Transactions of the ASME®

Journal of Heat Transfer

Published Quarterly by The American Society of Mechanical Engineers

VOLUME 121 • NUMBER 3 • AUGUST 1999

Transactions of the ASME, Journal of Heat Transfer (ISSN 0022-1481) is published quarterly (Feb., May, Aug., Nov.) for $250.00 per year by The American Society of Mechanical Engineers, Three Park Avenue, New York, NY 10016. Periodicals postage paid at New York, NY and additional mailing offices. POSTMASTER: Send address changes to Transactions of the ASME, Journal of Heat Transfer, c/o THE AMERICAN SOCIETY OF MECHANICAL ENGINEERS, 22 Law Drive, Box 2300, Fairfield, NJ 07007-2300. ***CHANGES OF ADDRESS*** *must be received at Society* headquarters seven weeks before they are to be effective. Please send old label and new address. **PRICES:** To members, $40.00, annually: to nonmembers, $250.00. Add $40.00 for postage to countries outside the United States and Canada.

1999 JHT HEAT TRANSFER GALLERY—SPECIAL INSERT

TECHNICAL PAPERS

(Contents continued on Outside Back Cover)

This journal is printed on acid-free paper, which exceeds the ANSI Z39.48-1992 specification for permanence of paper and library materials. ♾™
♻ 85% recycled content, including 10% post-consumer fibers.

(Contents continued)

TECHNICAL NOTES

(Contents continued on Inside Back Cover)

(Contents continued)

ERRATA

ANNOUNCEMENTS AND SPECIAL NOTICES

1998 Max Jakob Memorial Award Lecture

Heat and Mass Transfer Problems for Film Cooling

A. I. Leontiev
National Committee for Heat and Mass Transfer of the Russian Academy of Sciences,
17A Krasnokazarmennaya,
IVT RAN,
Moscow 111250, Russia
e-mail: nchmt@iht.mpei.ac.ru
Mem. ASME

In the paper, a review of calculation methods and of experimental results for heat transfer under film cooling is presented. The effects of arrangement of film cooling, longitudinal pressure gradient, nonisothermality and compressibility of the gas, injection of a foreign gas, surface roughness, swirling of flow, and turbulent pulsations of the main gas flow on the effectiveness of film cooling are considered. A generalized correlation for the effectiveness of film cooling, is proposed, which makes it possible to take into account the influence of the above factors. It is shown, that in determination of the heat transfer coefficient in the region of film cooling, it is necessary to take into account the influence of injected gas on the development of the thermal boundary layer. A method of calculation for combined cooling (film, porous or transpiration and convective), which accounts for effect of longitudinal heat conductivity of the wall on the film cooling effectiveness is proposed. An estimation of profile losses on a gas turbine blade is given for the cases of film and porous or transpiration cooling.

Introduction

Advances in many branches of engineering are connected with the use of higher and higher working temperatures, perfection of cooling systems for power installations and further development of the theory of heat transfer (Kays and Crawford, 1987). One of the most promising methods of thermal protection of heating surfaces is the use of gas film cooling. Despite intensive development of numerical methods for calculation of film cooling problems (for instance, Garg (1989)), simple and reliable correlations, which are based on clear physical models, that make it possible to generalize experimental data for complex boundary conditions, are necessary for complex engineering calculations.

Hartnett (1985) unites all kinds of cooling connected with injection of a cooling fluid to a heat transfer surface (film cooling, transpiration cooling, ablation) under the single label of mass transfer cooling. In Fig. 1, taken from the paper of Hartnett, we can see that all kinds of cooling differ only with by the method of submission of a cooling fluid onto a heat transfer surface. In most practical cases, mass transfer cooling is used when traditional convective cooling is insufficient to maintain the temperature of the wall at a given level. The greatest application of mass transfer cooling has been to aircraft and space engineering, where it is used to protect a surface of a turbine blade or flying vehicle from the impact of the influence high enthalpy gas flow. In Fig. 2 the comparison of various methods of cooling gas turbine blades (Leontiev, 1993a, b) is presented.

It is well known that an increase in the gas temperature at the turbine inlet is the basic method to advance technical and economical parameters of the gas turbine units and engines. Modern gas turbine engines are designed to operate at inlet temperatures of 1800–2000 K, which are far above the allowable temperatures of the metal. Under these conditions, the turbine blades must be cooled in order to ensure a reasonable lifetime. This calls for an efficient cooling system (see Fig. 3). In Fig. 3 a typical scheme for gas turbine blade cooling of an aviation engine is shown.

A considerable effort has been devoted to understanding the coolant film behavior and its interaction with the mainstream flow. The film cooling performance is influenced by the wall curvature, three-dimensional external flow structure, freestream turbulence, compressibility, flow unsteadiness, the hole size, shape and location, and the angle of injection. Many studies on film cooling have been confined to a simple geometry, for example, two-dimensional flat or curved plates in steady, incompressible flow. An excellent survey of the work up to 1971 has been provided by Goldstein (1971). To the present time many survey papers on film and porous or transpiration cooling (Garg, 1999; Hartnett, 1985; Ito et al., 1978; Ko et al., 1985; Kopelev, 1984; Leontiev et al., 1995; Metzger et al., 1993; Polezhaev, 1997; Volchkov, 1983; Volchkov et al., 1965) are known. Several further studies in this field have been summarized by Garg and Gaugler (1997).

There are excellent computational codes, which allow calculation of film cooling of rotating turbine blades. In the paper of Garg (1999), the results of predictions using three models of turbulence and three-dimensional Navier-Stokes equations are presented.

It is necessary to note, that numerical calculations, especially for turbulent flows, require experimental checking.

The purpose of this paper is to demonstrate opportunities for developing correlations on the basis of simple physical models. Methods for developing correlation equations for the analysis and generalization of experimental data are shown. Certainly, the accuracy of these equations depends on the accuracy of the necessary approximations used in the physical models as well as the accuracy of empirical constants based on experimental data, and therefore on the accuracy of the experimental data itself.

A problem is also posed to demonstrate opportunities for the use of simple physical models in developing correlations that do not contain empirical constants. Even such simple formulas allow qualitative (and in some cases quantitative) generalization of experimental heat transfer data in complex conditions. Moreover, the formulas presented in many cases can be used as a basis for developing more exact correlations that use additional empirical constants. Examples are given in the paper.

In this review we shall consider only these problems of film and porous cooling which, from our point of view require further investigation.

The first idea of calculation of heat transfer in a presence of gas film cooling using the equilibrium temperature of the wall was stated by Prof. E. Eckert (Eckert and Cho, 1994; Eckert and Drake, 1972) who received the first Max Jacob award in 1961 (Jakob, 1957). For conditions of gas film cooling it was suggested to define the heat flux using the following correlation:

Contributed by the Heat Transfer Division for publication in the JOURNAL OF HEAT TRANSFER. Manuscript received by the Heat Transfer Division, Feb. 16, 1999; revision received, Apr. 20, 1999. Associate Technical Editor: J. Howell.

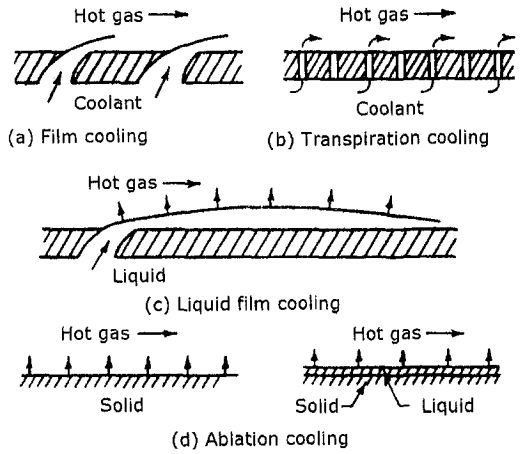

Fig. 1 Various mass transfer cooling schemes

$$q_w = \alpha(T_w^* - T_w), \tag{1}$$

where T_w^* is the temperature of an insulated wall in the presence of gas film cooling; α is the heat transfer coefficient in the absence of gas film cooling.

Thus the problem was reduced to a determination of the insulated wall temperature.

Effectiveness of Film Cooling

Many researches have been made and many empirical correlations have been offered for the determination of the temperature of the insulated wall.

The effectiveness of the cooling system is determined by the parameter Θ, where

$$\Theta = (T_0 - T_w^*)/(T_0 - T'), \tag{2}$$

and T_0 is the gas temperature, T' is the temperature of an injected gas, and T_w^* is the temperature of the insulated wall or adiabatic temperature of the wall.

In the paper by Hartnett (1985) a comprehensive review of these correlations is presented and a comparison of the calculated results for gas film cooling effectiveness when using three different formulas is given. These formulas are as follows.

Librizzi and Cresci (1964):

$$\Theta = \frac{1}{1 + \left(\frac{C_{p0}}{C_p'}\right) \cdot [0.329 \cdot (4.01 + \zeta)^{0.8} - 1]}; \tag{3}$$

Nomenclature

a = velocity of sound
b = $(j_w/\rho_0 W_0)(2/c_{f0})$, b_T = $(j_w/\rho_0 W_0)(2/\mathrm{St}_0)$, b_T = $(j_w/\rho_0 W_0)(1/\mathrm{St}_M)$ = blowing parameters
b_{cr} = critical blowing parameter
Bi = $\alpha\Delta_m/\lambda$ = Biot number
c_f = $2\tau_w/(\rho_0 W_0^2)$ = skin friction coefficient
c_{f0} = skin friction coefficient at the "standard condition" (in the absence of various influences)
c_w = mass concentration of blown component
C_p = specific heat at constant pressure, J/kg K
G_c = the discharge of cooling gas, kg/s
G_g = the summarized discharge of gas trough turbine, kg/s
$\bar{g}_c$ = G_c/G_g = specific discharge of cooling gas
i = specific enthalpy, J/kg
i^* = stagnation specific enthalpy, J/kg
i_w^* = adiabatic wall enthalpy, J/kg
j_s = $\rho_s W_s$ = mass flow rate of injected gas per unit area of the slot per unit time, kg/(m^2 s)
$\bar{j}_s$ = $\rho_s W_s/(\rho_0 W_0)$ = dimensionless mass flow rate of injected gas through the slot
j_w = $\rho_w W_w$ = mass flow rate of injected gas per unit area of the porous section per unit time, kg/(m^2 s)
$\bar{j}_w$ = $\rho_w W_w/(\rho_0 W_0)$ = dimensionless mass flow rate of injected gas through the porous section or the wall
K_s = height of roughness, mm
L = reference length, m
M = W_0/a = Mach number
Nu = $\alpha x/\lambda$ = Nusselt number
Pr = $\mu C_p/\lambda$ = Prandtl number
Pr_T = $\mu_T C_p/\lambda_T$ = turbulent Prandtl number
q_w = heat flux on the wall, W/m^2
r = recovery factor
Re** = $\rho_0 W_0 \delta^{**}/\mu_0$ = Reynolds number based on the momentum thickness
Re_i^{**} = $\rho_0 W_0 \delta_i^{**}/\mu_0$ = Reynolds number based on the enthalpy thickness
S = width of the slot, m
St = $q_w/\rho_0 W_0(i_w - i_w^*)$ = Stanton Number
St_0 = Stanton Number at the "standard condition" (in the absence of various influences)
T = temperature, K
T_g' = local temperature in the boundary layer on the insulated surface
T_w = wall temperature, K
T_w^* = adiabatic temperature of the wall, K
T' = temperature of an injected gas for porous section, K
Tu = $\sqrt{w'^2}/W_0$ = freestream turbulence
W = velocity, m/s
W_x = longitudinal component of velocity, m/s
x = longitudinal coordinate, m
α = local heat transfer coefficient, W/(m^2 K)
δ = thickness of velocity boundary layer, m
δ_T = thickness of thermal boundary layer, m
δ^* = displacement thickness
δ^{**} = momentum thickness
δ_i^{**} = enthalpy-deficit thickness, m
δ_T^{**} = temperature-deficit thickness, m
Δ_m = thickness of the wall, m
Θ = effectiveness of film cooling
λ = thermal conductivity, W/(m K)
λ_T = turbulent thermal conductivity, W/(m K)
Π = material porosity
ρ = density, kg/m^3
τ_w = shear stress on the wall, N/m^2
ψ = i_w/i_0 or T_w/T_0, ψ^* = i_w^*/i_0 or T_w^*/T_0, ψ_0^* = i_{w0}^*/i_0 or T_{w0}^*/T_0 = enthalpy or temperature factor
Ψ = $(c_f/c_{f0})_{\mathrm{Re}^{**}}$ = relative skin friction law
Ψ_s = $(\mathrm{St}/\mathrm{St}_0)_{\mathrm{Re}_i^{**}}$ = relative heat transfer law

Subscripts

cr = critical parameters
f = friction and film cooling parameters
M = parameters for the case of compressible main gas flow
pfc = porous-film-convective cooling parameters
s = injected gas parameters for the exit from a slot
x = parameters for the section x
w = parameters on the wall
0 = parameters on the outer margin of the boundary layer (main gas flow) or for "standard conditions"
$'$ = parameters of injected gas for transpiration cooling
1 = parameters for $x = x_1$

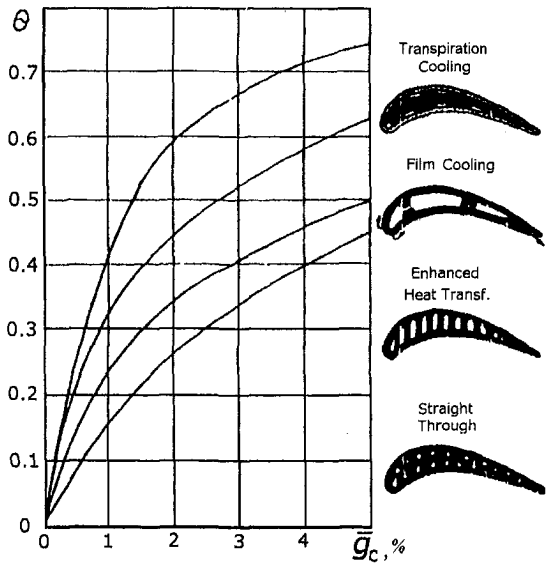

Fig. 2 Comparison of different systems for cooling of vanes. $\bar{g}_c = G_c/G_g$, G_c—the discharge of the cooling gas, G_g—the total discharge of the gas through the turbine.

Kutateladze and Leontiev (1963) and Leontiev (1966):

$$\Theta = \frac{1}{1 + 0.329\left(\frac{C_{p0}}{C'_p}\right)\cdot \zeta^{0.8}}; \tag{4}$$

Goldstein and Haji-Sheikh (1971):

$$\Theta = \frac{1.9\ \mathrm{Pr}^{2/3}}{1 + 0.329\left(\frac{C_{p0}}{C'_p}\right)\cdot \zeta^{0.8}}; \tag{5}$$

where Θ is an effectiveness of the film cooling,

$$\Theta = \frac{T_0 - T^*_w}{T_0 - T'}, \quad \zeta = \frac{x}{\bar{j}_s S}\left(\frac{\mu'}{\mu_0}\mathrm{Re}_s\right)^{-1/4},$$

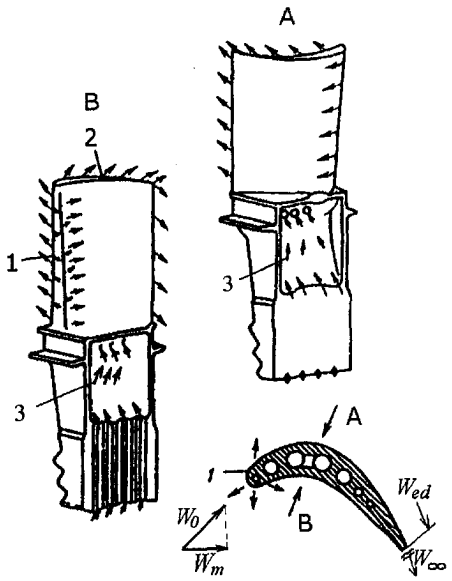

Fig. 3 Typical aircraft cooled blade. 1–gas injection on the leading edge of the blade, 2–gas injection on the end of the blade, 3–cooling gas flow inside of the blade body.

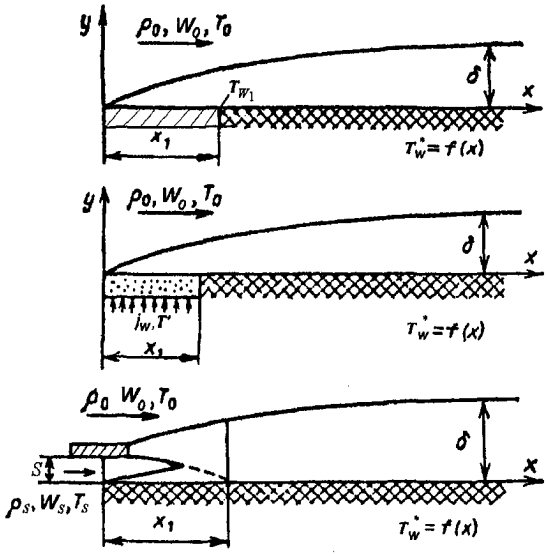

Fig. 4 Schemes for film cooling

$$\mathrm{Re}_s = \frac{\rho_s W_s S}{\mu'}, \quad \bar{j}_s = \frac{\rho_s W_s}{\rho_0 W_0}.$$

As compared to the other correlations, Eq. (4) has the following advantage. The idea used in developing this formula allows one to obtain the equation for Θ in the most general form. It takes into account the influence of a longitudinal pressure gradient, nonisothermality and compressibility of the flow, the roughness of the surface, and the method of organization of the gas film cooling on its effectiveness. Equation (4) is based on a very simple idea, which we can see from Fig. 4. For a flat boundary layer an integral equation of energy can be written as follows (Kutateladze and Leontiev, 1990):

$$\frac{d\ \mathrm{Re}^{**}_T}{d\bar{x}} + \frac{\mathrm{Re}^{**}_T}{\Delta T}\frac{d(\Delta T)}{d\bar{x}} = \mathrm{Re}_L\ \mathrm{St}_0(\psi_S + b_T), \tag{6}$$

where $\mathrm{Re}^{**}_T = \delta^{**}_T \rho_0 W_0/\mu_0$, $\Delta T = T_0 - T_w$,

$$\delta^{**}_T = \int_0^\infty \frac{\rho W}{\rho_0 W_0}\left(1 - \frac{T - T_w}{T_0 - T_w}\right)dy$$

is the enthalpy-deficit thickness,

$$\mathrm{Re}_L = \frac{\rho_0 W_0 L}{\mu_0}, \quad \bar{x} = \frac{x}{L}, \quad \psi_S = \left(\frac{\mathrm{St}}{\mathrm{St}_0}\right)_{\mathrm{Re}^{**}_T}, \quad b_T = \frac{j_w}{\rho_0 W_0}\cdot\frac{1}{\mathrm{St}_0}$$

is the blowing parameter,

$$\mathrm{St}_0 = \frac{q_w}{C_p\cdot\rho_0 W_0 \Delta T} \quad \text{is the Stanton Number.} \tag{7}$$

For the region $x > x_1$, the heat flux $q_w = 0$ and the energy equation becomes:

$$\frac{d(\mathrm{Re}^{**}_T \Delta T)}{dx} = 0 \tag{8}$$

and

$$\mathrm{Re}^{**}_T \Delta T = \mathrm{Re}^{**}_{T_1}\Delta T_1, \tag{9}$$

where $\mathrm{Re}^{**}_{T_1}$ and ΔT_1 is the Reynolds number and temperature difference at section $x = x_1$.

Hence

$$\Theta = \frac{\Delta T}{\Delta T_1} = \frac{\mathrm{Re}_{T_1}^{**}}{\mathrm{Re}_T^{**}}. \tag{10}$$

If at $x > x_1$ the condition $T_w = T_{w1} = \text{const}$ is imposed and

$$\mathrm{St}_0 = \frac{B}{2\,\mathrm{Re}_T^{**}\,\mathrm{Pr}^n} \tag{11}$$

then from Eq. (6) we can find

$$\mathrm{Re}_{T_0}^{**} = \left[(\mathrm{Re}_{T_1}^{**})^{m+1} + \frac{m+1}{2} B \cdot \frac{\mathrm{Re}_{L_1}}{\mathrm{Pr}^n} \int_{\bar{x}_1}^{\bar{x}} \tilde{W}_0 d\bar{x} \right]^{1/(m+1)}, \tag{12}$$

where $\tilde{W}_0 = W_0/W_{01}$.

For the boundary layer on an insulated surface with $x > x_1$, the following conditions must be met:

$$\left.\begin{array}{lll} \text{for} & y = 0, & q_w = 0, \quad \partial T/\partial y = 0 \\ \text{for} & y = \delta_T, & q = 0, \quad \partial T/\partial y = 0 \end{array}\right\}. \tag{13}$$

Thus, inside of the boundary layer the tendency toward temperature equilibrium takes place only due to molecular or turbulent mixing and suction from the outside flow. The most intensive mixing is reached near the wall where the derivative $\partial W_x/\partial y$ is a maximum. As a result, the temperature profile becomes deformed in such a way that the region where $\partial T/\partial y \cong 0$ (or where $T = T_w = \text{const}$) increases continuously along x. Simultaneously, through gas inflow from the main stream the temperature in the boundary layer approaches T_0, i.e., with $x \to \infty$, $T \to T_w \to T_0$.

The enthalpy-deficit thickness, by definition is

$$\delta_{T_0}^{**} = \int_0^{\infty} \frac{W_x}{W_0} \left(1 - \frac{T - T_w}{T_0 - T_w} \right) dy.$$

Consequently, on an insulated surface for $x \to \infty$

$$\delta_T^{**} \to \int_0^{\infty} \frac{W_x}{W_0} dy. \tag{14}$$

Introduce the coefficient $\beta = \delta_T^{**}/\delta_{T0}^{**}$, satisfying the following boundary conditions: for $x \to x_1$, $\beta \to 1$ and for $x \to \infty$, $\beta \to \beta_{\max}$, where

$$\beta_{\max} = \int_0^{\infty} \frac{\rho W_x}{\rho_0 W_0} dy \Bigg/ \int_0^{\infty} \frac{\rho W_x}{\rho_0 W_0} \left(1 - \frac{T - T_w}{T_0 - T_w} \right) dy. \tag{15}$$

For a laminar boundary layer

$$\omega = \frac{W_x}{W_0} = 2(\xi - \xi^3) + \xi^4; \quad \beta_{\max} = 6.0, \quad \text{where} \quad \xi = y/\delta.$$

In most practical cases film cooling is used when the Reynolds numbers are large and the boundary layer is turbulent. Then, taking $\omega = \omega_0 = \xi^{1/7}$, we obtain $\beta_{\max} = 9.0$.

Taking into consideration Eqs. (12) and (13) for $x \to \infty$, $\beta \to \beta_{\max}$, we obtain the relation for film cooling effectiveness

$$\Theta = \left[1 + \frac{m+1}{2} \frac{B}{\mathrm{Pr}^n} \left(\frac{\beta_{\max}}{\mathrm{Re}_{T_1}^{**}} \right)^{m+1} \int_{\bar{x}_1}^{\bar{x}} \mathrm{Re}_L d\bar{x} \right]^{-(1/(m+1))}. \tag{16}$$

For the laminar boundary layer ($m = 1$ and $B/2 = 0.22$) and $\mathrm{Pr} = 0.725$,

$$\Theta = \left[1 + \frac{10.6}{(\mathrm{Re}_{T_1}^{**})^2} \int_{\bar{x}_1}^{\bar{x}} \mathrm{Re}_L d\bar{x} \right]^{-0.5}. \tag{17}$$

For the turbulent boundary ($m = 0.25$ and $B/2 = 0.0128$),

$$\Theta = \left[1 + \frac{0.254}{(\mathrm{Re}_{T_1}^{**})^{1.25}} \int_{\bar{x}_1}^{\bar{x}} \mathrm{Re}_L d\bar{x} \right]^{-0.8}. \tag{18}$$

In particular, for the flow along a flat plate ($\mathrm{Re}_L = \text{const}$) for the laminar boundary layer

$$\Theta = \left[1 + \frac{10.6}{(\mathrm{Re}_{T_1}^{**})^2} \mathrm{Re}_{\Delta x} \right]^{-0.5}, \tag{19}$$

and for the turbulent boundary layer

$$\Theta = \left[1 + \frac{0.254}{(\mathrm{Re}_{T_1}^{**})^{1.25}} \mathrm{Re}_{\Delta x} \right]^{-0.9}, \tag{20}$$

where

$$\mathrm{Re}_{\Delta x} = \frac{\rho_0 W_0 (x - x_1)}{\mu_0}.$$

If we introduce $\mathrm{Re}_{\Delta x}^* = \int_{\bar{x}_1}^{\bar{x}} \mathrm{Re}_L d\bar{x}$, then Eqs. (19) and (20) can be extended to the case of an arbitrary law of velocity change along the body surface.

In particular, for the case of a power law $\tilde{W}_0 = \bar{x}^n$ for the change of velocity we obtain

$$\mathrm{Re}_{\Delta x}^* = \mathrm{Re}_{L_1} (\bar{x}^{n+1} - 1)/(n+1), \tag{21}$$

where

$$\bar{x} = x/x_1; \quad \tilde{W}_0 = W_0/W_{01}, \quad \mathrm{Re}_{L_1} = \frac{\rho_0 W_0 x_1}{\mu_0}.$$

Then the film cooling effectiveness for the laminar boundary layer is

$$\Theta = \left[1 + \frac{10.6}{(\mathrm{Re}_{T_1}^{**})^2} \mathrm{Re}_{L_1} \frac{\bar{x}^{n+1} - 1}{n+1} \right]^{-0.5}. \tag{22}$$

The result for the turbulent boundary layer is

$$\Theta = \left[1 + \frac{0.254}{(\mathrm{Re}_{T_1}^{**})^{1.25}} \mathrm{Re}_{L_1} \frac{\bar{x}^{n+1} - 1}{n+1} \right]^{-0.8}. \tag{23}$$

As follows from Eqs. (22) and (23), the cooling effectiveness decreases with accelerating flow ($(dW_0/dx) > 0$, $n > 0$) and increases with decelerating flow ($(dW_0/dx) < 0$, $n < 0$).

Equation (16) extended to compressible gas flow becomes

$$\Theta = \left[1 + \frac{B}{2} (1+m) \beta_{\max}^{m+1} \int_{\bar{x}_1}^{\bar{x}} \frac{\psi_S \mathrm{Re}_L \left(\frac{\mu_w}{\mu_0^*} \right)^m d\bar{x}}{(\mathrm{Re}_{T_1}^{**})^{m+1}} \right]^{-(1/(m+1))}, \tag{24}$$

where

$$\psi_S = \left[\frac{2 \operatorname{arctg} M_0 \sqrt{0.5 r (k-1)}}{(\sqrt{\bar{\psi}} + 1) M_0 \sqrt{0.5 r (k-1)}} \right]^2, \quad \bar{\psi} = T_w/T_w^*,$$

$$\beta_{\max} = \left(\int_0^1 \frac{\rho}{\rho_0} \omega d\xi \right) \left(\int_0^1 \frac{\rho}{\rho_0} (1 - \omega) d\xi \right)^{-1}.$$

To assess the influence of compressibility on $\beta_{\max}$ consider $\omega = \xi^{1/7}$ and $\rho/\rho_0 = \psi^* - (\psi^* - 1)\omega^2$. The results of the calculation for $\beta_{\max}$ for this case are given in Table 1.

Thus, the influence of gas compressibility on film cooling effectiveness with the accepted approximations is reflected by the coefficient $\beta_{\max}$ and ψ_S.

Table 1 Values of β_{max} depending upon M_0

M_0	0	1	2	3	4	5
β_{max}	9.0	9.2	9.8	10.4	11.5	12.0

Film Cooling Created by Gas Blowing Through a Porous or Transpiration Section

Here we obtain equations for film cooling effectiveness created by gas blowing through a permeable section x_1 in length (Fig. 5). Equation (5) can be written in the form

$$\frac{d(\mathrm{Re}_i^{**}\Delta i)}{d\bar{x}} = \mathrm{Re}_w(i_w^* - i').$$

Hence, for the case i_w = const., we have

$$\mathrm{Re}_{i1}^{**} = \mathrm{Re}_{w1}(1 + K_i), \tag{25}$$

where

$$\mathrm{Re}_{w1} = \frac{1}{\mu_0^*}\int_0^{x_1} j_w dx, \quad K_1 = \frac{i_{w1} - i'}{i_w^* - i_{w1}}.$$

For the case $M \ll 1$ and C_p = const., $K_1 = (T_{w1} - T')/(T_0 - T_{w1})$.

The equations for the film cooling effectiveness with a gas blowing through a porous wall, considering Eqs. (16) and (25), have the following form:

for a laminar boundary layer,

$$\Theta = \left[1 + \frac{10.6}{[\mathrm{Re}_{w1}(1 + K_1)]^2}\int_0^{\bar{x}} \mathrm{Re}_{x_1} d\bar{x}\right]^{-0.5}; \tag{26}$$

for a turbulent boundary layer,

$$\Theta = \left[1 + \frac{0.254}{[\mathrm{Re}_{w1}(1 + K_1)]^{1.25}}\int_0^{\bar{x}} \mathrm{Re}_{x_1} d\bar{x}\right]^{-0.8}. \tag{27}$$

In Figs. 6 and 7 the results obtained from Eq. (27) are compared with experimental data from several investigators.

For compressible gas flow, taking into account Eq. (24), we obtain

$$\Theta = \left\{1 + \frac{\beta_{max}^{1+m}}{(1 + K_1)^{m+1}\Theta^{1+m}} \frac{B(1 + m)\,\mathrm{Re}_{00}}{2\,\mathrm{Pr}^{0.75}\,\mathrm{Re}_w^{m+1}} \times \int_{\bar{x}_1}^{\bar{x}} \psi_S\left(\frac{\mu_w}{\mu_0^*}\right)^m U(1 - U^2)^{1/(k-1)}\Theta^{1+m} d\bar{x}\right\}^{-(1/(m+1))}, \tag{28}$$

where

$$\mathrm{Re}_{00} = \frac{W_{max}\rho_0^* L}{\mu_0^*}, \quad U = \frac{W_0}{W_{max}}, \quad W_{max} = \sqrt{2i_0^*}.$$

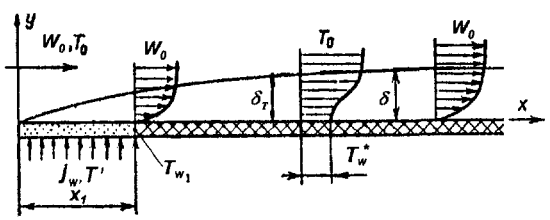

Fig. 5 Scheme for film cooling with a porous section

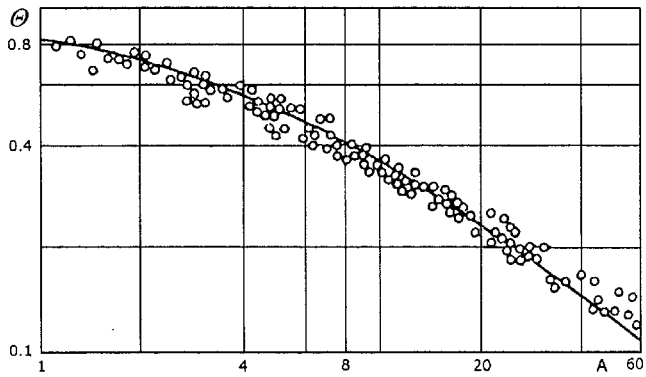

Fig. 6 Film cooling effectiveness with a porous section for pressure-gradient flow: curve–calculation from Eq. (27), points–experimental data [Komarov and Leontiev (1970)]. $A = (\mathrm{Re}_{\Delta x}/\mathrm{Re}_{w1}^{1.25}(1 + K_1)^{1.25})(\ln \bar{W}_0/tg\alpha)$, $\bar{W}_0 = W_0/W_{01}$, α–an angle of wall inclination to horizontal.

For gas flow in a supersonic nozzle

$$\Theta = \left\{1 + \frac{\beta_{max}^{1+m}}{\Theta^{1+m}(1 + K_1)^{1+m}} \frac{B(1 + m)}{2\,\mathrm{Pr}^{0.75}} \frac{\mathrm{Re}_{00}}{(\mathrm{Re}_{w1}\bar{D})^{1+m}} \times \int_{\bar{x}_1}^{\bar{x}} \psi_S\left(\frac{\mu_w}{\mu_0^*}\right)^m \bar{D}^{m-1}\Theta^{m+1} d\bar{x}\right\}^{-(1/(m+1))}. \tag{29}$$

Equations (28) and (29) are solved with respect to Θ by the method of successive approximations. For preliminary estimation the following equation may be used:

$$\Theta = \left\{1 + \frac{0.25\,\mathrm{Re}_{00}\psi_{t_1}\left(\frac{\mu_{w1}}{\mu_0^*}\right)^{0.25}\int_{\bar{x}_1}^{\bar{x}} \psi_M U(1 - U^2)^{1/(k-1)} d\bar{x}}{(1 + K_1)^{1.25}\,\mathrm{Re}_{w1}^{1.25}}\right\}^{-0.8}. \tag{30}$$

For a supersonic nozzle the following equation can be used:

$$\Theta \approx \left\{1 + \frac{0.25\,\mathrm{Re}_{00}(\psi_{t1})\left(\frac{\mu_{w1}}{\mu_0^*}\right)^{0.25}}{(1 + K_1)^{0.25}(\mathrm{Re}_{w1}\bar{D})^{1.25}}\int_{\bar{x}_1}^{\bar{x}} \psi_M \bar{D}^{-0.75} d\bar{x}\right\}^{-0.8}. \tag{31}$$

For a flow along a flat plate we have

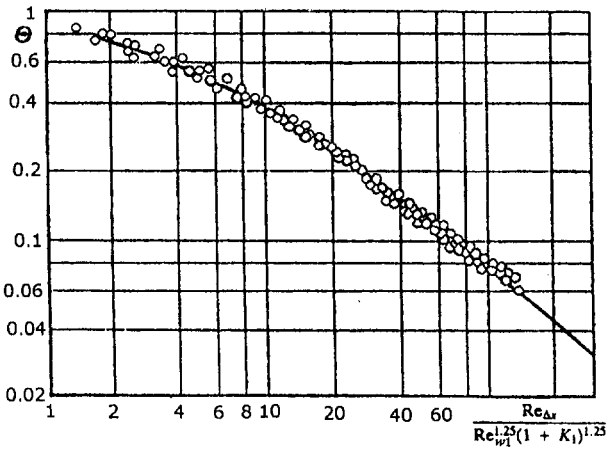

Fig. 7 Film cooling effectiveness with a porous section: curve–calculation from Eq. (27); points–experimental data [Goldstein et al. (1965)]

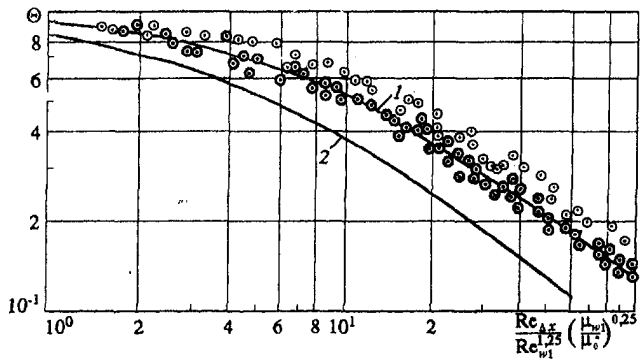

Fig. 8 Film cooling effectiveness downstream of a porous section for supersonic gas flow. 1, 2–results of calculation from Eq. (32) at $M_0 = 2.9$ and $M_0 \to 0$. Experimental points [Goldstein et al. (1968)] at $M_0 = 2.9$.

$$\Theta = \left\{1 + \psi_{t1}\psi_M \frac{0.25\ \mathrm{Re}_{\Delta x}}{[(1 + K_1)\ \mathrm{Re}_{w1}]^{1.25}} \left(\frac{\mu_{w1}}{\mu_0^*}\right)^{0.25}\right\}^{-0.8}, \quad (32)$$

where

$$\mathrm{Re}_{\Delta x} = \rho_0 W_0 (x - x_1)/\mu_0^*; \quad \psi_{t1} = \left(\frac{2}{\sqrt{\bar{\psi}_1} + 1}\right)^2;$$

$$\bar{\psi}_1 = \frac{T_{w1}}{T_w^*}, \quad \psi_M = \left[\frac{\mathrm{arctg}\ M_0\sqrt{0.5r(k-1)}}{M_0\sqrt{0.5r(k-1)}}\right]^2.$$

In Fig. 8 a comparison of Eq. (32) with the experiments of Goldstein et al. (1968) is presented. The experiments were carried out with $T_{w1}/T_w^* \sim 1.0$. Then it is convenient to write Eq. (32) as follows:

$$\Theta = \left\{1 + 0.25 \frac{\psi_M\ \mathrm{Re}_{\Delta x}}{[(1 + K_1)\ \mathrm{Re}_{w1}]^{1.25}} \left(\frac{\mu_{w1}}{\mu_0^*}\right)^{0.25}\right\}^{-0.8} \quad (33)$$

where $\mathrm{Re}_{w1} = j_w x_1/\mu_{w1}$.

As seen in Fig. 8, the experiments are in satisfactory agreement with Eq. (32). It is interesting to note that the film cooling effectiveness increases considerably with an increase in Mach number.

Such parameters as the turbulence of the main flow, the arrangement of the gas film cooling, the angle of injection of the cooling gas and the curvature of the cooled surface affect considerably the effectiveness of gas film cooling (Goldstein et al., 1965; Golovanov et al., 1996; Ito et al., 1978; Lebedev et al., 1999; Leontiev and Epifanov, 1992; Leontiev and Polyakov, 1998; Leontiev et al., 1997; Metzger et al., 1993; Motulevich et al., 1981).

Convective Heat Transfer in a Presence of Gas Film Cooling

It is suggested to define the heat transfer coefficient in Eq. (1), using a corresponding correlation for the case of the absence of gas film cooling (Hartnett, 1985; Hartnett et al., 1961). One can show, that in several cases this assumption can result to an essential error in the heat flux value. The enthalpy-deficit thickness δ_T^{**} on the insulated wall can differ considerably from that for the case of an absence of the film cooling because of essential difference in Re_{T01}^{**}.

From Eq. (12) it follows that $\mathrm{Re}_{T01}^{**} = [(m + 1)/2 \cdot B \cdot \mathrm{Re}_{x1}]^{1/(m+1)}$. On the other hand, from Eq. (25) after some transformation for the case $b_T = \mathrm{const.}$, it follows that $(\mathrm{Re}_{T0}^{**})_x = [(m + 1)/2 \cdot B \cdot (\psi_S + b_T)\ \mathrm{Re}_{x1}]^{1/(m+1)}$.

Hence

$$\frac{\mathrm{Re}_{T0}^{**}}{\mathrm{Re}_{T01}^{**}} = (\psi_S + b_T)^{1/(m+1)}. \quad (34)$$

From here

$$\frac{\alpha_{01}^*}{\alpha_{01}} = \frac{1}{(\psi_S + b_T)^{m/(m+1)}}. \quad (35)$$

Here α_{01}^* is the heat transfer coefficient in the section x_1, which is using the enthalpy-deficit thickness δ_T^{**} with the account of injection (Re_{T0}^{**}) and α_{01} is the heat transfer coefficient in the section x_1, which is determined using the corresponding correlation for a flow along an impermeable plate.

From Eq. (35), it follows that for the case of a turbulent boundary layer, when

$$\psi_S = (1 - b_T/4)^2 \text{ and } m = 0.25,$$

$$\frac{\alpha_{01}^*}{\alpha_{01}} = \frac{1}{\left(1 + \frac{b_T}{4}\right)^{2m/(m+1)}} = \frac{1}{\left(1 + \frac{b_T}{4}\right)^{0.4}}. \quad (36)$$

For critical blowing, when $b_T = 4$, the ratio $\alpha_{01}^*/\alpha_{01} = 0.76$. This is corroborated by measurements, presented in Goldstein (1971).

For the laminar boundary layer ($m = 1$) and $\psi_S = (1 - b_T/2)$, this effect can be more significant:

$$\frac{\alpha_0^*}{\alpha_{01}} = \frac{1}{\left(1 + \frac{b_T}{2}\right)^{0.5}}. \quad (37)$$

With critical blowing $b_T \approx 2$, we have $\alpha_{01}^*/\alpha_{01} \approx 0.7$.

Thus when calculating heat flux using Eq. (1) it is possible to obtain more exact results, if the heat transfer coefficient is defined from the law of heat transfer:

$$\mathrm{St}_0 = \frac{B}{2(\mathrm{Re}_T^{**})^m\ \mathrm{Pr}^n}, \quad (38)$$

$$\text{and } \mathrm{Re}_T^{**} = \left[(\mathrm{Re}_{T1}^{**})^{m+1} + \beta \frac{m+1}{2} B \cdot \frac{\mathrm{Re}_{L1}}{\mathrm{Pr}^n} \int_{\bar{x}_1}^{\bar{x}} \tilde{W}_0 d\bar{x}\right]^{1/(m+1)}.$$

However, in this case the validity of applying the law of heat transfer of the form (38) to the area of gas film cooling is not obvious.

In Kutateladze and Leontiev (1990), a more consecutive method of determination of the heat transfer coefficient in Eq. (1) is offered.

The integral energy equation for the region $x > x_1$ may be written in the form

$$\frac{d}{dx}[(T_w - T_w^*)\delta_T^{**} + (T_w^* - T_0)\delta_{T1}^{**}] = \frac{q_w}{C_p \rho_0 W_0}, \quad (39)$$

where

$$\left.\begin{aligned} \delta_T^{**} &= \int_0^\delta \frac{\rho W}{\rho_0 W_0}\left(\frac{T - T_g'}{T_w - T_w^*}\right) dy \\ \delta_{T1}^{**} &= \int_0^\delta \frac{\rho W}{\rho_0 W_0}\left(\frac{T_g' - T_0}{T_w^* - T_0}\right) dy \end{aligned}\right\}. \quad (40)$$

Here T_g' is the local temperature in the boundary layer on an insulated surface and T_w^* is the temperature of the insulated surface.

In accordance with Eq. (8)

$$\frac{d}{dx}[(T_w^* - T_0)\delta_{T1}^{**}] = 0. \quad (41)$$

Consequently

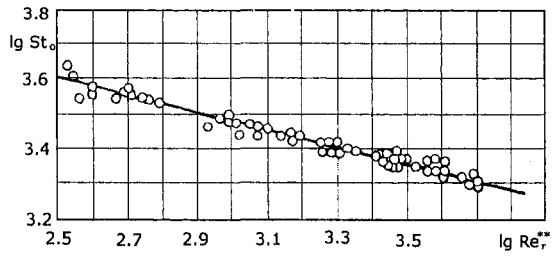

Fig. 9 Heat-transfer law in the presence of gas film cooling. Solid curve–Eq. (44); point–experimental data [Komarov and Leontiev (1970)]; St_0 is determined using Eq. (43), Re_T^{**} is determined using Eq. (6) taking into account δ_T^{**} by Eq. (40).

$$\frac{d\,\mathrm{Re}_T^{**}}{d\bar{x}} + \frac{\mathrm{Re}_T^{**}}{\Delta T^*}\frac{d(\Delta T^*)}{d\bar{x}} = \mathrm{Re}_L\,\mathrm{St}_0 \tag{42}$$

where

$$\mathrm{St}_0 = \frac{q_w}{C_p\rho_0 W_0 \Delta T^*}; \quad \Delta T^* = T_w - T_w^*. \tag{43}$$

Thus, the integral energy equation for a heat transfer surface in the presence of gas film cooling is of the usual form, if instead of ΔT we substitute $\Delta T^* = T_w - T_w^*$.

Suppose a heat transfer law in the form of Eq. (11) is true for the conditions under consideration, if we determine δ_T^{**} from Eq. (40), and St_0 from Eq. (43), i.e.,

$$\mathrm{St}_0 = \frac{B}{2}(\mathrm{Re}_T^{**})^{-m}\,\mathrm{Pr}^{-n}. \tag{44}$$

In Fig. 9 a comparison of Eq. (44) with the experiments of Komarov and Leontiev (1970) is presented.

In Fig. 10 is given the distribution of temperatures across the boundary layer on a plate with stepped heat supply obtained from the work of Volchkov (1983). The ratio of heat flux at the first and the second steps is varied between $0.3 \le q_{w1}/q_{w2} \le 7.0$. As seen from Fig. 10, the temperature profile in coordinates $(T - T_g')/(T_w - T_w^*) = f(y/\delta_T^{**})$ obeys an ordinary exponential relation.

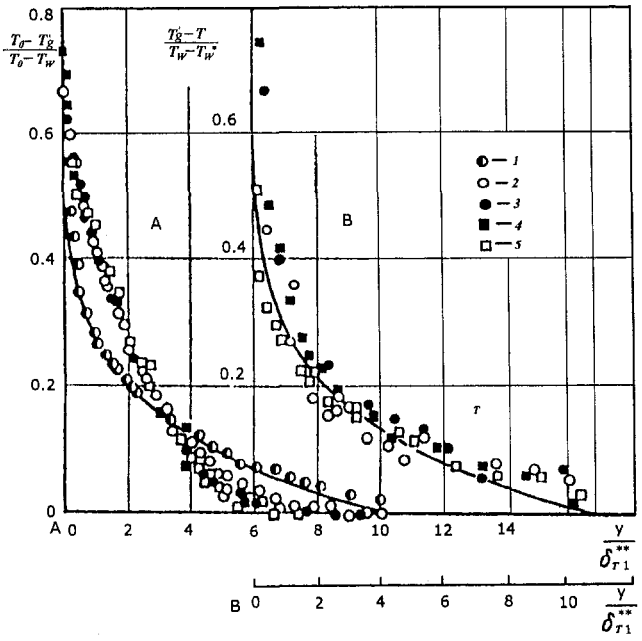

Fig. 10 Distribution of temperature across the section of a turbulent boundary layer with stepped heat flux distribution: solid curve–power law $(T_0 - T)/(T_0 - T_w) = 1 - 0.715(y/\delta_T^{**})$; *A*–in variables $(T_0 - T_g')/(T_0 - T_w) = f(y/\delta_{T1}^{**})$, *B*–in variables $(T_g' - T)/(T_w - T_w^*) = f(y/\delta_{T1}^{**})$. 1–4: experimental data [Volchkov (1983)] for q_w = const.–1 and for (q_{w1}/q_{w2}) = 6, 2–x/x_0 = 0.1, 3–0.23, 4–0.57, 5–0.77.

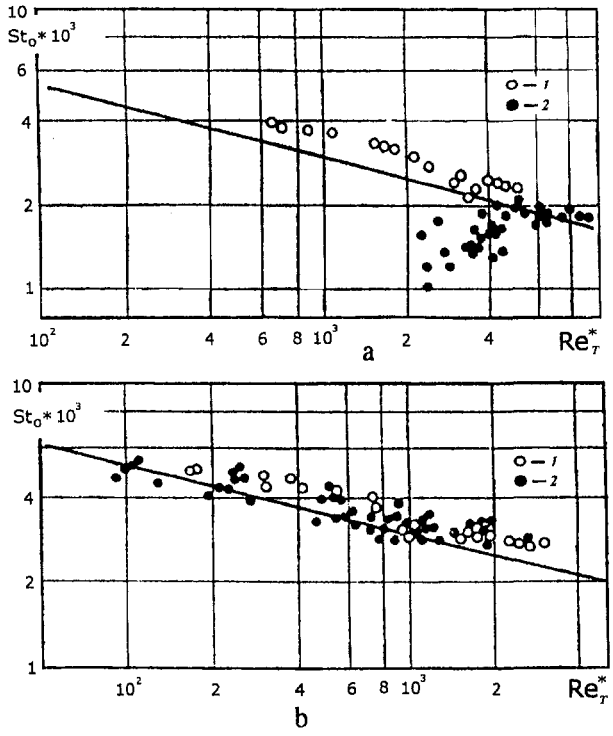

Fig. 11 Heat transfer law with stepped heat flux distribution. (*a*) calculation for $\Delta T = T_w - T_0$ and δ_T^{**} from Eq. (40); (*b*) calculation from $\Delta T = T_w - T_w^*$ and δ_T^{**} from Eq. (40), solid line–Eq. (44), 1, 2: experimental data [Volchkov (1983)], 1–$0.3 < q_{w1}/q_{w2} < 1.0$, 2–$3.1 < q_{w1}/q_{w2} < 6.7$.

In Fig. 11 comparison of the results of calculations from Eq. (44) with the experiments of Volchkov (1983) is presented. In Fig. 11 the experiments are generalized with the usual dimensionless groups, and with $q_{w1}/q_{w2} > 1$ the experimental points deviate considerably from the calculations using Eq. (44). When introducing the equilibrium temperature of the wall all the experimental points coincide with Eq. (44) (see Fig. 10, *B*).

As seen from Fig. 12, the introduction of the equilibrium temperature allows us also to generalize experiments on heat transfer on a rough surface. It should be noted that in the absence of gas film cooling of the same surface Volchkov (1983) obtained the following formula: $\mathrm{Nu}_x = 2.6 \cdot 10^{-3}\,\mathrm{Re}_x$, which is applicable for $x/A > 6$.

An integral of the energy Eq. (42), taking into consideration Eq. (44), has the form of

$$\mathrm{Re}_T^{**} = \frac{1}{\left(\Theta - \dfrac{T_0 - T_w}{T_0 - T_{w1}}\right)}\left[\frac{(m+1)B}{2\,\mathrm{Pr}^{0.75}} \times \mathrm{Re}_L\int_{\bar{x}_1}^{\bar{x}}\left(\Theta - \frac{T_0 - T_w}{T_0 - T_{w_1}}\right)^{m+1} d\bar{x} + (\mathrm{Re}_T^{**})_{\bar{x}=\bar{x}_1}^{m+1}\right]^{1/(m+1)}.$$

In the specific case, when $T_w = T_{w1}$, we obtain

$$\mathrm{Re}_T^{**} = \frac{1}{[\Theta - 1]}\left[\frac{(m+1)B}{2\,\mathrm{Pr}^{0.75}}\,\mathrm{Re}_L\int_{\bar{x}_1}^{\bar{x}} \tilde{W}_0(\Theta - 1)d\bar{x} + (\mathrm{Re}_T^{**})_{\bar{x}=\bar{x}_1}^{m+1}\right]^{1/(m+1)}. \tag{45}$$

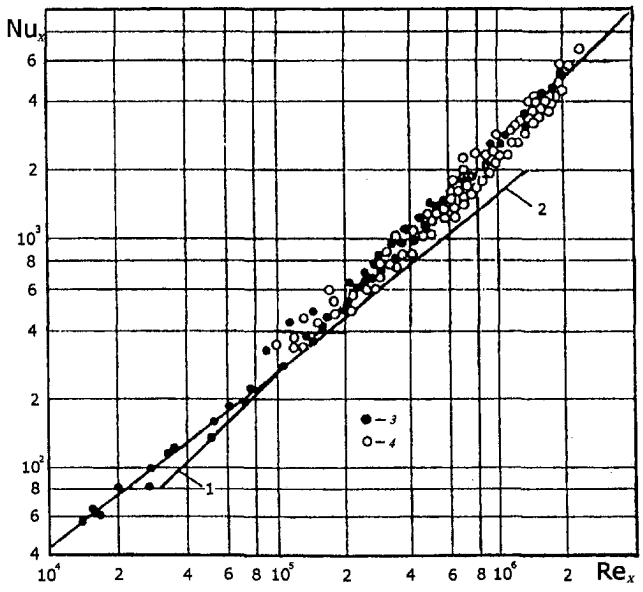

Fig. 12 Heat transfer on a rough surface in the presence of gas film cooling: 1–$Nu_x = 2.6\,10^{-3}\,Re_x$, 2–$Nu_x = 2.53\,10^{-2}\,Re_x^{0.8}$; 3, 4: experimental data [Volchkov and Levchenko (1965)], 3–in the absence of film cooling, 4–in the presence film cooling ($W_s/W_0 < 1$)

From Eq. (45), the local Re_T^{**} values are defined and then by Eq. (44) and the local values of Stanton number and heat transfer coefficient are found.

From Eq. (33) it follows that the effectiveness of gas film cooling depends on a total amount of gas injected through a porous section, since

$$Re_{T_0}^{**} = \frac{\int_0^{x_0} \rho_w W_w dx}{\mu_0} = \frac{G_c}{\mu_0}.$$

However, experiments show that, when gas is blown through a permeable section, separation of the boundary layer can occur with formation of a stagnant region with return flows (Hacker, 1956; Weighard, 1944).

In Fig. 13 and 14 a schematic diagram of the gas flow in the zone of the film cooling with intensive injection and the dependence of the separation area dimensions on the intensity of blowing are shown.

We see that with relative blowing $\bar{j}_w = j_w/\rho_0 W_0 = 0.017$, which approximately corresponds to critical injection, the zone of circulating flows disappears. Thus, on a porous section the regime of critical injection is the most optimal. It is interesting to compare this critical injection value with the amount of the gas that is sucked in the flat flooded turbulent jet. From Tollmien (1926), it follows that the specific mass flow rate of the gas that is sucked by a turbulent jet is equal to $\bar{j}_w = j_w/\rho_0 W_0 = 0.035$. That is approximately twice as much as the critical injection.

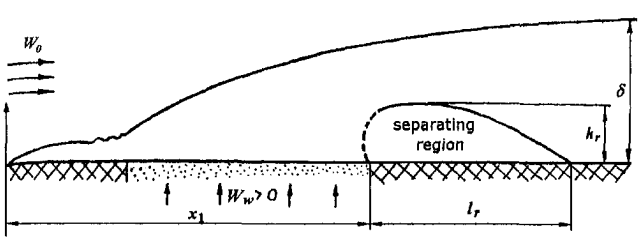

Fig. 13 Near-wall flow for a zone of intensive blowing through a porous section (results of visual investigations)

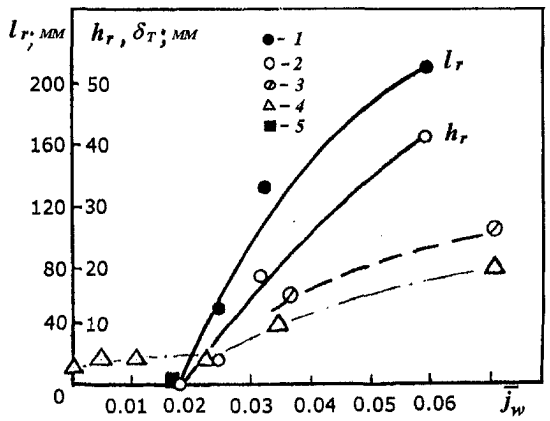

Fig. 14 The characteristics of the near wall flow downstream a zone of intensive porous blowing. l_r–length, h_r–height of a circulating zone (l_r, h_r–see Fig. 13), δ_T–thickness of a thermal boundary layer. 1–4: experimental data [Vasechkin (1986)]; 1–l_r, visual results on the plate; 2–h_r, visual results on the plate; 3–h_r, visual results on the cylinder; 4–δ_T, cylinder; 5–experimental data [Romanenko and Voloshchuk (1970)], l_r, h_r = 0, $\bar{j}_w = \rho_w W_w/\rho_0 W_0 = 0.017$.

In this connection the data of Motulevich (1981) are of interest. The results of the influence of the angle of blowing the gas onto a porous surface on the critical parameters of injection are presented. From these data it follows that by reducing the angle of injection, it is possible to increase by 1.5 times the value of critical injection and, accordingly, the effectiveness of gas film cooling.

Conjugate Heat Transfer Under Film Cooling

When calculating real systems of mass transfer cooling it is necessary to take into account the thermal resistance of the wall which separates the hot and cold flows of gases, a thermal resistance from the cooling gas site and a temperature distribution of the cooling gas along the channel length.

Let derive the equation for the general case of the film, porous or transpiration and convective cooling (Fig. 15).

Assuming that the temperature of the porous wall is equal to the temperature of the cooling gas, we have

$$C_p' j_w dT/dy = \lambda_e d^2T/dy^2. \tag{46}$$

Integrating Eq. (46) we obtain

$$(T_{w_1} - T)/(T_{w_1} - T_{w_2}) = [\exp((C_p'/C_{p_0})b_T\,\mathrm{Biy}) - 1]/[\exp((C_p'/C_{p_0})b_T\,\mathrm{Bi}) - 1] \tag{47}$$

where $\lambda_e = \lambda/(1 - \Pi)$ is the effective thermal conductivity.

The system of balance equations for the heat flux can be written as follows:

$$q_{w1} = \alpha_{q1}(T_w^* - T_{w1}),$$

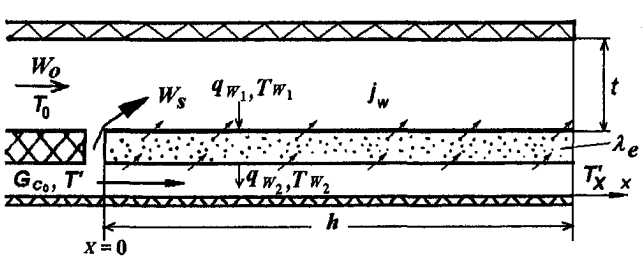

Fig. 15 Complex cooling of a wall

$$q_{w1} = C'_p j_w (T_{w1} - T_{w2}) \exp((C'_p/C_p) b_T \mathrm{Bi})/ [\exp((C'_p/C_p) b_T \mathrm{Bi}) - 1],$$

$$q_{w2} = q_{w1} \exp(-(C'_p/C_p) b_T \mathrm{Bi}),$$

$$q_{w2} = \alpha_{q2}(T_{w2} - T'_x), \quad (48)$$

where T^*_w is the temperature of the insulated wall with film cooling

$$T^*_w = T_0 - \Theta_f (T_0 - T'_x). \quad (49)$$

From the system of Eqs. (48) we obtain

$$\Theta_{\mathrm{pfc}} = [1 + (\psi_{in}/(C'_p/C_{p0}) b_T)(1 - e^{-(C'_p/C_{p0}) b_T \mathrm{Bi}}) + [(\psi_{in}\alpha_{q10})/(\psi_{\mathrm{suc}}\alpha_{q20})] e^{-(C'_p/C_{p0}) b_T \mathrm{Bi}}]^{-1}. \quad (50)$$

From Eqs. (1) and (50) it follows that

$$\Theta_x = (T_0 - T_{w1})/(T_0 - T'_x) = \Theta_{\mathrm{pfc}} + \Theta_f - \Theta_{\mathrm{pfc}}\Theta_f. \quad (51)$$

From Eq. (50) it is possible to obtain several special cases. For the case without film cooling ($T_0 = T^*_w$, $\Theta_f = 0$), we have

$$\Theta_x = \Theta_{pCx} = [1 + \psi_{in}(1 - e^{-(C'_p/C_{p0}) b_T \mathrm{Bi}})/(C'_p/C_{p0}) b_T + [(\psi_{in}\alpha_{q10})/(\psi_{\mathrm{suc}}\alpha_{q20})] e^{-(C'_p/C_{p0}) b_T \mathrm{Bi}}]^{-1}. \quad (52)$$

If only convective cooling is present from Eq. (52) we obtain

$$\Theta = [(1 + \mathrm{Bi}) + (\alpha_{q1}/\alpha_{q2})]^{-1}. \quad (53)$$

For the case of asymptotic suction, when $\alpha_{q2} = C'_p j_w$ (Kutateladze and Leontiev, 1990) from Eq. (52) we have

$$\Theta_{px} = (C'_p/C_{p0}) b_T / [\psi_{in} + (C'_p/C_{p0}) b_T]. \quad (54)$$

For the case $C'_p = C_{p0}$ by introducing the parameter $\bar{T}_{wx} = 1 - \Theta_x$, from Eq. (54) we can obtain

$$\bar{T}_{wx} = \psi_{in}/\psi_{\mathrm{suc}} = (1 - b_T/4)^2/(1 + b_T/4)^2. \quad (55)$$

Equation (51) can be transformed to

$$\bar{T}_{wx} = \bar{T}_{\mathrm{pfc}} \bar{T}_{wf}, \quad (56)$$

and for the case of asymptotic suction we have

$$\bar{T}_{wx} = (\psi_{in}/\psi_{\mathrm{suc}})(1 - \Theta_f). \quad (57)$$

For the case when $\mathrm{Bi} \to 0$, from Eq. (52) we obtain

$$\Theta_x = [1 + (\psi_{in}\alpha_{q10})/(\psi_{\mathrm{suc}}\alpha_{q20})]^{-1}. \quad (58)$$

Let us obtain the relation between Θ_x and Θ. For the case of porous or transpiration cooling we have

$$d[C'_p G_c T]/dx = q_{w2} z, \quad (59)$$

where z is the width of the channel. Then

$$T'_x = (C'_p G_c T' + q_{w2} z x)/C'_p (G_{c0} - j_w z x). \quad (60)$$

For the midspan cross section ($x = h/2$), we have

$$T'_x = 2T' + (q_{w2} z h)/C'_p G_c \quad (61)$$

or

$$T'_x = 2T' + (\psi_{in}/(C'_p/C_{p0}) b_T)(\exp(C'_p/C_{p0}) b_T \mathrm{Bi})(T^*_w - T_{w1}). \quad (62)$$

Consequently

$$1/\Theta = 1/\Theta_{x=h/2} + (\psi_{in}/(2C'_p/C_{p0}) b_T) \exp((C'_p/C_{p0}) b_T \mathrm{Bi}). \quad (63)$$

We obtain the same result as for the case of convective cooling.

For this case $C_p G_c dT/dx = q_w z$ and after integrating, we have

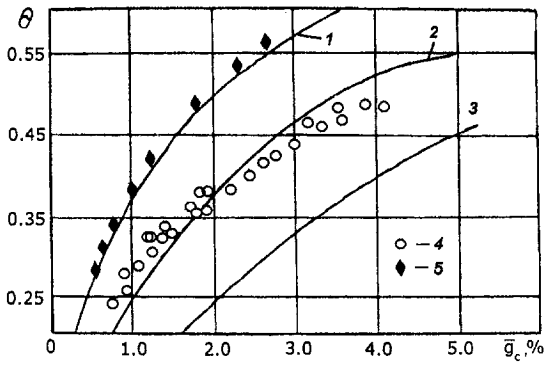

Fig. 16 Effectiveness of different cooling systems; 1–transpiration cooling, 2–transpiration-convective cooling, 3–convective-film cooling, 4–convective-porous cooling, 5–transpiration cooling (Lamelloy). 1–Eq. (50); 2–Eq. (52) for $b_T \to 0$; 3–Eq. (53); 4, 5–experimental data [Leontiev and Epifanov (1992)].

$$(T'_x - T')/(T_q - T_{w1}) = l\ \mathrm{St}_1/t\bar{g}_c$$

or

$$\Theta = [1 + \mathrm{Bi} + \alpha_{q1}/\alpha_{q2} \cdot z\ \mathrm{St}_1/t\bar{g}_c]^{-1}. \quad (64)$$

Thus, in all cases $\Theta < \Theta_x$.

In Fig. 16 experimental data (Leontiev and Epifanov, 1992) obtained with different cooling systems are presented.

From Fig. 16 we see that the system of porous or transpiration cooling is the most effective.

However, specific characteristics of permeable materials impede extensive practical application of this method of cooling.

First of all, internal channels of the porous structure can be clogged by solid particles. This is especially the case when powder or mesh porous materials with random micro structure of the cooling channels are used.

Laminated porous material with given initial micro structure such as Lamelloy developed by Detroit Diesel seems to be more promising. We have investigated three alternatives for the vane structure of the first-stage nozzle cascade of a power unit with 150 MW capacity. Five local parts of the vane profile were fabricated of laminated porous material, which was manufacturing using the methods and the technology developed in the Moscow State Technical University. The remaining part of the hollow vane was made of an impermeable material, and this part was not cooled. Thus, we have local transpiration cooling.

Convective cooling of the impermeable portion of the vane was arranged by installing a deflector. This was the case of combined convective-transpiration cooling (see Fig. 16, curve 2). The vane, which was entirely manufactured of laminated porous material, was investigated as well. From Fig. 16 it is clear that the cooling effectiveness of the vanes, which were fully made of laminated porous materials, is a little lower than that of the vane with local injection. The effectiveness of transpiration cooling was higher than when conventional methods of connective-film or film-impingement cooling were used.

However, with local injection a highly nonuniform distribution of the temperature along the vane surface takes place.

Naturally, the distribution of $T_{w2} = T_{w2}(S)$ is more smooth in the cases of convective-porous or transpiration cooling and transpiration cooling of the entire profile of the vane.

Figure 17 shows the comparison of the experimental data of Leontiev and Epifanov (1992) with the calculation using Eq. (52).

Hydrodynamic Losses on Porous Blades

When a coolant is injected through the pores of a permeable surface, the boundary layer structure undergoes secondary change, namely, the flow mode changes, the velocity profile shape and its

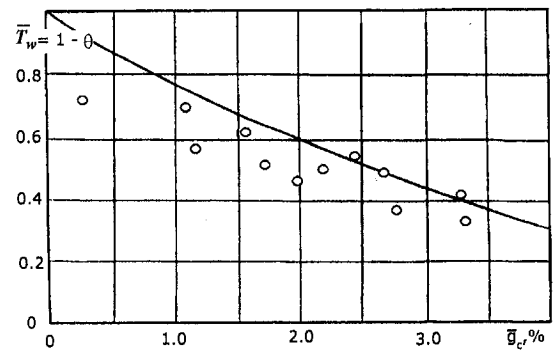

Fig. 17 Effectiveness of transpiration cooling for j_w = const. Curve–Eq. (55), points–experimental data [Leontiev and Epifanov (1992)].

thickness changes and the separation point shifts. This confirms the supposition of a considerable effect of porous or transpiration cooling upon gas-dynamic losses in turbines.

It is known that profile losses are determined as

$$\zeta_{pr} = 2(W_{ed}/W_m)^{3.2}(W_m/W_\infty)^{0.2}\delta^{**}_{ed}/C, \quad (65)$$

where δ^{**}_{ed} is momentum thickness at the edge of the vane, W_{ed}, W_∞, and W_m are the velocities of the main flow in the edge section, the velocity at an infinite distance from the vane and the average velocity, respectively (see Fig. 4).

The integral momentum equation for a two-dimensional boundary layer on a permeable surface may be written in the following form (Kutateladze and Leontiev, 1990):

$$d\,\mathrm{Re}^{**}_w/dx + [(1 + H)\,\mathrm{Re}^{**}_w/W_0]dW_0/dx = (\mathrm{Re}_L C_{f0}/2)(\psi + b), \quad (66)$$

where

$$\mathrm{Re}^{**}_w = \rho_0 W_0 \delta^{**}/\mu_w, \quad H = \delta^*/\delta^{**},$$

$$\mathrm{Re}_L = \rho_0 W_0 L/\mu_w, \quad \bar{x} = x/L.$$

For a constant value of the blowing parameter b (independent of the surface temperature) we obtain

$$\mathrm{Re}^{**}_w = \tilde{W}_0^{-k}\left[\frac{1+m}{2} B\,\mathrm{Re}_{0w}(\psi + b)\int_0^x \tilde{W}_0^{(1+(1+m)k)}dx\right]^{1/(1+m)}, \quad (67)$$

where $\tilde{W}_0 = W_0/W_{01}$ and $k = 1 + H$, the parameter ψ is determined from Eq. (36). For the turbulent boundary layer $m = 0.25$ and $B = 0.0128$.

For the turbulent boundary layer the dependence of the form parameter H on the blowing factor is determined by Kutateladze and Leontiev (1990),

$$H = (1 + 0.05b)H_0. \quad (68)$$

As a first approximation it is possible not to take into account the effect of blowing on the value of H. Then, from Eqs. (65) and (67) we have

$$\zeta_p/\zeta_{p0} = (\psi + b)^{0.2}, \quad (69)$$

where ζ_{p0} is the coefficient of the profile losses on an impermeable surface.

Taking into account Eq. (36) we obtain

$$\zeta_p/\zeta_{p0} = (1 + b/4)^{0.4} \quad (70)$$

or

$$\zeta_p/\zeta_{p0} = [1 + (t/4lc_{f0})\bar{g}_c]^{0.4}. \quad (71)$$

For more accurate calculation it is necessary to use Eq. (68). Our study of the characteristics of a straight subsonic cascade of blades was performed using a test rig for a cascade with three porous (in the center) and six solid blades.

In Fig. 18 the results of comparison of Eq. (71) with experimental data (Leontiev and Epifanov, 1992) are presented.

There is one essential fact, which attracts special attention. Namely, in all cascades the variation g_c from 0 to 4 percent have resulted in not more than a 12 percent increase in ζ_p. The increase in ζ_p in comparison with smooth impermeable cascades is caused by a combined effect of injection and roughness.

Influence of Longitudinal Thermal Conductivity on Effectiveness of Gas Film Cooling

In several cases, when calculating mass transfer cooling, it is necessary to take into account the effect of longitudinal thermal conductivity; that is, to solve a conjugate problem. Equation (24), which determines a temperature of the insulated wall under conditions of gas film cooling, is valid for the case when thermal conductivity of the wall material tends to zero ($\lambda \to 0$). The other limiting case corresponds to the condition when thermal conductivity of the wall material tends to infinity ($\lambda \to \infty$). In this case, the temperature of the wall remains constant along the plate and equal to the temperature of the wall on a porous plate. With a finite value of the thermal conductivity coefficient λ_m, the curve of the temperature of the wall will occupy an intermediate position between the above limiting cases. It is not so difficult to determine the equation for this curve, accepting an assumption of uniform distribution of the temperature along the thickness of the plate. In this case, the differential equation of a heat balance for the plate is

$$\lambda_m \cdot \Delta \frac{d^2T_w}{dx^2} = \alpha \cdot (T^*_w - T_w), \quad (72)$$

where Δ is the thickness of the plate.

Reducing Eq. (72) to a dimensionless form, we receive

$$\Theta^* = \Theta_w + \frac{1}{\dot{m}^2}\frac{d^2\Theta_w}{d\bar{x}^2}, \quad (73)$$

where

$$\Theta^* = \frac{T_0 - T^*_w}{T_0 - T'}; \quad \Theta_w = \frac{T_0 - T_w}{T_0 - T'};$$

$$\dot{m} = \frac{L}{\Delta}\sqrt{\mathrm{Bi}}; \quad \mathrm{Bi} = \frac{\alpha\Delta}{\lambda_m}; \quad \bar{x} = \frac{x}{L}.$$

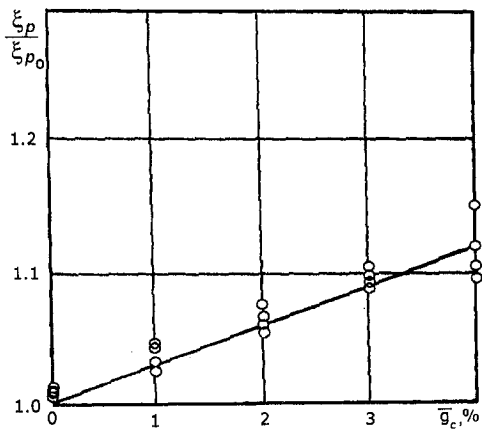

Fig. 18 Comparison of calculations using Eq. (71) with experimental data [Leontiev and Epifanov (1992)]

The general solution of Eq. (73) is

$$\Theta_w = \frac{\dot{m}}{2}\left\{ e^{-\dot{m}\bar{x}} \int e^{\dot{m}\bar{x}}\Theta^* d\bar{x} - e^{\dot{m}\bar{x}} \int e^{-\dot{m}\bar{x}}\Theta^* d\bar{x} \right\} + C_1 e^{\dot{m}\bar{x}} + C_2 e^{-\dot{m}\bar{x}}, \quad (74)$$

where the constants C_1 and C_2 are determined from the boundary conditions.

For the case of film-convective cooling

$$\lambda_e \Delta \frac{d^2 T_w}{dx^2} = \alpha_1 (T_w^* - T_w) - \alpha_2 (T_w - T'). \quad (75)$$

Transforming to a dimensionless form we find

$$\frac{1}{\dot{m}^2}\frac{d^2\Theta_w}{d\bar{x}^2} + \Theta_w = \frac{\alpha_1}{\alpha_1 + \alpha_2}\Theta^* + \frac{\alpha_2}{\alpha_1 + \alpha_2}, \quad (76)$$

with $\mathrm{Bi} = (\alpha_1 + \alpha_2)L/\lambda_e$, $\lambda_e = \lambda_m(1 - \Pi)$.

The general solution of Eq. (76) looks like

$$\Theta_w = \frac{\dot{m}}{2}\left\{ e^{-\dot{m}\bar{x}} \int e^{\dot{m}\bar{x}}(\Theta^* + B)d\bar{x} - e^{\dot{m}\bar{x}} \int e^{-\dot{m}\bar{x}}(\Theta^* + B)d\bar{x} \right\} + C_1 e^{\dot{m}\bar{x}} + C_2 e^{-\dot{m}\bar{x}}, \quad (77)$$

where $B = \alpha_2/(\alpha_1 + \alpha_2)$.

Figure 19 shows the comparison of the calculation results for the temperature of the blade wall with combined film and convective cooling, which were obtained using Eqs. (74) and (76), with experimental data (Leontiev and Epifanov, 1992). We see the effect of longitudinal thermal conductivity along the wall of the blade can be significant.

Gas Film Cooling Effectiveness on a Rough Wall

The roughness of the surface can significantly influence the effectiveness of gas film cooling. In this case, as is shown in Leontiev et al. (1995), the formula for determination of the effectiveness of gas film cooling takes the following form:

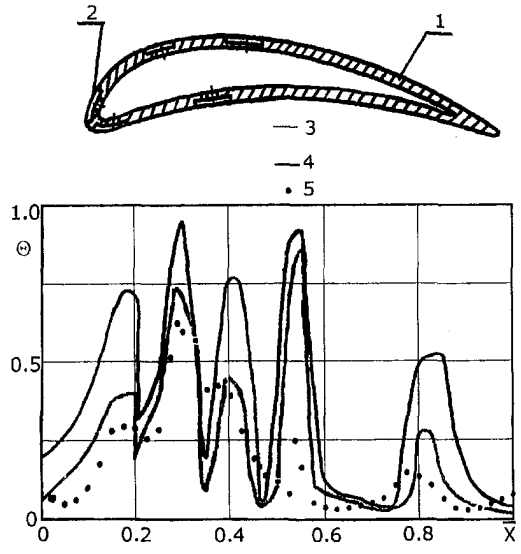

Fig. 19 Distribution of local convective-transpiration cooling effectiveness along the contour of the blade profile. 1–impermeable part of the wall; 2–insert from layers of permeable material; 3–accounting for longitudinal thermal conductivity; 4–without longitudinal thermal conductivity; 5–experimental data [Leontiev and Epifanov (1992)].

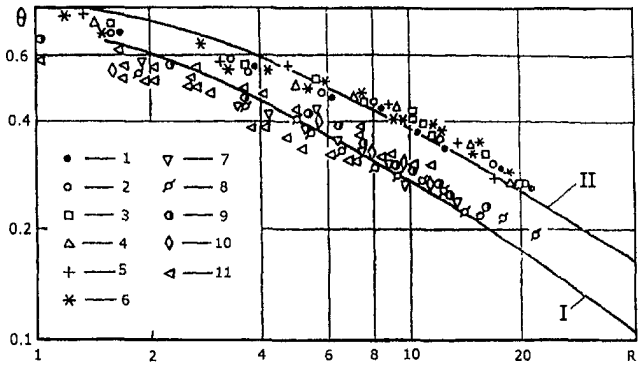

Fig. 20 Comparison of the measured values of gas film cooling effectiveness with the results of calculations. I–Eq. (80), II–Eq. (27). Experiment on a smooth plate: 1–$\bar{j}_w$ = 0.089; 2–0.087; 3–0.0083; 4–0.011; 5–0.01; 6–0.012. Experiment on a rough plate: 7–$\bar{j}_w$ = 0.012; 8–0.011; 9–0.01; 10–0.084; 1–10: experimental data [Komarov et al. (1982)]; 11–experimental data [Osipov (1994)]. $R = \mathrm{Re}_L/[\mathrm{Re}_w^{1.25}(1 + (T' - T_{w1})/(T_{w1} - T_0))^{1.25}]$.

$$\Theta = \left[1 + 0.016\beta_{\max}^{1+m} \times \frac{\mathrm{Re}_L \int_{\bar{x}_1}^{\bar{x}} \psi_f d\bar{x}}{\left(\frac{\rho_w W_w}{\mu'} x_1\right)^{1+m}\left[1 + \frac{T' - T_{w1}}{T_{w1} - T_0}\right]^{1+m}} \right]^{1/(1+m)}. \quad (78)$$

The law of friction on a rough surface can be presented as (Komarov et al., 1982)

$$\psi_f = 1 + 1.792\left(\frac{K_s}{x}\right)^{0.11}. \quad (79)$$

For the zone of the square-law of friction ($b_{\max} = 7.85$, $\psi_f = 2$) (Komarov et al., 1982) we have

$$\Theta = \left[1 + 0.42 \frac{\mathrm{Re}_{\Delta x}}{\mathrm{Re}_{w1}^{1.25}}\left[1 + \frac{T' - T_{w1}}{T_{w1} - T_0}\right]^{-1.25} \right]^{-0.8}. \quad (80)$$

For the region $0.1 < K_s/\delta^{**} < 0.5$, $\beta_{\max} = 7.81$, and

$$\Theta = \left[1 + 0.209 \frac{\mathrm{Re}_L \int_{\bar{x}_1}^{\bar{x}} \left[1 + 1.742\left(\frac{K_s}{x}\right)^{0.11}\right] d\bar{x}}{\mathrm{Re}_{w1}^{1.25}\left[1 + \frac{T' - T_{w1}}{T_{w1} - T_0}\right]^{1.25}} \right]^{-0.8}. \quad (81)$$

Figure 20 shows the comparison of the results calculating using Eqs. (80) and (27) with experimental data of Komarov et al. (1982) and Osipov (1994).

For the case of slot cooling of a tubular surface with macro roughness presented in Fig. 21, it is possible to recommend the formula of Volchkov and Levchenko (1965)

$$\Theta = \left[1 + 0.24 \cdot a_\Delta \frac{\mathrm{Re}_{\Delta x}}{\mathrm{Re}_s^{1.25}}\left(\frac{\mu_0}{\mu_s}\right)^{1.25} \right]^{-0.8}, \quad (82)$$

where

$$a_\Delta = 1 + \frac{4\Delta x \cdot \Delta}{(1 + \bar{j}_s^2)(\Delta x + 2\Delta)^2}; \quad \bar{j}_s = \frac{\rho_s W_s}{\rho_0 W_0}.$$

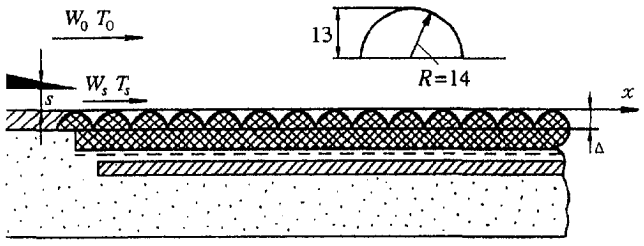

Fig. 21 Lot cooling surface with macro roughness

The results of generalization of experimental data using Eq. (82) are presented in Fig. 22.

Film Cooling for Flow of a Compressible Gas

The integral energy equation for the flow of a compressible gas can be written as

$$\frac{d\,\mathrm{Re}_T^{**}}{d\bar{x}} + \frac{\mathrm{Re}_T^{**}}{\Delta T}\frac{d(\Delta T)}{d\bar{x}} = \frac{q_w}{C_{p0}\rho_0 W_0 \Delta T}\mathrm{Re}_L, \tag{83}$$

where

$$\Delta T = T_{w0}^* - T_w; \quad T_{w0}^* = T_0\left\{1 + r\frac{k-1}{2}M^2\right\},$$

$$\mathrm{Re}_L = \frac{\rho_0 W_0 L}{\mu_0^*}, \quad \bar{x} = x/L.$$

T_w^* is the temperature of an insulated wall,

$$\mathrm{Re}_T^{**} = \frac{\rho_0 W_0 \delta_T^{**}}{\mu_0^*}; \quad \delta_T^{**} = \int_0^\delta \frac{\rho W}{\rho_0 W_0}\left(\frac{T_{w0}^* - T^*}{T_{w0}^* - T_w}\right)dy.$$

For of an insulated wall, $q_w = 0$ and

$$\Theta = \frac{T_{w0}^* - T_w^*}{T_{w01}^* - T_{w0}} = \frac{\mathrm{Re}_{T_1}^{**}}{\mathrm{Re}_T^{**}}, \tag{84}$$

and from here

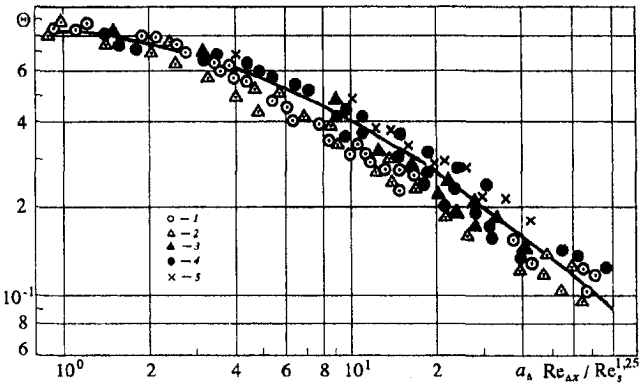

Fig. 22 Generalization of experimental data for film cooling effectiveness on a tubular surface, $\bar{j}_s < 1$. Curve–Eq. (82). Points–experimental data [Volchkov and Levchenko (1965)].

Symbols	S, mm	$\bar{j}_s$
1	13	0.23
2	10	0.23
3	6.5	0.65
4	3.5	0.88
5	2.0	0.73, 1.0

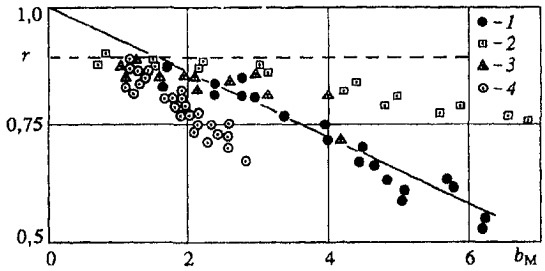

Fig. 23 Recovery factor on a porous surface. Experimental data: 1–M = 2.5 [Baryshev et al. (1972)]; 2–M = 3.2 Bartley, Leadon [see Leontiev et al. (1995)]; 3–M = 3.0 Leadon, Scott [see Leontiev et al. (1995)]; 4–M = 2.7 Rubesin [see Leontiev et al. (1995)]. Solid curves–Eq. (89), dotted curve–impermeable plate.

$$T_w^* = T_{w0}^* - \Theta(T_{w01}^* - T_{w0}). \tag{85}$$

The effectiveness of the gas film cooling Θ is defined by the formula

$$\Theta = \left[1 + \frac{B(m+1)\beta^{(m+1)}}{2\,\mathrm{Pr}^n}\frac{\mathrm{Re}_{00}}{\mathrm{Re}_{T_0}^{**(m+1)}} \times \int_1^x \psi_S\left(\frac{\mu_w}{\mu_0^*}\right)^m U(1-U^2)^{1/(k-1)}d\bar{x}\right]^{-(1/(m+1))}. \tag{86}$$

However, for definition of the temperature T_w^*, which appears in the formula for heat flux

$$q_w = \alpha(T_{w0}^* - T_w), \tag{87}$$

it is necessary to determine an equilibrium temperature of the wall in the zone of the gas film cooling T_{w0}^*, which, in a general case, differs from T_{w01}^*. The temperature T_{w01}^*, that is the equilibrium temperature of the insulated porous wall, is defined from the equation

$$T_{w01}^* = T_0 + r\frac{W_0^2}{2C_p}. \tag{88}$$

As experiments show, the recovery factor r depends on blowing intensity (Fig. 23). It is possible to approximate the experimental data by the empirical formula (Baryshev et al., 1972)

$$\frac{r}{r_0} = 1 - 0.4\frac{b_M}{b_{M_{cr}}}, \tag{89}$$

where

$$b_M = \frac{j_w}{\rho_0 W_0}\frac{1}{\mathrm{St}_M}; \quad b_{M_{cr}} = b_{cr0}\cdot\psi_M; \quad b_{cr0} = \frac{4}{\frac{1}{3} + \frac{2}{3}\bar{\psi}}; \quad \bar{\psi} = \frac{T_w}{T_{w0}^*}.$$

With critical injection, $(r/r_0)_{cr} = 0.6$.

Using the analogy between critical injection of gas and a quantity of gas sucked in the flat turbulent jet, it is possible to assume that Pr_T, that is the turbulent Prandtl number, under these conditions will approach to 0.5. Then from the Rubezin's formulas as presented in Jakob (1957)

$$r = \mathrm{Pr}_T\left[1 - \left(1 - \frac{\mathrm{Pr}}{\mathrm{Pr}_T}\right)\left(\frac{W_l}{W_0}\right)^2\right], \tag{90}$$

(W_l is a velocity on the viscosity sublayer edge), it follows that for $\mathrm{Pr}/\mathrm{Pr}_T \approx 1$,

$$\frac{r}{r_0} = \mathrm{Pr}_T \approx 0.5,$$

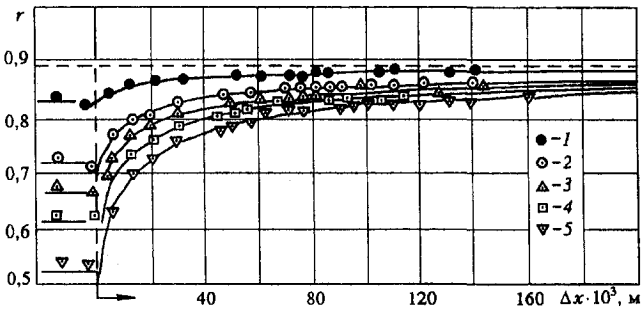

Fig. 24 Recovery factor on and downstream of a porous section. 1–5: experimental data [Baryshev et al. (1972)]; 1–$\bar{j}_w = 5 \cdot 10^{-3}$; 2–$6.4 \cdot 10^{-3}$; 3–$7.4 \cdot 10^{-3}$; 4–$8.0 \cdot 10^{-3}$; 5–$9.0 \cdot 10^{-3}$. Solid curves–Eq. (91). Dotted line–impermeable wall.

which is confirmed by the experimental results in Fig. 23.

Naturally, in the zone of gas film cooling, the recovery factors will increase with length of the plate, approaching the corresponding value for an impermeable wall (Jakob, 1957) $r_0 = \sqrt[3]{\mathrm{Pr}}$, (Fig. 24).

The condition of $T_{w1} = T^*_{w01}$ corresponds to the special case of Eq. (28); therefore, it is not surprising that the experimental data on recovery factors (Baryshev et al., 1972) are readily generalized by the formula (Fig. 25):

$$\frac{r_0 - r}{r_0 - r_1} = \left[1 + \frac{0.25\psi_M \,\mathrm{Re}_{\Delta x}}{\mathrm{Re}_{w1}^{1.25}} \left(\frac{\mu_0}{\mu_{w1}}\right)^{0.25}\right]^{-0.8}. \qquad (91)$$

It is interesting to note that Eq. (91) can be taken as a basis for generalization of experimental data with gas blowing through a porous disk (Vinogradov et al., 1997). The layout of the test section with which experiments were carried out is shown in Fig. 26.

In (Bengles et al., 1977; Goldstein et al., 1968; Schetz, 1980; Vinogradov et al., 1997), it is shown that with injection of the cooling fluid through a single hole, the flow pattern turns out to be rather complex: three-dimensional, with a formation downstream the hole of two intensive vortexes which are concurrent the flow. For considerable intensity of injection, an area of the lowered pressure with a suction of gas from the main flow is formed downstream of the jet. In this zone the effectiveness of gas film cooling decreases. A similar picture is observed with gas injection in supersonic flow Vinogradov et al. (1997). Figure 27 shows the results of measurements of recovery factors and the effectiveness of gas film cooling when blowing the gas into the supersonic flow through a flat porous disk. Also in Fig. 27, the results of calculations of gas film cooling effectiveness using the following formula are presented:

$$\Theta = \left\{1 + 0.25\,\frac{\psi_M K_0 \,\mathrm{Re}_{\Delta x}}{\mathrm{Re}_{w1}^{1.25}} \left(\frac{\mu_0}{\mu'}\right)^{0.25}\right\}^{-0.8} \qquad (92)$$

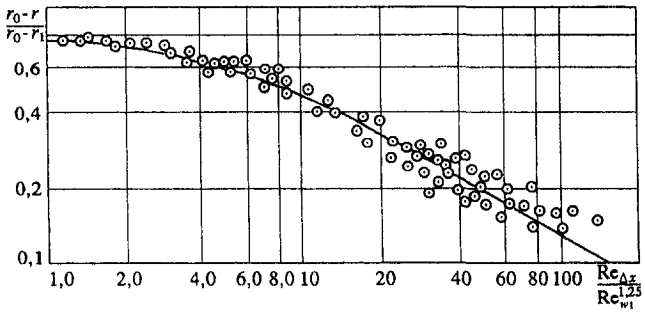

Fig. 25 Generalization of experimental data [Baryshev et al. (1972)] (see Fig. 24) for recovery factor in the zone of gas film cooling. Solid curve–Eq. (91).

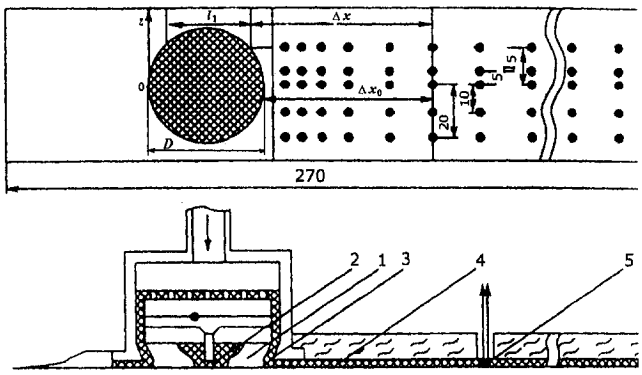

Fig. 26 Thermally insulated plate. 1–injection section with a permeable part; 2–Chromel-Copel Thermocouple; 3–textolite inserts thermally insulated from the model; 4–thermally insulated textolite plate; 5–Chromel-Copel Thermocouple.

and

$$\frac{r_0 - r}{r_0 - r_1} = \left[1 + \frac{0.25K_0\psi_M \,\mathrm{Re}_{\Delta x}}{\mathrm{Re}_{w1}^{1.25}} \left(\frac{\mu_0}{\mu'}\right)^{0.25}\right]^{-0.8}, \qquad (93)$$

where

$$\mathrm{Re}_{\Delta x} = \frac{\rho_0 W_0 \Delta x}{\mu_0}; \quad \mathrm{Re}_{w1} = \frac{\rho_w W_w}{\mu'} l_1;$$

$$r_0 = 0.895; \quad l_1 = D - 2z.$$

l_1 is the length of the permeable section in the flow direction, K_0 is the empirical factor, which takes into account a three-dimensional structure of the flow, r_1 is the recovery factor on a permeable surface, and r is the recovery factor in the zone of gas film cooling.

In Fig. 27 the continuous lines correspond to calculations using Eqs. (92) and (93) with $K_0 = 3$.

Thus, using Eqs. (89) and (93), it is possible to determine recovery factor values on a permeable and insulated wall and,

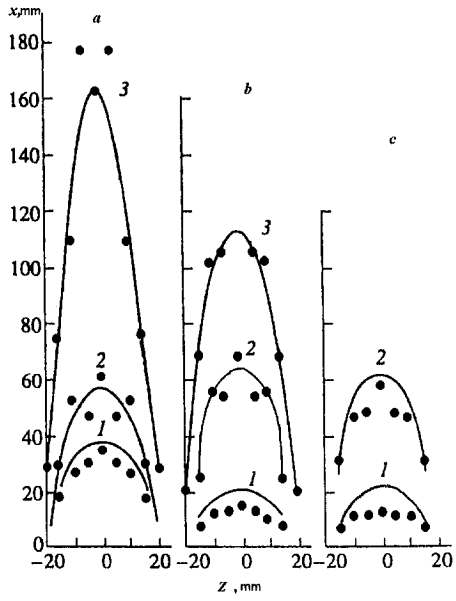

Fig. 27 Curves for the (*a*, *b*) constant recovery factors and (*c*) effectiveness of gas film cooling. (*a*) $\bar{j}_w = 0.012$; (*b*, *c*) $\bar{j}_w = 0.005$. (*a*) 1–$r = 0.78$, 2–0.8, 3–0.85; (*b*) 1–$r = 0.85$, 2–0.87, 3–0.88; (*c*) 1–$r = 0.2$, 2–0.1. Points–experimental data [Vinogradov et al. (1997)], the solid curves–Eq. (93).

using Eq. (92), to find equilibrium temperature in the region of gas film cooling.

It is known (Kutateladze and Leontiev, 1990) that blowing of gas significantly affects the coefficient of friction, and at $b = b_{cr}$, $c_f \to 0$.

In Baryshev et al. (1976), Eq. (27) was used for generalization of experimental data on local coefficients of friction in the zone of the gas film cooling.

We shall now introduce a parameter which is similar to the effectiveness of the gas film cooling

$$\Theta_f = \frac{c_{f0} - c_f}{c_{f0} - c_{f1}}, \tag{94}$$

where c_f is the coefficient of friction in the zone of the gas film cooling downstream the permeable portion, c_{f1} is the coefficient of friction at the end of the porous section, c_{f0} is the coefficient of friction under "standard" conditions, which is calculated using the formula

$$\frac{c_{f0}}{2} = \frac{0.0128}{(\mathrm{Re}^{**})^{0.25}}.$$

From Fig. 28, we see that experimental data on friction are well generalized by the relation

$$\Theta_f = \left[1 + 0.1\,\frac{\mathrm{Re}_{\Delta x}}{(\mathrm{Re}^{**}_{T_1})^{1.25}}\right]^{-0.8}. \tag{95}$$

Film Cooling Effectiveness With Blowing Foreign Gas

It should be noted that all the equations obtained for film cooling effectiveness can be extended to the case of blowing a foreign gas. In this case, the effectiveness of the gas film cooling is determined on the basis of gas enthalpies:

$$\Theta_i = \frac{i_0 - i^*_w}{i_0 - i_{w1}}. \tag{96}$$

For Sc = 1, there should exist similarity in distribution of the enthalpy and the total concentrations of the gas blown. Consequently

$$\Theta_i = \frac{i_0 - i^*_w}{i_0 - i_{w1}} = \frac{c_0 - c^*_w}{c_0 - c_{w1}}. \tag{97}$$

Hence,

$$c^*_w = c_0 - \Theta_i(c_0 - c_{w1}), \tag{98}$$

where c^*_w is the concentration of the blown gas on the insulated wall and c_{w1} is the concentration of the blown gas on the wall in section x_1. c_0 is the concentration of the blowing gas in the main flow.

The heat capacity of the binary gas mixture at the wall can be determined from

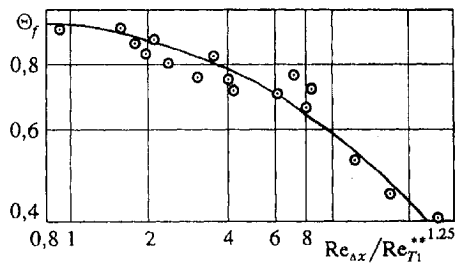

Fig. 28 Coefficient of friction downstream of a permeable section. Curve–Eq. (95); points–experimental data [Baryshev et al. (1976)] at x_0 = 0.04 and 0.16, j_w = 0.003–0.04.

$$C^*_{pw} = C'_p c^*_w + C_{p0}(1 - c^*_w) = C_{p0} + (C'_p - C_{p0})c^*_w. \tag{99}$$

From Eq. (96) it follows that

$$\Theta_i = \frac{C_{p0}T_0 - C^*_{pw}T^*_w}{C_{p0}T_0 - C_{pw1}T_{w1}}. \tag{100}$$

Hence, taking into account Eq. (99), we have

$$\Theta_t = \frac{T_0 - T^*_w}{T_0 - T_{w1}} = \frac{\Theta_i(C_{p0}T_0 - C_{pw1}T_{w1}) - (C_{pw1} - C_{p0})T_0c^*_w}{[C_{p0} + (C_{pw1} - C_{p0})c^*_w](T_0 - T_{w1})}. \tag{101}$$

In the case of blowing a foreign gas through a tangent slot, $c_0 = 0$, $c_{w1} = 1$, $T_{w1} = T_s$, and $C_{pw1} = C_{ps}$, and then from Eq. (101) we obtain

$$\Theta_t = \frac{\Theta_i C_{ps}}{\Theta_i(C_{ps} - C_{p0}) + C_{p0}}. \tag{102}$$

For the region $x > x_1$, where $q_w = 0$, the integral energy equation is written in the form

$$\frac{d(R^{**}_i \Delta i)}{d\bar{x}} = 0. \tag{103}$$

Hence,

$$\Theta_i = \frac{\mathrm{Re}^*_{i1}}{\mathrm{Re}^{**}_i} = \beta\,\frac{\mathrm{Re}^{**}_1}{\mathrm{Re}^{**}}, \tag{104}$$

where

$$\Theta_i = \frac{i^*_{w0} - i^*_w}{i^*_{w0} - i^*_{w1}}, \quad \mathrm{Re}^{**} = \frac{\rho_0 W_0 \delta^{**}}{\mu^*_0},$$

$$\mathrm{Re}^{**}_{i1} = \frac{\rho_0 W_0 \delta^{**}_{i1}}{\mu^*_0}, \quad \frac{i^*_{w0}}{i_0} = 1 + r\,\frac{k-1}{2}M^2_0.$$

Here i^*_w is the gas enthalpy at the insulated wall.

Taking into consideration Eq. (30) we obtain the following general equation for the gas film cooling effectiveness:

$$\Theta_i = \left[1 + \frac{B}{2\,\mathrm{Pr}^{0.75}}(1 + m)\beta^{m+1} \times \frac{\mathrm{Re}_L}{(\mathrm{Re}^{**}_{i1})^{m+1}} \int_{\bar{x}_1}^{\bar{x}} \psi_S \left(\frac{\mu_w}{\mu^*_0}\right)^{0.25} d\bar{x}\right]^{-0.8}, \tag{105}$$

where

$$\psi_S = \left[\frac{2\ \mathrm{arctg}\ M_0\sqrt{0.5r(k-1)}}{(\sqrt{\bar{\psi}} + 1)M_0\sqrt{0.5r(k-1)}}\right]^2$$

and $\bar{\psi} = i_w/i^*_w$.

The parameter Re^{**}_{i1} is determined by taking into account the method of creating film cooling:

(a) for a cooled section,

$$\mathrm{Re}^{**}_{i1} = \left[\frac{B}{2}(m + 1)\psi_{S1}\left(\frac{\mu_{w1}}{\mu^*_0}\right)^{0.25}\mathrm{Re}_{x1}\right]^{0.8}; \tag{106}$$

(b) for a porous section,

$$\mathrm{Re}^{**}_{i1} = \mathrm{Re}_{w1}(1 + K_1); \tag{107}$$

(c) for gas blowing through a slot,

$$\mathrm{Re}^{**}_{i1} = \frac{\rho_s W_s S}{\mu^*_0}. \tag{108}$$

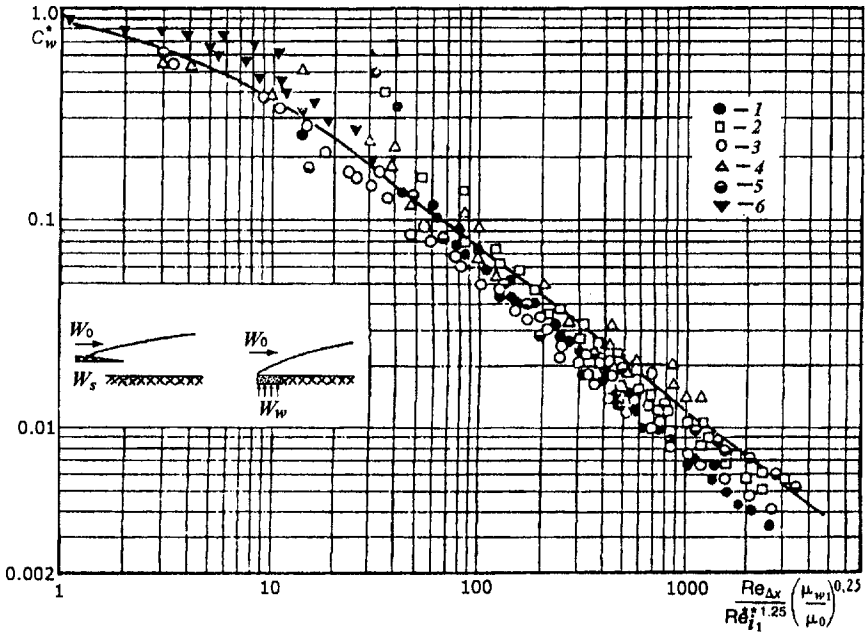

Fig. 29 Distribution of concentration on the wall. Film cooling effectiveness with foreign gas blowing: curve–Eqs. (98) and (109) for $\psi_s = 1$; points-experimental data:

Designation	Gas blown	Reference	Kind of film cooling
1	Helium	Volchkov (1983)	Porous section
2		Goldstein et al. (1966)	
3	Helium	Volchkov (1983)	Slot
4	Helium		
5	Hydrogen		
6	Freon-12		

For the region of subsonic velocity, Eq. (105) for $\beta = 9$ is written as follows:

$$\Theta_i = \left[1 + 0.25\,\frac{\mathrm{Re}_{L1}}{(\mathrm{Re}_{i1}^{**})^{1.25}}\int_{\bar{x}_1}^{\bar{x}} \psi_S\left(\frac{\mu_w}{\mu_0}\right)^{0.25} d\bar{x}\right]^{-0.8}. \quad (109)$$

The exact solution of the problem is carried out by the method of successive approximations since the function ψ_S depends on Θ_i. For practical calculations it is possible to assume as a first approximation that $\psi_S = \psi_{S1}$ and to obtain limiting values of the gas film cooling effectiveness under the conditions considered.

Figure 29 presents the comparison of Eqs. (98) and (109) with the experiments of Volchkov and Sinayko (1983) and Goldstein et al. (1966), where a concentration of the gas blown at the wall by different arrangements of film cooling was measured. The curve corresponds to the calculations of c_w^* from Eqs. (98) and (109) with the approximation $\psi_S \sim 1$. As is seen from Fig. 29, there is satisfactory agreement between the experimental data and the calculations. It is possible to achieve even better agreement; however, for this purpose it is necessary to take into account the actual value of ψ_S in Eq. (109).

In Fig. 30, the comparison of effectiveness of gas film cooling is shown for the cases of injection of air and helium Hartnett (1985). In addition, the results of calculations using Eq. (109) and Eq. (5) from Goldstein and Haji-Sheikh (1971) are shown.

Effectiveness of Gas Film Cooling in Swirled Flow

As is shown in Repukhov (1998) and Volchkov (1983), swirling the flow at the channel inlet can significantly influence the film cooling effectiveness. For injection of gas through a slot, the formula (109) proves to be true. Accounting for swirling the gas, this formula turns to be as

$$\Theta = \left[1 + 0.24\cdot \mathrm{Re}_s^{-1.25}\left(\frac{\mu_0}{\mu_s}\right)^{1.25} \times \frac{\rho_0 W_0}{\mu_0}\left(1 - \frac{S}{D}\right)^{-1.25}\int_{x_0}^{x} \psi_S dx\right]^{-0.8}, \quad (110)$$

where $\mathrm{Re}_s = \rho_s W_s S/\mu_s$; ψ_S is the relative law of heat transfer, which takes into account the effect of swirling the flow and other factors.

For a nonswirled jet,

$$\Theta = \left[1 + 0.24\cdot \mathrm{Re}_{\Delta x}\,\mathrm{Re}_s^{-1.25}\left(1 - \frac{S}{D}\right)^{-1.25}\right]^{-0.8}, \quad (111)$$

where $\mathrm{Re}_{\Delta x} = \rho_0 W_0 \Delta x/\mu_0$; $\Delta x = x - x_0$ and x_0 is the length of a starting section, where $\Theta = 1$.

As experimental results have shown, swirling the flow strongly effects the length of a starting section:

$$\frac{x_0}{S} = 28\left(\frac{W_s}{W_0}\right)^{1.25}. \quad (112)$$

The intensity of swirling reduces sharply with length of the channel and practically disappears in the length of the starting section. In Fig. 31 the experimental data on effectiveness of gas film cooling in swirled jets are generalized with the help of the formula (111), the influence of flow swirling is taken into account only within the starting section, with the latter being determined using the Eq. (112). As follows from Fig. 31, the experimental data are satisfactorily generalized by Eq. (111); however, for more accurate calculations, it is necessary to take into account an influence of swirling on the relative law of heat transfer ψ_S.

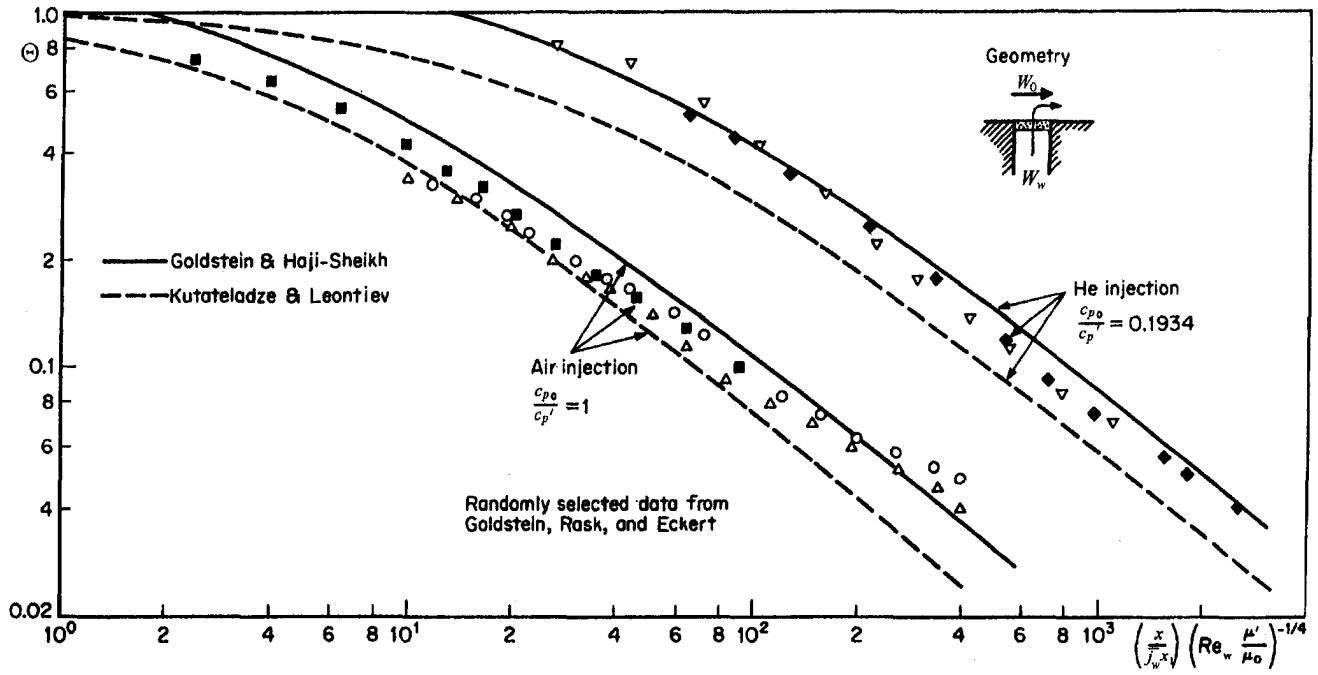

Fig. 30 Comparison of predictions and experimental results [Goldstein et al. (1966)] for injection through a porous slot-subsonic flow over a flat plate

Effectiveness of Gas Film Cooling in Turbulized Flows

In practical conditions, especially in the application of gas film cooling for cooling the blades of gas turbines, the main flow of gas can be strongly turbulized.

The question of influence of the degree of turbulence of the main flow on the effectiveness of gas film cooling has been investigated in detail (Carlson and Talmor, 1968; Chanay et al., 1976; Green, 1973; Lebedev et al., 1995; Ligrani et al., 1996; Mironov et al., 1981; Pichal, 1972; Romanenko et al., 1970; Vashechkin, 1986; Volchkov et al., 1995). Vasechkin (1986) shows that for film cooling by injection of gas through a slot, an increase in the degree of turbulence of the main flow by up to ten percent does not appreciably influence the effectiveness of gas film cooling, and the following relation remains valid:

$$\Theta = \left[1 + 0.25 \frac{\mathrm{Re}_{\Delta x}}{\mathrm{Re}_s^{1.25}}\right]^{-0.8}. \qquad (113)$$

However, for film cooling by injection of gas through a porous section, the level of turbulence of the main flow significantly reduces the effectiveness of the gas film cooling, (Fig. 32). Flow visualization shows that with $\mathrm{Tu}_0 > 0.1$, a destruction of the vortical zones downstream the porous section takes place.

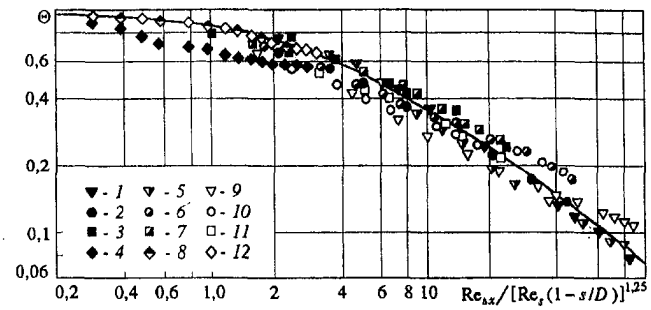

Fig. 31 Generalization of experimental data [Volchkov (1983)] on swirled film cooling effectiveness for air injection in air. Curve–Eq. (111). For φ deg = 0: 1–m = 0.3, 2–0.5, 3–0.9, 4–5.0; for φ deg = 58: 5–m = 0.3, 6–0.5, 7–0.9, 8–5.0; for φ deg = 74: 9–m = 0.3, 10–0.5, 11–0.9, 12–5.0.

In Fig. 33, experimental data Vasechkin (1986) are generalized by introduction of an empirical function in Eq. (113)

$$\Theta = \left[1 + A \frac{\mathrm{Re}_{\Delta x}}{\mathrm{Re}_{w1}^{1.25}(1 + K_1)^{1.25}}\right]^{-0.8}, \qquad (114)$$

where

$$A = \bar{j}_w(3.44\ \mathrm{Tu}_{\Delta x}10^2 + 16) + 0.12\ \mathrm{Tu}_{\Delta x}10^2, \qquad (115)$$

$\mathrm{Tu}_{\Delta x}$ is the degree of turbulence of the main flow averaged on the length of the film cooling, $\bar{j}_w = j_w/\rho_0 W_0$.

In papers by Andreev et al. (1998), Cho et al. (1998), Leontiev et al. (1995), Repukhov (1998), and Seo et al. (1998), the results of detailed studies on the influence of arrangement of the gas film cooling (injection of gas through a single hole, row of holes, perforated edges angles of injection and etc.) on its effectiveness are given. In particular, it is shown that at gas injection of $W_s/W_0 < 0.1$, the geometry of holes does not appreciably influence the effectiveness of film cooling (Fig. 34). In the above works the problems of film cooling under multi-slot injection conditions are considered in detail.

Figure 35 shows comparison of effectiveness of the film cooling created by injection of gas through the porous section and the slot (Mironov et al., 1981; Schetz, 1980). As is seen from Fig. 35 with the same amount of blowing gas, the effectiveness of slot injection is approximately two times higher than that for the gas injection through the porous section.

Conclusion

In this review, it is shown that gas film cooling is one of the most promising methods of thermal protection for heating surfaces in prospective energetic installations. The analysis of assumptions usually accepted in calculation of heat transfer in the presence of gas film cooling, is presented. It is shown that the heat transfer coefficient in the zone of gas film cooling can differ essentially from that found in the absence of film cooling.

1 The correlations presented for the effectiveness of gas film cooling make it possible to take into account the influence of the arrangement of film cooling, the longitudinal pressure gradient,

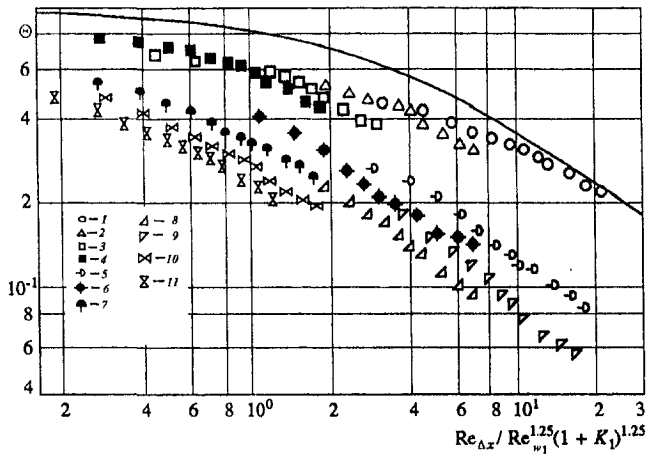

Fig. 32 Transpiration film cooling effectiveness for a strongly turbulized flow on a longitudinally streamed cylinder. Solid curve–Eq. (27). Experimental data [Vasechkin (1986)]:

Designation	1	2	3	4	5	6	7	8	9	10	11
$Tu_{\Delta x}$		0.006			0.13–0.095			0.17–0.13			
$\bar{j}_w$	0.007	0.016	0.032	0.048	0.007	0.015	0.044	0.007	0.015	0.045	0.063

nonisothermality and compressibility, swirling of the flow, roughness of the surface, and turbulence of the main flow. For confirmation of the proposed dependences, comparison with experimental data from various researchers is conducted. This allows recommendation of these correlations for engineering estimation of gas film cooling. The advantage of these formulas manifests itself in complex numerical calculations and optimization for designs of power installations, when the calculation of cooling systems is only a small part of a complex program or code.

2 To determine heat transfer coefficients in the presence of gas film cooling, it is proposed that we use the law of heat transfer, in which the energy displacement thickness is in excess to that on an insulated wall.

3 In calculation of film cooling for particular devices, it is necessary to solve a conjugate problem, taking into account the thermal resistance of walls, boundary layers on the side of cooling gas, and longitudinal heat conductance along the wall. A longitudinal thermal conductivity of the wall can influence considerably the value of heat flux to a cooled wall; however, calculation of this effect does not cause difficulties.

4 As compared to other methods, transpiration cooling is the most effective, and makes it possible to obtain required wall temperatures with minimal discharge of coolant. However, use of transpiration cooling is connected with several basic thermophysi-

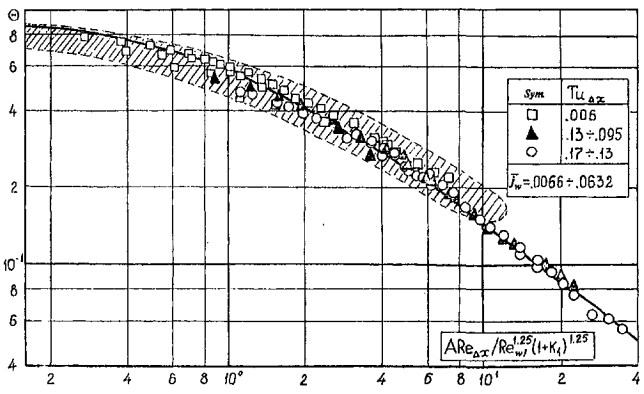

Fig. 33 Generalization of experimental distributions on Fig. 32 with the help of dependence Eq. (114). Shaded area–experimental data [Vasechkin (1986)] on a plate at l_p = 138 mm and 276 mm and $Tu_{\Delta x}$ = 0.08–0.091.

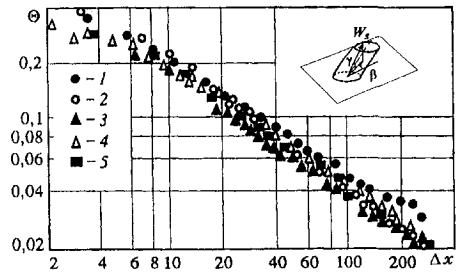

Fig. 34 Comparison of effectiveness of thermal protection of adiabatic flat plate for continuous slot and punched "belt" at injection coefficient $\bar{j}_s$ = 0.117. 1–continuous slot for γ = 30 deg; 2–continuous slot for γ = 90 deg; 3–two rows of round holes for γ = 90 deg; 4–two rows of round holes for γ = 30 deg and β = 0 deg; 5–two rows of round holes for γ = 30 deg and β = +90 deg.

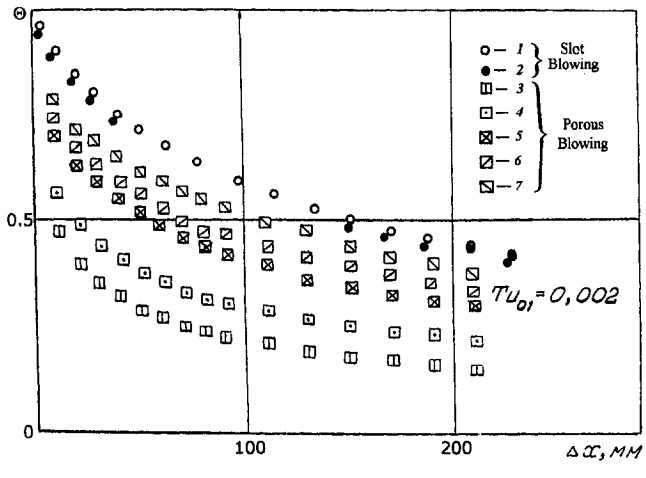

Fig. 35 Comparison of experimental distribution of film cooling effectiveness along protected zone for gas injection through porous section and slot, l_p = 138 mm and G_c = var. Experimental data [Vasechkin (1986)]. 1, 2: slot blowing; 1–G_c = 6.56 g/s, $\bar{M} = W_s/W_0$ = 1.51; 2–G_c = 4.68 g/s, $\bar{M} = W_s/W_0$ = 1.02; 3–7: porous blowing; 3–G_c = 2.43 g/s, $\bar{j}_w$ = 0.0062; 4–G_c = 4.59 g/s, $\bar{j}_w$ = 0.0115; 5–G_c = 7.03 g/s, $\bar{j}_w$ = 0.018; 6–G_c = 9.53 g/s, $\bar{j}_w$ = 0.024; 7–G_c = 14.35 g/s, $\bar{j}_w$ = 0.035.

cal and technological problems, which require special consideration.

5 For application of film cooling for gas turbines blades, it is necessary to take into account an increase in profile losses due to film cooling effects. The increase in the profile losses as compared to smooth, impermeable blades, is caused by the combined effects of injection and roughness.

6 The effectiveness of film cooling is more optimal when a cooling gas is injected through a slot rather than blowing the gas through a porous section, and the influence of velocity pulsation of the main flow on the effectiveness of gas film cooling in case of slot injection is less than for injection of gas through porous section.

Acknowledgment

The author appreciates Dr. N. V. Medvetskaya and Mrs. R. S. Gromadskaya for their very fruitful help in preparing this paper.

References

Andreev, K. D., Arseniev, L. V., and Polishchuk, V. G., et al., 1998, "Design of System of Cooling of Nozzle Vane of Gas Turbine for Driving GTI," *Heat Transfer 1998, Proceedings of 11th IHTC,* Vol. 6, Taylor and Francis, London, pp. 481–490.

Baryshev, Yu. V., Vinogradov, Yu. A., Leontiev, A. I., et al., 1972, "Recovery Coefficients on a Permeable Surface and in the Region of Gas Film Cooling in the Supersonic Turbulent Boundary Layer," *Mechanika Zhidkosti i Gaza,* pp. 131–136 (in Russian).

Baryshev, Yu. V., Leontiev, A. I., and Peiker, N. K., 1976, "Turbulent Boundary Layer on a Permeable Surface with Intensive Blowing," *Inzhenerno-Fizichesky Zhurnal,* Vol. 30, No. 5, pp. 773–779 (in Russian).

Bergles, G., Gosman, A., and Launder, B. E., 1977, "Near Field Character of a Jet Discharged through Wall at 30° to a Main Stream," *AIAA Journal,* Vol. 15, No. 4.

Carlson, N. M., and Talmor, E., 1968, "Gaseous Film Cooling at Various Degree of Hot-Gas Acceleration and Turbulence Levels," *Int. J. Heat and Mass Transfer,* Vol. 11, No. 11, pp. 1695–1713.

Chanay, G., Comte-Bellot, G., and Mathieu, J., 1976, "Development of a Turbulent Boundary Layer to Random Fluctuations in the External Stream," *Phys. Fluids,* Vol. 19, No. 9, pp. 1261–1272.

Cho, H. H., Kim, B. G., and Rhee, D. H., 1998, "Effects of Hole Geometry on Heat (Mass) Transfer and Film Cooling Effectiveness," *Heat Transfer 1998, Proceedings of the 11th IHTC,* Vol. 6, Taylor and Francis, London, pp. 499–504.

Eckert, E. R. G., and Cho, H. H., 1994, "Transition from transpiration to film cooling," *Int. J. Heat and Mass Transfer,* Vol. 37, Sup. 1, pp. 3–8.

Eckert, E. R. G., and Drake, R. M., 1972, *Analysis of Heat Transfer,* McGraw-Hill, New York.

Garg, V. K., 1999, "Heat Transfer on A Film-Cold Rotating Blade Using Different Turbulence Models," *Int. J. Heat and Mass Transfer,* Vol. 42, No. 5, pp. 789–802.

Garg, V. K., and Gaugler, R. E., 1997, "Effect of Coolant Temperature And Mass Flow on Film Cooling Of Turbine Blades," *Int. J. Heat and Mass Transfer,* Vol. 40, No. 2, pp. 435–443.

Goldstein, R. J., 1971, "Film Cooling," *Advances in Heat Transfer,* Irvine T. F. and J. P. Hartnett, eds., Vol. 7, Academic Press, New York, pp. 321–379.

Goldstein, R. J., Eckert, E. R., and Ramsey, J. W., 1968, "Film Cooling with Injection through Holes: Adiabatic Wall Temperatures Downstream of a Circular Hole," ASME *Journal of Engineering for Gas Turbines and Power,* Vol. 90, pp. 384–395.

Goldstein, R. G., Eckert, E. R. G., and Wilson, D. J., 1968, "Film Cooling with Normal Injection into a Supersonic Flow," *Transactions of the ASME,* Ser. B, Vol. 90, No. 4, pp. 584–589.

Goldstein, R. G., Rask, R. B., and Eckert, E. R. G., 1966, "Film Cooling with Helium Injection into an Incompressible Air Flow," *Int. J. Heat and Mass Transfer,* Vol. 9, pp. 1341–1350.

Goldstein, R. G., Shavit, G., and Chen, T. S., 1965, "Film-Cooling Effectiveness with Injection through a Porous Section," *Transactions of the ASME,* Ser. G, Vol. 87, No. 3, pp. 353–363.

Golovanov, A. V., Zeigarnik, Yu. A., and Polyakov, A. F. et al., 1996, "The Comparative Effectiveness of Steam and Air Cooled Gas Turbine Blades," *Thermal Engineering,* Vol. 43, No. 10, pp. 846–851.

Green, J. E., 1973, "On the Influence of Free Stream Turbulence on a Turbulent Boundary Layer, as it Relates to Wind Tunnel Testing at Subsonic Speeds," AGARD Report, No. 602, pp. 36–43.

Hacker, D. S., 1956, "Empirical Prediction of Turbulent Boundary Layer Instability along a Flat Plate with Constant Mass Addition at the Wall," *Jet Propulsion,* Vol. 26, No. 9.

Hartnett, J. P., 1985, "Mass Transfer Cooling," *Handbook of Heat Transfer Applications,* Editors: W. M. Rohsenow, J. P. Hartnett, and E. N. Ganic, eds., McGraw-Hill, New York, pp. 1–111.

Hartnett, J. P., Birkebak, R. C., and Eckert, E. R. G., 1961, "Velocity Distributions, Temperature Distributions, Effectiveness and Heat Transfer for Air Injected through a Tangential Slot into a Turbulent Boundary Layer," ASME JOURNAL OF HEAT TRANSFER, Vol. 83, pp. 293–306.

Ito, S., Goldstein, R. J., and Eckert, E. R. G., 1978, "Film Cooling of a Gas Turbine," ASME *Journal of Engineering for Gas Turbines and Power,* Vol. 100, pp. 476.

Jakob, Max, 1957, *Heat Transfer,* John Wiley and Sons, New York, p. 516.

Kays, W. M., and Crawford, M. E., 1987, *Convective Heat and Mass Transfer,* 3rd Ed., McGraw-Hill, New York, p. 600.

Ko, Shao-Yen, Liu, Deng-Ying, Xu, Jing-Zhong, and Li, Jing, 1985, *Film Cooling,* Science Press, Beijing, pp. 276–297.

Komarov, V. P., and Leontiev, A. I., 1970, "Experimental Investigation of the Effectiveness of Gas Film Cooling in the Turbulent Boundary Layer," *Teplofizika Vysokih Temperature,* Vol. 8, No. 2, pp. 353–358 (in Russian).

Komarov, V. P., Leontiev, A. I., Okolito, L. A. et al., 1982, "Investigation of the Effectiveness of Gas Film Cooling on a Rough Surface," *Inzhenerno-Fizichesky Zhurnal,* Vol. 13, No. 6, pp. 855–892 (in Russian).

Kopelev, S. Z., 1984, *Projecting Turbine Flowing Part of Aircraft Gas-Turbine Engine,* Moscow, p. 225 (in Russian).

Kutateladze, S. S., and Leontiev, A. I., 1963, "Film Cooling in Turbulent Boundary Layer in Gas," *Teplofizika Vysokih Temperatur,* Vol. 1, No. 2, pp. 281–290 (in Russian).

Kutateladze, S. S., and Leontiev, A. I., 1990, *Heat Transfer, Mass Transfer and Friction in Turbulent Boundary Layers,* Hemisphere, New York, p. 305.

Lebedev, V. P., Lemanov, V. V., Misyura, Y. A., and Terekhov, V. I., 1995, "Effects of Flow Turbulence on Film Cooling Effectiveness," *Int. J. Heat and Mass Transfer,* Vol. 38, No. 11, p. 2117.

Lebedev, V. P., Lemanov, V. V., and Terekhov, V. I., 1999, "Heat Transfer in a Wall Jet at High Turbulence of Cocurrent Stream," *Int. J. Heat and Mass Transfer,* Vol. 42, No. 4, pp. 599–612.

Leontiev, A. I., 1993a, "Perspectives of Porous Cooling: Application for Gas Turbine," *The 6th International Symposium on Transport Phenomena in Thermal Engineering,* Vol. II, May 9–13, Seoul, Korea, Taylor and Francis, London, pp. 39–48.

Leontiev, A. I., 1993b, "The Method of Calculation of Cooling of the Gas-Turbine Blades," *Izvestiya Akademie Nauk, Energetika,* No. 6, pp. 85–92 (in Russian).

Leontiev, A. I., 1966, "Heat and Mass Transfer in Turbulent Boundary Layers," *Advanced in Heat Transfer,* Editors: T. F. Irvine and J. P. Hartnett, eds., Vol. 3, Academic Press, New York, pp. 33–100.

Leontiev, A. I., and Epifanov, V. M., 1992, "Heat Mass Transfer and Hydrodynamics of Flow of Transpiration Cooled Gas Turbines," *Heat Transfer in Turbomachinery, Proceedings of the International Symposium on Heat Transfer in Turbomachinery,* Aug. 24–28, Athens, Greece, Begell House, New York.

Leontiev, A. I., and Polyakov, A. F., 1998, "The Conditions of Convective Heat Transfer on Porous Permeable Wall," *Izvestia RAN, Seria "Energetika,"* No. 6, p. 120 (in Russian).

Leontiev, A. I., Puzach, V. G., and Puzach, S. V., 1997, "Features of Thermal Permeable Wall Streamlined of High Temperature Gas Flow," *Izvestiya Akademie Nauk, Seria "Energetica,"* No. 2 (in Russian).

Leontiev, A. I., Volchkov, E. P., and Lebedev, V. P. et al., 1995, *Thermal Protection of Plasma Generator Walls,* Institute Thermophysics of SB of RAS, Novosibirsk, p. 335 (in Russian).

Librizzi, I., and Cressi, R. J., 1964, "Transpiration Cooling of a Turbulent Boundary Layer in an Axisymmetric Nozzle," *AIAA J.,* No. 2, p. 617.

Ligrani, P. M., Gong, R., and Cuthrell, J. M., et al., 1996, "Bulk Flow Pulsations and Film Cooling–II. Flow Structure and Film Effectiveness," *Int. J. Heat and Mass Transfer,* Vol. 39, No. 11, pp. 2283–2292.

Metzger, D. E., Kim, Y. W., and Yu, Y., 1993, "Turbine cooling: An overview and some focus topics," *The 6th International Symposium on Transport Phenomena (JSTP-6) in Thermal Engineering,* Vol. II, May 9–13, Seoul, Korea, pp. 49–60.

Mironov, B. P., Vasechkin, V. N., and Yarygina, N. I., et al., 1981, "Heat and Mass Transfer at High Free Stream Turbulence as a Function of Injection Rate," *Heat Transfer–Soviet Research,* Vol. 13, No. 5, pp. 54–65.

Motulevich, V. P., Sergievsky, E. D., and Yanovsky, L. S., 1981, "Influence Direction of Injection on Coefficient of Turbulent Skin Friction," *Heat Transfer Problems, Proceedings of Moscow Forest Engineering Institute,* Sup. 138, MFEI, pp. 104–113 (in Russian).

Osipov, M. I., 1994, "Efficiency of Film Cooling with Influence of Surface Roughness," *Heat Transfer 1994, Proceedings of 10th Int. Heat Transfer Conference,* Vol. 3, Taylor and Francis, London, pp. 95–99.

Pichal, M., 1972, "Lie turbulente Grenzschicht bei hochturbulenten Aubenstromung," *ZAMM,* Vol. 52, No. 10, pp. 407–416.

Polezhaev, Yu. V., 1997, "The Transpiration Cooling for Blades of High Temperatures Gas Turbine," *Energy Convers. Mgmt,* Vol. 38, No. 1013, pp. 1123–1133.

Romanenko, P. N., and Voloshchuk, A. Ya, 1970, "Effectiveness of Film Cooling with Gas Injection in Turbulent Boundary Layer through a Porous Section," *Teplofizika Vysokih Temperatur,* Vol. 8, No. 5, pp. 1025–1031 (in Russian).

Repukhov, V. M., 1998, "Thermal Protection and Effectiveness of Air-Water Film Cooling under Tangential and Normal Injection," *Proceeding of 2nd Russian Heat Transfer Conference,* Vol. 5, Oct. 26–30, Moscow, pp. 89–92 (in Russian).

Schetz, I. A., 1980, "Injection and Mixing in Turbulent Flow," *AIAA Journal,* Vol. 18, No. 5.

Seo, H. J., Lee, J. S., and Ligrani, P. M., 1998, "The Effect of Injection Hole Length on Film Cooling with Bulk Flow Pulsations," *Int. J. Heat and Mass Transfer,* Vol. 41, No. 22, pp. 3515–3528.

Tollmien, W., 1926, "Berechnung der turbulenten Ausbreitungsvorgange," *ZAMM,* Bd. IV, p. 468.

Vasechkin, V. N., 1986, "Influence of Hydrodynamic and Thermal Development of Boundary Layer on Heat Transfer at Different Level of Free Stream Turbulence," Ph.D. thesis, Institute of Thermophysics, Novosibirsk, p. 250.

Vinogradov, Yu. A., Ermolaev, I. K., and Leontiev, A. I., 1997, "Coefficients of Recovery and Efficiency of the Gas Curtain Injection of Gas through a Porous Disc," *High Temperatures,* Vol. 35, No. 6, pp. 1005–1008.

Volchkov, E. P., 1983, *Wall Gas Film Cooling,* Nauka, Novosiborsk, p. 259 (in Russian).

Volchkov, E. P., Lebedev, V. P., and Nizovtsev, M. I. et al., 1995, "Heat Transfer in a Channel with a Counter-Current Wall Injection," *Int. J. Heat and Mass Transfer,* Vol. 38, No. 14, pp. 2677–2687.

Volchkov, E. P., and Levchenko, V. Ya., 1965, "Effectiveness of gas film cooling in the turbulent boundary layer," *Prikl. Mech. I Tekh. Fiz.,* No. 5, pp. 142–146 (in Russian).

Wieghard, K., 1944, "Uber die turbulente Stromung im Rohr und langs der Platte," *ZAMM,* Vol. 24, pp. 294–303.

A Phase-Sensitive Technique for the Thermal Characterization of Dielectric Thin Films

S. W. Indermuehle
e-mail: indermuehles@asme.org

R. B. Peterson[1]
Associate Professor,
e-mail: Richard.Peterson@orst.edu
Assoc. Mem. ASME

Department of Mechanical Engineering,
Oregon State University,
Rogers Hall 204,
Corvallis, OR 97331

A phase-sensitive measurement technique for determining two independent thermal properties of a thin dielectric film is presented. The technique involves measuring a specimen's front surface temperature response to a periodic heating signal over a range of frequencies. The phase shift of the temperature response is fit to an analytical model using thermal diffusivity and effusivity as fitting parameters, from which the thermal conductivity and specific heat can be calculated. The method has been applied to 1.72-μm thick films of SiO_2 thermally grown on a silicon substrate. Thermal properties were obtained through a temperature range from 25°C to 300°C. One interesting outcome stemming from analysis of the experimental data is the ability to extract both thermal conductivity and specific heat of a thin film from phase information alone. The properties obtained with this method are slightly below the bulk values for fused silica with a measured room temperature (25°C) thermal conductivity of 1.28 ± 0.12 W/m-K.

Introduction

Many technologically important microstructures for microelectromechanical systems (MEMS) are often fabricated in a layered fashion. Thin films comprise the material for these microstructures, and devices fabricated with a particular film material can exhibit novel functionality and performance characteristics that depend on the film type used. Both mechanical and thermal properties are of interest. However, the latter category is especially important where microdevice operation is thermally based such as heat transfer in microchannel arrays, thermal sensor operation, and heat dissipation from integrated microelectronic components. A necessary first step in understanding the thermal response of these systems is obtaining accurate values for the thermal conductivity and specific heat. However, obtaining reliable thermal properties for thin films can be challenging due to the small dimensions involved.

A variety of measurement techniques have been developed for determining thin film properties. Lambropoulos et al. (1989, 1992) have given a thorough review of various techniques and have shown the effect of different variables on the thermal properties of dielectric materials. Cahill et al. (1989) also presented several methods that are applicable to thin film property measurement over a range of thicknesses. DeVecchio et al. (1995) developed a phase-sensitive technique for determining the thermal diffusivity of highly conductive samples where periodic heating was applied to one side of the sample and the temperature response was measured at the other. Chen and Tien (1993) presented a phase-sensitive method that allowed for diffusivity measurements in both the perpendicular and parallel directions to a sample's surface. Zhang and Grigoropoulos (1995) used silicon nitride films to demonstrate phase, amplitude, and heat pulse methods. A 3ω/ decay technique where thermal diffusivity and effusivity can both be determined has been studied by Frank et al. (1993). The technique involved using phase data to determine diffusivity while a thermal decay method, applied separately after phase measurements, yielded effusivity. Ju et al. (1998) have demonstrated a periodic surface heating method where optical thermometry was used to detect the magnitude of the front surface temperature signal. The method was applied to SiO_2 and polymeric films. Several techniques that involve the extraction of thermal information from a photoacoustic signal have also been described in the literature (Rosencwaig and Gersho, 1976; Bennett and Patty, 1982; Charpentier et al., 1982; Lachaine and Poulet, 1984; Swimm, 1983).

This paper describes a new phase-sensitive technique that allows the simultaneous determination of thermal diffusivity and effusivity (and hence, thermal conductivity and specific heat) for a dielectric thin film. The technique involves measuring the phase difference between a specimen's front surface temperature response and a periodic heating signal. To analyze the experimental data, an analytical expression is developed for the temperature response that includes the thermal properties of the substrate and thin film. The technique has been validated using 1.72-μm thick films of SiO_2 thermally grown on a silicon substrate.

Theory

Two analytical models are developed in this section, both of which contain a periodic boundary condition that drives heat conduction. Each model is based on a rectilinear coordinate system where the temperature response is sought at the same location that the periodic boundary condition is applied, namely at $x = 0$. One-dimensional conduction is assumed with heat flow perpendicular to the surface exposed to heating. With no energy generation within the domain and assuming constant thermal properties, the governing differential equation becomes

$$\frac{\partial^2 T}{\partial x^2} = \frac{1}{\alpha}\frac{\partial T}{\partial \theta} \tag{1}$$

where x is the spatial coordinate, θ is the time coordinate, and temperature is given by T. Other quantities can be found in the Nomenclature. The use of Eq. (1) assumes a continuum model for the analysis. In the work presented here, the film thickness is greater than one micron. Using the thermal properties for bulk SiO_2, a simplified analysis gives a phonon mean-free path of less than a nanometer thus validating the use of the continuum approach.

[1] To whom correspondence should be addressed.

Contributed by the Heat Transfer Division for publication in the JOURNAL OF HEAT TRANSFER. Manuscript received by the Heat Transfer Division, Aug. 5, 1998; revision received, Feb. 1, 1999. Keywords: Heat Transfer, Measurement Techniques, Periodic, Properties, Thin Films. Associate Technical Editor: A. Majumdar.

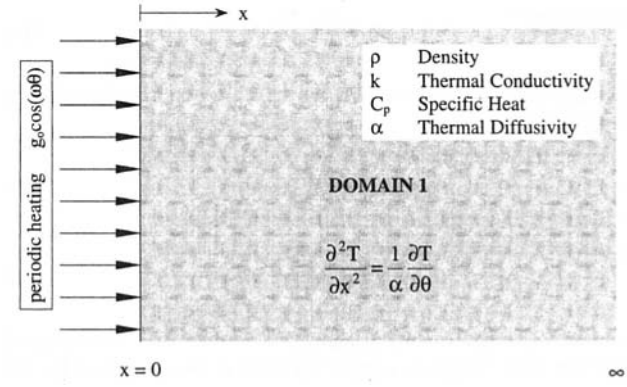

Fig. 1 Analytical domain of the one-dimensional heat conduction model for the reference

There are numerous techniques available for solving Eq. (1). When a periodic boundary condition is present, analysis commonly results in a periodic solution summed with a transient solution that decays to zero with time. If the "transient" part of the complete solution is of no interest, the problem can be solved by a method known as complex combination (Arpaci, 1966; Meyers, 1971). The details of this method will not be given here, but the method is used to obtain analytical results for both models presented in this section. Note that the resulting solution for the temperature distribution $T(x, \theta)$ will not be a truly steady-state solution, but pseudo-steady-state due to its periodicity.

The first model examines a semi-infinite domain whose front surface is exposed to periodic heating. The physical situation being modeled is that of I^2R heating imposed on the surface of a fused silica substrate. In actuality, two layers exist: a thin metal film heater (nichrome) and the thick substrate. However, because the film heater is very thin (50 nm) and its thermal conductivity is large compared to that of the substrate, its physical dimensions are neglected in the analytical model. Also, the substrate is assumed thermally thick. Thus, periodic heating at the front surface is not expected to produce a periodic response at the back. Results of this model are used later to correct sample data obtained in the experiment.

The second model examines a two-layered structure, also with its front surface exposed to periodic heating. In this model, the top layer represents the thin film under study and the back layer is the substrate. The latter is considered thermally thick, again permitting the use of a semi-infinite domain in the model.

Single-Domain Model. Figure 1 shows the analytical domain used for developing the first model. As stated previously, one-dimensional conduction with constant properties and zero energy generation is assumed for the analysis. As periodic heating is applied to the front surface, the solid is expected to reach a "baseline," or mean temperature upon which the periodic response will fluctuate. For simplicity, the mean temperature and initial temperature are considered equal and are given a value of zero. Mathematically, the initial condition is stated as $T(x, 0) = 0$. The periodic heat source at the front surface ($x = 0$) is expressed as a boundary condition of the form

$$q''(0, \theta) = -k \left.\frac{\partial T}{\partial x}\right|_{x=0} = g_0 \cos(\omega\theta) \tag{2}$$

where ω represents the angular frequency ($\omega = 2\pi f$) of the heating signal and g_0 is the amplitude. The second boundary condition is imposed at a position far removed from the periodic heat source where the thermal waves traveling through the solid are completely dampened, thus

$$T(x \to \infty, \theta) = 0. \tag{3}$$

As stated previously, the method of complex combination is used as a solution technique yielding

$$T(x, \theta) = \frac{g_0}{k}\sqrt{\frac{\alpha}{\omega}}\, e^{-\sqrt{\omega/2\alpha}x} \cos\left(\omega\theta - \sqrt{\frac{\omega}{2\alpha}}\, x - \frac{\pi}{4}\right). \tag{4}$$

A few key points are evident in this solution. First of all, the amplitude of the temperature response at the front surface is not only a function of surface heating strength, but also of two material properties and heating frequency. As expected, the amplitude of the temperature response decreases with increasing frequency and also decays with depth from the front surface. Of more importance is the phase shift between the periodic temperature response and heating signal. Phase shift within the solid is dependent on heating frequency and material properties. However, it reduces to a constant value at the front surface. Because the front surface-temperature response is desired, only the solution at $x = 0$ is of interest,

$$T(0, \theta) = \frac{g_0}{k}\sqrt{\frac{\alpha}{\omega}} \cos\left(\omega\theta - \frac{\pi}{4}\right). \tag{5}$$

Equation (5) clearly shows that for a one-dimensional semi-infinite region exposed to periodic heating, the temperature response at the front surface will lag the heating signal by a value of 45 deg, regardless of material properties and heating frequency.

Two-Domain Model. The analytical domains used for developing the second model are shown in Fig. 2. Domain 1 is the thin film and domain 2 is the thermally thick substrate. To produce periodic heating, a thin metal strip is physically present at the front surface. This gives a situation in which three layers actually exist. However, because the metal strip is very thin (50 nm) and highly conductive compared to the thin film, it is neglected in the analytical model. Furthermore, in addition to the conditions assumed for the one-domain model, the thermal properties of the film are assumed isotropic. If significant anisotropic behavior is present in thermally grown SiO_2 films, then the thermal conductivity results reported here would have to be considered effective values normal to the plane of the thin film.

The conduction problem represented by this model requires writing Eq. (1) for each domain, yielding a piecewise continuous solution. Two boundary conditions and one initial condition must accompany each of the equations in order to describe the physical

Nomenclature

C_p = specific heat, J/kg K
e_1 = film effusivity, W $s^{1/2}/m^2$ K
e_2 = substrate effusivity, W $s^{1/2}/m^2$ K
E = simplification variable
f = frequency of heat source, Hz
g_0 = amplitude of heat source, W/m^2
I = electrical current, Amp
k = thermal conductivity, W/m K
L = film thickness, m
MAG = amplitude of temperature response, K
q'' = flux of periodic heat source, W/m^2
R = electrical resistance, Ω
T = temperature, K
x = spatial coordinate, m

Greek Symbols

α = thermal diffusivity, m^2/s
ρ = mass density, kg/m^3
θ = time coordinate, sec
ω = angular heating frequency, rad/s
ϕ = phase shift, rad
Γ = simplification variable

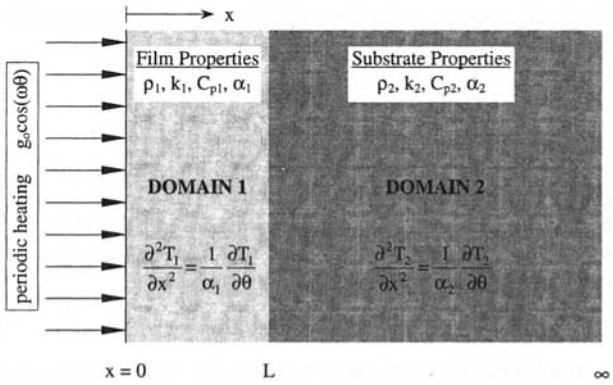

Fig. 2 Analytical domain of the one-dimensional heat conduction model for the layered sample

situation in full. Similar to the previous model, initial conditions state that temperature is equal to zero throughout both regions prior to heating,

$$T_1(x, 0) = 0 \tag{6}$$

$$T_2(x, 0) = 0. \tag{7}$$

A periodic heat flux is imposed at $x = 0$. This boundary condition is stated mathematically as

$$q''(0, \theta) = -k_1 \left.\frac{\partial T_1}{\partial x}\right|_{x=0} = g_0 \cos(\omega\theta). \tag{8}$$

The second boundary condition is at $x = L$. By using energy considerations at this location it is apparent that the heat flux leaving the back surface of domain 1 must equal the heat flux entering the front surface of domain 2, thus,

$$-k_1 \left.\frac{\partial T_1}{\partial x}\right|_{x=L} = -k_2 \left.\frac{\partial T_2}{\partial x}\right|_{x=L}. \tag{9}$$

Next, it is assumed that superior thermal contact exists between the domains. If thermal resistance is neglected then a temperature drop will not exist across the interface, giving

$$T_1(L, \theta) = T_2(L, \theta). \tag{10}$$

Finally, as the spatial coordinate (x) increases to values much larger than L, the magnitude of the periodic temperature response decreases. For very large values of x, the thermal wave will be completely dampened such that

$$T_2(x \to \infty, \theta) = 0. \tag{11}$$

Again, the method of complex combination is used for solving the equations. The pseudo-steady-state solution for the temperature response at $x = 0$ is placed in the simplified form of

$$T_1(0, \theta) = \text{MAG} \cdot \cos(\omega\theta + \phi) \tag{12}$$

where the amplitude and phase shift are expressed as

$$\text{MAG} = \frac{g_0}{e_1\sqrt{\omega}}\left(\frac{\sqrt{(1 - e^{-2\Gamma}E^2)^2 + 4E^2e^{-2\Gamma}\sin^2(\Gamma)}}{1 + e^{-2\Gamma}E^2 + 2Ee^{-\Gamma}\cos(\Gamma)}\right) \tag{13}$$

$$\phi = \text{atan}\left(-\frac{1 - e^{-2\Gamma}E^2 - 2Ee^{-\Gamma}\sin(\Gamma)}{1 - e^{-2\Gamma}E^2 + 2Ee^{-\Gamma}\sin(\Gamma)}\right). \tag{14}$$

In the above expressions, Γ and E are used for simplifying the equations. They have the functional form of

$$\Gamma = \sqrt{\frac{2\omega}{\alpha_1}}L \tag{15}$$

$$E = \frac{e_2 - e_1}{e_2 + e_1}. \tag{16}$$

Also, the effusivities of the film and substrate found in Eq. (16) are defined as

$$e_1 = \sqrt{k_1\rho_1C_{p1}} = \frac{k_1}{\sqrt{\alpha_1}} \tag{17}$$

$$e_2 = \sqrt{k_2\rho_2C_{p2}} = \frac{k_2}{\sqrt{\alpha_2}}. \tag{18}$$

Note that the phase shift at the front surface of a multilayered structure is no longer a simple constant as was the case for the single domain exposed to periodic surface heating.

Curve Fitting. The second model gives the phase shift in terms of five different quantities, three of which are embedded in the expression for Γ and two in the relationship for E. Of these five variables, three are considered known; the frequency of the periodic heat source (ω), the film thickness (L), and the effusivity of the silicon substrate (e_2). This leaves the film's effusivity (e_1) and diffusivity (α_1) as unknown thermal properties. Once these two independent properties are obtained, the thermal conductivity and specific heat of the thin film can readily be determined.

Before the curve-fitting process can begin, accurate thermal property data for the silicon substrate are required in order to utilize Eq. (18). A literature survey yielded values with up to ten percent uncertainty for the thermal conductivity of silicon (Glassbrenner and Slack, 1964; Touloukian et al., 1970a). Possible contributors to this uncertainty are doping level and property measurement technique. It is known that the silicon substrate used in this study is of n type, lightly doped with phosphorus (10^{15}/cm^3). This material has not been "well" characterized thermally; however, its properties are not expected to vary significantly from those for high-purity silicon. Therefore, both thermal conductivity and specific heat for high-purity single-crystal silicon are used in the effusivity calculations (Touloukian et al., 1970a; Touloukian and Buyco, 1970). For density, a constant value of $\rho_2 = 2330$ kg/m^3 is chosen.

From an examination of Eq. (14), the phase shift is clearly dependent upon the two parameters Γ and E. Through Eqs. (15) and (16), these two parameters are in turn dependent on α_1 and e_1 (the other terms in Γ and E are assumed known). Thus, the fitting process uses phase-shift data recorded over a range of frequencies to find a unique pair of values for α_1 and e_1 from which the thin-film thermal conductivity and specific heat can be determined. Nonlinear regression analysis software, available in a commercial package, was used to perform the fits. The package used the Marquardt-Levenberg algorithm for finding the best fit to each data set. Best fit was defined as a minimization of the sum of the squared differences between the observed and predicted data.

In order to use the fitting routine, absolute phase shift data are needed. However, the experimental data varies significantly from values predicted by the analytical model due to nonideal system behavior. One contributor is the physical thickness of the nichrome heating strip. Contributions here are thought small, mainly because of the small relative thickness and high thermal conductivity of nichrome compared to the SiO_2 film. Experimentally, heating-strip thicknesses of 50 and 100 nm have been studied with no apparent differences in the results. A more pronounced contribution comes from the finite response time of the measurement circuitry. This leads to increasing phase shifts with increasing frequency. This effect can be compensated for by using phase data from measurements on a reference as a means for producing absolute sample-phase data. To accomplish this, phase data collected for the reference substrate exhibits greater phase lags than the constant -45 deg predicted by Eq. (5). This excess phase lag (the difference between the measured phase and -45 deg) is used as an indicator of the response time of the electronic circuitry. It is frequency

dependent and assumed to be equally present in the data for both the reference and test sample. In the tests described in the following, the reference substrate was fused silica. One other substrate material (borosilicate glass) has been studied as a reference standard. Compared to fused silica, it gave similar phase-shift corrections.

The results of the curve fitting process was the thermal diffusivity and effusivity of the thin film. Once these properties are available, the specific heat is determined with

$$C_{p1} = \frac{e_1}{\rho_1 \sqrt{\alpha_1}}. \tag{19}$$

A density of $\rho_1 = 2220$ kg/m^3 is used for the thin film, corresponding to that of bulk SiO_2. The density of the film is expected to be lower than that of the bulk material, but in most cases only by a few percent (Decker et al., 1984). Therefore, the use of bulk values is thought to be sufficient for this work. With the specific heat, the thermal conductivity is easily calculated using

$$k_1 = \rho_1 \alpha_1 C_{p1}. \tag{20}$$

Experimental Method

The procedure described above requires absolute phase shift data as a function of frequency. In order to collect this data, a method was developed to detect and measure relative temperature variations having peak-to-peak amplitudes in the milli-Kelvin range. The following provides a detailed description of the apparatus.

Apparatus. The experimental configuration is shown in Fig. 3 and is centered about a sample emitting infrared radiation in a periodic manner as a result of rapid changes in surface temperature. The sample is mounted on a heat sink having an external bulk heater capable of providing temperatures in excess of 400°C, although only a temperature range of 25°C–300°C was studied in this work. The temperature fluctuations on the surface of the sample are produced by a thin-film nichrome strip heater.

The function generator of Fig. 3 provided the periodic voltage across the nichrome strip. Infrared emission from the strip was captured by an IR lens and was focused with a 1-to-1 imaging configuration onto the active element of an IR detector. The lens (Janos Technology Model A1200-012) was fabricated from Zinc Selenide and transmitted IR radiation between 0.63 μm and 18 μm with an efficiency near 70 percent. The IR detector (EG&G Judson Model J15D12-M204-S01M) consisted of a one-square-mm HgCdTe photoconductive element operating at 77 K. It was responsive to wavelengths between 2 μm and 10 μm. In order to sense the change in conductivity, a bias current was applied through the detector element by a pre-amplifier circuit, which also increased the signal strength by a factor of 100. The signal was then sent to a digital lock-in amplifier (Stanford Research Systems Model SR830 DSP). At the lock-in, the signal was compared with the function generator's synchronous output, which was in phase with the voltage signal applied across the nichrome heating strip. Internally, the lock-in manipulated both signals using a phase-sensitive detection scheme to produce values for magnitude and phase shift of the input signal.

Figure 4 shows the heat sink used for specimen mounting. Although only half of the sink is depicted in the figure, the entire heat sink surface was designed to accept a side-by-side placement of both the thin film sample and fused silica reference standard. For each, the substrate was placed closest to the heat sink with the nichrome layer facing outward. Both specimens were attached independently to the heat sink with stainless steel bolts and machinable ceramic mounting bars. The ceramic bars provided electrical isolation between the heat sink and the contact blocks. Leads from the function generator were attached to each contact block. The function generator supplied a periodic voltage in the form of a modified square wave having minimum and maximum values of 0 V and 10 V, respectively.

A scaled side view of the experimental apparatus is shown in Fig. 5. The heat sink was mounted onto two adjustment stages. The first was a three-axis micro-adjustment stage used to fine tune the alignment between the emitting surface, the IR lens, and the IR detector. The micro-adjustment stage was mounted directly to a macro-adjustment stage. The macro-adjustment stage was used solely for alternating between the measurement of the thin film sample and the fused silica standard. The lens system and detector also had translation capabilities for alignment purposes. The base of each component was rigidly fixed to an optical table.

Specimen Preparation. Each sample started out as a section of a 675-μm thick silicon wafer, 15.24 cm (6″) in diameter. The wafer was placed in a heated oxygen-rich environment and a 1.72-μm thick oxide layer was allowed to form. The wafer was then sliced into rectangular pieces with dimensions of 3.5 cm × 2.0 cm. The reference standards for the experiment were produced from 1-mm thick fused silica laboratory slides.

The nichrome (80 percent Nickel/20 percent Chromium) heating strip was deposited on each specimen using an e-beam evaporation process. Nichrome thicknesses of 50 and 100 nm were used in the study; however, only results for the 50-nm thick strip are reported here. No significant difference was observed between the two cases. The heating strip had a width of 2 mm and a length of 1 cm. Nichrome was concurrently deposited onto both the thin film sample and the fused silica standard in a side-by-side aluminum shadow mask fixture. Nichrome thickness was monitored continuously during deposition with a crystal oscillator. The width of the nichrome strip was chosen to minimize fringing effects in the collected IR emissions. The center of the strip was imaged with a 1-to-1 ZnSe lens configuration onto the 1 mm^2 active element of the HgCdTe detector. Thus, signals originating near the sides of the strip were rejected by the detection system.

A visual examination was performed on each specimen after completion of the deposition process. By holding the fused silica standard up to a source of white light, it was found that the 50-nm thick nichrome strip was not completely opaque to the visible spectrum. However, for IR wavelengths between 5 and 10 μm, and using a conservatively estimated extinction coefficient of 25 (the imaginary component of the complex index of refraction), a 50-nm film has a calculated IR transmittance of less than five percent. Thus the film was nearly opaque to thermal emissions originating under its surface. The e-beam deposition process produced an excellent bond at the nichrome/specimen interface. All interfacial bonds were strong enough so that the nichrome could not be removed by rubbing with a cloth or finger, but required heavy scratching in order to degrade the surface.

Technique. Recording of experimental data for determining thin film properties was straightforward. First, a specimen pair (sample/standard) was placed in the sample holder. Then, with the detector focused on the sample, phase data were recorded from 500 Hz to 20 kHz. The sample holder was then shifted to place the fused silica reference in front of the detector. The frequency sweep was repeated by recording phase data at the same frequencies, again starting at 500 Hz. As shown by Eq. (5), the phase shift for the reference should be constant at -45 deg. However, greater phase lags were observed due to the finite response time of the electronic circuitry. From the difference in predicted and measured phase lags, a phase correction was determined and applied to the sample data. The corrected values were then used in the curve-fitting routine as explained previously.

The temperature variations at the front surface were small and required a sensitive technique for signal detection and phase measurement. The electrical resistance of the nichrome film was approximately 110 Ω. With the function generator supplying a 0 to 10 V nominal square wave, the peak power dissipated was 0.909 W. However, the fundamental frequency component (for lock-in detection) to this heating signal had a corresponding g_0 (see Eq.

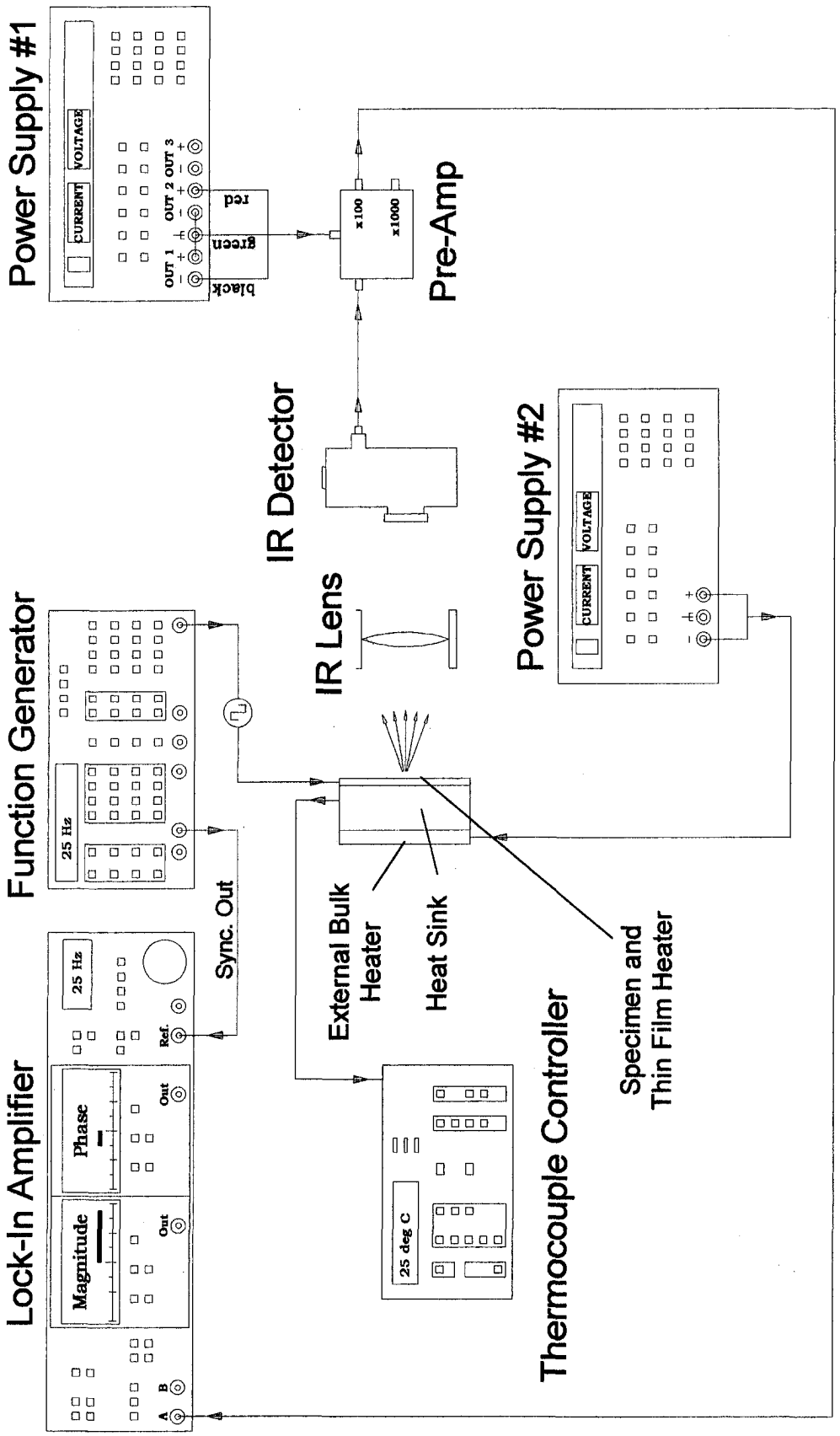

Fig. 3 Schematic diagram of the instrumentation setup for the experimental apparatus

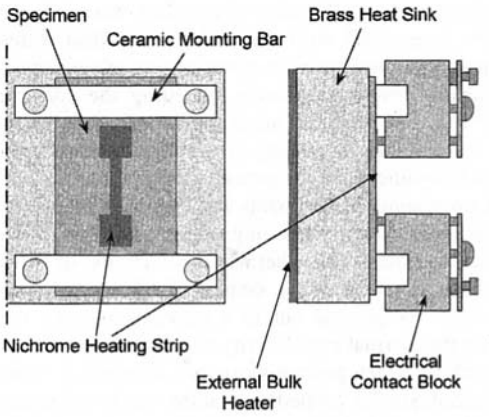

Fig. 4 Mounting arrangement for the samples

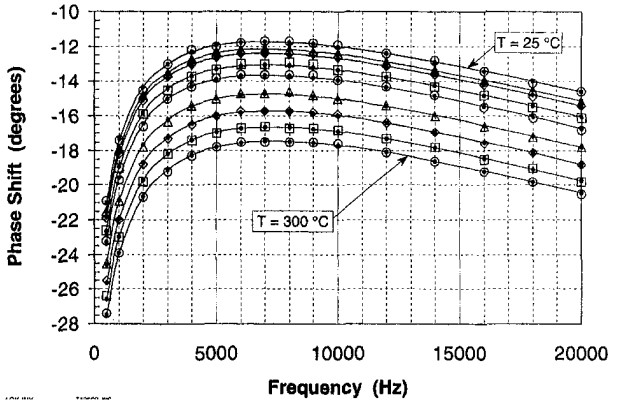

Fig. 6 Sample phase shift as a function of frequency curves at nine different temperatures. Open symbols are experimental data, solid line and small filled symbols are the analytical curve fit.

(13)) of 29,000 W/m^2. With this value, the temperature variations at the front surface of the sample had calculated magnitudes of 0.063 K and 0.038 K at 500 Hz and 20 kHz, respectively. Experimentally, a signal strength of 195 μV was measured by the lock-in amplifier at 500 Hz, and at 20 kHz the signal strength was 115 μV. These signals should be compared to the noise level of the detection system which was 42 μV/Hz$^{1/2}$ (as measured by the model SR830 lock-in amplifier) at 500 Hz and less than 3 μV/Hz$^{1/2}$ at 20 kHz. Thus, the detection scheme must be able to detect small rapid temperature signals amid substantial background noise. However, the lock-in amplifier had the capability of accomplishing this detection at the signal-to-noise ratios encountered in this experiment. It should be emphasized, however, that only qualitative detection of magnitude is needed since all quantitative information is collected in the form of phase shift data.

Results

The phase data obtained are in excellent agreement with Eq. (14) as shown by Fig. 6. The corrected phase data are shown as open symbols and the result of each curve fit is shown as a solid line. The uppermost curve represents 25°C while the lowest curve is for 300°C. Each curve corresponds to one thermal diffusivity/effusivity pair, and thus a single conductivity and specific heat. Note that small filled circles are provided on the solid line near each corrected value (open symbols) to display the analytically derived phase shift at that point. The front surface phase data rapidly increases in value at the lower frequencies, reaches a maximum at approximately 7000 Hz, and then decreases in a steady manner. If the curves were extended to much higher frequencies, a limit of −45 deg would eventually be reached.

The data at the lowest frequency shown for each curve displays a small deviation from the analytical fit. This deviation could be a result of the finite thickness of the silicon substrate. A characteristic length for determining whether the substrate is thermally thick is $\pi\mu$, where

$$\mu = \sqrt{\frac{2\alpha}{\omega}}. \tag{21}$$

This characteristic length has been derived by examining the thermal wave propagation into a semi-infinite domain and determining that the $\pi\mu$ depth gives thermal wave amplitudes that are approaching zero. At 500 Hz, the value of $\pi\mu$ for silicon is 748 μm. This is slightly larger than the 675 μm of the actual substrate. At 1000 Hz, $\pi\mu$ for silicon is 529 μm which is less than the actual substrate. Although 500 Hz is questionable for being thermally thick, it has been included in the data set for comparison purposes. Its affect on the curve fitting process is not significant in terms of changing the numerical results. Note that the rest of the fit is excellent.

The thermal conductivity and specific heat values obtained by utilizing this technique are presented in Fig. 7 and Fig. 8, respectively. The experimentally determined values are shown as open circles and the solid line of each figure represents a set of recommended values for the thermal conductivity (Touloukian, 1970b) and specific heat (Incropera, 1990) of SiO_2 in bulk form. The experimental values of thermal conductivity fall below the bulk values while the specific heat closely matches those of bulk fused silica, as expected. Table 1 also shows the results of the analysis. Included in the table are the thermal properties of silicon used to calculate the thermal effusivities required in the fitting routine.

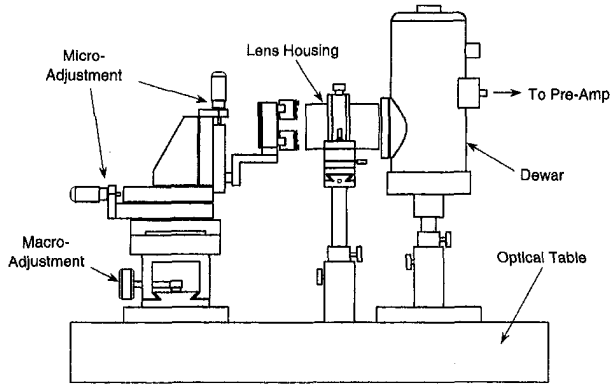

Fig. 5 Side view of the experimental apparatus showing translatable sample holder, lens holder, and IR detector

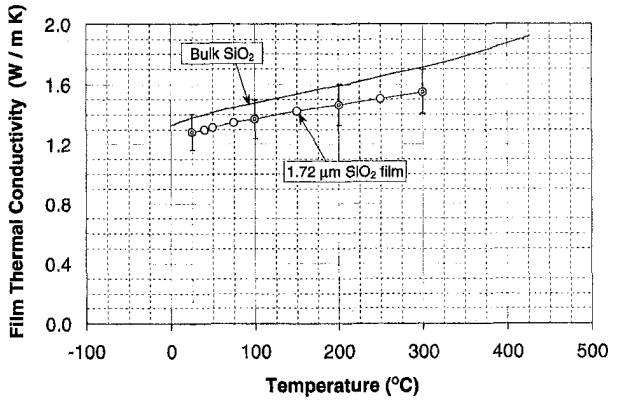

Fig. 7 Thermal conductivity of 1.72 micron-thick film and bulk SiO_2 as a function of sample temperature

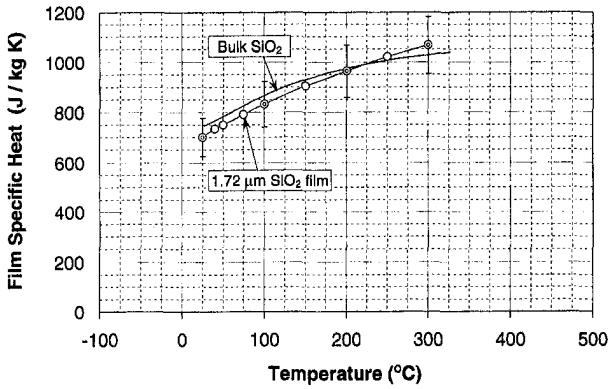

Fig. 8 SiO_2 specific heat as a function of sample temperature

Also shown are the nominal film properties that result from each fit of the experimental data to the analytical model. Uncertainty in these values is fully discussed in the following section.

Uncertainty Analysis. It is recognized that uncertainty exists within several elements of this measurement technique, and that the uncertainty associated with a single-system element will propagate toward uncertainty in the resulting thin film thermal properties. To place an estimate on how far the thermal conductivity and specific heat might differ from the "nominal" values as a result of uncertainty, two situations were investigated. First, uncertainty in the experimentally derived data was examined. Then, uncertainty associated with each variable used in the fitting routine was studied. The film properties found by applying the nominal values of silicon in the fitting routine were used as a baseline for comparison. All uncertainties in the following development should be viewed as an estimate of the 95 percent confidence level. That is, a 1 in 20 chance exists for a measured value to fall outside the given uncertainty range.

As with data obtained by any measurement system, uncertainty is inherent in the recorded phase data. The phase shift at the lock-in output is not expected to be in exact agreement with the physical phenomena occurring at the surface of the sample. However, this difference is kept to a minimum by using the reference standard. Therefore, the uncertainty in recording the phase data is expected to be largely due to resolution in a reading taken at the display of the lock-in.

During experimentation it was found that random fluctuations at the lock-in enabled a reading of phase to within ± 0.1 deg. A simple test was performed using this knowledge. Data from the 25°C sample run were used to explore the possible effect that an error in phase shift might have on the final film properties calculated. To do this, each of the corrected phase-shift values was systematically offset by twice the observed resolution, or +0.2 deg. A fit was then performed with the analytical model using the nominal properties of silicon. From these results, the thermal conductivity and specific heat of the film were calculated. The properties determined with the offset phase data differed from properties determined with the actual data by less than two percent. Repeating the test by randomly offsetting the corrected phase shifts by ± 0.2 deg produced much smaller uncertainties in the final results. It is felt that uncertainty in reading the phase at the lock-in output is insignificant in the overall measurement scheme.

Next, uncertainty in the results was estimated due to uncertainty in the variables used in the fitting routine. The variables explored were film thickness (L), thermal conductivity of silicon (k_2), specific heat of silicon (C_{p2}), density of silicon (ρ_2), and the film density (ρ_1). As pointed out in a previous section, a literature survey on the thermal conductivity of silicon produced a range of values with up to ten percent variation. Although it is not as well characterized, similar property variation was found in the specific heat of silicon. With this in mind, the thermal properties of silicon were allowed to vary by ten percent from their nominal values in the analysis presented in the following paragraphs. On the other hand, density was considered a well-characterized material property. The density of both the fused silica film and the silicon substrate were not expected to deviate from their respective bulk values by more than a few percent. Therefore, a conservative bound of five percent was placed on the possible variation in density for each. Finally, considering inaccuracy associated with the measurement of film thickness, this quantity was assigned an uncertainty of five percent with respect to its nominal value of 1.72 μm.

A change in each of the five "variables" above was examined at temperatures of 25°C, 100°C, 200°C, and 300°C to show their affect on the thin film thermal property calculations. Thus, a total of five separate fits are required at any temperature, one for each property. In any given fit, four of the variables are held to their nominal values and the fifth variable is altered by the percentage stated above. The properties of the thin film were calculated with the fit results and each property is compared to that determined when nominal values for all five variables are used.

A simple RSS (root-sum-square) technique was used on the "error" associated with each variable. For instance, by using the nominal value of each at 25°C, a film thermal conductivity of 1.284 W/m K was determined. When the silicon substrate's thermal conductivity was varied by ten percent while holding all other properties to their nominal values, the fit produced 1.219 W/m K for the film conductivity. The new value is 0.065 W/m K less than the nominal. This difference was considered the "error." Similarly, by varying the substrate density, substrate specific heat, film thickness, and film density, the film thermal conductivity produced by each fit yielded errors of 0.033 W/m K, 0.065 W/m K, 0.067 W/m K, and finally 0.000 W/m K. Note that the thin film density does not affect the result for the thermal conductivity—density effectively cancels when using the curve fitting results together with Eqs. (19) and (20). At 25°C, the RSS technique gives a total uncertainty of

Table 1 Thermal property values

	Silicon substrate		SiO_2 film results			
	k_2 W/m K	C_{p2} J/kg K	$a_1 \times 10^7$ m^2/s	e_1 W s$^{1/2}$/m^2 K	k_1 W/m K	C_{p1} J/kg K
25°C	150	712	8.244	1414	1.284	701.5
40°C	139	726	7.970	1456	1.300	734.6
50°C	133	735	7.874	1479	1.312	750.8
75°C	120	755	7.663	1539	1.347	791.9
100°C	109	773	7.403	1590	1.368	832.4
150°C	93	800	7.101	1690	1.424	903.4
200°C	81	821	6.854	1769	1.465	962.5
250°C	72	838	6.625	1846	1.503	1021.6
300°C	65	853	6.555	1916	1.551	1066.0

$$\text{RSS} = \sqrt{0.065^2 + 0.033^2 + 0.065^2 + 0.067^2 + 0.000^2}$$

$$= 0.118. \quad (22)$$

From the above calculation, the final thermal conductivity (using three significant figures) at room temperature becomes 1.28 ± 0.12 W/m K. In other words, the true value of the thermal conductivity is not expected to deviate more than 9.2 percent from the "nominal" value at this temperature for the 95 percent confidence level. Through this analysis, it was determined that the cumulative error associated with the variables propagated toward an uncertainty no larger than ten percent from the nominal film properties (specific heat and thermal conductivity) over the entire temperature range studied. The uncertainties in thermal conductivity and specific heat are presented as error bars in Fig. 7 and Fig. 8, respectively.

Discussion. In past work on the determination of thin film properties, Decker et al. (1984) found the thermal conductivity of fused silica films to be lower than bulk values by using a steady-state method based on thermocouple measurements. They studied films from two different deposition processes. Their measurements produced a thermal conductivity of 0.17 W/m K for a 1.05-μm thick *e*-gun evaporated film, which was less than the bulk value by a factor of 8. Also studied was a 0.50-μm thick reactively sputtered film of SiO_2 for which a thermal conductivity of 0.28 W/m K was measured. They concluded that film thermal conductivity depends strongly on deposition technique.

Lambropoulos et al. (1992) used a modified thermal comparator to determine the conductivity of various film materials with thicknesses between 0.50 μm–4.40 μm. Their results showed a smaller effective conductivity for *e*-beam evaporated films of SiO_2 as compared to bulk values. Films fabricated from an ion beam sputtering process also produced conductivities lower than the bulk material. The thermal properties obtained with their method differed from the bulk solid by a factor of approximately 3–5, in contrast to the factor of 8 found in the reference cited above. However, they have stated that uncertainty inherent within their method can affect the final film conductivity by a factor of two. Unlike the previous method, as well as the method presented here, they were able to provide an estimate for interfacial resistance along with film conductivity. They did not believe that thin film thermal conductivity was sensitive to the method of film preparation. Also noted was a strong dependence between film thickness and thermal conductivity for SiO_2 over the thickness range of 0.5 μm to 4 μm.

Silicon dioxide films fabricated with three different processes have been studied by Goodson et al. (1993), with film thickness ranging between 0.03 μm to 0.70 μm. Their work indicated that the fabrication process does have a strong influence on the conductivity of SiO_2. Of interest from the study are results found for a thermally grown film of SiO_2 with a thickness close to 0.5 μm. The film's effective conductivity was determined to be approximately 1.27 W/m K. Although the film thickness is much smaller than the 1.72 μm thick film of the current work, the resulting thermal conductivity is extremely close to that presented here.

Thermally grown and chemical vapor deposited (CVD) silicon dioxide layers were also studied by Kading et al. (1994) by using a noncontact technique. In their work, film thickness ranged from 20 nm to 200 nm. No significant dependence on thickness was observed, but it was found that the thermal conductivity of the CVD films was smaller than that of the thermally grown films. Their experiment involved a set of the thermally grown specimens with a 2-μm layer of gold sputtered on the top surface. For purposes of comparison, another specimen had a 20-nm layer of chromium evaporated on its front surface prior to sputtering the 2-μm layer of gold. Two interfaces existed in a specimen, one at the silicon dioxide/silicon substrate boundary and the other at the silicon dioxide/metal boundary. They did not find a significant thermal boundary resistance at the silicon dioxide/silicon interface. However, they concluded that the thermal boundary resistance at the metal interface was strongly dependent on the metallization process and was sometimes comparable to the internal resistance of the oxide layer itself. Ju et al. (1998) as well as Okuda and Ohkudo (1992) also presented SiO_2 film property data. In the former investigation, a technique was developed using front surface heating and optical thermometry to obtain the magnitude of the in-phase temperature variations. For a 1.56-μm thick SiO_2 film, an analytical model matched the experimental results for a thermal conductivity of 1.5 W/m-K, which is slightly higher than the bulk value for fused silica. Although some variations exist in the investigations cited above, the results found in the present study are consistent with this past body of work.

The phase-sensitive technique described in the present work has yielded values for the thermal conductivity and specific heat of a thin silicon dioxide film (1.72 μm) through a temperature range of 25°C–300°C. The film was thermally grown and had a thin layer of nichrome on its top surface, thus two interfaces. The experimentally obtained thermal conductivities of the thin film were never more than ten percent lower than the corresponding thermal conductivity of fused silica in bulk form over this temperature range. The results are in good agreement with previous work presented in the literature on thermally grown films of SiO_2. Although the thermal conductivity values produced by this method are lower than the bulk values, a larger variation has been reported for films fabricated by processes other than that used here. The values of specific heat that were found with the new method closely agree with the bulk values of fused silica, which was expected. No attempt was made at determining the extent of each interfacial resistance, although for the film thickness studied in this work, both resistances are thought to be much smaller than the thermal resistance of the film.

Acknowledgment

The authors would like to express their appreciation to Prof. T. K. Plant of the Electrical and Computer Engineering Department at Oregon State University for his help in depositing the thin nichrome films for the project.

References

Arpaci, V. S., 1966, *Conduction Heat Transfer*, Addison-Wesley, Reading, MA.

Bennett, C. A., Jr., and Patty, R. R., 1982, "Thermal Wave Interferometry: A Potential Application of the Photoacoustic Effect," *Appl. Opt.*, Vol. 21, pp. 49–54.

Cahill, D. G., Fischer, H. E., Klitsner, T., Swartz, E. T., and Pohl, R. O., 1989, "Thermal Conductivity of Thin Films: Measurements and Understanding," *J. Vac. Sci. Technol.*, A, Vol. 7, pp. 1259–1266.

Charpentier, P., Lepoutre, F., and Bertrand, L., 1982, "Photoacoustic Measurements of Thermal Diffusivity Description of the 'Drum Effect'," *J. Appl. Phys.*, Vol. 53, pp. 608–614.

Chen, G., and Tien, C. L., 1993, "Thermal Diffusivity Measurement of GaAs/AlGaAs Thin-Film Structures," presented at the ASME Winter Annual Meeting, Nov. 28–Dec. 3, New Orleans, LA.

Decker, D. L., Koshigoe, L. G., and Ashley, E. J., 1984, "Thermal Properties of Optical Thin Film Materials*," *Laser Induced Damage in Optical Materials*, NBS Special Publication 727 (Government Printing Office, Washington, DC, 1986), pp. 291–297.

DeVecchio, D., Russell, D., and Taborek, P., 1995, "Measurement of Thermal Diffusivity of Small, High Conductivity Samples Using a Phase Sensitive Technique," *Rev. Sci. Instrum.*, Vol. 66, pp. 3601–3605.

Frank, R., Drach, V., and Fricke, J., 1993, "Determination of Thermal Conductivity and Specific Heat by a Combined 3ω/Decay Technique," *Rev. Sci. Instrum.*, Vol. 64, pp. 760–765.

Glassbrenner, C. J., and Slack, G. A., 1964, "Thermal Conductivity of Silicon and Germanium from 3°K to the Melting Point," *Phys. Rev.*, Vol. 134, pp. A1058–A1069.

Goodson, K. E., Flik, M. I., Su, L. T., and Antoniadis, D. A., 1993, "Annealing-Temperature Dependence of the Thermal Conductivity of LPCVD Silicon-Dioxide Layers," *IEEE Electron Device Lett.*, Vol. 14, pp. 490–492.

Incropera, F. P., and Dewitt, D. P., 1990, Fundamentals of Heat and Mass Transfer, 3rd Ed., John Wiley and Sons, New York.

Ju, Y. S., Kurabayashi, K., and Goodson, K. E., 1998, "Thermal Characterization of IC Passivation Layers Using Joule Heating and Optical Thermometry," *Microscale Thermophysical Engineering*, Vol. 2, pp. 101–110.

Kading, O. W., Skurk, H., and Goodson, K. E., 1994, "Thermal Conduction in Metallized Silicon-Dioxide Layers on Silicon," *Appl. Phys. Lett.*, Vol. 65, pp. 1629–1631.

Lachaine, A., and Poulet, P., 1984, "Photoacoustic Measurement of Thermal Properties of a Thin Polyester Film," *Appl. Phys. Lett.*, Vol. 45, pp. 953–954.

Lambropoulos, J. C., Jolly, M. R., Amsden, C. A., Gilman, S. E., Sinicropi, M. J., Diakomihalis, D., and Jacobs, S. D., 1989, "Thermal Conductivity of Dielectric Thin Films," *J. Appl. Phys.,* Vol. 66, pp. 4230–4242.

Lambropoulos, J. C., Burns, S. J., Jacobs, S. D., and Shaw-Klein, L., 1992, "Effects of Anisotropy, Interfacial Thermal Resistance, Microstructure, and Film Thickness on the Thermal Conductivity of Dielectric Thin Films," ASME HTD-Vol. 227, pp. 37–49.

Meyers, G. E., 1971, *Analytical Methods in Conduction Heat Transfer,* McGraw-Hill, New York.

Okuda, M., and Ohkubo, S., 1992, "A Novel Method for Measuring the Thermal Conductivity of Submicrometer Thick Dielectric Films," *Thin Solid Films,* Vol. 213, pp. 176–181.

Rosencwaig, A., and Gersho, A., 1976, "Theory of the Photoacoustic Effect with Solids," *J. Appl. Phys.,* Vol. 47, pp. 64–69.

Swimm, R. T., 1983, "Photoacoustic Determination of Thin-Film Thermal Properties," *Appl. Phys. Lett.,* Vol. 42, pp. 955–957.

Touloukian, Y. S., and Buyco, E. H., 1970, "Specific Heat: Metallic Elements and Alloys," *Thermophysical Properties of Matter,* Vol. 4, IFI/Plenum Data Corporation, New York.

Touloukian, Y. S., Powell, R. W., Ho, C. Y., and Klemens, P. G., 1970a, "Thermal Conductivity: Metallic Elements and Alloys," *Thermophysical Properties of Matter,* Vol. 1, IFI/Plenum Data Corporation, New York.

Touloukian, Y. S., Powell, R. W., Ho, C. Y., and Klemens, P. G., 1970b, "Thermal Conductivity: Nonmetallic Solids," *Thermophysical Properties of Matter,* Vol. 2, IFI/Plenum Data Corporation, New York.

Zhang, X., and Grigoropoulos, C. P., 1995, "Thermal Conductivity and Diffusivity of Free-Standing Silicon Nitride Thin Films," *Rev. Sci. Instrum.,* Vol. 66, pp. 1115–1120.

B. H. Dennis
Graduate Assistant
Department of Aerospace Engineering,
The Pennsylvania State University,
University Park, PA 16802
e-mail: bhd102@psu.edu

G. S. Dulikravich
Professor,
Department of Mechanical and
Aerospace Engineering,
The University of Texas,
Arlington, TX 76019
e-mail: gsd@mae.uta.edu
Fellow ASME

Simultaneous Determination of Temperatures, Heat Fluxes, Deformations, and Tractions on Inaccessible Boundaries

A finite element method formulation for the detection of unknown steady boundary conditions in heat conduction and linear elasticity and combined thermoelasticity continuum problems is presented. The present finite element method formulation is capable of determining displacements, surface stresses, temperatures, and heat fluxes on the boundaries where such quantities are unknown or inaccessible, provided such quantities are sufficiently overspecified on other boundaries. Details of the discretization, linear system solution techniques, and sample results for two-dimensional problems are presented.

Introduction

It is often difficult and even impossible to place temperature probes, heat flux probes, or strain gauges on certain parts of a surface of a solid body. This can be either due to its small size or geometric inaccessibility or because of the hostile environment on that surface. With an appropriate inverse method these unknown boundary values can be deduced from additional information that should be made available at a finite number of points within the body or on some other surfaces of the solid body. In the case of steady thermoelasticity, the objective of an inverse boundary condition determination problem is to deduce displacements, tractions, temperatures, and heat fluxes on any surfaces or surface elements where such information is unknown. This represents a multidisciplinary (combined heat conduction and linear elasticity) inverse problem. A separate problem of inverse determination of unknown boundary conditions in steady heat conduction has been solved by a variety of methods (Larsen, 1985; Martin and Dulikravich, 1996a; Hensel and Hills, 1989). Similarly, a separate inverse boundary condition determination problem in linear elastostatics has been solved by different methods (Maniatty and Zabaras, 1994; Martin et al., 1995).

Our objective is to develop and demonstrate a novel approach for the simultaneous determination of both thermal and elasticity conditions on parts of a solid body surface. It should be pointed out that the iterative method for the solution of inverse problems to be discussed in this paper is entirely different from the noniterative approach based on boundary element method that has been used separately in linear heat conduction (Martin and Dulikravich, 1996a) and linear elasticity (Martin et al., 1995). Moreover, the current method has nothing in common with a more familiar inverse shape design problem (Kassab et al., 1994; Martin and Dulikravich, 1996b).

For inverse problems, the unknown boundary conditions on parts of the boundary can be determined by overspecifying the boundary conditions (enforcing both Dirichlet and Neumann-type boundary conditions) on at least some of the remaining portions of the boundary, and providing either Dirichlet or Neumann type boundary conditions on the rest of the boundary. It is possible, after a series of algebraic manipulations, to transform the original system of equations into a system which enforces the overspecified boundary conditions and includes the unknown boundary conditions as a part of the unknown solution vector. This formulation is an adaptation of a method by Martin and Dulikravich (1996a) for the inverse detection of boundary conditions in steady heat conduction and by Martin et al. (1995) for finding unknown boundary tractions and deformations in elastostatics using the boundary element method.

The main novelty of the current method is that it is capable of treating heat conduction and linear elasticity simultaneously (Dennis and Dulikravich, 1998a, b). Specifically, it represents an extension of the conceptual work presented by the authors (Dennis and Dulikravich, 1998a) by adding several regularization formulations. It also represents a more complete version of the work presented recently (Dennis and Dulikravich, 1998b).

Analytical and Numerical Formulation

When analyzing steady-state elasticity problems, either displacement vectors or surface traction vectors are specified everywhere on the boundary of the object. This way, one of these quantities is known, while the other is unknown at every point on the boundary.

When performing an inverse evaluation of the steady-state elasticity problem, both displacement vectors and surface traction vectors must be specified on a part of the body surface, while both are unknown on another part of the surface. Elsewhere on the body surface, either displacement vectors or surface traction vectors should be provided. The surface section where both displacement vectors and surface traction vectors are specified simultaneously is called the overspecified boundary.

Finite Element Method Formulation for Thermoelasticity. The Navier equations for linear static deformations u, v, w in three-dimensional Cartesian x, y, z coordinates are

$$(\lambda + G)\left(\frac{\partial^2 u}{\partial x^2} + \frac{\partial^2 v}{\partial x \partial y} + \frac{\partial^2 w}{\partial x \partial z}\right) + G\nabla^2 u + X = 0 \quad (1)$$

$$(\lambda + G)\left(\frac{\partial^2 u}{\partial x \partial y} + \frac{\partial^2 v}{\partial y^2} + \frac{\partial^2 w}{\partial y \partial z}\right) + G\nabla^2 v + Y = 0 \quad (2)$$

$$(\lambda + G)\left(\frac{\partial^2 u}{\partial x \partial z} + \frac{\partial^2 v}{\partial y \partial z} + \frac{\partial^2 w}{\partial z^2}\right) + G\nabla^2 w + Z = 0 \quad (3)$$

where

Contributed by the Heat Transfer Division for publication in the JOURNAL OF HEAT TRANSFER and presented at the '98 IMECE, Anaheim. Manuscript received by the Heat Transfer Division, Aug. 14, 1998; revision received, Apr. 4, 1999. Keywords: Computational, Finite Element, Heat Transfer, Inverse, Nonintrusive Diagnostics, Stress. Associate Technical Editor: D. Kaminski.

$$\lambda = \frac{E\nu}{(1+\nu)(1-2\nu)}, \quad G = \frac{E}{2(1+\nu)}.$$

Here X, Y, Z are body forces per unit volume due to stresses from thermal expansion.

$$X = -(3\lambda + 2G)\frac{\partial \alpha \Delta\Theta}{\partial x} \tag{4}$$

$$Y = -(3\lambda + 2G)\frac{\partial \alpha \Delta\Theta}{\partial y} \tag{5}$$

$$Z = -(3\lambda + 2G)\frac{\partial \alpha \Delta\Theta}{\partial z} \tag{6}$$

This system of differential Eqs. (1)–(3) can be written in the following matrix form:

$$[L]^T([C][L]\{\delta\} - [C]\{\epsilon_0\}) - \{f\} = 0 \tag{7}$$

where the differential operator matrix, $[L]$, is defined as

$$[L] = \begin{bmatrix} \frac{\partial}{\partial x} & 0 & 0 \\ 0 & \frac{\partial}{\partial y} & 0 \\ 0 & 0 & \frac{\partial}{\partial z} \\ \frac{\partial}{\partial y} & \frac{\partial}{\partial x} & 0 \\ \frac{\partial}{\partial z} & 0 & \frac{\partial}{\partial x} \\ 0 & \frac{\partial}{\partial z} & \frac{\partial}{\partial y} \end{bmatrix} \tag{8}$$

and the elastic modulus matrix, $[C]$, is defined as

$$[C] = \frac{\lambda}{\nu}\begin{bmatrix} 1-\nu & \nu & \nu & 0 & 0 & 0 \\ \nu & 1-\nu & \nu & 0 & 0 & 0 \\ \nu & \nu & 1-\nu & 0 & 0 & 0 \\ 0 & 0 & 0 & \frac{1-2\nu}{2} & 0 & 0 \\ 0 & 0 & 0 & 0 & \frac{1-2\nu}{2} & 0 \\ 0 & 0 & 0 & 0 & 0 & \frac{1-2\nu}{2} \end{bmatrix}. \tag{9}$$

Casting the system of Eq. (7) in integral form using the weighted residual method yields

$$\int_\Omega [V][L]^T([C][L]\{\delta\} - [C]\{\epsilon_0\})d\Omega - \int_\Omega [V]\{f\}d\Omega = 0 \tag{10}$$

where the matrix, $[V]$, is the weight matrix which is a collection of test functions and Ω is the domain where the equations are to be solved.

$$[V] = \begin{bmatrix} V_1 & 0 & 0 \\ 0 & V_2 & 0 \\ 0 & 0 & V_3 \end{bmatrix} \tag{11}$$

Equation (10) should now be integrated by parts to get the weak form of (7)

$$\int_\Omega ([L][V]^T)^T[C][L]\{\delta\}d\Omega - \int_\Omega ([L][V]^T)^T[C]\{\epsilon_0\}d\Omega - \int_\Omega [V]\{f\}d\Omega - \int_\Gamma [V]\{T\}d\Gamma = 0 \tag{12}$$

where $\{T\}$ is the vector of surface tractions on surface Γ.

$$\{T\} = [n][C][L]\{\delta\} \tag{13}$$

The matrix $[n]$ contains the Cartesian components of the unit vector normal to the surface Γ.

The displacement field in the x, y, and z-directions can now be represented with approximation functions

$$u(x, y, z) \approx \sum_{i=1}^{n} N_i(x, y, z)u_i \tag{14}$$

$$v(x, y, z) \approx \sum_{i=1}^{n} N_i(x, y, z)v_i \tag{15}$$

$$w(x, y, z) \approx \sum_{i=1}^{n} N_i(x, y, z)w_i. \tag{16}$$

Equations (14)–(16) can be rewritten in matrix form

$$\begin{Bmatrix} u(x, y, z) \\ v(u, x, y) \\ w(x, y, z) \end{Bmatrix} \approx [N]\{\delta\} \tag{17}$$

where $[N]$ is the interpolation matrix which contains the trial functions for each equation in the system. Also note that with

Nomenclature

$[C]$ = elastic modulus matrix
$[D]$ = damping matrix
E = elastic modulus of elasticity
$\{f\}$ = force vector
G = shear modulus
k = Fourier coefficient of heat conduction
$[K]$ = stiffness matrix
$[N]$ = interpolation matrix
$[n]$ = unit vector matrix
Q = heat flux
R = uniform random number between 0 and 1
S = heat source
u, v, w = deformations in the x, y, z-directions
X, Y, Z = body force components in x, y, z directions
x, y, z = Cartesian body axes
α = coefficient of thermal expansion
$\{\delta\}$ = displacement vector
$\{\epsilon_0\}$ = initial strain vector
ϵ = strain
Γ = boundary surface
λ = Lame's constant
Λ = damping parameter
ν = Poisson's ratio
$\{\sigma\}$ = stress component vector
$\bar{\sigma}$ = standard deviation
Θ = temperature
$\Delta\Theta$ = difference between local and reference temperature

Galerkin's method the weight matrix and the interpolation matrix are equal, $[N] = [V]^T$. If the matrix $[B]$ is defined as

$$[B] = [L][N] \tag{18}$$

then the substitution of the approximation functions (17) into the weak statement (12) creates the weak integral form for a finite element expressed as

$$\int_\Omega [B]^T[C][B]\{\delta\}d\Omega - \int_\Omega [B]^T[C]\{\epsilon_0\}d\Omega - \int_\Omega [N]^T\{f\}d\Omega - \int_{\Gamma_1} [N]^T\{T\}d\Gamma = 0. \tag{19}$$

This can also be written in the matrix form as

$$[K]\{\delta\} = \{f\}. \tag{20}$$

For thermal stresses, the initial elemental strain vector, ϵ_0, becomes

$$\{\epsilon_0\} = \lfloor \alpha\Delta\Theta \quad \alpha\Delta\Theta \quad \alpha\Delta\Theta \quad 0 \quad 0 \quad 0 \rfloor^T. \tag{21}$$

The local stiffness matrix, $[K]$, and the force per unit volume vector, $\{f\}$, are determined for each element in the domain and then assembled into the global system

$$[K]\{\delta\} = \{f\}. \tag{22}$$

After applying boundary conditions, the global displacements are found by solving this system of linear algebraic equations. The stresses, $\{\sigma\}$, can then be found in terms of the displacements, $\{\delta\}$, as

$$\{\sigma\} = [C][L]\{\delta\} - [C]\{\epsilon_0\}. \tag{23}$$

Finite Element Method Formulation for Thermal Problem. The temperature distribution throughout the domain can be found by solving Poisson's equation for steady linear heat conduction with a distributed steady heat source function, S, and thermal conductivity coefficient, k.

$$-k\left(\frac{\partial^2\Theta}{\partial x^2} + \frac{\partial^2\Theta}{\partial y^2} + \frac{\partial^2\Theta}{\partial z^2}\right) = S \tag{24}$$

Applying the method of weighted residuals to (24) with a weight function, ϕ, over an element results in

$$\int_\Omega \left(\frac{\partial^2\Theta}{\partial x^2} + \frac{\partial^2\Theta}{\partial y^2} + \frac{\partial^2\Theta}{\partial z^2} - \frac{S}{k}\right)\phi d\Omega = 0. \tag{25}$$

Integrating this by parts once (25) creates the weak statement for an element

$$-\int_\Omega k\left(\frac{\partial\phi}{\partial x}\frac{\partial\Theta}{\partial x} + \frac{\partial\phi}{\partial y}\frac{\partial\Theta}{\partial y} + \frac{\partial\phi}{\partial z}\frac{\partial\Theta}{\partial z}\right)d\Omega = \int_\Omega N_i S d\Omega - \int_\Gamma N_i(Q\cdot\hat{n})d\Omega. \tag{26}$$

Variation of the temperature across an element can be expressed by

$$\Theta(x, y, z) \approx \sum_{i=1}^{m} N_i(x, y, z)\Theta_i. \tag{27}$$

Using Galerkin's method, the weight function ϕ and the interpolation function for Θ are chosen to be the same. By defining the matrix $[E]$ as

$$[E] = \begin{bmatrix} \frac{\partial N_1}{\partial x} & \frac{\partial N_2}{\partial x} & \cdots & \frac{\partial N_m}{\partial x} \\ \frac{\partial N_1}{\partial y} & \frac{\partial N_2}{\partial y} & \cdots & \frac{\partial N_m}{\partial y} \\ \frac{\partial N_1}{\partial z} & \frac{\partial N_2}{\partial z} & \cdots & \frac{\partial N_m}{\partial z} \end{bmatrix}, \tag{28}$$

the weak statement (26) for a single element can be written in the matrix form as

$$[K_c]^e\{\Theta\}^e = \{Q\}^e \tag{29}$$

where

$$[K_c]^e = \int_\Omega k[E]^T[E]d\Omega^e \tag{30}$$

$$\{Q\}^e = -\int_\Omega S\{N\}d\Omega^e + \int_\Gamma Q\{N\}d\Gamma^e. \tag{31}$$

The local stiffness matrix, $[K_c]^e$, and heat flux vector, $\{Q\}^e$, are determined for each element in the domain and then assembled into the global system

$$[K_c]\{\Theta\} = \{Q\}. \tag{32}$$

Direct and Inverse Formulations

The above equations for linear elastostatics and steady heat conduction were discretized separately by using a Galerkin's finite element method. This results in two linear systems of algebraic equations,

$$[K]\{\delta\} = \{f\}, \quad [K_c]\{\Theta\} = \{Q\}. \tag{33}$$

These systems are large, sparse, symmetric, and positive definite. Once these global systems have been formed, the boundary conditions can be applied. For a well-posed (analysis or direct) problem, the boundary conditions must be known on all boundaries of the domain. For heat conduction, either the temperature, Θ, or the heat flux, Q, must be specified at each point of the boundary. For elasticity, the displacement vector components, u_s, v_s, w_s, or the surface traction vector components, T_{xs}, T_{ys}, T_{zs}, must be specified on the entire boundary.

Consider the linear system (29) for steady heat conduction on a quadrilateral finite element with boundary conditions given at points 1 and 4.

$$\begin{bmatrix} K_{11} & K_{12} & K_{13} & K_{14} \\ K_{21} & K_{22} & K_{23} & K_{24} \\ K_{31} & K_{32} & K_{33} & K_{34} \\ K_{41} & K_{42} & K_{43} & K_{44} \end{bmatrix}\begin{Bmatrix} \Theta_1 \\ \Theta_2 \\ \Theta_3 \\ \Theta_4 \end{Bmatrix} = \begin{Bmatrix} Q_1 \\ Q_2 \\ Q_3 \\ Q_4 \end{Bmatrix} \tag{34}$$

As an example of an inverse problem, one could specify both the temperature and the heat flux at point 1, flux only at points 2 and 3, and assume the boundary conditions at point 4 as being unknown. The original system of Eq. (34) can be modified by grouping all available boundary conditions in a vector on the right-hand side

$$\begin{bmatrix} K_{12} & K_{13} & K_{14} & 0 \\ K_{22} & K_{23} & K_{24} & 0 \\ K_{32} & K_{33} & K_{34} & 0 \\ K_{42} & K_{43} & K_{44} & -1 \end{bmatrix}\begin{Bmatrix} \Theta_2 \\ \Theta_3 \\ \Theta_4 \\ Q_4 \end{Bmatrix} = \begin{Bmatrix} Q_1 - \Theta_1 K_{11} \\ Q_2 - \Theta_1 K_{21} \\ Q_3 - \Theta_1 K_{31} \\ 0 - \Theta_1 K_{41} \end{Bmatrix}. \tag{35}$$

The same procedure can be applied to the system matrices for both steady heat conduction and elasticity in two or three dimensions. The resulting systems of equations will remain sparse, but will become unsymmetric and possibly rectangular depending on the ratio of the number of known to unknown boundary conditions. The next section will discuss techniques for solving such systems.

Regularization

Three regularization methods were applied separately to the solution of the systems of equations in attempts to increase the method's tolerance for measurement errors in the overspecified boundary conditions. Here, we consider the regularization of the inverse heat conduction problem.

The general form of a regularized system is given as (Neumaier, 1998)

$$\begin{bmatrix} K_c \\ \Lambda D \end{bmatrix} \{\Theta\} = \begin{Bmatrix} Q \\ 0 \end{Bmatrix}. \tag{36}$$

The traditional Tikhonov regularization (Tikhonov and Arsenin, 1977) is obtained when the damping matrix, $[D]$, is set equal to the identity matrix. Solving (36) in a least-squares sense minimizes the following error function:

$$\text{error}\,(\Theta) = \|[K_c]\{\Theta\} - \{Q\}\|_2^2 + \|\Lambda[D]\{\Theta\}\|_2^2. \tag{37}$$

This is the minimization of the residual plus a penalty term. The form of the damping matrix determines what penalty is used and the damping parameter, Λ, weights the penalty for each equation. These weights should be determined according to the error associated with the respective equation.

Method 1. This method of regularization uses a constant damping parameter Λ over the entire domain and the identity matrix as the damping matrix. This method can be considered the traditional Tikhonov method. The penalty term being minimized in this case is the square of the L_2 norm of the solution vector $\{x\}$. Minimizing this norm will tend to drive the components of $\{x\}$ to uniform values thus producing a smoothing effect. However, minimizing this penalty term will ultimately drive each component to zero, completely destroying the real solution. Thus, great care must be exercised in choosing the damping parameter Λ so that a good balance of smoothness and accuracy is achieved.

Method 2. This method of regularization uses a constant damping parameter Λ only for equations corresponding to the unknown boundary values. For all other equations $\Lambda = 0$ and $[D] = [I]$ since the largest errors occur at the boundaries where the temperatures and fluxes are unknown.

Method 3. This method uses Laplacian smoothing of the temperatures only on the boundaries where the boundary conditions are unknown. A penalty term could be constructed such that curvature of the solution on the boundary where conditions are unknown is minimized along with the residual.

$$\|\nabla^2\Theta_{ub}\|_2^2 \rightarrow \min \tag{38}$$

Equation (38) can be discretized using the method of weighted residuals to determine the damping matrix, $[D]$.

$$\|[D]\Theta_{ub}\|_2^2 = \int_\Gamma (\nabla^2\Theta_{ub})^2 d\Gamma = \|[K_c]\Theta_{ub}\|_2^2 \tag{39}$$

In two-dimensional planar problems, $[K_c]$ and $[D]$ can be thought of as an assembly of the linear or quadratic rod elements that discretize the boundary of the object where the boundary conditions are unknown. The main advantage of this method is its ability to smooth the solution vector without necessarily driving the components to zero and away from the true solution.

Solution of the Linear System

In general, the resulting finite element method systems for the inverse thermoelastic problems are sparse, unsymmetric, and often rectangular. These properties make the process of finding a solution to the system very challenging. Three approaches will be discussed here.

The first is to normalize the equations by multiplying both sides by the matrix transpose and solve the resulting square system with common sparse solvers.

$$[K]^T[K]\{\delta\} = [K]^T\{f\} \tag{40}$$

This approach has been found to be effective for certain inverse problems (Boschi and Fischer, 1996). The resulting normalized system is less sparse than the original system, but it is square, symmetric, and positive definite with application of regulariza-

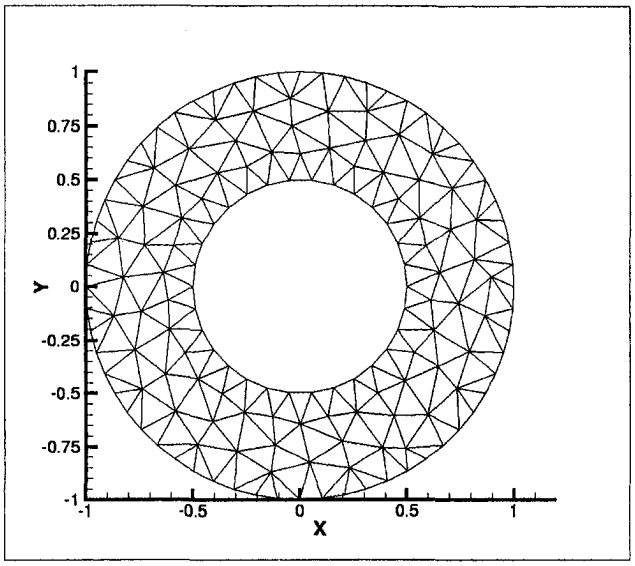

Fig. 1 Triangular mesh for an annular disk test case geometry

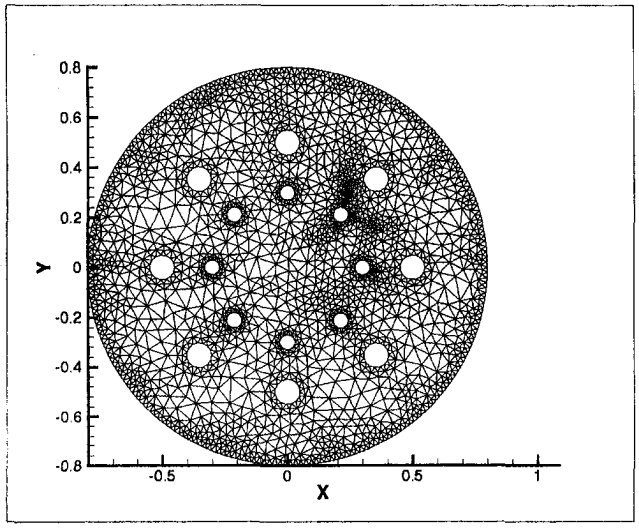

Fig. 2 Triangular mesh for a multiply connected domain test case geometry

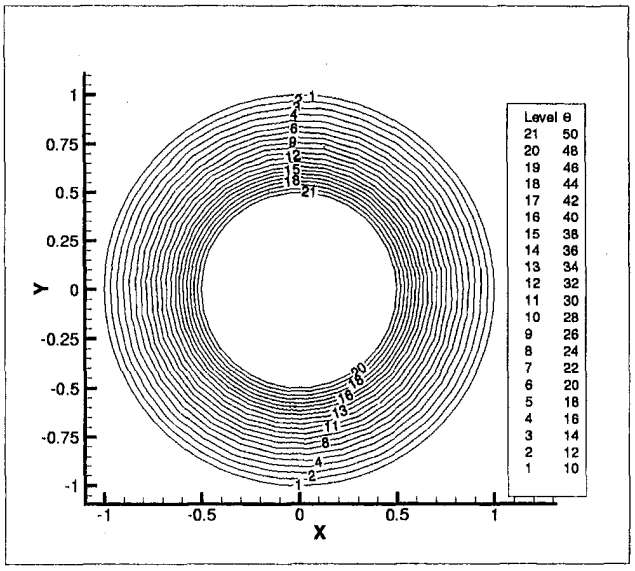

Fig. 3 Computed isotherms with inner and outer boundary temperatures specified

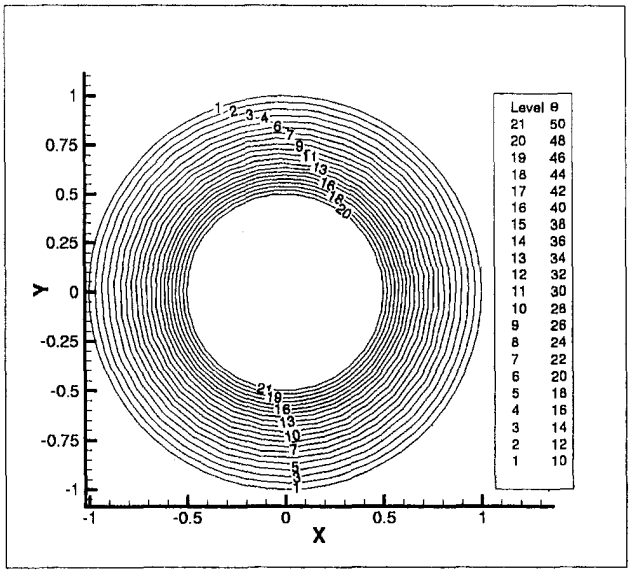

Fig. 4 Computed isotherms with outer boundary temperatures and fluxes specified. Nothing was specified on the inner boundary.

tion. The normalized system is solved with a direct method (Cholesky or LU factorization) or with an iterative method (preconditioned Krylov subspace). There are several disadvantages to this approach, among them being the computational expense of computing $[K]^T[K]$, the large in-core memory requirements, and the roundoff error incurred during the $[K]^T[K]$ multiplication.

A second approach is to use iterative methods suitable for unsymmetrical and least-squares problems. One such method is the least squares QR method, which is an extension of the well-known conjugate gradient method (Paige and Saunders, 1982). The least-squares QR method and other similar methods, such as the conjugate gradient for least squares, solve the normalized system, but without explicit computation of $[K]^T[K]$. However, convergence rates of these methods depend strongly on the condition number of the normalized system which is roughly the condition number of $[K]$ squared. Convergence can be slow when solving the systems resulting from the inverse finite element discretization since they are ill-conditioned.

A third approach is to use a noniterative method for unsymmetrical and least-squares problems such as QR factorization (Golub and Van Loan, 1996) or singular value decomposition (Golub and Van Loan, 1996). However, sparse implementations of QR or singular value decomposition solvers are needed to reduce the in-core memory requirements for the inverse finite element problems.

Numerical Results

The accuracy and efficiency of the finite element inverse formulation was tested on several simple two-dimensional problems with known analytic solutions. The method was implemented in an object-oriented finite element code written in $C++$. Elements used in the calculations were triangles with linear and quadratic interpolation functions. The triangular meshes were generated by an automatic Delauney triangulation technique (Shewchuk, 1996).

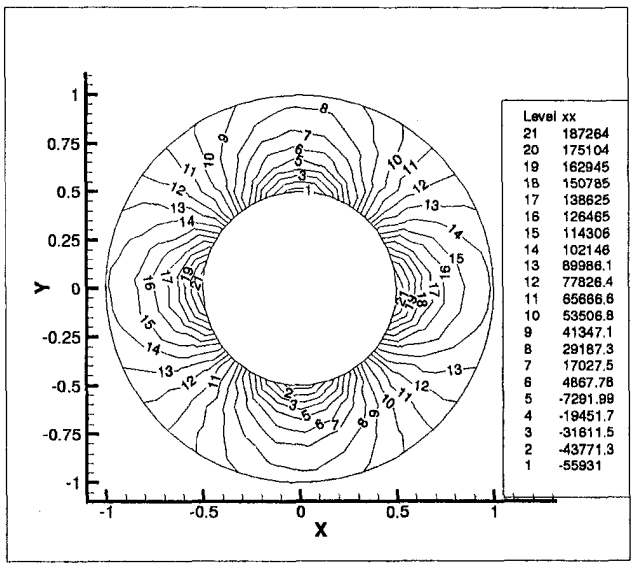

Fig. 5 Computed normal stress distribution with inner and outer boundary tractions specified

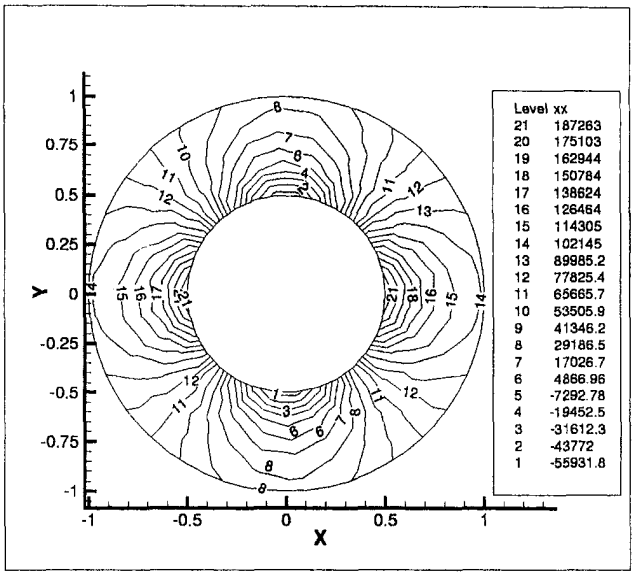

Fig. 6 Computed normal stress distribution with outer boundary tractions and displacements specified. Nothing was specified on the inner boundary.

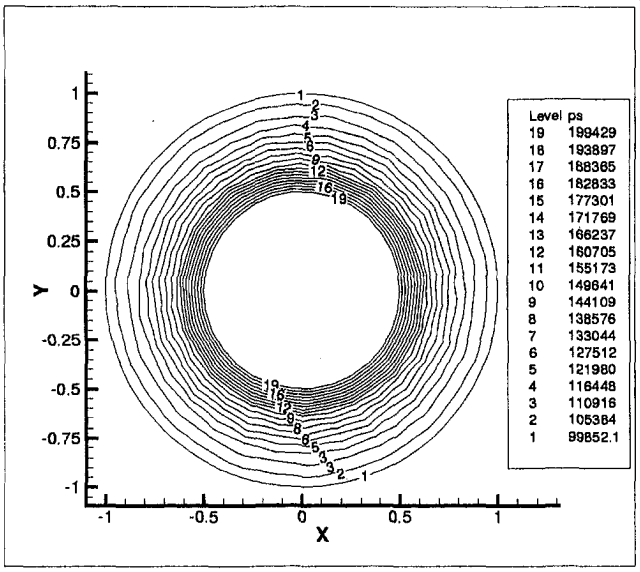

Fig. 7 Computed principal stress distribution with inner and outer boundary tractions specified

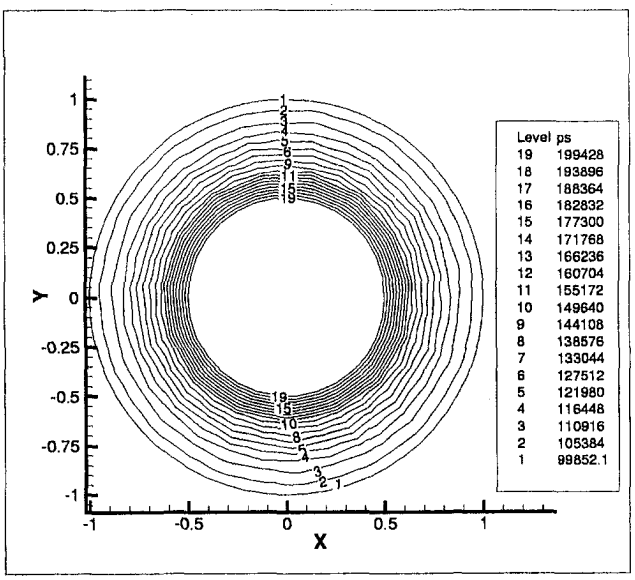

Fig. 8 Computed principal stress distribution with outer boundary tractions and displacements specified. Nothing was specified on the inner boundary.

Three different solution techniques were tested: a sparse QR factorization (Matstoms, 1991), a conjugate gradient for least squares method and least-squares QR code, and a CG solver applied to solving the normalized equations. The two basic test geometries included a rectangular plate and an annular disk (Fig. 1).

For heat conduction, one analytical test problem consisted of a rectangular homogeneous plate with uniform temperatures specified at the opposite boundaries and adiabatic conditions specified at the remaining two opposite boundaries. The finite element method solution of this direct problem was less than one percent in error compared to the analytical solution. Another simple test case was steady heat conduction in an annular homogeneous disk. In a direct (well-posed) problem a uniform temperature of 50.0 K was enforced on the inner circular boundary while a temperature of 10.0 K was enforced on the outer circular boundary. The temperature field computed with the finite element method had a maximum error of 1.0 percent compared to the analytical solution.

For elasticity, one analytical test problem consisted of a rectangular homogeneous plate under uniform tension at one end while having a fixed opposite boundary and zero tractions on the side walls. The finite element method solution of this direct problem was less than 1.0 percent in error. Another elasticity test case was also utilized where an annular pressure vessel was used to test the finite element method code (Martin et al., 1995). The finite element method solution of a direct problem was obtained when specifying tractions on both the inner and outer circular boundaries. The computed stress distributions were less than 2.0 percent in error compared to the analytical solution (Dennis and Dulikravich, 1998a).

Next, the combined thermoelastic analysis and inverse problems were attempted on an annular disk shown in Fig. 1. The outer circular boundary was constructed with 60 points while 30 points were used for the inner circular boundary. The triangular mesh contained 574 nodes and 242 quadratic elements. For the analysis problem, a temperature of 50.0 K was specified on the outer

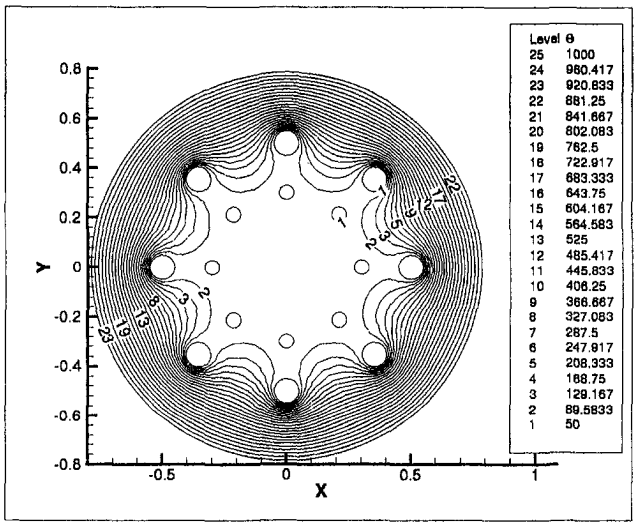

Fig. 9 Computed isotherms with inner and outer boundary temperatures specified

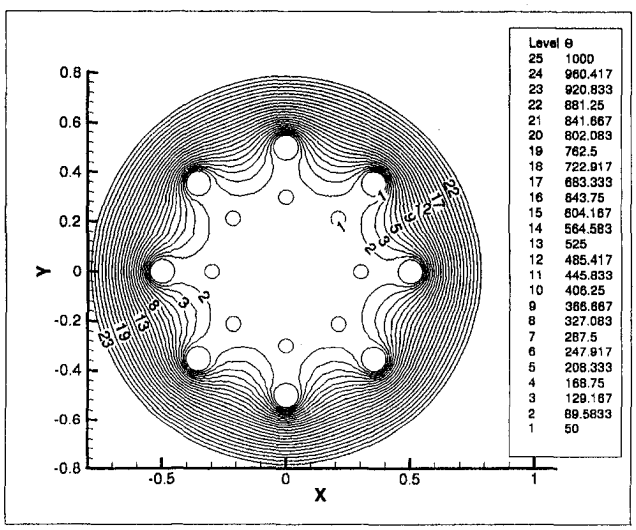

Fig. 10 Computed isotherms with outer boundary temperatures and fluxes specified. Nothing was specified on the inner boundary.

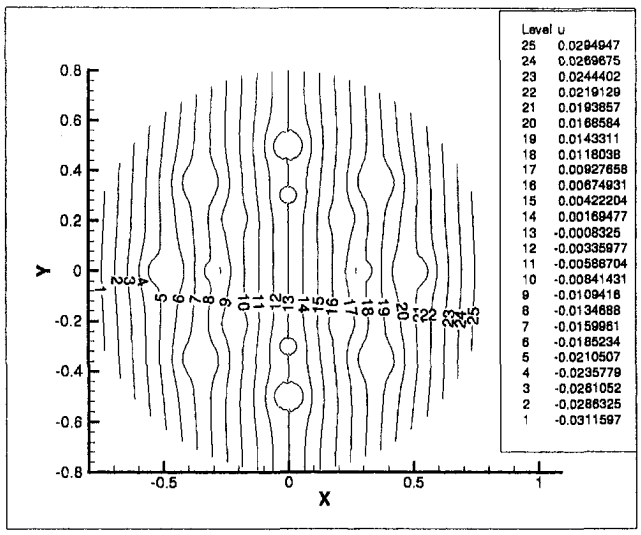

Fig. 11 Computed displacements in *x*-direction with inner and outer boundary tractions specified

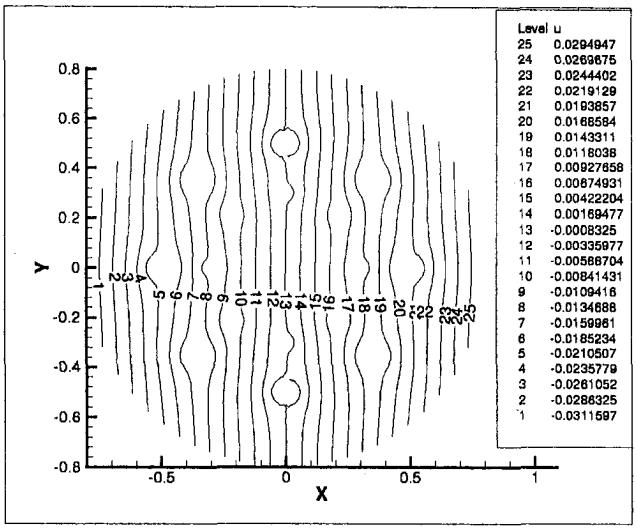

Fig. 12 Computed displacements in *x*-direction with outer boundary tractions and displacements specifies. Nothing was specified on the inner boundary.

circular boundary and 10.0 K was specified on the inner circular boundary. Simultaneously, a tensile surface stress of 101.0 kPa was specified on the outer circular boundary and a tensile stress of 202.0 kPa was specified on the inner circular boundary. The following material properties were used: $E = 2.0 \times 10^3$ Pa, $\nu = 2 \times 10^{-1}$, $\alpha = 2.0 \times 10^{-3}$ K^{-1}, and $k = 1.0$ Wm^{-1} K^{-1}. The computed temperature and stress distributions are shown in Figs. 3, 5, and 7.

The inverse problem was then created by overspecifying the outer circular boundary with the double-precision values of temperatures, fluxes, displacements, and tractions obtained from the numerical solution of the analysis problem. At the same time, no boundary conditions were specified on the inner circular boundary (Martin and Dulikravich, 1996a). A damping parameter of $\Lambda = 0$ was used. The computed temperature and stress distributions are shown in Figs. 4, 6, and 8. The maximum relative differences in temperatures, displacements, and stresses between the analysis and inverse results were less than 0.1 percent when solved with a QR factorization.

As a second thermoelastic test case, an analysis and an inverse problem were solved on the domain shown in Fig. 2. The domain was composed of 16 internal holes, each defined with 15 nodes. The outer circular boundary was constructed with 250 nodes. The triangular mesh contained 2310 nodes and 4170 linear elements.

For the analysis problem, a temperature of 1000.0 K was specified on the outer circular boundary and 50.0 K was specified on the 16 inner circular boundaries. A pressure of 101.0 kPa was applied to the outer boundary while a pressure of 202.0 kPa was applied to each of the 16 inner boundaries. The following material properties were used: $E = 2 \times 10^6$ Pa, $\nu = 10^{-1}$, $\alpha = 10^{-6}$ K^{-1}, $k = 1.0$ Wm^{-1} K^{-1}. The computed temperature and stress distributions from this well-posed (direct or analysis) problem are shown in Figs. 9, 11, and 13.

For the inverse problem, the boundary temperatures, fluxes, displacements, and tractions obtained from the forward analysis were specified on the outer circular boundary. No boundary conditions were specified on any of the 16 inner circular boundaries. Regularization method 3 was used. A damping parameter was $\Lambda = 1 \times 10^{-8}$ when determining the temperature field and $\Lambda = 1 \times 10^{-4}$ was used when computing the displacement field.

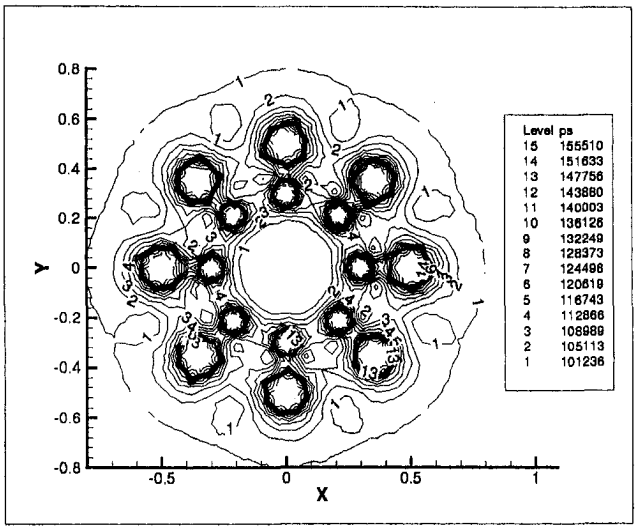

Fig. 13 Computed principal stress distribution with inner and outer boundary tractions specified

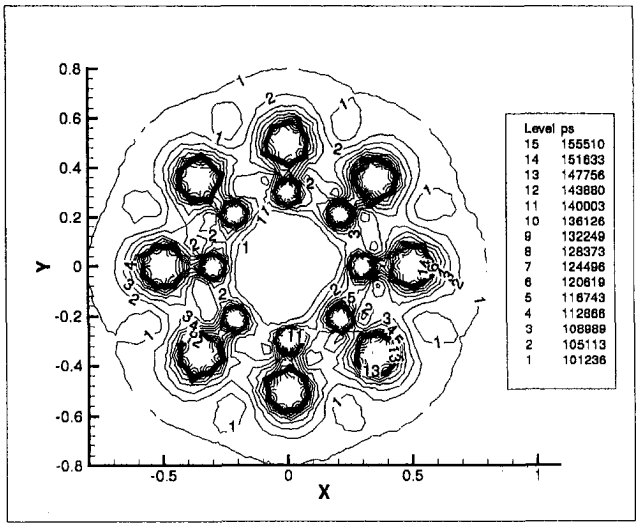

Fig. 14 Computed principal stress distribution with outer boundary tractions and displacements specified. Nothing was specified on the inner boundary.

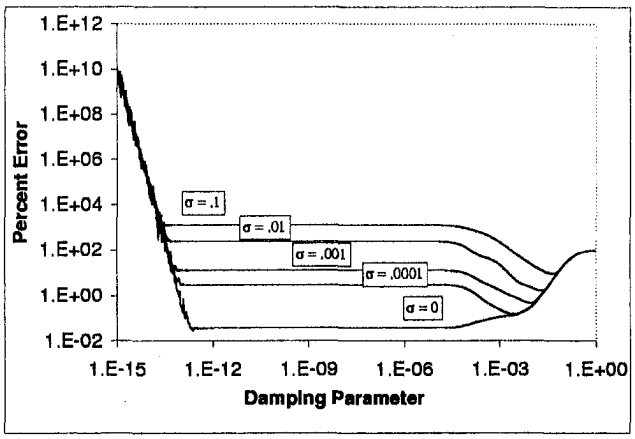

Fig. 15 Average error of predicted temperatures on unknown boundaries for regularization method 1 on annular region

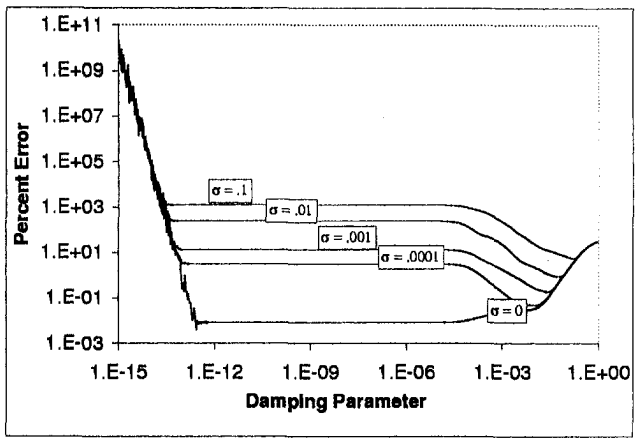

Fig. 16 Average error of predicted temperatures on unknown boundaries for regularization method 2 on annular region

The computed temperature and stress distributions from this ill-posed (inverse) problem are shown in Figs. 10, 12, and 14. The average relative differences between the numerical solutions of the forward and inverse temperatures, fluxes, displacements, and stresses were less than 0.1 percent when solved using a QR factorization.

Sensitivity to Input Error

The inverse heat conduction problem on the annular disk and multiply connected domain problems were tested with simulation of random measurement errors in the overspecified temperatures and fluxes. Random errors in the known boundary temperatures and fluxes were generated using the following equations (Martin and Dulikravich, 1996a):

$$\Theta = \Theta_{bc} \pm \sqrt{-2\bar{\sigma}^2 \ln R} \tag{41}$$

$$Q = Q_{bc} \pm \sqrt{-2\bar{\sigma}^2 \ln R} \tag{42}$$

For each case, Eqs. (41)–(42) were used to generate errors in both the known boundary temperatures and fluxes obtained from the numerical solution of the forward problem.

For the annular disk case, Figs. 15, 16, and 17 show the effect of the standard deviation, $\bar{\sigma}$, and damping parameter, Λ, on the average error of the temperatures recovered on the unknown boundaries compared to the temperatures given by the forward solution. Regularization method 3 gave the best results for all values of $\bar{\sigma}$. It produced errors in the unknown boundary conditions of the same magnitude as the input errors in the known boundary conditions.

For the multiply connected domain case, Figs. 18, 19, and 20 show the effect of the standard deviation, $\bar{\sigma}$, and damping parameter, Λ, on the average error of the temperatures recovered on the unspecified boundaries compared to the values given by the forward solution. None of the regularization methods worked well with this case when simulated measurement errors were applied. The input errors in the overspecified boundary conditions were amplified by several orders of magnitude in the temperatures predicted on the unspecified boundary. These results indicate that this finite element method inverse method requires better regularization if measurement errors are to be used with complicated multidomain geometries.

Discussion of Results

All three sparse matrix solvers performed well for test cases with relatively small number of variables. The QR factorization was found to provide the highest accuracy in the shortest computing time. For each of the test problems presented here the total solution time was less than five seconds on a Pentium 200 MHz PC. However, the QR factorization failed for larger problems where the number of grid points was greater than about 2000. This is most likely due to the instability of the QR

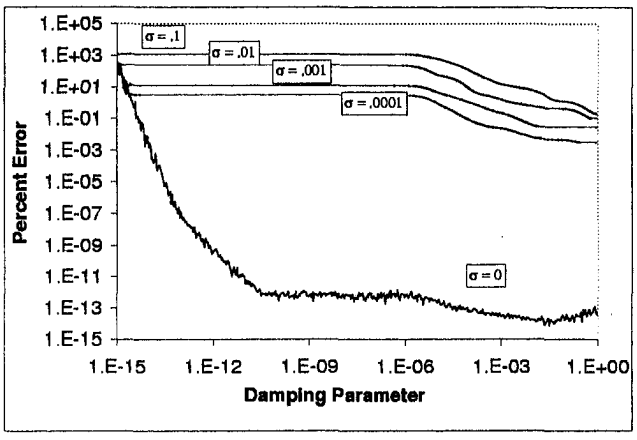

Fig. 17 Average error of predicted temperatures on unknown boundaries for regularization method 3 on annular region

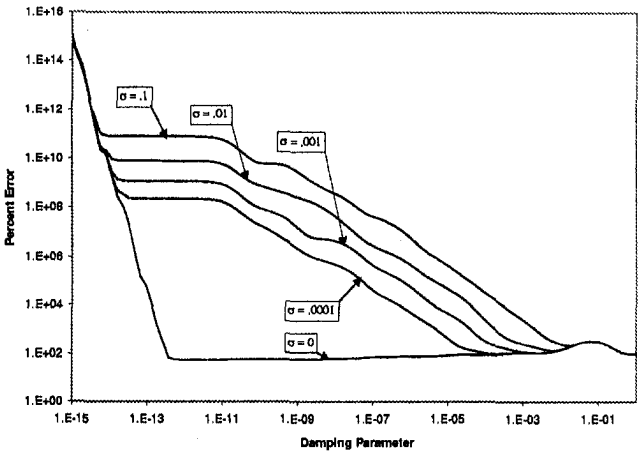

Fig. 18 Average error of predicted temperatures on unknown boundaries for regularization method 1 on multiply connected domain

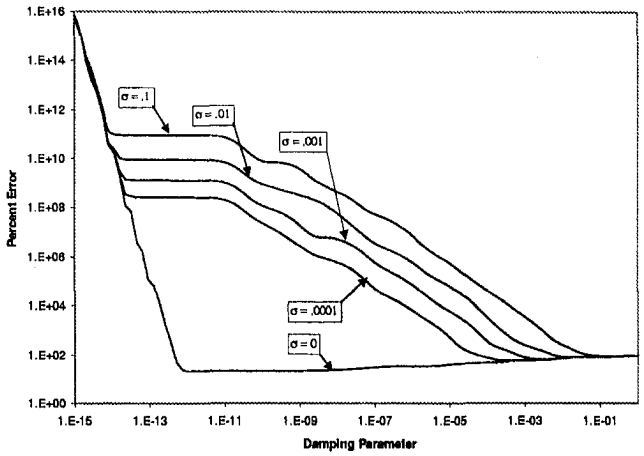

Fig. 19 Average error of predicted temperatures on unknown boundaries for regularization method 2 on multiply connected domain

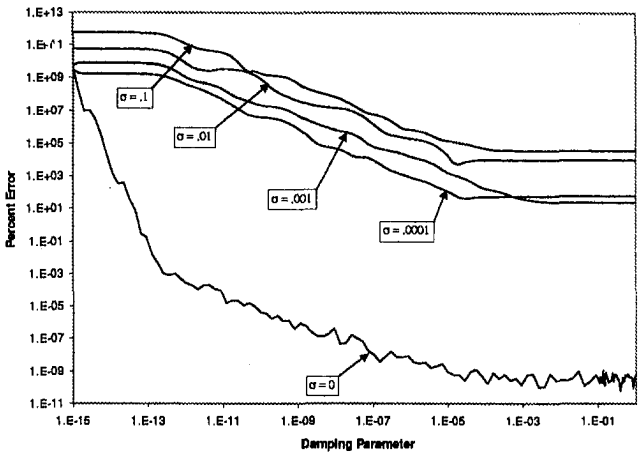

Fig. 20 Average error of predicted temperatures on unknown boundaries for regularization method 3 on multiply connected domain

algorithm when dealing with systems with high condition numbers (Golub and Van Loan, 1996). Applying small amounts of regularization ($\Lambda > 10^{-16}$) to the sparse matrix eliminated the instability. The CG method applied to the normalized equations worked well for problems with less than 100 nodes. For more than 100 nodes, this method required many iterations to converge to a solution less accurate than the QR solution. When regularization was applied to the sparse matrix, the CG convergence improved dramatically but the QR factorization was still much faster by comparison. The conjugate gradient least-square and least-squares QR methods were found to be slow for problems with more than 500 nodes, but were able to provide better solutions than those obtained with the CG applied to the normal equations.

Conclusion

A unified formulation for inverse determination of unknown steady boundary conditions in thermoelasticity has been developed and tested numerically using finite element method on several two-dimensional multiply connected configurations. The main conclusion is that the type and the amount of regularization used can significantly affect the accuracy of the results. This is true for the cases with no errors in the overspecified boundary conditions and for the cases with a random input error taken into account.

Acknowledgments

The authors are grateful for the National Science Foundation Grant DMI-9522854 monitored by Dr. George A. Hazelrigg, the NASA Glenn Research Center Grant NAG3-1995 facilitated by Dr. John Lytle and supervised by Dr. Kestutis Civinskas, for ALCOA Foundation Faculty Research Award facilitated by Dr. Yimin Ruan and Dr. Owen Richmond, and for Lockheed Martin Skunk Works grant supervised by Mr. Thomas Oatway.

References

Boschi, L., and Fischer, R. P., 1996, "Iterative Solutions for Tomographic Inverse Problems: LSQR and SIRT," Tech. Rep. Seismology, Harvard University, Cambridge, MA.

Dennis, B. H., and Dulikravich, G. S., 1998a, "A Finite Element Formulation for the Detection of Boundary Conditions in Elasticity and Heat Transfer," *International Symposium on Inverse Problems in Engineering Mechanics-ISIP'98,* M. Tanaka and G. S. Dulikravich, eds., Nagano City, Japan, Mar. 24–27, 1998, Elsevier Science, Dordrecht, The Netherlands, pp. 61–70.

Dennis, B. H., and Dulikravich, G. S., 1998b, "Simultaneous Determination of Temperatures, Heat Fluxes, Deformations, and Tractions on Inaccessible Boundaries," *Symposium on Inverse Problems in Mechanics, ASME IMECE'98,* L. G. Olson and S. Saigal, eds., Anaheim, CA, Nov. 15–20, ASME-AMD-Vol. 228, ASME, New York, pp. 1–10.

Golub, G. H., and Van Loan, C. F., 1996, *Matrix Computations,* 3rd Ed., Johns Hopkins, Baltimore, MD.

Hensel, E. H., and Hills, R., 1989, "Steady-State Two-Dimensional Inverse Heat Conduction," *Numerical Heat Transfer,* Vol. 15, pp. 227–240.

Kassab, A. J., Moslehy, F. A., and Daryapurkar, A., 1994, "Detection of Cavities by Inverse Elastostatics Boundary Element Method: Experimental Results," *Boundary Element Technology IX,* C. A. Brebbia and A. J. Kassab, eds., Computational Mechanics Publications, Southampton, UK, pp. 85–92.

Larsen, M. E., 1985, "An Inverse Problem: Heat Flux and Temperature Prediction for a High Heat Flux Experiment," Tech. Rep. SAND-85-2671, Sandia National Laboratories, Albuquerque, NM.

Maniatty, M. M., and Zabaras, N. J., 1994, "Investigation of Regularization Parameters and Error Estimating in Inverse Elasticity Problems," *International Journal of Numerical Methods in Engineering,* Vol. 37, pp. 1039–1052.

Martin, T. J., and Dulikravich, G. S., 1996a, "Inverse Determination of Boundary Conditions in Steady Heat Conduction With Heat Generation," ASME JOURNAL OF HEAT TRANSFER, Vol. 118, pp. 546–554.

Martin, T. J., and Dulikravich, G. S., 1996b, "Inverse Shape and Boundary Condition Problems and Optimization in Heat Conduction," *Advances in Numerical Heat Transfer,* W. J. Minkowycz and E. Sparrow, eds., Taylor & Francis, London, pp. 324–367.

Martin, T. J., Halderman, J., and Dulikravich, G. S., 1995, "An Inverse Method for Finding Unknown Surface Tractions and Deformations in Elastostatics," *Computers and Structures,* Vol. 56, No. 5, pp. 825–836.

Matstoms, P., 1991, "The Multifrontal Solution of Sparse Least Squares Problems," Ph.D. thesis, Linköping University, Sweden.

Neumaier, A., 1998, "Solving Ill-Conditioned and Singular Linear Systems: A Tutorial on Regularization," SIAM Review, to appear.

Paige, C. C., and Saunders, M. A., 1982, "LSQR: An Algorithm for Sparse Linear Equations and Sparse Least Squares," *ACM Transactions on Mathematical Software,* Vol. 8, No. 1, pp. 43–71.

Shewchuk, J. R., 1996, "Triangle: Engineering a 2D Quality Mesh Generator and Delaunay Triangulator," *First Workshop on Applied Computational Geometry,* Philadelphia, PA.

Tikhonov, A. N., and Arsenin, V. Y., 1977, *Solutions of Ill Posed Problems,* V. H. Wistom & Sons, Washington, DC.

K. Ezato
Kyushu University, Fukuoka, and
Japan Atomic Energy Research Institute,
Ibaraki, Japan

A. M. Shehata
Xerox Corporation,
Webster, NY

T. Kunugi
Kyoto University, Kyoto, and
Japan Atomic Energy Research Institute,
Ibaraki, Japan

D. M. McEligot
Idaho National Engineering and
Environmental Laboratory/LMITCo,
Idaho Falls, ID, and
University of Arizona,
Tucson, AZ
Fellow ASME

Numerical Prediction of Transitional Features of Turbulent Forced Gas Flows in Circular Tubes With Strong Heating

In order to treat strongly heated, forced gas flows at low Reynolds numbers in vertical circular tubes, the k-ϵ turbulence model of Abe, Kondoh, and Nagano (1994), developed for forced turbulent flow between parallel plates with the constant property idealization, has been successfully applied. For thermal energy transport, the turbulent Prandtl number model of Kays and Crawford (1993) was adopted. The capability to handle these flows was assessed via calculations at the conditions of experiments by Shehata (1984), ranging from essentially turbulent to laminarizing due to the heating. Predictions forecast the development of turbulent transport quantities, Reynolds stress, and turbulent heat flux, as well as turbulent viscosity and turbulent kinetic energy. Overall agreement between the calculations and the measured velocity and temperature distributions is good, establishing confidence in the values of the forecast turbulence quantities—and the model which produced them. Most importantly, the model yields predictions which compare well with the measured wall heat transfer parameters and the pressure drop.

Introduction

Gas cooling offers the advantages of inherent safety, environmental acceptability, chemical inertness, high thermal efficiency, and a high-temperature working fluid for electrical energy generation and process heating. Consequently, helium and other gas systems are considered as coolants for advanced power reactors, both fission and fusion. To advance technology for gas-cooled reactors, the High Temperature Engineering Test Reactor (HTTR) is under construction at the Oarai Research Establishment of the Japan Atomic Energy Research Institute (Takase, Hino, and Miyamoto, 1990). Concepts for fusion power plants with helium coolants include ARIES-I and ARIES-IV (Najmabadi et al., 1991, 1992), DEMO (Wong et al., 1995) and Prometheus (Waganer, 1993) in the United States and SSTR-2 (Yamazaki, 1992) and DREAM-2 (Nishio, 1993, 1995) in Japan.

These applications have in common turbulent flow with significant gas temperature variation along and/or across the cooling channels. The temperature range causes variation of the gas properties, invalidating the use of design relations such as the popular Dittus-Boelter correlation (Dittus and Boelter, 1930). An alternate approach is to apply computational thermal fluid dynamics (CTFD) using a turbulence model that provides reasonable predictions in such flow fields (Iacovides and Launder, 1995). Unfortunately, many proposed models provide poor predictions for convective heat transfer for forced flow in simple circular tubes even when the properties can be idealized as constant (Mikielewicz, 1994); property variation and/or possible buoyancy forces increase the difficulty.

General effects of strong heating of a gas are variation of the transport properties, reduction of density causing acceleration of the flow in the central core, and, in some cases, significant buoyancy forces. Growth of the internal thermal boundary layer leads to readjustment of any previously fully developed turbulent momentum profile. No truly fully established conditions are reached because the temperature rises—leading, in turn, to continuous axial and radial variation of properties such as the gas viscosity.

In an application such as the HTTR (or reduction of flow scenarios in other plants) another complication arises. To obtain high outlet temperatures, design gas flow rates are kept relatively low. For example, at the exit of the HTTR cooling channels, the Reynolds number is about 3500. In this range the heat transfer parameters may appear to correspond to turbulent flow or to laminar flow or to an intermediate behavior, depending on the heating rate (Bankston, 1970), with consequent differences in their magnitudes. The situation where laminar values are measured at Reynolds numbers typifying turbulent flow is called "laminarization" by some authors (Perkins, 1975). Several authors have developed approximate criteria for the transitions between these regimes as shown in Fig. 1 (McEligot, 1963; Coon, 1968; Coon and Perkins, 1970; McEligot, Coon, and Perkins, 1970; Akino, 1978; Ogawa et al., 1982). If the designer is to have confidence in a CTFD code, its turbulence model must demonstrate the "right" predictions in these conditions. The ultimate goal of the present study is to reach that state.

Most popular turbulence models have been developed for conditions approximating the constant properties idealization. Before they can be applied with confidence to gas-cooled components with high heat fluxes, they must be verified by comparison to careful measurements of the heat transfer, pressure drop, and mean flow and thermal fields with significant gas property variation.

Previous Work. By comparison to the thermal entry measurements of Perkins and Worsoe-Schmidt (1965), of McEligot, Magee and Leppert (1965) and of Petukhov, Kirillov, and Maidanik (1966), Bankston and McEligot (1970) were able to examine the application of 11 simple turbulence models for high-Reynolds-number turbulent gas flows with properties varying strongly in both axial and radial directions. Best agreement was found with a van Driest mixing length model (van Driest, 1956) with the expo-

Contributed by the Heat Transfer Division for publication in the JOURNAL OF HEAT TRANSFER and presented at the ASME Fluids Engineering Conference, Vancouver, June 1997. Manuscript received by the Heat Transfer Division, Oct. 23, 1996; revision received, Nov. 1, 1998. Keywords: Flow Transition, Forced Convection, Turbulence. Associate Technical Editor: S. Ramadhyani.

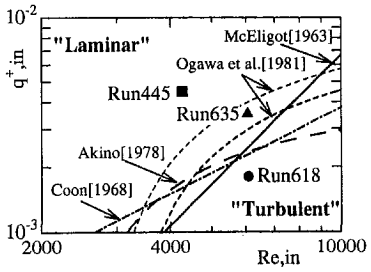

Fig. 1 Proposed criteria for laminarization of heated gas flow in circular tubes with approximately constant heat flux (Fujii, 1991); symbols = experimental conditions of Shehata (1984)

nential term evaluated with wall properties. To accommodate low-Reynolds-number turbulent and laminarizing flows, McEligot and Bankston (1969) modified this model further. This modification was developed by comparison to integral quantities, such as the local Stanton number, since internal profile measurements were not then available for guidance.

The first investigator to succeed in applying an "advanced" turbulence model to laminarization by heating apparently was Kawamura (1979). He tested predictions for low-Reynolds-number turbulence models, k–kL, k–ϵ, k–W and modified k–kL, by comparison to the heat transfer coefficients measured by Perkins and Worsoe-Schmidt (1965), Coon (1968), Coon and Perkins (1970), and Bankston (1970). Kawamura concluded that the modified k–kL model gave good agreement with the experiments. Ogawa and Kawamura (1986, 1987) also observed that the k–kL model predicted their local friction factor data well during laminarization. Extending the work of Kawamura, Fujii et al. (1991) employed three types of turbulence models, k–ϵ, k–ϵ–$\overline{uv}$ and k–kL–$\overline{uv}$, for comparisons to their measurements of strongly heated turbulent gas flow in an annulus; they preferred the predictions seen with the latter model. Recently, this code has been extended to flow in a circular tube (Nishimura et al., 1997).

Torii et al. (1990) and Torii and Yang (1997) modified a k–ϵ model originally developed by Nagano, Hishida, and Asano (1984) (Nagano and Hishida, 1987) and found that it compared favorably with that of the k–kL model for predicting the streamwise variation of the heat transfer coefficient in laminarizing flows in circular tubes. Torii et al. (1991) then compared predictions from this model to their wall measurements for an annulus with the inner wall and with both walls heated; agreement was good at low and high heating rates but not at intermediate values (their $q^+ \approx 0.0031$). Torii et al. (1993) also attempted to apply the Reynolds-stress model of Launder and Shima (1989) to Bankston's St {Re} data for a circular tube. They concluded that the adopted model can generally reproduce the streamwise variation of laminarizing flows, but again predictive accuracy is comparatively poor in the subtle range of turbulent-to-laminar transition.

Objectives and Approach. All of the aforementioned turbulence models for high heating rates were developed without the benefit of internal velocity and temperature distributions in dominant forced flow for guidance or testing. Thus, it is not certain whether their agreements with wall data were fortuitous or not when such agreement occurred. For *dominant forced convection with significant gas property variation,* in low Mach number flow of common gases through a circular tube, apparently the only published profile data available to guide (or test) the development of predictive turbulence models have been K. R. Perkins's measurements of mean temperature distributions (Perkins, 1975). Shehata obtained the first mean velocity distributions for this situation. His careful measurements are now available (Shehata and McEligot, 1995, 1998) to examine this problem and these serve as the bases for evaluation of the predictive technique employed in the present work. Shehata's experiment concentrated on three characteristic cases with gas property variation: turbulent, laminarizing and intermediate or "subturbulent" (as denoted by Perkins).

Recently Abe, Kondoh, and Nagano (1992, 1994) improved the turbulence model of Nagano and Tagawa (1990) which, in turn, was an improvement over the model of Nagano and Hishida employed by Torii et al. The new version (AKN) can be considered "more universal" as it has been developed to treat separated flows as well as flows with pressure gradients; for this reason the principal change is use of the Kolomogorov velocity scale instead of the friction velocity to account for near-wall and low-Reynolds-number effects. Model constants in the transport equations for turbulent kinetic energy and its dissipation rate were also reevaluated for improvement of overall accuracy.

The objectives of the present study are (1) to extend the AKN model to treat strongly heated gas flows in circular tubes and (2) to examine the validity of that extension by comparison to careful measurements for the same conditions. The major new contribution is the use of internal velocity profiles, in addition to internal temperature profiles and integral parameters, in the validation for these air flows with strongly varying fluid properties.

In the following, we first describe the numerical technique and the model used for the predictions. Since the AKN model was developed for flows in wide rectangular ducts (two-dimensional), the predictions are first verified by comparison to accepted correlations and thermal entry measurements for low-Reynolds-number flows in circular tubes under the constant properties idealization.

Nomenclature

c_p = specific heat at constant pressure
C_f = friction factor, $\tau_w/(\rho_b W_b^2/2)$
$C_{\epsilon 1}$, $C_{\epsilon 2}$, C_μ = constants in turbulence model
D = diameter; D_h, hydraulic diameter
f_2, f_μ = functions in turbulence model
G = mass flux, $(\rho W)_{in}$
Gr* = modified Grashof number, gD^3/ν^2
Gr_q = local Grashof number based on heat flux, $gD^4 q''_w/\nu_b^2 \lambda_b T_b$
g_c = units conversion factor, e.g., 1 kg m/(N s^2)
g_i = acceleration of gravity in i-direction
k = turbulent kinetic energy, $-\overline{u_i u_j}/2$
L = characteristic turbulence length scale
Nu = Nusselt number, $\alpha D/\lambda$
P = mean static pressure
P^+ = nondimensional pressure drop, $\rho_{in}(P_{in} - P)/G^2$
Pe_t = turbulent Peclet number, (ν_t/ν) Pr
Pr, Pr_t = molecular and turbulent Prandtl numbers, $\mu c_p/\lambda$ and $\mu_t c_p/\lambda_t$
q^+ = nondimensional wall heat flux, $q''_w/(Gc_pT_{in})$
q''_t = turbulent heat flux, $\rho c_p \overline{ut}$
q''_w = wall heat flux
r = coordinate in radial direction
r_w = tube radius
Re = Reynolds number, $WD/\nu = GD/\mu$
R_t = turbulent Reynolds number, $k^2/\nu\epsilon$
St = Stanton number, Nu/(Re Pr)
T, t = mean temperature and temperature fluctuation
U_i, u_i = mean velocity and velocity fluctuation in i-direction

After a brief description of Shehata's experiment, the *predicted* effects and trends induced by heating at the experimental conditions are examined in terms of key turbulence quantities. Then the predicted mean velocity and temperature distributions are compared to the measurements for verification. For the thermal design engineer, the main questions usually involve wall heat transfer rates and pressure drop so the predictions of these quantities are assessed with the data and we then close with a few concluding remarks.

Predictive Technique

Governing Equations and Numerical Procedure. In analysis of the strongly heated gas flow with significant variation of thermal properties, it is necessary to consider their temperature dependencies in the momentum and energy equations. However, we assume that the fluctuations of the thermal properties are sufficiently small compared with their mean values that we can neglect the terms including the fluctuations of the thermal properties. We deal with the steady state and axisymmetric thermofluid field flowing upward in a circular tube. The working gas is taken as air in the comparisons and viscous dissipation is neglected because the Mach number is small. The low-Re k–ϵ turbulence model proposed by Abe, Kondoh, and Nagano (1994) is employed for predicting the turbulent flow field. This model was developed for predicting separating and reattaching flows and its capabilities for channel flows at various Reynolds numbers were confirmed by the original authors.

The governing equations are as follows:
Continuity:

$$\frac{\partial}{\partial x_i}(\rho U_i) = 0. \tag{1}$$

Momentum:

$$\frac{\partial}{\partial x_j}(\rho U_j U_i) = -\frac{\partial P}{\partial x_i} + \frac{\partial}{\partial x_j}\left[\mu\left(\frac{\partial U_i}{\partial x_j} + \frac{\partial U_j}{\partial x_i}\right) - \rho\overline{u_i u_j}\right] - \rho g_i. \tag{2}$$

Energy:

$$\frac{\partial}{\partial x_j}(\rho c_p U_j T) = \frac{\partial}{\partial x_j}\left(\lambda\frac{\partial T}{\partial x_j} - \rho c_p\overline{u_j t}\right). \tag{3}$$

Turbulent kinetic energy:

$$\frac{\partial}{\partial x_j}(\rho U_j k) = \frac{\partial}{\partial x_j}\left\{\left(\mu + \frac{\mu_t}{\sigma_k}\right)\frac{\partial k}{\partial x_j}\right\} - \rho\overline{u_i u_j}\frac{\partial U_i}{\partial x_j} - \rho\epsilon. \tag{4}$$

Dissipation rate of turbulent kinetic energy:

$$\frac{\partial}{\partial x_j}(\rho U_j \epsilon) = \frac{\partial}{\partial x_j}\left\{\left(\mu + \frac{\mu_t}{\sigma_\epsilon}\right)\frac{\partial \epsilon}{\partial x_j}\right\} - \rho C_{\epsilon 1}\frac{\epsilon}{k}\overline{u_i u_j}\frac{\partial U_i}{\partial x_j} - \rho C_{\epsilon 2} f_2 \frac{\epsilon}{k}\epsilon \tag{5}$$

where turbulence quantities are defined as

$$-\rho\overline{u_i u_j} = \mu_t\left(\frac{\partial U_i}{\partial x_j} + \frac{\partial U_j}{\partial x_i}\right) - \frac{2}{3}\rho k\delta_{ij} \tag{6}$$

$$\mu_t = \rho C_\mu f_\mu \frac{k^2}{\epsilon} \tag{7}$$

$$-\rho c_p\overline{u_j t} = \lambda_t\frac{\partial T}{\partial x_j} \tag{8}$$

$$\lambda_t = \frac{c_p\mu_t}{\mathrm{Pr}_t}. \tag{9}$$

We consider the buoyancy effect only in the momentum equation and not in the turbulence model. Model constants and functions in Eqs. (4), (5), and (7) are taken to be the same as in the AKN model: $C_\mu = 0.09$, $C_{\epsilon 1} = 1.5$, $C_{\epsilon 2} = 1.9$, $\sigma_k = 1.9$, $\sigma_\epsilon = 1.4$,

$$f_\mu = \{1 - \exp(-y^*/14)\}[1 + (5/R_t^{3/4})\exp\{-(R_t/200)^2\}] \quad \text{and}$$

$$f_2 = [1 - 0.3\exp\{-(R_t/6.5)^2\}][1 - \exp(-y^*/3.1)]^2.$$

The turbulent Prandtl number, Pr_t, in Eq. (9) is treated as a function of the distance from the wall, as suggested by Kays and Crawford (1993),

$$\mathrm{Pr}_t = \left[\frac{1}{2\,\mathrm{Pr}_{t\infty}} + \frac{c\,\mathrm{Pe}_t}{\sqrt{\mathrm{Pr}_{t\infty}}} - (c\,\mathrm{Pe}_t)^2\left\{1 - \exp\left(\frac{-1}{c\,\mathrm{Pe}_t\sqrt{\mathrm{Pr}_{t\infty}}}\right)\right\}\right]^{-1} \tag{10}$$

where $\mathrm{Pe}_t = (\mu_t/\mu)\mathrm{Pr}$, $\mathrm{Pr}_{t\infty}$ is the value of Pr_t far from the wall (=0.8) and c is an empirical constant (=0.3).

Equations (1)–(5) are discretized with a finite control volume method, employing the QUICK scheme (Leonard, 1979) for the

Nomenclature (cont.)

U, u = mean velocity and velocity fluctuation in radial direction
u_ϵ = Kolomogorov velocity scale, $(\nu\epsilon)^{1/4}$
u_τ = friction velocity, $\sqrt{|\tau_w|/\rho}$
W, w = mean velocity and velocity fluctuation in axial direction
x_i = coordinate in i-direction
y = distance from wall surface
y^+ = nondimensional distance from wall surface, $u_\tau y/\nu$
y^* = nondimensional distance from wall surface, $u_\epsilon y/\nu$
z = coordinate in axial direction
$\overline{(\ )}$ = ensemble-average value
$\{\ \}$ = function of

Greek symbols

α = heat transfer coefficient, $q''_w/(T_w - T_b)$
δ_{ij} = Kronecker delta
ϵ = dissipation rate of turbulent kinetic energy, $\nu\overline{(\partial u_i/\partial x_j)(\partial u_i/\partial x_j)}$
λ, λ_t = molecular and turbulent thermal conductivities
μ, μ_t = molecular and turbulent viscosities
ν, ν_t = kinetic viscosity and eddy diffusivities
ρ = density
σ_k, σ_ϵ = model constants for turbulent diffusion of k and ϵ
τ_w = wall shear stress

Subscripts

b = evaluated at bulk temperature
in = evaluated at start of heating
w = evaluated at wall surface
z = evaluated at local axial position

convective term in Eqs. (2)–(5). Other terms were discretized by second-order central differences. In conjunction with the momentum equations, the continuity equation was converted to a pressure correction equation, which was solved via the SIMPLE algorithm (Patankar, 1980). The set of the algebraic equations is solved with Gauss elimination. The convergence criteria of the residuals of all equations were assumed to be less than 10^{-6} of their total inflow rates. The thermal properties are estimated at every iteration by numerical functions described in the following section. The computations are performed on the FUJITSU VPP500 machine.

For the results presented, the numerical grid employed eighty nodes with variable spacing between the centerline and the wall, concentrated near the wall. The first node from the wall was located at $y^+ \approx 0.5$ or less. A length of 150 diameters was employed with 2000 nodes for predicting the constant properties flow. The nodes in the streamwise direction were distributed uniformly. For comparison to Shehata's experiment, a length 60 diameters long was chosen with 1000 axial nodes; the last axial node was set at about ten diameters beyond the last useful data point.

Grid dependency was tested by repeating calculations for the "subturbulent" experimental case with 60, 80, and 100 nonuniform nodes in the radial direction. The velocity and temperature profiles in the fully developed region agreed within about one percent. To investigate the streamwise grid spacing, calculations were conducted with 500, 1000, and 1500 nodes. For all three cases, wall temperature, Nusselt number, and pressure drop predictions agreed within one percent. In addition, predictions with 80 nodes in the radial direction and 1000 nodes in the axial direction were compared to experimental results, as presented in coming sections.

Thermal Properties. For air, the thermal properties are evaluated as power-law functions of the pointwise temperature with density estimated via the perfect gas approximation (Perkins, 1975; Shehata, 1984) as follows:

$$\rho = \rho_{\text{ref}}(P/P_{\text{ref}})(T_{\text{ref}}/T) \tag{11}$$

$$\mu = \mu_{\text{ref}}(T/T_{\text{ref}})^{0.67} \tag{12}$$

$$c_p = c_{p,\text{ref}}(T/T_{\text{ref}})^{0.095} \tag{13}$$

$$\lambda = \lambda_{\text{ref}}(T/T_{\text{ref}})^{0.805}. \tag{14}$$

The subscript ref indicates that the value was taken at the reference state, typically at the inlet gas temperature and pressure (near 25°C and 0.09 MPa). For the range $270 < T < 900$ K, the tabulated values by the National Bureau of Standards (NBS 564) show agreement with the perfect gas approximation within 0.04 percent and with the power laws for specific heat, viscosity, and thermal conductivity within about $2\frac{1}{2}$, 2, and 3 percent, respectively; these levels are of about the same order as the departures of the tables from measured properties (Hilsenrath et al., 1955).

Boundary Conditions. The governing equations are the elliptic sets of partial differential equations. Thus, they require specification of boundary conditions at the entrance, wall, and exit along with axisymmetry. Nonslip impermeable wall conditions are assumed and the dissipation rate of turbulent energy at the wall is estimated as $\epsilon_w = 2\nu_w(\partial\sqrt{k}/\partial y)_w^2$, where y represents the coordinate normal to the wall.

The classic case of a fully developed flow at the thermal entry is approximated as follows. The thermal condition at the wall is taken to be adiabatic for the first 25 diameters, followed by a specified uniform wall heat flux. Entering conditions are isothermal temperature and approximations of fully developed mean velocity and turbulence profiles, estimated from the literature (Schlichting, 1968; Hinze, 1975; Kays and Crawford, 1993); these quantities then are allowed to readjust in accordance with the AKN model through the adiabatic entry to yield a new approximation of fully developed profiles at the start of heating that is consistent with the model. Outlet conditions are specified by setting streamwise gradients to zero (first partial derivatives for w, u, k, and ϵ, and the second for T).

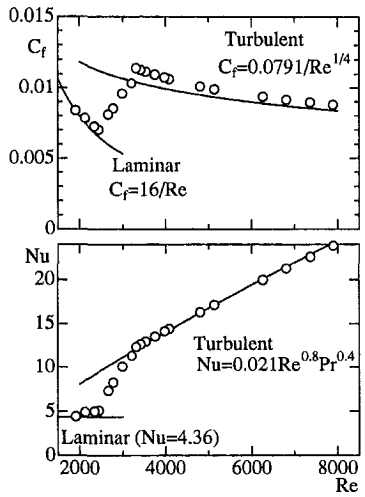

Fig. 2 Comparison of predictions from present model (circles) to empirical turbulent correlations and theoretical laminar results for fully established flow with constant fluid properties

Predictions of Constant Properties Flows

To validate the numerical code and the turbulence model used in the present study for low-Reynolds-number turbulent flows, we calculated the heat transfer coefficients and friction factors for gas flows in a circular tube with uniform wall heat flux and the constant properties idealization. The flow range was $1900 < \text{Re} < 8000$ and the gas properties were selected for air. For these calculations, the heated region was taken as 125 diameters long, starting at $z/D = 25$. Predicted values of the Nusselt number and friction factor at the outlet are compared to empirical correlations for turbulent flow and to analytic values for laminar flow in Fig. 2; the circles represent the present numerical predictions.

McEligot, Ormand, and Perkins (1966) showed that the Dittus-Boelter correlation (1930) with the coefficient taken as 0.021 for common gases (McAdams, 1954; Kawamura, 1979) is valid to within about five percent for $\text{Pr} \approx 0.7$ and Reynolds numbers greater than about 2500. The present predictions agree closely for $\text{Re} > 3200$. Shehata (1984) found his measured friction factors for fully developed turbulent flow to fall between the Blasius relation (Schlichting, 1968) and the Drew, Koo, and McAdams correlation (1932). The agreement with the present friction calculations is also reasonable above $\text{Re} \approx 3200$, ours being about five percent high. Below this Reynolds number, the predicted Nusselt numbers and friction factors decrease smoothly towards the theoretical laminar values as the Reynolds number decreases, approaching closely for $\text{Re} < 2500$. Below $\text{Re} \approx 2000$, the values for heat transfer differ by about one percent while friction results differ by about 0.3 percent.

In their study, Torii et al. (1989, 1990) found that their ability to predict laminarizing flows coincided with the capability of the fully established, constant properties calculations to indicate a transition from turbulent to laminar flow near $\text{Re} \approx$ 2-3000. The original Nagano and Hishida model (1987) lacked this capability (Fig. 2 in Torii et al. (1990)), with the turbulent prediction gradually merging with the laminar value as the Reynolds number decreased to about 1000. It is interesting to the present authors that, for flow between parallel plates, the AKN model shows the latter behavior (Fig. 2(*a*) in Abe, Kondoh, and Nagano (1994)). However, with no change in model constants or functions, the same AKN model predicts reasonable behavior in this sense for a circular tube (our Fig. 2)! It is worth warning thermal designers that caution is appropriate in applying a turbulence model to a geometry other than one for which it has been adequately tested.

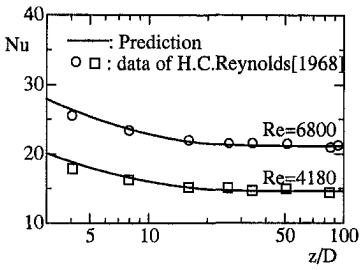

Fig. 3 Comparison of predictions from present model to thermal entry measurements of H. C. Reynolds (1968), constant fluid properties.

As noted in the section on predictive techniques, the present heat transfer predictions are based on the turbulent Prandtl number model recommended by Kays and Crawford (KC). Before choosing this model, we attempted a "two-equation heat transfer model" and a different Pr, model. In both cases, predictions for the fully established Nusselt numbers were about ten percent or more higher than the Dittus-Boelter correlation, so we selected the KC model as better for our purposes.

In addition to predictions for fully established flow, it is desirable to determine whether the turbulence model predicts the thermal entry development adequately in the Reynolds number range of interest. Reynolds (1968) and Reynolds, Swearingen, and McEligot (1969) conducted experimental and analytic studies of the thermal entry for low-Reynolds-number flows, providing semi-analytic correlations with the constant property idealization. The local experimental measurements were extrapolated to unity versus T_w/T_b, i.e., constant properties, for comparison (and verification) of the analytic predictions. In Fig. 3, predictions from the present model are compared to Reynolds's data at Re $\approx$ 6800 and 4180. For $z/D \approx 4$ and greater, agreement of the predictions presented is within the experimental uncertainty of the measurements.

In summary, the proposed AKN/KC model appears to perform satisfactorily for constant-properties flow of common gases in pure forced convection in circular tubes.

Predicted Distributions of Mean Turbulence Quantities With High Heat Fluxes

The experimental objective of Shehata (1984) and Shehata and McEligot (1998) was to measure the distributions of the mean streamwise velocity and temperature for *dominant forced convection* in a well-defined axisymmetric experiment involving significant variation of the gas transport properties across the viscous layer. Experiments were conducted for air flowing upwards in a vertical circular tube heated resistively at atmospheric pressure. Experimental conditions concentrated on three characteristic cases with gas property variation as follows: (1) essentially turbulent flow with slight, but significant, air property variation, (2) severe air property variation evolving to near laminar flow (as implied by the integral heat transfer parameters), and (3) moderate gas property variation, yielding behavior that could be intermediate or transitional between the first two. Inlet Reynolds numbers of about (1) 6080, (2) 6050, and (3) 4260 with nondimensional heating rates, q^+, of about 0.0018, 0.0035, and 0.0045, respectively, yielded this range. For ease of reference to the reader, these conditions are called Runs 618, 635, and 445. Internal flow data were obtained at five axial locations: 3.17, 8.73, 14.20, 19.87, and 24.54 diameters. Over the range $5 < z/D < 26$ the wall heat flux was uniform to within about three percent of the average value. Details plus tabulations of resulting data are available in a report by Shehata and McEligot (1995) with some additional information given by Perkins (1975).

As shown by Torii et al. (1990) and Fujii (1991), several functions of $q^+_{in}\{\mathrm{Re}_{in}\}$ have been suggested by investigators as criteria for flow regime prediction. Figure 1 presents Shehata's experimental conditions in these terms. One sees that the characterization of his data as turbulent, intermediate, and laminarizing is consistent with these criteria.

The predicted effects of the model on turbulence quantities of interest are presented next, calculated for the conditions of the three experimental runs for which measurements of the mean velocity distributions are available. In these cases, the grid only extended 35 diameters beyond the start of the heating. The values of the uniform heat fluxes were chosen to coincide with the average values of $q''_w\{z\}$ in the experiment.

The predicted pointwise values of the turbulent viscosity (μ_t/μ) and the behavior of the related turbulent kinetic energy are shown in Fig. 4, where symbols are used to identify axial locations, not data (there were no direct measurements of turbulence quantities); these locations are the same as those where mean velocity and temperature profiles have been measured by Shehata. The abscissae are the normalized wall coordinate; the physical distance from the wall to the centerline. In all three cases, the quantity μ_t/μ is predicted to decrease first near the wall and then further into the core. The axial rates at which these phenomena happen increase with q^+. As a measure of an effective viscous layer thickness, y_v, we can choose the location where $(\mu_t/\mu) = 1$. The value y_v/r_w of the inlet profile for $\mathrm{Re}_{in} \approx 6000$ (runs 618 and 635) is 0.05, and is 0.07 in case of $\mathrm{Re}_{in} \approx 4300$ (run 445). By the last measurement station, it is predicted to grow to $y_v/r_w \approx 0.09$, 0.15 and 0.4 for "conditions" 618, 635, and 445, respectively. These predictions are consistent with the earlier suggestion of one of the present authors that the cause of the unexpected reduction in heat transfer parameters could be a thickening of the viscous sublayer (McEligot, 1963, p. 131). Between $z/D \approx 3$ and 9, the flattened profile of μ_t/μ in the core disappears as the region affected by the wall grows.

The turbulent kinetic energy profiles show some of the same trends (Fig. 4(*b*)). Normalization of the turbulent kinetic energy is by a constant, $u^2_{\tau,in}$, giving a direct measure of the magnitude of the its variation along the tube (i.e., no scaling related to μ, which varies locally with the pointwise temperature). The profiles increase from the wall to a maximum and then decrease to the order of unity at the centerline. An effect of heating appears to be to reduce k near the wall; the higher the heating rate, the greater this effect is calculated to be.

No large changes to the turbulent kinetic energy profiles are forecast for run 618. After $z/D \approx 9$, the magnitude near the wall only varies slightly; it seems near self-preserving. Further towards the center (about $0.1 < y/r_w < 1$), the variation of the expected profiles is nearly negligible until $z/D > 14$; then the peak increases and values near the centerline decrease as the distance increases. At the last station the peak of $k\{y/r_w\}$ is slightly further from the wall than y_v and is further for run 635 than run 618—but, in terms of local wall units, this peak remains at $y^+ \approx 14$ for $3 < z/D < 25$. The profiles $k\{y^+\}$ are forecast to remain almost invariant from the wall to $y^+ \approx 10$ while the flow accelerates and the Reynolds number decreases.

For run 635, initially k decreases near the wall and the peak values decrease as well. After $z/D \approx 9$ the rate of change decreases and for the last half of the tube the change is slight, but one could not claim that it appears to become self-preserving. This run might be considered to laminarize near the wall; this effect leads to lower peaks for $3 < z/D < 14$, then the maxima are predicted to become approximately constant but become further from the wall than for run 618, consistent with a physically thicker effective viscous layer. In wall coordinates (y^+) the variation is less but the trends are the same. With the exception of the entering profile, the peak value occurs near $y^+ \approx 15$, approximately the same as run 618.

The calculations for run 445 show a significant reduction in turbulence kinetic energy along the tube. A region of low values near the wall grows continuously, giving near zero values from the wall to $y/r_w \approx 0.15$ ($y^+ \approx 10$) at the last station. Simultaneously,

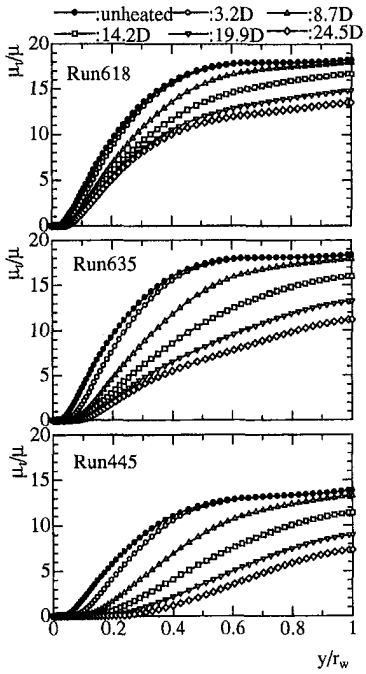

Fig. 4 (*a*)

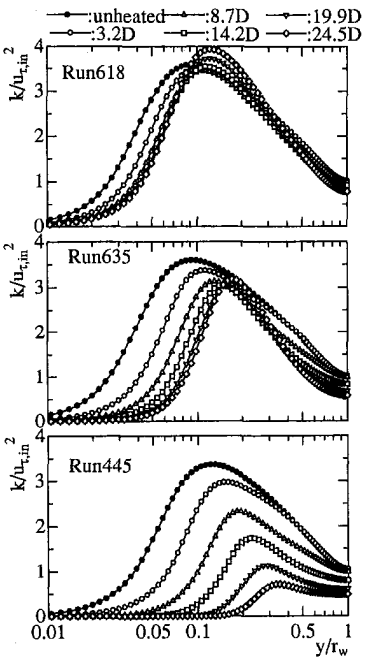

Fig. 4 (*b*)

Fig. 4 Predicted axial development of turbulence quantities for conditions of experiments by Shehata (1984): (*a*) turbulent viscosity and (*b*) turbulent kinetic energy

the peak values decrease continuously and move closer to the center. The centerline value decreases as well but is still nonzero at the last station. These same trends also appear when presented as a function of y^+; no near invariant section is predicted as the profiles continuously decrease in the streamwise direction. Clearly, a laminarization process is being forecast but a hot wire sensor at the centerline would still show turbulent fluctuations (Bankston, 1970; Ogawa et al., 1982).

It is of interest that the predicted maximum values of the turbulent kinetic energy increase in the downstream direction for run 618 but not for the others. In all cases the flow accelerates in the downstream direction, so the wall shear stress is expected to increase approximately as W_b^2. (The acceleration parameter, $K = (\nu_b/W_b^2)(dW_b/dz)$, was approximately 1×10^{-6}, 2×10^{-6}, and 4×10^{-6} for runs 618, 635, and 445, respectively.) Consequently, near the wall the gradient $\partial W/\partial y$ would increase so that the production term in the governing equation for turbulent kinetic energy would as well. For run 618 apparently this increase is predicted to be more rapid with respect to axial distance than the stabilization of the viscous layer due to the acceleration. An alternative explanation could invoke the effects on the dissipation rate. One could calculate the magnitudes of the individual terms as part of the numerical solution and then compare their values to see the predicted relative effects on the local value of the squared difference from the mean (known as the turbulent kinetic energy), but that exercise is beyond the present intended scope. For run 635 the countering effects at $y^+ \approx 15$ apparently balance so the predicted maxima do not change significantly. Then in run 445 the countering effects near the wall are predicted to be greater than the production term and the profiles of this defined turbulence quantity decrease continuously.

Resulting predictions for turbulent shear stress (Reynolds stress) and turbulent heat flux are presented in Fig. 5; these are normalized by local wall values, e.g., $\tau_w\{z\}$. The wall coordinate y^+ is unambiguously defined as $y[g_c\tau_w/\rho_w]^{1/2}/\nu_w$ with local wall values. These two transport quantities show mostly the same effects as each other except the turbulent heat flux is affected by the growth of the thermal boundary layer at "large" values of y^+.

For run 618 the normalized Reynolds stress profiles are forecast to approach a self-preserving condition after $z/D \approx 9$ while the normalized turbulent heat flux appears to be approaching a near asymptotic profile as the thermal boundary layer grows. Predictions for run 635 give lower magnitudes than run 618 for both quantities at equivalent stations. For example, at the last station and $y^+ = 10$ the normalized Reynolds stress profile for run 618 is only slightly lower than the adiabatic entry profile whereas for 635 the comparable profile is forecast to decrease by about 50 percent. Peak values are correspondingly lower.

The normalized turbulent heat flux profile, $q_t''\{y^+\}/q_w''$, is predicted to be almost invariant to $y^+ \approx 15$ in run 618. However, for run 635 at $y^+ = 10$, it is calculated to decrease by about $\frac{2}{3}$ between $z/D \approx 3$ and 25. Peak values of $q_t''\{y^+\}/q_w''$ are predicted to be less for run 635 than for run 618. For both momentum and thermal energy, run 635 shows significantly less turbulent transport than run 618, which is considered to be representative of gas flow with property variation that retains its turbulent character. In that sense, run 635 is predicted to be laminarized to some extent; the viscous-dominated region is forecast to become thicker in wall units as well as in physical distance.

Expectations for run 445 are more extreme suppression of turbulent transport than for run 635. The calculations forecast continuous thickening of the viscous-dominated region and reduction in the maximum values of the normalized Reynolds stresses within the usual viscous layer ($y^+ < 30$–40). Beyond $z/D \approx 9$ the same comments hold for the normalized turbulent heat fluxes. The benefits of turbulent transport are predicted to be significantly decreased as the axial distance increases. For example, within 25 diameters the maximum normalized Reynolds stress is calculated to decrease to about 0.05, about an order of magnitude less than its value for the entering adiabatic profile.

For a slightly higher heating rate ($q^+ \approx 0.0055$), Perkins (1975) showed that his "laminar" turbulence model predicted the development of the mean temperature profile well. With his approach, turbulent adiabatic entering profiles were specified and then the governing equations were solved with turbulent viscosity and turbulent thermal conductivity set to zero through the thermal entry region. The present predictions of the development of the turbulent shear stresses and heat fluxes for run 445 demonstrate why Perkins's approach could be successful at higher heating rates; these turbulent transport quantities are forecast to become negligible quickly after the application of the high heating rate.

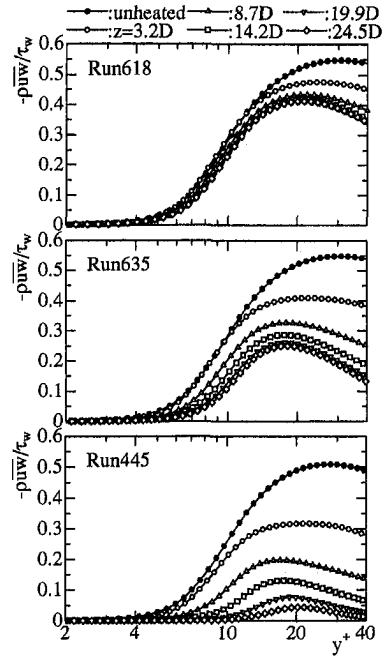

Fig. 5 (*a*)

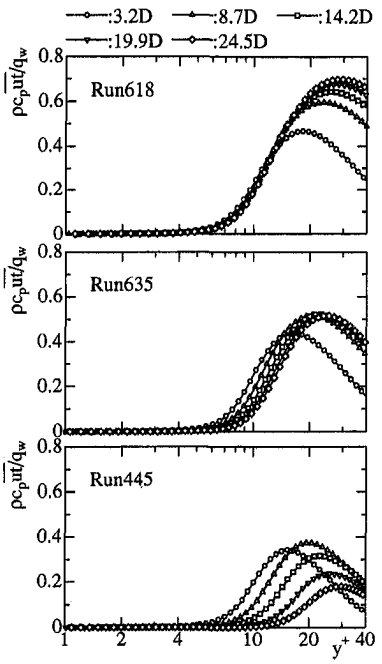

Fig. 5 (*b*)

Fig. 5 Predicted axial development of turbulent transport quantities for conditions of experiments by Shehata (1984): (a) Reynolds stress and (b) turbulent heat flux

One may wonder what are the effects of heating on the "law of the wall." To address this concern, Fig. 6 provides the predicted mean velocity distributions in terms of wall coordinates from $y^+ \approx 3$ to its centerline value. One sees that at these conditions the entire cross section can be considered to be in the "near-wall" region. The figure demonstrates a continual variation of the centerline value of y^+ with axial position and heating rate; this result precludes conveniently presenting the axial development in terms of both wall (y^+) and physical (y/r_w) coordinates on the same graph. At $z/D \approx 3$ one could fit logarithmic curves to the predictions for the two lower heating rates; however, the intercepts and slopes

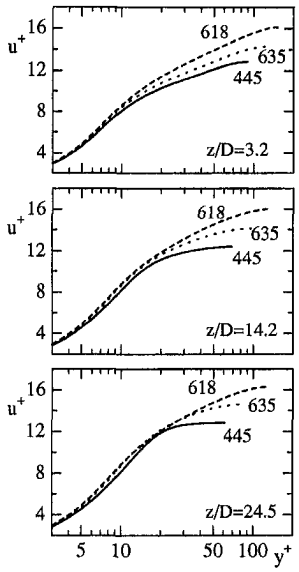

Fig. 6 Predicted development of mean velocity in terms of wall coordinates

differ from the accepted values for the so-called "universal velocity profile." For the remainder of the predictions on this figure, no logarithmic curve can be reasonably fitted. At small values of y^+, the predictions for Run 445 are slightly lower than for the other two runs; this observation is consistent with the predicted trend induced by a favorable streamwise pressure gradient in unheated flows (McEligot, 1985). Consequently, use of turbulence models employing wall functions would not be a reasonable approach for these strongly heated flows.

Comparisons to Measurements

Necessary conditions to consider a turbulence model seriously are that it predict mean velocity and temperature profiles, plus wall heat transfer parameters and pressure drop, satisfactorily for the conditions of interest. The present model is now assessed in those terms. Figure 7 provides direct comparisons of the predictions to measured profiles. The region shown emphasizes the normal viscous layer with coordinates chosen to avoid the uncertainties involved in the determination of u_τ for nondimensionalization. For example, for the temperature profiles t_w^+ is represented by $(T_w - T)/T_{in}$. These comparisons of predictions and data are more severe tests than using coordinates based on a wall shear stress which has been fitted in the viscous layer. Accordingly, no measurements are presented in terms of wall coordinates in the present paper. The measured points nearest the wall correspond to y^+ of about 3 to 5, depending on the heating rate and station. The location $y/r_w = 0.1$ is approximately equivalent to $y^+ \approx 20$ for the entering profiles of runs 618 and 635. At the last station, $y/r_w = 0.5$ is about $y^+ \approx 60$ and 30 for runs 618 and 445, respectively.

Direct measurements of the local wall shear stress are generally not feasible for the conditions of this experiment (and it cannot be deduced from local estimates of dp/dz as in unheated flow since $u\{y\}$ varies continuously in the streamwise direction). The approach of fitting profile data with a Clauser plot is not valid for low Reynolds numbers or for flows changing significantly in the axial direction; the Clauser analysis is based on the assumption that $\tau_w \approx \tau\{y\}$ for $y^+ > \sim 30$, a poor approximation in these situations. Figure 6 has shown that a meaningful "log law" region cannot reasonably be identified for the conditions of these experiments (although the unsuspecting can usually draw a straight line through data on a semi-logarithmic graph).

Experimental uncertainties were estimated employing the technique of Kline and McClintock (1953). Examples of the resulting

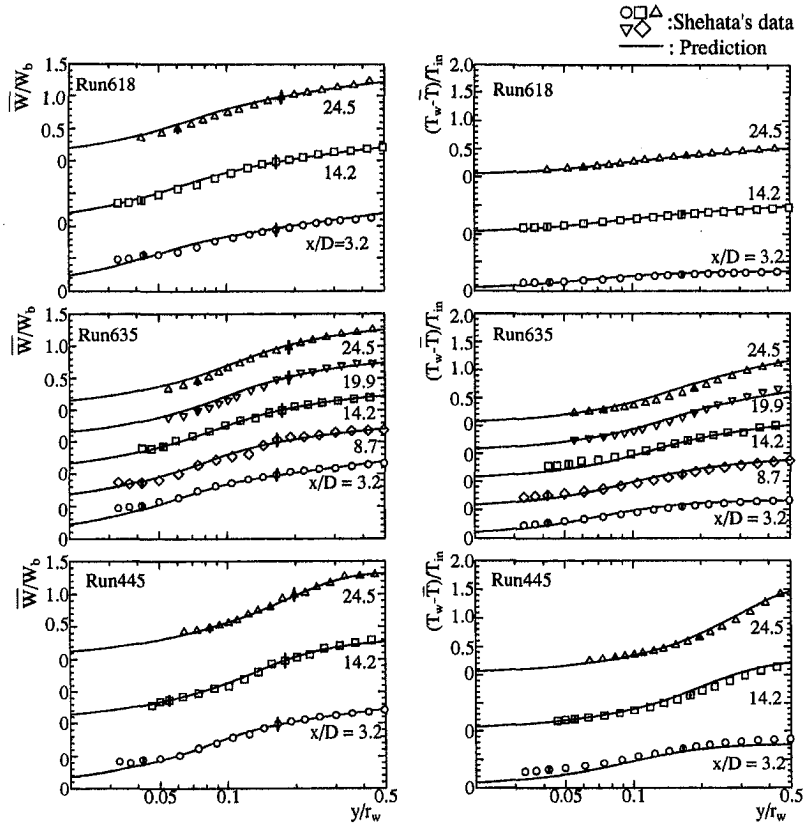

Fig. 7 Predicted axial development of mean streamwise velocity and mean temperature (solid lines) compared to measurements (symbols) of Shehata (1984), with strong heating of air in a vertical circular tube.

uncertainties in velocity and temperature are tabulated as functions of position and experimental run by Shehata (1984). In general, the uncertainty in velocity was calculated to be in the range of eight to ten percent *of the pointwise value,* with the larger percent uncertainties occurring near the wall. The uncertainty in temperature was typically one to two percent of the pointwise absolute temperature. Typical values of these estimates are indicated in Fig. 7 as vertical lines. These estimates are believed to be conservative (i.e., pessimistic) since comparisons of the integrated and measured total mass flow rates for each profile showed better agreement—of the order of three percent or less, except near the exit in the runs with the two highest heating rates. The estimated experimental uncertainty in the Stanton number was six percent or less for the range $3 < x/D < 20$ and for the nondimensional pressure defect it was about four percent at the last measuring station (Perkins, 1975).

The quantity $(T_w - T)/T_{in}$ provides a measure of the gas property variation across the tube. For example, in run 618 $(T_w - T)/T_{in}$ varies by about 50 percent to $y/r_w = 0.5$ at the last station, so μ and k vary by about 40 percent in that region. In contrast, in run 445 they vary by more than that in the first three diameters. At the first station for all runs, the first few velocity data points near the wall appear slightly high relative to appropriate asymptotic behavior, a common feature in experimental measurements (and a good reason not to determine u_τ by fitting $u^+ = y^+$). This location required the longest insertion of the probe support in the experiment so some aspects of the data reduction are more difficult to calculate there.

Overall agreement between the predictions and the measurements is encouraging. Though close examination reveals some differences in detail, the predictions can be considered to be satisfactory at least.

Perkins (1975) and Torii et al. (1993) found the intermediate conditions most difficult to predict (run 635 here). Run 618 shows a slight overprediction of the velocity profile at $z/D \approx 25$ but otherwise all profiles are good. Run 445 predictions look good throughout despite having the largest fluid property variation; this result probably occurs because molecular transport increases in importance once the laminarizing process has begun. So if one wishes the most sensitive test of a turbulence model for low-Reynolds-number flows with gas property variation, conditions like those of run 635 may be key.

Since run 635 was recognized in advance as most difficult, two extra sets of internal profiles were measured in the experiment. Agreement between calculations and data is good for the first three stations. Then at $z/D \approx 20$ and 25 the velocity is overpredicted near the wall and at $z/D \approx 25$ the quantity $(T_w - T)/T_{in}$ is overpredicted in the range $0.1 < y/r_w < 0.25$ (corresponding approximately to $8 < y^+ < 20$), i.e., $T\{y\}$ is *under*predicted. In the viscous layer, a higher velocity is caused by a lower value of μ_t, which also leads to a higher thermal resistance in the layer; this higher thermal resistance would interfere with thermal energy transport beyond the region leading, in turn, to lower temperatures further from the heated wall. If one wishes to improve the model further, these observations could provide a starting point. For the present purposes, the level of agreement seen is considered satisfactory.

Thermal design engineers usually find prediction of the wall heat transfer parameters and friction to be most important. Figure 8 provides these tests for the present model; vertical lines denote the estimated experimental uncertainties. Figure 8(*a*) compares local Stanton numbers; since viscosity increases as the gas is heated, the Reynolds number decreases with an increase in z and the axial progression is from right to left. Dashed lines represent asymptotes for fully established flow of constant property gases ($Pr \approx 0.7$) as references. High values at the right are the usual high (nondimensionalized) heat transfer coefficients of the immediate

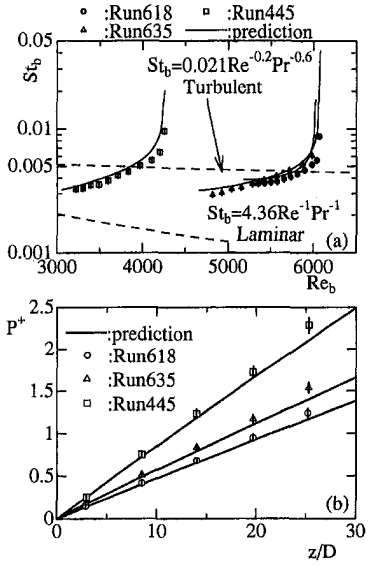

Fig. 8 Predicted local integral parameters (solid lines) compared to measurements (symbols) of Shehata (1984): (*a*) wall heat transfer and (*b*) nondimensional pressure defect

thermal entry; the first data point is at $z/D \approx 0.2$ and the last valid data are at $z/D \approx 25$.

The results are not perfect. But they are within acceptable design accuracy despite the challenging conditions of these flows. The calculations display the trends of the data, e.g., they appear to be laminarizing or not as the case may be. After $z/D \approx 6$ the predictions lie within about eight percent of the measurements or better. Of the three sets of conditions, calculations for the conditions of run 635 seem best despite being considered the most difficult test. It is probably appropriate here to reemphasize that the constants and functions in the AKN and KC models have not been readjusted for these calculations.

Wall shear stresses and friction factors are not directly measured in the experiments; pressure differences are. In contrast to fully developed flows with constant properties, τ_w and C_f cannot be deduced from the raw data without questionable assumptions and approximations, so we compare the predictions to the nondimensional pressure drops directly. In making these comparisons, one must be careful to use the same definition as employed in the data reduction, specifically $P^+ = \rho_{in} g_c (P_{in} - P)/G^2$ here. For the conditions of these flows, $P^+\{z\}$ provides a test of the combined effects of thermal energy addition, wall friction, and vertical elevation change. The relative contributions can be estimated via a local approximation of the one-dimensional momentum equation (McEligot, Smith, and Bankston, 1970),

$$-[2\rho_z g_c D_h (dP/dz)/G^2] \approx 8q_z^+ + 4C_{f,z} + 2(\mathrm{Gr}_z^2/\mathrm{Re}_z^2) \quad (15)$$

with the subscript z representing evaluation at local bulk properties. For run 618 these terms are approximately in the ratios 1:4:3, respectively, so wall friction would account for about half the pressure drop; for run 445, they are about 4:5:5 so friction contributes only about one-third. In the predictions, the turbulence model primarily affects only the friction contribution so it is not surprising that the velocity profiles of Fig. 7 yield the good predictions of Fig. 8(*b*).

It would be interesting to examine whether the apparent laminarization is due to viscosity variation or due to acceleration of the flow. One would need measurements at the same conditions for (1) an incompressible fluid with significant viscosity variation and (2) a compressible constant viscosity fluid. The implication of Fig. 1 is that the stabilizing effect of acceleration ($K_v \approx 4q^+/\mathrm{Re}$) provides a significant, if not dominant, cause.

Concluding Remarks

The k–ϵ turbulence model of Abe, Kondoh, and Nagano (1994), developed for forced turbulent flow between parallel plates with the constant property idealization, has been successfully extended to treat strongly heated gas flows at low Reynolds numbers in vertical circular tubes. For thermal energy transport, the turbulent Prandtl number model of Kays and Crawford (1993) was adopted. No constants or functions in these models were readjusted.

Under the idealization of constant fluid properties, predictions for fully established conditions agreed with the Dittus-Boelter correlation for common gases (coefficient = 0.021 (McAdams, 1954)) within about five percent for Re > 3200. Predicted friction coefficients were about five percent higher than the Drew, Koo, and McAdams (1932) correlation in this range. Below Re ≈ 2000 both predictions agreed with theoretical laminar values within about one percent. The local thermal entry behavior, Nu $\{z/D\}$, was further confirmed by comparison to the measurements of Reynolds (1968) for Re ≈ 4180 and 6800.

The capability to treat forced turbulent flows with significant gas property variation was assessed via calculations at the conditions of experiments by Shehata (1984), ranging from essentially turbulent to laminarizing due to the heating. The apparatus was a vertical circular tube with an unheated entry length for flow development, followed by a resistively heated section which gave an approximately uniform wall heat flux. Inlet Reynolds numbers of about 6080, 6050, and 4260 with nondimensional heating rates, $q^+ = q''_w/(Gc_pT_{in})$, of about 0.0018, 0.0035, and 0.0045, respectively, were employed as internal mean velocity and temperature distributions were measured by hot wire anemometry.

Predictions forecast the development of turbulent transport quantities, Reynolds stress and turbulent heat flux, as well as turbulent viscosity and turbulent kinetic energy. Results suggest that the run at the lowest heating rate behaves as a typical turbulent flow, but with a reduction in turbulent kinetic energy near the wall. For the highest heating rate all turbulence quantities showed steady declines in the viscous layer as the axial position increased—representative of conditions called laminarizing. For the intermediate run, predictions showed the same trends as the highest heating rate but occurred more gradually with respect to axial distance. These observations are consistent with empirical criteria for these regimes, expressed in terms of $q_{in}^+\{\mathrm{Re}_{in}\}$. No direct measurements are available to confirm or refute these distributions; they must be assessed by examination of the mean velocity and temperature distributions that result from these predictions of the turbulent transport quantities.

Overall agreement between the predictions and the measured velocity and temperature profiles is good, establishing confidence in the values of the forecast turbulence quantities—and the model which produced them. Most importantly, the model yields predictions which compare well to the measured wall heat transfer parameters and the pressure drop. Thus, thermal design engineers should find calculations based on the present turbulence model to be satisfactory for forced low-Reynolds-number turbulent flows with significant gas property variation.

It should be recognized that, while confidence in the numerical model has been established through agreement of mean quantities with experiments, the forecast turbulence quantities (particularly the exact shapes of their profiles) cannot be assured yet. However, obtaining measurements of those quantities, without blockage effects on one hand or dominant buoyant effects on the other, will be a difficult experimental challenge to accomplish.

Acknowledgments

The study reported was supported by the Japan Atomic Energy Research Institute (JAERI) and by the Long Term Research Initiative and Laboratory Directed Research and Development Programs of the Idaho National Engineering and Environmental Laboratory/Lockheed Martin Idaho Technologies Company under DoE Idaho Field Office Contract DE-AC07-94ID13223. Dr. Ezato

received support as a JAERI Research Scholar and Professor McEligot as a JAERI Distinguished Foreign Scientist. The experiments of Dr. Shehata were funded by the Office of Naval Research, the National Science Foundation and the University of Arizona. To all we are extremely grateful.

References

Abe, K., Kondoh, T., and Nagano, Y., 1994, "A new turbulence model for predicting fluid flow and heat transfer in separating and reattaching flows—I. Flow field calculations," *Int. J. Heat Mass Transfer,* Vol. 37, pp. 139–151.

Abe, K., Nagano, Y., and Kondoh, T., 1992, "An improved k-ϵ model for prediction of turbulent flows with separation and reattachment," *Trans., JSME,* Vol. 58, No. 554, pp. 57–64 (in Japanese).

Akino, N., 1978, "On the criterion for laminarization in a heated circular tube," *Proc., Fall Meeting, Atomic Energy Soc. Japan,* Vol. A36, Kobe, p. 36 (in Japanese).

Bankston, C. A., 1970, "The Transition From Turbulent to Laminar Gas Flow in a Heated Pipe," ASME JOURNAL OF HEAT TRANSFER, Vol. 92, pp. 569–579.

Bankston, C. A., and McEligot, D. M., 1970, "Turbulent and laminar heat transfer to gases with varying properties in the entry region of circular ducts," *Int. J. Heat Mass Transfer,* Vol. 13, pp. 319–344.

Coon, C. W., 1968, "The transition from the turbulent to the laminar regime for internal convective flow with large property variations," Ph.D. thesis, University of Arizona.

Coon, C. W., and Perkins, H. C., 1970, "Transition From the Turbulent to the Laminar Regime for Internal Convective Flow With Large Property Variations," ASME JOURNAL OF HEAT TRANSFER, Vol. 92, pp. 506–512.

Drew, T. B., Koo, E. C., and McAdams, W. M., 1932, "The friction factor in clean round pipes," *Trans., A.I.Ch.E.,* Vol. 38, pp. 56–72.

Dittus, F. W., and Boelter, L. M. K., 1930, "Heat transfer in automobile radiators of the tubular type," *Pub. in Engrg.* (Univ. California), Vol. 2, pp. 443–461.

Fujii, S., 1991, "Studies on heat transfer of strongly heated turbulent gas flow in annular ducts," Ph.D. thesis, University of Tokyo (in Japanese).

Fujii, S., Akino, N., Hishida, M., Kawamura, H., and Sanokawa, K., 1991, "Experimental and theoretical investigations on heat transfer of strongly heated turbulent gas flow in an annular duct," *JSME International J., Ser II,* Vol. 34, No. 3, pp. 348–354.

Hilsenrath, J., et al., 1955, "Tables of thermal properties of gases," NBS Circular 564.

Hinze, J. O., 1975, *Turbulence,* 2nd Ed., McGraw-Hill, New York.

Iacovides, H., and Launder, B. E., 1995, "Computational fluid dynamics applied to internal gas-turbine blade cooling: A review," *Int. J. Heat Fluid Flow,* Vol. 16, pp. 454–470.

Kawamura, H., 1979, "Prediction of heated gas with large property variations using a two-equation model of turbulence," *Trans., JSME,* Vol. 45, No. 395B, pp. 1038–1046 (in Japanese).

Kawamura, H., 1979, "Analysis of laminarization of heated turbulent gas using a two-equation model of turbulence," *Proc., 2nd Intl. Symp. Turb. Shear Flow,* London, pp. 18.16–18.21.

Kays, W. M., and Crawford, M. E., 1993, *Convective heat and mass transfer,* 3rd Ed., McGraw-Hill, New York.

Kline, S. J., and McClintock, F. A., 1953, "Describing uncertainties in single-sample experiments," *Mech. Engr.,* Vol. 75, No. 1, pp. 3–8.

Launder, B. E., and Shima, N., 1989, "Second-moment closure for the near-wall sublayer: Development and application," *AIAA Journal,* Vol. 27, No. 10, pp. 1319–1325.

Leonard, B. P., 1979, "A stable and accurate convective modeling procedure based on quadratic upstream interpolation," *Comp. Meth. Appl. Mech. and Engrg.,* Vol. 19, pp. 59–98.

McAdams, W. H., 1954, *Heat transmission,* 3rd Ed., McGraw-Hill, New York, p. 219.

McEligot, D. M., 1963, "The effect of large temperature gradients on turbulent flow of gases in the downstream region of tubes," Ph.D. thesis, Stanford Univ; also TID-19446.

McEligot, D. M., 1985, "Measurement of wall shear stress in favorable pressure gradients," *Lecture Notes Phys.,* Vol. 235, pp. 292–303.

McEligot, D. M., and Bankston, C. A., 1969, "Turbulent predictions for circular tube laminarization by heating," ASME paper 69-HT-52.

McEligot, D. M., Coon, C. W., and Perkins, H. C., 1970, "Relaminarization in tubes," *Int. J. Heat Mass Transfer,* Vol. 9, pp. 1151–1152.

McEligot, D. M., Magee, P. M., and Leppert, G., 1965, "Effect of Large Temperature Gradients on Convective Heat Transfer: The Downstream Region," ASME JOURNAL OF HEAT TRANSFER, Vol. 87, pp. 67–76.

McEligot, D. M., Ormand, L. W., and Perkins, H. C., 1966, "Internal Low Reynolds Number Turbulent and Transitional Gas Flow With Heat Transfer," ASME JOURNAL OF HEAT TRANSFER, Vol. 88, pp. 239–245.

McEligot, D. M., Smith, S. B., and Bankston, C. A., 1970, "Quasi-Developed Turbulent Pipe Flow With Heat Transfer," ASME JOURNAL OF HEAT TRANSFER, Vol. 92, pp. 641–650.

Mikielewicz, D. P., 1994, "Comparative studies of turbulence models under conditions of mixed convection with variable properties in heated vertical tubes," Ph.D. thesis, University of Manchester.

Nagano, Y., Hishida, M., and Asano, T., 1984, "Improved form of the k-ϵ model for wall turbulent shear flows," *Trans., JSME,* Vol. 50, No. 457B, pp. 2022–2031 (in Japanese).

Nagano, Y., and Hishida, M., 1987, "Improved form of the k-ϵ model for wall turbulent shear flows," *J. Fluids Engr.,* Vol. 109, pp. 156–160.

Nagano, Y., and Tagawa, M., 1990, "An improved k-ϵ model for boundary layer flows," *J. Fluids Engr.,* Vol. 112, pp. 33–39.

Najmabadi, F., et al., 1991, "The ARIES-I Tokamak reactor study," Final Rpt. UCLA-PPG-1323, University of California, Los Angeles.

Najmabadi, F., et al., 1992, "The ARIES-II and ARIES-IV second-stability Tokamak reactors," *Fusion Tech.,* Vol. 21, pp. 1721–1728.

Nishimura, M., Fujii, S., Shehata, A. M., Kunugi, T., and McEligot, D. M., 1997, "Prediction of forced gas flows in circular tubes at high heat fluxes," *Proc., Eighth Int. Topical Meeting on Nuclear Reactor Thermal-hydraulics,* Kyoto, pp. 294–304.

Nishio, S., et al., 1993, "A concept of DRastically EAsy Maintenance (DREAM) Tokamak reactor," *Proc., IAEA Tech. Comm. Meeting on Fusion Reactor Design and Technology,* UCLA, Sept.

Nishio, S., 1995, "DRastically EAsy Maintenance reactor: DREAM-2," *Proc., Japan-US Workshop on Fusion Power Reactors P246,* JAERI-memo 07-100, Naka, June, pp. 160–169.

Ogawa, M., and Kawamura, H., 1986, "Experimental and analytical studies on friction factor of heated gas flow in circular tube," *J. At. Energy Soc., Japan,* Vol. 28, No. 10, pp. 957–965 (in Japanese).

Ogawa, M., and Kawamura, H., 1987, "Effects of entrance configuration on pressure loss and heat transfer of transitional gas flow in a circular tube," *Heat Transfer-Japanese Research,* Vol. 15, No. 5, pp. 77–91.

Ogawa, M., Kawamura, H., Takizuka, T., and Akino, N., 1982, "Experiment on laminarization of strongly heated gas flow in a vertical circular tube," *J. At. Energy Soc., Japan,* Vol. 24, No. 1, pp. 60–67 (in Japanese).

Patankar, S., 1980, *Numerical Heat Transfer and Fluid Flow,* Hemisphere, Washington, DC.

Perkins, H. C., and Worsoe-Schmidt, P. M., 1965, "Turbulent heat and momentum transfer for gases in a circular tube at wall-to-bulk temperature ratios to seven," *Int. J. Heat Mass Transfer,* Vol. 8, pp. 1011–1031.

Perkins, K. R., 1975, "Turbulence structure in gas flows laminarizing by heating," Ph.D. thesis, University of Arizona.

Petukhov, B. S., Kirillov, V. V., and Maidanik, V. N., 1966, "Heat transfer experimental research for turbulent gas flow in pipes at high temperature difference between wall and bulk fluid temperature," *Proc., 3rd Int. Heat Transfer Conf.,* Vol. I, pp. 285–292.

Reynolds, H. C., 1968, "Internal low-Reynolds-number, turbulent heat transfer," Ph.D. thesis, University of Arizona. Also DTIC AD-669-254.

Reynolds, H. C., Swearingen, T. B., and McEligot, D. M., 1969, "Thermal entry for low-Reynolds-number turbulent flow," *J. Basic Engrg.,* Vol. 91, pp. 87–94.

Schlichting, H., 1968, *Boundary layer theory,* 6th Ed., McGraw-Hill, New York.

Shehata, A. M., 1984, "Mean turbulence structure in strongly heated air flows," Ph.D. thesis, University of Arizona.

Shehata, A. M., and McEligot, D. M., 1995, "Turbulence structure in the viscous layer of strongly heated gas flows," Tech. report INEL-95/0223, Idaho National Engineering Laboratory.

Shehata, A. M., and McEligot, D. M., 1998, "Mean turbulence structure in the viscous layer of strongly-heated internal gas flows: Measurements," *Int. J. Heat Mass Transfer,* Vol. 41, pp. 4297–4313.

Takase, K., Hino, R., and Miyamoto, Y., 1990, "Thermal and hydraulic tests of standard fuel rod of HTTR with HENDEL," *J. Atomic Energy Soc. Japan,* Vol. 32, No. 11, pp. 1107–1110 (in Japanese).

Torii, S., Shimizu, A., Hasegawa, S., and Higasa, M., 1989, "Analysis of the laminarization phenomena in a circular tube by use of a modified k-ϵ model," *Trans., JSME,* Vol. 55, No. 518B, pp. 3144–3150 (in Japanese).

Torii, S., Shimizu, A., Hasegawa, S., and Higasa, M., 1990, "Laminarization of strongly heated gas flows in a circular tube (Numerical analysis by means of a modified k-ϵ model)" *JSME International J., Ser II,* Vol. 33, No. 3 pp. 538–547.

Torii, S., Shimizu, A., Hasegawa, S., and Higasa, M., 1993, "Numerical analysis of laminarizing circular tube flows by means of a Reynolds stress turbulence model," *Heat Transfer—Japanese Research,* Vol. 22, pp. 154–170.

Torii, S., Shimizu, A., Hasegawa, S., and Kusama, N., 1991, "Laminarization of strongly heated annular gas flows," *JSME International J., Ser II,* Vol. 34, No. 2, pp. 157–168.

Torii, S., and Yang, W.-J., 1997, "Laminarization of turbulent gas flow inside a strongly heated tube," *Int. J. Heat Mass Transfer,* Vol. 40, pp. 3105–3117.

van Driest, E. R., 1956, "On turbulent flow near a wall," *J. Aerospace Sci.,* Vol. 23, pp. 1007–1011, 1036.

Waganer, L. M., 1993, "Innovation leads the way to attractive IFE reactors—Prometheus-L & Prometheus—H," *Proc., IAEA Tech. Comm. Meeting on Fusion Reactor Design and Technology,* UCLA, Sept.

Wong, C. P. C., Czechowicz, D. G., McQuillan, B. W., Sleicher, R. W., and Cheng, E. T., 1995, "Evaluation of U. S. DEMO helium-cooled blanket options," *Symp. Fusion Engrg.,* Champaign, IL, Oct.

Yamazaki, S., 1992, "Divertor design of SSTR-2," *Proc., Japan-US Workshop on Tokamak Fusion Power Reactors with EC Contribution,* JAERI-memo 04-171, Naka, pp. 186–195.

Laminar Convective Heat Transfer of a Bingham Plastic in a Circular Pipe With Uniform Wall Heat Flux: The Graetz Problem Extended

T. Min
Ph.D. Student,
e-mail: tmin@eddy.snu.ac.kr

J. Y. Yoo[1]
Professor,
e-mail: jyyoo@plaza.snu.ac.kr
Mem. ASME

Department of Mechanical Engineering,
Seoul National University,
Seoul 115 742, Korea

Thermally developing laminar flow of a Bingham plastic in a circular pipe with uniform wall heat flux has been studied analytically. Expressions for the fully developed temperature and Nusselt number are presented in terms of the yield stress, Peclet number, and Brinkman number. The solution to the Graetz problem has been obtained by using the method of separation of variables, where the resulting eigenvalue problem is solved approximately by using the method of weighted residuals. The effects of the yield stress, Peclet, and Brinkman numbers on the Nusselt number are discussed. In particular, it is shown that the heat transfer characteristics in the entrance region are significantly affected by the yield stress with the inclusion of viscous dissipation.

1 Introduction

The problem of laminar forced convective heat transfer in pipe flows is of foremost importance to the design of practical thermal systems. A large number of fluids used extensively in industrial applications exhibit yield stresses that must be overcome before they start to flow, which are called Bingham plastic. Some examples are electrorheological fluids, magnetorheological fluids, suspensions, drilling muds, paints, greases, aqueous foams, slurries, and food products like margarine, mayonnaise, and ketchup, etc. While these fluids are receiving more attention these days due to their extensive applicability and great importance in many industries, the literature on their flow and heat transfer characteristics is surprisingly limited (Vradis and Ötügen, 1997) and accordingly only little is known of them.

The first studies of heat transfer in a duct flow of a Newtonian fluid were made more than a century ago by Graetz in 1883–1885, and independently by Nusselt in 1910. These studies, known as the Graetz problems or thermally developing flow problems and their various extensions, have evoked many research efforts. Comprehensive reviews of the works on heat transfer in laminar duct flow was compiled by Shah and London (1978) and Kakaç et al. (1987).

The classical Graetz problem for Newtonian fluids has been extended by Sellars et al. (1956) and Siegel et al. (1958) to the case of prescribed wall heat flux neglecting both axial conduction and viscous dissipation. Hsu (1967) considered a uniform entrance temperature profile and analyzed the Graetz problem for a Newtonian fluid including axial conduction, but still neglecting viscous dissipation, by using the method of separation of variables. He numerically obtained the first 12 eigenvalues and eigenfunctions for Pe = 5, 10, 20, 30, 50, and 100. Pirkle and Sigillito (1972) pointed out two errors in Hsu's analysis and presented corrected formulas. However, they did not quite present any quantitative results. In the meantime, Ou and Cheng (1973) obtained solutions to the Graetz problem with uniform wall heat flux for a Newtonian fluid including viscous dissipation. However, at this time, the effect of axial conduction was neglected.

For a Bingham plastic, Wissler and Schechter (1959) and Blackwell (1985) studied thermally developing flow with constant wall temperature, neglecting axial conduction and viscous dissipation. The Levéque solution of a Bingham plastic was given by Beek and Eggink (1962). Johnston (1991) extended the Graetz problem of a Bingham plastic to the case including axial conduction, but still neglecting viscous dissipation. Recently, Min et al. (1997a) included both axial conduction and viscous dissipation and showed that axial conduction is negligible for Pe $>$ 500. They have also shown that the yield stress does not have a strong effect on the thermal field when viscous dissipation is ignored, but it significantly affects the thermal field when viscous dissipation is included.

In most industrial applications more complex governing equations than those of the idealized Graetz problem are involved, which are fully elliptic. Therefore, numerical methods are inevitably required to be used and results for complex heat transfer problems have been widely reported for Newtonian fluids (Shah and London, 1978). Vradis et al. (1993) reported numerical solutions to the hydrodynamically developing flow problem and the simultaneously developing flow problem by employing the fully elliptic governing equations for a Bingham plastic in a circular pipe. Very recently, Min et al. (1997b) pointed out some shortcomings involved in Vradis et al. (1993) and reported that the heat transfer characteristics obtained by their improved method exhibited consistent trends as those predicted from their earlier analytical approach (Min et al., 1997a). They also argued that the fully developed velocity assumption for the Graetz problem is valid when Pr $>$ 10 in the case of Bingham plastic.

As far as is known, there has been no work in the literature that studied thermally developing flow of a Bingham plastic, not to mention a Newtonian fluid, with uniform wall heat flux, which considers both axial conduction and viscous dissipation. For Newtonian fluid flows, it is known that viscous dissipation is important only at high speeds (Kays and Crawford, 1993). However, the same argument does not hold for the case of non-Newtonian fluid flows even at relatively low speeds because of high viscosities and relatively high-velocity gradients occurring within the flow fields (Bird et al., 1987). A possible question is raised whether the yield stress has a strong effect on the thermal field with the inclusion of viscous dissipation, as is the case with uniform wall temperature

[1] To whom correspondence should be addressed.

Contributed by the Heat Transfer Division for publication in the JOURNAL OF HEAT TRANSFER and presented at IMECE '96 Atlanta. Manuscript received by the Heat Transfer Division, June 11, 1997; revision received, Feb. 10, 1999. Keywords: Forced Convection, Materials Processing and Manufacturing Process, Non-Newtonian Flows and Systems. Associate Technical Editor: S. Ramadhyani.

(Min et al., 1997a). Therefore, the objective of the present paper is to investigate thermally developing flow (the Graetz problem extended) of a Bingham plastic including both axial conduction and viscous dissipation subject to uniform wall heat flux, which can be used as a reference for future numerical and experimental studies on this subject. The solution to this problem is obtained by using the method of separation of variables, where the resulting eigenvalue problem is solved approximately by using the method of weighted residuals.

2 Statement of the Problem

For constant properties, the fully developed velocity profile for a laminar pipe flow of a Bingham plastic is given as follows (Bird et al., 1960):

$$u(r) = \begin{cases} \dfrac{2(1-c)^2}{1-\dfrac{4}{3}c+\dfrac{c^4}{3}} & \text{for } 0 \le r \le c, \\ \dfrac{2(1-r^2-2c(1-r))}{1-\dfrac{4}{3}c+\dfrac{c^4}{3}} & \text{for } c \le r \le 1, \end{cases} \tag{1}$$

where $r = 0$ and $r = 1$ correspond, respectively, to the centerline and the wall, and c is the dimensionless radius of the plug-flow region. As c approaches 1, $u(r)$ becomes a complete plug flow ($u = 1$), while $c = 0$ corresponds to a laminar Newtonian flow since Bingham plastic becomes a Newtonian fluid in the limiting case of vanishing yield stress.

Since a fully developed velocity profile is assumed for thermally developing flow, the nondimensionalized energy equation of a Bingham plastic including axial conduction and viscous dissipation for a circular pipe flow can be represented as (Min et al., 1997a)

$$\frac{u}{2}\frac{\partial\Theta}{\partial x^+} = \frac{1}{\mathrm{Pe}^2}\frac{\partial^2\Theta}{\partial x^{+2}} + \frac{1}{r}\frac{\partial}{\partial r}\left(r\frac{\partial\Theta}{\partial r}\right) + \mathrm{Br}\cdot\eta_{\mathrm{eff}}\cdot\left(\frac{du}{dr}\right)^2, \tag{2a}$$

$$\eta_{\mathrm{eff}} = \begin{cases} \infty & \text{for } 0 \le r \le c, \\ 1 + \dfrac{\tau_y R/\mu_0 U_{av}}{|du/dr|} & \text{for } c \le r \le 1, \end{cases} \tag{2b}$$

where $\Theta(r, x^+) = (T - T_e)/(q_w R/k)$ is the nondimensionalized temperature. For uniform wall heat flux and uniform inlet temperature, the boundary conditions are written as

$$\Theta(r, 0) = 0, \tag{2c}$$

$$\Theta(r, x^+) \to \Theta_\infty(r, x^+) \quad \text{as } x^+ \to \infty, \tag{2d}$$

$$\frac{\partial\Theta(0, x^+)}{\partial r} = 0, \tag{2e}$$

$$\frac{\partial\Theta(1, x^+)}{\partial r} = 1. \tag{2f}$$

Unlike the case for uniform wall temperature condition, here the dimensionless temperature for a fully developed flow Θ_∞ does depend on both r and x^+ (Kays and Crawford, 1993). Thus, we decompose $\Theta(r, x^+)$ as $\Theta(r, x^+) = \Theta_\infty(r, x^+) + \theta(r, x^+)$, where $\Theta_\infty(r, x^+)$ is the fully developed temperature and $\theta(r, x^+)$ is the excessive temperature. The fully analytic expression of Θ_∞ is given in the next section. For the moment, we show how the energy equation is decomposed into two parts, and what boundary conditions are applied to each part.

Nomenclature

$\mathbf{A}, \mathbf{B}, \mathbf{C}$ = matrices
A_{ji}, B_{ji}, C_{ji} = elements of matrices
Br = Brinkman number, $\mu_0 U_{av}^2/q_w R$
Br_{cr} = critical Brinkman number
C_n = coefficients used in the solution of eigenvalue problem
C_p = specific heat at constant pressure
c = dimensionless radius of the plug flow region, or ratio of yield shear stress to wall shear stress, τ_y/τ_w
$\mathbf{c}, \mathbf{d}$ = eigenvectors
c_i, d_i = components of eigenvectors
D = pipe diameter
h = heat transfer coefficient based on bulk temperature
k = thermal conductivity
N = number of finite eigenmodes
Nu = local Nusselt number, hD/k
Nu_∞ = fully developed Nusselt number
Pr = Prandtl number, $\mu_0/(\rho\alpha)$
Pe = Peclet number, $2U_{av}R/\alpha$
q_w = uniform wall heat flux per unit area, $k(\partial T/\partial y)$
R = pipe radius
R_n = eigenfunction
r = dimensionless radial coordinate, y/R
S_i = trial function
$T(y, z)$ = temperature
T_e = entrance temperature
$T_m(z)$ = bulk temperature
$T_w(z)$ = wall temperature
U = axial velocity
U_{av} = average axial velocity
u = dimensionless axial velocity, U/U_{av}
w_j = weight function used in the method of weighted residuals
x = dimensionless axial coordinate, z/R
x^+ = dimensionless axial coordinate, $(z/R)/\mathrm{Pe}$
y = radial coordinate
z = axial coordinate
α = thermal diffusivity
η = apparent viscosity for a Bingham model
η_{eff} = dimensionless apparent viscosity, η/μ_0
$\Theta(r, x^+)$ = dimensionless temperature, $(T - T_e)/(q_w R/k)$
$\Theta_m(x^+)$ = dimensionless bulk temperature, $(T_m - T_e)/(q_w R/k)$
$\Theta_w(x^+)$ = dimensionless wall temperature, $(T_w - T_e)/(q_w R/k)$
$\Theta_\infty(r, x^+)$ = dimensionless temperature for $x^+ \to \infty$
$\Theta_{\infty,m}(r, x^+)$ = dimensionless bulk temperature for $x^+ \to \infty$
$\Theta_{\infty,w}(r, x^+)$ = dimensionless wall temperature for $x^+ \to \infty$
$\theta(r, x^+)$ = dimensionless excessive temperature, $\Theta - \Theta_\infty$
λ_n = eigenvalue
μ_0 = plastic viscosity
μ_n = coefficients used in the solution of eigenvalue problem
ρ = density
τ = shear stress
τ_w = wall shear stress
τ_y = yield shear stress
Φ = viscous dissipation function
$\phi(r)$ = dimensionless temperature, $(\Theta_{\infty,w} - \Theta_\infty)/(\Theta_{\infty,w} - \Theta_{\infty,m})$

The fully developed temperature profile for laminar pipe flow with uniform wall heat flux can be expressed (Kays and Crawford, 1993) as

$$\frac{\partial \Theta_\infty}{\partial x^+} = \frac{d\Theta_{\infty,m}}{dx^+} = \text{const.} \tag{3}$$

In other words, the dependence of $\Theta_{\infty,m}$ on x^+ is only linear. Thus we can split Eqs. (2) into two sets of equations as follows:

$$\frac{u}{2}\frac{d\Theta_{\infty,m}}{dx^+} = \frac{1}{r}\frac{\partial}{\partial r}\left(r\frac{\partial \Theta_\infty}{\partial r}\right) + \text{Br}\cdot\eta_{\text{eff}}\cdot\left(\frac{du}{dr}\right)^2, \tag{4a}$$

$$\frac{\partial \Theta_\infty(0, x^+)}{\partial r} = 0, \tag{4b}$$

$$\frac{\partial \Theta_\infty(1, x^+)}{\partial r} = 1 \tag{4c}$$

and

$$\frac{u}{2}\frac{\partial \theta}{\partial x^+} = \frac{1}{\text{Pe}^2}\frac{\partial^2 \theta}{\partial x^{+2}} + \frac{1}{r}\frac{\partial}{\partial r}\left(r\frac{\partial \theta}{\partial r}\right), \tag{5a}$$

$$\theta(r, 0) = -\Theta_\infty(r, 0), \tag{5b}$$

$$\theta(r, x^+) \to 0 \quad \text{as } x^+ \to \infty, \tag{5c}$$

$$\frac{\partial \theta(0, x^+)}{\partial r} = \frac{\partial \theta(1, x^+)}{\partial r} = 0. \tag{5d}$$

3 Analysis

3.1 Fully Developed Flow. In this subsection, we obtain Θ_∞ from Eqs. (4). $d\Theta_{\infty,m}/dx^+$ of Eq. (4*a*) can be obtained by nondimensionalizing the energy conservation relation. This is expressed for a cross section of a pipe as

$$\rho C_p U_{av}\pi R^2\frac{dT_{\infty,m}}{dz} = q_w\cdot 2\pi R + 2\pi\int_0^R \eta\left(\frac{dU}{dy}\right)^2 y dy, \tag{6a}$$

$$\frac{d\Theta_{\infty,m}}{dx^+} = 4(1 + 4A\cdot\text{Br}), \tag{6b}$$

where $A = 3/(3 - 4c + c^4)$. Replacing the left-hand side of Eq. (4*a*) by Eq. (6*b*) and integrating Eq. (4*a*) with respect to r subject to boundary conditions (4*a*) and (4*c*), one can obtain the fully developed temperature as

$$\Theta_\infty(r, x^+) = \begin{cases} A\left((1-c)^2r^2 - \dfrac{27 - 40c + 13c^4}{36}\right) \\ \quad + 2A\cdot\text{Br}(2A(1-c)^2r^2 - 1) \\ \quad + A\dfrac{c^4}{3}\ln c + \Theta_{\infty,w}(x^+) \quad \text{for } 0 \le r \le c, \\ 4A\left(\dfrac{5c}{18} - \dfrac{3}{16} + (1-2c)\dfrac{r^2}{4} + \dfrac{2c}{9}r^3 - \dfrac{r^4}{16}\right) \\ \quad + 16A^2\,\text{Br}\left(\dfrac{c}{6} - \dfrac{1}{8} + (1-2c)\dfrac{r^2}{4} + \dfrac{c}{3}r^3 - \dfrac{r^4}{8}\right) \\ \quad + A\dfrac{c^4}{3}\ln r + \Theta_{\infty,w}(x^+) \quad \text{for } c \le r \le 1. \end{cases} \tag{7}$$

Now, $\Theta_{\infty,w}(x^+)$ can be determined in conjunction with $\Theta_{\infty,m}(x^+)$ which can be obtained in two ways. One is the integration of Eq. (6*b*) between $x^+ = 0$ and $x^+ = x^+$:

$$\Theta_{\infty,m} = 4(1 + 4A\cdot\text{Br})x^+ - \frac{4}{\text{Pe}^2}\int_0^1 \frac{\partial \theta(r, 0)}{\partial x^+} r dr, \tag{8a}$$

where $\theta(r, 0) = -\Theta_\infty(r, 0)$. Note that the nonvanishing axial conduction at the pipe entrance ($x^+ = 0$) produces $(4/\text{Pe}^2)\int_0^1 (\partial\theta(r, 0)/\partial x^+) r dr$ (Pirkle and Sigillito, 1972). The other is simply the definition of the bulk temperature

$$\Theta_{\infty,m} = 2\int_0^1 u\Theta_\infty r dr = 2B - A\cdot\text{Br} + \Theta_{\infty,w}, \tag{8b}$$

where B is a constant which can be expressed as

$$B = A^2\left(-\frac{11}{48} + \frac{68c}{105} - \frac{62c^2}{135} - \frac{c^4}{4} + \frac{10c^5}{27} + \frac{c^6}{15} - \frac{2c^7}{15} - \frac{13c^8}{1008} + \frac{c^8\ln c}{18}\right). \tag{9}$$

By equating Eqs. (8*a*) and (8*b*), one can get $\Theta_{\infty,w}$. Incidentally, Hsu (1967) dropped the term $(4/\text{Pe}^2)\int_0^1 (\partial\theta(r, 0)/\partial x^+) r dr$ in his analysis for a Newtonian fluid. Pirkle and Sigillito (1972) pointed out that this and another error described in the next subsection were made by Hsu, but somehow they did not quite complete their calculations to give any numerical values for Θ_∞. Now, the complete expression of Θ_∞ for a Bingham plastic is

$$\Theta_\infty(r, x^+) = \begin{cases} A\left((1-c)^2r^2 - \dfrac{27 - 40c + 13c^4}{36}\right) + 2A\cdot\text{Br}(2A(1-c)^2r^2 - 1) + A\dfrac{c^4}{3}\ln c + 4(1 + 4A\cdot\text{Br})x^+ \\ \quad - \dfrac{4}{\text{Pe}^2}\displaystyle\int_0^1 \frac{\partial\theta(r, 0)}{\partial x^+} r dr - 2B + A\cdot\text{Br} \quad \text{for } 0 \le r \le c, \\ 4A\left(\dfrac{5c}{18} - \dfrac{3}{16} + (1-2c)\dfrac{r^2}{4} + \dfrac{2c}{9}r^3 - \dfrac{r^4}{16}\right) + 16A^2\text{Br}\left(\dfrac{c}{6} - \dfrac{1}{8} + (1-2c)\dfrac{r^2}{4} + \dfrac{c}{3}r^3 - \dfrac{r^4}{8}\right) \\ \quad + A\dfrac{c^4}{3}\ln r + 4(1 + 4A\cdot\text{Br})x^+ - \dfrac{4}{\text{Pe}^2}\displaystyle\int_0^1 \frac{\partial\theta(r, 0)}{\partial x^+} r dr - 2B + A\cdot\text{Br} \quad \text{for } c \le r \le 1. \end{cases} \tag{10}$$

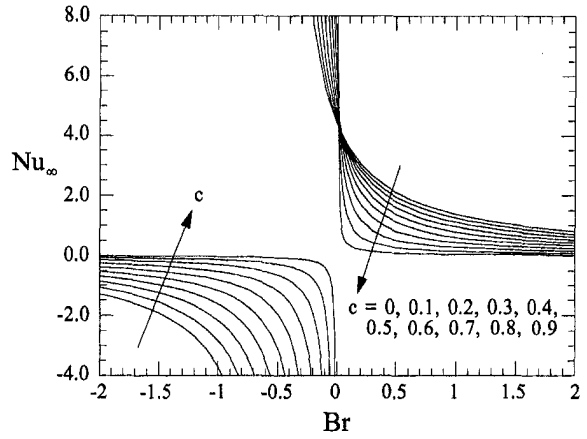

Fig. 1 Variation of fully developed Nusselt number with respect to Br for c = 0, 0.1, 0.2, 0.3, 0.4, 0.5, 0.6, 0.7, 0.8, and 0.9

One can easily verify that Eq. (10) is the same as the solution of Ou and Cheng (1973) for a Newtonian fluid ($c = 0$) when axial conduction is negligible (Pe $\rightarrow \infty$), which is written as

$$\Theta_\infty(r, x^+) = 4x^+ + r^2\left(1 - \frac{r^2}{4}\right) - \frac{7}{24} + \mathrm{Br}(16x^+ + 4r^2 - 2r^4 - 1). \quad (11)$$

In the case of including axial conduction, numerical values of the fully developed temperature $\Theta_\infty(r, x^+)$ cannot be given until $\theta(r, 0)$ is known. Fortunately, the dimensionless excessive temperature $\theta(r, x^+)$ can be calculated as a solution to an eigenvalue problem, which is explained in the next subsection. Since we are more interested in the fully developed Nusselt number, we instead define a new dimensionless fully developed temperature $\phi = (\Theta_{\infty,w} - \Theta_\infty)/(\Theta_{\infty,w} - \Theta_{\infty,m})$ which is similar to the one used in the case of uniform wall temperature (Min et al., 1997a). Then, it can be easily shown from Eq. (7) and Eq. (8*b*) that ϕ is invariant with x^+, and the fully developed Nusselt number can be obtained as

$$\mathrm{Nu}_\infty = -2 \cdot \phi'(1) = \frac{2}{\Theta_{\infty,w} - \Theta_{\infty,m}} = \frac{2}{A \cdot \mathrm{Br} - 2B}. \quad (12)$$

For a Newtonian fluid ($c = 0$), $\mathrm{Nu}_\infty = 2/(\mathrm{Br} + 11/24)$, which is coincident with the result of Ou and Cheng (1973). For a Bingham plastic with uniform wall temperature (Min et al., 1997a, b), the thermally fully developed solutions are by definition independent of both Pe and Br when viscous dissipation is included (Br $\neq$ 0), while they are dependent on Pe when it is negligible (Br = 0). However, from Eqs. (7), (8*b*), and (12), the thermally fully developed temperature profile ϕ and Nusselt number Nu_∞ for a Bingham plastic with uniform wall heat flux are independent of Pe, whether Br is zero or not.

Figure 1 shows the variation of Nu_∞ with respect to Br for c = 0, 0.1, 0.2, 0.3, 0.4, 0.5, 0.6, 0.7, 0.8, and 0.9. It can be clearly seen that there are singularities in Nu_∞ for Br $<$ 0 (cooling

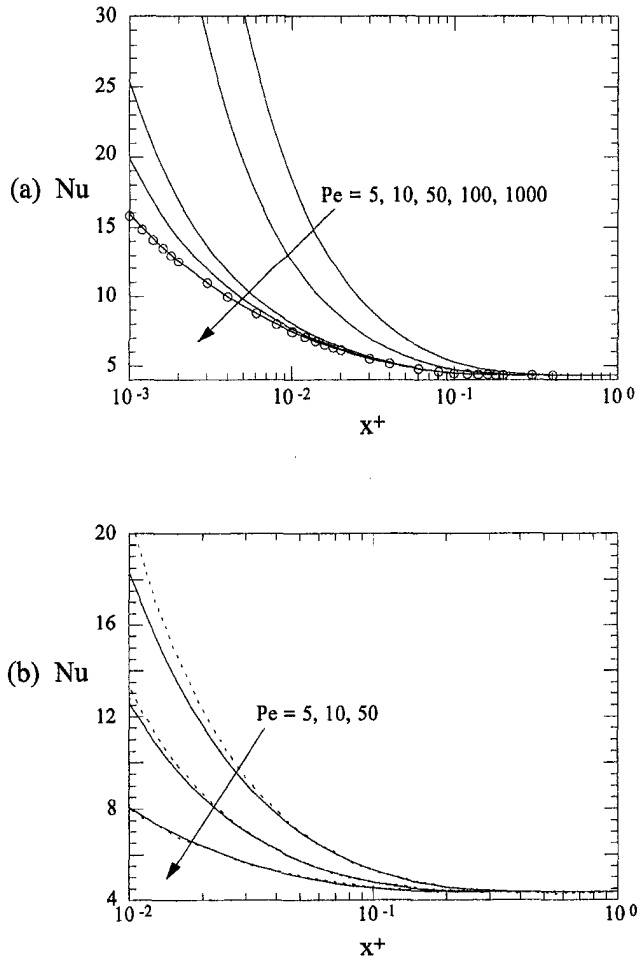

Fig. 2 (*a*) Local Nusselt number with respect to axial distance for c = 0 (excluding viscous dissipation): , present study; ○, Shah (1975). (*b*) Local Nusselt number with respect to axial distance for c = 0 (excluding viscous dissipation): ———, present study; - - - - -, Hsu (1967).

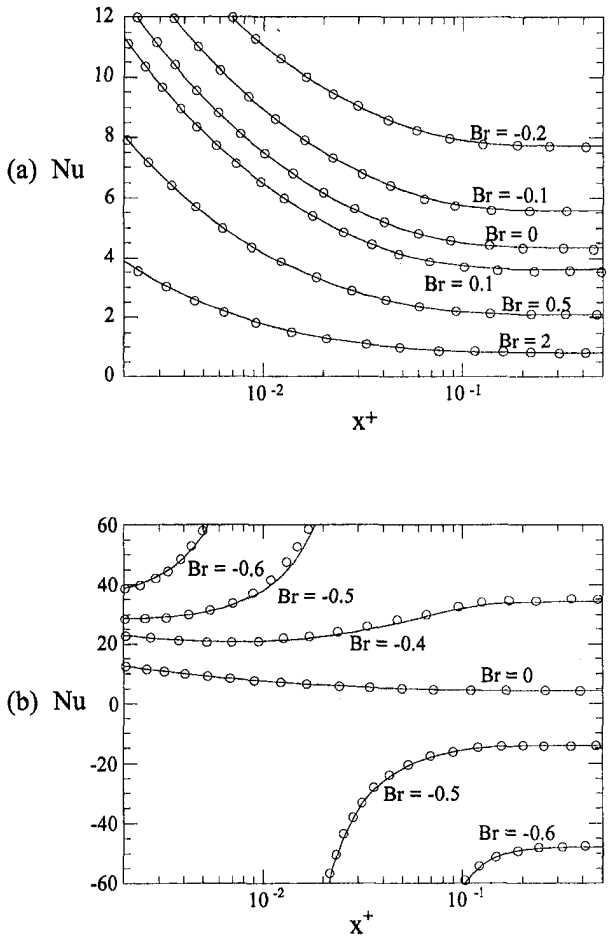

Fig. 3 (*a*) Local Nusselt number with respect to axial distance for c = 0 and $-0.2 \leq \mathrm{Br} \leq 2$ (including viscous dissipation): ———, present study; ○, Ou and Cheng (1973). (*b*) Local Nusselt number with respect to axial distance for c = 0 and $-0.6 \leq \mathrm{Br} \leq 0$ (including viscous dissipation): ———, present study; ○, Ou and Cheng (1973).

condition). The existence of a singularity in the curve of fully developed Nusselt number means that fully developed bulk temperature equals fully developed wall temperature, making the denominator of Eq. (12) become zero. This results from the fact that the heat removed at the wall is equivalent to the heat generated by viscous dissipation at a certain downstream location (Ou and Cheng, 1973). More details on this subject are discussed in the next section. From Eq. (12) the critical Brinkman number $\mathrm{Br}_{cr} = 2B/A \cong -0.4583, -0.3224, -0.1944, -0.0892$, and -0.0219 for $c = 0$, 0.2, 0.4, 0.6, and 0.8, respectively. One should note that the singularities in the Nusselt number are due to its definition (12) and represent the inadequacy of the conventional definition for the physical problem with $\mathrm{Br} < 2B/A$ (Ou and Cheng, 1973). It can be argued, however, that the variation of Nu_∞ with respect to Br decreases for larger c. This statement can be supported by the observation that from Eq. (12), the viscous dissipation is closely related to A, which increases for larger c and increases even to infinity as c approaches 1.

3.2 Thermally Developing Flow. In order to obtain the dimensionless temperature profile $\Theta(r, x^+) = \Theta_\infty(r, x^+) + \theta(r, x^+)$ for thermally developing flow, we have to calculate the dimensionless excessive temperature $\theta(r, x^+)$ which satisfies Eqs. (5). The solution to this problem is sought in the form

$$\theta(r, x^+) = \sum_{n=1}^{\infty} C_n R_n(r) \exp(-\lambda_n x^+), \tag{13}$$

where λ_n and $R_n(r)$ are the eigenvalues and eigenfunctions, respectively, of the following eigenvalue problem:

$$(rR_n')' + \left(\frac{\lambda_n^2}{\mathrm{Pe}^2} + \lambda_n \frac{u}{2}\right) \cdot rR_n = 0, \tag{14a}$$

$$R_n'(0) = 0, \quad R_n'(1) = 0. \tag{14b}$$

Since the axial conduction term, $(1/\mathrm{Pe}^2)\partial^2\theta/\partial x^{+2}$, is retained in Eq. (5*a*), the mathematical problem (14*a*) and (14*b*) does not reduce to a classical Sturm-Liouville system with a complete set of eigenfunctions orthonormal with respect to a weighting function (LeCroy and Eraslan, 1969). Hence, we determine the coefficients C_n approximately by considering finite N eigenmodes (λ_n, $R_n(r)$) adequate for a converged solution. The method of weighted residuals through which these finite N eigenmodes are determined is explained in the Appendix. Applying the boundary condition at the entrance, multiplying Eq. (13) by R_m, and integrating over $0 \le r \le 1$, we obtain

$$\sum_{n=1}^{N} C_n \int_0^1 R_m R_n dr = -\int_0^1 R_m \Theta_\infty(r, 0) dr,$$

$$m = 1, 2, \ldots, N. \tag{15}$$

Solving the above set of N simultaneous Eqs. (15), we can determine C_n. Note that Hsu (1967) obtained C_n from the following relation, which Pirkle and Sigillito (1972) proved to be incorrect:

$$C_n = \frac{-\int_0^1 \left(\frac{2\lambda_n}{\mathrm{Pe}^2} + \frac{u}{2}\right) \Theta_\infty(r, 0) R_n r dr}{\int_0^1 \left(\frac{2\lambda_n}{\mathrm{Pe}^2} + \frac{u}{2}\right) R_n^2 r dr}. \tag{16}$$

The complete expression for the temperature now becomes

$$\Theta(r, x^+) = \Theta_\infty(r, x^+) + \sum_{n=1}^{\infty} C_n R_n(r) \exp(-\lambda_n x^+). \tag{17}$$

The bulk temperature, the wall temperature, and the Nusselt number are of interest and given by

$$\Theta_m(x^+) = 4(1 + 4A \cdot \mathrm{Br})x^+, \tag{18}$$

$$\Theta_w(x^+) = 4(1 + 4A \cdot \mathrm{Br})x^+ - 2B + A \cdot \mathrm{Br} + \sum_{n=1}^{N} C_n \mu_n \exp(-\lambda_n x^+) + \sum_{n=1}^{N} C_n R_n(1) \exp(-\lambda_n x^+), \tag{19}$$

$$\mathrm{Nu} = \frac{2}{\Theta_w - \Theta_m} = \frac{2}{-2B + A \cdot \mathrm{Br} + \sum_{n=1}^{N} C_n \mu_n \exp(-\lambda_n x^+) + \sum_{n=1}^{N} C_n R_n(1) \exp(-\lambda_n x^+)}, \tag{20}$$

where $\mu_n = (4/\mathrm{Pe}^2)\lambda_n[\int_0^1 R_n(r) r dr]$ was introduced due to the presence of the term $(4/\mathrm{Pe}^2)\int_0^1 (\partial\theta(r, 0)/\partial x^+) r dr$ in the expression $\Theta_\infty(r, x^+)$ (refer to Eq. (10)).

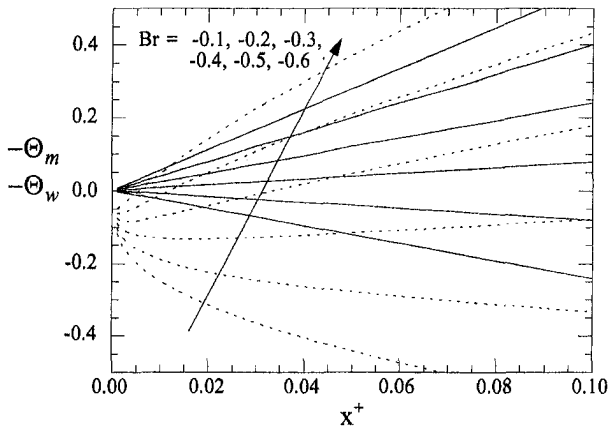

Fig. 4 Bulk and wall temperatures with respect to axial distance for c = 0 and Pe = 1000: ———, Θ_m (bulk temperature); - - - - -, Θ_w (wall temperature)

4 Results and Discussions

We performed our analysis for Pe = 5, 10, 100, 1000, with various values of Br and c = 0, 0.4, 0.6 over the range of $0.001 \le x^+ \le 1$. About 300 eigenmodes are required to obtain a converged solution with the criterion $(\mathrm{Nu}^{N+1} - \mathrm{Nu}^N)/\mathrm{Nu}^N < 10^{-5}$ over the entire range of x^+ except at the singularities; for this range of x^+, the relative error was typically less than 10^{-4} for all values

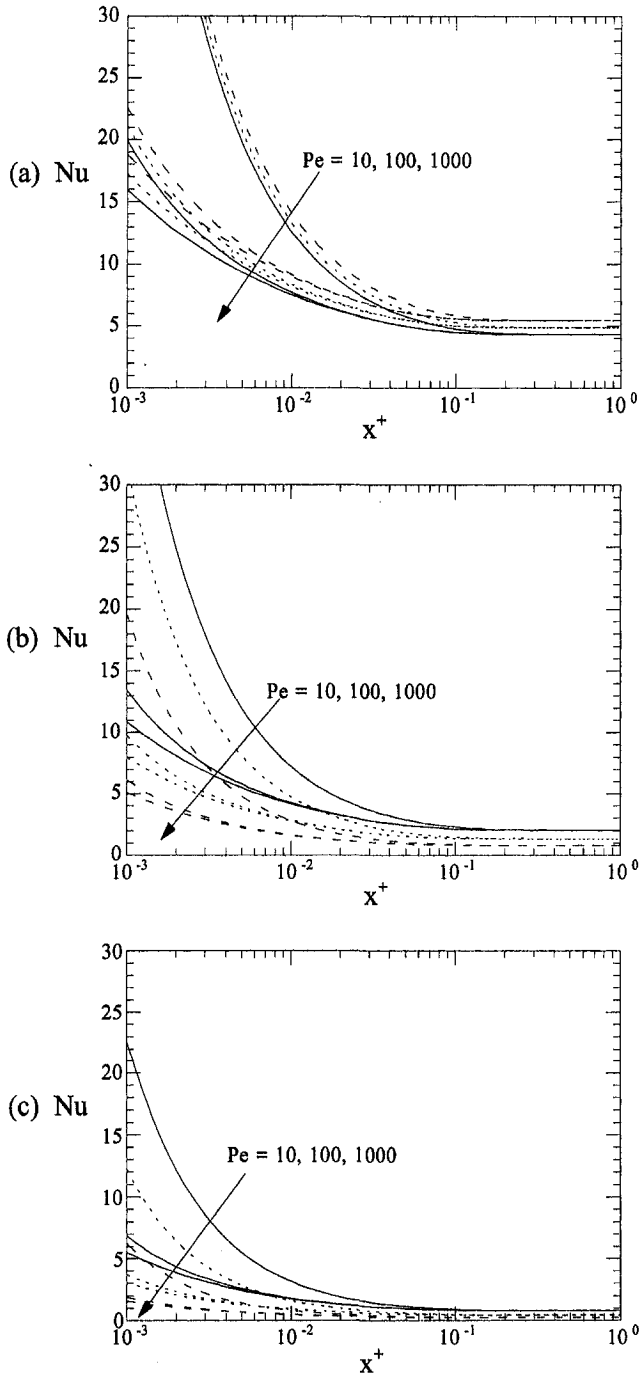

Fig. 5 Local Nusselt number with respect to axial distance for Br ≥ 0: ———, c = 0; - - - - -, c = 0.4; – – –, c = 0.6: (*a*) Br = 0; (*b*) Br = 0.5; (*c*) Br = 2

of c. It is emphasized that these are the first results in the literature obtained as the solution to the Graetz problem not only for a Bingham plastic but also for a Newtonian fluid, which includes both axial conduction and viscous dissipation with uniform wall heat flux.

4.1 Newtonian Fluid. Figures 2(*a*) and 2(*b*) show the local Nusselt number distributions for $c = 0$ neglecting viscous dissipation (Br = 0), compared with those obtained by Shah (1975) and Hsu (1967), respectively.[2] As expected, when Pe increases, the curves approach that of infinite Pe reported by Shah (1975), who solved the problem of laminar Newtonian fluid by neglecting axial conduction. It can be seen that the present result is in good agreement with the result of Shah (1975) when Pe = 1000. Therefore, it is deduced that the effect of axial conduction on the Nusselt number can be neglected when Pe is larger than 1000. It is also shown from Fig. 2(*b*) that there exists a substantial difference between the present result and Hsu (1967) for Pe < 50.

Figures 3(*a*) and 3(*b*) show the local Nusselt number distributions for $c = 0$ and Pe = 1000, including viscous dissipation. These results also show good agreement with previous results of Ou and Cheng (1973) who ignored axial conduction for a Newtonian fluid. It is reminded that from Eq. (12) Br_{cr} is again $2B/A$, below which the singularity in Nu_∞ exists. For a Newtonian fluid ($c = 0$), it is $-\frac{11}{24}$ which is the same as Ou and Cheng (1973) reported. Then it can be clearly seen that for Br ≤ −0.5 in Fig. 3(*b*) the Nusselt number does not decrease monotonically and there are singularities in the Nusselt number distributions.

The characteristics of Nu can be better understood by considering the differences between the wall and bulk temperatures. Figure 4 shows the variations of the wall and bulk temperatures in the axial direction for Br = 0, −0.1, −0.2, −0.3, −0.4, −0.5, and −0.6 with Pe = 1000 and $c = 0$. It is of particular interest to note that, for Br = −0.5 and −0.6 (i.e., for $\mathrm{Br} < \mathrm{Br}_{cr} = -0.4583$), the wall temperatures (T_w) become equal to the bulk temperatures (T_m) at some axial distances ($x^+ = (x^+)^*$), respectively. Note also that $\Theta < 0$ under a cooling condition means by definition $(\Theta(r, x^+) = (T - T_e)/(q_w R/k))$ that the temperature is larger than the entrance temperature because q_w is negative, which is equivalent to $\Theta > 0$ under a heating condition. Thus, for a cooling condition, it is more convenient to represent the temperature in terms of $-\Theta$ instead of Θ (Ou and Cheng, 1973).

The increase of |Br| under cooling condition means by definition the decrease of heat removed at the wall, $|q_w|$. For $\mathrm{Br}_{cr} < \mathrm{Br} < 0$, the cooling effect on the wall dominates over the viscous dissipation so that $T_w < T_m < T_e$ holds throughout the whole flow field ($x^+ > 0$). Naturally, $\Theta_w > \Theta_m$, resulting in Nu > 0 (see Fig. 3). For $\mathrm{Br} = \mathrm{Br}_{cr}$, the heat removed at the wall is equivalent to the heat generated by the viscous dissipation, resulting in $\Theta_w = \Theta_m$. The Nusselt number becomes infinite for this case, because the denominator of Eq. (12) becomes zero. For $\mathrm{Br} < \mathrm{Br}_{cr}$, the heat generation by the viscous dissipation dominates over the cooling effect on the wall (Ou and Cheng, 1973) and the fluid is rather heated in the downstream region of $x^+ = (x^+)^*$ where $T_w = T_m$. Therefore, for $x^+ > (x^+)^*$, $T_w > T_m$ and $\Theta_w < \Theta_m$ (Fig. 4), resulting in Nu < 0 (Fig. 3(*b*)).

[2] Physically, thermal boundary layer develops faster for smaller Pe. This means that Nu decreases for smaller Pe. Therefore, the present results (Figs. 2(*a*) and 2(*b*)) may appear to be contradictory to this fact, if we do not consider carefully the definitions of dimensionless coordinates. Note that the nondimensional axial distance used in the present study is $x^+ = x/\mathrm{Pe} = (z/R)/\mathrm{Pe}$. When we plot Nu with respect to x, we recover smaller Nu for smaller Pe. This problem has been also discussed in Min et al. (1997b).

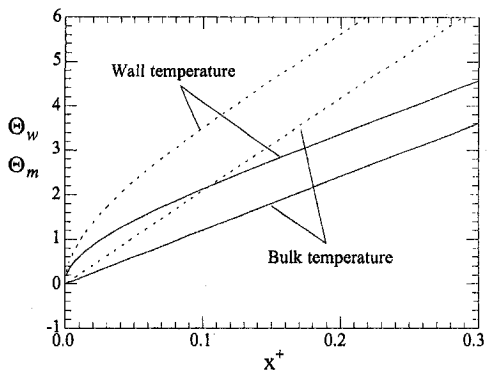

Fig. 6 Bulk and wall temperatures with respect to axial distance for Br = 0.5 and Pe = 1000: ———, c = 0; - - - - -, c = 0.4

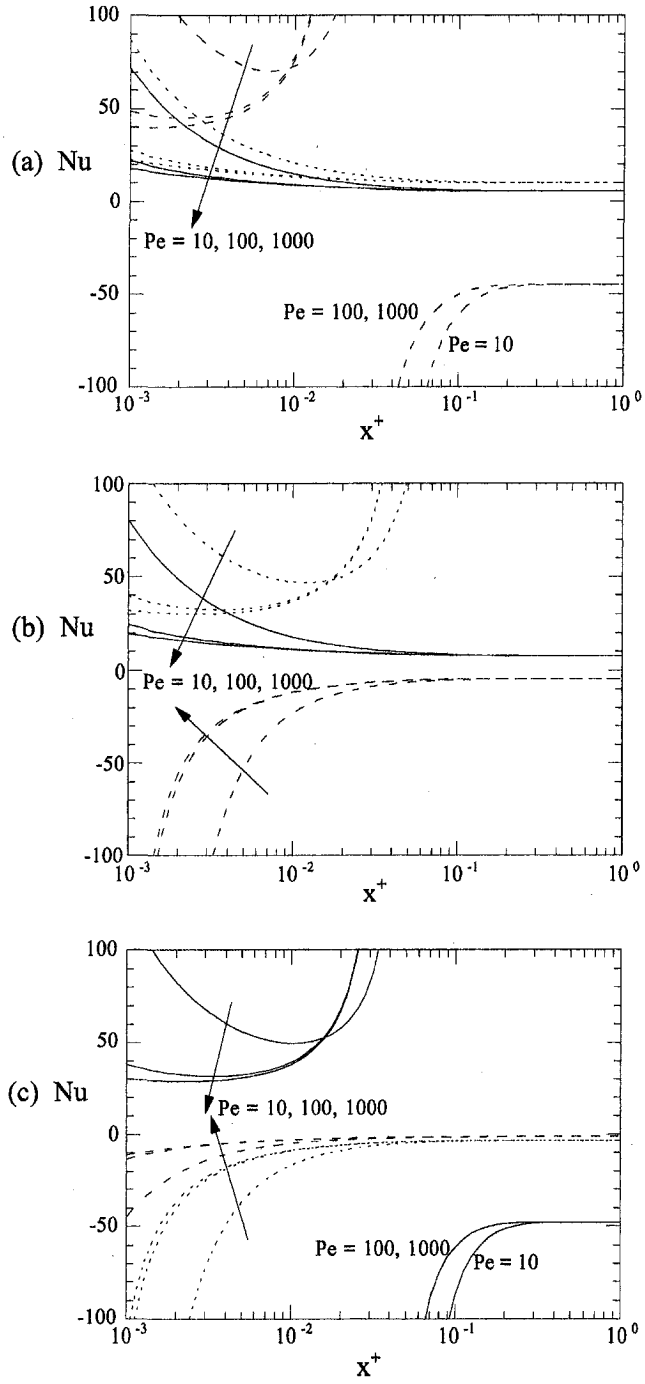

Fig. 7 Local Nusselt number with respect to axial distance for Br < 0: ———, $c = 0$; - - - -, $c = 0.4$; – – –, $c = 0.6$: (*a*) Br = −0.1; (*b*) Br = −0.2; (*c*) Br = −0.5

4.2 Bingham Plastic. Figures 5(*a*)–5(*c*) show the local Nusselt number for Br = 0, 0.5, and 2 with respect to Pe and c. For Br = 0, the local Nusselt number does not vary significantly with respect to c for the whole range of x^+ (Fig. 5(*a*)). However, when viscous dissipation is included (Br ≠ 0), the local Nusselt number is significantly affected by c in the entrance region, where the axial conduction effect is important. Qualitatively, for Br = 0 (Fig. 5(*a*)), the shape of the Nusselt number is very similar to that with uniform wall temperature (Min et al., 1997a, b). When the viscous dissipation is excluded (Br = 0), Nu increases with an increase of c because the thickness of the boundary layer decreases (Fig. 5(*a*)). However, when we consider the viscous dissipation under heating condition (Br > 0), the heat transfer characteristics in terms of c is completely different. Figures 5(*b*) and 5(*c*) show that Nu rather decreases with an increase of c. This can be explained from the variations of the wall and bulk temperatures in the axial direction. For example, Fig. 6 shows the variations of the wall and bulk temperatures with respect to axial distance for Br = 0.5 and Pe = 1000 with $c = 0$ and 0.4. It is noted that, with an increase of c, the increase of T_w becomes larger than that of T_m. It is because the heat generation by dissipation near the wall becomes larger due to the increased velocity gradient there. Thus $T_w - T_m$ increases and Nu decreases with an increase of c, considering the definition of $\mathrm{Nu} = 2/(\Theta_w - \Theta_m)$.

Figures 7(*a*)–7(*c*) show the local Nusselt number for Br = −0.1, −0.2, and −0.5 with respect to Pe and c. For Br < 0 (cooling condition), the dependence of the Nusselt number on c is more complex than for Br > 0 (heating condition), because there exists a Br_{cr} for each c. it is reminded that, $\mathrm{Br}_{cr} = 2B/A \cong -0.4583$, −0.1944, and −0.0892 for $c = 0$, 0.4, 0.6, respectively. Therefore, in Fig. 7(*a*) for Br = −0.1, only curves for $c = 0.6$ have singularities. Similarly, in Fig. 7(*b*) for Br = −0.2, curves for $c = 0.4$ and 0.6 have singularities and in Fig. 7(*c*) for Br = −0.5, all the curves of Nu for $c = 0$, 0.4 and 0.6 have singularities. It is also noted that as |Br| increases for a given c, the location of the singularity approaches the inlet, if it exists. It is because the wall temperature increases faster for larger |Br|, compared to the bulk temperature. However, the Nusselt number varies little with respect to Pe for $x^+ > 0.02$, where the axial conduction effect is not so important. Through a similar analysis to the one given for the case of heating condition, it can be deduced that increasing c causes the increase of T_w to become larger than that of T_m, as shown in Figs. 8(*a*) and 8(*b*). In other words, with an increase of

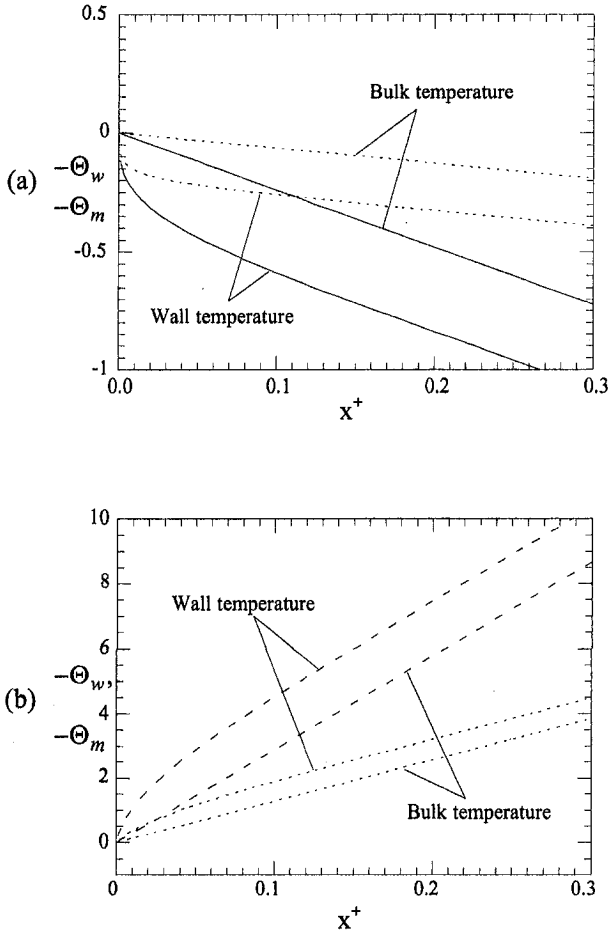

Fig. 8 Bulk and wall temperatures with respect to axial distance for Pe = 1000: ———, $c = 0$; - - - -, $c = 0.4$; – – –, $c = 0.6$: (*a*) Br = −0.1; (*b*) Br = −0.5

c for Br $= -0.1$, $\Theta_w - \Theta_m$ becomes smaller and Nu increases because $T_w < T_m < T_e$ (Fig. 8(a)). However, for Br $= -0.5$, $|\Theta_w - \Theta_m|$ becomes larger and |Nu| decreases when Nu is negative because $T_w > T_m$ (Fig. 8(b)).

5 Conclusion

Thermally fully developed flow as well as thermally developing flow (the Graetz problem) including both axial conduction and viscous dissipation have been investigated analytically for a Bingham plastic in a laminar pipe flow with uniform wall heat flux. In particular, the Graetz problem is solved by the method of separation of variables, incorporating an approximate solution to the resultant eigenvalue problem, which is obtained by using the method of weighted residuals.

For thermally fully developed flow, the temperature profiles and the Nusselt number are obtained. When c is zero and Pe $\rightarrow \infty$, the solutions agree exactly with those reported in previous studies for Newtonian fluids. It has been found that the Nusselt number for a Bingham plastic is less affected by the Brinkman number for larger yield stress. For thermally developing flow, it is shown that viscous dissipation plays a significantly different role on heat transfer, depending on heating and cooling conditions, respectively. The Nusselt number for a Bingham plastic is not so significantly affected by the yield stress when viscous dissipation is excluded. However, the Nusselt number is significantly changed by the yield stress in the entrance region with the inclusion of viscous dissipation, i.e., for Br > 0. Therefore, in the study on heat transfer of a Bingham plastic, it is emphasized that the viscous dissipation must be considered.

Acknowledgment

This study was supported by the Science & Technology Policy Institute, Republic of Korea through project number 97-I-01-03-A-024.

References

Beek, W. J., and Eggink, R., 1962, "Heat Transfer to Non-Newtonian Fluids in Laminar Flow through Circular Pipes," *De Ingenieur,* Vol. 74, No. 35, pp. 81–89 (in Dutch).

Bird, R. B., Armstrong, R. C., and Hassager, O., 1987, *Dynamics of Polymeric Liquids,* (Vol. 1, Fluid Mechanics), John Wiley and Sons, New York.

Bird, R. B., Stewart, W. E., and Lightfoot, E. N., 1960, *Transport Phenomena,* John Wiley and Sons, New York.

Blackwell, B. F., 1985, "Numerical Solution of the Graetz Problem for a Bingham Plastic in Laminar Tube Flow With Constant Wall Temperature," ASME JOURNAL OF HEAT TRANSFER, Vol. 107, pp. 466–468.

Finlayson, B. A., 1972, *The Method of Weighted Residuals and Variational Principles,* Academic Press, New York.

Hsu, C. J., 1967, "An Exact Mathematical Solution for Entrance-Region Laminar Heat Transfer with Axial Conduction," *Applied Scientific Research,* Vol. 17, pp. 359–376.

Johnston, P. R., 1991, "Axial Conduction and the Graetz Problem for a Bingham Plastic in Laminar Tube Flow," *International Journal of Heat and Mass Transfer,* Vol. 34, pp. 1209–1217.

Kakaç, S., Shah, R. K., and Aung, W., 1987, *Handbook of Single-Phase Convective Heat Transfer,* John Wiley and Sons, New York.

Kays, W. M., and Crawford, M. E., 1993, *Convective Heat and Mass Transfer,* 3rd Ed., McGraw-Hill, New York.

LeCroy, R. C., and Eraslan, A. H., 1969, "The Solution of Temperature Development in the Entrance Region of an MHD Channel by the B. G. Galerkin Method," ASME JOURNAL OF HEAT TRANSFER, Vol. 91, pp. 212–220.

Min, T., Yoo, J. Y., and Choi, H., 1997a, "Laminar Convective Heat Transfer of a Bingham Plastic in a Circular Pipe—I. Analytical Approach—Thermally Fully Developed Flow and Thermally Developing Flow (the Graetz Problem Extended)," *International Journal of Heat and Mass Transfer,* Vol. 40, pp. 3025–3037.

Min, T., Yoo, J. Y., Choi, H. G., and Choi, H., 1997b, "Laminar Convective Heat Transfer of a Bingham Plastic in a Circular Pipe—II. Numerical Approach—Hydrodynamically Developing Flow and Simultaneously Developing Flow," *International Journal of Heat and Mass Transfer,* Vol. 40, pp. 3689–3701.

Ou, J. W., and Cheng, K. C., 1973, "Viscous Dissipation Effects on Thermal Entrance Region Heat Transfer in Pipes with Uniform Wall Heat Flux," *Applied Scientific Research,* Vol. 28, pp. 289–301.

Pirkle, J. C., and Sigillito, V. G., 1972, "Laminar Heat Transfer with Axial Conduction," *Applied Scientific Research,* Vol. 26, pp. 108–112.

Sellars, J. R., Tribus, M., and Klein, J. S., 1956, "Heat Transfer to Laminar Flow in a Round Tube or Flat Conduit—The Graetz Problem Extended," ASME *Transactions,* Vol. 78, pp. 441–448.

Shah, R. K., 1975, "Thermal Entry Length Solutions for the Circular Tube and Parallel Plates," *Proceedings of National Heat and Mass Transfer Conference,* 3rd, Indian Institute of Technology, Bombay, Vol. 1, Paper No. HMT-11-75.

Shah, R. K., and London, A. L., 1978, "Laminar Flow Forced Convection in Ducts," *Advances in Heat Transfer,* Supplement 1, Academic Press, New York.

Siegel, R., Sparrow, E. M., and Hallman, T. M., 1958, "Steady Laminar Heat Transfer in a Circular Tube with Prescribed Wall Heat Flux," *Applied Scientific Research,* Sect. A7, pp. 386–392.

Vradis, G. C., Dougher, J., and Kumar, S., 1993, "Entrance Pipe and Heat Transfer for a Bingham Plastic," *International Journal of Heat and Mass Transfer,* Vol. 36, pp. 543–552.

Vradis, G. C., and Ötügen, M. V., 1997, "The Axisymmetric Sudden Expansion Flow of a Non-Newtonian Viscoplastic Fluid," ASME *Journal of Fluids Engineering,* Vol. 119, pp. 193–200.

Wissler, E. H., and Schechter, R. S., 1959, "The Graetz-Nusselt Problem (with Extension) for a Bingham Plastic," *Chemical Engineering Progress Symposium* Series 29, Vol. 55, pp. 203–208.

APPENDIX

The Method of Weighted Residuals

It is well known that the construction of an exact analytical solution to the eigenvalue problem of thermally developing flow is very difficult even in the case of negligible axial conduction. Although numerical solutions to the eigenvalue problem (5) are possible, higher modes of the system for large eigenvalues necessitate extensive computational effort, as Sellars et al. (1956) reported. Therefore, in this paper, an approximate solution to the eigenvalue problem (5) is obtained by the method of weighted residuals.

We expand the eigenfunction R_n in terms of some known functions $S_i(r)$ which satisfy the boundary conditions, Eq. (5b) (Finlayson, 1972):

$$R_n = \sum_{i=1}^{N} c_i^{(n)} S_i(r), \quad n = 1, 2, \ldots, N, \tag{A1}$$

where $c_i^{(n)}$ are undetermined coefficients. In the present study, we set $S_i = \cos(i - 1)\pi r$. Integrating Eq. (5a) multiplied by the weight function w_j, it can be written as (Finlayson, 1972)

$$\int_0^1 (rR_n')' w_j dr + \int_0^1 \left(\frac{\lambda_n^2}{\mathrm{Pe}^2} + \lambda_n \frac{u}{2}\right) r R_n w_j dr = 0. \tag{A2}$$

In the Galerkin method, $w_j = S_j$ and Eq. (A2) becomes (for more details, see Finlayson (1972))

$$\sum_{i=1}^{N} (A_{ji} + \lambda_n^2 B_{ji} + \lambda_n C_{ji}) c_i^{(n)} = 0, \quad n = 1, 2, \ldots, N, \tag{A3}$$

where A_{ji}, B_{ji}, and C_{ji} are elements of matrices such that

$$A_{ji} = -\int_0^1 r S_i' w_j' dr, \tag{A4a}$$

$$B_{ji} = \frac{1}{\mathrm{Pe}^2} \int_0^1 r S_i w_j dr, \tag{A4b}$$

$$C_{ji} = \int_0^1 \frac{u}{2} r S_i w_j dr. \tag{A4c}$$

This can be turned into a $2N \times 2N$ linear matrix problem by adding an unknown eigenvector $\mathbf{d}$

$$\begin{pmatrix} \mathbf{O} & \mathbf{I} \\ -\mathbf{B}^{-1}\mathbf{A} & -\mathbf{B}^{-1}\mathbf{C} \end{pmatrix} \begin{pmatrix} \mathbf{c} \\ \mathbf{d} \end{pmatrix} = \lambda \begin{pmatrix} \mathbf{c} \\ \mathbf{d} \end{pmatrix}, \tag{A5}$$

where $\mathbf{A} = \{A_{ji}\}$, $\mathbf{B} = \{B_{ji}\}$, and $\mathbf{C} = \{C_{ji}\}$. Solving Eq. (A5), we can obtain N real positive eigenvalues and the corresponding eigenvectors.

Experimental Study of the Local Convection Heat Transfer From a Wall-Mounted Cube in Turbulent Channel Flow

E. R. Meinders[1]
Philips Research,
Prof. Holstlaan 4,
Building WB 151,
5656 AA Eindhoven,
The Netherlands

K. Hanjalic

Delft University of Technology,
Faculty of Applied Physics,
2628 CJ Delft, The Netherlands

R. J. Martinuzzi

University of Western Ontario,
Faculty of Engineering Science,
London, ON Canada

This paper presents some results of the experimental investigation of the local convective heat transfer on a wall-mounted cube placed in a developing turbulent channel flow for Reynolds numbers between 2750 $< Re_H <$ 4970. Experiments were conducted using a specially designed cubic assembly made of heated copper core and a thin epoxy layer on its surface. The distribution of the local heat transfer coefficient was obtained from the surface heat flux evaluated from the heat input and computed temperature field in the epoxy layer, and from the surface temperature distribution acquired by infrared thermography. In parallel, the flow field was studied using laser doppler anemometer and flow visualizations, aimed at correlating the local heat transfer with the flow pattern and turbulence field. The complex vortex structure around the cube, in particular at the top and the side faces, caused large variation in the local convective heat transfer. The largest gradients in the distributions of the surface heat transfer were found at locations of flow separation and reattachment. Areas of flow recirculation are typically accompanied by a minimum in the heat transfer coefficient. It is argued that the local temperature rise of the air in the recirculation zone is caused by the trapped vortex, which acts as an insulation layer preventing the removal of heat from the surface of the cubes. In contrast, the intermittent reattachment of the low-temperature shear flow was found to produce large heat transfer coefficients.

1 Introduction

The convective heat transfer and flow field characteristics of heated surface-mounted prismatic obstacles in a channel flow is of both fundamental scientific and practical interest. Sharp-edged obstacles mounted on solid walls give rise to complex flow patterns with regions of flow separation, reattachment, and recirculation. The fundamental interest lies in understanding the interaction between these large-scale structures and the local surface heat transfer. From the application point of view, these geometries have a diagnostic value of practical relevance to the electronics industry, where local overheating is a major cause of technical failure on printed circuit boards. Avoiding component damage relies on accurate predictions of the local convective heat transfer, which requires detailed knowledge of the local flow patterns. Typically, the interior of an electronic cabinet is compact and geometrically complex with electronic components resembling prismatic obstacles. In spite of generally low fluid velocities, these configurations give rise to complicated flow patterns with regions of high-turbulence intensities. Combined with the concentrated heat dissipation within the board-mounted elements, these unsteady, strongly three-dimensional flow patterns may cause a high nonuniformity of the convective heat transfer, resulting in local hot spots. In this study, the local convective heat transfer from a single surface-mounted element, modeled as a cube obstacle placed in a developing channel flow, is investigated as a simplified, reference diagnostic case.

In the past few decades, much research was already devoted to the flow around bluff-bodies. Cubical geometries are often chosen as a reference. The literature review of Schofield and Logan (1990) showed that a consensus exists for the general flow features around a single wall-mounted cube. These features include: the horseshoe vortex, originating in the windward stagnation region at the base of the cube and extending downstream; two intense wall-bound vortices along the side faces; the vortex on top of the cube; and the near wake recirculation region. Hunt et al. (1978) discussed the applications of the topology principles to oil-film visualizations of the surface streaks to deduce the flow field around single wall-mounted prismatic obstacles in boundary layer flows. This technique allows to identify several characteristic flow features, such as the secondary structure of the horseshoe vortex, which are difficult to assert from single-point velocimetry measurements alone. The studies of Martinuzzi (1992), Larousse et al. (1991), Hussein and Martinuzzi (1996), and Martinuzzi and Tropea (1993) were focussed on the flow structure around a cube in a fully developed channel flow at the Reynolds number of Re_H = 40,000, based on the bulk velocity and the cube height. The channel-to-cube-height ratio was 2. In addition to the aforementioned features, they showed that periodic vortex shedding existed in the wake and that the dynamic behavior of the flow in the horseshoe vortex region was bimodal, but nonperiodic. Hot-wire anemometry data (Castro and Robins, 1997) showed that the extent of the wake recirculation depends on the relative boundary layer thickness of the on-coming flow, which also determines whether or not the flow reattachment occurs on the obstacle top face.

Several studies in the accessible literature focussed on distributions of the local heat transfer coefficients for two-dimensional configurations. Examples include square cylinders suspended in a flow (Igarashi, 1986) and wall-mounted square bars (Igarashi, 1986; Igarashi and Yamasaki, 1991; Aliaga et al., 1994; Lorenz et al., 1995). Other investigations deal with the convective heat transfer downstream of a step in the surface of a plate (Seban, 1964), the heat transfer in the recirculation region behind a double

[1] To whom correspondence should be addressed. e-mail: erwin@natlab.research.philips.com.

Contributed by the Heat Transfer Division for publication in the JOURNAL OF HEAT TRANSFER. Manuscript received by the Heat Transfer Division, Aug. 4, 1997; revision received, Apr. 12, 1999. Keywords: Augmentation and Enhancement, Conjugate Heat Transfer, Flow Separation, Forced Convection, Turbulence. Associate Technical Editor: J. Han.

step (Filetti and Kays, 1967), and the heat transfer in the recirculation region on a blunt flat plate (Ota and Kon, 1974). In all these cited studies, a heated thin sheet of metal at the obstacle surface provided the local heat flux. The studies showed that for these two-dimensional geometries, flow impingement and separation had a significant impact on the local heat transfer coefficient. Regions of flow separation were typically characterized by low convective heat transfer, while regions where the flow reattached coincided with maxima in the local heat transfer coefficient. The constant heat flux method was used by Olsen et al. (1989) to measure local heat transfer coefficients at two faces of the cube. The coverage of the entire cube surface with these metal foils proved to be difficult. The heat transfer was also strongly nonuniform in their case, in particular at the side face of the cube where the side vortex, enveloping the entire side face, caused the monotonic increase in the heat transfer coefficient in the streamwise direction.

To the knowledge of the authors, no results have been published on the direct measurement of the distributions of the local convective heat transfer for *all* faces of a single cube exposed to convective cooling. Natarajan and Chyu (1991, 1994) investigated the local mass transfer from a single wall-mounted cube in a boundary layer flow with the naphthalene sublimation method for a cube in a boundary layer flow ($\delta/H = \frac{1}{4}$, δ is the boundary layer thickness and H is the cube size). The heat transfer was then derived from a mass/heat transfer analogy. The Reynolds numbers, based on the cube height and freestream velocity, ranged between 3.1×10^4 and 1.1×10^5. They observed significant differences in the mass transfer rates for the different cube faces which were directly related to the complex flow structure around the cube.

Much more research was devoted to the element-averaged convective heat transfer from isothermal obstacles. A study of the convective heat transfer for an isolated single protrusion in channel flow was performed by Roeller et al. (1991), for Reynolds numbers based on the channel height between 500 and 10,000, which included variation of obstacle dimensions, geometry, and blockage ratio. The results showed that the averaged heat transfer coefficient increases with increasing blockage ratio mainly due to local flow acceleration. Nakayama and Park (1996) studied the conjugate heat transfer from a wall-mounted block in channel flow both experimentally and numerically for Reynolds numbers between 2200 to 16,000 for two different situations: a heated copper block on an adiabatic wall and an adiabatic block on a heated wall. They found that the conjugate effects were strong and that the local convective heat transfer from the channel wall was closely related to the three-dimensional flow field around the protrusion. Morris and Garimella (1996) studied the thermal wake downstream of a three-dimensional obstacle in a water tunnel flow for uniform inlet conditions and Reynolds numbers between 500–1000 (laminar) and 10,000–25,000 (turbulent). Mean flow patterns were deduced from flow visualization experiments. It was shown that buoyancy affected the thermal wake structure only for the lower Reynolds number cases. Recently, Chyu and Natarajan (1996) performed a comparative study on the local mass transfer characteristics on the base surface of three-dimensional basic geometries (cylinder, cube, diamond, pyramid, and hemisphere) placed in a boundary layer flow at a Reynolds number of 17,000, based on the object height. The results showed a mass transfer enhancement especially in vicinity of the horseshoe vortex system and wake vortices downstream of the protrusions.

From the foregoing literature review, it is seen that the flow around a single surface-mounted cube was documented in great detail mainly for Reynolds numbers typically an order of magnitude higher than those encountered in electronic cooling applications. This lower Reynolds number range is the primary interest of our study. Hence, the flow field in the Reynolds number range $2750 < \mathrm{Re}_H < 4970$, where Re_H is based on the cube height and the bulk velocity, is investigated using oil-film visualization, smoke visualization, and laser doppler anemometry (LDA). It is observed that several large-scale flow features are, superficially at least, similar in this case as in the high Reynolds number case which is well documented in the literature. However, it is important to note that at least four important differences exist. First, unlike the case in the fully developed turbulent channel flow, the flow in the present case reattaches at the top and side faces of the cube. It will be shown later in the paper that the location of the flow reattachment points has a major effect on the local convective heat transfer. Second, as a result of the flow reattachment on the top face, the wake recirculation region is shorter in the present study, which affects the curvature of the shear layer and, in turn, the vortex shedding dynamics. A third difference between the two cases is found in the vortex shedding frequency: The Strouhal number was 0.095 for the present case versus 0.14 for the fully developed case. Finally, the windward separation point is much further upstream than for the fully developed case while the stagnation point on the obstacle front face is lower, indicating that the horseshoe vortex is smaller at lower Reynolds numbers.

Since the flow around single wall-mounted cubes is well documented, it suffices to discuss only the major differences between the high and low Reynolds number flows. Further, some relevant flow aspects will be highlighted to facilitate the interpretation of the convective heat transfer. The focus will primarily be on the discussion of distributions of the local convective heat transfer for cubes in a low Reynolds number turbulent channel flow. In addition to providing a comprehensive data set for benchmark purposes, we attempt to describe the interaction between the flow and surface heat transfer as well as to identify similarities or dissimilarities between momentum and heat transfer.

Nomenclature

A, B = coefficient
D = channel width, m
f = frequency, Hz
h_{ad}, h = adiabatic heat transfer coefficient, W/m^{2}K
$\bar{h}$ = average heat transfer coefficient, W/m^{2}K
H = cube size, mm
$\mathrm{Re}_\theta = U\theta/\nu$ = Reynolds number based on momentum thickness
$\mathrm{Re}_H = u_B H/\nu$ = Reynolds number based on cube height
$\mathrm{St} = fH/u_B$ = Strouhal number, based on bulk velocity
T_{ad} = adiabatic component temperature, °C
T_{sur} = surface temperature, °C
$\bar{u}$ = mean velocity in x-direction, m/s
u_B = bulk velocity, m/s
$u_\tau = \sqrt{\tau_w/\rho}$ = shear velocity, m/s
U_∞ = freestream velocity, m/s
$\overline{u'^2}$ = Reynolds normal stress in x-direction, m^2/s^2
$\overline{w'^2}$ = Reynolds normal stress in z-direction, m^2/s^2
x = coordinate in streamwise direction, m
y = coordinate in span direction, m
z = coordinate in normal direction, m

Greek Symbols

δ = boundary layer thickness, m
θ = momentum thickness, m
λ = thermal conductivity, W/mK
ν = kinematic viscosity, m/s^2
ρ = fluid density, kg/m^3
τ_w = wall shear stress, N/m^2
ϕ''_{cond} = conductive heat flux at surface, W/m^2
ϕ''_{conv} = convective heat flux, W/m^2
ϕ''_{rad} = radiative heat flux, W/m^2

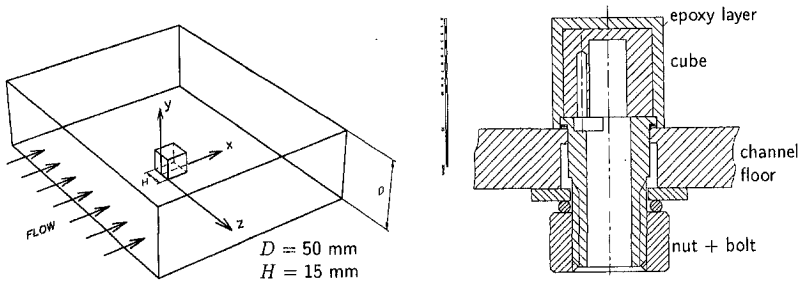

Fig. 1 A three-dimensional view of the wall-mounted cube in the channel with the coordinate system used and a detailed drawing of the measurement cube assembly

2 Experimental Details

The experiments were carried out in a two-dimensional wind tunnel of height $D = 50$ mm and of width 600 mm. A cube with dimension $H = 15$ mm ($D/H = 3.3$) was placed on one of the walls along the channel centerline. In-flow conditions were controlled by tripping the boundary layer 75 cm upstream of the cube leading face. A sketch of the experimental configuration and the Nomenclature are given in Fig. 1. The x, y, and z-coordinates denote the streamwise, normal, and spanwise direction, respectively. The different faces are classified as front face, side faces, top face, and rear face. A detailed drawing of the measurement assembly is also given in Fig. 1. This measurement cube consists of a 12-mm cubical copper core covered by a thin epoxy layer machined to 1.5-mm uniform thickness. The high thermal conductivity of the heated copper core allowed its temperature to be kept uniform within 0.05°C. The three-dimensional temperature distribution in the epoxy substrate was obtained by solving the conduction problem with temperature boundary conditions for the internal surface (the uniform copper temperature) and the outer surface (the temperature distribution acquired from Infrared thermography). The local mean conductive heat flux at the surface of the cube is determined from the local mean temperature derivative normal to the surface. At the surface, equilibrium of heat fluxes yields the local convective heat flux ϕ''_{conv}, and thus the adiabatic heat transfer coefficient,

$$h_{ad} = \frac{\phi''_{\text{cond}} - \phi''_{\text{rad}}}{T_{\text{sur}} - T_{ad}}; \tag{1}$$

where the difference between the conductive heat flux, ϕ''_{cond} and the radiative heat flux ϕ''_{rad} denote ϕ''_{conv}; T_{sur} and T_{ad} denote, respectively, the surface and the adiabatic temperatures. The local radiative heat flux was approximated from the Stefan-Boltzmann relationship using the local surface temperature, the surface emissivity, and the ambient temperature. The adiabatic temperature is defined as the surface temperature (and thus the local ambient temperature) of an element in the adiabatic situation. For these single cube experiments, T_{ad} corresponds to the inlet temperature of the air stream (Moffat and Anderson, 1990). A detailed discussion of the experimental techniques and calibration methods are discussed in Meinders et al. (1997, 1999) and Meinders (1998) and here we summarize in brief the major aspects.

The surface temperature distribution was acquired using an infrared (IR) imaging system, mounted at a 45-deg scan angle to enable the measurement on the lateral faces of the cube. A major difficulty in measuring surface temperature distributions of small three-dimensional bodies is maintaining high accuracy and large depth of field without reducing the spatial resolution. This problem was resolved by using a restoration technique for infrared images with a Wiener filter. This technique is based on the measured two-dimensional optical transfer function, which is a characteristic of the used infrared imaging system. The cube surface is coated with a thermal black paint of emissivity 0.95 to enhance thermal radiation. This experimentally determined emissivity is uniform for scan angles up to approximately 60 deg. An in situ calibration was used to account for miscellaneous environmental contributions to the total received radiosity and relate the local emitted intensity and surface temperature distribution.

The estimated accuracy of the heat transfer coefficients is within five to ten percent based on the analysis using the standard single sample uncertainty estimation method (Moffat, 1988). The local convective heat transfer is determined directly from the local conductive heat fluxes. Hence, the overall accuracy depends strongly on the accuracy of the surface temperature measurements which are within 0.4°C using infrared thermography with in situ calibration and image restoration. This accuracy was verified using liquid crystal thermography. The spatial accuracy of the thermography measurements is within 0.5 mm. The uncertainties of the ambient and adiabatic reference temperatures (within 0.5°C) have little impact on the overall accuracy. The other main contributions to inaccuracy include: the machining tolerance for the epoxy layer thickness (<1 percent); the thermal conductivity of the epoxy substrate ($\lambda = 0.24 \pm 2$ percent W/mK); and the copper core temperature measured with an embedded thermocouple (±0.1°C).

Qualitative information of the flow field was obtained via flow visualizations. A two-component back-scatter LDA system (TSI 9230/9201) was used to obtain mean and instantaneous flow field details around the obstacle. The maximum overall experimental uncertainty is estimated to be five percent for the mean velocities and ten percent for the Reynolds stresses based on methods reviewed in the literature (Absil, 1996; Durst et al., 1976). Reference is made to Meinders (1998) for a more detailed discussion of the LDA results and technique used.

3 Characterization of Channel Flow

The laminar-turbulent boundary layer transition was forced by a tripping strip located on the channel floor 75 cm upstream of the cube. The resulting flow consisted of a developing turbulent boundary layer on the floor and an almost laminar boundary layer at the opposing wall while the core flow remained uniform. The core stream velocity gradient dU_∞/dx was 0.67 1/s. The momentum thickness θ at the floor was used to determine a local Reynolds number Re_θ. In the absence of the cube, $\text{Re}_\theta = 660$ at $x = 0$ which is the location of the cube leading edge. Profiles of the mean velocity and second moments were measured at five locations in the streamwise direction which included three positions upstream and two downstream of the cube. Log-law fitting, as proposed by Coles (1962), was used to determine the shear velocities u_τ. The mean velocity gradients evaluated from the measured velocity profiles close to the wall agreed with Coles method within about five to ten percent. These shear velocities were used to nondimensionalize the mean velocity and the y-coordinate. A typical value for the shear velocity is $u_\tau = 0.25$ m/s at $x = 0$. The dimensionless mean velocity $\bar{u}/u_\tau$ and turbulent intensities $\sqrt{u'^2}/u_\tau$ are plotted on a semi-log scale in Fig. 2 and compared with results of Erm et al. (1978) for $\text{Re}_\theta = 617$. Although these measurements represent a turbulent developing boundary layer in the absence of

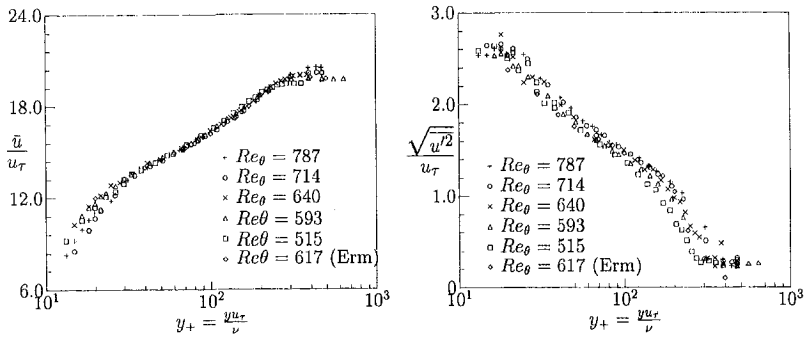

Fig. 2 Velocity profiles and turbulence intensities scaled with inner variables for different Reynolds numbers; comparison between present data and literature (Erm et al., 1978)

a pressure gradient, they are in good agreement with the present data.

A consistency check was conducted by verifying conservation of mass at the five subsequent stations. The mass flow was obtained from a numerical integration yielding an average mass flow rate of 0.262 kg/s per unit area. The average bulk velocity, derived from the ratio of the mass flow rate and the integration area, was 4.47 m/s. The discrepancies in the bulk velocities between the five profiles were within one percent. The Reynolds number based on the averaged bulk velocity (4.47 m/s) and the cube height was $\mathrm{Re}_H = 4440$.

4 Results and Discussion

4.1 Flow Field. The flow field structure around the single cube in the turbulent developing channel flow was deduced from the LDA measurements and complementary information obtained from the flow visualization experiments. The LDA measurements were conducted at $\mathrm{Re}_H = 4440$. The flow visualizations were performed for $2000 < \mathrm{Re}_H < 7000$. The results were independent of Re_H in the range studied.

4.1.1 Time-Averaged Flow Field. The flow field in front of the cube is characterized by the horseshoe vortex system which originates at the base of the windward stagnation region and extends downstream along the channel floor past the sides of the cube. The surface imprint of this system can be observed from the oil-film results of Fig. 3. The location of the main horseshoe vortex is denoted by the pigment pattern marked **A**. Secondary vortices at the upwind base of the main structure result in clear pigment patterns. The flow separation line originates at the saddle point $\mathbf{S}_b$, located approximately 1.4 cube heights upstream of the leading face, and is delimited by the pigment line extending laterally and then downstream from this point. This location differs from the high Reynolds number case of Martinuzzi et al. who found the separation line to be at one cube distance H upstream. A separation saddle is also observed close to the windward face (marked $\mathbf{S}_a$). The flow pattern in the wake recirculation region is dominated by an arch vortex. This structure results in the two vorticity concentration nodes marked **B** in the oil-film results in Fig. 3, which are the two counterrotating footprints of the arch-shaped vortex. The shear layer separates at the top leading edge and reattaches at approximately $1.5H$ downstream of the trailing face, $x/H = 2.5$ (marked with **C** in Fig. 3). The top face is characterized by a bound vortex in the vicinity of the leading edge. The oil-surface image of Fig. 3 shows two counterrotating vorticity concentration nodes marked **D**, which are attributed to the footprints of this vortex. The two sides of the cube show a symmetric pattern with vortex tubes close to the leading edge, confined by the main stream and the cube. These vortex tubes have origins at the nodes close to the leading edge corner on the channel floor marked **E** in Fig. 3. The time-averaged vortical pattern around the single wall-mounted cube is sketched in Fig. 4. The horseshoe vortex, top, and side vortices and the wake vortex are clearly identifiable from the sketch.

LDA data of the mean streamwise velocity $\bar{u}$ and the Reynolds normal stresses in the streamwise and spanwise direction, $\overline{u'^2}$ and $\overline{w'^2}$, respectively, are plotted in Fig. 5(*a*), (*c*), and (*e*) for five heights at the front centerline (upstream) of the cube. The location of the horseshoe vortex can be identified as the region of negative streamwise velocities and extends up to approximately half of the cube height. The peaks in the Reynolds normal stresses $\overline{u'^2}$ coincide with maximum turbulence production areas due to large velocity shear gradients and bimodal behavior. LDA measurements in the wake region are given in Fig. 5(*b*), (*d*), and (*f*) for $z/H = 0$ at five different heights y/H. The flow recirculation induced by the arch vortex appears as negative mean velocities.

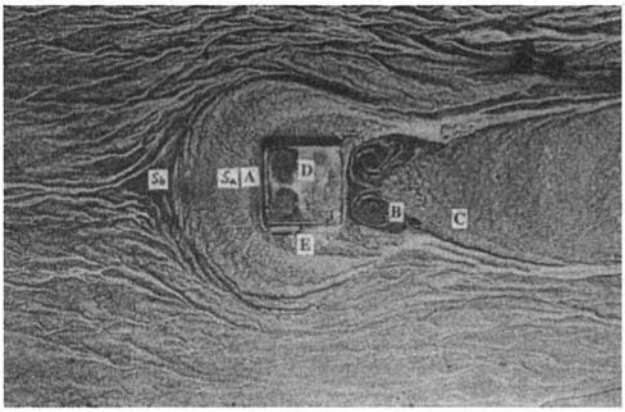

Fig. 3 Visualization of the surface flow pattern using the oil-film technique. Flow is from left to right.

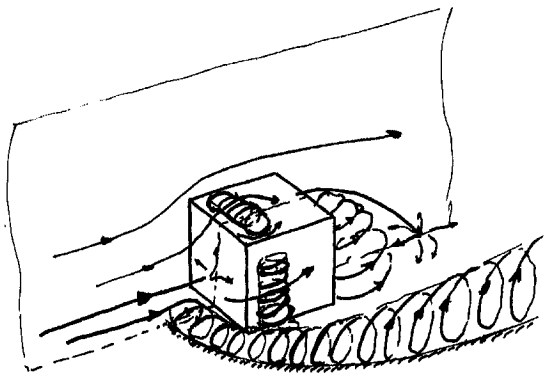

Fig. 4 "Artist's impression" of the flow structure around the single cube in a turbulent channel flow

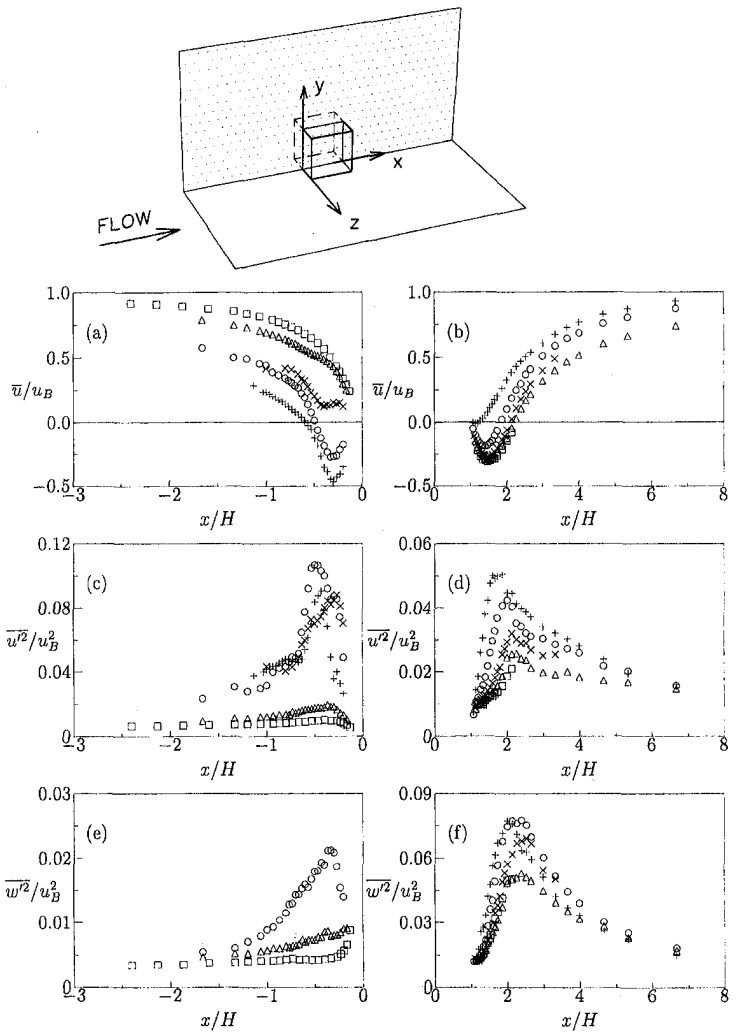

Fig. 5 Profiles of $\bar{u}$(*a*), $\overline{u'^2}$ (*c*), and $\overline{w'^2}$ (*e*) upstream of the obstacle along $z/H = 0$; (+) $y/H = 0.07$, (○) $y/H = 0.1$, (×) $y/H = 0.13$, (△) $y/H = 0.3$, and (□) $y/H = 0.5$ and profiles of $\bar{u}$ (*b*), u'^2 (*d*), and w'^2 (*f*) downstream of the obstacle along $z/H = 0$; (+) $y/H = 0.9$, (○) $y/H = 0.7$, (×) $y/H = 0.5$, (△) $y/H = 0.3$, and (□) $y/H = 0.1$

The reattachment point, obtained from an extrapolation of the separation line to the channel floor, is found at $x/H = 2.4$–2.5, which is in agreement with the oil graphite observations. As would be expected, the magnitude for $\overline{u'^2}$ and $\overline{w'^2}$ are high in the shear layer ($y/H = 0.7$ and 0.9). Downstream of the reattachment point ($x/H = 2.5$), the shear layer has broadened significantly due to diffusion and the turbulence level is decaying.

4.1.2 Vortex Shedding. The frequencies of the velocity fluctuations associated with the vortex shedding phenomenon were determined from the peaks in power density spectra of the spanwise velocity component. The spectra showed peaks centered around the predominant frequency indicating that the large-scale coherent structure contains a substantial amount of the turbulent kinetic energy, Fig. 6. The wake frequencies were measured for the Reynolds number range in which the convective heat transfer measurements were performed. These frequencies are expressed in terms of the dimensionless Strouhal number St ($St = fH/u_B$, where f is the frequency and u_B is the bulk velocity). The results are plotted versus the Reynolds number Re_H in Fig. 7 yielding an average value of $St = 0.095$. From the constant Strouhal numbers it can be concluded that the results are independent of the Reynolds number. This value differs significantly from the Strouhal number $St = 0.145$ found by Martinuzzi (1992) for the single cube in the fully developed channel flow at $Re_H = 40{,}000$, and a channel-height-to-cube-height ratio of 2. It is believed that these effects are caused by different levels of the freestream turbulence, which was much higher in the fully developed case. Another reason may be the difference in aspect ratios which impose different blockage effects.

4.2 Heat Transfer. Distributions of the local heat transfer coefficient are discussed for channel flow bulk velocities of 2.8, 3.2, 4.0, 4.5, and 5.0 m/s which correspond to Reynolds numbers $Re_H = 2750$, 3200, 4000, 4440, and 4970. As was demonstrated

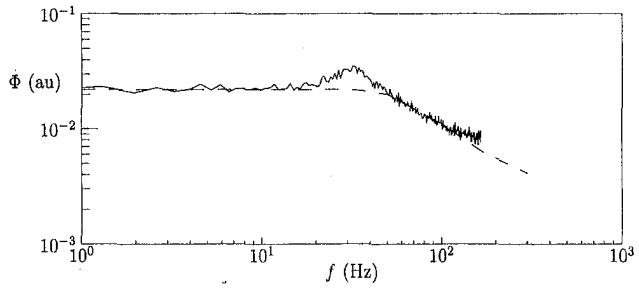

Fig. 6 Spectral power density function of the *w* velocity measured at the location $x/H = 2.7$, $y/H = 0.5$, and $z/H = 0.5$ ($Re_H = 5305$)

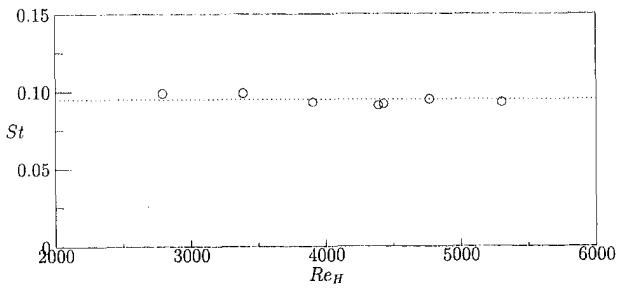

Fig. 7 Strouhal numbers (St = fH/u_B) as a function of the Reynolds number

from the LDA (vortex shedding measurements) and visualization experiments, the flow field is essentially independent of Re_H for this range of Reynolds numbers. The temperature of the internal copper core was adjusted to 75.0°C, which was regulated through a feedback loop to the supplied power. The inlet temperature of the air was kept at 21°C.

Verification of the accuracy of the IR thermography was made by comparing the surface temperature distributions with liquid crystal (LC) temperature measurements. In order to allow direct quantitative comparison, measurements were conducted for both thermographic techniques with identical experimental conditions (i.e., inlet temperature, power input, bulk airspeed). A mixture of five different LCs was used. The calibration of the LCs was based on the a priori known temperature field of the calibration set-up and incorporated the angle of view, the source of illumination, etc. It yielded five objectively determined isotherms, i.e., the sharp transitions between the green and red appearance at 47.6, 55.8, 60.6, 65.3, and 72.8°C. The spatial and temperature accuracy of the LC measurements are 0.5 mm and 0.4°C, respectively. Although restricted in spatial resolution, the LC measurements provide good absolute accuracy for validation of the infrared measurements. Results for two Reynolds numbers, Re_H = 3200 and 4440, are shown in Fig. 8 along path **ABCDA**, which is a plane parallel to the mounting base at $y/H = 0.5$, and path **ABCD** which denotes a plane perpendicular to the mounting base at $z/H = 0$. The LC measurements, only available at discrete locations at the cross sections of isotherms, are indicated with △ and □ for Re_H = 3200 and 4440, respectively. Profiles of the infrared temperature measurements are denoted by ○ and ×, for Re_H = 3200 and 4400. For both Reynolds numbers, the temperature measurements obtained with these techniques coincide within the experimental uncertainty of 0.4°C.

Surface temperature distributions on the five faces exposed to airflow are represented as isotherm maps in Fig. 9 (the five faces are folded out and mapped in one plane). The isotherm plots for the five Reynolds numbers studied are very similar. It is, therefore, reasonable to assume that the surface heat transfer and flow field are qualitatively similar throughout the Re_H-range studied, as was already suggested from oil-film visualizations and LDA measurements. Since the cubes are mounted vertically, it is important to note that the isotherm distributions are symmetric. These results indicate that buoyancy effects are negligible, which is to be expected since the ratio of the Grashof number to the square of the Reynolds number is significantly smaller than one.

4.2.1 Averaged Convective Heat Transfer. The cube-averaged heat transfer coefficient $\bar{h}$ is given on log-log scale in Fig. 10 as a function of Re_H. It is defined as the ratio of the cube-averaged convective heat flux and the difference between the cube-averaged surface temperature and the reference temperature. The cube-averaged heat flux and surface temperature were determined by integrating the measured distributions over the five exposed cube faces. The linear regression of the data points suggests a fit of the type $\bar{h} = A(Re_H)^B$ which is widely adopted for forced convective heat transfer problems. A and B denote constants. For the present study, the coefficient B had a value of 0.65 as compared to 0.626 from the naphthalene sublimation experiments of Chyu and Natarajan (1991) and Natarajan and Chyu (1994). Although the Reynolds number range considered in their study differed approximately one decade from the present Reynolds number range, the exponent is in good agreement. The face-averaged heat transfer coefficients are based on the face-integrated convective heat flux and the face-averaged surface temperature. The results, also given in Fig. 10 as a function of Re_H, are also linearly dependent on Re_H (when plotted in log-log coordinates). The high heat transfer coefficient at the front face is indicative for the impinging flow present at the front face. The low-temperature

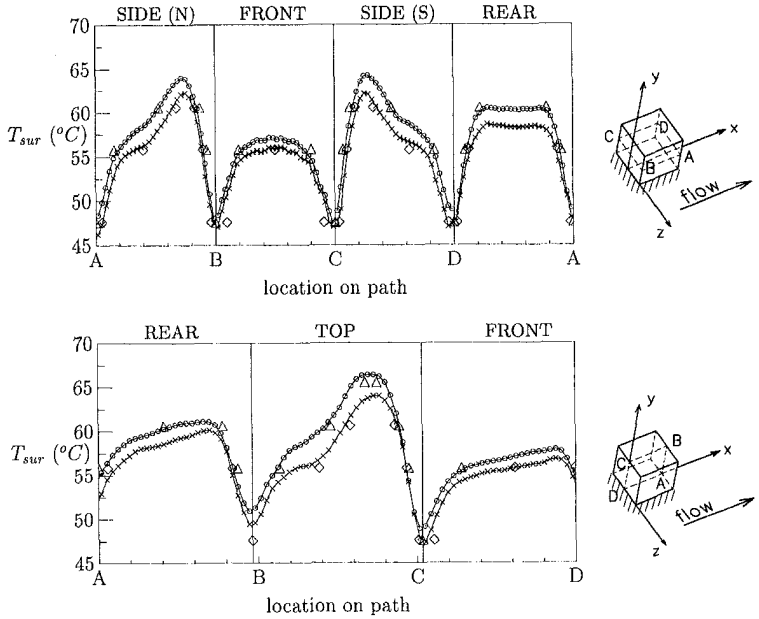

Fig. 8 Surface temperatures along path ABCDA (upper plot) and along path ABCD (lower plot) for Re_H = 3200 and Re_H = 4440, respectively; comparison between LC (△ and □) and infrared thermography (lines with ○ and ×)

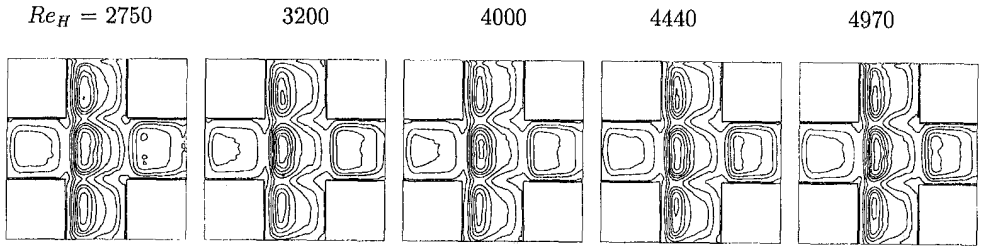

Fig. 9 Infrared surface temperature maps for Reynolds numbers Re_H = 2750, 3200, 4000, 4440, and 4970. Flow is from left to right.

oncoming flow causes high rates of convective heat transfer. The average heat transfer at the remaining faces is of comparable order of magnitude but markedly smaller (about 50 percent) than that at the front face. The enthalpy of the fluid entrained in the strong flow recirculation over these faces increases, resulting in a reduction of the convective heat transfer. The top face has the lowest averaged heat transfer coefficient. Besides the strong top vortex found at this face, it is assumed that a blockage effect is present. The channel roof imposes a significant constraint since the channel-width-to-cube-size ratio was 3.4. Although flow is trapped over the top face of the cube, the corresponding flow rate is somewhat smaller than that along the side faces. A further effect which intensifies the convective heat transfer at the sides is vortex shedding from the trailing side edges. Chyu and Natarajan (1991) and Natarajan and Chyu (1994) found exponents between $B = 0.538$ (front face) and $B = 0.666$ (side face) for the different faces of the cubical obstacle, which are in reasonably good agreement with the present results.

4.2.2 Distributions of the Local Convective Heat Transfer. Profiles of the surface temperature and the heat transfer coefficient are given in Figs. 11 and 12 along path **ABCDA** and path **ABCD**, respectively. The local heat transfer coefficients were made dimensionless with the cube-averaged heat transfer coefficient $\bar{h}$. The coinciding profiles again illustrate that similarity is verified and that the flow field determined for $Re_H = 4440$ applies for the whole range of Reynolds numbers considered for the heat transfer measurements. The temperature profiles are added to support the discussion on the marked variations in the local convective heat transfer.

Front face. From the flow study it was found that the oncoming flow impinges at the front face leading to a flow stagnation point at about $y/H \approx \frac{2}{3}$ along the symmetry line $z/H = 0$. Flow impingement generally causes a large and uniform convective heat transfer around the stagnation point, as is clearly seen in the profiles along path **ABCDA** and **ABCD**, section BC and CD, respectively. The small minimum in the heat transfer coefficient, found at the foot of the front face close to the mounting base (see Fig. 12) corresponds to the center of the horseshoe vortex while h slightly increases towards the channel floor, point D, which is in opposite direction to the local fluid velocity in the horseshoe vortex. The study of the flow field revealed that the Reynolds normal stresses (or turbulent kinetic energy) showed large peaks in the proximity of the horseshoe vortex. The peaks in the Reynolds normal stresses coincided with maximum turbulence production areas due to large velocity shear gradients. Furthermore, the unstable behavior of the horseshoe vortex contributed to the increased turbulence production. Since this region was identified as an area of minimum convective heat transfer, it is suggested that a dissimilarity existed between the heat and momentum transfer: Although the level of turbulence generally intensifies the heat transport leading to higher h values, this does not apply for the horseshoe vortex region. An explanation for this departure was sought in the local fluid temperature. The rotational behavior of the horseshoe vortex caused the residence time of the fluid in the vortex to be high, allowing the local fluid temperature to increase and, in turn, reducing the local convective heat transfer. Further, heat leakage via conduction from the cube through the mounting base might cause a slight increase in temperature of the base plate upstream of the cube. The rotating horseshoe vortex was, therefore, also heated by this secondary effect, although the effect was estimated to be smaller then five percent (estimated from a global energy balance). An opposite observation was made around the stagnation point. Although the heat transfer coefficients are high and rather uniform, the turbulent kinetic energy was moderate compared to that measured in the horseshoe vortex region. But for this area, the high-velocity and low-enthalpy impinging flow caused a beneficial convective cooling.

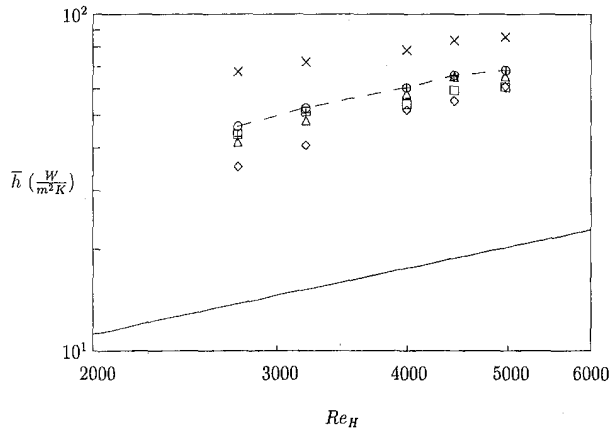

Fig. 10 Cube-averaged and face-averaged heat transfer coefficients as a function of the Reynolds number Re_H; (—○—) cube average, (+) side (N), (×) front, (△) side (S), (□) rear, and (◇) top. The solid line denotes the relation $\bar{h} = A(Re_H)^{0.65}$.

Similar observations were made by Chyu and Natarajan (1991) and Natarajan and Chyu (1994) for distributions of the mass transfer coefficient of a cube in a thin boundary layer flow at Reynolds numbers between 3.1×10^4 and 1.1×10^5. The horseshoe vortex region was also indicative for lower mass transfer coefficients while the remainder of the front face exhibited a nearly constant mass transfer rate.

Rear face. The convective heat transfer from the leeward face of the cube was almost uniform, except for the local maximum at the cube upper edge (see partition DA and AB in Fig. 11 and Fig. 12, respectively). The flow on this face was dominated by the arch-shaped vortex. Although the turbulence intensity was rather low in the core of the vortex (destabilization) the outer region of the vortex was rather turbulent because of the vortex shedding and turbulence production due to large average velocity gradients. Partially due to the mechanism of vortex shedding, the recirculation of fluid in the wake resulted in more efficient mixing which led to higher and more uniformly distributed local fluid temperatures. This in turn caused uniform distributions of the local heat transfer coefficients. The local maximum at the cube upper edge of the leeward face is explained by entrainment of cold air along the

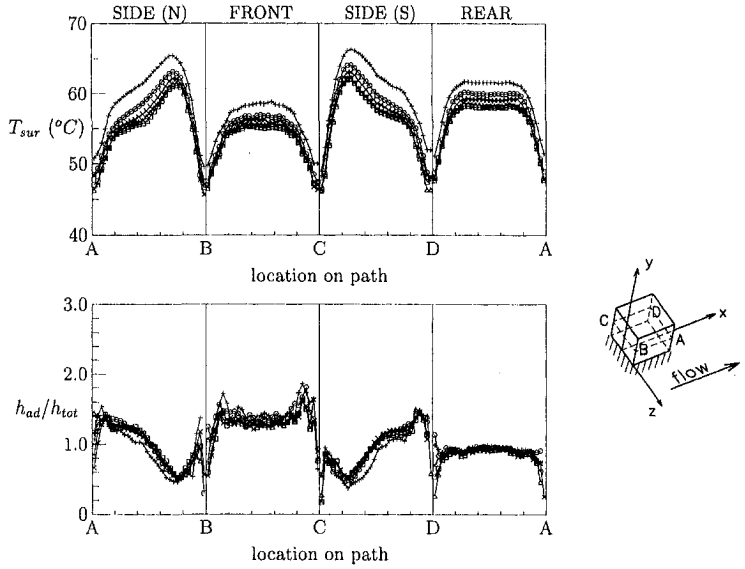

Fig. 11 Surface temperature and heat transfer coefficient distributions along path ABCDA parametric in Reynolds number; (+) Re_H = 2750, (○) Re_H = 3200, (×) Re_H = 4000, (△) Re_H = 4440, and (□) Re_H = 4970

shear layer over the top face. This locally benefited the convective heat transfer.

Chyu and Natarajan (1991) and Natarajan and Chyu (1994) reported different local mass transfer coefficients at the rear face of the cube. While in the present study the distributions of h were more or less uniform except in the vicinity of the upper top edge, where a local maximum and sharp minima at the edges were found, the mass transfer coefficient distributions showed uniform coefficients across the entire face with exception of a maximum towards the channel floor. They argued that close to the channel floor, high-rotational fluid from the horseshoe vortex is entrained into the wake region leading to a local maximum in the mass transfer. The shear layer reattachment, as found to be the primary mechanism at the side faces in the present study, caused the flow to be directed away from the side walls, and therefore, such a pronounced entrainment was not detected.

Side faces. The profiles of the heat transfer coefficients at the side faces are shown between AB and CD of path **ABCDA** in Fig. 11. A local minimum is found at the upstream part of the side face and a local maximum exists downstream, close to the trailing side edge. The variation in h along the face is up to 100 percent. The mean flow separated at the leading side edge and reattached downstream at the side face at approximately $x/H = 0.9$. However, the instantaneous behavior of the flow was strongly affected by vortex shedding, which resulted in intermittent quasi-periodic separation and reattachment along the sides. The side vortex, therefore, fluctuated somewhat around an equilibrium state. From the h-profiles in Fig. 11 it is seen that the location of minimum heat transfer coefficients corresponds to that of the vortex core. This center of the vortex is associated with a region of high-wall shear stress. According to Reynolds analogy, regions of high-wall shear stress should imply large heat transfer coefficients and this obser-

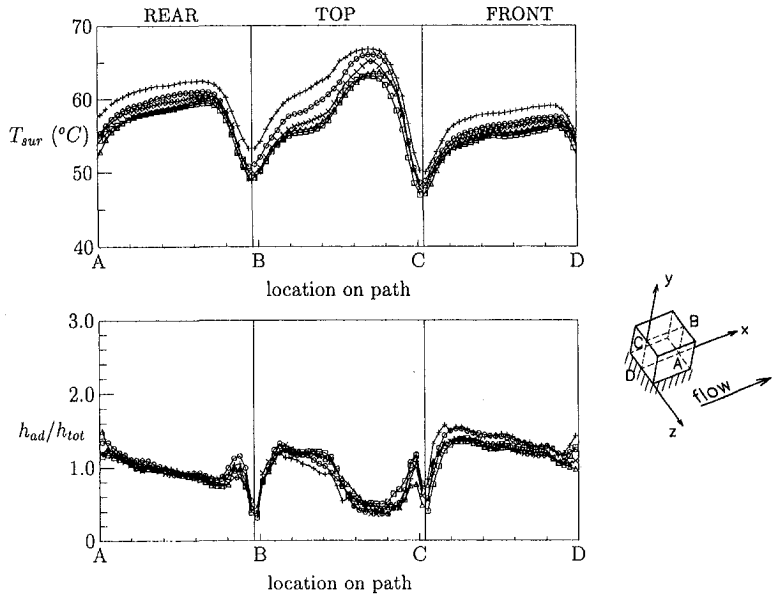

Fig. 12 Surface temperature and heat transfer coefficient distributions along path ABCD parametric in Reynolds number; (+) Re_H = 2750, (○) Re_H = 3200, (×) Re_H = 4000, (△) Re_H = 4440, and (□) Re_H = 4970

vation thus suggests that Reynolds' analogy fails locally. An explanation is again found in the local fluid temperature in the vortex. Heat is convected in the recirculation region, leading to an increased fluid temperature and, therefore, acting as a kind of insulation layer. This buffer prevents beneficial convective heat transfer. On the contrary, the intermittent flow reattachment convects relatively cold surrounding fluid to the surface together with strong velocity fluctuations normal to the wall. This mechanism causes the convective heat transfer intensification observed from the local maximum of the heat transfer coefficient in the proximity of the reattachment point ($x/H \approx 0.9$). The areas around flow reattachment are characterized by low-wall shear stresses, and contrary to Reynolds analogy, it is the large-velocity fluctuations normal to the wall as well as the low-enthalpy fluid which intensify the local removal of heat.

The mass transfer coefficients of Chyu and Natarajan (1991) and Natarajan and Chyu (1994) showed a slight increase in streamwise direction. This was caused by the flow recirculation which enveloped the entire side face. The oncoming flow conditions prevented the separated shear layers to reattach on the side faces. Therefore, the gradients remained moderate in contradiction to the present results which were primary dominated by the flow separation and subsequent reattachment.

Top face. Profiles of the heat transfer coefficients of the top face are shown in Fig. 12, between BC. These profiles show large spatial streamwise gradients: The heat transfer coefficients drop to a minimum and recover downstream to reach the plateau of maximum heat transfer coefficient. Similarly to the side faces, the vortex over the top face dictates the local heat transfer. It was concluded from LDA-measurements that no detectable vortex shedding occurred from the top trailing edge. Instabilities in the flow over the top face did not lead to vortex shedding since the necessary second shear layer was absent. Further, it is also believed that due to the vicinity of the opposing channel wall (roof) and the channel floor possible flow oscillations were suppressed. Despite that, the separated top shear layer reattached intermittently at approximately $x/H = 0.9$ at the top face. This caused local heat transfer intensification and led to the local maximum in the convective heat transfer towards the trailing edge. Again, a local heat transfer minimum is observed in an area of high-wall shear stress (on the wall directly below the bound vortex core) and a maximum in an area of low-wall shear stress (the reattachment region).

Chyu and Natarajan (1991) and Natarajan and Chyu (1994) observed monotonically increasing mass transfer coefficients in streamwise direction at the top face which they attributed to the recirculation of the top vortex enveloping the entire face. Again the significant differences in the local heat/mass transfer distributions are caused by the different oncoming conditions.

5 Conclusion

The experimental work presented in this paper was primarily focused on the local convective heat transfer from a single surface-mounted cube placed in a developing low Reynolds number turbulent channel flow. This flow displayed some noticeable differences as compared to the fully developed high Reynolds number channel flow, studied by Martinuzzi (1992). We found shear layer reattachment at the side and top faces of the cube while this was absent in the fully developed case. Further, the flow reattachment at the channel floor downstream of the cube occurred at a shorter distance than in the fully developed channel flow. The flow dynamics is also different as reflected in different vortex shedding frequencies. Although the present flow is qualitatively comparable to the fully developed channel flow, these noticeable differences in the flow have a significant effect on the local convective heat transfer from the cube.

At the windward face it was observed that the heat transfer coefficient is uniform about the stagnation point, as found commonly for impinging flows. A local heat transfer minimum was found close to the base corner corresponding to the position of the horseshoe vortex core. Although this location coincided with an area of high-wall shear stresses it was argued that the local increase in the fluid temperature prevented a beneficial removal of heat. Flow separation occurred at the leading side edges and flow instabilities caused significant vortex shedding behind these faces. The maximum of the heat transfer coefficient occurred in the proximity of the reattachment points, where the wall shear stress is small, but the velocity fluctuations normal to the wall are large. Minima in h were found below the recirculation vortex cores, where the wall shear stress approaches its maximum, but where the local fluid temperature is locally higher. The increased temperature of the flow recirculation acted as an insulation layer and prevented convective removal of heat. Similar features were found at the top face, although random flow instabilities (rather than vortex shedding) caused the maxima in the heat transfer coefficient close to the trailing edge. The arch vortex in the wake of the cube caused fairly uniform distributions of the local convective heat transfer.

The major findings are significant differences in the convective heat transfer (up to 100 percent) observed at the five faces of the cube. The differences were attributed to the structure of the turbulent velocity field around the cube. Strong local shear does not necessarily correspond to high surface heat transfer: The trapped fluid in a flow recirculation gains in temperature, decreasing thus far the local heat removal. Although marked differences were observed between the distributions of the mass transfer coefficient for a single cube in a boundary layer flow (Chyu and Natarajan, 1991; Natarajan and Chyu, 1994), the trends are similar.

Acknowledgment

This work, performed at the Faculty of Applied Physics of the Delft University of Technology, was financially supported by Philips, Nederlandse Philips Bedrijven B.V., The Netherlands. The technical support of Jaap Beekman and Bart Hoek is gratefully acknowledged.

References

Absil, L. H. J., 1996, "Analysis of the laser Doppler measurement technique for application in turbulent flows," Ph.D. thesis, Faculty of Aerospace Engineering, Delft University of Technology, Delft, The Netherlands.

Aliaga, D. A., Lamb, J. P., and Klein, D. E., 1994, "Convective heat transfer distributions over plates with square ribs from infrared thermography measurements," *Int. J. Heat Mass Transfer,* Vol. 37, No. 3, pp. 363–374.

Castro, I. P., and Robins, A. G., 1977, "The flow around a surface-mounted cube in uniform and turbulent streams," *J. Fluid Mech.,* Vol. 79, Part 2, pp. 307–335.

Chyu, M. K., and Natarajan, V., 1991, "Local Heat/Mass Transfer Distribution on the Surface of a Wall-Mounted Cube," ASME JOURNAL OF HEAT TRANSFER, Vol. 113, pp. 851–857.

Chyu, M. K., and Natarajan, V., 1996, "Heat transfer on the base surface of three-dimensional protruding elements," *Int. J. Heat Mass Transfer,* Vol. 39, No. 14, pp. 2925–2935.

Coles, D. E., 1962, "The turbulent boundary layer in a compressible fluid," Rand Report R-403-PR.

Durst, F., Melling, A., and Whitelaw, J. H., 1976, *Principles and Practice of Laser Doppler Anemometry,* Academic Press, New York.

Erm, L. P., Smits, A. J., and Joubert, P. N., 1978, "Low Reynolds number turbulent boundary layers on a smooth flat surface in a zero pressure gradient," *5th Symp. on Turbulent Shear Flows,* F. Durst et al., Springer-Verlag, New York, pp. 186–196.

Filetti, E. G., and Kays, W. M., 1967, "Heat Transfer in Separated, Reattached, and Redeveloped Regions Behind a Double Step at Entrance to a Flat Duct," ASME JOURNAL OF HEAT TRANSFER, pp. 163–168.

Hunt, J. C. R., Abell, C. J., Peterka, J. A., and Woo, H., 1978, "Kinematical studies of the flows around free or surface-mounted obstacles; applying topology to flow visualizations," *J. Fluid Mech.,* Vol. 86, Part 1, pp. 179–200.

Hussein, H. J., and Martinuzzi, R. J., 1996, "Energy balance for turbulent flow around a surface mounted cube placed in a channel," *Physics. Fluids,* Vol. 8, No. 3, pp. 764–780.

Igarashi, T., 1986, "Local heat transfer from a square prism to an air stream," *Int. J. Heat Mass Transfer,* Vol. 29, No. 5, pp. 777–784.

Igarashi, T., and Yamasaki, H., 1991, "Fluid flow and heat transfer of a two-dimensional rectangular block in the turbulent boundary layer on a plate," *Proceedings of the ASME/JSME Thermal Engineering Joint Conference,* ASME, New York, pp. 341–347.

Larousse, A., Martinuzzi, R., and Tropea, C., 1991, "Flow around surface-mounted, three-dimensional obstacles," *Selected papers of the 8th Symp. on Turbulent Shear Flows,* Springer Verlag, New York, pp. 127–139.

Lorenz, S., Mukomilow, D., and Leiner, W., 1995, "Distribution of the heat transfer coefficient in a channel with periodic transverse grooves," *Experimental Thermal and Fluid Science,* Vol. 11, pp. 234–242.

Martinuzzi, R. J., 1992, "Experimentelle Untersuchung der Umstroming wandgebundener, rechteckiger, prismatischer Hindernisse," Ph.D. thesis, Erlangen, Germany.

Martinuzzi, R. J., and Tropea, C., 1993, "The Flow Around Surface Mounted, Prismatic Obstacles Placed in a Fully Developed Channel Flow," ASME *Journal of Fluids Engineering,* Vol. 115, pp. 85–92.

Meinders, E. R., 1998, "Experimental study of heat transfer in turbulent flows over wall-mounted cubes," Ph.D. thesis, Faculty of Applied Physics, Delft University of Technology, Delft, The Netherlands.

Meinders, E. R., Meer, T. H. van der Hanjalić, K., and Lasance, C. J. M., 1997, "Application of infrared thermography to the evaluation of local convective heat transfer on arrays of cubical protrusions," *Int. J. of Heat and Fluid Flow,* Vol. 18, No. 1, pp. 152–159.

Meinders, E. R., van Kempen, G. M. P., van Vliet, L. J., and van der Meer, T. H., 1999, "Measurement and application of an infrared image restoration filter to improve the accuracy of surface temperature measurements of cubes," *Experiments in Fluids,* Vol. 26, No. 1–2, pp. 86–96.

Moffat, R. J., 1988, "Describing the uncertainties in experimental results," *Experimental Thermal and Fluid Science,* Vol. 1, No. 1, pp. 3–17.

Moffat, R. J., and Anderson, A. M., 1990, "Applying Heat Transfer Coefficient Data to Electronics Cooling," ASME JOURNAL OF HEAT TRANSFER, Vol. 112, pp. 882–890.

Morris, G. K., and Garimella, S. V., 1996, "Thermal wake downstream of a three-dimensional obstacle," *Experimental Thermal and Fluid Science,* Vol. 12, pp. 65–74.

Nakayama, W., and Park, S.-H., 1996, "Conjugate heat transfer from a single surface-mounted block to forced convective air flow in a channel," ASME JOURNAL OF HEAT TRANSFER, Vol. 118, pp. 301–309.

Natarajan, V., and Chyu, M. K., 1994, Effect of Flow Angle of Attack on the Local Heat/Mass Transfer From a Wall-Mounted Cube, ASME JOURNAL OF HEAT TRANSFER, Vol. 116, pp. 552–560.

Olsen, J., Webb, B. W., and Queiroz, M., 1989, "Local three-dimensional heat transfer heat transfer from a heated cube," Proceedings, *ASME Winter Annual Meeting,* San Francisco, ASME, New York.

Ota, T., and Kon, N., 1974, "Heat Transfer in the Separated and Reattached Flow on a Blunt Flat Plate," ASME JOURNAL OF HEAT TRANSFER, Vol. 96, pp. 459–462.

Roeller, P. T., Stevens, J., and Webb, B. W., 1991, "Heat Transfer and Turbulent Flow Characteristics of Isolated Three-Dimensional Protrusions in Channels," ASME JOURNAL OF HEAT TRANSFER, Vol. 113, pp. 597–603.

Schofield, W. H., and Logan, E., 1990, "Turbulent shear flow over surface mounted obstacles," ASME *Journal of Fluids Engineering,* Vol. 113, p. 405.

Seban, R. A., 1964, "Heat Transfer to the Turbulent Separated Flow of Air Downstream of a Step in the Surface of a Plate," ASME JOURNAL OF HEAT TRANSFER, Vol. 86, pp. 259–264.

Transition of Chaotic Flow in a Radially Heated Taylor-Couette System

R. Kedia[1]
e-mail: rajesh@rrt.arco.com

M. L. Hunt
e-mail: hunt@caltech.edu
Mem. ASME

T. Colonius
e-mail: colonius@caltech.edu

Division of Engineering and Applied Science,
California Institute of Technology,
Pasadena, CA 91125

Numerical simulations have been performed to study the stability of heated, incompressible Taylor-Couette flow for a radius ratio of 0.7 and a Prandtl number of 0.7. As Gr is increased, the Taylor cell that has the same direction of circulation as the natural convection current increases in size and the counterrotating cell becomes smaller. The flow remains axisymmetric and the average heat transfer decreases with the increase in Gr. When the cylinder is impulsively heated, the counterrotating cell vanishes and n = 1 spiral is formed for Gr = 1000. This transition marks an increase in the heat transfer due to an increase in the radial velocity component of the fluid. By slowly varying the Grashof number, the simulations demonstrate the existence of a hysteresis loop. Two different stable states with same heat transfer are found to exist at the same Grashof number. A time-delay analysis of the radial velocity and the local heat transfer coefficient time is performed to determine the dimension at two Grashof numbers. For a fixed Reynolds number of 100, the two-dimensional projection of the reconstructed attractor shows a limit cycle for Gr = −1700. The limit cycle behavior disappears at Gr = −2100, and the reconstructed attractor becomes irregular. The attractor dimension increases to about 3.2 from a value of 1 for the limit cycle case; similar values were determined for both the local heat transfer and the local radial velocity, indicating that the dynamics of the temperature variations can be inferred from that of the velocity variations.

Introduction

Taylor-Couette flow (Taylor, 1923) is an interesting nonlinear, dissipative dynamical system. The inner rotating cylinder provides a driving force, and as its rotation rate is increased, a series of transitions and bifurcations occur, starting with stable Taylor vortices, and leading to fully developed turbulent flow. These transitions have been widely explored (e.g., the review by Koschmieder, 1993) as a function of Reynolds number. However, buoyancy effects caused by the imposition of a radial temperature gradient cause important changes to the transitions (Kedia et al., 1998). These are important to a number of practical devices such as high-speed pumps (Narabayashi et al., 1993).

It is useful to review the transitions for an unheated flow, such as found in the experiments of Brandstater and Swinney (1987). They considered Taylor-Couette flow with a radius ratio of 0.875 and an aspect ratio of 20. On starting the rotation of the inner cylinder, the first flow encountered is circular steady Couette flow. The only nonzero velocity is the azimuthal velocity, which has a radial dependence. Upon increasing the Reynolds number ($R = \omega r_i b/\nu$), the next transition is to Taylor vortex flow (TVF) at a critical Reynolds number ($R_c = 118.4$). The TVF arises from a symmetrical supercritical steady bifurcation of the base flow. The flow remains time independent but with a periodic disturbance in the axial direction. Upon further increasing the Reynolds number, another transition is made to Wavy vortex flow (WVF) at approximately $R/R_c = 1.3$. The WVF is a time-periodic supercritical bifurcation (a Hopf bifurcation) of the TVF characterized by unsteady travelling waves. This is a first time-dependent solution with breaking of the azimuthal symmetry. Since the trajectory is a limit cycle in phase space, the corresponding attractor dimension (the dimension is roughly the number of independent variables needed to model the underlying phenomenon in a dynamical system) is 1. A power spectrum would show a fundamental frequency corresponding to the azimuthal wave number and its harmonics. As the Reynolds number is increased further, modulated wavy vortex flow (MWVF) is formed at $R/R_c = 10$. This is doubly periodic with an attractor dimension of 2; hence, there are two incommensurate frequencies, and the phase space portrait is a torus. At higher Reynolds number ($R/R_c = 11.7$), the flow becomes chaotic or "weakly turbulent." Brandstater and Swinney calculated the fractal dimension as 2.4 for $R/R_c = 12.4$. Thereafter, with a continuous increase of Reynolds number, the flow becomes "fully turbulent" and the fractal dimension continues to increase monotonically.

The present work explores the effect of a radial temperature gradient quantified by the Grashof number ($Gr = g\beta(T_1 - T_2)b^3/\nu^2$) and the acceleration ratio ($A = \omega^2 r_i/g$). An earlier study by Kedia, Hunt, and Colonius (1998) presented local and average heat transfer coefficients for a fixed Reynolds number ($R = 100$) and for a range of Grashof numbers. The study also discussed previous investigations of heated Taylor-Couette flows. Based on the heat transfer results, the flow was found to undergo a series of transitions that depend on the direction and magnitude of the imposed temperature gradient. The current work presents more detailed results on the evolution of the flow structures as the Grashof number increases, and indicates the coupling between the variations in the heat transfer rates and the changes in the size and shape of the Taylor vortices. The relation between the average wall shear stress and mean equivalent conductivity are presented in terms of the Colburn analogy. The mean equivalent conductivity, K_{eq}, is defined as the ratio of the average convective heat transfer coefficient ($h_{\bar{\theta},\bar{z},\bar{t}}$) to the heat transfer coefficient for pure conduction. In addition, local measurements of the radial velocity component and the heat transfer coefficient are used to characterize the flow in terms of the attractor dimension at two different Grashof numbers.

[1] Presently at ARCO Exploration and Production Technology, Plano, TX 75075.

Contributed by the Heat Transfer Division for publication in the JOURNAL OF HEAT TRANSFER and presented at '98 IMECE, Anaheim. Manuscript received by the Heat Transfer Division, July 7, 1998; revision received, Mar. 26, 1999. Keywords: Annular Flow, Computational, Heat Transfer, Instability, Mixed Convection. Associate Technical Editor: D. Zumbrunnen.

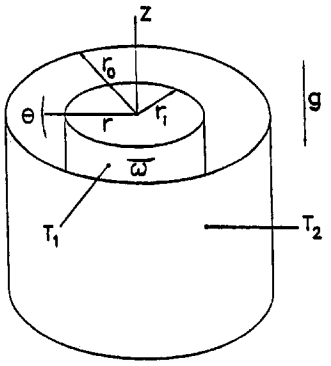

Fig. 1 Flow geometry

Numerical Method

A sketch of the flow configuration in (r, θ, z) cylindrical coordinates is shown in Fig. 1. The radii of the inner and the outer cylinders are r_i and r_o, respectively, and the radius ratio is η. The inner cylinder rotates with a constant angular velocity ω about the vertical z-axis while the outer cylinder is stationary. The two cylinders are at different uniform temperatures. The temperature of the inner cylinder is T_1 and that of the outer one is T_2. Gravity acts in the negative z-direction. The centrifugal force is parallel to the mean temperature gradient. The temperature difference can be assumed to be sufficiently small such that the density is treated as a constant everywhere in the Navier-Stokes equations with the exception of the gravitational (z-momentum equation) and the centrifugal (r-momentum equation) terms. All other fluid properties are assumed to be independent of temperature. The flow is axially periodic (i.e., infinite aspect ratio) and no slip boundary conditions are used at the inner and the outer cylinders. Without heating, the Taylor cells are of uniform size. The axial distance between a pair of Taylor cells is defined as axial wavelength (λ) and b is the gap width. The axial wavelength is normalized by the gap width to define L_z.

The study by Kedia, Hunt and Colonius (1998) outlines the solution to the three-dimensional incompressible equations of motion with the energy equation using a Chebyshev/Fourier spectral method. Viscous terms are integrated implicitly with a Crank-Nicholson scheme, while the convective terms are integrated explicitly with an Adams-Bashforth scheme. The results are calculated on a 32^3 mesh and dealiased with the $\frac{3}{2}$ rule. To verify the adequacy of the 32^3 simulations, a series of higher resolution simulations (64^3) with a smaller time step were also performed. The three components of velocity and the temperature were monitored at the same physical location as for the coarser resolution. The two gave an identical time trace which proved the sufficiency of the coarser simulation. The real time requirement is 13.5 s per time step on a SGI Onyx (IP21 processor) for a typical 32^3 simulation.

The nondimensional equations and boundary conditions are given below, and follow from the earlier study by Kedia et al. (1998).

Continuity:

$$\frac{\partial u_r}{\partial r} + \frac{u_r}{r} + \frac{1}{r}\frac{\partial u_\theta}{\partial \theta} + \frac{\partial u_z}{\partial z} = 0. \tag{1}$$

Momentum:

$$\frac{\partial u_r}{\partial t} + \frac{u_\theta}{r}\frac{\partial u_r}{\partial \theta} + u_z\frac{\partial u_r}{\partial z} - u_z\frac{\partial u_z}{\partial r} - u_\theta\frac{\partial u_\theta}{\partial r} - (1 - \beta^*(T - \overline{T_o}))\frac{u_\theta^2}{r} = -\frac{\partial P}{\partial r} + \frac{1}{R}\left(\frac{1}{r^2}\frac{\partial^2 u_r}{\partial \theta^2} - \frac{1}{r^2}\frac{\partial u_\theta}{\partial \theta} - \frac{1}{r}\frac{\partial^2 u_\theta}{\partial \theta \partial r} + \frac{\partial^2 u_r}{\partial z^2} - \frac{\partial^2 u_z}{\partial r \partial z}\right) \tag{2}$$

Nomenclature

A = acceleration ratio, $\omega^2 r_i/g$
b = gap width, $(r_o - r_i)$
C_f = friction factor, $\tau_w|_{\bar{\theta},\bar{z},\bar{t}}/\frac{1}{2}\rho(\omega r_i)^2$
C_p = heat capacity at constant pressure
D_1 = pointwise dimension
D_2 = correlation dimension
f = frequency of heat transfer coefficient fluctuation
f_c = inner cylinder frequency
f_{sp} = normalized fundamental frequency for $n = 2$ spiral flow
Gr = Grashof number, $g\beta(T_1 - T_2)b^3/\nu^2$
g = acceleration due to gravity
h = local heat transfer coefficient, $q/(T_b - T_2)$
$h_{\bar{\theta},\bar{z},\bar{t}}$ = spatially and temporally averaged heat transfer coefficient
$I(\tau)$ = mutual information function
j_H = Colburn factor
K_{eq} = mean equivalent conductivity, $r_i \ln(1/\eta)h_{\bar{\theta},\bar{z},\bar{t}}/k$
k = thermal conductivity of the fluid,
L_z = normalized axial wavelength, λ/b
m = embedding dimension
$N(\epsilon)$ = number of points in a hypersphere of radius ϵ
n = number of starts, $2\pi r_o \tan \Psi/L_z$
P = nondimensional dynamic pressure, nondimensionalized by $\omega^2 r_i^2$
Pr = Prandtl number, ν/α
$P(X)$, $P(Y)$ = probability density
$P(X, Y)$ = joint probability density
q = heat flux on the outer cylinder
R = Reynolds number, $\omega r_i b/\nu$
R_c = critical Reynolds number for the onset of Taylor vortex flow
r, θ, z = cylindrical coordinates
r_i = inner cylinder radius
r_o = outer cylinder radius
St = Stanton number, $h_{\bar{\theta},\bar{z},\bar{t}}/\rho(\omega r_i)C_p$
T = nondimensional temperature, nondimensionalized by $T_1 - T_2$ after subtracting T_2
T_1 = inner cylinder temperature
T_2 = outer cylinder temperature
$\overline{T_b}$ = bulk temperature
$\overline{T_o}$ = dimensionless reference temperature
t = time
u_r, u_θ, u_z = nondimensional velocity component in cylindrical coordinate system, nondimensionalized by ωr_i
$v(t)$ = time series
ω = inner cylinder angular velocity
ρ = density of the fluid
ν = kinematic viscosity of the fluid
α = thermal diffusivity of the fluid
β = thermal expansion coefficient of the fluid
β^* = $\beta(T_1 - T_2)$
μ = dynamic viscosity of the fluid
λ = wavelength of a pair of vortices
η = radius ratio, r_i/r_o
τ = delay time
$\tau_w|_{\bar{\theta},\bar{z},\bar{t}}$ = spatially and temporally averaged wall shear stress
Ψ = the angle of inclination of the cell from the horizontal

$$\frac{\partial u_\theta}{\partial t} + \frac{u_r u_\theta}{r} + u_r \frac{\partial u_\theta}{\partial r} - \frac{u_r}{r}\frac{\partial u_r}{\partial \theta} - \frac{u_z}{r}\frac{\partial u_z}{\partial \theta} + u_z \frac{\partial u_\theta}{\partial z}$$
$$= -\frac{1}{r}\frac{\partial P}{\partial \theta} + \frac{1}{R}\left(\frac{1}{r}\frac{\partial u_\theta}{\partial r} - \frac{u_\theta}{r^2} + \frac{\partial^2 u_\theta}{\partial r^2} + \frac{1}{r^2}\frac{\partial u_r}{\partial \theta} - \frac{1}{r}\frac{\partial^2 u_r}{\partial r \partial \theta} - \frac{1}{r}\frac{\partial^2 u_z}{\partial z \partial \theta} + \frac{\partial^2 u_\theta}{\partial z^2}\right) \quad (3)$$

$$\frac{\partial u_z}{\partial t} - u_r \frac{\partial u_r}{\partial z} + u_r \frac{\partial u_z}{\partial r} + \frac{u_\theta}{r}\frac{\partial u_z}{\partial \theta} - u_\theta \frac{\partial u_\theta}{\partial z} = -\frac{\partial P}{\partial z}$$
$$+ \frac{1}{R}\left(\frac{1}{r}\frac{\partial u_z}{\partial r} - \frac{1}{r}\frac{\partial u_r}{\partial z} - \frac{\partial^2 u_r}{\partial r \partial z} + \frac{\partial^2 u_z}{\partial r^2} + \frac{1}{r^2}\frac{\partial^2 u_z}{\partial \theta^2} - \frac{1}{r}\frac{\partial^2 u_\theta}{\partial z \partial \theta}\right)$$
$$+ \frac{\mathrm{Gr}}{\mathrm{Re}^2}(T - \overline{T_o}) \quad (4)$$

with $(u_r, u_\theta, u_z) = (0, 1, 0)$ at the nondimensional inner radius, $\eta/(1-\eta)$ and $(u_r, u_\theta, u_z) = (0, 0, 0)$ at the nondimensional outer radius, $1/(1-\eta)$.

Energy:

$$\frac{\partial T}{\partial t} + u_r \frac{\partial T}{\partial r} + \frac{u_\theta}{r}\frac{\partial T}{\partial \theta} + u_z \frac{\partial T}{\partial z}$$
$$= \frac{1}{\mathrm{PrR}}\left(\frac{1}{r}\frac{\partial T}{\partial r} + \frac{\partial^2 T}{\partial r^2} + \frac{1}{r^2}\frac{\partial^2 T}{\partial \theta^2} + \frac{\partial^2 T}{\partial z^2}\right) \quad (5)$$

with $T = 1$ at the nondimensional inner radius, $\eta/(1-\eta)$ and $T = 0$ at the nondimensional outer radius, $1/(1-\eta)$.

The code was validated by comparing the critical Reynolds number and the corresponding wave speeds with a linear stability analysis that included the effects of radial heating on the centrifugal and gravitational potentials (Chen and Kuo, 1990). In addition, the simulations were also compared with the results of Kataoka et al. (1977) for the local mass transfer coefficient in the limit of small Grashof number, and with the average heat transfer coefficients from the experiments of Ball et al. (1989) for a range of Grashof numbers. Further validations can also be found in Kedia (1997).

It is well known that the axial wavelength depends on Gr. At the outset, it was unclear whether the flow states ($n = 1$ spiral, $n = 2$ spiral, or aperiodic) would be sensitive to the imposed axial wavelength, L_z. However, the numerical experiments showed that the flow states were invariant as L_z was varied by as much as 30 percent. As L_z was varied, the size of the cells were proportionally increased. In the absence of any published results on the exact axial wavelength for nonzero Grashof number and the robustness of the flow states with regard to L_z, the wavelength for heated flow was chosen as the wavelength at zero Grashof number (widely available from both linear stability analysis and experimental results).

Results

Flow Transitions and Hysteresis. The variation of the size of the Taylor cells (for a fixed axial wavelength) with the increase in the value of Gr is shown in Fig. 2. The axial velocity contours (there are two circular contours in the radial direction which corresponds to one Taylor cell) are plotted in the r-z plane for $\eta = 0.7$, $L_z = 2.001$, $A = 0.67$, R = 100 and Pr = 0.7. Note that the critical Reynolds number for the onset of isothermal Taylor cells for a radius ratio of 0.7 is 79.49. The figure illustrates two important phenomena. The first is the change in the size of Taylor cells and the second is the formation of $n = 1$ spiral flow. The spirals move an axial distance of nL_z for one rotation around the inner cylinder (Kedia et al., 1998). For Gr = 0, there is no effect of natural convection, and both the Taylor cells are of equal size. As

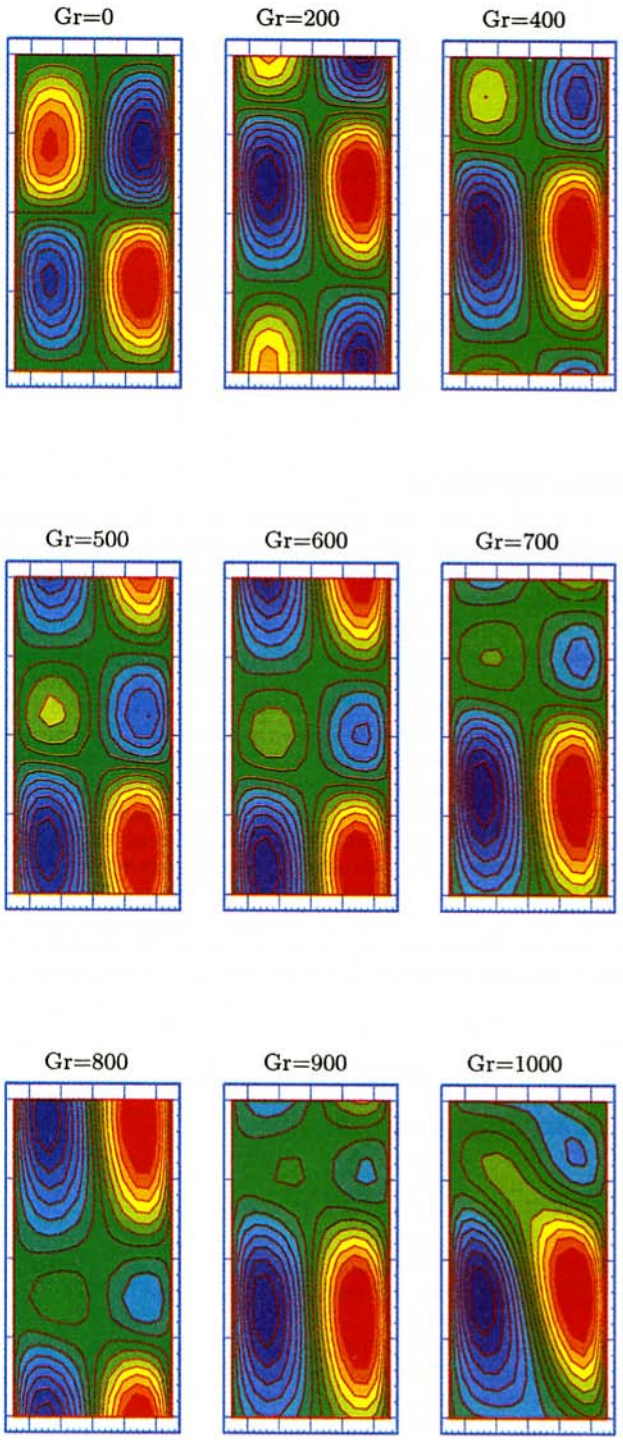

Fig. 2 Change in the size of Taylor vortices with Grashof number for η = 0.7, L_z = 2.001, A = 0.67, R = 100, and Pr = 0.7

Gr is increased, a natural convection current is set up. For a positive Gr, the direction of the convection current is upwards near the inner cylinder and downwards near the outer cylinder. As a result of this, the Taylor cell that has the same direction of circulation as the natural convection current increases in size. The counterrotating cell, on the other hand, decreases in size. The counterrotating cell becomes very small for Gr = 900, but the flow remains axisymmetric. As Gr is increased to 1000, the cell cannot become any smaller and $n = 1$ spiral flow is formed. The spiral flow is a Hopf bifurcation of the axisymmetric Taylor vortex flow which occurs between the Grashof numbers of 900 and 1000. Also

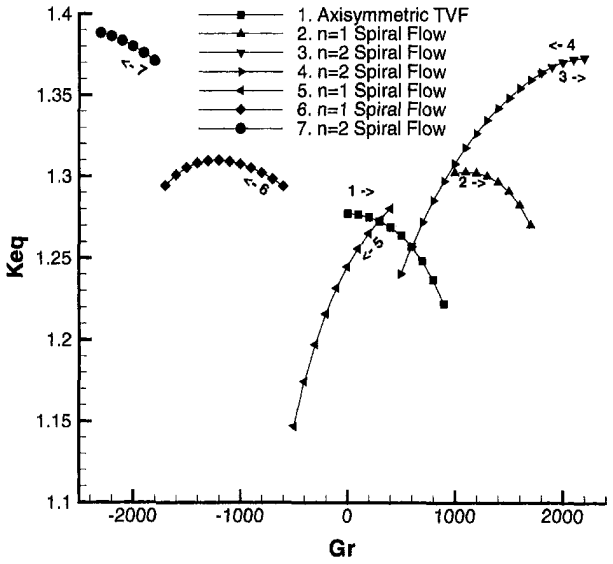

Fig. 3 Map showing different stable states present in the flow by slowly varying the Grashof numer for $\eta = 0.7$, $L_z = 2.001$, $A = 0.67$, R = 100, and Pr = 0.7

the Taylor cells are convected in the axial direction, with the direction depending on the direction of the radial heating. As Gr is increased to 1300, the flow becomes aperiodic. For negative Gr (heating of the outer cylinder), Kedia et al. (1998) showed that the flow became aperiodic at higher absolute values of Gr. For $\eta = 0.7$, the flow transitioned from axisymmetric to $n = 1$ spiral at Gr $= -900$, and then transitioned to $n = 2$ spiral at -1500. The flow became aperiodic at Gr $= -2100$. Onset of spiral ($n = 1$ and $n = 2$) flows have also been observed by Kuo and Ball (1997) in certain Gr and R parameter space.

The results shown in Fig. 2 were calculated for conditions that would correspond with an impulsive heating and simultaneous acceleration of the cylinder. However, as shown by experimental data, different stable states can be reached by varying the initial conditions of the flow. For example, Coles (1965) observed as many as 25 different stable states at a given cylinder speed for isothermal Taylor-Couette flow. The speed was reached by varying the acceleration rates of the rotating cylinder. The final state in Taylor-Couette flow is thus widely believed to be dependent on its previous history. Figure 3 shows the value of the mean equivalent conductivity and different stable states present in the flow as Gr is slowly varied. The case is for $\eta = 0.7$, $L_z = 2.001$, $A = 0.67$, Pr = 0.7, and a fixed Reynolds number (R = 100). A random disturbance of magnitude one percent of the velocity of the inner cylinder was introduced to the laminar state (circular Couette flow) and allowed to grow into Taylor vortices. The Reynolds number was slowly increased (in steps of 5) to achieve the desired Reynolds number. The result with the lower Reynolds number was used as initial condition for the next higher Reynolds number. Once the desired Reynolds number was reached, another random disturbance of magnitude one percent of the temperature difference between the two cylinders was imposed on the temperature initial condition in order to trigger transitions. Grashof number was then varied in steps of 100 to achieve the next desired Gr with the previous result used as initial condition. The different states are marked from 1 to 7 in the symbol table in the order in which Gr is slowly increased and then decreased at a constant rotation of the cylinder. As Gr is slowly increased from 0 to 900, axisymmetric TVF is formed. From Gr = 1000 to 1700, $n = 1$ spiral flow is formed; $n = 2$ spiral flow is formed from Gr = 1800 to 2200. As Gr is decreased from 2200, $n = 2$ spiral flow exists until Gr = 500. There exist two different stable states (axisymmetric TVF and $n = 2$ spiral flow) for Gr = 600, but with the same heat transfer coefficient. Axisymmetric TVF is achieved by slowly increasing Gr; then $n = 2$ spiral flow is achieved by slowly decreasing Gr. For Gr = 400 to -1700, $n = 1$ spiral flow is formed. With a further decrease in Gr, $n = 2$ spiral flow is formed for Gr = -1800 to -2300. The figure shows the property of nonuniqueness by the existence of a hysteresis loop.

Heat Transfer and Colburn's Analogy. Figure 3 shows the mean equivalent conductivity, $K_{eq} = r_i \ln (1/\eta) h_{\bar{\theta},\bar{z},\bar{t}}/k$, as a function of Grashof number for the Grashof numbers steadily increased and then decreased. As shown in the figure, there is a seven percent increase in the average heat transfer coefficient as the flow transitions from an axisymmetric flow to $n = 1$ spiral, and an additional eight percent increase in transitioning from a $n = 1$ to a $n = 2$ spiral. These increases coincide with an increase in the radial velocity component. In the study by Kedia et al. (1998) in which the cylinders were impulsively heated, the flow was aperiodic beyond Gr = 1300, and the equivalent conductivity was lower, with a value of approximately 1.24. The previous study also showed that the heat transfer was sensitive to the imposed axial wavelength (K_{eq} decreased by 6 percent for a 30 percent increase in L_z). Similar variations in the equivalent conductivity occur as the Grashof number is decreased and the flow changes state.

Often it is of interest to compare the variations in the wall shear stress and the effective transport properties for a scalar, as done in the work by Lathrop et al. (1992), for turbulent Taylor-Couette flow. Hence, the results for the average wall shear stress and heat transfer coefficient are presented in terms of the Colburn analogy:

$$\mathrm{St} \cdot j_H(\mathrm{Pr}, \mathrm{Gr}, A, \mathrm{R}, \eta) = C_f/2 \tag{6}$$

where St is the Stanton number, C_f is the friction factor, and j_H is the Colburn factor, which may be a function of Pr, Gr, A, R, and η. For planar Couette flow, $j_H(\mathrm{Pr}) = \mathrm{Pr}$, but it is usually equal to $\mathrm{Pr}^{2/3}$ for turbulent boundary layers. For circular Couette flow, there is an additional geometric dependence on η. However, as η approaches 1, $j_H(\mathrm{Pr}, \mathrm{R}) = \mathrm{Pr}$. For planar Couette flow and boundary layers, there is no dependence on Reynolds numbers. This invariance with Reynolds numbers was also found for the turbulent Couette flow study by Lathrop et al. (1992).

Figure 4 shows the variation of j_H with R for $\eta = 0.7$, $L_z = 2.001$, Pr = 0.7, and Gr = 0. The geometric factor has been incorporated into j_H such that for $\eta = 0.7$, $j_H = \mathrm{Pr}$ for circular Couette flow. The dots are the simulation results. For R = 60 and 70 (circular Couette flow), which are below the critical Reynolds number, $j_H = \mathrm{Pr}$. As the Reynolds number is increased, j_H

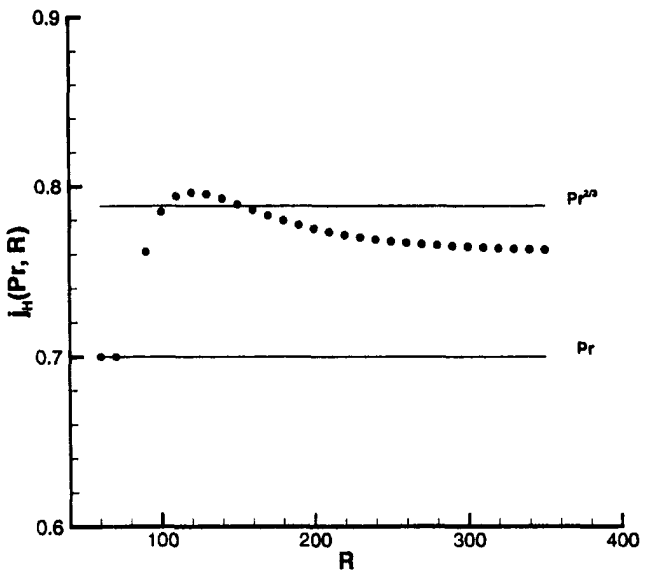

Fig. 4 Variation of j_H(Pr, R) with Reynolds number for $\eta = 0.7$, $L_z = 2.001$, Pr = 0.7, and Gr = 0

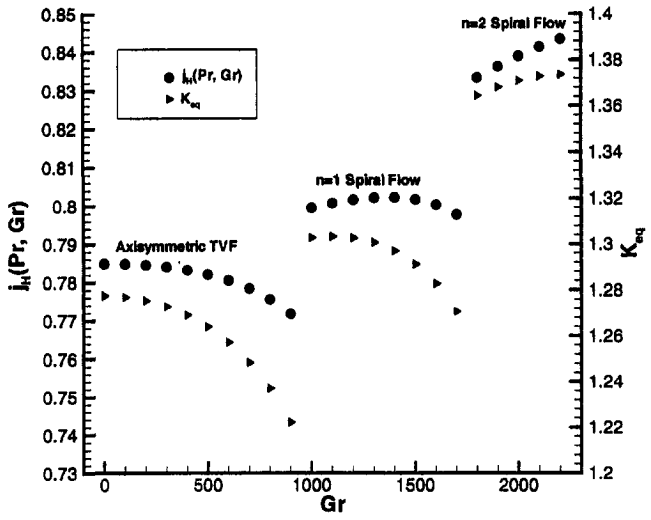

Fig. 5 Variation of j_H(Pr, Gr) and K_{eq} with Grashof number for η = 0.7, L_z = 2.001, A = 0.67, Pr = 0.7, and R = 100

increases and reaches a maximum just above $Pr^{2/3}$ and finally becomes constant at $0.76 = Pr^{0.77}$. Hence, just beyond the critical Reynolds number, the Colburn factor does depend on the Reynolds number, but the dependence decreases for higher Reynolds numbers. Figure 5 shows a similar correlation for $\eta = 0.7$, $L_z = 2.001$, $A = 0.67$, Pr = 0.7, and R = 100. Here j_H(Pr, Gr) is plotted with Gr for a fixed Reynolds number (R = 100). At the Grashof numbers corresponding to changes from axisymmetric to $n = 1$ spiral flow, and from $n = 1$ spiral to $n = 2$ spiral, both the friction factor and the equivalent conductivity exhibit similar increases in value.

Time-Delay Analysis. To characterize the flow as the Grashof number is changed, an analysis of the temporal variations of radial velocity and heat transfer coefficient is performed. The radial velocity halfway between the inner and the outer cylinders at the mid-axial position is recorded at every time step. Figure 6 shows the fluctuating component of the radial velocity (the mean velocity has been subtracted) for $\eta = 0.7$, $L_z = 2.001$, R = 100, Pr = 0.7, and Gr = −1700. The time is nondimensionalized using the time period of the inner rotating cylinder. The flow is in the $n = 2$ spiral flow regime. The time trace looks regular and periodic. Shown in Fig. 7 is a similar velocity trace for Gr = −2100. The time trace has become irregular and the flow is in the aperiodic regime. Both

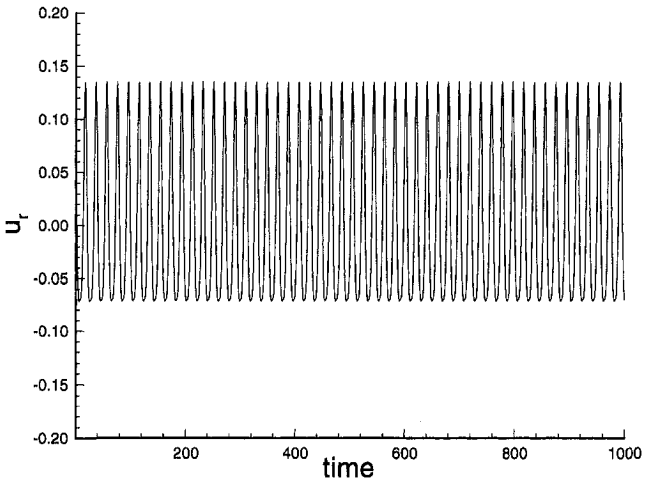

Fig. 6 Radial velocity signal for η = 0.7, L_z = 2.001, R = 100, Pr = 0.7, and Gr = −1700

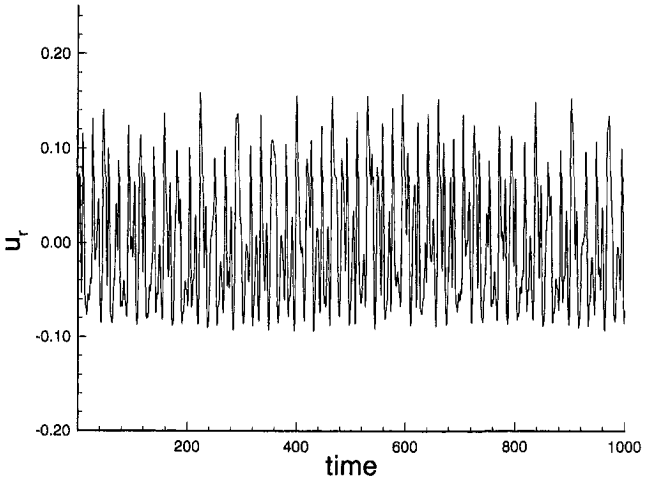

Fig. 7 Radial velocity signal for η = 0.7, L_z = 2.001, R = 100, Pr = 0.7, and Gr = −2100

the time traces are shown after the initial transients have died down. The power spectra of the radial velocity time series were obtained by performing a fast Fourier transform. Shown in Figs. 8

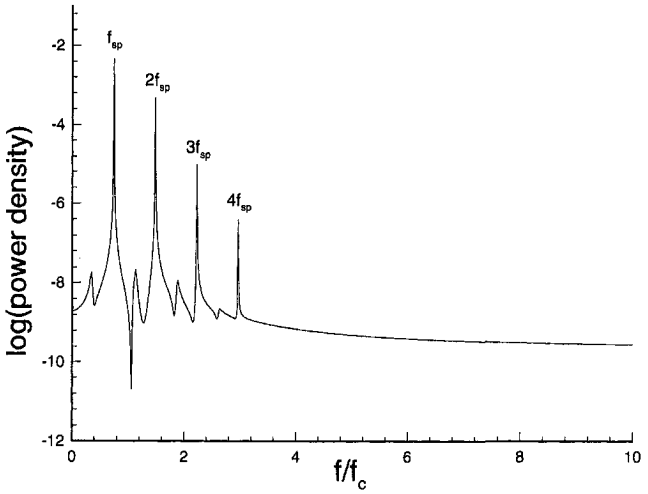

Fig. 8 Power spectrum of the radial velocity for η = 0.7, L_z = 2.001, A = 0.67, R = 100, Pr = 0.7, and Gr = −1700

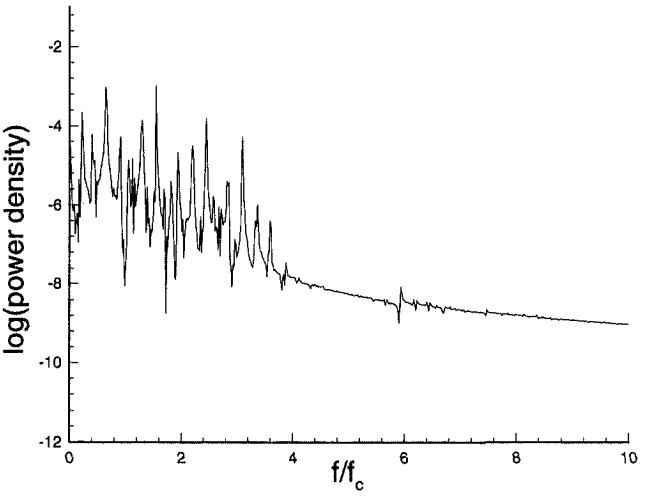

Fig. 9 Power spectrum of the radial velocity for η = 0.7, L_z = 2.001, A = 0.67, R = 100, Pr = 0.7, and Gr = −2100

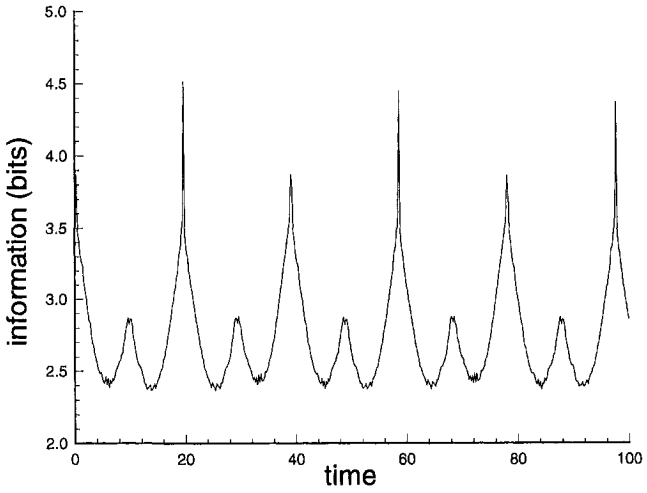

Fig. 10 Mutual information of the radial velocity for $\eta = 0.7$, $L_z = 2.001$, $A = 0.67$, R = 100, Pr = 0.7, and Gr = −1700

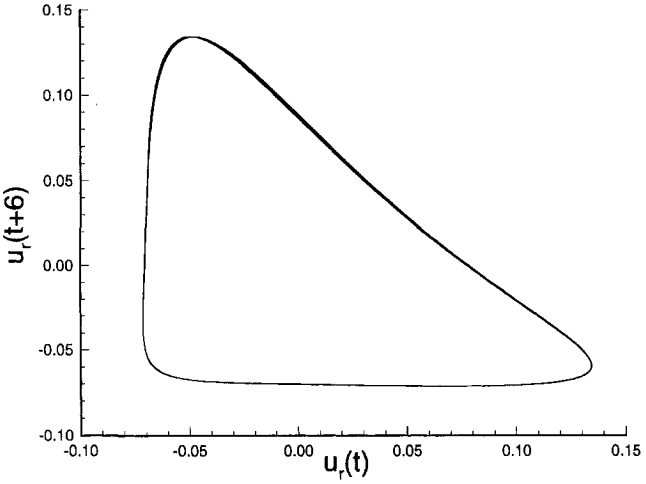

Fig. 12 Phase plot of the radial velocity for $\eta = 0.7$, $L_z = 2.001$, $A = 0.67$, R = 100, Pr = 0.7, and Gr = −1700

and 9 are the respective power spectra for Gr = −1700 ($n = 2$ spiral flow) and Gr = −2100 (aperiodic flow). Figure 8 shows a fundamental frequency at $f/f_c = 0.74$ and its harmonics. Here, the frequency is nondimensionalized using the inner cylinder frequency (f_c). The flow is clearly periodic in nature. For the case of Gr = −2100 (Fig. 9), the peaks for Gr = −1700 are still present but their amplitudes have slightly decreased. Also, other frequencies have appeared in the flow that are of comparable power density.

For the broadband spectra at Gr = −2100, the flow may be represented as a low dimensional dynamical system using time-delay coordinates to reconstruct the phase space (Takens, 1981). To calculate the dimension of the attractor, a suitable time delay must be determined. For this purpose, the mutual information function, $I(\tau)$, is used (Fraser and Swinney, 1986)

$$I(\tau) = \int\int P(X, Y) \log_2[P(X, Y)/P(X)P(Y)]dXdY \quad (7)$$

where $X = v(t)$ and $Y = v(t + \tau)$; $P(X)$ and $P(X, Y)$ are the probability density and the joint probability density and τ is a suitable time delay. Given the value of $v(t)$, the mutual information function gives the accuracy with which $v(t + \tau)$ can be predicted. Since $v(t)$ and $v(t + \tau)$ denote the coordinates of the reconstructed phase space, they should be independent of each other. Therefore, a good choice for the time delay is the first local minimum (Fraser et al., 1986) of the mutual information. The mutual information function is shown for Gr = −1700 and Gr = −2100 in Figs. 10 and 11, and the first local minimums occur at $t = 6$ and $t = 3$, respectively. Note that for Gr = −1700, the mutual information function is periodic as expected for a periodic signal.

The phase plots for Gr = −1700 and Gr = −2100 are shown in Figs. 12 and 13. For Gr = −1700, a clean limit cycle is seen for $n = 2$ spiral flow (periodic). For Gr = −2100, the reconstructed attractor has become vastly irregular and the limit cycle has disappeared.

In the present study both the pointwise dimension, D_1, and the correlation dimension, D_2, are calculated using the following definitions (Farmer et al., 1983):

$$D_1 = \lim_{\epsilon \to 0} \frac{\langle \log N(\epsilon) \rangle_x}{\log \epsilon} \quad (8)$$

where $N(\epsilon)$ is the number of points in a hypersphere of radius ϵ. The averaging is done over different referencing points x. The correlation dimension is similar to the pointwise dimension but the averaging is done over the number of points $N(\epsilon)$,

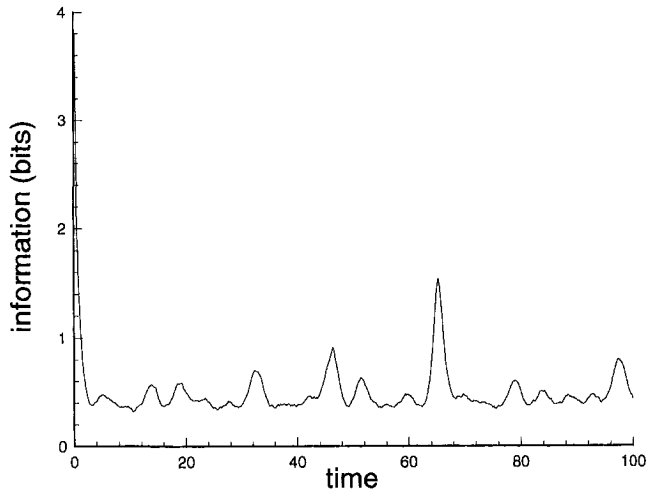

Fig. 11 Mutual information of the radial velocity for $h = 0.7$, $L_z = 2.001$, $A = 0.67$, R = 100, Pr = 0.7, and Gr = −2100

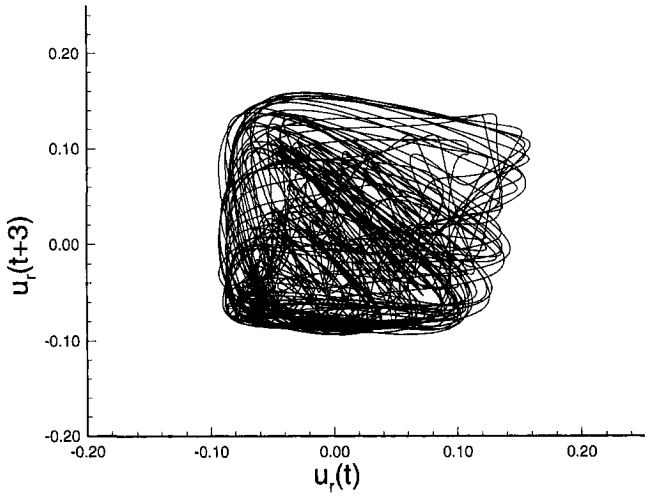

Fig. 13 Phase plot of the radial velocity for $\eta = 0.7$, $L_z = 2.001$, $A = 0.67$, R = 100, Pr = 0.7, and Gr = −2100

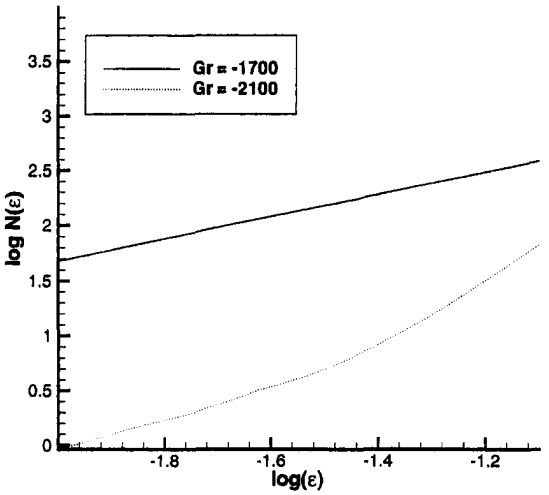

Fig. 14 Plot of log $N(\epsilon)$ versus log (ϵ) from the radial velocity for $\eta = 0.7$, $L_z = 2.001$, $A = 0.67$, R = 100, and Pr = 0.7

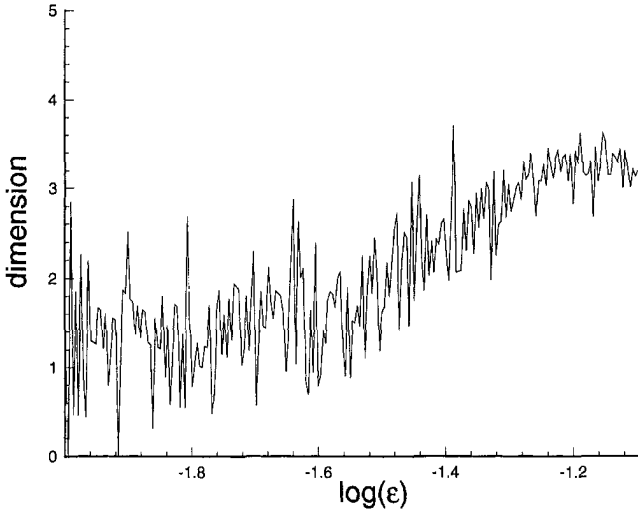

Fig. 16 Plot of the slope from the radial velocity for $\eta = 0.7$, $L_z = 2.001$, $A = 0.67$, R = 100, Pr = 0.7, and Gr = −2100

$$D_2 = \lim_{\epsilon \to 0} \frac{\log \langle N(\epsilon) \rangle_x}{\log \epsilon}. \quad (9)$$

Both the pointwise dimension D_1 and the correlation dimension D_2 were computed using the same algorithms, once by averaging the logarithm of the number of points and again by taking the logarithm of the averaged points. There was no appreciable change in these two calculated dimensions. Therefore, only D_1 is reported here. Embedding was done in six-dimensional phase space. Higher dimensional embedding was also done with no change in the attractor dimension. For a six-dimensional embedding, 256 reference points were chosen. These reference points were selected using uniformly generated random numbers, so that the reference points are spread out through the entire attractor equally. The pointwise dimension D_1 is shown for the two different flows ($n = 2$ spiral flow and aperiodic flow). Plots of log $N(\epsilon)$ versus log (ϵ) for Gr = −1700 and Gr = −2100 are shown in Fig. 14. The slopes of the graphs give the dimension of the reconstructed attractor. The slopes for the above cases are shown in Figs. 15 and 16. For Gr = −1700, a constant slope of approximately 1 is seen which reflects the periodic nature of the reconstructed attractor. For Gr = −2100 (Fig. 16), a slope of about 3.2 in the log (ϵ) interval of (−1.3, −1.1) is visible. The attractor dimension reaches an asymptotic value as the embedding dimension is increased (Table 1). If three irrationally related frequencies exist in the flow, the dimension of the flow would be 3.

The same process of time delay analysis is repeated for the local heat transfer coefficient (h) at one location within the flow. The time series for the local heat transfer coefficient and the radial velocity look very similar. The power spectra for the two Grashof numbers are given in Figs. 17 and 18. The magnitude of the power is two orders of magnitude higher than the corresponding power spectra for the radial velocity. However, the peaks occur at virtually the same frequencies. Shown in Figs. 19 and 20 are the dimension calculations for the local coefficients of heat transfer.

Table 1 Pointwise dimension as a function of the embedding dimension

m	D_1
3	2.50 ± 0.1
4	3.00 ± 0.1
5	3.15 ± 0.1
6	3.20 ± 0.1
7	3.20 ± 0.1
8	3.20 ± 0.1

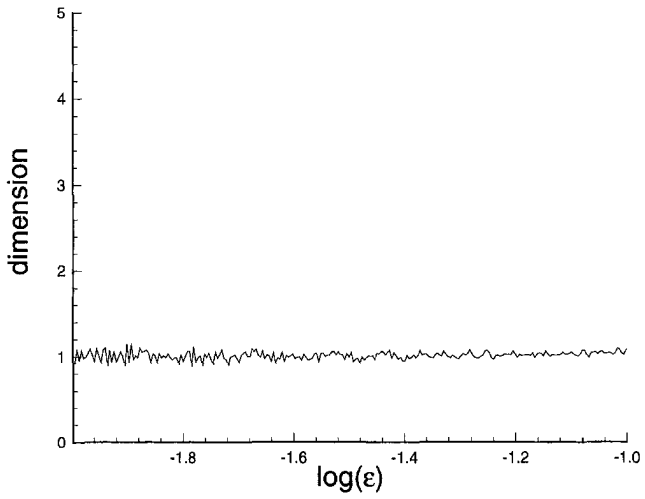

Fig. 15 Plot of the slope from the radial velocity for $\eta = 0.7$, $L_z = 2.001$, $A = 0.67$, R = 100, Pr = 0.7, and Gr = −1700

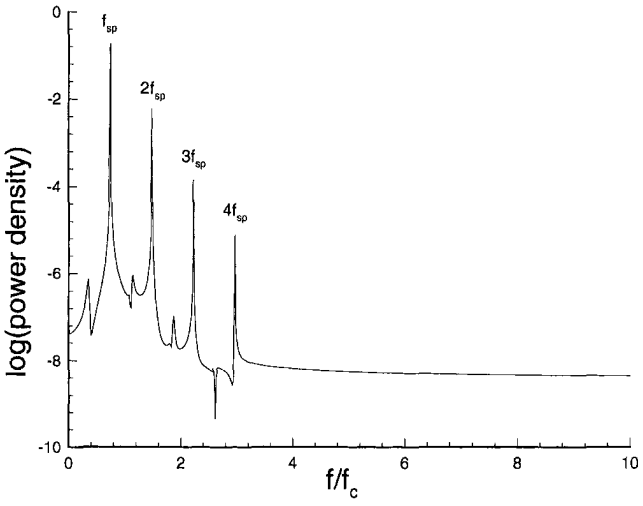

Fig. 17 Power spectrum of the local heat transfer coefficient for $\eta = 0.7$, $L_z = 2.001$, $A = 0.67$, R − 100, Pr = 0.7, and Gr = −1700

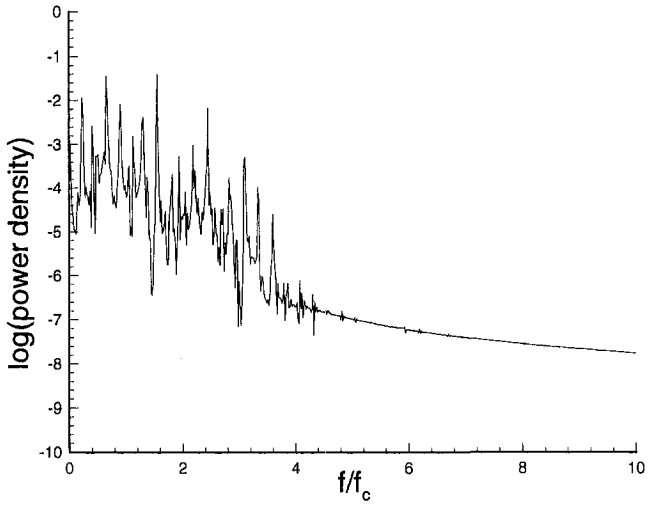

Fig. 18 Power spectrum of the local heat transfer coefficient for $\eta = 0.7$, $L_z = 2.001$, $A = 0.67$, R = 100, Pr = 0.7, and Gr = −2100

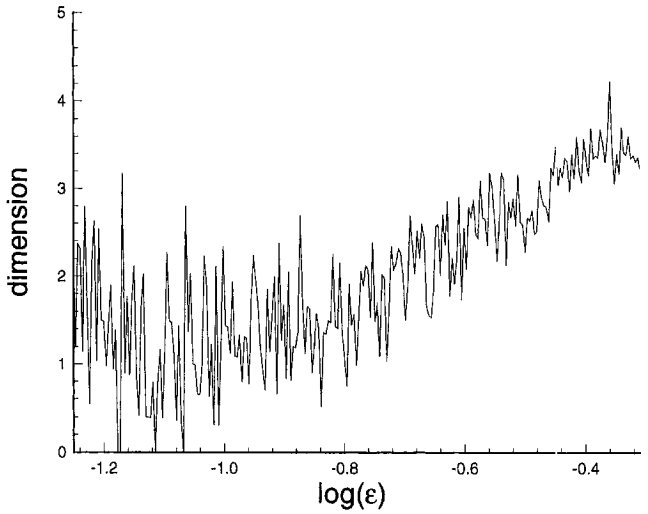

Fig. 20 Plot of the slope from the local heat transfer coefficient for $\eta = 0.7$, $L_z = 2.001$, $A = 0.67$, R = 100, Pr = 0.7, and Gr = −2100

The dimension for Gr = −2100 is approximately 3.2, which agrees well with the dimension obtained from the radial velocity time trace. Therefore, it is concluded that the local heat transfer coefficient follows the radial velocity pattern, with the reason being the active role of the radial velocity component in transferring heat between the two cylinders. The information about the phase space, such as the temporal evolution of the trajectories and the dimension of the attractor, can be used for making models such as predicting the value of the heat transfer coefficient for aperiodic flow. These models can then be used for predicting future behavior of the dynamical system, i.e., extracting the value of $v(t + 1)$ given a long time series of $v(t)$.

Conclusion

Heat transfer in an incompressible three-dimensional Taylor-Couette flow with a rotating inner cylinder has been numerically investigated to study the interaction of gravity and centrifugal potentials with the radial temperature gradient. Both the aforementioned effects have not been considered together in previous numerical simulations. For a fixed axial wavelength, the individual size of the Taylor vortex pair changes with the Grashof number, corresponding to a transition to a spiral flow regime with a significant increase in the average heat transfer.

One of the interesting properties of the nonlinear Navier-Stokes equations is nonuniqueness. With all other parameters fixed, the Grashof number was slowly varied to examine the existence of a hysteresis loop in heated Taylor-Couette flow. It was found that two stable states existed for the same Grashof number. One state was reached by increasing the Grashof number and the other by slowly decreasing it.

The validity of Colburn's correlation was also investigated to indicate the coupling between the wall stress and the transport of a scalar. The function $j_H(\mathrm{Pr}, \mathrm{R})$ was found to be slightly lower than $\mathrm{Pr}^{2/3}$ (note that the exponent is 0.77, which is higher than $\frac{2}{3}$) for the range of Reynolds number numerically investigated and to be dependent on the Reynolds number near the critical speed. For a fixed Reynolds number, the friction factor and the equivalent conductivity followed similar trends with Grashof number.

The frequency power spectrum for $n = 2$ spiral flow showed the single fundamental frequency and its harmonics for Gr = −1700. For Gr = −2100, new frequencies appeared in the power spectrum. The power spectrum became broadbanded for even lower Grashof numbers. The two-dimensional projection of the reconstructed attractor showed a limit cycle for Gr = −1700. The limit cycle behavior disappeared at Gr = −2100 and the reconstructed attractor became irregular. The pointwise dimension calculation was approximately 1 for Gr = −1700. The dimension value increased to about 3.2 for Gr = −2100 and the constant dimension region was found to be small. These dimensions were found from the trace of the radial velocity, and from the variation in the local heat transfer. Hence, the dynamics of the heat transfer variations can be modelled exactly the same as that of the radial velocity, which may be easier to assess in certain physical arrangements.

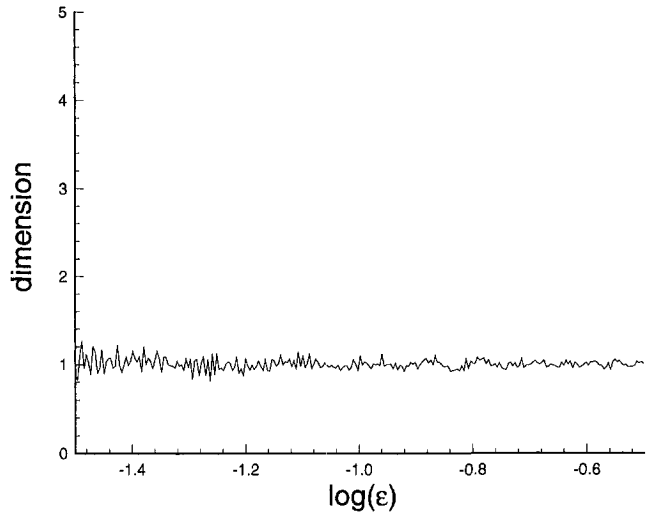

Fig. 19 Plot of the slope from the local heat transfer coefficient for $\eta = 0.7$, $L_z = 2.001$, $A = 0.67$, R = 100, Pr = 0.7, and Gr = −1700

Acknowledgments

This research was performed in part using the CSCC parallel computer system operated by Caltech on behalf of the Concurrent Supercomputing Consortium. Access to this facility was provided by Caltech. The authors would also like to thank Dr. A. Leonard at Caltech and Dr. R. D. Moser at University of Illinois at Urbana-Champagne for valuable discussions.

References

Ball, K. S., Farouk, B., and Dixit, V. C., 1989, "An experimental study of heat transfer in a vertical annulus with a rotating inner cylinder," *Int. J. Heat Mass Transfer*, Vol. 32, No. 8, pp. 1517–1527.

Brandstater, A., and Swinney, H. L., 1987, "Strange attractors in weakly turbulent Couette-Taylor flow," *Phys. Rev. A,* Vol. 35, No. 5, pp. 2207–2220.

Chen, J., and Kuo, J., 1990, "The linear stability of steady circular Couette flow with a small radial temperature gradient," *Phys. Fluids A,* Vol. 2, No. 9, pp. 1585–1591.

Coles, D., 1965, "Transition in circular Couette flow," *J. Fluid Mech.,* Vol. 21, pp. 385–425.

Farmer, J. Doyne, Ott, E., and Yorke, J. A., 1983, "The dimension of chaotic attractors," *Physica 7D,* pp. 153–180.

Fraser, A. M., and Swinney, H. L., 1986, "Independent coordinates for strange attractors from mutual information," *Physical Review A,* Vol. 33, No. 2, pp. 1134–1140.

Kataoka, K., Doi, H., and Komai, T., 1977, "Heat/Mass transfer in Taylor vortex flow with constant axial flow rates," *Int. J. Heat Mass Transfer,* Vol. 20, pp. 57–63.

Kedia, R., 1997, "An investigation of velocity and temperature fields in Taylor-Couette flows," Ph.D. thesis, California Institute of Technology, Pasadena, CA.

Kedia, R., Hunt, M. L., and Colonius, T., 1998, "Numerical Simulations of Heat Transfer in Taylor-Couette Flows," ASME JOURNAL OF HEAT TRANSFER, Vol. 120, pp. 65–71.

Koschmieder, E. L., 1993, *Benard Cells and Taylor Vortices,* Cambridge University Press, New York.

Kuo, D. C., and Ball, K. S., 1997, "Taylor-Couette flow with buoyancy: Onset of spiral flow," *Phys. Fluids A,* Vol. 9, No. 10, pp. 2872–2884.

Lathrop, D. P., Fineberg, J., and Swinney, H. L., 1992, "Turbulent flow between concentric rotating cylinders at large Reynolds number," *Physical Review Letters,* Vol. 68, No. 10, pp. 1515–1518.

Narabayashi, T., Miyano, H., Komita, H., Iikura, T., Shiina, K., Kato, H., Watanabe, A., and Takahashi, Y., 1993, "Study on temperature fluctuation mechanisms in an annulus gap between PLR Pump shaft and casing cover," *Proceedings of the Second ASME/JSME Joint Conference on Nuclear Engineering,* P. F. Peterson, ed., Mar. 21–24, San Francisco, CA, ASME, New York.

Takens, F., 1981, "Detecting strange attractors in turbulence," *Lecture Notes in Mathematics, 898,* D. Rand and L. S. Young, eds., Springer, Berlin, pp. 366–381.

Taylor, G. I., 1923, "Stability of a viscous liquid contained between two rotating cylinders," *Phils. Trans. R. Soc. London,* Vol. A223, pp. 289–343.

Heat Transfer of Compressed Air Flow in a Spanwise Rotating Four-Pass Serpentine Channel[1]

G. J. Hwang
Professor,
e-mail: gjhwang@faculty.nthu.edu.tw
Fellow ASME

S. C. Tzeng
Ph.D. Candidate

C. P. Mao
M. Sc. Student

Department of Power Mechanical Engineering,
National Tsing Hua University,
Hsinchu 30043, Taiwan

Convective heat transfer of compressed air flow in a radially rotating four-pass serpentine channel is investigated experimentally in the present study. The coolant air was compressed at 5 atmospheric pressure to achieve a high rotation number and Reynolds number simultaneously. The main governing parameters are the Prandtl number, the Reynolds number for forced convection, and the rotation number for the Coriolis-force-induced cross-stream secondary flow and the Grashof number for centrifugal buoyancy. To simulate the operating conditions of a real gas turbine, the present study kept the parameters in the test rig approximately the same as those in a real engine. The air in the present serpentine channel was pressurized to increase the air density for making up the low rotational speed in the experiment. The air flow was also cooled to increase the density ratio before entering the rotating ducts. Consequently, the order of magnitude of Grashof number in the present study was the same as that in real operating conditions. The local heat transfer rate on the walls of the four-pass serpentine channel are correlated and compared with that in the existing literature.

1 Introduction

Inside a rotating heated serpentine channel, the hydrodynamic and the thermal behaviors of the fluid flow are not only affected by the main flow but also modified by the Coriolis-induced cross-stream and centrifugal-buoyancy radial secondary flows. Consequently, the heat transfer rate on the leading edge, the trailing edge and the side walls are quite different from each other. High heat transfer rate is always desirable and gives a better cooling of a heated channel. On the contrary, a low heat transfer rate may yield a hot spot on the channel wall and damage the turbine blade. For cooling and maintaining the structural integrity of blades and vanes in gas turbine engines, the cooling system requires complex airflow passages to be incorporated inside the rotating airfoil section. Internal cooling is achieved by passing the coolant through serpentine passages inside the blade and extracting the heat to the outside.

Generally, the convective heat transfer in radially rotating channels can be categorized into a single-pass flow passage, U-type two-pass flow passages, and multipass serpentine flow passages. The cross section of the channel can be circular, rectangular, square, or triangular. In addition, the channel wall can be smooth or ribbed. The different experimental conditions including rotational speeds, flow regimes, wall thermal boundary conditions, channel dimensions/configuration, and temperature differences may have scattering results. The dimensional variables can be reduced to dimensionless parameters, such as the Reynolds number, indicating the effect of forced convection; the Rotation number, representing the effect of Coriolis force; and the Grashof number, signifying the effect of centrifugal buoyancy. Some recent experiments in radially rotating U-type or serpentine channels with a variety of geometry, dimensions, and dimensionless parameters are listed in Table 1. It is indicated that the compressed air flow used by Wagner et al. (1991a, b, 1992) and the present study makes the parameters, including Re, Ro, and Gr*, reach the values for an aircraft engine as shown in Table 2.

Wagner et al. (1991a, b) investigated the local heat transfer for radially outward and inward flows in rotating serpentine passages with uniform wall temperature. Depending on the flow direction, the rotational effects on the heat transfer coefficients are markedly different. Buoyancy is found to be favorable for heat transfer on both the trailing and leading edges. However, the increase in heat transfer for inward flow was relatively less than that for outward flow. Yang et al. (1992) investigated the rotational effect on the heat transfer coefficient of cooling air in a four-pass serpentine flow passage with smooth walls. The results revealed significant changes in the heat transfer performance at the turning sections and considerable differences between the inward and outward flows in the straight sections of the flow passage.

Han and Zhang (1992) and Han et al. (1993) examined the effect of uneven wall temperature on heat transfer in a rotating two-pass square channel. They studied three cases of thermal boundary conditions: four-wall at the same temperature, four-wall at the same heat flux, and the trailing wall hotter than the leading wall with side walls unheated and insulated. Han et al. (1994) investigated the effect of a surface heating condition on the local heat transfer rates of outward flow in a radially rotating square channel. Four surface heating conditions were tested: four-wall at uniform temperature; the temperature ratio of leading surface to the side wall and the trailing surface to the side wall is 1.05 and 1.10, respectively; the trailing surface hot and remaining three walls cold; and the leading surface hot and remaining three walls cold.

Mochizuki et al. (1994) studied experimentally the heat transfer characteristics of a three-pass serpentine flow passage with rotation. They found that the heat transfer rate in the radially outward flow passages diminishes on the leading edge, but increases on the trailing edge, with an increase in rotational speed. The trend is reversed in the radially inward flow passages. Since the heat transfer rate in the bend is substantially higher than that in the straight flow passages, the average heat transfer rate over the entire flow passage is greatly affected by flow at the 180-deg bends. Hwang and Kuo (1997) summarized the heat transfer results. The Nusselt number ratios on the trailing and leading sides for three-

[1] Part of this paper was presented at the 5th ASME/JSME Thermal Engineering Joint Conference, San Diego, CA.

Contributed by the Heat Transfer Division for publication in the JOURNAL OF HEAT TRANSFER. Manuscript received by the Heat Transfer Division, Nov. 15, 1998; revision received, Apr. 21, 1999. Keywords: Channel Flow, Heat Transfer, Mixed Convection, Rotating, Turbines, Turbulent. Associate Technical Editor: J.-C. Han.

Table 1 Some recent experimental investigations on heat transfer in radially rotating serpentine channel

AUTHOR S	AIR PRESSURE (MPa)	PASS OF CHANNEL	B. C.	MAX. RPM	D(mm)	L/D	$\overline{R}$/D	Re $\times 10^{-3}$	ReRe_Ω $\times 10^{-6}$	$\overline{Gr_\Omega}$ $\times 10^{-5}$
Wagner et al. (1991a, b)	1	2	UWT	1100	12.7	14	33, 49	12.5 - 50	300-1200	2030
Wagner et al. (1992)	1	2	UWT	1100	12.7	14	33, 49	12.5 - 50	300-1200	2030
Han & Zhang (1992, 1993 and 1994)	0.1	2	UWT/UHF	800	12.7	12	30	2.5 - 25	22-220	23.3
Yang et al. (1992)	0.1	3	UHF	327	25.4	8.86	—	44-110	200-508.125	218
Mochizuki et al. (1994)	0.1	3	UHF	500	20	10.5	44	4.0 - 20	18.7-92.75	2500
Hwang & Kuo (1997)	0.1	3	UHF	1800	4	25	60	5.0 - 20	12.8-51.2	2.5
Present study	0.5	4	UHF	1250	10	10	53	20 - 40	118-336	1800

pass serpentine flow passages are correlated by different equations. The equations for the first passage are the same as that for the single outward flow passage. The correlation for the first passage can also be used for the third passage.

This paper deals with the rotational effects, by varying through-flow Reynolds numbers, rotational speeds, and wall heat flux on the local heat transfer in a radially rotating four-pass serpentine square-sectioned smooth flow passage. The main flow directions were two radially outward and two radially inward. The rotational effects in these four passages of the serpentine channels may be different due to the different main flow direction and the presence of 180-deg bends. One of the major attempts in the present study is to pressurize the air flow in the serpentine channel to keep the values of parameters, including the Reynolds number, the rotation number, and the Grashof number, approximately the same as those of a real engine.

2 Parametric Analysis

The flow in a heated, rotating four-pass serpentine channel is three-dimensional and extremely complex. The combined effects of the Coriolis-induced cross-stream secondary flow and centrifugal-buoyancy radial flows influence the forced longitudinal flow. Normally the Coriolis-induced vorticity tends to enhance the heat transfer, on the trailing edge when the flow is outward. The centrifugal buoyancy enhances the heat transfer in radially outward flow.

As seen in Table 2, it is not difficult to have the geometry of the test rig including coolant passage diameter D, length L, and mean rotating radius $\bar{R}$ similar to that in a real engine. On the other hand, the temperature and rotational speed of the test rig are much lower than that of the aircraft engine. The low rotational speed yields a low rotation number and a low rotational Grashof number. Therefore, the air in the present serpentine channel was pressurized to increase the air density for making up the low rotational speed in

Nomenclature

A = cross-sectional area of the flow passage, mm^2
Cp = specific heat, J/(Kg · K)
D = hydraulic diameter = $2ab/(a + b)$, mm
F_{in} = correlation function for inward flow
F_{out} = correlation function for outward flow
Gr_Ω = rotational Grashof number = $\beta(T_{W,Z} - T_{b,Z})(\epsilon + Z/D)\ Re^2\ Ro^2$
$\overline{Gr_\Omega}$ = mean rotational Grashof number = $\beta(T_{b,o} - T_{b,i})(\epsilon + \bar{Z}/D)\ Re^2\ Ro^2$
Gr^* = rotational buoyancy parameter = Gr_Ω/Re^2
$\overline{Gr^*}$ = mean rotational buoyancy parameter = $\overline{Gr_\Omega}/Re^2$
h_Z = heat transfer coefficient = $q_{net,Z}/(T_{W,Z} - T_{b,Z})$, watt/($m^2$ · °C)
k_{air} = thermal conductivity of air, watt/(m · °C)
L = coolant passage length, mm
Nu = Nusselt number = $h_Z D/k_{air}$
Nu_Ω = Nusselt number for rotating condition
Nu_∞ = Nusselt number for fully developed turbulent flow in a nonrotating circular tube
Pr = Prandtl number = $Cp \cdot \mu/k_{air}$
q_{net} = net wall heat flux, watt/m^2
$\bar{R}$ = mean rotational radius = $Z_o + L/2$, mm
Re = through-flow Reynolds number = $\rho W_o D/\mu$
Re_Ω = rotational Reynolds number = $\rho\Omega D^2/\mu$
rms = root mean square
Ro = rotation number = $Re_\Omega/Re = \Omega D/W_o$
$T_{b,i}$ = inlet coolant bulk temperature, °C
$T_{b,o}$ = outlet coolant bulk temperature, °C
$T_{b,Z}$ = local coolant bulk temperature, °C
$T_{W,Z}$ = local wall temperature, °C
W_o = mean coolant velocity, m/s
U, V, W = velocity component, m/s
UHF = uniform heat flux
UWT = uniform wall temperature
Z_o = distance between rotating axis and heater, mm
X, Y, Z = system coordinates

Greek Symbols

β = volume expansion coefficient, 1/K
ϵ = eccentricity = Z_o/D
ρ = coolant density, kg/m^3
Ω = rotational speed, rad/s

Superscripts

$\overline{(\ )}$ = mean quantity

Table 2 Parameters for aircraft engine and present test rig

Parameters	Aircraft engine*	Present test rig** (Present study)
Coolant passage diameter D (mm)	~4	10
Coolant passage length L (mm)	48 ~ 70	100
Mean rotational radius $\bar{R}$ (mm)	200~360	530
Mean rotational radius/diameter ratio $\bar{R}/D$	50~90	53
Maximum passage wall temperature T_w (K)	1256 (1800°F)	393 (343)
Inlet coolant bulk temperature $T_{b,i}$ (K)	867 (1100°F)	283
Density ratio $(\Delta\rho/\rho)_i = (\rho_{b,i}-\rho_w)/\rho_{b,i} = (T_w - T_{b,i})/T_w$	0.366	0.325 (0.192)
Rotational speed Ω (rpm)	0~15000	0~1250
Mean coolant velocity W_o (m/s)	34.5 ~ 69.0	6.17 ~ 12.34
Flow Reynolds number Re	2.0 ~ 4.0×10^4	2.0 ~ 4.0×10^4
Rotation number $Ro = Re_\Omega/Re$	0.091 ~ 0.182	0.105~ 0.21
Mean rotational Buoyancy parameter $\overline{Gr^*} = \overline{Gr_\Omega}/Re^2$	0.152 ~ 0.608	0.156 ~ 0.624 (0.112~0.449)

* The thermophysical properties for an aircraft engine are valued at P = 17 atm, ρ = 6.002 kg/m^3, T=1000 K and $\bar{R}/D$ = 50

** The thermophysical properties for the present test rig are valued at P = 5 atm, ρ = 5.94 kg/m^3, T=300 K and $\bar{R}/D$ = 53

the experiment. Keeping the same value of the Reynolds number, the axial velocity can be decreased by using the compressed air flow. Thus, the low axial velocity yields a high rotation number. The air flow was also cooled to gain a high density ratio before entering the rotating duct. This high density ratio will give a similar order of magnitude of Grashof number as that in a real engine. The relative dimensionless parameters were similar to those of real engine at the same time. The functional relationship is expressed as

$$Nu_\Omega = F_1(Re, Re_\Omega, Gr_\Omega, Pr, \bar{R}/D, Z/D)$$
$$= F_2(Re, Ro, Gr^*, Pr, \bar{R}/D, Z/D) \quad (1)$$

where $Ro = Re_\Omega/Re$ and $Gr^* = Gr_\Omega/Re^2$. The ranges of parameters in an aircraft engine and the present test rig are also listed in Table 2. The values in the present study are slightly lower than those in the designed test rig. This was due to the limitation of electrical power input to the wall heaters.

3 Experimental Apparatus and Test Section

The experimental apparatus, as shown in Fig. 1, consists of five major parts: (1) the coolant air supply system, (2) the heater and power control system, (3) the speed controller, (4) the test section, and (5) the data acquisition system. The coolant air was supplied from a storage tank with a 0.7 MPa air compressor. A bypass valve at the exit of the storage tank and a flow rate control valve at the exit of the piping system are utilized to maintain the desired flow rate and pressure. They are not shown in Fig. 1. Two electric digital flowmeters with the ranges of 0 ~ 670 and 0 ~ 1700 liter/min were mounted on the piping system. Also, two electrical digital pressure gauge with the range of 0 ~ 1.0 MPa were installed. Therefore, one could detect the pressures and flow rates of the coolant air at both ends of the test section. The average values were used to evaluate the parameters in this study. The differences of the values of pressure and flow rate at both ends signified the pressure drop and the flow leakage, respectively. A chiller was used to decrease the coolant temperature to about −2°C before entering the rotating shaft. The rotating shaft had two coaxial cylinders. One was an annular passage for the coolant inlet, the other was an inner passage for the coolant outlet. A high-speed rotating joint and four sets of mechanical seals were used in the rotating shaft to prevent air flow leakage. The flow leakage was kept within ±3 percent for minimum flow rate. The pressure was measured at 0.53 MPa for inlet and 0.47 MPa for outlet. A water cooling-cycle system was used to cool the mechanical seals.

A 3.73 kW AC induction motor drove the hollow rotating shaft with a belt drive pulley system. The rotational speed was adjusted continuously by an inverter to a maximum rotating speed of 2500 rpm. The rotational speed was detected by a photoelectric tachometer. The shaft rotating direction could be clockwise or counterclockwise to measure both the leading and trailing wall temperature distributions with only one wall thermocouple installation.

Along the flow passage, TT-T-30-SLE type thermocouples of 0.24-mm diameter for measuring the wall temperature were embedded on the interior wall surface of the flow passage. Two T-type thermocouples were positioned at the duct inlet and outlet for measuring the inlet and exit coolant bulk temperature. A 20-contact-point slip ring was used to transfer outputs of 58 thermocouples to a 60-point hybrid recorder by a switching device.

3.1 Test Section. As shown in Fig. 2, the test section of the serpentine channel had two outward flow passages and two inward flow passages, along with three 180-deg turn sections. To compare with the data of Han et al. (1993) without using the compressed air, the 180-deg turn section consisted of two 90-deg bends, 10 mm apart.

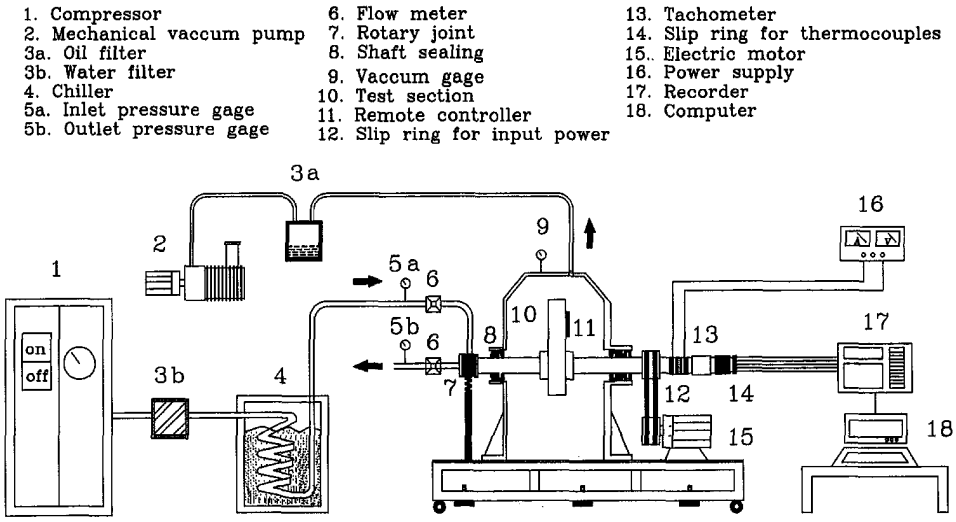

Fig. 1 Schematic of experimental apparatus

For distinguishing the thermal behavior on each wall, the circumferential wall heat conduction was deliberately suppressed by using material of low thermal conductivity. Four stainless-steel film heaters, with 0.02-mm thickness, were used to heat the flow passages. The film heater was plated separately on each interior wall surface of the flow passages. The wall thermal boundary condition of uniform heat flux could be achieved. The heaters started at Z_o = 480 mm, and attached on the walls including straight sections and sections of 180-deg bends. The test section had a hydraulic diameter of 10 mm and a mean rotational radius of 530 mm.

A thermocouple was positioned at the duct inlet for measuring the inlet coolant bulk temperature. A mixing chamber with staggered rod bundles was attached on the exit plane to provide a well-mixed condition. The outlet bulk temperature was read by the installation of another thermocouple behind the mixing chamber. Twenty-six thermocouples were installed on the trailing wall (the direction of rotation is indicated in Fig. 2.). The thermocouples were located along the center line on the trailing wall at positions Z/D (listed in Table 3). Sixteen thermocouples on the side wall A and 14 thermocouples on the side wall B were mounted at the same axial distance as that of the trailing wall. The measurement of temperature on the leading wall could be obtained by just changing the rotation direction. In the present study, the thermocouples were embedded in a copper block of dimension 0.5 × 3 × 7 mm. The copper blocks were electrically insulated from the heater by a polyethylene film of thickness 0.014 mm.

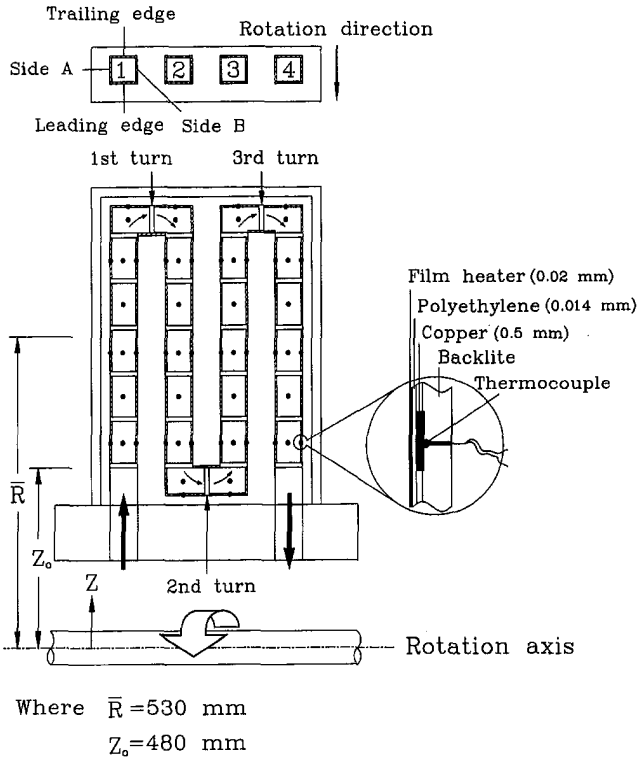

Fig. 2 Schematic of the four-pass heat transfer test section

Table 3 The value of local Nusselt number for Ω = 0 in four-pass smooth serpentine passage

Position	Z/D	Re=20000	Re=30000	Re=40000
1st Passage	1.0	64.63	83.76	103.93
	2.5	63.63	83.22	102.09
	4.0	59.44	79.39	100.36
	5.5	58.40	77.85	99.11
	7.0	58.67	74.67	99.12
1st Turn	8.5	79.71	105.22	128.36
	10.5	93.00	122.14	144.87
2nd Passage	12.0	76.05	101.94	127.21
	13.5	69.28	93.34	118.14
	15.0	62.94	83.79	108.54
	16.5	58.94	77.88	102.65
	18.0	60.73	79.56	103.73
2nd Turn	19.5	86.15	112.99	138.60
	21.5	87.19	118.22	143.59
3rd Passage	23.0	71.12	95.38	121.25
	24.5	67.04	90.76	117.77
	26.0	62.77	84.95	111.45
	27.5	59.26	79.89	105.62
	29.0	55.26	73.69	98.76
3rd Turn	30.5	83.38	95.58	114.52
	32.5	94.08	107.47	127.71
4th Passage	34.0	75.43	90.14	112.72
	35.5	70.17	84.77	106.84
	37.0	64.36	81.07	103.44
	38.5	60.59	77.19	99.23
	40.0	56.93	73.55	93.88

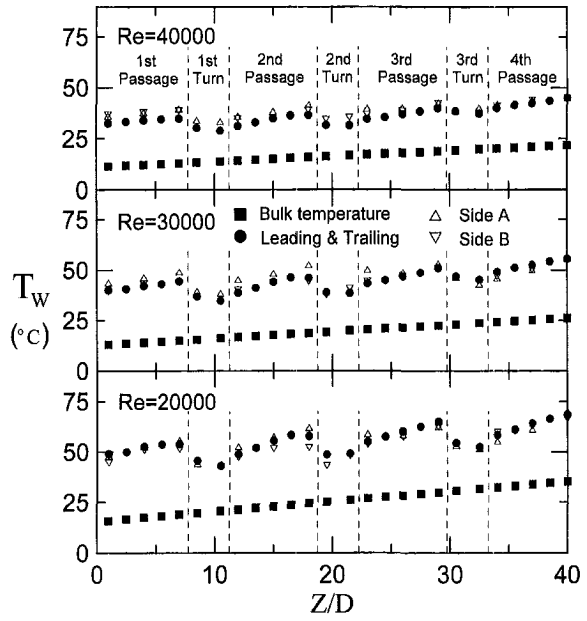

Fig. 3 The wall and coolant temperatures for Ω = 0 at selected Reynolds numbers

An adapter made of Bakelite, of 420-mm length, was mounted between the test section and the rotating shaft to increase the radial length of the test section. The data of heater power input and wall temperature distribution were recorded and analyzed to obtain the value of heat transfer coefficient. A balance was done for the assembly of a rotating shaft and test section. The main flow direction of the passage was perpendicular to the centerline of the rotating shaft.

3.2 Data Reduction. The local heat transfer coefficient h_z was evaluated as the ratio of the net wall heat flux q_{net} to the temperature difference between the local wall temperature $T_{w,z}$ and the local coolant bulk temperature $T_{b,z}$, i.e., $h_Z = q_{net}/(T_{w,z} - T_{b,z})$. The net wall heat flux from the duct walls to the air flow was obtained by subtracting the external heat loss from the electric power supplied to the film heaters. The heat loss test at each measurement point of the test section is obtained under the no-flow condition for 0, 250, 500, 750, 1000, and 1250 rpm. The average value of heat loss with two vertical and two horizontal orientations of the test cylinder was taken. The measured electrical power input and steady-state temperature determine the amount of heat loss at the measured temperature. By varying the electrical power input, the relationship between the heat loss and temperature can be obtained. The external heat loss including the axial conduction and convection was attributed to both conduction from the heated test section to the model support structure and convection to the ambient air in the test cell. The value is about 457.32 watt/m^2 for the extreme cases. It had a 7.5 percent heat loss for total input power. The local Nusselt number was calculated from the local heat transfer coefficient, hydraulic diameter, and thermal conductivity of air as

$$\mathrm{Nu}_\Omega = h_Z D/k_{\mathrm{air}}. \tag{2}$$

The thermal conductivity of air was based on the local bulk temperature.

3.3 Uncertainty Analysis. The errors in the temperature reading can be obtained from the calibration of the thermocouples. The uncertainty was ±0.1°C from the readout of the data recorder. The difference between the wall temperature and bulk temperature is greater than 15°C. The calibration of the flow rate was carried out with compressed air at 5 atmospheric pressure. The maximum error in the flow rate was about three percent at 43 liter/min. The rotational speed was detected by a tachometer with a bit of oscillation. The maximum error of the rotational speed was two percent at 250 rpm. The uncertainties of air thermophysical properties were included in the analysis. Uncertainties in parameters were estimated by using the root-sum-square method of Kline and McClintock (1953). The measured value and its uncertainty can be expressed as $R = R \pm \delta R$. The uncertainties of cross-sectional area, power, volume flow rate, pressure, temperature, Reynolds number, Nusselt number, Rotation number, and Rayleigh number were estimated within ±1.41 percent, ±4.03 percent, ±2.33 percent, ±2 percent, ±4 percent, ±2.73 percent, ±7.23 percent, ±3.24 percent, and ±10.33 percent for a flow rate of 43 liter/min and a rotational speed of 250 rpm, respectively.

4 Results and Discussion

The experiment was conducted to determine the distribution of the local Nusselt number along the four duct walls for the ranges of Reynolds number (Re = 20,000, 30,000 and 40,000), rotational speed (0, 250, 500, 750, 1000, and 1250 rpm), and outlet-to-inlet temperature differences ($T_{b,o} - T_{b,i}$ = 10, 15, and 20°C).

4.1 Nonrotating Condition on Wall Temperature and Heat Transfer. Figure 3 gives the wall and coolant bulk temperatures at Re = 20,000, 30,000, and 40,000 for Ω = 0. The temperature differences among those of leading (trailing) and side walls are not significant. As the Reynolds number increases, the gradient of the coolant bulk temperature decreases. The average slope of the wall temperature distribution is the same as the slope of the coolant bulk temperature distribution at the selected Reynolds numbers. The temperature difference in the regions of two 90-deg bends drops due to a large heat transfer rate in this region. As the Reynolds number increases, the effect of bends on the wall temperature is less pronounced.

Figure 4 shows the effect of Reynolds number on the local Nusselt number at Re = 20,000, 30,000 and 40,000. The results are also compared with the Dittus-Boelter (1930) correlation

$$\mathrm{Nu}_\infty = 0.023\ \mathrm{Re}^{0.8}\ \mathrm{Pr}^{0.4} \tag{3}$$

for fully developed turbulent flow in a smooth circular duct with uniform wall temperature. It is believed that the Nusselt number shown in Eq. (3) is about the same as that in a square duct with

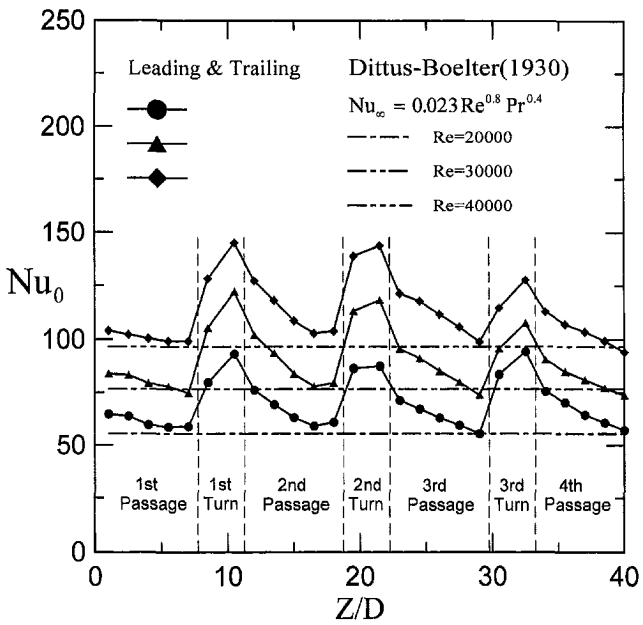

Fig. 4 Effect of Reynolds number on the local Nusselt number for Ω = 0

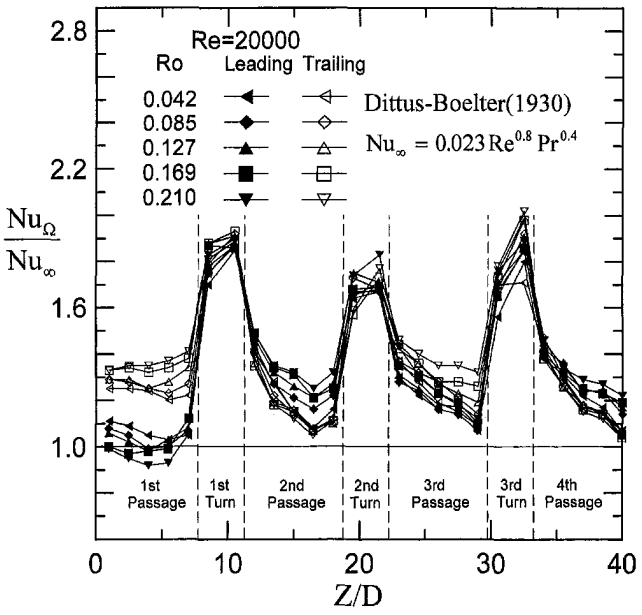

Fig. 5 Effect of Rotation number ratio on the Nusselt number ratio at Re = 20,000

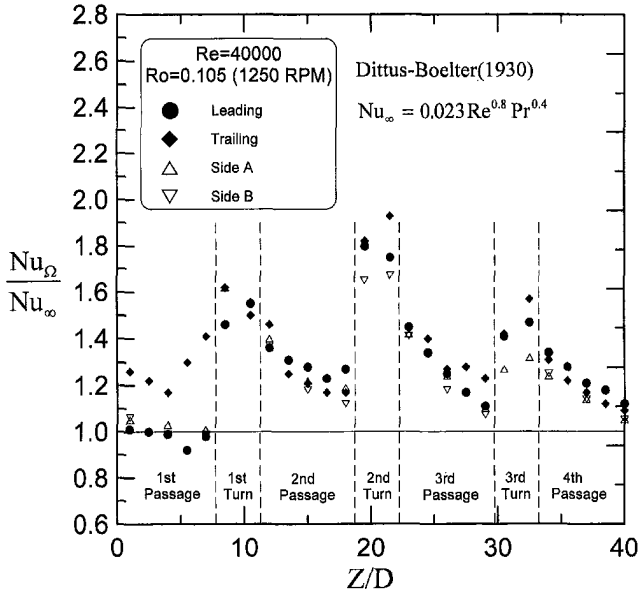

Fig. 6 The four-wall local Nusselt numbers ratio for Re = 40,000 and Ro = 0.105

uniform wall heat flux (Holman, 1989). The measured results show that the values of Nu of these passages increase with the increase in Re and reasonably agree with those of the Dittus-Boelter (1930) correlation near the end of each passage. On the first, second, and third turn, the Nusselt numbers are higher than those in the passages due to the secondary flow induced by the two 90-deg bends. The Nusselt number achieves its highest value at the second 90-deg bend.

4.2 Rotational Effects on Heat Transfer. Figure 5 reveals the effects of rotation number on the local Nusselt number ratio at Re = 20,000 and Ro = 0.042, 0.085, 0.127, 0.169, and 0.210. The Nusselt number on the trailing edge for the first and the third passages increases with the increase in the rotation number. Similarly the Nusselt number on the leading edge for the second and fourth passages also increases with the rotation number. This tendency is more noticeable at a higher rotation number than that at a lower rotation number. On the trailing edge for the outward flow (e.g., the first and third passages) and on the leading edge for the inward flow (e.g., the secondary and fourth passages), the heat transfer coefficients are increased. It is seen that the difference between Nusselt numbers on the trailing and leading edges are larger in the first passage than that in the second, third, and fourth passages.

Figure 6 shows the four-wall local Nusselt number ratios for Re = 40,000 and Ro = 0.105. Generally speaking, the Nusselt numbers on side walls are close to the lower values on leading and trailing edges except in the region of first turn. The local Nusselt number ratio on the trailing edge for the outward flow and on the leading edge for the inward flow is also increased. The Nusselt number ratio of the first passage is different from that of the second, third, and fourth passage. This may be due to the entrance effect in the first passage. Generally, the Nusselt number ratios in the second, third, and fourth passage drop monotonically from higher values to values greater than one. The Nusselt number ratios in the bend regions are higher than that in the straight passages. The Nusselt number ratio of the second turn is different from those of the first and third turn. The flow is accelerated by the centrifugal force near the channel wall in the second passage.

4.3 Rotation Number Effects on Heat Transfer Rate. Figure 7 shows the local Nusselt number ratio Nu_0/Nu_0 with Ro at selected Z/D for Re = 20,000, 30,000, 40,000. The values of Nu_0, indicating the Nusselt number under the stationary condition, are shown in Fig. 4 and Table 3. It is not shown in Fig. 4 that the enhancement in heat transfer at smaller Z/D is less than that at higher Z/D. In the regions of 180-deg bends the enhancement of the heat transfer rate is observed due to the rotation. It is also noted that there is no appreciable difference between the Nusselt numbers of leading and trailing edges in the regions of first, second, and third turns. In the second and fourth passages, the Nusselt numbers of leading edge are higher than that of trailing edge.

4.4 Rotational Buoyancy Effect on Heat Transfer Rate. Figure 8 shows the centrifugal buoyancy effect on the mean heat transfer rate at each passage for Re = 20,000. The inlet-to-outlet bulk temperature was kept at $T_{b,o} - T_{b,i}$ = 10, 15, and 20°C. In a rotational flow field like this, centrifugal force exerts in the main flow by producing a radial pressure gradient. With density varia-

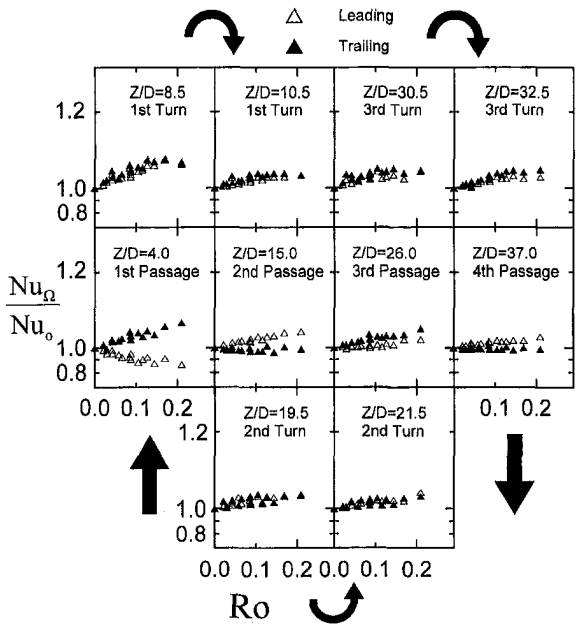

Fig. 7 The local Nusselt number ratio (to Nu_0) with variations of Ro at the selected cross section of flow passage for Re = 20,000, 30,000, 40,000

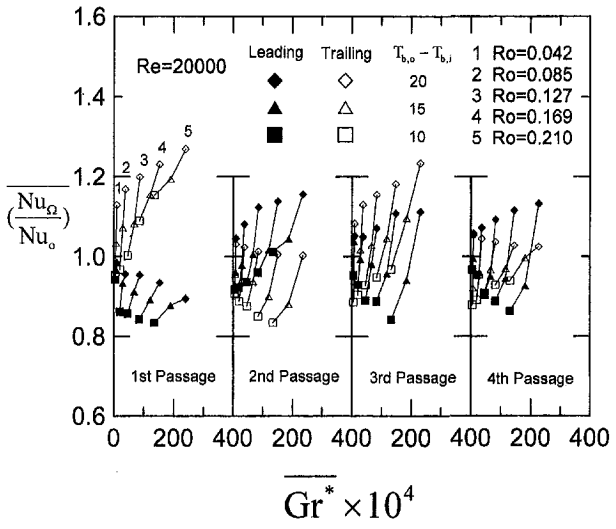

Fig. 8 The centrifugal buoyancy effect on heat transfer rate at each passage for Re = 20,000

tion in the nonisothermal flow, additionally, the thermal buoyancy stemmed from centrifugal force emerges, and alters flow and heat transfer characteristics significantly. In the extreme case of the present study, $T_{b,o} - T_{b,i} = 20°C$, the ratio of thermal centrifugal force to hydrodynamic centrifugal force is $\beta\Delta T$, which is smaller. The values is about 0.068. Due to the increasing heat flux, the mean heat transfer rate increases on both the leading edge and trailing edge of all passages. The heat transfer enhancement is gradually increased for a higher temperature difference. Under different conditions, buoyancy flow may provide opposing or aiding effect to the main flow. In the outward flow passage, the direction of forced flow opposes the buoyancy flow (opposing flow). In the inward flow passage, these two forces are in the same direction (aiding flow). The Nusselt number ratio increases with the increase in the Grashof number in all passages. This observation is different from that observed by Hwang and Kuo (1997) at Re = 5000. These phenomena can be found by analyzing mixed convection of the buoyancy-induced opposing and aiding flows in a vertical heated tube (Buhr et al., 1974; Abdelmeguid and Spalding, 1979; Cotton and Jackson, 1987). With increasing the rotational buoyancy parameters in the outward flow passage, the increased tendencies on heat transfer were found by Wagner et al. (1991a, b), Morris and Ghavami-Nasr (1991), and Han and Zhang (1992). The combined effect on the heat transfer rates is obtained. The increase in the Nusselt number ratio with $T_{b,o} - T_{b,i} =$ 10–20°C can be more than 20 percent in the third passage.

4.5 Correlation of the Heat Transfer Results. Figures 9(*a*) and (*b*) show the correlation of heat transfer data for the serpentine flow passage on the leading and trailing edges. Note that the correlations are for the outlet and inlet temperature difference $T_{b,o} - T_{b,i} = 20°C$ and Reynolds number = 20,000, 30,000 and

Leading edge	rms (%)				$Re \times 10^{-3}$
	1st	2nd	3rd	4th	
● Present study	6.81	6.90	7.12	7.13	20, 30, 40
◆ Hwang and Kuo (1997)	6.64	7.21	6.62	----	5, 10, 15, 20
▼ Yang et al. (1992)	7.51	6.05	8.85	----	44, 110
▲ Han et al. (1993)	11.71	12.64	----	----	2.5, 5, 10, 25
× Wanger et al. (1991 b)	22.83	13.43	----	----	4, 20
■ Mochizuki et al. (1994)	20.00	----	----	----	12.5, 25, 50

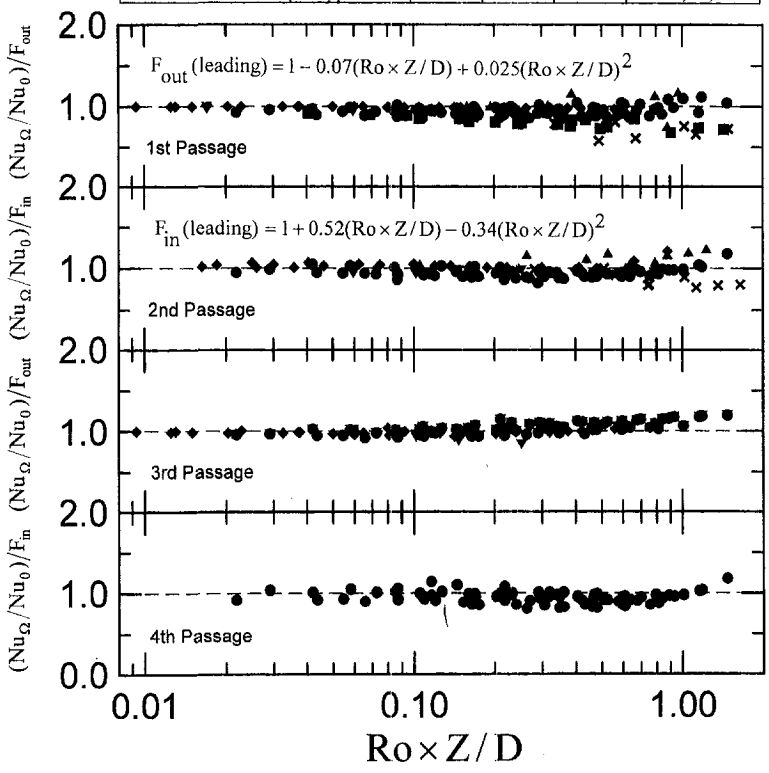

Fig. 9(*a*) on the leading edge

Trailing edge	rms (%)				$Re \times 10^{-3}$
	1st	2nd	3rd	4th	
● Present study	6.31	4.04	8.91	7.17	20, 30, 40
◆ Hwang and Kuo (1997)	7.76	4.25	8.46	----	5, 10, 15, 20
▼ Yang et al. (1992)	8.05	4.89	4.55	----	44, 110
▲ Han et al. (1993)	9.52	6.59	----	----	2.5, 5, 10, 25
× Wanger et al. (1991 b)	16.98	19.32	----	----	4, 20
■ Mochizuki et al. (1994)	10.52	----	----	----	12.5, 25, 50

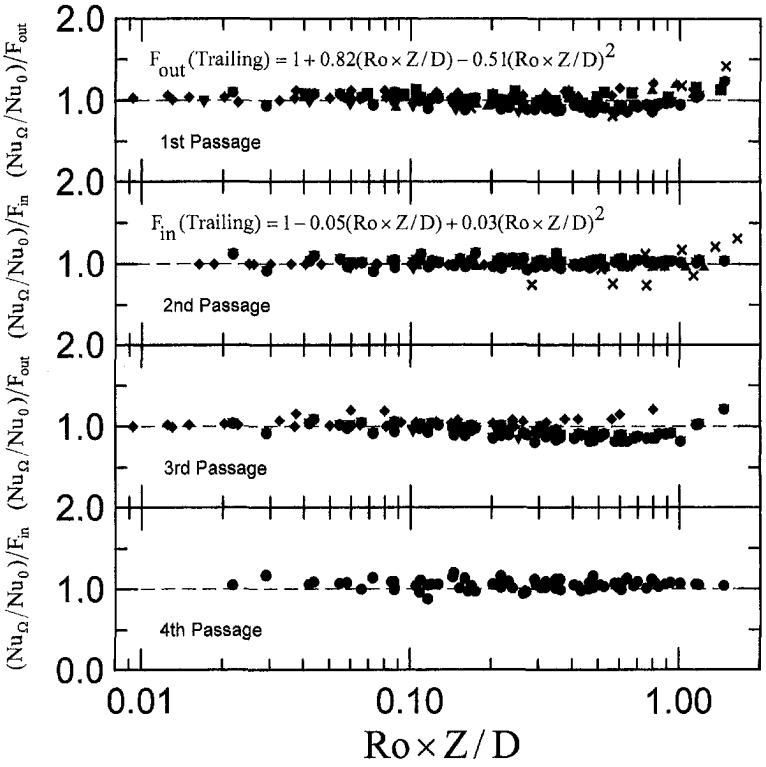

Fig. 9(*b*) on the trailing edge

Fig. 9 The correlation of heat transfer data for the serpentine flow passage

40,000. By using the ratio of Nu_Ω/Nu_0, Hwang and Kuo (1997) correlated the data of outward and inward flows on the leading and trailing edges of a single straight tube, including those of Wagner et al. (1991a), Han et al. (1993), and Mochizuki et al. (1994) for inward and outward flow in a serpentine passage. The rms values in Kuo and Hwang (1997) should be multiplied by the square root of the number of data.

Hwang and Kuo (1997) correlated the experimental data for the rotation numbers 0 to 0.032. Due to the effects of the high Rotation number, the correlation (Hwang and Kuo (1997)) is modified with the present experimental data. The values of the second coefficient in function F are changed. Also, due to the effects of the first passage and the 180-deg bend, the correlation of the inward flow passage cannot be used for the second flow passage. However, new correlations are derived to fit the data of the serpentine passage. For the leading edge, root-mean-square differences of 6.81 percent and 7.12 percent are found in the first and third passage, and 6.90 percent and 7.13 percent are in the second and fourth passage. Also for the trailing edge root-mean-square, differences of 6.31 percent and 8.91 percent are in the first and third passage and 4.04 percent and 7.17 percent are in the second and fourth passage. The experimental data of Wagner et al. (1991b) for uniform wall temperature, and Yang et al. (1992), Han et al. (1993), and Mochizuki et al. (1994) for uniform wall heat flux are also presented. The data of Yang et al. (1992), Han et al. (1993), and Mochizuki et al. (1994) fit generally well with the present correlations on both the trailing and leading edges. Possibly due to the thermal boundary condition of constant wall temperature, the data of Wagner et al. (1991b) show large rms (root-mean-square) errors from the present correlation.

4.6 Heat Transfer in Bend Regions. There are three bend regions in the present four-pass serpentine channel. The cooling area and the cooling capacity of bend regions cannot be overlooked. Figure 10 shows the Nusselt number ratio Nu_Ω/Nu_∞ versus Re at the first and second points of these three bends. It is easy to understand that the trailing wall at the first point and the leading wall at the second point have larger values of the Nusselt number in $Re \leq 10{,}000$ (Han et al., 1993). At higher values of Reynolds number, say $Re \geq 20{,}000$, no appreciable difference in the heat transfer of trailing and leading walls is observed, regardless of the position of measurement. Yang et al. (1992) obtained higher values of the Nusselt number ratio than the present study did. Yang et al. (1992) used a round turn in their serpentine channel instead of rectangular ones in Han et al. (1993) and the present study. Although the flow in a bend region of a rotating passage is extremely complicated, it seems reasonable to speculate that the rectangular bend has a more complex secondary vortex system and better mixing than a round turn and, in turn, a higher heat transfer rate.

5 Concluding Remarks

In heated, radially rotating flow passages, the experiments have provided a comprehensive discussion of heat transfer characteristics in a serpentine channel. To meet the real engine conditions, the

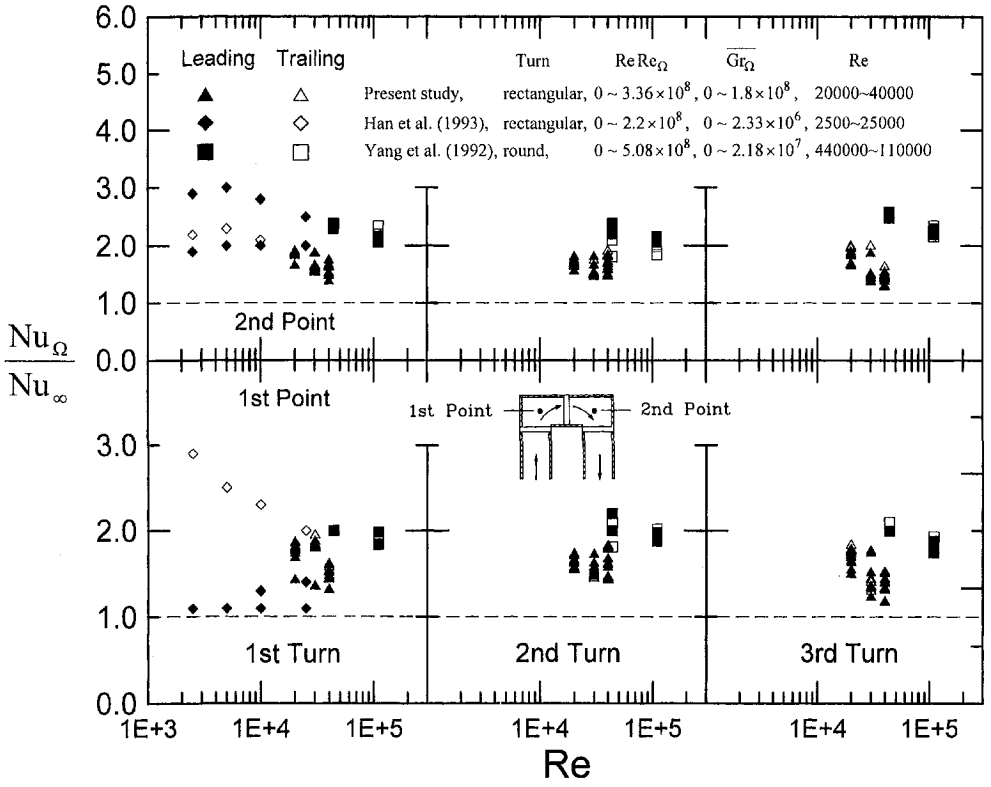

Fig. 10 The Nusselt number ratio Nu_Ω/Nu_∞ versus Re in bend regions

intake coolant was pressurized at 5 atmospheric and cooled to increase the density ratio before entering the rotating ducts to achieve a high rotation number and Grashof number simultaneously. Therefore, one is able to obtain, in the test rig, the values of the Reynolds number, Rotation number, and Grashof number similar to that of a real turbine engine.

This investigation has presented results of the effect of the Coriolis-induced cross-stream and centrifugal-buoyancy radial secondary flows on the convective heat transfer of flow in a rotating square serpentine channel. The secondary flow associated with the Coriolis and buoyancy forces results in the difference between the rotating and nonrotating flow cases. In the outward flow, the rotation-induced cross-stream secondary flow enhances the heat transfer on the trailing edge. On the contrary, the heat transfer on the leading edge is not enhanced. In a turbulent flow regime (Re $\geq$ 20,000), the heat transfer rate increases with an increase in centrifugal buoyancy effect characterized by a rotational Grashof number. It is noted that the effects of the rotation number on heat transfer coefficients are the most pronounced in the first passage due to an increase in the rotational Grashof number. Due to the stronger secondary flow and better vortex-generation capability, it is not continue that heat transfer enhancement is significant at all bend regions. The heat transfer data of the serpentine flow passage on the leading and trailing edges are correlated for Re = 20,000 ~ 40,000, Ro = 0.042–0.21, and Gr* ~ 0.024. The data of constant wall heat flux in the present study and existing literature lie within ten percent of these correlation equations. The data of constant wall temperature show large deviations from the correlation.

Acknowledgment

The authors wish to express their appreciation to the National Science Council, Taiwan (Grant No. NSC-87-2212-E-007-048), for the financial support.

References

Abdelmeguid, A. M., and Spalding, D. B., 1979, "Turbulent Flow and Heat Transfer in Pipes with Buoyancy Effects," *Journal of Fluid Mechanics,* Vol. 94, pp. 383–400.

Buhr, H. O., Horsten, E. A., and Carr, A. D., 1974, "The Distortion of Turbulent Velocity and Temperature Profiles on Heating for Mercury in a Vertical Pipe," ASME JOURNAL OF HEAT TRANSFER, Vol. 96, pp. 152–158.

Cotton, M. A., and Jackson, J. D., 1987, "Calculation of Turbulent Mixed Convection in a Vertical Tube Using a Low-Reynolds-Numerical κ-ϵ Turbulence Model," presented at the 6th Symposium on Turbulent Shear Flows, Toulouse, France.

Dittus, F. W., and Boelter, L. M. K., 1930, "Heat Transfer in Automobile Radiators of the Tubular Type," University of California Publications in Engineering, Vol. 2, No. 13, pp. 443–461, reprinted in *Int. Comm. Heat Mass Transfer,* Vol. 12, 1985, pp. 3–22.

Han, J. C., and Zhang, Y., 1992, "Effect of Uneven Wall Temperature on Local Heat Transfer in a Rotating Square Channel With Smooth Walls and Radial Outward Flow," ASME JOURNAL OF HEAT TRANSFER, Vol. 114, pp. 850–858.

Han, J. C., Zhang, Y. M., and Kalkuehler, K., 1993, "Uneven Wall Temperature Effect on Local Heat Transfer in a Rotating Two-Pass Square Channel With Smooth Walls," ASME JOURNAL OF HEAT TRANSFER, Vol. 115, pp. 912–920.

Han, C. J., Zhang, Y. M., and Lee, C. P., 1994, "Influence of Surface Heating Condition on Local Heat Transfer in a Rotating Square Channel With Smooth Walls and Radially Outward Flow," ASME *Journal of Turbomachinery,* Vol. 116, pp. 149–158.

Holman, J. P., 1989, *Heat Transfer,* McGraw-Hill, New York.

Hwang, G. J., and Kuo, C. R., 1997, "Experimental Study and correlations of Convective Heat Transfer in a Radially Rotating Serpentine Passage," ASME JOURNAL OF HEAT TRANSFER, Vol. 119, pp. 460–466.

Ito, H., and Nanbu, K., 1971, "Flow in Rotating Straight Pipe of Circular Cross Section," ASME *Journal of Basic Engineering,* Vol. 93, pp. 383–394.

Kline, S. J., and McClintock, F. A., 1953, "Describing Uncertainties in Single Sample Experiments," *Mechanical Engineering,* Jan., pp. 3–8.

Mochizuki, S., Yamawaki, S., and Yang, W. J., 1994, "Heat Transfer in Serpentine Flow Passages With Rotation," ASME *Journal of Turbomachinery,* Vol. 116, pp. 133–140.

Morris, W. D., and Ghavami-Nasr, G., 1991, "Heat Transfer in Rectangular Channel with Orthogonal Mode Rotation," ASME *Journal of Turbomachinery,* Vol. 113, pp. 339–345.

Wagner, J. H., Johnson, B. V., and Hajek, T. J., 1991a, "Heat Transfer in Rotating Passages with Smooth Walls and Radial Outward Flow," ASME *Journal of Turbomachinery,* Vol. 113, pp. 42–51.

Wagner, J. H., Johnson, B. V., and Kopper, F. C., 1991b, "Heat Transfer in Rotating Serpentine Passages With Smooth Walls," ASME *Journal of Turbomachinery,* Vol. 113, pp. 321–330.

Yang, W. J., Zhang, N., and Chiou, J., 1992, "Local Heat Transfer in a Rotating Serpentine Flow Passage," ASME JOURNAL OF HEAT TRANSFER, Vol. 114, pp. 354–361.

Free Jet Impingement Heat Transfer of a High Prandtl Number Fluid Under Conditions of Highly Varying Properties

J. E. Leland
Air Force Research Laboratory,
Wright Patterson AFB, OH 45433-7251
e-mail: john.leland@afrl.af.mil
Assoc. Mem. ASME

M. R. Pais
Cudo Technologies,
Chicago, IL 60010
Assoc. Mem. ASME

An experimental investigation was performed to determine the heat transfer rates for an impinging free-surface axisymmetric jet of lubricating oil for a wide range of Prandtl numbers (48 to 445) and for conditions of highly varying properties (viscosity ratios up to 14) in the flowing film. Heat transfer coefficients were obtained for jet Reynolds numbers from 109 to 8592, nozzle orifice diameters of 0.51, 0.84 and 1.70 mm and a heated surface diameter of 12.95 mm. The effect of nozzle to surface spacing (1 to 8.5 mm), was also investigated. Viscous dissipation was found to have an effect at low heat fluxes. Distinct heat transfer regimes were identified for initially laminar and turbulent jets. The data show that existing constant property correlations underestimate the heat transfer coefficient by more than 100 percent as the wall to fluid temperature difference increases. Over 700 data points were used to generate Nusselt number correlations which satisfactorily account for the highly varying properties with a mean absolute error of less than ten percent.

Introduction

Interest in using lubricating oils as coolants is increasing in spite of their being poor heat transfer fluids, especially in sophisticated systems such as electrical drive systems in aircraft (Pais et al., 1995), integrated starter/generator turbine engines (Ferreira and Richter, 1993), and terrestrial engine/generator sets. Lubricating oil is an attractive coolant for aircraft applications because it is generally in close proximity to the electrical generating equipment. It is also pre-existing on aircraft and therefore does not require (1) flight qualification, (2) new maintenance procedures, (3) additional inventory space and logistics procedures, and (4) additional environmental protection guidelines. These four advantages translate into greatly reduced operational costs which may far outweigh any loss in cooling efficiency. Lubricating oils such as Coolanol and its replacement, polyalphaolephin (PAO), and even jet fuel (being considered as a coolant alternative (Pais et al., 1993)) are generally known for their large Prandtl number and strong dependance of viscosity on temperature. These oil-cooled systems must operate over a large-temperature range, 233–393 K, and consequently large variation in coolant Prandtl number. Because of the lack of applicable correlations, it is of great interest to the aircraft industry to obtain jet impingement heat transfer prediction capability using these fluids over wide Prandtl number ranges.

Jet impingement heat transfer is known for its ease of implementation and high heat transfer coefficients. It has been employed for the drying of paper and textiles, tempering glass, bearing cooling, turbine blade cooling, and electronics cooling. Many excellent surveys have been performed for air jet impingement (Livingood and Hrycak, 1973; Martin, 1977; Downs and James, 1987), liquid jet impingement (Webb and Ma, 1995), comparison of jet impingement versus spray impingement (Gu et al., 1993), numerical modeling of jet impingement (Polat et al., 1989), and boiling jet impingement (Wolf et al., 1993).

Metzger et al. (1974) were perhaps the first to investigate the effects of Prandtl number on jet impingement heat transfer. Their experiments were conducted using both water and synthetic lubricating oil issued from a long pipe type nozzle and impinging on a heated copper disk. For the oil, $85 \leq \mathrm{Pr} \leq 151$ and $2.2 \times 10^3 \leq \mathrm{Re} \leq 12.1 \times 10^3$. The following correlation was proposed for the lubricating oil:

$$\mathrm{Nu}_d = 2.65\ \mathrm{Re}_d^{0.47}\ \mathrm{Pr}^{0.24}(D/d)^{-0.68}(\mu_{aw}/\mu_w)^{0.37} \qquad (1)$$

where all properties are based on T_{aw}, except μ_w, which is based on T_w. The adiabatic wall temperature was obtained from

$$r^* = \mathrm{Pr}^n = 2c_p(T_{aw} - T_j)/U^2 \qquad (2)$$

where $n = 0.6$. The data also showed a definite dependence of r^* on the nozzle diameter, d. Metzger et al. (1974) obtained the majority of their heat transfer data for $T_w - T_{aw} = 3.3$ K to avoid the problem of variable properties. The effect of viscous dissipation for large Prandtl numbers becomes extremely important in the calculation of the heat transfer coefficient for temperature differences of this order because $T_{aw} - T_j$ is of the same order as $T_w - T_{aw}$. A limited number of data were obtained for $T_w - T_{aw}$ equal 8.9 and 17.8 K to study the effects of variable properties. Increasing the temperature difference had the effect of increasing the heat transfer coefficient. The ratio, μ_{aw}/μ_w, specifically accounts for the variable properties and Eq. (1), was stated to be valid for $1.0 \leq \mu_{aw}/\mu_w \leq 1.7$.

Ma et al. (1990) later studied the effects of Prandtl number on local heat transfer. They obtained results for a jet of transformer oil or ethylene glycol issuing from a pipe-type nozzle onto a resistively heated 20-μm thick constantan foil. The Prandtl number ranges were 202 to 260 and 80 to 127, respectively. The exponent, n, in Eq. (2) was experimentally found to equal 0.5, which is also equal to that generally used for high-speed air flows. The majority of their results were obtained for the submerged jet although a few data were obtained for the free jet. Although the free-jet data were not explicitly correlated, it was found to match the submerged-jet data very near the stagnation zone, $r/d < 2.5$. No attempt was made to account for variable properties although data were obtained for $T_w - T_j$ up to 49.8 K.

Ma et al. (1997a) studied free-surface obliquely impinging jets for transformer oil issuing from a pipe-type nozzle onto a 10-μm

Contributed by the Heat Transfer Division for publication in the JOURNAL OF HEAT TRANSFER. Manuscript received by the Heat Transfer Division, Oct. 24, 1997; revision received, Apr. 12, 1999. Keywords: Cooling, Forced Convection, Heat Transfer, Jets. Associate Technical Editor: J. Han.

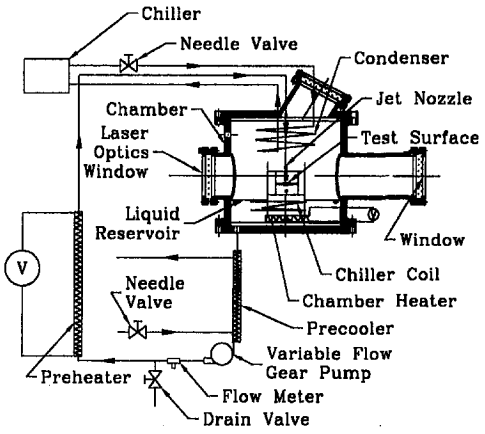

Fig. 1 Flow loop schematic

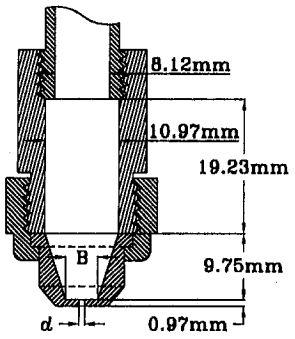

Fig. 2 Nozzle schematic

thick constantan foil. The angle of the jet was varied from 45 deg to 90 deg. Local heat transfer results were correlated by the equation

$$\mathrm{Nu}_r = 0.00275\ \mathrm{Re}^{1/2}\ \mathrm{Pr}^{1/3}\ \frac{\mathrm{Re}^{0.0274|r/d|}}{1 + 0.145|r/d|^{1.733}} \qquad (3)$$

which has been simplified for the case of an orthogonally impinging jet. All properties were based on the film temperature, which was the average of the jet and wall temperatures. In their experiments, Ma et al. (1997a) were careful to maintain the difference between T_w and T_{aw} at 10 K, thus also avoiding the issue of variable properties.

For aircraft systems, the lubricating oil systems may operate at temperature extremes of from 233 K to over 393 K. The typical operating temperature range is from 303 K to 373 K, though, and the cooled component temperature may reach as high as 423 K, (i.e., $T_w - T_{aw} = 120$ K and $\mu_{aw}/\mu_{aw} > 14$. This study explores the effects of extended Prandtl number and property variation due to large wall-to-fluid temperature differences on free-jet impingement heat transfer.

Experimental Apparatus

The experimental apparatus (see Fig. 1) has three primary components, the flow loop, nozzle, and heat transfer surface. The flow loop consists of a magnetically coupled gear pump, preheater, flow meter, chiller, and test chamber. The preheater is used to obtain the desired jet temperature. The test fluid flows into the pool/reservoir in the chamber after impinging on the test heater. Chilled water flowing through a coil heat exchanger is used to maintain the reservoir fluid at a preset temperature. The test chamber was well insulated and a kapton heater was used to maintain the air space at the fluid temperature to prevent heat loss from the jet. The test chamber allowed independent control of system pressure, but was left open to the atmosphere for all tests with lubricating oil.

The geometry and dimensions of the jet nozzle are shown in Fig. 2. The nozzle body was supplied by a 8.12-mm ID tube 16 diameters long. The supply tube passed through the chamber wall via an o-ring seal. This allowed the nozzle-to-surface distance to be adjusted by sliding the tube up or down. Three different orifice diameters were used and are listed in Table 1. This orifice design was selected because it most closely models what would be used in application, (see Pais et al. (1995) or Jiji and Dagan (1987, 1992) and Pan et al. (1992)).

The heat transfer surface is shown in Fig. 3 and consists of a 12.95-mm diameter oxygen-free copper block. The copper block was enclosed in low thermal conductivity (0.3 W/mK) rigid insulation and heated from below by a resistively heated nichrome wire sandwiched between two plates of boron nitride. The sides of the copper block were well sealed against the insulating enclosure to prevent fluid from leaking into the module. High-temperature silicone sealant was used for this purpose. The exposed face of the copper block was sanded and glass beaded (34 μm nominal bead dia.). The surface was then cleaned with potassium hydroxide followed with methanol to remove finger oil, silicone residue, and other residue. The surface roughness was measured and an ISO roughness standard, R_a, was found to be 5 nm $\pm$ 1 nm. Three 0.12-mm wire diameter type-T thermocouples were imbedded in the copper block through 0.5-mm diameter holes and were used to calculate the heat flux. The heat loss was calculated as the difference between the measured flux at the surface and the electrical power in. Heat loss was greater than 40 percent for Nu_d less than 10 but decreased to less than 15 percent for Nu_d greater than 50.

The presently used surface configuration was selected because it most closely models the heat transfer situations of interest such as the cooling of aluminum stator housings (Pais et al., 1995) or power electronics which are typically packaged with thick (>2.5 mm) copper bases. Wang et al. (1989) analytically studied the effect of surface thickness and thermal conductivity on heat transfer for a laminar free surface impinging jet of water. For a thick surface or high surface thermal conductivity, large radial variations

Nomenclature

c_p = specific heat
d = jet diameter
D = heated surface diameter
h = heat transfer coefficient
k = fluid thermal conductivity
L = length of square heater, Eq. (5)
m = number of jets, Eq. (5)
Nu_d = surface averaged Nusselt number, hd/k
Pr = Prandtl number, $\mu c_p/k$
q = heat flux
r = radial coordinate
r^* = recovery factor
R_a = ISO R468 parameter for surface roughness
Re_d = Reynolds number, Ud/ν
T_f = film temperature $(T_{aw} + T_w)/2$
U = bulk average jet velocity
z = nozzle to surface distance
ρ = density
μ = dynamic viscosity

Subscripts

aw = property based on adiabatic wall temperature
avg = average
j = property based on jet temperature
max = maximum
w = property based on wall temperature

Table 1 Nozzle dimensions

d [mm]	B [mm]
0.508	2.79
0.838	4.83
1.702	4.83

of the imposed temperature or heat flux profiles had a negligible impact on local heat transfer coefficients. For thinner and low thermal conductivity surfaces, the same imposed temperature and heat flux profiles caused large radial variation, (>20 percent), in the local heat transfer values. Rahman et al. (1998a) performed a numerical investigation of the effects of heat transfer surface thickness and thermal conductivity on jet impingement heat transfer. To illustrate the dramatic effect of surface configuration, their results are summarized in Table 2 for the present surface configuration and an alternate configuration more commonly used in jet impingement studies. Note that while the thick copper surface has a much lower h_{avg}, it also has a lower maximum surface temperature and a much lower maximum surface temperature variation, ΔT_{max}.

Uncertainty Analysis

A Hewlett Packard 3852A data acquisition system was used to make all voltage and temperature measurements. This device has a resolution of 0.02°C and rated accuracy of 0.65°C for type-T thermocouples. The data acquisition unit and type-T thermocouples were calibrated as a unit, using a precision digital RTD, (0.03°C rated accuracy), over the temperature range of interest. The system accuracy for temperature measurement was better than 0.1°C after calibration. The uncertainty of the velocity calculation was dominated by the uncertainty of the positive displacement flow meter which was 0.5 percent of the reading. Flow velocity was based on the orifice cross-sectional area.

The individual temperatures given by two type-T thermocouples, 2.54 and 7.44 mm from the top surface (see Fig. 3) and one-dimensional approximation of the heat conduction were used to calculate the heat flux, q. A third thermocouple, 12.3 mm below the surface, was used to obtain a corroborating measurement for heat flux. The validity of the one-dimensional approximation was confirmed by a detailed numerical model of the conjugate heat transfer problem (Rahman et al., 1998b). The uncertainty of the thermal conductivity, bead location in the holes, hole locations, and the temperatures were considered as well (see Leland (1994) for details). The standard Kline and McClintock (1953) approach to random uncertainty shows that the error of the heat flux calculation decreases rapidly as the heat flux increases. Random uncertainty analysis also shows that the heat flux calculation is dominated by the uncertainty of the temperature measurements for heat fluxes less than 30 W/cm^2. For heat fluxes of 11.9, 31.2, and 65.1 W/cm^2, random uncertainties were 10.0, 4.9, and 3.7 percent, respectively.

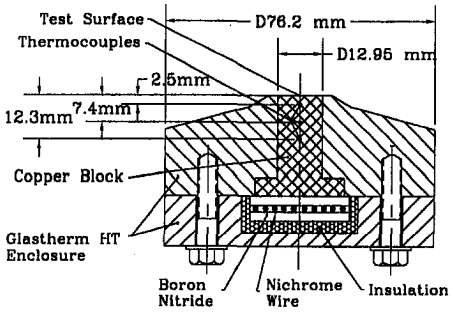

Fig. 3 Heater schematic

Table 2 Surface-dependent heat transfer and temperature data

Material	Thickness [mm]	h_{avg} [W/m^{2}K]	T_{max} [K]	ΔT_{max} [K]
copper	10	3.9	388	1.3
constantan	0.125	10.9	404	18

$Re_d = 550$, $T_j = 348$ K, $z = 8.5$ mm, $q = 63$ kW/m^2

The wall temperature, T_w, was extrapolated using the same temperature difference for calculating the heat flux. The uncertainty in T_w ranged from 0.26 to 0.32 K over the range of experimental values obtained. The error in T_w increased with heat flux so the impact on Nusselt number became less for larger film coefficients. The average jet temperature, T_j, was measured with an exposed bead 0.76-mm diameter type-T probe thermocouple. This thermocouple was also calibrated to 0.1°C. The film coefficient was calculated from the following equation:

$$h = q/(T_w - T_{aw}) \tag{4}$$

where T_{aw} is obtained from Eq. (2). With $n = 0.47$, Eq. (2) correlated the present results with a mean absolute error of 25 percent. This error was used to establish the uncertainty of T_{aw}. The random uncertainty in T_{aw} thus ranged from 0.10 K for combinations of small Prandtl numbers and velocities to 1.8 K for combinations of large Prandtl numbers and velocities. The first approximation of the film temperature, $(T_w + T_j)/2$, was used to calculate the Prandtl number in Eq. (2). Thus, the uncertainty of T_{aw} was smaller for higher heat fluxes. The average uncertainty in T_{aw} for all the data was 0.35 K.

Finally, the equations for the random uncertainties of q, T_{aw}, and T_w were combined to obtain the uncertainty of the heat transfer coefficient Eq. (4). The Kline and McClintock (1953) approach to random uncertainty analysis shows that the heat transfer coefficient calculation is dominated by the uncertainty in q and T_{aw} for small heat transfer coefficients and by the other temperature measurements for larger heat transfer coefficients. Remember that the uncertainty in T_{aw} is greatest for large Prandtl numbers and especially for large-jet velocities. For 83 percent of the data, the uncertainty was between three and five percent. Another 13 percent of the heat transfer coefficient data had an uncertainty of between five and ten percent. The remaining four percent of the data had an uncertainty of between 10 and 31 percent with the majority of these data tending toward ten percent uncertainty. The random uncertainty in the Nusselt number is essentially equal to the uncertainty in the heat transfer coefficient. Thus, the accuracy of the measured Nusselt numbers is quite good.

Several runs for increasing and decreasing heat flux were conducted to determine the repeatability of the results. The repeatability was well within the experimental error, thus indicating that the above results are conservative.

Experimental Procedure

For each series of tests with a particular nozzle, the nozzle-to-wall distance was adjusted to attain a desired distance. This distance was then measured with a dial indicator and recorded. For each test run, the desired flow rate was attained and power to the preheater and coolant flow rate of the chiller were then adjusted to obtain the desired jet temperature. Once test conditions were reached, the surface was allowed to come to steady-state and adiabatic wall temperature measurements were made. Power to the test heater was then increased in 10-W increments until an input power of 100 W or a maximum heater temperature of about 455 K was achieved. Temperatures were held at steady-state for a period of ten minutes before readings were recorded.

Results

Over 700 data points have been obtained covering $109 \leq Re_d \leq 8592$, $48 \leq Pr \leq 445$, and surface to jet-diameter ratios, D/d, of

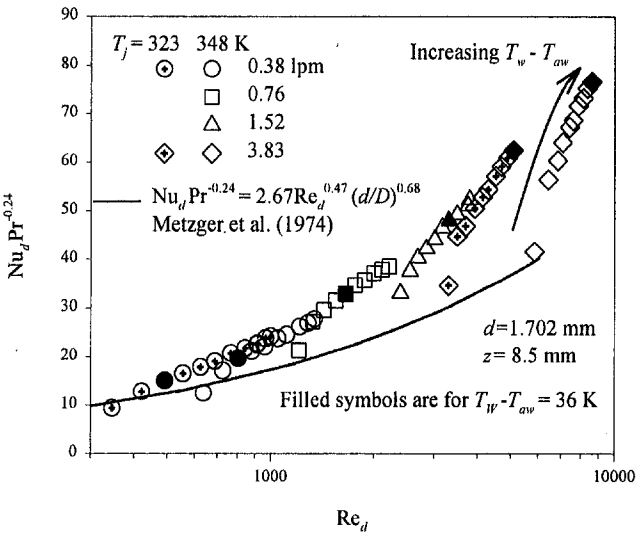

Fig. 4 Nu_d versus Re_d for T_j = 343 K and constant flow rates

7.61, 15.45, and 25.49 which correspond to the nozzle diameters listed in Table 1 and a surface diameter of 12.95 mm. The surface to nozzle spacing, z, was varied from 1 to 8.5 mm which yielded z/d ratios of 1.19 to 7.87. Variable properties in the post impingement film were the result of large wall-to-jet temperature differences, $T_w - T_j$. A maximum wall-to-jet temperature difference of 130 K was measured during these experiments. The effect of variable properties is embodied in the adiabatic wall-to-wall viscosity ratio, μ_{aw}/μ_w, which ranged from 1 to 14.28. It is important to note that all properties are based on the film temperature, $T_f = (T_{aw} + T_w)/2$, unless otherwise noted by a subscript.

Adiabatic Wall Temperature

The adiabatic wall temperature, T_{aw}, is predicted using Eq. (2) where $n = 0.47$ was found by correlation with experimental data. For the prediction of T_{aw}, the Prandtl number in Eq. (2) was based on the first approximation of the film temperature or $(T_j + T_w)/2$ rather than T_j alone. This was done because Pr will change under increased T_w and viscous dissipation should reduce as the film heats up across the surface. This approach also led to better correlations for Nu_d

Equation (2) is commonly used to calculate the adiabatic wall temperature (Kays and Crawford, 1980). Metzger et al. (1974) were the first to show the significance of viscous dissipation for impinging jets of high Prandtl number yet moderate velocity. They showed a clear dependance of T_{aw} on d. Gardon and Cobonpue (1961) using air jets noted a dependence of T_{aw} on parameters, z/d and d, as well as the Prandtl number. They noted that $(T_{aw} - T_j)$ was a maximum at z/d = 10. Goldstein et al. (1986) in his study with air jets showed that the recovery factor r^* varies dramatically with r near the stagnation zone. A dependence on nozzle-to-wall spacing and a possible, albeit slight, dependence on the Reynolds number was also noted. During the process of the present study, several significant experimental investigations by Ma et al. (1997a, b, c) and one numerical investigation by Lee et al. (1997) concerning the recovery factor were published. Data for the fully developed axisymmetric free jet (Ma et al., 1997a) using transformer oil is qualitatively similar to that of Goldstein et al. (1986) but showed a strong dependency on radial position outside of the stagnation zone and an added dependence on impingement angle. A numerical confirmation of these results was performed by Lee et al. (1997). The numerical results confirmed most of the observed trends but showed no dependence of r^* on d for a small range of d.

Although the above works conclusively show that the recovery factor is sensitive to many parameters other than the Prandtl number, Eq. (2) has been found by previous researchers to give adequate results. Metzger et al. (1974) correlated Eq. (2) with n = 0.6 for a fully developed jet of lubricating oil issuing from a tube-type nozzle onto a 3-mm thick copper surface. Ma et al. (1990) correlated Eq. (2) with $n = 0.5$ for a fully developed jet of transformer oil issuing from a tube-type nozzle onto a 20-μm thick constantan surface. Thus, the exponent of 0.47 found in this study compares well with previous work and the use of Eq. (2) is more than adequate because T_{aw} is less important in calculating the heat transfer coefficient for the large $T_w - T_j$ data which are the focus of this study.

Nusselt Number Data

Figure 4 illustrates the importance of considering varying properties when utilizing existing correlations. The effect of $T_w - T_{aw}$ on Nu_d is plotted for different flow rate and T_j pairs. At very low values of $T_w - T_{aw}$, the data compare very well with the correlation generated by Metzger et al. (1974) for transformer oil. This correlation was derived from data for $T_w - T_{aw}$ = 3.3 K. As $T_w - T_{aw}$ increases for a given flow rate and T_j, the data diverge from the correlation. The error increases beyond 100 percent for large Re_d and $T_w - T_{aw}$. For each flow rate and T_j pair the data points for $T_w - T_{aw} \approx 36$ K are filled. These data points show how the data for a given value of $T_w - T_{aw}$ diverge from the correlation with increasing Re_d. Figure 5 shows the effect of Pr, T_j and $T_w - T_{aw}$ on Nu_d. For each flow rate and T_j pair, $T_w - T_{aw}$ increases to the left and upward. For T_j = 303 K, increasing $T_w - T_{aw}$ causes a large reduction in Pr but modest increase Nu_d. As T_j increases, the same $T_w - T_{aw}$ causes a smaller decrease in Pr but a larger increase in Nu_d. The filled symbols represent data for $T_w - T_{aw}$ = 31 K. Note that the effect of $T_w - T_{aw}$ on Nu_d is stronger for larger flow rates, (or $Re_{d,j}$). Finally, note that the data for different flow rates begins to converge as Pr increases. Thus, for a sufficiently high Pr, a change in $Re_{d,j}$ may have little or no effect on Nu_d.

The effect of nozzle diameter is shown in Fig. 6. Higher Nusselt numbers are achieved for the larger nozzle diameter for the same Re_d. However, this does not imply that h is greater. In fact, given the same flow rate, T_f and T_j, h is higher for the 0.508-mm nozzle. Metzger et al. (1974) obtained similar results for a constant nozzle diameter and varying heater diameter, D. Ma et al. (1990) have shown that the nozzle-to-wall separation distance has a negligible effect on stagnation point heat transfer $z/d \leq 8$ for free-surface jet impingement. The present data taken for $1.9 < z/d < 4.8$ corroborates their results.

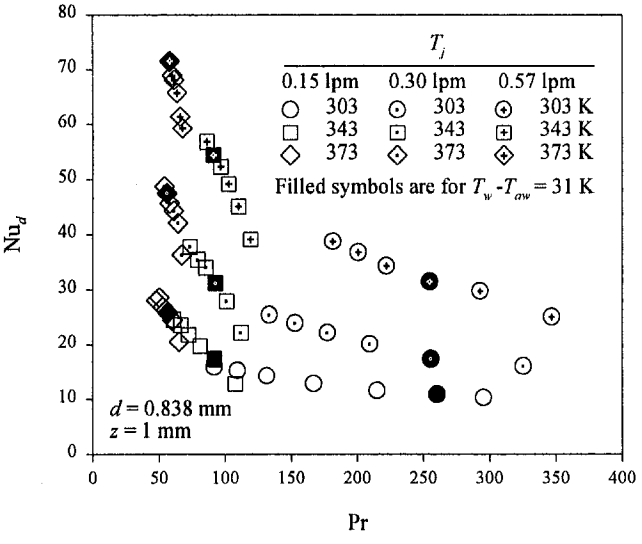

Fig. 5 Nu_d versus Pr for various jet temperatures

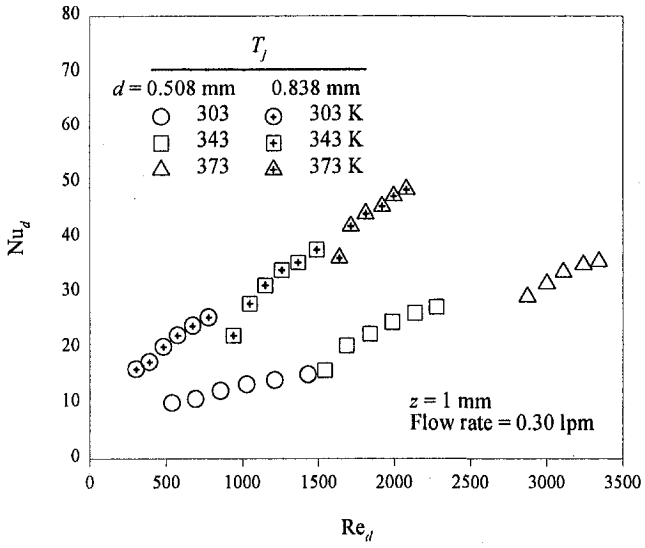

Fig. 6 Comparison of Nu_d for different nozzle diameters

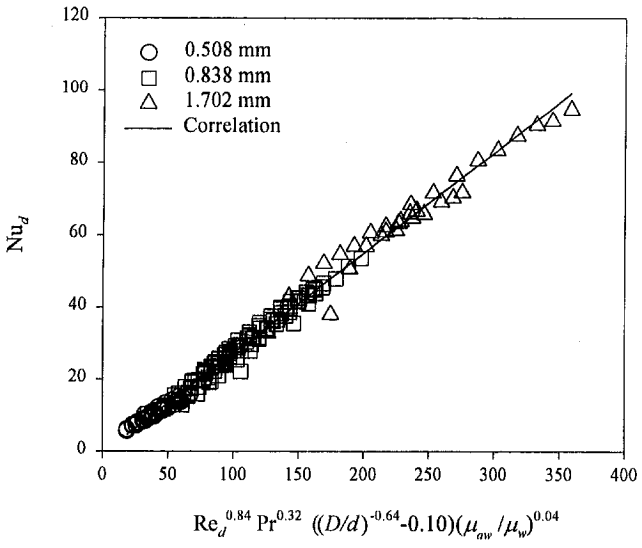

Fig. 7 Comparison of data to correlation for laminar jet

Nusselt Number Correlations

The results presented in the previous section show that the Nusselt number is a function of Re_d, Pr, D/d, and $T_w - T_{aw}$ but not z/d for the range of the variables studied. The effect of variable properties is generally accounted for by including the ratios of μ_j/μ_w, T_w/T_j. Metzger et al. (1974) correlated data for synthetic lubricating oil for, $85 \le Pr \le 151$, $2200 \le Re_d \le 12100$, $1.75 \le D/d \le 25.1$, and $1.0 < \mu_{aw}/\mu_w < 1.7$ where Re_d and Pr are based on T_{aw} rather than T_f, to obtain Eq. (1). The present data match their results for small values of $T_w - T_{aw}$, (i.e., $\mu_{aw}/\mu_w < 2$). However, for larger values of $T_w - T_{aw}$, the correlation either under or over predicts even though the other parameters are within range. Another possible reason for the incongruence is the type of nozzles used (orifice in the present as opposed to pipe type in theirs). For data outside the valid range of Re_d and Pr, Eq. (1) under and over predicts by as much as 36 percent and 340 percent, respectively.

Jiji and Dagan (1987) obtained the following correlation for single and multiple-jet impingement of water and FC-77 for $5 \le Pr \le 27$, $3100 \le Re_d \le 12{,}300$, $12.7 \le L/d \le 25.4$ and $m = 1$, 4, or 9, where the properties are based on $T_f = (T_w + T_j)/2$:

$$Nu_L = 3.84\ Re_d^{1/2}\ Pr^{1/3}(0.008mL/d + 1). \quad (5)$$

This equation fits the present data well for $Re_d > 1000$ and $Pr < 100$. The correlation rapidly diverges and significantly overestimates Nu_d for $Re_d < 1000$ and modestly underestimates Nu_d for $Pr > 100$.

The realistic use of high Pr fluids with large $T_w - T_{aw}$ in actual applications has created a need for correlations that account for large variations of properties within the boundary layer. Based on the correlations of Azuma and Hoshino (1984a and 1984b) and Liu et al. (1991) it was determined that the films generated in the current experiments were laminar and far from transition to turbulence. In a numerical study of the present experiment, Rahman (1998b) has determined that a transition to turbulence begins to occur at the very edge of the heat transfer surface for large values of Re_d. Nevertheless, analysis of the current data indicates a clear distinction in the Nu_d for $Re_{d,j} < 800$ and $Re_{d,j} > 1100$. For intermediate $800 < Re_{d,j} < 1100$, the data follows either trend or falls in between. This disparity is explained by the results of Ellison and Webb (1994) who showed that the state of the jet being laminar or turbulent prior to impingement can have an effect on the heat transfer. The current results were correlated for $Re_d < 800$ and $Re_d > 1100$ and are represented by Eqs. (6) and (7), respectively. The data were first subdivided to accurately determine the dependancies on Re_d, Pr and the other variables. A weighted least-squares technique was used to calculate the constants and coefficients: For an initially laminar jet

$$Nu_d = 0.28\ Re_d^{0.84}\ Pr^{0.32}\left(\left(\frac{D}{d}\right)^{-0.64} - 0.10\right)\left(\frac{\mu_{aw}}{\mu_w}\right)^{0.04}, \quad (6)$$

and for an initially turbulent jet

$$Nu_d = 1.78\ Re_d^{0.58}\ Pr^{0.22}\left(\left(\frac{D}{d}\right)^{-0.32} - 0.30\right)\left(\frac{\mu_{aw}}{\mu_w}\right)^{0.27}. \quad (7)$$

Note that the Prandtl number exponent is very near the commonly used value of $\frac{1}{3}$ for the laminar jet case and is very close to the value found by Metzger et al. (1974) (see Eq. (1)) for the turbulent case. It is also interesting to note that the Reynolds number dependencies are very similar to those found by Ellison and Webb (1994) for laminar and turbulent jets. Figures 7 and 8 show how the data compare to these correlations. The laminar and turbulent correlations fit the data with mean absolute errors of 5.4 percent and 7.0 percent, respectively. To predict Nu_d for $800 \le Re_d \le$

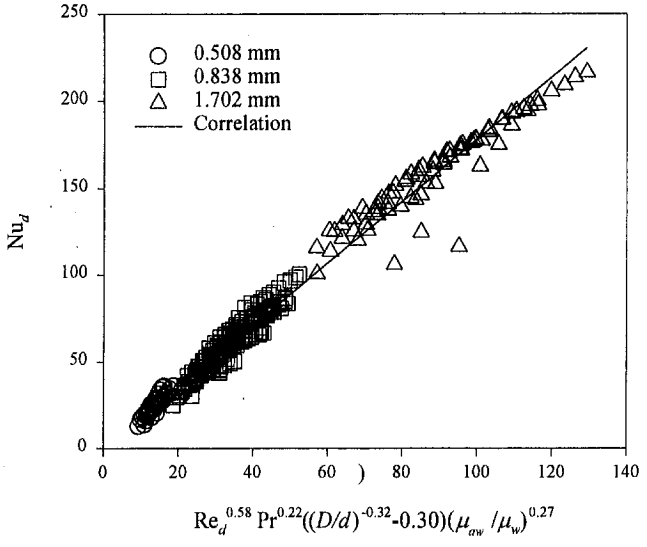

Fig. 8 Comparison of data to correlation for turbulent jet

1100, it is suggested that Eqs. (6) and (7) be averaged. The outlying points are for very low $T_w - T_{aw}$ and large flow rates where the random uncertainty is greatest and variable properties are hardest to compensate for, (see Fig. 4). Thus, the correlation of Metzger et al. (1974) is recommended for very low $T_w - T_{aw}$ conditions.

Conclusions

Over 700 data points were obtained for a wide range of conditions, (i.e., $109 \leq \mathrm{Re}_d \leq 8592$, $48 \leq \mathrm{Pr} \leq 445$, and surface-to-jet diameter ratios, D/d, of 7.61, 15.45, and 25.49), and highly varying properties, (a wall to jet temperature difference of 130 K was measured). The effect of variable properties is embodied in the adiabatic wall to wall viscosity ratio, μ_{aw}/μ_w, which ranged from 1 to 14.28. The data were correlated with excellent accuracy. A division in the data for laminar and turbulent jet conditions led to the generation of two correlations, Eqs. (6) and (7), with mean absolute errors of 5.4 percent and 7.0 percent, respectively. The use of the film temperature for the calculation of the properties was critical to obtaining such an excellent fit. These equations will provide a predictive capability that is useful in the design of practical heat transfer equipment for the cooling of electronics, generators, and other systems utilizing high Pr coolants. Other conclusions are summarized as follows:

1 Heat transfer surface configuration has an important effect on the Nusselt number and should be considered when choosing a correlation. More research is needed on this topic.

2 The effect of recovery temperature should not be ignored for small Nu_d. The recovery factor was correlated by $\mathrm{Pr}^{0.47}$ although a dependance on other parameters such as the surface-to-nozzle diameter ratio and Reynolds number was witnessed.

3 In agreement with the literature, the effect of nozzle-to-surface spacing on Nu_d was found to have a negligible effect for $z/d \leq 4.8$.

4 For constant Re_d, larger nozzle diameters yielded higher Nu_d. However, for constant Re_d, T_f, and T_j, h is higher for smaller nozzles.

5 For high Prandtl number fluids and very low wall to adiabatic wall temperature differences, the correlation of Metzger et al. (1974) Eq. (1) is recommended in place of Eqs. (6) and (7).

Acknowledgment

The authors greatly appreciate the diligent work of Mr. Richard J. Harris, University of Dayton Research Institute, in preparing the experimental setup and acquiring the large amount of data necessary for this study.

References

Azuma, T., and Hoshino, T., 1984a, "The Radial Flow of a Thin Liquid Film. First Report, Laminar-Turbulent Transition," *Bulletin of the Japanese Society of Mechanical Engineers,* Vol. 27, No. 234, pp. 2739–2746.

Azuma, T., and Hoshino, T., 1984b, "The Radial Flow of a Thin Liquid Film. Second Report, Liquid Film Thickness," *Bulletin of the Japanese Society of Mechanical Engineers,* Vol. 27, No. 234, pp. 2747–2754.

Downs, S. J., and James, E. H., 1987, "Jet Impingement Heat Transfer—A Literature Survey," ASME Paper No. 87-HT-35.

Ellison, B., and Webb, B. W., 1994, "Local Heat Transfer to Impinging Liquid Jets in the Initially Laminar, Transitional, and Turbulent Regimes," *International Journal of Heat and Mass Transfer,* Vol. 37, No. 8, pp. 1207–1216.

Ferreira, C. A., and Richter, E., 1993, "A Detailed Design of a 250 kw Switched Reluctance Starter/generator for an Aircraft Engine," *SAE Journal of Aerospace,* Vol. 102, pp. 289–300.

Gardon, R., and Cobonpue, J., 1961, "Heat Transfer Between a Flat Plate and Jets of Air Impinging on it," *Proceedings of the Second International Heat Transfer Conference,* Boulder CO, ASME, New York, pp. 454–460.

Goldstein, R. J., Behbahani, A. I., and Kieger Heppelmann, K., 1986, "Streamwise Distribution of the Recovery Factor and the Local Heat Transfer Coefficient to an Impinging Circular Air Jet," *International Journal of Heat and Mass Transfer,* Vol. 29, No. 8, pp. 1227–1235.

Gu, C. B., Su, G. S., Chow, L. C., and Pais, M. R., 1993, "Comparison of Spray and Jet Impingement Cooling," ASME Paper No. 93-HT-20.

Jiji, L. M., and Dagan, Z., 1987, "Experimental Investigation of Single Phase Multi-Jet Impingement Cooling of an Array of Microelectronic Heat Sources." *Proceedings of the International Symposium on Cooling Technology,* Pacific Institute for Thermal Engineering, pp. 265–283.

Kays, W. M., and Crawford, M. E., 1980, *Convective Heat and Mass Transfer,* McGraw-Hill, New York, pp. 296–297.

Kline, S. J., and McClintock, F. A., 1953, "Describing Uncertainties in Single-Sample Experiments," *Mechanical Engineering,* Vol. 75, Jan., pp. 3–8.

Lee, X. C., Ma, C. F., Zheng, Q., Zhuang, Y., and Tian, Y. Q., 1997, "Numerical Study of Recovery Effect and Impingement Heat Transfer with Submerged Circular Jets of Large Prandtl Number Liquid," *International Journal of Heat and Mass Transfer,* Vol. 40, No. 11, pp. 2647–2653.

Leland, J. E., 1994, "The Effects of Channel Curvature and Protrusion Height on Nucleate Boiling and the Critical Heat Flux of a Simulated Electronic Chip," Ph.D. dissertation, University of Kentucky, Lexington, KY.

Liu, X., Lienhard, V, J. H., and Lombara, J. S., 1991, "Convective Heat Transfer by Impingement of Circular Liquid Jets," ASME JOURNAL OF HEAT TRANSFER, Vol. 113, pp. 571–582.

Livingood, J. N. B., and Hrycak, P., 1973, "Impingement Heat Transfer from Turbulent Air Jets to Flat Plates—A Literature Survey," NASA TM X-2778.

Ma, C.-F., Sun, H., Auracher, H., and Gomi, T., 1990, "Local Convective Heat Transfer From Vertical Heated Surfaces to Impinging Circular Jets of Large Prandtl Number Liquids," *Proceedings of the 9th International Heat Transfer Conference,* Vol. 2, Jerusalem, Hemisphere, Washington, DC, pp. 441–446.

Ma, C. F., Zheng, Q., Sun, H., and Wu, K., 1997a, "Local Characteristics for Impingement Heat Transfer with Oblique Round Free-Surface Jets of Large Prandtl Number Liquid," *International Journal of Heat and Mass Transfer,* Vol. 40, No. 10, pp. 2249–2259.

Ma, C. F., Zheng, Q., Lee, S. C., and Gomi, T., 1997b, "Impingement Heat Transfer and Recovery Effect with Submerged Jets of Large Prandtl Number Liquid—I. Unconfined Circular Jets," *International Journal of Heat and Mass Transfer,* Vol. 40, No. 6, pp. 1481–1490.

Ma, C. F., Zhuang, Y., Lee, S. C., and Gomi, T., 1997c, "Impingement Heat Transfer and Recovery Effect with Submerged Jets of Large Prandtl Number Liquid—II. Initially Laminar Confined Slot Jets," *International Journal of Heat and Mass Transfer,* Vol. 40, No. 6, pp. 1491–1500.

Martin, H., 1977, "Heat and Mass Transfer Between Impinging Gas Jets and Solid Surfaces," *Advances in Heat Transfer,* Vol. 13, Academic Press, New York, pp. 1–60.

Metzger, D. E., Cummings, K. N., and Ruby, W. A., 1974, "Effects of Prandtl Number on Heat Transfer Characteristics of Impinging Liquid Jets," *Proceedings of the 5th International Heat Transfer Conference,* Vol. 2, Tokyo, Hemisphere, Washington, DC, pp. 20–24.

Pais, M. R., Leland, J. E., Chang, W. S., and Chow, L. C., 1993, "Jet Impingement Cooling Using a Jet Fuel," ASME Paper No. 93-HT-22.

Pais, M. R., Chow, L. C., Knee, J., Bonneau, V., Leland, J. E., and Beam, J. E., 1995, "Jet Impingement Cooling in VSCF Generators," SAE Paper No. SAE 951451, SAE Aerospace Atlantic Conference, Dayton, OH.

Pan, Y., Stevens, J., and Webb, B. W., 1992, "Effect of Nozzle Configuration of Transport in the Stagnation Zone of Axisymmetric, Impinging Free-Surface Liquid Jets: Part 2—Local Heat Transfer," ASME JOURNAL OF HEAT TRANSFER, Vol. 114, pp. 880–886.

Polat, S., Huang, B., Mujumdar, A. S., and Douglas, W. J. M., 1989, "Numerical Flow and Heat Transfer Under Impinging Jets: A Review," *Annual Review of Numerical Fluid Mechanics and Heat Transfer,* Vol. 2, Hemisphere, New York, pp. 157–197.

Rahman, M. M., Bula, A. J., and Leland, J. E., 1998, "Numerical Modeling of Conjugate Heat Transfer During Free Liquid Jet Impingement," *Proceedings of the ASME Advanced Energy Systems Division,* AES-Vol. 38, ASME, New York, pp. 475–486.

Rahman, M. M., Bula, A. J., and Leland, J. E., 1998, "Conjugate Heat Transfer During Free Jet Impingement of a High Prandtl Number Fluid," *Numerical Heat Transfer, Part A: Applications,* submitted for publication.

Wang, X. S., Dagan, Z., and Jiji, L. M., 1989, "Conjugate Heat Transfer Between a Laminar Impinging Liquid Jet and a Solid Disk," *International Journal of Heat and Mass Transfer,* Vol. 32, No. 11, pp. 2189–2197.

Webb, B. W., and Ma, C.-F., 1995, "Single-Phase Liquid Jet Impingement Heat Transfer," *Advances in Heat Transfer,* Vol. 26, Academic Press, New York, pp. 105–217.

Wolf, D. H., Incropera, F. P., and Viskanta, R., 1993, "Jet Impingement Boiling," *Advances in Heat Transfer,* Vol. 23, Academic Press, New York, pp. 1–132.

Plume Dynamics in Natural Convection in a Horizontal Cylindrical Annulus

C. E. Fisher
Fiber Optics and Electronics Technology Center,
3M Company
Building A143-5N-01,
6801 River Place Boulevard,
Austin TX 78726-9000
Assoc. Mem.

K. S. Ball
Department of Mechanical Engineering,
The University of Texas at Austin,
Austin, TX 78712-1063
e-mail: kball@burst.me.utexas.edu
Mem. ASME

Measurements of the unsteady temperature fluctuations in the plume region between differentially heated horizontal concentric cylinders are reported. In particular, power spectral density estimates of the temperature fluctuations within the plume show the development and breakdown of the oscillatory plume structure at high Rayleigh number, Ra_d, by two relatively independent processes: (1) the development of harmonic oscillations related to the dominant plume oscillation frequency, and (2) interactions between the oscillating plume and the adjacent relatively stagnant core flow (shear and entrainment). The harmonic oscillations are shown to be the dominant energy transfer mode at moderate Ra_d (up to $Ra_d = 10^8$), acting to disperse the plume energy without generating a broadband spectrum. The spectral density estimates show that while a distinct plume oscillation is still present near the inner cylinder at $Ra_d = 10^9$, the plume becomes increasingly turbulent as the outer cylinder is approached. A new correlation for the plume oscillation frequency, which is found to be proportional to $Ra_d^{0.5}$, is also presented.

Introduction

Natural convection heat transfer is an important component of many engineering systems. The existence of thermal plumes that rise from heated surfaces is a common characteristic of natural convection flows, whether the flow is in an enclosure or is unconfined. The structure of these thermal plumes is of considerable interest due to their dominant effect on the behavior of the flow (Turner, 1973). In the 1960s, researchers began investigating the development and dynamics of turbulence in buoyant flows along heated vertical plates and in free plumes, in the latter case focusing on the flowfield in the self-preserving region far away from the origin of the buoyant flow. Several theories have been put forth on the details of the spectral development of turbulent flows that include buoyancy, like stratified shear flows (Turner, 1973) or buoyant jets (Papanicolaou and List, 1987). The recent research of Dai et al. (1994, 1995) and Sangras et al. (1998) shows power spectral density (PSD) estimates from velocity and mixture fraction measurements in the self-preserving regions of buoyant turbulent plumes.

The research reported here provides new detailed measurements of the fluctuating temperature in the thermal plume arising in the natural convection flow in a differentially heated horizontal cylindrical annulus. This study examines the dynamics of the flow in the plume region, investigating primarily the breakdown of the well-defined oscillation that develops at the onset of instability in the laminar flow at low Ra_d. From the instantaneous measurements, PSD are extracted. These data show the development of fluctuations in the plume, leading to transition to turbulence in the natural convection flow.

The notion of an inertial subrange, where the energy transfer from one wave number to the next is only a function of the wave number and the spectral energy flux (or more clearly, that viscosity is unimportant in the transfer process) comes from the scaling arguments of Kolmogorov and Oboukhov for incompressible flow. In this range, the velocity spectrum is expected to decay with wave number (or frequency) as $\kappa^{-5/3}$. Other authors have extended this theory to encompass flows with small density variations, in which temperature may be considered to be a passive scalar (Tennekes and Lumley, 1972). In this instance, the inertial subrange is known as a "convective subrange" and exhibits the same $\kappa^{-5/3}$ decay.

In a buoyancy-driven flow where temperature is not a passive scalar, additional subranges with different scaling relations may develop. In stable stratification, a buoyancy subrange may develop, characterized by a κ^{-3} scaling at lower wavenumbers changing to $\kappa^{-5/3}$ at higher wave numbers (Turner, 1973). Turner explains this phenomenon by noting that the local rate of energy transfer will be larger than the eventual dissipation rate when buoyancy is present since energy is extracted by working against gravity at larger scales. Bill and Gebhart (1979) observed a κ^{-3} decay in the spectral density of velocity and temperature fluctuations at frequencies above 0.5 Hz for turbulent natural convection in air adjacent to a heated vertical surface. Papanicolaou and List (1987) present PSD measurements for turbulent round buoyant jets showing the existence of a $\kappa^{-5/3}$ inertial-convective subrange followed by an "inertial-diffusive subrange" where the spectrum decays as κ^{-3} at higher wave numbers. This inertial-diffusive subrange has also been observed by Dai et al. (1994, 1995) and Sangras et al. (1998), and is attributed to buoyancy-generated inertia forces by Papanicolaou and List (1987). The existence of inertial subranges that are influenced by buoyancy underscores important buoyancy-turbulence interactions, as noted by Sangras et al. (1998), and warrants further study.

Natural convection in the cylindrical annulus formed by horizontal concentric cylinders has been widely investigated, and numerous studies have been published describing the flow phenomena (Bishop et al., 1968; Powe et al., 1969; Kuehn and Goldstein, 1976a) and providing correlations for the mean heat transfer rates between the cylinders (Kuehn and Goldstein, 1976b, 1978, 1980; Bishop, 1988). With the exception of Lis (1966), who reported mean heat transfer results up to $Ra_d = 10^{10}$, earlier studies of this problem were limited to $Ra_d < 10^8$.

In a series of experiments using helium at cryogenic temperatures, Fersner (1986), McLeod (1987), Bishop (1988), and McLeod and Bishop (1989) obtained measurements of the fluctuating temperature field at Ra_d up to $Ra_d = 2 \times 10^9$. They present mean temperature profiles and PSD measurements showing an increase in temperature fluctuations as Ra_d is increased from 10^7 to 10^8, and an even more dramatic increase as Ra_d is increased further

Contributed by the Heat Transfer Division for publication in the JOURNAL OF HEAT TRANSFER and presented at '98 AIAA/ASME Joint Thermophysics & HT Conf., Albuquerque. Manuscript received by the Heat Transfer Division, Feb. 2, 1998; revision received, Mar. 2, 1999. Keywords: Enclosure Flows, Heat Transfer, Natural Convection, Plumes, Turbulent. Associate Technical Editor: D. A. Zumbrunnen.

to 10^9. However, the PSD measurements are presented on a linear scale, making it difficult to identify harmonics at higher frequencies and impossible to observe any inertial subranges, if they exist. The change in the turbulence level is attributed to a change in the plume structure above the inner cylinder from a quasi-laminar oscillating flow to a steady turbulent plume composed of small-scale eddies. Sketches of the postulated flow structure showing the extent of the turbulence, which originates in the plume as it reaches the outer cylinder, are included in McLeod and Bishop (1989).

In contrast to the research of Bishop and co-workers described above, the goal of the present research is to characterize the spectral distribution of the temperature fluctuation measurements to obtain fundamental information to understand the transition process and development of turbulence in buoyancy-induced flows in enclosures. Because of the relatively simple geometry presented by an annular enclosure, natural convection between horizontal cylinders is amenable to direct numerical simulations and the PSD data will also be invaluable for benchmarking numerical results and developing improved turbulence models that account for buoyancy-turbulence interactions.

Experimental Facility and Data Acquisition

This study considers the flow between two horizontal concentric stainless steel cylinders, which form an annulus with $L = 265.0$ mm, $r_i = 9.5$ mm, and $r_o = 79.5$ mm. The resulting gap width, d, radius ratio, R, and aspect ratio, A, are 70.0 mm, 0.12, and 3.786, respectively. The inner cylinder is heated to 500 K while the outer cylinder is maintained at 300 K by a constant temperature bath. Ra_d is varied by changing the fluid pressure within the annulus, which has Pyrex windows to seal each end while allowing optical access. Complete details on the annulus assembly are given in Fisher (1996). Experiments are performed using air and xenon as the working fluids. Despite the relatively small aspect ratio, end-effects are confined to a limited region of the annulus as verified by smoke visualization studies reported earlier (Fisher et al., 1994).

The fluid temperature is measured by seven 40-μm diameter chromel-constantan (Type E) thermocouples located in a vertical line centered directly above the inner cylinder in the middle of the annulus. The thermocouples are mounted and evenly distributed in a rake structure at radial positions corresponding to $r^* = 0.1$ to $r^* = 0.7$. Compensation due to the thermal inertia of the wire is not performed, since the time constant of the wire (approximately 12 ms) is small enough to satisfy the Nyquist criterion for sampling over the dynamic frequency range of the temperature measurements. Temperature data are acquired by a National Instruments, Inc. (Austin, Texas) 12-bit A/D system which is interfaced to an Apple Macintosh Centris 650 microcomputer running the National Instruments LabViewII virtual instrument software. The continuous voltage output from each thermocouple is sampled at 100 or 200 Hz and stored in data files containing 4096 (4 K) points. Typically 40 records of data are acquired at each operating condition for each thermocouple location.

The PSD of the temperature fluctuations are obtained by applying a standard 2^n fast Fourier transform (FFT) algorithm to segmented portions of the data record. Before processing, each ensemble is modified by a Hamming window on the first and last ten percent of the data to reduce spectral leakage. For this study, the ensemble size is fixed at 1024 (1 K) points, with an overlap of 50 percent. This was found to be a suitable tradeoff between spectral resolution and statistical independence. After FFT processing, the individual PSDs are ensemble-averaged. Further details about these procedures can be found in Fisher (1996) and Fisher et al. (1994, 1995).

Experimental uncertainties (95 percent confidence) were determined by multiple measurements of a steady variable (Moffat, 1982). The uncertainties in the geometric parameters d, R, and A are small (less than one percent). The uncertainty in the thermocouple probe positioning is 2.0 percent. Maximum experimental uncertainties of the reported flow properties are as follows: 12 percent for Ra_d; 38 percent for $E_T(f)/\bar{T}'^2$ at $\mathrm{Ra}_d = 10^8$ increasing to 63 percent for $E_T(f)/\bar{T}'^2$ at $\mathrm{Ra}_d = 10^9$.

Results

As noted earlier, detailed descriptions of the natural convection flow in horizontal annuli have already been published. It is well known that the steady laminar plume that develops above the heated inner cylinder becomes unstable above a critical Ra_d, and begins to oscillate in the wide gap annulus (Powe et al., 1969). The plume oscillation is characterized by a longitudinal travelling wave. Although the critical value of Ra_d for the onset of oscillatory flow was not determined in the present study, a strong plume oscillation was evident for $\mathrm{Ra}_d = 10^6$. There is little qualitative change in the characteristics of the PSD obtained from the fluctuating temperature measurements in the range $10^6 \leq \mathrm{Ra}_d \leq 10^8$. The spectral energy transfer is between discrete frequencies (harmonics of the fundamental plume oscillation frequency, f_1). The absence of spectral subranges where a continuous transfer of energy between frequencies exists indicates that the flow in this range of Ra_d is still laminar. In the vicinity of the inner cylinder, only the fundamental frequency, f_1, has any significant energy content. As the outer cylinder is approached, harmonics of f_1 increasingly begin to appear. As Ra_d increases, harmonics of f_1 first appear at larger values of r^* (i.e., further away from the inner cylinder). Above $\mathrm{Ra}_d = 10^8$, significant changes in the PSD occur. Thus, results will only be presented for $\mathrm{Ra}_d = 10^8$ and above.

$\mathrm{Ra}_d = 10^8$. Figure 1 shows the changes in the PSD of the temperature measurements with increasing distance from the inner cylinder, r^*, on the vertical centerline above the heated inner

Nomenclature

A = aspect ratio, L/d
d = gap width, $r_o - r_i$
$E_T(f)$ = temporal PSD of T
f = frequency
g = gravitational acceleration
L = axial length of annulus
r = radial coordinate
r^* = normalized radial location, $(r - r_i)/d$
R = radius ratio, r_o/r_i
Ra_d = Rayleigh number, $g\beta\Delta T d^3/(\nu\alpha)$
T = temperature

Greek Symbols

α = thermal diffusivity
β = volumetric coefficient of thermal expansion
ΔT = temperature difference, $T_i - T_o$
κ = wave number
ν = kinematic viscosity

Subscripts

i = inner cylinder
o = outer cylinder

Superscripts

$()'$ = root-mean-squared fluctuating value

Acronyms

A/D = analog-to-digital
FFT = fast Fourier transform
PSD = power spectral density

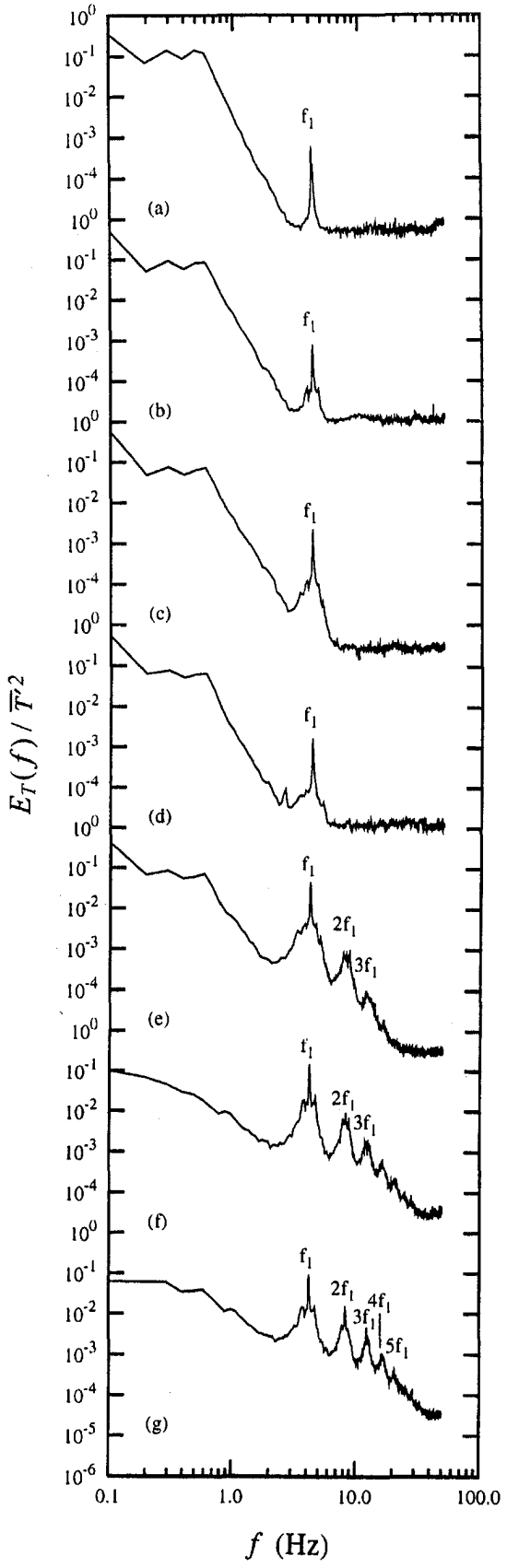

Fig. 1 Temporal PSD of temperature fluctuations for $Ra_d = 10^8$: (*a*) $r^* = 0.1$, (*b*) $r^* = 0.2$, (*c*) $r^* = 0.3$, (*d*) $r^* = 0.4$, (*e*) $r^* = 0.5$, (*f*) $r^* = 0.6$, (*g*) $r^* = 0.7$

cylinder for $Ra_d = 10^8$. The spectrum at $r^* = 0.1$ indicates the existence of an oscillatory flow with a frequency of 4 Hz. The identification of the fundamental frequency at 4 Hz was also confirmed by flow visualization studies (see Fisher, 1996 and Fisher et al., 1995 for details). The implication of this single peak at $r^* = 0.1$ is that the plume structure for $Ra_d = 10^8$ is robust and does not begin to break down until further downstream; the temperature spectrum retains essentially the same shape up to $r^* = 0.4$. Above $r^* = 0.4$, harmonics of the fundamental plume oscillation frequency begin to appear, with the frequency bands between the peaks becoming more energetic as nonlinear interactions occur within the plume. The appearance of harmonics indicates that energy is being transferred selectively to remote frequencies, consistent with a set of interacting waves (Turner, 1973). At $r^* = 0.5$, the fundamental frequency can be seen at 4 Hz, along with the first two harmonics at 8 and 12 Hz. There is also some evidence of a third harmonic starting to appear at 16 Hz. The flow continues to develop in this fashion as the outer cylinder is approached. At $r^* = 0.7$, the fourth harmonic frequency of 20 Hz is evident. Above this frequency, a continuous cascade begins to form, indicating the development of turbulence. However, no inertial subranges are found for $Ra_d \leq 10^8$.

$Ra_d = 5.0 \times 10^8$. The temperature PSD estimates obtained at $Ra_d = 5.0 \times 10^8$, shown in Fig. 2, are markedly different than those obtained at lower Ra_d. Nearer to the inner cylinder, there is a continuous cascade of energy at frequencies below about 10 Hz. However, the decay rate is very large and not characteristic of fully developed turbulence. The plume oscillates with a fundamental frequency of 14 Hz, although the peak in the PSD at this frequency is not well defined until $r^* = 0.5$. At $r^* = 0.5$, the first harmonic at 28 Hz is also evident and the second harmonic at 42 Hz is beginning to develop. The energy extracted by the oscillation of the plume results in the large rates of energy transfer from the lower frequencies.

As the outer cylinder is approached, the plume oscillation begins to break down. At $r^* = 0.6$, the harmonics have disappeared and the peak at the fundamental frequency is much smaller. At $r^* = 0.7$, the plume oscillation is gone, and the spectrum shows a continuous cascade of energy with two identifiable subranges. Between approximately 1 Hz to 12 Hz, the spectrum decays as $f^{-5/3}$, characteristic of the inertial-convective subrange seen by other investigators in buoyant jets and plumes. At higher frequencies, between about 12 Hz and 40 Hz, the spectrum decays as f^{-3} typical of the inertial-diffusive subrange previously discussed. These PSD results are the first signs of fully developed turbulence within the plume.

$Ra_d = 10^9$. The PSD of the temperature measurements obtained at $Ra_d = 10^9$ are shown in Fig. 3. The flow near the inner cylinder ($r^* \leq 0.3$) is weakly turbulent. There is a continuous energy cascade, although no inertial subranges can be identified. The fundamental plume oscillation frequency is indicated by a small peak in the spectrum at 15 Hz. The cascade of energy from the lower frequencies occurs at rates higher than expected for fully developed turbulence in the presence of the plume oscillation, as noted above. As the plume oscillates, it interacts with the adjacent relatively stagnant core flow in two significant ways. First, entrainment of the surrounding fluid results in an increase in the spatial extent of the plume, as observed by McLeod and Bishop (1989). Second, the local shear produced at the interface results in instability and the production of turbulence (Turner, 1973). These two effects, which become increasingly important as both Ra_d and r^* increase, contribute to the breakdown of the plume. At $r^* = 0.4$, the plume oscillation has broken down and distinct peaks in the PSD are no longer evident, corresponding with the emergence of the inertial-convective and inertial-diffusive subranges, characterized by $f^{-5/3}$ and f^{-3} decay rates, respectively.

Plume Oscillation Frequency. By using the temperature PSD results, it is possible to develop a correlation for the fundamental plume oscillation frequency:

$$f_1 = 5.172 \times 10^{-4} (Ra_d)^{0.5}. \quad (1)$$

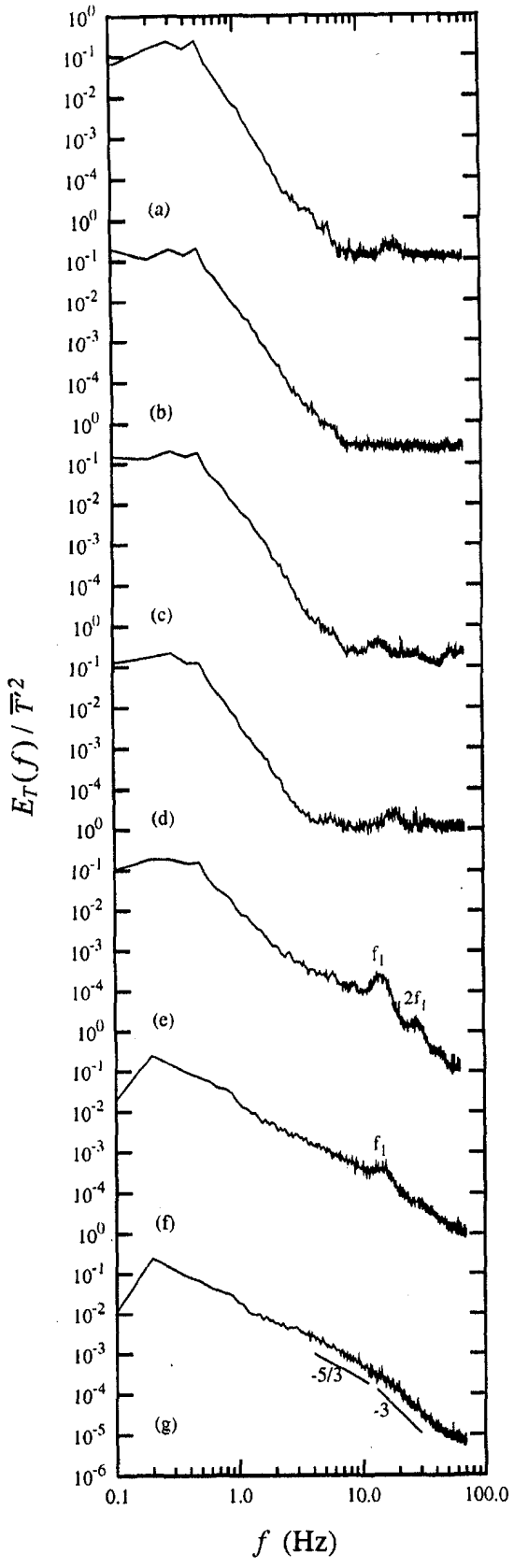

Fig. 2 Temporal PSD of temperature fluctuations for $Ra_d = 5 \times 10^8$: (*a*) $r^* = 0.1$, (*b*) $r^* = 0.2$, (*c*) $r^* = 0.3$, (*d*) $r^* = 0.4$, (*e*) $r^* = 0.5$, (*f*) $r^* = 0.6$, (*g*) $r^* = 0.7$

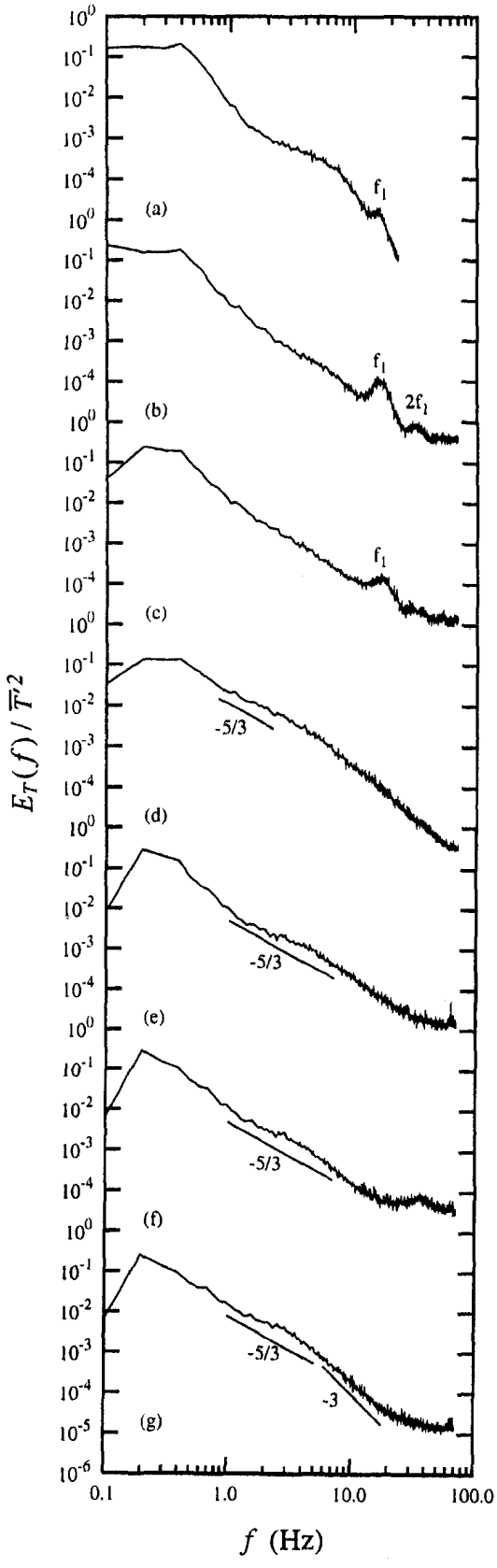

Fig. 3 Temporal PSD of temperature fluctuations for $Ra_d = 10^9$: (*a*) $r^* = 0.1$, (*b*) $r^* = 0.2$, (*c*) $r^* = 0.3$, (*d*) $r^* = 0.4$, (*e*) $r^* = 0.5$, (*f*) $r^* = 0.6$, (*g*) $r^* = 0.7$

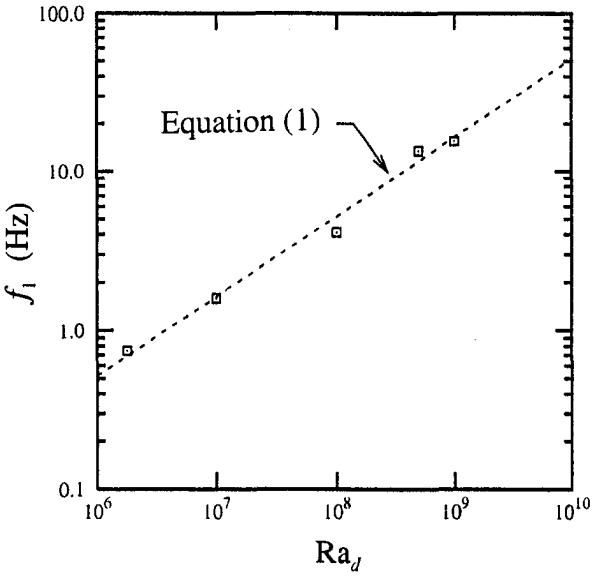

Fig. 4 Variation of fundamental frequency of plume oscillation with Ra_d

Figure 4 shows this correlation along with the data from this study. Earlier correlations proposed by Bishop et al. (1968) are limited to lower values of Ra_d.

Conclusions

This study has added information to the observations of previous authors about the dynamics of the thermal plume in a horizontal annulus, showing that the single dominant oscillation that exists at low Ra_d is modulated and eventually breaks down during the transition to turbulence with increasing Ra_d. The fundamental plume oscillation frequency is found to be proportional to the square root of Ra_d, with the oscillatory flow beginning very close to the inner cylinder. The plume is still largely laminar at $Ra_d = 10^8$, although as the outer cylinder is approached the number of higher harmonics of the fundamental oscillation frequency increases dramatically. At $Ra_d = 5 \times 10^8$, the plume is weakly turbulent and exhibits a continuous energy cascade, although the decay rates are much larger than expected for fully developed turbulence due to the energy extracted by the plume oscillations. The plume oscillation breaks down near the outer cylinder, and the flow becomes fully turbulent. As Ra_d increases further, the radial location at which the plume becomes fully turbulent moves inward. At $Ra_d = 10^9$, the plume oscillation breaks down near $r^* = 0.4$, and there is evidence of inertial-convective and inertial-diffuse subranges characterized by decay rates of $f^{-5/3}$ and f^{-3}, respectively.

Acknowledgment

This material is based upon work supported by the National Science Foundation under Award No. CTS-9258006.

References

Bill, R. G., and Gebhart, B., 1979, "The Development of Turbulent Transport in a Vertical Natural Convection Boundary Layer," *International Journal of Heat and Mass Transfer,* Vol. 22, pp. 267–277.

Bishop, E. H., 1988, "Heat Transfer by Natural Convection of Helium Between Horizontal Isothermal Concentric Cylinders at Cryogenic Temperature," ASME JOURNAL OF HEAT TRANSFER, Vol. 110, pp. 109–115.

Bishop, E. H., Carley, C. T., and Powe, R. E., 1968, "Natural Convective Oscillatory Flow in Cylindrical Annuli," *International Journal of Heat and Mass Transfer,* Vol. 11, pp. 1741–1752.

Dai, Z., Tseng, L. K., and Faeth, G. M., 1994, "Structure of Round, Fully Developed, Buoyant Turbulent Plumes," ASME JOURNAL OF HEAT TRANSFER, Vol. 116, pp. 409–417.

Dai, Z., Tseng, L. K., and Faeth, G. M., 1995, "Velocity Statistics of Round, Fully Developed, Buoyant Turbulent Plumes," ASME JOURNAL OF HEAT TRANSFER, Vol. 117, pp. 138–145.

Fersner, J. W., 1986, "Natural Convection Between Horizontal Isothermal Concentric Cylinders: The Temperature Field," M.S. thesis, Clemson University, Clemson, SC.

Fisher, C. E., 1996, "An Experimental Study of Plume Dynamics in Turbulent Natural Convection in a Horizontal Annulus," Ph.D. dissertation, The University of Texas at Austin, Austin, TX.

Fisher, C. E., Kohli, A., and Ball, K. S., 1995, "An Experimental Study of High Rayleigh Number Natural Convection in a Horizontal Annulus," *Proceedings of the 30th National Heat Transfer Conference,* Vol. 8, I. S. Habib et al., eds., ASME, New York, pp. 69–78.

Fisher, C. E., Kohli, A., and Ball, K. S., 1994, "Measurement of Power Spectral Density in Turbulent Natural Convection using a Laser Doppler Velocimeter," ASME Paper No. 94-WA/HT-16.

Kuehn, T. H., and Goldstein, R. J., 1976a, "An Experimental and Theoretical Study of Natural Convection in the Annulus between Horizontal Concentric Cylinders," *Journal of Fluid Mechanics,* Vol. 74, pp. 695–719.

Kuehn, T. H., and Goldstein, R. J., 1976b, "Correlating Equations for Natural Convection Heat Transfer between Horizontal Circular Cylinders," *International Journal of Heat and Mass Transfer,* Vol. 19, pp. 1127–1134.

Kuehn, T. H., and Goldstein, R. J., 1978, "An Experimental Study of Natural Convection Heat Transfer in Concentric and Eccentric Horizontal Cylindrical Annuli," ASME JOURNAL OF HEAT TRANSFER, Vol. 100, pp. 635–640.

Kuehn, T. H., and Goldstein, R. J., 1980, "A Parametric Study of Prandtl Number and Diameter Ratio Effects on Natural Convection Heat Transfer in Horizontal Cylindrical Annuli," ASME JOURNAL OF HEAT TRANSFER, Vol. 102, pp. 768–770.

Lis, J., 1966, "Experimental Investigation of Natural Convection Heat Transfer in Simple and Obstructed Horizontal Annuli," *Proceedings of the Third International Heat Transfer Conference,* AIChE, New York, pp. 196–204.

McLeod, A. E., 1987, "Heat Transfer by Natural Convection of Helium Between Horizontal Isothermal Concentric Cylinders at Cryogenic Temperatures," M.S. thesis, Clemson University, Clemson, SC.

McLeod, A. E., and Bishop, E. H., 1989, "Turbulent Natural Convection of Gases in Horizontal Cylindrical Annuli at Cryogenic Temperatures," *International Journal of Heat and Mass Transfer,* Vol. 32, pp. 1967–1978.

Moffat, R. J., 1982, "Contribution to the Theory of Single-Sample Uncertainty Analysis," ASME *Journal of Fluids Engineering,* Vol. 104, pp. 250–258.

Papanicolaou, P. N., and List, E. J., 1987, "Statistical and Spectral Properties of Tracer Concentration in Round Buoyant Jets," *International Journal of Heat and Mass Transfer,* Vol. 30, pp. 2059–2071.

Powe, R. E., Carley, C. T., and Bishop, E. H., 1969, "Free Convective Flow Patterns in Cylindrical Annuli," ASME JOURNAL OF HEAT TRANSFER, Vol. 91, pp. 310–314.

Sangras, R., Dai, Z., and Faeth, G. M., 1998, "Mixing Structure of Plane Self-Preserving Buoyant Turbulent Plumes," ASME JOURNAL OF HEAT TRANSFER, Vol. 120, pp. 1033–1041.

Tennekes, H. and Lumley, J. L., 1972, *A First Course in Turbulence,* MIT Press, Cambridge, MA.

Turner, J. S., 1973, *Buoyancy Effects in Fluids,* Cambridge University Press, New York.

T. S. Fisher[1]
Assoc. Mem. ASME

K. E. Torrance
Professor,
Fellow ASME

Sibley School of Mechanical and Aerospace Engineering,
Cornell University,
Ithaca, NY 14853

Experiments on Chimney-Enhanced Free Convection

Experimental results are presented for thermal systems consisting of a vertical, parallel-plate, isothermal heat sink and a chimney. A ridge of maximum total heat transfer is observed with respect to the plate spacing and heat-sink height. The magnitude of heat transfer and the location of optima confirm prior theoretical predictions by Fisher et al. (1997) to within 11 percent. Averaged velocity measurements closely match theoretical predictions of mean velocity. Cold inflow at the chimney exit is quantified and shown to decrease overall heat transfer by approximately four percent.

1 Introduction

The present paper addresses the use of chimneys to enhance heat transfer from free-convection heat sinks. Prior theoretical work by Fisher et al. (1997) and Fisher and Torrance (1998) suggests that significant improvements are possible by adding a chimney to plate-fin and pin-fin heat sinks. The underlying analysis, however, relies on several assumptions (i.e., two-dimensional flow, fins of infinite thermal conductivity for plate-fin heat sinks, inviscid flow in the chimney, and negligible unfinned-base heat transfer and radiation). In order to test the theory (and the assumptions), a series of experiments was conducted on plate-fin heat sinks with chimneys.

Laminar natural convection from parallel plates without a chimney has been widely studied. The data of Elenbaas (1942) provide the foundation for heat transfer from a single isothermal channel without chimney enhancement. For flows without chimneys, the parallel-plate analysis described by Fisher et al. (1997) reduces to the analysis of Quintiere and Mueller (1973), which compares favorably to Elenbaas' experimental data. Based on single-channel correlations, Elenbaas (1942) and Bar-Cohen and Rohsenow (1984) predicted the optimal plate spacing of an array of parallel plates of fixed total width.

Other studies have addressed the parallel-plate problem for different boundary conditions. In separate studies, Ostrach analytically treated the problems of fully developed flow with internal heat sources (Ostrach, 1952) and linear wall temperature variation (Ostrach, 1954). The problem of asymmetric wall heating has been considered under developing conditions by Aung et al. (1972) and fully developed conditions by Aung (1972). Mixed convection from uniform heat-flux plates was analytically treated by Tao (1960).

Very few prior experiments have considered chimney-enhanced convection, and none have included parallel-plate or pin-fin heat exchangers below the chimney. Perhaps the work of Straatman et al. (1993) resembles the present work most closely. However, their experiments included only a single isothermal channel with a chimney cross-sectional area of the same order as that of the heated channel. Under such conditions, the assumption of inviscid flow in the chimney becomes questionable.

2 Background

The aforementional theoretical study by Fisher et al. (1997), for parallel-plate finned heat sinks with chimneys, introduced two useful nondimensional variables. The first is a nondimensional heat-sink channel width, which is scaled by the Grashof number based on total system height as

$$b^*\mathrm{Gr}_H^{1/4} = \frac{b}{H}\left(\frac{g\beta\Delta T_w H^3}{\nu^2}\right)^{1/4} \tag{1}$$

where b is the heat-sink channel half-width, H is the total system height (heat-sink height H_H plus chimney height H_C), and ΔT_w is the temperature difference between the heat-sink surface and the ambient air. A sketch of a heat sink is shown in Fig. 1; the heat-sink/chimney orientation is shown in Fig. 2. The theory also defines a scaled rate of total heat transfer as

$$Q_{\mathrm{tot}}^{**} = \frac{Q_{\mathrm{tot}}}{Lk_f\Delta T_w\phi W^*\mathrm{Gr}_H^{1/2}} \tag{2}$$

where L is the fin length, k_f is the fluid's thermal conductivity, ϕ [$\equiv b/(b+t)$] is the heat-sink porosity, and W^* ($\equiv W/H$) is the nondimensional heat-sink width.

The theoretical results indicate that the maximum rate of heat transfer $Q_{\mathrm{tot,max}}^{**}$ remains nearly constant, with a value of approximately 0.35, as the fraction of total system height devoted to the heat sink, H_H^* ($\equiv H_H/H$), is varied. The foregoing assumes a Prandtl number of 0.7 (gases) and a constant chimney cross-sectional area. The maximum rate of heat transfer corresponds to an optimal scaled channel width, $(b^*\mathrm{Gr}_H^{1/4})_{\mathrm{opt}}$, which decreases as the relative heat-sink height decreases. The relative invariance of $Q_{\mathrm{tot,max}}^{**}$ suggests that systems with chimneys ($H_H^* < 1$) with optimal channel widths can produce the same rates of heat transfer as optimal systems without chimneys (but with taller heat sinks because $H_H^* = 1$).

The maximization of heat transfer with respect to channel width reflects a compromise between convective surface area and local rates of heat transfer. For very large channel widths, convective surface area is small, but local rates of heat transfer are large due to boundary-layer-type flow over the fin surfaces. As the channel width decreases, total convective surface area increases (due to an increasing number of fins), and the boundary layers merge, resulting in fully developed channel flow and lower rates of local heat transfer. The theoretical results indicate that for systems with and without chimneys, the optimal channel widths correspond to fully developed flow at the channel exit, but that the degree of development within the channel depends on the relative heat-sink height.

The present experimental work attempts to test the accuracy of the parallel-plate analysis of Fisher et al. (1997). In particular, the system-level characteristics of several heat-sink/chimney combinations are reported, together with velocity measurements obtained by hot-wire anemometry. Further, the phenomenon of cold inflow at the chimney exit is studied and related to a loss of theoretical performance. The following sections describe the experimental

[1] To whom correspondence should be addressed: Assistant Professor, Department of Mechanical Engineering, Vanderbilt University, Box 1592–Station B, Nashville, TN 37235. e-mail: tim.fisher@vanderbilt.edu.

Contributed by the Heat Transfer Division for publication in the JOURNAL OF HEAT TRANSFER. Manuscript received by the Heat Transfer Division, Aug. 1, 1998; revision received, Feb. 15, 1999. Keywords: Channel, Enhancement, Heat Transfer, Natural Convection. Associate Technical Editor: R. Douglass.

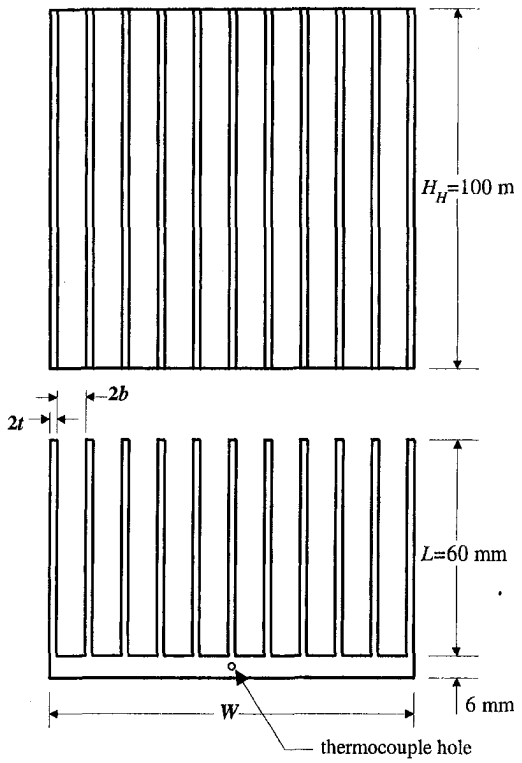

Fig. 1 Dimensioned plate-fin heat-sink drawing

apparatus and present results, which are compared with theoretical predictions.

3 Experimental Setup

3.1 Heat Sinks and Chimneys. Two experimental heat sinks were fabricated via a precision sawing technique. The heat-sink material is 6063-T6 aluminum. The plate spacings were selected to span the ridge of maximum heat transfer identified by Fisher et al. (1997) for different chimney heights.

A drawing of a heat sink with channel width $2b$, fin thickness $2t$, and overall width W, appears in Fig. 1. The overall fin height and length for each heat sink are 100 mm and 60 mm, respectively. The base conduction thickness of 6 mm allows sufficient heat spreading to achieve an isothermal base condition. Originally, the plate spacing and fin thickness of each heat sink were designed to produce a porosity of $\phi = 80$ percent. However, due to manufacturing constraints, the fin thickness of the narrow-channel heat sink

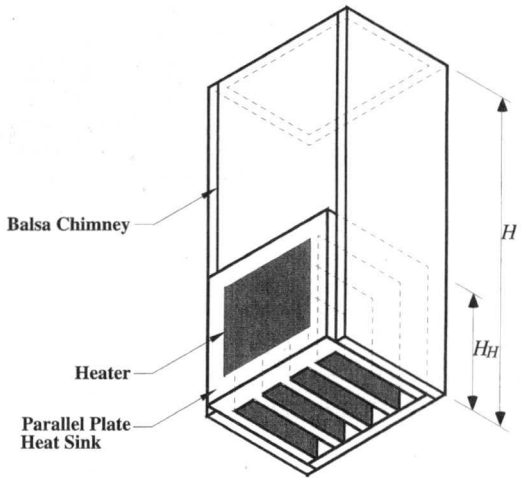

Fig. 2 Isometric view from below of the heat-sink/chimney system

was increased, resulting in a porosity of 74 percent. The variable dimensions of each heat sink appear in Table 1.

The two channel widths, which differ by 45 percent, provide a variation of the scaled (nondimensional) channel width $b^*\mathrm{Gr}_H^{1/4}$, given in Eq. (1). By varying the scaled channel width (via b, H, and/or ΔT_w), we expect to be able to cross and thus verify the ridge of maximum heat transfer predicted by Fisher et al. (1997).

The heat sinks were attached to chimneys made of 0.635-cm thick balsa wood ($k = 0.055$ W/mK), as shown in Fig. 2. Two chimneys with heights $H_C = 67$ mm and $H_C = 233$ mm produce relative heat-sink heights of $H_H^* (\equiv H_H/H) = 0.6$ and $H_H^* = 0.3$, respectively. The chimneys also include shrouds on three sides of the heat sinks. The two shrouds parallel to the fin length provide thermal insulation for the edge fins. The other shroud along the fin tips promotes nearly two-dimensional flow in the heat-sink channels. The chimneys maintain constant flow cross-sectional areas of 60 mm by 102 mm throughout their heights, resulting in a chimney contraction ratio of $\Gamma (\equiv W/W_C) \approx 1$ for each heat sink. Heating power to each heat sink was supplied by a 185 Ω resistance heater. The heating element was encased in silicone rubber, and a thin-film adhesive secured the heater to the heat-sink base.

The chimney walls contain two additional layers of materials. The inner layer is made of a highly reflective aluminum sheet to minimize thermal radiation. The outer layer is made of 1.27-cm thick fiberglass pipe insulation ($k = 0.033$ W/mK). Thin neoprene sheets cover the inner surfaces of the shroud walls to eliminate gaps between the heat sink and shroud.

3.2 Guard Heating and Insulation. The experimental apparatus was constructed to minimize heat transfer from the back

Nomenclature

b = channel half-width (m), see Fig. 1
b^* = nondimensional channel half-width, b/H
Fr = Froude number, see Eq. (4)
g = gravitational acceleration (m/s^2)
Gr_H = system Grashof number, see Eq. (1)
H = total system height (m)
H_C = chimney height (m)
H_H = heat-sink height = 0.1 m
H_H^* = nondimensional heat-sink height, H_H/H
k = thermal conductivity (W/mK)
L = fin length = 0.06 m
Q_{tot} = total heat flow rate (W)
Q_{tot}^{**} = scaled heat flow rate, see Eq. (2)
t = plate half-thickness (m), see Fig. 1
T = temperature (K)
W = total width of plate array (m), see Fig. 1
W^* = nondimensional heat-sink width, W/H
W_C = width of chimney exit (m)
x, y = coordinates of chimney cross section (m)
β = coefficient of thermal expansion (1/K)
ΔT = temperature rise above ambient (K), $T - T_0$
Γ = chimney contraction ratio, W/W_C
ϕ = volume-based heat-sink porosity (percent), $b/(b + t)$
ν = fluid kinematic viscosity (m^2/s)
ρ = density (kg/m^3)

Subscripts

0 = ambient
w = heat-sink wall

Table 1 Variable dimensions of experimental heat sinks

Dimension	Narrow-channel heat sink	Wide-channel heat sink
number of channels	13	10
channel width $2b$	5.5 mm	8.0 mm
fin thickness $2t$	2.0 mm	2.0 mm
overall width W	99.5 mm	102.0 mm

side of the heat sink and through the chimney walls. The guard heating arrangement shown in Fig. 3 was designed to minimize losses from the back side of the primary heater. The guard stack consists of a sequence of neoprene sheets and copper plates.

The copper plate nearest the heat sink provides a nearly uniform reference temperature surface. Due to its high thermal conductivity, the reference copper plate used in the present work serves as a heat compensator, taking heat lost from the back side of the heater and returning it to the heat sink at the edges of the base that the heater does not cover. By matching the guard and reference plate temperatures, no heat is allowed to flow between them, thereby ensuring that the heat lost from the heater is returned to the heat sink. Guard heat was generated from a 25 Ω resistance heater with Kapton insulation.

Thermocouple locations on the heat sink and guard plates are also shown in Fig. 3. Type-T (copper-constantan), 36-gauge thermocouples from a single spool were employed for all temperature measurements. The spool was calibrated using a two-point method at the ice and steam points. Thermocouples were located at the center of each copper plate, at the interior of the base through a 1.59-mm diameter hole, and at the tip of a centrally located fin.

Fiberglass pipe insulation (1.27-cm thick) covered the entire assembly's exposed vertical sides, including the back of the guard stack, chimney shrouds, and chimney walls. The smallest effective thermal resistance through the chimney walls was calculated to be approximately 9 K/W. Considering the observed chimney fluid temperatures and heating conditions described in later sections, heat transfer through the chimney walls is estimated to be less than four percent of the total heat dissipation.

3.3 Configuration and Data Acquisition. Significant care was taken to ensure calm thermal and hydrodynamic conditions in the laboratory. The windows were sealed with duct tape and covered with a plastic sheet. Horizontal window blinds blocked the majority of solar radiation into the room. Under these conditions, room drafts in the laboratory were negligible, and measured thermal gradients in the vertical direction were less than 1.5°C/m.

To create a quiescent ambient environment, four vertical window screens enclosed the heat-sink/chimney system. The screens suppressed horizontal room drafts that might affect flow conditions at the system inlet and/or outlet. The system itself was attached to a support structure made of a combination of angle steel and basswood. The system inlet was nine hydraulic diameters (9 × 8 cm = 72 cm) above the floor to ensure unencumbered flow induction.

In addition to the thermocouples shown in Fig. 3, several others were placed on and around the heat-sink/chimney system. Two thermocouples measured the local ambient temperature at the heat-sink inlet and chimney exit, respectively. The thermocouples were shrouded in aluminum foil (containing small punctures to allow air flow) in order to eliminate radiation effects. Other thermocouples were placed, during various experiments, on the perimeter of the heat-sink base and copper plates to evaluate temperature uniformity, which was found to be uniform to about 0.4°C. Other temperature measurements were taken in the fin tips and on the chimney wall.

To obtain data and control the experiment, the heat-sink/chimney system was connected to various electronic equipment. A personal computer provided a central means of data acquisition and control. For each power setting, the guard heater was automatically adjusted until the temperature difference between the two guard plates remained below 0.35 K for a period of five minutes. Data collection was then performed, followed by a 20 minute pause. The computer program then cycled through the guard setting, data collection, and pause procedures three additional times. Output data were averaged over the last three of four measurements to minimize the effects of random fluctuations in the temperature and voltage readings and of changes in the local ambient environment.

3.4 Flow Measurement. A constant temperature anemometer (DISA 55M) was used to measure air velocities at the chimney exit. Because of the variability of fluid temperatures in the experiment, a temperature-compensated probe was utilized instead of a standard, single-sensor probe. The temperature compensator uses a two-sensor probe to automatically compensate for changes in the fluid temperature.

The hot-wire probe was calibrated as described by Mendez and Torrance (1998). To ensure temperature independence, the probe was placed in a heated cavity, where its zero-velocity output voltage matched the voltage observed without heating. The minimum velocity allowed by the calibration system is 0.5 m/s, which exceeds most of the measured velocities presented in later sections. Consequently, velocity measurements were generally extrapolated, as opposed to interpolated, from the calibration curve. However, the calibration data exhibited a well-ordered, linear relationship between voltage^2 and velocity$^{0.5}$, thus suggesting that extrapolation does not introduce excessive error.

3.5 Experimental Uncertainty. Uncertainties were present in various experimental measurements. The maximum random uncertainties in temperature and heating power measurements are ±0.4 K and ±2 percent, respectively. The resulting uncertainties in system Grashof number Gr_H and nondimensional heat transfer rate Q^{**}_{tot} can be computed by the method of Kline and McClintock (1953) as

$$\delta Z = \left\{ \sum_{i=1}^{n} \left(\frac{\partial Z}{\partial X_i} \delta X_i \right)^2 \right\}^{1/2} \tag{3}$$

where $Z = Gr_H$ or Q^{**}_{tot} and $X_i = T_w$, T_0, or Q_{tot}. Using Eq. (3), the estimated random uncertainties for Gr_H are ±5 percent and ±1 percent for $\Delta T_w = 10$ K and 50 K, respectively. For Q^{**}_{tot}, the uncertainties are ±7 percent and ±3 percent, respectively, for $\Delta T_w = 10$ K and 50 K.

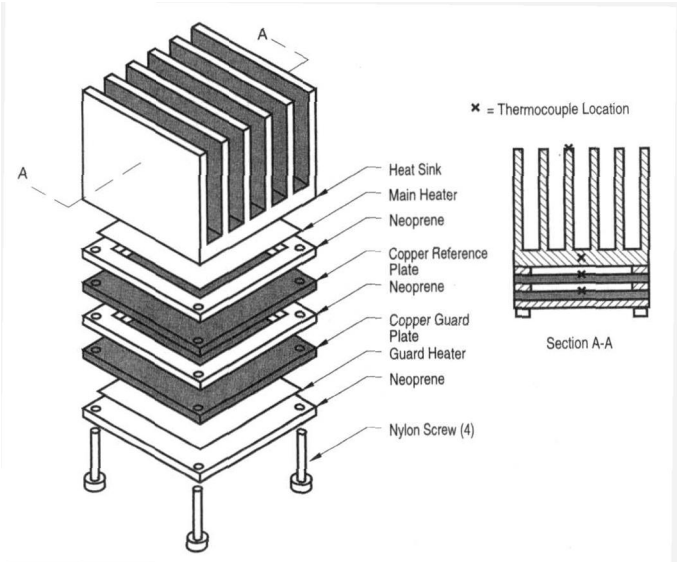

Fig. 3 Isometric view of the guard heating stack and cross-section showing thermocouple locations

For velocity measurements, uncertainties arise from the calibration procedure and random signal noise. The calibration velocities are accurate to within ±2 percent (DISA, 1985). The deviation of measured points from the calibration line was found to be approximately ±5 percent (Mendez and Torrance, 1998). Further, as described in Section 3.4, the use of extrapolation, as opposed to interpolation, may cause additional uncertainty, estimated here to be ±5 percent. The resulting overall uncertainty in velocity based on the sum-of-squares approach in Eq. (3) is estimated to be ±8 percent.

4 Results and Discussion

Each of the previously described heat sinks (of height H_H = 100 mm) was tested at two different total system heights, H = 333 mm and 167 mm, with heating powers ranging from 5 to 100 W. In subsequent sections, all material properties appearing in nondimensional parameters, such as Gr_H and Q^{**}_{tot}, were evaluated at the film temperature, $(T_w + T_0)/2$, where T_w is the arithmetic average of the heat-sink base and fin-tip temperatures. The average temperature T_w is used to compare the results to the two-dimensional theoretical model, which does not include fin effects. The difference between the base and fin-tip temperatures was generally less than ten percent, and always less than 15 percent, of the base-to-ambient temperature difference. The Ph.D. dissertation by Fisher (1998) contains tabulated data, including material properties, from all experiments.

4.1 Heat Transfer Results. With the large chimney (H = 333 mm), the relative heat-sink height is $H^*_H = 0.3$, and the relative channel half-widths are $b^* = 0.00826$ and 0.0120 for the narrow and wide-channel heat sinks, respectively. For the narrow-channel heat sink, the main heating power was cycled through heating powers of 5 to 50 W in 5 W increments and 60 to 100 W in 10 W increments, with steady-state temperatures recorded at each heating power. For the wide-channel heat sink, heating levels of 10 to 45 W in 5 W increments were employed.

The experimental results for the large chimney ($H^*_H = 0.3$) are presented in nondimensional form in Fig. 4(a), where the scaled heat transfer rate Q^{**}_{tot} (see Eq. (2)) is graphed versus the scaled channel half-width, $b^*\mathrm{Gr}_H^{1/4}$ (see Eq. (1)). Results for both narrow and wide-channel heat sinks appear in the figure. The solid lines represent the theoretical predictions from Fisher et al. (1997). The two solid lines do not intersect because they represent different heat-sink porosities of ϕ = 74 percent for the narrow-channel heat sink and ϕ = 80 percent for the wide-channel heat sink. However, extrapolation of the curves indicates that the porosity difference produces only a slight change in the theoretical prediction. The theoretical predictions match the experimental results to within 11 percent and 9 percent for the narrow and wide-channel heat sinks, respectively, and consistently overpredict the measured heat dissipation rates. The overprediction may be the result of neglecting chimney viscous forces in the model, which leads to an overprediction of the system air flow rate.

The most distinguishing feature of Fig. 4(a) is the agreement between theory and experiment for the maximum nondimensional heat transfer rate. Experimental scatter prevents the precise definition of an optimal point. However, the experiments suggest a maximum in the range $0.84 \le b^*\mathrm{Gr}_H^{1/4} \le 0.92$. The theory predicts a maximum heat transfer rate at $b^*\mathrm{Gr}_H^{1/4} = 0.89$, which falls within the experimental range. Good agreement in trend and magnitude also exists away the maximum, thus confirming the theory's ability to predict the influence of geometric and thermal parameters.

For the small chimney system (H = 167 mm), the relative heat-sink height is $H^*_H = 0.6$. The main heating power was cycled through heating powers of 10 to 80 W in 10 W increments for the narrow-channel heat sink, and heating powers of 5 to 14 W in 1 W increments and 15 to 60 W in 5 W increments for the wide-channel heat sink. The smaller heating increments for the wide-channel heat sink enabled better definition of the region of maximum nondimensional heat transfer.

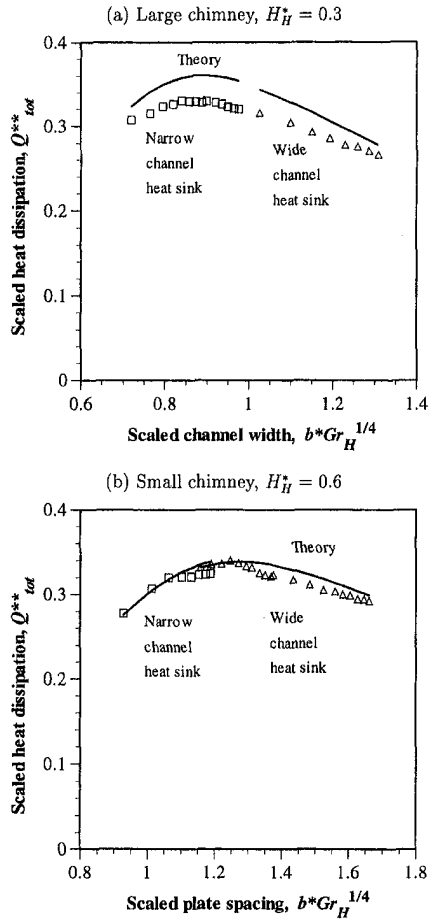

Fig. 4 Scaled total heat dissipation, Q^{**}_{tot}, as a function of scaled channel width, $b^*\mathrm{Gr}_H^{1/4}$. (*a*) Large chimney, $H^*_H = 0.3$; (*b*) small chimney, $H^*_H = 0.6$. Narrow-channel heat sink, ϕ = 74 percent. Wide-channel heat sink, ϕ = 80 percent. Theoretical data from Fisher et al. (1997). Maximum uncertainty in Q^{**}_{tot} is ±7 percent.

A nondimensional graph of Q^{**}_{tot} versus $b^*\mathrm{Gr}_H^{1/4}$ for the small chimney $H^*_H = 0.6$ is shown in Fig. 4(b). The separate lines for the narrow and wide-channel heat sinks overlap, illustrating the small effect of the porosity difference. Again, the agreement between theory and experiment is very good in the region of maximum nondimensional heat transfer. The theoretical predictions closely match the experimental data, in this case to within five percent for both heat sinks. The closer agreement in Fig. 4(b) between theory and experiment for the small-chimney system, as compared to that for the large chimney system (see Fig. 4(a)), may be the result of a reduced effect of the inviscid chimney flow assumption in the model.

The experimental maximum in Fig. 4(b) is observed near $b^*\mathrm{Gr}_H^{1/4} = 1.25$, whereas the theory predicts a maximum heat transfer rate at $b^*\mathrm{Gr}_H^{1/4} = 1.27$. Also, good agreement exists away from the maximum. However, a slightly larger difference between theory and experiment appears just to the right of the maximum in Fig. 4(b), and is discussed further in Section 4.3.

4.2 Flow Rates in the Chimney. The results of the previous section indicate generally good agreement between theory and experiment for the overall system-level energy transfer for the chimney-enhanced heat sinks under study. The present section considers more detailed local measurements. The theory of Fisher et al. (1997) is appropriate for predicting *local* velocities within the heat-sink channels but only *average* velocities within the chimney. Local velocity measurements in the heat-sink channels were not

possible due to instrument limitations, but local velocities at the chimney exit were possible, and were carried out for heating powers of 60, 80, and 100 W for the narrow-channel heat sink with the large chimney, $H_H^* = 0.3$.

Fifteen velocity measurements in the chimney cross section were taken for each power setting. Measurements were taken at $x = 5.1, 15.3, 25.5, 35.7, 45.9$ mm and $y = -20, 0, 20$ mm (using a centered x–y coordinate system in the 102-mm by 60-mm chimney cross section). Several additional measurements were taken with $x < 0$ to confirm symmetry about $x = 0$. Velocity measurements for $Q_{tot} = 60$, 80, and 100 W are shown in Figs. 5(*a*), (*b*), and (*c*), respectively. The three y-values of -20, 0, and 20 mm correspond to the heated, centerline, and unheated sides of the cross section. Turbulence intensities were measured at each x–y location and found to be less than four percent, with the highest measurements near the chimney walls.

In Fig. 5, the one-sided heating produces asymmetric local velocities about the $y = 0$ centerline. Indeed, for the higher heating powers, velocities near the heated side are generally larger than the centerline velocities. The theory, which assumes isothermal fins and one-dimensional flow in the chimney, does not capture this asymmetry. Nor does the theory account for viscous effects in the chimney, which are evident from the boundary layers

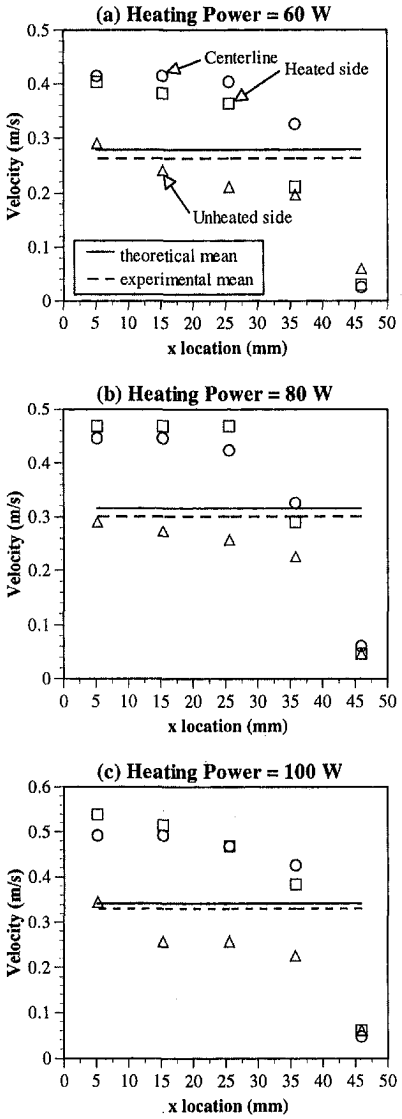

Fig. 5 Profiles of local velocity at the chimney exit. $H_H^* = 0.3$. (*a*) Q_{tot} = 60 W; (*b*) Q_{tot} = 80 W; (*c*) Q_{tot} = 100 W. Uncertainty in velocity is ±8 percent.

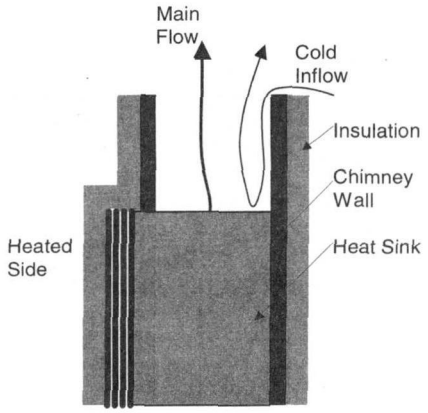

Fig. 6 Sketch of cold inflow

in the centerline velocity data. However, the mean velocities, shown by the straight lines, indicate excellent agreement between theory and experiment, with the theory being slightly higher due to the neglect of viscous forces in the chimney. The agreement in both mean velocity and overall heat transfer suggests that the theory captures the dominant thermo-fluid processes of the heat-sink/chimney system.

4.3 Effects of Cold Inflow. An unexpected "kink" appears in the nondimensional heat transfer data in Fig. 4(*b*) for the small chimney ($H_H^* = 0.6$) for both narrow and wide-channel heat sinks. For each heat sink, the agreement between theory and experiment degrades as the heat sink temperature increases (i.e., as $b^*\mathrm{Gr}_H^{1/4}$ increases). The divergence occurs over a narrow abscissa range, followed by a range in which the relative differences are nearly constant. We here postulate that cold inflow at the chimney exit starts to occur in the narrow range of divergence and persists for higher abscissa values.

The phenomenon of cold inflow has been previously studied in connection with constant-area ducts (Jorg and Scorer, 1967; Sparrow et al., 1984) and contracting channels, such as those in natural draft cooling towers (Moore, 1978; Modi and Moore, 1987; Modi and Torrance, 1987). Although the theory of cold inflow is not complete, Modi and Moore (1987) and Modi and Torrance (1987) have suggested that the presence of cold inflow is related to the Froude number

$$\mathrm{Fr} = \frac{\rho_c U^2}{g r_H(\rho_c - \rho_h)} = \frac{U^2}{g\beta r_H(T_h - T_c)} \tag{4}$$

where U is the mean fluid velocity in the chimney, the subscripts h and c represent the hot and cold fluids, and r_H is the chimney's hydraulic radius. The second equality in Eq. (4) is a consequence of a linearized equation of state. The prior work suggests that cold inflow occurs when Fr is less than a critical value, typically of the order $\mathrm{Fr}_{crit} \sim 1$.

A schematic of the cold inflow phenomenon is shown in Fig. 6. Cold inflow events in the present work were episodic and time dependent. They were nearly time-periodic and occurred along the unheated side of the chimney. This is consistent with the work of Sparrow et al. (1984) who observed cold inflow on the unheated wall of an asymmetrically heated, vertical channel. Cold inflow is driven by a density gradient between the heated chimney fluid and the unheated ambient fluid. Cold ambient fluid enters in the low-velocity wall layer of the chimney. Cold inflow decreases the overall flow rate (and heat transfer) by restricting the exit cross section and by cooling the chimney fluid, thereby reducing the effective draft height. Because the dynamic head is completely lost to the ambient (Fisher and Torrance, 1998), the system's flow and heat transfer rates decrease as exit losses increase.

Preliminary experiments on cold inflow are reported in the present

work. Cold inflow events were quantified by observing the behavior of cotton fiber strands located along the periphery of the chimney exit. The strands were approximately 1.5 cm in length and initially oriented perpendicularly to the upward chimney velocity. In the absence of cold inflow, the flow caused the strands to point upward. In the presence of cold inflow, the strands shifted, usually in a very abrupt manner, from an upward to a downward orientation.

Typically, cold inflow events lasted for approximately two seconds. Because of its periodic nature in the present study, cold inflow was quantified in terms of the frequency, f_{cold}, of the strands' shifting from an upward to downward orientation. Events were recorded for one minute at each of six locations around the perimeter of the chimney exit, with two locations on the unheated side of the chimney. The frequency of cold inflow reported here is an average from the two locations on the unheated side of the chimney.

An increase in cold inflow frequency coincided with the aforementioned slight divergence between theory and experiment for both narrow and wide-channel heat sinks. Figure 7 shows the frequency of cold inflow and the percentage error (i.e., the difference between theory and experiment) as functions of the system Grashof number. The results in Fig. 7 suggest a strong correlation between cold inflow frequency and error for both heat sinks. As the frequency increases, the error between theory and experiment increases. For the wide-channel heat sink (Fig. 7(*b*)), an abrupt increase in cold inflow frequency is closely matched by a similar increase in error between theory and experiment. For the narrow-channel heat sink (Fig. 7(*a*)), the abrupt increases are less well correlated. This could be due to the unstable hydrodynamic conditions and attendant fluctuations, or to obtaining the cold inflow data separately from the error data. All other data support the correlation between cold inflow and error.

Prior work (Modi and Moore, 1987; Modi and Torrance, 1987) has suggested that cold inflow occurs when the Froude number is less than a critical value. To test this conjecture, Froude numbers

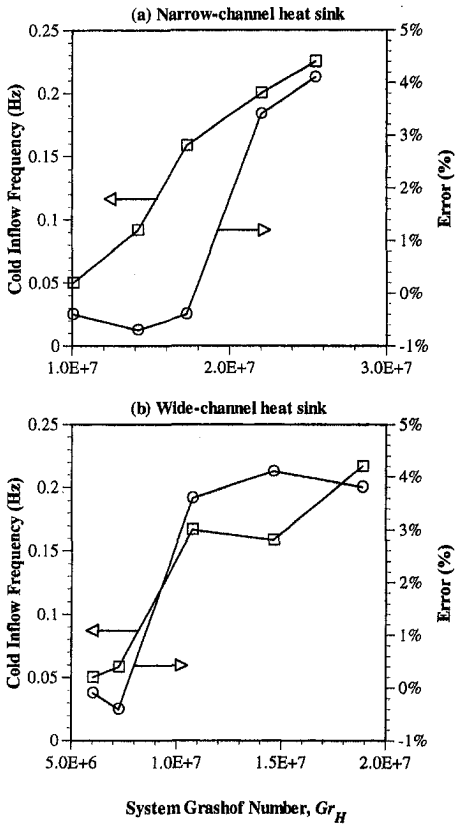

Fig. 7 Frequency of cold inflow and error between theory and experiment as functions of the system Grashof number, Gr_H. (*a*) Narrow-channel heat sink; (*b*) wide-channel heat sink. $H_H^* = 0.6$.

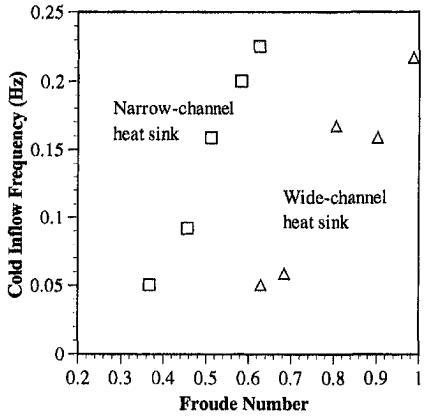

Fig. 8 Frequency of cold inflow as a function of Froude number, Fr. $H_H^* = 0.6$.

were calculated from the theoretical values for velocity and temperature. The resulting relationship between cold inflow frequency and Froude number appears in Fig. 8 for both narrow and wide-channel heat sinks. The results suggest a transition range of Froude numbers, and a dependence of the transition region on channel spacing. The transition range is of the order of the critical value suggested by Modi and Torrance (1987).

5 Summary and Conclusions

The experiments described herein document the performance improvement achievable with parallel-plate free-convection heat sinks that employ chimneys. Results are compared with theoretical predictions (Fisher et al., 1997). In general, the experiments confirm the use of the theoretical model, and the existence of optimal geometries to produce maximum heat transfer.

The agreement between theory and experiment is displayed in Fig. 4 for heat-sink heights of $H_H^* = 0.3$ and 0.6. The nondimensional channel width, $b^*Gr_H^{1/4}$, that produces maximum heat transfer was confirmed to within six percent by the experiments.

Flow-field measurements validate momentum transfer and cold inflow at the chimney exit. The measured average chimney velocity is close to that predicted by the theory (see Fig. 5). Periodic cold inflow at the chimney exit was quantified by its frequency (see Fig. 7), and found to reduce overall heat transfer by approximately four percent.

The experiments confirm that chimneys, when combined with conventional free-convection heat sinks, provide significant heat transfer enhancement and can thus reduce the size and weight of conventional heat-sink systems.

Acknowledgments

The authors thank Prof. F. K. Moore and Dr. K. K. Sikka for helpful conversations, F. A. Mendez and W. W. Thrasher for assistance with the experiments, and The Metals Group of La Selva Beach, CA, for graciously providing the heat sinks. The research was funded by the Industry-Cornell University Alliance for Electronic Packaging, with corporate support from AMP, IBM, and 3M, and was carried out at the Advanced Facility for Electronic Packaging, which is supported by the National Science Foundation, Cornell University, and the New York State Center for Advanced Technology (part of NYSSTF). TSF was supported by a graduate fellowship from the Semiconductor Research Corporation.

References

Aung, W., 1972, "Fully Developed Laminar Free Convection between Vertical Plates Heated Asymmetrically," *International Journal of Heat and Mass Transfer*, Vol. 15, pp. 1577–1580.

Aung, W., Fletcher, L. S., and Sernas, V., 1972, "Developing Laminar Free

Convection between Vertical Flat Plates with Asymmetric Heating," *International Journal of Heat and Mass Transfer,* Vol. 15, pp. 2293–2308.

Bar-Cohen, A., and Rohsenow, W. M., 1984, "Thermally Optimum Spacing of Vertical, Natural Convection Cooled, Parallel Plates," ASME JOURNAL OF HEAT TRANSFER, Vol. 106, pp. 116–123.

DISA, 1985, *DISA 55D90 Calibration Equipment Instruction Manual,* DISA/DANTEC Inc.

Elenbaas, W., 1942, "Heat Dissipation of Parallel Plates by Free Convection," *Physica,* Vol. 9, No. 1, pp. 1–28.

Fisher, T. S., 1998, "Optimal Free- and Forced-Convection Cooling of Electronics," Ph.D. thesis, Cornell University, Ithaca, NY.

Fisher, T. S., and Torrance, K. E., 1998, "Free Convection Limits for Pin-Fin Cooling," ASME JOURNAL OF HEAT TRANSFER, Vol. 120, pp. 633–640.

Fisher, T. S., Torrance, K. E., and Sikka, K. K., 1997, "Analysis and Optimization of a Natural Draft Heat Sink System," *IEEE Transactions on Components, Packaging and Manufacturing Technology—Part A,* Vol. 20, No. 2, pp. 111–119.

Jorg, O., and Scorer, R. S., 1967, "An Experimental Study of Cold Inflow into Chimneys," *Atmospheric Environment,* Vol. 1, pp. 645–654.

Kline, S. L., and McClintock, F. A., 1953, "Describing Uncertainties in Single-Sample Experiments," *Mechanical Engineering,* Vol. 75, pp. 3–8.

Mendez, F. A., and Torrance, K. E., 1998, "Thermal Anemometry for Electronic Packaging Applications," Technical Report, Sibley School of Mechanical and Aerospace Engineering, Cornell University, Ithaca, NY.

Modi, V., and Moore, F. K., 1987, "Laminar Separation in Buoyant Channel Flows," *Journal of Fluid Mechanics,* Vol. 177, pp. 37–47.

Modi, V., and Torrance, K. E., 1987, "Experimental and Numerical Studies of Cold Inflow at the Exit of Buoyant Channel Flows," ASME JOURNAL OF HEAT TRANSFER, Vol. 109, pp. 392–399.

Moore, F. K., 1978, "Cold Inflow and Its Implications for Dry Tower Design," *Proceedings of the 2nd Conference on Waste Heat Management and Utilization,* University of Miami, Miami Beach, FL.

Ostrach, S., 1952, "Laminar Natural-Convection Flow and Heat Transfer of Fluids with and without Heat Sources in Channels with Constant Wall Temperature," Technical Note 2863, NACA.

Ostrach, S., 1954, "Combined Natural- and Forced-Convection Laminar Flow and Heat Transfer of Fluids with and without Heat Sources in Channels with Linearly Varying Wall Temperatures," Technical Note 3141, NACA.

Quintiere, J., and Mueller, W. K., 1973, "An Analysis of Laminar Free and Forced Convection Between Finite Vertical Parallel Plates," ASME JOURNAL OF HEAT TRANSFER, Vol. 95, pp. 53–59.

Sparrow, E. M., Chrysler, G. M., and Azevedo, L. F., 1984, "Observed Flow Reversals and Measured-Predicted Nusselt Numbers for Natural Convection," ASME JOURNAL OF HEAT TRANSFER, Vol. 106, pp. 325–332.

Straatman, A. G., Tarasuk, J. D., and Floryan, J. M., 1993, "Heat Transfer Enhancement From a Vertical, Isothermal Channel Generated by the Chimney Effect," ASME JOURNAL OF HEAT TRANSFER, Vol. 115, pp. 395–402.

Tao, L. N., 1960, "On Combined Free and Forced Convection in Channels," ASME JOURNAL OF HEAT TRANSFER, Vol. 82, pp. 233–238.

Combined Natural Convection and Volumetric Radiation in a Horizontal Annulus: Spectral and Finite Volume Predictions

D.-C. Kuo

J. C. Morales
Mem. ASME

K. S. Ball
e-mail: kball@burst.me.utexas.edu
Mem. ASME

Department of Mechanical Engineering,
The University of Texas at Austin,
Austin, TX 78712

Combined natural convection and radiation in a two-dimensional horizontal annulus filled with a radiatively participating gray medium is studied numerically by using a control-volume-based finite difference method and a spectral collocation method coupled with an influence matrix technique. The mathematical model includes the continuity equation, the incompressible Navier-Stokes equations, the energy equation, and the radiative transfer equation (RTE), which is modeled using the P_1 differential approximation. Computed results for two Rayleigh numbers, $Ra = 10^4$ and $Ra = 10^5$, for several combinations of the radiation-conduction parameter, N_R, and the optical thickness, τ, are presented. The differences observed in the predicted flow structures and heat transfer characteristics are described. Furthermore, an unusual flow structure is studied in detail, and multiple solutions are found. Finally, the potential benefits of applying spectral methods to problems involving radiative heat transfer are demonstrated.

Introduction

Natural convection in a horizontal annulus is important in many applications. Due to its simple geometry and well-defined boundary conditions, the system has been studied extensively by researchers (Bishop et al., 1968; Kuehn and Goldstein, 1976; Farouk and Güçeri, 1981; Vafai and Desai, 1993). Among them, Kuehn and Goldstein reported a widely referenced series of experimental and numerical results for Rayleigh number up to $Ra = 10^5$. Though natural convection in an annulus has been explored in detail, the problem of combined natural convection and thermal radiation of a radiatively participating medium within a concentric annulus has received little attention. One major reason for this lack of research is that the inclusion of thermal radiation increases the complexity of the analysis significantly. The already complex equations of motion for pure convection become even more complicated with the addition of the integro-differential radiative transfer equation.

In the absence of natural convection, the heat transfer in an annulus is determined by conduction and radiation and is independent of its orientation; therefore, the system degenerates to a one-dimensional problem. The theoretical analysis for this asymptotic condition has been performed by Fernandes and Francis (1982) and by Pandey (1989). With the introduction of buoyancy, the presence of the radiatively participating medium will influence the temperature field and therefore affects the resulting flow field.

Onyegegbu (1986) was one of the first to investigate the combined heat transfer problem of a radiatively participating medium within a horizontal annulus. In his study, a finite difference based iterative method was used along with the Milne-Eddington approximation for modeling the radiative transfer. The Milne-Eddington approximation results in a differential equation which is identical to the P_1 approximation (Modest, 1993). Tan and Howell (1989) also simulated the horizontal annulus flow using a finite difference method, but they employed the YIX method to handle the integral part of the radiative transfer equation (RTE). Morales and Campo (1992) conducted a series of numerical investigations for flows within a horizontal annulus using the P_1 approximation with a control-volume-based finite difference method. Burns et al. (1995) solved the same problem using a finite element formulation for the combined mode heat transfer. Tan and Howell (1989), Morales and Campo (1992), and Burns et al. (1995) all considered the same radius ratio ($\eta = 2.6$), and in all three studies an unusual quadracellular flow was obtained as the steady-state solution for $Ra = 10^5$, $N_R = 1$, and $\tau = 1$. All of the above studies assumed symmetry in the vertical midplane and solved the two-dimensional steady-state form of the model equations. Based on these assumptions, possible asymmetries or unsteadiness in the flows would have been precluded.

To the best of the authors' knowledge, no previous studies of combined natural convection and volumetric thermal radiation in a horizontal annulus using spectral methods have been reported. In this study, the problem investigated by the above researchers is revisited using a hybrid Chebyshev/Fourier collocation method coupled with an influence matrix technique. The results are then compared to those from control-volume-based finite difference methods. Unlike previous works, midplane symmetry is not assumed and the two-dimensional equations of motion are solved in transient form in order to admit any possible unsteady or asymmetric solutions. Special focus is placed on the stability of the unusual quadracellular flow pattern reported previously and the existence of multiple solutions.

As noted by Yang (1988), transitions in flows observed in experiments are physically possible, while those in numerical simulations may not be. Thus, it is important to be able to simulate numerically the bifurcations in a flow and to determine what factors lead to bifurcations and to the existence of multiple solutions. While bifurcation phenomena in natural convection flows have been widely studied (see, for example, Saric and Szewczyk, 1985; Bau et al., 1987; Simpkins and Liakopoulos, 1992) and the existence of multiple solutions is well documented in certain problems such as buoyant flow in three-dimensional rectangular enclosures (Yang, 1988), parallel studies dealing with radiation-convection interactions are lacking. The horizontal annulus problem provides a simple geometry to investigate such interactions, which are present in many important engineering applications.

Contributed by the Heat Transfer Division for publication in the JOURNAL OF HEAT TRANSFER and presented at the '96 NHTC, Houston. Manuscript received by the Heat Transfer Division, Feb. 9, 1998; revision received, Apr. 16, 1999. Keywords: Heat Transfer, Mixed Mode, Natural Convection, Numerical Methods, Radiation. Associate Technical Editor: P. Menguc.

Formulation

The problem considered in this study is the natural convection of a radiatively participating, Boussinesq fluid with Pr = 0.72 in an infinitely long horizontal annulus. The radius ratio of the annulus is $\eta = 2.6$. A temperature difference is imposed between the inner and outer cylinders of the annulus, resulting in buoyancy-induced fluid motion (gravitational acceleration is in the vertical direction) and volumetric thermal radiation. The thermal boundary conditions correspond to an isothermal hot inner cylinder and isothermal cold outer cylinder. The hydrodynamic boundary conditions correspond to the no-slip condition on the solid surfaces.

The set of equations to be solved are the two-dimensional, incompressible continuity, momentum, energy, and radiative transfer equations expressed in the cylindrical coordinate system:

$$\frac{1}{r}\frac{\partial}{\partial r}(ru_r) + \frac{1}{r}\frac{\partial u_\theta}{\partial \theta} = 0 \tag{1}$$

$$\frac{\partial u_r}{\partial t} + u_r\frac{\partial u_r}{\partial r} + \frac{u_\theta}{r}\frac{\partial u_r}{\partial \theta} - \frac{u_\theta^2}{r} = -\frac{1}{\rho}\frac{\partial P}{\partial r} - g\beta(T_i - T)\cos\theta + \nu\left\{\frac{\partial}{\partial r}\left[\frac{1}{r}\frac{\partial}{\partial r}(ru_r)\right] + \frac{1}{r^2}\frac{\partial^2 u_r}{\partial \theta^2} - \frac{2}{r^2}\frac{\partial u_\theta}{\partial \theta}\right\} \tag{2}$$

$$\frac{\partial u_\theta}{\partial t} + u_r\frac{\partial u_\theta}{\partial r} + \frac{u_\theta}{r}\frac{\partial u_\theta}{\partial \theta} + \frac{u_r u_\theta}{r} = -\frac{1}{\rho r}\frac{\partial P}{\partial \theta} + g\beta(T_i - T)\sin\theta + \nu\left\{\frac{\partial}{\partial r}\left[\frac{1}{r}\frac{\partial}{\partial r}(ru_\theta)\right] + \frac{1}{r^2}\frac{\partial^2 u_\theta}{\partial \theta^2} + \frac{2}{r^2}\frac{\partial u_r}{\partial \theta}\right\} \tag{3}$$

$$\frac{\partial T}{\partial t} + u_r\frac{\partial T}{\partial r} + \frac{u_\theta}{r}\frac{\partial T}{\partial \theta} = \alpha\left\{\frac{1}{r}\frac{\partial}{\partial r}\left(r\frac{\partial T}{\partial r}\right) + \frac{1}{r^2}\frac{\partial^2 T}{\partial \theta^2}\right\} + \frac{a}{\rho c_p}(G - 4\sigma T^4) \tag{4}$$

$$\frac{1}{r}\frac{\partial}{\partial r}\left(r\frac{\partial G}{\partial r}\right) + \frac{1}{r^2}\frac{\partial^2 G}{\partial \theta^2} = 3(a + \sigma_s)a(G - 4\sigma T^4). \tag{5}$$

The P_1 differential approximation for a gray gas (see, for example, Modest, 1993) has been used to model the radiative transfer. By applying an energy balance, the boundary conditions for the RTE (Eq. 5) are

$$\left.\frac{\partial G}{\partial r}\right|_{r=r_i} = \frac{3\epsilon_w(a + \sigma_s)}{4 - 2\epsilon_w}(G - 4\sigma T^4)|_{r=r_i} \tag{6a}$$

and

$$\left.\frac{\partial G}{\partial r}\right|_{r=r_o} = -\frac{3\epsilon_w(a + \sigma_s)}{4 - 2\epsilon_w}(G - 4\sigma T^4)|_{r=r_o}. \tag{6b}$$

The above set of equations are cast into dimensionless form by introducing length, time, velocity, pressure, irradiation, and temperature scales of r_i, r_i^2/ν, ν/r_i, $\rho\nu^2/r_i^2$, σT_i^4, T_i, respectively. A radiation-conduction parameter, N_R, is commonly used to indicate the relative importance of the radiation effect. It is defined as

$$N_R = \frac{r_i\sigma T_o^3}{k}. \tag{7}$$

Larger values of N_R indicate stronger effects of radiation.

Solution Technique

The model equations are solved numerically using both a spectral method and a control-volume-based finite difference method. The spectral method used is a hybrid Chebyshev/Fourier collocation method. Compared to lower-order finite difference or finite element methods, it has been shown that spectral methods are better able to resolve fine scale flow features and provide greater accuracy in the simulation of transport phenomena in simple geometries (Ku et al., 1987a, b; Le Quéré and Pécheux, 1989; Hyun et al., 1995). Details of the collocation method used are briefly described below.

The velocity components, pressure, temperature, and irradiation are represented by Fourier series expansions in the periodic azimuthal direction and by Chebyshev polynomial expansions in the radial direction:

$$\varphi(r, \theta) = \sum_{m=-M/2}^{M/2-1}\sum_{n=0}^{N}\hat{\varphi}_{mn}T_n(r)\exp(-im\theta). \tag{8}$$

In Eq. (8), φ represents any dependent variable, $\hat{\varphi}_{mn}$ is the corresponding time-dependent Fourier-Chebyshev coefficient (to be determined), and $T_n(r)$ are the Chebyshev polynomials. The Chebyshev-Gauss-Lobatto collocation points (Canuto et al., 1988) are used to determine the grid points in the radial direction, while a uniform grid is used in the azimuthal direction.

In order to solve the pressure-velocity coupling, a Poisson equation is obtained by taking the divergence of the momentum equations. This equation is solved with Dirichlet boundary conditions determined from an influence matrix calculation. The influence matrix technique allows boundary conditions for the pressure

Nomenclature

a = absorption coefficient of the medium (m^{-1})
c_p = specific heat (J/kg · K)
g = gravitational acceleration (m/s^2)
G = irradiation (W/m^2)
k = thermal conductivity (W/m · K)
k_{eq} = mean equivalent conductivity
M = grid points in θ-direction
N = grid points in r-direction
N_R = radiation-conduction parameter, $r_i\sigma T_o^2/k$
P = pressure (N/m^2)
Pr = Prandtl number ($=\nu/\alpha$)
q'' = heat flux (W/m^2)
r = radial coordinate or radius (m)
Ra = Rayleigh number, $g\beta\Delta T(r_o - r_i)^3/(\nu\alpha)$
t = time (s)
T = temperature (K)
ΔT = temperature difference, $T_i - T_o$
u_r = radial velocity component (m/s)
u_θ = azimuthal velocity component (m/s)

Greek Symbols

α = thermal diffusivity (m^2/s)
β = coefficient of thermal expansion (K^{-1})
ϵ_w = emissivity of the cylinder wall
ϕ = temperature ratio, T_o/T_i
η = radius ratio, r_o/r_i
θ = azimuthal coordinate
ν = kinematic viscosity (m^2/s)
σ = Stefan-Boltzmann constant ($W/m^2 \cdot K^4$)
σ_s = scattering coefficient of the medium (m^{-1})
τ = optical thickness, $(r_o - r_i)(a + \sigma_s)$
ψ = dimensionless streamfunction

Subscripts

i = inner cylinder
o = outer cylinder

Superscripts

* = dimensionless quantity

Table 1 k_{eq} without radiation

Study	Ra = 10^4	Ra = 10^5
Kuehn and Goldstein (1976)	2.01	—
Morales and Campo (1992)	1.98	3.47
current study (spectral)	1.98	3.47

Table 2 Maximum ψ without radiation

Study	Ra = 10^4	Ra = 10^5
Tan and Howell (1989)	13.27	31.36
Morales and Campo (1992)	12.97	29.32
current study (spectral)	12.99	29.37

to be determined in such a way that the divergence of the velocity on the boundaries is eliminated; i.e., the incompressibility constraint posed by the continuity Eq. (1) is enforced. It is based on the fact that the pressure distribution at the boundary is linearly related to the divergence of the velocity there. The influence matrix technique has been widely implemented and is discussed in considerable detail elsewhere (see, for example, Le Quéré and Alziary, 1985).

After the pressure has been determined, the momentum and energy equations (2)–(4) are integrated in time following the second-order accurate, semi-implicit Adams-Bashforth/second-order backward Euler scheme (Ehrenstein and Peyret, 1989), which results in a set of two-dimensional Helmholtz equations to be solved at each time step. The use of Fourier series to represent the azimuthal variation of the dependent variables allows the two-dimensional equations to be factored into M one-dimensional equations for each Fourier wave number, m. The resulting one-dimensional equations are solved efficiently by constructing the matrix operators representing the Chebyshev collocation derivatives (using the Chebyshev-Gauss-Lobatto collocation points), as detailed by Ku et al. (1987a, b). The solution of the Helmholtz equations is thus reduced to evaluating a series of matrix products.

Finally, the Poisson equation for the irradiation is solved. Note that no special treatment is required to solve Eq. (5) for the irradiation (under the P_1 approximation, the radiative transport equation has the same form as that of the energy equation). The time level is then advanced, and the procedure is repeated until a steady-state condition is obtained.

The finite difference method follows the well-known procedure described by Patankar (1980), with the SIMPLEX algorithm chosen to solve the pressure-velocity coupling (Van Doormal and Raithby, 1985). Uniformly spaced control volumes are used, and the integration in time is accomplished using a backward Euler scheme. Both central difference and the power-law schemes are employed to evaluate the advection and diffusion fluxes. The pressure, temperature, and irradiation are computed at the center of each control volume, while velocities are determined at the control volume interfaces.

The steady-state condition is identified when the maximum change in the temperature between time steps is less than 10^{-7}. The number of time steps required to reach the steady-state condition varied with grid size, which also dictated the maximum time step that could be used without incurring stability problems. Dimensionless time steps on the order of 10^{-4}–10^{-5} are used for all computations. All computations were performed on IBM RS/6000 workstations, using double-precision arithmetic.

Results

Simulations for two Rayleigh numbers, Ra = 10^4 and Ra = 10^5, are conducted with and without the effects of volumetric radiation. When considering radiation, different combinations of N_R and τ are studied, while $\epsilon_w = 1$ (black surfaces) and ϕ is fixed ($\phi = 0.5$ unless otherwise noted). Ranges for these parameters are taken from previous works for comparison purposes and do not correspond to a particular fluid. In all calculations (unless otherwise noted), the entire annulus is considered without symmetry assumptions. Streamfunction values are obtained from the calculated velocity field by solving a Poisson equation with $\psi = 0$ at the boundaries. The mean equivalent conductivity, k_{eq}, is defined as the ratio of the total heat flux through the annulus due to convection and radiation to the heat flux due to conduction only. The convection and radiation heat fluxes are calculated by differentiating the temperature and irradiation, respectively, at the cylinder walls using the Chebyshev coefficients for the spectral simulations and one-sided finite differences for the control volume simulations. A numerical grid (r, θ) of (65×64) points is used for the spectral results, while (41×80) grid points are used for the finite volume computations. Increasing the resolutions further had no appreciable effects on the results obtained; see the convergence study.

The spectral and finite volume numerical codes developed based on the methods described above are validated using two limiting cases. The first limiting case corresponds to pure natural convection in a horizontal annulus with $\eta = 2.6$ and Pr = 0.72. A comparison of k_{eq} obtained from different numerical schemes for Ra = 10^4 and Ra = 10^5 is presented in Table 1. (The present finite volume results are identical to those of Morales and Campo (1992).) Table 2 shows the maximum streamfunction evaluated in different studies. Both tables show excellent agreement between the current results and the results from others.

The second limiting case corresponds to one-dimensional conduction and radiation in an annulus with $\eta = 2$, $\phi = 0.1$, $\tau = 1$, and Pr = 0.72. The heat flux at the inner cylinder from the spectral simulations along with the analytical solutions by Fernandes and Francis (1982) and the results from Morales and Campo (1992) are shown in Table 3. The results from the spectral simulations agree well with the finite difference results from Morales and Campo. Compared to the analytical results, however, the P_1 approximation for radiation in the participating media overpredicts the heat transfer rate. For weak radiation ($N_R = 0.5$), the difference is small, while for strong radiation ($N_R = 5.0$), the difference is about 12 percent.

Ra = 10^4. Figure 1(*a*) shows the isotherms and streamlines obtained from the spectral simulations for Ra = 10^4 without radiation. Fluid close to the inner cylinder is heated and rises along the inner cylinder wall and a thin boundary layer develops. Around the top of the inner cylinder, the boundary layers from both sides of the inner cylinder meet and detach from the cylinder wall, forming a thermal plume. The thermal plume rises, impinges upon the top of the outer cylinder, and separates to form two currents, which then descend along the outer cylinder. The major fluid motion occurring in the upper half of the annulus includes a thermal plume, boundary layer flow, and two large circulation cells. In contrast, a significant portion of the lower half of the annulus, excluding the boundary layer attached to the inner cylinder wall, remains sluggish.

Figures 1(*b–d*) show the isotherms and streamlines obtained spectrally for Ra = 10^4 with increasing radiation effect. It is seen that the introduction of radiation affects the flow structure significantly. Fluid close to the lower half of the inner cylinder is still being heated and rises along the inner cylinder but detaches from the cylinder wall earlier than that in the pure convection case,

Table 3 Scaled total heat flux at inner cylinder for radiation and conduction, $q''/[k(a + \sigma_s)T_i]$

Study	$N_R = 0.5$	$N_R = 2.5$	$N_R = 5.0$
Fernandes and Francis (1982)	1.660	3.144	5.019
Morales and Campo (1992)	1.721	3.457	5.645
current study (spectral)	1.710	3.462	5.656

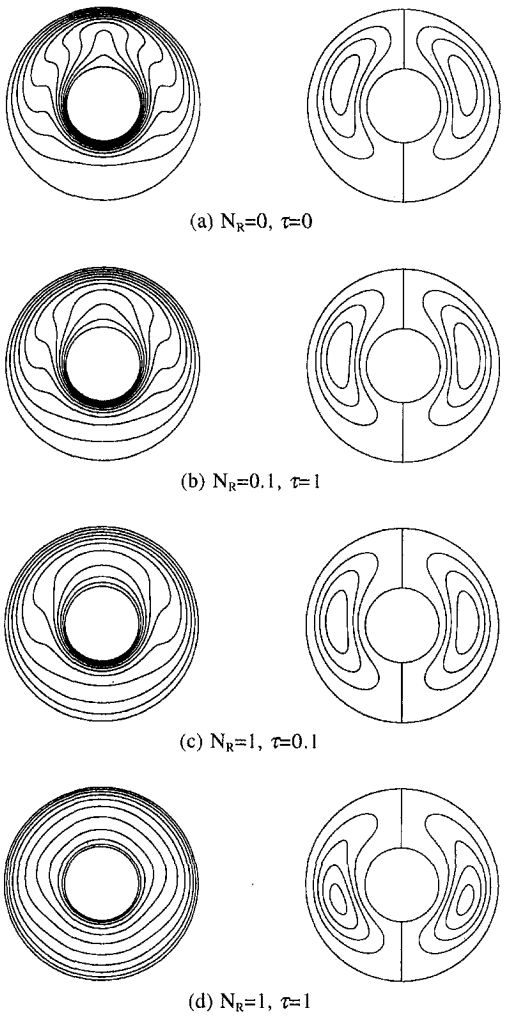

Fig. 1 Isotherms and streamlines ($\Delta\psi$ = 5) for Ra = 10^4 from spectral simulations

causing a downward shift of the centers of circulations. It is noticed that the stronger the radiation (higher N_R and/or τ), the lower the centers of circulations. With increasing radiation effects, the flow circulation increases in vigor (indicated by larger maximum values of the streamfunction). Despite the increased advective effect, the temperature distribution becomes more uniform and is dominated by the diffusive radiative transport. The temperature gradients on the cylinder surfaces also become more uniform, although there is a net increase in the mean heat transfer rate. It is concluded that the radiation tends to redistribute the thermal energy more evenly inside the domain. Finally, at this Rayleigh number, there are no significant differences between the results using finite volume computations and the ones obtained from the spectral method.

Ra = 10^5. Figure 2(*a*) shows the spectral results for Ra = 10^5 without radiation. The basic flow structure is the same as that for Ra = 10^4. The differences are the thinner boundary layers and the stronger thermal plume associated with the higher Ra. Also noticeable is the significant temperature inversion in the radial direction for Ra = 10^5 due to the stronger fluid circulation.

Figures 2(*b–c*) are the results with relatively weak radiation (N_R = 0.1, τ = 1, and N_R = 1, τ = 0.1). Because of the much stronger advection and relatively weaker radiation, most of the effects due to radiation observed in the cases for Ra = 10^4 are not seen. The only radiation effect noticeable is the more evenly distributed isotherms at the bottom of the annulus, indicating a more evenly distributed thermal energy in this area.

With strong radiation effects (N_R = 1, τ = 1), if the simulation is started from rest without disturbance, a steady-state solution, SS1, is reached (Fig. 2(*d*)). This symmetric quadracellular flow is dominated by three thermal plumes: One plume descends beneath the top of the outer cylinder toward the top of the inner cylinder while two plumes on both sides of the descending plume rise radially from the inner cylinder toward the outer cylinder. Such a flow structure is inconsistent with the weaker radiation cases shown in Figs. 2(*a–c*), suggesting that it may be nonphysical in nature. As discussed in the cases for Ra = 10^4, stronger radiation tends to redistribute the thermal energy more evenly. Thus, it is expected that the sole (central) thermal plume should become less distinct and the isotherms less distorted as the relative effects of radiation increase. However, in SS1 (Fig. 2(*d*)), three thermal plumes occur in the upper half of the annulus resulting in a reversal in the direction of flow directly above the inner cylinder and drastic variations in the temperature profile. Tan and Howell (1989) reported that they could not obtain converged solutions for $N_R > 10$, which may be an indication that the SS1 solution for N_R = 1 is probably unstable too. Burns et al. (1995) noted that the SS1 solution is probably numerical in nature and might not reflect a physical solution, due to ignored three-dimensional effects.

To see if SS1 is a stable solution, numerical experiments were conducted by introducing various disturbances into the system. For example, a random disturbance with a magnitude of less than one percent of ΔT was superimposed on the SS1 temperature field. Simulations for Ra = 10^5, N_R = 1, τ = 1 were then redone using the perturbed SS1 temperature fields as initial conditions. Regardless of

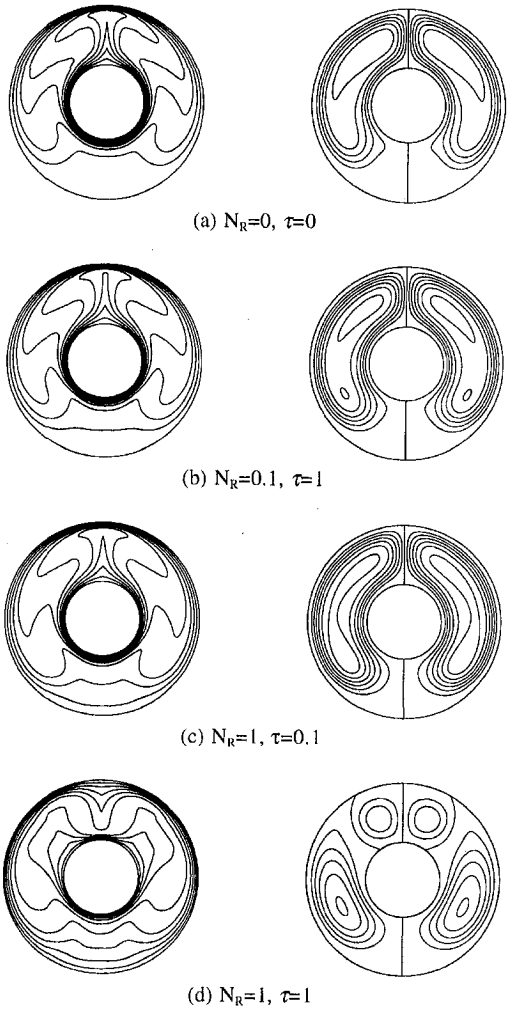

Fig. 2 Isotherms and streamlines ($\Delta\psi$ = 7) for Ra = 10^5 from spectral simulations

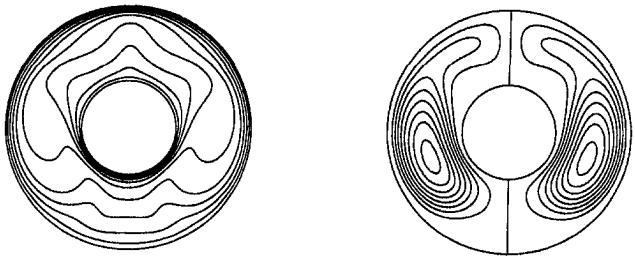

Fig. 3 Isotherms and streamlines ($\Delta\psi = 10$) for Ra = 10^5, $N_R = 1$, $\tau = 1$; SS2 solution from spectral simulations

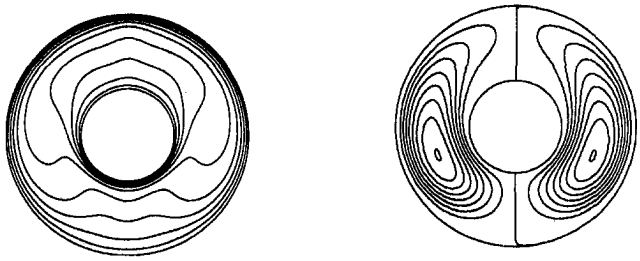

Fig. 5 Isotherms and streamlines ($\Delta\psi = 10$) for Ra = 10^5, $N_R = 1$, $\tau = 1$; SS2 solution from power-law scheme

the exact form of the perturbation, the SS1 solution was found to be unstable and a new steady-state solution, SS2, emerges (Fig. 3).

Instead of a descending thermal plume on top of the annulus and two rising ones on both sides as observed in SS1, a slow, broad upward current is present causing a weaker thermal plume in SS2. By comparing SS2 (Fig. 3) to Figs. 2(*a–c*), the characteristics of the radiation effects discussed for the case Ra = 10^4 are all shown: decreasing advection, downward shift of the centers of circulation, a weaker thermal plume, and less distorted isotherms. Therefore, in comparison with SS1, the steady-state solution SS2 is more reasonable.

This new steady-state solution, SS2, was also perturbed and it was observed that the disturbance dies out without affecting the final flow pattern. Also, a simulation for Ra = 10^5, $N_R = 1$, $\tau = 1$ using the steady-state solution for Ra = 10^4, $N_R = 1$, $\tau = 1$ as the initial condition was performed. Without introducing the disturbance, SS2 emerges as the steady-state solution directly without reaching SS1 first. This simulation further suggests that the SS2 solution is physically more plausible.

The pursuit of SS2 for Ra = 10^5, $N_R = 1$, $\tau = 1$ as described above was repeated using the finite volume method without any symmetry assumption. Computed results corroborate the existence of a second steady-state solution, SS2, which is more stable than the one obtained when starting from rest, SS1. Finite volume results obtained using the central difference scheme, Fig. 4, are similar to the results shown in Fig. 2(*d*) for the spectral method, while results obtained using the power-law scheme, Fig. 5 (which are identical to the results reported by Morales and Campo (1992)), have significant differences. In the power-law results, the SS2 temperature distribution has considerably less distinct features; such smoothing is consistent with larger numerical dissipation.

Because the SS2 flow has not been reported previously, the stability of both the SS1 and SS2 solutions in the half-domain problem, i.e., under the assumption of symmetry, was investigated by introducing various perturbations to the flow similar to the procedure described earlier for the full-domain problem. Both steady-state solutions are found to be stable in the half-domain problem. From these results, it is concluded that SS1 is stable to symmetric disturbances but unstable to asymmetric disturbances. Since previous studies on the half-domain preclude the introduction of asymmetric disturbances, SS2 was never observed. (Note that the SS2 solution evolves in the transient simulations after SS1 is randomly perturbed, thereby breaking its symmetry.)

Finally, a comparison of the mean equivalent conductivity for Ra = 10^5, $N_R = 1$, $\tau = 1$ is listed in Table 4. It is shown that k_{eq} from the spectral simulation agrees well with that from the finite volume method. As in the one-dimensional radiation and conduction case discussed earlier, the P_1 approximation for radiation overpredicts the heat transfer rate by 8.5 percent compared to the finite element calculations. Regardless of the radiative transfer model used, including the YIX method of Tan and Howell (1989), similar results are obtained for the structure of the flow field and temperature distribution. Note that Tan and Howell did not report k_{eq} values for the case being discussed.

Convergence Study. In order to assess the numerical uncertainty (grid-independence or convergence) of the solutions, the discrete error in the L^2 norm (Fletcher, 1984), defined by

$$\|\varphi - \varphi_{MN}\|_{2,d} = \left[\sum_{l=1}^{L} (\varphi - \varphi_{MN})_l^2\right]^{1/2} \tag{9}$$

is computed, where φ_{MN} represents the dependent variable of interest obtained numerically using $M \times N$ grid points. The solution obtained with the largest grid size for each case (129×128) is used to approximate the exact solution, φ, for the purpose of constructing the L^2 error in Eq. (9). The difference between the solution φ_{MN} and the "exact" solution φ is evaluated and summed over a fixed set of points common to all grid resolutions $M \times N$.

Convergence rates for the case Ra = 10^5, $N_R = 1$, $\tau = 1$ are presented in Fig. 6. In Fig. 6(*a*), the radial velocity components obtained with increasing resolution are compared to those from the highest resolution solution, while in Fig. 6(*b*) the mean equivalent conductivities are compared. In both figures, similar convergence trends are observed. For the spectral simulations, a rapid and increasing rate of convergence (greater than eighth order at the highest resolutions considered) is observed, while for the control-volume simulations a fairly constant second-order convergence rate is obtained. (The order of convergence corresponds to the slope of the L^2 error curves.) These trends are as expected, indicating that the respective numerical schemes are convergent and that the grid sizes used in this study are adequate.

The results shown in Fig. 6 clearly demonstrate that much greater accuracy can be obtained in spectral simulations compared to finite control volume simulations at the same resolution. Furthermore, it is noted that the computation times required by the spectral simulations and the finite volume simulations are comparable at the same resolu-

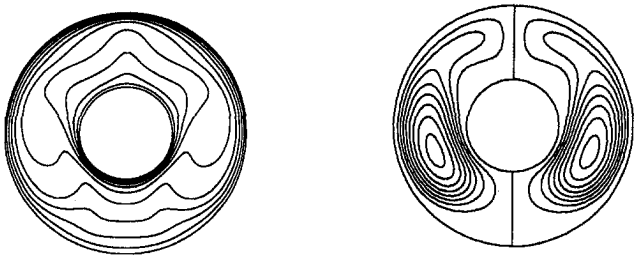

Fig. 4 Isotherms and streamlines ($\Delta\psi = 10$) for Ra = 10^5, $N_R = 1$, $\tau = 1$; SS2 solution from central difference scheme

Table 4 k_{eq} for Ra = 10^5, $N_R = 1$, $\tau = 1$

Study	SS1	SS2
Burns et al. (1995) (finite element method)	13.0	—
current study (central difference)	14.1	13.6
current study (power law)	14.0	13.7
current study (spectral)	14.1	13.6

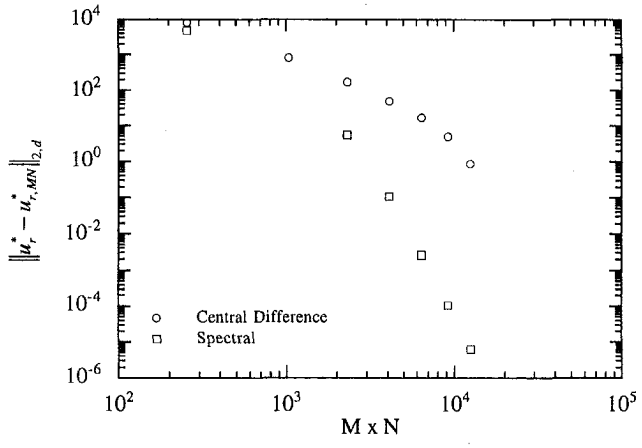

a) Radial velocity component

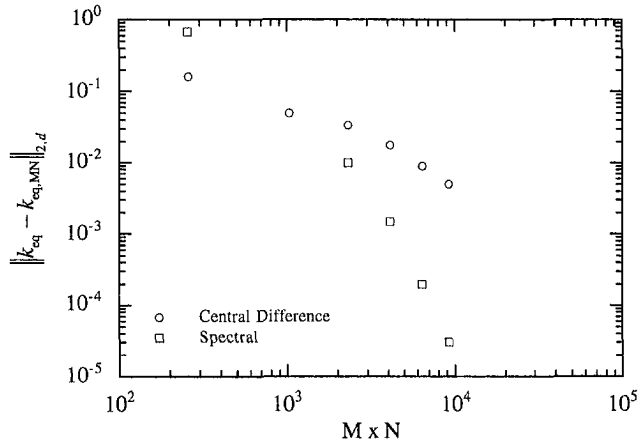

b) Mean equivalent conductivity

Fig. 6 Rates of convergence for spectral and finite volume solutions for Ra = 10^5, $N_R = 1$, $\tau = 1$

tion. While the spectral method presented has a larger fixed operation count per time step, it employs a direct method for satisfying the continuity equation; the SIMPLEX algorithm used in the finite volume calculations is iterative. Performing iterations offsets the larger operation count of the spectral method. Thus, except for the more complicated programming effort required by the spectral method, there are no other significant tradeoffs between the two methodologies as applied to this problem besides accuracy.

Conclusions

Combined natural convection and radiation of a radiatively participating medium in a differentially heated horizontal annulus has been studied numerically. The P_1 approximation is applied to model the radiative transfer. A hybrid Chebyshev/Fourier collocation method coupled with an influence matrix technique is used to solve the time-dependent equations of motion in the full domain (i.e., without symmetry assumptions). Comparisons show that the results from the spectral simulations are in good agreement with the results from finite difference simulations and from other numerical schemes, and that greater accuracy can be achieved for the same grid resolution by using a spectral method.

For Ra = 10^5, $N_R = 1$, $\tau = 1$, two steady-state solutions, SS1 and SS2, exist. It is demonstrated that the quadracellular SS1 is nonphysical and unstable while the bicellular SS2 is stable and reasonable, so the SS2 solution is preferred. It is also shown that the development of SS2 is tied to a symmetry breaking in the system. Therefore the entire domain must be taken into account without symmetry assumptions; otherwise the path towards SS2 may be artificially broken. This demonstrates two extremely important caveats when performing numerical simulations of combined natural convection-radiation problems: multiple solutions may exist due to the nonlinear thermal radiation, and expected symmetries may be broken. Considerable care should be exercised when modeling these flows.

Acknowledgment

This material is based upon work supported by the National Science Foundation under Award No. CTS-9258006.

References

Bau, H. H., Bertram, L. A., and Korpela, S. A., eds., 1987, *Bifurcation Phenomena in Thermal Processes and Convection,* ASME, New York.

Bishop, E. H., Carley, C. T., and Powe, R. E., 1968, "Natural Convective Oscillatory Flow in Cylindrical Annuli," *International Journal of Heat and Mass Transfer,* Vol. 11, pp. 1741–1752.

Burns, S. P., Howell, J. R., and Klein, D. E., 1995, "Application of the Finite Element Method to the Solution of Combined Natural Convection-Radiation in a Horizontal Cylindrical Annulus," *Numerical Methods in Thermal Problems,* Vol. IX, R. W. Lewis and P. Durbetaki, eds., Pineridge Press, Swansea, UK, pp. 327–338.

Canuto, C., Hussaini, M. Y., Quarteroni, A., and Zang, T. A., 1988, *Spectral Methods in Fluid Dynamics,* Springer-Verlag, New York.

Ehrenstein, U., and Peyret, R., 1989, "A Chebyshev Collocation Method for the Navier-Stokes Equations with Application to Double-Diffusive Convection," *International Journal for Numerical Methods in Fluids,* Vol. 9, pp. 427–452.

Farouk, B., and Güçeri, S. I., 1981, "Natural Convection from Horizontal Cylinder—Laminar Regime," ASME JOURNAL OF HEAT TRANSFER, Vol. 103, pp. 522–527.

Fernandes, R., and Francis, J., 1982, "Combined Conductive and Radiative Heat Transfer in an Absorbing, Emitting, and Scattering Cylindrical Medium," ASME JOURNAL OF HEAT TRANSFER, Vol. 104, pp. 594–601.

Fletcher, C. A. J., 1984, *Computational Galerkin Methods,* Springer-Verlag, New York.

Hyun, M. T., Kuo, D. C., Bergman, T. L., and Ball, K. S., 1995, "Simulation of Thermosolutal Convection in Pb-Sn: FVM and Spectral Predictions," *Proceedings of the 30th 1995 National Heat Transfer Conference,* Vol. 4, R. L. Mahajan, ed., ASME, New York, pp. 63–69.

Ku, H. C., Hirsh, R. S., and Taylor, T. D., 1987a, "A Pseudospectral Method for Solution of the Three-Dimensional Incompressible Navier-Stokes Equations," *Journal of Computational Physics,* Vol. 70, pp. 439–462.

Ku, H. C., Taylor, T. D., and Hirsh, R. S., 1987b, "Pseudospectral Methods for Solution of the Incompressible Navier-Stokes Equations," *Computers and Fluids,* Vol. 15, No. 2, pp. 195–214.

Kuehn, T. H., and Goldstein, R. J., 1976, "An Experimental and Theoretical Study of Natural Convection in the Annulus Between Horizontal Concentric Cylinders," *Journal of Fluid Mechanics,* Vol. 74, pp. 695–719.

Le Quéré, P., and Alziary de Roquefort, T., 1985, "Computation of Natural Convection in Two-Dimensional Cavities with Chebyshev Polynomials," *Journal of Computational Physics,* Vol. 57, pp. 210–228.

Le Quéré, P., and Pécheux, J., 1989, "Numerical Simulations of Multiple Flow Transitions in Axisymmetric Annulus Convection," *Journal of Fluid Mechanics,* Vol. 206, pp. 517–544.

Modest, M., 1993, *Radiative Heat Transfer,* McGraw-Hill, New York.

Morales, J. C., and Campo, A., 1992, "Radiative Effects on Natural Convection of Gases Confined in Horizontal, Isothermal Annuli," *Developments in Radiative Heat Transfer,* S. T. Thynell et al., eds., ASME, New York, pp. 231–238.

Onyegegbu, S. O., 1986, "Heat Transfer Inside a Horizontal Cylindrical Annulus in the Presence of Thermal Radiation and Buoyancy," *International Journal of Heat and Mass Transfer,* Vol. 29, pp. 659–671.

Pandey, D. K., 1989, "Combined Conduction and Radiation Heat Transfer in Concentric Cylindrical Media," *Journal of Thermophysics and Heat Transfer,* Vol. 3, pp. 75–82.

Patankar, S. V., 1980, *Numerical Heat Transfer and Fluid Flow,* Hemisphere, New York.

Saric, W. S., and Szewczyk, A. A., eds., 1985, *Stability in Convective Flows,* ASME, New York.

Simpkins, P. G., and Liakopoulos, A., eds., 1992, *Stability of Convective Flows,* ASME, New York.

Tan, Z., and Howell, J. R., 1989, "Combined Radiation and Natural Convection in a Participating Medium between Horizontal Concentric Cylinders," *Heat Transfer Phenomena in Radiation, Combustion and Fires,* R. K. Shah, ed., ASME, New York, pp. 87–94.

Vafai, K., and Desai, C. P., 1993, "Comparative Analysis of the Finite-Element and Finite-Difference Methods for Simulation of Buoyancy-Induced Flow and Heat Transfer in Closed and Open Ended Annular Cavities," *Numerical Heat Transfer,* Part A, Vol. 23, pp. 35–59.

Van Doormal, J. P., and Raithby, G. D., 1985, "An Evaluation of the Segregated Approach for Predicting Incompressible Fluid Flows," 1985 National Heat Transfer Conference, Denver, Aug., Paper 85-HT-9, ASME, New York.

Yang, K. T., 1988, "Transitions and Bifurcations in Laminar Buoyant Flows in Confined Enclosures," ASME JOURNAL OF HEAT TRANSFER, Vol. 110, pp. 1191–1204.

Effect of Surface Radiation and Partition Resistance on Natural Convection Heat Transfer in a Partitioned Enclosure: An Experimental Study

N. Ramesh
Research Scholar

S. P. Venkateshan[1]
Professor,
e-mail: spv35@hot.mail.com

Department of Mechanical Engineering,
Indian Institute of Technology,
Madras 600 036, India

The heat transfer across an air-filled partitioned square enclosure is studied experimentally using a differential interferometer. The partition was located centrally inside the enclosure, parallel to the two isothermal differentially heated vertical walls, and extended the full height of the enclosure. The top and bottom horizontal walls of the enclosure were maintained adiabatic. A parametric study has been carried out using different partitions, focusing attention on the effect of partition thermal resistance as well as the interaction of surface radiation and natural convection, and on the total heat transfer between the vertical walls, inside the enclosure. Correlations, valid for the laminar range, are proposed.

Introduction

The study of heat transfer in enclosures and partitioned enclosures is important in the design of various thermal systems such as building components for energy conservation, double-pane windows, nuclear reactor cooling, and so on. Buoyancy-driven flow and transport in such enclosures has received widespread attention. However, the study of interaction of surface radiation and natural convection occurring in such systems has attracted only limited attention. Partitions are provided in enclosures in order to cut down the rate of heat transfer from the hot wall to the cold wall. Results reported in the literature include vertical and horizontal enclosures having partitions of different heights and attached to different walls of the enclosure. However, from considerations of brevity and purpose, the literature review reported in the present paper pertains only to vertical enclosures having differentially heated vertical walls and adiabatic horizontal walls with vertical partitions.

Experimental and/or theoretical studies carried out for large Rayleigh numbers on partitioned enclosures containing glycerin (Emery, 1969) and water (Anderson and Bejan, 1981; Lin and Bejan, 1983; Nansteel and Greif, 1984; Nishimura et al., 1985 and 1988) are available. Because the present study considers air as the medium, a review of relevant literature on partitioned enclosures containing air is presented next.

Bajorek and Lloyd (1982) used a Mach-Zehnder interferometer to study a partially partitioned square enclosure whose surfaces and partitions (Plexiglas™, 6.35 mm thick) were coated with black paint. Air and carbon dioxide were used as working fluids and the study was carried out for $10^5 \leq Gr \leq 10^6$. Kangni et al. (1991) studied laminar natural convection and conduction in enclosures filled with air, having multiple vertical partitions with finite thickness and conductivity using a finite difference solution procedure. The study covered the Rayleigh number range 10^3–10^7 and aspect ratio 5–20. Apart from different spacing of the partition, the ratio of thermal conductivity of the partition to the fluid was varied from 1 to 10^4 and the ratio of the thickness of the partition to the width of the enclosure was varied from 0.01 to 0.1. The number of partitions were varied from one to five. However, no correlations were reported in the study. Kangni et al. (1995) carried out a similar numerical study for an inclined enclosure filled with air and provided a correlation for convective Nusselt number.

Kelkar et al. (1990) carried out a finite difference numerical study of a square enclosure containing air for two different configurations of an incomplete partition inside the enclosure. The study pointed out that the finite thickness and thermal conductivity of the partition significantly affect the heat transfer in enclosures having full length vertical partitions.

Sri Jayaram (1996) and Sri Jayaram et al. (1997) were the first to consider the effects of interaction of surface radiation among the enclosure walls and partition. Two-dimensional finite difference modeling based on a control volume formulation was adopted to study the interaction between laminar free convection ($4.54 \times 10^4 \leq Ra \leq 1.2 \times 10^6$) and surface radiation in a partitioned square enclosure (1996), and a tall enclosure (1997) using air as the medium. The partition was assumed to be very thin and perfectly conducting. The effect of an off-centered partition was also studied. For the case of tall enclosures, the aspect ratio was varied from 2 to 35. Both studies were carried out for a range of emissivity values from 0.05–0.95. A detailed parametric study has resulted in correlations for convective and radiative Nusselt numbers.

Experimental studies conducted so far on fully partitioned enclosures have used water or glycerin as the medium inside the enclosure. In general, enclosures were also of large dimensions, resulting in very high values of Rayleigh number, typically 10^9 to 10^{13}. Moreover, the interaction of surface radiation and natural convection has never been studied experimentally. The present work therefore, is aimed at providing fundamental understanding on (i) the effect interaction of surface radiation and natural convection and (ii) the effect of partition resistance on total heat transfer between the vertical walls of a partitioned enclosure, using air, for $5 \times 10^4 \leq Ra \leq 1 \times 10^5$. A series of carefully controlled experiments have been carried out to cover a wide range of parameters, as given in Table 1.

[1] To whom correspondence should be addressed.

Contributed by the Heat Transfer Division for publication in the JOURNAL OF HEAT TRANSFER. Manuscript received by the Heat Transfer Division, Oct. 1, 1998; revision received, Mar. 19, 1999. Keywords: Enclosure Flows, Heat Transfer, Interferometry, Natural Convection, Radiation. Associate Technical Editor: M. P. Menguc.

Table 1 Range of parameters considered in the present study

Parameter	Range
T_h, °C	50–100
T_c, °C	35
ϵ_h	0.05, 0.85
ϵ_c	0.05, 0.85
ϵ_p	0.03, 0.17, 0.22, 0.85
$\epsilon_t = \epsilon_b$	0.85
Ra	5×10^4–1×10^6
λ	1.74×10^{-7}–1.0×10^{-3}
N_{rc}	23–65

Experimental Apparatus and Procedure

The experimental apparatus used to investigate the heat transfer phenomena in the present study is an optical device, the differential interferometer (DI). The core element of the DI is a shearing element (Wollaston prism), the use of which produces the required split of the incident wave front into two wave fronts traveling through the test section separated by a definite distance. Figure 1 shows the schematic of the DI. The light from the mercury vapor lamp is allowed to pass through a condenser, heat filter, polarizer, interference filter (monochromater) and then through the partial mirror to a Wollaston prism in that order. The light leaving the biconvex lens, is of very high spectral quality, satisfying the conditions for interference. It is this light which is then allowed to pass through the test section. In the present study, light from the green interference filter (wave length = 549 nm) is chosen. The light, after passing through the test section and arriving at the plane mirror, retraces its path and is deflected sideways by the partial mirror PM. The second Wollaston prism WP_2, in the image plane of the telescope, causes interference fringes, which are used for quantitative analysis. The object is seen with the help of the telescope. The achromatic objective AO and the Ocular O together form the telescope. Excellent description of the DI is available in Black and Carr (1971) and Sobhan et al. (1990).

The sectional view of the partitioned enclosure test cell used in the present study is shown in Fig. 2. Two test cells (40 mm × 40 mm × 200 mm and 60 mm × 60 mm × 300 mm) were used in order to cover the range of Rayleigh numbers shown in Table 1. The hot and cold vertical walls were made of aluminum. The Nichrome™ wire-wound strip heater in the hot wall was energized by means of stabilized electric power supply through a variac. The variac could be adjusted to any input voltage in order to control the hot wall temperature. The cold wall was connected to a precision thermostat, containing water, which when circulated through a channel milled in the cold wall, maintained it at the desired temperature. The top and bottom horizontal walls were made of 1-inch thick Perspex™. By careful design and assembly, it was ensured that the hot and cold aluminum walls do not have any physical contact with the top and bottom adiabatic walls. A small air gap (<1 mm) running all along the depth of the enclosure at the meeting corners of the walls was provided to ensure that the walls do not have physical contact. The slots at the four corners (see Fig. 2) were loosely filled with glass wool (k = 0.035 W/m-K) to suppress air circulation inside the slots. The front and rear walls were made of optical quality glass plates in order to allow monochromatic light from the interference filter to pass through. Both the enclosures had a depth to width ratio of 5:1 so that two dimensional conditions prevail inside the enclosure (see, for example, Ozoe et al., 1975).

Table 2 shows the partitions used in the present study. In the present work, the surfaces of metallic partitions were highly polished using a buffing wheel and metal polish in order to obtain the required low emissivities. Application of two coats of blackboard paint on the walls of the enclosure and metallic partitions provided a high emissivity value of 0.85 (Rao and Venkateshan, 1996). The partitions were inserted into the enclosure through a small groove (0.6 mm × 1 mm) milled throughout the depth, at the center of the horizontal walls of the enclosure. The temperatures at various locations along the partition height from bottom to top were measured by means of 0.2-mm diameter Type-T thermocouples. The hot and cold wall temperature, and the temperature at various locations along the adiabatic walls of the enclosure were measured using 0.3-mm dia. Type-K thermocouples. The thermocouples were calibrated and the error accounted for as per guidelines given in ASTM standard (1989). All sides of the enclosure except the front and rear windows were covered with layers of glass wool insulation (k = 0.035 W/m-K) built up to a thickness of approx. 25 cm. This was necessary so that the heat loss from the inside to the outside of the enclosure was negligible. This heat loss was found to be less than three percent of the heat input from the hot wall, into the enclosure, for the case where largest temperature difference existed between the hot and cold walls. The insulation

Nomenclature

d = width of the enclosure, m
g = acceleration due to gravity, 9.81 m/s^2
k_f = thermal conductivity of air at T_m, W/m-K
k_p = thermal conductivity of partition material, W/m-K
n = number of partitions
N_{rc} = black body radiation conduction interaction parameter $\{\sigma T_h^4 d/k_f(T_h - T_c)\}$
$\bar{Nu}_c$ = average Nusselt number due to convection, $\{q_c d/(T_h - T_c)k_f\}$
$\bar{Nu}_r$ = average Nusselt number due to radiation, $\{q_r d/(T_h - T_c)k_f\}$
$\bar{Nu}_t$ = total (average) Nusselt number $(\bar{Nu}_c + \bar{Nu}_r)$
$\bar{Nu}_o$ = total (average) Nusselt number for a nonpartitioned square enclosure
$\bar{Nu}_p$ = total (average) Nusselt number for a partitioned square enclosure $(\bar{Nu}_p = \bar{Nu}_t)$
Pr = Prandtl number of air
q_c = convective heat flux entering the enclosure from hot wall, W/m^2
q_r = radiative heat flux entering the enclosure from hot wall, W/m^2
Ra = Rayleigh number, $\{g\beta(T_h - T_c)d^3 \text{Pr}/\nu^3\}$
t_p = thickness of partition, m
T = temperature, K
T_c = cold wall temperature, K
T_h = hot wall temperature, K
T_m = mean temperature, $(T_h + T_c)/2$, K
T_r = temperature ratio, (T_c/T_h)
x = distance along hot wall, cold wall or partition height, m

Greek Symbols

β = thermal expansion coefficient, $(1/T_m)$, K^{-1}
ϵ = hemispherical emissivity
λ = dimensionless partition resistance parameter, $\{(t_p k_f)/(k_p d)\}$
ν = kinematic viscosity of air at T_m, m^2/s
θ = dimensionless temperature, $(T - T_c)/(T_h - T_c)$
σ = Stefan-Boltzmann constant, $(5.667 \times 10^{-8}$ W/m^2 K$^4)$
ξ = dimensionless distance along partition height, (x/d)

Subscripts

b = bottom wall
c = cold, convection
f = fluid
h = hot
o = without partition
p = partition
r = radiation
t = total, top wall

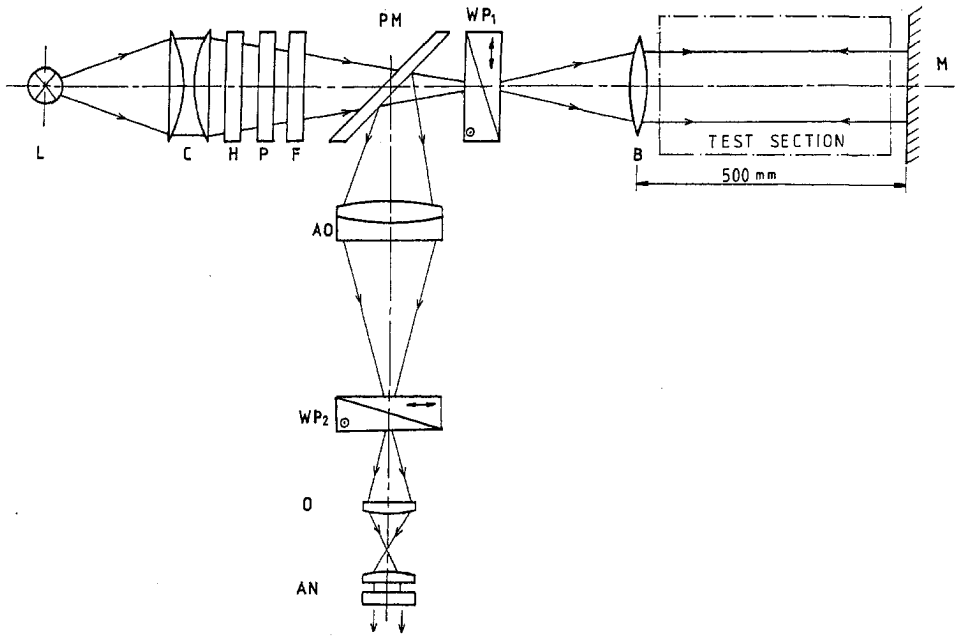

Fig. 1 Schematic of the Differential Interferometer (L–light source, C–condenser, H–heat filter, P–polarizer, F–interference filter, PM–partial mirror, WP_1–Wollaston prism, WP_2–Wollaston prism, B–Biconvex lens, M–plane mirror, AO–achromatic objective, O–ocular, AN–analyzer)

cover ensured nearly adiabatic boundary conditions along the top and bottom walls of the enclosure under laboratory conditions.

A typical experimental run lasted about ten hours. During the experiments, the temperature readings of points at identical locations both along the top wall and the bottom wall at two different cross-sectional locations along the depth of the enclosure were compared for any variations with time. It was found that after about eight hours these temperatures showed no variations with time. As an extra caution the experiments were allowed to run for another two hours before data was recorded. Interferograms and temperature readings were recorded only after attaining steady-state conditions. The thermocouples along the hot and cold isothermal vertical walls showed a maximum temperature variation of ± 0.2°C over the surface of the hot wall and a maximum variation of ± 0.3°C over the surface of the cold wall, at a temperature of 67°C between both walls. The interferograms were analyzed (Sobhan et al., 1990) to evaluate the average convective heat transfer coefficient from the hot wall of the enclosure.

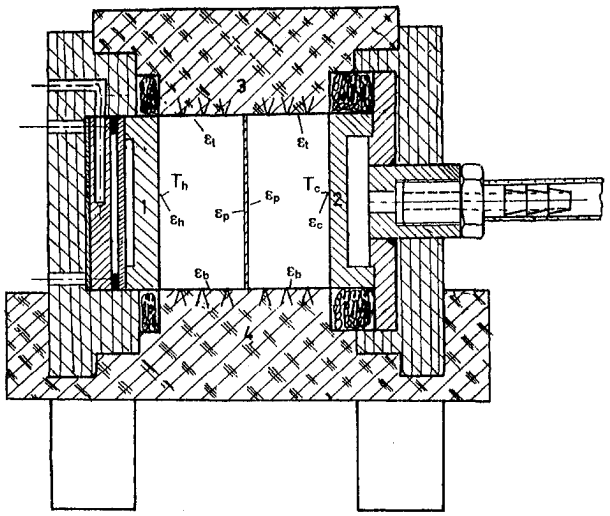

Fig. 2 Sectional view of the partitioned enclosure test cell (1–hot wall, 2–cold wall, 3–top wall, 4–bottom wall). Thermocouple locations along the top and bottom walls are indicated thus >.

The total heat transferred from the left wall of the enclosure is the sum of the convective and radiative heat transfer components. The convective part is evaluated from the interferogram. The radiative part is evaluated analytically using the measured temperatures of the hot and cold walls, the top and bottom walls, and the temperature of partition at various locations. The required shape factors were evaluated using Hottel's crossed string method (Siegel and Howell, 1972). Using the measured temperatures as input variables, the radiative heat transfer from all walls of the enclosure and partition was calculated by the method of enclosure analysis as outlined by Siegel and Howell (1972). The total heat transferred from the hot wall is represented by means of a total (average) Nusselt number ($\bar{N}u_t$), calculated as the sum of the average convective ($\bar{N}u_c$) and average radiative ($\bar{N}u_r$) Nusselt numbers. The following experimental uncertainties apply for the measured quantities: temperature—less than ± 0.04°C, length (fringe deflection measurement)—less than ± 0.02 mm, emissivity—less than ± 0.01. These would result in the overall experimental uncertainty (Coleman and Steele Jr., 1989) in the estimation of total (average) Nusselt number ($\bar{N}u_t$) to within ± 5 percent. However, the average convective Nusselt number ($\bar{N}u_c$) evaluated using the interferogram is subject to an uncertainty of ± 2.5 percent only.

Results and Discussion

A large number of experiments were carried out on two fully partitioned square enclosures for two different cases: (a) enclosures with highly polished hot and cold walls and partitions (low

Table 2 Type of partitions

Partition Material	Thickness (mm)	Conductive Resistance (K/W)	Emissivity
Pure Copper	0.10	2.5×10^{-7}	0.03
	0.28	6.98×10^{-7}	0.03
SS 316	0.10	6.7×10^{-6}	0.22
	0.38	2.6×10^{-5}	0.17
Teflon™	0.50	1.43×10^{-7}	0.85

emissivity case) and (b) enclosures with walls and partitions painted black (high emissivity case). For all experiments carried out in the present study, the top and bottom walls of the enclosure were painted black, so as to have a surface emissivity of 0.85. For example, wooden walls (Eckert and Carlson, 1961) typically have an emissivity of 0.85. In what follows, description of the results obtained from the experiments is presented.

Figure 3 shows the variation of dimensionless temperature along the partition height for the case of an enclosure having highly polished hot and cold walls. The metallic partitions were also highly polished. The Teflon™ partition was used without any surface treatment. As can be seen from the figure, the partition wall temperature distribution is linear for all partitions, increasing from bottom to top. The temperatures measured at various points along the partition height correspond to locations on the side of the partition wall which faces the vertical hot wall of the enclosure. In an enclosure with a single vertical partition located centrally, the temperature attained by the partition is due to (i) the result of the interaction between a falling boundary layer along one side i.e. the side facing the hot wall of the enclosure and a rising boundary layer along the other side, facing the cold wall of the enclosure; (ii) the longitudinal and transverse conduction occurring along and across the partition; and (iii) the radiative heat transfer to or from the partition. In fact, the temperature actually attained is an equilibrium temperature, which is a consequence of a balance among the competing factors mentioned above. The partition emissivity influences the radiative interactions among the walls which form the hot and cold cells of the enclosure. Even though all metallic partitions are highly polished to a mirror finish, all of them do not possess the same value of surface emissivity (see Table 2). The effect of thermal conductivity, thickness and surface emissivity of partitions on the partition surface temperature can be inferred from the above figure. It can be seen that the graphs for SS 316, and Teflon™, (both materials have low thermal conductivity) are steeper than for pure copper. For the same value of temperature difference between the hot and cold vertical walls of the enclosure, the above figure shows the following temperature difference between the top and bottom of the partition: Teflon™: 11.01°C, 0.1 mm copper: 3.45°C, 0.28 mm copper: 4.18°C, 0.1 mm SS 316: 10.81°C, 0.38 mm SS 316: 7.11°C.

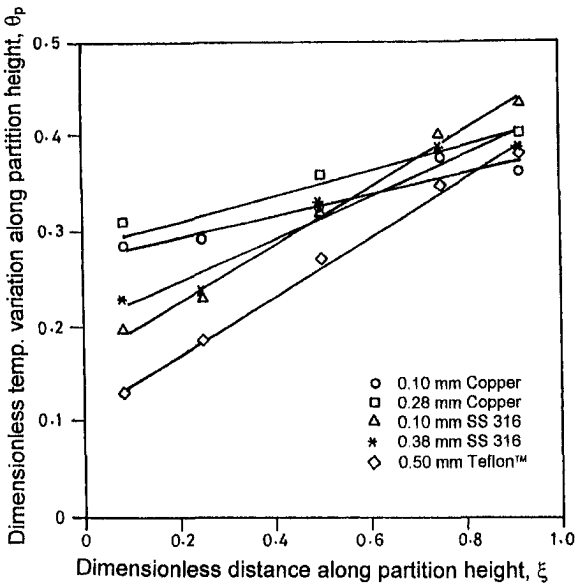

Fig. 3 Variation of dimensionless temperature along partition height. The hot and cold vertical walls of the enclosure have the same emissivity ($\epsilon_h = \epsilon_c = 0.05$). The temperature difference (T_h-T_c) lies in the range 44.8 ± 1.13°C. Table 2 shows the emissivity of partitions.

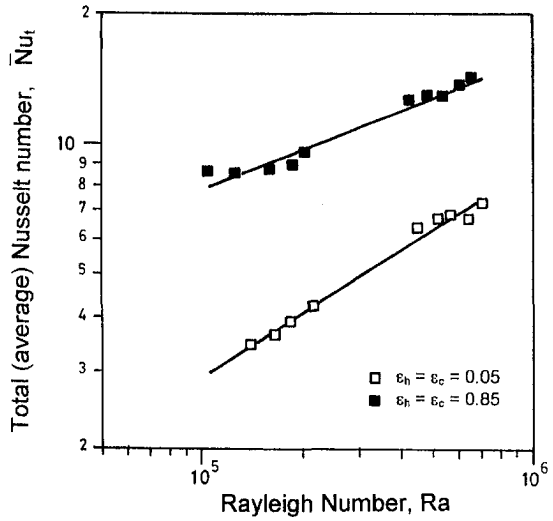

Fig. 4 Effect of emissivity of hot and cold enclosure walls on total heat transfer for the same partition (Teflon™ partition, $\epsilon_p = 0.85$)

The surface emissivity of the hot and cold walls of the enclosure has a significant effect on the partition wall temperature. If the partition is made of a material having a high value of surface emissivity, the radiative interactions occurring between the enclosure walls and the partition become severe. For the same value of temperature difference (≈31°C) maintained between the hot and cold walls of the enclosure it was found that the overall surface temperature of the Teflon™ partition increases by about 6°C in a partitioned enclosure having highly emissive hot and cold vertical walls as compared to a partitioned enclosure with highly polished hot and cold walls. This enhancement is due to the effect of strong radiative interaction among the walls of the enclosure and the partition. This interaction has a dramatic effect on $\bar{N}u_t$ evaluated at the hot wall of the partitioned enclosure, as shown in Fig. 4. The value of $\bar{N}u_t$ in an enclosure with highly emissive hot and cold walls and partition (Teflon™, in the present case) is found to be almost twice that of the value obtained by using the same partition in an enclosure with highly polished hot and cold walls. The above figure emphasizes the importance of the role of surface radiation.

The important factors that affect the heat transfer in a partitioned enclosure are the thickness, surface emissivity and thermal conductivity of the partition, medium inside the enclosure and the size of the enclosure. A dimensionless parameter (as used by Kelkar et al., 1990), called the partition resistance parameter is defined, based on the geometric and thermophysical properties, as

$$\lambda = \{t_p k_f\}/\{k_p d\}. \quad (1)$$

In a partitioned enclosure with a full partition, the overall cross-cavity heat transfer from hot to cold wall is influenced by the conductive resistance imposed by the partition. In the present study, five different partitions (Table 2) were independently studied in order to understand the effect of the presence of partition on fluid flow and heat transfer. The conductive resistances (per unit area basis) of the partitions are also given in Table 2. It is to be noted that the conductive resistance of each of the above partitions is very much lower than that of an equivalent thickness of air.

Table 3 shows values of partition resistance parameter λ, temperature difference along the partition (between top and bottom of partition) and values of $\bar{N}u_t$ evaluated for two extreme cases—pure copper and Teflon™—for increasing values of Rayleigh number. Experiments on pure copper and Teflon™ partitions were carried out, maintaining approximately the same

Table 3 Variation of $\bar{Nu}_r$ with λ

Material	λ	$T_h - T_c$ °C	ϵ_h	ϵ_c	ϵ_p	Ra	Temp. diff. °C	$\bar{Nu}_r$
Copper	1.74×10^{-7}	24.96	0.85	0.85	0.85	108269	1.46	7.781
Teflon	1.0×10^{-3}	23.83	0.85	0.85	0.85	103912	2.92	8.591
Copper	1.74×10^{-7}	52.99	0.85	0.85	0.85	188042	3.2	8.911
Teflon	1.0×10^{-3}	53.90	0.85	0.85	0.85	188599	7.87	8.876
Copper	1.16×10^{-7}	42.23	0.85	0.85	0.85	532822	3.95	12.207
Teflon	6.67×10^{-4}	42.62	0.85	0.85	0.85	535431	10.08	12.899
Copper	1.16×10^{-7}	53.35	0.05	0.05	0.03	636376	4.44	6.092
Teflon	6.67×10^{-4}	52.55	0.05	0.05	0.85	644639	13.75	6.591

value of temperature difference ($T_h - T_c$), between the hot and cold walls as shown in the table. Temperature measurements at locations along the partition height, from bottom of the partition to the top, reveal an interesting feature. As discussed earlier (Fig. 3), partition temperature increases from bottom to top. It was found that the magnitude of the temperature difference between the top and bottom of the partition wall is dependent on the thermal conductivity, thickness, and surface emissivity of the partition wall, the surface emissivity of hot and cold walls of the enclosure, and Rayleigh number of flow inside the enclosure. It can be found from Table 3, that, for more or less the same Rayleigh number, this temperature difference for the Teflon™ partition is always higher than that of a pure copper partition. It is also clear from the table, that at low value of Rayleigh number, this temperature difference for a pure copper partition (1.46°C) and Teflon partition (2.92°C) is not significant. As Rayleigh number increases, Teflon™ partition has a larger value of temperature difference between top and bottom of the partition (13.75°C) compared to that of a pure copper partition (4.44°C). This temperature difference affects the flow inside the hot and cold cells of the partitioned enclosure. Due to surface emissivity of enclosure walls and partition, this temperature difference affects the radiative interactions among the walls of the enclosure and the partition. Therefore, the radiative Nusselt number ($\bar{Nu}_r$) is strongly influenced for an enclosure having highly polished hot and cold walls and partitions. Figure 5 shows the variation of $\bar{Nu}_r$ with partition resistance parameter λ, for a partitioned enclosure with highly reflecting hot and cold vertical walls. As the Rayleigh number and partition resistance increases, the temperature difference between the top and bottom of the partition wall also increase. This temperature difference was found to be higher for an enclosure with highly reflecting hot and cold walls and partitions, as compared to an enclosure with highly emissive walls. The increase in heat transfer is reflected in the increase in average radiative Nusselt number, $\bar{Nu}_r$. Radiation contributes significantly to the overall heat transfer between the hot and cold vertical walls of the enclosure and therefore the total Nusselt number, $\bar{Nu}_t$, is also increased. Therefore, it can be concluded that it is not natural convection alone, but the coupling of the two modes of heat transfer which characterizes the transport phenomena inside the partitioned enclosure.

As pointed out earlier, the engineering objective of the present study is to investigate the effect of surface radiation and partition resistance in a partitioned enclosure. Figure 6 shows a representative graph obtained from experiments conducted in a nonpartitioned as well as a partitioned enclosure using a 0.1-mm thick copper partition. It can be seen from the graph, that at any given value of Ra, $\bar{Nu}_t$ is always higher for a nonpartitioned enclosure having highly emissive walls. For an enclosure with high emissivity walls and high emissivity partition, $\bar{Nu}_t$ at any Ra is lower than that for a similar nonpartitioned enclosure. However, even for this case, the total is higher compared to that for the case of an nonpartitioned enclosure having highly reflecting hot and cold vertical walls. At any given value of Ra, the lowest value of $\bar{Nu}_t$ is obtained for the case of a partitioned enclosure having highly reflecting hot and cold vertical walls and partitions. The trends seen in the above figure are similar for all experiments carried out on partitioned enclosures in the present study.

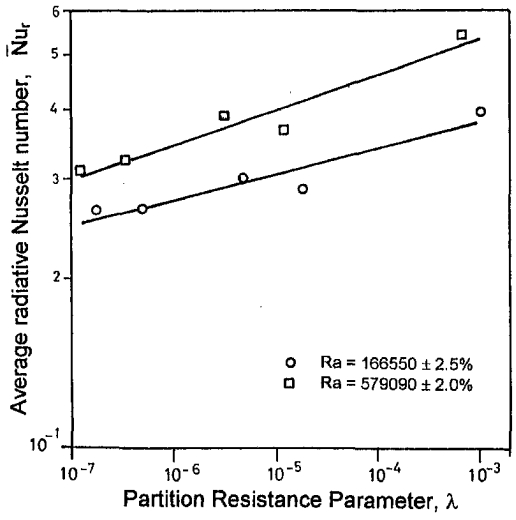

Fig. 5 Effect of partition resistance parameter on radiative heat transfer. Two enclosures (40 × 40 × 200 mm and 60 × 60 × 300 mm) were used in the experiments. The hot and cold vertical walls of the enclosure were highly polished ($\epsilon_h = \epsilon_c = 0.05$). Table 2 shows emissivity of partitions.

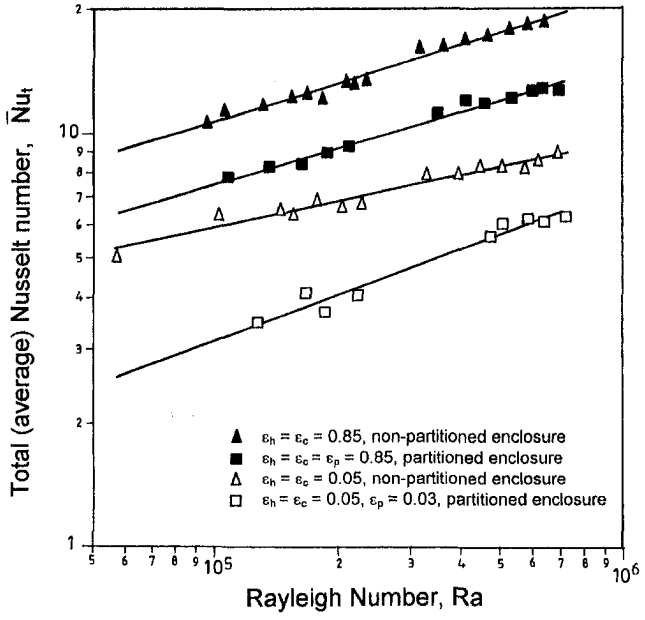

Fig. 6 Comparison of total (average) Nusselt number obtained for a partitioned enclosure with a nonpartitioned enclosure for various surface emissivities of walls and partition. The graph is for a pure copper partition, 0.1 mm thick.

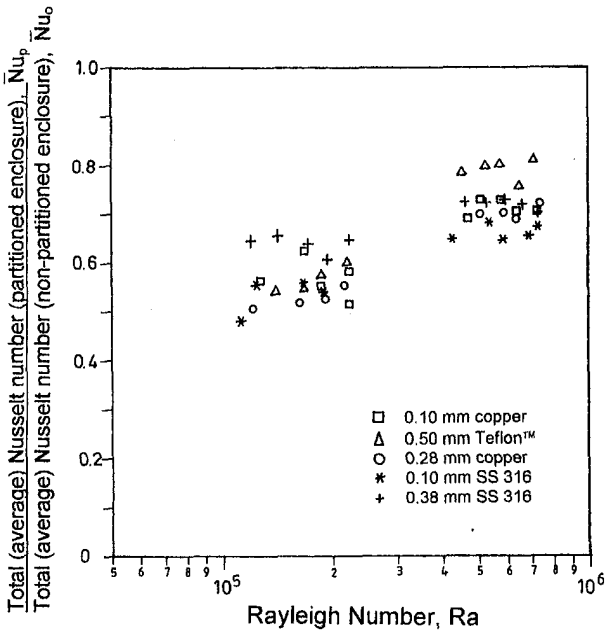

Fig. 7 Reduction in total (average) Nusselt number for a partitioned enclosure. The hot and cold vertical walls of the enclosure have same emissivity ($\epsilon_h = \epsilon_c = 0.05$). Partition emissivity as in Table 2.

Figure 7 shows the reduction ratio obtained by using highly polished partitions in an enclosure with highly polished hot and cold vertical walls. The reduction ratio is defined as the ratio of the total (average) Nusselt numbers obtained for an enclosure with and without partition. The reduction ratio is found to be a function of Rayleigh number. For the range of Rayleigh numbers considered in the present study, it can be seen from Fig. 7 that the reduction ratio lies between 0.45–0.8. For the case of natural convection being the only mode of heat transfer in enclosures with a single vertical partition, reduction ratio of 0.6 (Anderson and Bejan, 1981) and 0.5 (Nishimura et al., 1985; Sri Jayaram, 1996) have been reported earlier. The effect of surface radiation on reduction ratio can best be appreciated when this figure is compared with Fig. 8, which shows the variation of the reduction ratio with Rayleigh number for the case of a partitioned enclosure having highly emissive hot and cold vertical walls and partitions. For low Rayleigh numbers it can be inferred from Fig. 8 that surface radiation has effected a shift of the values of reduction ratio from a band 0.45–0.65 (as seen in Fig. 7) to a band 0.65–0.80. The spread in reduction ratio values seen earlier in Fig. 7, is found to be smaller in Fig. 8. For the case of a partitioned enclosure having highly emissive hot and cold vertical walls and partitions the reduction ratio is found to be independent of Rayleigh number for the range of parameters considered in the present study.

Correlations

Based on experimental data (100 points), two correlations are proposed in order to evaluate $\bar{Nu}_c$ and $\bar{Nu}_r$ for a partitioned enclosure. The correlations are obtained as functions of Rayleigh number, radiation conduction interaction parameter, emissivity of the hot and cold wall, emissivity of the partition, temperature ratio, and the partition resistance parameter.

Average Convective Nusselt Number

$$\bar{Nu}_c = 0.024\ Ra^{0.353}\ N_{rc}^{0.216}(1 + \epsilon_h)^{-0.152}(1 + \epsilon_p)^{0.061}$$

Standard error of the estimate of $\bar{Nu}_c = 0.03$

Correlation coefficient = 0.967

Deviation of data from fit = ±15 percent (max.) (2)

Average Radiative Nusselt Number

$$\bar{Nu}_r = 0.629\ Ra^{0.081}\ N_{rc}^{0.373}(\epsilon_h)^{0.974}(\epsilon_p)^{0.086}(T_r)^{-2.64}(\lambda)^{0.019}$$

Standard error of the estimate of $\bar{Nu}_r = 0.02$

Correlation coefficient = 0.999

Deviation of data from fit = ±10 percent (max.) (3)

The total (average) Nusselt number ($\bar{Nu}_t$) can be obtained as the sum of the average Nusselt number due to convection ($\bar{Nu}_c$) and the average Nusselt number due to radiation ($\bar{Nu}_r$). One of the objectives of the present investigation was to study the effect of partition resistance parameter λ on cross-cavity heat transfer between the hot and cold vertical walls of the enclosure. From graphs of $\bar{Nu}_c$ versus λ, for all partitions considered in the study, it was found that $\bar{Nu}_c$ has very little or negligible dependence on λ. Hence, λ is not included in the correlation for $\bar{Nu}_c$. The hot wall emissivity ϵ_h has a negative index. The negative value shows that as the emissivity of the hot wall increases, suppression of natural convection takes place (Balaji and Venkateshan, 1993) and hence $\bar{Nu}_c$ decreases. The radiation conduction interaction parameter N_{rc} indicates the relative role of heat transfer by radiation to that by conduction through the air layer between the two isothermal vertical walls of the enclosure. For the range of N_{rc} considered in the present study, the percentage change in $\bar{Nu}_c$ is 25 percent, whereas for the same range, $\bar{Nu}_r$ changes by 47 percent.

$\bar{Nu}_r$ has a strong dependence on ϵ_h, ($=\epsilon_c$, in the present study) which has a power of 0.974. The importance of the interaction can be seen from the index of radiation conduction interaction parameter N_{rc}, which has a relatively high value of 0.373. The partition emissivity ϵ_p is found to play an important role in both correlations. With increase in partition emissivity, enhancement of both $\bar{Nu}_c$ and $\bar{Nu}_r$ takes place. The partition resistance parameter λ was found to affect $\bar{Nu}_r$ significantly (see Fig. 5). Hence λ is included in the correlation for $\bar{Nu}_r$. For example, in the present study, λ varies from 1.74×10^{-7} to 1×10^{-3}. The corresponding percentage change in $\bar{Nu}_r$ for this range of λ is about 18 percent.

Earlier studies have concluded that the Nusselt number in a partitioned enclosure is reduced by a factor of $(n + 1)^a$ where $a = -0.61$ (Anderson and Bejan, 1981) and $a = -1$ (Nishimura et al., 1988) when compared to the Nusselt number obtained for a

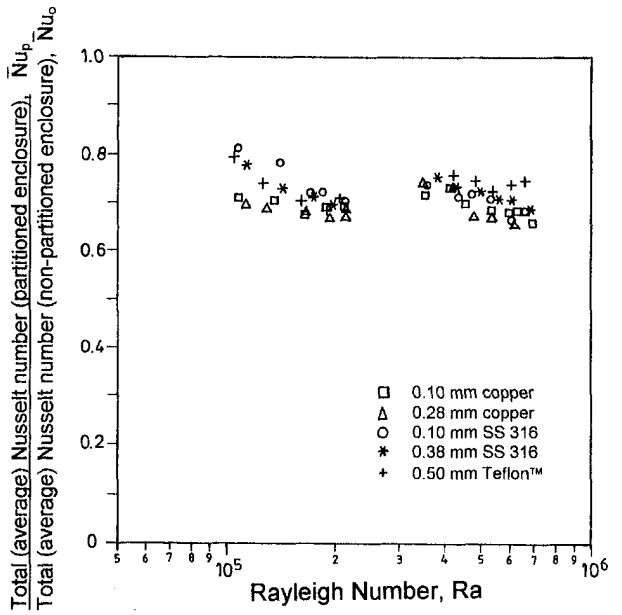

Fig. 8 Reduction in total (average) Nusselt number for a partitioned enclosure. All walls of the enclosure and partitions have the same emissivity (=0.85).

nonpartitioned enclosure, where "n" is the number of partitions. The results of Sri Jayaram et al. (1997) and the present experimental study have shown that the reduction of Nusselt number by a factor of the type $(n + 1)^a$, where "a" is a fixed quantity, is not correct for all situations. Enclosure and partition walls have nonzero emissivity and therefore there occur transfer of heat by radiation also. Hence, the interaction of surface radiation with natural convection brings about a marked deviation of results obtained considering radiation from those obtained without considering radiation. This deviation is large, particularly if the surfaces of enclosure walls and partitions are of very high emissivity. A comparison of Figs. 7 and 8 will enable us to understand this better. The heat transfer mechanism in a partitioned enclosure with highly emissive walls and partitions is therefore entirely different from that of a partitioned enclosure having highly reflecting walls and partitions.

Conclusion

In this paper we have reported the results of an experimental study carried out on fully partitioned square enclosures, focusing attention on the effect of surface emissivity of walls and partition on the overall heat transfer inside the enclosure. The following conclusions can be drawn from the study:

1 Natural convection heat transfer is supplemented by surface radiation between the walls of the enclosure and the partition. Even though there is a reduction of natural convection because of the presence of surface radiation, the overall heat transfer represented by $\bar{N}u_t$ is augmented substantially.

2 A temperature difference occurs along the partition height between top and bottom (top being always at a higher temperature) and this difference which depends on Ra and partition properties, affects the surface radiation to a large extent, thereby increasing $\bar{N}u_r$ and therefore $\bar{N}u_t$ as partition resistance parameter increases.

3 The reduction in total Nusselt number for a partitioned enclosure having highly emissive enclosure walls and partition was found to be independent of the Rayleigh number, for the range considered in the present study.

4 Two correlations were also presented.

Acknowledgment

The authors thank Dr. C. Balaji, Assistant Professor, Department of Mechanical Engineering, Indian Institute of Technology, Madras, for his comments while reviewing the original manuscript.

References

Anderson, R., and Bejan, A., 1981, "Heat Transfer Through Single and Double Vertical Walls in Natural Convection: Theory and Experiment," *International Journal of Heat and Mass Transfer,* Vol. 24, No. 10, pp. 1611–1620.

Bajorek, S. M., and Lloyd, J. R., 1982, "Experimental Investigation of Natural Convection in Partitioned Enclosures," ASME JOURNAL OF HEAT TRANSFER, Vol. 104, pp. 527–532.

Balaji, C., and Venkateshan, S. P., 1993, "Interaction of Surface Radiation with Free Convection in a Square Cavity," *International Journal of Heat and Fluid Flow,* Vol. 14, No. 3, pp. 260–267.

Black, W. Z., and Carr, W. W., 1971, "Application of Differential Interferometer to the Measurement of Heat Transfer Coefficients," *Review of Scientific Instruments,* Vol. 42, pp. 337–340.

Coleman, H. W., and Steele, Jr., W. G., 1989, *Experimentation and Uncertainty Analysis for Engineers,* John Wiley and Sons, New York.

Eckert, E. R. G., and Carlson, W. O., 1961, "Natural Convection in an air layer enclosed between two vertical plates with different temperatures," *International Journal of Heat and Mass Transfer,* Vol. 2, pp. 106–120.

Emery, A. F., 1969, "Exploratory Studies of Free Convection Heat Transfer Through an Enclosed Vertical Liquid Layer With a Vertical Baffle," ASME JOURNAL OF HEAT TRANSFER, Vol. 91, pp. 163–165.

Kangni, A., Ben Yedder, R., and Bilgen, E., 1991, "Natural Convection and Conduction in Enclosures with Multiple Vertical Partitions," *International Journal of Heat and Mass Transfer,* Vol. 34, No. 11, pp. 2819–2825.

Kangni, A., Vasseur, P., and Bilgen, E., 1995, "Natural Convection in Inclined Enclosures with Multiple Conducting Partitions," *AIAA Journal of Thermophysics and Heat Transfer,* Vol. 9, No. 2, pp. 270–277.

Kelkar, K. M., and Patankar, S. V., 1990, "Numerical Prediction of Natural Convection in Square Partitioned Enclosures," *Numerical Heat Transfer,* Part A, Vol. 17, pp. 269–285.

Lin, Nienchuan N., and Bejan, A., 1983, "Natural Convection in a Partially Divided Enclosure," *International Journal of Heat and Mass Transfer,* Vol. 26, No. 12, pp. 1867–1878.

Nansteel, M. W., and Greif, R., 1984, "An Investigation of Natural Convection in Enclosures with Two and Three Dimensional Partitions," *International Journal of Heat and Mass Transfer,* Vol. 27, No. 4, pp. 561–571.

Nishimura, T., Shiraishi, M., and Kawamura, Y., 1985, "Analysis of Natural Convection Heat Transfer in Enclosures Divided by a Vertical Partition Plate," *Proceedings of the International Symposium on Heat Transfer, Beijing,* Paper No. 85-ISHT-1-6, pp. 129–136.

Nishimura, T., Shiraishi, M., Nagasawa, F., and Kawamura, Y., 1988, "Natural Convection Heat Transfer in Enclosures with Multiple Vertical Partitions," *International Journal of Heat and Mass Transfer,* Vol. 31, No. 8, pp. 1679–1686.

Ozoe, H., Sayama, H., and Churchill, S. W., 1975, "Natural Convection in an Inclined Rectangular Channel at Various Aspect Ratios and Angles—Experimental Measurements," *International Journal of Heat and Mass Transfer,* Vol. 18, pp. 1425–1431.

Rao, Rammohan V., and Venkateshan, S. P., 1996, "Experimental Study of Free Convection and Radiation in Horizontal Fin Arrays," *International Journal of Heat and Mass Transfer,* Vol. 39, No. 4, pp. 779–789.

Siegel, R., and Howell, J. R., 1972, *Thermal Radiation Heat Transfer,* McGraw-Hill, New York.

Sobhan, C. B., Venkateshan, S. P., and Seetharamu, K. N., 1990, "Experimental Studies on Steady Free Convection Heat Transfer from Fins and Fin Arrays," *Warme-und-Stoffubertragung,* Vol. 25, pp. 345–352.

Sri Jayaram, K., 1996, "Interaction of Surface Radiation and Free Convection in Partitioned Enclosures," M.S. thesis, Indian Institute of Technology, Madras, India.

Sri Jayaram, K., Balaji, C., and Venkateshan, S. P., 1997, "Interaction of Surface Radiation and Free Convection in an Enclosure With a Vertical Partition," ASME JOURNAL OF HEAT TRANSFER, Vol. 119, pp. 641–645.

"Temperature Measurement," Annual Book of ASTM Standards, Vol. 14.03, ASTM, Philadelphia, pp. 96–97.

Dynamics and Heat Transfer Associated With a Single Bubble During Nucleate Boiling on a Horizontal Surface

G. Son

V. K. Dhir
Mem. ASME

N. Ramanujapu

Mechanical and Aerospace Engineering Department, University of California, Los Angeles, CA 90095

In this study, a complete numerical simulation of a growing and departing bubble on a horizontal surface has been performed. A finite difference scheme is used to solve the equations governing conservation of mass, momentum, and energy in the vapor-liquid layers. The vapor-liquid interface is captured by a level set method which is modified to include the influence of phase change at the liquid-vapor interphase. The disjoining pressure effect is included in the numerical analysis to account for heat transfer through the liquid microlayer. From the numerical simulation, the location where the vapor-liquid interface contacts the wall is observed to expand and then retract as the bubble grows and departs. The effect of static contact angle and wall superheat on bubble dynamics has been quantified. The bubble growth predicted from numerical analysis has been found to compare well with the experimental data reported in the literature and that obtained in this work.

Introduction

Nucleate boiling is a liquid-vapor phase-change process associated with bubble formation. As it is a very efficient mode of heat transfer, the boiling process has been studied extensively during the last half century. Although significant progress has been made in modeling the nucleate boiling process, a mechanistic model to describe the phenomena and predict the heat transfer coefficients without employing empirical constants has not yet been developed for isolated bubble regime (partial nucleate boiling) on a horizontal surface. In most previous studies, modeling of bubble dynamics including the growth and departure of the bubble has been overly simplified and the flow and temperature fields influenced by the bubble motion have not been correctly treated.

Fritz (1935) was the first to develop a criterion for bubble departure by balancing buoyancy with surface tension forces acting on a static bubble. He proposed an empirical expression for the bubble departure diameter as

$$D_d = 0.0208\varphi\sqrt{\sigma/g(\rho_l - \rho_v)} \tag{1}$$

where the contact angle φ is measured in degrees. Although deviations of predictions made from Eq. (1) with the data for the bubble diameter at departure reported in the literature have been observed, Eq. (1) provides an appropriate length scale for the boiling process. Including the effect of the bubble growth velocity, Staniszewski (1959) suggested an equation for the bubble diameter at departure as

$$D_d = 0.0071\varphi\sqrt{2\sigma/g(\rho_l - \rho_v)}\left(1 + 0.435\frac{dD}{dt}\right) \tag{2}$$

where dD/dt is given in inches per second just prior to departure. This correlation was based on his experimental observation that faster growing bubbles grew bigger before departure. The criterion for bubble departure has been improved by including several other forces such as liquid inertia and drag (Hsu and Graham, 1976). However, the evaluation of these forces requires knowledge of the bubble growth rate.

An expression for the asymptotic growth of a spherical bubble placed in a superheated liquid layer of infinite extent was obtained by Plesset and Zwick (1954):

$$D = 4\sqrt{\frac{3}{\pi}}\sqrt{\alpha_l t}\frac{\rho_l c_{pl}\Delta T}{\rho_v h_{fg}}. \tag{3}$$

This expression suggests that the growth rate of a bubble is linearly proportional to liquid superheat, ΔT. However, for a bubble attached to a heater surface, the growth rate cannot be obtained analytically because the temperature field around the bubble is not uniform and the bubble shape changes continuously. Mikic et al. (1970) used a geometric factor to relate the shape of a bubble growing on the heater surface to a perfect sphere. Accounting for the thermal energy that is stored in the superheated liquid layer prior to bubble inception, they obtained an approximate solution for the bubble growth rate. Since the initial energy content of the superheated liquid layer surrounding the bubble depends on the waiting time, the model exhibits the dependence of bubble growth rate on the waiting time. However, the model did not include the evaporation from the liquid microlayer underneath the base of a bubble.

The existence of the microlayer underneath a bubble was confirmed experimentally by Cooper and Lloyd (1969) through the observation of fluctuations in the heater surface temperature. Using the lubrication theory for the liquid flow in the microlayer, they deduced the thickness of the microlayer as

$$\delta = 0.8\sqrt{\nu_l t}. \tag{4}$$

Although Cooper and Lloyd proved the importance of microlayer evaporation, they did not account for long range forces when the microlayer is very thin. Complete analysis for the microlayer including disjoining pressure, vapor recoil pressure, and interfacial heat transfer resistance has been carried out by Lay and Dhir (1995). As a result, they were able to predict the maximum diameter of vapor stems in fully developed nucleate boiling. According to their analysis, local heat fluxes as high as 1.54×10^8 W/m^2 can exist in the very thin film.

Recently, Lee and Nydahl (1989) have numerically simulated

Contributed by the Heat Transfer Division for publication in the JOURNAL OF HEAT TRANSFER. Manuscript received by the Heat Transfer Division, Aug. 2, 1998; revision received, Feb. 3, 1999. Keywords: Boiling, Bubble Growth, Heat Transfer, Multiphase, Numerical Methods. Associate Technical Editor: P. Ayyaswamy.

the bubble growth in nucleate boiling including the microlayer. For the thickness of the microlayer, they have used the formulation of Cooper and Lloyd. To match the predicted bubble growth with the experimental data reported in the literature, they reduced the lead constant in Eq. (4) to 0.55. Although Lee and Nydahl accounted for the flow field and temperature field correctly by solving the momentum and energy equations in the liquid, they had to assume that the bubble remained hemispherical in shape during its growth and as such they could not demonstrate the departure process of the bubble.

The objective of this study is to perform a complete simulation of the hydrodynamics and heat transfer associated with a single bubble, the shape of which changes continuously during the growth. Through the analysis new physical insights can be gained into partial nucleate boiling, which has eluded the simplified models developed previously. As such the equations governing conservation of mass, momentum, and energy in the vapor and liquid phases are solved numerically. The vapor-liquid interface is captured by a level set method which can easily handle breaking and merging of the interface. This method has been applied to adiabatic incompressible two-phase flow by Sussman et al. (1994) and to film boiling near critical pressures by Son and Dhir (1998). In this work, the level set formulation, modified to accommodate the liquid-vapor phase change, is applied for simulation of partial nucleate boiling on a horizontal surface.

Analysis

In analyzing the growth of a single bubble, the computational domain is divided into micro and macro regions as shown in Fig. 1. The micro region contains the thin film that forms underneath the bubble whereas the macro region consists of the bubble and the liquid surrounding the bubble. In carrying out the analysis the flows are assumed to be axisymmetric and laminar and the fluid properties including density, viscosity, and thermal conductivity are assumed to be constant in each phase. For the low-wall superheats investigated in this study, the liquid viscosity changes by less than nine percent and the other thermophysical properties change by less than three percent. Therefore, the assumption of constant property is not too restrictive so long as the computations are performed for low superheats.

Liquid Microlayer. Lubrication theory for the microlayer has been used and validated by a number of investigators in the literature (refer to Wayner (1992) and Lay and Dhir (1995)). The equation of mass conservation in the microlayer is written as

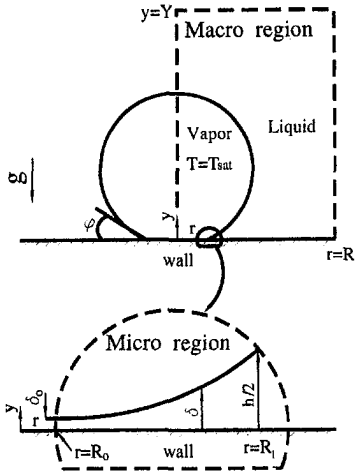

Fig. 1 Macro and micro regions used in numerical simulation

$$\frac{\partial \delta}{\partial t} = v_l - q/\rho_l h_{fg}. \tag{5}$$

In Eq. (5), the liquid velocity normal to the vapor-liquid interface, v_l, is obtained from the continuity equation as

$$v_l = -\frac{1}{r}\frac{\partial}{\partial r}\int_o^\delta r u_l dy. \tag{6}$$

The momentum equation for the microlayer is written as

$$\frac{\partial p_l}{\partial r} = \mu_l \frac{\partial^2 u_l}{\partial y^2}. \tag{7}$$

The energy conservation equation for the film yields

$$q = k_l(T_w - T_{int})/\delta. \tag{8}$$

Nomenclature

A = dispersion constant
c_p = specific heat at constant pressure
D = bubble diameter
D_c = cavity diameter
D_d = bubble diameter at departure
$\mathbf{g}$ = gravity vector
H = step function
h = grid spacing for the macro region
h_{ev} = evaporative heat transfer coefficient
h_{fg} = latent heat of evaporation
k = thermal conductivity
l_o = characteristic length, $\sqrt{\sigma/g(\rho_l - \rho_v)}$
M = molecular weight
$\mathbf{m}$ = mass flux vector defined in Eq. (17)
Nu = Nusselt number, $l_o q/k\Delta T$
p = pressure
q = heat flux
R = radius of computational domain
$\bar{R}$ = universal gas constant
R_o = radius of dry region beneath a bubble
R_1 = radial location of the interface at $y = h/2$
r = radial coordinate
T = temperature
ΔT = temperature difference, $T_w - T_{sat}$
t_o = characteristic time, l_o/u_o
u = r-directional velocity
$\mathbf{u}$ = velocity vector, (u, v)
$\mathbf{u}_{int}$ = interfacial velocity vector
u_o = characteristic velocity, $\sqrt{gl_o}$
$\dot{V}_{micro}$ = rate of vapor volume production from the microlayer
ΔV_{micro} = control volume near the micro region
v = y-directional velocity
Y = height of computational domain
y = vertical coordinate
α = thermal diffusivity
β_T = coefficient of thermal expansion
δ = liquid film thickness
δ_T = thermal layer thickness
θ = dimensionless temperature, $(T - T_{sat})/\Delta T$
κ = interfacial curvature
μ = dynamic viscosity
ν = kinematic viscosity
ρ = density
σ = surface tension
σ_T = variation of surface tension with temperature
ϕ = level set function
φ = contact angle

Subscripts

int = interface
l, v = liquid, vapor
r, y, t = $\partial/\partial r$, $\partial/\partial y$, $\partial/\partial t$
sat, w = saturation, wall

The inertial terms in the momentum equation and convection terms in the energy equation can be neglected because the Reynolds number based on the liquid film thickness and the liquid velocity (smaller than 0.05 m/sec for $\Delta T = 8.5$ K) in the micro region is less than unity.

Using a modified Clausis Clayperon equation, (e.g., Wayner, 1992), the evaporative heat flux is written as

$$q = h_{ev}[T_{int} - T_v + (p_l - p_v)T_v/\rho_l h_{fg}] \tag{9}$$

where

$$h_{ev} = 2(M/2\pi\bar{R}T_v)^{0.5}\rho_v h_{fg}^2/T_v; \quad T_v = T_{sat}(p_v). \tag{10}$$

The pressures in the vapor and liquid phases are related (Lay and Dhir, 1995) as

$$p_l = p_v - \sigma\kappa - \frac{A}{\delta^3} + \frac{q^2}{\rho_v h_{fg}^2} \tag{11}$$

where surface tension, σ, is taken to be a function of temperature and A is the dispersion constant relating disjoining pressure to the film thickness. In Eq. (11), the second term on the right-hand side accounts for the capillary pressure, the third term for the disjoining pressure, and the last term originates from the recoil pressure. The curvature of the interface is defined as

$$\kappa = \frac{1}{r}\frac{\partial}{\partial r}\left(r\frac{\partial\delta}{\partial r}\Big/\sqrt{1+\left(\frac{\partial\delta}{\partial r}\right)^2}\right). \tag{12}$$

The combination of the mass, momentum, and energy equations for the microlayer yields

$$\delta'''' = f(\delta,\ \delta'\delta''\delta''') \tag{13}$$

where $'$ denotes $\partial/\partial r$.

The boundary conditions for the above equation are as follows:

at $r = R_o$,

$$\delta = \delta_o; \quad \delta' = \delta''' = 0 \tag{14}$$

where δ_o is of the order of molecular size (refer to Lay and Dhir (1995)).

at $r = R_1$,

$$\delta = h/2; \quad \delta'' = 0 \tag{15}$$

where $h/2$ is the distance to the first computational node for the level set function, ϕ, from the wall. In implementing the above boundary conditions the radius R_1 was determined from the solution of macro region. For a given dispersion constant, the microlayer formulation, Eq. (13), and R_o are solved with five boundary conditions, Eqs. (14) and (15). In this study an apparent contact angle is defined as

$$\tan\varphi = h/2(R_1 - R_o). \tag{16}$$

Macro Region. For numerically analyzing the macro region, the level set formulation developed by Son and Dhir (1998) for film boiling is used. The interface separating the two phases is captured by ϕ, which is defined as a signed distance from the interface. The negative sign is chosen for the vapor phase and the positive sign for the liquid phase. The momentum and energy equations for the vapor-liquid region are written as

$$\rho\left(\frac{\partial\mathbf{u}}{\partial t} + \mathbf{u}\cdot\nabla\mathbf{u}\right) = -\nabla p + \rho\mathbf{g} - \rho\beta_T(T - T_{sat})\mathbf{g} - \sigma\kappa\nabla H + \nabla\cdot\mu\nabla\mathbf{u} + \nabla\cdot\mu\nabla\mathbf{u}^T$$

$$\rho c_{pl}\left(\frac{\partial T}{\partial t} + \mathbf{u}\cdot\nabla T\right) = \nabla\cdot k\nabla T \quad \text{for } H > 0$$

$$T = T_{sat}(p_v) \quad \text{for } H = 0$$

where

$$\rho = \rho_v + (\rho_l - \rho_v)H$$

$$\mu^{-1} = \mu_v^{-1} + (\mu_l^{-1} - \mu_v^{-1})H$$

$$k^{-1} = k_l^{-1}H$$

$$H = 1 \quad \text{if } \phi \geq +1.5h$$

$$= 0 \quad \text{if } \phi \leq -1.5h$$

$$= 0.5 + \phi/(3h) + \sin[2\pi\phi/(3h)]/(2\pi) \quad \text{if } |\phi| \leq 1.5h$$

where h is a grid spacing. The step function, H, is smoothed over three grid spacings to prevent numerical instability arising from discontinuous material properties (refer to Sussman et al., 1994). The mass conservation equation including the effect of volume expansion due to liquid-vapor phase change is derived from the conditions of the mass continuity and energy balance at the interface:

$$\mathbf{m} = \rho(\mathbf{u}_{int} - \mathbf{u}) = k\nabla T/h_{fg} \tag{17}$$

$$\nabla\cdot\mathbf{u} = -\frac{1}{\rho}\left(\frac{\partial\rho}{\partial t} + \mathbf{u}\cdot\nabla\rho\right) + \dot{V}_{\text{micro}}$$

$$= \frac{\mathbf{m}}{\rho^2}\cdot\nabla\rho + \dot{V}_{\text{micro}}. \tag{18}$$

In Eq. (18), $\dot{V}_{\text{micro}}$ is obtained from the microlayer solution as

$$\dot{V}_{\text{micro}} = \int_{R_o}^{R_1}\frac{k_l(T_w - T_{\text{int}})}{\rho_v h_{fg}\delta\Delta V_{\text{micro}}}rdr \tag{19}$$

where ΔV_{micro} is a vapor-side control volume near the micro region, which was arbitrarily chosen to be $R_1 - 3h \leq r \leq R_1$ and $0 \leq y \leq h$. In the level set formulation, the level set function, ϕ, is advanced as

$$\frac{\partial\phi}{\partial t} = -\mathbf{u}_{\text{int}}\cdot\nabla\phi \tag{20}$$

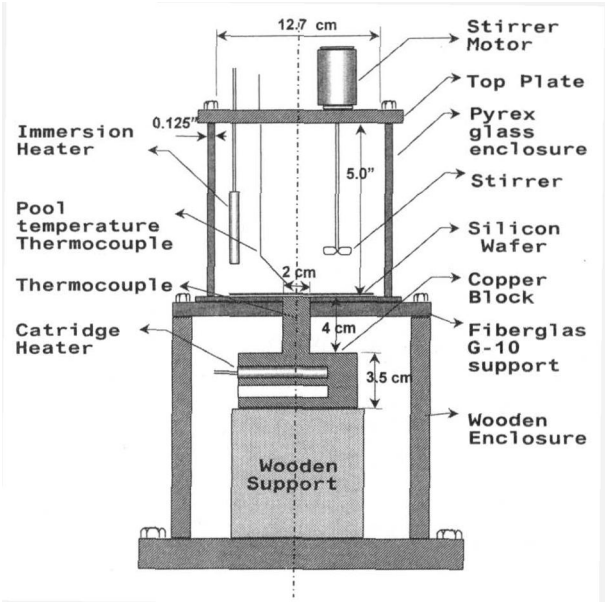

Fig. 2 Experimental setup

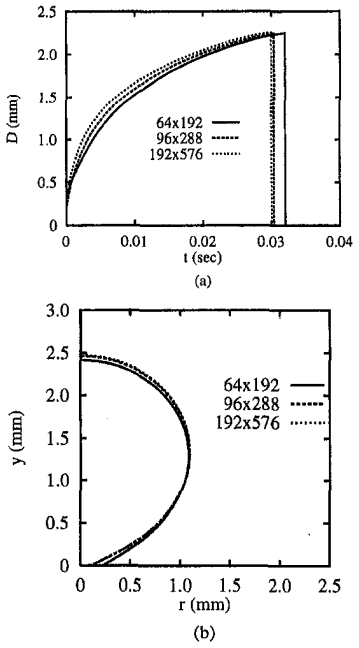

Fig. 3 Effect of mesh size on the numerical results for $\Delta T = 6.2$ K and $A = -8.5 \times 10^{-21}$ J; (*a*) the bubble growth and (*b*) the bubble shape at $t = 0.03$ sec

and is reinitialized as

$$\frac{\partial \phi}{\partial t} = \frac{\phi_o}{\sqrt{\phi_o^2 + h^2}}(1 - |\nabla \phi|) \tag{21}$$

where ϕ_o is a solution of Eq. (20).

The boundary conditions for the governing equations for the macro region are:

at the wall ($y = 0$),

$$u = v = 0,\ T = T_w,\ \phi = -\cos \varphi; \tag{22}$$

at the planes of symmetry ($r = 0, R$),

$$u = \frac{\partial v}{\partial r} = \frac{\partial T}{\partial r} = \frac{\partial \phi}{\partial r} = 0; \tag{23}$$

at the top of computational domain (free surface, $y = Y$),

$$\frac{\partial u}{\partial y} = \frac{\partial v}{\partial y} = \frac{\partial \phi}{\partial y} = 0,\ T = T_{sat}. \tag{24}$$

The procedure used to match asymptotically the solutions for the micro and macro regions is as follows: (i) guess a contact angle, (ii) solve the macro-region equations, (iii) determine R_1 (radial location of the vapor-liquid interface at $y = h/2$), (iv) solve the microlayer formulation with five boundary conditions for a given dispersion constant and determine R_o, (v) obtain the apparent contact angle from Eq. (16), and (vi) repeat steps (i)–(v) if the contact angle obtained in step (v) is different from the guessed value in step (i).

Experiments

In order not to cloud the bubble growth and departure data obtained on a test nucleation site by the activity at spurious cavities surrounding the test site, a single cavity was micromachined at the center of a mirror-polished 100 silicon wafer. The wafer had a diameter of 10 cm and a 10 μm square cavity with a depth of 20 μm was formed in the geometric center of the wafer. The wafer was heated in the central portion with power supplied from a cartridge heater embedded in a copper cylinder having a diameter of 2 cm. The silicon wafer was bonded to the copper block by using Omega Bond (OB-200) conductive adhesive. Four Type K thermocouples were placed in the copper block at a distance of 10 mm apart with the top thermocouple being 2 mm from the upper surface of the copper block. The wafer was supported not only by the copper block, but also by G-10 insulation surrounding the copper block. The test surface was housed in a 15 × 15 × 15 cm cubic chamber. Figure 2 shows the experimental apparatus. The boiling chamber is open at the top, but has stainless steel support for mounting the auxiliary heater, stirrer, and a movable thermocouple to measure the pool temperature.

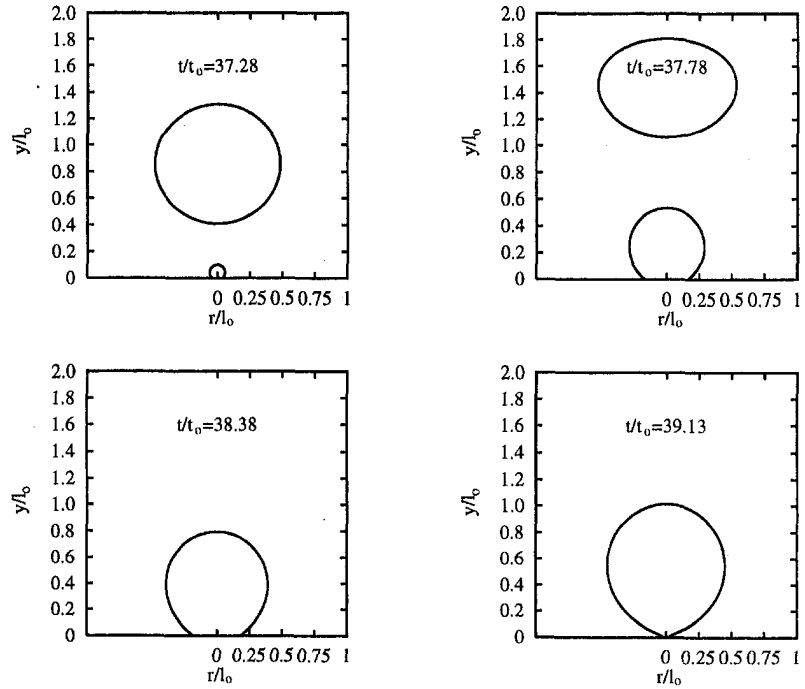

Fig. 4 Bubble growth pattern for $\Delta T = 6.2$ K and $A = -8.5 \times 10^{-21}$ J

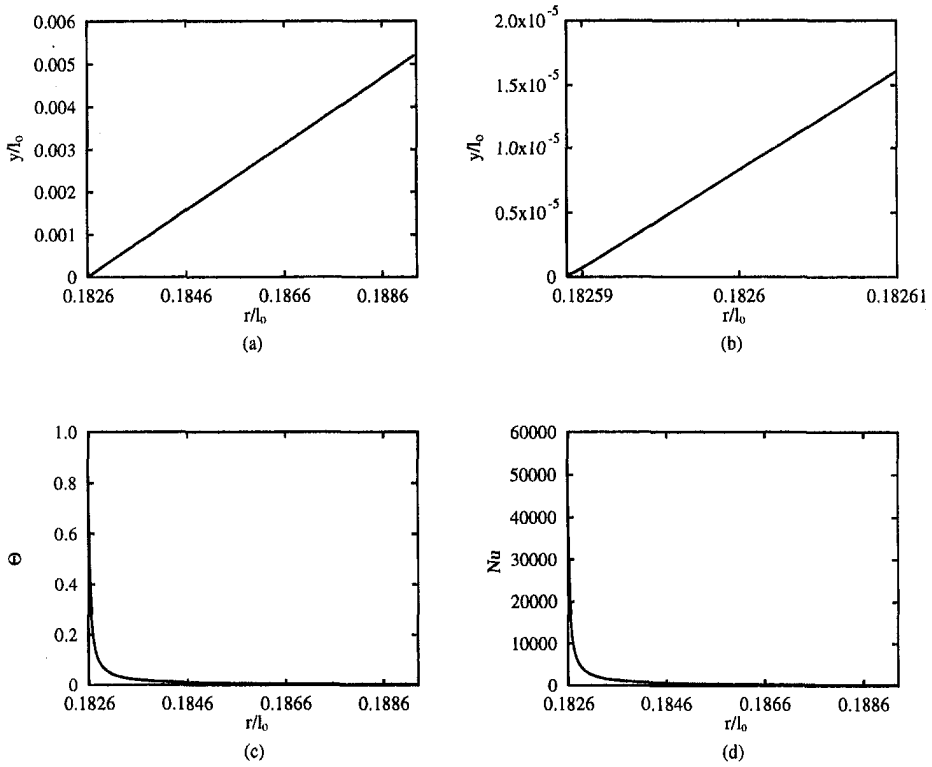

Fig. 5 Results for the micro region at $t/t_o = 38.38$; (*a*) and (*b*) interface shape, (*c*) interfacial temperature, and (*d*) heat transfer coefficient for $\Delta T = 6.2$ K and $A = -8.5 \times 10^{-21}$ (J)

Prior to conducting of the boiling experiments, the test surface was thoroughly cleaned with isopropanol followed by methanol. The surface was then blow-dried and was heated to 100°C to remove any residual film of cleansing agents. A small droplet of the test liquid was placed on the wafer surface and a photograph was taken. From the photograph, a static contact angle of the liquid with the silicon wafer surface was determined. The test liquid (distilled water) was boiled for at least half an hour to remove any dissolved air in the liquid. A calibration for the cumulative thermal resistance of the conductive adhesive layer joining the copper substrate with the wafer and the wafer itself was made. This thermal resistance was used to determine the temperature of the boiling surface as a function of heat flux. The calculated temperature was verified by placing a thermocouple directly on the boiling surface of the silicon wafer exposed to the saturated liquid.

Subsequently, the energy was supplied to the cartridge heater embedded in the copper block and the surface temperature of the silicon wafer was brought to the saturation temperature of water. Preboiled water was poured into the test chamber and auxiliary heater and stirrer were turned on in order to maintain the liquid pool at the saturation temperature. Just prior to recording of the bubble growth and departure data, the power to the auxiliary heater and the stirrer was shut off in order to obtain a quasi-static pool. The bubble growth and departure processes were recorded on a video camera operating at 450 frames per second. At a given time, the data were recorded for several bubble growth and departure cycles.

Results and Discussion

In carrying out numerical simulation, the characteristic length, l_o, the characteristic velocity, u_o, and the characteristic time, t_o, are defined as

$$l_o = \sqrt{\sigma/g(\rho_l - \rho_v)};\ u_o = \sqrt{gl_o};\ t_o = l_o/u_o. \qquad (25)$$

During numerical simulations of partial nucleate boiling, the properties of water at 1 atm. are used. The computation domain is chosen to be $(R/l_o, Y/l_o) = (1, 3)$ so that the bubble growth is not affected by the computational boundary. To initiate the computations, the initial fluid temperature profile is taken to be linear in the natural convection thermal boundary layer and fluid velocity is set equal to zero. The initial thermal boundary layer thickness, δ_T, is evaluated from the correlation for the turbulent natural convective heat transfer (refer to Kays and Crawford, 1980) as

$$\delta_T = 7.14(\nu_l\alpha_l/g\beta_T\Delta T)^{1/3}.$$

Since in reality partial nucleate boiling on a horizontal surface is a cyclic process, the computations should be carried out over several cycles until no cycle-to-cycle change in the bubble growth pattern or in the temperature profile in the thermal boundary layer is observed.

To select an appropriate mesh size, convergence for grid resolutions was tested with mesh points of 64×192, 96×288 and 192×576. The results are plotted in Fig. 3. As the mesh points increase, the relative difference of the bubble growth rates between successive mesh sizes becomes small. For 96×288 and 192×576 meshes, the difference of the bubble growth periods is less than two percent. Also, the bubble shapes at departure for the two finest grids have shown insignificant differences. Therefore, most of computations in this study are performed on 96×288 grid points to save the computing time without losing the accuracy of numerical results. During the computations, time steps were chosen to satisfy the CFL condition, $\Delta t \le h/(|u| + |v|)$, due to the explicit treatment of the convection terms and the condition that the numerical results should not change if the time steps are halved. An appropriate time step is approximately a dimensionless time of 5×10^{-4}.

Figure 4 shows the bubble growth pattern during one cycle for $\Delta T = 6.17$ K and $A = -8.5 \times 10^{-21}$ J. As mentioned earlier, the solution for the macro region is coupled with the solution for the micro region. The results for the micro region corresponding to the bubble at $t/t_o = 38.38$ are plotted in Fig. 5. The value of the radius of the bubble base, $(r/l_o, y/l_o) = (R_1/l_o, h/2l_o) = (0.189, 0.005)$ at $t/t_o = 38.38$ in Fig. 4, obtained in the macro region

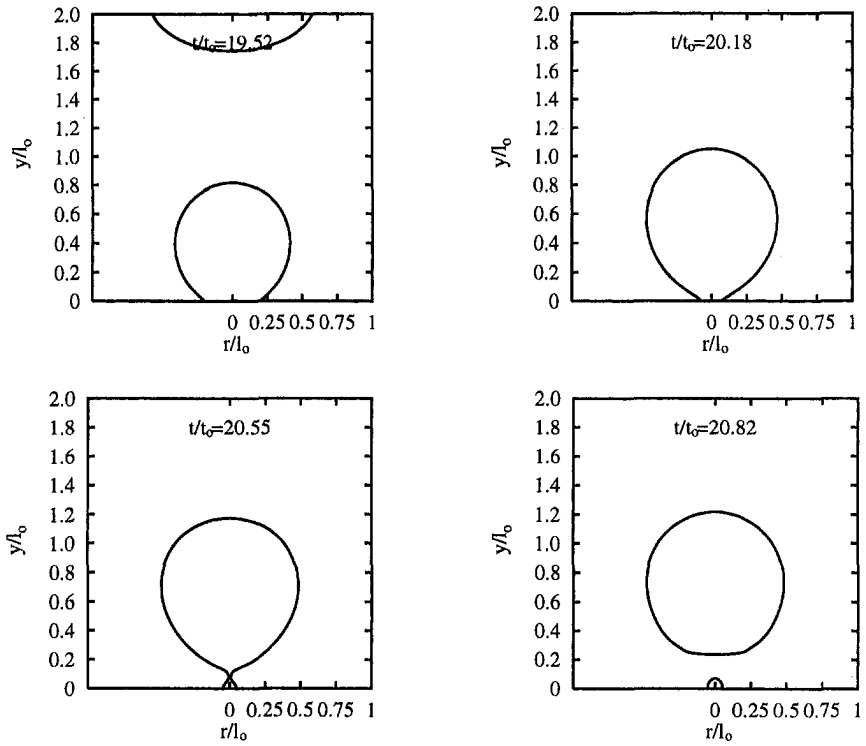

Fig. 6 Bubble growth pattern for $\Delta T = 6.2$ K and $A = -8.5 \times 10^{-21}$ J with a cavity of $D_c = 250$ μm

serves as a boundary condition for the governing equations for the micro region in Fig. 5(*a*). From Fig. 5(*b*), it is seen that due to the contribution of disjoining pressure the slope of the interface decreases to zero rapidly near the nonevaporating region ($\delta = \delta_o$). As the thickness of the liquid microlayer decreases, the interface temperature rises up to the wall temperature as shown in Fig. 5(*c*). Also, significant evaporative heat transfer is observed in the micro region. The apparent contact angle (38 deg from Fig. 5(*a*)) and the total energy removal integrated over the micro region plotted in Fig. 5(*d*) are used in the calculations for the macro region. In the present calculations, for a given dispersion constant (A), the apparent contact angle is nearly independent of the bubble growth process. In reality, however, the dynamic contact angles (advancing and receding contact angles) differ from the static contact angle. The hysteresis of contact angle on a real solid surface is not modeled in this study and this may have some effect on the shape of the vapor-liquid interface at the heated surface during bubble departure.

It is seen from Fig. 4 that during the early period of bubble growth ($37.28 < t/t_o < 38.38$), the location where the vapor-liquid interface contacts the solid wall moves radially outwards. However, the horizontal movement of the bubble base is retarded by the wall friction and the surface tension forcing the bubble shape to satisfy the geometric condition (contact angle). This in turn tends to push the upper portion of the bubble outwards and as a result leads to increased buoyancy force. The nonuniform bubble motion induces a clockwise vortex in the liquid layer. When liquid vortex becomes stronger with the increase of the bubble diameter, the bubble base moves inwards ($38.38 < t/t_o < 39.13$). The departure process occurs rapidly because the dominance of buoyancy over surface tension accelerates as the bubble base shrinks. According to the experimental observation of Siegel and Keshock (1964) for the bubble departure process, the bubble neck forms near the wall and thereafter the bubble breaks off. The small vapor portion left after the bubble departure serves as a nucleus for the next bubble. This condition can be achieved through the simulation of the bubble growth with a cavity of $D_c = 250$ μm as demonstrated in Fig. 6. The computation are performed with grid points of 128×384. Also, to satisfy the condition that the bubble base can not shrink beyond the cavity mouth at $t/t_o = 20.18$ and $t/t_o = 20.55$ in Fig. 6, an additional constraint is imposed for evaluation of the level set function at the wall:

$$\phi \leq 0 \qquad \text{for } r \leq D_c/2. \tag{26}$$

In Fig. 6 the numerical simulation including a cavity shows clearly the departure process that is consistent with the experimental observation of Siegel and Keshock (1964). However, the cavities existing on a real surface are one or two orders of magnitude smaller than the cavity used in this computation, $D_c = 250$ μm. For an extremely small cavity, the cavity does not affect the overall

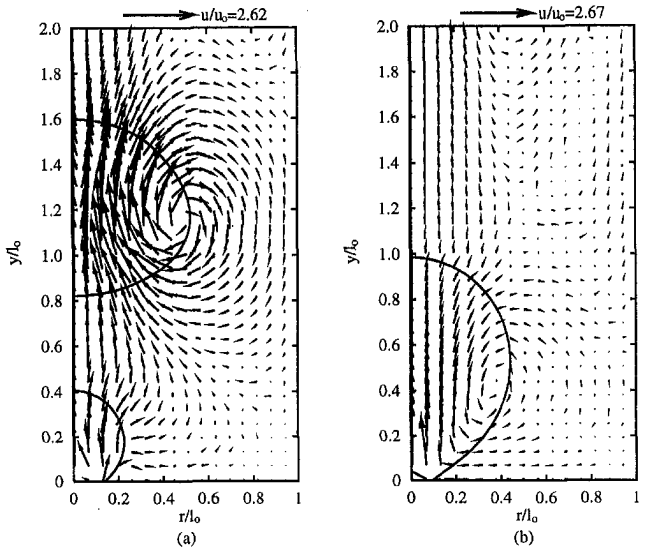

Fig. 7 Flow patterns during growth and detachment of single bubbles for $\Delta T - 6.2$ K and $A = -8.5 \times 10^{-21}$ J; (*a*) $t/t_o = 37.58$ and (*b*) $t/t_o = 39.03$

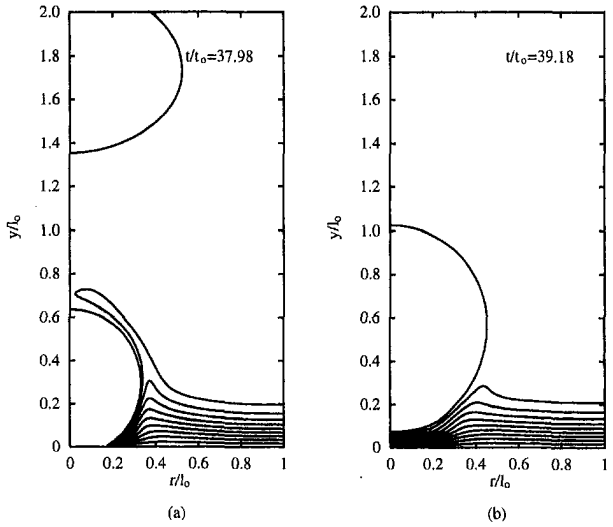

Fig. 8 Temperature fields with temperature interval of 0.62 K for ΔT = 6.2 K and $A = -8.5 \times 10^{-21}$ J

bubble growth because the breakoff period of a bubble is very short compared with the overall bubble growth period. As such the effect of cavity on the bubble growth is not included in most of computations of the present study and the small bubble serving as nucleus for the next cycle is placed on the surface after the previous bubble departs (at t/t_o = 37.28 in Fig. 4). The initial bubble size chosen in the present computations is small enough to have no significant effect on the overall bubble growth. The waiting periods for the cavity considered in the present work are practically zero because the wall temperature is assumed to remain constant. In the experiment with a constant heat flux condition, the wall temperature decreases when the cold pool liquid fills the area vacated by the departing bubble. The liquid layer and the heater surface have to be heated to a temperature necessary to initiate the next bubble. Such a waiting period can be predicted when a conjugate problem involving conduction in the solid is solved simultaneously. In the present computations the waiting period was chosen so that a growing bubble was not disturbed by the previously departed bubble.

The flow field in and around a bubble growing on the wall and for a detached bubble is shown in Fig. 7(*a*). During the early period of bubble growth, the liquid around the bubble is seen to be pushed out. A circulatory flow pattern inside the bubble as well as in the liquid outside is clearly seen for the freely rising detached bubble. The vapor velocity vectors in the bubble are reflective of the bulk movement of the bubble in the upward direction and the changes in the bubble shape as the bubble rises in the pool. There is no inflow or outflow of vapor at the vapor-liquid interface. Figure 7(*b*) shows the flow pattern in and around the bubble shortly before detachment. On the upper portion of the bubble, the liquid is being pushed outwards whereas the liquid flow is radially inward in the lower portion of the bubble. The temperature field around the bubble is shown in Fig. 8. The crowding of the isotherms underneath the bubble is reflective of the very high heat flux in that region. Initially when a bubble locates inside the thermal boundary layer, the bubble grows as a result of evaporation all around of the bubble interface including the micro region. As the bubble grows out of the thermal layer, the energy required for evaporation is supplied through only the portion around the bubble base. Also it is seen from Fig. 8(*b*) that just after bubble detachment a thin thermal layer forms on the area vacated by the departing bubble and the thickness of the thermal layer increases with time due to transient thermal conduction.

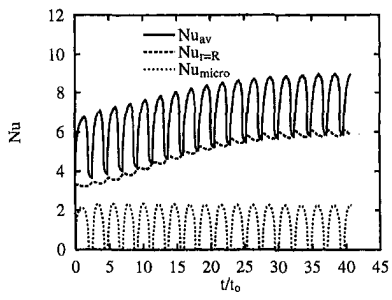

Fig. 9 Variation of Nusselt number with time for various bubble growth cycles for ΔT = 6.2 K and $A = -8.5 \times 10^{-21}$ J

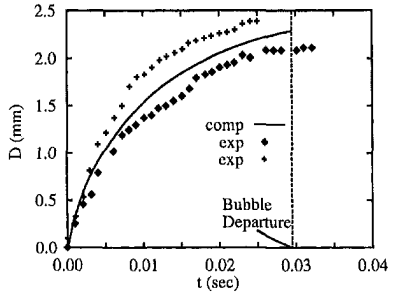

Fig. 10 Comparison of bubble diameter predicted from numerical simulation with experimental data obtained by Siegel and Keshock (1964) for ΔT = 6.2 K and φ = 38 deg ($A = -8.5 \times 10^{-21}$ J)

Figure 9 shows temporal variation of predicted Nusselt number based on the area averaged heat flux at the wall, Nu_{av}, and the local Nusselt number at the edge of the domain, $Nu_{r=R}$. Because of the uncertainty in the specification of the initial condition, magnitude of Nusselt number is seen to change from cycle to cycle. However, after about 14 cycles, the steady-state condition appears to have been achieved. Nu_{micro} is the Nusselt number based on the contribution of microlayer. It is seen that for this set of calculations the microlayer contributes about 20 percent to the total flux. Also, it is noted that local heat transfer at $r = R$ is 80 percent higher than that obtained from the correlation for the turbulent natural convection. This indicates that the liquid vortex associated with a growing and departing bubble is much stronger than the motion induced by pure natural convection.

In Fig. 10 a comparison of the bubble growth predicted from the numerical calculations is made with the data reported by Seigel and Keshock (1964) for ΔT = 6.2 K and φ = 38 deg. The numerical predictions are bounded by the upper and lower limits of the data. The model also predicts correctly the bubble diameter at departure and time for departure.

A similar comparison of the predictions of the bubble diameter as a function of time is made in Fig. 11 and 12 with the data obtained from the present experiments. The data and predictions

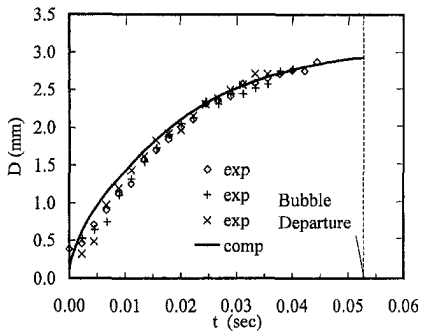

Fig. 11 Comparison of bubble diameter predicted from numerical simulation with experimental data for ΔT = 7.0 K and φ = 50 deg ($A = -14.4 \times 10^{-21}$ J)

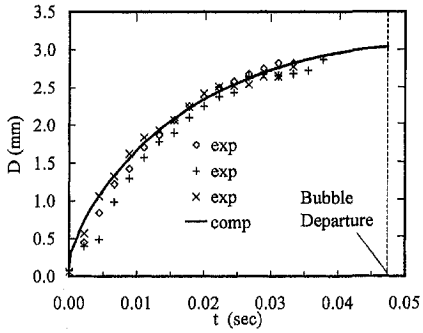

Fig. 12 Comparison of bubble diameter predicted from numerical simulation with experimental data for ΔT = 8.5 K and φ = 50 deg (A = -14.4×10^{-21} J)

plotted in Fig. 11 and 12 are for saturated water at one atmosphere pressure and for wall superheats of 7 K and 8.5 K, respectively. The static contact angle for water on silicon wafer was found to be 50 deg. The advancing and receding contact angles during bubble growth were also measured (Ramanujapu and Dhir (1998)) and found to vary between ±5 deg of the static value. In making the predictions, plotted in Fig. 11 and 12, the contact angle was kept constant at 50 deg. Different values of the contact angle were obtained by changing the value of A. Thus a proportionality relationship was developed between the dispersion constant and the contact angle. For both superheats the predictions of bubble growth, bubble diameter at departure and bubble growth time are found to be in good agreement with the data except that model generally tends to overpredict the growth period. In Fig. 13 the bubble shape just prior to departure, obtained from the usual observations for a superheat of 8.5 K is compared with that obtained from numerical simulation. Overall the agreement between the two is quite good. However, slight differences are observed in the neck region.

The dependence of bubble growth on surface wettability is plotted in Fig. 14. Computations were made for three different contact angles (φ) of 25 deg, 30 deg, and 38 deg which correspond to dispersion constants of -3×10^{-21} (J), -5×10^{-21} (J) and -8.5×10^{-21} (J). It is seen from Fig. 14 that as the contact angle increases, the bubble growth period increases. Also, the bubble diameter at departure becomes larger as the contact angle increases. This is caused by the fact that as the contribution of surface tension increases with increase in the contact angle, the vapor volume required for bubble departure also increases. The increase of bubble departure diameter with contact angle is found to be generally in agreement with the correlations proposed by Fritz (1935) and Staniszewski (1959).

Figure 15 shows the effect of wall superheat on the bubble growth. The bubble diameter at departure and the bubble growth period are listed in Table 1. With increase in wall superheat vapor production rate increases. As a result the growth period decreases

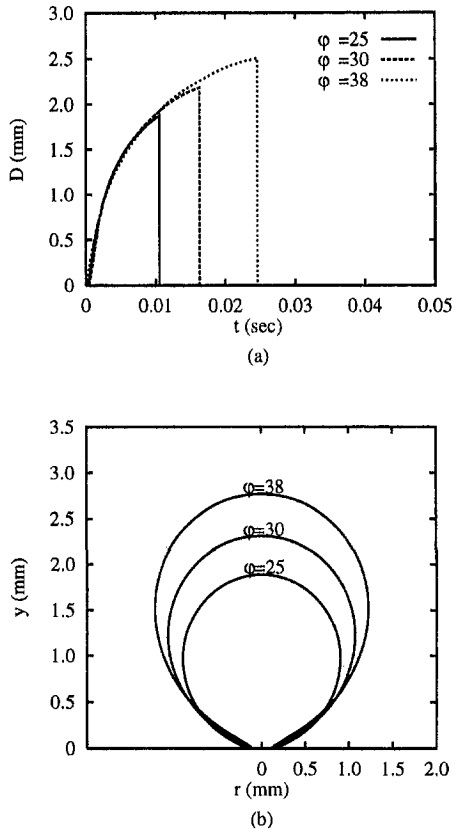

Fig. 14 Effect of contact angle (φ) on bubble growth; (*a*) variation of bubble diameter with time and (*b*) bubble shape at departure for ΔT = 8.5 K

from 29.5 msec to 20.5 msec when ΔT is increased from 6.2 K to 12.5 K. Also, the bubble diameter at departure increases with wall superheat. This indicates that for a fixed contact angle, the bubble diameter at departure depends on the growth rate (bubble dynamics) which increases with wall superheat.

Nusselt numbers based on heat transfer coefficient averaged over the cell area are plotted in Fig. 16. During early period of bubble growth, the Nusselt number increases because the area of the microlayer increases as the bubble base expands. Thereafter, the Nusselt number decreases during a bubble departure period. Also, it is seen from Fig. 16 that as the wall superheat increases the Nusselt number increases. This is caused by the fact that the bubble growth rate increases with ΔT and this in turn induces a stronger vortex motion. The time and area-averaged Nusselt numbers are listed in Table 1. The Nusselt numbers and heat fluxes for the partial nucleate boiling on a single nucleation site vary as $\Delta T^{0.4}$ and $\Delta T^{1.4}$ respectively. However, on a real surface with various sizes of cavities, the heat fluxes vary much steeply with ΔT

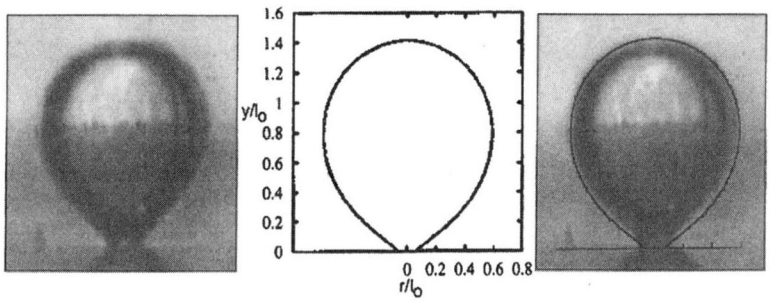

Fig. 13 Comparison of prediction of bubble shape at departure with data for ΔT = 8.5 K and φ = 50 deg

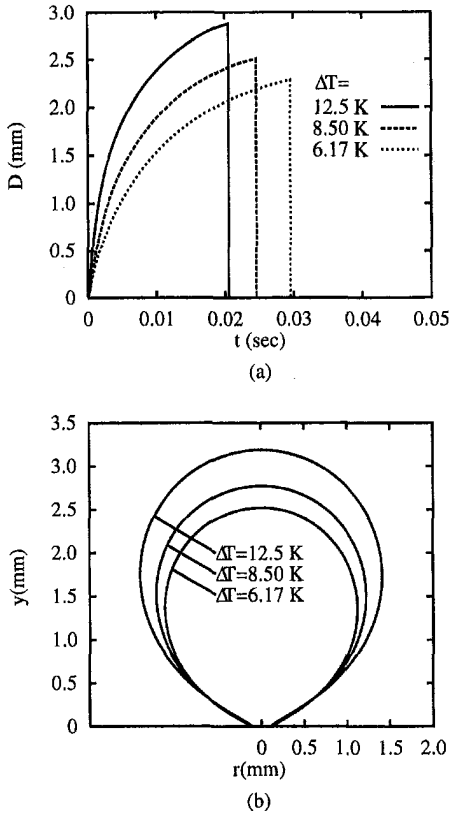

Fig. 15 Effect of wall superheat (ΔT) on bubble growth; (*a*) variation of bubble diameter with time and (*b*) bubble shape at departure for φ = 38 deg

because the number density of active sites strongly depends on the wall superheat. To predict nucleate boiling heat flux values on a real surface, the effect of cavity number density should be included in the numerical model. This can be achieved from the numerical simulation of a single bubble on an effective surface area corresponding to the number density of cavities on a real surface, which will be done in the future.

Conclusions

1 A numerical simulation of a growing and departing bubble on a horizontal surface has been carried out without any approximation of the bubble shape. The effect of microlayer evaporation is included in the analysis.

Table 1 Predicted bubble growth and heat transfer rate for different wall superheat for φ = 38 deg

ΔT (K)	D_d (mm)	Growth period (msec)	Nu	q (W/cm^2)
6.2	2.28	29.5	7.86	1.32
8.50	2.51	24.6	8.83	2.04
12.5	2.88	20.5	10.4	3.54

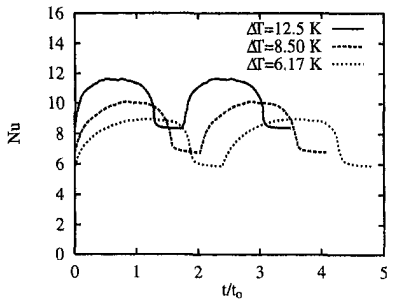

Fig. 16 Effect of wall superheat (ΔT) on Nusselt number for φ = 38 deg

2 From the numerical simulation, the location where the vapor-liquid interface contacts the wall is observed to move outwards and then inwards as the bubble grows and departs.

3 The local wall heat flux is seen to vary cyclically during the bubble growth. The contribution of microlayer to the total heat flux is found to be about 20 percent.

4 The departing bubble becomes larger with the increase in contact angle and wall superheat. The bubble growth scenario predicted from numerical analysis compares well with that observed in the experiments.

Acknowledgment

This work received support from NASA Microgravity Fluid Physics Program.

References

Cooper, M. G., and Lloyd, A. J. P., 1969, "The Microlayer in Nucleate Pool Boiling," *Int. J. Heat Mass Transfer,* Vol. 12, pp. 895–913.

Fritz, W., 1935, "Maximum Volume of Vapor Bubbles," *Physik Zeitschr.,* Vol. 36, pp. 379–384.

Hsu, Y. Y., and Graham, R. W., 1976, *Transport Processing in Boiling and Two Phase Systems,* Hemisphere, Washington, DC.

Kays, W. M., and Crawford, M. E., 1980, *Convective Heat and Mass Transfer,* McGraw-Hill, New York, p. 328.

Lay, J. H., and Dhir, V. K., 1995, "Shape of a Vapor Stem During Nucleate Boiling of Saturated Liquids," ASME JOURNAL OF HEAT TRANSFER, Vol. 117, pp. 394–401.

Lee, R. C., and Nydahl, J. E., 1989, "Numerical Calculation of Bubble Growth in Nucleate Boiling From Inception Through Departure," *ASME Journal of Heat Transfer*, Vol. 111, pp. 474–479.

Mikic, B. B., Rohsenow, W. M., and Griffith, P., 1970, "On Bubble Growth Rates," *Int. J. Heat Mass Transfer,* Vol. 13, pp. 647–666.

Plesset, M. S., and Zwick, S. A., 1954, "Growth of Vapor Bubbles in Superheated Liquids," *J. Appl. Phys.,* Vol. 25, pp. 493–500.

Ramanujapu, N., and Dhir, V. K., 1999, "Dynamics of Contact Angle During Growth and Detachment of a Vapor Bubble at a Single Nucleation Site," presented at ASME-JSME Conference in San Diego, CA.

Siegel, R., and Keshock, E. G., 1964, "Effects of Reduced Gravity on Nucleate Boiling Bubble Dynamics in Saturated Water," *AICHE Journal,* Vol. 10, pp. 509–517.

Son, G., and Dhir, V. K., 1998, "Numerical Analysis of Film Boiling Near Critical Pressure With a Level Set Method," ASME JOURNAL OF HEAT TRANSFER, Vol. 120, pp. 183–192.

Staniszewski, B. E., 1959, "Nucleate Boiling Bubble Growth and Departure," Technical Report No. 16, Division of Sponsored Research, Massachusetts Institute of Technology, Cambridge, MA.

Sussman, M., Smereka, P., and Osher, S., 1994, "A Level Set Approach for Computing Solutions to Incompressible Two-Phase Flow," *J. of Comput. Phys.,* Vol. 114, pp. 146–159.

Wayner, P. C., Jr., 1992, "Evaporation and Stress in the Contact Line Region," *Proceedings of the Engineering Foundation Conference on Pool and External Flow Boiling,* V. K. Dhir and A. E. Bergles, eds., Santa Barbara, CA, pp. 251–256.

Gibbs-Thomson Effect on Droplet Condensation

Chun-Liang Lai
Department of Mechanical Engineering,
National Taiwan University,
Taipei, Taiwan 106, R.O.C.
Mem. ASME

The present study is primarily aimed at theoretically investigating the growth of a single spherical droplet due to condensation. The droplet is either at the center of a large spherical container or in an infinite domain. The effect on the droplet growth due, respectively, to the subcooling, the Gibbs-Thomson condition, and the density-difference-induced convection will be analyzed and discussed systematically. Dimensional analysis indicates that three different time scales exist during the droplet growth due to condensation. The first and second small time scales describe, respectively, the transient temperature distributions of the gas phase and droplet, while the largest time scale describes the droplet growth. With the aid of multiple time-scale analysis, the analytic solutions for the droplet growth and the temperature distribution are obtained. The results indicate that, with a large Stefan number, the subcooling effect is stronger and the droplet grows faster. The Gibbs-Thomson effect, on the contrary, suppresses the droplet growth. However, the effect becomes smaller as time proceeds. Moreover, if the density difference between the liquid and the gas phases becomes larger, the induced convection will be stronger, which is conducive to the droplet growth.

1 Introduction

The Gibbs-Thomson equation is a well-developed thermodynamic relation describing the equilibrium condition at the interface where the phase transition occurs (Hsieh, 1975). When the Gibbs-Thomson relationship is applied to droplet condensation, it indicates that the vapor has to be subcooled below the saturation temperature at the same vapor pressure. The degree of subcooling is determined by the Gibbs-Thomson relation and is a function of the surface tension and interface curvature (Mutaftschiev, 1993). Nevertheless, there is no experimental evidence to justify the existence and correctness of the Gibbs-Thomson relation when it is applied to droplet condensation. The primary difficulty comes from the following two facts, First, to avoid the gravity effect, the droplet has to be very small, which makes the measurements very difficult. Secondly, in order to have a larger droplet for the experiment, the gravitational force makes the droplet not purely spherical which, with two main radii of curvature, makes the measurements even more difficult. However, with the advent of manned spacecraft, the reduced-gravity environment provides an opportunity for such an experiment (Ostrach, 1982). It becomes possible to generate a large spherical droplet in the spacelab, which makes the measurements straightforward and easier. Therefore, it is worthwhile to study droplet growth due to condensation at this moment to facilitate the design and prediction of the related experiments. The experimental justification of the Gibbs-Thomson relation applied to droplet condensation will be very interesting and important from an academic point of view.

Although condensation has been well studied and applied in many ways, most of the studies emphasized film condensation and nucleation (Akers et al., 1959; Carpenter and Colburn, 1951; Chaddock, 1957; Lee, 1964; Sardesai et al., 1982; Feder et al., 1966; Mason, 1951; Bear and McCormick, 1963; Sugawara and Katsuta, 1966). Most of the studies about droplet condensation were semi-empirical (Sugawara and Katsuta, 1966; O'Bara et al., 1967; Gose et al., 1967; Welch and Westwater, 1961) or with a simplified model (Avedisian, 1986; Sideman and Taitel, 1964; Mokhtarzadeh and El-Shirbini, 1979). A fully theoretical analysis appropriately describing droplet condensation and growth, especially considering the Gibbs-Thomson effect and the density-difference induced convection, is not found. Droplet condensation is basically a Stefan problem or the so-called moving boundary problem (Crank, 1984; Hill, 1987; Meirmanov, 1992). However, the analysis is different from the treatment for the solidification problem. The convective flow induced by the density difference during solidification is usually very small and negligible while it is large and cannot be neglected during condensation. Moreover, when the Gibbs-Thomson relation is considered, the boundary condition for the temperature at the interface becomes nonlinear and is a function of the interface curvature. All these features make the analytic solutions more difficult to obtain for the condensation problem than for the solidification problem.

In the next section a simplified physical model and the corresponding mathematical formulation will be given. With the introduction of dimensional analysis, three time scales are determined for droplet condensation. The smallest and the second large time scales describe the transient temperature variation of the gas phase and the droplet, respectively, while the largest time scale describes the droplet growth. In Section 3, with the aid of multiple-time-scale analysis, the analytic solutions for droplet growth and the temperature distributions are obtained. The results will be presented in Section 4. Conclusion and remarks for present and future works will be given in the last section.

2 Mathematical Formulation

The system to be analyzed is a spherical container filled with vapor initially at a uniform pressure P_g^* and a subcooled temperature T_o^*. The radius of the container is b^*. In the center of the container there is a spherical droplet originally with a radius a, which is larger than the critical radius corresponding to P_g^* and T_o^*. As time proceeds, the vapor starts to condense on the surface of the droplet, making the droplet grow constantly. It is assumed that $a \ll b^*$ and the droplet growth due to condensation is so slow that the vapor pressure P_g^* remains constant during the condensation process. The schematic diagram is shown in Fig. 1. The main concern of this study is the effect on the droplet growth and the temperature distribution due, respectively, to the Gibbs-Thomson condition and the convection induced by the density difference between the liquid and gas phases during condensation.

The following assumptions are first made to simplify the problem.

Contributed by the Heat Transfer Division for publication in the JOURNAL OF HEAT TRANSFER. Manuscript received by the Heat Transfer Division, Dec. 1, 1998; revision received, Mar. 23, 1999. Keywords: Condensation, Droplet, Heat Transfer. Associate Technical Editor: M. Kaviany.

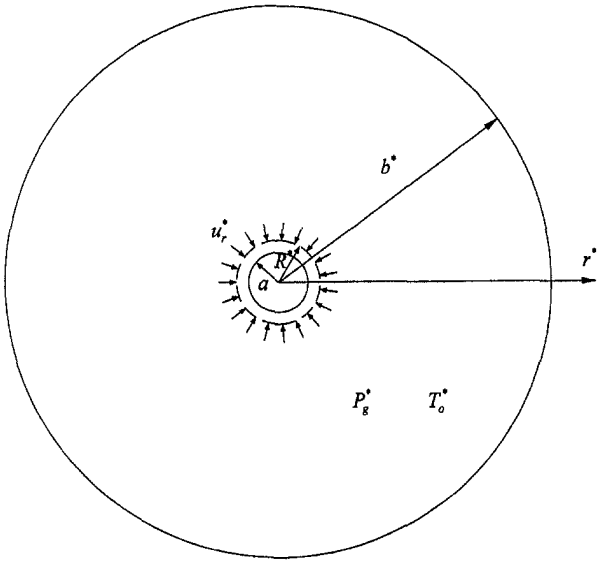

Fig. 1 Schematic diagram of the physical model

1 The system is retained in a microgravity environment. The gravitational force and buoyancy effects are negligibly small. Therefore, the droplet remains spherical is shape during the condensation process.

2 The vapor in the container is initially at a uniform pressure P_g^* and a subcooled temperature T_o^*, which is less than T_s^*, the saturation temperature corresponding to P_g^*.

3 The system and the accompanying processes due to condensation are assumed spherically symmetrical.

4 The convection is mainly induced by the density difference between the liquid and gas phases during condensation.

5 The container is so large, compared to the droplet, and the growth rate of the droplet is so small, that the vapor pressure remains nearly constant during the condensation process.

6 The equation of state for an ideal gas is used as an approximation for the vapor when the Gibbs-Thomson condition is derived. However, when dealing with the convection effect, the flow is assumed incompressible.

The governing equations for the problem under the above assumptions are simply the unsteady, spherically symmetrical heat transfer equations subjected to appropriate boundary conditions on the droplet surface. They are described as follows:

Liquid phase:

$$\frac{\partial T_l^*}{\partial t^*} = D_l\left(\frac{2}{r^*}\frac{\partial T_l^*}{\partial r^*} + \frac{\partial^2 T_l^*}{\partial r^{*2}}\right), \quad 0 < r^* < R^* \tag{1}$$

Vapor phase:

$$\frac{\partial T_g^*}{\partial t^*} + u_r^*\frac{\partial T_g^*}{\partial r^*} = D_g\left(\frac{2}{r^*}\frac{\partial T_g^*}{\partial r^*} + \frac{\partial^2 T_g^*}{\partial r^{*2}}\right), \quad R^* < r^* < b^* \tag{2}$$

The boundary conditions are

(1) Stefan condition: conservation of enthalpy during condensation

$$L\frac{dR^*}{dt^*} = D_l C_l \left.\frac{\partial T_l^*}{\partial r^*}\right|_{R^*} - D_g C_g \left.\frac{\partial T_g^*}{\partial r^*}\right|_{R^*} \tag{3}$$

(2) Gibbs-Thomson condition:

$$T_l^*(R^*, t^*) = T_g^*(R^*, t^*) = T_s^*\left(1 - \frac{\sigma}{L}\frac{2}{R^*(t^*)}\right) \tag{4}$$

(3) T_l^* is regular at $r^* = 0$: (5)

(4) $T_g^* = T_o^*$ at $r^* = b^*$. (6)

In the above expressions, T^* is the temperature with subscript l denoting the liquid phase and g, the gas phase. D_l and D_g represent, respectively, the thermal diffusivities of the liquid and gas phases with C_l and C_g the corresponding heat capacities. u_r^* is the induced radial velocity due to the density difference during condensation. L and σ are the latent heat of condensation and the surface tension of the droplet. t^* and r^* represent time and the radial coordinate. $R^*(t^*)$ is the instant radius of the droplet which is initially equal to a.

The radial velocity u_r^* induced by the density difference during condensation can be solely determined by the continuity equation and the conservation of mass at the droplet surface. Since the flow is assumed incompressible, the continuity equation becomes

$$\nabla \cdot \mathbf{V} = \frac{1}{r^{*2}}\frac{\partial}{\partial r^*}(r^{*2}u_r^*) = 0. \tag{7}$$

In the equation, $\mathbf{V}$ represents the velocity vector. From Eq. (7), u_r^* can be easily determined as

$$u_r^* = \frac{R^{*2}}{r^{*2}}u_R^* \tag{8}$$

wherein u_R^* is the radial velocity at the droplet surface, i.e., at $r^* = R^*$. The mass conservation must be satisfied at the droplet surface during condensation, which gives

$$\rho_l^*\frac{dR^*}{dt^*} = \rho_g^*\left[\frac{dR^*}{dt^*} - u_R^*\right] \tag{9}$$

with ρ_l^* and ρ_g^* denoting the density of the liquid phase and gas phase, respectively. From Eq. (9), u_R^* can then be solved in terms of the droplet growth rate dR^*/dt^*, i.e.,

$$u_R^* = \frac{\rho_g^* - \rho_l^*}{\rho_g^*}\frac{dR^*}{dt^*} = -\delta\frac{dR^*}{dt^*}. \tag{10}$$

Nomenclature

a = initial radius of droplet
b = radius of spherical container
C = heat capacity
D = thermal diffusivity
L = latent heat of condensation
P = pressure
P_s = saturation pressure
R = instant radius of droplet
r = radial coordinate
T = temperature
T_o = subcooled temperature
T_s = saturation temperature
t = time
u_R = droplet growth rate
u_r = radial velocity
$\mathbf{V}$ = velocity vector
Δ = Stefan number
δ = defined as $(\rho_l^* - \rho_g^*)/\rho_g^*$
Γ = parameter representing the Gibbs-Thomson effect
ρ = density
σ = surface tension

Superscripts

* = dimensional variables

Subscripts

g = gas phase
l = liquid phase

In Eq. (10), $\delta \equiv (\rho_l^* - \rho_g^*)/\rho_g^*$, with an order of magnitude about $O(10^3)$. Substituting Eq. (10) into Eq. (8), u_r^* can be expressed as

$$u_r^* = -\delta \frac{R^{*2}}{r^{*2}} \frac{dR^*}{dt^*}. \tag{11}$$

With this expression for u_r^*, Eq. (2), the energy equation for the gas phase, can then be rewritten as follows:

$$\frac{\partial T_g^*}{\partial t^*} - \delta \frac{R^{*2}}{r^{*2}} \frac{dR^*}{dt^*} \frac{\partial T_g^*}{\partial r^*} = D_g \left(\frac{2}{r^*} \frac{\partial T_g^*}{\partial r^*} + \frac{\partial^2 T_g^*}{\partial r^{*2}} \right), \quad R^* < r^* < b^*. \tag{12}$$

For the convenience of analysis and discussion, the following nondimensionalization scheme is introduced:

$$T_i = \frac{T_i^* - T_s^*}{T_o^* - T_s^*}, \quad i = g, l$$

$$t = \frac{t^*}{a^2/D_g}, \quad r = \frac{r^*}{a}, \quad R = \frac{R^*}{a}, \quad b = \frac{b^*}{a}.$$

With the above nondimensional variables, the governing equations, Eq. (1) and Eq. (12), and the associated boundary conditions, Eqs. (3)–(6), can now be expressed in the following dimensionless forms:

$$\frac{\partial T_l}{\partial t} = \frac{D_l}{D_g} \left(\frac{2}{r} \frac{\partial T_l}{\partial r} + \frac{\partial^2 T_l}{\partial r^2} \right), \quad 0 < r < R \tag{13}$$

$$\frac{\partial T_g}{\partial t} - \delta \frac{R^2}{r^2} \frac{dR}{dt} \frac{\partial T_g}{\partial r} = \frac{2}{r} \frac{\partial T_g}{\partial r} + \frac{\partial^2 T_g}{\partial r^2}, \quad R < r < b \tag{14}$$

$$\frac{dR}{dt} = \Delta \frac{\partial T_g}{\partial r} - \Delta \frac{D_l C_l}{D_g C_g} \frac{\partial T_l}{\partial r}, \quad \text{at } r = R \tag{15}$$

$$T_l = T_g = \frac{\Gamma}{R}, \quad \text{at } r = R \tag{16}$$

$$T_l \text{ is regular}, \quad \text{at } r = 0 \tag{17}$$

$$T_g = 1, \quad \text{at } r = b. \tag{18}$$

The initial condition for the droplet growth is

$$R = 1, \quad \text{at } t = 0. \tag{19}$$

The initial distribution of the temperature field, however, depends on the condition specified which, as can be seen later, affects only the transient part of the temperature solution and has little effect on the droplet growth.

In Eqs. (15) and (16) two important dimensionless parameters are introduced. Their expressions and physical meanings are as follows:

$$\Delta \equiv \frac{C_g(T_s^* - T_o^*)}{L} \tag{20}$$

and

$$\Gamma \equiv \frac{2\sigma T_s^*}{aL(T_s^* - T_o^*)}. \tag{21}$$

Δ is called the Stefan number, which is an index of subcooling while Γ represents, in a sense, the Gibbs-Thomson effect.

Since the order of magnitude of D_l/D_g is about 10^{-2}~10^{-3} and that for Δ is about 10^{-5}~10^{-7} (Daubert and Danner, 1985; Haar et al., 1984), it becomes evident that there exist another two time scales, i.e., a^2/D_l and $a^2/\Delta D_g$ from Eqs. (13) and (15), respectively. The time scales for the present problem are now redefined as follows:

$$t_1 = \frac{a^2}{D_g} \tag{22}$$

$$t_2 = \frac{a^2}{D_l} \tag{23}$$

and

$$t_3 = \frac{a^2}{\Delta D_g}. \tag{24}$$

t_1 is the smallest time scale describing the transient development of the temperature field of the surrounding gas phase. t_2 is for the temperature field of the droplet. t_3, the largest time scale of the whole process, describes the droplet growth. Since both t_1 and t_2 are much smaller than t_3, only the steady-state solutions of the droplet and surrounding gas phase, which will be solved in the next section, are important to the droplet growth. The transient parts, which are closely related to the initial conditions specified and are case dependent, will then be omitted without deterioration to the analysis.

3 Solutions With Multiple-Time-Scale Analysis

According to the analysis of last section, there exist three time scales whose orders of magnitude are $O(t_1) \ll O(t_2) \ll O(t_3)$. Therefore, with the aid of multiple-time-scale analysis, analytic solutions for the droplet growth and temperature distribution can then be obtained.

(A) Solutions With Time Scale t_1: By choosing $t_1 = a^2/D_g$ as the characteristic time scale, the governing equations and boundary conditions can be simplified as follows:

$$\frac{\partial T_l}{\partial t} = 0 \tag{25}$$

$$\frac{dR}{dt} = 0 \tag{26}$$

$$\frac{\partial T_g}{\partial t} = \frac{2}{r} \frac{\partial T_g}{\partial r} + \frac{\partial^2 T_g}{\partial r^2}, \quad 1 < r < b \tag{27}$$

$$T_g = \Gamma, \quad \text{at } r = 1 \tag{28}$$

$$T_g = 1, \quad \text{at } r = b. \tag{29}$$

It means, within the time scale t_1, the variations of the temperature distribution and the size of the droplet are negligibly small. Only the development of the temperature field of the surrounding gas phase is important. The solution for Eq. (27) satisfying boundary conditions (28) and (29) can now be obtained as follows:

$$T_g = (\text{transient part}) + \frac{\Gamma - b}{1 - b} + \frac{b(1 - \Gamma)}{1 - b} \frac{1}{r}. \tag{30}$$

The transient part of the solution is initial-condition dependent, which is very difficult to determine exactly at the moment when the droplet is generated and the measurement is started. However, since only the steady-state solution is crucial to the droplet growth, it becomes unnecessary to solve explicitly the transient part.

(B) Solutions With Time Scale t_2: When t_2 is chosen as the time scale, the problem is reduced to the following:

$$\frac{dR}{dt} = 0 \tag{31}$$

$$T_g = \frac{\Gamma - b}{1 - b} + \frac{b(1 - \Gamma)}{1 - b} \frac{1}{r}, \quad 1 < r < b \tag{32}$$

$$\frac{\partial T_l}{\partial t} = \frac{2}{r}\frac{\partial T_l}{\partial r} + \frac{\partial^2 T_l}{\partial r^2}, \quad 0 < r < 1 \tag{33}$$

$$T_l \text{ is regular}, \quad \text{at } r = 0 \tag{34}$$

$$T_l = \Gamma, \quad \text{at } r = 1. \tag{35}$$

The expression for T_g is obtained from the steady-state solution of Eq. (30). Within this time scale, the droplet growth is still negligibly small. The solution for Eq. (33) with boundary conditions (34) and (35) possesses the following form:

$$T_l = (\text{transient part}) + \Gamma. \tag{36}$$

The steady-state solution of T_l is simply a constant determined by the Gibbs-Thomson relation. The transient part of T_l is still not important to the droplet growth.

(C) Solutions With Time Scale t_3: When the one associated with the droplet growth is chosen as the reference time scale, the whole problem is then reduced to the following form:

$$\frac{2}{r}\frac{\partial T_l}{\partial r} + \frac{\partial^2 T_l}{\partial r^2} = 0, \quad 0 < r < R \tag{37}$$

$$-\delta\Delta \frac{R^2}{r^2}\frac{dR}{dt}\frac{\partial T_g}{\partial r} = \frac{2}{r}\frac{\partial T_g}{\partial r} + \frac{\partial^2 T_g}{\partial r^2}, \quad R < r < b \tag{38}$$

$$\frac{dR}{dt} = \frac{\partial T_g}{\partial r} - \frac{D_l C_l}{D_g C_g}\frac{\partial T_l}{\partial r}, \quad \text{at } r = R \tag{39}$$

$$T_l = T_g = \frac{\Gamma}{R}, \quad \text{at } r = R \tag{40}$$

$$T_l \text{ is regular}, \quad \text{at } r = 0 \tag{41}$$

$$T_g = 1, \quad \text{at } r = b \tag{42}$$

$$R = 1, \quad \text{at } t = 0. \tag{43}$$

Although Δ is very small, the convective term, i.e., the left-hand side term of Eq. (38), still needs to be included because the density ratio $\delta \equiv (\rho_l^* - \rho_g^*)/\rho_g^*$ is usually very large.

Within this time scale, the droplet grows constantly. Consequently, the temperature distributions of the droplet and the surrounding gas phase are essentially quasi-steady with the unsteady nature displaying implicitly through the droplet growth. The whole set of equations, i.e., Eqs. (37)–(43) can now be solved. They are

$$T_l = \frac{\Gamma}{R}, \quad 0 < r < R \tag{44}$$

$$T_g = -\frac{g(t)}{f(t)}\exp\left(\frac{f(t)}{r}\right) + h(t), \quad R < r < b \tag{45}$$

$$\frac{dR}{dt} = \frac{g(t)}{R^2}\exp\left(\frac{f(t)}{R}\right) \tag{46}$$

with

$$f(t) = \Delta\delta R^2\frac{dR}{dt} \tag{47}$$

$$g(t) = \frac{f(t)\left(\frac{\Gamma}{R} - 1\right)}{\exp\left(\frac{f(t)}{b}\right) - \exp\left(\frac{f(t)}{R}\right)} \tag{48}$$

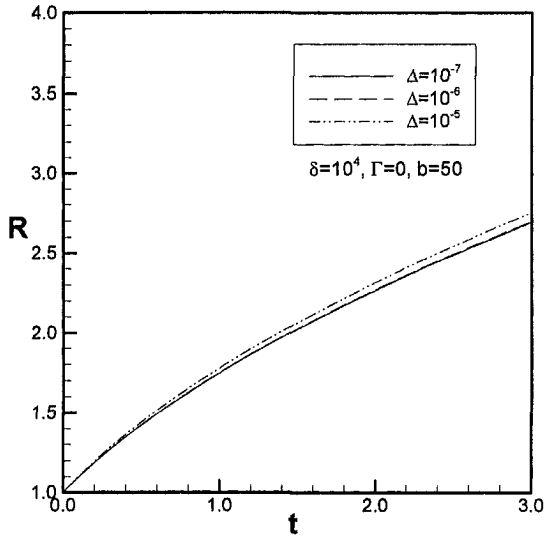

Fig. 3 Subcooling effect on the droplet growth

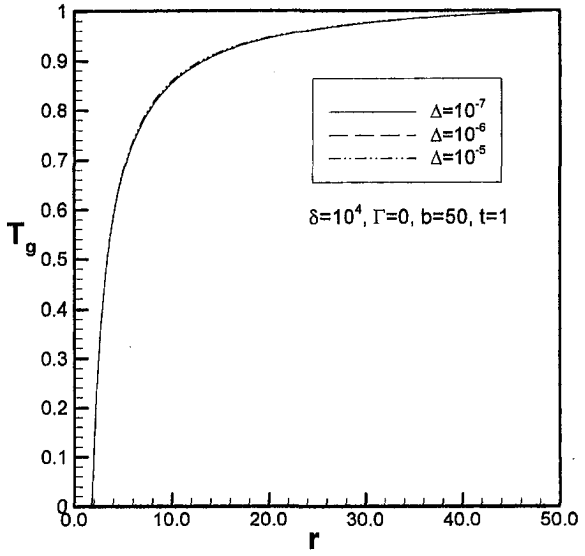

Fig. 2 Subcooling effect on the temperature distribution of the gas phase

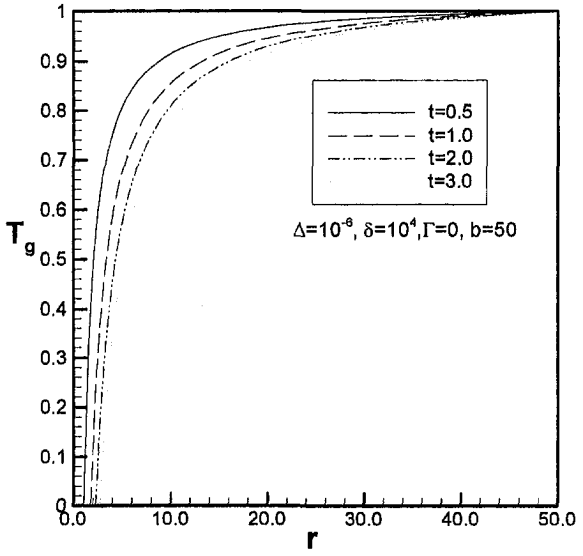

Fig. 4 Temperature distribution of the gas phase at different time instants

$$h(t) = \frac{\exp\left(\frac{f(t)}{R}\right) - \frac{\Gamma}{R}\exp\left(\frac{f(t)}{b}\right)}{\exp\left(\frac{f(t)}{R}\right) - \exp\left(\frac{f(t)}{b}\right)}. \quad (49)$$

If the droplet is growing by condensation in an infinite domain, the above solutions can be reduced to the following forms by simply letting b approach infinity. The expressions for T_l, T_g, dR/dt and $f(t)$ are the same as those shown in Eqs. (44)–(47), with

$$g(t) = \frac{f(t)\left(\frac{\Gamma}{R} - 1\right)}{1 - \exp\left(\frac{f(t)}{R}\right)} \quad (50)$$

and

$$h(t) = \frac{\exp\left(\frac{f(t)}{R}\right) - \frac{\Gamma}{R}}{\exp\left(\frac{f(t)}{R}\right) - 1} \quad (51)$$

as $b \to \infty$.

To obtain the analytic solution of R from Eq. (46) is formidable. Simple numerical iterations are needed to calculate the solutions of R. The steady-state solutions of T_l and T_g will be used in Eq. (39) for the first estimation of dR/dt. Then numerical iterations are performed until certain appropriate criterion of convergence is reached.

4 Results and Discussion

The results to be presented in the following are calculated based on the data of water vapor.

The $R - t$, $V - t$, and $T_g - r$ relations are to be presented and discussed in the following, with $V \equiv dR/dt$ denoting the droplet growth speed. The parametric ranges investigated are Δ: 10^{-5}~10^{-7}, δ: 10^3~10^5, and Γ: 10^{-3}~10^{-6}, which are typical for the water vapor with a: 0.1 cm~2.0 cm, ΔT (subcooled temperature): 1°C~10°C, and P_s (the saturation pressure): 0.1 atm~2.0 atm.

Figure 2 is the temperature distribution of gas phase at $t = 1$ with $\delta = 10^4$, $\Gamma = 0$, and $b = 50$ for various values of Δ, i.e., $\Delta = 10^{-5}$, 10^{-6}, and 10^{-7}. All three curves are pretty close, which indicates that the effect due to subcooled temperature within the range $\Delta = 10^{-5}$~10^{-7} is not obvious. However, from the figure, it can still be seen that the temperature distribution for $\Delta = 10^{-5}$ is steeper than those for $\Delta = 10^{-6}$ and 10^{-7}. As a result, the droplet will grow faster in the case with $\Delta = 10^{-5}$ than those with $\Delta = 10^{-6}$ and 10^{-7}. In other words, it indicates that the droplet will grow faster with a larger subcooled temperature. This phenomena is reflected in the $R - t$ diagram and is shown in Fig. 3. Figure 4 is the temperature distribution of gas phase at $t = 0.5$, 1.0, 2.0, and 3.0 for the situation with $\Delta = 10^{-6}$, $\delta = 10^4$, $\Gamma = 0$, and $b = 50$. It can be seen from this figure that, as time proceeds, the temperature distribution near the droplet becomes less and less steep. Consequently, the droplet will grow more and more slowly as time proceeds. This phenomenon is also reflected in the variation of the slope of the $R - t$ curve shown in Fig. 3.

In order to demonstrate the convection effect due to the density difference during condensation, the temperature distribution of the gas phase at $t = 1$ with $\Delta = 10^{-6}$, $\Gamma = 0$, and $b = 50$ for various values of δ, i.e., $\delta = 10^3$, 10^4, and 10^5 and the corresponding droplet growth, i.e., the $R - t$ curve, are calculated and shown respectively in Figs. 5 and 6. Two conclusions can be drawn from these two figures. First, the convection toward the droplet due to

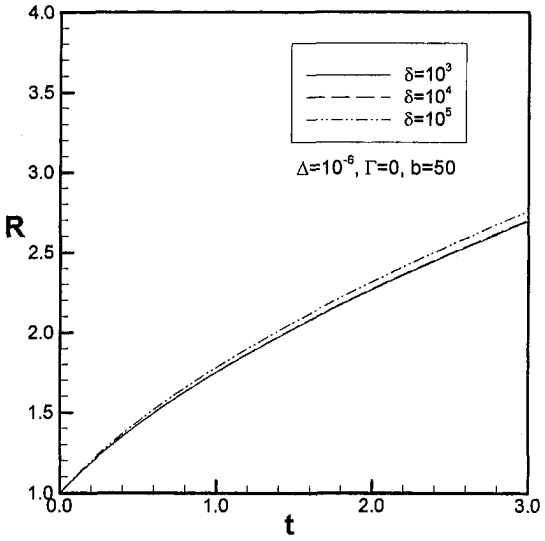

Fig. 6 Convection effect on the droplet growth

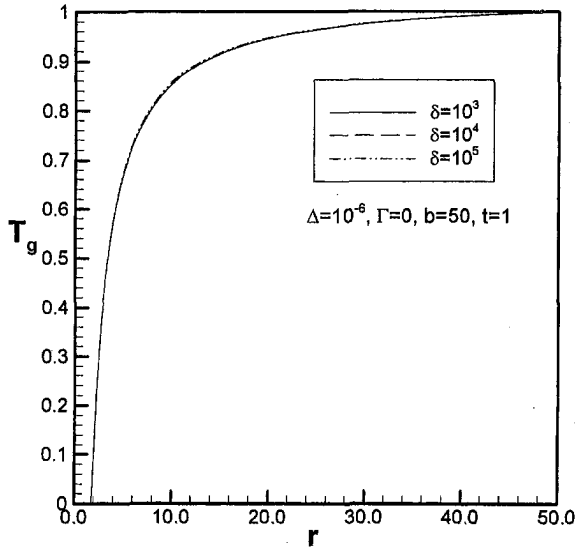

Fig. 5 Convection effect on the temperature distribution of the gas phase

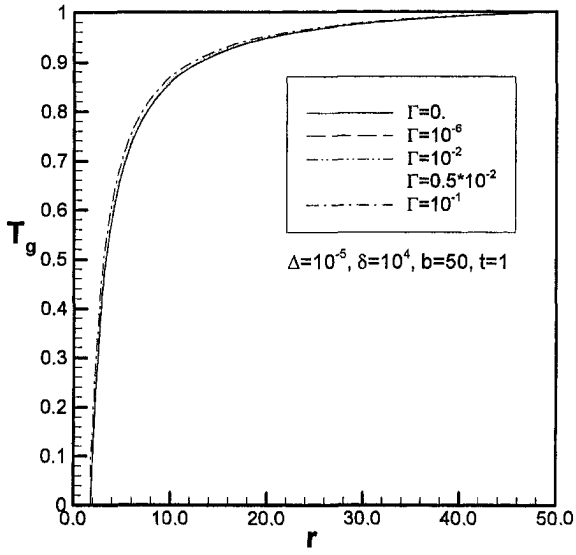

Fig. 7 Gibbs-Thomson effect on the temperature distribution of the gas phase

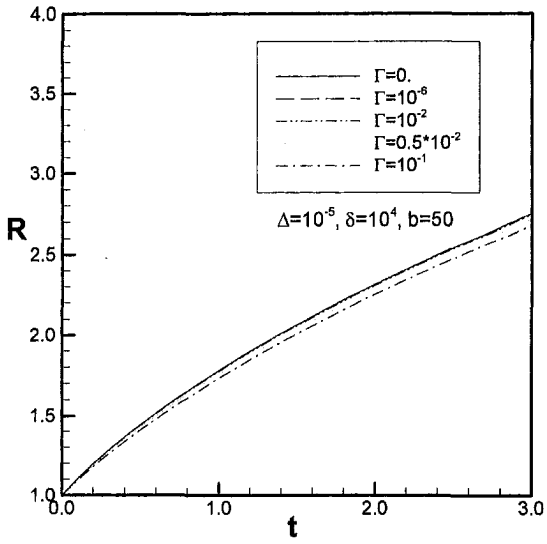

Fig. 8 Gibbs-Thomson effect on the droplet growth

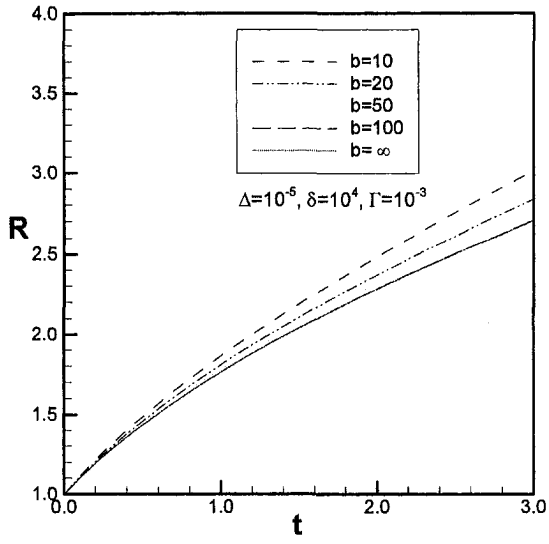

Fig. 10 Boundary effect on the droplet growth

the density difference during condensation is conducive to the droplet growth. That is, at the same instant, the droplet with $\delta = 10^5$ possesses the largest radius compared to those with $\delta = 10^3$ and 10^4. Secondly, the convection effects on the droplet growth within the parametric range of $\delta = 10^3 \sim 10^5$ are nearly the same.

The Gibbs-Thomson effect on the temperature distribution and the droplet growth are demonstrated in Figs. 7–9. Figure 7 is the temperature distribution of the gas phase at $t = 1$ with $\Delta = 10^{-5}$, $\delta = 10^4$, and $b = 50$ for various values of Γ, i.e., $\Gamma = 0$, 10^{-6} 10^{-2}, 0.5×10^{-2} and 10^{-1}. Figure 8 is the corresponding $R - t$ curves displaying the droplet growth during condensation. From Fig. 8, it can be concluded that the droplet growth due to condensation is suppressed by the Gibbs-Thomson condition. In other words, it means that, with a stronger Gibbs-Thomson effect, i.e., a larger value of Γ, the droplet growth will become slower. Physically, this phenomenon can be explained as follows: When a system possesses a stronger Gibbs-Thomson effect, the effective subcooled temperature becomes smaller in a relative sense (Eqs. (16) and (18)), which is then less conducive to the droplet growth. Figure 9 is the corresponding $V - t$ curves with $V \equiv dR/dt$, the droplet growth rate. The difference in the droplet growth due to different values of Γ becomes much more obvious in the $V - t$ curves than in the $R - t$ curves. This result indicates that using the droplet growth speed as an index might be a better way to demonstrate the Gibbs-Thomson effect on the droplet growth due to condensation. However, as can be seen in Figs. 7–9, when Γ is less than 10^{-2}, the Gibbs-Thomson effect on the droplet growth becomes very small. Unfortunately Γ is usually less than 10^{-3} for a water-vapor system with P_s (the saturation pressure) between 0.1 atm and 2.0 atm. Therefore, in order to facilitate the experimental measurements, using a water-vapor system with a higher P_s or other liquid-vapor systems becomes necessary.

The boundary effect of the container on the droplet growth is illustrated in Fig. 10, with $b = 10$, 20, 50, 100, and ∞. It can be seen from this figure that as $b \geq 50$ with $R \leq 2.0$, the wall effect becomes negligibly small. The droplet grows just like in an infinite domain. Physically, it means that if the distance between the droplet and any wall of the container is greater than 50 times the droplet radius, the shape of the container becomes unimportant to the droplet growth. In other words, the container can be any shape easy to construct once it is large enough.

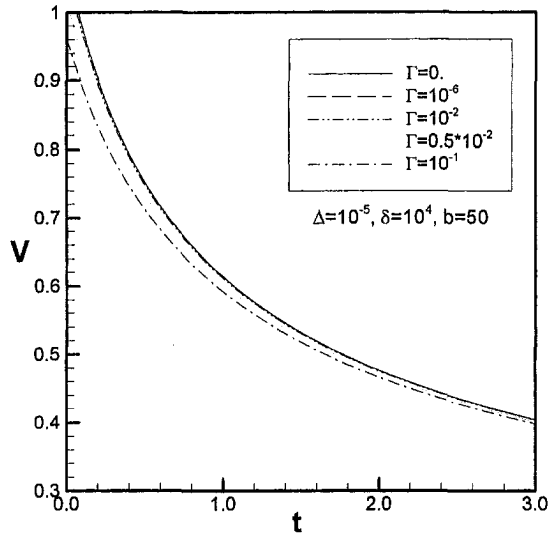

Fig. 9 Gibbs-Thomson effect on the droplet growth rate

5 Conclusions

The Gibbs-Thomson effect on the droplet growth due to condensation is theoretically studied herein. With the aid of multiple-time-scale analysis, the analytical solutions for the droplet growth and the temperature distribution are obtained. The following conclusions are drawn from the present study.

1 The subcooled temperature and the convection due to density difference during condensation are conducive to the droplet growth. The Gibbs-Thomson effect suppresses the droplet growth due to condensation.

2 The droplet growth rate might be a better index to demonstrated the Gibbs-Thomson effect on the droplet growth due to condensation.

3 The shape of the container becomes unimportant to the droplet growth if the distance between the droplet and each wall of the container is greater that 50 times the droplet radius.

Since the Gibbs-Thomson effect on the droplet growth due to condensation is very small for a water-vapor system with P_s between 0.1 atm to 2.0 atm, to find other liquid-vapor systems or use a water-vapor system with a higher P_s becomes necessary to facilitate the experimental measurements.

Acknowledgment

Support from the National Center for Microgravity Research on Fluids and Combustion at Case Western Reserve University is greatly acknowledged.

References

Akers, W. W., Deans, H. A., and Crosser, O. K., 1959, "Condensation Heat Transfer Within Horizontal Tubes," *Chem. Engr. Prog. Symp. Ser.*, Vol. 55, pp. 171–176.

Avedisian, C. T., 1986, "Bubble Growth in Superheated Liquid Droplets," *Encyclopedia of Fluid Mechanics,* Vol. 3, Gulf Publishing, Houston, pp. 130–190.

Bear, E., and McCormick, J. L., 1963, "On the Mechanism of Heat Transfer in Dropwise Condensation," *J. Colloid Sci.,* Vol. 18, pp. 208–215.

Carpenter, E. F., and Colburn, A. P., 1951, "The Effect of Vapour Velocity on Consensation Inside Tubes," *Proc. of the General Discussion on Heat Transfer,* pp. 450–544.

Chaddock, J. B., 1957, "Condensation of Vapours in Horizontal Tubes," *Refrig. Engng.,* Vol. 65, pp. 36–41 and 90–95.

Crank, J., 1984, *Free and Moving Boundary Problems,* Claredon Press, Oxford.

Daubert, T. E., and Danner, R. P., 1985, *Data Compilation Tables of Properties of Pure Compounds: Design Institute for Physical Property Data,* AIChE, New York.

Feder, J., et al., 1966, "Homogeneous Nucleation and Growth of Droplets in Vapors," *Advances in Physics,* Vol. 15, pp. 111–178.

Gose, E., Macciordi, A. N., and Baer, 1967, "Model for Dropwise Condensation on Randomly Disturbed Sites," *Int. J. Heat Mass Transfer,* Vol. 10, pp. 15–22.

Haar, L., Gallagher, J. S., and Kell, G. S., 1984, *NBS/NRC Steam Tables,* Hemisphere, New York.

Hill, J. M., 1987, *One-Dimensional Stefan Problem: An Introduction,* Longman's, London, pp. 105–133.

Hsieh, J. S., 1975, *Principles of Thermodynamics,* McGraw-Hill, New York.

Lee, J., 1964, "Turbulent Film Condensation," *AIChE J.,* pp. 450–544.

Mason, B. J., 1951, "Spontaneous Condensation of Water Vapour in Expansion Chamber Experiments," *Proc. Phys. Soc.,* Vol. 64, pp. 773–779.

Meirmanov, A. M., 1992, *The Stefan Problem,* Walter de Gruyter, Hawthorn, NY.

Mokhtarzadeh, M. R., and El-Shirbini, A. A., 1979, "A Theoretical Analysis of Evaporating Droplets in an Immiscible Liquid," *Int. J. Heat Mass Transfer,* Vol. 22, pp. 27–37.

Mutaftschiev, B., 1993, "Nucleation Theory," *The Handbook of Crystal Growth,* (Volume 1, Fundamentals, Part A: Thermodynamics and Kinetics), D. T. J. Hurle, ed., North-Holland, Amsterdam, pp. 187–247.

O'Bara, J. T., Killion, E. S., and RobLee, L. H. S., 1967, "Dropwise Condensation of Steam at Atmospheric and Above Atmospheric Pressure," *Chem. Engr. Sci.,* Vol. 22, pp. 1305–1314.

Ostrach, S., 1982, "Low-Gravity Fluid Flow," *Ann. Rev. Fluid Mech.,* Vol. 14, pp. 313–345.

Sardesai, R. G., Owen, R. G., and Pulling, D. J., 1982, "Pulling, Pressure Drop for Condensation of a Pure Vapour in Down Flow in a Vertical Tube," *Heat Transfer,* Vol. 5, pp. 139–145.

Sideman, S., and Taitel, Y., 1964, "Direct-Contact Heat Transfer With Change of Phase: Evaporation of Drops in an Immiscible Liquid Medium," *Int. J. Heat Mass Transfer,* Vol. 7, pp. 1273–1289.

Sugawara, S., and Katsuta, K., 1966, "Fundamental Study on Dropwise Consensation," *Proceedings of the Third International Heat Transfer Conference,* Vol. 2, pp. 354–361.

Welch, J. F., and Westwater, J. W., 1961, "Microscopic Study of Dropwise Condensation," *International Developments in Heat Transfer,* Part II, ASME, New York.

Forced Convection in Microstructures for Electronic Equipment Cooling

S. J. Kim
e-mail: sungkim@me.kaist.ac.kr
Mem. ASME

D. Kim

Department of Mechanical Engineering,
Korea Advanced Institute of
Science and Technology,
Taejon 305-701, Korea

This paper reports analytical solutions for both velocity and temperature profiles in microchannel heat sinks by modeling the microchannel heat sink as a fluid-saturated porous medium. The analytical solutions are obtained based on the modified Darcy model for fluid flow and the two-equation model for heat transfer. To validate the porous medium model and the analytical solutions based on that model, the closed-form solution for the velocity distribution in the fully-developed channel flow and the numerical solutions for the conjugate heat transfer problem, comprising the solid fin and the fluid, are also obtained. The analytical solutions based on the porous medium model are shown to predict the volume-averaged velocity and temperature distributions quite well. Using the analytical solutions, the aspect ratio and the effective thermal conductivity ratio are identified as variables of engineering importance and their effects on fluid flow and heat transfer are studied. As either one of these variables increases, the fluid temperature is shown to approach the solid temperature. Finally, the expression for the total thermal resistance, derived from the analytical solutions and the geometry of the microchannel heat sink for which the thermal resistance of the heat sink is minimal, is obtained.

1 Introduction

The trend in the electronic equipment industry toward denser and more powerful products requires a higher level of performance from cooling technology. Many ideas for cooling methods have been proposed, including a microchannel heat sink. The microchannel heat sink was first introduced by Tuckerman and Pease (1981, 1982), and is based on the idea that the heat transfer coefficient is inversely proportional to the hydraulic diameter of the channel. Since its emergence, much research has been conducted, as summarized in a critical review of microchannel heat sinks by Phillips (1990). However, most of this research is limited to conventional methods which use the Navier-Stokes equation for fluid flow and fin theory for heat transfer. Since the work of Tuckerman and Pease (1981), which was subject to several constraints such as the fully developed laminar flow, the fixed fin-channel width ratio, the high aspect ratio, and the constant fin efficiency, many researchers have been interested in eliminating such constraints and designing better microchannel heat sinks. Knight et al. (1991) suggested a design method for microchannel heat sinks in which both laminar and turbulent flow regimes were considered. Using their method, they reported the total thermal resistance of a microchannel could be lowered by 35 percent compared to that obtained by Tuckerman and Pease (1981).

Since the mid 1980s, studies that came out of conventional methods started to emerge. Koh and Colony (1986) modeled the microstructures as a porous medium using Darcy's law to describe the flow. Later Tien and Kuo (1987) proposed a model using the modified Darcy equation by Vafai and Tien (1981), which accounts for the boundary effect on convection problems. For heat transfer, they used the two-equation model which treats the fluid and the solid regions separately. They reported the analytical solution for the velocity distribution and the numerical solution for the temperature distribution.

In this paper, laminar fully developed flow in a microchannel heat sink subjected to a constant heat flux at its bottom is studied. When the microchannel heat sink is modeled as a porous medium, analytical solutions for both velocity and temperature profiles within it can be obtained. The analytical solutions are based on the modified Darcy model for fluid flow and the two-equation model for heat transfer. To validate the porous medium model of the microchannel heat sink and the analytical solutions based on that model, the conjugate heat transfer problem is also solved numerically and the numerical results are compared with analytical solutions. By using the analytical solutions, variables of engineering importance can be identified and their effects on fluid flow and heat transfer studied. Finally, the analytical results made possible by the use of the porous medium model are applied to the thermal optimization of the microchannel heat sink. The total thermal resistance derived from the analytical solutions is minimized in order to optimize the thermal performance of the microchannel heat sink. The point of this example is to demonstrate the cost and speed advantage of the new analytical solutions compared to more time-consuming numerical procedures when used in design applications.

2 Problem Description and Modeling

The problem under consideration in this paper concerns forced convective flow through a microchannel as shown in Fig. 1. The direction of fluid flow is parallel to x. The top surface is insulated and the bottom surface is uniformly heated. A coolant passes through the microchannel and takes heat away from a heat dissipating component attached below. In analyzing the problem, the flow is assumed to be laminar and both hydrodynamically and thermally fully developed. All thermophysical properties are assumed to be constant.

The microchannel is modeled as a fluid-saturated porous structure as proposed by Tien and Kuo (1987). The governing equations for the velocity and temperature fields in the microstructure are established by applying the volume-averaging technique. The extended Darcy equation, which has been developed for describing fluid flow in a porous medium, is used in place of the Darcy equation in order to account for the boundary effect. The two-equation model, which treats the solid and the fluid as separate entities, is used in the present analysis because the temperature difference between the solid and the fluid in general cannot be

Contributed by the Heat Transfer Division for publication in the JOURNAL OF HEAT TRANSFER. Manuscript received by the Heat Transfer Division, Sept. 28, 1998; revision received, Mar. 8, 1999. Keywords: Cooling, Heat Transfer, Microstructures, Optimization, Porous Media. Associate Technical Editor: M. Kaviany.

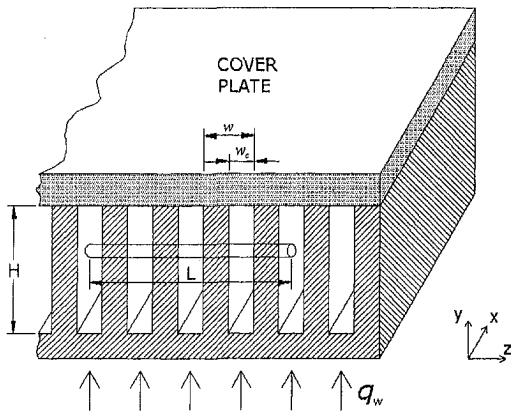

Fig. 1 Microchannel heat sink

neglected. In this work, the representative elementary volume (REV hereafter) for the volume-averaging is a slender cylinder aligned parallel to the wall but perpendicular to the flow direction as shown in Fig. 1. For the volume-averaging to be valid, the REV should be much longer than the width of the fin and the channel combined (Kaviany, 1995) and the direction of volume-averaging should be independent of the paths of fluid flow and heat transfer. In the microchannel heat sink, the chip size is typically much greater than the width of the fin and the channel combined. Also, fluid flows in the x direction, and heat is mainly transferred in the x and y directions. Hence the volume-averaged equations can be applied to microstructures without any problem.

3 Mathematical Formulation and Solutions

To analyze fluid flow and heat transfer through the microchannel heat sink the extended Darcy equation and volume-averaged energy equations for solid and fluid phases should be solved. For the present problem, the extended Darcy equation and boundary conditions are (Vafai and Tien, 1981)

$$-\frac{d}{dx}\langle p\rangle_f + \mu_f \frac{d^2}{dy^2}\langle u\rangle_f - \frac{\mu_f}{K}\epsilon\langle u\rangle_f = 0 \tag{1}$$

$$\langle u\rangle_f = 0 \quad \text{at} \quad y = 0, H \tag{2}$$

where $\langle\ \rangle_f$ denotes a volume-averaged value over the fluid region and p, μ_f, u, ϵ, K, and H are pressure, viscosity, velocity, porosity, permeability, and channel height, respectively.

The volume-averaged energy equations for the solid and fluid phases and boundary conditions are (Tien and Kuo, 1987)

$$k_{se}\frac{\partial^2\langle T\rangle_s}{\partial y^2} = h_t a(\langle T\rangle_s - \langle T\rangle_f) \tag{3}$$

$$\epsilon\rho_f c_f\langle u\rangle_f\frac{\partial\langle T\rangle_f}{\partial x} = h_t a(\langle T\rangle_s - \langle T\rangle_f) + k_{fe}\frac{\partial^2\langle T\rangle_f}{\partial y^2} \tag{4}$$

$$\langle T\rangle_s = \langle T\rangle_f = T_w \quad \text{at} \quad y = 0 \tag{5}$$

$$\frac{\partial\langle T\rangle_s}{\partial y} = \frac{\partial\langle T\rangle_f}{\partial y} = 0 \quad \text{at} \quad y = H \tag{6}$$

where $\langle\ \rangle_s$ means a volume-averaged value over the solid region and k_{se}, T, h_t, a, ρ_f, c_f, and k_{fe} are effective thermal conductivity of the solid, temperature, interstitial heat transfer coefficient, wetted area per volume, density, heat capacity and effective thermal conductivity of fluid, respectively. The interstitial heat transfer coefficient h_t is the proportionality constant between the interfacial heat flux and the solid-fluid temperature difference within the REV.

For the microchannel heat sink, the porosity, the permeability, and the effective conductivities can be represented as

$$\epsilon = \frac{w_c}{w}, \quad K = \frac{\epsilon w_c^2}{12}, \quad k_{se} = (1-\epsilon)k_s, \quad k_{fe} = \epsilon k_f, \tag{7}$$

where w_c, k_s, and k_f are channel width, thermal conductivity of solid and thermal conductivity of fluid, respectively.

Equations (1), (3), and (4) can be nondimensionalized by using the following variables:

$$U = \frac{\langle u\rangle_f}{u_m}, \quad \mathrm{Da} = \frac{K}{H^2}, \quad Y = \frac{y}{H}, \quad P = \frac{K}{\epsilon\mu_f u_m}\frac{d\langle p\rangle_f}{dx},$$

$$\theta_s = \frac{\langle T\rangle_s - T_w}{\frac{q_w H}{(1-\epsilon)k_s}}, \quad \theta_f = \frac{\langle T\rangle_f - T_w}{\frac{q_w H}{(1-\epsilon)k_s}} \tag{8}$$

Nomenclature

a = wetted area per volume
$A_{c,\mathrm{fin}}$ = cross-sectional area of the fin
A_{fs} = interfacial area between the fin and the fluid
C = effective thermal conductivity ratio, $\epsilon k_f/(1-\epsilon)k_s$
c_f = heat capacity of fluid
D = equivalent Biot number, $h_t a H^2/(1-\epsilon)k_s$
Da = Darcy number, K/H^2
h = heat transfer coefficient based on the bulk-mean temperature
h_t = interstitial heat transfer coefficient based on the local temperature
H = channel height
k_f = thermal conductivity of fluid
k_{fe} = effective thermal conductivity of fluid
k_s = thermal conductivity of solid
k_{se} = effective thermal conductivity of solid
K = permeability
L = length of heat sink
Nu_∞ = local Nusselt number for the fully developed flow in the microchannel, $h_t D_h/k_f$
p = pressure
P = dimensionless pressure, $(K/\epsilon\mu_f u_m)(d\langle p\rangle_f/dx)$
P_{fin} = perimeter of the fin
q_w = heat flux over the bottom surface
T = temperature
T_b = bulk mean temperature of fluid
u = velocity
u_m = mean velocity in the fluid region
U = dimensionless velocity, $\langle u\rangle_f/u_m$
$\dot{V}$ = volume flow rate
w_c = channel width
W = width of heat sink
Y = dimensionless vertical coordinate, y/H
α_s = aspect ratio of the microchannel, H/w_c
Δp = pressure difference between upstream and downstream
ϵ = porosity
ρ_f = density of fluid
θ_f = dimensionless temperature of fluid, $(\langle T\rangle_f - T_w)/(q_w H/(1-\epsilon)k_s)$
θ_{fin} = thermal resistance for conduction and convection through and around the fin
θ_{flow} = thermal resistance for the flow of a coolant
θ_s = dimensionless temperature of solid, $(\langle T\rangle_s - T_w)/(q_w H/(1-\epsilon)k_s)$
θ_{total} = total thermal resistance
μ_f = viscosity of fluid
$\langle\ \rangle_f$ = volume-averaged value over the fluid region
$\langle\ \rangle_s$ = volume-averaged value over the solid region

where u_m and q_w are the mean velocity in the fluid region and the heat flux over the bottom surface, respectively.

For the fully developed flow subject to a constant heat flux,

$$\frac{\partial\langle T\rangle_f}{\partial x} = \frac{\partial\langle T\rangle_s}{\partial x} = \frac{dT_w}{dx} = \text{constant} \tag{9}$$

and from the energy balance,

$$q_w = \epsilon\rho_f c_f u_m H \frac{\partial\langle T\rangle_f}{\partial x}. \tag{10}$$

Then nondimensionalized equations and boundary conditions are expressed as follows:

$$U = \frac{\mathrm{Da}}{\epsilon}\frac{d^2U}{dY^2} - P \tag{11}$$

$$\frac{d^2\theta_s}{dY^2} = \frac{h_i a H^2}{(1-\epsilon)k_s}(\theta_s - \theta_f) \tag{12}$$

$$U = \frac{h_i a H^2}{(1-\epsilon)k_s}(\theta_s - \theta_f) + \frac{\epsilon k_f}{(1-\epsilon)k_s}\frac{d^2\theta_f}{dY^2} \tag{13}$$

$$U = \theta_s = \theta_f = 0 \quad \text{at} \quad Y = 0 \tag{14}$$

$$U = \frac{d\theta_s}{dY} = \frac{d\theta_f}{dY} = 0 \quad \text{at} \quad Y = 1. \tag{15}$$

When Eq. (11) is solved with B.C.'s (14), (15), the velocity distribution is obtained as follows:

$$U = A\cosh\left(\sqrt{\frac{\epsilon}{\mathrm{Da}}}Y\right) + B\sinh\left(\sqrt{\frac{\epsilon}{\mathrm{Da}}}Y\right) - P \tag{16}$$

where

$$A = P, \quad B = P\frac{1-\cosh\left(\sqrt{\frac{\epsilon}{\mathrm{Da}}}\right)}{\sinh\left(\sqrt{\frac{\epsilon}{\mathrm{Da}}}\right)}.$$

Since

$$\int_0^1 U dY = 1,$$

$$P = \frac{\sinh\left(\sqrt{\frac{\epsilon}{\mathrm{Da}}}\right)}{2\sqrt{\frac{\mathrm{Da}}{\epsilon}}\left\{\cosh\left(\sqrt{\frac{\epsilon}{\mathrm{Da}}}\right) - 1\right\} - \sinh\left(\sqrt{\frac{\epsilon}{\mathrm{Da}}}\right)}. \tag{17}$$

Now energy Eqs. (12) and (13) with B.C.'s (14), (15) can be solved by the following method:
(12)–(13);

$$\frac{d^2}{dY^2}\left(\theta_s + \frac{\epsilon k_f}{(1-\epsilon)k_s}\theta_f\right) = U. \tag{18}$$

$$\frac{\epsilon k_f}{(1-\epsilon)k_s} \times (12) + (13);$$

$$-\frac{\epsilon k_f}{(1-\epsilon)k_s}\frac{d^2}{dY^2}(\theta_s - \theta_f) + \frac{h_i a H^2}{(1-\epsilon)k_s}\left(1 + \frac{\epsilon k_f}{(1-\epsilon)k_s}\right)(\theta_s - \theta_f) = U. \tag{19}$$

By letting $C = \epsilon k_f/(1-\epsilon)k_s$ and $D = h_i a H^2/(1-\epsilon)k_s$, Eqs. (18) and (19) with B.C.'s (14), (15) result in

$$\theta_s + C\theta_f = P\left[-\frac{1}{2}Y^2 + C_1 Y + C_2\left\{1 - \cosh\left(\sqrt{\frac{\epsilon}{\mathrm{Da}}}Y\right) - \frac{1-\cosh\left(\sqrt{\frac{\epsilon}{\mathrm{Da}}}\right)}{\sinh\left(\sqrt{\frac{\epsilon}{\mathrm{Da}}}\right)}\sinh\left(\sqrt{\frac{\epsilon}{\mathrm{Da}}}Y\right)\right\}\right] \tag{20}$$

$$\theta_s - \theta_f = P\left[-\frac{1}{D(1+C)} + C_3\cosh\left(\sqrt{\frac{D(1+C)}{C}}Y\right) + C_4\sinh\left(\sqrt{\frac{D(1+C)}{C}}Y\right) + C_5\left\{\cosh\left(\sqrt{\frac{\epsilon}{\mathrm{Da}}}Y\right) + \frac{1-\cosh\left(\sqrt{\frac{\epsilon}{\mathrm{Da}}}\right)}{\sinh\left(\sqrt{\frac{\epsilon}{\mathrm{Da}}}\right)}\sinh\left(\sqrt{\frac{\epsilon}{\mathrm{Da}}}Y\right)\right\}\right] \tag{21}$$

where

$$D_1 = D(1+C) - C\frac{\epsilon}{\mathrm{Da}}$$

$$N_1 = D(1+C)\sqrt{\frac{\epsilon}{\mathrm{Da}}}\left\{1 - \cosh\left(\sqrt{\frac{\epsilon}{\mathrm{Da}}}\right)\right\}$$

$$N_2 = C\frac{\epsilon}{\mathrm{Da}}\sqrt{\frac{D(1+C)}{C}}\sinh\left(\sqrt{\frac{\epsilon}{\mathrm{Da}}}\right)\sinh\left(\sqrt{\frac{D(1+C)}{C}}\right)$$

$$C_1 = 1 - \frac{\sqrt{\frac{\mathrm{Da}}{\epsilon}}\left(\cosh\left(\sqrt{\frac{\epsilon}{\mathrm{Da}}}\right) - 1\right)}{\sinh\left(\sqrt{\frac{\epsilon}{\mathrm{Da}}}\right)}$$

$$C_2 = -\frac{\mathrm{Da}}{\epsilon}$$

$$C_3 = -\frac{C\frac{\epsilon}{\mathrm{Da}}}{D(1+C)D_1}$$

$$C_4 = \frac{N_1 + N_2}{D(1+C)\sqrt{\frac{D(1+C)}{C}}\cosh\left(\sqrt{\frac{D(1+C)}{C}}\right)\sinh\left(\sqrt{\frac{\epsilon}{\mathrm{Da}}}\right)D_1}$$

$$C_5 = \frac{1}{D_1}.$$

Finally, Eqs. (20) and (21) can be solved algebraically. Hence, analytical solutions for the dimensionless temperature profiles for fluid and solid phases are obtained as follows:

$$\theta_f = \frac{P}{1+C}\left[-\frac{1}{2}Y^2 + C_1 Y + C_6 - C_3\cosh\left(\sqrt{\frac{D(1+C)}{C}}Y\right) - C_4\sinh\left(\sqrt{\frac{D(1+C)}{C}}Y\right) + C_7\left\{\cosh\left(\sqrt{\frac{\epsilon}{\mathrm{Da}}}Y\right) + \frac{1-\cosh\left(\sqrt{\frac{\epsilon}{\mathrm{Da}}}\right)}{\sinh\left(\sqrt{\frac{\epsilon}{\mathrm{Da}}}\right)}\sinh\left(\sqrt{\frac{\epsilon}{\mathrm{Da}}}Y\right)\right\}\right] \tag{22}$$

$$\theta_s = P\left[\frac{\mathrm{Da}}{\epsilon}\left\{\cosh\left(\sqrt{\frac{\epsilon}{\mathrm{Da}}}\,Y\right) + \frac{1-\cosh\left(\sqrt{\frac{\epsilon}{\mathrm{Da}}}\right)}{\sinh\left(\sqrt{\frac{\epsilon}{\mathrm{Da}}}\right)} \times \sinh\left(\sqrt{\frac{\epsilon}{\mathrm{Da}}}\,Y\right)\right\} - \frac{1}{2}Y^2 + C_1 Y + C_2\right] - C\theta_f \quad (23)$$

where

$$C_6 = -\frac{\mathrm{Da}}{\epsilon} + \frac{1}{D(1+C)} \quad \text{and} \quad C_7 = \frac{\mathrm{Da}}{\epsilon} - \frac{1}{D_1}.$$

4 Discussion on Velocity and Temperature Distributions

To validate the porous medium model of the microchannel heat sink and the analytical solutions based on that model, Eqs. (16), (22), and (23) are compared with the corresponding velocity and temperature distributions for the conjugate heat transfer problem comprising both the solid fin and the fluid. The formulation and the numerical method for the conjugate heat transfer problem are very similar to those in Sparrow et al. (1978), and are not repeated here for brevity. Only the conventional energy equation is solved numerically, because a closed-form solution exists for the fully developed channel flow in the form of (Shah and London, 1978)

$$U = \frac{\sum_{n=1,3,\ldots}^{\infty} -\frac{1}{n^4}\left[1 - \frac{\cosh\left(\frac{n\pi H}{w_c}(Y-0.5)\right)}{\cosh\left(\frac{n\pi H}{2w_c}\right)}\right]}{\sum_{n=1,3,\ldots}^{\infty} -\frac{1}{n^4}\left[1 - \frac{2w_c}{n\pi H}\tanh\left(\frac{n\pi H}{2w_c}\right)\right]}. \quad (24)$$

Note that the velocity distribution given in Eq. (24) is the result of volume-averaging in the z-direction so that it may be compared with Eq. (16), which is the solution of the extended Darcy equation. In Fig. 2(a), Eq. (24) is compared with the analytical solution of the present study (Eq. (16)), together with the analytical solution of Tien and Kuo (1987). In Fig. 2(a), Eq. (16) is shown to predict the velocity profile of Eq. (24) within one percent. For the REV, the unidirectional flow in the x-direction can be modeled as the flow between two parallel plates. Hence, the permeability based on the Hagen-Poiseuille flow between two parallel plates is used in the present analysis while Tien and Kuo (1987) used the hydraulic diameter of the channel instead of the channel width in Eq. (7) for the permeability. About seven percent deviation of their analytical solution for the velocity distribution from the exact solution seems to be attributable to their choice of the geometric length scale in the permeability.

Similarly in Fig. 2(b), Eqs. (22) and (23) are compared with the corresponding volume-averaged temperature distributions from the numerical solutions. As mentioned before, numerical solutions for the fully developed temperature distribution are obtained by using the finite difference method for the conjugate heat transfer problem composed of the fins and the microchannel between them. In Fig. 2(b), Eqs. (22) and (23) from the porous medium model are shown to be accurate in comparison with these numerical solutions to within 4.0 percent. The error in the temperature distribution is due to the volume-averaging in the porous medium model, which deals with thermal conduction in the y-direction only. This point of view can be manifested by comparing the analytical solution with the one-dimensional numerical solution, which neglects the heat conduction in the z-direction as in Sparrow et al. (1978). As shown in Fig. 2(b), Eqs. (22) and (23) match with the one-dimensional numerical solution better than with the two-dimensional numerical solution. It goes without saying that these analytical solutions from the porous medium model are helpful to identifying and studying the effects of variables of engineering importance. So the extension to more practical research, such as optimization of the microchannel, is possible without tedious numerical computations, which will be illustrated in Section 5.

In Eq. (16), the normalized velocity U is a function of ϵ/Da only. Since $\epsilon/\mathrm{Da} = 12\alpha_s^2$, where α_s is the aspect ratio of the microchannel, U is a function of the aspect ratio only. Similarly Eqs. (22) and (23) show that dimensionless temperatures, θ_f and θ_s, are functions of ϵ/Da, C and D. Note that D depends on the aspect ratio α_s and the effective thermal conductivity ratio C, since

$$D = \frac{H^2}{(1-\epsilon)k_s} h_t a = C\,\mathrm{Nu}_\infty \alpha_s(\alpha_s + 1). \quad (25)$$

In addition, a functional relationship of Nu_∞ in terms of α_s can be deduced from the values of $h_t a$ which are obtained from numerical solutions for various aspect ratios. Data fitting of Nu_∞ with respect to the aspect ratio, as shown in Fig. 3, yields

$$\mathrm{Nu}_\infty = 2.253 + 8.164\left(\frac{\alpha_s}{\alpha_s + 1}\right)^{1.5}, \quad (26)$$

where Nu_∞ is the local Nusselt number for the fully developed flow in the microchannel. This data fitting is accurate to within 4.3 percent. Hence, θ_f and θ_s are functions of the aspect ratio α_s and the effective thermal conductivity ratio C.

Figure 4(a) shows the effect of α_s on the dimensionless velocity distribution while Figs. 4(b) and (c) show the relationships between the dimensionless temperature distributions and the parameters of engineering importance, α_s and C. The solid temperature decreases from its maximum value at the bottom wall as Y increases. On the other hand the fluid temperature decreases from its

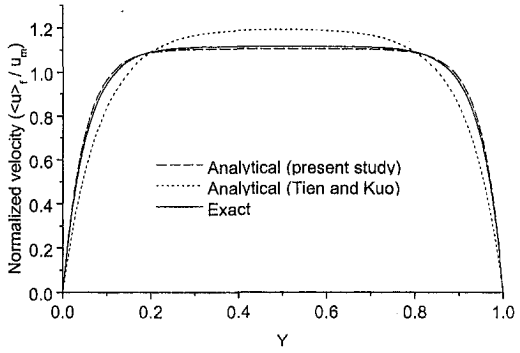

Fig. 2(a)

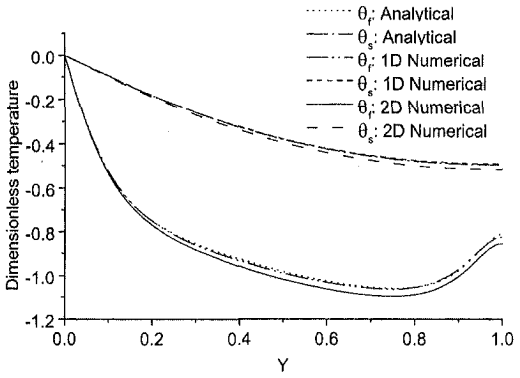

Fig. 2(b)

Fig. 2 Comparisons with numerical solutions (α_s = 6); (a) velocity, (b) temperature (C = 0.005)

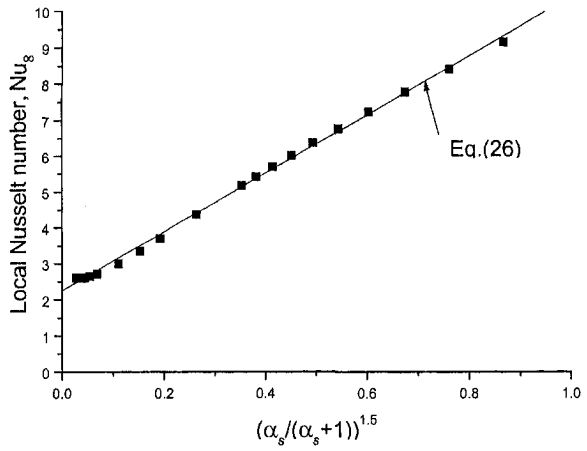

Fig. 3 Fitting of the local Nusselt number

maximum at the bottom wall to a minimum. It then increases until it becomes the top wall temperature, which is due to the small velocity near the wall. The solid temperature distribution is almost insensitive to the geometry of the fin/channel and the thermal conductivity ratio while the fluid temperature distribution strongly depends on α_s and C. Figures 4(a) and (b) show that the velocity distribution flattens and the temperature difference between θ_f and θ_s decreases as α_s increases. As α_s increases, the velocity distribution deviates little from its mean value because the region insensitive to the boundary effect increases. And as α_s increases while C and the channel height H are fixed, the channel width w_c decreases. The channel height (a length scale used for nondimensionalization) is arbitrarily fixed to help to better explain the effect of α_s on the temperature distributions. The increase in α_s results in the increase in the interstitial heat transfer coefficient as well as the decrease in the heat transfer rate dissipated into the channel. Both of these are responsible for the decrease in the temperature difference between the phases.

Now the effect of the effective thermal conductivity ratio C on the temperature distributions is shown in Fig. 4(c). It is clear from the definition of C that C increases with the porosity, ϵ, and the thermal conductivity ratio between the fluid and solid phases, k_f/k_s. As ϵ increases while α_s, k_f/k_s, and H are held constant, the fin base area decreases. This results in the decrease in the heat transfer rate between the fin and the fluid, which makes the temperature difference between θ_f and θ_s decreases because the heat transfer coefficient does not depend on ϵ. Similarly, as k_f/k_s increases while α_s, ϵ, and H are held constant, the difference in temperature gradients between the solid and fluid phases decreases, which in turn results in the decrease in the temperature difference between the phases. Overall the fluid temperature approaches the solid temperature as any one of α_s and C increases, in which the local thermal equilibrium may be assumed and the one-equation model would be appropriate.

5 Optimization of the Microchannel Heat Sink

In this section it is illustrated that the analytical results made possible by the porous medium model obtained in the previous section can be applied to thermal optimization of the microchannel heat sink. To optimize the thermal performance of the microchannel heat sink the minimization of the total thermal resistance is sought. The thermal resistance is the temperature difference between two points of concern per unit heat flux. So, minimizing the thermal resistance for a constant heat flux means minimizing the temperature difference between the heat sink base temperature at the exit and the coolant temperature at the inlet. The latter is a fixed value because a coolant at a normal temperature is continuously provided during operation. Therefore, the minimization of the total thermal resistance can be realized by minimizing the heat sink base temperature at the exit. The total thermal resistance is the sum of the thermal resistance for the flow of the coolant and that for conduction through and convection between the fins.

$$\theta_{\text{total}} = \theta_{\text{flow}} + \theta_{\text{fin}} \tag{27}$$

The thermal resistance for the flow of the coolant is responsible for the temperature rise of the coolant from the inlet to the exit. From the energy balance this resistance can be expressed as

$$\theta_{\text{flow}} = \frac{1}{\rho_f c_f \dot{V}} = -\frac{12\nu_f LP}{c_f w_c^3 \alpha_s \Delta p W \epsilon}. \tag{28}$$

From the definition of the bulk mean temperature the thermal resistance for conduction through and convection between the fins can be represented by

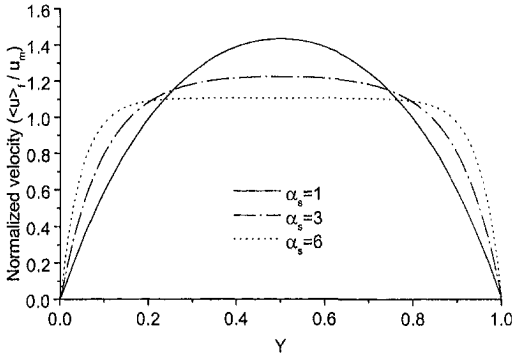

Fig. 4(a)

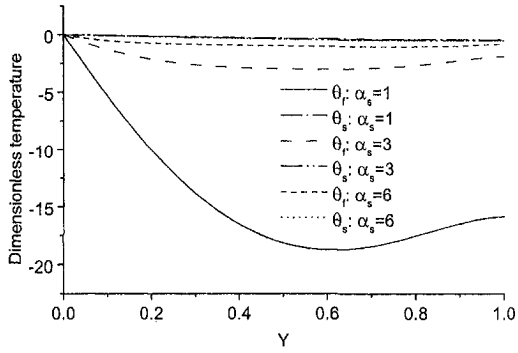

Fig. 4(b)

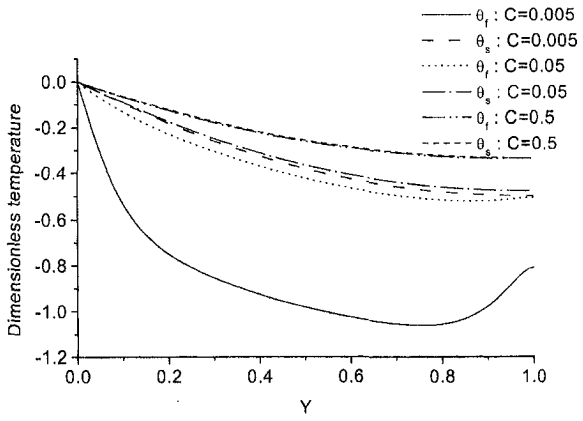

Fig. 4(c)

Fig. 4 Effects of various parameters; (a) effect of α_s on velocity profiles, (b) effect of α_s on temperature profiles, (c) effect of C on temperature profiles

$$\theta_{\text{fin}} = \frac{1}{hA_{fs}} = \frac{T_w - T_b}{q_w LW} = -\frac{\theta_{f,b} H}{(1-\epsilon)k_s LW}$$

$$= -\frac{w_c \alpha_s \int_0^1 U\theta_f dY}{(1-\epsilon)k_s LW} \tag{29}$$

where T_b, h, A_{fs}, $\dot{V}$, Δp, L, and W are bulk-mean temperature of fluid, heat transfer coefficient between the fin and the fluid based on the bulk-mean temperature of the fluid, interfacial area between the fin and the fluid, volume flow rate, pressure difference between upstream and downstream, length and width of the heat sink, respectively. To validate the expressions (28) and (29), the experimental results for the total thermal resistance except the effect of the substrate thickness (Tuckerman and Pease, 1981) are compared with those calculated from Eqs. (28) and (29) in Table 1. Note that their experimental results include the effects of the entrance region and the substrate conduction. Table 1 shows the predicted values are in good agreement with the experimental ones within 7.6 percent even considering these effects. Hence, it is valid to optimize the thermal performance of the microchannel with Eqs. (28) and (29) based on the porous medium model.

In minimizing the total thermal resistance, conductivities of the fluid and the solid and the size of the chip which is to be cooled are assumed to be fixed. Also, the maximum pressure difference across the microchannel heat sink and the maximum pumping power are practically chosen, as shown in Table 2. With these assumptions, Eqs. (28) and (29) show that the total thermal resistance is now a function of α_s, ϵ, and w_c. For large α_s, the heat transfer coefficient is directly related to the Nusselt number, which does not change significantly with α_s as pointed out by Tuckerman and Pease (1981), and the fluid flow becomes a Darcian flow, i.e., $U \approx 1$ and $P \approx 1$. It can be inferred from Eqs. (28) and (29) that, for large α_s, θ_{fin} mainly depends on the interfacial area between the fin and the fluid; $A_{fs} = LW\epsilon(1 + 2\alpha_s)$ and θ_{flow} is mainly affected by the cross-sectional area of the channel, $W\epsilon w_c \alpha_s$. Consequently, the total thermal resistance tends to decrease as the aspect ratio α_s increases. Therefore, there is no optimum value for α_s, as pointed out by Tuckerman and Pease (1981). In reality, the aspect ratio is usually limited by the manufacturing capability and the cost for machining the microchannel.

In this paper the results of Tuckerman and Pease (1981) and Knight et al. (1991) for optimum geometry of the microchannel heat sink are compared with those of the present study. Tuckerman and Pease (1981) and Knight et al. (1991) used the friction factor of the channel for the pressure drop and the fin theory, assuming one-dimensional conduction along the fin height for heat transfer.

Case I: Tuckerman and Pease. Tuckerman and Pease (1981) simplified the optimization problem by using various constraints; they assumed $\epsilon = 0.5$ and the fixed Nusselt number of 6 and they approximated the hydraulic diameter of the channel as $2w_c$ by using the high aspect ratio assumption. They also used the fin efficiency of 0.76 to restrict the aspect ratio to within a practical limit. When the tip is insulated, the fin efficiency, η, is

Table 1 Comparison with experimental results of Tuckerman and Pease (1981)

w_c (μm)	w (μm)	H (μm)	Thermal resistance		Relative error (%)
			prediction (℃/W)	experiment (℃/W)	
56	100	320	0.097	0.105	7.6
55	100	287	0.101	0.105	3.8
50	100	302	0.079	0.083	4.8

Table 2 Comparison with previous papers

	Case I		Case II	
	Tuckerman and Pease	Present study	Knight et al.	Present study
Constraints				
Size, Length(L) by Width(W)	1 cm × 1 cm	same	same	same
Maximum pressure drop	206.8 kPa	same	same	same
Maximum pumping power	2.27 W	2.27 W	2.56 W	2.56 W
Fin efficiency	0.76	N/A	0.76	N/A
Coolant	Water	same	same	same
Fin material	Silicon	same	same	same
k_f/k_s	0.004069	same	same	same
High aspect ratio assumption	Yes	Yes	No	No
Nusselt number	6	same (α_s limitation)	unrestricted	unrestricted
Calculated Results				
Number of channels	88	85	83	82
Channel height, H, μm	365	378	357	360
Fin thickness, μm	57	59	60	61
Channel width, w_c, μm	57	59	61	61
Porosity, ϵ	0.5	0.5	0.504	0.5
Reynolds number	730	733	834	826
Volumetric flow rate, cm³/s	11	11.3	12.4	12.6
Aspect ratio, α_s	6.4	6.4	5.8	5.9
θ_{flow}, ℃/W	0.022	0.022	0.019	0.020
θ_{fin}, ℃/W	0.064	0.053	0.058	0.050
θ_{total}, ℃/W	0.086	0.075	0.077	0.070

$$\eta = \frac{\tanh N}{N} \tag{30}$$

where

$$N^2 = \frac{hP_{\text{fin}}}{k_s A_{c,\text{fin}}} \approx \frac{2h}{k_s \dfrac{1-\epsilon}{\epsilon} w_c} \tag{31}$$

and P_{fin} and $A_{c,\text{fin}}$ are the perimeter of the fin and the cross-sectional area of the fin, respectively. As an approximation, they assumed that the length of the fin, L, is much longer than the thickness of the fin, $((1-\epsilon)/\epsilon)w_c$. Tuckerman and Pease practically chose $N = 1$, which results in $\eta = 0.76$. From Eq. (31), this is equivalent to the following condition:

$$\alpha_s = 0.408 \sqrt{\frac{k_s}{k_f}}. \tag{32}$$

With k_f/k_s as given in Table 1, this results in $\alpha_s = 6.4$. Therefore, the optimization problem in the case of Tuckerman and Pease is to determine the optimum value of w_c for which the total thermal resistance is minimal.

In our case we obtain optimum values of parameters by minimizing the total thermal resistance under the conditions and the constraints of Tuckerman and Pease. Under the constraints of Tuckerman and Pease, θ_{total} is the function of w_c only. Hence, the minimum of θ_{total} can be found using $d\theta_{\text{total}}/dw_c = 0$ and the optimum value of the channel width is

$$w_{c,\text{opt}} = \left[\frac{36 k_s \nu_f L^2 P}{\alpha_s^2 c_f \Delta p \int_0^1 U\theta_f dY}\right]^{1/4}. \tag{33}$$

Case II: Knight et al. Recently, Knight et al. (1991) extended the work of Tuckerman and Pease (1981) in thermal optimization of the microchannel heat sink. They excluded most constraints of Tuckerman and Pease (1981), such as $\epsilon = 0.5$, the

fixed Nusselt number of 6 and the high aspect ratio in the calculation of the hydraulic diameter, while they also restricted the aspect ratio by assuming the fixed fin efficiency of 0.76. In this case, Eq. (31) expresses the relationship between α_s and ϵ as (Eq. (47) in Knight et al. (1991))

$$\left(-1.047 + 9.326\,\frac{\alpha_s^2 + 1}{(\alpha_s + 1)^2}\right)\alpha_s(\alpha_s + 1) - \frac{k_s(1-\epsilon)}{k_f\epsilon} = 0. \quad (34)$$

Equation (34) can be solved numerically and the optimization in their case is progressed with respect to ϵ and w_c.

In our case we obtain optimum values of parameters by minimizing θ_{total} with the limitation on the aspect ratio imposed by Eq. (34). In this case, θ_{total} is a complex function of ϵ and w_c. Therefore a search method should be used to find optimum values of ϵ and w_c which result in a minimum total thermal resistance and the procedure is as follows (Stoecker, 1989):

1 Start at one point in the region of interest, i.e., $0.1 \leq \epsilon \leq 0.9$ and $1\ \mu\text{m} \leq w_c \leq 1000\ \mu\text{m}$, and solve Eq. (34) if ϵ changes.

2 Check eight points in a grid surrounding the central point. The surrounding point having the smallest total thermal resistance is chosen as the central point for the next search.

3 If no surrounding point provides a smaller total thermal resistance than the central point, the central point is the optimum point.

4 A common practice is first to use a coarse grid and after the optimum point has been found for that grid subdivide the grid into smaller elements for a further search.

The results of Cases I and II are summarized in Table 2.

As shown in Table 2, optimum values of parameters in the paper of Tuckerman and Pease (1981) and Knight et al. (1991) are in agreement with those from the porous medium model to within 3.3 percent and to within 1.6 percent, respectively. This example demonstrates the advantages of the porous medium model and the new analytical solutions based on it in determining the optimum geometry of the microchannel heat sink. The cost and speed advantage of the analytical solutions compared to more time consuming numerical procedures in design applications cannot be overemphasized.

Also, the resultant thermal resistances for the flow of the coolant agree with those from the porous medium model very well. However, the resultant thermal resistances for conduction through and convection between the fins are different by 17.2 percent and 13.8 percent, respectively. This can be explained as follows:

First, in the case of Tuckerman and Pease, they used the high aspect ratio in the calculation of the hydraulic diameter of the channel. Under the high aspect ratio assumption, the heat transfer at the bottom of the channel is neglected and this can cause noticeable error in the thermal resistance calculation for high ϵ. Also they used the fixed Nusselt number of 6 which is in good agreement with that resulted from a boundary condition of constant heat flux around the channel, while in the present problem, the heat flux varies along the fin height.

Second, in the case of Knight et al., they used the Nusselt number which results from a boundary condition of constant heat flux around the channel. As mentioned before, this approximate Nusselt number can produce noticeable error in this problem. Additionally, in the paper of Knight et al. (1991), they pointed out that the relaxation of the constraint on ϵ results in a reduction of the total thermal resistance from that of Tuckerman and Pease (1981). However, as shown in Table 2, the optimum values of ϵ remained almost constant at 0.5. We think the assumption of the high aspect ratio and the fixed Nusselt number of 6 result in the difference between the results of Tuckerman and Pease (1981) and that of Knight et al. (1991).

Overall, the porous medium model can be successfully and effectively applied to the thermal optimization and the prediction of the thermal resistance of the microchannel heat sink.

6 Conclusion

In this paper, analytical solutions for velocity and temperature distributions through microchannel heat sinks are presented by modeling the microchannel heat sink as a fluid-saturated porous medium. The analytical solutions are obtained based on the modified Darcy model for fluid flow and the two-equation model for heat transfer. To validate the porous medium model and the analytical solutions based on that model, the closed-form solution for the velocity distribution in the fully developed channel flow and the numerical solutions for the conjugate heat transfer problem comprising the solid fin and the fluid are also obtained. The analytical solutions are shown to predict the volume-averaged velocity and temperature distributions in the microchannel heat sink quite well. Using the analytical solutions, variables of engineering importance are identified as α_s and C and the fluid temperature approaches the solid temperature as either one of α_s and C increases, in which case the local thermal equilibrium may be assumed and the one-equation model would be appropriate. Finally, the expression for the total thermal resistance is derived from the analytical solutions, which is found to be the function of α_s, ϵ, and w_c. The geometries of the microchannel heat sink for which the thermal resistance of the heat sink is minimal are obtained under the constraints of Tuckerman and Pease (1981) and Knight et al. (1991), respectively. Comparisons with the results of Tuckerman and Pease (1981) and Knight et al. (1991) show that the porous medium model can be successfully used for the thermal optimization and the prediction of the thermal resistance of the microchannel heat sink.

Acknowledgments

This work was supported by EPRC (Electronic Packaging Research Center) at KAIST, and KOSEF (Korea Science and Engineering Foundation).

References

Bejan, A., and Morega, A. M., 1993, "Optimal Arrays of Pin Fins and Plate Fins in Laminar Forced Convection," ASME JOURNAL OF HEAT TRANSFER, Vol. 115, pp. 75–81.

Kaviany, M., 1995, *Principles of Heat Transfer in Porous Media,* Springer-Verlag, New York.

Knight, R. W., Goodling, J. S., and Hall, D. J., 1991, "Optimal Thermal Design of Forced Convection Heat Sinks–Analytical," ASME *Journal of Electronic Packaging,* Vol. 113, pp. 313–321.

Koh, J. C. Y., and Colony, R., 1986, "Heat Transfer of Microstructures for Integrated Circuits," *Int. Comm. Heat Mass Transfer,* Vol. 13, pp. 89–98.

Phillips, R. J., 1990, "Micro-channel heat sinks," *Advances in Thermal Modeling of Electronic Components and Systems,* Vol. 2, A. Bar-Cohen and A. D. Kraus, eds., ASME, New York, Chapter 3.

Shah, R. K., and London, A. L., 1978, *Laminar Flow Forced Convection in Ducts,* Academic Press, San Diego, CA.

Sparrow, E. M., Baliga, B. R., and Patankar, S. V., 1978, "Forced Convection Heat Transfer From a Shrouded Fin Array With and Without Tip Clearance," ASME JOURNAL OF HEAT TRANSFER, Vol. 100, pp. 572–579.

Stoecker, W. F., 1989, *Design of Thermal Systems,* McGraw-Hill, New York.

Tien, C. L., and Kuo, S. M., 1987, "Analysis of Forced Convection in Microstructures for Electronic System Cooling," *Proc. Int. Symp. Cooling Technology for Electronic Equipment,* Honolulu, HI, pp. 217–226.

Tuckerman, D. B., and Pease, R. F. W., 1981, "High-Performance Heat Sinking for VLSI," *IEEE Electron Device Letter,* Vol. 2, pp. 126–129.

Tuckerman, D. B., and Pease, R. F. W., 1982, "Ultrahigh Thermal Conductance Microstructures for integrated Circuits," *IEEE Proc. 32nd Electronics Conference,* pp. 145–149.

Vafai, K., and Tien, C. L., 1981, "Boundary and Inertia Effects on Flow and Heat Transfer in Porous Media," *Int. J. Heat Mass Transfer,* Vol. 24, pp. 195–203.

Variations of Buoyancy-Induced Mass Flux From Single-Phase to Two-Phase Flow in a Vertical Porous Tube With Constant Heat Flux

T. S. Zhao[1]
Assistant Professor,
e-mail: metzhao@ust.hk
Assoc. Mem. ASME

Q. Liao[2]
Research Associate

P. Cheng
Professor,
Fellow ASME

Department of Mechanical Engineering,
The Hong Kong University of Science and Technology,
Clear Water Bay, Kowloon,
Hong Kong, China

This paper presents an experimental study of a buoyancy-induced flow of water with phase-change heat transfer in a vertical porous tube heated at a constant heat flux. Experiments were carried out from subcooled liquid flow to convective boiling by varying the imposed heat fluxes. At a prescribed heat flux the steady-state mass flux of water, as well as the temperatures along the tube wall and along the centerline of the packed tube, were measured. It is shown that for both single-phase flow and the two-phase flow with a rather low vapor fraction, the induced mass flux increased as the heat flux was increased. However, as the imposed heat flux was increased further, the induced mass flux dropped drastically, and remained relatively constant afterwards. The influences of various parameters such as the porous tube diameter, the particle sizes, and the hydrostatic head on the induced mass flux are also examined.

Introduction

Buoyancy-induced convective fluid flow with and without phase-change heat transfer in a porous medium is frequently encountered in numerous important technological applications (Cheng, 1978; Wang and Cheng, 1997). Examples include thermal energy storage, nuclear waste isolation, geothermal systems, porous medium heat pipes, food drying, porous insulation moisture transport, and post-accident analysis of liquid-cooled nuclear reactors, electronic cooling, etc. In this paper, we shall consider single-phase and two-phase convection in a vertical packed tube as depicted in Fig. 1, where subcooled water enters from the bottom and flows against gravity through a porous medium tube heated at a uniform heat flux. If the imposed heat flux is low such that the flow is single phase, the motion of water inside the packed tube is solely driven by the buoyancy force when the hydrostatic head $\Delta h = 0$. An order-of-magnitude estimate gives the following expression for the variation of the mass flux raising through the packed tube with the applied heat load:

$$m'' = \rho u \sim \frac{K\rho\beta g\Delta T}{\nu}, \tag{1}$$

which can be readily obtained based on Darcy's equation under the Boussinesq approximation (Cheng, 1978). In Eq. (1), K is permeability and $\Delta T = T_{out} - T_{in}$ with T_{out} and T_{in} denoting the fluid temperatures at the top and the bottom of the packed tube, respectively, while the other symbols are explained in the Nomenclature. It is clear from Eq. (1) that the buoyancy-induced mass flux is proportional to the applied heat load, a higher heat flux leading to a higher induced mass flux. At a sufficiently high heat load, a liquid-vapor two-phase zone will form adjacent to the walls, with the subcooled liquid zone existing elsewhere. It is of interest to know how the mass flux varies with the applied heat load as the fluid changes from single phase to two phase. One might speculate that the induced mass flux for the two-phase flow in the packed channel would be higher as compared with single-phase flow of subcooled liquid because the liquid/vapor meniscus inside the two-phase region may create a wicking effect to pump the subcooled liquid from the liquid pool into the packed structure, in addition to the buoyancy effect. However, such a speculation has never been verified experimentally. Since this problem involves a number of complex and interacting physical phenomena such as phase change, capillary action, and the presence of a moving and irregular interface between the single and two-phase regions, both analytical and numerical treatments are rather complicated.

There are several papers in the literature which may be relevant to the present work. Guo and Wu (1993) investigated natural convection in vertical empty parallel plates with variable properties taken into account and found that the mass flow rate of the buoyancy-induced flow in the channel exhibits a nonmontonic change as the applied heat becomes sufficiently high; i.e., the mass flow rate goes up first, reaches a peak value and drops drastically afterwards. They attributed this sharp fall in the mass flow rate to the higher viscous drag at higher temperatures. Most recently, Xia and Guo (1996) experimentally investigated natural convective boiling in vertical rectangular narrow channels. They found that the buoyancy-induced mass flow rate in the boiling channel underwent a drastic fall at a rather high heat flux. They suggested that the reason for this sharp fall was due to the boiling crisis.

In this paper we shall present a peculiar vapor-choking phenomenon associated with the behavior of the induced mass flux as a function of the prescribed heat flux for the physical problem depicted in Fig. 1. For both single-phase flow and the two-phase flow with a rather low vapor fraction, the induced mass flux increases as the prescribed heat flux is increased. However, as the heat flux is increased, the induced mass flux drops drastically and then remains relatively constant afterwards. We shall then focus ourselves on discussing the underlying mechanisms leading to such a choking phenomenon. Finally, the influences of various parameters such as particle sizes, the porous tube diameters, and a superimposed aiding flow (with $\Delta h \neq 0$) on the induced mass flux are also experimentally examined.

[1] To whom correspondence should be addressed.

[2] Permanent Address: Department of Thermal Power Engineering, Chongqing University, Chongqing, China.

Contributed by the Heat Transfer Division for publication in the JOURNAL OF HEAT TRANSFER. Manuscript received by the Heat Transfer Division, Sept. 10, 1998; revision received, Feb. 26, 1999. Keywords: Boiling, Heat Transfer, Mixed Convection, Porous Media, Two-Phase. Associate Technical Editor: M. Kaviany.

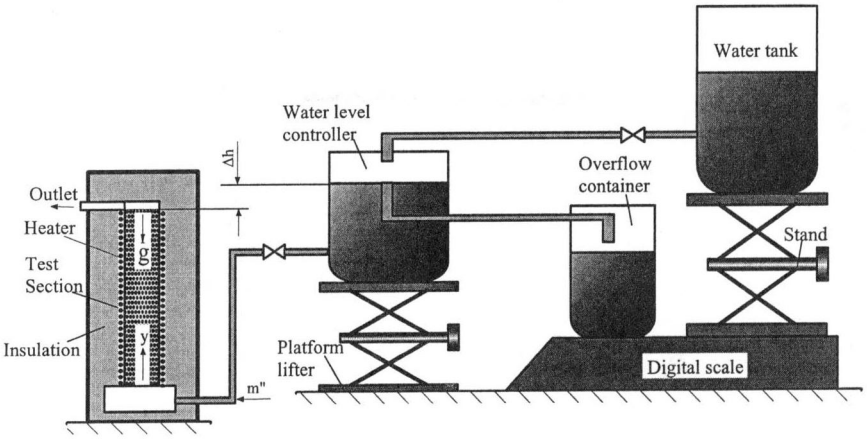

Fig. 1 Schematic of the experimental apparatus

Experimental Apparatus and Procedure

Test Section. The experimental investigation was carried out in the apparatus shown in Fig. 1, which consisted of two major assemblies: a vertically oriented test section and a water supply assembly. The circular test section was made of a copper tube with length $L = 215$ mm, inside diameter $D_i = 13.5$ mm (or $D_i = 20.0$ mm), and outside diameter $D_o = 15.0$ mm (or $D_o = 22.0$ mm). The tube was packed with glass beads, essentially spherical in shape with an average particle diameter of $d_p = 1.09$ mm (or $d_p = 0.50$ mm). The test section was heated uniformly outside by a wrapped-around insulated steel wire (0.6 mm in diameter). This steel wire was connected to an adjustable voltage controller. A mixing chamber made of steel screens was installed on the bottom of the test section to promote a more uniform velocity profile entering the test section while a short tube of 8 mm in diameter was connected to the top of the test section to lead the working fluid to a reservoir. The test section was well insulated outside with fiber glass wool. The locations of various thermocouples are shown in Fig. 2. Eight T-type thermocouples of 0.2 mm in diameter were embedded along the tube wall to measure wall temperatures while another eight T-type thermocouples of 0.8 mm in diameter were inserted in the glass beads for measuring temperature distributions in the porous structure. A data acquisition system, consisting of a personal computer, an A/D converter board (MetraByte DAS-20), and two universal analog input multiplexers (MetraByte EXP-20), was employed to record temperature measurements.

Water Supply Assembly. As shown in Fig. 1, the liquid supply assembly was placed adjacent to the test section. The deionized water draining from the water tank was bifurcated into two streams in the water-level controller: One stream was directed toward the test section while the remainder was directed toward the overflow container. As such, the water level in the water-level controller could be kept constant during the experiments. The hydrostatic head Δh (the distance between the top of the packed tube and the water level) was controlled by adjusting the elevation of the platform lifter, on which the water-level controller was placed. Both the water tank and the overflow container were placed on a digital scale such that the mass flow rate passing through the test section could be measured by reading the mass change per unit time.

In order to degas the air from the packed tube, the water level of the water-level controller was adjusted above the top of the packed tube and a moderate heat flux was applied for two hours prior to each experiment. Then, the water level was adjusted to the required elevation. For each test case, it took about one to two hours for the system to be stabilized. The experimental data were collected under steady-state conditions.

Experimental Uncertainties. The three physical parameters measured during the experiments were: the imposed heat flux, the temperatures along the tube wall and along the centerline of the packed column (see Fig. 2), as well as the mass flux of water. The thermocouples were calibrated to ensure the accuracy within ± 0.2°C. It was estimated that the uncertainty of the mass flux was ± 0.4 percent while the uncertainty of the imposed heat flux was ± 8 percent, which was primarily caused by the heat loss.

An Approximate Analysis

For the purpose of enhancing the interpretation of the experimental data presented in the next section, we now present a one-dimensional approximate analysis. Consider a vertically oriented porous media tube heated at a constant heat flux, as de-

Nomenclature

D_i = inside diameter of the porous tube
d_p = diameter of the porous medium
$\mathbf{g}$ = gravitational acceleration
$J(s)$ = Levertt's function
k_r = relative permeability
K = absolute permeability
L = height of the porous tube
m'' = induced mass flux
p = pressure
q_w = imposed heat flux
s = liquid saturation
T = temperature
$\mathbf{u}$ = superficial or Darcian velocity vector
x = coordinate in vertical direction

Greek Symbols

β = thermal expansion coefficient
Δh = hydrostatic head
ϵ = porosity
λ = relative mobility
μ = viscosity
ν = kinetic viscosity
ρ = density
σ = surface tension

Subscripts

c = capillary
h = heating
i = inside
in = inlet
l = liquid phase
o = outside
sat = saturated state
v = vapor phase
w = wall

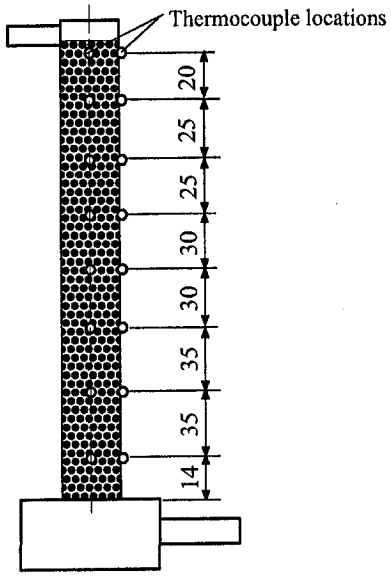

Fig. 2 Arrangement and the locations of thermocouples

scribed above and illustrated in Fig. 1. The porous tube is initially saturated with a subcooled liquid. As heat is added to the tube wall, the liquid rises up in the packed column from the adjacent liquid pool due to the buoyancy force, and the superimposed pressure gradient, if $\Delta h \neq 0$. When the heat flux exceeds a certain value, boiling occurs in the vicinity of the tube wall near the exit and extends to the neighboring region. As a consequence, a two-phase region consisting simultaneously of liquid and vapor is formed adjacent to the tube wall. Under this situation, the liquid/vapor meniscus inside the two-phase region can create a wicking effect to pump the subcooled liquid into the packed tube, in addition to the buoyancy effect, and the superimposed pressure gradient, if any. Under a steady-state condition, the momentum equation for a buoyancy-driven two-phase flow in a porous medium is (Wang and Cheng, 1997)

$$\rho \mathbf{u} = -\frac{K}{\nu(s)}[\nabla p_l + \lambda_v(s)\nabla p_c - \lambda_l(s)\rho_l \mathbf{g}]. \tag{2}$$

The mixture variables in Eq. (2) are defined as

Density:

$$\rho = \rho_l s + \rho_v(1 - s), \tag{3}$$

Velocity:

$$\rho \mathbf{u} = \rho_l \mathbf{u}_l + \rho_v \mathbf{u}_v, \tag{4}$$

Viscosity:

$$\nu(s) = \mu(s)/\rho = \frac{\rho_l s + \rho_v(1 - s)}{\rho\left(\frac{k_{rl}}{\nu_l} + \frac{k_{rv}}{\nu_v}\right)}, \tag{5}$$

Relative mobility:

$$\lambda_l(s) = \frac{k_{rl}/\nu_l}{\frac{k_{rl}}{\nu_l} + \frac{k_{rv}}{\nu_v}}; \quad \lambda_v(s) = \frac{k_{rv}/\nu_v}{\frac{k_{rl}}{\nu_l} + \frac{k_{rv}}{\nu_v}}, \tag{6}$$

where s represents the liquid saturation, the subscripts "l" and "v" denote the quantities for liquid and vapor, respectively, while all the other symbols used are explained in the Nomenclature. The empirical expressions for relative permeabilities k_{rl} and k_{rv} can be found elsewhere (Kaviany, 1991). Equation (2) suggests that for a two-phase flow there are three force components which may influence the mass flux. These force components include the superimposed pressure gradient, the capillary pressure gradient, and the gravity force, as represented, respectively, by the first term, the second term, and the last term in Eq. (2). The capillary pressure p_c represents the difference between the pressures of the liquid and vapor phases due to interfacial tension, which can be evaluated by

$$p_c = p_v - p_l = \left(\frac{\epsilon}{K}\right)^{1/2} \sigma J(s), \tag{7}$$

with $J(s)$ being the Levertt function (Leverett, 1941) and σ the vapor-liquid interfacial tension. Various forms of the J-function can be found elsewhere (Kaviany, 1991). With reference to Fig. 1, the hydrostatic pressure difference between the inlet and the outlet of the porous tube Δp is

$$\Delta p = \rho_{li} g(\Delta h + L), \tag{8}$$

where L is the height of the porous tube and ρ_{li} is the density of water at the inlet of the porous tube corresponding to the inlet temperature T_{li}. We now assume that the pressure gradient along the vertical x-axis is constant throughout the porous tube, i.e.,

$$\frac{\partial p}{\partial x} = \text{const.} = \frac{\Delta p}{L} = \rho_{li} g \Delta h/L + \rho_{li} g. \tag{9}$$

Substituting Eq. (9) into Eq. (2), we obtain a one-dimensional approximation of force balance in the vertical x-axis as

$$\rho u = \frac{K}{\nu(s)}[\rho_{li} g \Delta h/L - \lambda_v \nabla p_c + (\rho_{li} - \lambda_l \rho_l)g], \tag{10}$$

where u denotes the velocity component in the vertical direction. Although Eq. (10) is an approximate equation, the physical significance of each term is clear. For example, in the case without the superimposed pressure gradient ($\Delta h = 0$), the motion of the fluid in the porous tube is due to both the capillary and the buoyancy effect. Moreover, as the liquid saturation (s) approaches unity (subcooled liquid, then $\lambda_v = 0$) or zero (superheated vapor, then $\lambda_l = 0$), Eq. (10) is reduced, respectively, to

$$\rho_l u_l = \frac{K}{\nu_l}[\rho_{li} g \Delta h/L + (\rho_{li} - \rho_l)g], \tag{11}$$

or

$$\rho_v u_v = \frac{K}{\nu_v}(\rho_{li} g \Delta h/L + \rho_{li} g). \tag{12}$$

As will be shown in the next section, Eqs. (10)–(12) are helpful for the interpretation of experimental results.

Results and Discussion

A series of experiments were carried out by varying the heat flux from 0.2 kW/m^2 to 16.5 kW/m^2. Two porous tubes, one with D_i = 13.5 mm and the other with D_i = 20.0 mm, packed with glass beads with an average diameter of either 1.09 mm or 0.5 mm were tested. Both pure natural convection (with hydrostatic head Δh = 0) and aided mixed convection (Δh = 10 mm and 20 mm) were examined. In what follows, we shall first present the temperature distributions and the general trend of the variations of the buoyancy-induced mass flux versus the imposed heat flux. We shall then examine and discuss the effects of various parameters, such as the diameter of the packed tube D_i, the particle diameters d_p, and the hydrostatic head Δh on the mass flux. It should be pointed out that all the experimental data presented in the following paragraphs were connected by lines in order to clearly show the trend of each curve.

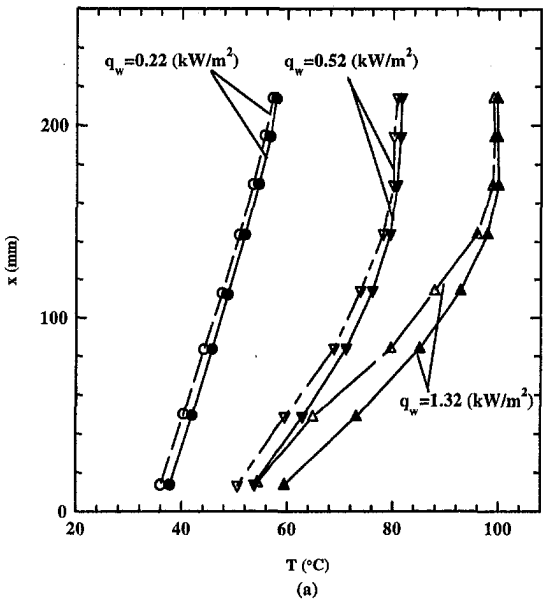

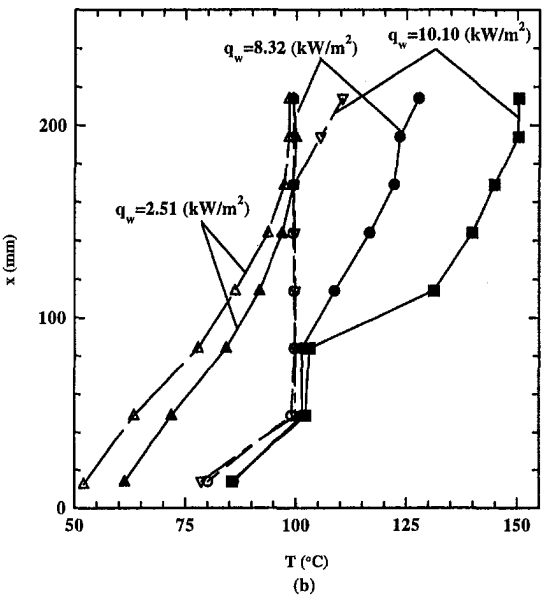

Fig. 3 Variation of the temperatures at the tube wall (represented by solid symbols) and at the tube centerline (represented by empty symbols) along the vertical direction for D_i = 20.0 mm, d_p = 1.09 mm, and Δh = 0

I General Observations.

Temperature Distributions. The variations of the temperatures along the tube wall (represented by solid symbols) and along the vertical centerline (represented by empty symbols) of the packed tube for various heat fluxes are presented in Fig. 3. For the sake of clarity, the data before the initiation of boiling (i.e., at small heat fluxes) are shown in Fig. 3(*a*) while the data after boiling occurred (i.e., at larger heat fluxes) are presented in Fig. 3(*b*). We now focus our attention to the temperature profiles for the single-phase flow presented in Fig. 3(*a*). Generally, the wall temperatures were higher than those along the centerline of the tube due to heat transfer from the wall to the flowing fluid. As expected, both wall and fluid temperatures increased with the increase of the imposed heat flux. Another observation from Fig. 3(*a*) is that both the wall and fluid temperatures increased nearly linearly along the vertical direction for a small heat flux (q_w = 0.22 kW/m^2). At higher heat fluxes (q_w = 0.52 and 1.32 kW/m^2); however, the temperatures increased rapidly in the inlet zone but increased slowly toward the exit of the packed tube. This is because at a low heat flux the induced mass flux of water was relatively small (as will be shown in Fig. 4). Thus, the heat convection due to the corresponding movement of water was insignificant for this case. Since in the single-phase flow regime the induced mass flux due to buoyancy force is increased with the increase of the imposed heat flux (again, as will be evident from Fig. 4), convection became more significant as the imposed heat flux is increased. Therefore, both the wall and fluid temperature profiles varied nonlinearly with height at higher heat fluxes. When the heat flux was increased to about q_w = 2.02 kW/m^2, it was observed during the experiments that vapor departed from the exit of the packed tube, indicating boiling began. An examination of both the wall and fluid temperatures at the exit presented in Fig. 3(*b*) show that they were at the saturated value when q_w = 2.51 kW/m^2. As the heat flux was further increased to q_w = 8.32 kW/m^2 and 10.10 kW/m^2, even though the temperature difference between the tube wall and the centerline in the inlet zone was relatively small, it became much larger toward the exit of the packed tube. This is due to the lower conductivity of superheated vapor formed adjacent to the tube wall.

Variation of the Mass Flux. Figure 4 presents the variation of the mass flux with the imposed heat flux for the D_i = 20.0 mm packed tube with glass beads of d_p = 1.09 mm under the condition of pure natural convection (Δh = 0). It is seen that the induced mass flux increased as the prescribed heat flux was increased. When the imposed heat flux reached about 2.02 (kW/m^2) (i.e., at point B in Fig. 4), boiling occurred near the wall at the outlet. After boiling occurred, the induced mass flux kept increasing for a small increment of the imposed heat flux. However, as the heat flux was further increased, the induced mass flux dropped rapidly, and remained relatively constant afterwards. For the convenience of discussion, we now divide the variation of the mass flux versus the imposed heat flux shown in Fig. 4 into three regions, namely, an increasing mass flux region (A–C), a dropping mass flux region (C–D), and a constant mass flux region (D–E). Let us first focus on discussing the increasing mass flux region (A–C). This region (A–C) consists two subregions separated by the boiling point at B: the subcooled liquid flow region (A–B) and the two-phase flow region (B–C). In the subcooled liquid flow region (A–B), the increase of the mass flux with the increase of the heat flux can be explained from Eq. (11), where the drag force becomes smaller while the buoyancy becomes stronger due to both the viscosity and the density become smaller with the increase of temperature. After the point B, boiling began and the flow of water

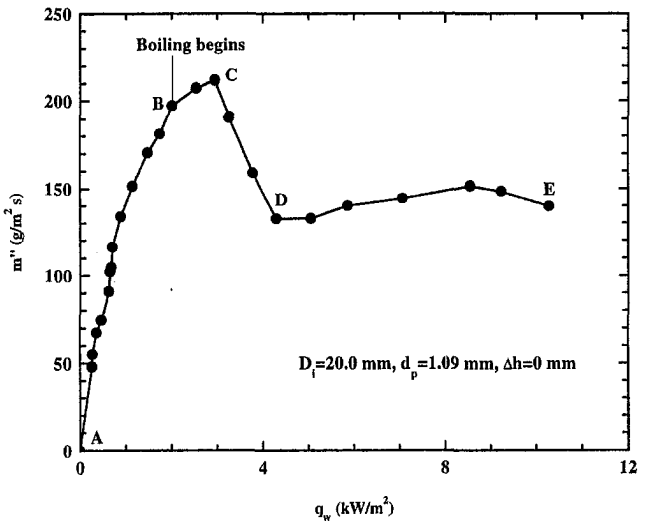

Fig. 4 Variations of the mass flow flux versus the imposed heat flux for D_i = 20.0 mm, d_p = 1.09 mm, and Δh = 0

inside the packed tube consisted of a subcooled water zone and a two-phase zone. Under the condition without the superimposed pressure gradient ($\Delta h = 0$), the motion of the two-phase flow is essentially influenced by three force components such as the capillary force, the drag force, and the buoyancy force, as indicated in Eq. (10). Inspection of Eq. (10) also shows that the relative importance of each term strongly depends on the liquid saturation distribution, which are subject to changing with heat fluxes. Typical liquid saturation distributions in the porous tube under various heat fluxes are depicted in Fig. 5. In the initial period of boiling (B–C), as shown in Figs. 5(*a*) and 5(*b*), a two-phase zone was formed only adjacent to the tube wall near the exit while the central part of the cross section of the porous tube at the exit was filled with subcooled liquid. Under this situation, the capillary force began to affect the motion of the fluid in the porous tube due to the existence of liquid/vapor meniscus in the two-phase zone. Its primary function, however, was to draw liquid toward the heated wall but would not help much in the increase of the overall mass flux flowing in the porous tube. As the heat flux was increased, the buoyancy force was increased further because the density difference became larger while the drag force in the subcooled liquid zone decreased because the viscosity became smaller. This leads to an increase of the mass flux. On the other hand, however, the thermal drag force (Guo et al., 1993) near the exit became relatively larger due to the lower density of the vapor in the two-phase zone, which tended to reduce the mass flux of water. Consequently, in the initial period of boiling (B–C), the induced mass flux of water was increasing but at a slower rate as compared with the subcooled liquid flow region (A–B). After point B, a small increment of the heat flux would lead to a fast expansion of the two-phase zone adjacent to the tube wall and soon the whole cross section of the porous tube near the exit was occupied by the two-phase zone, as shown in Fig. 5(*c*). As a result, the drag force in the two-phase zone near the exit became extremely large which caused a drastic drop in the mass flux in the C–D region. Once the cross section of the porous tube near the exit was completely filled by the two-phase flow, the change of the drag force in the two-phase zone due to the increase of the heat flux became relatively slow as compared with the C–D region, even though it remained increasing. On the other hand, as the heat flux is increased, both the capillary force and the buoyancy force are increased because the saturation gradient and the density difference become larger in the system. This leads to an increase of the mass flux. Therefore, the relatively constant mass flux versus the heat flux at high heat fluxes

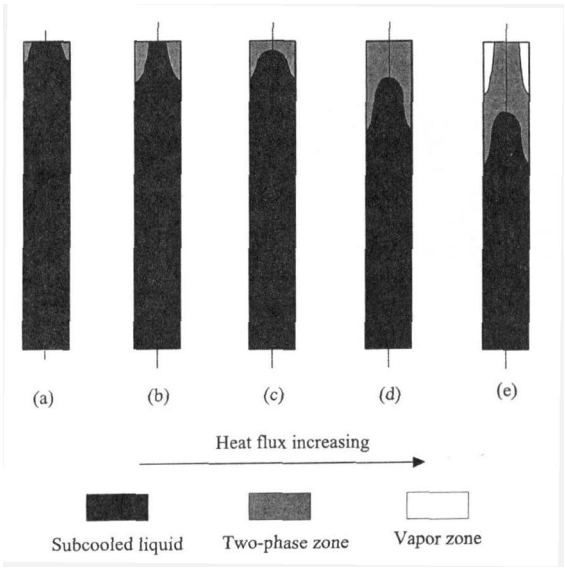

Fig. 5 Typical possible liquid saturation distributions at various heat fluxes

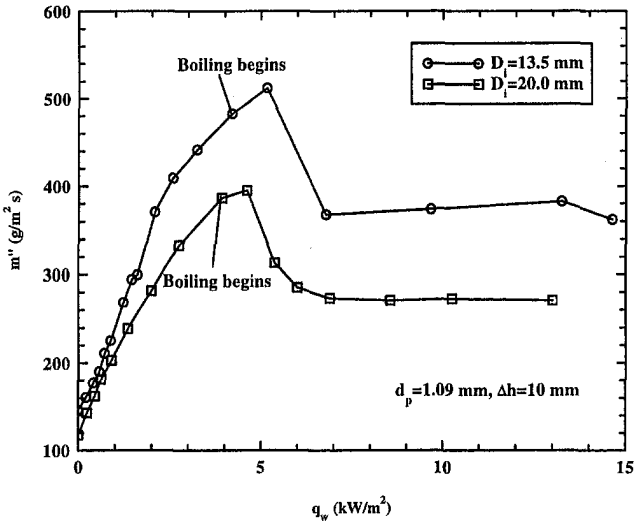

Fig. 6 Effect of the porous tube diameter on the variation of the induced mass flux for d_p = 1.09 mm and Δh = 10 mm

in the D–E region may be attributed to the fact that the balance of the aforementioned three forces.

II Case Studies. In the following, we shall examine the effect of the porous tube diameter D_i, the particle diameters d_p, and the hydrostatic head Δh on the induced mass flux.

Effect of the Tube Diameter D_i. Figure 6 shows the variation of mass flux with the imposed heat flux for different porous tube diameters for a given particle size (d_p = 1.09 mm) and a fixed hydrostatic head (Δh = 10 mm). Generally it is seen from Fig. 6 that the behavior of the mass flux versus heat flux is similar to that in Fig. 4 with $\Delta h = 0$ for both D_i = 13.5 mm and D_i = 20.0 mm. It is observed from Fig. 6 that the diameter of the porous tube has a significant influence on the magnitude of the induced mass flux: a packed tube with a smaller diameter leading to a larger mass flux over the whole range of the imposed heat flux for both the single-phase and the two-phase flow. The increase of the mass flux due to the decrease of tube diameter in the range of the single-phase flow can be explained based on the energy balance over the entire porous tube, which gives

$$q_w \pi D_i L = \dot{m} c_p (T_{\text{out}} - T_{\text{in}}), \tag{13}$$

with c_p denoting the specific heat of fluid. Considering the mass flow rate $\dot{m} = m''(\pi/4) D_i^2$ and $\Delta T = (T_{\text{out}} - T_{\text{in}})$, Eq. (13) can be rewritten as

$$q_w \pi D_i L = m'' \frac{\pi}{4} D_i^2 c_p \Delta T. \tag{14}$$

The relationship between the temperature difference ΔT and m'' can be obtained from Eq. (1) to give

$$\Delta T \sim \frac{\nu}{K \rho \beta g} m''. \tag{15}$$

Combining Eqs. (14) and (15), we obtain

$$m'' \sim \sqrt{\frac{4 q_w L K \rho \beta g}{\nu c_p}} \sqrt{\frac{1}{D_i}}, \tag{16}$$

and

$$\Delta T \sim \sqrt{\frac{4 q_w L \nu}{c_p K \rho \beta g}} \sqrt{\frac{1}{D_i}}. \tag{17}$$

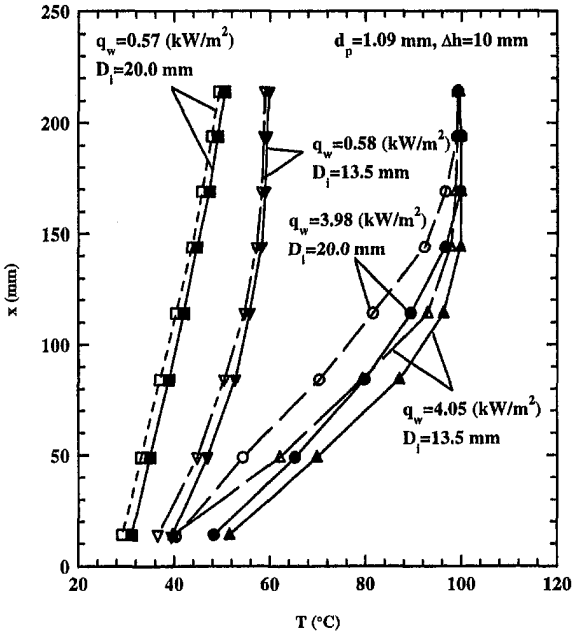

Fig. 7 Effect of the porous tube diameter on the variation of the temperature distributions of the wall (represented by solid symbols) and centerline of the packed tube (represented by empty symbols) for d_p = 1.09 mm and Δh = 10 mm

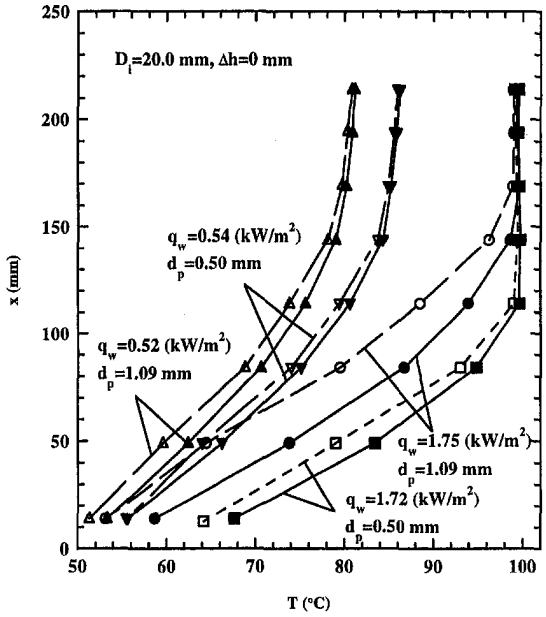

Fig. 9 Effect of the particle size on the variation of the temperature distributions of the wall (represented by solid symbols) and the centerline of the packed tube (represented by empty symbols) for D_i = 20.0 mm and Δh = 0

Equation (16) explains why the decrease of the tube diameter leads to the increase of the induced mass flux in the range of the single-phase flow, as shown in Fig. 6. Equation (17) indicates that the temperature difference is also inversely proportional to the tube diameter. This is evident from the measured temperature profiles shown in Fig. 7: At almost the same heat fluxes the temperatures along the tube wall and along the tube centerline for a smaller porous tube (D_i = 13.5 mm) were higher than those for a larger porous tube (D_i = 20.0 mm). It is also seen from Fig. 6 that the induced mass flux is also higher for the smaller tube (D_i = 13.5 mm) in the range of the two-phase flow. This may be attributed to the fact that the buoyancy force was higher for the porous tube with a smaller diameter due to higher temperatures in the porous tube. On the other hand, the higher temperatures lead to a smaller viscosity. As indicated from Eqs. (10) to (12), a larger buoyancy force and a lower viscosity lead to a higher mass flux.

Effect of the Particle Sizes. The effect of the particle sizes on the mass flux for the porous tube of D_i = 20.0 mm and the head Δh = 0 mm is presented in Fig. 8. Again, a trend similar to those presented in Figs. 4 and 6 is observed. It is seen that the induced mass flux for d_p = 1.09 mm is higher than that for d_p = 0.50 mm over the whole range of the imposed heat flux. This may be attributed to the fact that the porous tube with a smaller particle size has a lower permeability, which lead to a larger drag force. As indicated in Eqs. (10)–(12), the mass flux, therefore, is reduced with the decrease of particle diameter. A comparison of the curves presented in Fig. 8 also shows that the heat flux at which boiling began for d_p = 1.09 mm was higher than that for d_p = 0.50 mm. This is because a lower mass flux causes a higher fluid temperature at the same heat flux, which is evident from Fig. 9. Therefore, boiling initiated earlier for the porous tube with smaller particles. Worthy of note is the fact that the increase of the fluid temperature leads to an increase of buoyancy force and a decrease in viscosity

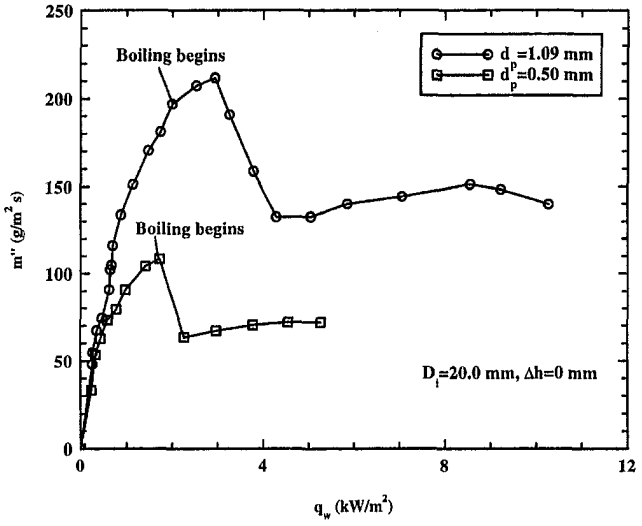

Fig. 8 Effect of the particle size on the variation of the induced mass flux for D_i = 20.0 mm and Δh = 0

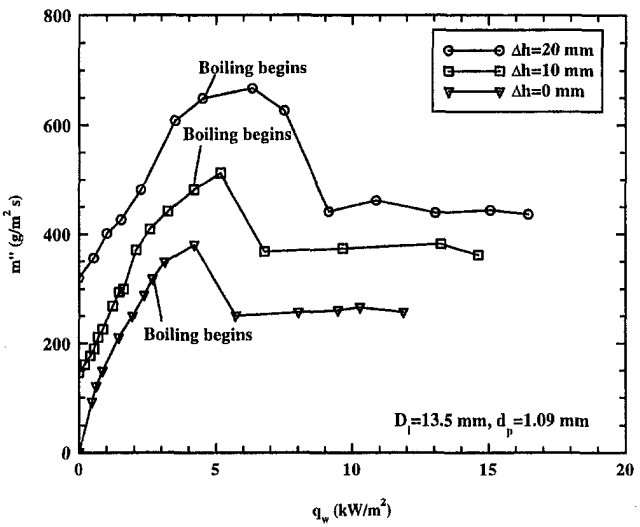

Fig. 10 Effect of the hydrostatic head on the variation of the induced mass flux for D_i = 13.5 mm and d_p = 1.09 mm

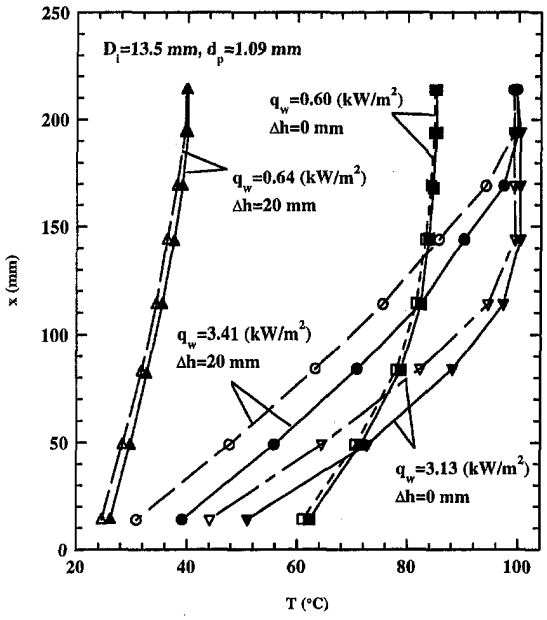

Fig. 11 Effect of the hydrostatic head on the variation of the temperature distributions of the wall (represented by solid symbols) and the centerline of the packed tube (represented by empty symbols) for D_i = 13.5 mm and d_p = 1.09 mm

which may cause a higher mass flux. But the decrease of the permeability due to smaller particles has a predominate influence on the variation of the mass flux, thus resulting in a decrease in the mass flux for a tube packed with smaller diameter glass beads.

Effect of the Hydrostatic Head Difference. Figure 10 shows the variation of mass flux with heat flux for three different heads (Δh = 0 mm, 10 mm, and 20 mm) for the porous tube of D_i = 13.5 mm packed with particles of d_p = 1.09 mm. It is clear from this figure that the mass flux increased with the increase of Δh for a given heat flux. This behavior can readily be explained based on Eqs. (10) to (12), where it is seen that the mass flux is directly proportional to the head Δh. It is also noted from Fig. 10 that the heat flux, at which boiling began, became higher than with the increases of the hydrostatic head Δh. The primary reason responsible for this behavior is that the higher mass flux caused by a larger hydrostatic head Δh leads to lower fluid temperatures, as evident from Fig. 11, where the temperature profiles for different hydrostatic heads at almost the same heat fluxes are illustrated.

Concluding Remarks

Experiments were carried out from subcooled liquid flow to convective boiling in a vertical porous tube heated at a constant heat flux. The measurements of the steady-state mass flux of water shows that for both single-phase flow and two-phase flow with a low vapor fraction in a system without (or with a small) imposed pressure gradient, the induced mass flux increased as the heat flux was increased. However, as the imposed heat flux was further increased with a corresponding increase in the vapor fraction, the induced mass flux dropped drastically, and remained relatively constant afterwards. It is shown that the diameter of the porous tube, the particle size, and the hydrostatic head have a significant influence on the mass flux of water. The mass flux is increased with the increase of the porous tube diameter, the particle size, and the hydrodynamic head.

Acknowledgment

This work was supported by Hong Kong RGC Earmarked Research Grant No. HKUST 809/96E.

References

Cheng, P., 1978, "Heat Transfer in Geothermal Systems," *Advances in Heat Transfer,* Vol. 14, Academic Press, New York, pp. 1–105.

Guo, Z. Y., and Wu, X. B., 1993, "Thermal Drag and Critical Heat Flux for Natural Convection of Air in Vertical Parallel Plates," ASME JOURNAL OF HEAT TRANSFER, Vol. 115, pp. 124–129.

Kaviany, M., 1991, *Principles of Heat Transfer in Porous Media,* Springer-Verlag, New York.

Leverett, M. C., 1941, "Capillary Behavior in Porous Solids," *AIME Transaction,* Vol. 142, pp. 152–169.

Topin, F., Rahli, O., Tadrist, L., and Pantaloni, J., 1996, "Experimental Study of Convective Boiling in a Porous Medium: Temperature Field Analysis," ASME JOURNAL OF HEAT TRANSFER, Vol. 118, pp. 230–233.

Wang, C. Y., and Cheng, P., 1997, "Multiphase Flow and Heat Transfer in Porous Media," *Advances in Heat Transfer,* Vol. 30, Academic Press, New York, pp. 93–196.

Xia, C. L., Hu, W. L., and Guo, Z. Y., 1996, "Natural Convection Boiling in Vertical Rectangular Narrow Channels," *Experimental Thermal and Fluid Science,* Vol. 12, pp. 313–324.

Y. Yokoyama
CAMPmode,
Department of Mechanical Engineering,
University of Colorado,
Boulder, CO 80309-0427
e-mail: yokoyama@spot.colorado.edu
Mem. ASME

F. A. Kulacki
Department of Mechanical Engineering,
University of Minnesota,
Minneapolis, MN 55455

R. L. Mahajan
CAMPmode,
Department of Mechanical Engineering,
University of Colorado,
Boulder, CO 80309-0427

Mixed Convection in a Horizontal Porous Duct With a Sudden Expansion and Local Heating From Below

Results are reported for an experimental and numerical study of forced and mixed convective heat transfer in a liquid-saturated horizontal porous duct. The cross section of the duct has a sudden expansion with a heated region on the lower surface downstream and adjacent to the expansion. Within the framework of Darcy's formulation, the calculated and measured Nusselt numbers for $0.1 < Pe < 100$ and $50 < Ra < 500$ are in excellent agreement. Further, the calculated Nusselt numbers are very close to those for the bottom-heated flat duct. This finding has important implications for convective heat and mass transfer in geophysical systems and porous matrix heat exchangers. The calculations were also carried out for glass bead-packed beds saturated with water using non-Darcy's formula. The streamlines in the forced convection indicate that, even with non-Darcy effects included, recirculation is not observed downstream of an expansion and the heat transfer rate is decreased but only marginally.

1 Introduction

Convective heat transfer in fluid-saturated porous media has important applications in geophysics, energy systems engineering, and agricultural engineering. Although a large part of previous work deals either with natural or forced convection, recent research includes mixed convection in which both of the two modes of heat transfer interact. Most of the studies of mixed convection have been limited to simple flow systems e.g., horizontal and vertical layers. Of these, experimental investigations are rather few.

The first studies of mixed convection in porous layers were reported by Wooding (1963), Prats (1966), Elder (1967), Sutton (1970), and Homsy and Sherwood (1976). These studies considered the effects of through-flow on free convection in a saturated porous medium heated uniformly from below. Particular attention was paid to the impact of the through-flow on the critical Rayleigh number that characterizes the onset of buoyancy induced flow. Cheng (1977a, b) considered mixed convection along horizontal, vertical, and inclined surfaces in an infinite porous medium and obtained similarity solutions for several special cases. Prasad et al. (1988), Lai et al. (1988), and Lai and Kulacki (1991) investigated mixed convection in horizontal and vertical layers with localized heating. Studies of mixed convection in porous annuli have been reported by Reda (1988), Clarksean et al. (1988), and Choi and Kulacki (1992).

Earlier studies present heat transfer correlations in simple geometries. However, those encountered in most of the practical applications are generally not that simple. To address this gap, the present study considers mixed convection in a porous duct with a sudden expansion of its cross-sectional area. This specific geometry can be encountered, for instance, around a nuclear waste repository embedded under a permeable layer of rock with impermeable layer protruding from one side.

Forced convective flow fields and heat transfer characteristics in irregular geometries have been investigated for pure fluid cases (without porous media) and composite systems (partially filled with porous media). For pure fluid case, Gooray et al. (1981) performed a numerical study on separated forced convective flow behind a backstep, while Yamamoto et al. (1979) and Sinha et al. (1981) reported the experimental results for separating flow and heat transfer for backsteps and cavities. For composite systems of porous media/pure fluid, Vafai and Huang (1994) numerically analyzed forced convection over intermittently placed porous cavities, while Abu-Hijleh (1997) investigated convective laminar flow over a two-dimensional backward facing step with a porous floor segment.

The present study differs from these in that the system is completely filled with porous media. Our particular attention is in mixed and forced convection regimes. Heat transfer coefficients are reduced to correlations in terms of Nusselt, Rayleigh, and Peclet numbers and are compared with the results of Lai and Kulacki (1991) for a layer in which there is no expansion.

2 Problem Formulation and Numerical Procedure

The geometry considered in the present study is a two-dimensional horizontal porous duct with a step change of the cross section (Fig. 1). The ratio of the inlet height to outlet height is fixed at 0.5. The heat source has a length equal to the duct height after the expansion and is assumed maintained either at constant temperature or constant heat flux condition. It is located on the bottom wall adjacent to the step. The bottom wall downstream of the heat source is adiabatic while the top wall is at a constant temperature. Flow in the duct is introduced at a mean axial velocity, u_0, at a temperature equal to that of the top wall far upstream of the step.

First consider the Darcy formulation. Assuming that (i) the thermophysical properties of the fluid and the porous medium are homogeneous and isotropic, (ii) the medium is isotropic and homogeneous, (iii) the fluid and the solid matrix are in local thermodynamic equilibrium everywhere, (iv) the flow is steady, laminar, incompressible and two-dimensional, and (v) the Boussinesq approximation is valid, the governing equations are

$$\frac{\partial^2\psi}{\partial X^2} + \frac{\partial^2\psi}{\partial Y^2} = -\frac{\mathrm{Ra}}{\mathrm{Pe}}\frac{\partial\theta}{\partial X} \tag{1}$$

$$\frac{\partial\psi}{\partial Y}\frac{\partial\theta}{\partial X} - \frac{\partial\psi}{\partial X}\frac{\partial\theta}{\partial Y} = \frac{1}{\mathrm{Pe}}\left(\frac{\partial^2\theta}{\partial X^2} + \frac{\partial^2\theta}{\partial Y^2}\right) \tag{2}$$

Contributed by the Heat Transfer Division for publication in the JOURNAL OF HEAT TRANSFER. Manuscript received by the Heat Transfer Division, Feb. 3, 1997; revision received, Mar. 23, 1999. Keywords: Geophysical Heat Transfer, Mixed Convection, Porous Media. Associate Technical Editor: T. Tong.

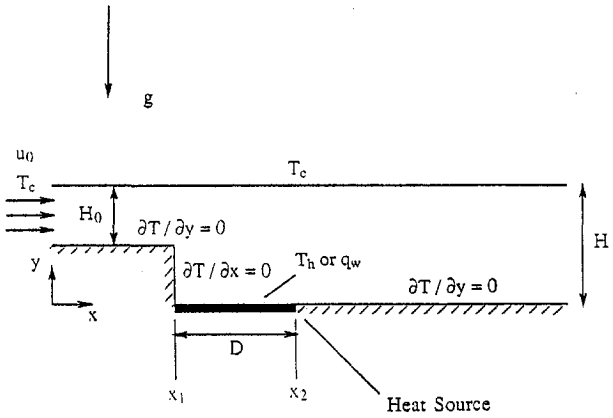

Fig. 1 Fluid layer with a step change in cross section

and boundary conditions are

$$\text{at } X = 0 \quad \psi = Y - 1/2,\ \theta = 0 \tag{3}$$

$$\text{for } X \gg 0 \quad \partial\psi/\partial X = \partial\theta/\partial Y = 0 \tag{4}$$

$$\text{at } Y = 0,\ X > X_2 \quad \psi = 0,\ \partial\theta/\partial Y = 0 \tag{5}$$

$$Y = 1/2,\ X < X_1$$

$$\text{at } X = X_1,\ 0 < Y < 1/2 \quad \partial\theta/\partial X = 0 \tag{6}$$

$$\text{at } Y = 0,\ X_1 < X < X_2 \quad \psi = 0,\ \theta = 1 \text{ (isothermal heating)} \tag{7a}$$

$$\partial\theta/\partial Y = -1 \text{ (constant flux heating)} \tag{7b}$$

$$\text{at } Y = 1 \quad \psi = 1/2,\ \theta = 0. \tag{8}$$

In these formulations, velocity components have the usual definition in terms of the stream function, and the dimensionless temperature is given by

$$\theta = \frac{T - T_c}{T_h - T_c} \tag{9a}$$

for an isothermal source, and

$$\theta = \frac{k_m(T - T_c)}{q_w H} \tag{9b}$$

for a constant heat flux source. Rayleigh numbers for isothermal and uniform flux heating are correspondingly given by

$$\text{Ra} = \frac{Kg\beta H(T_h - T_c)}{\alpha_m \nu} \tag{10a}$$

$$\text{Ra} = \frac{Kg\beta q_w H^2}{\alpha_m \nu k_m}. \tag{10b}$$

Finally, the Peclet number is defined in terms of duct height as follows:

$$\text{Pe} = \frac{u_0 H}{\alpha_m}. \tag{11}$$

Downstream boundary conditions are derived from the assumption that far from the heat source, the flow becomes parallel once again after releasing a large portion of its energy through the top wall. Axial conduction is then negligible at this location (Roache, 1976).

In non-Darcy's case, the velocity is normalized with the average velocity at the inlet, u_a, for the forced convection regime, and with the convective velocity, u_c, defined as

$$u_c = \sqrt{\frac{Kg\beta(T_h - T_c)\alpha_m}{\nu H}} \tag{12}$$

for the natural convection regime. The nondimensional mass conservation equation is

$$\frac{\partial^2\psi}{\partial X^2} + \frac{\partial^2\psi}{\partial Y^2} = -\omega \tag{13}$$

for both the regimes. The resulting nondimensional momentum equations are

$$(1 + \text{Re Fs}|V|)\omega = \frac{\text{Da}}{\epsilon}\left(\frac{\partial^2\omega}{\partial X^2} + \frac{\partial^2\omega}{\partial Y^2}\right) + \frac{\text{Ra}}{\text{Pe}}\frac{\partial\theta}{\partial X} + \text{Re Fs}\left(\frac{\partial\psi}{\partial X}\frac{\partial|\mathbf{V}|}{\partial X} + \frac{\partial\psi}{\partial X}\frac{\partial|\mathbf{V}|}{\partial X}\right) \tag{14}$$

Nomenclature

A = area, m^2
b = porous structure property associated with inertia term, m
D = length of heat source, m
Da = Darcy number, Eq. (17)
E_e = energy balance, Eq. (21*b*)
E_m = mass balance, Eq. (21*a*)
Fs = Forchheimer number, Eq. (18)
g = gravitational acceleration, m/s^2
h = heat transfer coefficient, $W/m^2 \cdot K$
H = duct height, m
H_0 = duct height upstream of expansion, m
k = thermal conductivity, $W/m \cdot K$
K = permeability, m^2
Nu = overall Nusselt number, Eq. (23)
Nu_x = local Nusselt number, Eq. (22)
P_{net} = net power to heater, W
Pe = Peclet number, Eq. (11)
Pe* = modified Peclet number, Eq. (24)
Pr = Prandtl number, ν/α_m
q_w = wall heat flux, W/m^2
Ra = Rayleigh number, Eq. (10)
Re = Reynolds number, Eq. (16)
T = temperature, K
u = velocity in x-direction, m/s
u_0 = inlet velocity for Darcy's case, m/s
u_c = convective velocity, m/s
$\mathbf{V}$ = nondimensional velocity vector
X = nondimensional horizontal Cartesian coordinate
X_1 = X-coordinate denoting upstream edge of heat source
X_2 = X-coordinate denoting downstream edge of heat source
Y = nondimensional vertical Cartesian coordinate
α = thermal diffusivity, m^2/s
β = thermal expansion coefficient, K^{-1}
Δn = mesh size at the wall
ϵ = porosity
θ = nondimensional temperature, Eq. (9)
λ = convergence criterion
ν = kinematic viscosity, m^2/s
ϕ = dependent variable, Eq. (20)
ψ = nondimensional stream function
ω = nondimensional vorticity

Subscripts

1 = value at the wall, Eq. (19)
2 = value at the grid point adjacent to the wall, Eq. (19)
a = average
c = cold
H = heat source
h = heated
m = medium
x = local

Superscripts

N = number of iteration, Eq. (20)
— = average

for forced convection regime, and

$$\left(1 + \frac{\mathrm{Fs}\sqrt{\mathrm{Ra}}}{\mathrm{Pr}}\left|\mathbf{V}\right|\right)\omega = \frac{\mathrm{Da}}{\epsilon}\left(\frac{\partial^2\omega}{\partial X^2} + \frac{\partial^2\omega}{\partial Y^2}\right) + \sqrt{\mathrm{Ra}}\frac{\partial\theta}{\partial X} + \frac{\mathrm{Fs}\sqrt{\mathrm{Ra}}}{\mathrm{Pr}}\left(\frac{\partial\psi}{\partial X}\frac{\partial|\mathbf{V}|}{\partial X} + \frac{\partial\psi}{\partial X}\frac{\partial|\mathbf{V}|}{\partial X}\right) \quad (15)$$

for natural convection regime.

Initial numerical experiments were carried out at different Ra, Pe combinations to select the suitable form of momentum equation that would give faster convergence. For instance, for Ra = 100, Eq. (14) was used for Pe $\geq$ 10 and Eq. (15) for Pe $<$ 10. In these equations

$$\mathrm{Re} = \frac{\mathrm{Pe}}{\mathrm{Pr}} = \frac{u_a H}{\nu} \quad (16)$$

$$\mathrm{Da} = \frac{K}{H^2} \quad (17)$$

$$\mathrm{Fs} = \frac{b}{H}. \quad (18)$$

The Darcy number and Forchheimer number include permeability and inertia resistance, which can be evaluated empirically using Ergun model (Kladias and Prasad, 1991). As suggested by Nield (1991), the expression for effective viscosity associated with the viscous term has not been well established for glass-bead packed bed, due to small amount of available experimental data. In the present study, it was assumed to be equal to that of the fluid.

At the inlet, the flow is assumed to be fully developed in porous medium under consideration. The velocity profile at the inlet was calculated using the transient momentum equation in X-direction. The inlet stream function and vorticity values follow this velocity profile. At the exit, the horizontal gradients of stream function, vorticity, and temperature are assumed to be zero. The assumption here is that far downstream of the heated section, the flow is parallel again and changes in the streamwise direction are small. The vorticity at the wall is calculated by using Thom's first-order formula (Roache, 1976):

$$\omega_1 = \frac{-2(\psi_2 - \psi_1)}{(\Delta n)^2}. \quad (19)$$

The governing equations are transformed into finite difference form via an integration over a control volume following the upwind differencing procedure described by Gosman et al. (1969) and Patankar (1980). The Gauss-Seidel point iterative method is used to solve the resulting system of algebraic equations for Darcy's case, and line-by-line method for non-Darcy's case. The convergence criterion is determined from a simple comparison of successive iterates

$$|\phi^N - \phi^{N-1}| < \lambda \quad (20)$$

where ϕ^N denotes the dependent variable at the Nth iteration, and λ is the convergence criterion.

Based on a series of numerical experiments, the convergence criterion was selected to be 10^{-4} for Ra $\geq$ 100 and 10^{-5} for Ra $<$ 100. Although using smaller values usually had no significant effect on the final results, they were changed to smaller values when the $|E_e| > 0.04$ (see Eq. (21b)). Convergence of the numerical scheme was accelerated by overrelaxation of both the stream function and temperature, with the relaxation parameter taken between 1.1 and 1.6.

Several trial runs were made to select the proper length of the unheated sections to satisfy upstream and downstream boundary conditions. It was found that for the dimensionless lengths upstream and downstream of the heat source greater than three and eight, respectively, the improvement in the overall Nusselt number was less than two percent. With these lengths, the boundary conditions are well satisfied at reasonable computational time without sacrificing accuracy. In most of the test cases, we adopted a 483 $\times$ 43 semi-uniform mesh, it being uniform throughout the domain except adjacent to the boundary where it is halved. It is noted that there is a discontinuity of the thermal boundary condition at the downstream edge of the heat source. With the present numerical scheme, the control volume can be designed so as to avoid the presence of this discontinuity within the control volume surface. Numerical experiments showed that further refinement of the mesh size to 963 $\times$ 83 changed the overall Nusselt number by less than 0.5 percent. The accompanying increase in the CPU time, however, is tenfold. Despite this large increase in CPU time, the mesh size was refined to 963 $\times$ 83 or 1923 $\times$ 163 at high Peclet number regime, where steep velocity and temperature gradient are expected above the heat source.

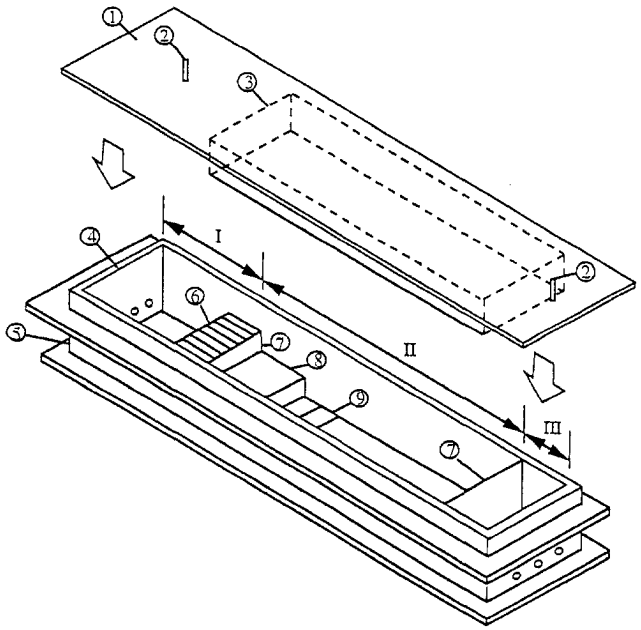

Fig. 2 Experimental apparatus. I: Entrance section; II: Test section; and III: Exit section. (1) Upper plate; (2) air vent; (3) cooling chamber; (4) gasket; (5) side walls; (6) tube bundle; (7) screen; (8) step; and (9) heater.

Overall mass and energy balances are defined by

$$E_m = \frac{(\text{Mass Inflow}) - (\text{Mass Outflow})}{(\text{Mass Inflow})} \quad (21a)$$

$$E_e = \frac{(\text{Total Energy Input}) - (\text{Energy Outflow})}{(\text{Total Energy Input})} \quad (21b)$$

and were checked after each calculation. For all of the results reported here, the error in the mass balance is 10^{-4} or less, and the error in the energy balance is within one percent. The uncertainty in the calculated Nusselt number is estimated to be three percent. Additional details of the convergence tests and numerical scheme are given by Yokoyama (1993).

3 Apparatus and Procedure

The overall design of the apparatus is shown in Fig. 2. It is a rectangular box made of Plexiglas and is 304.8 mm wide and 101.6 mm deep. The entrance section is 203.2 mm long and is equipped with a flow distributor. The exit section is 152.4 mm long and provides a return passage for circulating water via a drain at the bottom. The test section is comprised of two parts: (1) the upstream region with the step and (2) the downstream, heated region. The step is made of polystyrene insulation covered with a sheet of

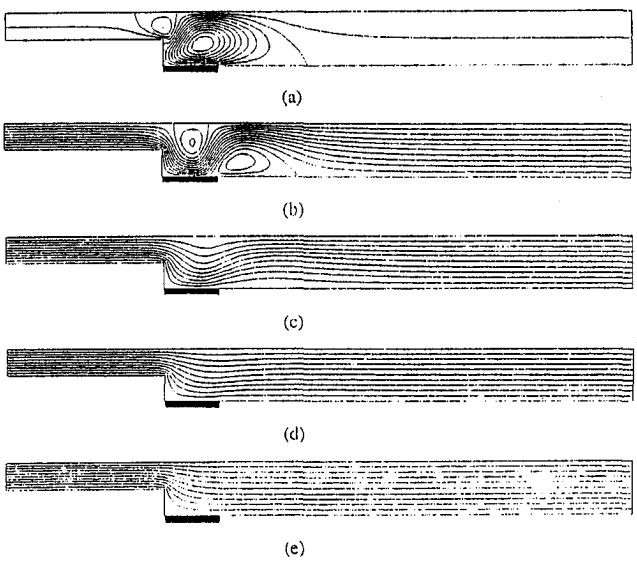

Fig. 3 Streamlines for Ra = 100 and constant flux heating. (*a*) Pe = 1, $\Delta\psi$ = 0.25; (*b*) Pe = 5, $\Delta\psi$ = 0.05; (*c*) Pe = 10, $\Delta\psi$ = 0.05; (*d*) Pe = 20, $\Delta\psi$ = 0.05; and (*e*) Pe = 100, $\Delta\psi$ = 0.05.

Plexiglas. Just upstream of the step is a tube bundle that serves as a flow straightener. Thin foil heaters are mounted on the bottom of the box in the downstream region. The sidewalls are thermally insulated with three layers of polystyrene, each 50.8 mm thick. The entrance and exit walls and the top and bottom are also insulated with the same material.

On the bottom wall of the test section beneath the foil heaters, grooves are provided for three 36-gage copper-constantan (Type T) thermocouples underneath each heater. Three thermocouples are also installed on the bottom surface of the Plexiglas box such that three pairs of thermocouples monitor the temperature of the heater. With this arrangement, heat losses can be estimated in both the lateral and longitudinal directions. All thermocouples were fixed in place with a high-temperature highly conductive adhesive applied to the junctions.

The upper boundary is maintained at a constant temperature with a cooling chamber that is a rectangular box with a copper plate bottom. Cooling water is provided from a constant temperature bath, and the mixing of water above the plate is sufficient to maintain it at a constant temperature. Twelve thermocouples are mounted on the surface of the plate to monitor temperature. The temperature variation across the plate was found to be less than 0.3°C.

Other components of the apparatus include a power supply with a variable voltage controller, digital multimeters, a variable speed pump, and variable area flow meters. Thermocouple readings are made against an ice-point reference, and signals are converted to temperature reading via the standard calibration in a data acquisition system. (See Yokoyama (1993) for a more detailed description.)

Experiments were performed using 3-mm diameter glass beads and water. After sealing the entire apparatus, and establishing flow in the cooling chamber and in the test section, power was applied to the heaters to reach a desired constant heat flux level. Once steady state had been achieved, thermocouple readings were taken five times over a ten-minute period. These sets of readings were averaged and used in the computation of nondimensional parameters.

The porosity was measured while packing the system with glass beads, and was found to be 0.3750. The permeability was then calculated using the Kozeny-Carman equation, and was determined to be 6.750×10^{-9} m^2. Using CRC Handbook of Chemistry and Physics (1967–1968) and Perry's Chemical Engineers Handbook (1963), thermophysical properties were evaluated at the average of the upper surface and heat source temperatures. The medium thermal conductivity was calculated using the weighted mixing rule.

Based on the summation of fractional errors, the estimated experimental uncertainties in the Rayleigh and Peclet numbers are 5.9 and 3.9 percent, respectively. The uncertainty in the Nusselt number ranges from 3.5 to 14.3 percent, depending on the average temperature difference. Larger uncertainties in the Nusselt number occur when the temperature difference is very small and the uncertainty in the temperature difference is large relative to the overall temperature difference.

4 Results

Measurements cover the ranges $0.1 \leq \mathrm{Pe} \leq 100$ and $50 \leq \mathrm{Ra} \leq 500$. These ranges are expected to include convective transport from natural to forced convection. We first present numerical results obtained using Darcy formulations. These are then compared with the experimental data.

The computed steady-state flow and temperature fields for Ra = 100 or $1 < \mathrm{Pe} < 100$ for constant-flux surface heating are presented in Figs. 3 and 4, respectively. When the Peclet number is small, cellular flows arise above the heated surface along with the associated thermal plume. As the Peclet number increases, these characteristics of natural convection disappear. Cellular flows are swept downstream and eventually vanish altogether. When forced convection dominates, the recirculating motion is entirely absent. We also note that the flow field differs from that of a pure fluid (i.e., no porous matrix present). The neglect of both inertia and viscous effects in the momentum equation along with the use of Darcy's law accounts for this difference.

Local Nusselt number is defined

$$\mathrm{Nu}_x = \frac{h_x H}{k_m} \tag{22a}$$

where h_x is the local heat transfer coefficient. In dimensionless variables, local Nusselt numbers can be written as

$$\mathrm{Nu}_x = (\theta_{Y=0})^{-1}. \tag{22b}$$

Figure 5 shows the computed dimensionless temperature distribution and the experimental data along the length of the duct. Recall that $X = 3$ corresponds to the leading edge of the heated surface. A fair agreement is seen between the experimental and

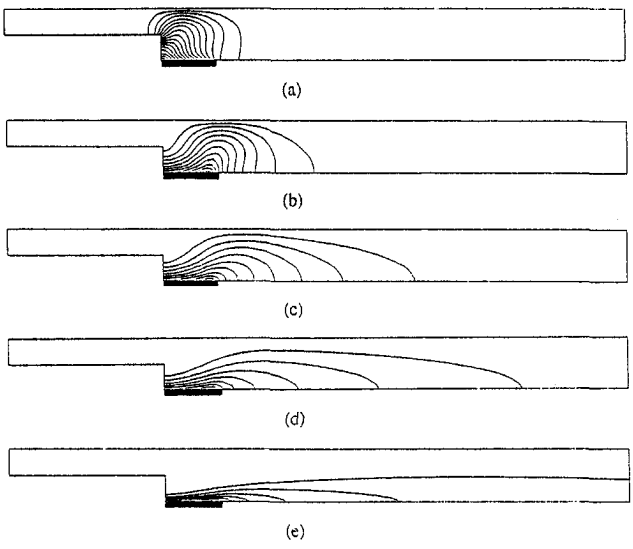

Fig. 4 Isotherm contours for Ra = 100 and constant flux heating. (*a*) Pe = 1, $\Delta\theta$ = 0.04; (*b*) Pe = 5, $\Delta\theta$ = 0.04; (*c*) Pe = 10, $\Delta\theta$ = 0.04; (*d*) Pe = 20, $\Delta\theta$ = 0.04; and (*e*) Pe = 100, $\Delta\theta$ = 0.02.

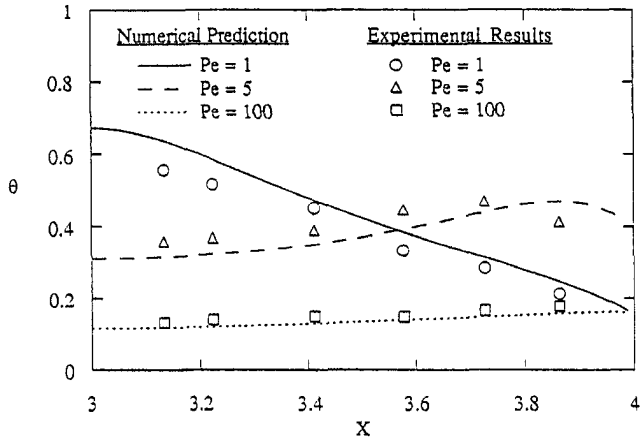

Fig. 5 Temperature distribution on the heat source for constant flux heating, Ra = 100

numerical results. The deviations between the two are generally within ten percent. However, the deviation seems to follow a trend. The numerical results overpredict the experimental results for Pe = 1, and underpredict for Pe = 100 and most of Pe = 5. This is possibly due to a measuring error in the location of the thermocouple. This is discussed in detail later in this section.

We note in Fig. 5 that the local temperature decreases with distance at Pe = 1. This is consistent with the existence of backward flow over the heater due to the buoyancy-induced cell. The temperature distribution for Pe = 5 shows the maximum temperature to be near the downstream edge. This behavior can be explained from the streamline plot in Fig. 3(*b*). As seen there, the buoyancy cell on the left side is dominant above the heat source but the backward flow exists at the downstream edge. Near the downstream edge, the two cells meet causing an elevated temperature. At Pe = 100, the temperature increases slightly with distance as forced flow begins to dominate. Generally the experimental results confirm our qualitative observations on the flow structure, including the absence of recirculating motion at downstream edge of the step in the forced convection regime.

The overall Nusselt number is defined by

$$\mathrm{Nu} = \frac{1}{\theta_{Y=0}}. \tag{23a}$$

The numerically calculated values are presented in Fig. 6 and are also listed in Table 1. The experimental Nusselt numbers are calculated as

$$\mathrm{Nu} = \frac{HP_{\mathrm{net}}}{k_m A_H \Delta T} \tag{23b}$$

and also plotted in Fig. 6. The experimental uncertainties in the data are indicated on the figure. It is seen that the experimental results agree well with the numerical results. The maximum discrepancy is 15 percent, but is mostly within ten percent. The deviation, however, seems systematic especially at lower Rayleigh numbers. The experimental results give higher values of Nusselt number than the numerical results in the natural convection regime, and lower value in the forced convection regime. This discrepancy may be attributed to a measurement error in distance X. Figure 5 indicates that a less than one percent undermeasurement in X would cause the local temperature to be lower than numerical prediction in the natural convection regime, and higher in the forced convection regime. This would lead to the Nusselt number discrepancy observed in Fig. 6.

It is noted that there exists a Peclet number at which the overall Nusselt number reaches a minimum for a given Rayleigh number. This "critical" Peclet number was also reported by Prasad et al. (1988) and *Lai and Kulacki* (1991) for both isothermal and constant flux heating in channel flow without the step. The minimum occurs because of the complex interaction of buoyancy and momentum forces as flow restructuring takes place in the Rayleigh-Peclet number plane. At low Pe, the contributions of each of the co-existing cellular flows to heat transfer are about the same. As Pe is increased, the right-hand cell is pushed downstream and eventually leaves the region of the heat source; the left-hand cellular flow then dominates the transport process, but it alone cannot increase mixing sufficiently to compensate for the departure of the other flow. The result is a decrease in heat transfer coefficient. At much higher Pe, mixing is sufficient to produce the higher Nusselt numbers expected in forced convection.

From the present data, a minimum in the Nusselt number appears most noticeably at high Rayleigh numbers (Ra = 500). Peclet numbers at which minimum Nusselt numbers occur are on the order of ten. More experimental data are needed to validate this observation. For more details see Yokoyama (1993).

The numerical and experimental heat transfer results for the constant flux case are reduced to correlations in terms of Nusselt, Rayleigh, and Peclet numbers. To compare Nusselt numbers to the case without step change in channel height, the Peclet number is redefined in terms of the mass average velocity at the exit, i.e.,

$$\mathrm{Pe}^* = (H/H_0)\,\mathrm{Pe}. \tag{24}$$

Correlations in the same form as developed by Lai and Kulacki (1991) are sought. A nonlinear regression analysis, results in the following relations:

Numerical Predictions: $0.2 < \mathrm{Pe}^* < 200$, $10 < \mathrm{Ra} < 500$.

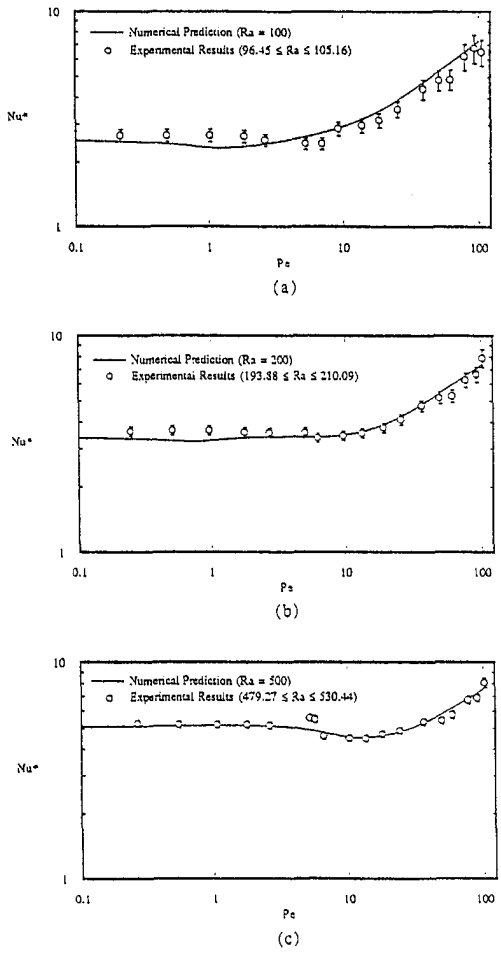

Fig. 6 Overall Nusselt numbers for constant flux heating. (*a*) Ra = 100; (*b*) Ra = 200; and (*c*) Ra = 500.

Table 1 Experimental data

Pnet [W]	ΔT [°C]	Ra	Pe	Nu
2.91	4.55	102.10	0.21	2.67
2.88	4.49	100.87	0.47	2.67
2.88	4.49	101.00	1.01	2.67
2.88	4.52	101.18	1.81	2.65
2.88	4.70	101.91	2.56	2.55
2.82	4.79	99.67	5.17	2.45
2.85	4.83	101.75	6.90	2.46
2.83	4.09	101.06	9.11	2.88
2.83	3.95	97.70	13.60	2.98
2.85	3.77	96.45	18.29	3.15
2.91	3.41	99.50	25.33	3.56
2.97	2.82	98.14	39.17	4.39
3.07	2.66	101.45	51.19	4.81
3.09	2.65	103.72	61.89	4.85
3.07	2.07	101.69	78.51	6.19
3.12	1.92	103.92	92.41	6.76
3.12	2.00	105.16	104.25	6.50
5.41	6.21	197.97	0.24	3.62
5.49	6.23	201.62	0.50	3.66
5.49	6.24	201.80	0.96	3.66
5.46	6.31	199.53	1.75	3.59
5.47	6.37	200.52	2.65	3.57
5.57	6.46	204.97	4.91	3.58
5.57	6.84	208.56	6.15	3.38
5.45	6.54	205.57	9.55	3.46
5.40	6.29	196.97	13.14	3.57
5.49	6.05	198.39	19.01	3.77
5.56	5.62	193.88	25.72	4.12
5.88	5.16	210.09	36.68	4.74
5.71	4.59	201.74	49.90	5.17
5.75	4.53	205.22	61.78	5.28
5.93	3.95	208.66	77.09	6.24
5.76	3.61	200.45	92.30	6.64
5.88	3.09	204.57	101.79	7.90
12.24	9.63	506.99	0.26	5.27
12.19	9.70	505.79	0.54	5.21
12.19	9.70	509.08	1.06	5.21
12.17	9.68	508.91	1.74	5.21
12.17	9.78	510.54	2.55	5.16
12.05	8.93	489.76	5.15	5.59
12.07	9.08	495.92	5.65	5.51
12.28	11.08	530.44	6.61	4.59
12.11	11.17	518.82	10.21	4.49
12.09	11.19	518.84	13.52	4.47
11.89	10.47	504.79	17.92	4.70
11.88	10.08	501.50	24.32	4.88
12.07	9.32	496.21	36.55	5.37
12.06	9.21	492.21	49.70	5.43
12.81	8.20	515.83	59.22	5.77
12.36	7.62	489.49	76.83	6.73
12.81	7.72	512.77	89.19	6.89
12.54	6.45	479.27	101.49	8.07

$$\frac{\mathrm{Nu}}{\mathrm{Pe}^{*0.5}} = \left[1.019 + 0.53\left(\frac{\mathrm{Ra}}{\mathrm{Pe}^{*1.5}}\right)\right]^{0.351} \tag{25}$$

Experiments: $0.42 < \mathrm{Pe}^* < 208.5$, $96.5 < \mathrm{Ra} < 530.4$.

$$\frac{\mathrm{Nu}}{\mathrm{Pe}^{*0.5}} = \left[0.810 + 0.119\left(\frac{\mathrm{Ra}}{\mathrm{Pe}^{*1.5}}\right)\right]^{0.383} \tag{26}$$

The standard error associated with each of those correlations is 0.213 and 0.335, respectively.

The corresponding correlations obtained by Lai and Kulacki (1991) without a step are as follows.

Numerical Predictions:

$$\frac{\mathrm{Nu}}{\mathrm{Pe}^{*0.5}} = \left[1.917 + 0.210\left(\frac{\mathrm{Ra}}{\mathrm{Pe}^{*1.5}}\right)\right]^{0.372}. \tag{27}$$

Experiments:

$$\frac{\mathrm{Nu}}{\mathrm{Pe}^{*0.5}} = \left[1.274 + 0.079\left(\frac{\mathrm{Ra}}{\mathrm{Pe}^{*1.5}}\right)\right]^{0.506}. \tag{28}$$

These four equations are presented in Fig. 7. It is observed that the predictions are in excellent agreement with the measurements. Furthermore, the present results are also in very good agreement with those obtained for channels in which there is no step change in height. Additional calculations showed that this observation is true for the cases when the step height is $\frac{3}{4}$ and $\frac{1}{4}$ of the duct height after the expansion (Yokoyama, 1993). Thus, with the heat source length equal to the duct height after expansion, it can be concluded that within the uncertainty of both the numerical results and measurements, Nusselt numbers are not much influenced by the presence of the step change in channel height.

Numerical Results for Non-Darcy's Case. To assess the effect of Darcy approximation, we also obtained numerical results for non-Darcy formulation, Eqs. (13)–(15). The test case considers a packed bed with 3-mm diameter glass beads saturated with water. The duct height $H = 50.8$ mm and the heat source provides isothermal heating. The motivation of this calculation was a postulation that non-Darcy effects may cause recirculating motion downstream of the expansion in the forced convection regime. It is well known that, for non-Darcy forced convection, the thermal dispersion and variable porosity near a solid wall may have significant effects on heat transfer (e.g., Vafai, 1984, Cheng and Vortmeyer, 1988, and Cheng et al., 1988). In the present study, these effects are neglected to clearly demonstrate the non-Darcy effects on the restructuring of flow

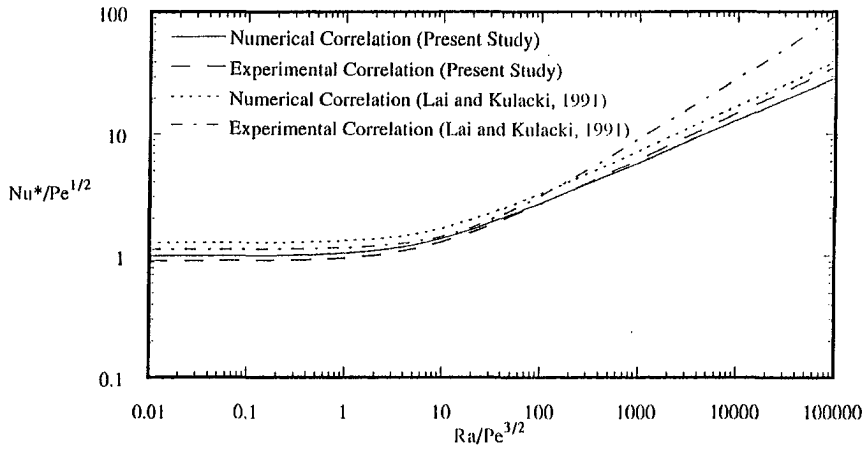

Fig. 7 Correlations for constant flux heating. Correlations of Lai and Kulacki (1991) are for horizontal layer without a step change in height.

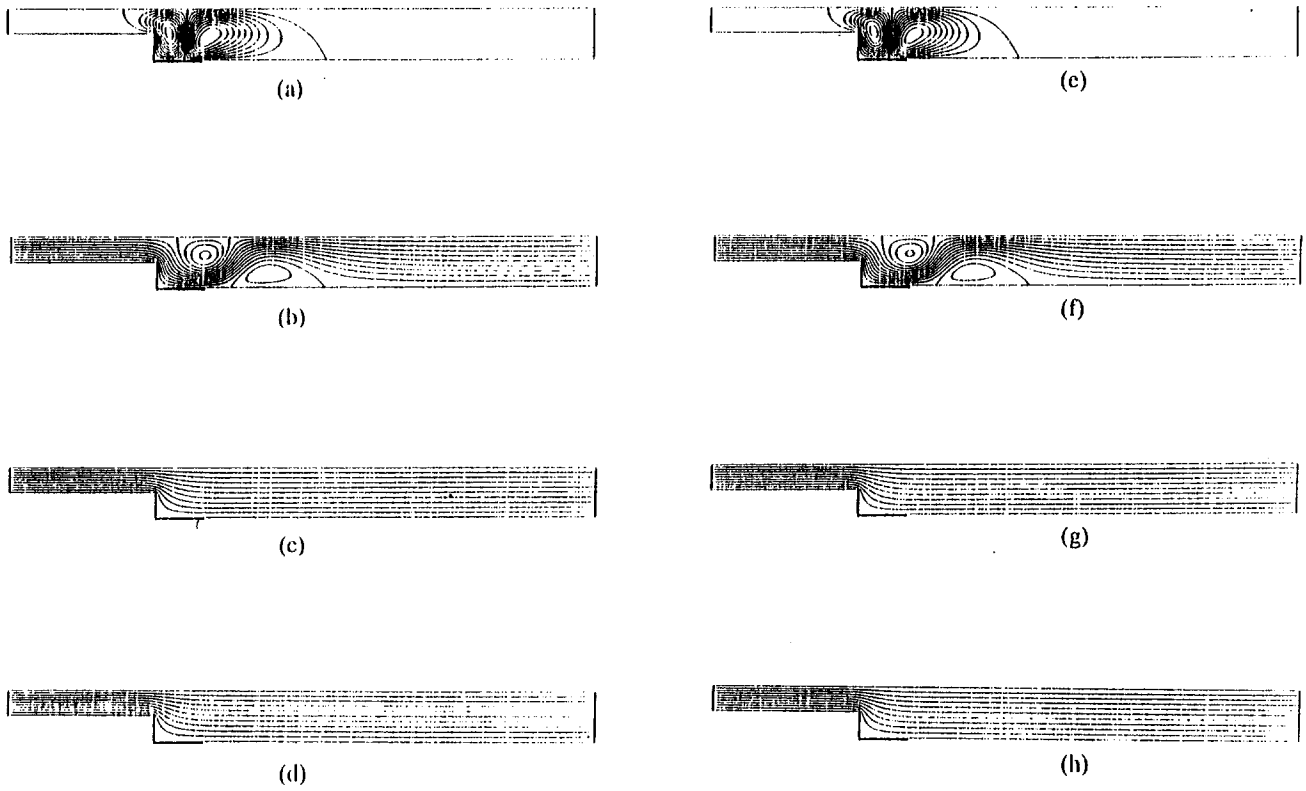

Fig. 8 Streamlines for Ra = 100 and isothermal heating. (*a*)–(*d*): Darcy's case, (*e*)–(*h*): nonDarcy's case. (*a*) Pe = 1, $\Delta\psi$ = 0.5; (*b*) Pe = 10, $\Delta\psi$ = 0.05; (*c*) Pe = 100, $\Delta\psi$ = 0.05; (*d*) Pe = 1000, $\Delta\psi$ = 0.05; (*e*) Pe = 1, $\Delta\psi$ = 0.5; (*f*) Pe = 10, $\Delta\psi$ = 0.05; (*g*) Pe = 100, $\Delta\psi$ = 0.05; and (*h*) Pe = 1000, $\Delta\psi$ = 0.05.

and heat transfer characteristics. The glass-bead packed bed was chosen due to its well-established empirical correlations for the structural and thermophysical parameters.

Figures 8 and 9 show the streamlines and isotherms for isothermal heating case. Both Darcy's case and non-Darcy's case are presented. It is noted from Fig. 8 that the inclusion of non-Darcy

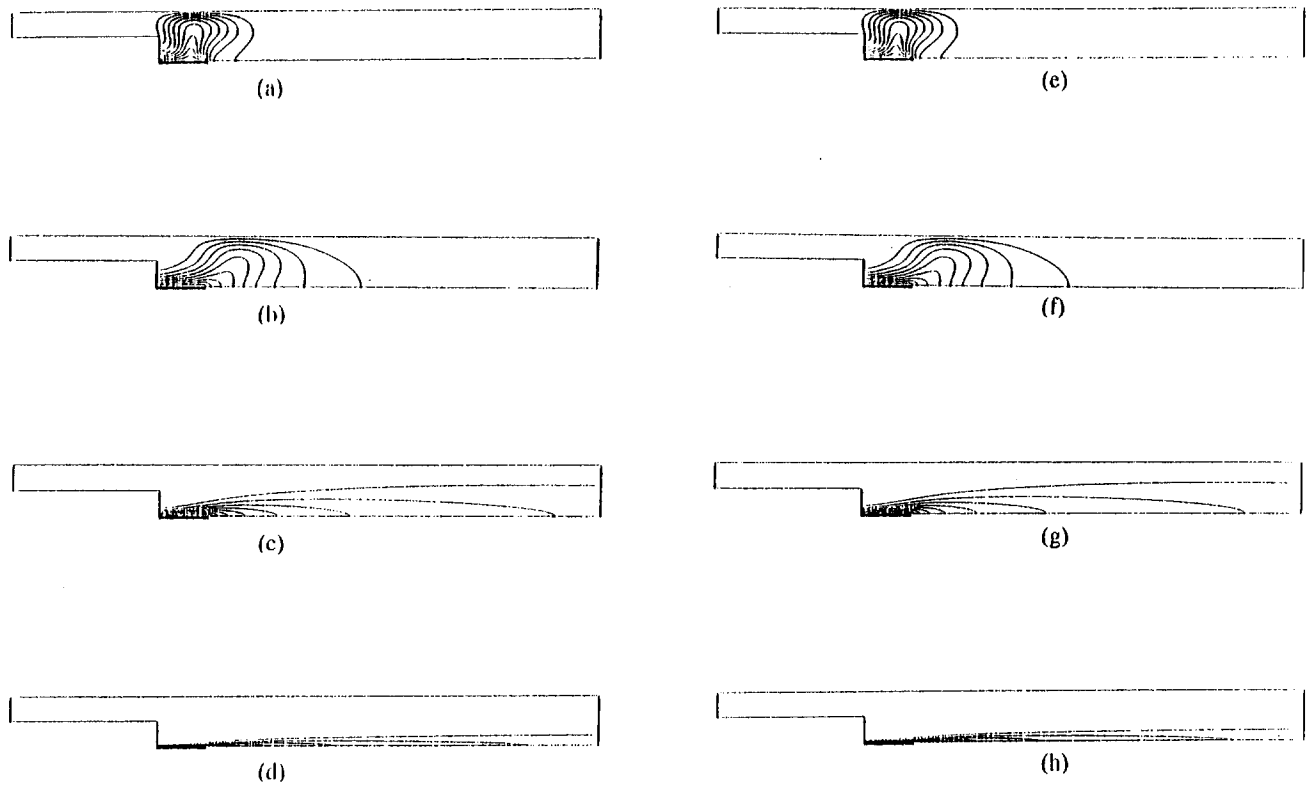

Fig. 9 Isotherm contours for Ra = 100 and isothermal heating. (*a*)–(*d*) Darcy's case, (*e*)–(*h*): non-Darcy's case. $\Delta\theta$ = 0.1. (*a*) Pe = 1; (*b*) Pe = 10; (*c*) Pe = 100; (*d*) Pe = 1000; (*e*) Pe = 1; (*f*) Pe = 10; (*g*) Pe = 100; and (*h*) Pe = 1000.

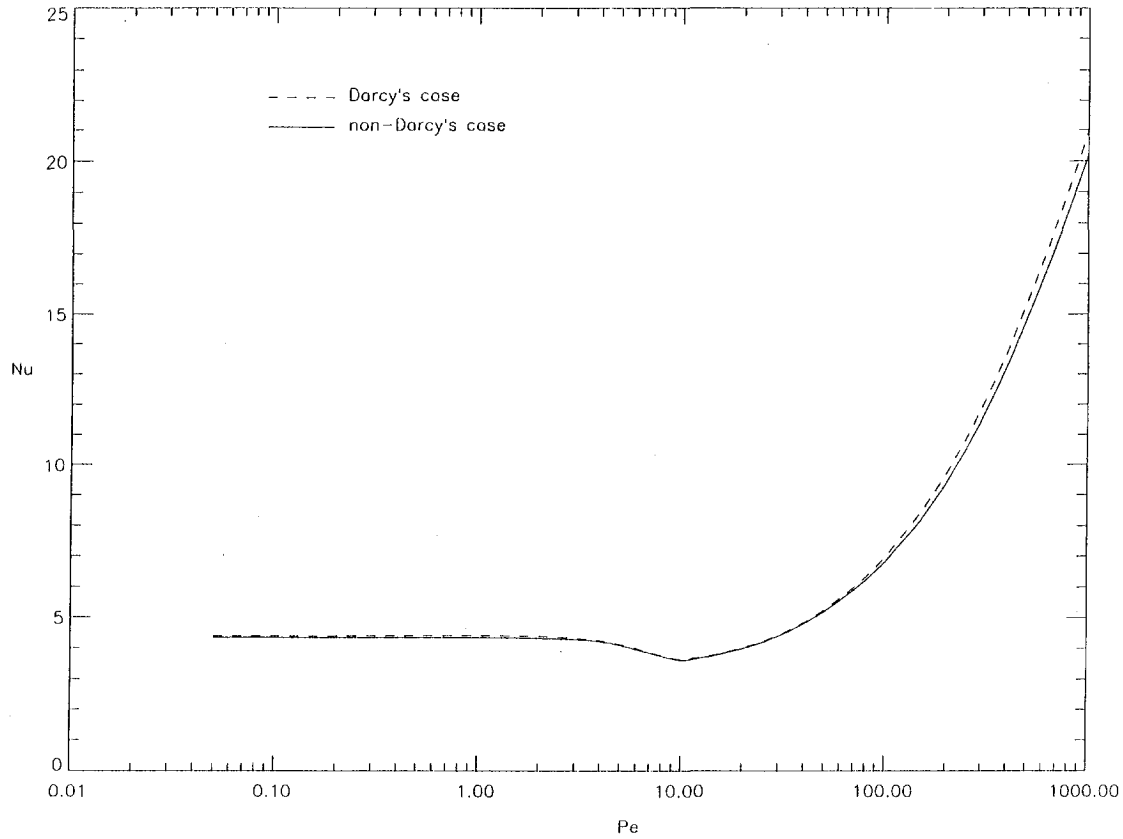

Fig. 10 Overall Nusselt numbers for isothermal heating

effects does not cause recirculating flow downstream of the expansion, even in the high Peclet number region. Therefore, it can be concluded that, with this specific porous structure and fluid, the non-Darcy effects do not alter the flow and temperature field. One can argue that a recirculating motion may appear at high Peclet number. However, in such a case, the fluid flow is likely to be in turbulent regime, and the assumption that the flow is laminar is no longer valid.

The little change in flow field as mentioned above is reflected in the overall Nusselt number, which is defined as

$$\mathrm{Nu} = \int_{X_1}^{X_2} \left(-\frac{\partial \theta}{\partial Y} \right) \Big|_{Y=0} dX \tag{29}$$

for isothermal heating. Figure 10 presents the overall Nusselt number for Ra = 100, for both Darcy's and non-Darcy's cases. The non-Darcy effects reduce the heat transfer coefficient, but the difference from the Darcy's case is four percent at most. Thus, for the specific combination of porous structure and fluid considered here, the non-Darcy effects have little effect on the heat transfer characteristics.

5 Concluding Remarks

Mixed convection in a horizontal porous duct with a sudden expansion of its cross-sectional area has been numerically and experimentally investigated. Predicted Nusselt numbers are in good agreement with measured values despite the limitations imposed by use of the stagnant thermal conductivity.

For the restricted heating length considered here, i.e., $(X_2 - X_1)/H = 1$, heat transfer results, when compared with those for a duct without a step, are unaffected by the presence of the step, and the inclusion of non-Darcy effects. This result has important implications for the analysis of convective heat transport in a variety of geophysical and engineering systems, e.g., hydrothermal systems, insulation systems, and porous matrix heat exchangers. For geophysical systems, cross-sectional area changes are gradual and generally less abrupt than the step change considered here. Thus, correlations and interpretations of flow regimes based on flat channel analysis appear to form a sufficient basis for the analysis of convective transport for coupled hydrothermal and geochemical processes.

We also note that one feature of flow in the flat duct that was observed by Lai and Kulacki (1991), namely the onset of oscillatory flow, was not observed here. Perhaps, the presence of the step tends to stabilize effect the flow at the larger Peclet numbers. Additional experiments will be needed, however, to fully determine the nature and parameter space of flow instabilities.

Acknowledgments

The authors acknowledge Mr. C. P. Malhotra at the University of Colorado for his assistance in the calculation and in preparation of figures presented in this study.

References

Abu-Hijleh, B., 1997, "Convection Heat Transfer from a Laminar Flow over a 2-D Backward Facing Step with Asymmetric and Orthotropic Floor Segments," *Numerical Heat Transfer, Part A: Applications,* Vol. 31, pp. 325–335.

Cheng, P., 1977a, "Combined Free and Forced Convection Flow about Inclined Surfaces in Porous Media," *Int. J. Heat Mass Transfer,* Vol. 20, pp. 807–814.

Cheng, P., 1977b, "Similarity Solutions for Mixed Convection from Horizontal Impermeable Surfaces in Saturated Porous Media," *Int. J. Heat Mass Transfer,* Vol. 20, pp. 893–898.

Cheng, P., Hsu, C. T., and Chowdhury, A., "Forced Convection in the Entrance Region of a Packed Channel With Asymmetric Heating," ASME JOURNAL OF HEAT TRANSFER, pp. 946–954.

Cheng, P., and Vortmeyer, D., 1988, "Transverse Thermal Dispersion and Wall Channeling in a Packed Bed with Forced Convective Flow," *Chemical Eng. Sci.,* Vol. 43, pp. 2523–2532.

Choi, C. Y., and Kulacki, F. A., 1992, "Mixed Convection Through Vertical Porous

Annuli Locally Heated From the Inner Cylinder," ASME JOURNAL OF HEAT TRANSFER, Vol. 114, pp. 143–151.

Clarksean, R., Kwendakwema, N., and Boehm, R., 1988, "A Study of Mixed Convection in Porous Medium Between Vertical Concentric Cylinders," *Proceedings of the 1988 National Heat Transfer Conference,* Vol. 2, ASME, New York, pp. 339–344.

Elder, J. W., 1967, "Steady Free Convection in a Porous Medium Heated from Below," *J. Fluid Mech.,* Vol. 27, pp. 29–48.

Gooray, A. M., Watkins, C. B., and Aung, W., 1981, "Numerical Calculations of Turbulent Heat Transfer Downstream of a Rearward-Facing Step," *Proceedings of the 2nd International Conference on Numerical Method in Laminar and Turbulent Flow,* Venice, Italy, John Wiley and Sons, New York, pp. 639–651.

Gosman, A. D., Pun, W. M., Runchal, A. K., Spalding, D. B., and Wolfshtein, M., 1969, *Heat and Mass Transfer in Recirculating Flows,* Academic Press, New York.

Homsy, G. M., and Sherwood, A. E., 1976, "Convective Instabilities in Porous Media with Through Flow," *AIChE J.,* Vol. 22, pp. 168–174.

Kladias, N., and Prasad, V., 1991, "Experimental Verification of Darcy-Brinkman-Forchheimer Flow Model for Natural Convection in Porous Media," *J. Thermophysics and Heat Transfer,* Vol. 5, pp. 560–576.

Lai, F.-C., and Kulacki, F. A., 1988, "Aiding and Opposing Mixed Convection in a Vertical Layer with a Finite Wall Heat Source," *Int. J. Heat Mass Transfer,* Vol. 31, pp. 1049–1061.

Lai, F. C., and Kulacki, F. A., 1991, "Experimental Study of Free and Mixed Convection in Horizontal Porous Layers Heated From Below," *Int. J. Heat Mass Transfer,* Vol. 34, pp. 525–541.

Nield, D. A., 1991, "The Limitation of the Brinkman-Forchheimer Equation in Modeling Flow in a Saturated Porous Medium and at an Interface," *Int. J. Heat Fluid Flow,* Vol. 12, pp. 269–272.

Patankar, S. V., 1980, *Numerical Heat Transfer and Fluid Flow,* Hemisphere/McGraw-Hill, New York.

Prasad, V., Lai, F. C., and Kulacki, F. A., 1988, "Mixed Convection in Horizontal Porous Layers Heated From Below," ASME JOURNAL OF HEAT TRANSFER, Vol. 110, pp. 395–402.

Prats, M., 1966, "The Effect of Horizontal Fluid Flow on Thermally Induced Convection Currents in Porous Mediums," *J. Geophysical Research,* Vol. 71, pp. 4835–4837.

Reda, D. C., 1988, "Mixed Convection in a Liquid-Saturated Porous Medium," ASME JOURNAL OF HEAT TRANSFER, Vol. 110, pp. 147–154.

Roache, P. J., 1976, *Computational Fluid Dynamics,* Hermosa Publishers, Albuquerque, NM.

Sinha, S. N., Gupta, A. K., and Oberai, M. M., 1981, "Laminar Separating Flow over Backsteps and Cavities—Part II: Cavities," *AIAA J.,* Vol. 20, pp. 370–375.

Sutton, F. M., 1970, "The Onset of Convection in a Porous Channel with Net Through Flow," *Physics of Fluids,* Vol. 13, pp. 1931–1934.

Vafai, K., 1984, "Convective Flow and Heat Transfer in Variable-Porosity Media," *J. Fluid Mech.,* Vol. 147, pp. 233–259.

Vafai, K., and Huang, P. C., 1994, "Analysis of Heat Transfer Regulation and Modification Employing Intermittently Emplaced Porous Cavities," ASME JOURNAL OF HEAT TRANSFER, Vol. 116, pp. 604–613.

Wooding, R. A., 1963, "Convection in a Saturated Porous Medium at Large Rayleigh or Peclet number," *J. Fluid Mech.,* Vol. 15, pp. 527–544.

Yamamoto, H., Seki, N., and Fukusako, S., 1979, "Forced Convection Heat Transfer on Heated Bottom Surface of Cavity," ASME JOURNAL OF HEAT TRANSFER, Vol. 101, pp. 475–479.

Yokoyama, Y., 1993, *Convective Heat Transfer in Porous Medium Downstream of a Sudden Expansion,* Doctoral dissertation, Colorado State University, Fort Collins, CO.

Air-Side Heat Transfer and Friction Correlations for Plain Fin-and-Tube Heat Exchangers With Staggered Tube Arrangements

N. H. Kim
Department of Mechanical Engineering,
University of Inchon,
177 Dohwa-Dong, Nam-Gu,
Inchon 402-749, Korea

B. Youn
Air Conditioning & Refrigeration Division,
Samsung Electronics, Korea

R. L. Webb
Department of Mechanical Engineering,
Pennsylvania State University,
University Park, PA 16802

This paper deals with heat exchangers having plain fins on a staggered array of circular tubes. Correlations are developed to predict the air-side heat transfer coefficient and friction factor as a function of the Reynolds number and geometric variables of the heat exchanger such as tube diameter, tube pitch, fin spacing, etc. A multiple regression technique was used to correlate 47 sets of heat exchanger data to develop the heat transfer and friction correlation. The correlations are applicable to heat exchangers having small diameter tubes (or large tube pitch to tube diameter ratio), whose performance previous correlations failed to predict adequately. The heat transfer correlation applicable to three or more row configuration predicts 94 percent of the data within ±20 percent, and the heat transfer correlation applicable to one- or two-row configuration predicts 94 percent of the data within ±20 percent. The friction correlation predicts 90 percent of the data within ±20 percent.

1 Introduction

Air-cooled plate finned-tube heat exchangers have been used for exchange between gases and liquids for many years. The heat exchangers may have plain fins or specially configured fins. Specially configured fins may provide increased heat transfer coefficients. Another recent trend is toward use of smaller tube diameter (Webb, 1998). As the tube diameter decreases, the low-performance wake region behind the tube decreases, which improves the overall air-side performance. In addition, the profile drag by the tube also decreases, which reduces the air-side pressure drop.

The flow pattern in finned-tube heat exchangers is very complex, due to its three-dimensional nature and flow separations (Neal and Hitchcock, 1966; Saboya and Sparrow, 1974, 1976). The use of specially configured fin geometries introduces further complications. Pioneering experiments on the air-side transfer coefficients were conducted by Saboya and Sparrow (1974, 1976). They used the naphthalene mass transfer technique to measure the local coefficients. The measurement revealed that, near the leading edge of the fin, the developing boundary layer produces a relatively high transfer coefficients. On the front of the tube, a vortex develops, which is then swept around the tube. This vortex produces a natural heat transfer augmentation. Behind the tube, a very-low-performance wake region exists. Small tube diameter will reduce this low-performance region. Recently, several attempts have been made to address the problem numerically (Rosman et al., 1984; Torikoshi et al., 1994; Torikoshi and Xi, 1995; and Jang et al., 1996). The numerical results generally confirmed the findings by Saboya and Sparrow. One interesting finding by Torikoshi and Xi (1995) was that increasing the tube diameter did not improve the heat transfer coefficients, but increased the friction factor. Although some progress has been made in the numerical approach, designers still rely on experimental data-based correlations to predict the thermal performance of a heat exchanger.

Several correlations are available for plain finned-tube heat exchangers (McQuiston, 1978a; Gray and Webb, 1986; Seshimo and Fujii, 1991; etc.). Of them, the state-of-the art correlation is that of Gray and Webb (1986). They developed the heat transfer and friction correlations based on six data sources (18 heat exchangers). Recent heat exchangers have small diameter tubes, whose geometric parameters may be outside of the applicable range of Gray and Webb correlation. For example, S_t/D of Wang and Chi's (1998) coils with 7-mm outer diameter tube is 2.88, which is outside of Gray and Webb's correlation range ($1.97 < S_t/D < 2.55$). The characteristic dimensions of plain finned-tube heat exchangers are shown in Fig. 1.

Available data of coils with 7-mm diameter tube (Wang and Chi, 1998; Youn, 1997) are predicted the by Gray and Webb correlation, and the results are shown in Figs. 2 and 3. Figure 2 shows an error plot of the Colburn "j" factor. All the data are highly (8 percent to 256 percent) underpredicted. The discrepancy increases as Reynolds number decreases. The friction error plot is shown in Fig. 3. The data are highly (up to 122 percent) underpredicted at low Reynolds numbers and overpredicted (up to 44 percent) at high Reynolds numbers. Gray and Webb's friction correlation consists of two parts—that of fin and that of tube. For the tube friction correlation, Gray and Webb recommend the use of the Zukauskas and Ulinskas (1983) correlation, which is limited to $S_t/D = 2.5$. The S_t/D of both Wang and Chi (1998) and Youn's (1997) coils is 2.88, which is outside of the correlation range. Thus, Jakob's (1938) correlation, which is applicable to $S_t/D = 3.0$, was used instead. The adequacy of this will be elaborated later.

In this paper, new heat transfer and friction correlations for plain finned-tube heat exchangers are provided. The data sources used to develop the correlations are listed in Table 1. Symbols "H" and "F" in the last column of Table 1 denote that the data were used for the development of the heat transfer correlation or for the friction correlation, respectively. The 47 coil data consist of those used by Gray and Webb to develop their correlations, and those by Wang et al. (1997), Wang and Chi (1998), and Youn (1997). Wang

Contributed by the Heat Transfer Division for publication in the JOURNAL OF HEAT TRANSFER. Manuscript received by the Heat Transfer Division, Sept. 24, 1997; revision received, Feb. 1, 1999. Keywords: Finned Surfaces, Forced Convection, Heat Transfer, Heat Exchangers. Associate Technical Editor: J.-C. Han.

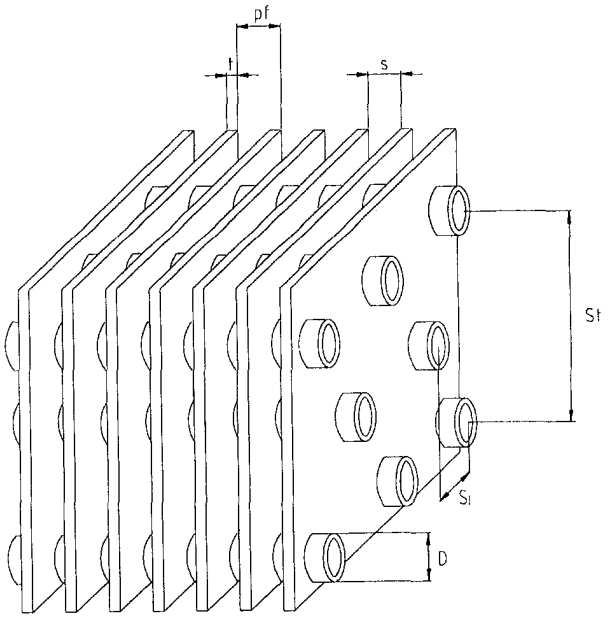

Fig. 1 Schematic drawing of the plain finned tube heat exchanger

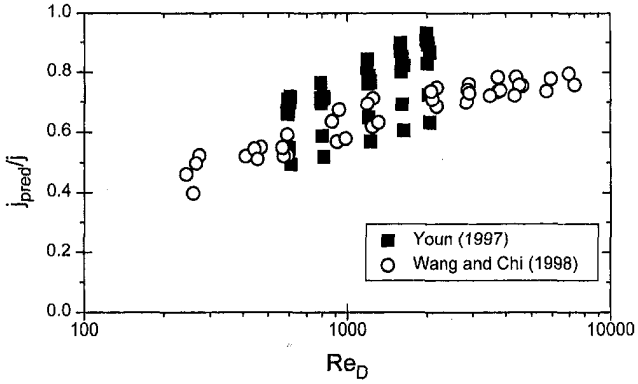

Fig. 2 Error plot of the *j* factor of coils with 7-mm diameter tube compared with Gray and Webb (1986) correlation

et al.'s data are obtained from coils with 10-mm tube diameter, and Wang and Chi's and Youn's data are obtained from coils with 7-mm tube diameter. All of the present data are limited to a staggered tube layout. Multirow inline tube layouts yield lower heat transfer coefficients as discussed in Chapter 6 of Webb (1994). So, little use is made of the inline geometry.

It is noted that moderate errors may exist in the published data. This is because of the particular water-side circuiting employed, the ϵ-NTU relationship used to obtain UA, the fraction of the total resistance on the air side, and the fin efficiency equation used. Wang et al. (1998) discuss these concerns. Table 2 provides some detail on the methodologies used by various authors. McQuiston (1978b) and McQuiston and Tree (1971) reduced the data assuming that the heat exchangers were of counterflow arrangement. The Dittus and Boelter (1930) equation was used to determine the tube-side heat transfer coefficient, and Schmidt's (1949) approximate equation was used to calculate the fin efficiency. The contact resistance between the fin and the tube was implicitly included in the air-side heat transfer coefficient. To determine the friction factor, the entrance and exit losses were extracted from the measured pressure drop. Rich (1973, 1975) tested heat exchangers of one to six row configuration. He assumed counterflow for configurations of more than two rows. He argued that the deviation from pure counterflow is less than two percent for all the heat exchangers he tested. The tube-side heat transfer coefficient was obtained from Wilson Plot results, and the fin efficiency was obtained by the sector method. His samples had copper fins, which were oven-soldered to the copper tube. Thus, no contact resistance existed. His friction factor implicitly included the entrance and exit losses. Wang et al. (1997) and Wang and Chi (1998) used an unmixed-unmixed cross flow formula to reduce the heat transfer data. Gnielinski's (1976) equation was used to determine the tube-side heat transfer coefficient, and Schmidt's equation was used for the fin efficiency. The fin-tube contact resistance was implicitly included in the air-side heat transfer coefficient. The entrance and exit losses were explicitly accounted for to determine the friction factor. Wang et al. (1998) reports that no significant difference exists whether the entrance and exit losses are included or not. Youn (1997) analyzed the heat exchanger by the tube-by-tube method. In this method, heat exchangers are subdivided into a number of single cross flow passes, and the unit passes are analyzed using the cross flow, ϵ-NTU formula. Tube-side heat transfer coefficients were determined from separate tests, and the fin efficiency was obtained using the Schmidt equation. The contact resistance was included in the air-side heat transfer coefficient, and the entrance and exit losses were included in the friction factor.

2 Correlating Method

The heat transfer and friction correlations were developed through a multiple linear regression analysis. Details of the multiple regression technique are available somewhere else (Ryan et

Nomenclature

A = air-side surface area (fins and tubes), m^2
A_c = flow cross-sectional area in minimum flow area, m^2
$A_{c,t}$ = flow cross-sectional area in minimum flow area for tube bank, m^2
A_f = surface area of fins, m^2
c_p = specific heat, J/kgK
D = tube outer diameter (including collar), m
f = Fanning friction factor, dimensionless
f_f = friction factor associated with fin area, dimensionless
f_t = friction factor associated with tube area, dimensionless
G_c = mass velocity ($=\rho u_{max}$), kg/m^2s
h = heat transfer coefficient, W/m^2K
j = Colburn j factor ($=St\ Pr^{2/3}$), dimensionless
k = thermal conductivity, W/mK
N = number of tube row, dimensionless
p_f = fin pitch, m
Pr = Prandtl number, dimensionless
Re_D = Reynolds number based on D ($=\rho u_{max} D/\mu$), dimensionless
s = spacing between adjacent fins, m
S_l = tube spacing in air flow direction, m
S_t = tube spacing normal to flow, m
St = Stanton number ($=h/G_c c_p$), dimensionless
t = fin thickness, m
u_{max} = maximum velocity based on A_C, m/s
ΔP = pressure drop across a heat exchanger, Pa
ΔP_t = pressure drop assignable to bare tube bank, Pa
ΔP_f = pressure drop assignable to fin area, Pa
μ = dynamic viscosity, kg/ms
ρ = density, kg/m^3

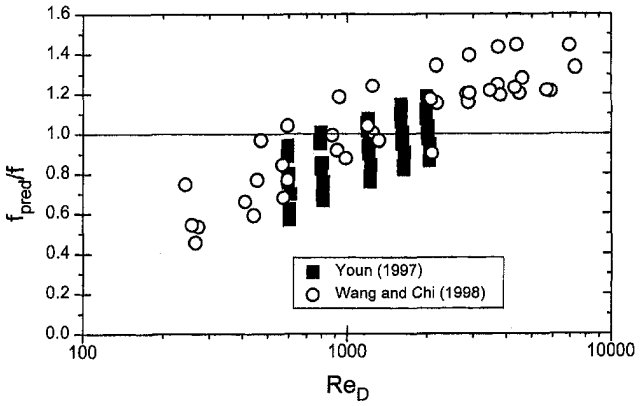

Fig. 3 Error plot of the friction factor of coils with 7-mm diameter tube compared with Gray and Webb (1986) correlation

al., 1985) and only a short description is provided. A commercial statistical package (Ryan et al., 1985) was used to perform a multiple regression analysis, which provided the best fit of data. The accuracy of the correlation is evaluated using the "R-squared" value, which is defined as the fraction of the variability in the logarithm of dependent variable (e.g., j factor) that can be accounted for by means of the linear regression equation using the independent variables (e.g., dimensionless geometric parameters). The objective is to select independent variables that give the highest R-squared value. This may be done by trial and error. This method of correlating the data is strictly empirical and requires knowledge of the geometric and flow parameters that affect the heat transfer coefficient.

Table 1 Geometry of sample configurations

No.	Author	S_t (mm)	S_l (mm)	D (mm)	s (mm)	t	N	H/F
1	McQuiston (1978b)	25.40	22.00	9.66	3.023	0.152	4	H/F
2					6.198			
3					1.964			
4					2.398			
5					1.662			
6	Rich(1973)	31.75	27.51	13.34	8.547	0.152	4	H/F
7					5.593			
8					2.169			
9					3.160			
10					3.655			
11					2.019			
12					1.599			
13					1.081			
14	Cox and Jallouk (1982)	50.80	43.99	19.51	1.599	0.279	8	H
15					1.611			
16	McQuiston and Tree (1971)	20.32	17.58	10.34	1.611	0.165	5	H/F
17					3.010			
18	Kays and London (1984)	25.40	22.00	10.21	2.845	0.330	∞	H/F
19		38.1	44.45	17.17	2.870	0.406		
20	Rich(1975)	31.75	27.51	12.23	1.599		1	H
21							2	
22							3	
23							4	
24							5	
25							6	
26	Wang et al. (1997)	25.40	22.00	10.23	1.691	0.130	2	H/F
27					2.113		2	
28					3.067		2	
29					1.898		4	
30					2.101		4	

Table 1 (Continued)

No.	Author	S_t (mm)	S_l (mm)	D (mm)	s (mm)	t	N	H/F
31	Wang et al. (1997)	25.40	22.00	10.23	2.870	0.130	4	H/F
32					1.720		6	
33					2.084		6	
34					3.035		6	
35	Wang & Chi (1998)	21.00	12.70	7.59	1.104	0.115	2	H/F
36					1.595		2	
37					1.104		3	
38					1.600		3	
39	Youn (1997)	21.00	12.70	7.30	0.990	0.11	1	H/F
40					1.190		1	
41					1.390		1	
42					0.990		2	
43					1.190		2	
44					1.390		2	
45					0.990		3	
46					1.190		3	
47					1.390		3	

The potentially significant variables are: flow parameters (Re_D and Pr), tube bank parameters (S_t, S_l, D, N), and the fin spacing(s). Several different groupings of the dimensionless variables were tried in the development of the correlation. The set finally chosen was based on groupings that provided the best correlation. For each coil, two or three data points were used, which spanned the range of Reynolds numbers tested. Some authors (Rich, 1973, 1975; Wang et al., 1997; Wang and Chi, 1998) provide data to Reynolds numbers as low as 200. At these low Reynolds numbers, some data for large tube rows and small fin spacing show somewhat different behavior than others (a flattening characteristic). At this operating condition, the thermal effectiveness is very high, and the data are subject to significant experimental error. Thus, data for Reynolds numbers lower than 500 were not considered in this study. Care was taken to avoid biasing the correlation by including a large number of data points having a small range of particular geometric parameters.

3 Heat Transfer Correlation

For low-to-moderate Reynolds number, Rich's (1975) Fig. 14 shows that the heat transfer coefficient decreases as the number of tube row increases. However, at high Reynolds numbers, turbulence produced by the tubes can make the multirow heat transfer

Table 2 Data reduction details used by various investigators

Authors	Number of row	H-X analysis method	Tube-side heat transfer	Fin efficiency	Contact resistance	Entrance and exit loss in Δp
McQuiston (1978b) McQuiston and Tree (1971)	4 ∞	Counter flow	Dittus-Boelter (1930)	Schmidt (1949)	Included in h_o	Explicitly appear
Rich(1973) Rich(1975)	4 1 to 6	Cross flow for row Counter flow for two and more	Wilson Plot(1915)	Sector method	Zero contact resistance	Implicitly included
Wang et al. (1997) Wang and Chi (1998)	2 to 6 2 to 3	Unmixed-unmixed cross flow	Gnielinski (1976)	Schmidt (1949)	Included in h_o	Explicitly appear
Youn(1997)	1 to 3	Tube-by-tube method	Experiment	Schmidt (1949)	Included in h_o	Implicitly included

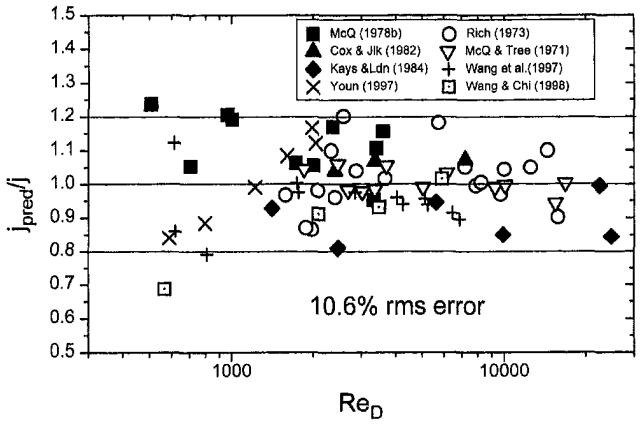

Fig. 4 Error plot of the *j* factor correlation (Eq. (1))

coefficient greater than that for one row. The heat transfer correlation was developed in two steps. The first step developed a correlation for finned tube geometry having three tube rows. Then a multiplier was developed to account for the row effect of the coils having one or two tube rows. It is assumed that the heat transfer coefficients of the coils having three or more rows are negligibly different from that of three row coil. This procedure was taken by Gray and Webb (1986) to develop their own correlation. The number of tube rows, beyond which they assumed to have the same heat transfer coefficients, was four. In this study, three rows was chosen because new data of coils with 7-mm diameter tube by Wang and Chi (1998) and Youn (1997) do not contain four-row data as shown in Table 1. Three row was the largest value they tested.

For a fin-tube heat exchanger, the fin area typically comprises more than 90 percent of the total air-side heat transfer area. Thus, no attempt was made to separate the heat transfer by the tube and that by the fin. After trying different combinations of the dimensionless parameters, Eq. (1), which yielded the largest R-squared value, was finally chosen for the three-row j-factor correlation. One should note that Eq. (1) is the row-average value, not the local row value.

$$j_{N=3} = 0.163\ \mathrm{Re}_D^{-0.369}(S_t/S_l)^{0.106}(s/D)^{0.0138}(S_t/D)^{0.13} \quad (1)$$

Figure 4 shows an error plot of the j-factor correlation. Examination of the figure shows that 94 percent of the data are predicted within ±20 percent, and 82 percent of the data are predicted within ±15 percent. The rms error of the correlation is 10.6 percent. The greatest data scatter occurs at low Reynolds numbers. At low Reynolds numbers, Wang and Chi's (1998) three-row data of coils with 7-mm diameter tube are generally underpredicted, and McQuiston's (1978b) four-row data are generally overpredicted.

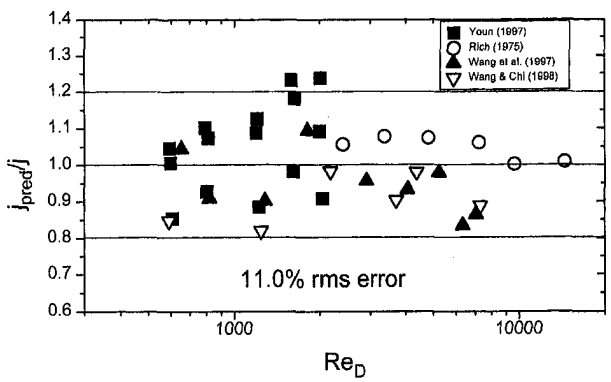

Fig. 5 Error plot of the *j* factor correlation (Eq. (2))

Table 3 Limitations on correlations

Heat Transfer Correlation (N≥3)
$505 \le Re_D \le 24707$, $0.857 \le S_t/S_l \le 1.654$ $1.996 \le S_t/D \le 2.881$, $0.081 \le s/D \le 0.641$
Heat Transfer Correlation (N = 1, 2)
$591 \le Re_D \le 14430$, $1.154 \le S_t/S_l \le 1.654$ $2.399 \le S_t/D \le 2.877$, $0.135 \le s/D \le 0.300$
Friction Correlation
$505 \le Re_D \le 19766$, $0.857 \le S_t/S_l \le 1.654$ $1.966 \le S_t/D \le 2.876$, $0.081 \le s/D \le 0.641$

Several data sources were used to determine the effect of number of tube rows on the j-factor. These include Rich's (1975) one and two-row data, Wang et al.'s (1997) two-row data, Wang and Chi (1998) two-row data, and Youn's (1997) one and two-row data. Rich's data were obtained from coils with 13-mm diameter tube, Wang et al.'s data were from coils with 10-mm diameter tube, and Wang and Chi's and Youn's data for coils with 7-mm diameter tube. The previously described regression procedure was used to correlate the data, with results given by Eq. (2). It is noted that Eq. (2) is also the row average value.

$$j_{N=1,2}/j_{N=3} = 1.043[\mathrm{Re}_D^{-0.14}(S_t/S_l)^{-0.564}(s/D)^{-0.123}(S_t/D)^{1.17}]^{(3-N)} \quad (2)$$

An error plot of Eq. (2) is shown in Fig. 5. The figure shows that 94 percent of the data are predicted within ±20 percent and 83 percent of the data are predicted within ±15 percent. The rms error is 11.0 percent. Gray and Webb (1986) also developed a row-effect correlation. Their correlation is, however, based on single data source of Rich (1975). Several data sources were used for the present correlation, and thus, may yield a better row-effect predic-

Table 4 rms errors of various correlations

Correlations	j		f		Data sources
	All data	7 mm tube data	All data	7 mm tube data	
Present Correlation	10.7%	13.1%	12.6%	12.7%	Shown in Table 1
Gray and Webb(1986)	17.8%	31.4%	12.1%	16.9%	McQuiston(1978b) McQuiston and Tree (1971) Rich(1973,1975) Cox and Jallouk (1982) Kays and London (1984)
McQuison (1978a)	40.3%	63.7%	51.6%	66.4%	Rich(1973,1975) Kays and London (1984) McQuiston(1978b) McQuiston and Tree (1971)
Kayansayan (1993)	42.7%	56.1%			Kayansayan (1993)
Seshimo and Fujii (1991)	28.5%	40.5%	33.9%	45.9%	Seshimo and Fujii (1991)
Elmahdy and Briggs (1979)	41.5%	27.9%			Rich (1973) Kays and London (1984) Myers (1967) Briggs and Young (1963)

tion. Equation (2) implicitly shows that, as Reynolds number or tube-row increases, the ratio ($j_{N=1,2}/j_{N=3}$) approaches 1.0, which coincides with the general behavior of the heat transfer data of finned-tube heat exchangers. Limitations on the correlations are listed in Table 3.

One may choose different sets of dimensionless variables to correlate the data. For example, McQuiston (1978) and Kayansayan (1993) chose a single "finning factor" (defined as fin area divided by total surface area) as the representative dimensionless geometric parameter. The present correlation has three geometric parameters (S_t/S_l, s/D, S_t/D). For a single or two-row configuration, Seshimo and Fujii (1993) used an entrance length-based correlation. Table 4 compares the predictability of existing correlations. Present correlations (Eqs. (1) and (2)) show the best performance with 10.7 percent rms error when all data are considered and 13.1 percent when only data of coils with 7-mm diameter tube are considered. The Gray and Webb (1986) correlation reasonably predicts the data. However, the prediction on data of coils with 7-mm diameter tube is rather poor. The reason for this is that the S_t/D of the coils with 7 mm-diameter tube (Wang and Chi, 1998; Youn, 1997) is outside of the range of their correlation. The rms errors of other correlations are relatively large, which may be due to the limited data source used to develop the correlations. The data sources are listed in the last column of Table 4.

4 Pressure Drop Correlation

Unlike the heat transfer, a significant portion of the total pressure drop may be attributed to the tube because of the profile drag. Thus, the friction correlation was developed based on a superposition model as discussed by Gray and Webb (1986). The total pressure drop ΔP is written as

$$\Delta P = \Delta P_f + \Delta P_t \tag{3}$$

where ΔP_t is the pressure drop caused by the drag force on the tubes, and ΔP_f is that caused by the friction on the fins. One may write equations for ΔP_t and ΔP_f as

$$\Delta P = f \frac{A}{A_c} \frac{G_c^2}{2\rho} \tag{4}$$

$$\Delta P_f = f_f \frac{A_f}{A_c} \frac{G_c^2}{2\rho} \tag{5}$$

$$\Delta P_t = f_t \frac{A_t}{A_{c,t}} \frac{G_c^2}{2\rho}. \tag{6}$$

Substituting Eqs. (4)–(6) into (3), and solving for f gives

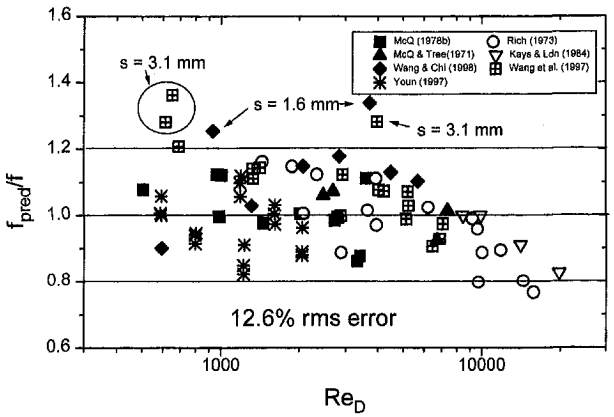

Fig. 6 Error plot of the friction factor correlation (Eq. (9))

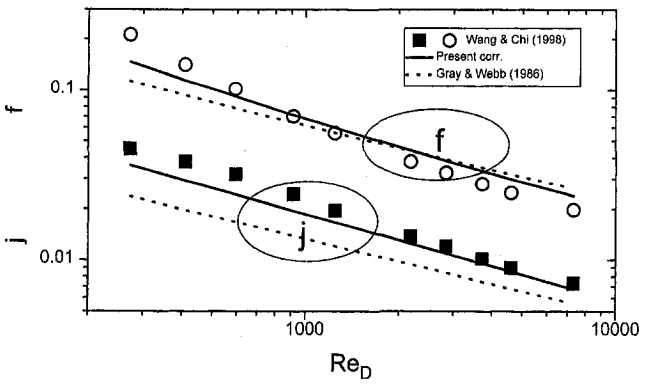

Fig. 7 Wang and Chi (1986) 7-mm tube coil data (s = 1.1 mm) compared with the present correlation and with Gray and Webb (1986) correlation

$$f = f_f \frac{A_f}{A} + f_t \left(1 - \frac{A_f}{A}\right)\left(1 - \frac{t}{p_f}\right). \tag{7}$$

One may solve for f_f if the tube bank friction factor f_t is known. The state-of-the-art tube bank friction correlation is that of Zukauskas and Ulinskas (1983). The correlation is, however, limited to $S_t/D \leq 2.5$. The S_t/D of the 7 ϕ coils considered in this study is 2.88, which is outside range of the Zukauskas and Ulinskas correlation. Thus, the Jakob (1938) correlation, which is applicable to $S_t/D = 3.0$, was used instead. The Jakob correlation applicable to staggered tube layout is as follows:

$$f_t = \frac{4}{\pi}\left(0.25 + \frac{0.118}{[(S_t/D) - 1]^{1.08}} \mathrm{Re}_D^{-0.16}\right)[(S_t/D) - 1]. \tag{8}$$

The present authors have compared the Zukauskas and Ulinskas correlation and Jakob correlation using the present data with $S_t/D \leq 2.5$, where both correlations apply. Comparison revealed that the Zukauskas and Ulinskas correlation predicted 5.3 percent (on rms average, maximum 8.8 percent) higher values than the Jakob correlation. Using f_t, as given by Eq. (8), f_f was calculated. Then, the multiple regression method was used to develop the f_f correlation, which is given by

$$f_f = 1.455\ \mathrm{Re}_D^{-0.656}(S_t/S_l)^{-0.347}(s/D)^{-0.134}(S_t/D)^{1.23}. \tag{9}$$

The friction factor of the finned-tube heat exchanger is obtained by substituting Eqs. (8) and (9) into Eq. (7), and solving for f. Unlike the heat transfer, the pressure drop generally do not show row effects. Thus, no attempt was made to make a separate row effect correlation.

Figure 6 shows the ability of the correlation to predict the friction factor. The figure shows that 90 percent of the data are predicted within ±20 percent. The rms error is 12.6 percent. The greatest data scatter occurs at low Reynolds numbers. Wang et al.'s (1997) and Wang and Chi's (1998) data, which are overpredicted at high Reynolds numbers, correspond to coils with large fin spacing. The fin spacings are shown in the figure. A similar trend was noted by Kim et al. (1997) for wavy plate-finned coils. The limitations on the correlation are listed in Table 3.

The predictability of the existing correlations is shown in Table 4. The present correlation (Eq. (9)) and the Gray and Webb (1986) correlation show approximately equal predictability when all the data are considered. However, the present correlation predicts the data of coils with 7-mm diameter tube better than the Gray and Webb correlation. The rms error of other correlations are rather large.

Figure 7 shows Wang and Chi's (1998) data of the coil with 7-mm diameter tube and 1.1-mm fin spacing compared with the predictions of the present (Eqs. (1), (2), and (9)) and Gray and Webb (1986) correlations. Present correlations reasonably predict

both the heat transfer and friction data, while the Gray and Webb correlation underpredicts the heat transfer data.

5 Conclusions

In this study, air-side heat transfer and friction correlations are developed for plate finned-tube heat exchangers having plain fins. The present correlations extend the Gray and Webb (1986) correlation by adding new data with small tube diameter. The correlations were developed from a database containing tube diameters between 7.3 mm and 19.3 mm. The heat transfer correlation (Eq. (1)) is valid for three or more rows and predicts 94 percent of the data within ±20 percent. Equation (2) is the multiplier to account for the row effect for one or two-row configurations, which predicts 94 percent of the data within ±20 percent. The rms error of the heat transfer correlation is 10.7 percent. The friction correlation (Eq. (9)) predicts 90 percent of the data within ±20 percent. The rms error is 12.6 percent. Limitations on the correlations are listed in Table 3.

Acknowledgment

The authors are very grateful to Dr. C. C. Wang of ITRI, Taiwan for providing the key data.

References

Briggs, D. E., and Young, E. H., 1963, "Convective Heat Transfer and Pressure Drop of Air Flowing across Triangular Pitch Bank of Finned Tubes," *Chem. Eng. Progress Symposium Series—Heat Transfer,* Vol. 59, No. 41, pp. 1–10.

Cox, B., and Jallouk, P. A., 1982, "Experimental Data on the Performance Characteristics of Eight Compact Heat Transfer Surfaces," Report K-1832, Union Carbide Corp., Oak Ridge, TN.

Dittus, F. W., and Boelter, L. M. K., 1930, *Publications on Engineering,* University of California, Berkeley, Vol. 2, p. 443.

Elmahdy, A. H., and Briggs, R. C., 1979, "Finned Tube Heat Exchangers; Correlation of Dry Surface Data," *ASHRAE Trans.,* Vol. 85, No. 2, pp. 262–273.

Gnielinski, V., 1976, "New Equation for Heat and Mass Transfer in Turbulent Pipe and Channel Flow," *Int. Chem. Engng.,* pp. 359–368.

Gray, D. L., and Webb, R. L., 1986, "Heat Transfer and Friction Correlations for Plate Fin-and-Tube Heat Exchangers Having Plain Fins," *Proceedings of the 9th International Heat Transfer Conference,* Taylor & Francis, London, San Francisco, pp. 2745–2750.

Jacob, M., 1938, "Heat Transfer and Flow Resistance in Cross Flow of Gases over Tube Banks," *Trans. ASME,* Vol. 60, p. 384.

Jang, J-Y., Wu, M-C., and Chang, W-J., 1996, "Numerical and Experimental Studies of Three-Dimensional Plate-Fin and Tube Heat Exchangers," *International Journal Heat Mass Transfer,* Vol. 39, No. 14, pp. 3057–3066.

Kayansayan, N., 1993, "Heat Transfer Characterization of Flat Plain Fins and Round Tube Heat Exchangers," *Experimental Thermal and Fluid Science,* Vol. 6, pp. 263–272.

Kays, W. M., and London, A. L., 1984, *Compact Heat Exchangers,* 3rd Ed., McGraw-Hill, New York. p. 224.

Kim, N-H., Yun, J-H., and Webb, R. L., 1997, "Heat Transfer and Friction Correlations for Wavy Plate Fin-and-Tube Heat Exchangers," ASME JOURNAL OF HEAT TRANSFER, Vol. 119, pp. 560–567.

McQuiston, F. C., 1978a, "Correlation for Heat, Mass and Momentum Transport Coefficients for Plate-Fin-Tube Heat Transfer Surfaces with Staggered Tube," *ASHRAE Trans.,* Vol. 84, Part 1, pp. 294–309.

McQuiston, F. C., 1978b, "Heat, Mass and Momentum Transfer Data for Five Plate-Fin-Tube Heat Transfer Surfaces," *ASHRAE Trans.,* Vol. 84, Part 1, pp. 266–293.

McQuiston, F. C., and Tree, D. R., 1971, "Heat Transfer and Flow Friction Data for Two Fin-Tube Surfaces," ASME JOURNAL OF HEAT TRANSFER, Vol. 93, pp. 249–250.

Neal, S. B. H. C., and Hitchcock, J. A., 1966, "A Study of the Heat Transfer Process in Banks of Finned Tubes in Cross Flow, Using a Large Scale Model Technique," *Proceedings of the Third International Heat Transfer Conference,* Vol. 3, Chicago, IL, Taylor & Francis, London, pp. 290–298.

Myers, R., 1967, "The Effect of Dehumidification on the Air-Side Heat Transfer Coefficient for a Finned Tube Coil," M. Sc. thesis, University of Minnesota.

Rich, D. G., 1973, "The Effect of Fin Spacing on the Heat Transfer and Friction Performance of Multi-Row, Smooth Plate Fin-and-Tube Heat Exchangers," *ASHRAE Trans.,* Vol. 79, Part 2, pp. 137–145.

Rich, D. G., 1975, "The Effect of Number of Tube Rows of the Heat Transfer Performance of Smooth Plate-Fin-Tube Heat Exchangers," *ASHRAE Trans.,* Vol. 81, Part 1, pp. 307–317.

Rosman, E. C., Carajilescov, P., and Saboya, F. E. M., 1984, "Performance of One- and Two-Row Tube and Plate Fin Heat Exchangers," ASME JOURNAL OF HEAT TRANSFER, Vol. 106, pp. 627–632.

Ryan, B. F., Joiner, B. L., and Ryan, Jr., T. A., 1985, *MINITAB Handbook,* 2nd Ed., Duxbury Press, Boston, MA.

Saboya, F. E. M., and Sparrow, E. M., 1974, "Local and Average Heat Transfer Coefficients for One-Row Plate Fin and Tube Heat Exchanger Configurations," ASME JOURNAL OF HEAT TRANSFER, Vol. 96, pp. 265–272.

Saboya, F. E. M., and Sparrow, E. M., 1976, "Transfer Characteristics of Two-Row Plate Fin and Tube Heat Exchanger Configurations," *International Journal of Heat Mass Transfer,* Vol. 19, pp. 41–49.

Schmidt, Th. E., 1949, "Heat Transfer Calculations for Extended Surfaces," *Refrig. Eng.,* Apr., pp. 351–357.

Seshimo, Y., and Fujii, M., 1991, "An Experimental Study of the Performance of Plate Fin-and-Tube Heat Exchangers at Low Reynolds Numbers," *Proceedings of the 3rd ASME/JSME Thermal Engineering Joint Conference,* Vol. 4, ASME, New York, pp. 449–454.

Torikoshi, K., Xi, G., Nakazawa, Y., and Asano, H., 1994, "Flow and Heat Transfer Performance of a Plate Fin-and-Tube Heat Exchanger (1st Report: Effect of Fin Pitch)," *10th Int. Heat Transfer Conf.,* Paper 9-HE-16, pp. 411–416.

Torikoshi, K., and Xi, G., 1995, "A Numerical Study of Flow and Thermal Fields in Finned Tube Heat Exchangers (Effect of Tube Diameter)," Paper No. ASME HTD-Vol. 317-1, pp. 453–458.

Wang, C-C., and Chi, K., 1998, "Heat Transfer and Friction Characteristics of Plain Fin-and-Tube Heat Exchangers, Part 1: New Experimental," *Int. J. Heat Mass Transfer,* submitted for publication.

Wang, C-C., Chi, K., and Webb, R. L., 1998, "Data Reduction for the Air-Side Performance of Fin-and-Tube Heat Exchangers," ASME JOURNAL OF HEAT TRANSFER, submitted for publication.

Wang, C-C., Hsieh, Y-C., and Lin, Y-T., 1997, "Performance of Plate Finned Tube Heat Exchangers Under Dehumidifying Conditions," ASME JOURNAL OF HEAT TRANSFER, Vol. 119, pp. 109–117.

Webb, R. L., 1994, *Principles of Enhanced Heat Transfer,* Wiley Inter-Science, New York.

Webb, R. L., 1998, "Advances in Air-Cooled Heat Exchanger Technology," *Proceedings of Int. Conference on Heat Exchangers for Sustainable Development,* Lisbon, Portugal, Instituto Superior Technico, pp. 677–692.

Wilson, E. E., 1915, "A Basis for Rational Design of Heat Transfer Apparatus," *ASME Trans.,* Vol. 37, p. 47.

Youn, B., 1997, internal report, Samsung Electric Corp.

Zukauskas, A., and Ulinskas, R., 1983, "Banks of Plain and Finned Tubes," *Heat Exchanger Design Handbook,* Vol. 2, Hemishere Publishing Corporation, New York, pp. 72–80.

M. K. Chyu
e-mail: mc47@andrew.cmu.edu
Fellow ASME

Y. Hsing

Department of Mechanical Engineering,
Carnegie Mellon University,
Pittsburgh, PA 15213

V. Natarajan
The BOC Group Technical Center,
Murray Hill, NJ 07947

J. S. Chiou
Department of Mechanical Engineering,
National Cheng Kung University,
Tainan, Taiwan

Effects of Perpendicular Flow Entry on Convective Heat/Mass Transfer From Pin-Fin Arrays

Convective heat transfer with pin-fin arrays have been studied extensively in laboratory experiments where flow is introduced to the array uniformly over the channel span. However, the flow path in actual cooling designs is often serpentine-shaped with multiple turns, and the pin-fin array section is often located immediately downstream of a turn. The present study, using an analogous mass transfer technique based on naphthalene sublimation, investigates the effects of three different, nonaxial flow entries on array heat transfer for both an inline and a staggered arrangement of pins. The measurement acquires the mass transfer rate of each individual pin in a five row by seven column array for the Reynolds number varying from 8000 to 25,000. The mass transfer and associated flow visualization results indicate that the highly nonuniform flow distribution established at the array entrance and persisting through the entire array can have significant effects on the array heat transfer characteristics. Compared to the conventional case with axial-through flow entrance, the overall array heat transfer performance can be either enhanced or degraded, depending on the actual inlet arrangements and array configurations.

Introduction

Heat transfer with flow over an array of circular pin-fins has been the subject of extensive research in the past because of its importance in a wide variety of engineering applications. Pin-fins with small height-to-diameter ratios, namely on the order of unity, are often used as heat transfer augmentation devices for cooling of electronic components or turbine blades and vanes. For the latter, use of pin-fin arrays (the so-called pedestals) is especially viable for internal cooling passage near the blade trailing section where the pin-fins also serve a structural purpose in bridging the narrow span between the pressure and suction surfaces.

Because of comparable sizes in fin height and diameter, implementing a pin-fin array in a cooling channel has a rather insignificant effect on increasing the area for heat transfer. The additional fin surface area is offset by the area covered underneath the fin base. Here the total heat transfer must include heat transfer from both the fin surface and the uncovered region on the endwall. Hence the fin/endwall interaction is expected to be the dominant feature for the convective transport with pin-fin arrays. This represents a major divergence from the classical problem for long tube banks with crossflow (Zukauskas, 1972), where almost all the heat transfer takes place on the tube surface and the endwall effect is nonexistent. In general, short pin-fin arrays produce lower heat transfer than their long-cylinder counterparts.

Heat transfer and pressure loss for short pin-fin arrays primarily directed to turbine blade cooling applications have been studied extensively since the early 1980s. A significant contribution was made by groups at NASA-Lewis (VanFossen, 1982; Simoneau and VanFossen, 1984; Brigham and VanFossen, 1984) and Arizona State University (Metzger et al., 1982a, b, c, 1984, 1986). They have examined the effects of pin and array geometries, flow parameters, and thermal conditions. Heat transfer results obtained include array-averaged Re-Nu correlations and row-resolved heat transfer distributions. Armstrong and Winstanley (1987) have compiled these findings for the staggered arrays. Using a mass transfer subliming system, Chyu (1990) evaluated the effects of fillets at the cylinder-endwall junction. Without fillets, his mass transfer results agree very favorably with those reported earlier. Chyu and Goldstein (1991) investigated the influence of array geometry on the heat transfer from the uncovered region of the endwall. More recently, Chyu et al. (1998) made a comparison of heat transfer from the pin surface and from the uncovered endwall. They concluded that the magnitudes of spanwise-averaged heat transfer coefficient form these two participating surfaces are comparable, when $H/D = 1$ and $S/D = X/D = 2.5$.

Compared to previous research, the present study focuses on a different issue, namely the effects of flow nonuniformity at the array inlet. Typically, in experimental simulations, the inlet flow direction is modeled parallel to the channel axis, normal to array rows. The variation of transport features among different fin elements of the same row is virtually nonexistent. However, this is often not a realistic inlet configuration for heat exchangers, where coolant flow is usually subjected to severe turnings through a serpentine-shaped passage before entering the fin array. With the underlying goal of gaining further understanding toward the effects of inlet condition, this study examines the case where flow enters the array immediately following a 90-deg turn. Figure 1 shows a schematic view of the flow inlet along with two different, but parametrically related, array configurations; i.e. inline and staggered. Three different types of inlets were examined. One of them has flow entering from the side of the array (denoted as "S"), and the other two guides the flow vertically entering form the top wall of the array housing (normal to the figure plane, denoted as "C" and "L"). While all three inlets induce flow making a sharp 90-deg turn before entering the test section, the direction of inlet flow is perpendicular to the fin axis for the case of side entry, and parallel to the fin axis for the top entries. The major difference between the two cases of top entry is the actual inlet location. Inlet "C" is located on the center of the array span along the symmetry line, while inlet "L" is offset to the lower side of the figure. All three inlets have the same cross-sectional shape and area. The effects of such nontraditional inlets on the heat transfer from the pin-fin arrays can be assessed through comparison with results obtained under normal flow conditions.

Contributed by the Heat Transfer Division for publication in the JOURNAL OF HEAT TRANSFER and presented at '96 NHTC, Houston. Manuscript received by the Heat Transfer Division, Mar. 25, 1997; revision received, Mar. 2, 1999. Keywords: Analog Techniques, Augmentation and Enhancement, Finned Surfaces, Heat Exchangers, Turbines. Associate Technical Editor: J. C. Han.

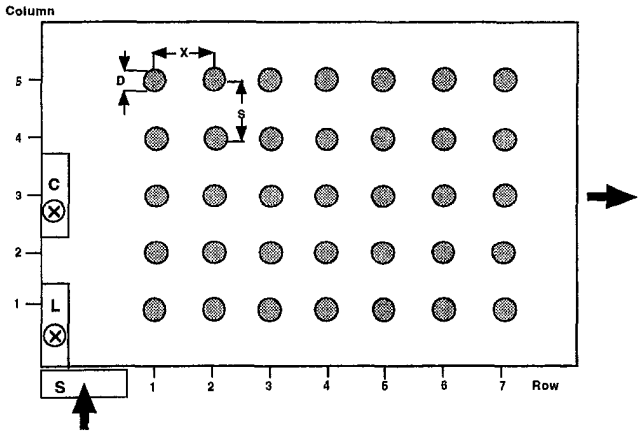

Fig. 1(*a*) In-line array

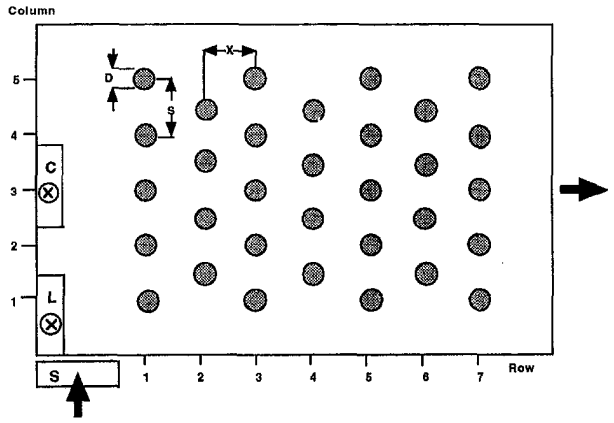

Fig. 1(*b*) Staggered array

Fig. 1 Pin-fin arrays with perpendicular inlet

Experimental Apparatus and Procedures

The pin-fin elements are perfectly cylindrical in shape and made of aluminum rods approximately 12.5 mm in diameter. Geometrically, an array is determined by the cylinder diameter (D), the cylinder height (H), and the spacings between neighboring fin elements in both spanwise and streamwise directions. To facilitate a rational comparison, the two arrays studied have identical geometric parameters that are very typical of those employed in practice; i.e., $H/D = 1$, $S/D = X/D = 2.5$. These array geometries can be achieved by shifting the even number rows of one array by one-half spanwise fin spacing relative to those of the other array. There are seven rows for both arrays, but the total number of fin elements is different. For the in-line array, each row has five pins giving a total of 35 pins. On the other hand, the number of pins per row in the staggered array alternates with five in the odd number row and four in the even number row, a total of 32 pins.

The test channel which houses the fin arrays is made of aluminum tooling plate and has a rectangular cross-section, 159 mm wide and 12.7 mm high. Downstream of the test section is a 230-mm long discharge duct, which is approximately ten times the hydraulic diameter of the test section. Inlet flow to the array is introduced through a rectangular opening (25.4 mm wide and 12.5 mm high) on one side of the test channel. The center of the first row of pins is about two pin-spacings from the furthest edge (lower-left corner in Fig. 1) of the test section. Attached to the opening is an approximate 455-mm long aluminum duct which serves as the entrance section. Airflow is supplied by a 50 HP compressor and is monitored by a pressure regulator, a control valve, and an orifice before reaching the test section.

The present experiment uses an analogous mass transfer technique with subliming naphthalene instead of direct heat transfer measurements. The same technique has been employed earlier pin-fin studies by Chyu et al. (1990, 1991, 1998). To ease the experiment and to facilitate a direct comparison with the baseline data reported by Chyu (1990), only the surface of each pin element is mass transfer active. Understandably this arrangement may present a different thermal condition compared to reality. However, earlier studies (Metzger et al., 1982; Chyu, 1990) have suggested that, within the present test range, the spanwise-averaged heat transfer coefficients on the pin surface and on the uncovered endwall are quite comparable, within ten percent in most cases. Chyu et al. (1998) recently also confirmed this finding and reported that the heat transfer coefficient on the pin surface varies insignificantly with different thermal boundary conditions on the endwall. This implies that the values of heat transfer coefficient obtained from the heated pins alone are reasonably representative over the entire array. In addition, since the primary focus of this study lies in the effect of array inlet geometry, which is largely hydrodynamic in nature, the exactness of thermal condition is deemed to be a secondary issue, provided that it is the same for all of the cases compared.

Each experiment starts with preparation of naphthalene coating on the pin-fin surface. This is achieved by dipping the cylinder, with both ends taped, into a pool of nearly boiling, molten naphthalene. During the dip, the cylinder is held by a tweezers at both ends and immersed in the liquid naphthalene for about one second. The naphthalene solidifies almost instantly after removal from the pool and forms a nearly 2-mm thick layer on the cylinder surface.

Nomenclature

D = pin-fin diameter
H = pin-fin height
h = heat transfer coefficient, Eq. (1)
h_m = pin-resolved naphthalene mass transfer coefficient, Eq. (2)
k = thermal conductivity
m = mass transfer flux of naphthalene from pin-fin surface
n = power index
Nu = Nusselt number, hD/k
Pr = Prandtl number, ν/α
q = heat flux from pin-fin surface
Re = Reynolds number, $U_m D/\nu$
S = pin spacing in spanwise direction
Sc = naphthalene-air Schmidt number, $\nu/K = 2.5$
Sh = pin-resolved naphthalene mass transfer Sherwood number, $h_m D/K$
T = temperature
U_m = mean flow in the minimum flow area
X = pin spacing in streamwise direction

Greek Symbols

α = thermal diffusivity
K = naphthalene-air diffusion coefficient
ν = kinematic viscosity of air
$\rho_{v,w}$ = vapor mass concentration or density of naphthalene on pin-fin surface
$\rho_{n,b}$ = vapor mass concentration or density of naphthalene in flow bulk
ρ_s = density of solid naphthalene

Subscript

A = array-averaged
b = bulk
C = column-averaged
R = row-averaged
w = wall, fin surface

Such a coating process generally results in a quality surface, so no additional polishing or machining procedure is necessary. After the coating process, the cylinders are stored in a tightly sealed plastic box for at least 15 hours to ensure that they attain thermal equilibrium with the surrounding air.

Before a test run, all fins are separately weighed using an electronic balance with an accuracy of 10^{-2} mg in a 166-g range. The pin fins are then screw-mounted on the bottom wall of the test section in the desired array geometry. The entire assembly is completed when the top wall is fastened and sealed. When in place, the top wall touches the upper end of each pin-fin, ensuring that no apparent gap is present between the wall and fin. Having assembled the test section, the compressed air is induced and flows through the channel for about 30 minutes. During the test run, the system temperature is determined by the average readings of four thermocouples embedded on the inner surface of the two endwalls. The system temperature is used to evaluate the naphthalene vapor concentration, $\rho_{v,w}$, on the fin surface. Since the value of $\rho_{v,w}$ is very temperature sensitive, an isothermal system is highly desirable. A test is considered to be a failure and discarded if any two of the four thermocouple readings differ more than 0.2°C. After the test run, all fins are unscrewed and removed from the channel and each is weighed again. The weight difference for each individual fin yields the amount of naphthalene sublimed during the test run. The average naphthalene mass sublimed is approximately 20 mg, which amounts to less than ten percent of initial mass of naphthalene coated on the pin surface.

As an auxiliary study, the streakline patterns on the endwall are visualized using the oil-graphite technique. These patterns directly substantiate the interpretation of the mass transfer results. To facilitate appropriate visual access for the streakline photographs, the aluminum wall atop the test channel is replaced by a transparent Plexiglas plate.

Heat/Mass Transfer Analogy and Data Reduction

The convective heat transfer coefficient, h, of each fin element is given by

$$h = q/(T_w - T_b) \tag{1}$$

where T_w and T_b are the element wall temperature and the bulk mean temperature in the channel, respectively. By analogy (Eckert, 1976), the mass transfer coefficient, h_m, of each circular fin is

$$h_m = m/(\rho_{v,w} - \rho_{n,b}) \tag{2}$$

where m is the mass transfer rate per unit area which can be calculated from the weight change of the coated pin before and after the experiment. The naphthalene concentration at the wall, $\rho_{v,w}$, is obtained by evaluating the time-averaged naphthalene vapor pressure using the pressure-temperature correlation of Ambrose et al. (1975) in conjunction with the ideal gas law.

The value of naphthalene concentration in the bulk flow at a given row is determined by the total mass transfer upstream. The increase in bulk concentration naphthalene vapor within the domain of a specific row j can be expressed as

$$\Delta\rho_{n,b} = M_j/Q \tag{3}$$

where Mj is the mass transfer per unit time from all fin surfaces of the entire row j, and Q is the volumetric air flow rate through the channel. Since the air flow at the channel inlet is naphthalene free, it leads to

$$\Delta\rho_{n,b} = \sum_{1}^{j-1} M_j/Q. \tag{4}$$

As the mass transfer system is essentially isothermal, the naphthalene vapor pressure and vapor concentration at the wall are constant. In heat transfer, this is equivalent to a wall boundary condition of constant temperature on the fin surface, and the fins thus can be regarded to have an ideal 100 percent efficiency.

The dimensionless pin-resolved mass transfer coefficient, Sherwood number, Sh, is defined by

$$\mathrm{Sh} = h_m D/\mathrm{K} \tag{5}$$

where K is the naphthalene-air diffusion coefficient which is determined by taking the Schmidt number equal to 2.5 (Sparrow and Ramsey, 1978); i.e.,

$$\mathrm{Sc} = \nu/\mathrm{K}. \tag{6}$$

Since the naphthalene concentration in the boundary layer is extremely small, the kinematic viscosity, ν, uses the value of air under the operating conditions. By analogy, the Sherwood number can be transformed to its heat transfer counterpart, the Nusselt number (Nu), using the relation

$$\mathrm{Nu}/\mathrm{Sh} = (\mathrm{Pr}/\mathrm{Sc})^n \tag{7}$$

where Pr is the Prandtl number and the power index n is approximately equal to 0.4, according to Sparrow and Ramsey (1978). Using air (Pr = 0.7) as the coolant, a direct conversion relationship can be obtained,

$$\mathrm{Nu} = 0.6\ \mathrm{Sh}. \tag{8}$$

Most of the results presented in this study are in the form of pin-resolved mass transfer Sherwood number (Sh). The uncertainty analysis with a 95 percent confidence level in the measured parameters is based on the method of Kline and McClintock (1953). One of the major errors contributing to the value of Sh is the uncertainty of naphthalen-to-air diffusion coefficient, K, which, in turn, is a strong function of temperature during the experiment. The uncertainty of temperature reading is about ±0.1 C, which corresponds to approximately two percent. error in K. The second major error is the uncertainty in measuring the flow rate or Reynolds number in the air supply system, which is about four percent. The third error, which is relatively insignificant (<1 percent), is the uncertainty of the naphthalene weighing system as well as excessive natural sublimation before and after the experiment. Combining all these errors leads to about seven percent overall uncertainty for Sh. The repeatability for all the test runs is about the same value.

Results and Discussion

One of the most important features inherited in pin fin arrays with conventional, through-flow entries is the variation of the row-resolved heat transfer coefficient. According to Metzger et al. (1982a), and Chyu et al. (1990, 1998), the maximum Nusselt number occurs at the second row and the third row for the inline and staggered array, respectively. Such a maximum is a result of two competing effects. Heat transfer from a fin element can be substantially promoted by direct wake shedding generated from the elements situated upstream. On the other hand, heat removed from the elements upstream elevates the bulk mean temperature in the channel, which reduces the driving potential for convective heat transfer. With this notion in mind, the highest row-resolved heat transfer should occur at the upstream-most row that is subjected to direct wake shedding. The Nusselt number in the downstream row to the maximum displays virtually a constant value as the heat convection in the housed channel reaches a fully developed status.

Figures 2 and 3 show the relative magnitude of mass transfer among all individual elements for the inline array and staggered array, respectively. The numerical value marked beside each element is the ratio of its pin-resolved Sherwood number to the Sherwood number averaged over the entire array, Sh_A. The values marked outside the figure border are the normalized row-average (Sh_R, top border) and column-average Sherwood numbers (Sh_c,

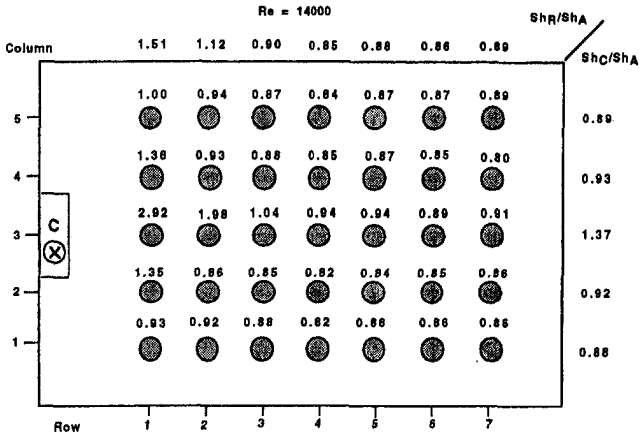

Fig. 2(*a*) Central inlet, Re = 1.4 × 104

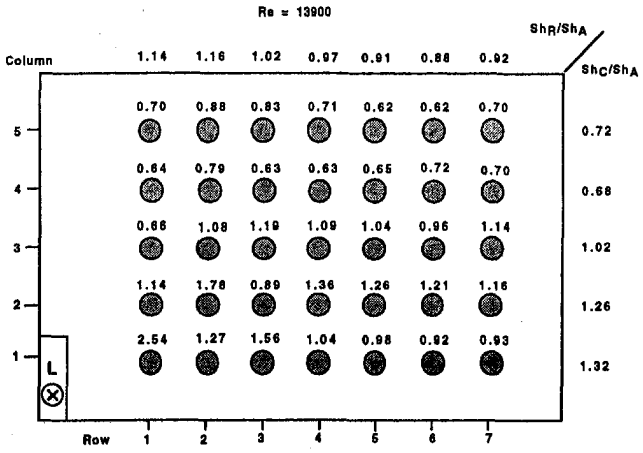

Fig. 2(*b*) Lower inlet, Re = 1.39 × 104

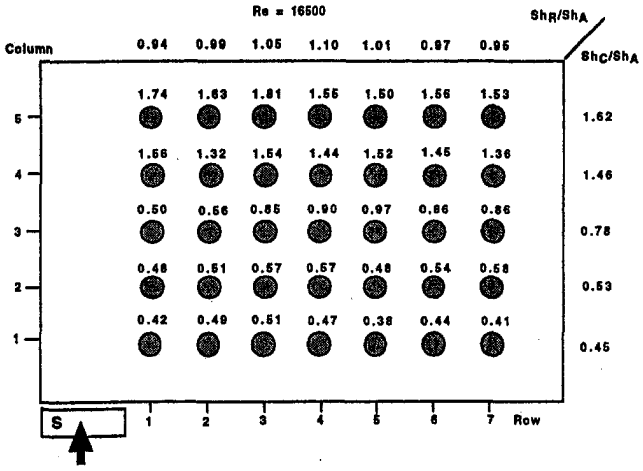

Fig. 2(*c*) Side inlet, Re = 1.65 × 104

Fig. 2 Pin-resolved mass transfer–in-line array

right border). Although the cases shown in Figs. 2 and 3 have different Reynolds numbers, the normalized mass transfer data revealed in each figure are representative of the specific array geometry and are relatively independent of the Reynolds number. According to Chyu (1990), the reference values of Sh_R/Sh_A from row 1 to row 7 for the inline array with a uniform flow entry without a reduced inlet-area and turn are 0.92, 1.08, 1.04, 1.01, 1.00, 0.99, and 0.98. The corresponding values for the staggered array are 0.88, 1.01, 1.11, 1.04, 1.01, 0.99, and 0.97. As a result, the maximum variation in row-resolved mass transfer for both reference arrays is about ±10 percent. Note that, due to symmetry, no variation in Sh_c exists in these cases.

As a contrast to the case with straight entry, Figs. 2 and 3 reveal strong spatial nonuniformity and complex distribution in pin-resolved mass transfer. The variation between the highest and the lowest Sherwood number in an array is by a factor of 3 to 5. Except for the case with side entry (Figs. 2(*c*) and 3(*c*)), the pin immediately downstream to the inlet always experiences the highest transfer coefficient over the entire array. The magnitude of such a maximum is about 2 to 2.5 times the array averaged value. This localized mass transfer elevation appears to be induced by a

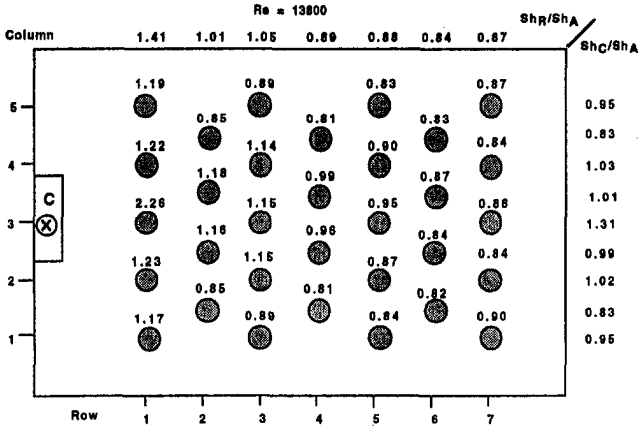

Fig. 3(*a*) Central inlet, Re = 1.38 × 104

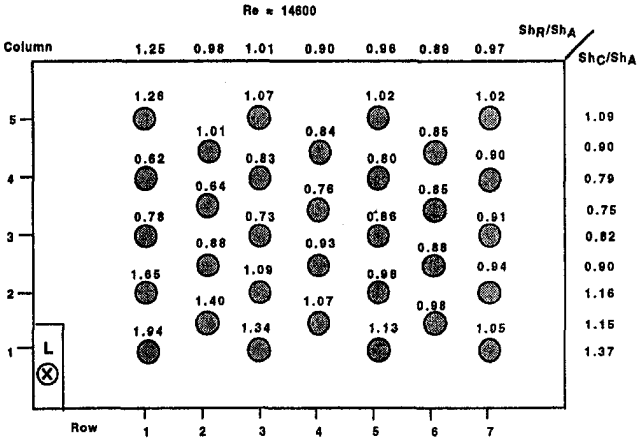

Fig. 3(*b*) Lower inlet, Re = 1.46 × 104

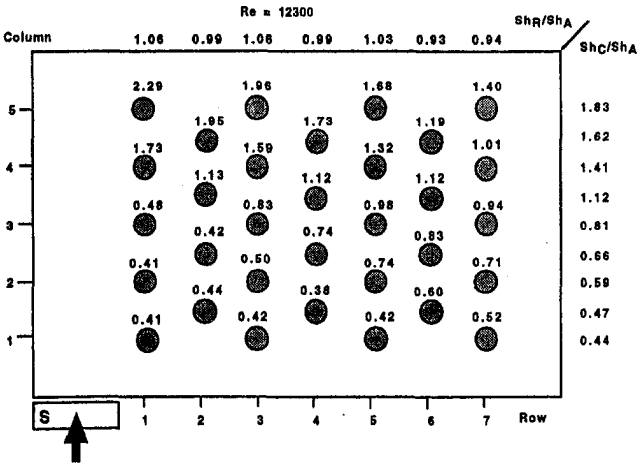

Fig. 3(*c*) Side inlet, Re = 1.23 × 104

Fig. 3 Pin-resolved mass transfer–staggered array

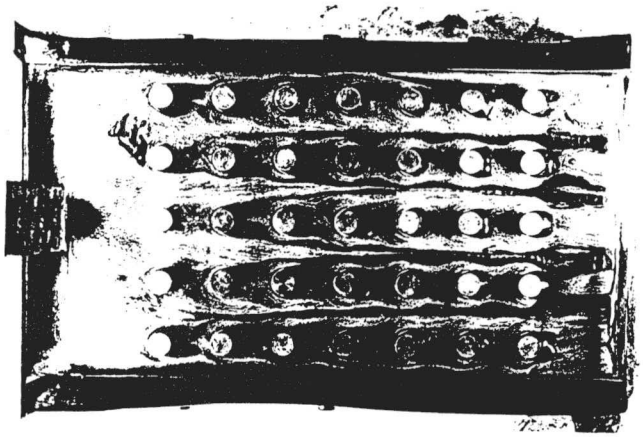

Fig. 4(*a*) Central inlet

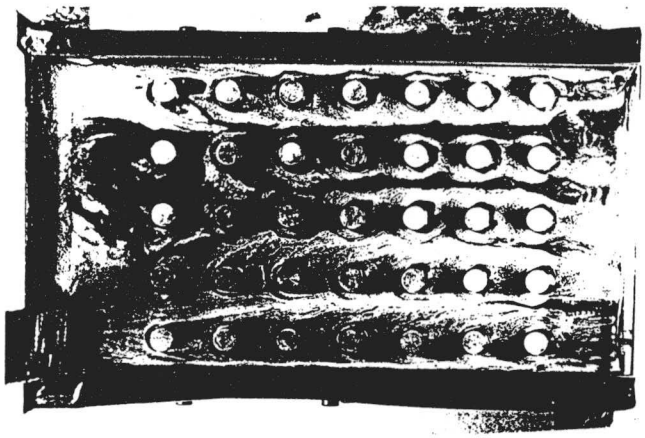

Fig. 4(*b*) Lower inlet

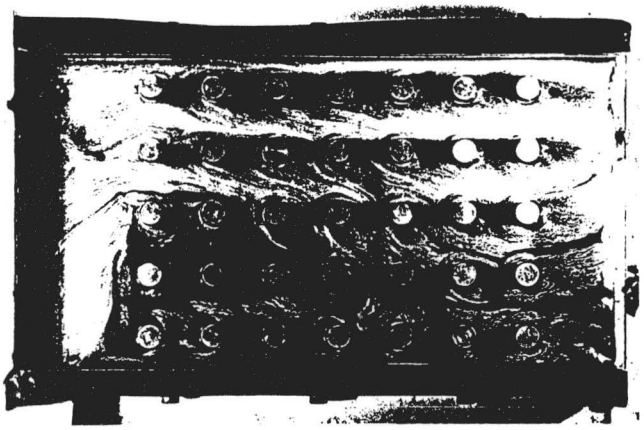

Fig. 4(*c*) Side inlet

Fig. 4 Endwall flow visualization–in-line array

distinct flow feature near the inlet region, which can be described as jet impingement in a confined space. Figures 4 and 5 show the photos of streakline patterns of an oil-graphite mixture on the array endwall. Such a flow visualization study not only exhibit salient features of horseshoe vortex around individual pin elements but also reveal qualitative information concerning convective transport in an array. A brighter spot in the photo generally implies greater convective transport in the region than a darker spot. Because the lighting conditions and the mixture batch used may vary among different cases, comparison of local transport variation based on brightness contrast should be limited to the same photo.

For the cases with a top entry, the flow turns 90 deg and spreads into the pin fin array after impinging on the base plate. The streakline traces revealed in Figs. 4(*a*), 4(*b*), 5(*a*), and 5(*b*) indicate that flow spreading near the impingement region produces a very nonuniform velocity profile across the span just ahead of the array. Such an unevenness in flow distribution is responsible for the spanwise variation of mass transfer for pins located in the same row. The elevated mass transfer from the pin closest to the inlet appears to be induced by the combination of high-flow speed and impingement-enhanced turbulent mixing near the region. This effect is especially evident in the first two rows of the cases with a central inlet (Figs. 2(*a*) and 3(*a*)). In addition to spanwise nonuniformity, the mass transfer in these upstream rows also shows a decreasing trend toward downstream. Due mainly to the mixing promoted by pins upstream, the mass transfer coefficient

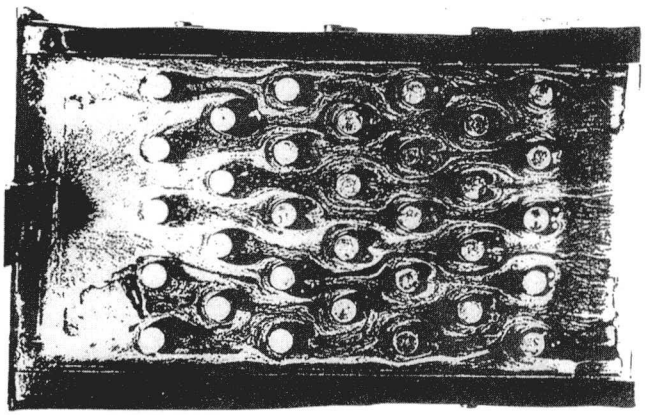

Fig. 5(*a*) Central inlet

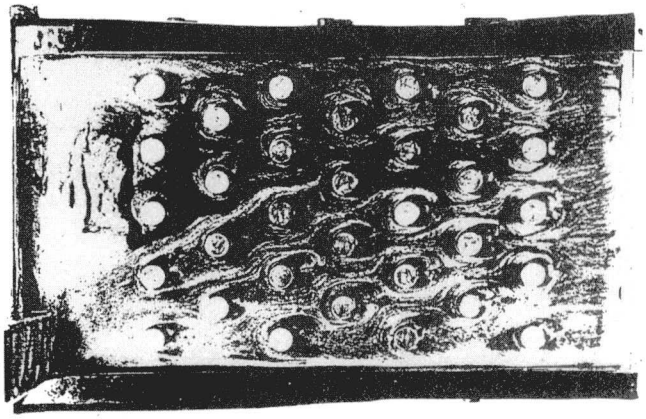

Fig. 5(*b*) Lower inlet

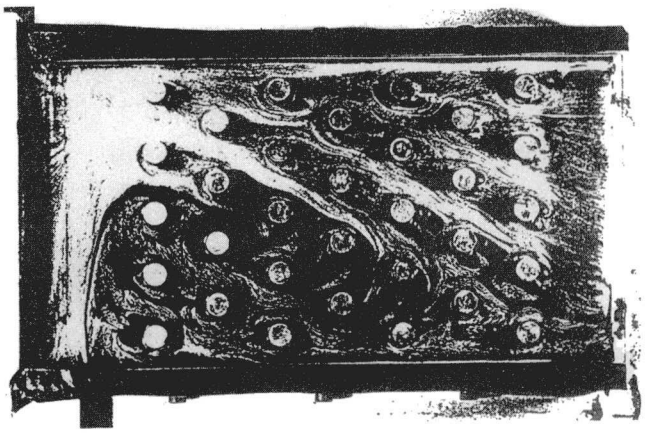

Fig. 5(*c*) Side inlet

Fig. 5 Endwall flow visualization–staggered array

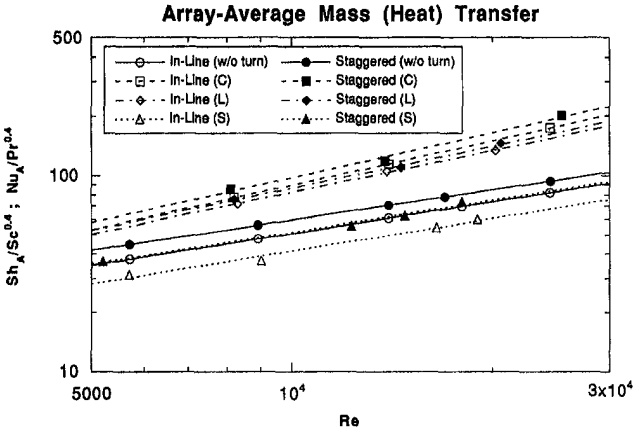

Fig. 6 Array averaged mass transfer

for pins located downstream to the third row becomes quite uniform. These features prevail in both inline and staggered arrays.

Influenced by the peculiar inlet location and sidewall presence, the mass transfer results for the lower top-wall entry (Figs. 2(*b*) and 3(*b*)) exhibit a great asymmetry. Pins located along the paths of higher flow rate (columns 1 to 3) inherit higher mass transfer coefficients than those located off the main flow paths (columns 3 to 5). The unevenness of flow distribution is quite evident, according to the endwall streakline photos (Figs. 4(*b*) and 5(*b*)). The region of dark, graphite accumulation corresponds well to the zone of low mass transfer. One distinct feature between the two streakline photos is that the main flow tends to move diagonally across the staggered array, while the flow moves primarily straight through the inline array. This may be caused by differences in array geometry and form-induced pressure characteristic. Further examining the streakline photos reveal that the inlet flow is subjected to a second impingement on the farther sidewall of the test channel. As a result, the pins located in the first few rows of column 5 exhibit substantially higher mass transfer than those of the neighboring columns.

The normalized pin-resolved mass transfer for arrays with a side entry are shown in Figs. 2(*c*) and 3(*c*). Compared to the cases with a top entry, one marked distinction here is the absence of direct impingement of inlet flow on the base plate. The pin elements of higher mass transfer are all located in columns 4 and 5, far away from the flow inlet. This implies that a large fraction of the entrance flow proceeds from the side entrance toward the opposite side of the housed channel before turning into the array. The streakline photos (Figs. 4(*c*) and 5(*c*)) confirm such a speculation. The appearance shows clearly that the entrance flow proceeds in the perpendicular entry direction past columns 1 to 3 and only at the end of its spanwise travel turns into columns 4 and 5. The patterns further reveal that the flow, after turning, is largely concentrated around the pins of columns 4 and 5 for its travel through the upstream portion of the array. In other words, the pins in columns 1 and 2 are in relatively stagnated or slow moving flow regions virtually throughout the array. In fact, flow in this region is subjected to a mild recirculation oriented in the clockwise direction. The flow encircling the recirculating zone shows a diagonal movement, particularly for the staggered case. Although photos of flow patterns for other Reynolds numbers are not shown here, the actual size of such a low-speed zone appears to decrease with an increase in Re.

Figure 6 shows the average mass transfer results over the entire array. Note that the figure ordinate uses $Sh_A/Sc^{0.4}$ which is analogous to $Nu_A/Pr^{0.4}$ for heat transfer. Corresponding data for the baseline cases with a straight, uniform flow entry reported by Chyu (1990) are also included in the figure for comparison. The collective results confirm a general notion that, for a given Reynolds number or flow rate, the overall heat transfer of a staggered array is higher than that of a corresponding in-line array. This trend is consistent regardless of different arrangements in flow entry. However, varying the flow inlet conditions can substantially change the heat transfer characteristics, both in the amount involved and the extent of Reynolds number dependency. The values of an average Sherwood number for the cases with a perpendicular flow entry from the top wall are significantly higher than those of the baseline cases with a uniform flow entry. For the staggered array, the increase is about 35 to 60 percent for the lower inlet ("L"), and an another 15 to 20 percent increase for the central inlet ("C"). On the other hand, the increase for the in-line array is virtually the same, approximately 100 percent, for both types of inlets. The actual Sh_A values of these in-line cases, in fact, are comparable to that of the staggered array with a lower inlet. In contrast, the corresponding magnitudes of an array-averaged transfer coefficient with a side entry are nearly 20 percent lower compared to the baseline case. The level of such a reduction is virtually the same for both arrays. The sizable low-speed zone with degraded mass transfer adjacent to the flow inlet is responsible for this phenomenon.

Also revealed in Fig. 6 is a general trend of pin-fin heat transfer that the array-averaged Sherwood number or Nusselt number increases with the Reynolds number. However, the level of Re-dependency varies among different entry arrangements. The power index for both arrays with a side entry shows a value about 0.6, which is comparable to that with a conventional through-flow entry. The corresponding power indices for the other two top-wall entries ("C" and "L") are higher, around 0.7 to 0.75. Apparently, the flow impingement followed by a sharp, 90-deg turn near the array inlet has altered the general features of pin-fin heat transfer collectively reported in the open literature.

Concluding Remarks

An experimental study, using a mass transfer analogy, has investigated the effects of three different perpendicular flow entries on pin-fin array heat transfer performance for both in-line and staggered pin configurations. Mass transfer rates are determined for each pin in 7 row by 5 column arrays and are then reduced to pin-resolved Sherwood numbers. The mass transfer and associated flow visualization results indicate that the effects of perpendicular flow entry on the array heat transfer characteristics can be severe. A large variation in mass (heat) transfer across the rows associated with highly nonuniform flow distribution prevails at the array entrance and persists through the entire array. For both arrays, the perpendicular flow always produces two distinctly different regions with differences of pin-resolved mass transfer as high as three to five times. All tests reveal one region of fast-moving through-flow with elevated mass transfer while the remaining regions of the array experienced relatively stagnant flow and consequently much lower mass transfer. The specific locations of these regions depend critically on the actual arrangement and geometry of flow inlet. The highly localized mass transfer variation has a significant implication to the overall array-averaged heat transfer performance. The present results indicate that implementation of flow entering from the top wall can further enhance the array heat transfer by nearly a factor of 2 compared to the case with the conventional, uniform flow entry. In contrast, a side entry can result in an about 20 percent reduction in overall heat transfer from the array. The quantitative information obtained from this study may be used as an adjusting factor for the existing pin-fin heat transfer data when the actual applications involve nonaxial flow inlets.

References

Ambrose, D., Lawenson, I. J., and Sprake, C. H. S., 1975, "The Vapor Pressure of Naphthalene," *J. Chem. Thermo.*, pp. 1173–1176.

Armstrong, J., and Winstanly, D., 1987, "A Review of Staggered Array Pin Fin Heat Transfer for Turbine Cooling Applications," ASME Paper 87-GT-201.

Brigham, B. A., and VanFossen, G. J., 1984, "Length-to-Diameter Ratio and Row Number Effects in Short Pin Fin Heat Transfer," ASME *Journal of Engineering for Gas Turbine and Power,* Vol. 106, pp. 241–246.

Chyu, M. K., 1990, "Heat Transfer and Pressure Drop for Short Pin-Fin Arrays With Pin-Endwall," ASME JOURNAL OF HEAT TRANSFER, Vol. 112, pp. 926–932.

Chyu, M. K., and Goldstein, R. J., 1991, "Influence of Cylindrical Elements on Local Mass Transfer from a Flat Surface," *Int. J. Heat and Mass Transfer,* Vol. 34, pp. 2175–2186.

Chyu, M. K., Hsing, Y. C., Shih, T. I-P., and Natarajan, V., 1998, "Heat Transfer Contributions of Pins and Endwall in Pin-Fin Arrays: Effects of Thermal Boundary Condition Modeling," ASME Paper 98-GT-175. ASME *Journal of Turbomachinery,* accepted for publication.

Eckert, E. R. G., 1976, "Analogies to Heat Transfer Processes," *Measurements in Heat Transfer,* E. R. G. Eckert and R. J. Goldstein, eds., Hemisphere, New York.

Metzger, D. E., Berry, R. A., and Benson, J. P., 1982a, "Developing Heat Transfer in Rectangular Ducts With Staggered Arrays of Short Pin Fins," ASME JOURNAL OF HEAT TRANSFER, Vol. 104, pp. 700–706.

Metzger, D. E., and Haley, S. W., 1982b, "Heat Transfer Experiments and Flow Visualization of Arrays of Short Pin Fins," ASME Paper 82-GT-138.

Metzger, D. E., Fan, Z. X., Shepard, W. B., 1982c, "Pressure Loss and Heat Transfer Through Multiple Rows of Short Pin Fins," *Heat Transfer 1982,* Vol. 3, Hemisphere, New York, pp. 137–142.

Metzger, D. E., Fan, C. S., and Haley, S. W., 1984, "Effects of Pin Shape and Array Orientation on Heat Transfer and Pressure Loss in Pin Fin Arrays," ASME *Journal of Engineering for Gas Turbines and Power,* Vol. 106, pp. 252–257.

Metzger, D. E., and Sheppard, W. B., 1986, "Row Resolved Heat Transfer Variations in Pin Fin Arrays Including Effects of Non-Uniform Arrays and Flow Convergence," ASME Paper 86-GT-132.

Simoneau, R. J., and VanFossen, G. J., 1984, "Effect of Location in an Array on Heat Transfer to a Short Cylinder in Crossflow," ASME JOURNAL OF HEAT TRANSFER, Vol. 106, pp. 42–48.

Sparrow, E. M., and Ramsey, J. W., 1978, "Heat Transfer and Pressure Drop for a Staggered Wall-Attached Array of Cylinders with Tip Clearance," *Int. J. Heat Mass Transfer,* Vol. 21, pp. 1369–1378.

VanFossen, G. J., 1982, "Heat Transfer Coefficient for Staggered Arrays of Short Pin Fins," ASME *Journal of Engineering for Gas Turbine and Power,* Vol. 104, pp. 268–274.

Zukauskas, A. A., 1972, "Heat Transfer from Tubes in Cross Flow," *Advances in Heat Transfer,* Vol. 8, pp. 116–133.

Constructal Trees of Convective Fins

A. Bejan
J. A. Jones Professor of Mechanical Engineering,
e-mail: abejan@aduke.edu
Fellow ASME

N. Dan

Department of Mechanical Engineering and Materials Science,
Duke University,
Durham, NC 27708-0300

This paper extends to the field of convective heat transfer the constructal theory *of optimizing the access of a current that flows between one point and a finite-size volume, when the volume size is constrained. The volume is bathed by a uniform stream. A small amount of high-conductivity fin material is distributed optimally through the volume, and makes the connection between the volume and one point (fin root) on its boundary. The optimization proceeds in a series of volume subsystems of increasing sizes (elemental volume, first construct, second construct). The shape of the volume and the relative thicknesses of the fins are optimized at each level of assembly. The optimized structure emerges as a tree of fins in which every geometric detail is a result of minimizing the thermal resistance between the finite-size volume and the root point (source, sink). Convection occurs in the interstitial spaces of the tree. The paper shows that several of the geometric details of the optimized structure are robust, i.e., relatively insensitive to changes in other design parameters. The paper concludes with a discussion of constructal theory and the relevance of the optimized tree structures to predicting* natural *self-organization and self-optimization.*

1 Constructal Theory

Constructal theory is the thought that the geometric form visible in natural flow systems is generated by (i.e., it can be deduced from) a single principle that holds the rank of law (Bejan, 1996, 1997a, b). The *constructal law* was first stated for open (flow) systems: "For a finite-size system to persist in time (to live), it must evolve in such a way that it provides easier access to the imposed currents that flow through it." This statement has two parts. First, it recognizes the natural tendency of imposed currents to construct shapes, i.e., paths of optimal access through constrained open systems. The second part accounts for the evolution (i.e., improvements) of these paths, which occurs in an identifiable *direction that is time itself.*

The above formulation of the constructal law refers to a system with imposed flow streams, in and out. If the system is isolated and initially in a state of internal nonequilibrium, it will create optimal geometric paths for its internal currents. The constructal law then is the statement that the isolated system selects and optimizes its internal structure (flow paths) to maximize its speed of approach to equilibrium (uniformity, no flow, death).

The constructal law was conceived as a purely theoretical way of accounting for the billions and billions of natural patterns that have been recognized empirically as "self-organization" and "self-optimization." Some of these patterns (e.g., tree networks) have been subjected to the descriptive (not theoretical) technique of fractal geometry.

The constructal optimization of paths for internal currents was first proposed in the context of urban growth (Bejan, 1996) and pure heat conduction (Bejan, 1997a, b). In the latter, the channels were inserts of high thermal conductivity in a background medium (the interstitial material) that had lower thermal conductivity. The volume generated heat at every point, and was cooled from a single point (the sink). The method was since extended to fluid flow (Bejan, 1997c; Bejan and Errera, 1997) by recognizing the heterogeneity associated with low-resistance flow through tubes embedded through a diffusive material with higher resistance (e.g., Darcy flow). Additional extensions of the method are reviewed in Bejan (1997b, d) and Section 6.

In his Donald Q. Kern award lecture, Kraus (1997) showed that complex networks of fins constitute an important class of heat transfer devices that can be analyzed based on the linear transformations involving the solutions to the individual fin equations. The most common type of fin network is the "tree," in which several fins are attached to a central stem that makes the ultimate connection between the convective space and the wall (the fin root). This is an important heat transfer augmentation technique in the cooling of electronics packages, where it is also known as the "fin bush" or the "fin tower" (Kraus, 1997; Hamburgen, 1986). Most recently, the same structure has generated interest in chemical engineering (Lin and Lee, 1997a) and entropy generation minimization (Lee and Lin, 1995; Lin and Lee, 1997b), where the analyses were based on concepts of fractal geometry.

Kraus' (1997) lecture on fin networks coincides with the development of constructal theory as a method of optimizing geometrically the heat-flow path between one point and a finite-size volume, and a physics principle for the existence of geometrical form in natural systems far from equilibrium. This coincidence is an excellent opportunity to optimize the geometry of a fin tree from the constructal point of view, because the very reason for the existence of the fin tree in engineering is the maximization of the thermal conductance between the root point and the fixed volume (with convective flow) that is allocated to that point.

The objective of the present paper is to optimize the architecture (shapes, structure, dimensions) of a tree of fins by using constructal theory. It is to take the constructal method out of the field of conduction, pure conduction and pure fluid mechanics, where it has been applied until now, and to extend it to volume-constrained systems in which the transfer of heat at the smallest (interstitial) scales is by convection. Unlike in the fin-tree studies mentioned in the above paragraphs, the focus of the present paper is on geometric optimization, not on analysis. We are interested in a simple and robust method that leads not only to the optimal architecture of the point-to-volume heat path, but also the existence of the fin tree as the visible component of that path.

2 Elemental System

For simplicity, we consider the two-dimensional volume of frontal area A and length W, where W is aligned with the freestream (U_∞, T_∞) (Fig. 1(a)). The problem consists of distributing optimally through this volume a fixed amount of high-conductivity (k_p) material, which takes heat from one spot on the

Contributed by the Heat Transfer Division for publication in the JOURNAL OF HEAT TRANSFER. Manuscript received by the Heat Transfer Division, Oct. 1, 1998; revision received, Apr. 5, 1999. Keywords: Finned Surfaces, Geometry, Heat Transfer, Optimization, Thermodynamics. Associate Technical Editor: T. F. Chung.

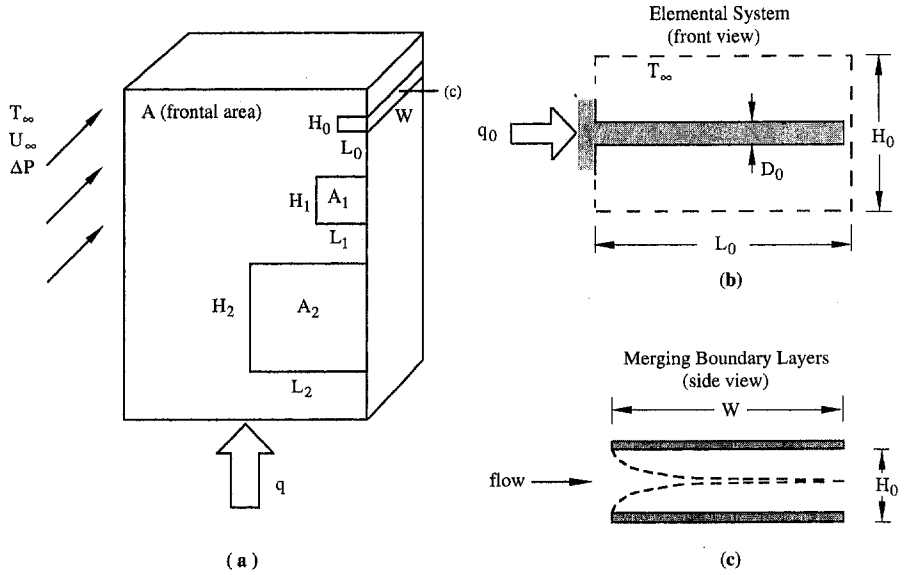

Fig. 1 (*a*) Volume (AW) serving as convective heat sink for a concentrated heat current (q), and (*b*) the smallest volume element defined by a single plate fin

boundary and discharges it throughout the volume. We may think of the boundary spot as the external surface of an electronic module that must be cooled. In this case the volume AW is the space that is allocated for the purpose of cooling the module by forced convection. This volume constitutes an overall constraint.

As in the conduction applications of the constructal method, we start the space-filling optimization sequence from the smallest finite size scale. The smallest system (the "elemental system" in constructal terminology) consists of a two-dimensional volume H_0L_0W, in which there is only one blade of k_p material (Fig. 1(*b*)). The thickness of this blade is D_0. Heat is transferred from one boundary spot (T_0, at the root of the fin) to the entire elemental volume. If we neglect the heat transfer through the fin tip, and if we adopt the most common unidirectional fin conduction model based on the assumptions listed by Gardner (1945), then the heat transfer rate is

$$\frac{q_0}{(T_0 - T_\infty)W} = (2k_pD_0h_0)^{1/2} \tanh\left[\left(\frac{2h_0}{k_pD_0}\right)^{1/2} L_0\right]. \quad (1)$$

Unlike the conduction applications of the constructal method, where it was possible to optimize the shape of the elemental volume, in the present problem the thickness of the elemental volume (H_0) is fixed because it is the same as the optimal spacing between two successive D_0-thick plate fins. The spacing is optimal when the laminar boundary layers that develop over the sweep length W became thick enough to touch at the trailing edge of each plate fin (Watson et al., 1996). This feature is illustrated in Fig. 1(*c*). Specifically, the optimal spacing ($H_0 - D_0 \sim H_0$) is determined uniquely by the swept length W and the pressure difference ΔP maintained across the swept volume (Bejan and Sciubba, 1992),

$$\frac{H_0}{W} \cong 2.73\left(\frac{\mu\alpha}{W^2\Delta P}\right)^{1/4}. \quad (2)$$

Using the solution reported in Bejan (1995), it can be shown that the minimized thermal resistance that corresponds to this spacing is also characterized by an average heat transfer coefficient that is given approximately by

$$h_0 \cong 0.55\,\frac{k}{W}\left(\frac{W^2\Delta P}{\mu\alpha}\right)^{1/4}. \quad (3)$$

The factor ΔP that appears in Eqs. (2), (3) refers to the pressure difference that is maintained in the W direction (e.g., by a fan), where $H_0 \times L_0$ is the cross section of a duct. If the H_0-wide channel is open to one side (the side that would connect the tips of two successive fins), and if the entire assembly is immersed in a stream of velocity U_∞, then Eqs. (2), (3) are adequate if ΔP is replaced by the dynamic pressure associated with the free stream, $\Delta P \cong \rho U_\infty^2/2$. The correctness of Eqs. (2), (3) in correlating the optimal spacing between parallel plates immersed in a freestream has been demonstrated numerically (e.g., Morega and Bejan, 1994).

Nomenclature

A = frontal area, m^2
A_p = frontal area occupied by the fin profile, m^2
D = fin thickness, m
h = heat transfer coefficient, W/m^2K
$\hat{h}$ = dimensionless heat transfer coefficient, Eq. (27)
H = height, m
k = fluid thermal conductivity, W/mK
k_p = fin thermal conductivity, W/mK
L = length, m
n = number of constituents in an assembly
q = heat current, W
$T_{0,1,2}$ = root temperature, K
T_∞ = freestream temperature, K
U_∞ = freestream velocity, m/s
W = width, m
α = fluid thermal diffusivity, m^2/s
ΔP = pressure difference, bar
μ = viscosity, kg/sm
ρ = fluid density, kg/m^3
ϕ = volume fraction of fin material, $\phi = A_p/A$
Φ = dimensionless parameter proportional to ϕ, Eq. (14)
$(\,)_m$ = maximized once
$(\,)_{mm}$ = maximized twice
$(\,)_0$ = elemental system
$(\,)_1$ = first construct
$(\,)_2$ = second construct
$(\tilde{\ })$ = dimensionless variables, Eqs. (6)–(8), (11), and (15)–(17)
$(\hat{\ })$ = dimensionless variables, Eq. (26)

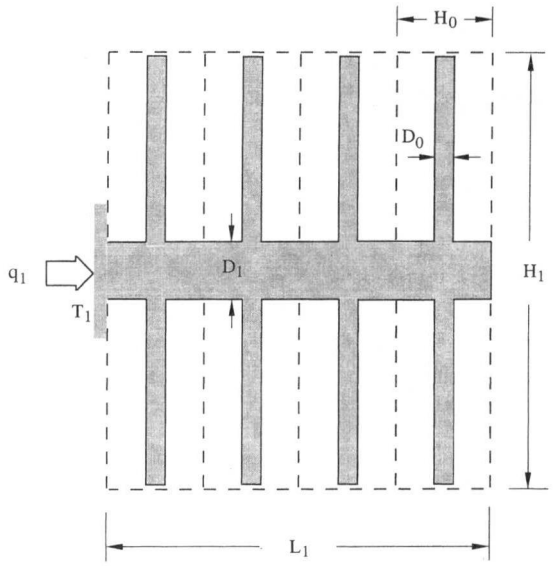

Fig. 2 The first assembly consisting of a large number of elemental volumes (Fig. 1(*b*))

We now proceed toward larger scales by recognizing that at the elemental level the h_0 and H_0 values provided by Eqs. (2), (3) are two known constants. The known and fixed scales of the smallest volume element are essential features of the constructal method of minimizing the flow resistance between a volume and one point (Bejan, 1997a, b). The length L_0 will be determined next, based on the optimization of the first construct, because it is equal to half of the transversal dimension of the first construct ($L_0 = H_1/2$, Fig. 2).

3 First Construct

The next volume subsystem is the first assembly of constant frontal area $H_1L_1 = A_1$, which is shown in Fig. 2. The shape of this volume (H_1/L_1) is free to vary. The assembly is defined by a central blade of thickness D_1, which is connected to all the elemental volumes that are needed to fill the A_1W volume. Note that the D_1 blade connects the roots of all the D_0 fins. When the number of elemental volumes in this assembly is large, the cooling effect provided by the D_0 fins is distributed almost uniformly along the D_1 stem. In this limit the D_1 stem functions as a fin immersed in a convective medium with constant heat transfer coefficient. The effective heat transfer coefficient of this medium (h_1) can be deduced from Eq. (1) by noting that each q_0 current flows out of the D_1 blade through an area of size H_0W. In other words, we combine $h_1 = q_0/[H_0W(T_0 - T_\infty)]$ with Eq. (1) and $L_0 = H_1/2$, and obtain

$$h_1 = \frac{1}{H_0}(2k_pD_0h_0)^{1/2}\tanh\left[\left(\frac{2h_0}{k_pD_0}\right)^{1/2}\frac{H_1}{2}\right]. \quad (4)$$

The D_1 blade functions as a fin with insulated tip, therefore we write cf. Eq. (1)

$$\frac{q_1}{(T_1 - T_\infty)W} = (2k_pD_1h_1)^{1/2}\tanh\left[\left(\frac{2h_1}{k_pD_1}\right)^{1/2}L_1\right]. \quad (5)$$

We will show that the geometry of the first assembly represented by Eqs. (4) and (5) has two degrees-of-freedom. The search for the optimal geometry is aided by the introduction of the dimensionless quantities

$$\tilde{q}_1 = \frac{q_1}{(T_1 - T_\infty)Wh_0H_0} \quad \tilde{h}_1 = \frac{h_1}{h_0} \quad (6)$$

$$\tilde{D}_0 = \frac{D_0k_p}{h_0H_0^2} \quad \tilde{D}_1 = \frac{D_1k_p}{h_0H_0^2} \quad (7)$$

$$\tilde{H}_1 = \frac{H_1}{H_0} \quad \tilde{L}_1 = \frac{L_1}{H_0}. \quad (8)$$

Equations (4) and (5) become

$$\tilde{h}_1 = (2\tilde{D}_0)^{1/2}\tanh\left[(2\tilde{D}_0)^{-1/2}\tilde{H}_1\right] \quad (9)$$

$$\tilde{q}_1 = (2\tilde{D}_1\tilde{h}_1)^{1/2}\tanh\left[\left(\frac{2\tilde{h}_1}{\tilde{D}_1}\right)^{1/2}\tilde{L}_1\right]. \quad (10)$$

There are two constraints that must be satisfied. First, the volume constraint $H_1L_1 = A_1$ now reads

$$\tilde{H}_1\tilde{L}_1 = \tilde{A}_1. \quad (11)$$

The total frontal area of all the k_p blades is

$$A_{p,1} = D_1L_1 + n_1D_0L_0 \quad (12)$$

where n_1 is the number of elemental systems contained by the first assembly, $n_1 = 2L_1/H_0$. The k_p material in constraint (12) assumes the dimensionless form

$$\Phi_1 = \frac{\tilde{D}_1}{\tilde{H}_1} + \tilde{D}_0 \quad (13)$$

in which we wrote Φ_1 for the design parameter that accounts for the volume fraction $\phi_1 = A_{p,1}/A_1$ occupied by the high-conductivity material,

$$\Phi_1 = \phi_1\frac{k_p}{h_0H_0}. \quad (14)$$

The objective is to maximize the $\tilde{q}_1$ expression of Eq. (10) subject to Eqs. (9), (11) and (13), and to determine the optimal geometry represented by the aspect ratios H_1/L_1 and D_1/D_0. Figure 3 shows that $\tilde{q}_1$ can be maximized twice, by selecting the two aspect ratios: their optimal values are approximately $(H_1/L_1)_{opt} \sim 2$ and $(D_1/D_0)_{opt} \sim 4$. The exact results of this double maximization procedure are reported in Figs. 3–5 as functions of $\tilde{A}_1$ and Φ_1.

The lower part of Fig. 3 shows that the optimal aspect ratio of the assembly is approximately 2 in the entire ($\tilde{A}_1$, Φ_1) range that we considered. This is a robust optimization result, which also agrees numerically with a corresponding shape optimum in tree networks for heat conduction (Bejan, 1997a, b). An alternate presentation of the optimal shape information of Fig. 3 is the optimal number of elemental systems, which is shown in the upper part of Fig. 4. Recall that $n_{1,opt} = 2L_{1,opt}/H_0$. The large $\tilde{A}_1$ values used on the abscissa are required by the geometric relation $A_1 \gg H_0^2$. The large Φ_1 values are due to the factor k_p/h_0H_0 on the right side of Eq. (14), in spite of the fact that the volume fraction ϕ_1 is generally small. To see the origin of the large Φ_1 values, assume that the fluid and its velocity are such that Eq. (2) yields $H_0/W = 0.1$. The corresponding result deduced from Eq. (3) using for k the thermal conductivity of room-temperature air is $h_0W = 0.38$ W/mK. Next, in Eq. (14) we substitute for k_p the thermal conductivity of commercial copper, and obtain $\Phi_1 \cong \phi_1 \cdot 10^4$.

The second geometric feature that was optimized is the ratio of the two plate thicknesses, which is shown in the lower part of Fig. 4. The ratio $(D_1/D_0)_{opt}$ varies as $(D_1/D_0)_{opt} \cong 1.4\tilde{A}_1^{1/2}$ when $\Phi_1 \gtrsim 10^3$. The effect of the volume fraction Φ_1 is weak. Most interesting is that the two graphs of Fig. 4 are very similar: the optimal ratio of fin thicknesses is almost equal to the optimal number of elemental systems assembled. This means that in the first construct the cross section for fin conduction is conserved in going from the elemental constituents to the central stem, i.e., $n_1D_0 \cong D_1$.

Figure 5 shows the results obtained for the twice-maximized overall heat transfer rate of the first assembly, $\tilde{q}_{1,max}$. This quantity

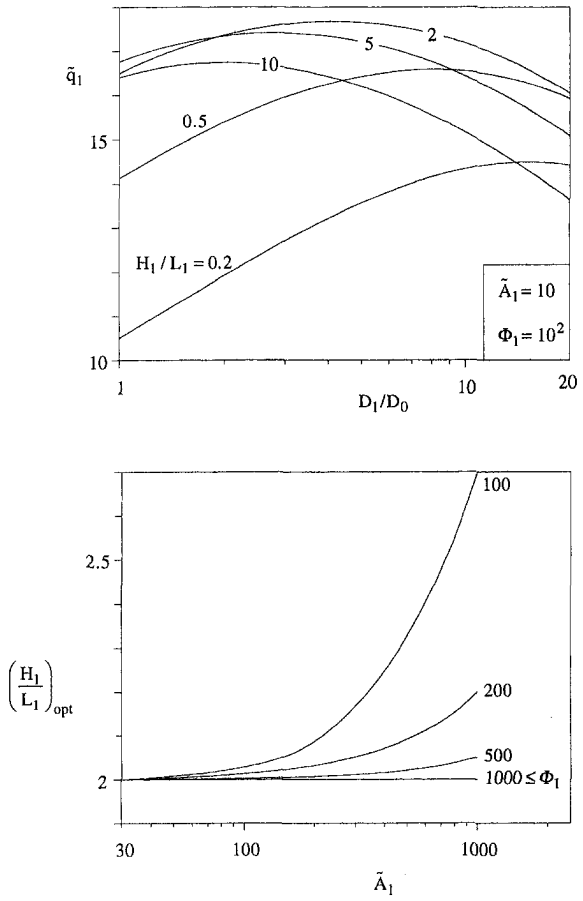

Fig. 3 The double maximization of the overall thermal conductance, and the optimal shape of the first assembly

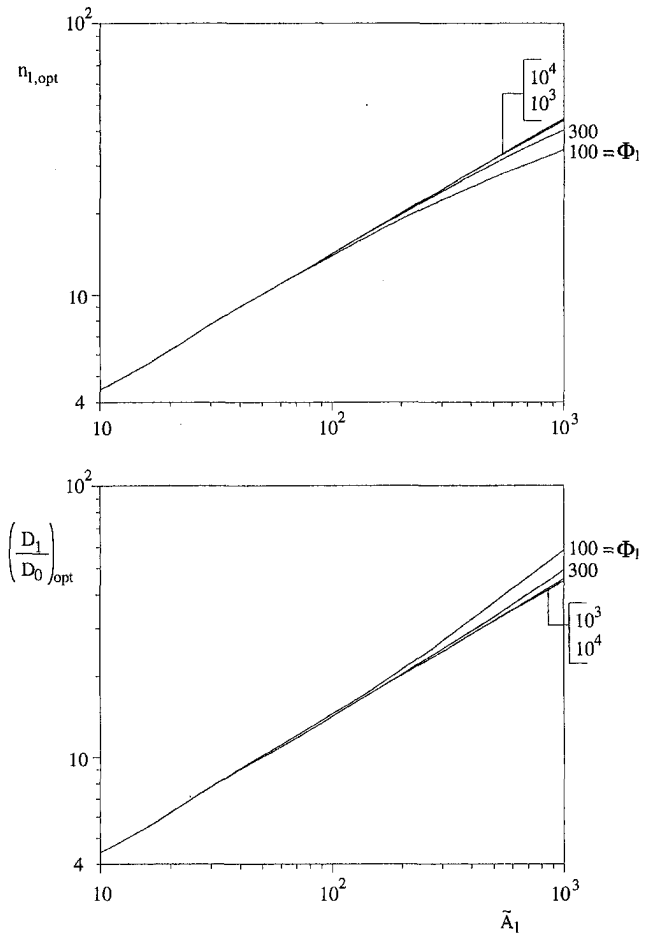

Fig. 4 The optimal number of elemental volumes and the optimal ratio of the plate thicknesses in the first assembly

is almost proportional to $\tilde{A}_1$, i.e., proportional to the size of the volume allocated for the removal of the heat current q_1 by convection. The Φ_1 effect is weaker but not negligible: The heat transfer rate decreases as the amount of high-conductivity material decreases. The effects of the volume size ($\tilde{A}_1$) and fin material (Φ_1) on the heat transfer rate are not unexpected: More space and more fin material mean more heat transfer.

In Fig. 6 we show the evolution of the twice-optimized geometry of the first assembly, while the size parameter $\tilde{A}_1$ increases at constant volume fraction of fin material ($\Phi_1 = 1000$). In other words, the amount of fin material increases in proportion to the volume occupied by the fin tree. The drawing was made by assuming that $\phi_1 = 0.1$, or $\Phi_1 = 10^4\phi_1$ as in the preceding numerical example. Each frame was drawn to scale in order to show the growth of the volume occupied by the assembly. The role of unit length is played by the thickness of the elemental volume (H_0), which is constant according to the discussion that followed Eqs. (2), (3). The exhibited structures were selected to correspond to even values of n_1; the corresponding values of the assembly size parameter $\tilde{A}_1$ are also listed.

Two invariant features of the fin trees of Fig. 6 are worth noting. The overall shape of the volume occupied by the assembly does not change much as the volume size increases. This feature is an illustration of the $(H_1/L_1)_{opt}$ results reported in Fig. 3. Another feature is the thickness of the elemental fin, $D_{0,opt}$, which does not vary from frame to frame in Fig. 6. It can be verified that when the elemental spacing H_0 and the volume fraction Φ_1 are fixed, the optimized thickness of the elemental fins is also fixed. If in the preceding numerical example $H_0 = 0.5$ cm, then $D_{0,opt} = 0.025$ cm in all the frames of Fig. 6. The corresponding thickness of the trunk, $D_{1,opt}$, takes the values 0.25 cm, 0.5 cm, and 0.75 cm as $n_{1,opt}$ increases.

Future work may address various improvements and refinements of the classical fin conduction model that was used in setting up the analysis and optimization. For example, the effects of temperature-dependent thermal conductivity, radiative heat transfer, and spatially varying heat transfer coefficient can be incorporated at the elemental level, while paying a penalty through the increased complexity of the analysis, and the need for numerical work even at the elemental level. Equation (2) will most definitely have to be determined numerically for the refined model.

We were not able to compare the presently optimized geome-

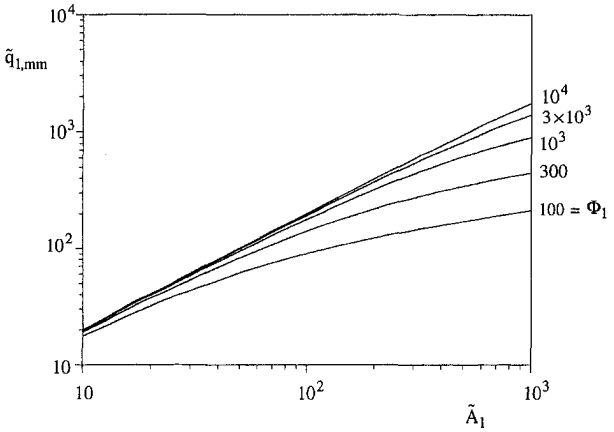

Fig. 5 The twice-maximized heat transfer rate of the first assembly

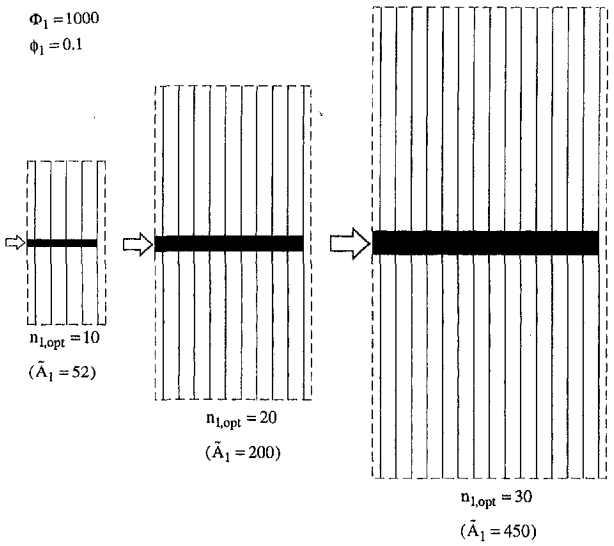

Fig. 6 The changes exhibited by the optimized architecture of the first assembly as the total volume increases

tries (e.g., Fig. 6) with designs based on earlier methods, because, contrary to Eqs. (2), (3), the earlier methods are based on the assumption that the heat transfer coefficient is a constant not affected by the fin-to-fin spacing. The work that we published on optimal plate-to-plate spacings (e.g., Morega and Bejan, 1994) showed that the approach based on Eqs. (2), (3) leads to superior designs in a wide variety of plate surfaces and heating configurations. Another reason why the present architectures can be expected to perform better than the classical designs that fill the same volume, is that the present architectures have been *optimized* while holding the volume fixed. Any other structure that fills the same volume and uses the same amount of fin material will have a higher resistance than the structures optimized based on the constructal method. For the same reason the constructal method is not applicable if the volume that houses the fin assembly is infinite. The global constraints (volume, material) are essential elements of constructal theory (Bejan, 1997a, b).

4 Second Construct

We concluded that the twice-maximized heat transfer rate accommodated by the first assembly increases monotonically as the volume ($\tilde{A}_1$) increases (Fig. 5). Can this increase continue forever? No, because the invariant thickness of the elemental fins leads eventually to mechanical problems (bending, vibrations, warpage). There is also the effect of the fin efficiency, which decreases as the fin contact area increases. This second effect was taken into account at every optimization step via Eq. (1).

In this section we study an alternative to increasing heat transfer rate by increasing the volume of the fin tree. That alternative is to increase the *complexity* of the fin tree. This step is presented in Fig. 7, which shows the "second assembly" recommended by constructal theory. The volume of the second assembly (A_2) contains a large number ($n_2 \gg 1$) of the first assemblies optimized in the preceding section. In other words, we write $A_2 = n_2 A_1$, or

$$\tilde{A}_2 = n_2 \tilde{A}_1 \tag{15}$$

where $\tilde{A}_2 = A_2/H_0^2$. In the following optimization analysis we fix the second-assembly size $\tilde{A}_2$, and vary the number n_2. This means that the size of each first assembly varies according to n_2.

The second assembly is held together by a central stem of length L_2 and thickness D_2. The total heat transfer rate q_2 can be estimated by treating the stem as a fin with insulated tip. The analysis repeats the steps shown at the start of Section 3. The "effective" heat transfer coefficient h_2 comes from $q_{1,mm} = h_2 H_1 W(T_1 - T_\infty)$, which becomes

$$\tilde{h}_2 = \frac{\tilde{q}_{1,mm}}{\tilde{H}_1} \tag{16}$$

where $\tilde{h}_2 = h_2/h_0$. For the heat transfer rate through the root of the D_2-thick stem we start with the equivalent of Eq. (5) and arrive at

$$\tilde{q}_2 = (2\tilde{D}_2\tilde{h}_2)^{1/2} \tanh\left[\left(2\frac{\tilde{h}_2}{\tilde{D}_2}\right)^{1/2}\tilde{L}_2\right] \tag{17}$$

where $\tilde{q}_2 = q_2/[(T_2 - T_\infty)Wh_0H_0]$, $\tilde{D}_2 = D_2k_p/[h_0H_0^2]$, and $\tilde{L}_2 = L_2/H_0$. Note that the nondimensionalization of the second-assembly variables is the same as for the first assembly, Eqs. (6)–(8).

Next, we constrain the amount of k_p material in the second assembly. This volume is proportional to the shaded area $A_{p,2}$ shown in Fig. 7,

$$A_{p,2} = \left(L_2 - \frac{H_1}{2}\right)D_2 + n_2 A_{p,1}. \tag{18}$$

The length of the D_2 fin is taken as $(L_2 - H_1/2)$ instead of L_2, because it is the distance from the root (T_2) to the connection (T_1) with the D_1 fins of the farthest first constructs. In other words, the insulated nose of length $H_1/2$ of the D_2 fin of Fig. 7 is left out: This feature is shown in Fig. 8, where only two first constructs are shown. The dimensionless constraint that corresponds to Eq. (18) is

$$\Phi_2 = \left(\tilde{L}_2 - \frac{\tilde{H}_1}{2}\right)\frac{\tilde{D}_2}{\tilde{A}_2} + \Phi_1 \tag{19}$$

where $\Phi_2 = \phi_2 k_p/[h_0H_0]$ and $\phi_2 = A_{p,2}/A_2$. The second geometric constraint is the total volume (or frontal area A_2), which has the following dimensionless form:

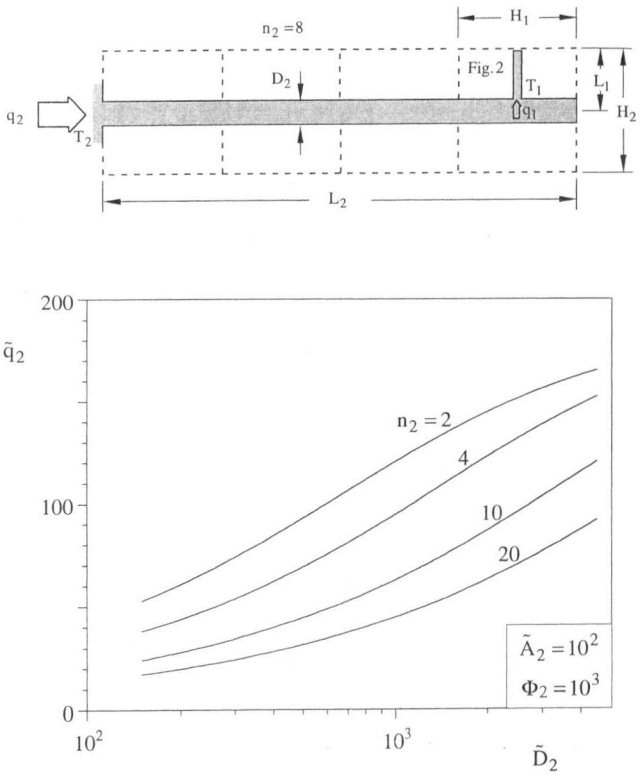

Fig. 7 Second assembly consisting of a large number of shape-optimized first assemblies, and the effect of n_2 and $\tilde{D}_2$ on the heat current

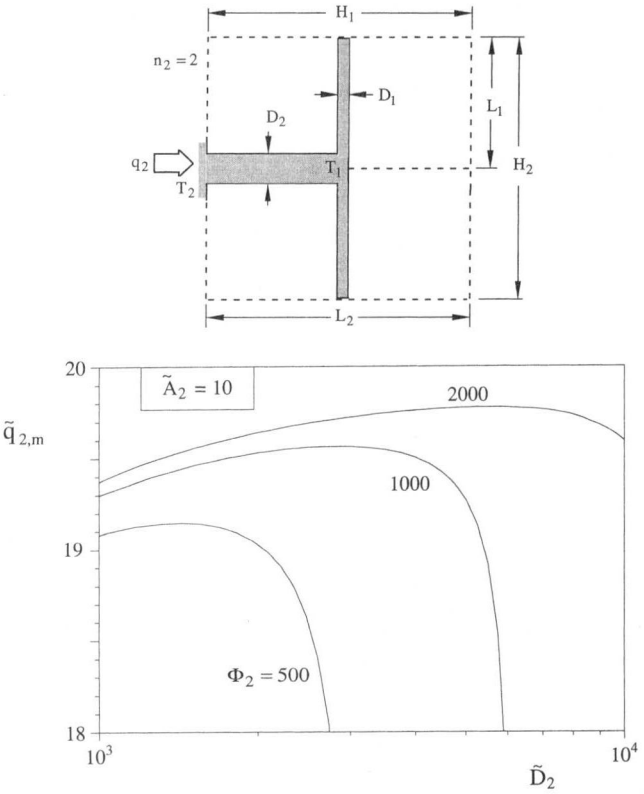

Fig. 8 Second assembly containing only two first assemblies, and the optimization with respect to the thickness of the central stem

$$\tilde{H}_2\tilde{L}_2 = \tilde{A}_2. \tag{20}$$

We hold the second-assembly parameters $\tilde{A}_2$ and Φ_2 fixed. For the shape of each first assembly we use the optimal value deduced in the preceding section, $(H_1/L_1)_{opt}$ = function $(\tilde{A}_1, \Phi_1)$. Under these conditions, the geometry of the second assembly has two degrees-of-freedom. The overall shape H_2/L_2 and the stem thickness $\tilde{D}_2$. It can be shown that to vary H_2/L_2 is equivalent to varying n_2,

$$\frac{H_2}{L_2} = \frac{4}{n_2}\left(\frac{L_1}{H_1}\right)_{opt}. \tag{21}$$

Other useful relations are $\tilde{H}_1 = 2\tilde{L}_2/n_2$ and $\tilde{L}_2 = (L_2/H_2)\tilde{A}_2^{1/2}$.

The two degrees-of-freedom are reflected in the function $\tilde{q}_2(n_2, \tilde{D}_2)$, which was determined numerically and illustrated for one case in the lower part of Fig. 7. Important in this figure is the effect of n_2: The heat transfer rate is larger when n_2 is smaller. Other cases $(\tilde{A}_2, \Phi_2)$ show the same trend. This leads to a powerful conclusion that also holds for conduction trees (Bejan, 1997a, b): The best second assembly contains only two first constructs; note that $n_2 = 2$ is the smallest number of first constructs that can be mounted on the D_2 stem of the second construct. Pairing (or bifurcation)—the integer 2—emerges as one of the many results of the minimization of thermal resistance in point-to-volume flow.

The conclusion that $n_2 = 2$ also means that we must revise the analysis, because Eqs. (16), (17) are based on the model of Fig. 7 in which it was assumed that $n_2 \gg 1$. The appropriate structure for a second assembly with only two first assemblies is shown in Fig. 8, where it is worth noting that the length of the D_2 stem stops at $L_2/2$. The frontal shape was drawn almost square because we know that each first assembly will have a frontal aspect ratio $(H_1/L_1)_{opt} \cong 2$, in accordance with Fig. 3. The analysis of the flow of heat into the assembly of Fig. 8 consists of writing that the overall temperature difference $(T_2 - T_\infty)$ is equal to the drop of temperature along the D_2 stem, plus the temperature difference sustained by one of the first assemblies,

$$T_2 - T_\infty = \frac{q_{2,m}}{2}\left(\frac{L_2}{k_p D_2 W} + \frac{1}{\tilde{q}_{1,mm} W h_0 H_0}\right) \tag{22}$$

or, in dimensionless terms,

$$\tilde{q}_{2,m} = 2\left(\frac{\tilde{L}_2}{\tilde{D}_2} + \frac{1}{\tilde{q}_{1,mm}}\right)^{-1}. \tag{23}$$

Note that the heat current $q_{2,m}$ has been maximized once already, in the move from an arbitrary n_2 (Fig. 7) value to the best value of $n_2 = 2$ (Fig. 8). In place of the k_p-material constraint (19) we now have

$$\Phi_2 = \frac{\tilde{H}_1\tilde{D}_2}{2\tilde{A}_2} + \Phi_1. \tag{24}$$

The shape of the second assembly is no longer variable, because it is set by the shape of the first assembly, $(H_2/L_2) = 2(L_1/H_1)_{opt}$. There is only one degree-of-freedom in the design of the structure of Fig. 8, namely, the stem thickness $\tilde{D}_2$.

The numerical maximization of the $\tilde{q}_{2,m}$ expression of Eq. (23) begins with the observation that $\tilde{q}_{1,mm}$ is a known function of $\tilde{A}_1$ and Φ_1, cf. Fig. 5. In view of the volume constraint $\tilde{A}_1 = \tilde{A}_2/2$ and the constraint (24), this means that $\tilde{q}_{2,m}$ = function $(\tilde{D}_2, \tilde{A}_2, \Phi_2)$ where $\tilde{A}_2$ and Φ_2 are parameters. The existence of the $\tilde{q}_{2,m}$ maximum with respect to $\tilde{D}_2$ is demonstrated in the lower part of Fig. 8, in an operation that was repeated for many combinations of $\tilde{A}_2$ and Φ_2. The key results are the twice-maximized heat current of the second assembly (Fig. 9) and the optimal thickness of its central stem (Fig. 10, top). Both $\tilde{q}_{2,mm}$ and $\tilde{D}_{2,opt}$ increase with $\tilde{A}_2$ and Φ_2; for example, the formula $\tilde{D}_{2,opt} = 0.9\tilde{A}_2^{1/2}\Phi_2$ correlates the data of Fig. 10 (top) with a relative error of 4.02 percent. These trends are expected, because they parallel what we learned from the optimization of the first assembly.

More interesting is the lower part of Fig. 10, which is a replotting of the data of the upper part as the ratio $(D_2/D_1)_{opt}$. We arrive in this way at new invariant in the geometry of the second assembly. The stem thickness increases by a nearly constant factor in going from the first assembly to the second assembly. A similar characteristic was found in the optimization of the second assembly of the conduction heat tree (Bejan, 1997a, b). In the present case, the ratio $(D_2/D_1)_{opt}$ is equal to 3.54 with a standard deviation of 0.048. The slight lack of smoothness in some of the results of Fig. 10 is due to the shallow maximum of the $\tilde{q}_{2,m}$ versus $\tilde{D}_2$ curves (Fig. 8); we prescribed discrete values when varying $\tilde{D}_2$, and the ratio D_2/D_1 may not have been read with sufficient accuracy from the data. Nevertheless, the constancy of the ratio $(D_2/D_1)_{opt}$ and the large size of the $(\tilde{A}_2, \Phi_2)$ domain are worth noting.

Figure 11 provides a pictorial summary to the analysis and

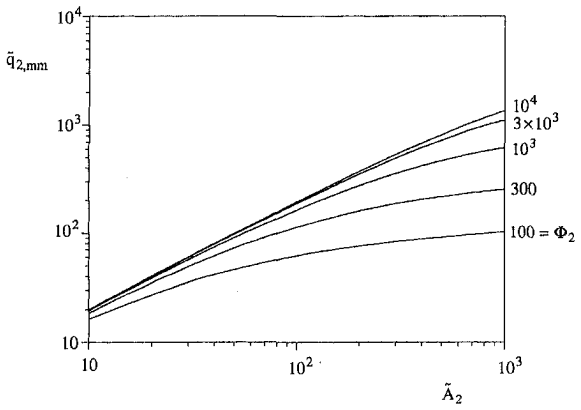

Fig. 9 The twice-maximized heat transfer rate of the second assembly

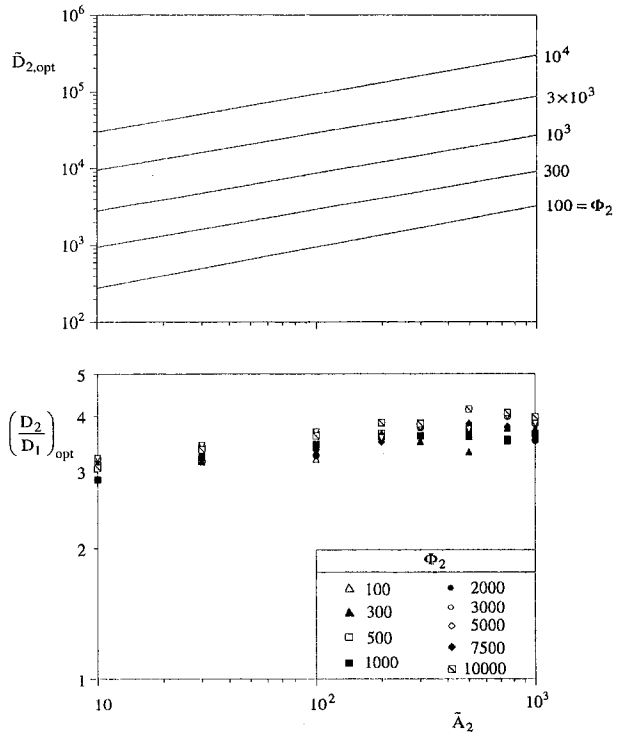

Fig. 10 The optimal thickness of the main stem of the second assembly, and the stem thickness ratio $(D_2/D_1)_{opt}$

quantitative results developed in this section. The figure is a scale drawing of the optimized architecture of the second assembly, when the volume fraction and properties of the fin material are characterized by $\Phi_2 = 10^3$ and $\phi_2 = 0.1$. As in Fig. 6, the construction is based on the assumption that the external flow is such that the elemental spacing is $H_0 = 0.5$ cm. This leads to $D_{0,opt} = 0.014$ cm. The two frames of Fig. 11 show how the architecture changes as the tree of fins spreads over a larger volume. The shape of the occupied volume remains almost the same (square frontal area), and the thickness of the central stem increases relative to the other fin thicknesses. The calculated fin thicknesses $(D_0, D_1, D_2)_{opt}$ are indicated under each frame of Fig. 11.

5 Numerical Simulation and Optimization of Two-Dimensional Conduction in a Tree of Fins

As an alternative to the analytical approach pursued until now, we subjected the first-assembly configuration to direct numerical simulation of the two-dimensional heat flow pattern. With reference to the domains defined in Figs. 2 and 8, we solved the equation for conduction in the solid

$$\frac{\partial^2 \hat{T}}{\partial \hat{x}^2} + \frac{\partial \hat{T}}{\partial \hat{y}^2} = 0 \tag{25}$$

where x and y are the horizontal and vertical directions, respectively. The y-axis coincides with the symmetry plane of the central stem. The dimensionless variables are

$$(\hat{x}, \hat{y}) = (x, y)/H_0 \quad \hat{T} = (T - T_\infty)/(T_b - T_\infty) \tag{26}$$

where T_b is the base temperature of the central stem (e.g., T_1 in Fig. 2). Because of symmetry, we solved Eq. (25) only in the upper half of the solid domain ($\hat{y} > 0$), using $\partial \hat{T}/\partial \hat{y} = 0$ as boundary condition along the plane of symmetry ($\hat{y} = 0$). The condition at the root of the central stem is $\hat{T} = 1$. The remaining surfaces are in contact with fluid, and are characterized by the boundary condition $-\partial \hat{T}/\partial \hat{n} = \hat{h}\hat{T}$, where $\hat{n}$ is the normal to the surface ($\hat{x}$ or $\hat{y}$), and $\hat{h}$ is the dimensionless heat transfer coefficient (assumed uniform):

$$\hat{h} = h/(k_p/H_0). \tag{27}$$

We solved this two-dimensional steady conduction problem for many, slightly different configurations subjected to the same overall size constraint ($\tilde{A}_1$) and total volume of solid (ϕ_1). For this purpose we used a commercial finite elements code (FIDAP, 1993), because we needed a rapid and reliable solver capable of handling many simulations. The accuracy of this code was tested and documented in an earlier study of conduction in tree-shaped domains (Ledezma et al., 1997).

In the optimization of the first construct we used the constraints $\tilde{A}_1 = 50$ and $\phi_1 = 0.1$, and selected the case $\hat{h} = 4$, which corresponds to a set of plausible physical values: $H_0 = 1$ cm, $k_p = 150$ W/mK and $h = 6$ W/m^{2}K. To start with, we fixed the ratio $D_1/D_0 = 12$, and maximized the overall conductance of the assembly with respect to n_1 and H_1/L_1. The overall conductance was defined as $\hat{q}'''_{base}/(\hat{T}_b - \hat{T}_{min}) = -\hat{k}(\partial \hat{T}/\partial \hat{x})|_{base}/(1 - \hat{T}_{min})$, where $\hat{q}'''_{base} = q'''_{base}H_0/[k_p(T_b - T_\infty)]$ is the base heat flux, $\hat{k} = k/k_p$ is the dimensionless fluid thermal conductivity, and $\hat{T}_{min}$ is the lowest temperature on the fin (the upper right corner in Fig. 2). We found that the optimal combination is $n_1 = 6$ and $H_1/L_1 = 1.6$. In the next phase, we set $n_1 = 6$ and $H_1/L_1 = 1.6$, maximized the conductance with respect to D_1/D_0, and found the optimal ratio $D_1/D_0 = 7.2$. These values (n_1, H_1/L_1, D_1/D_0) agree already (approximately) with the results anticipated analytically, which were not very sensitive to Φ_1 (e.g., Figs. 3 and 4). To refine the optimal configuration further, we would have to repeat this cycle several times, by starting with the recently optimized value of D_1/D_0.

In the optimization of the second construct we used the same constraints, $\tilde{A}_2 = 50$, $\phi_1 = 0.1$ and $\hat{h} = 4$. We relied on the conclusion derived from Fig. 7 (bottom) and set $n_2 = 2$, which left four degrees-of-freedom: n_1, H_2/L_2, D_1/D_0 and D_2/D_1. In the first phase we fixed $D_2/D_1 = 4$ and $D_1/D_0 = 10$, and sought the maximization of the overall conductance with respect to n_1 and H_2/L_2. We used $n_1 = 4$, 6, 8, 10, and 12, and found no maximum: The conductance increases monotonically as n_1 decreases. The optimal external shape is $H_2/L_2 = 3.0$ when $n_1 = 4$, and $H_2/L_2 = 2.6$ when $n_1 = 10$. Next, for each n_1 value we fixed H_2/L_2 at its optimal value, and then optimized D_1/D_0 and D_2/D_1. We found that for $4 \le n_1 \le 12$ the optimal ratios for maximal overall conductance are adequately represented by $D_1/D_0 = 12$ and $D_2/D_1 = 3$.

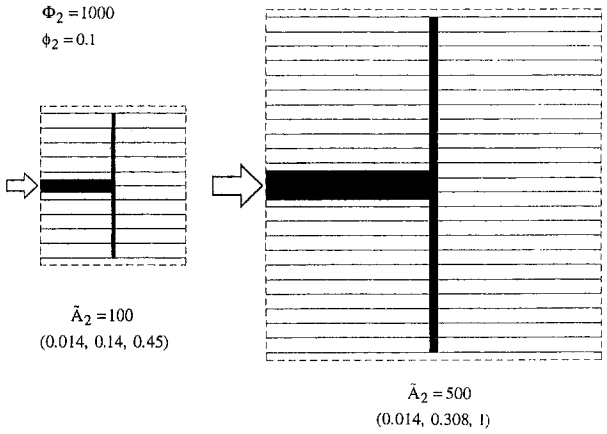

Fig. 11 The changes exhibited by the optimized architecture of the second assembly as the total volume increases. The three numbers listed in parentheses represent, in order, D_0, D_1 and D_2, expressed in centimeters.

6 Tree Structures and Their Relevance to Natural Design

The chief characteristic of the fin network analysis presented in this paper is that the same analysis—the same geometric optimization—is repeated at each level of assembly. We illustrated this characteristic of constructal theory by considering only the elemental volume (Section 2), the first construct (Sections 3 and 5) and the second construct (Section 4). The procedure could be continued toward higher-order assemblies, however, an interesting feature characterizes the trees of fins optimized in this paper. If we compare on the same basis ($\tilde{A}_2 = \tilde{A}_1$ and $\Phi_2 = \Phi_1$) the twice-maximized conductances of the second construct (Fig. 9) and the first construct (Fig. 5), we find virtually no difference between the two when $\tilde{A}_{1,2}$ is of the order of 10 or smaller. At larger $\tilde{A}_{1,2}$ values, the second construct is inferior to the first construct. This finding represents a departure from the trend known in pure-conduction and pure-fluid heat trees. It is also an invitation to more realistic modeling, numerical and experimental work in the future, on the performance and optimization of first and second constructs. When the elemental fin dimensions are small enough, realistic formulations may also be constructed by modeling the elemental fin-to-fin spaces as pores in a fluid-saturated medium with different fluid and solid temperatures (e.g., Lee and Vafai, 1999).

Practical constraints must be taken into account before continuing the optimization with more complex constructs. Manufacturing constraints will certainly rule the decision with regard to the complexity of the fin design (e.g., first construct versus second construct). In this regard, the practical value of the work presented in this paper has two facets. First, the constructal optimization represents a *strategy* (a road map) for pursuing optimal structure in a design subjected to volume constraint. Second, many of the geometrical features that are determined by this method are *robust* (relatively insensitive to other design parameters): Examples are the optimized shapes of the frontal areas and the ratios between successive fin thicknesses.

These robust geometric shapes (ratios) are also found in other volume-to-point flow optimization studies (Bejan, 1997a–d; Bejan and Tondeur, 1998), and are now intrinsic parts of the geometrical form "tree." They explain why natural tree networks "look the same," even though, from the river basin to the lung, their function and fine details are not identical. In other words, the geometrical form "tree" that we know so well is more than a "stick figure" that connects one point to a finite size volume (an infinity of points). It is also a structure that is based on building blocks (constructs, assemblies) that are relatively "round" (not very slender), in which the high-conductivity fibers become thicker in fixed proportions in going from one construct to the next assembly of constructs.

The relevance of constructal theory to explaining shape and structure in natural nonequilibrium (flow) systems is discussed further in Bejan, 1997b, d). The theory was extended more recently to three-dimensional tree networks (Bejan, 1997c; Ledezma and Bejan, 1998), time-dependent discharge from a volume to one point, as in river basins and lightning (Dan and Bejan, 1998; Errera and Bejan, 1998), turbulence and Bénard convection (Nelson and Bejan, 1998; Bejan, 1997b, 1998), dendritic crystals in rapid solidification (Bejan, 1997b), patterns of cracks in volumetrically shrinking solids (Bejan et al., 1998), street patterns and urban growth (Bejan and Ledezma, 1998), cross sections of ducts and rivers (Bejan, 1997b), and pulsating physiological processes such as breathing and heart beating (Bejan, 1997e). The road to new extensions and a compelling theory (a single law) of organization in nature is wide open.

Acknowledgment

This work was supported by the National Science Foundation.

References

Bejan, A., 1995, *Convection Heat Transfer,* 2nd Ed., John Wiley and Sons, New York, pp. 132–136.

Bejan, A., 1996, "Street Network Theory of Organization in Nature," *Journal of Advanced Transportation,* Vol. 30, No. 2, pp. 85–107.

Bejan, A., 1997a, "Constructal-Theory Network of Conducting Paths for Cooling a Heat Generating Volume," *International Journal of Heat and Mass Transfer,* Vol. 40, pp. 799–816.

Bejan, A., 1997b, *Advanced Engineering Thermodynamics,* 2nd Ed., John Wiley and Sons, New York.

Bejan, A., 1997c, "Constructal Tree Network for Fluid Flow between a Finite-Size Volume and One Source or Sink," *Revue Générale de Thermique,* Vol. 36, pp. 592–604.

Bejan, A., 1997d, "How Nature Takes Shape," *Mechanical Engineering,* Vol. 119, Oct., pp. 90–92.

Bejan, A., 1997e, "Theory of Organization in Nature: Pulsating Physiological Processes," *International Journal of Heat and Mass Transfer,* Vol. 40, pp. 2097–2104.

Bejan, A., 1998, "Questions in Fluid Mechanics: Natural Tree-Shaped Flows," ASME *Journal of Fluids Engineering,* Vol. 120, pp. 429–430.

Bejan, A., and Errera, M. R., 1997, "Deterministic Tree Networks for Fluid Flow: Geometry for Minimal Flow Resistance between a Volume and One Point," *Fractals,* Vol. 5, pp. 685–695.

Bejan, A., and Ledezma, G. A., 1998, "Streets Tree Networks and Urban Growth: Optimal Geometry for Quickest Access Between a Finite-Size Volume and One Point," *Physica A,* Vol. 255, pp. 211–217.

Bejan, A., and Sciubba, E., 1992, "The Optimal Spacing of Parallel Plates Cooled by Forced Convection," *International Journal of Heat and Mass Transfer,* Vol. 35, pp. 3259–3264.

Bejan, A., and Tondeur, D., 1998, "Equipartition, Optimal Allocation, and the Constructal Approach to Predicting Organization in Nature," *Revue Générale de Thermique,* Vol. 37, pp. 165–180.

Bejan, A., Ikegami, Y., and Ledezma, G. A., 1998, "Constructal Theory of Natural Crack Pattern Formation for Fastest Cooling," *International Journal of Heat and Mass Transfer,* Vol. 41, pp. 1945–1954.

Dan, N., and Bejan, A., 1998, "Constructal Tree Networks for the Time-Dependent Discharge of a Finite-Size Volume to One Point," *Journal of Applied Physics,* Vol. 84, pp. 3042–3050.

Errera, M. R., and Bejan, A., 1998, "Deterministic Tree Networks for River Drainage Basins," *Fractals,* Vol. 6, pp. 245–261.

FIDAP Theory Manual, 1993, V. 7.0, Fluid Dynamics International, Evanston, IL.

Gardner, K. A., 1945, "Efficiency of Extended Surfaces," *Transactions of the ASME,* Vol. 67, pp. 621–631.

Hamburgen, W. R., 1986, "Optimal Finned Heat Sinks," WRL Research Report 86/4, Digital, Western Research Laboratory, Palo Alto, CA.

Kraus, A. D., 1997, "Developments in the Analysis of Finned Arrays," the Donald Q. Kern Award Lecture, National Heat Transfer Conference, Aug. 11, Baltimore, MD.

Ledezma, G. A., and Bejan, A., 1998, "Constructal Three-Dimensional Trees for Conduction Between a Volume and One Point," ASME JOURNAL OF HEAT TRANSFER, Vol. 120, pp. 977–984.

Ledezma, G. A., Bejan, A., and Errera, M. R., 1997, "Constructal Tree Networks for Heat Transfer," *Journal of Applied Physics,* Vol. 82, pp. 89–100.

Lee, D. J., and Lin, W. W., 1995, "Second-Law Analysis on a Fractal-Like Fin under Crossflow," *AIChE Journal,* Vol. 41, pp. 2314–2317.

Lee, D.-Y., and Vafai, K., 1999, "Analytical Characterization and Conceptual Assessment of Solid and Fluid Temperature Differentials in Porous Media," *International Journal of Heat and Mass Transfer,* Vol. 42, pp. 423–435.

Lin, W. W., and Lee, D. J., 1997a, "Diffusion-Convection Process in a Branching Fin," *Chemical Engineering Communications,* Vol. 158, pp. 59–70.

Lin, W. W., and Lee, D. J., 1997b, "Second-Law Analysis on a Pin-Fin Array under Cross-Flow," *International Journal of Heat and Mass Transfer,* Vol. 40, pp. 1937–1945.

Morega, Al. M., and Bejan, A., 1994, "The Optimal Spacing of Parallel Boards with Discrete Heat Sources Cooled by Laminar Forced Convection," *Numerical Heat Transfer, Part A,* Vol. 25, pp. 373–392.

Nelson, R. A., Jr., and Bejan, A., 1998, "Constructal Optimization of Internal Flow Geometry in Convection," ASME JOURNAL OF HEAT TRANSFER, Vol. 120, pp. 357–364.

Watson, J. C., Anand, N. K., and Fletcher, L. S., 1996, "Mixed Convective Heat Transfer Between a Series of Vertical Parallel Plates with Planar Heat Sources," ASME JOURNAL OF HEAT TRANSFER, Vol. 118, pp. 984–990.

Augmented Heat Transfer in a Triangular Duct by Using Multiple Swirling Jets

J.-J. Hwang
Professor,
e-mail: jjhwhang@chu.edu.tw
Mem. ASME

C.-S. Cheng
Graduate Student

Department of Mechanical Engineering,
Chung-Hua University,
Hsinchu, Taiwan 300, R.O.C.

Measurements of detailed heat transfer coefficients on two principal walls of a triangular duct with a swirling flow are undertaken by using a transient liquid crystal technique. The vertex corners of the triangular duct are 45, 45, and 90 deg. The swirl-motioned airflow is induced by an array of tangential jets on the side entries. The effects of flow Reynolds number ($8600 \leqq Re \leqq 21000$) and the jet inlet angle (α = 75, 45, and 30 deg) are examined. Flow visualization by using smoke injection is conducted for better understanding the complicated flow phenomena in the swirling-flow channel. Results show that the heat transfer for α = 75 deg is enhanced mainly by the wall jets as well as the impinging jets; while the mechanisms of heat transfer enhancement for α = 45 and 30 deg could be characterized as the swirling-flow cooling. On the bottom wall, jets at α = 75 deg produce the best wall-averaged heat transfer due to the strongest wall-jet effect among the three angles (α) investigated. On the target wall, however, the heat transfer enhancements by swirling flow (α = 45 and 30 deg) are slightly higher than those by impinging jets (α = 75 deg). Correlations for wall-averaged Nusselt number for the bottom and target walls of the triangular duct are developed in terms of the flow Reynolds number for different jet inlet angles.

Introduction

In the modern gas turbine design, the trend is toward high inlet gas temperature (1400–1500°C) for improving thermal efficiency and power density. Since these temperatures are far above the allowable metal temperature, the gas turbine blades must be cooled in order to operate without failure. Various blade cooling methods have been developed over the years, for example, impingement cooling for the leading edge (Bunker and Metzger, 1990; Parsons, et al., 1998), and augmented convection by rib-turbulators for the mid-chord region (Chyu and Wu, 1989; Han, et al., 1991; Hwang, 1998) and by pin fins for the trailing edge (Chyu et al., 1998; Hwang et al., 1999). This investigation focuses on the leading edge cooling of blades, as shown in Fig. 1, and studies the heat transfer in a triangular duct with swirling flow created by multiple side-entry jets that are tangential to the inner surface of the duct.

Blum and Oliver (1967) measured the local heat transfer coefficients in an electrically heated tube with swirling flow. An initial swirl generator with four square slots was used to inject the gas tangentially into the tube. The heat transfer coefficients were derived from the tube wall temperature assuming a uniform heat flux and a linear temperature rise for the fluid. The directions of the flow were explored in the separate experiment. Ivanova (1967) and Narezhnyy and Sudarev (1971) used different swirl generators at the pipe inlet only, in the form of vane swirl generators and helically twisted inserts, respectively, to produce a free swirling flow in the test section. Both results indicated that the heat transfer rates were highly dependent on the inlet angle of the swirling flow. Lipina and Bergles (1969) carried out a test with full-length twisted tapes along the tube, with water as the working fluid. For a constant pumping power a comparison of swirling and straight flows indicated an improvement in heat transfer rate of the least 20 percent with swirling flows. Gutstein et al. (1970) used helical vane inserts along the heated tubular test section in which air was the working fluid. The heat transfer rates and pressure drops increased substantially as the insert pitch-to-tube diameter ratio decreased. Migay and Golubev (1970) carried out a theoretical analysis to predict the heat transfer coefficient based on the evaluation of the equivalent friction factors for free swirling flows. Results showed that the free swirling flow increases the heat transfer rate, and the present theoretical results and the experimental data were in satisfactory agreement. Senoo and Nagato (1972) used the swirling number to adequately correlate the friction coefficient measurements for swirling flow in pipes. Hay and West (1975) measured the local heat transfer coefficients for swirling flow generated by a slot jet at the upstream end of a pipe. Results showed that, at some locations, the heat transfer augmentation could be as much as eight times the value of a fully developed internal flow. Algrifri and Bhardwaj (1985) presented an analytical study of heat transfer characteristics in decaying turbulent swirling flow in a pipe. Heat transfer was predicted by assuming the flow to be a rotating slug, which was the case for the swirling flow generated by a short-twisted tape. Recently, a screw-shaped swirl cooling technique was used for blade leading edge cooling (Glezer et al., 1996, 1998; Hedlum et al., 1998), which showed improved cooling performance of a circular passage in comparison to conventional internal cooling method. Ligrani et al. (1998) performed a flow visualization study to examine the relation between the generation of Görtler vortices and the augmented heat transfer characteristics in the cooling passage. Huang et al. (1998) utilized a transient liquid crystal technique to measure the detailed heat transfer coefficients on a target wall with an array of orthogonal impinging jets. Three different crossflow directions are examined by changing the test section open ends. Results showed that the flow exiting from both sides of the test duct performed the best heat transfer on the target wall.

From the above review, it may be inferred that the related published data are mostly for a circular tube with either decaying or continuous swirling flow. However, the published literature contains little information about the heat transfer and fluid flow in a triangular duct with swirling flow. Strictly speaking, the detailed heat transfer coefficients in such kinds of ducts have not been reported yet. Therefore, the aim and objective of this study is to provide heat transfer characteristics in a triangular duct with swirl-motioned airflow induced by multiple jets from the side entry of

Contributed by the Heat Transfer Division for publication in the JOURNAL OF HEAT TRANSFER. Manuscript received by the Heat Transfer Division, Sept. 28, 1998; revision received, Apr. 12, 1999. Keywords: Augmentation, Heat Transfer, Impingement, Swirling, Turbines. Associate Technical Editor: J. C. Han.

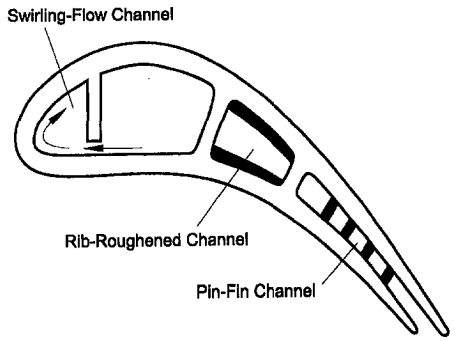

Fig. 1 Conceptual view of the swirling cooling at the leading edge of the turbine blade

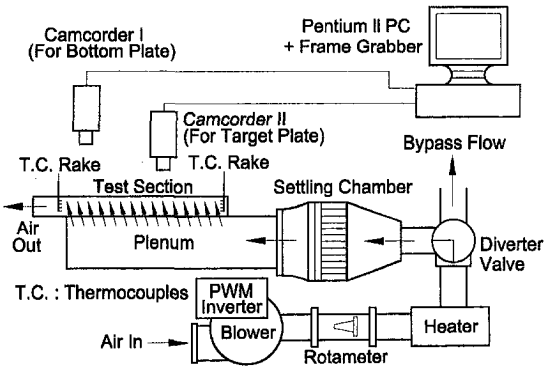

Fig. 2 Schematically drawing of the experimental apparatus

the duct. A transient liquid-crystal technique is employed to measure the local heat transfer on two principal walls of the triangular duct (jet wall exclusive). This technique is similar to that presented by Ekkad and Han (1995). During this work, the angle between the swirling jet and the duct axial direction and the Reynolds number (based on the duct hydraulic diameter and average velocity at duct exit) are varied from 30 deg $\leqq \alpha \leq$ 75 deg, and 8600 $\leqq$ Re $\leqq$ 21,000, respectively, to examine their effects on the heat transfer characteristics. Moreover, to better understand the mechanisms of heat transfer enhancement in triangular ducts with various jet inlet angles, smoke injection is used to visualize the secondary-flow structures in the swirling-flow channel.

Experimental Apparatus and Procedure

Apparatus. The entire apparatus shown schematically in Fig. 2 consists of an open airflow circuit, the test section, and an image-processing system. Air from a 5-hp blower passes through a rotameter that measures the volume flow rate of the air. Adjusting the motor speed via a PWM (pulse wave modulation) inverter controls the airflow rate. It then flows into an electric heater to be heated to a required temperature. The hot air from the heater subsequently traverses a settling chamber for reducing the possible noise, a plenum, and then flows through the swirling holes into the test section. Finally, the air exits from the straight outlet to the outside of building via an exhaust system. Figure 3 shows a detailed configuration of dimension and coordinate system of the test section. The test section associated with the plenum is made of Plexiglas®. The cross section of the test duct is an isosceles right triangle (i.e., 45, 45, and 90 degs). The triangular duct has a closed upstream end and the multiple jets are ejected from the plenum through the sidewall, which models the swirling cooling passage at the blade leading edge. The three walls of the triangular duct shown in Fig. 3(*a*) are referred to the divider wall, the bottom wall and the target wall, respectively, in the following discussion. The divider wall is 30 mm in height (also the bottom-wall width) and 10 mm in thickness (also the length of the jet hole). Fifteen swirled holes of 5-mm diameter (d) are drilled through the low end of the divider and ensure that their edges are tangent to the inner surface of the bottom wall. The angle between the jet flow and the axial direction (z) of the test duct is varied from α = 30 to 75 deg, and the jet-hole spacing is fixed at s = 15 mm. Note that in practical situations of leading edge cooling of blades, most heat is removed from two principal walls that form the vertex corner angle β, i.e., the bottom and target walls. Therefore, as shown in Fig. 3(*b*), only these two principal walls are coated with liquid crystals for heat transfer measurements.

The image-processing system includes two digital color cam-

Nomenclature

c_p = specific heat at constant pressure, kJ kg^{-1} K^{-1}
De = equivalent hydraulic diameter at the triangular duct, m
d = diameter of jet hole, Fig. 3, m
h = heat transfer coefficient, kJ m^{-2} K^{-1}
k = thermal conductivity of the duct wall material, W m^{-1} K^{-1}
k_f = air thermal conductivity, W m^{-1} K^{-1}
Nu = local Nusselt number, hDe/k_f
Nu_d = local jet Nusselt number, hd/k_f
$\overline{\text{Nu}}$ = area-averaged Nusselt number based on the duct hydraulic diameter
$\overline{\text{Nu}}_s$ = Nusselt number for fully developed smooth pipe flows, i.e., $\overline{\text{Nu}}_s = 0.023\ \text{Re}^{0.8}\ \text{Pr}^{0.4}$
$\overline{\text{Nu}}_d$ = area-averaged jet Nusselt number, i.e., $\overline{\text{Nu}}_d = \overline{\text{Nu}}(d/De)$
n = distance normal to the test surface, m
P = wall static pressure, kPa
Pr = Prandtl number
Re = Reynolds number, $U \cdot De/\nu$
Re_d = jet Reynolds number, $u \cdot d/\nu$
s = jet spacing, Fig. 3, m
T_m = mixed mainstream temperature, K
T_i = initial wall temperature, K
T_w = wall temperature, K
t = transient test time, s
U = mean throughflow velocity at the exit of the triangular duct, m s^{-1}
u = jet hole velocity, m s^{-1}
x, y, z = coordinate system of the test duct, Fig. 3

Greek Symbols

α = jet inlet angle, Fig. 3
α_w = thermal diffusivity of the duct wall material, m^2 s^{-1}
β = vertex angle between the target wall and the bottom wall, Fig. 3
ρ = air density, kg m^{-3}
γ = vertex angle between the target wall and the divider, Fig. 3
ν = viscosity of the air, m^2 s^{-1}
τ_j = time step, s

Subscripts

b = bulk mean
d = jet hole
i = initial
m = mainstream
s = smooth
w = wall

Superscripts

$^-$ = averaged

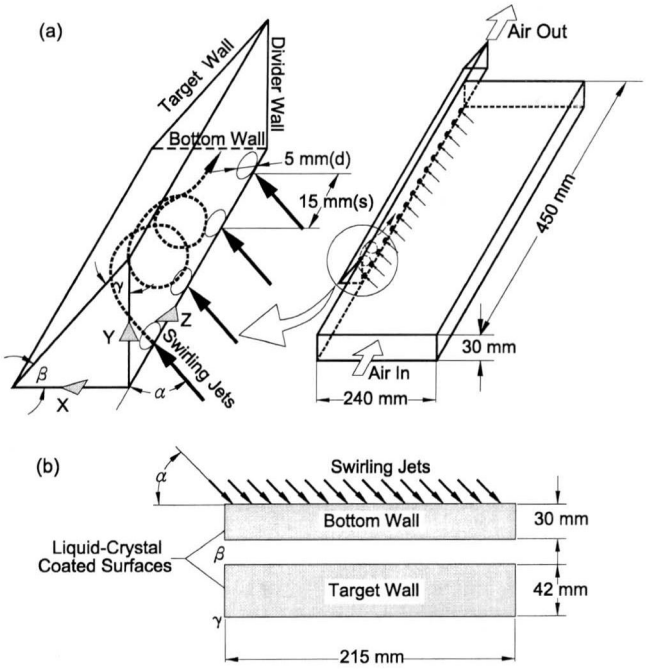

Fig. 3 Dimension and coordinate system of the test section

corders (SONY DCR-TRV7) and a frame grabber interface associated with a Pentium II PC. The camcorders view and record the color changes on the liquid-crystal coated surfaces during the transient test. The frame grabber interface is programmed to analyze the color changes using image-processing software. The software analyzes the picture frame by frame and simultaneously records the time lapse of the liquid crystals from colorless to green during the transient test.

Experimental Procedure. In contrast to the coating procedure used in Huang et al. (1998), the inner surfaces of the target and bottom walls are sprayed with a thin film of liquid crystals (Hallcrest, BW/R38C5W/C17-10) first and then the opaque background paints. Two camcorders view the color changes on the target and bottom surfaces, respectively, from outside. The calibration of color to temperature is carried out on a copper rod coated with liquid crystals (Vedula and Metzger, 1991). The liquid crystals are colorless at room temperature. They then change to red, green, blue, and finally colorless again during the heating process. The color-change temperatures to red, green, and blue are 38.2°C, 39.0°C and 43.5°C, respectively. Each test run is thermal transient, initiated by suddenly exposing the hot air to the test section, which results in a color change of the surface coatings. Before the test run, the hot air bypasses the test section so that the walls remain at the laboratory ambient temperature. The three-way ball valve keeps in the diverted position until a required mainstream temperature has been achieved in the bypass loop. Then, the valve turns to route the hot air into the test section and, simultaneously, the recorder is switched on to record the mainstream temperature history. Note that the diversion of the flow will lead to a little and instantaneous pulsation of the float in the rotameter due to an alternation of friction loss in the flow loops, which causes an uncertainty in the volume flow rate less than 3.0 percent. The image-processing system records the transition time for the color change to green, and transfers the data into a matrix of time of the color change over the entire surface. The time and temperature data are entered into a computer program to obtain the local heat transfer coefficient.

Data Analysis and Uncertainty. The local heat transfer coefficients over the test surface can be obtained by assuming one-dimensional transient conduction over a semi-infinite solid. The one-dimensional transient conduction, the initial condition, and boundary conditions on the liquid crystal coated surface are

$$k\frac{\partial^2 T}{\partial n^2} = \rho c_p \frac{\partial T}{\partial t} \tag{1}$$

$$\text{as } t = 0, \quad T = T_i; \quad \text{as } t > 0, \quad k\frac{\partial T}{\partial n} = h(T_w - T_m)$$

$$\text{at} \quad n = 0; \quad T = T_i, \quad \text{as } n \to \infty.$$

The surface temperature response to the equation above is shown as

$$\frac{T_w - T_i}{T_m - T_i} = 1 - \exp\left(\frac{h^2\alpha_w t}{k^2}\right) \cdot \text{erfc}\left(\frac{h\sqrt{\alpha_w t}}{k}\right). \tag{2}$$

The heat transfer coefficient h can be calculated from the above equation, by knowing the wall temperature (T_w), the initial surface temperature (T_i), the oncoming mainstream temperature (T_m), and the corresponding time (t) required to change the coated-surface color to green at any location. The time required for the color changes in a typical run is about 15 to 90 seconds, depending on the location, mainstream temperature, and throughflow rate. This testing time is so short that the heat flow can hardly penetrate the depth of Plexiglas®. Therefore, the assumption of the semi-infinite solid on the test surface is valid. The local mainstream temperature at any axial location of the swirling channel is linearly interpolated between the inlet and outlet temperatures measured by two thermocouple rakes (each has four beads, Fig. 2). Since T_m is time-dependent, the solution in Eq. (2) should be modified. First, the mainstream temperature history is simulated as a series of time-step changes. Then, the time-step changes of the mainstream temperature are included in the solution for the heat transfer coefficient using Duhamel's superposition theorem. The solution for the heat transfer coefficient at every location is therefore represented as eject

$$T_w - T_i = \sum_{j=1}^{n} \left\{ 1 - \exp\left[\frac{h^2\alpha_w(t-\tau_j)}{k^2}\right] \times \text{erfc}\left[\frac{h\sqrt{\alpha_w(t-\tau_j)}}{k}\right]\right\} [\Delta T_{m(j,j-1)}] \tag{3}$$

where $\Delta T_{m(j,j-1)}$ and τ_j are the temperature and time-step changes obtained from the recorder output. The maximum uncertainty of h is an order of ±6.8 percent. The individual contributions to the uncertainty of h for the measured or physical properties are: time of the color change t, ±2.8 percent, mainstream temperature T_m, ±3.0 percent, and wall material properties α_w and k, ±3.0 percent.

Two kinds of the nondimensional heat transfer coefficients are presented in this work. One is the Nusselt number based on the duct parameters, i.e.,

$$\text{Nu} = hDe/k_f. \tag{4a}$$

The value above can give an indication of the extent of heat transfer enhancement by the multiple swirling jet flows with respect to the nonswirling fully developed pipe flow. The other is the so-called jet Nusselt number, i.e.,

$$\text{Nu}_d = hd/k_f. \tag{4b}$$

This reduction is widely used in the impinging-cooling study, which can provide the information of heat transfer enhancement on a plate by an individual jet. By using the estimation method of Kline and McClintock (1958), the maximum uncertainties are 8.5 percent and 8.6 percent for Nu and Nu_d, respectively.

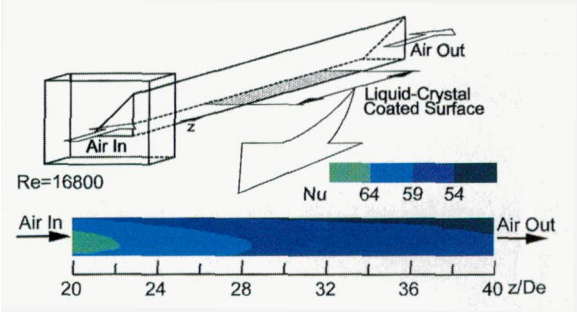

Fig. 4 Detailed heat transfer coefficient distribution on the bottom wall of the triangular duct with straight flow

Results and Discussion

As a verification of the experimental procedure, the present results obtained for a triangular duct with straight flow were compared with some previous results. Figure 4 shows the transient liquid-crystal measurements of detailed distributions of the heat transfer coefficient on the bottom wall of the triangular duct. Airflow of a fixed throughflow rate (Re = 16,800) is introduced from an upstream plenum through a sharp-edge inlet into the triangular duct. Results displayed are between $20 \leqq z/De \leqq 40$. It is seen from this figure that the heat transfer coefficient is gradually decreased along the axial distance, especially the region before $z/De \leqq 30$, indicating that the flow is still developing in this region. In addition, tongue-shaped distributions of the iso-Nusselt number are slightly deflected toward to the right-angled corner, which reflects the difference in the sidewall effects caused by the altitude and the hypotenuse of the triangular duct. Figure 5 shows the comparison between the present triangular-duct results and those in a circular pipe (Dittus-Boelter correlation) and in a triangular duct (Zhang, et al., 1994). The dashed line represents the well-known Dittus-Bolter correlation for fully developed pipe flow, and the triangular symbols are the results of Zhang et al. (1994) in a 35–55–90 deg triangular duct. The present data shown in this figure are taken the average results between $z/De = 36$ and 40. It is seen that the Nusselt numbers measured are in qualitative agreement with the Dittus-Boelter correlation and the data of Zhang et al. (1994). Quantitatively, present data are slightly higher than the correlation, typically about 12 percent. The trend is very consistent with the previous results of Mills (1962) and Kays and Crawford (1980), both which showed that the entrance effect at axial location of 40 diameters from a sharp-edge inlet is about 15 percent. Generally speaking, the agreement for the comparison above is satisfactory, indicating that the data obtained by the present transient method are reliable and representative of the steady-state conditions.

Flow Distributions. The local heat transfer characteristics are closely related to the flow rate from each jet hole. Therefore, the static pressure differences between the plenum and the triangular test section are measured to determine the jet flow rates. The local pressure distributions are measured by placing the static pressure taps inside the test section and the plenum. A typical axial distribution of the static pressure difference between the plenum and the test duct is shown in Fig. 6(*a*) for Re = 13,200, and while the corresponding distribution of the flow rate through each jet hole is displayed in Fig. 6(*b*). As the flow enters the plenum from one end of the channel, it is expected that there is an uneven distribution of the flow through each hole. However, from this figure, it is evident that the entrance effect is small. At the most, the jet flow rate increases slightly with increasing z/d. Strictly speaking, the volume flow rate of the on each jet hole has an average value of 23.2 l/min ± 8.2 percent. In addition, the sum of each jet flow rate is checked with the total flow rate measured by the rotameter, and a satisfactory agreement is achieved.

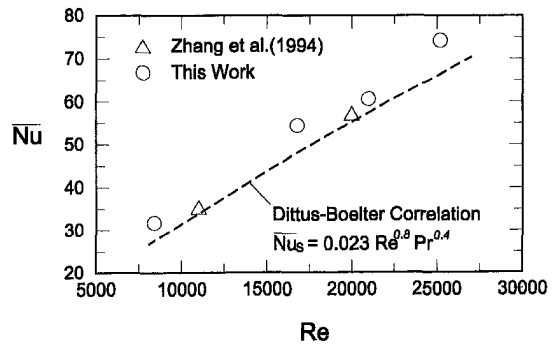

Fig. 5 Comparison of the present Nusselt number averaged over $36 \leqq z/De \leqq 40$ with previous results obtained from fully developed pipe and triangular duct flows

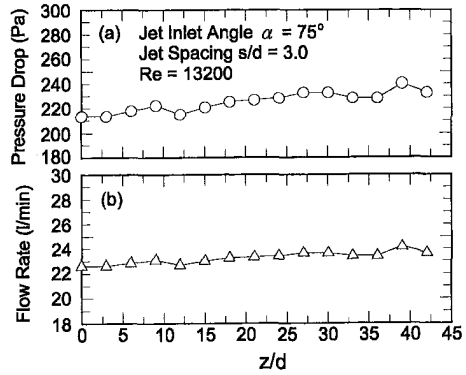

Fig. 6 Static pressure drop and jet flow rate of the triangular duct along the axial distance

Detailed Heat Transfer Coefficient Distribution. Figures 7–9 show the detailed heat transfer coefficients on the bottom and target walls for three different jet inlet angles, i.e., α = 75, 45, and 30 deg. Each graph has three different Reynolds numbers (Re = 8600, 11,700, and 16,900). The results are presented for axial

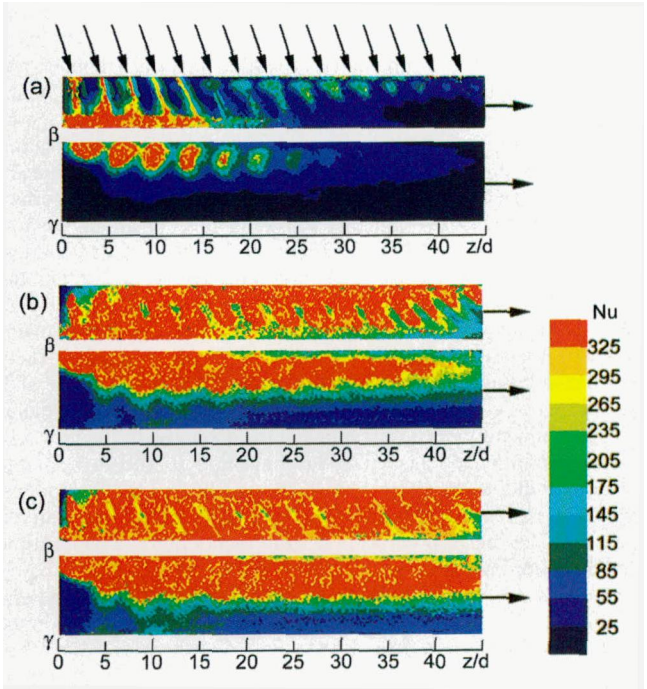

Fig. 7 Detailed heat transfer coefficient distribution on the bottom and target walls for α = 75 deg, (*a*) Re = 8600, (*b*) Re = 11,700, and (*c*) Re = 16,900

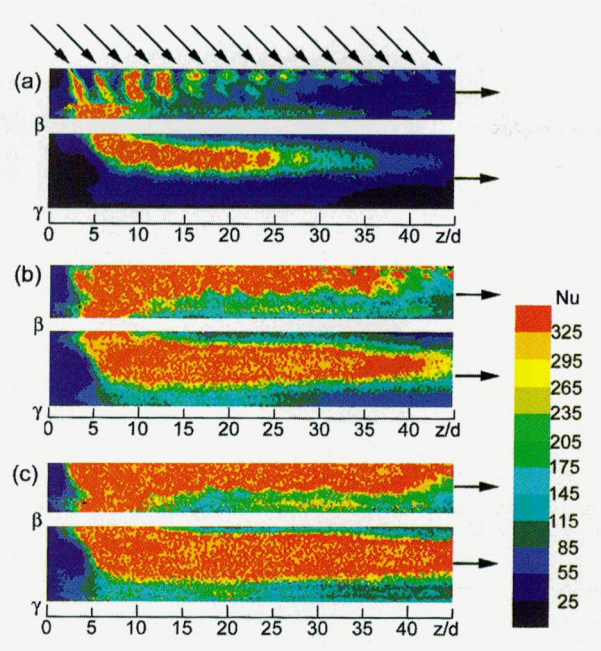

Fig. 8 Detailed heat transfer coefficient distribution on the bottom and target walls for α = 45 deg, (*a*) Re = 8600, (*b*) Re = 11,700, and (*c*) Re = 16,900

distance from $z/d = 0$ to 45 over the entire span of the target and bottom walls. The locations of two corners of the triangular duct, i.e., β and γ, are denoted on each figure. In addition, the small arrows indicate the locations and directions of the jets and the throughflow (large arrow) exits from the right end of the graphs.

The primary effect of increasing Re is to increase Nu on both the target and bottom walls monotonically. Such a behavior is indicative of a consistency of flow pattern as flow rate is increased. Figure 7 presents the results of $\alpha = 75$ deg. Near the upstream closed end ($z/d = 0$) of the duct, high heat transfer bends span across the bottom wall from the jet entry to the corner β because of the strong wall-jet effect. Meanwhile, the target wall at the corresponding axial locations has round zones of high heat transfer due to jet impingement. As the flow moves downstream, the penetration depth of the wall jet on the bottom wall is reduced gradually and the wall jet direction is slightly deflected toward the z-direction due to crossflow. On the target wall, the crossflow not only reduces the impingement heat transfer but also moves the apparent impingement away from the leading-edge apex (β). In addition, a dead zone (very poor heat transfer) exists on the target wall adjacent the corner γ. It is interesting to note that the previous work of Bunker and Metzger (1990) also found a similar trend of the off-axis impingement as the jets aimed normally at a symmetric leading-edge apex and exited from the chordwise direction. In contrast to the present work, however, the off-axis impingement in their work is due to an existence of recirculating flow in the leading-edge apex but is not due to the crossflow effect.

As for the results of $\alpha = 45$ deg (Fig. 8), the Nu distributions are somewhat different from those for $\alpha = 75$ deg, especially on the target wall. The wall-jet phenomenon on the bottom wall for $\alpha = 45$ deg is less apparent than those for $\alpha = 75$ deg since the jets for $\alpha = 45$ deg lift off from the bottom wall (will be shown later). In addition, the impinged traces on the target wall can be hardly observed for $\alpha = 45$ deg. This is because the jet momentum in the span direction is reduced, such that, in turn, the penetrability of the wall jet across the bottom wall is lessened. Consequently, the corresponding jets impinging on the target wall are weakened. In fact, in this circumstance, the bottom and target walls of the triangular duct are washed by the swirled motion of multiple jet flows, rather than enhanced by the wall/impinged jets. Further, comparing Figs. 7 and 8 reveals that the high heat transfer band along the z-direction on the target wall moves toward the span center as α changes from 75 to 45 deg. Consequently, the dead zone on the target wall adjacent the corner angle γ for $\alpha = 75$ deg has been greatly improved. However, in the meanwhile, another dead zone appears near the corner angle β, which is caused by the angle of the jets away from that corner. These phenomena become more significant for $\alpha = 30$ deg in Fig. 9. Note that the region of poor heat transfer near the upstream closed end of the duct has been enlarged as α decreases.

According to the detailed Nu distributions above, generally speaking, the mechanisms of heat transfer enhancement in the triangular duct for $\alpha = 45$ and 30 deg could be characterized as a swirl-flow cooling, while the duct for $\alpha = 75$ deg is cooled by wall/impinged jets. To further confirm the heat transfer mechanisms above, flow visualizations of $\alpha = 75$ and 45 deg are undertaken and are compared in Fig. 10. The smoke generated by a smoke generator is injected into the plenum before the blower is turned on. The flow visualization is realized by a laser sheet which is constructed by passing a Helium-Neon laser beam (60 mW, Spectra Physics 120) through a glass rod (Hwang et al., 1998). A 35-mm single-lens reflect camera is focused on the illuminating plane. Photographs of the flow are taken on Agfa film with a shutter speed of 1/1000 s for the capture of highly fluctuating flows. Figures 10(*a*) and (*b*) show the secondary-flow structures of $\alpha = 75$ and 45 deg, respectively. The laser sheet cuts across the center of the second hole ($z/d = 4.5$) from the upstream end. It is seen that the jet for $\alpha = 75$ deg washes thoroughly the bottom wall and directly impinges on the target plate near the corner β. A counterrotating vortex pair seems to be created around the upper portion of the duct. These vortices are, in fact, transient and relatively stagnant as compared to the jet flow, resulting in a lower heat transfer near the corner γ (Fig. 7). Note also that the Görlter vortices along the concave surface of a circular swirl chamber that were observed by Ligrani et al. (1998) are not found in the present sharp-edge triangular duct. As for $\alpha = 45$ deg (Fig. 10(*b*)), rather than directly impinging on the target wall, the jet lifts off from the bottom wall and turns into the main stream, resulting in a swirl motion of the fluid in the duct center. This single swirl flow presents continually, and is much stronger than the double swirl motions in Fig. 10(*a*). In addition, the swirling jet contacts the target wall at about one-third span distance from the corner β,

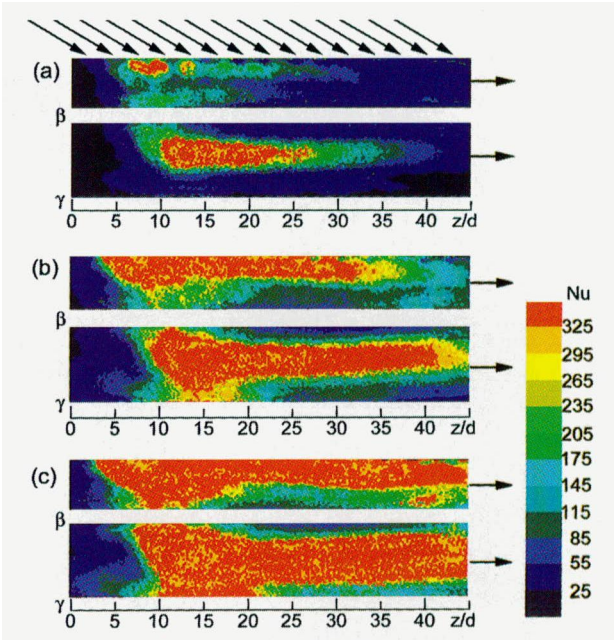

Fig. 9 Detailed heat transfer coefficient distribution on the bottom and target walls for α = 35 deg, (*a*) Re = 8600, (*b*) Re = 11,700, and (*c*) Re = 16,900

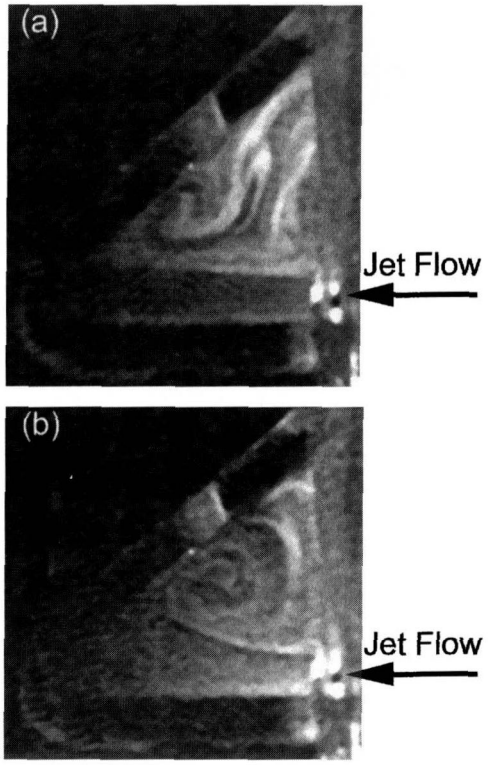

Fig. 10 Smoke-injection visualization of the secondary flow structures of the triangular duct at z/d = 4.5, (*a*) α = 75 deg (*b*) α = 45 deg

which gives an explanation that high heat transfer region moves toward the span center of the target plate as α reduces from 75 to 45 deg. In summary, the jets appear to be coalescing with the decrease in jet-inlet angle. There seems to some kind of increased mixing induced by the swirl for shallow angle. Further efforts about the measurement in mean and fluctuating velocities are required to improve the understanding of the turbulent transportation mentioned above.

Span-Averaged Nusselt Number Distribution. The effects of Reynolds number on the span-averaged Nusselt number distributions along the axial distance of the duct are shown in Figs. 11 to 13 for different jet inlet angles. The upper and lower parts of each graph represent the results of the bottom and target walls, respectively. An array of arrows on each graph indicates the

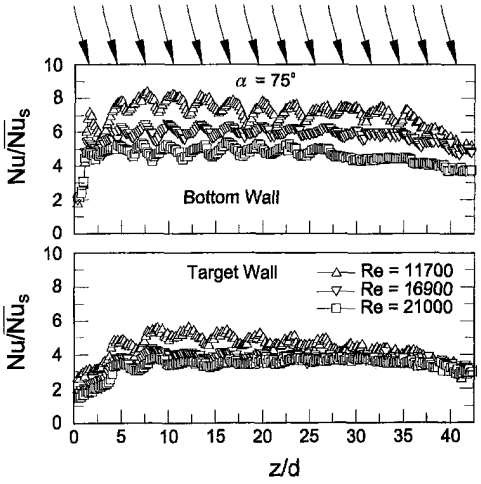

Fig. 11 Span-averaged Nusselt number distribution along axial distance for α = 75 deg

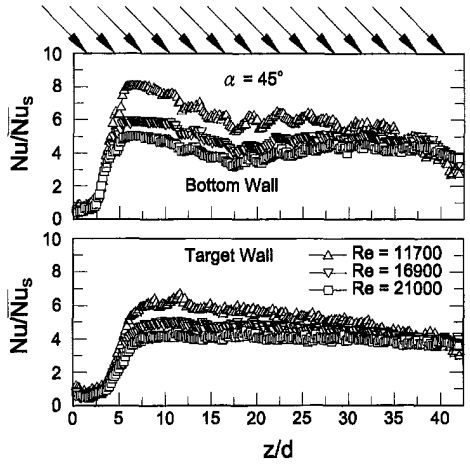

Fig. 12 Span-averaged Nusselt number distribution along axial distance for α = 45 deg

location and direction of the swirling jets. All heat transfer coefficients are normalized by the well-known Dittus-Boelter correlation for the fully developed pipe flow. The Nusselt number ratios on the bottom and target walls of the duct decrease with increasing Re for all jet inlet angles investigated. Again, the trends of the Nusselt number ratio distributions for α = 75 deg are significantly different from those of α = 45 and 30 deg. As shown in Fig. 11, the Nusselt number ratio has a repeated peak-valley distribution along the axial distance on both the bottom wall and the target wall, especially for Re = 11,700. The local maximum of Nusselt number ratio on the bottom and target walls corresponds, respectively, to the wall and impinged jets. In the present study, the jets flow over the bottom wall but do not penetrate through the duct core region. Therefore, the crossflow effect is not as strong as that in Huang et al. (1998) with jets across the mainstream. Consequently, only a slight decrease in the Nusselt number ratio due to the crossflow is observed in Fig. 11. As for the results of α = 45 and 30 deg shown in Figs. 12 and 13, the distributions of Nusselt number ratio on the bottom and target walls are roughly similar. It starts with a local minimum from the upstream end, increases downstream, and reaches to a local maximum at about z/d = 5–7 for α = 45 deg and z/d = 10–12 for α = 30 deg, and then decreases gradually downstream. The locations of local maximum values are well washed by the swirl jets without initial crosssflow.

Wall-Averaged Nusselt Number.

Correlation. Detailed heat transfer results from the present study are the average of the entire bottom and target plates to

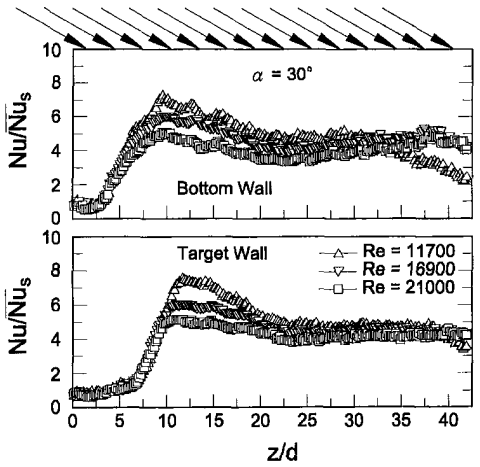

Fig. 13 Span-averaged Nusselt number distribution along axial distance for α = 30 deg

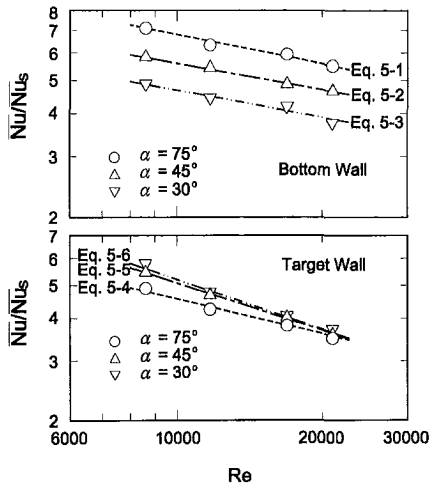

Fig. 14 Wall-averaged Nusselt number as a function of Reynolds number

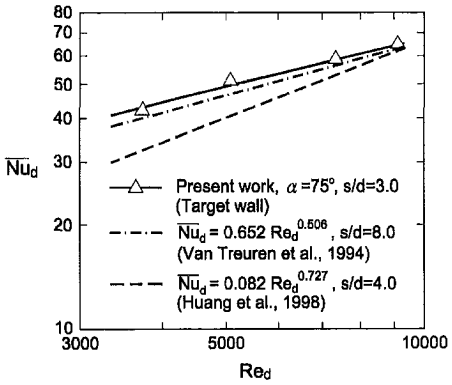

Fig. 15 Comparison of the target wall heat transfer between the present work of α = 75 deg and the previous works

produce the wall-averaged Nusselt number. The wall-averaged Nusselt number for each jet inlet angle is plotted against the Reynolds number in Fig. 14. The results of the bottom and target walls for different α respectively correlate for Reynolds-number dependence as $\overline{Nu} = C_1 Re^{C_2}$. The coefficients of C_1 and C_2 for each α and the deviations between the actual experiments and these correlations are displayed in Table 1. It is seen that α affects the bottom-wall heat transfer more significantly than the target-wall heat transfer. On the bottom wall, the wall-averaged Nusselt number ratios for α = 75 deg are higher than those for α = 45 deg, and subsequently higher than those for α = 30 deg. That is the stronger the wall jet, the higher the bottom-wall heat transfer. On the target wall, however, ducts of α = 45 and 30 deg have almost the same heat transfer enhancement, and slightly higher than that of α = 75 deg, indicating that the swirl-motioned flow could produce a higher target-wall heat transfer than impinged jets.

Comparison With Previous Works. Figure 15 shows the comparison of the present target-wall results of α = 75 deg with the correlations by Van Treuren et al. (1994) and Huang et al. (1998) for the wall cooled by arrays of impinged jets. The case α = 75 deg, selected for comparison, is because it is closely related to the jet impingement. To place all results on the common basis, the present Nusselt number and Reynolds number have been plotted based on the jet parameters (i.e., jet hole diameter and the average jet velocity). The correlation by Van Treuren et al. (1994) was developed based on an array of five by eight jets. The jet spacing was eight hole diameters (s/d = 8.0) in both spanwise and streamwise directions. In Huang et al. (1998), a total of 4 by 12 jet holes was distributed on the jet plate, and the jet spacing was fixed at s/d = 4.0. In both works, the jets impinge normally on the target wall. It is seen from this figure that the jet Reynolds number (Re_d) dependence of the jet Nusselt number ($\overline{Nu}_d$) are largely similar between the present work and Van Treuren et al. (1994). The present heat transfer data are higher than those obtained by Van Treuren et al. (1994) and by Huang et al. (1998) although the present jet has an inclined angle with respect to the target wall. The fact may be due to the small jet spacing (s/d = 3.0) employed in the present work and, partly, due to the less crossflow effect for the present wall-jet impingement.

Concluding Remarks

Heat transfer characteristics in a swirling triangular duct with an array of side-entry jets have been studied experimentally. Detailed heat transfer coefficient distributions on two principal walls of the triangular duct are measured using a transient liquid crystal technique to examine the effects of flow Reynolds number and jet inlet angle. These detailed distributions not only provide a better understanding of the heat transfer enhancement by swirling jets in a triangular duct encountered in the leading-edge cooling of the turbine blade, but also provide a reference for computational fluid dynamic-based studies relating to the swirling-flow heat transfer. Main findings based on the experiments are as follows.

1 From the traces of heat transfer coefficient distribution on two principal walls of the triangular duct and the secondary-flow structures visualized by smoke injection, in general, the enhancements of heat transfer for α = 75 deg are attributed mainly to the wall as well as impinged jets. As for α = 45 and 30 deg, the mechanisms of heat transfer enhancements in the triangular duct are characterized as the swirling-flow cooling.
2 The dead zone appearing near the corner γ for α = 75 deg can be improved by decreasing α to enhance the swirling flow. Meanwhile, however, another two dead zones are created near the corner β and the upstream closed end of the duct.
3 The jet inlet angle affects strongly the averaged bottom-wall heat transfer but relatively insignificantly the averaged target-wall heat transfer. Among the three jet inlet angles investigated, α = 75 deg has the highest bottom-wall heat transfer coefficient due to the strongest wall-jet effect. However, on the target wall, the heat transfer enhancement by the impinged jet as done by α = 75 deg seems to be less notable than that by the swirl-motioned flow as done by α = 45 and 30 deg.
4 The average heat transfer coefficients on the bottom wall are higher than those on the target wall for all three jet inlet angles

Table 1 Coefficients of wall-averaged heat transfer correlations

	$\overline{Nu} = C_1 Re^{C_2}$							
	Bottom Wall				Target Wall			
α	C_1	C_2	Error	Eq.	C_1	C_2	Error	Eq.
75 deg	1.8902	0.5178	6.7%	5-1	2.2466	0.4574	5.4%	5-4
45 deg	1.2329	0.5459	3.1%	5-2	6.0231	0.3609	3.6%	5-5
30 deg	1.0831	0.5382	8.2%	5-3	9.4831	0.3160	5.3%	5-6

investigated, especially for $\alpha = 75$ deg. Correlations for the wall-averaged Nusselt number for the bottom and target walls of the triangular duct have been developed in terms of the flow Reynolds number for three different jet inlet angles.

Acknowledgment

The National Science Council of Republic of China provides supports of this work under the contract number of NSC-89-2212-216-004. Acknowledgments also go to Pitotech Co., Ltd. (Web site: www.pitotech.com.tw) for the development of the software of LCIA (Liquid Crystat Imaging Analyzer) for analyzing the color transient.

References

Algrifri, A. H., and Bhardwaj, R. K., 1985, "Prediction of the Heat Transfer for Decaying Turbulent Swirl Flow in a Tube," *Int. J. Heat Mass Transfer,* Vol. 28, pp. 1637–1643.

Blum, H. A., and Oliver, L. R., 1967, "Heat Transfer in a Decaying Vortex System," ASME Paper No. 66-WA/HT-62.

Bunker, R. S., and Metzger, D. E., 1990, "Local Heat Transfer in Internally Cooled Turbine Airfoil Leading Edge Regions: Part I—Impingement Cooling Without Film Coolant Extraction," ASME *Journal of Turbomachinery,* Vol. 112, pp. 451–458.

Chyu, M. K., and Wu, L. X., 1989, "Combined Effects of Rib Angle-of-Attack and Pitch-to-Height Ratio on Mass Transfer From a Surface with Transverse Ribs," *Experimental Heat Transfer,* Vol. 2, pp. 291–308.

Chyu, M. K., Hsing, Y. C., and Natarajan, V., 1998, "Convective Heat Transfer of Cube Fin Arrays in a Narrow Channel," ASME *Journal of Turbomachinery,* Vol. 120, pp. 362–367.

Ekkad, S. V., and Han, J. C., 1995, "Local Heat Transfer Distributions Near a Sharp Turn of a Two-Pass Smooth Square Channel Using a Transient Liquid Crystal Image Technique," *Journal of Flow Visualization and Image Processing,* Vol. 2, pp. 285–297.

Glezer, B., Moon, H.-K., and O'Connell, T., 1996, "A Novel Technique for the Internal Blade Cooling," ASME Paper No. 96-GT-181.

Glezer, B., Moon, H.-K., Kerrebrock, J., and Guenette, G., 1998, "Heat Transfer in a Rotating Radial Channel with Swirling Internal Flow," ASME Paper No. 98-GT-214.

Gutstein, M. U., Converse, G. L., and Peterson, J. R., 1970, "Augmentation of Single-Phase Heat Transfer in Tubes by Use of Helical Van Inserts," *4th International Heat Transfer Conference,* Paper No. F. C. 4.7.

Han, J. C., Zhang, Y. M., and Lee, C. P., 1991, "Augmented Heat Transfer in Square Channels With Parallel, Crossed, and V-Shaped Angled Ribs," ASME JOURNAL OF HEAT TRANSFER, Vol. 113, pp. 590–596.

Hay, N., and West, P. D., 1975, "Heat Transfer in Free Swirling Flow in a Pipe," ASME JOURNAL OF HEAT TRANSFER, Vol. 97, pp. 411–416.

Hedlund, C. R., Ligrani, P. M., Moon, H.-K., and Glezer, B., 1998, "Heat Transfer and Flow Phenomena in a Swirl Chamber simulating Turbine Blade Internal Cooling," ASME Paper No. 98-GT-466.

Huang, Y., Ekkad, S. V., and Han, J. C., 1998, "Detailed Heat Transfer Distributions Under an Array of Orthogonal Impinging Jets," *AIAA Journal of Thermophysics and Heat Transfer,* Vol. 12, pp. 73–79.

Hwang, J. J., 1998, "Heat Transfer-Friction Characteristic Comparison in Rectangular Ducts With Slit and Solid Ribs Mounted on One Wall," ASME JOURNAL OF HEAT TRANSFER, Vol. 120, pp. 709–716.

Hwang, J. J., and Lai, D. Y., 1998, "Three-Dimensional Laminar Flow in a Rotating Multiple-Pass Square Channel with Sharp 180-deg Turns," ASME *Journal of Fluids Engineering,* Vol. 120, pp. 488–495.

Hwang, J. J., Lai, D. Y., and Tsia, Y. P., 1999, "Heat Transfer and Pressure Drop in a Pin-Fin Trapezoidal Duct," ASME *Journal of Turbomachinery,* Vol. 21, pp. 264–271.

Ivanova, A. V., 1967, "Increasing the Rate of Heat Transfer in a Round Air-Cooled Tube," *Proceedings of 2nd All-Soviet Union Conference on Heat and Mass Transfer,* Vol. 1, pp. 243–250.

Kays, W. M., and Crawford, M. E., 1980, *Convective Heat and Mass Transfer,* 2nd Ed., McGraw-Hill, New York.

Kline, S. J., and McClintock, F. A., 1953, "Describing Uncertainties in Single-Sample Experiments," *Mechanical Engineering,* Vol. 75, pp. 3–8.

Ligrani, P. M., Hedlund, C. R., Thambu, R., Babinchak, B. T., Moon, H.-K., and Glezer, B., 1998, "Flow Phenomena in Swirl Chambers," *Experiments in Fluids,* Vol. 24, pp. 254–264.

Lipina, R. F., and Bergles, A. E., 1969, "Heat Transfer and Pressure Drop in Tape-Generated Swirl Flow of Single Phase Water," ASME JOURNAL OF HEAT TRANSFER, Vol. 91, pp. 434–441.

Migay, V. K., and Golubev, L. K., 1970, "Friction and Heat Transfer in Turbulent Swirl Flow With a Variable Swirl Generator in a Pipe," *Heat Transfer-Soviet Research,* Vol. 2, pp. 68–73.

Mills, A. F., 1962, "Experimental Investigation of Turbulent Heat Transfer in the Entrance Region of a Circular Conduit," *J. Mech. Eng. Sci.,* Vol. 4, pp. 63–77.

Narezhnyy, E. G., and Sudarev, A. V., 1971, "Local Heat Transfer in Air Flowing in Tubes With a Turbulence Promoter at the Inlet," *Heat Transfer-Soviet Research,* Vol. 3, pp. 62–66.

Parsons, J. A., Han, J. C., and Lee, C. P., 1998, "Rotation Effect on Jet Impingement Heat Transfer in Smooth Rectangular Channels With Four Heated Walls and Radially Outward Crossflow," ASME JOURNAL OF HEAT TRANSFER, Vol. 120, pp. 79–85.

Senoo, Y., and Nagato, T., 1972, "Swirl Flow in Long Pipes With Different Roughness," *Bulletin of the JSME,* Vol. 15, pp. 1514–1521.

Van Treuren, K. W., Wang, Z., Ireland, P. T., Jones, T. V., 1994, "Detailed Measurements of Local Heat Transfer Coefficient and Adiabatic Wall Temperature Beneath an Array of Impinging Jets," ASME *Journal of Turbomachinery,* Vol. 116, pp. 369–374.

Vedula, R. J., and Metzger, D. E., 1991, "A Method for the Simultaneous Determination of Local Effectiveness and Heat Transfer Distributions in Three-Temperature Convection Situation," ASME Paper No. 91-GT-345.

Zhang, Y. M., Gu, W. Z., and Han, J. C., 1994, "Augmented Heat Transfer in Triangular Ducts with Full and Partial Ribbed Walls," *AIAA Journal of Thermophysics and Heat Transfer,* Vol. 8, pp. 574–597.

Y. P. Wan
Research Scientist,
e-mail: ywan@ccmail.sunysb.edu
Mem. ASME

V. Prasad
Professor,
Fellow ASME

G.-X. Wang[1]
Assistant Professor,
Mem. ASME

S. Sampath
Associate Professor

Center for Thermal Spray Research, and
Process Modeling Laboratory,
State University of New York at Stony Brook,
Stony Brook, NY 11794-2275

J. R. Fincke
Consulting Scientist,
Idaho National Engineering and Environmental Laboratory,
ID 83415-2211
e-mail: jf1@inel.gov

Model and Powder Particle Heating, Melting, Resolidification, and Evaporation in Plasma Spraying Processes

A comprehensive model is developed to study the heating, melting, evaporation, and resolidification of powder particles in plasma flames. The well-established LAVA code for plasma flame simulation is used to predict the plasma gas field under given power conditions, and provide inputs to the particle model. The particle is assumed to be a spherical and one-dimensional heat conduction equation with phase change within the particle is solved numerically using an appropriate coordinate transformation and finite difference method. Melting, vaporization, and resolidification interfaces are tracked and the particle vaporization is accounted for by the mass diffusion of vapor through the boundary layer around the particle. The effect of mass transfer on convective heat transfer is also included. Calculations have been carried out for a single particle injected into an $Ar–H_2$ plasma jet. Zirconia and nickel are selected as solid particles because of their widespread industrial applications as well as significant differences in their thermal properties. Numerical results show strong nonisothermal effect of heating, especially for materials with low thermal conductivity, such as zirconia. The model also predicts strong evaporation of the material at high temperatures.

1 Introduction

The quality of thermal spray coatings is directly determined by the velocity, temperature, melt fraction, and size of the sprayed powder particles when they impact the substrate. A reliable description of transport phenomena associated with the sprayed particles is therefore essential to improved understanding of the relationship between the key process parameters and effective control of the coating quality.

Particle motion and heating is a well-researched topic in fluid mechanics and heat transfer. Many well-established models for particle-gas interaction can be conveniently employed in the modeling of plasma spray processes by adding some special effects of the thermal plasma. These effects, are due to special characteristics of the thermal plasma such as high temperature and temperature gradients, low pressure, noncontinuum effects, strongly varying plasma properties, thermophoresis, turbulent dispersion, evaporation, etc. These effects have been discussed extensively by Pfender and his co-workers (Pfender and Lee, 1985). Their work on noncontinuum effects (Chen and Pfender, 1983a, b) and the influence of varying plasma properties (Lee et al., 1981) on particle drag and heat transfer has been widely cited in the literature.

The vaporization of molten droplets has also drawn significant research attention. A number of papers have been published on this issue. Mostly, a simple heat transfer model has been used (Proulx et al., 1985; Das and Sivakumar, 1990), which assumes that the vaporization takes place only when the particle temperature (or the temperature at the surface) reaches the boiling point and the vaporization rate is controlled only by the heat flux at the particle surface. As we know, most materials can be vaporized at temperatures much lower than the boiling point and the vaporization rate can be very high near the boiling point. A model that can consider vaporization at any temperature is therefore necessary to properly account for the rate of evaporation at the particle surface. In an early work, Fiszdon (1979) included the effect of diffusion of the vaporized particle materials in his model and investigated the phase change of an alumina particle into a known plasma jet field. A comprehensive model considering both the Langmuir evaporation and mass transfer of species across the boundary layer has been recently proposed by Westhoff et al. (1992). The model is based on the harmonic average of mass transfer coefficients due to Langmuir evaporation and the mass transfer through the boundary layer. This treatment can introduce errors by allowing the particle temperature to become much higher than the boiling point if the heat transfer rate is very high, which can allow the heat gain to exceed the energy needed to overcome the latent heat of vaporization. This became evident when we tried to use this model. Vardelle et al. (1997) have recommended the use of the Langmuir expression for evaporation under the vacuum environment and the mass diffusion expression under atmospheric conditions. Although no detailed evaporation calculations under the real plasma spray condition are reported in their paper, it outlines the basic transport phenomena related to the vaporization of powder particles.

The effect of mass transport (vaporization) on convective heat transfer is another important issue related to vaporization. This problem has been well documented in the combustion literature. The review papers by Law (1982) and Faeth (1983) present detailed descriptions of the mass diffusion-controlled vaporization as well as its effect on heat transfer. Although the importance of this effect in plasma spraying has been noted by Boulos et al. (1993) in their comprehensive review, no detailed calculations and discus-

[1] Current address: Department of Mechanical Engineering, The University of Akron, Akron, OH.

Contributed by the Heat Transfer Division for publication in the JOURNAL OF HEAT TRANSFER and presented at '98 IMECE, Anaheim. Manuscript received by the Heat Transfer Division, Aug. 1, 1998; revision received, Feb. 15, 1999. Keywords: Evaporation, Heat Transfer, Melting, Modeling, Plasma. Associate Technical Editor: C. Beckermann.

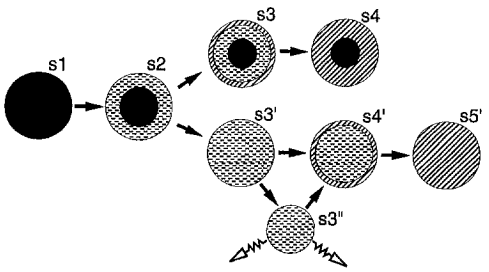

Fig. 1 Illustration of the possible phase-change paths and conditions of the powder particle in-flight

sions were presented. In fact, this effect has been mostly ignored in thermal spray modeling (Chen and Pfender, 1982), even though it can be as significant as the Knudsen effect. This has been incorporated into the particle-plasma heating model presented here.

In addition to evaporation, the powder particles may also experience other phase changes, like melting and resolidification (Fiszdon, 1979). As illustrated in Fig. 1, a solid powder particle is partially melted to condition $S2$ during the early heating stage. It may impact the substrate under this condition or it may undergo two different phase-change paths depending on the local plasma gas conditions. One possible path is that it continues to be heated up and fully melted ($S3'$). Meanwhile, evaporation can occur at the surface and cause decrease in particle size ($S3''$). If it does not hit the substrate soon, resolidification will start on its surface layer ($S4'$) due to lower plasma temperatures and eventually it will get fully solidified ($S5'$). Another possible path is that the particle is cooled down before it is fully melted and it starts getting resolidified at its outer surface ($S3$). It is also possible that the entire melt will be resolidified before the particle reaches the substrate. Evidently, the particle may end up impacting the substrate under any condition between $S2 - S4$ or $S2 - S5'$ and the condition under which it reaches the substrate will have a strong influence on the coating quality. A particle model is developed here that is capable of predicting all of these possible conditions.

Furthermore, most of the plasma spray analyses have assumed a uniform temperature within the particle, which is reasonable for metal and alloy powders. However, for the materials with low thermal conductivity, or to be exact, for the particle with a large Biot number, the temperature gradient within the particle can become high. In fact, during the transient heating of a particle, internal heat conduction should be accounted for, if the Biot number is greater than 0.02 (Wei et al., 1988).

Models for particle heating with consideration of internal conduction, melting, evaporation, and solidification were applied or verified without the coupling with the plasma flow field (Fiszdon, 1979; Chen and Pfender, 1982; Lee, 1988; Das and Sivakumar, 1990). Comprehensive studies on both plasma gas and particle heating with different applications such as DC plasma, RF induction plasma and supersonic plasma processing systems have been reported by Proulx et al., (1985), Wei et al., (1987, 1988), and Westhoff et al., (1992). In this paper, we simulate an Ar–H_2 DC plasma spraying system with the consideration of plasma chemistry, turbulence mixing, and interaction between the plasma gas and the powder particles.

Here, we present a model that accounts for the temperature variation in the particle based on heat transfer by convection and radiation at its surface, and phase change of the powder particles

Nomenclature

a = thermal accommodation coefficient
B = mass transfer number
c_p = specific heat capacity, J/kg-K
C_D = drag coefficient, Eq. (28)
d = particle initial diameter, m
D = diffusion coefficient, m^2/s
f_{Kn} = factor of Knudsen effect, Eq. (16)
f_{prop} = factor to account property variation, Eq. (15)
f_v = factor for mass transfer, Eq. (14)
k = thermal conductivity, W/m-K
$\tilde{k}$ = turbulence kinetic energy, J/kg
Kn* = effective Knudsen number
L_m = latent heat of fusion, J/kg
L_v = latent heat of vaporization, J/kg
$\dot{m}_v$ = vaporization rate, kg/s
Pr = Prandtl number, Eq. (13)
$\dot{Q}_{conv}$ = convective heat transfer rate, J/s
$\dot{Q}_{rad}$ = radiative heat transfer rate, J/s
$\dot{Q}_{vap}$ = heat transfer rate for vaporization, J/s
r = radial coordinate for the particle, m
r_i^- = inner radius of domain i, m
r_i^+ = outer radius of domain i, m
r_m = position of the melting interface, m
r_m^-, r_m^+ = vicinity of the melting interface, m
r_p = particle radius, m
r_s = position of the solidification interface, m
r_s^-, r_s^+ = vicinity of the solidification interface, m
$\mathcal{R}$ = gas constant, J/mole-K
$\tilde{p}$ = gas pressure, N/m^2
p_v = vapor pressure, N/m^2
Re_p = Reynolds number, Eq. (12)
Sc = Schmidt number, Eq. (23)
Sh = Sherwood number, Eq. (23)
t = time coordinate, t
T = temperature, K
T_i = temperature at the melting interface, K
$\tilde{T}_\infty$ = temperature outside boundary layer, K
T_s = particle surface temperature, K
T_m = melting point, K
$\mathbf{U}$ = Favre-averaged velocity vector, m/s
$\mathbf{U}'$ = velocity fluctuation, m/s
$\mathbf{U}_p$ = particle velocity vector, m/s
v_w = mean molecular speed, m/s
W = molecular weight of the gas mixture, kg/mole
W_0 = molecular weight of gas without vapor, kg/mole
W_p = molecular weight of the particle, kg/mole
Y^* = mass fraction of vapor at surface
$\tilde{Y}_\infty$ = vapor mass fraction outside boundary layer

Greek Symbols

γ_w = specific heat ratio of gas, c_p/c_v
ϵ = surface emissivity coefficient
$\tilde{\epsilon}$ = dissipation rate of $\tilde{k}$, 1/s
μ = viscosity, N-s/m^2
ξ_i = transformed coordinate for domain i
ρ_p = particle density, kg/m^3
$\tilde{\rho}$ = turbulent mean density of gas, kg/m^3
σ = Stefan-Boltzmann constant, J/m^2-s-K^4
ϕ = general representation of variable

Subscripts

c = the cell where the particle is located
f = the film temperature
p = particle
w = the vicinity of particle surface

Superscript

$\tilde{}$ = Favre-averaged quantity

including melting, evaporation, and resolidification. A numerical scheme based on coordinate transformation is used to treat the heat conduction with moving interfaces and boundaries. The coupling between plasma jet and particles is considered and the effect of evaporation on the heat flux to particles is discussed.

2 Governing Equations

2.1 Powder Particles. In the computer model, LAVA, the injected powder particles are discretely treated in a Lagrangian manner. Computational particles are created at the point of injection and tracked throughout their flight. By solving the plasma gas equations, LAVA provides the information on conditions external to the particle. Heat transfer and phase change within the particle and mass transfer from its surface can be calculated based on this information if a suitable particle model can be developed.

2.1.1 Energy Transport in a Particle. To develop a particle heating, melting, resolidification, and evaporation model we assume that the spherical symmetry is applicable and internal convection within the molten part of the particle is negligible. The spherical particle is heated up (or cooled down) by surrounding plasma gas (local conditions) by heat convection and thermal radiation. The temperature distribution within the particle is then governed by heat conduction, and can be obtained from

$$\rho_p c_p \frac{\partial T}{\partial t} = \frac{1}{r^2}\frac{\partial}{\partial r}\left(k_p r^2 \frac{\partial T}{\partial r}\right) \tag{1}$$

where the subscript p represents the particle and the properties ρ_p, c_p, and k_p are taken as local values. Although they can be easily considered as functions of both temperature and phase, they are only allowed to change upon phase change in the present model.

Because the particle may undergo phase change during the flight, such as melting, vaporization, and even resolidification, there may exist internal phase-change interfaces other than the particle surface. The phase-change interface can be treated either as a heat source (Groma and Vetö, 1986) or as a boundary for the heat conduction system. We prefer to treat it as an additional boundary between the two different phase domains. The number of such phase-change interfaces will depend on the temperature distribution inside the particle. For example, there is no phase-change interface in the case of a solid particle ($S1$ in Fig. 1) or completely molten particle ($S3'$), one interface for a partially molten particle ($S2$ and $S4'$), and two interfaces for a partially molten and then a resolidified particle ($S3$). All these phase-change interfaces, including the particle surface if vaporization occurs, are moving boundaries. The boundary conditions for a partially melted particle (with one internal interface) are given below, with the geometry illustrated in Fig. 2:

$$\left.\frac{\partial T}{\partial r}\right|_{r=0} = 0 \tag{2}$$

$$\left.\left(k_p \frac{\partial T}{\partial r}\right)\right|_{r=r_m^-} - \left(k_p \frac{\partial T}{\partial r}\right)_{r=r_m^+} = L_m \rho_p \frac{dr_m}{dt} \tag{3}$$

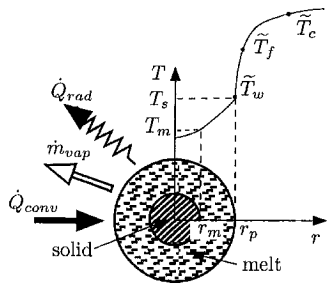

Fig. 2 Schematic of the particle geometry and heating model

$$4\pi r_p^2 \left(k_p \frac{\partial T}{\partial r}\right)\Big|_{r=r_p} = \dot{Q}_{\text{conv}} - \dot{Q}_{\text{vap}} - \dot{Q}_{\text{rad}}. \tag{4}$$

The following boundary condition at the resolidification interface r_s is needed if resolidification occurs:

$$\left.\left(k_p \frac{\partial T}{\partial r}\right)\right|_{r=r_s^+} - \left.\left(k_p \frac{\partial T}{\partial r}\right)\right|_{r=r_s^-} = L_m \rho_p \frac{dr_s}{dt}. \tag{5}$$

In the above equations, $r_p(t)$ is the radius of the particle, which may change due to vaporization. The rate of heat transfer by convection, vaporization and radiation are given below:

$$\dot{Q}_{\text{conv}} = 4\pi r_p^2 h(\tilde{T}_c - T_s) \tag{6}$$

$$\dot{Q}_{\text{vap}} = \dot{m}_v L_v \tag{7}$$

$$\dot{Q}_{\text{rad}} = 4\pi r_p^2 \epsilon\sigma(T_s^4 - \tilde{T}_\infty^4) \tag{8}$$

where, the overhead $\sim$ refers to the Favre-averaged value for all dependent variables in the plasma phase. Favre-averaged quantities are used to account for steep variation of density in the plasma flame, since this kind of mass-averaging allows a direct correlation between the turbulent fluctuations of density and other variables (Williams, 1985). The subscript c represents the location surrounding the particle, which is in fact the computational cell in LAVA for the plasma gas in which the particle is located and subscript ∞ represents the condition far away from the particle. In Eq. (7), L_v is the latent heat of vaporization and $\dot{m}_v$ is the vaporization rate that can be obtained using a vaporization model, to be discussed later. The plasma gas is assumed to be optically thin and therefore only the radiation between the particle surface and far-away environment is considered (Boulos et al., 1994). A small content of metal vapor in plasma gas will significantly affect the radiative property of the surrounding plasma, and hence, the assumption of optically thin vapor layer in the plasma gas may be questionable (Boulos et al., 1994). However, we make this assumption for the sake of simplification of calculations, and also, because the information on radiation properties of zirconia and nickel vapors are lacking. This area needs further investigation, particularly by conducting experimental measurements, to account for the radiation effects of vaporization.

The convection heat transfer coefficient, h, in Eq. (6) can be calculated from

$$h = \frac{k_f \text{Nu}}{2r_p}. \tag{9}$$

Here, the subscript f denotes the value calculated at the film temperature, $\tilde{T}_f$, which is introduced to deal with the steep temperature gradient in the boundary layer surrounding the particle and strong dependence of the physical properties of plasma gas on the temperature, see Fig. 2. The film temperature $\tilde{T}_f$ is defined as

$$\tilde{T}_f \equiv (\tilde{T}_c + \tilde{T}_w)/2. \tag{10}$$

The subscript w indicates the immediate vicinity in the gas phase.

The Nusselt number, Nu in Eq. (9), can be evaluated using an appropriate correlation, for example,

$$\text{Nu} = (2.0 + 0.6\ \text{Re}_p^{1/2}\ \text{Pr}^{1/3})\left(\frac{c_{p,c}}{c_{p,w}}\right)^{0.38}(f_{\text{prop}})^{0.6} f_{\text{Kn}} f_v. \tag{11}$$

In the above equation, the terms in the first bracket is the Nusselt number expression that accounts for forced convection heat transfer from a sphere (Ranz and Marshall, 1952), where the Reynolds number and Prandtl number of plasma gas are defined as

$$\text{Re}_p \equiv \frac{2\bar{\rho}_f r_p |\tilde{\mathbf{U}} + \mathbf{U}' - \mathbf{U}_p|}{\mu_f} \tag{12}$$

$$\mathrm{Pr} \equiv \frac{\mu_f c_{p,f}}{k_f}. \tag{13}$$

The factor f_v accounts for the effect of mass transfer due to vaporization, and is given by (Faeth, 1983)

$$f_v = \frac{\dot{m}_v c_{p,f}/2\pi r_p k_f}{\exp\{\dot{m}_v c_{p,f}/2\pi r_p k_f\} - 1}. \tag{14}$$

The factors f_{prop} and f_{Kn} in Eq. (11) represent the effects of variable plasma properties and noncontinuum, respectively. They can be obtained from (Lee et al., 1981; Chen and Pfender, 1983a):

$$f_{\text{prop}} = \frac{\rho_c \mu_c}{\rho_w \mu_w} \tag{15}$$

$$f_{\text{Kn}} = \left[1 + \left(\frac{2-a}{a}\right)\left(\frac{\gamma_w}{1+\gamma_w}\right)\frac{4}{\mathrm{Pr}_w}\mathrm{Kn}^*\right]^{-1} \tag{16}$$

where a is the thermal accommodation coefficient with a recommended value of 0.8 (Chen and Pfender, 1983a), γ_w and Pr_w are the specific heat ratio and the Prandtl number of the plasma gas evaluated at the surface temperature. Here, Kn* is the Knudsen number based on an effective mean free path and can be obtained from an appropriate expression, e.g., Chen and Pfender (1983a):

$$\mathrm{Kn}^* = \frac{\mathrm{Pr}_w}{\bar{\rho}_w v_w r_p}\frac{k_f}{c_{pf}} \tag{17}$$

where v_w is the mean molecular speed that is dependent upon the average molecular weight W of the gas mixture as well as on the gas temperature near the particle surface, $\tilde{T}_w$, and is given by

$$v_w = \left(\frac{8\mathcal{R}\tilde{T}_w}{\pi W}\right)^{1/2}. \tag{18}$$

2.1.2 Melting, Resolidification, and Vaporization. Both equilibrium and nonequilibrium melting models have been reported in the literature, that can yield the solid/melt interface velocity, dr_m/dt, to be substituted in Eq. (3). In the equilibrium model, the interface temperature is taken as the equilibrium melting point, T_m, and dr_m/dt is directly obtained from the melting interface condition, Eq. (3).

In the nonequilibrium model for rapid melting, the interface temperature, T_i, is correlated to the interface velocity through the following linear kinetics relationship (Wang and Matthys, 1996):

$$\frac{dr_m}{dt} = \mu_k(T_m - T_i) \tag{19}$$

where μ_k is the linear kinetic coefficient, a property of the material. Its value for nickel and zirconia is estimated as 0.85 and 10^{-2}, respectively (Wang and Matthys, 1996).

Resolidification can be treated in the same way as melting. In the equilibrium model, the interface temperature is set to the melting point and dr_s/dt is directly obtained from Eq. (5). In the nonequilibrium model, the formulation for interface velocity, similar to Eq. (19), can be written as

$$\frac{dr_s}{dt} = \mu_k(T_i - T_m). \tag{20}$$

For plasma spraying under atmospheric conditions, the evaporation rate $\dot{m}_v$ in Eq. (7) is generally controlled by the vapor diffusion through the boundary layer around the particle (Vardelle et al., 1997), which can be expressed as (Faeth, 1983)

$$\dot{m}_v = 2(\bar{\rho}D)_f \pi r_p \ln(1+B)\,\mathrm{Sh} \tag{21}$$

where the Sherwood number, Sh, accounts for the convective mass transfer. Considering the effect of noncontinuum on mass transfer to be negligible, the Sherwood number can be evaluated from (Faeth, 1983)

$$\mathrm{Sh} = 2.0 + 0.6\,\mathrm{Re}_p^{1/2}\,\mathrm{Sc}^{1/3} \tag{22}$$

with the Schmidt number Sc defined as

$$\mathrm{Sc} \equiv \frac{\mu_f}{(\bar{\rho}D)_f}. \tag{23}$$

The mass transfer number B in Eq. (21) is defined as

$$B \equiv \frac{Y^* - \tilde{Y}_\infty}{1 - Y^*} \tag{24}$$

where $\tilde{Y}_\infty$ is the mass fraction of vapor outside the boundary layer whose value is usually taken as that at the computational cell, and Y^* is the mass fraction of vapor in the vicinity of the particle surface, given by

$$Y^* = \frac{W_p}{W_p + W_0(\tilde{p}_c/p_v - 1)}. \tag{25}$$

In the above equation, W_p is the molecular weight of the powder material, W_0 is the molecular weight of the gas mixture excluding the vapor species, $\tilde{p}_c$ is the pressure in the computational cell, and $p_v(T_s)$ is the vapor pressure, which is a strong function of the particle surface temperature.

As the particle surface temperature T_s approaches the boiling point T_b, the value of Y^* becomes larger and larger and finally approaches unity. In this situation, the vaporization rate $\dot{m}_v$ becomes so high that the energy needed to overcome the latent heat of vaporization $\dot{Q}_{\text{vap}}$ is balanced by the net heat transfer to the particle, i.e., the right-hand side of the particle surface boundary condition in Eq. (4) reduces to zero. This leads to the expression of the widely used heat transfer controlled vaporization model,

$$\dot{m}_{v,\text{heat}} = (\dot{Q}_{\text{conv}} - \dot{Q}_{\text{rad}})/L_v. \tag{26}$$

The particle surface temperature in this situation is usually taken as the boiling point.

2.1.3 Momentum Transport. The driving forces on a particle immersed into a plasma jet include the viscous drag, the pressure gradient, the Basset history, and the gravitational force. As already discussed by many researchers (Pfender and Lee, 1985), most of the driving forces, except the viscous drag force, can be neglected for a particle with a size smaller than 100 μm. When drag is the only driving force, the momentum equation can be written as

$$\frac{d\mathbf{U}_p}{dt} = \frac{3}{8}\frac{\bar{\rho}}{\rho_p}\frac{C_D}{r_p}|\tilde{\mathbf{U}} + \mathbf{U}' - \mathbf{U}_p|(\tilde{\mathbf{U}} + \mathbf{U}' - \mathbf{U}_p). \tag{27}$$

Here, the velocity fluctuation, $\mathbf{U}'$ approximates the fluctuating effects of turbulence on tiny particles, which is still an unclear topic in turbulent two-phase flow. By considering the effects of variable plasma properties and Knudsen noncontinuum on drag (Lee et al., 1981; Chen and Pfender, 1983b), the drag force coefficient C_D can be written as

$$C_D = \left(\frac{24}{\mathrm{Re}_p} + \frac{6}{1+\sqrt{\mathrm{Re}_p}} + 0.4\right) f_{\text{prop}}^{-0.45} f_{\text{Kn}}^{0.45} \tag{28}$$

where the dependence of drag coefficient on Reynolds number, Re_p, is taken from a simple form proposed by White (1974), which is valid for $\mathrm{Re}_p < 100$. For evaporating droplets, the formulation of drag coefficient in Eq. (28) still provides a good correlation (Faeth, 1983).

2.2 Plasma Gas. In this study, the plasma jet is calculated using the well-established LAVA code (Ramshaw and Chang, 1993), which is a three-dimensional CFD code developed for transient simulation of thermal plasma. Here, we use only a two-

Table 1 Processing Parameters

Processing Parameters	Value
current	600 Amps
voltage	70 Volts
power efficiency	0.7
primary gas flow	40 SLM Ar
secondary gas flow	12 SLM H_2

dimensional version of the LAVA code because of the following two reasons: the two-dimensional version is fully tested (including the validation in our laboratory) and three-dimensional calculations require enormous computational resources for any realistic calculation. The comprehensive model employed in this algorithm treats the plasma as a compressible, multicomponent, chemically-reacting ideal gas with temperature-dependent thermodynamic and transport properties. In LAVA, the ionization, dissociation, recombination, and other chemical reactions are treated using a general kinetic algorithm (Ramshaw and Chang, 1995). A reduced set of reactions is used for the argon-hydrogen plasma considered here and is listed in the Appendix. This set of reactions is a combination of the reaction mechanism for argon plasma provided by Chang and Ramshaw (1993) and that for the nitrogen-hydrogen plasma used by Chang and Ramshaw (1996). The following chemical species were therefore included in the calculations: Ar, Ar^+, H_2, H, H^+, N_2, N_2^+, N, N^+, O_2, O, O^+, and e^-.

A detailed description of the physical model and numerical techniques incorporated into LAVA can be found in the article by Ramshaw and Chang (1993). The governing equation that is solved in LAVA is given in its general form, for a two-dimensional cylindrical coordinate system, as

$$\frac{\partial(\bar{\rho}\tilde{\phi})}{\partial t} + \frac{1}{x}\frac{\partial(\bar{\rho}x\tilde{u}\tilde{\phi})}{\partial x} + \frac{\partial(\bar{\rho}\tilde{v}\tilde{\phi})}{\partial y} = \frac{1}{x}\frac{\partial}{\partial x}\left(\frac{\mu+\mu_t}{\sigma_{\tilde{\phi}}}x\frac{\partial\tilde{\phi}}{\partial x}\right) + \frac{\partial}{\partial y}\left(\frac{\mu+\mu_t}{\sigma_{\tilde{\phi}}}\frac{\partial\tilde{\phi}}{\partial y}\right) + S_{\tilde{\phi}}. \quad (29)$$

Here, ϕ represents all of the dependent variables, including velocities in the x and y directions, $\tilde{u}$ and $\tilde{v}$, the mass fraction $\tilde{Y}_i$ of chemical species or component i, and the thermal internal energy $\tilde{e}$. $S_{\tilde{\phi}}$ is a general representation of the source term for variable $\tilde{\phi}$. The standard $\tilde{k} - \tilde{\epsilon}$ model (Launder and Spalding, 1972) is used to estimate the turbulent viscosity μ_t and the equations for $\tilde{k}$ and $\tilde{\epsilon}$ follow the general form of Eq. (29). Local thermodynamic equilibrium is assumed in the plasma jet for the calculations reported here.

3 Numerical Method and Validation

The numerical method for the solution of plasma gas equations is described by Ramshaw and Chang (1993) and will be omitted here for brevity. Only the numerical technique used to solve the particle heat conduction equation with moving phase-change interfaces is addressed here. To fix the solid/melt and melt/vapor interfaces in the computational domain, the original physical coordinate is transformed into a new dimensionless coordinate by introducing a new coordinate,

$$\xi_i = \frac{r - r_i^-}{r_i^+ - r_i^-}, \quad (30)$$

where r_i^- and r_i^+ represent the inner and outer radii of the subdomain, respectively, that may be solid or liquid. Therefore, for different subdomains separated by various phase interfaces, the coordinates after transformation will be different. For example, as shown in Fig. 2, in the case of only one solid/melt interface, r_i^- and r_i^+ for the solid domain are 0 and r_m, respectively, while they are r_m and r_p, for the melt domain.

After the coordinate transformation, each physical domain separated by the phase-change interface are transformed to a corresponding computational domain starting from 0 to 1. Equation (1) is then transformed to

$$\rho_p c_p \frac{\partial T}{\partial t} = \frac{1}{(r_i^+ - r_i^-)^2[(r_i^+ - r_i^-)\xi_i + r_i^-]^2}\frac{\partial}{\partial\xi_i} \times [k_p[(r_i^+ - r_i^-)\xi_i + r_i^-]^2]\frac{\partial T}{\partial\xi_i} + \rho_p c_p\left[\frac{\xi_i}{r_i^+ - r_i^-}\frac{dr_i^+}{dt} + \frac{1-\xi_i}{r_i^+ - r_i^-}\frac{dr_i^-}{dt}\right]\frac{\partial T}{\partial\xi_i}. \quad (31)$$

The boundary conditions for each individual computational domain in the case of one solid/melt interface, for example, are given as

$$\left.\frac{\partial T}{\partial\xi_1}\right|_{\xi_1=0} = 0 \quad (32)$$

$$\frac{1}{r_m}\left(k_p\frac{\partial T}{\partial\xi_1}\right)\Big|_{\xi_1=1} - \frac{1}{r_p - r_m}\left(k_p\frac{\partial T}{\partial\xi_2}\right)\Big|_{\xi_2=0} = L_m\rho_p\frac{dr_m}{dt} \quad (33)$$

$$4\pi r_p^2\frac{1}{r_p - r_m}\left(k_p\frac{\partial T}{\partial\xi_2}\right)\Big|_{\xi_2=1} = \dot{Q}_{\text{conv}} - \dot{Q}_{\text{vap}} - \dot{Q}_{\text{rad}}. \quad (34)$$

A boundary condition similar to Eq. (33) can be obtained if the particle starts solidifying at the outer surface when it passes through a low temperature field. Under such conditions, Eq. (34) will also need modifications, essentially $\dot{Q}_{\text{vap}} = 0$. The transformed heat conduction Eq. (31) is solved using the finite volume method ((Wang et al., 1997), see Wan et al. (1998) for the discretized equations).

The computer model developed here has been validated against the analytical results of Solomon (1979) and the numerical solution of Anselmo et al. (1991) for melting of a sphere. An excellent agreement is achieved. Sensitivity analysis for the influence of grid resolution has also been carried out with 10, 20, 40, and 80 grids. The variation in melt/solid interface positions with 10 and 80 grids is less than five percent while the CPU requirement increases by a factor of ten. Most of the calculations reported here have been carried out with ten grids in each subdomain.

No effort has been made to validate the LAVA algorithm for plasma jet simulation since it is well established in the literature (Ramshaw and Chang, 1993; Chang and Ramshaw, 1993). A grid resolution of 56 in the x-direction and 65 in the y-direction is selected for the plasma gas calculation performed here.

4 Results and Discussion

The present study is conducted for a DC plasma system at Idaho National Engineering and Environment Laboratory that uses a Metco 9MB plasma gun (Smith et al., 1997). In order to display the effect of evaporation of molten droplets, we have selected high-power and high H_2 flow rates as processing conditions, as listed in Table 1. The nozzle diameter of the plasma gun is 7.5 mm and the powder is fed from outside the plasma gun, as illustrated in Fig. 3. The powder port is located axially 6.0 mm downstream from the nozzle exit and vertically 8.0 mm above the nozzle axis. For present calculations, the particles are injected into the stream at 5

Table 2 Values of dimensional and nondimensional parameters for zirconia to show the particle-plasma interaction

C_D	$2 \sim 16$	V_{rel}	$10 \sim 1200$ m/s
Re_p	$5 \sim 25$	μ_f	$2 \times 10^{-5} \sim 2 \times 10^{-4}$ kg/s.m
f_{Kn}	$0.8 \sim 1.0$	k_f	$2 \times 10^{-2} \sim 1.2$ W/m.K
Sc	0.7	$(\bar{\rho}D)_f$	$5 \times 10^{-5} \sim 3.5 \times 10^{-4}$ kg/s.m
Nu	$2.5 \sim 5$	h	$10^3 \sim 10^5$ W/K.m^2
Sh	$2.5 \sim 5$	Pr	$0.35 \sim 0.65$

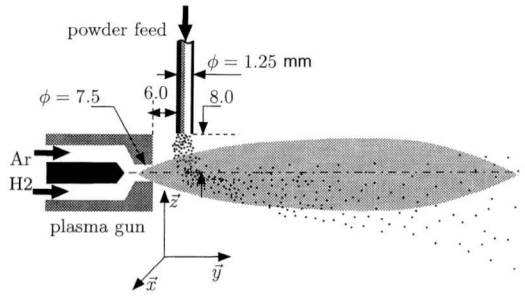

Fig. 3 Schematic of a plasma spray system

ms when the transient simulation of the plasma jet has reached the steady state. The initial velocity of the particle is taken as 11 m/s in a direction perpendicular to the axis of the plasma jet.

Except for the validation calculations in which multiple particles are simulated simultaneously, most calculations are performed for single zirconia and nickel particles with diameters of 20, 40, and 80 μm. The thermophysical properties of these materials are taken from Hultgen et al. (1973) and Samsonov (1973). The influence of the carrier gas flow on plasma flow field is neglected because of two reasons: (1) The carrier gas causes the flow pattern of the plasma jet to be somewhat nonsymmetrical which will require three-dimensional calculations. This will greatly increase the requirements of computational resources with very little effect on the particle behavior. (2) The carrier gas flow rate of 5 slm (standard liter per minute) is relatively low compared with the flow rate of the primary and secondary plasma gas, which is about 52 slm. Moreover, the cooling effect of the carrier gas is appreciable only in the vicinity of the powder injection nozzle. The heating of particles in this region is, however, relatively insignificant. Therefore, the assumption of negligible carrier gas effect is not expected to affect, in any significant manner, the results obtained for in-flight particles and the conclusions based on these results.

4.1 Comparison With Experimental Data. To validate the particle heating and phase-change model, the experiments conducted by Smith et al. (1997) were simulated by using the above formulation. The operating conditions are the same as that listed in Table 1 and the particle size for zirconia powder varies between 30 to 99 μm. The particles are injected at an average velocity of 14.5 m/s.

Before we attempt to compare the calculations with the measurements, it is necessary to reexamine the methods used in the measurements of Smith et al. (1997), so that the experimental data can be interpreted accurately and a fair comparison can be made. In the experiment of Smith et al., the transverse and axial particle trajectory patterns were obtained using a spray pattern trajectory (SPT) sensor. In addition, a laser doppler velocimetry system capable of spectral width measurements is used to measure the average velocity and size of the particles. For the measurement of the particle velocity along the axis (Fig. 4(a)), the SPT sensor is focused on a very small region near the axis, and therefore, the average axial velocity of particles is in reality the velocity of the particles that are traveling along the axis. These are mostly the particles with small sizes, since most of the large particles move to the periphery of the flame due to larger inertia. The average in-flight particle temperatures are determined via two-color pyrometry, using IPP 2000. Obviously, the measured particle temperatures represent the averaged temperature of many of the particles moving through the focused cross section.

Results presented in Fig. 4 are the particle velocity and temperature along the axial distance in this viewing frame. The particle velocity plotted in Fig. 4(a) are the number-averaged values for the particles within the selected size group, three curves representing three different size groups. Figure 4(a) clearly shows that the smaller particles have much higher axial velocity than the larger particles. The number-averaged temperature of the particles is shown in Fig. 4(b). While the smaller particles exhibit much larger overheating, the larger particles just reach the melting point (2950 K) with many of them only partially melted or even not melted. This is because the larger particles have much higher heat capacity and need more time to get heated. Also, the general trajectories of the larger particles are away from the hot core of the plasma flame. Figure 4(b) also shows that the smaller particles cool down rapidly while the larger particles keep their temperature around the melting point for a longer time during the flight.

The agreement between the simulation and measurements, as shown in Fig. 4, is considered quite reasonable considering the uncertainty in measurements and only smaller particles passing through the viewing frame. Measurements in a plasma spraying system is very challenging. Although significant progress has been made to develop techniques for measurements of averaged particle velocity and temperature under plasma conditions, the data must be interpreted carefully and should be rather used for qualitative analysis and physical understanding than as exact quantitative values.

The details of the model-predicted results on particle heating, melting, evaporation, and solidification are presented below for a single particle.

4.2 Particle Heating History. Figure 5 shows the typical evolution of the particle surface temperature, T_s, together with its surrounding plasma temperature, T_g. The zirconia particle injected at time 5 ms takes about one-fourth of its dwell time to get into the hot core of the plasma jet and about the same length of time to be heated up to its maximum temperature. There is a short standstill as the surface temperature reaches the melting point (about 2590 K) because the heat transferred to the particle at this point is mostly used to overcome the latent heat of fusion. As the surface temperature approaches the boiling point (about 5000 K), the vaporization of the particle becomes more and more significant, as indirectly demonstrated by the curve for f_v in Fig. 5. Although the

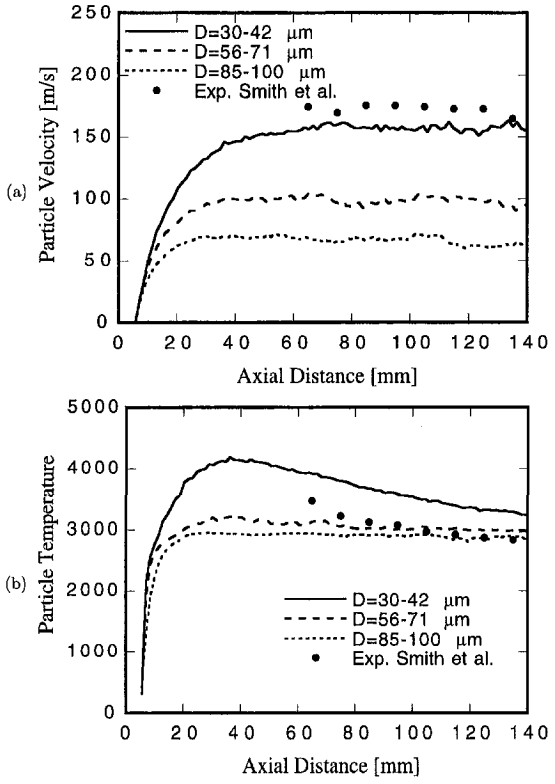

Fig. 4 (a) Axial velocity, and (b) surface temperature of a zirconia particle of different diameters. Experimental data for particle size 30 ~ 99 μm taken from Smith et al. (1997).

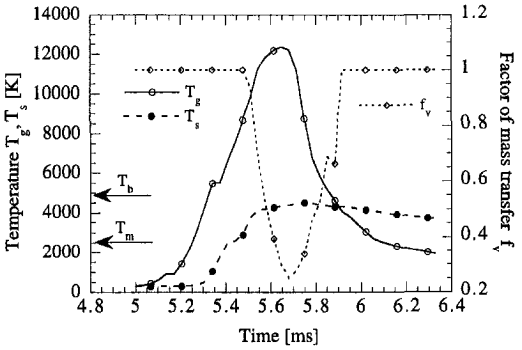

Fig. 5 Evolution of the temperature of the particle surface and the surrounding plasma gas, and the influence factor, f_v, of mass transfer on heat transfer, for Zirconia particle of 40 μm

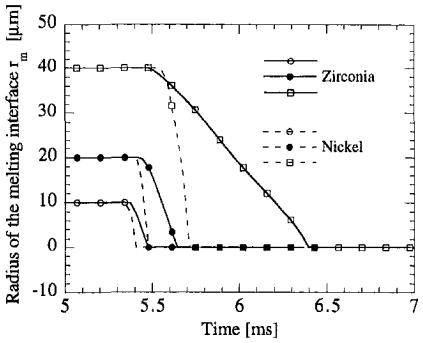

Fig. 7 Comparison of the movement of the melt/solid interface for zirconia and nickel particles of three different sizes

temperature of the surrounding plasma gas is still rising, the increase in surface temperature of the particle is very small. One reason for this behavior is that the heat transferred to a particle is mostly used for vaporization, and the other reason is that the convective heat transfer from the plasma gas to the particle is significantly reduced by the mass transfer due to vaporization. This reduction can be as high as about 70 percent as displayed by a sharp drop in f_v. The decrease in convective heat transfer results from the net outward mass transfer that reduces the Nusselt number, an effect very similar to that observed in blowing (Faeth, 1983). At some point the plasma gas temperature $\tilde{T}_g$ decreases below the particle surface temperature as the particle moves away from the plasma core. The particle then loses heat primarily by radiation and the surface temperature starts decreasing.

To examine the contribution of radiation and convective heat transfer, they are calculated separately and presented in Fig. 6. Negative values of $\dot{Q}_{\text{conv}}$ and positive values of $\dot{Q}_{\text{rad}}$ represent heat loss from the particle surface and different scales are applied to $\dot{Q}_{\text{conv}}$ and $\dot{Q}_{\text{rad}}$ on this plot. During the heating of a particle, the convective heat transfer dominates, which is about two orders of magnitude larger than the radiative heat transfer. Indeed, the heat transfer by convection increases during the heat-up stage since the temperature difference between the particle and plasma gas increases and the thermal conductivity of plasma gas is larger at higher temperatures. Similarly, the radiative heat transfer rate increases rapidly as the surface temperature increases. And it becomes relatively important only when the temperature of the surrounding plasma gas drops down significantly, i.e., the convective heat transfer decreases. To show the importance of various parameters and their effect on transport mechanisms between the particle and plasma gas, the values of many useful dimensional and nondimensional parameters for a zirconia particle of 40 μm are listed in Table 2.

As already shown in Fig. 4(*b*), the particle temperature reaches a peak after traveling for a very short distance in the plasma jet. The actual time needed for the particle to reach the maximum temperature is, however, almost half of the particle dwell time in the plasma jet, as shown in Fig. 5. This means that within almost half of its in-flight time, the particle travels just a few centimeters downstream. This is because of the small particle velocity at the early stages of acceleration.

The heat-up history of nickel particle is very similar to that of the zirconia particle, except for some small differences in the magnitude due to the variations in thermophysical properties. For example, a nickel particle of 40 μm reaches the maximum temperature of about 2900 K at almost the same time as a zirconia particle of the same size. The vaporization, however, lasts much longer and more mass is vaporized in the case of nickel because of its lower boiling point (3187 K).

4.3 Melting of a Particle. The movement of the melt/solid interface is shown in Fig. 7 for both the zirconia and nickel particles of three different sizes. Although the melt/solid interface velocity does not change much with the particle size, the rate of melting is quite different for the two different materials selected here. As represented by the slopes of the curves in Fig. 7, the velocity of zirconia melt/solid interface is much smaller than that in the case of nickel. This can be explained through the melting interface condition, Eq. (3); the larger latent heat of fusion for zirconia leads to its slower interface movement.

The results (not shown here) on the melt interface movement obtained by using the nonequilibrium kinetic model, Eq. (19), are the same as that with the equilibrium assumption. This indicates that the net rate of heat transfer to the solid side of the interface is the controlling factor for particle melting and the simple equilibrium model can be employed without any appreciable inaccuracy introduced into the model predictions.

4.4 Resolidification of a Particle. No resolidification is observed in the case of particle sizes of 20, 40 and 80 μm. However, it occurs at a 100-μm zirconia particle. As shown in Fig. 8, the

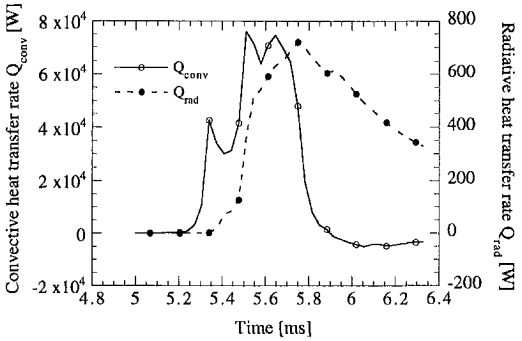

Fig. 6 Convective heat transfer versus the radiative heat transfer

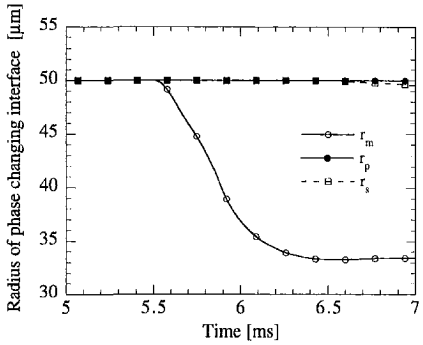

Fig. 8 Movement of the phase-change interfaces of a 100 μm zirconia particle

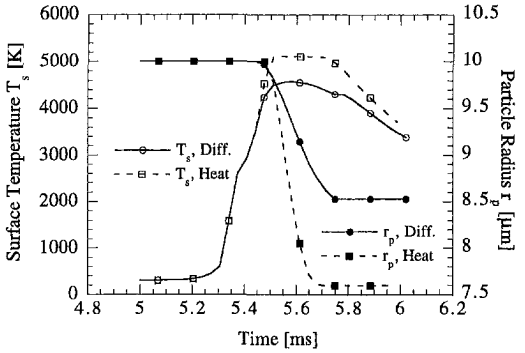

Fig. 9 Particle temperature and radius of a 20-μm zirconia particle obtained using two different vaporization models

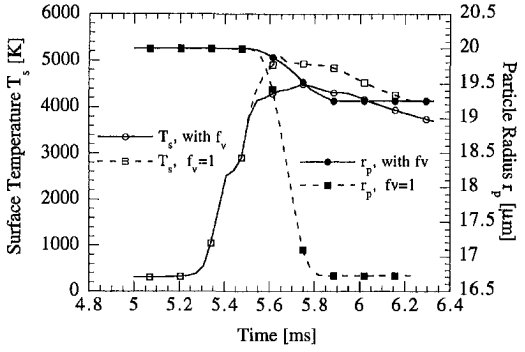

Fig. 10 Temperature and radius of Zirconia particle calculated with and without the effect of mass transfer on heat transfer

resolidification begins at about 6.6 ms, which corresponds to the axial distance of approximately 7.5 cm. This means that this particle will be partially resolidified when it impacts the substrate placed 10 cm away from the plasma torch. The thickness of the solidified layer grows slowly, indicating a relatively slow cooling rates because the heat must be diffused through the solid layer as soon as it is formed on the surface. The reason for resolidification of larger particles is that the trajectories of large particles deviate much more from the center line of the plasma jet due to their larger inertia. They fly quickly to the peripheral region where the plasma gas has much lower temperatures. They start to cool down and resolidify shortly after passing through the hot core of the plasma flame. The larger the particle, the faster it will start to resolidify. Additionally, because of the short residence time in the hot flame region, a larger particle does not get fully melted, as shown by the radius of the melting interface, r_m, in Fig. 8. The melting interface stops moving towards the particle center at about 6.5 ms and then moves back due to resolidification at this interface. The melting interface has now become a solidification interface. At this point two resolidification interfaces, one moving inward and the other moving outward, appear. The outer resolidification has much higher velocity because of direct thermal interaction with the surrounding gas.

4.5 Vaporization at the Surface and Effect of Mass Transfer. In order to compare the different vaporization models the particle temperature and radius obtained by using the mass diffusion controlled vaporization model and the heat transfer controlled model are plotted in Fig. 9. In the heat transfer controlled vaporization calculations, the boiling point of zirconia was chosen as 5000 K, at which the vapor pressure is almost the same as the atmospheric pressure. As shown in Fig. 9, the surface temperature calculated with the heat transfer controlled model is higher than that with the mass transfer model, and the mass that has been vaporized is predicted to be more. The reason for the higher vaporization rate as predicted by the heat transfer controlled model is that a much larger amount of available heat is used for vaporization in this case.

The effect of mass transfer on heat transfer, or on the particle temperature and diameter is further displayed in Fig. 10. These results show that without the correction of the mass transfer on heat transfer the particle temperature will be a little larger than that with the correction. This small increase in the surface temperature has a strong influence on the vaporization rate as reflected by the change of the particle radius.

4.6 Effect of Internal Conduction. The computational results with and without internal conduction for nickel and zirconia particles have also been obtained to examine the significance of internal conduction with respect to the material properties. Figure 11 presents the temperature at the particle center and the surface. As expected, the nickel particles have negligible temperature difference between the surface and the center, while in the case of zirconia the temperature difference is quite large. Obviously, this difference tends to be larger for larger particles and for higher rates of heat transfer at the surface. The result for an 80-μm zirconia particle is very interesting. In this case, the temperature at the particle center reaches the melting point so late that the surface temperature has already fallen. This implies that in the case of a larger particle with low thermal conductivity, the central portion may not melt. This is consistent with the result obtained for a 100-μm zirconia particle and is shown in Fig. 8. Figure 11 also shows that the particles with larger sizes have longer dwell time in the plasma jet; about 1.0, 1.4, and more than 2.0 ms for the particles of size 20, 40, and 80 μm, respectively. The difference between the zirconia and nickel on the dwell time is not so obvious because of the small difference in density of these two materials.

5 Conclusions

A comprehensive mathematical model has been developed to study the interaction of a plasma jet with powder particles while accounting for the temperature gradients within the particle, melt/solid interface movement and particle vaporization. Special attention has been paid to the modeling of vaporization and the influence of vaporization on convective heat transfer. An effective numerical scheme based on coordinate transformation for the solution of internal heat conduction with moving interfaces and

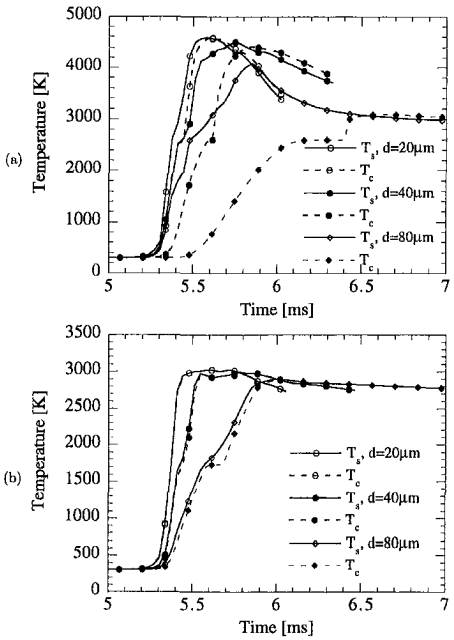

Fig. 11 Temperatures at the particle center and particle surface for different particle sizes, for (*a*) zirconia and (*b*) nickel

boundaries has been developed. Computations have been performed for a single particle of zirconia and nickel with different sizes injected into an Ar–H_2 plasma jet. Following are major conclusions:

- In the case of powder fed from the outside of the plasma gun, the powder particles need about one-fourth of the dwell time to travel into the hot plasma core and about the same length of time to be heated to their maximum temperature.
- Convective heat transfer dominates the heat-up stage while radiative heat transfer becomes important after the particle reaches its maximum temperature and the particle flies into the plasma plume with a relatively lower temperature.
- Vaporization becomes significant even when the particle temperature is much below the boiling point. The mass diffusion-controlled model for vaporization modeling is therefore necessary to replace the simple heat transfer controlled model.
- Mass transfer due to vaporization significantly reduces the convective heat transfer at the particle surface, thereby constraining the vaporization rate.
- Resolidification at the particle surface is possible in the case of large particles.
- The movement of melt interface is controlled by heat transfer through the interface. The equilibrium model is adequate for the modeling of melting process.

Acknowledgments

Acknowledgments are due to NSF (MRSEC Program under Award No. DMR-9632570) and the Idaho National Engineering and Environment Laboratory, University Research Consortium Program, managed by Lockheed Martin Corporation for DoE.

References

Anselmo, A., Prasad, V., and Koziol, J., 1991, "Melting of a Sphere when Dropped in a Pool of Melt with Applications to Partially-Immersed Silicon Pellets," 27th National Heat Transfer Conf., Minneapolis.

Boulos, M. I., Fauchais, P., Vardelle, A., and Pfender, E., 1993, "Fundamentals of Plasma Particle Momentum and Heat Transfer," *Plasma Spraying,* R. Suryanarayanan, ed., World Scientific, Singapore, pp. 3–57.

Boulos, M. I., Fauchais, P., and Pfender, E., 1994, *Thermal Plasmas, Fundamentals and Applications,* Vol. 1, Plenum Press, New York, p. 367, 372.

Chang, C. H., and Ramshaw, J. D., 1993, "Numerical Simulations of Argon Plasma Jets Flowing into Cold Air," *Plasma Chemistry and Plasma Processing,* Vol. 13, No. 2, pp. 189–209.

Chang, C. H., and Ramshaw, J. D., 1996, "Modeling of nonequilibrium effects in a High-Velocity Nitrogen-Hydrogen Plasma Jet," *Plasma Chemistry and Plasma Processing* (Supplement), Vol. 16, No. 1, pp. 5S–17S.

Chen, X., and Pfender, E., 1982, "Heat Transfer to a Single Particle Exposed to a Thermal Plasma," *Plasma Chemistry and Plasma Processing,* Vol. 2, No. 2, pp. 185–212.

Chen, X., and Pfender, E., 1983a, "Effect of the Knudsen Number on Heat Transfer to a Particle Immersed into a Thermal Plasma," *Plasma Chemistry and Plasma Processing,* Vol. 3, No. 1, pp. 97–112.

Chen, X., and Pfender, E., 1983b, "Behavior of Small Particles in a Thermal Plasma Flow," *Plasma Chemistry and Plasma Processing,* Vol. 3, No. 3, pp. 351–366.

Das, D. K., and Sivakumar, R., 1990, "Modeling of the Temperature and the Velocity of Ceramic Powder Particles in A Plasma Flame-I. Alumina," *Acta Metall. Mater.,* Vol. 38, No. 11, pp. 2187–2192.

Faeth, G. M., 1983, "Evaporation and Combustion of Sprays," *Prog. Energy Combust. Sci.,* Vol. 9, pp. 1–76.

Fiszdon, J. K., 1979, "Melting of Powder Grains in a Plasma Flame," *Int. J. Heat Mass Transfer,* Vol. 22, pp. 749–761.

Groma, I., and Vetö, B., 1986, "Melting of Powder Grains in Plasma Spraying," *Int. J. Heat Mass Transfer,* Vol. 29, No. 4, pp. 549–554.

Hultgen, R., Desai, P. D., Hawkins, D. T., Gleiser, M., Kelley, K. K., and Wagman, D. D., 1973, *Selected Values of the Thermodynamics Properties of the Elements,* American Society of Metals.

Launder, B. E., and Spalding, D. B., 1972, *Mathematical Models of Turbulence,* Academic Press, New York.

Law, C. K., 1982, "Recent Advances in Droplet Vaporization and Combustion," *Prog. Energy Combust. Sci.,* Vol. 8, pp. 171–201.

Lee, H. E., 1988, "Heat Transfer of Particles in Plasma Flow," *J. Phys. D: Appl. Phys.,* Vol. 21, pp. 73–78.

Lee, Y. C., Hsu, K. C., and Pfender, E., 1981, "Modeling of Particles Injected into a d.c. Plasma Jet," *Proc. 5th Int. Symposium on Plasma Chemistry,* Vol. 2, p. 795.

Pfender, E., and Lee, Y. C., 1985, "Particle Dynamics and Particle Heat and Mass Transfer in Thermal Plasma, Part I, The Motion of a Single Particle without Thermal Effects," *Plasma Chemistry and Plasma Processing,* Vol. 5, No. 3, pp. 211–237.

Proulx, P., Mostaghimi, J., and Boulos, M. I., 1985, "Plasma-particle Interaction Effects in Induction Plasma Modeling under Dense Loading Conditions," *Int. J. Heat Mass Transfer,* Vol. 28, No. 7, pp. 1327–1336.

Ramshaw, J. D., and Chang, C. H., 1993, "Computational Fluid Dynamics Modeling of Multi-component Thermal Plamsmas," *Plasma Chemistry and Plasma Processing,* Vol. 12, No. 3, pp. 299–325.

Ramshaw, J. D., and Chang, C. H., 1995, "Iteration Scheme for Implicit Calculations of Kinetics and Equilibrium Chemical Reactions in Fluid Dynamics," *J. of Computational Physics,* Vol. 116, pp. 359–364.

Ranz, W. E., and Marshall, W. R., 1952, "Evaporation from Drops," *Chem. Engrg. Prog.,* Vol. 48, No. 3, pp. 141–173.

Samsonov, G. V., 1973, *The Oxide Handbook,* Plenum, New York (translation from Russian).

Smith, W., Jewett, T. J., Sampath, S., Swank, W. D., and Fincke, J. R., 1997, "Plasma Processing of Functionally Graded Materials Part I: Process Diagnostics," *Proc. United Thermal Spray Conf.,* C. C. Berndt, ed., ASM International, Materials Park, OH, pp. 599–605.

Solomon, A. D., 1979, "Melt Time and Heat Flux for a Simple PCM Body," *Solar Energy,* Vol. 22, pp. 251–257.

Vardelle, A., Themelis, N. J., Dussoubs, B., Vardelle, M., and Fauchais, P., 1997, "Transport and Chemical Rate Phenomena in Plasma Sprays," *J. of High Temp. Proc.,* Vol. 1, No. 3, pp. 295–314.

Wan, Y. P., Prasad, V., Wang, G.-X., Sampath, S., and Fincke, J. R., 1998, "Modeling of Powder Particle Heating, Melting and Evaporation in Plasma Spraying Progresses," *Proc. ASME Heat Transfer Division,* Vol. 4, HTD-Vol. 361-4, ASME, New York, pp. 67–77.

Wang, G.-X., and Matthys, E. F., 1996, "Modeling of Nonequilibrium Surface Melting and Resolidification for Pure Metals and Binary Alloys," ASME JOURNAL OF HEAT TRANSFER, Vol. 118, pp. 944–951.

Wang, G.-X., Prasad, V., and Matthys, E. F., 1997, "An Interface-tracking Numerical Method for Rapid Planar Solidification of Binary Alloys with Application to Microsegregation," *Materials Science & Engineering,* Vol. A225, pp. 47–58.

Wei, D. Y. C., Farouk, B., and Apelian, D., 1987, "Melting Powder Particles in a Low-Pressure Plasma Jet," ASME JOURNAL OF HEAT TRANSFER, Vol. 109, pp. 971–976.

Wei, D. Y. C., Farouk, B., and Apelian, D., 1988, "Melting Metal Powder Particles in an Inductively Coupled R. F. Plasma Torch," *Metall. Trans. B,* Vol. 19B, pp. 213–226.

Westhoff, R., Trapaga, G., and Szekely, J., 1992, "Plasma-Particle Interactions in Plasma Spraying Systems," *Metall. Trans. B,* Vol. 23B, pp. 683–693.

White, F. M., 1974, *Viscous Fluid Flow,* McGraw-Hill, New York.

Williams, F. A., 1985, *Combustion Theory,* 2nd Ed., Addison-Weslay, New York, p. 380.

APPENDIX

Reaction Mechanisms for an Ar + H_2 Plasma into Air

Kinetic reactions:

$$H_2 + M = 2H + M$$

$$O_2 + M = 2O + M$$

$$N_2 + M = 2N + M$$

Equilibrium reactions:

$$Ar + e^- = Ar^+ + 2e^-$$

$$H + e^- = H^+ + 2e^-$$

$$N + e^- = N^+ + 2e^-$$

$$O + e^- = O^+ + 2e^-$$

$$N_2 + N^+ = N_2^+ + N$$

$$N + N = N_2^+ + e^-$$

$$H + O_2 = OH + O$$

$$H_2 + O = OH + H$$

$$H_2O + O = 2OH$$

$$H_2 + OH = H_2O + H$$

Journal of Heat Transfer

Technical Notes

This section contains shorter technical papers. These shorter papers will be subjected to the same review process as that for full papers.

Thermal Contact Resistance of Silicone Rubber to AISI 304 Contacts

S. K. Parihar[1] and N. T. Wright[2]

Introduction

Elastomers are highly extensible, compliant, and easily processed into a variety shapes; other properties vary according to the specific constituents. Elastomers may deform easily to occupy cavities at an irregular metal surface—unlike metal to metal contacts, these interfaces may have more real contact area than apparent contact area. The typically low thermal conductivity and softness of elastomers, as compared with metals, often suggests that the total thermal resistance of a metal-elastomer-metal joint may be calculated using only the bulk thermal resistance of the elastomer, the interface resistances being neglected. For a thin elastomer layer or as additives increase its thermal conductivity, and as the bulk resistance of the elastomer thus decreases, the interface resistances may become significant. Existing contact resistance models (e.g., Cooper et al., 1969; Mikic, 1974; Sridhar and Yovanovich, 1994), developed for interfaces of two hard materials, are not applicable to elastomeric contacts because of the intrinsic properties of elastomers. Therefore, measurement of the thermal contact resistance (or its inverse, the contact conductance) for elastomeric interfaces is necessary.

Fletcher and Miller (1974) report the thermal conductance of metal-elastomer-metal joints composed of commercially available gasket materials for aerospace applications. The elastomer thicknesses ranged from 0.43 to 2.92 mm and many of the samples were filled with metal particles to enhance their thermal or electrical conductivity. The overall contact conductance of these joints increased with increasing contact pressure. Mohr et al. (1997) measured the total conductance of an elastomer-paper-elastomer joint. They found that the surface properties of the elastomers played a significant role in the overall thermal contact conductance of the joint, though the 1.78-mm thickness of their elastomer specimens prevented measurement of the temperature distribution within the elastomer. Others have measured the contact conductance at the interfaces of metals and rigid polymers (e.g., Hall et al., 1987; Yu et al., 1990; Rhee et al., 1994). Marotta and Fletcher (1996) measured the thermal contact conductance for a wide range of thermoplastic and thermosetting polymers. The thermal conductance increased with applied pressure, but the effect of temperature level on the conductance varied between polymers.

Reported here are the results of measurements of the interface resistances of a silicone rubber and AISI 304 stainless steel (SS) joint. Temperatures within the silicone rubber specimens were measured to facilitate determination of the interface resistances as well as the total resistance of the joint. Correlations were developed for the resistances in terms of mechanical load, heat flux, temperature level, and specimen thickness.

Methods and Materials

The device used for the measurements reported here is described in detail in Parihar and Wright (1997). Briefly, it is an insulated column consisting of a heater, two 304 SS cylinders, a specimen, and a heat sink assembled under a bell jar to reduce interaction with the ambient environment. At the top of the column are dead weights on a freely sliding carriage. A steel ball transmits only a normal force from the carriage to the column. An automatically regulated guard heater is mounted inside a copper cylinder and maintained to within 0.5°C of the main heater, which is a 30 W flexible electric heater mounted in another hollow copper cylinder just below the guard heater. Next is a 31.8-mm diameter, 17.8-mm long 304 SS cylinder that both measures the flux and provides the hot metal interface for the joint. Four 36-gauge, copper-constantan thermocouples are mounted in 0.4-mm dia., 4-mm deep holes equally spaced along the edge. An identical 304 SS cylinder below the specimen provides the cold metal interface. The heat sink is a hollow copper cylinder cooled with water pumped from a chilled bath, and underneath the heat sink is a load cell. The column is insulated by 50 mm of fiberglass wool.

Silicone rubber specimens, 31.8 mm in diameter, were cut from 4.76, 6.35, and 9.54-mm thick sheets (McMaster-Carr) using a specially machined die spun at high speed while cooled by a water spray to protect the specimens from heat-induced alterations. These specimens were also fitted with four 36-gauge T-type thermocouples mounted in 0.4-mm diameter, 4-mm deep holes. For each thickness, three specimens were tested and the results averaged.

The column was assembled and aligned with the silicone specimen in place between the two 304 SS cylinders. All metal-to-metal interfaces were coated with thermally conductive grease. The minimum dead weight was applied, and LVDT readings before and after the dead weight loading provided the displacement due to the mechanical loading alone. The heater powers were set to the minimum level to be used in the testing and the computer controlled data acquisition system was started to record the thermocouple and LVDT output and

[1] Department of Mechanical Engineering, University of Maryland, Baltimore, MD 21250. Current address: National Instrument Company, 4119 Fordleigh Road, Baltimore, MD 21215.

[2] To whom correspondence should be addressed. Department of Mechanical Engineering, University of Maryland, Baltimore, MD 21250. e-mail: wright@umbc.edu. Mem. ASME.

Contributed by the Heat Transfer Division for publication in the JOURNAL OF HEAT TRANSFER. Manuscript received by the Heat Transfer Division, Aug. 5, 1998; revision received, Dec. 16, 1998. Keywords: Conduction, Contact Resistance, Heat Transfer, Polymers. Associate Technical Editor: A. Majumdar.

Table 1 Surface properties of the 304 SS cylinders

	Upper flux meter		Lower flux meter	
Hardness	1020 MPa		1020 MPa	
Side in contact with	Heater	Rubber	Heat sink	Rubber
RMS surface roughness (μm)	0.407	2.334	0.364	2.004
Mean asperity slope (μm/m)	0.143	0.193	0.427	0.238

Table 2 Surface properties of a typical silicone rubber specimen

Hardness	50 Shore A (manufacturer's value)			
Side in contact with	Hot interface		Cold interface	
	Before test	After test	Before test	After test
RMS surface roughness (μm)	2.345	2.231	2.425	2.479
Mean asperity slope (μm/m)	1.931	1.825	2.009	1.977

the heater input voltage and current at 30-minute intervals. Seven hours was the longest time required to reach steady-state from the start-up condition, so eight hours were allowed between each change of the operating conditions.

The surface properties of the 304 SS cylinders, listed in Table 1, were measured using an optical profilometer (Zygo) and a hardness tester (Buehler Micromet). The ends that were in contact with either the heater or heat-sink were relatively smooth. Those in contact with the specimen had been bead-blasted and were considerably rougher. A representative sampling of the rubber specimens were similarly examined with the profilometer before and after the tests (see Table 2). No significant permanent change to the surfaces resulted from the testing.

Data Reduction. The heat flux through each stainless steel cylinder was calculated from the measured temperature gradient and the thermal conductivity of 304 SS at the mean temperature of the cylinder. The temperatures of the metal at the hot and cold interfaces with the specimen, T_1 and T_4, respectively, were estimated by extrapolating the temperature gradient to the surface. The heat flux through the silicone was estimated by averaging the heat flux through the two 304 SS cylinders, which differed by a maximum of 15 percent. A polynomial fit through the measured silicone temperatures was used to extrapolate the temperatures of the hot and cold surfaces of the silicone T_2 and T_3, respectively. The positions of these thermocouples

Table 3 Correlations of contact resistance at a silicone rubber–304 SS joint, where resistances have units of m² K/kW, T_h and T_s of K, q'' of kW/m², σ of MPa, and δ of mm

Correlation	R^2
$R_t = -18.52 - 0.73 \ln(\sigma) + 0.06T_s + 2.48\delta - 0.36q''$	0.994
$R_h = -23.68 - 0.22 \ln(\sigma) + 0.13T_s + 0.034\delta - 0.32q'' - 0.042T_h$	0.704
$R_c = -4.72 - 1.63\sigma + 0.04T_s - 0.17\delta - 0.056q'' - 0.015T_h$	0.686
$T_h = 174 - 3.26 \ln(\sigma) + 12.6\delta + 21.9q''$	0.981
$T_s = 236 - 17.3\sigma + 6.2\delta + 11.0q''$	0.986

were corrected for displacement due to the mechanical and thermal loads by assuming a linear variation between the zero displacement at the bottom of the specimen and the maximum displacement at the top (0.2 to 0.7 mm), as measured by the LVDT. The total joint resistance R_t was calculated from

$$R_t = \frac{(T_1 - T_4)}{q''} \tag{1}$$

where q'' is the flux through the specimen. Similarly, the resistances at the hot and cold interfaces are $R_h = (T_1 - T_2)/q''$ and

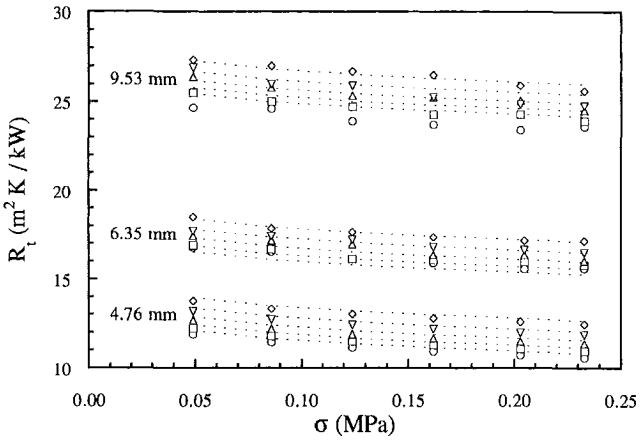

Fig. 2 Comparison of the correlation listed in Table 3 with measured R_t for the three specimen thicknesses. For 9.53 mm, T_s are ○ 311 K, □ 323 K, △ 338 K, ▽ 357 K, ◇ 378 K; for 6.53 mm, T_s are the same as for Fig. 1; and for 4.76 mm, T_s are ○ 290 K, □ 302 K, △ 317 K, ▽ 336 K, ◇ 358 K.

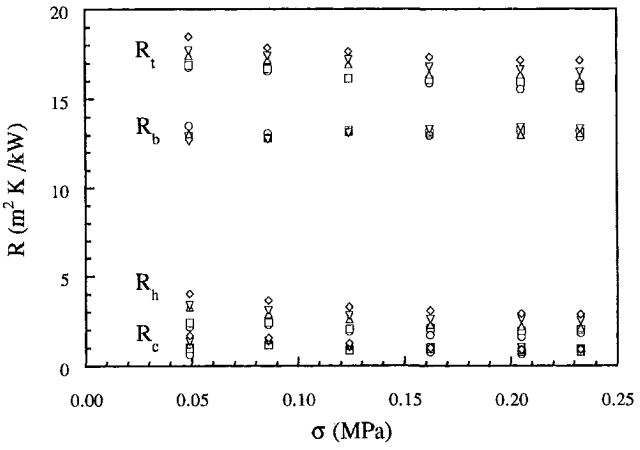

Fig. 1 Measured components of contact resistance for 6.53 mm silicone. The temperatures are T_s: ○ 297 K, □ 309 K, △ 324 K, ▽ 343 K, ◇ 364 K.

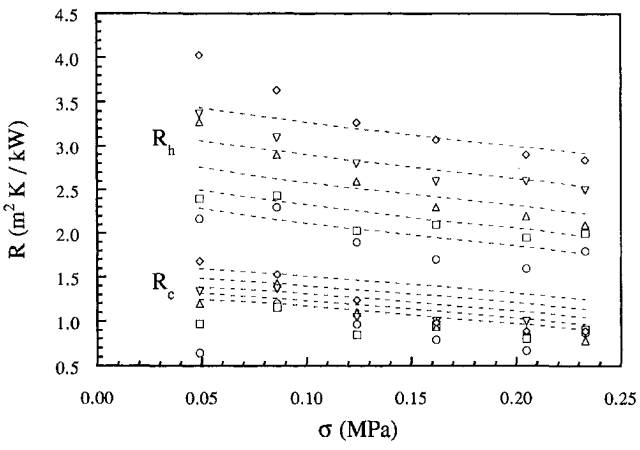

Fig. 3 Comparison of correlations listed in Table 3 with measured R_h and R_c for 6.35 mm silicone. Here, T_h are ○ 315 K, □ 338 K, △ 366 K, ▽ 398 K, ◇ 433 K; and T_c are ○ 286 K, □ 290 K, △ 294 K, ▽ 297 K, ◇ 301 K.

$R_c = (T_3 - T_4)/q''$, respectively. The bulk resistance is calculated by $R_b = R_t - R_h - R_c$.

Uncertainty. Using the propagation of uncertainty (Kline and McClintock, 1953), and the uncertainties in T_1, T_2, and q'', the uncertainty associated with R_t is 13 percent. The additional uncertainty of the position of the thermocouples in the silicone increase the uncertainty in the values of R_h and R_c to 29 percent.

Results and Discussion

Figure 1 shows R_t, R_h, and R_c decreasing with increasing applied normal stress σ for the 6.35-mm specimens. The interface temperatures are defined as $T_h = (T_1 + T_2)/2$ and $T_c = (T_3 + T_4)/2$ at the hot and cold interfaces, respectively. The behavior for the other two thicknesses is similar. The decreasing R_t results from the reduction in the interface resistances. The bulk resistance, averaged over the range of σ and the mean temperature of the silicone T_s, comprises 74, 77, and 85 percent of R_t for the 4.76, 6.35, and 9.53 mm specimens, respectively. Table 3 lists the correlations developed using the best fit linear regression from the results of the three specimens of each thickness. The specimen thickness δ dominates the correlation of R_t, as might be expected given the dominance of R_b. The high coefficient of determination ($R^2 = 0.994$) for R_t indicates a good correlation of the data. Figure 2 illustrates this good agreement between the correlation for R_t and the measurements at the three thicknesses. In each case, R_t decreases with increasing σ and decreasing T_s.

Figure 3 compares the correlations for R_h and R_c with the results for the 6.35 mm silicone. Again, increasing σ and decreasing T_h or T_c result in reduced R_h and R_c, respectively. These relations for the interface resistances are not as well correlated as was R_t, as is indicated by the lower values of R^2 listed in Table 3. This may be the result of the increased uncertainty in the measurements of the interface resistances.

The trends shown in Fig. 3 are typical of the three specimen thicknesses. The ratio R_c/R_h is less than one and decreases with increasing T_h. Heat transfer is from metal to elastomer at the upper interface, with a representative ratio of thermal conductivity of silicone k_r to thermal conductivity of metal k_m of 0.025. This may result in a constriction resistance at the asperities of the upper interface. For T_h increasing from 315 to 433 K, k_r decreases by 17 percent and k_m increases by 15 percent, further reducing the ratio of k_r/k_m. At the lower interface the heat flow is from the metal to elastomer with a representative k_m/k_r of 31. The heat transfer is from low to high thermal conductivity material, with the metal acting as a strong heat sink. Parihar (1997) calculated $T_1 - T_2$ to be 1.5 times greater than $T_3 - T_4$ using a finite difference model for conditions representative of the measurements. This calculation is in good agreement with the differences in the measured R_h and R_c.

These measurements suggest that the interface resistances for a silicone rubber to stainless steel joint may be a significant fraction of the overall resistance. The difference in the resistances at the two interfaces appears to result from a constriction resistance at the metal to elastomer interface.

References

Cooper, M. G., Mikic, B. B., and Yovanovich, M. M., 1969, "Thermal Contact Conductance," *J. Heat Mass Trans.*, Vol. 12, pp. 279–300.

Fletcher, L. S., and Miller, R. G., 1974, "Thermal Conductance of Gasket Materials for Spacecraft Joints," *Progress in Astronautics and Aeronautics, Thermophysics and Spacecraft Thermal Control,* AIAA, Vol. 35, pp. 335–349.

Hall, J. A., Ceckler, W. H., and Thompson, E. V., 1987, "Thermal Properties of Rigid Polymers. I. Measurement of the Thermal Conductivity and Questions Concerning Contact Resistance," *J. Appl. Poly. Sci.*, Vol. 33, pp. 2029–2039.

Kline, S. J., and McClintock, F. A., 1953, "Describing Uncertainties in Single Sample Experiments," *Mechanical Engineering,* Vol. 75, pp. 3–8.

Marotta, E., and Fletcher, L. S., 1996, "Thermal Contact Conductance of Selected Polymeric Materials," *J. Thermophysics Heat Trans.*, Vol. 10, No. 2, pp. 334–342.

Mikic, B. B., 1974, "Thermal Contact Conductance: Theoretical Considerations," *Int. J. Heat Mass Trans.*, Vol. 17, pp. 205–214.

Mohr, J. W., Seyed-Yagoobi, J., and Price, D. C., 1997, "Thermal Contact Conductance of a Paper/Elastomer Interface," ASME JOURNAL OF HEAT TRANSFER, Vol. 119, pp. 363–366.

Parihar, S. K., 1997, "Thermal Contact Resistance of Elastomer to Metal Contacts," Ph.D. dissertation, University of Maryland. Baltimore, MD.

Parihar, S. K., and Wright, N. T., 1997, "Thermal Contact Resistance at Elastomer to Metal Interfaces," *Int. Comm. Heat Mass Trans.*, Vol. 24, No. 8, pp. 1083–1092.

Rhee, B. O., Hieber, C. A., and Wang, K. K., 1994, "Experimental Investigation of Thermal Contact Resistance in Injection Molding," *ANTEC,* pp. 496–500.

Shridar, M. R., and Yovanovich, M. M., 1994, "Elastoplastic Contact Conductance Model for Isotropic Conforming Rough Surfaces and Comparison with Experiments," *Thermal Phenomena at Molecular and Microscales and in Cryogenic Infrared Detectors,* Vol. 277, ASME, New York, pp. 43–56.

Yovanovich, M. M., De Vaal, J. W., and Hegazy, A. H., 1994, "A Statistical Model to Predict Thermal Contact Gap Conductance between Conforming Rough Surfaces," AIAA-82-0888, June 1982, pp. 1–7.

Yu, C. J., Sunderland, J. E., and Poli, C., 1990, "Thermal contact Resistance in Injection Molding," *Poly. Engr. Sci.*, Vol. 30, pp. 1599–1606.

On the Wave Diffusion and Parallel Nonequilibrium Heat Conduction

M. Honner[1] and J. Kunes[2]

Introduction

Wave diffusion and parallel heat conduction in spite of total physical difference have such a similar mathematical description that they even led to the development of the unified model for both microscale nonequilibrium heat conduction processes (Tzou, 1997).

This contribution uses a physical approach coming from the nature of microscale heat transfer to remind us of differences between wave diffusion and parallel nonequilibrium heat transfer. The objective of this contribution is to introduce dimensionless criteria for microscale heat transfer standing on the criteria already established and used for equilibrium diffusion conduction. Applicability regions for individual modes of heat propagation can be defined by means of the criteria.

Wave Diffusion Heat Conduction

The wave heat conduction equation has been derived in the form

$$\frac{\partial^2 T}{\partial x^2} = \frac{1}{a}\frac{\partial T}{\partial \tau} + \frac{\tau_q}{a}\frac{\partial^2 T}{\partial \tau^2} \tag{1}$$

and mathematically represents wave fields with decay. The difference to the diffusion heat conduction equation is expressed by the wave term introducing the relaxation time of the material $\tau_q(s)$. However, the relaxation time does not represent the finite speed of heat propagation and has not been originally introduced in the wave heat conduction theory.

The diffusion theory has already used the relaxation time of materials as the time representing the mean free path of energy carriers. By means of the relaxation time the relations for thermal conductivity have been derived, for example, concerning phonon or electron scattering processes on phonons, lattice imperfections

[1] To whom correspondence should be addressed. Research Worker, Mechanical Engineering Research, Skoda Vyzkum s.r.o., Tylova 57, CZ 31600 Plzen, Czech Republic. e-mail: mhonner@vyz.ln.skoda.cz. Mem. ASME.

[2] Professor, Department of Physics, University of West Bohemia, Univerzitni 22, CZ 30614 Plzen, Czech Republic. e-mail: kunes@kfy.zcu.cz.

Contributed by the Heat Transfer Division for publication in the JOURNAL OF HEAT TRANSFER. Manuscript received by the Heat Transfer Division, Sept. 8, 1998; revision received, Apr. 6, 1999. Keywords: Conduction, Heat Transfer, Heat Waves, Microscale, Nonequilibrium, Thermophysical. Associate Technical Editor: A. Majumdar.

$R_c = (T_3 - T_4)/q''$, respectively. The bulk resistance is calculated by $R_b = R_t - R_h - R_c$.

Uncertainty. Using the propagation of uncertainty (Kline and McClintock, 1953), and the uncertainties in T_1, T_2, and q'', the uncertainty associated with R_t is 13 percent. The additional uncertainty of the position of the thermocouples in the silicone increase the uncertainty in the values of R_h and R_c to 29 percent.

Results and Discussion

Figure 1 shows R_t, R_h, and R_c decreasing with increasing applied normal stress σ for the 6.35-mm specimens. The interface temperatures are defined as $T_h = (T_1 + T_2)/2$ and $T_c = (T_3 + T_4)/2$ at the hot and cold interfaces, respectively. The behavior for the other two thicknesses is similar. The decreasing R_t results from the reduction in the interface resistances. The bulk resistance, averaged over the range of σ and the mean temperature of the silicone T_s, comprises 74, 77, and 85 percent of R_t for the 4.76, 6.35, and 9.53 mm specimens, respectively. Table 3 lists the correlations developed using the best fit linear regression from the results of the three specimens of each thickness. The specimen thickness δ dominates the correlation of R_t, as might be expected given the dominance of R_b. The high coefficient of determination ($R^2 = 0.994$) for R_t indicates a good correlation of the data. Figure 2 illustrates this good agreement between the correlation for R_t and the measurements at the three thicknesses. In each case, R_t decreases with increasing σ and decreasing T_s.

Figure 3 compares the correlations for R_h and R_c with the results for the 6.35 mm silicone. Again, increasing σ and decreasing T_h or T_c result in reduced R_h and R_c, respectively. These relations for the interface resistances are not as well correlated as was R_t, as is indicated by the lower values of R^2 listed in Table 3. This may be the result of the increased uncertainty in the measurements of the interface resistances.

The trends shown in Fig. 3 are typical of the three specimen thicknesses. The ratio R_c/R_h is less than one and decreases with increasing T_h. Heat transfer is from metal to elastomer at the upper interface, with a representative ratio of thermal conductivity of silicone k_r to thermal conductivity of metal k_m of 0.025. This may result in a constriction resistance at the asperities of the upper interface. For T_h increasing from 315 to 433 K, k_r decreases by 17 percent and k_m increases by 15 percent, further reducing the ratio of k_r/k_m. At the lower interface the heat flow is from the metal to elastomer with a representative k_m/k_r of 31. The heat transfer is from low to high thermal conductivity material, with the metal acting as a strong heat sink. Parihar (1997) calculated $T_1 - T_2$ to be 1.5 times greater than $T_3 - T_4$ using a finite difference model for conditions representative of the measurements. This calculation is in good agreement with the differences in the measured R_h and R_c.

These measurements suggest that the interface resistances for a silicone rubber to stainless steel joint may be a significant fraction of the overall resistance. The difference in the resistances at the two interfaces appears to result from a constriction resistance at the metal to elastomer interface.

References

Cooper, M. G., Mikic, B. B., and Yovanovich, M. M., 1969, "Thermal Contact Conductance," *J. Heat Mass Trans.*, Vol. 12, pp. 279–300.

Fletcher, L. S., and Miller, R. G., 1974, "Thermal Conductance of Gasket Materials for Spacecraft Joints," *Progress in Astronautics and Aeronautics, Thermophysics and Spacecraft Thermal Control,* AIAA, Vol. 35, pp. 335–349.

Hall, J. A., Ceckler, W. H., and Thompson, E. V., 1987, "Thermal Properties of Rigid Polymers. I. Measurement of the Thermal Conductivity and Questions Concerning Contact Resistance," *J. Appl. Poly. Sci.*, Vol. 33, pp. 2029–2039.

Kline, S. J., and McClintock, F. A., 1953, "Describing Uncertainties in Single Sample Experiments," *Mechanical Engineering,* Vol. 75, pp. 3–8.

Marotta, E., and Fletcher, L. S., 1996, "Thermal Contact Conductance of Selected Polymeric Materials," *J. Thermophysics Heat Trans.*, Vol. 10, No. 2, pp. 334–342.

Mikic, B. B., 1974, "Thermal Contact Conductance: Theoretical Considerations," *Int. J. Heat Mass Trans.*, Vol. 17, pp. 205–214.

Mohr, J. W., Seyed-Yagoobi, J., and Price, D. C., 1997, "Thermal Contact Conductance of a Paper/Elastomer Interface," ASME JOURNAL OF HEAT TRANSFER, Vol. 119, pp. 363–366.

Parihar, S. K., 1997, "Thermal Contact Resistance of Elastomer to Metal Contacts," Ph.D. dissertation, University of Maryland. Baltimore, MD.

Parihar, S. K., and Wright, N. T., 1997, "Thermal Contact Resistance at Elastomer to Metal Interfaces," *Int. Comm. Heat Mass Trans.*, Vol. 24, No. 8, pp. 1083–1092.

Rhee, B. O., Hieber, C. A., and Wang, K. K., 1994, "Experimental Investigation of Thermal Contact Resistance in Injection Molding," *ANTEC,* pp. 496–500.

Shridar, M. R., and Yovanovich, M. M., 1994, "Elastoplastic Contact Conductance Model for Isotropic Conforming Rough Surfaces and Comparison with Experiments," *Thermal Phenomena at Molecular and Microscales and in Cryogenic Infrared Detectors,* Vol. 277, ASME, New York, pp. 43–56.

Yovanovich, M. M., De Vaal, J. W., and Hegazy, A. H., 1994, "A Statistical Model to Predict Thermal Contact Gap Conductance between Conforming Rough Surfaces," AIAA-82-0888, June 1982, pp. 1–7.

Yu, C. J., Sunderland, J. E., and Poli, C., 1990, "Thermal contact Resistance in Injection Molding," *Poly. Engr. Sci.*, Vol. 30, pp. 1599–1606.

On the Wave Diffusion and Parallel Nonequilibrium Heat Conduction

M. Honner[1] and J. Kunes[2]

Introduction

Wave diffusion and parallel heat conduction in spite of total physical difference have such a similar mathematical description that they even led to the development of the unified model for both microscale nonequilibrium heat conduction processes (Tzou, 1997).

This contribution uses a physical approach coming from the nature of microscale heat transfer to remind us of differences between wave diffusion and parallel nonequilibrium heat transfer. The objective of this contribution is to introduce dimensionless criteria for microscale heat transfer standing on the criteria already established and used for equilibrium diffusion conduction. Applicability regions for individual modes of heat propagation can be defined by means of the criteria.

Wave Diffusion Heat Conduction

The wave heat conduction equation has been derived in the form

$$\frac{\partial^2 T}{\partial x^2} = \frac{1}{a}\frac{\partial T}{\partial \tau} + \frac{\tau_q}{a}\frac{\partial^2 T}{\partial \tau^2} \tag{1}$$

and mathematically represents wave fields with decay. The difference to the diffusion heat conduction equation is expressed by the wave term introducing the relaxation time of the material $\tau_q(s)$. However, the relaxation time does not represent the finite speed of heat propagation and has not been originally introduced in the wave heat conduction theory.

The diffusion theory has already used the relaxation time of materials as the time representing the mean free path of energy carriers. By means of the relaxation time the relations for thermal conductivity have been derived, for example, concerning phonon or electron scattering processes on phonons, lattice imperfections

[1] To whom correspondence should be addressed. Research Worker, Mechanical Engineering Research, Skoda Vyzkum s.r.o., Tylova 57, CZ 31600 Plzen, Czech Republic. e-mail: mhonner@vyz.ln.skoda.cz. Mem. ASME.

[2] Professor, Department of Physics, University of West Bohemia, Univerzitni 22, CZ 30614 Plzen, Czech Republic. e-mail: kunes@kfy.zcu.cz.

Contributed by the Heat Transfer Division for publication in the JOURNAL OF HEAT TRANSFER. Manuscript received by the Heat Transfer Division, Sept. 8, 1998; revision received, Apr. 6, 1999. Keywords: Conduction, Heat Transfer, Heat Waves, Microscale, Nonequilibrium, Thermophysical. Associate Technical Editor: A. Majumdar.

or electrons in Bhandari and Rowe (1988). Therefore, thermal conductivity is defined as

$$\lambda = \tfrac{1}{3}\rho c_p v^2 \tau_q. \tag{2}$$

Relaxation time is defined as the mean time between two collisions of energy carriers leading to the loss of momentum. Relation to the mean free path Λ is then

$$\Lambda = v\tau_q. \tag{3}$$

The wave heat conduction theory only adds the wave term into Eq. (1) to extract the second power of speed of heat propagation from thermal diffusivity

$$\frac{\tau_q}{a} = \frac{3}{v^2}, \tag{4}$$

in order for the mathematical description to reflect physical reality of finite speed conduction.

The wave diffusion heat conduction equation has the dimensionless form

$$\frac{\partial^2 \Theta}{\partial X^2} = \frac{\partial \Theta}{\partial \mathrm{Fo}} + \mathrm{Fo}_q \frac{\partial^2 \Theta}{\partial \mathrm{Fo}^2} \tag{5}$$

where the following dimensionless parameters appear. The *Fourier number,* dimensionless time of the process, expresses relations among the path traveled by the energy carrier during time τ, the mean free path, and the characteristic length L,

$$\mathrm{Fo} = \frac{a\tau}{L^2} = \frac{v\tau}{L}\frac{v\tau_q}{L}. \tag{6}$$

The *Fourier relaxation number* reflects the ratio of the mean free path Λ to the characteristic length L of the considered region

$$\mathrm{Fo}_q = \frac{a\tau_q}{L^2} = \left(\frac{\Lambda}{L}\right)^2. \tag{7}$$

The Fourier relaxation number is therefore the second power of the Knudsen number. By using the analogy to molecular heat and mass transfer in gas (Eckert, 1959), the following conclusion of the effect of Fo_q on the propagation character can be done:

$\mathrm{Fo}_q > 10^2$ *Wave conduction:* In the considered volume of the material heat carriers do not undergo collisions. Diffusion does not exist and carriers transport heat as free waves between boundaries of the considered material volume.

$10^{-4} < \mathrm{Fo}_q < 10^2$ *Wave diffusion conduction:* Transition state—the wave heat transport is attenuated strongly with the decrement of the Fourier relaxation number as the increasing effect of collisions takes place. The wave propagation character therefore changes to diffusion.

$\mathrm{Fo}_q < 10^{-4}$ *Diffusion conduction:* Collisions dominate the heat propagation character in the considered material volume. They slow down heat conduction and distribute propagation to all directions. The well-known diffusive heat transfer is the result.

When material surface is affected by a sudden rise of heat flux, the heat wave originating on the material surface propagates into the depth

$$X = \frac{\mathrm{Fo}}{\sqrt{\mathrm{Fo}_q}}. \tag{8}$$

According to the thermal resistivity of the material, the wave is continually decayed and the temperature of the wavefront is given by (Kuneš et al., 1996)

$$\Theta(\mathrm{Fo}) = \Theta(0)e^{-\mathrm{Fo}/2\mathrm{Fo}_q}. \tag{9}$$

The wave kinetic energy is scattered in collisions among energy carriers and is transformed into the internal energy of the material. Thus the wave propagation character transit to diffusion.

The dimensionless *criterion of nonequilibrium state of matter* is introduced as the ratio of the Fourier number and Fourier relaxation number

$$K_{\mathrm{NSM}} = \frac{\mathrm{Fo}}{\mathrm{Fo}_q}. \tag{10}$$

It defines the time range of nonequilibrium wave heat conduction as Fig. 1 demonstrates.

$K_{\mathrm{NSM}} < 10^{-2}$ *Nonequilibrium: wave conduction* (region A in Fig. 1). Energy carriers propagate in the material without collisions as thermal waves. Collision processes causing thermal resistance of the material have not yet taken place shortly after the origination of the nonequilibrium state due to the effect of heat sources. The heat conduction process is described by the pure wave equation.

$10^{-2} < K_{\mathrm{NSM}} < 10^{1}$ *Transition: wave diffusion conduction* (B in Fig. 1). The decay of the wave propagation becomes evident with increasing time as the material is directed to equilibrium. The heat conduction process is described by the wave diffusion equation.

$K_{\mathrm{NSM}} > 10^{1}$ *Equilibrium: diffusion conduction* (region C in Fig. 1). Sufficient time has passed from the origination of the nonequilibrium state to the decay of the wave heat propagation. The heat conduction process is further described by the diffusion equation.

The aforementioned wave diffusion theory has been expanded to incorporate the effect of elastic and inelastic collisions of phonons in solids (Guyer and Krumhansl, 1969). There are two basic phonon scattering mechanisms in solids: *R*-processes (umklapp scattering, mass-fluctuation scattering, etc.) and *N*-processes. Both are dependent on the frequency or energy of

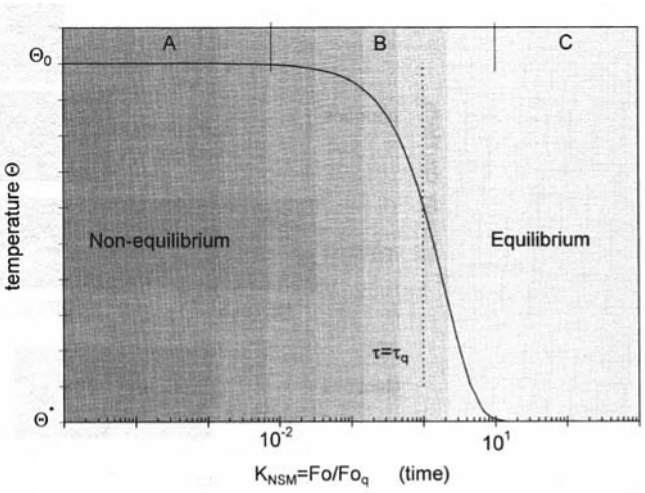

Fig. 1 Decay of thermal waves as dimensionless temperature of the wavefront in course of time represented by the criterion of nonequilibrium state of matter K_{NSM}

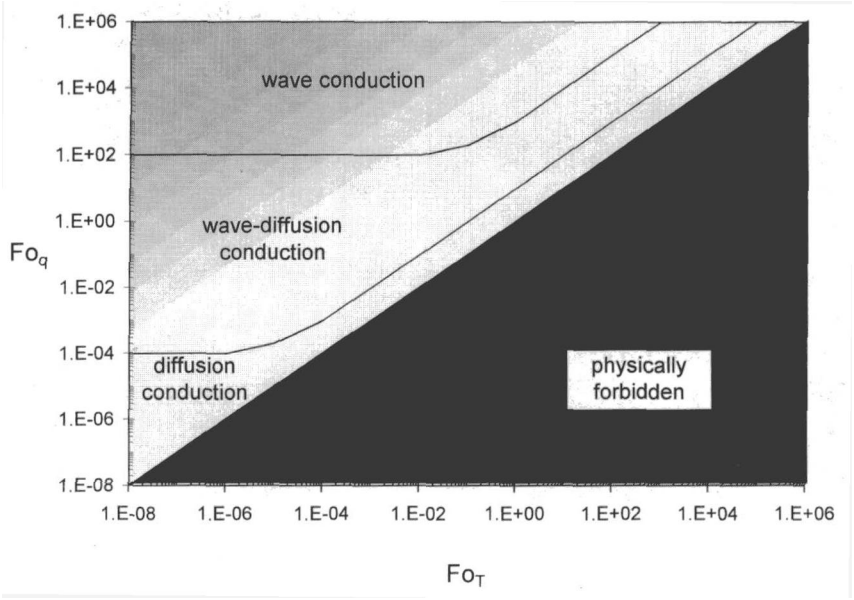

Fig. 2 Regions of application for wave, wave diffusion, and diffusion heat conduction

phonons. The role of the R and N-processes in creation of thermal resistance of the material and in equilibration of the phonon system is essentially different. R-processes are the processes causing the loss of momentum and thus creating thermal resistance. However, they destroy momentum selectively as a function of phonon state (resonance, etc). N-processes are the momentum conserving processes. They do not directly contribute to thermal resistance. However, they contribute indirectly because they act as an intermediate to interchange the phonon states.

The wave diffusion heat conduction equation is then, according to Tzou (1997), written as

$$\tau_T \frac{\partial}{\partial \tau}\frac{\partial^2 T}{\partial x^2} + \frac{\partial^2 T}{\partial x^2} = \frac{1}{a}\frac{\partial T}{\partial \tau} + \frac{\tau_q}{a}\frac{\partial^2 T}{\partial \tau^2}. \tag{11}$$

The dimensionless form of Eq. (11),

$$\mathrm{Fo}_T \frac{\partial}{\partial \mathrm{Fo}}\frac{\partial^2 \Theta}{\partial X^2} + \frac{\partial^2 \Theta}{\partial X^2} = \frac{\partial \Theta}{\partial \mathrm{Fo}} + \mathrm{Fo}_q \frac{\partial^2 \Theta}{\partial \mathrm{Fo}^2}, \tag{12}$$

introduces the further dimensionless parameter, the Fourier thermalization number, as a relation between paths traveled by the energy carrier during times τ_q and τ_T, and the characteristic length L,

$$\mathrm{Fo}_T = \frac{a\tau_T}{L^2} = \frac{v\tau_q}{L}\frac{v\tau_T}{L}. \tag{13}$$

The effect of thermalization time τ_T on the propagation character has already been discussed by Tzou (1997). If $\mathrm{Fo}_T = 0$, Eq. (12) describes the usual wave diffusion heat conduction. As Fo_T grows, heat conduction approaches diffusion. Finally, when Fo_T approaches Fo_q, the propagation character changes to purely diffusive as Eq. (12) reduces to the equation of the

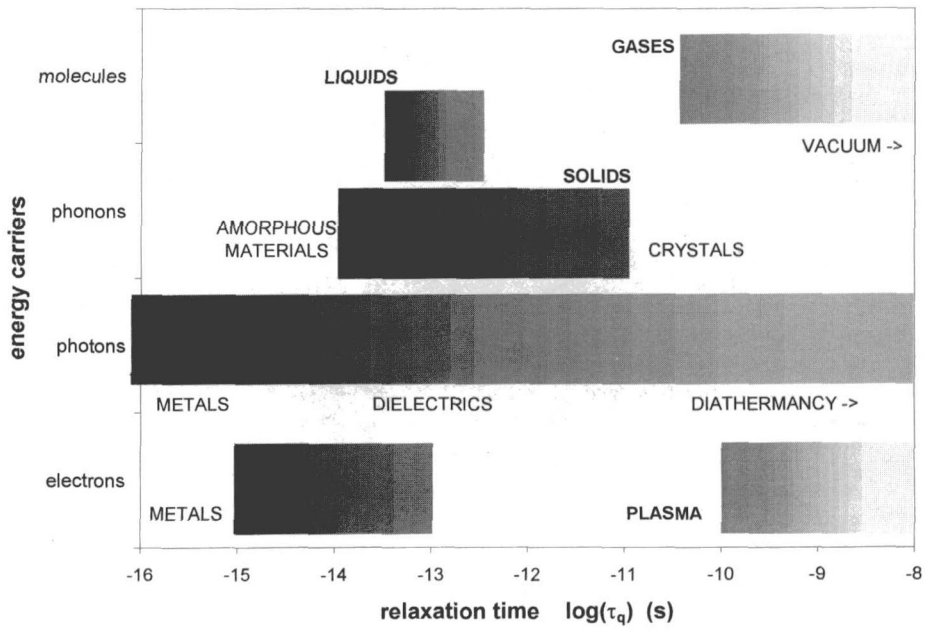

Fig. 3 Relaxation times corresponding to wave conduction by various heat carriers in different materials

Fourier diffusion heat conduction (Tzou, 1997). Values $Fo_T > Fo_q$ are physically forbidden for the case of wave diffusion heat conduction. Heat propagation in this interval appears, according to Tzou (1997), without wave effects and is quicker than diffusion. It is reserved for parallel heat conduction as will be shown later.

Criterion of the propagation character is introduced as

$$K_\tau = \frac{\tau_T}{\tau_q} = \frac{Fo_T}{Fo_q}. \tag{14}$$

The limit for wave diffusion conduction appears as $K_\tau = 1$, when Eqs. (11) or (12) describe diffusion heat conduction. The values of relaxation and thermalization time of the material are physically defined to satisfy

$$K_\tau < 1. \tag{15}$$

Application regions for pure wave, wave diffusion, and diffusion heat conduction are modified by the effect of the dimensionless thermalization time Fo_T, compared to the single effect of Fo_q, as shown in Fig. 2.

The following conclusion on wave diffusion heat conduction can be stated. Wave heat conduction proceeds from the wave behavior of elementary particles (heat carriers) in the microstructure of materials. Diffusion conduction arises from elastic and inelastic collisions when the original direction of propagation is lost and the energy distribution of heat carriers can be changed. The relaxation time of the material represents the inelastic collision process of the thermal wave decay when the energy of the wave is transformed into the internal energy of the material. Thermalization time represents, in the case of solids, the effect of elastic collisions when thermal wave momentum is conserved; however, the energy distribution of the carriers is produced. Both processes lead to the diffusion character of heat conduction and bring the material to the equilibrium. Value of the relaxation time specifies time range of nonequilibrium wave heat conduction. The ratio of thermalization and relaxation time describes superior heat propagation character.

Wave diffusion propagation occurs as phonon heat transfer in solids, electron heat transfer in metals, photon radiative heat transfer, and molecular heat transfer in gases. Values of relaxation time have been found by Honner (1998) according to Eq. (2) from tabulated thermophysical properties (see Fig. 3).

Parallel Heat Conduction

Similar mathematical description as the wave diffusion heat conduction is used also in the case of another nonequilibrium heat conduction process called parallel conduction. In nonhomogeneous materials, energy can be carried in several ways or by means of different heat carriers that constitute their own thermal subsystems in the material. Parallel nonequilibrium behavior can be found in various nonhomogeneous materials with more kinds of heat carriers as electrons and phonons in metals and semiconductors, or electrons and heavy particles in plasmas. It also occurs as parallel conduction in components of composites or parallel conduction, convection, and radiation in porous materials.

Heat conduction in the framework of the subsystem is generally represented by the wave diffusion heat conduction model. However, for simplicity, we will assume only diffusion. Parallel heat conduction in such a nonhomogeneous material is described by the coupled heat conduction equations

$$C_1 \frac{\partial T_1}{\partial \tau} = \lambda_1 \frac{\partial^2 T_1}{\partial x^2} + q_{V1} + \alpha_V (T_2 - T_1)$$

$$C_2 \frac{\partial T_2}{\partial \tau} = \lambda_2 \frac{\partial^2 T_2}{\partial x^2} + q_{V2} + \alpha_V (T_1 - T_2), \tag{16}$$

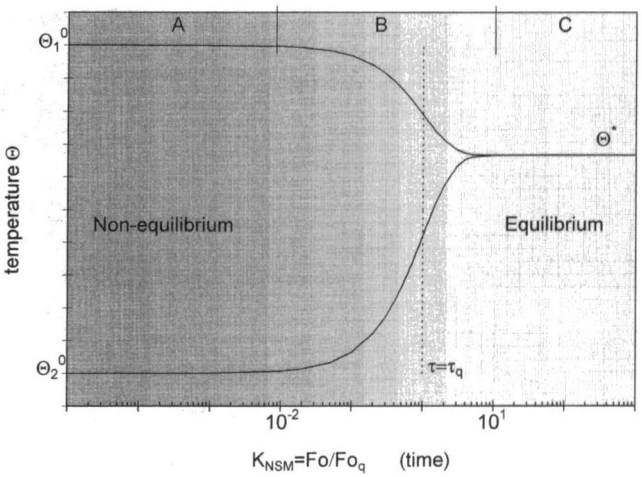

Fig. 4 Development of the material component temperatures in transition from the initial nonequilibrium back to equilibrium in course of time represented by the criterion of nonequilibrium state of matter K_{NSM}

where each thermal component of the material is represented by its thermal conductivity λ_i and heat capacity C_i. The thermal bond between the subsystems is expressed in the value of the coefficient of internal heat transfer α_V ($W \cdot m^{-3} \cdot K^{-1}$).

Two or more subsystems can occur in their own thermal equilibrium characterized by the temperature of the subsystem; however, the material in its entirety can occur in nonequilibrium. The state of the material is then characterized by different temperatures of individual subsystems caused by a different amount of energy in the subsystems.

Similarly to wave heat conduction, the base parallel heat conduction equation can be derived from Eq. (16) as

$$-a_P \tau_T \nabla^4 T + \tau_T \frac{\partial}{\partial \tau} \nabla^2 T + \nabla^2 T = \frac{1}{a} \frac{\partial T}{\partial \tau} + \frac{\tau_q}{a} \frac{\partial^2 T}{\partial \tau^2} \tag{17}$$

where the corresponding material properties are introduced in relation to wave conduction:

thermal diffusivity

$$a = \left(\frac{\lambda_1 + \lambda_2}{C_1 + C_2} \right), \tag{18}$$

parallel thermal diffusivity

$$a_P = \left(\frac{1}{a_1} + \frac{1}{a_2} \right)^{-1} = \left(\frac{\lambda_1 \lambda_2}{\lambda_1 C_2 + \lambda_2 C_1} \right), \tag{19}$$

relaxation time

$$\tau_q = \frac{1}{\alpha_V} \left(\frac{1}{C_1} + \frac{1}{C_2} \right)^{-1}, \tag{20}$$

thermalization time

$$\tau_T = \frac{1}{\alpha_V} \left(\frac{\lambda_1 C_2 + \lambda_2 C_1}{\lambda_1 + \lambda_2} \right), \tag{21}$$

heat propagation velocity

$$v_{ekv} = \sqrt{\frac{a}{\tau_q}} = \left(\alpha_V \frac{\lambda_1 + \lambda_2}{C_1 C_2} \right)^{1/2}. \tag{22}$$

Parallel and serial thermal conductivity and heat capacity are defined similarly as electrical conductivity and capacity in electric circuits.

Internal heat transfer can be dimensionally expressed as the *Biot volumetric number of microscale heat transfer,*

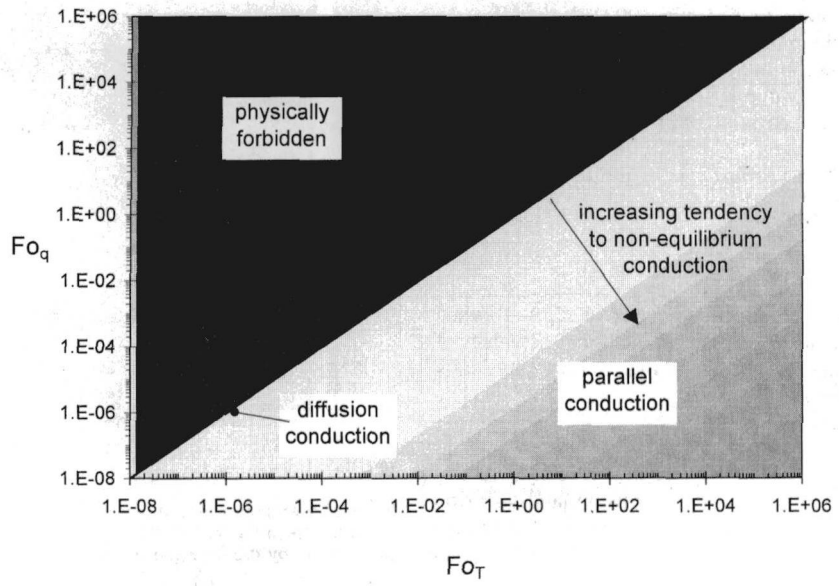

Fig. 5 Regions of application for parallel heat conduction

$$\mathrm{Bi}_V = \frac{\alpha_V L^2}{\lambda}. \tag{23}$$

It represents the ratio of the internal thermal conductivity (heat transfer among material components) to the standard thermal conductivity. If the internal heat transfer is intensive, heat is conducted as in a homogeneous material. On the other hand, if the internal heat transfer is too low, individual material components can be considered as separated thermal systems.

The characteristic length L can be defined as a product of the time of the thermal process and the equivalent heat propagation velocity

$$L = \tau\left(\alpha_V \frac{\lambda_1 + \lambda_2}{C_1 C_2}\right)^{1/2}. \tag{24}$$

The Biot number of microscale heat transfer is then defined as

$$\mathrm{Bi}_{V,eku} = \frac{\tau^2 \alpha_V^2}{C_1 C_2} = \mathrm{Fo}^2 \mathrm{Bi}_V^2 K_C. \tag{25}$$

The parallel heat conduction Eq. (17) is written in the dimensionless form

$$-\mathrm{Fo}_{PT}\nabla^4\Theta + \mathrm{Fo}_T \frac{\partial}{\partial \mathrm{Fo}} \nabla^2\Theta + \nabla^2\Theta = \frac{\partial \Theta}{\partial \mathrm{Fo}} + \mathrm{Fo}_q \frac{\partial^2 \Theta}{\partial \mathrm{Fo}^2} \tag{26}$$

where the following dimensionless parameters appear: The *Fourier relaxation number* represents the relation between the ratio of serial and parallel heat capacity K_C and internal heat transfer Bi_V, respectively, by

$$\mathrm{Fo}_q = \frac{a\tau_q}{L^2} = \mathrm{Bi}_V^{-1} K_C^{-1}. \tag{27}$$

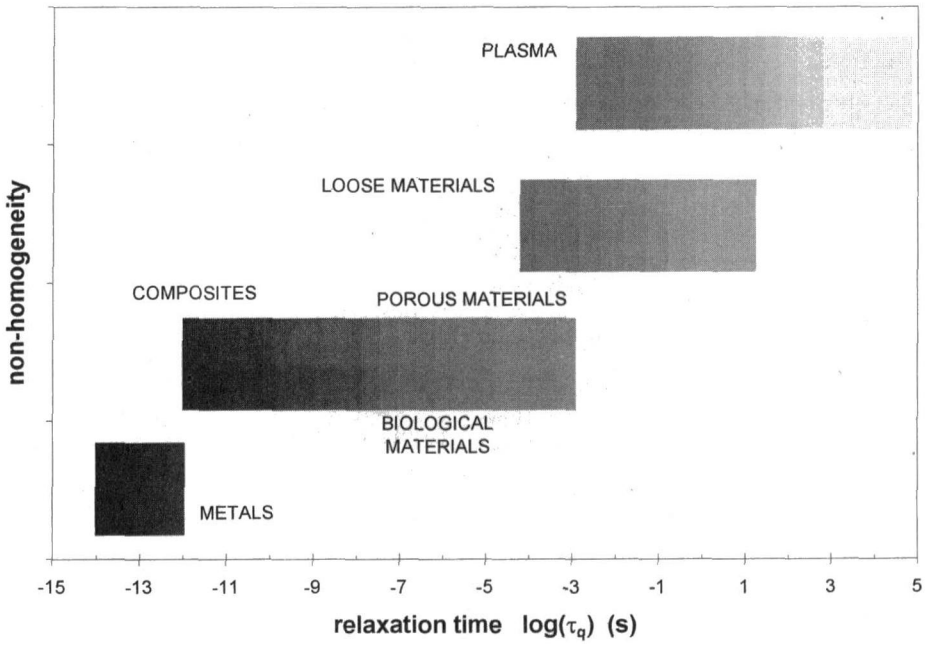

Fig. 6 Estimates of relaxation time of parallel conduction for various nonhomogeneous materials

The *Fourier parallel thermalization number* specifies the relation between the ratio of serial and parallel thermal conductivity K_λ of the material and internal heat transfer Bi_V,

$$\mathrm{Fo}_{PT} = \frac{a_P \tau_T}{L^2} = \mathrm{Bi}_V^{-1} K_\lambda^{-1}. \tag{28}$$

The *Fourier thermalization number* further modifies the Fourier parallel thermalization number by the ratio of serial and parallel thermal diffusivity K_a,

$$\mathrm{Fo}_T = \frac{a \tau_T}{L^2} = \mathrm{Bi}_V^{-1} K_\lambda^{-1} K_a^{-1} = \mathrm{Fo}_{PT} K_a^{-1}. \tag{29}$$

Heat supplied to the material, for example as an internal heat source, is usually absorbed by individual material components in different intensity. Thus, the material comes to the nonequilibrium state represented by different temperatures of the components. The material returns to the equilibrium through mutual heat transfer interactions among the components. This internal redistribution of energy is described by the relaxation time of the material. The value of this material property determines the time range of the parallel nonequilibrium state remaining after the heat source has been switched off.

Transition from the initial nonequilibrium to the equilibrium is shown in the following simple example. Consider material initially with different temperatures of two of its components $T_1^0 > T_2^0$. Internal heat transfer then redistributes heat inside the material. Finally, material comes to equilibrium with the same equilibrium temperature T^* of both components depending on the heat capacity of the components

$$T^* = \frac{C_1 T_1^0 + C_2 T_2^0}{C_1 + C_2}. \tag{30}$$

Development of temperatures in the course of time has been derived in the form

$$T_1(\tau) = T_1^0 + (T_2^0 - T_1^0) \frac{C_2}{C_1 + C_2} (1 - e^{-\tau/\tau_q})$$

$$T_2(\tau) = T_2^0 + (T_1^0 - T_2^0) \frac{C_1}{C_1 + C_2} (1 - e^{-\tau/\tau_q}), \tag{31}$$

reflecting the exponential character on the ratio of the time of the process and the relaxation time of the material. As Fig. 4 shows, the material reaches equilibrium at the time approximately equal to the relaxation time of the material. Estimates of relaxation times for various nonhomogeneous materials are shown in Fig. 6.

The *Criterion of nonequilibrium state of matter* is introduced:

$$K_{\mathrm{NSM}} = \frac{\tau}{\tau_q} = \frac{\tau \alpha_V}{C_S} = \frac{\mathrm{Fo}}{\mathrm{Fo}_q} = \mathrm{FoBi}_V K_C. \tag{32}$$

According to the criterion, one can discover the state of the material. This physically represents the ratio of heat transferred inside the material among its components to the overall heat capacity of the material. The nonequilibrium state of the material in time Fo after switching off the sources is determined by the intensity of internal heat transfer Bi_V and the ratio of parallel and serial heat capacity K_C.

$K_{\mathrm{NSM}} < 10^{-2}$ *Nonequilibrium* (region A in Fig. 4). In a short time interval after origination of nonequilibrium, the internal heat transfer among material components has not yet effectively taken place. The material has to be represented by different component temperatures and in this stage, the thermal process can be described as a system of independent heat conduction equations for individual material components.

$10^{-2} < K_{\mathrm{NSM}} < 10^{1}$ *Transition* (region B in Fig. 4). The heat transfer among material components manifests itself. Temperatures of the components approach the equilibrium value with increasing time. The heat conduction process has to be described by a system of coupled heat conduction equations or by one equation of parallel heat conduction (17).

$K_{\mathrm{NSM}} > 10^{1}$ *Equilibrium* (region C in Fig. 4). Sufficient time has past from the origination of nonequilibrium to reach equilibrium by the internal redistribution of energy. The state of the material is represented by the same temperature of all its components. The heat conduction process can be usually described by the diffusion heat conduction equation for the whole material.

The *criterion of propagation character* is defined similarly to the wave heat conduction theory

$$K_\tau = \frac{\tau_T}{\tau_q} = \frac{\mathrm{Fo}_T}{\mathrm{Fo}_q}. \tag{33}$$

According to the definition of relaxation and thermalization time for parallel conduction, Eq. (20) and Eq. (21), one can reveal that the only physically allowed region for parallel conduction is

$$K_\tau > 1. \tag{34}$$

It means no thermal waves can occur within the framework of nonequilibrium parallel heat conduction because of the dominance of the mixed derivative term in the base Eq. (26). Increasing K_τ (see Fig. 5) represents increasing material tendency to the parallel behavior due to the different thermophysical properties of material components. The manifestation of the nonequilibrium conduction is substantially influenced by the microscale internal heat transfer as the criterion of nonequilibrium state of matter (32) shows.

Figure 5 further demonstrates that the allowed region for parallel conduction is the physically forbidden region for wave conduction and vice versa. It also creates prerequisites for a simple differentiation of both nonequilibrium heat conduction modes in the unified model (Tzou, 1997).

Conclusion

The paper presents a unified description of two physically different wave diffusion and parallel nonequilibrium heat conductions. Dimensionless criteria specifying the nonequilibrium state of the material and the heat propagation character have been used to specify application regions of individual modes of heat propagation. The presented description of microscale heat transfer processes also proposes applications for analogous nonequilibrium mass transfer processes.

References

Bhandari, C. M., and Rowe, D. M., 1988, *Thermal Conduction in Semiconductors,* Wiley Eastern Ltd., New Delhi.

Eckert, E. R. G., 1959, *Einführung in den Wärme- und Stoffaustausch,* Springer-Verlag, Berlin.

Guyer, R. A., and Krumhansl, J. A., 1966, "Solution of the Linearized Phonon Boltzmann Equation," *Physical Review,* Vol. 148, No. 2, pp. 766–780.

Honner, M., 1998, "Micro-thermomechanics in advanced technologies," Ph.D. thesis, University of West Bohemia, Plzen (in Czech).

Kuneš, J., Krejčí, L., and Honner, M., 1996, "Wave Heat Conduction in Technologies," *Strojnicky Casopis,* Vol. 47, pp. 346–362.

Tzou, D. Y., 1997, *Macro- to Microscale Heat Transfer: The Lagging Behavior,* Taylor & Francis, London.

Nonlinear Inverse Heat Conduction With a Moving Boundary: Heat Flux and Surface Recession Estimation

V. Petrushevsky[1] and S. Cohen[2]

A one-dimensional, nonlinear inverse heat conduction problem with surface ablation is considered. In-depth temperature measurements are used to restore the heat flux and the surface recession history. The presented method elaborates a whole domain, parameter estimation approach with the heat flux approximated by Fourier series. Two versions of the method are proposed: with a constant order and with a variable order of the Fourier series. The surface recession is found by a direct heat transfer solution under the estimated heat flux.

Nomenclature

k = conductivity
c_p = specific heat
ρ = density
T = temperature
q = heat flux
t = time
z = surface coordinate measured from initial position at $t = 0$
nf = Fourier series order
A, B = Fourier series coefficients
H = latent heat of phase change
σ = standard deviation of temperature measurement noise

Subscripts and Superscripts

0 = initial condition
end = end of the process
pc = phase change
J = iteration number
$*$ = trial value
$\hat{}$ = updated value
true = true value
est = estimated by the inverse method
t = transpose

Introduction

The inverse heat conduction problem (IHCP) is concerned with the determination of surface boundary conditions (temperature, heat flux) based on temperature data measured inside the material. A number of methods have been developed to solve the IHCP. The least-squares technique is commonly used to find the surface heat flux, which forces the sensor temperature response to be close to the measured temperature data. Whole domain methods have used polynomial functional form to describe the entire heat flux history (Beck et al., 1985; Hensel, 1991). The sequential function specification approach (Beck and Blackwell, 1988) and dynamic programming method (Busby and Trujillo, 1985) have evaluated the heat flux as a sequence of finite duration pulses.

Most of the existing inverse methods consider linear heat transfer problems. Beck and Wolf (1965) applied finite difference analysis to handle a nonlinear problem with temperature-dependent thermal properties. Finite element algorithms have been used for nonlinear problems involving phase change in melting/solidification processes (Hsu et al., 1986; Quyang, 1992).

For some applications involving intensive convective heating of a solid material plate in a high speed, hot external flow, the material at the boundary can reach its phase-change temperature, and a nonlinear heat transfer process can occur due to surface ablation and energy absorption by latent heat. Contrary to the melting processes considered by the existing inverse methods, the present case involves the phase-change products being blown away by the external flow, and the solid material surface is continuously exposed to the external heat flux. Typically, temperature-dependent properties augment the nonlinearity, because a wide temperature range is present in the solid. For this kind of problem, estimation of the surface recession is important along with the heat flux.

The nonlinearity causes complex behavior of the measured temperature sensitivity to the heat flux. During the surface recession, the sensitivity drops sharply because the phase-change process at the surface absorbs a significant part of the heat flux, and the sensors' temperature is influenced mainly by the surface approaching. However, as the sensors become closer to the receding surface, the sensitivity tends to increase.

The varying sensitivity poses substantial numerical difficulties for the sequential inverse methods, severely affecting convergence stability and requiring recalculation of sensitivity coefficients at every time step. The whole domain, parameter estimation approach can be better suited for the considered nonlinear problem, suggesting better stability and fewer amount of computations.

In this paper, the surface heat flux is approximated by the Fourier series. The surface recession is found by a direct heat transfer solution under the estimated heat flux. Two versions of the method are considered: a constant order and a variable order of the Fourier series.

The Inverse Problem Solution Using the Fourier Series of a Constant Order

Consider a one-dimensional solid plate of finite thickness with an external heat flux $q(t)$ applied at its front surface. The plate may consist of several layers of different materials featuring temperature-dependent properties, and it may have a known heat transfer boundary condition at the back surface. A large Biot number is considered (Bi > 0.1). The plate material next to the front surface may reach the phase-change temperature level, and ablation may occur during the process.

The plate temperature response is measured by M sensors located at depths of δ_{sens_m} ($m = 1, \ldots, M$) from an initial position of the front surface. Location of the sensors is assumed to be deeper than the maximum expected surface recession, in order to ensure their survival to the end of the process. Readout of the sensors is available at N discrete times (not necessarily equally spaced), and it includes true temperature and measurement noise:

$$Y = T^{\text{true}} + \epsilon \tag{1}$$

where

Y is the $(N \times M)$ matrix of measured temperature values;
T^{true} is the $(N \times M)$ matrix of true temperature values at location points of the sensors;
ϵ is the $(N \times M)$ matrix of random measurement errors.

The unknown heat flux is approximated by the Fourier series of a constant order nf:

$$q(t) = \frac{A_0}{2} + \sum_{j=1}^{nf} \left(A_j \cos \frac{2\pi j t}{t_{\text{END}}} + B_j \sin \frac{2\pi j t}{t_{\text{END}}} \right). \tag{2}$$

[1] MobileComm Ltd., Argaman Industrial Park, P. O. Box 16, Yavne 81550, Israel. e-mail: fts@netvision.net.il.
[2] Heat Transfer Group, Israel Aircraft Industries, Ben Gurion International Airport, 70100, Israel.

Contributed by the Heat Transfer Division for publication in the JOURNAL OF HEAT TRANSFER. Manuscript received by the Heat Transfer Division, Aug. 4, 1997; revision received, Apr. 20, 1999. Keywords: Ablation, Heat Transfer, Inverse, Numerical Methods, Phase Change. Associate Technical Editor: R. Boyd.

It is assumed that all the plate configuration data (number of layers, thickness, the properties, the back surface boundary conditions) are known, and an adequate analytical or numerical direct heat transfer model is available. Then, for a given $q(t)$, the $(N \times M)$ matrix T of the computed temperature values at location points of the sensors and the $(N \times 1)$ vector z of the computed surface recession values can be obtained for the discrete time sequence using the model.

The inverse problem is formulated to find out a vector of the Fourier coefficients ($2nf + 1$ elements):

$$V = \{A_0 \quad A_1 \quad \cdot \quad \cdot \quad A_{nf} \quad B_1 \quad \cdot \quad \cdot \quad B_{nf}\}^t, \tag{3}$$

which determines the surface heat flux estimation causing the calculated sensors' temperature response to be close to the measured one in a sense of the least-squares criterion (LSC):

$$S = \sum_{m=1}^{M} \sum_{i=1}^{N} (T_{im} - Y_{im})^2. \tag{4}$$

To provide sufficient data for the solution of the problem, the number of the measured temperature data points $(N \times M)$ should equal or exceed amount of the unknown Fourier coefficients $(2nf + 1)$.

The Gauss method is used for iterative minimization of criterion (4). The method may be used either in its basic form or with convergence improving modifications (Beck and Arnold, 1977). In this paper, the Marquardt modification was applied. The algorithm involves the following steps:

1 An initial guess for a trial vector V^* of the Fourier coefficients.

2 A direct heat transfer solution under the heat flux history defined by the trial vector.

3 Evaluation of the LSC by Eq. (4), substituting T^* in place of T.

4 Calculation of derivatives of the sensors' temperatures and of the LSC on the Fourier coefficients in proximity of the trial set.

5 Matrix $X((N \cdot M) \times (2nf + 1)$ elements) is formed from M submatrices $P^{(m)}(N \times (2nf + 1)$ elements). Each of the latter ones contains the mth sensor temperature derivatives on the Fourier coefficients

$$X = \{P^{(1)} \quad P^{(2)} \quad \cdot \quad P^{(m)} \quad \cdot \quad P^{(M)}\}^t, \tag{5}$$

where

$$P^{(m)} = \begin{bmatrix} \frac{\partial T_{1m}}{\partial A_0} & \frac{\partial T_{1m}}{\partial A_1} & \cdot & \cdot & \frac{\partial T_{1m}}{\partial A_{nf}} & \frac{\partial T_{1m}}{\partial B_1} & \cdot & \cdot & \frac{\partial T_{1m}}{\partial B_{nf}} \\ \cdot & \cdot & \cdot & \cdot & \cdot & \cdot & \cdot & \cdot & \cdot \\ \cdot & \cdot & \cdot & \cdot & \cdot & \cdot & \cdot & \cdot & \cdot \\ \frac{\partial T_{Nm}}{\partial A_0} & \frac{\partial T_{Nm}}{\partial A_1} & \cdot & \cdot & \frac{\partial T_{Nm}}{\partial A_{nf}} & \frac{\partial T_{Nm}}{\partial B_1} & \cdot & \cdot & \frac{\partial T_{Nm}}{\partial B_{nf}} \end{bmatrix}.$$

Vector $g[(2nf + 1) \times 1$ elements] is formed from the LSC derivatives on the Fourier coefficients:

$$g = \left\{ \frac{\partial S}{\partial A_0} \quad \frac{\partial S}{\partial A_1} \quad \cdot \quad \cdot \quad \frac{\partial S}{\partial A_{nf}} \quad \frac{\partial S}{\partial B_1} \quad \cdot \quad \cdot \quad \frac{\partial S}{\partial B_{nf}} \right\}^t. \tag{6}$$

6 A step in the Fourier coefficients' space is done in the direction of the LSC descent, and the updated vector of the coefficients is obtained:

$$\hat{V} = V^* - \left\{ (2X^tX) + \frac{\lambda_0}{\nu^J} \cdot D \right\}^{-1} \cdot g \tag{7}$$

where λ_0 is a positive number chosen by numerical experiments or calculated by the Levenberg procedure (Beck and Arnold, 1977); ν is a constant greater than unity; and D is a diagonal matrix with positive elements (a unity matrix may be used).

7 The updated Fourier coefficient vector is used as a trial one, and the procedure is performed iteratively until relative decrease of the LSC per iteration becomes smaller than a limit value ξ_1:

$$\left| \frac{S^J - S^{J-1}}{S^J} \right| \le \xi_1. \tag{8}$$

The process results in estimation of the required heat flux and surface recession:

$$q^{\text{est}}(t) = q^*(t); \quad z^{\text{est}} = f\{q^*(t)\} \tag{9}$$

The straightforward procedure described above provides decent estimation of the surface recession (see the numerical example). However, if the Fourier series order is chosen inadequately high for a given application, the heat flux estimation will suffer from excursions related to nondamped high frequency terms of the series. The effect is caused by especially low sensitivity of the temperature measurements to the high-frequency heat flux content, since the latter is smoothed by thermal inertia of the plate material as well as by the phase change latent heat at the boundary. In other words, the LSC may have a wide area of local minima in the Fourier coefficients' space if the series order is inadequately high.

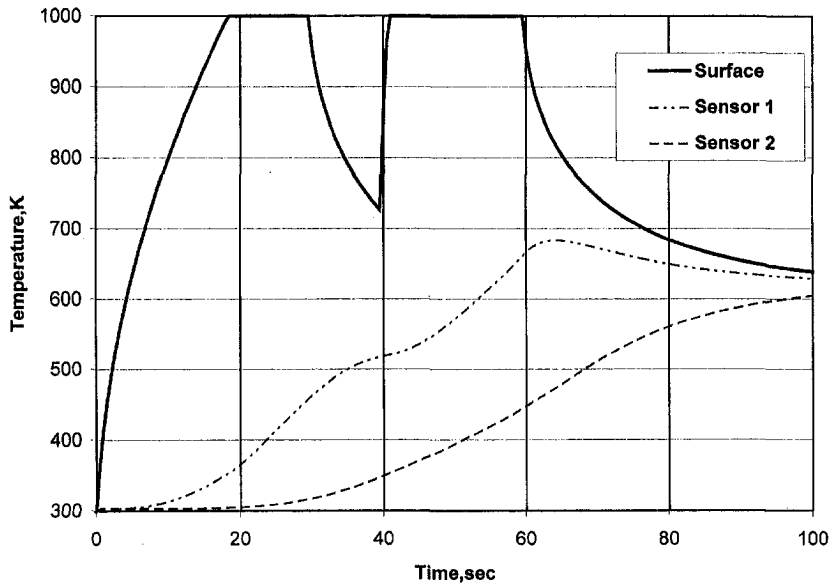

Fig. 1 Temperature histories of the surface and of the sensors

Table 1 Performance Summary
(The upper values are $\sigma = 2.0$ K, and the lower values are for $\sigma = 4.0$ K.)

The performance criteria	The constant order algorithm			The variable order approximation algorithm
	$nf = 3$	$nf = 6$	$nf = 12$	
S, $\times 10^3$ K^2	17.39 30.7	1.684 5.79	14.91 38.5	6.63 6.97
$i = 1N\,(q_i^{true} - q_i^{est})^2$, $\times 10^{10}$ W^2/m^4	10.14 10.11	6.82 7.23	8.64 8.67	6.66 7.29
$i = 1N\,(z_i^{true} - z_i^{est})^2$, $\times 10^{-6}$ m^2	8.83 13.01	2.67 2.35	0.550 0.667	1.526 2.41
$i = 1N\,q_i^{est} i = 1N\,q_i^{true}$	0.877 0.846	0.945 0.949	0.994 0.991	0.953 0.948

A rational nf value can be assigned if there is some adequate a priori data about the heat flux history shape. Alternatively, the LSC can be augmented by a regularization term in order to penalize excursions in the heat flux estimation (Beck and Blackwell, 1988). In this paper, another technique is proposed which varies the Fourier series order and chooses automatically an adequate one, avoiding the estimation excursions.

The Algorithm Modified by a Variable Order of the Fourier Series

A basic property of a function approximation by the Fourier series is its orthogonality: the approximation refinement by introducing a new frequency term does not change previously calculated coefficients for other frequencies terms (Korn and Korn, 1968). Though the property cannot be employed directly in the inverse problem case because the real function (the heat flux history) is not known a priori, it suggests that the Fourier coefficients of a coarse, low-order approximation can be used as good initial guesses for the corresponding frequency terms of a finer, higher order approximation.

The following procedure is proposed:

1 A small value of nf is assigned, and an initial guess is done for the Fourier coefficients to get a coarse initial heat flux approximation. For most applications, it is reasonable to begin with $nf = 1$ and with certainly low values of the coefficients, ensuring that the initial heat flux approximation does not cause severe surface recession, which would exceed the location depth of the most outward sensor.

2 The LSC minimization algorithm (see above) is applied iteratively until a relative decrease of the LSC per iteration becomes smaller than the limit value ξ_1. The trial vector of the Fourier coefficients is obtained as a result of this step:

$$V^* = \{A_0^* \quad A_1^* \quad \cdot \quad \cdot \quad A_{nf}^* \quad B_1^* \quad \cdot \quad \cdot \quad B_{nf}^*\}'. \quad (10)$$

3 The Fourier series order is increased by one, using the trial coefficients as an initial guess for the corresponding frequency terms, and assigning zeros to coefficients of the newly introduced, higher frequency term. The updated vector is formed as

$$\hat{V} = \{A_0^* \quad A_1^* \quad \cdot \quad \cdot \quad A_{nf}^* \quad 0.0 \quad B_1^* \quad \cdot \quad \cdot \quad B_{nf}^* \quad 0.0\}'. \quad (11)$$

4 The LSC minimization and the Fourier series order increment (steps 2, 3) are repeated until the relative reduction of the LSC achieved by the series order increase becomes smaller than prechosen value ξ_2:

$$\left| \frac{S_{nf-1} - S_{nf}}{S_{nf}} \right| \le \xi_2. \quad (12)$$

Number of the measured temperature data points ($N \times M$) limits the maximal possible series order nf (see the previous paragraph).

Numerical Example

A one-dimensional plate, 0.006 mm thick with an insulated back surface, consists of a single material which has the following second-order temperature-dependent conductivity and specific heat model:

$$k = 10^{-1} + 10^{-4} \cdot (T - T_0) - 10^{-7} \cdot (T - T_0)^2 \quad [\text{W/m} \cdot \text{K}]$$

$$c_p = 10^3 + 10^{-1} \cdot (T - T_0) + 10^{-3} \cdot (T - T_0)^2 \quad [\text{J/kg} \cdot \text{K}]$$

where $T_0 = 300$ K is an initial temperature of the plate; the density: $\rho = 1000$ kg/m^3; the phase-change temperature: $T_{pc} = 1000$ K; and the latent heat: $H_{pc} = 1 \cdot 10^6$ J/kg.

The process duration is 100 s, and an applied heat flux features two rectangular pulses of a different magnitude. The plate temperature field (see Fig. 1) as well as the surface recession is calculated using a moving boundary direct heat transfer procedure, which

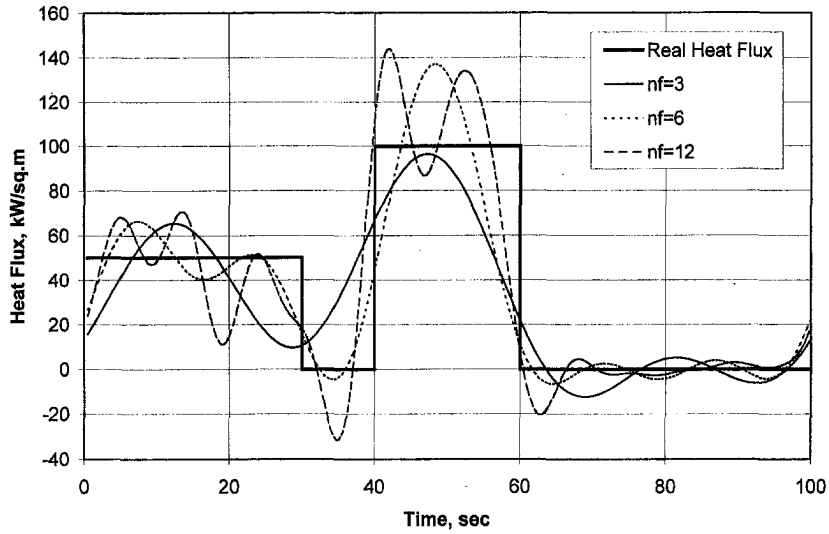

Fig. 2 The heat flux estimation by the constant-order algorithm ($\sigma = 4.0$ K)

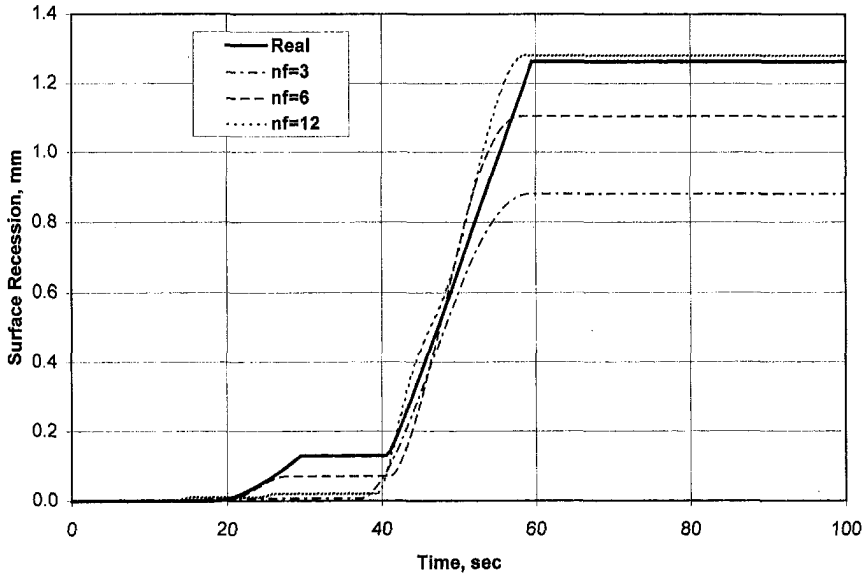

Fig. 3 The surface recession estimation by the constant-order algorithm (σ = 4.0 K)

involves the finite difference approach with an implicit integration. Two temperature sensors are considered: (M = 2): δ_{sens1} = 0.003 m, δ_{sens2} = 0.006 m. Normally distributed noise was added to the true sensors' temperature history in order to simulate measured data. Two noise levels are examined: σ = 2.0 K and σ = 4.0 K. The parameters of the least-squares numerical procedure were chosen by numerical experiments: $\Delta A = 1 \cdot 10^{-6}$, $\lambda_0 = 1 \cdot 10^{-5}$, ν = 5.0, $\xi_1 = \xi_2$ = 0.01. The time step is equal to 0.5 s (for the inverse analysis as well as for the direct heat transfer procedure), which yields N = 200.

See Table 1 for the summary of the method performance. The constant order algorithm was applied with nf = 3, 6, 12 (graphs are presented in Figs. 2, and 3 for σ = 4.0 K). For nf = 3, the heat flux estimation is smoothed, but nevertheless the two heat flux peaks are coarsely reproduced. For nf = 12, the sharp rise and fall of the rectangular heat flux peaks are better reproduced, though high-frequency excursions are prominently visible. The case of nf = 6 represents some compromise between smoothness and accuracy, and yields the best heat flux estimation and the best measured temperature fitting (from the three cases). However, estimation of the heat flux integral improves with the series order increase. Since the surface recession is roughly proportional to this integral, its estimation also becomes more accurate as the series order grows.

The variable order algorithm was started with nf = 1, and it has stopped the series order increment process at nf = 8 for σ = 2.0 K and at nf = 6 for σ = 4.0 K. The achieved performance is close to the case for the constant order algorithm with nf = 6.

In this example, the surface recession is estimated quite accurate, especially by the constant-order algorithm for nf = 12. The heat flux estimation shows the amount of the pulses and their magnitude, but it is unable to restore the rectangular shapes accurately. The reason: the sensors have very low sensitivity to the high-order harmonics, which the rectangular shapes contain.

For both versions of the method, the measurement noise increase has only a slight affect on the estimation performance. This is a logical result for the whole domain approach.

Conclusions

This paper describes the use of the whole-domain parameter estimation method for the inverse analysis of a nonlinear one-dimensional heat conduction process with surface ablation. The method applies the least-squares technique to obtain estimation for the surface heat flux in the form of Fourier series. The surface recession is found by a direct heat transfer solution using the estimated heat flux.

Two versions of the algorithm were proposed. The first version applies a constant order of the Fourier series. Accuracy of the surface recession estimation by this algorithm improves with an increase in the series order. However, the heat flux estimation can suffer from excursions if the series order is chosen too high for a given application.

The second version involves an initial coarse solution using a low order of the Fourier series, and consequent increment of the series order with a parallel solution refinement. The series order increment continues until the LSC improvement ceases, which means that the adequate series order has been reached. This version avoids the heat flux estimation excursions, though the surface recession estimation can be less accurate in comparison with the constant-order version.

The method features low sensitivity to measurement noise, and can be applied to a variety of one-dimensional problems.

References

Beck, J. V., and Arnold, K. J., 1977, *Parameter Estimation in Engineering and Science,* John Wiley and Sons, New York, pp. 340–371.

Beck, J. V., and Blackwell, B., 1988, "Inverse Problems," *Handbook of Numerical Heat Transfer,* edited by W. J. Minkowycz, E. M. Sparrow, G. E. Schneider, and R. H. Pletcher, eds., John Wiley and Sons, New York, pp. 787–834.

Beck, J. V., Blackwell, B., and St. Clair, C. R., Jr., 1985, *Inverse Heat Conduction: Ill-Posed Problems,* Wiley-Interscience, New York.

Beck, J. V., and Wolf, H., 1965, "Nonlinear Inverse Heat Conduction Problem," ASME Paper 65-HT-40, presented at the ASME/AIChE Heat Transfer Conference and Exhibit, Los Angeles.

Busby, H. R., and Trujillo, D. M., 1985, "Numerical Solution to a Two-dimensional Inverse Heat Conduction Problem," *Intl. J. for Numerical Methods in Engineering,* Vol. 21, pp. 349–359.

Hensel, E., 1991, *Inverse Theory and Applications for Engineers,* Prentice-Hall, Englewood Cliffs, NJ.

Hsu, Y. F., Rubinsky, B., and Mahin, K., 1986, "An Inverse Finite Element Method for the Analysis of Stationary Arc Welding Processes," ASME JOURNAL OF HEAT TRANSFER, Vol. 108, pp. 734–741.

Korn, G. A., and Korn, T. M., 1968, *Mathematical Handbook For Scientists and Engineers,* McGraw-Hill, New York.

Quyang, T., 1992, "Analysis of Parameter Estimation Heat Conduction Problems with Phase Change Using the Finite Element Method," *Intl. J. for Numerical Methods in Engineering,* Vol. 33, pp. 2016–2037.

Improved Modeling of Turbulent Forced Convective Heat Transfer in Straight Ducts

M. Rokni[1] and B. Sunden[2]

This investigation concerns numerical calculation of turbulent forced convective heat transfer and fluid flow in their fully developed state at low Reynolds number. The authors have developed a low Reynolds number version of the nonlinear k-ϵ model combined with the heat flux models of simple eddy diffusivity (SED), low Reynolds number version of generalized gradient diffusion hypothesis (GGDH), and wealth $\propto$ earning $\times$ time (WET) in general three-dimensional geometries. The numerical approach is based on the finite volume technique with a nonstaggered grid arrangement and the SIMPLEC algorithm. Results have been obtained with the nonlinear k-ϵ model, combined with the Lam-Bremhorst and the Abe-Kondoh-Nagano damping functions for low Reynolds numbers.

Nomenclature

A_{cross} = cross section area
A_w = area of the wall
C_P = specific heat at constant pressure
C_E, C_D, C_t = closure coefficient
$C_{\epsilon 1}$, $C_{\epsilon 2}$, C_μ = closure coefficient
D_h = hydraulic diameter
f = Fanning friction factor
f_1, f_2, f_3 = damping functions
$\overline{f_j t}$ = buoyancy-driven heat flux
k = kinetic energy
L = duct length
Nu = Nu number
Nu_{ov} = overall Nu number
Nu_{xp} = local Nu number at each point
Nu_{DB} = Nu Number due to Dittus-Boelter
P = pressure
P^* = cyclic pressure
P_k = production terms
Pr = Prandtl number
Q = heat flux
q_w = heat flux through the walls
Re = Reynolds number
S_{ij} = mean strain rate
$\dot{S}_{ij}$ = Oldroyd derivative of S_{ij}
T = temperature
T_b = bulk temperature
T_p = point temperature
T_w = wall temperature
U_j = velocity
U_b = bulk velocity
$-\rho\overline{u_i u_j}$ = turbulent stresses
$\rho C_p \overline{u_j t}$ = turbulent heat fluxes
x_j = coordinate
β = cyclic pressure coefficient
δ_{ij} = Kroneckers delta
ϵ = dissipation of kinetic energy
Φ_{ij} = pressure-strain
γ = cyclic parameter, see Eq. (22)
Γ = numerical diffusivity
η = distance normal to the wall
λ = cyclic parameter, see Eq. (20)
μ = molecular viscosity
μ_τ = turbulent viscosity
Θ = dimensionless temperature
ρ = density
σ = turbulent Prandtl number
Ω = cyclic temperature source term

1 Introduction

Ducts with noncircular cross sections are frequently encountered in industrial heat transfer equipment, e.g., compact heat exchangers, cooling channels in gas turbine blades, nuclear reactors, etc. The main flow in such ducts is influenced by the secondary motions in the plane perpendicular to the streamwise direction. In wavy ducts, centrifugal forces occur and these influence the main flow. This motion is pressure-induced and commonly it is said to be of Prandtl's *first* kind. This kind of motion exists even in curved circular ducts for laminar flow. Secondary motion of Prandtl's *second* kind takes place in the smooth corner of noncircular straight ducts for turbulent flow. These motions are of major concern since they redistribute the turbulence kinetic energy at the cross section of a duct which in turn affects the wall shear stresses and the turbulent heat fluxes.

Close to each corner of an orthogonal straight duct there exist two counter rotating vortices that transport high momentum fluid towards the duct corner and then outwards along the walls. However, Speziale and Gatski (1997) predicted another two much smaller counter rotating vortices (in addition to the two main vortices) by using an isotropic dissipation equation and an RSM model (with SSG for pressure strain). To avoid these nontrivial small vortices, they exchanged the isotropic dissipation by a nonisotropic dissipation equation. In the present study, the isotropic dissipation equation is used with a nonlinear eddy viscosity model combined with the damping functions and no extra vortices are predicted. The study may therefore contribute to assess simple turbulence models which requires less computational effort and time but may provide reasonable accurate results from an engineering point of view.

In order to obtain a reasonable prediction of the flow from numerical simulations, the turbulence model must allow for the secondary flows. In the present investigation Speziale's nonlinear k-ϵ model is combined with Lam-Bremhorst's as well as Abe-Kondoh-Nagano's damping functions to predict turbulent Reynolds stresses. The simple eddy diffusivity (SED) concept, low Reynolds number version of the general gradient diffusion hypothesis (GGDH), and the low Reynolds number version of wealth $\propto$ earning $\times$ time (WET) models are employed to determine turbulent heat fluxes.

The results obtained from different models are compared with the existing correlation in terms of friction factor and Nusselt number. A fully developed condition is achieved by imposing cyclic boundary conditions in the main flow direction.

Several fundamental investigations concerning turbulent flow in square and rectangular ducts exist. The nonlinear k-ϵ model proposed by Speziale (1987) has been employed for predicting the flow and heat flux in straight and corrugated ducts with trapezoidal cross sections (see Rokni and Sundèn, 1996, 1998). However, the wall function approach was used to handle the wall boundary condition. Direct numerical simulations have been performed for a square duct by Huser and Biringen (1993) and Gavrilakis (1991). Kim et al. (1987) provided valuable data for evaluation of turbulence models for a plane duct. Large eddy simulations for square

[1] Division of Heat Transfer, Lund Institute of Technology, 221 00 Lund, Sweden. e-mail: masoud@emvox7.vok.lth.se.
[2] Division of Heat Transfer, Lund Institute of Technology, 221 00 Lund, Sweden. e-mail: bengts@emvox2.vok.lth.se. Mem. ASME.

Contributed by the Heat Transfer Division for publication in the JOURNAL OF HEAT TRANSFER and presented at '97 NHTC, Baltimore. Manuscript received by the Heat Transfer Division, Mar. 30, 1998; revision received, Mar. 22, 1999. Keywords: Channel Flow, Heat Transfer, Modeling, Turbulence. Associate Technical Editor: R. Douglass.

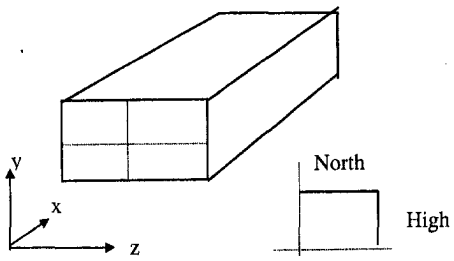

Fig. 1 Duct under consideration

ducts are reported by Su and Friedrich (1994) at a Reynolds number of 49,000 and by Madabhushi and Vanka (1991) at a Reynolds number of 5800.

In the literature no numerical investigations have been presented on turbulent flow in ducts at relatively low Reynolds number using turbulence models. In this work, the numerical calculation is focused on fully developed periodic flow and may be regarded as a further application and evaluation of the computational method developed by Rokni and Sundèn (1996, 1998) which has successfully been applied in straight and wavy ducts of various cross sections using wall functions. At low Reynolds numbers the wall function approach is not appropriate and thus another procedure is needed.

2 Problem Statement

Straight ducts with square and rectangular cross sections are considered in this study. Only one quarter of the duct is considered by imposing symmetry conditions. A principle sketch of a duct is shown in Fig. 1.

The calculation method has been focused on fully developed turbulent flow in a three-dimensional duct.

Mean velocity distributions, friction factor, and Nu number are determined numerically for fully developed conditions.

3 Governing Equations

The governing equations are the continuity, momentum, and energy equations. Fully developed periodic turbulent flow is considered in this investigation. The following assumptions are employed: steady state, no-slip at the walls, and constant fluid properties. One then has

$$\frac{\partial}{\partial x_j}(\rho U_j) = 0 \tag{1}$$

$$\frac{\partial}{\partial x_j}(\rho U_i U_j) = -\frac{\partial P}{\partial x_i} + \frac{\partial}{\partial x_j}\left[\mu\left(\frac{\partial U_i}{\partial x_j} + \frac{\partial U_j}{\partial x_i}\right)\right] + \frac{\partial}{\partial x_j}(-\rho\overline{u_i u_j}) \tag{2}$$

$$\frac{\partial}{\partial x_j}(\rho U_j T) = \frac{\partial}{\partial x_j}\left[\frac{\mu}{\mathrm{Pr}}\frac{\partial T}{\partial x_j} + (-\rho\overline{u_j t})\right]. \tag{3}$$

The turbulent stresses $(-\rho\overline{u_i u_j})$ and the turbulent heat fluxes $(\rho C_p\overline{u_j t})$ are modeled as described in the following sections.

3 Turbulence Model for Reynolds Stresses

The most widely used two-equation turbulence model; namely the k-ϵ model, is also used here with the conventional *isotropic dissipation equation.* The model is combined with damping functions to increase the accuracy near the walls. The conventional low Reynolds number form of the k-ϵ model (Wilcox, 1993) for steady state is given by

$$\frac{\partial}{\partial x_j}(\rho U_j k) = \frac{\partial}{\partial x_j}\left[\left(\mu + \frac{\mu_\tau}{\sigma_k}\right)\frac{\partial k}{\partial x_j}\right] + P_k - \rho\epsilon \tag{4}$$

$$\frac{\partial}{\partial x_j}(\rho U_j \epsilon) = \frac{\partial}{\partial x_j}\left[\left(\mu + \frac{\mu_\tau}{\sigma_\epsilon}\right)\frac{\partial \epsilon}{\partial x_j}\right] + f_1 C_{\epsilon 1}\frac{\epsilon}{k}P_k - f_2 C_{\epsilon 2}\rho\frac{\epsilon^2}{k} \tag{5}$$

where P_k is the production term expressed as

$$P_k = \tau_{ij}\frac{\partial U_i}{\partial x_j} = -\rho\overline{u_i u_j}\frac{\partial U_i}{\partial x_j} \tag{6}$$

and f_1 and f_2 are damping functions.

The turbulent eddy viscosity μ_τ is calculated as

$$\mu_\tau = \rho f_\mu C_\mu \frac{k^2}{\epsilon} \tag{7}$$

where f_μ is the damping function for the turbulent viscosity. In the linear eddy viscosity model the Reynolds stresses τ_{ij} are expressed as

$$\tau_{ij} = -\tfrac{2}{3}\rho k\delta_{ij} + 2\mu_\tau S_{ij}. \tag{8}$$

A nonlinear constitutive relation for the Reynolds stresses in incompressible flow was proposed by Speziale (1987). The nonlinear terms in this model are a form of quadratic terms, which enable calculation of anisotropic normal stresses and consequently prediction of the secondary velocity field in ducts. The Reynolds stresses in this model are determined according to

$$\tau_{ij} = -\frac{2}{3}\rho k\delta_{ij} + 2\mu_\tau S_{ij} + 4C_D C_\mu \mu_\tau \frac{k}{\epsilon}\left(S_{ik}S_{kj} - \frac{1}{3}S_{mn}S_{nm}\delta_{ij}\right) + 4C_E C_\mu \mu_\tau \frac{k}{\epsilon}\left(\dot{S}_{ij} - \frac{1}{3}\dot{S}_{mm}\delta_{ij}\right) \tag{9}$$

$$S_{ij} = \frac{1}{2}\left(\frac{\partial U_i}{\partial x_j} + \frac{\partial U_j}{\partial x_i}\right) \tag{10}$$

and $\dot{S}_{ij}$ is the frame-indifferent Oldroyd derivative of S_{ij} (see, e.g., Wilcox, 1993). In steady state one has

$$\dot{S}_{ij} = U_k\frac{\partial S_{ij}}{\partial x_k} - \frac{\partial U_i}{\partial x_k}S_{kj} - \frac{\partial U_j}{\partial x_k}S_{ki}. \tag{11}$$

The standard values for the constants and coefficients in (3), (4), (5), (7), and (9) have been used:

$$\sigma_k = 1.0, \quad \sigma_\epsilon = 1.314, \quad C_{\epsilon 1} = 1.44, \quad C_{\epsilon 1} = 1.92$$

$$C_D = C_E = 1.68 \quad \text{and} \quad C_\mu = 0.09.$$

4 Turbulence Models for Heat Flux

Three models are used to express the turbulent heat flux.

(a) The SED based on the Boussinesq viscosity model as

$$\rho\overline{u_j t} = -\frac{\mu_\tau}{\sigma_T}\frac{\partial T}{\partial x_j} \tag{12}$$

Please note that the damping function f_μ appears in μ_τ. This model may be regarded as a low Reynolds number model.

(b) Low Reynolds number version of the GGDH is defined as

$$\overline{u_j t} = -C_t f_\mu \frac{k}{\epsilon}\left(\overline{u_j u_k}\frac{\partial T}{\partial x_k}\right). \tag{13}$$

(c) WET in its low Reynolds number version is defined by

$$\overline{u_j t} = -C_t f_\mu \frac{k}{\epsilon}\left(\overline{u_j u_k}\frac{\partial T}{\partial x_k} + \overline{u_k t}\frac{\partial U_j}{\partial x_k}\right). \tag{14}$$

The constant C_t is set to 0.3 in both Eqs. (13) and (14).

It should be noted that the authors suggest that low Reynolds number versions of the GGDH and WET models are created by only using the damping function f_μ as shown in Eqs. (13) and (14). A low Reynolds number version of GGDH and WET is needed to create consistency with the treatment of the flow field. However, such a formulation is not well known. This work is thus a first attempt to handle these methods at low Reynolds numbers for turbulent convective heat transfer in ducts.

5 The Damping Functions f_1, f_2, and f_μ

The high Reynolds number form of the k-ϵ model suggests that f_μ should approximately be equal to unity in the fully turbulent region remote from solid walls. However, in a region very close to a wall where the viscous effects become very important, f_μ will differ considerably from unity. In this study, two kinds of damping functions are used, the Lam-Bremhorst (1981), hereafter the LB model, and the Abe-Kondoh-Nagano (1995) model, hereafter the AKN model. The main difference between these two models is that the friction velocity u^* is used to account for the near-wall effect in the LB model while the Kolmogorov velocity scale $u_\epsilon \equiv (\nu\epsilon)^{0.25}$ is used in the AKN model. It is known that the friction velocity vanishes at separation (at the corner of an orthogonal duct) and reattachment points but the Kolmogorov velocity scale does not. In the LB model the formulation of f_1, f_2, and f_μ are expressed as

$$f_\mu = (1 - e^{-0.0165\mathrm{Re}_k})^2\left(1 + \frac{20.5}{\mathrm{Re}_t}\right) \tag{15}$$

where $\mathrm{Re}_k = \rho k^{0.5}\eta/\mu$ and $\mathrm{Re}_t = \rho k^2/\mu\epsilon$.

$$f_1 = 1 + \left(\frac{0.05}{f_\mu}\right)^3. \tag{16}$$

and

$$f_2 = 1 - e^{-\mathrm{Re}_t^2}. \tag{17}$$

In the AKN model the formulations of f_μ, f_1, and f_2 are given by

$$f_\mu = (1 - e^{-y^*/14})^2\left(1 + \frac{5}{\mathrm{Re}_t^{0.75}}\, e^{-\mathrm{Re}_t/200^2}\right) \tag{18}$$

where $y^* = u_\epsilon(\rho\eta/\mu) = (\mu\epsilon/\rho)^{0.25}\rho\eta/\mu$ and $\mathrm{Re}_t = \rho k^2/\mu\epsilon$.

$$f_1 = 1, \quad f_2 = (1 - e^{-y^*/3.1})^2(1 - 0.3e^{-(\mathrm{Re}_t/6.5)^2}). \tag{19}$$

It should be noted that when the AKN model is used, the constants are set as $\sigma_k = \sigma_\epsilon = 1.4$. In the above equations η is the normal distance to a wall.

6 Periodic Condition

It is obvious that the pressure P decreases in the main flow direction and therefore the pressure should be handled in a special way. It is expressed as

$$P(x, y, z) = -\beta x + P^*(x, y, z) \tag{20}$$

where β is a constant representing the nonperiodic pressure gradient and P^* behaves in a periodic manner from cycle to cycle in the flow direction.

The dimensionless temperature θ is defined in the cyclic case as

$$\theta(x, y, z) = \frac{T(x, y, z) - T_w}{T_b(x) - T_w} \tag{21}$$

where T_W is the constant wall temperature and T_b is the fluid bulk temperature. Using this expression and inserting it into the energy Eq. (3) one obtains

$$\frac{\partial}{\partial x_j}(\rho U_j\theta) = \frac{\partial}{\partial x_j}\left[\frac{\mu}{\mathrm{Pr}}\frac{\partial\theta}{\partial x_j} - (\rho\overline{u_j\theta})\right] + \Omega \tag{22}$$

where Ω is

$$\Omega = \lambda\left[\Gamma\frac{\partial\theta}{\partial x} + \frac{\partial}{\partial x}(\Gamma\theta) - \rho U\theta\right] + \Gamma\theta\left(\lambda^2 + \frac{\partial\lambda}{\partial x}\right). \tag{23}$$

In (23) λ is

$$\lambda = \frac{\partial(T_b - T_w)}{\partial x}\Big/(T_b - T_w). \tag{24}$$

$\Gamma = \mu/\mathrm{Pr}$ and both λ and Ω are periodic parameters.

In the GGDH method, $\overline{u_jt}$ is calculated from

$$\overline{u_jt} = -Cf_\mu\frac{k}{\epsilon}(T_b - T_w)\left\{\overline{u_ju}\left(\lambda\theta + \frac{\partial\theta}{\partial x}\right) + \overline{u_jv}\frac{\partial\theta}{\partial y} + \overline{u_jw}\frac{\partial\theta}{\partial z}\right\}. \tag{25}$$

In the WET method, $\overline{u_jt}$ is determined from

$$\overline{u_jt} = -C_tf_\mu\frac{k}{\epsilon}(T_b - T_w)\left\{\overline{u_ju}\left(\lambda\theta + \frac{\partial\theta}{\partial x}\right) + \overline{u_jv}\frac{\partial\theta}{\partial y} + \overline{u_jw}\frac{\partial\theta}{\partial z} + \overline{u_kt}\frac{\partial U_j}{\partial x_k}\right\}. \tag{26}$$

An additional condition is needed to close the problem since the energy equation contains two unknowns $\theta(x, y, z)$ and $\lambda(x)$. This condition is found from the definition of the bulk temperature. In dimensionless form one has

$$\int |U|\theta dA_c = \int |U| dA_c \tag{27}$$

where A_c is the cross-sectional area in the main flow direction. The shape of the nondimensional temperature profile $\theta(x, y, z)$ repeats itself in the fully developed periodic region.

7 Boundary Conditions

Periodicity conditions are imposed at the inlet and outlet for all variables. It then follows

$$\Phi(x, y, z) = \Phi(x + L, y, z)$$
$$\Phi = U, V, W, P^*, k, \epsilon. \tag{28}$$

In order to achieve stability in the numerical procedure, the following variables are also handled as periodic:

$$\overline{u_iu_j},\ \overline{u_j\theta},\ \lambda,\ S_{ij},\ f_\mu.$$

The boundary conditions $k = \partial\epsilon/\partial\eta = 0$ at the walls and $\partial k/\partial\eta = \partial\epsilon/\partial\eta = 0$ at the symmetry lines are adopted. η is the normal distance to a wall or a symmetry line. The effect of one wall, namely the nearest one is adopted in this investigation, $\eta = \min.(\eta_1, \eta_2)$.

8 Additional Equations

The Reynolds number is defined as

$$\mathrm{Re} = \frac{\rho U_bD_h}{\mu} = \frac{\dot{m}D_h}{A_{\mathrm{cross}}\cdot\mu} \tag{29}$$

where A_{cross} is the cross-sectional area and U_b is the bulk velocity which is related to the mass flow as

$$\dot{m} = \int_A \rho U\cdot dA. \tag{30}$$

The pressure drop per cycle is defined by

$$\Delta p = \beta L = 4f \frac{L}{D_h} \frac{\rho U_b^2}{2} \tag{31}$$

where f is the Fanning friction factor. One then has

$$f = \frac{\beta D_h/4}{\rho U_b^2/2}. \tag{32}$$

In the turbulent region the calculated friction factor is compared with the Blasius friction factor (Incropera and DeWitt, 1996) which is valid for $\mathrm{Re} \leq 2 \times 10^4$.

$$f = 0.079\ \mathrm{Re}^{-0.25} \tag{33}$$

However, in the laminar region the friction factor is compared to the following correlation for a square duct (see, e.g., Incropera and DeWitt, 1996):

$$f = \frac{57}{4\ \mathrm{Re}}. \tag{34}$$

The Nu number is calculated in two ways, by finding the Nu number at each point adjacent to the wall (Nu_x), or using the inlet and outlet bulk temperatures (Nu_{ov}). These are called the local and the overall Nu number, respectively.

Since the points adjacent to the walls are always in the viscous sublayer then the local Nu number can be found as follows:

$$\mathrm{Nu}_{xp} = D_h \frac{\theta_p}{y}. \tag{35}$$

If one takes the average of the local Nu numbers at all points adjacent to the walls for each cross section, one has

$$\mathrm{Nu}_{x\mathrm{cross}} = \frac{\Sigma\ \mathrm{Nu}_{iW} A_{iW}}{\Sigma A_{iW}} \quad i = \mathrm{NW}, \mathrm{HW} \tag{36}$$

where Nu_{iW} is expressed as

$$\mathrm{Nu}_{iW} = \left[\frac{\int\int \mathrm{Nu}_{xp}\, dA}{\int\int dA} \right]_{iW}$$

(where the indices stand for NW = North Wall and HW = High Wall. The main flow is through the west and east walls). Nu_x is then calculated according to

$$\mathrm{Nu}_x = \frac{\int \mathrm{Nu}_{x\mathrm{cross}}\, dx}{L}. \tag{37}$$

The Nu_{ov} number can be calculated as shown below. The overall heat transfer coefficient is calculated by

$$h_{ov} = \frac{\dot{Q}}{A_w \Delta T_{wb}} \tag{38}$$

where

$$\dot{Q} = \dot{m} C_p (T_{b2} - T_{b1}) \tag{39}$$

$$\Delta T_{wb} = \tfrac{1}{2}\{(T_w - T_{b2}) + (T_w - T_{b1})\}. \tag{40}$$

By combining these equations, one finds

$$\mathrm{Nu}_{ov} = \frac{2A_{\mathrm{cross}}}{A_w} \frac{(1-\gamma)}{(1+\gamma)} \mathrm{Pr\ Re} \tag{41}$$

where γ in the cyclic case can be derived as

$$\gamma = \exp\left(\int_0^L \lambda dx \right). \tag{42}$$

The Nu number is compared to the Dittus-Boelter equation for circular ducts (e.g., Incropera and DeWitt, 1995) in the turbulent region

$$\mathrm{Nu} = 0.023\ \mathrm{Re}^{0.8}\ \mathrm{Pr}^{0.3} \tag{43}$$

while in the laminar region the Nu number for a square duct is 2.98. The Dittus-Boelter correlation is usually recommended for Reynolds number greater than about 10,000 but experiments carried out by Lowdermilk et al. (1954) showed that it may be used even for lower Reynolds number in square and rectangular ducts. For a rectangular duct in laminar flow the Nu number depends on the aspect ratio (see, e.g., Incropera and DeWitt, 1996).

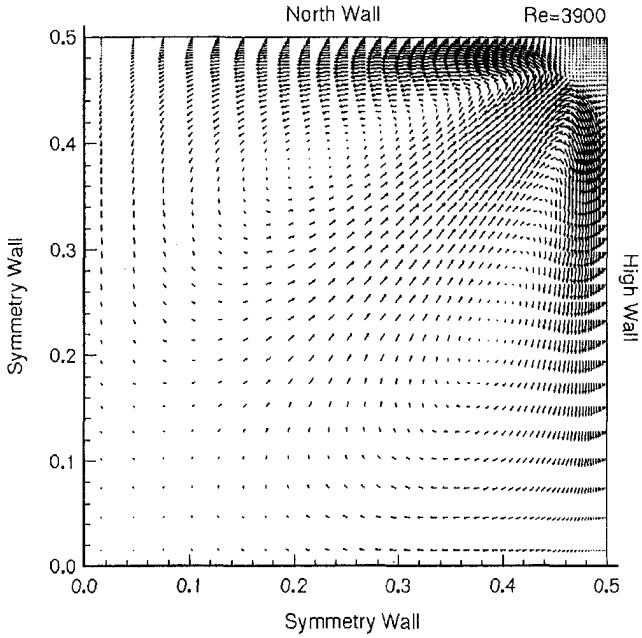

Fig. 2(*a*)

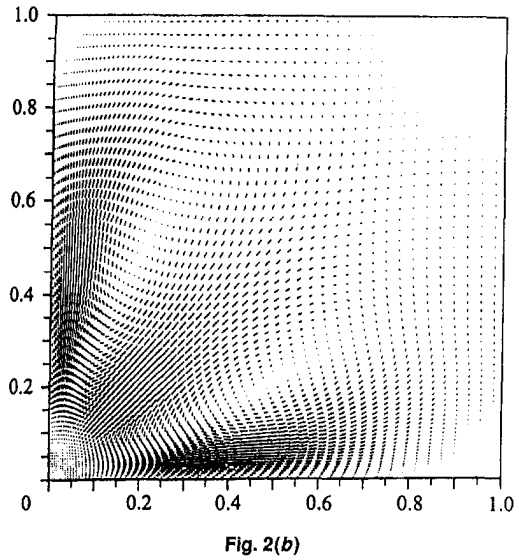

Fig. 2(*b*)

Fig. 2 Secondary velocity field predicted by the nonlinear *k-ε* model (*a*) compared with DNS work of Gavrilakis (see Speziale and Gatski, 1997)

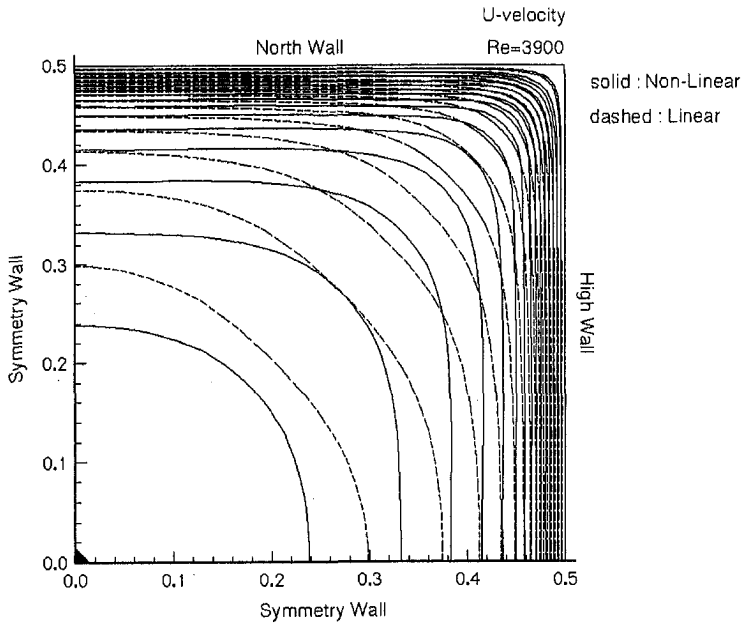

Fig. 3 Streamwise velocity contours predicted by the linear and the nonlinear k-ϵ model. Solid lines are the nonlinear model and dashed lines are the linear model.

9 Numerical Solution Procedure

The partial differential equations are transformed to algebraic equations by a general finite-volume technique. The momentum equations are solved for the velocity components on a nonstaggered grid arrangement. The Rhie-Chow interpolation method (Rhie and Chow, 1983) is used to interpolate the velocity components to the control volume faces from the grid points. The SIMPLEC-algorithm (Raithby and Schneider, 1988) is employed to handle the pressure velocity coupling. TDMA (see, e.g. Patankar, 1980) based algorithms are used for solving the equations. The convective terms are treated by the van Leer scheme (van Leer, 1974) while the diffusive terms are treated by the central-difference scheme. The hybrid scheme is used for solving k and ϵ.

The initial values for all variables are set to zero except for k and ϵ. These are set as

$$k = 0.005U_{in}^2 \quad \text{and} \quad \epsilon = 0.1k^2.$$

The initial values for k and ϵ are important *in periodic conditions and with LB damping functions.* If U_{in} is too low, k and ϵ may not be activated while a too high value of U_{in} may cause divergence problem. This property seems to impose a limitation of using the LB damping functions for periodic conditions. It is, however, favorable in terms of computational aspects, to use periodic conditions but care is recommended in choosing the initial values. Such a limitation does not exist for the AKN model. Rokni (1998) compared these two models, namely the LB and AKN models, and found that the AKN model is much more stable and less sensitive to initial values than the LB model. He also found that the AKN model demands less grid points in the sublayer. He also discussed the last two findings (stability and less grid points) and found that the LB damping functions have singularities (due to friction velocity) in contrast to the AKN model.

A nonuniform grid distribution is employed in the plane perpendicular to the main flow direction. Close to each wall, the number of grid points or control volumes is increased to enhance the resolution and accuracy. The computations were terminated when the sum of the absolute residuals normalized by the inflow was less than 3×10^{-6} for all variables. Different number of grid points was used in the cross-sectional plane. For instance, it was shown that the overall friction factors and Nu numbers, which are the most interesting parameters from an engineering point of view, did not change significantly (less than one percent) if the number of grid points were increased beyond 31×31 in a square duct at Reynolds number less than 9000. However, at least 41×41 grid points were needed for Reynolds number higher than 9000 if the LB model was used. It is obvious that the number of grid points should be increased by increasing Reynolds number, since some grid points must always be in the viscous sublayer near each wall. However, the AKN model does not need as many grid points as the LB model and showed to be much more robust. Only three grid points were applied in the main flow direction.

It might be of interest to point out that 21×21 grid points (in the plane perpendicular to the main flow direction) were sufficient if the law of the wall was used at Reynolds number about 10000.

As it is known, the results obtained from the low Reynolds k-ϵ model depend somewhat on the number of grid points. This problem has also been noticed in this investigation. However, the results change only slightly and can be neglected in this investigation. The grid dependence of the results was found to be less in the AKN model. Usually by changing the stretching factor, satisfactory results can be obtained by this model. It should be pointed out that the average value of $y+$ near each wall should not be too small since the turbulent Prandtl number in the temperature equation is not constant close to a wall. It has been found that if the average value of $y+$ near a wall is kept between 0.3 and 1.3 no significant changes in the computed friction factor and Nu number occur.

10 Results and Discussions

The predicted secondary velocity distribution using the nonlinear k-ϵ model is shown in Fig. 2. For sake of clarity, the secondary velocity field is shown for 51×51 mesh points. The secondary motion consists of two counter rotating vortices, which transport high momentum fluid towards the duct corner along the bisector and then outwards along the walls. Close to the duct center the secondary flow is weak and seems to have no influence on the streamwise flow. Near the corner the flow must be completely viscous which can be seen clearly in the figure. The velocity vectors are computed all the way down to the wall. The magnitude of the secondary velocity vectors decreases in the sublayer and becomes zero at the walls. The linear k-ϵ model does not predict any secondary flow and thus there is a large difference in the cross flow transport into the corner

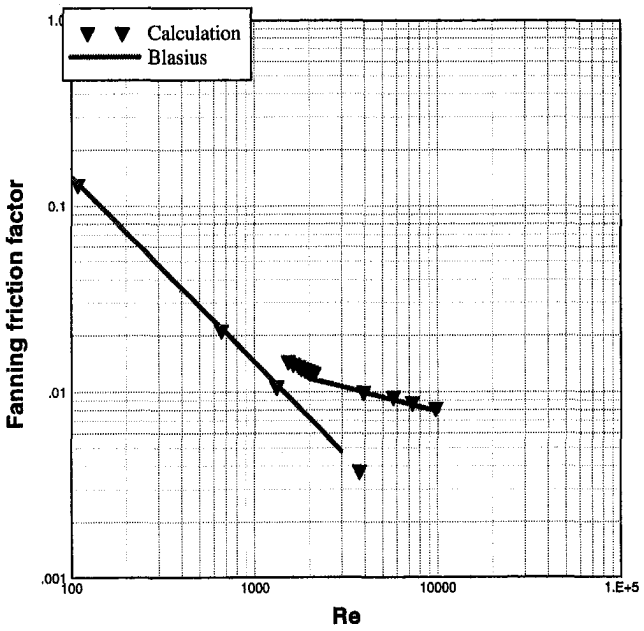

Fig. 4 Calculated Fanning friction factor compared with the Blasius correlation

between the linear and the nonlinear k-ϵ models. The corresponding secondary velocity pattern obtained from the DNS work of Gavrilakis (see Speziale and Gatski, 1997) has been displayed in Fig. 2(b) but rotated 180 degrees (the reader should be aware about the quality of the figure since it has first been scanned and then enclosed). The agreement is really good.

Figure 3 shows the streamwise velocity contours predicted by the linear and nonlinear k-ϵ models. The nonlinear k-ϵ model shows that in the region close to the corner, the contours are bulged towards the corner due to the presence of the secondary motion. However, the linear k-ϵ model shows no bulging at all and behaves in a similar way as a duct with circular cross section.

The center-to-bulk-velocity ratio (U_c/U_b), is 1.30 in the nonlinear k-ϵ model as well as in the linear k-ϵ model at Re $\approx$ 3900. This ratio can be compared to the value 1.33 obtained by Gavrilakis (1992) for a square duct at the Reynolds number 4410 by using direct numerical simulations.

The calculated Fanning friction factor is shown in Fig. 4. In the turbulent region, the results obtained from the nonlinear k-ϵ model agree excellently with the Blasius correlation and all the calculated values are within five percent.

Figure 4 shows results for both turbulent and laminar cases. Laminar solutions, obtained when the k and ϵ equations are not solved, were possible up to a Reynolds number of approximately 3500. It was possible to achieve turbulent solutions for Reynolds numbers as low as 1600. However, to achieve a reasonable prediction method in the Reynolds number range 1600–3500 obviously a transition model is needed. The transition region is, however, not within the scope of this investigation.

Both the linear k-ϵ and the nonlinear k-ϵ models give almost identical result in predicting the friction factors. This can be explained because the magnitude of the secondary velocities is small (only a few percent of the main flow velocity) in straight square ducts and their contribution to the calculated friction factor is small. However, the situation is completely different in wavy ducts since the magnitude of the secondary motions are much higher (more than 20 percent to 40 percent) and their contribution to the calculated friction factor may be of importance. Therefore the linear k-ϵ model is not an appropriate model in wavy ducts.

To show the effect of the secondary motion on the temperature field Fig. 5 is presented. The results from the linear and the nonlinear k-ϵ models combined with the SED concept are compared to each other. The temperature field predicted by the nonlinear model is bulged towards the corner while the linear model does not show any bulging at all. This can be explained by presence of the secondary motion. The effect of the secondary motions near the corner as well as near the walls are very small and both the linear and the nonlinear models gives very similar results (see Fig. 5).

The Nu number predicted by the nonlinear k-ϵ model combined with the SED concept is shown in Fig. 6. In the laminar region the predicted Nu number is 2.98 which is exactly equal to the analytical value for square ducts. In the turbulent region, the calculated Nu numbers are in good agreement with the Dittus-Boelter correlation, as shown in Fig. 6. The results obtained from the GGDH

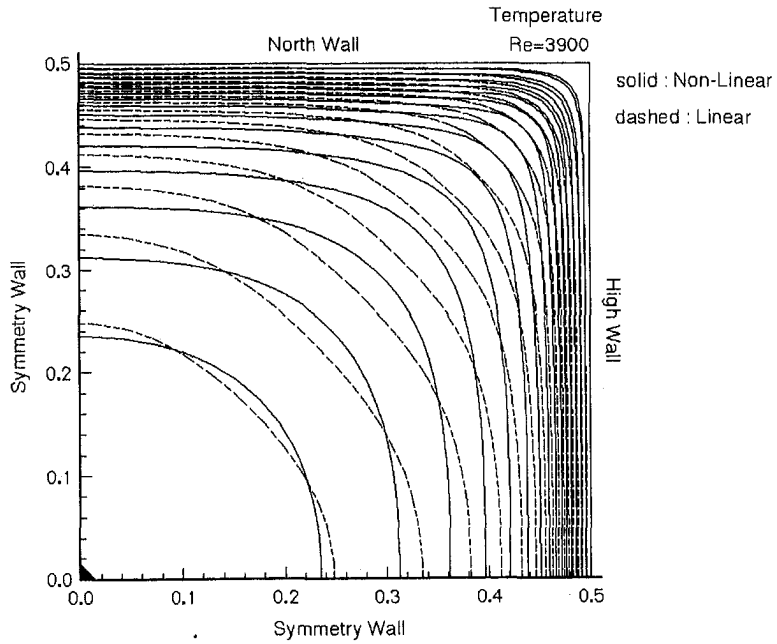

Fig. 5 The temperature field contours predicted by the linear and the nonlinear models

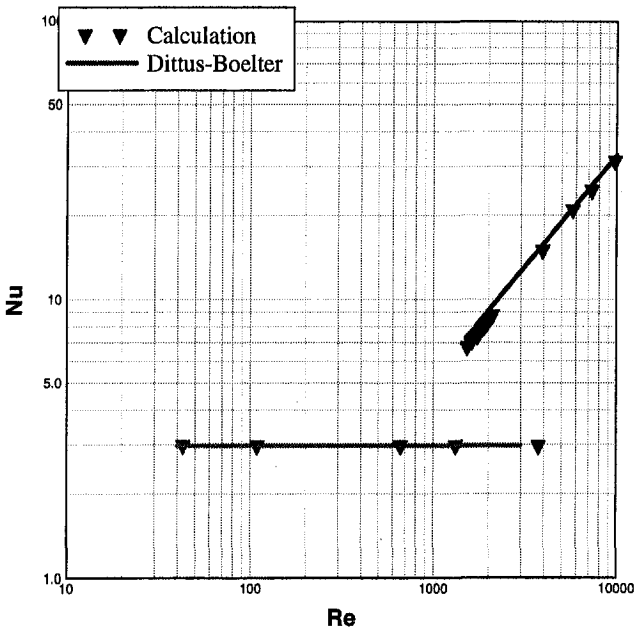

Fig. 6 Calculated Nu number in a square duct compared with the Dittus-Boelter correlation

Table 1 Comparison between the local Nu numbers, the overall Nu numbers and Dittus-Boelter correlation, and different heat flux models

Method	Re	Nu	Nu_{ov}	Nu_{DB}
k-ε	2482	10.3	10.2	10.8
SED	2495	10.2	10.1	10.9
GGDH	2495	10.4	10.4	10.9
WET	2495	10.4	10.4	10.9
k-ε	3964	15.1	15.0	15.8
SED	3929	15.1	15.1	15.6
GGDH	3929	15.6	15.5	15.6
WET	3929	15.5	15.4	15.6
k-ε	5753	20.0	20.0	21.2
SED	5743	21.0	20.9	21.2
GGDH	5743	21.9	21.8	21.2
WET	5743	21.9	21.7	21.2
k-ε	7303	24.3	24.3	25.7
SED	7327	24.7	24.8	25.8
GGDH	7327	25.8	25.8	25.8
WET	7327	25.8	25.8	25.8

and WET heat flux models compared with the SED concept are shown in Table 1.

To have a correct description in the overlapping Reynolds number range in Fig. 6, a transition model is needed. This is beyond the scope of this paper and is not discussed here.

It should be mentioned that in the turbulent region, SED, GGDH, and WET methods are combined with the nonlinear model. However, only the SED concept is combined with the linear k-ϵ model in the turbulent region. The table reveals that all the three models give almost the same results, while the results obtained from GGDH and WET are almost identical.

11 Other Correlations

The calculated friction factors are also compared with the Prandtl law and the Petukhov correlation, and good agreement was found. The predicted Nu numbers are also in good agreement with the Gnielinski correlation. These correlations can be found in, e.g., Incropera and DeWitt (1996).

12 Conclusions

A numerical method for turbulent and laminar flow and heat transfer in straight square ducts has been presented. Speziale's nonlinear eddy viscosity model has been used successfully in combination with the Lam-Bremhorst damping functions to predict the secondary velocity field, the streamwise velocity, friction factor, and Nusselt number. New versions of the GGDH and WET for low Reynolds numbers are suggested. Comparisons of the results obtained with the linear eddy viscosity model are also presented.

The average friction factors predicted with both models agree very well with the Blasius correlation, the Petukhov correlation as well as the Prandtl law. The calculated Nu numbers are in decent agreement with the Dittus-Boelter correlation and the Gnielinski correlation. The GGDH and WET methods agree best with the experimental correlations; however, a general conclusion cannot be drawn until the performance of these models have been shown in more complex channels.

To have a physical correct description of the secondary flow, local axial velocities and temperatures, the advanced models are needed.

The computational time for the nonlinear k-ϵ model is of the same order of magnitude as for the linear k-ϵ model. The nonlinear model thus presents a cheap method to improve the prediction of the turbulent stresses. It is faster and simpler than full Reynolds stress models (RSMs), LES and DNS simulations.

The GGDH and WET turbulent heat flux models present a computationally cheap method to take anisotropy into account. These models are simpler and more stable than the full turbulent heat flux models.

Two different damping functions were used to express the near-wall behavior, the Lam-Bremhorst and the Abe-Kondoh-Nagano models. The study showed that the Abe-Kondoh-Nagano model is very robust and demands fewer grid points than the Lam-Bremhorst model in all cases studied. Satisfactory results can be achieved by the Abe-Kondoh-Nagano with a limited number of grid points; changing the stretching factor might be more appropriate than increasing the number of grid points.

References

Abe, K., Kondoh, T., and Nagano, Y., 1995, "A New Turbulence Model for Predicting Fluid Flow and Heat Transfer in Separating and Reattaching Flows—II. Thermal Field Calculations," *Int. J. Heat Mass Transfer,* Vol. 38, No. 8, pp. 1467–1481.

Gavrilakis, S., 1992, "Numerical Simulation of Low-Reynolds-number Turbulent Flow Through A Straight Square Duct," *J. Fluid Mech.,* Vol. 244, pp. 101–129.

Huser, A., and Biringen, S., 1993, "Direct Numerical Simulation of Turbulent Flow In a Square Duct," *J. Fluid Mech.,* Vol. 257, pp. 65–95.

Incropera, F. P., and DeWitt, D. P., 1996, *Fundamentals of Heat and Mass Transfer,* Fourth Ed., John Wiley and Sons, New York.

Kim, J., Moin, P., and Moser, R., 1987, "Turbulence Statistics In Fully Developed Channel Flow at Low Reynolds Number," *J. Fluid Mech.,* Vol. 177, pp. 133–166.

Lam, C. K. G., and Bremhorst, K., 1981, "A Modified Form of the k-ϵ Model for Predicting Wall Turbulence," ASME *Journal of Fluids Engineering,* Vol. 103, pp. 456–460.

Lowdermilk, W. H., Wieland, W. F., and Livingood, J. N. B., 1954, "Measurements of Heat Transfer and Friction Coefficients for Flow of Air in Noncircular Ducts at High Surface Temperature," Report No. NACA RN E53J07.

Madabhushi, R. K., and Vanka, S. P., 1991, "Large Eddy Simulation of Turbulence-Driven Secondary Flow In a Square Duct," *Phys. Fluids,* Vol. A3, pp. 2734–2745.

Patankar, S. V., 1980, *Numerical Heat Transfer and Fluid Flow,* McGraw-Hill, New York.

Rhie, C. M., and Chow, W. L., 1983, "Numerical Study of the Turbulent Flow Past an Airfoil with Trailing Edge Separation," *AIAA J.,* Vol. 21, No. 11, pp. 1525–1532.

Rokni, M., 1998, "Numerical Investigation of Turbulent Fluid Flow and Heat Transfer in Complex Ducts," Doctoral thesis, ISSN 1104-7747, Department of Heat and Power Engineering, Lund Institute of Technology, Lund, Sweden.

Rokni, M., and Sundèn, B., 1996, "A Numerical Investigation of Turbulent Forced Convection in Ducts With Rectangular and Trapezoidal Cross-Section Area by Using Different Turbulence Models," *Num. Heat Transfer,* Vol. 30, No. 4, pp. 321–346.

Rokni, M., and Sundèn, B., 1998, "3D Numerical Investigation of Turbulent Forced Convection in Wavy Ducts With Trapezoidal Cross-Section," *Int. J. Num. Meth. for Heat & Fluid Flow,* Vol. 8, No. 1, pp. 118–141.

Speziale, C. G., 1987, "On Non-linear K-l and K-ϵ Models of Turbulence," *J. Fluid Mech.,* Vol. 178, pp. 459–475.

Speziale, C. G., and Gatski, T. B., 1997, "Analysis and Modelling of Anisotropies in the Dissipation Rate of Turbulence," *J. Fluid Mech.,* Vol. 344, pp. 155–180.

Su, M. D., and Friedrich, R., 1994, "Investigation of Fully Developed Turbulent

Flow In a Straight Duct With Large Eddy Simulation," ASME *Journal of Fluids Engineering*, Vol. 116, pp. 677–684.

Van Leer, B., 1974, "Towards the Ultimate Conservative Difference Scheme. II. Monotonicity and Conservation Combined in a Second Order Scheme," *J. Comp. Phys.*, Vol. 14, pp. 361–370.

Wilcox, D. C., 1993, *Turbulence Modeling for CFD*, DCW Industries, Inc.

Laminar Free Convection of Pure and Saline Water Along a Heated Vertical Plate

A. Pantokratoras[1]

1 Introduction

The classical problem of free-convection heat transfer from a heated vertical surface has been of interest to investigators for a very long time. An important method for finding a solution to this problem is the similarity method. Schuh (1948) gave solutions for the vertical isothermal plate for various values of Pr number (10, 100, 1000) employing approximate methods. Ostrach (1953) numerically obtained the solution for Pr range of 0.01 to 1000 for the same problem. Sparrow and Gregg (1956) presented results for the free-convection problem from a vertical plate with uniform surface heat flux. Liburdy and Faeth (1975) obtained numerical results for the free-convection problem along a vertical adiabatic wall for Pr numbers 0.01, 0.1, 0.7, 1, 10, and 100. Jaluria and Gebhart (1977) also gave results for the same problem for Pr number range 0.01–100. In all of the above research a linear relationship between fluid density and temperature has been used.

However, it is known that the density-temperature relationship for water is linear at high temperatures and nonlinear at low temperatures. The density of pure water is maximum at 3.98°C. The density increases as the temperature decreases approaching 3.98°C, while the density decreases as the temperature decreases from 3.98°C to 0°C.

Except for the above-mentioned studies there are some papers concerning water free convection in low-temperature range where the density-temperature relatinship is nonlinear. Goren (1966) solved the problem of water free convection along a vertical isothermal surface with ambient temperature equal to maximum density temperature. The obtained results are valid for surface temperatures until 8°C. Vanier and Tien (1967) extended the above work to surface temperatures until 35°C but the results were obtained again only for one ambient temperature equal to 4°C. Soundalgekar (1973) used an integral method to calculate the surface shear stress in water free convection over a vertical plate with variable temperature. The ambient water was again at 4°C. Gebhart and Mollendorf (1978) analyzed the problem of laminar free convection of water over a vertical plate with both thermal and saline diffusion and presented results for the vertical isothermal plate with temperature diffusion. The uniform surface heat flux problem was analyzed by Qureshi and Gebhart (1978) and similarity results were produced only when the ambient density coincides with density extremum temperature, that is only for one ambient temperature at a given salinity. Mollendorf, Johnson, and Gebhart (1981) presented self-similarity solutions for pure and saline water free convection over an adiabatic vertical plate in low-temperature range, again with the above-mentioned constraint. Gebhart, Carey, and Mollendorf (1979) developed a purturbation analysis to extend the range of the calculations beyond the density extremum temperature and produced results for the adiabatic and uniform heat flux plate. These results are valid only when the ambient temperature is near the maximum density temperature.

From the above literature review it is clear that the problem of water free convection in low-temperature range has been investigated but there are some situations that have not been treated. For the free convection over an adiabatic and uniform heat flux plate, results have been produced for ambient temperature equal to or near the density extremum temperature. Results for the maximum velocity have not been given for the isothermal plate. The objective of this paper is to present results for the above three cases in the entire temperature range between 20°C and 0°C for the following cases: (1) pure water (2) saline water with temperature diffusion and constant salinity. The results are obtained with the numerical solution of the boundary layer equations.

2 The Mathematical Model

Consider laminar free convection along a vertical plate placed in a calm environment with u and v denoting, respectively, the velocity components in the x and y direction, where x is vertically upwards and y is the coordinate perpendicular to x. The flow is assumed to be steady, of the boundary layer type. The governing equations of this flow with Boussinesq approximations are

$$\text{continuity equation: } \frac{\partial u}{\partial x} + \frac{\partial v}{\partial y} = 0 \tag{1}$$

$$\text{momentum equation: } u\frac{\partial u}{\partial x} + v\frac{\partial u}{\partial y} = \nu\frac{\partial^2 u}{\partial y^2} - \frac{\rho - \rho_a}{\rho_a} g \tag{2}$$

$$\text{energy equation: } u\frac{\partial T}{\partial x} + v\frac{\partial T}{\partial y} = \alpha\frac{\partial^2 T}{\partial y^2} \tag{3}$$

where T is the water temperature, ρ and ρ_a are the local and ambient water density, ν is the kinematic viscosity, and α is the thermal diffusivity. The density of saline water is a function of temperature, salinity, and pressure. In this paper the known from Oceanography International Equation of State for Seawater (UNESCO, 1981; Fofonoff, 1985) is used for the calculation of density. This equation is valid for temperatures from −2 to 40°C, salinities from zero percent to four percent and pressures from 1 to maximum oceanic pressure in bars. In this paper all calculations have been made for atmospheric pressure, that is for 1 bar.

In the boundary layer equations the kinematic viscosity and thermal diffusivity of water are included and must be calculated for each situation. These quantities are calculated from data given by Kukulka, Gebhart, and Mollendorf (1987).

The following boundary conditions were applied:

$$\text{at } y = 0: \quad u = v = 0, \quad T = T_o \text{ for isothermal plate}$$

$$u = v = 0, \quad \frac{\partial T}{\partial y} = 0 \text{ for adiabatic plate}$$

$$u = v = 0, \quad -k\left(\frac{\partial T}{\partial y}\right) = \text{const. for uniform heat flux plate}$$

$$\text{as } y \to \infty \quad u = 0, \quad T = T_a.$$

At the edge of the plate initial flat velocity and temperature profiles were assumed. These profiles were used only to start the computations and their shape had no influence on the results which were taken far downstream of the edge.

The Eqs. (1)–(3) form a parabolic system and are solved by a method described by Patankar (1980). The finite difference method is used with primitive coordinates x, y and a space marching procedure is used in the x direction with an expanding grid. For more information about the expanding grid see Jia (1984). Calcu-

[1] School of Engineering, Democritus University of Thrace, 67100 Xanthi, Greece. e-mail: pantokrator@xanthi.cc.duth.gr. Mem. ASME.

Contributed by the Heat Transfer Division for publication in the JOURNAL OF HEAT TRANSFER. Manuscript received by the Heat Transfer Division, Nov. 15, 1998; revision received, Apr. 12, 1999. Keywords: Heat Transfer, Natural Convection, Plate. Associate Technical Editor: Y. Jaluria.

Flow In a Straight Duct With Large Eddy Simulation," ASME *Journal of Fluids Engineering*, Vol. 116, pp. 677–684.

Van Leer, B., 1974, "Towards the Ultimate Conservative Difference Scheme. II. Monotonicity and Conservation Combined in a Second Order Scheme," *J. Comp. Phys.*, Vol. 14, pp. 361–370.

Wilcox, D. C., 1993, *Turbulence Modeling for CFD*, DCW Industries, Inc.

Laminar Free Convection of Pure and Saline Water Along a Heated Vertical Plate

A. Pantokratoras[1]

1 Introduction

The classical problem of free-convection heat transfer from a heated vertical surface has been of interest to investigators for a very long time. An important method for finding a solution to this problem is the similarity method. Schuh (1948) gave solutions for the vertical isothermal plate for various values of Pr number (10, 100, 1000) employing approximate methods. Ostrach (1953) numerically obtained the solution for Pr range of 0.01 to 1000 for the same problem. Sparrow and Gregg (1956) presented results for the free-convection problem from a vertical plate with uniform surface heat flux. Liburdy and Faeth (1975) obtained numerical results for the free-convection problem along a vertical adiabatic wall for Pr numbers 0.01, 0.1, 0.7, 1, 10, and 100. Jaluria and Gebhart (1977) also gave results for the same problem for Pr number range 0.01–100. In all of the above research a linear relationship between fluid density and temperature has been used.

However, it is known that the density-temperature relationship for water is linear at high temperatures and nonlinear at low temperatures. The density of pure water is maximum at 3.98°C. The density increases as the temperature decreases approaching 3.98°C, while the density decreases as the temperature decreases from 3.98°C to 0°C.

Except for the above-mentioned studies there are some papers concerning water free convection in low-temperature range where the density-temperature relatinship is nonlinear. Goren (1966) solved the problem of water free convection along a vertical isothermal surface with ambient temperature equal to maximum density temperature. The obtained results are valid for surface temperatures until 8°C. Vanier and Tien (1967) extended the above work to surface temperatures until 35°C but the results were obtained again only for one ambient temperature equal to 4°C. Soundalgekar (1973) used an integral method to calculate the surface shear stress in water free convection over a vertical plate with variable temperature. The ambient water was again at 4°C. Gebhart and Mollendorf (1978) analyzed the problem of laminar free convection of water over a vertical plate with both thermal and saline diffusion and presented results for the vertical isothermal plate with temperature diffusion. The uniform surface heat flux problem was analyzed by Qureshi and Gebhart (1978) and similarity results were produced only when the ambient density coincides with density extremum temperature, that is only for one ambient temperature at a given salinity. Mollendorf, Johnson, and Gebhart (1981) presented self-similarity solutions for pure and saline water free convection over an adiabatic vertical plate in low-temperature range, again with the above-mentioned constraint. Gebhart, Carey, and Mollendorf (1979) developed a purturbation analysis to extend the range of the calculations beyond the density extremum temperature and produced results for the adiabatic and uniform heat flux plate. These results are valid only when the ambient temperature is near the maximum density temperature.

From the above literature review it is clear that the problem of water free convection in low-temperature range has been investigated but there are some situations that have not been treated. For the free convection over an adiabatic and uniform heat flux plate, results have been produced for ambient temperature equal to or near the density extremum temperature. Results for the maximum velocity have not been given for the isothermal plate. The objective of this paper is to present results for the above three cases in the entire temperature range between 20°C and 0°C for the following cases: (1) pure water (2) saline water with temperature diffusion and constant salinity. The results are obtained with the numerical solution of the boundary layer equations.

2 The Mathematical Model

Consider laminar free convection along a vertical plate placed in a calm environment with u and v denoting, respectively, the velocity components in the x and y direction, where x is vertically upwards and y is the coordinate perpendicular to x. The flow is assumed to be steady, of the boundary layer type. The governing equations of this flow with Boussinesq approximations are

$$\text{continuity equation: } \frac{\partial u}{\partial x} + \frac{\partial v}{\partial y} = 0 \tag{1}$$

$$\text{momentum equation: } u\frac{\partial u}{\partial x} + v\frac{\partial u}{\partial y} = \nu\frac{\partial^2 u}{\partial y^2} - \frac{\rho - \rho_a}{\rho_a} g \tag{2}$$

$$\text{energy equation: } u\frac{\partial T}{\partial x} + v\frac{\partial T}{\partial y} = \alpha\frac{\partial^2 T}{\partial y^2} \tag{3}$$

where T is the water temperature, ρ and ρ_a are the local and ambient water density, ν is the kinematic viscosity, and α is the thermal diffusivity. The density of saline water is a function of temperature, salinity, and pressure. In this paper the known from Oceanography International Equation of State for Seawater (UNESCO, 1981; Fofonoff, 1985) is used for the calculation of density. This equation is valid for temperatures from −2 to 40°C, salinities from zero percent to four percent and pressures from 1 to maximum oceanic pressure in bars. In this paper all calculations have been made for atmospheric pressure, that is for 1 bar.

In the boundary layer equations the kinematic viscosity and thermal diffusivity of water are included and must be calculated for each situation. These quantities are calculated from data given by Kukulka, Gebhart, and Mollendorf (1987).

The following boundary conditions were applied:

$$\text{at } y = 0: \quad u = v = 0, \quad T = T_o \text{ for isothermal plate}$$

$$u = v = 0, \quad \frac{\partial T}{\partial y} = 0 \text{ for adiabatic plate}$$

$$u = v = 0, \quad -k\left(\frac{\partial T}{\partial y}\right) = \text{const. for uniform heat flux plate}$$

$$\text{as } y \to \infty \quad u = 0, \quad T = T_a.$$

At the edge of the plate initial flat velocity and temperature profiles were assumed. These profiles were used only to start the computations and their shape had no influence on the results which were taken far downstream of the edge.

The Eqs. (1)–(3) form a parabolic system and are solved by a method described by Patankar (1980). The finite difference method is used with primitive coordinates x, y and a space marching procedure is used in the x direction with an expanding grid. For more information about the expanding grid see Jia (1984). Calcu-

[1] School of Engineering, Democritus University of Thrace, 67100 Xanthi, Greece. e-mail: pantokrator@xanthi.cc.duth.gr. Mem. ASME.

Contributed by the Heat Transfer Division for publication in the JOURNAL OF HEAT TRANSFER. Manuscript received by the Heat Transfer Division, Nov. 15, 1998; revision received, Apr. 12, 1999. Keywords: Heat Transfer, Natural Convection, Plate. Associate Technical Editor: Y. Jaluria.

lations were made on a DEC ALPHA 7000 computer using quadruple precision accuracy.

3 Results and Discussion

In the similarity method commonly used in free convection over vertical surfaces, the following functions and variables are used. The nondimensional stream function $f(\eta)$ is connected with physical stream function as follows:

$$\psi = 4\nu\left[\frac{\mathrm{Gr}_x}{4}\right]^{1/4} f(\eta) \tag{4}$$

where the similarity variable η is defined by

$$\eta = \frac{y}{x}\left[\frac{\mathrm{Gr}_x}{4}\right]^{1/4} \tag{5}$$

where Gr_x is the local Grashof number. In the classical similarity analysis with linear relationship between density and temperature the local Grashof number is defined as

$$\mathrm{Gr}_x = \frac{gx^3\beta(T_a)(T_o - T_a)}{\nu^2} \tag{6}$$

where $\beta(T_a)$ is the thermal expansion coefficient of water at ambient temperature and T_o is the plate temperature. The above Grashof number is unsuitable for water free convection at low temperatures due to nonlinear relationship between density and temperature. For example, when the ambient temperature corresponds to density extremum, the $\beta(T_a)$ coefficient becomes zero and the Grashof number becomes zero, too. In this case no similarity variabale η can be defined. Therefore, the following Grashof number is further used:

$$\mathrm{Gr}_x = \frac{gx^3}{\nu^2}\frac{\rho_a - \rho_o}{\rho_a} \tag{7}$$

where ρ_a and ρ_o are the ambient and wall local density. In the similarity analysis the vertical velocity is given by

$$u = \frac{2\nu}{x}[\mathrm{Gr}_x]^{1/2} f' \tag{8}$$

or in nondimensional form as

$$f' = \frac{ux}{2\nu}[\mathrm{Gr}_x]^{-1/2}. \tag{9}$$

A profile of the velocity f' has zero value at the plate and far away from the plate and a maximum value $f'_{\max}$ in the intermediate region. Taking the derivative of f' with respect to η we have

$$f'' = \frac{x^2}{\nu\sqrt{2}}[\mathrm{Gr}_x]^{-3/4}\left(\frac{\partial u}{\partial y}\right) \tag{10}$$

and the value of f'' at the plate is

$$f''(0) = \frac{x^2}{\nu\sqrt{2}}[\mathrm{Gr}_x]^{-3/4}\left(\frac{\partial u}{\partial y}\right)_{y=0}. \tag{11}$$

This quantity is used for the calculation of the wall shear stress by the following equation:

$$\tau(x) = \mu\left(\frac{\partial u}{\partial y}\right)_{y=0} = \mu\nu\frac{\sqrt{2}}{x^2}[\mathrm{Gr}_x]^{3/4} f''(0). \tag{12}$$

Another useful quantity in this problem is the wall heat flux $\varphi'(0)$ that is the derivative of the nondimensional temperature at the plate. Taking the derivative of the nondimensional temperature $\varphi = (T - T_a)/(T_o - T_a)$ with respect to n we have

$$\varphi'(0) = \frac{x}{T_o - T_a}\left[\frac{\mathrm{Gr}_x}{4}\right]^{-1/4}\left(\frac{\partial T}{\partial y}\right)_{y=0}. \tag{13}$$

In the present work the above quantities have been calculated as follows: The numerical method used is a space-marching technique giving the downstream velocity and temperature profiles using the known upstream profiles. At every downstream distance x the wall density ρ_o was calculated using the International Equation of State for Seawater from the calculated downstream wall temperature. Then the Grashof number was calculated from Eq. (7). The next steps were the calculation of similarity variable η from Eq. (5) and the calculation of nondimensional vertical velocity profile f' from Eq. (9). The $f'_{\max}$ was calculated from known values across the boundary layer. The $f''(0)$ was calculated from Eq. (11) and the $\varphi'(0)$ from Eq. (13). The derivatives $(\partial u/\partial y)_{y=0}$ and $(\partial T/\partial y)_{y=0}$ were calculated from the following equations:

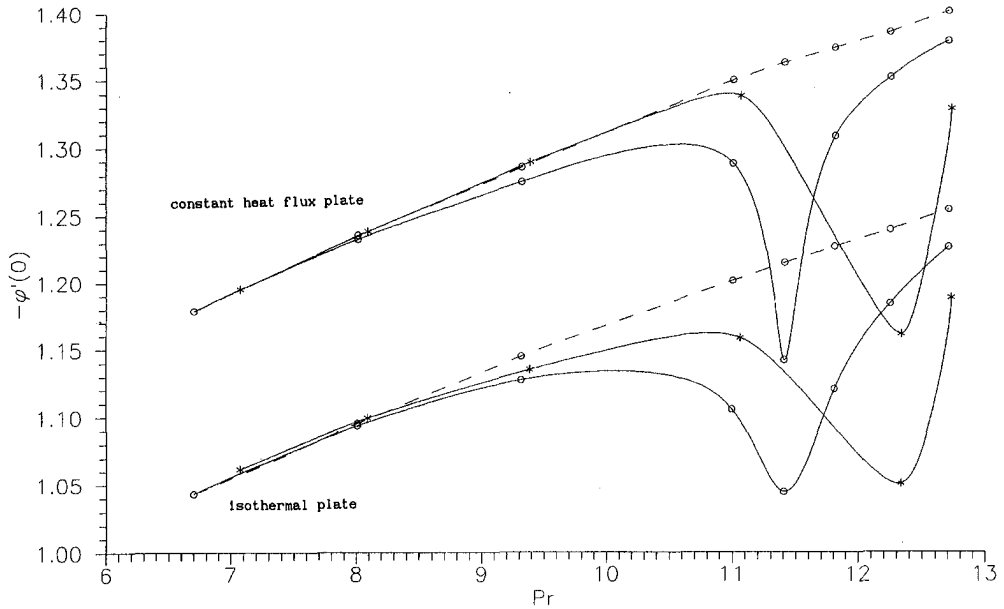

Fig. 1 Wall heat transfer as a function of the Prandtl number; ----, linear density-temperature relationship; —, real density-temperature relationship; ○, pure water; *, saline water (s = one percent)

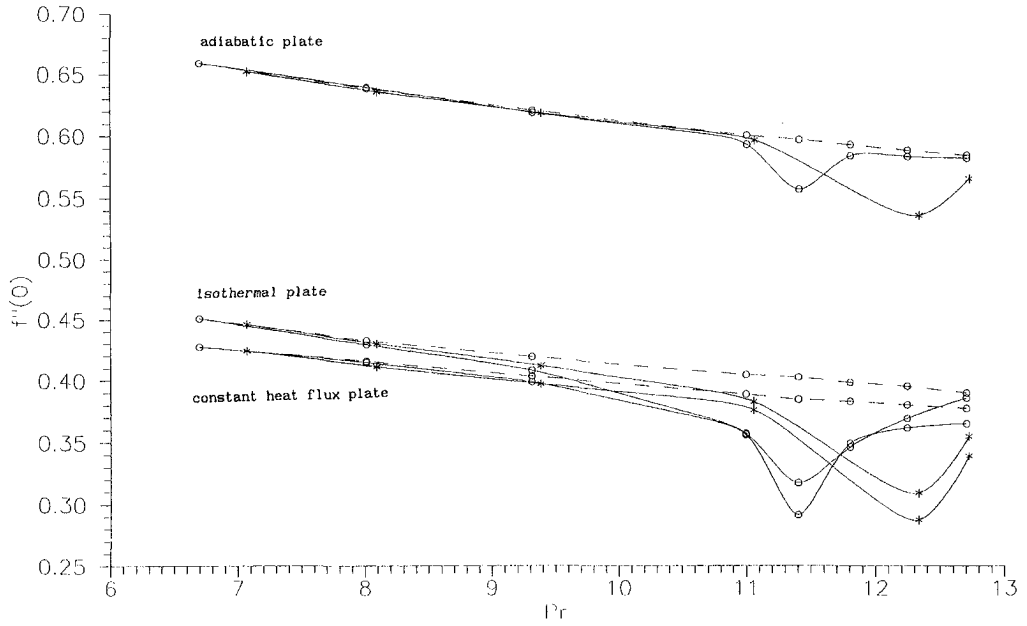

Fig. 2 Wall shear stress as a function of the Prandtl number: ----, linear density-temperature relationship; —, real density-temperature relationship; °, pure water; * saline water (*s* = ten percent)

$$\left(\frac{\partial u}{\partial y}\right)_{y=0} = \frac{u(2) - u(1)}{\Delta y} \tag{14}$$

$$\left(\frac{\partial T}{\partial y}\right)_{y=0} = \frac{T(2) - T(1)}{\Delta y} \tag{15}$$

where (1) is a grid point on the plate and (2) is an adjacent grid point along y. The calculated profiles f' and φ were not similar in the near-field region because the boundary layer approximation is not valid in this region but as the calculation procedure was promoted downwards similarity was reached. In order to test the accuracy of this method, the results were compared with results available in the literature. In the work of Gebhart (1985) a complete table is given with data concerning the transport quantities of free convection adjacent to vertical isothermal and adiabatic surfaces. This table was prepared by Krishnamurthy. For example, the quantities $-\varphi'(0)$, $f''(0)$, and $f'_{\max}$ for the isothermal case (Pr = 6.7) calculated in the present work were 1.0431, 0.4509, and 0.1334 and the corresponding results by Krishnamurthy were 1.0408, 0.4548, and 0.1335. The agreement is considered satisfactory and calculations were extended to temperature range between 20°C and 0°C. But does similarity exist in this range? The transformed momentum equation in similarity form is (Mollendorf, Johnson, and Gebhart, 1981)

$$f''' + \frac{c_x}{b} ff'' - \left(\frac{c_x}{b} + \frac{cb_x}{b^2}\right) f'^2 + \frac{g}{\nu^2 c b^3} \frac{\rho_a - \rho}{\rho_a} = 0 \tag{16}$$

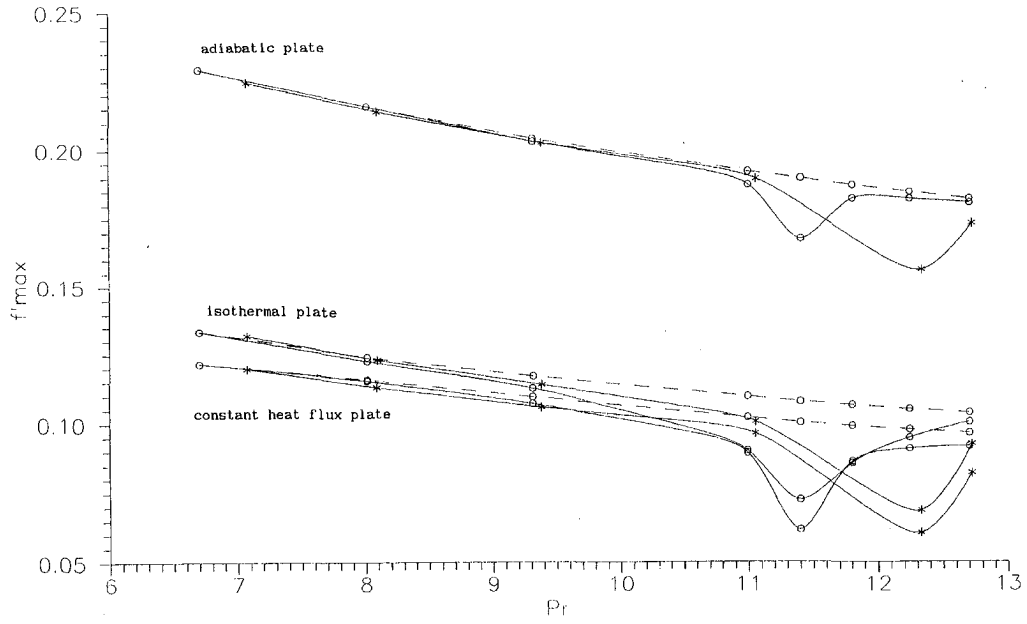

Fig. 3 Peak velocity as a function of the Prandtl number; ----, linear density-temperature relationship; —, real density-temperature relationship; °, pure water; * saline water (*s* = one percent)

where the subscript x indicates differentiation with respect to x and the primes derivatives with respect to η. Similarity requires that the coefficients and the buoyancy force in the above equation not be x-dependent. This is achieved when

$$b(x) = \frac{1}{4}\, c(x)/x \quad \text{and} \quad c(x) = 4\left(\frac{\mathrm{Gr}_x}{4}\right)^{1/4}. \tag{17}$$

Substituting the above b and c coefficients and the Grashof number from Eq. (7) into the buoyancy force gives

$$\frac{g}{\nu^2 c b^3}\,\frac{\rho_a - \rho}{\rho_a} = \frac{\rho_a - \rho}{\rho_a - \rho_o}. \tag{18}$$

In the classical similarity analysis with linear relationship between density and temperature the above buoyancy force takes the form

$$\frac{g}{\nu^2 c b^3}\,\frac{\rho_a - \rho}{\rho_a} = \frac{T - T_a}{T_o - T_a} \tag{19}$$

and is independent of x. The solution procedure used in the present work is equivalent to the classical similarity method except for the buoyancy force which is $(\rho_a - \rho)/(\rho_a - \rho_o)$ instead of $(T - T_a)/(T_o - T_a)$. The buoyancy force based on density is the real one and is independent of x not only in the linear range but in the entire temperature range. After that results were produced for the entire temperature range between 20°C and 0°C for pure water and saline water with s = one percent. The maximum density temperature for this salinity is 1.86°C.

The results are plotted in Figs. 1, 2, and 3. The wall heat transfer $-\varphi'(0)$, the wall shear stress $f''(0)$, and the peak velocity $f'_{\max}$ are shown as functions of Pr number for the three cases: isothermal, constant heat flux, and adiabatic plate. The above quantities that correspond to linear relationship between density and temperature for pure water are also shown in the figures (dashed lines). The corresponding quantities for the linear relationship and saline water are not shown because they are almost identical to those of pure water. Some very interesting conclusions can be drawn from these figures.

The wall heat transfer is greater in the uniform heat flux case than in the isothermal case. The wall heat transfer increases in a monotonic way as the Pr number increases when the density-temperature relationship is linear, but this trend changes dramatically when the water real density-temperature relationship is used. In the first region the heat transfer increases as the Pr number increases but as the ambient temperature decreases approaching the maximum density temperature the heat transfer decreases and reaches a minimum at maximum density temperature. Afterwards, when the ambient temperature decreases and the Pr number increases, the wall heat transfer increases approaching the linear density-temperature curve.

From Fig. 2 it is seen that the wall shear stress is much greater in adiabatic plate flow than that of isothermal and constant heat flux flow. The shear stress decreases in a monotonic way as the Pr number increases when the density-temperature relationship is linear. This trend changes when the water real density-temperature relationship is used. As the ambient water temperature decreases the wall shear stress decreases and reaches a minimum when the ambient temperature is equal to the density extremum temperature. Afterwards, when the ambient temperature decreases and the Pr number increases, the shear stress increases approaching the linear density-temperature curve. The results concerning the maximum velocity, which are shown in Fig. 3, are quite similar to that of wall shear stress.

References

Fofonoff, N. P., 1985, "Physical properties of seawater: A new salinity scale and equation of state for seawater," *Journal of Geophysical Research,* Vol. 90, No. C2, pp. 3332–3342.

Gebhart, B., and Mollendorf, J., 1978, "Buoyancy-induced flows in water under conditions in which density extrema may arise," *Journal of Fluid Mechanics,* Vol. 89, pp. 673–707.

Gebhart, B., Carey, V., and Mollendorf, J., 1979, "Buoyancy induced flows due to energy sources in cold quiescent pure and saline water," *Chemical Engineering Communications,* Vol. 3, pp. 555–575.

Gebhart, B., 1985, *Similarity solutions for laminar external boundary region flows, Natural Convection, Fundamentals and Applications,* Hemisphere Publishing Corporation, Washington, DC.

Goren, S. L., 1966, "On free convection in water at 4°C," *Chemical Engineering Science,* Vol. 21, pp. 515–518.

Jaluria, Y., and Gebhart, B., 1977, "Buoyancy-induced flow arising from a line thermal source on an adiabatic vertical surface," *Int. J. Heat Mass Transfer,* Vol. 20, pp. 153–157.

Jia, S. B., 1984, "Laminar jet issuing into stagnant surroundings," Computational Fluid Dynamics Unit, PDR/CFDU IC/15, Imperial College of Science and Technology, London.

Kukulka, D. J., Gebhart, B., and Mollendorf, J. C., 1987, "Thermodynamic and Transport Properties of Pure and Saline Water," *Advances in Heat Transfer,* Vol. 18, pp. 325–363.

Liburdy, J., and Faeth, G., 1975, "Theory of a steady laminar thermal plume along a vertical adiabatic wall," *Lett. Heat Mass Transfer,* Vol. 2, pp. 407–418.

Mollendorf, J. C., Johnson, R. S., and Gebhart, B., 1981, "Several plume flows in pure and saline water at its density extremum," *Journal of Fluid Mechanics,* Vol. 113, pp. 269–282.

Ostrach, S., 1953, "An analysis of laminar free convection flow and heat transfer about a flat plate parallel to the direction of the generating body force," NASA Tech. Rep. 1111.

Qureshi, Z., and Gebhart, B., 1978, "Vertical natural convection with the uniform flux condition in pure and saline water at the density extremum," *Proceedings, 6th International Heat Transfer Conf.,* Toronto.

Patankar, S. W., 1980, *Numerical Heat Transfer and Fluid Flow,* McGraw-Hill, New York.

Schuh, H., 1948, "Boundary layers of temperature," Section B.6 of W. Tollmien, *Boundary Layers,* British Ministry of Supply, German Document Center, Ref. 3220T.

Soundalgekar, V. M., 1973, "Laminar free convection flow of water at 4°C from a vertical plate with variable wall temperature," *Chemical Engineering Science,* Vol. 28, pp. 307–309.

Sparrow, E. M., and Gregg, J. L., 1956, "Laminar free convection from a vertical plate with uniform surface heat flux," *Trans. ASME,* Vol. 78.

UNESCO, 1981, "The Practical Salinity Scale 1978 and the International Equation of State of Seawater 1980," Tenth Report of the Joint Panel on Oceanographic Tables and Standards, UNESCO Technical Papers in Marine Science No. 36, UNESCO, Paris, France.

Vanier, C. R., and Tien, C., 1967, "Further work on free convection in water at 4°C," *Chemical Engineering Science,* Vol. 22, pp. 1747–1751.

Radiative Heat Transfer in Arbitrary Configurations With Nongray Absorbing, Emitting, and Anisotropic Scattering Media

S. Maruyama[1,2] and Z. Guo[3]

Introduction

Radiative heat transfer in absorbing, emitting, and scattering media is a problem of practical significance, e.g., in the design of industrial furnaces and many combustion devices, and in the prediction of the effect of ducts, CO_2 and other participating gases on the global environment. Recently, much attention has been given to solve the problem using numerical approaches such as the Monte Carlo method by Farmer and Howell (1994), the discrete ordinate method by Fiveland and Jessee (1995), and the YIX method by Hsu et al. (1992). A solution method that is reasonably accurate, efficient in both comput-

[1] Institute of Fluid Science, Tohoku University, Katahira 2-1-1, Aoba-ku, Sendai 980-8577, Japan.

[2] e-mail: maruyama@ifs.tohoku.ac.jp. Mem. ASME.

[3] Department of Mechanical, Aerospace and Manufacturing Engineering, Polytechnic University, 6 Metrotech Center, Brooklyn, NY 11201.

Contributed by the Heat Transfer Division for publication in the JOURNAL OF HEAT TRANSFER. Manuscript received by the Heat Transfer Division, Aug. 5, 1998; revision received, Jan. 5, 1999. Keywords: Heat Transfer, Numerical Methods, Participating Media, Radiation, View Factors. Associate Technical Editor: M. P. Menguc.

where the subscript x indicates differentiation with respect to x and the primes derivatives with respect to η. Similarity requires that the coefficients and the buoyancy force in the above equation not be x-dependent. This is achieved when

$$b(x) = \frac{1}{4}\, c(x)/x \quad \text{and} \quad c(x) = 4\left(\frac{\mathrm{Gr}_x}{4}\right)^{1/4}. \tag{17}$$

Substituting the above b and c coefficients and the Grashof number from Eq. (7) into the buoyancy force gives

$$\frac{g}{\nu^2 c b^3}\,\frac{\rho_a - \rho}{\rho_a} = \frac{\rho_a - \rho}{\rho_a - \rho_o}. \tag{18}$$

In the classical similarity analysis with linear relationship between density and temperature the above buoyancy force takes the form

$$\frac{g}{\nu^2 c b^3}\,\frac{\rho_a - \rho}{\rho_a} = \frac{T - T_a}{T_o - T_a} \tag{19}$$

and is independent of x. The solution procedure used in the present work is equivalent to the classical similarity method except for the buoyancy force which is $(\rho_a - \rho)/(\rho_a - \rho_o)$ instead of $(T - T_a)/(T_o - T_a)$. The buoyancy force based on density is the real one and is independent of x not only in the linear range but in the entire temperature range. After that results were produced for the entire temperature range between 20°C and 0°C for pure water and saline water with s = one percent. The maximum density temperature for this salinity is 1.86°C.

The results are plotted in Figs. 1, 2, and 3. The wall heat transfer $-\varphi'(0)$, the wall shear stress $f''(0)$, and the peak velocity $f'_{\max}$ are shown as functions of Pr number for the three cases: isothermal, constant heat flux, and adiabatic plate. The above quantities that correspond to linear relationship between density and temperature for pure water are also shown in the figures (dashed lines). The corresponding quantities for the linear relationship and saline water are not shown because they are almost identical to those of pure water. Some very interesting conclusions can be drawn from these figures.

The wall heat transfer is greater in the uniform heat flux case than in the isothermal case. The wall heat transfer increases in a monotonic way as the Pr number increases when the density-temperature relationship is linear, but this trend changes dramatically when the water real density-temperature relationship is used. In the first region the heat transfer increases as the Pr number increases but as the ambient temperature decreases approaching the maximum density temperature the heat transfer decreases and reaches a minimum at maximum density temperature. Afterwards, when the ambient temperature decreases and the Pr number increases, the wall heat transfer increases approaching the linear density-temperature curve.

From Fig. 2 it is seen that the wall shear stress is much greater in adiabatic plate flow than that of isothermal and constant heat flux flow. The shear stress decreases in a monotonic way as the Pr number increases when the density-temperature relationship is linear. This trend changes when the water real density-temperature relationship is used. As the ambient water temperature decreases the wall shear stress decreases and reaches a minimum when the ambient temperature is equal to the density extremum temperature. Afterwards, when the ambient temperature decreases and the Pr number increases, the shear stress increases approaching the linear density-temperature curve. The results concerning the maximum velocity, which are shown in Fig. 3, are quite similar to that of wall shear stress.

References

Fofonoff, N. P., 1985, "Physical properties of seawater: A new salinity scale and equation of state for seawater," *Journal of Geophysical Research,* Vol. 90, No. C2, pp. 3332–3342.

Gebhart, B., and Mollendorf, J., 1978, "Buoyancy-induced flows in water under conditions in which density extrema may arise," *Journal of Fluid Mechanics,* Vol. 89, pp. 673–707.

Gebhart, B., Carey, V., and Mollendorf, J., 1979, "Buoyancy induced flows due to energy sources in cold quiescent pure and saline water," *Chemical Engineering Communications,* Vol. 3, pp. 555–575.

Gebhart, B., 1985, *Similarity solutions for laminar external boundary region flows, Natural Convection, Fundamentals and Applications,* Hemisphere Publishing Corporation, Washington, DC.

Goren, S. L., 1966, "On free convection in water at 4°C," *Chemical Engineering Science,* Vol. 21, pp. 515–518.

Jaluria, Y., and Gebhart, B., 1977, "Buoyancy-induced flow arising from a line thermal source on an adiabatic vertical surface," *Int. J. Heat Mass Transfer,* Vol. 20, pp. 153–157.

Jia, S. B., 1984, "Laminar jet issuing into stagnant surroundings," Computational Fluid Dynamics Unit, PDR/CFDU IC/15, Imperial College of Science and Technology, London.

Kukulka, D. J., Gebhart, B., and Mollendorf, J. C., 1987, "Thermodynamic and Transport Properties of Pure and Saline Water," *Advances in Heat Transfer,* Vol. 18, pp. 325–363.

Liburdy, J., and Faeth, G., 1975, "Theory of a steady laminar thermal plume along a vertical adiabatic wall," *Lett. Heat Mass Transfer,* Vol. 2, pp. 407–418.

Mollendorf, J. C., Johnson, R. S., and Gebhart, B., 1981, "Several plume flows in pure and saline water at its density extremum," *Journal of Fluid Mechanics,* Vol. 113, pp. 269–282.

Ostrach, S., 1953, "An analysis of laminar free convection flow and heat transfer about a flat plate parallel to the direction of the generating body force," NASA Tech. Rep. 1111.

Qureshi, Z., and Gebhart, B., 1978, "Vertical natural convection with the uniform flux condition in pure and saline water at the density extremum," *Proceedings, 6th International Heat Transfer Conf.,* Toronto.

Patankar, S. W., 1980, *Numerical Heat Transfer and Fluid Flow,* McGraw-Hill, New York.

Schuh, H., 1948, "Boundary layers of temperature," Section B.6 of W. Tollmien, *Boundary Layers,* British Ministry of Supply, German Document Center, Ref. 3220T.

Soundalgekar, V. M., 1973, "Laminar free convection flow of water at 4°C from a vertical plate with variable wall temperature," *Chemical Engineering Science,* Vol. 28, pp. 307–309.

Sparrow, E. M., and Gregg, J. L., 1956, "Laminar free convection from a vertical plate with uniform surface heat flux," *Trans. ASME,* Vol. 78.

UNESCO, 1981, "The Practical Salinity Scale 1978 and the International Equation of State of Seawater 1980," Tenth Report of the Joint Panel on Oceanographic Tables and Standards, UNESCO Technical Papers in Marine Science No. 36, UNESCO, Paris, France.

Vanier, C. R., and Tien, C., 1967, "Further work on free convection in water at 4°C," *Chemical Engineering Science,* Vol. 22, pp. 1747–1751.

Radiative Heat Transfer in Arbitrary Configurations With Nongray Absorbing, Emitting, and Anisotropic Scattering Media

S. Maruyama[1,2] and Z. Guo[3]

Introduction

Radiative heat transfer in absorbing, emitting, and scattering media is a problem of practical significance, e.g., in the design of industrial furnaces and many combustion devices, and in the prediction of the effect of ducts, CO_2 and other participating gases on the global environment. Recently, much attention has been given to solve the problem using numerical approaches such as the Monte Carlo method by Farmer and Howell (1994), the discrete ordinate method by Fiveland and Jessee (1995), and the YIX method by Hsu et al. (1992). A solution method that is reasonably accurate, efficient in both comput-

[1] Institute of Fluid Science, Tohoku University, Katahira 2-1-1, Aoba-ku, Sendai 980-8577, Japan.

[2] e-mail: maruyama@ifs.tohoku.ac.jp. Mem. ASME.

[3] Department of Mechanical, Aerospace and Manufacturing Engineering, Polytechnic University, 6 Metrotech Center, Brooklyn, NY 11201.

Contributed by the Heat Transfer Division for publication in the JOURNAL OF HEAT TRANSFER. Manuscript received by the Heat Transfer Division, Aug. 5, 1998; revision received, Jan. 5, 1999. Keywords: Heat Transfer, Numerical Methods, Participating Media, Radiation, View Factors. Associate Technical Editor: M. P. Menguc.

ing time and storage, flexible with arbitrary three-dimensional geometry, and can be applied to real gas and particles is needed for the prediction of the radiation transport.

The radiation element method by the ray emission model, REM^2 (Maruyama and Aihara 1997), is an extension of the zone method and is a generalized numerical method for analyzing radiation transfer in participating media and specular and/or diffuse surfaces, with which arbitrary configurations can be coped with easily using finite element grids. This method has been applied to complex configurations such as a large helical device for the research of a fusion reactor (Maruyama and Higano 1997). An intrinsic weakness in REM^2 is the assumption of isotropic scattering, whereas scattering from most particles is anisotropic. A few numerical approaches such as the discrete ordinate method and the P_N method take into account anisotropic scattering. The REM^2 has been applied to one-dimensional anisotropic scattering media using zeroth-order delta function approximation (Maruyama, 1998). A very good agreement with the exact solution was found even for strong forward or backward scattering particles.

The gray assumption was also employed in previous studies. However, most of the radiation transfer problems in engineering are nongray in which participating gases, such as H_2O and CO_2, have very fine spectral absorption structures due to quantum effects. Hence, Beer's law cannot be applied to participating gases with moderate spectroscopic resolution. The REM^2 method assumes that temperature and radiative properties are uniform in each radiation element. The view factors are obtained by a ray tracing method in which path lengths in each radiation element can be specified. Therefore, all existing gas models are feasible in the present method to account the nongray characteristics of participating gas.

Accurate prediction of thermal radiation in a combustion chamber becomes a formidable task where the spectral absorption and anisotropic scattering characteristics of the medium are considered. Many investigators in the combustion field do not take the anisotropic scattering into account. The wide-band model is also widely employed for radiation in combustion gas, but it has not been compared with the narrow-band model in a realistic problem.

In this paper, the REM^2 is developed to incorporate the spectral dependence of radiation properties using the narrow band model and assuming anisotropic scattering. The zeroth-order delta function approximation is used to scale the anisotropic scattering. The radiative heat transfer within a complex three-dimensional boiler furnace is analyzed as an example of application of engineering interest. Both the Elsasser narrow band model and the exponential wide-band model are adopted to consider the spectral characteristics of CO_2 and H_2O gases. The results of heat flux on the walls and heat flux divergence in the boiler are compared between the analyses of the narrow-band model and the wide-band model. The effects of the anisotropic scattering and particle density are also discussed.

Method Description

The solution algorithm of REM^2 can be found in Maruyama and Aihara (1997), in which the gray assumption was employed. However, it is easy to extend the solution to nongray case when we introduce a spectral effective radation area $A^R_{i,\lambda}$ as

$$A^R_{i,\lambda} = \frac{1}{\pi}\int_{A_i(\hat{s})}\left[1-\exp\left(-\int_0^S \beta_{i,\lambda}dS'\right)\right]d\omega dA \approx \frac{1}{\pi}\int_{4\pi} A_i(\hat{s})\left[1-\exp\left(-\int_0^{\bar{S}} \beta_{i,\lambda}dS'\right)\right]d\omega \quad (1)$$

where $\bar{S}$ is the averaged thickness of the radiation element in the direction $\hat{s}$, $A(\hat{s})$ is the area projected onto the element surface normal to $\hat{s}$ and $\beta_{i,\lambda}$ is the extinction coefficient, respectively.

The Elsasser narrow band model is used in conjunction with the correlation parameters in Edwards wide-band model to determined the spectral absorption coefficients of CO_2 and H_2O as described by Tong and Skocypec (1992) in detail. Then the apparent extinction coefficient of the element in the direction $\hat{s}$ is reached as a function of the averaged path length as follows:

$$\beta_g = \ln\left[\int_{-\delta/2}^{\delta/2}\exp(-\kappa_\eta \bar{S})d\eta\right]. \quad (2)$$

The particles are assumed to be carbon spheres with a diameter of 30 μm. The values of scattering and extinction efficiencies are listed in Table 1 of Tong and Skocypec (1992). The scattering phase function was approximated by a delta-Eddington function as

$$\Phi(\Psi) = 2f\delta(1-\cos\theta) + (1-f)(1+3g\cos\theta) \quad (3)$$

where $f = 0.111$ and $g = 0.215$.

The phase function is scaled to the zeroth-order delta function approximation (Maruyama, 1998). The scaled extinction coefficient β^*_P and albedo Ω^D are

$$\beta^*_P = \beta_P(1-a_1\Omega/3), \quad \Omega^D = \frac{\Omega(1-a_1/3)}{1-a_1\Omega/3} \quad (4)$$

in which a_1 is a coefficient of the first term in Legendre polynomials. Maruyama (1998) examined the accuracy of the zeroth-order approximation in a one-dimensional system. The approximation has good accuracy with exact solution for the cases of a strong forward scattering medium and a backward scattering medium. A recent work by Guo and Maruyama (1998) compared the scaled isotropic results with the anisotropic calculations in three-dimensional nonhomogeneous media.

The final extinction coefficient of the mixture of particles and gases is expressed as

$$\beta = \sum_{k=1}^{N_g}\beta_{gk} + \beta^*_P \quad (5)$$

where β_{gk} is the apparent extinction coefficient of the kth gas, and N_g is the total number of gas components.

The radiation elements consisting of numerous polygons and polyhedrons modeled by arbitrary triangles, quadrilaterals, tetrahedrons, wedges, and hexahedrons, which are produced by applying the CAE software PATRAN, are used in the present method. As have been discussed by Maruyama and Aihara (1997), all the physical properties within each radiation element are assumed to be uniform. The view factors are calculated by the ray tracing method based on the ray emission model (Maruyama and Aihara, 1997).

The REM^2 method was compared with Monte Carlo method and YIX method in a benchmark problem (Hsu and Farmer, 1997) with gray nonhomogeneous participating medium. A general difference between the present method and the aforementioned methods was found to be within two percent (Guo and Maruyama, 1998). The present method is also compared with Monte Carlo method (Farmer and Howell, 1995) and YIX method (Hsu et al., 1992) in one and three-dimensional geometries containing a mixture of CO_2 and N_2 gases and carbon particles. Comparisons are performed with three carbon concentration levels of $Nc = 2.0\times10^7$, 2.0×10^8, and 2.0×10^9 particles per cubic meter, which represent participating media of optical thin, intermediate, and thick, respectively. The difference of predicted heat flux between the REM^2 and the Monte Carlo and YIX methods is three percent in the case of one-dimensional medium. For the three-dimensional medium, the differences of predicted heat flux and its divergence between the REM^2 and the Monte Carlo method are generally five percent, while ten percent differences of heat flux and its divergence are found between the present method and YIX method. The differences of heat flux and its divergence at the boundaries are usually within 20 percent between the REM^2 and the Monte Carlo and

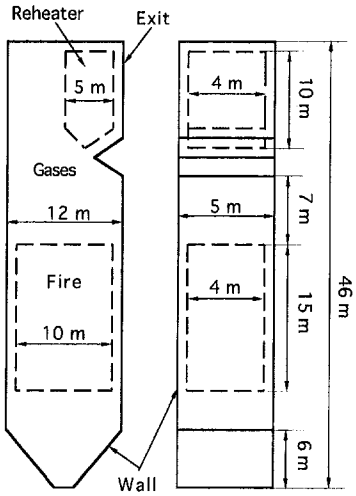

Fig. 1 Dimensions and arrangement of a boiler furnace

YIX methods. The values of radiative heat flux predicted by the present method are generally slightly lower than those predicted by Monte Carlo and YIX methods. A good agreement of predictions of heat flux and its divergence is found between the present solution and the Monte Carlo and YIX solutions for all three levels of particle density.

The computation efficiency is also of major concern in radiation transfer calculations of three-dimensional configurations. In the present computation of the aforementioned three-dimensional nongray problem, the number of spectral discretization was set to be 100 and the number of ray emission was set to be $Nr = 155$. When a personal computer VT-Alpha/533 is employed, the total CPU time including calculations of view factors and radiation transfer is about 240 seconds. It is also found that the CPU time decreases as the particle density increases.

The ray effect discussed by Chai et al. (1993) is a numerical error due to directional discretization of the RTE equation. As has been discussed by Maruyama and Aihara (1996), the ray effect is not serious for the case of a simple configuration. However, the effect is significant at the corner of a simple shape and for a complicated configuration.

Numerical error due to spatial discretization is of major interest to reduce the computational time. The aforementioned benchmark calculations of the three-dimensional nongray participating media have been carried out for several element numbers from 216 to 1331. These results agree with each other and show good agreement with the Monte Carlo result by Farmer and Howell (1994). The present method shows good agreement, even for the case of coarse spatial discretization. This trend has been shown in a previous report (Maruyama and Aihara, 1996) for gray media.

Results and Discussion

As an application of engineering interest, radiative heat transfer in a three-dimensional complex boiler furnace with CO_2, H_2O and carbon particles is considered. The furnace configuration is shown in Fig. 1. The boiler is modeled as that the temperature in the fire region is constant at 1896 K and the temperature in the gas region is constant at 1427 K. The total gas pressure in both gas and fire regions is uniform and constant at 1 atm. The mole fractions of CO_2 and H_2O are 0.126 and 0.113, respectively. The rest is N_2. This model is specified to adjust the example of a boiler furnace using heavy oil as a fuel in a handbook (JSME, 1993). The realistic model of a boiler has nonuniform temperature distribution. We have adopted the simple model to show the applicability of the present method to nongray calculation. The effect of nonuniform distribution has been discussed by Neghabat and Naragi (1998) and Guo and Maruyama (1998). The dimensions are decided to satisfy the specifications of the example problem. Hence, the dimensions are not realistic comparing with existing boilers for power plants. The same gas model as the benchmark analysis (Tong and Skocypec, 1992) is adopted, nevertheless the model exhibits inaccurate results, in particular, at low-temperature gases. The carbon particles are also taken into account in the fire region with uniform density, in which three different concentrations of $Nc = 2.0 \times 10^7$, 2.0×10^8 and 2.0×10^9 particles per cubic meter are selected for comparison. The reheater for super heating the steam is modeled by an opaque wall at a uniform temperature of 773 K. The wall-surface temperature in the combustion gas exit region is taken as 773 K, in which region another reheater is generally placed. The temperature in the rest wall surface is assumed to be 610 K. All the furnace wall surfaces are diffuse with emissivity of 0.8.

Figure 2 illustrates a half-symmetrical analysis model of the boiler furnace. The participating medium in Fig. 2 is divided into 453 polyhedrons as volume elements. The wall surface of the reheater is divided into 41 surface elements, while 323 surface elements are placed on the furnace surface. The number of total radiation elements in the half analysis model is 817. A totally specular reflecting wall was located on one surface in order to simulate the symmetry of the geometry. The number of ray emissions for each radiation element is set at $Nr = 155$ and the number of spectral discretization is set at 100. The calculations were performed on a VT-Alpha 533 personal computer.

First, the effect of anisotropic scattering of particles is investigated. The distributions of heat flux on the wall of the boiler and of the divergence of heat flux at the center plane of the boiler are illustrated in Figs. 3(*a*) and (*b*), respectively, for anisotropic scattering (left) and isotropic scattering (right) in the case of particle concentration of $Nc = 2.0 \times 10^9$. The heat flux and the divergence of heat flux in Figs. 3–5 are normalized by σT_0^4 and $\sigma T_0^4/W$, respectively, with $T_0 = 1896$ K and $W = 1$ m. The negative value of the heat flux depicts the heat flux from the participating media into the wall surface. As for the divergence of heat flux, a negative value means absorbing heat, while a positive value stands for heat generation. The larger the absolute value is, the larger is the heat flux or heat flux divergence. It is seen that larger heat flux is distributed in the wall surfaces near the fire region, while the heat flux on the surfaces in pure combustion gas and gas exit regions is very low. This reveals that the radiation from high-temperature particles is much stronger than that from high-temperature combustion gas. Comparing the results between anisotropic and isotropic scatterings in the particle region in Figs. 3(*a*) and (*b*), it was found that the heat flux as well as the divergence of heat flux increased when the anisotropic property was accounted for. This is because the transmitted radiation is increased for a strong forward anisotropic scattering medium compared with the assumption of isotropic scattering, while the emission coefficient does not

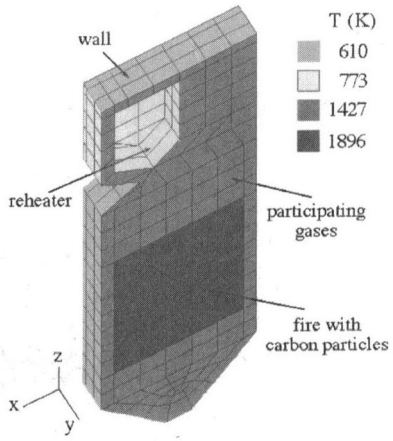

Fig. 2 Half symmetrical radiation element analysis model of the boiler furnace

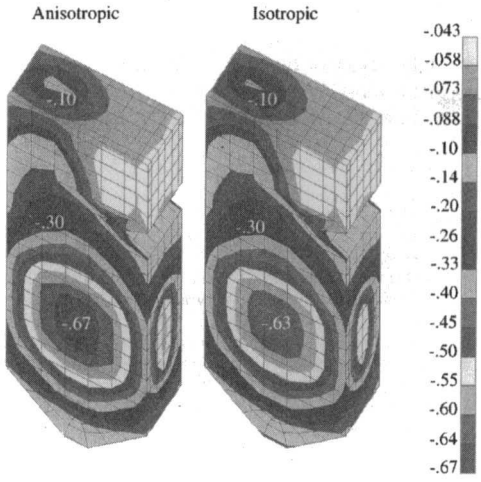

(a) Normalized heat flux.

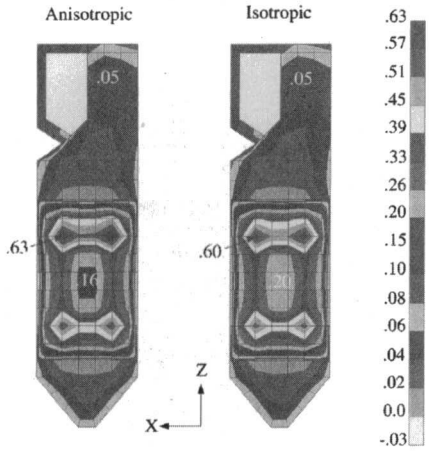

(b) Normalized heat flux divergence at center plane.

Fig. 3 Comparisons of normalized radiative heat flux (*a*) and its divergence (*b*) between anisotropic scattering and isotropic scattering in the case of $Nc = 2.0 \times 10^9$ and the adoption of Elsasser narrow band model

change. The radiation transfer is enhanced. The difference in the results between the anisotropic and isotropic scatterings is generally 15 percent. There are some locations where the difference is about 30 percent.

The comparison of numerical results of heat flux and heat flux divergence between narrow-band and wide-band gas models is demonstrated in Fig. 4 in the case of $Nc = 2.0 \times 10^7$ with anisotropic scattering. It is seen that the gas model influences the results of numerical prediction. The predicted results by a wide-band model are generally larger than those by a narrow-band model. Comparing two different models, the differences in heat flux are approximately ten percent, while the differences in the divergence of heat flux increase to 20 percent with 40 percent detected in some areas near the boundary.

Finally, the comparison is extended to solutions with anisotropic scattering and narrow-band models and with isotropic scattering and wide-band models. Figure 5 portrays the comparisons of heat flux on the wall and heat flux divergence in the center plane for particle density $Nc = 2.0 \times 10^8$. The wide-band model tends to increase the prediction of heat flux and its divergence, on the other hand, the effect of isotropic scattering is reversed. Hence, the differences between the two solutions in Fig. 10 are not so large as observed in Figs. 3 and 4. In general, ten percent difference in heat flux and divergence of heat flux is found. However, there are some cases where the difference in heat flux divergence reaches 30 percent. Comparing Figs. 3, 4, and 5, the influence of particle density is revealed. The heat flux as well as the divergence of heat flux increases as the particle density increases. However, the influence is mainly focused on the fire region and the wall surface near the fire. In the pure combustion gas regions, such as in the reheater and gas exit area, the distributions of heat flux and its divergence were slightly influenced by the particle radiation.

Inspecting the flux divergence distribution in the fire region in Figs. 3(*b*), 4(*b*), and 5(*b*), it is observed that the flux divergence values are smallest in the middle of the fire and largest near the surroundings. This trend is due to the specification that the high-temperature fire is surrounded by low-temperature combustion gas. The fire medium adjacent to the cold surrounding gives up more of its heat than that in the interior. The corners of the fire exhibit even higher divergence values, as there are more cold surrounding areas to heat. However, the surface heat flux near the corners is reduced as shown in Figs. 3(*a*), 4(*a*), and 5(*a*). This is because there is less media able to radiate heat to the corner area.

In the above calculations of boiler furnace, the total CPU time including the calculation of view factors is approximately 45 minutes on VT-Alpha/533 when the Elsasser narrow-band model is adopted, while about 40 minutes is needed if only the exponential wide-band model is employed (the number of band divisions, i.e., 100 discretization, is the same as in Elsasser model). The difference of CPU times between the anisotropic scattering and isotropic scattering is negligible. The CPU time increases as the ray emission number increases. For example, when increasing the ray emission number from $Nr = 155$ to $Nr = 561$ in the boiler, the total CPU time will increase to

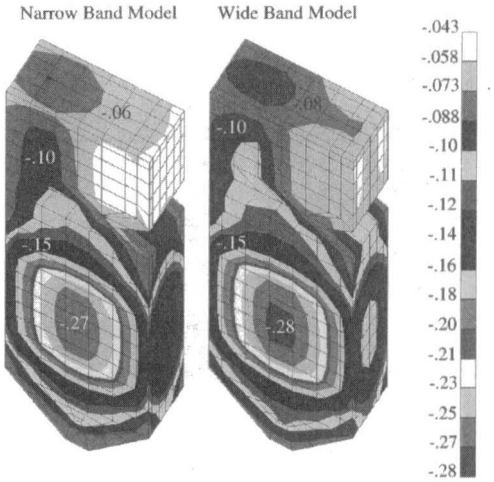

(a) Normalized heat flux.

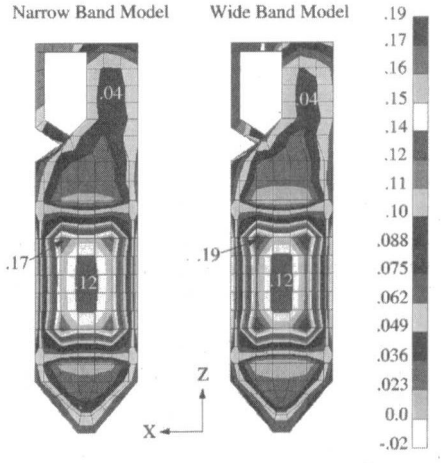

(b) Normalized heat flux divergence at center plane.

Fig. 4 Comparisons of normalized radiative heat flux (*a*) and its divergence (*b*) between different gas models in the case of $Nc = 2.0 \times 10^7$ and the consideration of anisotropic scattering

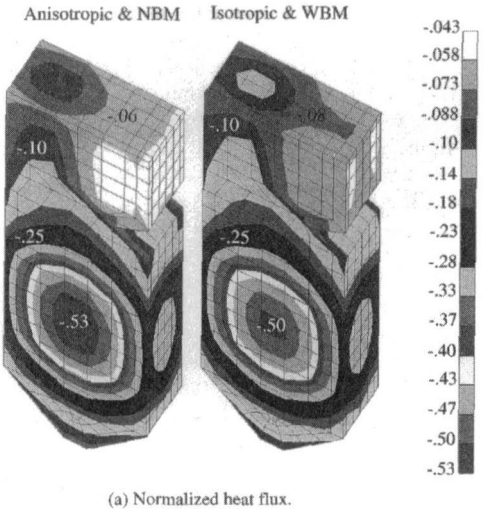

(a) Normalized heat flux.

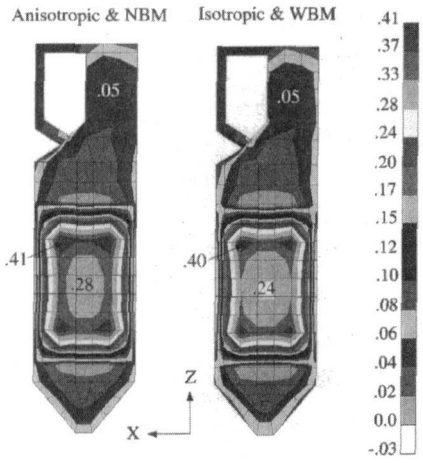

(b) Normalized heat flux divergence at center plane.

Fig. 5 Comparisons of normalized radiative heat flux (*a*) and its divergence (*b*) between the solution of narrow band model and anisotropic scattering and that of wide band model and isotropic scattering in the case of $Nc = 2.0 \times 10^8$

about 60 minutes due to the increase of CPU time in the calculation of view factors. However, the differences of predicted heat flux and its divergence between $Nr = 155$ and $Nr = 561$ are within five percent. Thus, a reasonable accuracy and small CPU time can be achieved for a small number of ray emissions. Numerical simulation for coarser spatial discretization has been carried out for the case of 510 radiation elements. Similar results compared with the case of 817 elements are obtained.

Conclusions

The REM^2 method has been applied to investigate radiative heat transfer in a boiler furnace with nongray combustion gas mixture and anisotropic scattering carbon particles. The distributions of heat flux and its divergence were obtained when the temperature was specified. Emphasis was placed on the examination of the influences of different gas models and scattering characteristics. The use of a purely wide-band model increases the heat flux and divergence of heat flux by a range of 10 to 40 percent compared with the results employed by the Elsasser narrow-band model. The assumption of isotropic scattering decreases the predictions of heat flux and its divergence by 10 to 30 percent of the anisotropic scattering. This tendency is consistent with the findings of Mengüc and Viskanta (1987) for the case of a pulverized coal-fired furnace, while the conditions are different from each other. It was found that larger heat flux exists in the wall surface near the fire. The influence of the particle density in this region is very important. As the particle density increases, the radiative heat flux and the divergence of heat flux increases. However, in the reheater and gas exit regions, little effect of direct radiation from the particle region was found, and most of the radiation comes from the high-temperature gas mixture.

References

Chai, J. C., Lee, H. S., and Patankar, S. V., 1993, "Ray Effect and False Scattering in the Disrete Ordinates Method," *Numerical Heat Transfer, Part B,* Vol. 24, pp. 373–389.

Farmer, J. T., and Howell, J. R., 1994, "Monte Carlo Prediction of Radiative Heat Transfer in Inhomogeneous, Anisotropic, Nongray Media," *J. Thermophysics Heat Transfer,* Vol. 8, pp. 133–139.

Fiveland, W. A., and Jessee, J. P., 1995, "Comparison of Discrete-Ordinate Method for Multidimensional Geometries," *J. Thermophysics Heat Transfer,* Vol. 8, pp. 426–433.

Guo, Z., and Maruyama, S., 1998, "Scaling Anisotropic Scattering in Radiative Transfer in Three-Dimensional Nonhomogeneous Media," *Int. Commun. Heat Mass Transfer,* submitted for publication.

Hsu, P.-F., and Farmer, J. T., 1997, "Benchmark Solution of Radiative Heat Transfer Within Nonhomogeneous Participating Media Using the Monte Carlo and YIX method," ASME JOURNAL OF HEAT TRANSFER, Vol. 119, pp. 185–188.

Hsu, P.-F., Tan, Z., and Howell, J. R., 1992, "Application of the YIX Method to Radiative Heat Transfer Within a Mixture of Highly Anisotropic Scattering Particles and Non-Gray Gas," *Developments in Radiative Heat Transfer,* ASME HTD-Vol. 203, pp. 285–300.

JSME, 1993, *JSME Heat Transfer Hand Book,* pp. 276–285.

Maruyama, S., and Aihara, T., 1996, "Radiative Heat Transfer of Arbitrary 3-D Participating Media and Surfaces With Non-Participating Media by a Generalized Numerical Method REM^2," *Radiative Transfer—I, Proc. the 1st Int. Symp. on Radiative Heat Transfer,* M. P. Mengue, ed., August, Kusadasi, Turkey, Begell House, New York, pp. 153–167.

Maruyama, S., and Aihara, T., 1997, "Radiation Heat Transfer Between Arbitrary Three-Dimensional Absorbing, Emitting and Scattering Media and Specular and Diffuse Surfaces," ASME JOURNAL OF HEAT TRANSFER, Vol. 119, pp. 129–136.

Maruyama, S., and Higano, M., 1997, "Radiative Heat Transfer of Torus Plasma in Large Helical Device by Generalized Numerical Method REM^2," *Energy Conversion and Management,* Vol. 38, pp. 1187–1195.

Maruyama, S., 1998, "Radiation Heat Transfer in Anisotropic Scattering Media With Specular Boundary Subjected to Collimated Irradiation," *Int. J. Heat Mass Transfer,* Vol. 41, pp. 2847–2856.

Mengüc, M. P., and Viskanta, R., 1987, "A Sensitivity Analysis for Radiative Heat Transfer in a Pulverized Coal-Fired Furnace," *Combustion Sci. & Tech.,* Vol. 51, pp. 51–74.

Neghabat, A., and Naraghi, M. H. N., 1998, "Analysis of Radiative Heat Transfer in Three-Dimensional Nonhomogeneous, Nongray, and Anisotropic Scattering Media," *Heat Transfer 1998, Proc. of 11th IHTC,* Vol. 7, Kyongju, Korea, Aug., pp. 415–420.

Tong, T. W., and Skocypec, R. D., 1992, "Summary on Comparison of Radiative Heat Transfer Solutions for a Specified Problem," *Developments in Radiative Heat Transfer,* ASME HTD-Vol. 203, ASME, New York, pp. 253–258.

Turbulence-Radiation Interactions in Nonreactive Flow of Combustion Gases

S. Mazumder[1,3] and M. F. Modest[1,2]

Nomenclature

B = width of bluff body (Fig. 1)
D = width of central injection duct (Fig. 1)
I_η = spectral radiative intensity
$I_{b\eta}$ = Planck function
s = position

[1] Department of Mechanical Engineering, The Pennsylvania State University, University Park, PA 16802.

[2] Fellow ASME.

[3] Presently at CFD Research Corporation, Huntsville, AL.

Contributed by the Heat Transfer Division for publication in the JOURNAL OF HEAT TRANSFER. Manuscript received by the Heat Transfer Division, Aug. 15, 1998; revision received, Jan. 20, 1999. Keywords: Channel Flow, Heat Transfer, Monte Carlo, Radiation, Turbulence. Associate Technical Editor: P. Menguc.

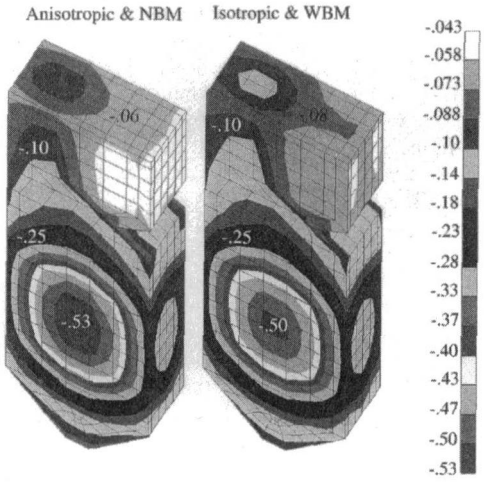

(a) Normalized heat flux.

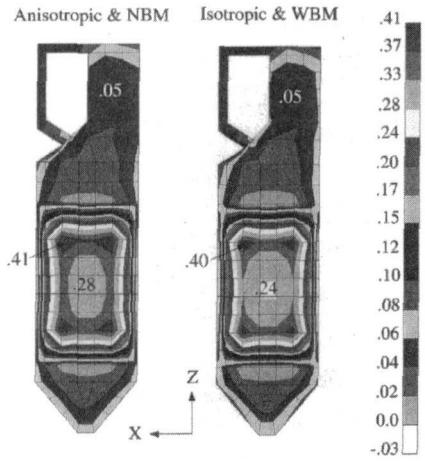

(b) Normalized heat flux divergence at center plane.

Fig. 5 Comparisons of normalized radiative heat flux (*a*) and its divergence (*b*) between the solution of narrow band model and anisotropic scattering and that of wide band model and isotropic scattering in the case of $Nc = 2.0 \times 10^8$

about 60 minutes due to the increase of CPU time in the calculation of view factors. However, the differences of predicted heat flux and its divergence between $Nr = 155$ and $Nr = 561$ are within five percent. Thus, a reasonable accuracy and small CPU time can be achieved for a small number of ray emissions. Numerical simulation for coarser spatial discretization has been carried out for the case of 510 radiation elements. Similar results compared with the case of 817 elements are obtained.

Conclusions

The REM^2 method has been applied to investigate radiative heat transfer in a boiler furnace with nongray combustion gas mixture and anisotropic scattering carbon particles. The distributions of heat flux and its divergence were obtained when the temperature was specified. Emphasis was placed on the examination of the influences of different gas models and scattering characteristics. The use of a purely wide-band model increases the heat flux and divergence of heat flux by a range of 10 to 40 percent compared with the results employed by the Elsasser narrow-band model. The assumption of isotropic scattering decreases the predictions of heat flux and its divergence by 10 to 30 percent of the anisotropic scattering. This tendency is consistent with the findings of Mengüc and Viskanta (1987) for the case of a pulverized coal-fired furnace, while the conditions are different from each other. It was found that larger heat flux exists in the wall surface near the fire. The influence of the particle density in this region is very important. As the particle density increases, the radiative heat flux and the divergence of heat flux increases. However, in the reheater and gas exit regions, little effect of direct radiation from the particle region was found, and most of the radiation comes from the high-temperature gas mixture.

References

Chai, J. C., Lee, H. S., and Patankar, S. V., 1993, "Ray Effect and False Scattering in the Disrete Ordinates Method," *Numerical Heat Transfer, Part B,* Vol. 24, pp. 373–389.

Farmer, J. T., and Howell, J. R., 1994, "Monte Carlo Prediction of Radiative Heat Transfer in Inhomogeneous, Anisotropic, Nongray Media," *J. Thermophysics Heat Transfer,* Vol. 8, pp. 133–139.

Fiveland, W. A., and Jessee, J. P., 1995, "Comparison of Discrete-Ordinate Method for Multidimensional Geometries," *J. Thermophysics Heat Transfer,* Vol. 8, pp. 426–433.

Guo, Z., and Maruyama, S., 1998, "Scaling Anisotropic Scattering in Radiative Transfer in Three-Dimensional Nonhomogeneous Media," *Int. Commun. Heat Mass Transfer,* submitted for publication.

Hsu, P.-F., and Farmer, J. T., 1997, "Benchmark Solution of Radiative Heat Transfer Within Nonhomogeneous Participating Media Using the Monte Carlo and YIX method," ASME JOURNAL OF HEAT TRANSFER, Vol. 119, pp. 185–188.

Hsu, P.-F., Tan, Z., and Howell, J. R., 1992, "Application of the YIX Method to Radiative Heat Transfer Within a Mixture of Highly Anisotropic Scattering Particles and Non-Gray Gas," *Developments in Radiative Heat Transfer,* ASME HTD-Vol. 203, pp. 285–300.

JSME, 1993, *JSME Heat Transfer Hand Book,* pp. 276–285.

Maruyama, S., and Aihara, T., 1996, "Radiative Heat Transfer of Arbitrary 3-D Participating Media and Surfaces With Non-Participating Media by a Generalized Numerical Method REM^2," *Radiative Transfer—I, Proc. the 1st Int. Symp. on Radiative Heat Transfer,* M. P. Mengue, ed., August, Kusadasi, Turkey, Begell House, New York, pp. 153–167.

Maruyama, S., and Aihara, T., 1997, "Radiation Heat Transfer Between Arbitrary Three-Dimensional Absorbing, Emitting and Scattering Media and Specular and Diffuse Surfaces," ASME JOURNAL OF HEAT TRANSFER, Vol. 119, pp. 129–136.

Maruyama, S., and Higano, M., 1997, "Radiative Heat Transfer of Torus Plasma in Large Helical Device by Generalized Numerical Method REM^2," *Energy Conversion and Management,* Vol. 38, pp. 1187–1195.

Maruyama, S., 1998, "Radiation Heat Transfer in Anisotropic Scattering Media With Specular Boundary Subjected to Collimated Irradiation," *Int. J. Heat Mass Transfer,* Vol. 41, pp. 2847–2856.

Mengüc, M. P., and Viskanta, R., 1987, "A Sensitivity Analysis for Radiative Heat Transfer in a Pulverized Coal-Fired Furnace," *Combustion Sci. & Tech.,* Vol. 51, pp. 51–74.

Neghabat, A., and Naraghi, M. H. N., 1998, "Analysis of Radiative Heat Transfer in Three-Dimensional Nonhomogeneous, Nongray, and Anisotropic Scattering Media," *Heat Transfer 1998, Proc. of 11th IHTC,* Vol. 7, Kyongju, Korea, Aug., pp. 415–420.

Tong, T. W., and Skocypec, R. D., 1992, "Summary on Comparison of Radiative Heat Transfer Solutions for a Specified Problem," *Developments in Radiative Heat Transfer,* ASME HTD-Vol. 203, ASME, New York, pp. 253–258.

Turbulence-Radiation Interactions in Nonreactive Flow of Combustion Gases

S. Mazumder[1,3] and M. F. Modest[1,2]

Nomenclature

B = width of bluff body (Fig. 1)
D = width of central injection duct (Fig. 1)
I_η = spectral radiative intensity
$I_{b\eta}$ = Planck function
s = position

[1] Department of Mechanical Engineering, The Pennsylvania State University, University Park, PA 16802.

[2] Fellow ASME.

[3] Presently at CFD Research Corporation, Huntsville, AL.

Contributed by the Heat Transfer Division for publication in the JOURNAL OF HEAT TRANSFER. Manuscript received by the Heat Transfer Division, Aug. 15, 1998; revision received, Jan. 20, 1999. Keywords: Channel Flow, Heat Transfer, Monte Carlo, Radiation, Turbulence. Associate Technical Editor: P. Menguc.

$\hat{s}$ = unit vector along a line of sight
T = temperature
Y_α = mass-fraction of αth species

Greek

η = wave number
κ_η = spectral absorption coefficient

Introduction

A nonreactive hot mixture of radiatively participating species, typically carbon dioxide and water vapor, may be found in the exhaust sections of almost all combustors. Since the scalar fluctuations in such nonreactive flows are substantially smaller than in flames, it is commonly believed that the effects of turbulence-radiation interactions (TRI) on altering wall heat fluxes in nonreactive flows are negligible. Such belief, however, has not been substantiated by evidence to date. The purpose of this note is to investigate the conditions under which TRI may be important in nonreactive flows. The final outcome was found to be largely dependent on how the scalar fluctuations correlate, rather than the magnitude of the fluctuations themselves. It was found that for most situations of practical interest, TRI effects are indeed negligible.

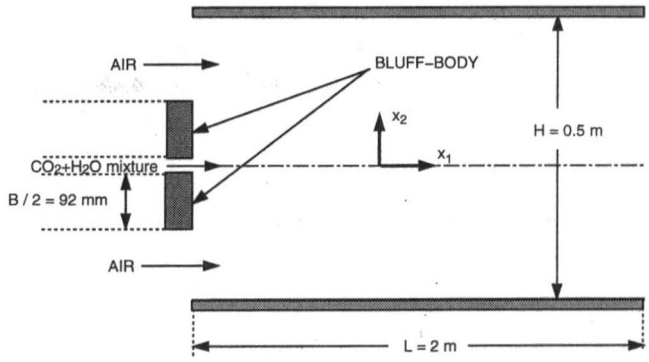

Fig. 1 Geometry used for sample calculations

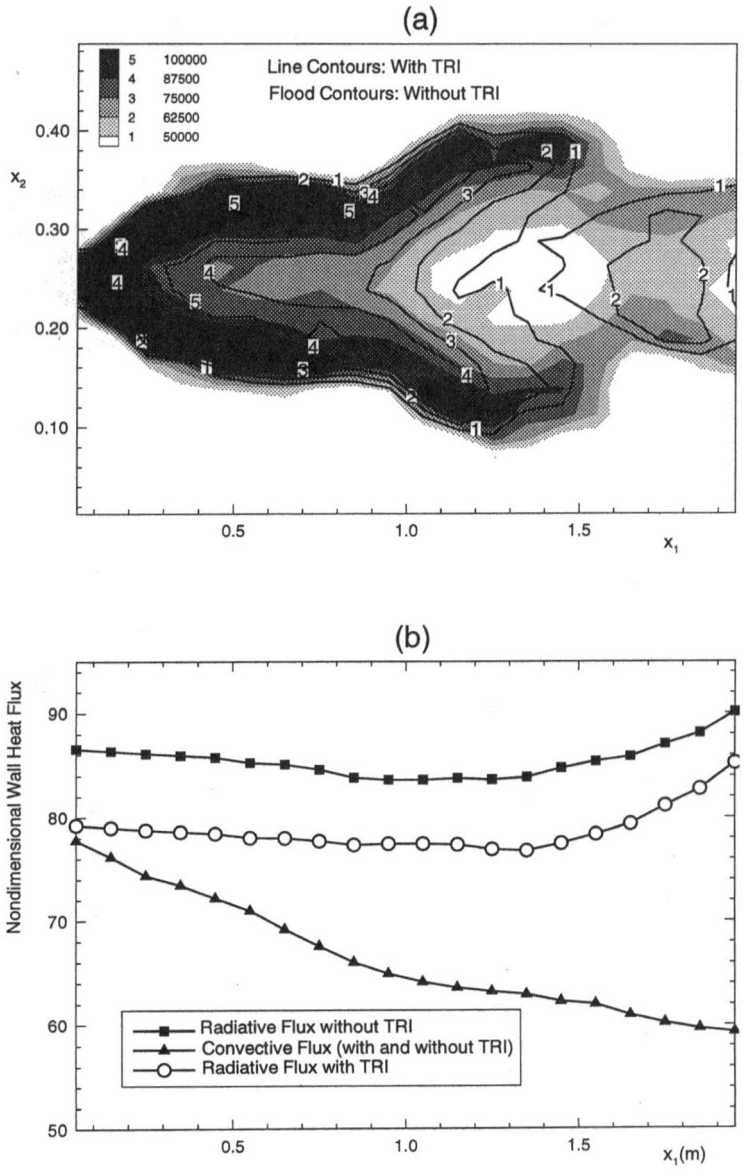

Fig. 2 Effect of TRI on (*a*) divergence of the radiative heat flux (in W/m^3), and (*b*) wall heat flux for the case when the inlet coflowing air temperature is 200 K higher than the inlet temperature of the CO_2–H_2O mixture

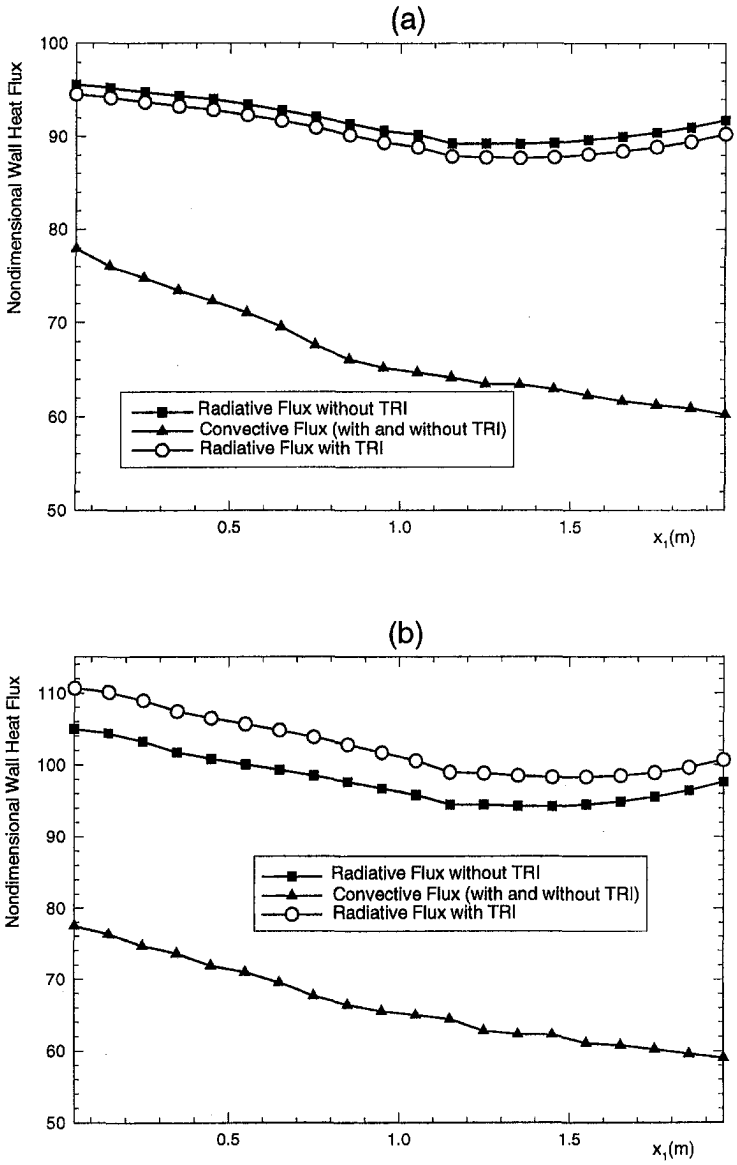

Fig. 3 Effect of TRI on wall heat fluxes for (*a*) equal inlet temperatures for CO_2–H_2O mixture and coflowing air, and (*b*) inlet CO_2–H_2O misture temperature 200 K higher than coflowing air inlet temperature

Theory

The absorption coefficient of a mixture of gases is a function of its temperature and composition (Modest, 1993). In a turbulent flow, the fluctuations in the scalar field cause the absorption coefficient to fluctuate, as well. These fluctuations may correlate with the fluctuations in the Planck function (which is a function of temperature) to result in so-called turbulence-radiation interactions (TRI).

The spectral radiative transfer equation for an absorbing-emitting medium is (Modest, 1993)

$$\frac{\partial I_\eta}{\partial s} = \kappa_\eta (I_{b\eta} - I_\eta) \tag{1}$$

where I_η is the spectral radiative intensity, $I_{b\eta}$ is the Planck function, κ_η is the spectral absorption coefficient, and η is the wave number. Scattering may be important when large soot agglomerates are present. Soot, however, is locally produced and destroyed within the flame itself, and hardly any soot is liable to be present in the exhaust section of a well-designed combustor and, therefore, scattering may be considered negligible.

Decomposition of I_η, $I_{b\eta}$, and κ_η into their mean and fluctuating parts, substitution into Eq. (1), and averaging, results in

$$\frac{\partial \langle I_\eta \rangle}{\partial s} = \langle \kappa_\eta \rangle \langle I_{b\eta} \rangle - \langle \kappa_\eta \rangle \langle I_\eta \rangle + \langle \kappa'_\eta I'_{b\eta} \rangle - \langle \kappa'_\eta I'_\eta \rangle, \tag{2}$$

where quantities within angled brackets represent averages, and quantities with primes denote fluctuations. The last two terms in Eq. (2) are a result of TRI. The correlation, $\langle \kappa'_\eta I'_\eta \rangle$, is generally negligible since the fluctuations in the absorption coefficient and the spectral radiative intensity act at completely different scales, except in an optically thick medium. Arguments to this effect have been provided in the past by Kabashnikov and co-workers (1985a, b) and by Song and Viskanta (1987).

In this work, the unknown correlation $\langle \kappa'_\eta I'_{b\eta} \rangle$, required for closure of the radiative transfer equation, was modeled using the velocity-composition joint probability density function (PDF) approach (Pope, 1985). Detailed descriptions on the modeling and solution procedure can be found in Mazumder (1997) and in Mazumder and Modest (1999).

Performing Taylor series expansions of κ_η and $I_{b\eta}$ about their mean values, it can be shown that, in general,

$$\langle \kappa'_\eta I'_{b\eta} \rangle = f(\langle T'^2 \rangle, \langle \underline{Y}' T' \rangle, \text{ higher order terms}), \quad (3)$$

where $\underline{Y}$ is a set consisting of all the species mass fractions. Of the two second-order correlations appearing in Eq. (3), the correlation $\langle \underline{Y}' T' \rangle$ is responsible for determining whether $\langle \kappa'_\eta I'_{b\eta} \rangle$ is positive or negative, since $\langle T'^2 \rangle$ is always positive. If $\langle \kappa'_\eta I'_{b\eta} \rangle$ is positive, the intensity of radiation along a line of sight will be enhanced (cf. Eq. (2)), and if $\langle \kappa'_\eta I'_{b\eta} \rangle$ is negative, the intensity will be attenuated. In other words, the role of TRI essentially reduces to how the concentration fluctuations correlate with the temperature fluctuations in the medium. In flames, this correlation is always positive because local production of CO_2 or H_2O is always accompanied by production of heat (or an increase in local temperature). For nonreactive flows, this is not the case, and the matter requires further investigation.

Sample Calculations

The geometry used for the sample calculations is shown in Fig. 1, and is two-dimensional planar. A mixture of carbon dioxide and water vapor (equal by mass) was injected along the centerline, as shown, at a temperature of 1000K and a velocity of 16.41 m/s. The coflowing air has a temperature of 1200K and a velocity of 10 m/s. The Reynolds number based on the inlet air properties and the bluff body size is 13,304. The wake behind the bluff body promotes intense mixing by recirculation.

In order to isolate the effect of TRI, the case described above was run with radiation but without TRI, and a restart file was stored after 460 ms. The divergences of the radiative heat flux and the wall heat fluxes were calculated and stored. The TRI terms were then turned on and the simulation was allowed to march forward for a single time-step of one nanosecond. The divergences and wall heat loads were recalculated. Figure 2 illustrates the divergences and wall heat fluxes with and without TRI. The exact opposite effect of what was observed for reactive flows in Mazumder and Modest (1999) is observed here. Figure 2(*a*) shows that the regions of strong emission contract to some extent when TRI is included. Consequently, the radiative wall heat fluxes decrease by approximately ten percent when TRI is included (Fig. 2(*b*)), although the relative change is much smaller than what was observed for a flame, where an increase of about 45 percent was noted (Mazumder and Modest, 1999). The smaller change was expected since it is well known that the fluctuations in a flame are significantly larger than in an inert flow. All of the above observations suggest that $\langle \kappa'_\lambda E'_{b\lambda} \rangle$ is negative in this case, which was indeed observed to be true when this term was printed out.

The negative magnitude of the correlation $\langle \kappa'_\lambda E'_{b\lambda} \rangle$ can be explained physically by examining a situation where pure carbon dioxide flows into still air. A blob of CO_2, as soon as it is exposed to the air, captures some oxygen and nitrogen, and loses some CO_2 to the surrounding air due to mixing. Consequently, the CO_2 concentration in the blob decreases. In the absence of turbulence this exchange takes place by molecular diffusion only, and is extremely slow. In the presence of turbulence the mixing proceeds at a rate governed by the local turbulent time scale, and is usually quite rapid. The important issue at this point is whether the temperature of the blob increases or decreases during this mixing process. This, of course, is governed by the relative temperature difference between the CO_2 stream and the surrounding air. If the CO_2 stream is colder than the surrounding air, which is the case here, the temperature of the blob will increase. The reverse is true if an air blob is considered, i.e., a positive concentration fluctuation will be associated with a negative temperature fluctuation. The net effect of these associations result in correlations such as $\langle Y'_i T' \rangle$ being negative if the surrounding or coflowing air is hotter than the species jet. By the same token, the correlation is expected to be almost zero or randomly behaving if the temperature of the two streams are equal, and positive if the CO_2–H_2O mixture stream is hotter than the coflowing air stream. To investigate this matter, two more simulations were performed. In the first case, the two inlet temperatures were maintained equal, and in the second case, the CO_2–H_2O mixture was injected at a temperature 200K hotter than the air injection temperature. The heat fluxes for these two cases are illustrated in Fig. 3. For the case with equal inlet temperatures of the two streams, as expected, the difference in the radiative flux with and without TRI is extremely small, and may be attributed to numerical uncertainty. When the temperature of the CO_2–H_2O mixture stream is higher than the temperature of the coflowing air, TRI plays the role of increasing the radiative wall heat flux, and thus lending strong support to the above physical explanation.

In most practical situations, the exhaust gas from a combustor is a mixture of all the different species, and all species are at the same temperature, rather than existing as separate streams with different temperatures. Therefore, it is reasonable to conclude that the effect of TRI in nonreactive flows is only marginal and may be neglected to simplify the analysis.

Conclusions

The effect of turbulence-radiation interactions in nonreactive flow of combustion gases was investigated numerically. The role of TRI largely depends on how the temperature fluctuations correlate with the concentration fluctuations. In most cases of practical interest, the fluctuations were found to be uncorrelated, resulting in almost negligible effect of TRI on the wall heat loads.

Acknowledgment

This research was supported in part by the Applied Research Laboratory at Penn State.

References

Kabashnikov, V. P., and Myasnikova, G. I., 1985a, "Thermal Radiation in Turbulent Flows—Temperature and Concentration Fluctuations," *Heat Transfer–Soviet Research,* Vol. 17, No. 6, pp. 116–125.

Kabashnikov, V. P., 1985b, "Thermal Radiation in Turbulent Flows—In the Case of Large Fluctuations of the Absorption Coefficient and the Planck Function," *Journal of Engineering Physics,* Vol. 49, No. 1, pp. 778–784.

Mazumder, S., 1997, "Numerical Study of Chemically Reactive Turbulent Flows with Radiative Heat Transfer," Ph.D. thesis in Mechanical Engineering, The Pennsylvania State University.

Mazumder, S., and Modest, M. F., 1999, "A PDF Approach to Modeling Turbulence-Radiation Interactions in Nonluminous Flames," *International Journal of Heat and Mass Transfer,* Vol. 42, pp. 971–991.

Modest, M. F., 1993, *Radiative Heat Transfer,* McGraw-Hill, New York.

Pope, S. B., 1985, "PDF Methods for Turbulent Reactive Flows," *Progress in Energy and Combustion Science,* Vol. 11, pp. 119–192.

Song, T. H., and Viskanta, R., 1987, "Interaction of Radiation with Turbulence: Application to a Combustion System," *Journal of Thermophysics,* Vol. 1, No. 1, pp. 56–62.

Coupled Liquid and Vapor Flow in Miniature Passages With Micro Grooves

D. Khrustalev[1,2] and A. Faghri[1,3]

Friction factor coefficients for liquid flow in a rectangular microgroove coupled with the vapor flow in a vapor channel of a

[1] Department of Mechanical Engineering, University of Connecticut, Storrs, CT 06269.

[2] Present address: Thermacore, Inc., Lancaster, PA 17601. e-mail: khrustalev@thermacore.com.

[3] e-mail: faghri@eng2.uconn.edu. Mem. ASME.

Contributed by the Heat Transfer Division for publication in the JOURNAL OF HEAT TRANSFER and presented at '98 IMECE, Anaheim. Manuscript received by the Heat Transfer Division, Aug. 8, 1998; revision received, Feb. 22, 1999. Keywords: Flow, Heat Transfer, Heat Pipes, Two-Phase. Associate Technical Editor: A. Majumdar.

$$\langle \kappa'_\eta I'_{b\eta} \rangle = f(\langle T'^2 \rangle, \langle \underline{Y}' T' \rangle, \text{ higher order terms}), \quad (3)$$

where $\underline{Y}$ is a set consisting of all the species mass fractions. Of the two second-order correlations appearing in Eq. (3), the correlation $\langle \underline{Y}' T' \rangle$ is responsible for determining whether $\langle \kappa'_\eta I'_{b\eta} \rangle$ is positive or negative, since $\langle T'^2 \rangle$ is always positive. If $\langle \kappa'_\eta I'_{b\eta} \rangle$ is positive, the intensity of radiation along a line of sight will be enhanced (cf. Eq. (2)), and if $\langle \kappa'_\eta I'_{b\eta} \rangle$ is negative, the intensity will be attenuated. In other words, the role of TRI essentially reduces to how the concentration fluctuations correlate with the temperature fluctuations in the medium. In flames, this correlation is always positive because local production of CO_2 or H_2O is always accompanied by production of heat (or an increase in local temperature). For nonreactive flows, this is not the case, and the matter requires further investigation.

Sample Calculations

The geometry used for the sample calculations is shown in Fig. 1, and is two-dimensional planar. A mixture of carbon dioxide and water vapor (equal by mass) was injected along the centerline, as shown, at a temperature of 1000K and a velocity of 16.41 m/s. The coflowing air has a temperature of 1200K and a velocity of 10 m/s. The Reynolds number based on the inlet air properties and the bluff body size is 13,304. The wake behind the bluff body promotes intense mixing by recirculation.

In order to isolate the effect of TRI, the case described above was run with radiation but without TRI, and a restart file was stored after 460 ms. The divergences of the radiative heat flux and the wall heat fluxes were calculated and stored. The TRI terms were then turned on and the simulation was allowed to march forward for a single time-step of one nanosecond. The divergences and wall heat loads were recalculated. Figure 2 illustrates the divergences and wall heat fluxes with and without TRI. The exact opposite effect of what was observed for reactive flows in Mazumder and Modest (1999) is observed here. Figure 2(*a*) shows that the regions of strong emission contract to some extent when TRI is included. Consequently, the radiative wall heat fluxes decrease by approximately ten percent when TRI is included (Fig. 2(*b*)), although the relative change is much smaller than what was observed for a flame, where an increase of about 45 percent was noted (Mazumder and Modest, 1999). The smaller change was expected since it is well known that the fluctuations in a flame are significantly larger than in an inert flow. All of the above observations suggest that $\langle \kappa'_\lambda E'_{b\lambda} \rangle$ is negative in this case, which was indeed observed to be true when this term was printed out.

The negative magnitude of the correlation $\langle \kappa'_\lambda E'_{b\lambda} \rangle$ can be explained physically by examining a situation where pure carbon dioxide flows into still air. A blob of CO_2, as soon as it is exposed to the air, captures some oxygen and nitrogen, and loses some CO_2 to the surrounding air due to mixing. Consequently, the CO_2 concentration in the blob decreases. In the absence of turbulence this exchange takes place by molecular diffusion only, and is extremely slow. In the presence of turbulence the mixing proceeds at a rate governed by the local turbulent time scale, and is usually quite rapid. The important issue at this point is whether the temperature of the blob increases or decreases during this mixing process. This, of course, is governed by the relative temperature difference between the CO_2 stream and the surrounding air. If the CO_2 stream is colder than the surrounding air, which is the case here, the temperature of the blob will increase. The reverse is true if an air blob is considered, i.e., a positive concentration fluctuation will be associated with a negative temperature fluctuation. The net effect of these associations result in correlations such as $\langle Y'_i T' \rangle$ being negative if the surrounding or coflowing air is hotter than the species jet. By the same token, the correlation is expected to be almost zero or randomly behaving if the temperature of the two streams are equal, and positive if the CO_2–H_2O mixture stream is hotter than the coflowing air stream. To investigate this matter, two more simulations were performed. In the first case, the two inlet temperatures were maintained equal, and in the second case, the CO_2–H_2O mixture was injected at a temperature 200K hotter than the air injection temperature. The heat fluxes for these two cases are illustrated in Fig. 3. For the case with equal inlet temperatures of the two streams, as expected, the difference in the radiative flux with and without TRI is extremely small, and may be attributed to numerical uncertainty. When the temperature of the CO_2–H_2O mixture stream is higher than the temperature of the coflowing air, TRI plays the role of increasing the radiative wall heat flux, and thus lending strong support to the above physical explanation.

In most practical situations, the exhaust gas from a combustor is a mixture of all the different species, and all species are at the same temperature, rather than existing as separate streams with different temperatures. Therefore, it is reasonable to conclude that the effect of TRI in nonreactive flows is only marginal and may be neglected to simplify the analysis.

Conclusions

The effect of turbulence-radiation interactions in nonreactive flow of combustion gases was investigated numerically. The role of TRI largely depends on how the temperature fluctuations correlate with the concentration fluctuations. In most cases of practical interest, the fluctuations were found to be uncorrelated, resulting in almost negligible effect of TRI on the wall heat loads.

Acknowledgment

This research was supported in part by the Applied Research Laboratory at Penn State.

References

Kabashnikov, V. P., and Myasnikova, G. I., 1985a, "Thermal Radiation in Turbulent Flows—Temperature and Concentration Fluctuations," *Heat Transfer–Soviet Research,* Vol. 17, No. 6, pp. 116–125.

Kabashnikov, V. P., 1985b, "Thermal Radiation in Turbulent Flows—In the Case of Large Fluctuations of the Absorption Coefficient and the Planck Function," *Journal of Engineering Physics,* Vol. 49, No. 1, pp. 778–784.

Mazumder, S., 1997, "Numerical Study of Chemically Reactive Turbulent Flows with Radiative Heat Transfer," Ph.D. thesis in Mechanical Engineering, The Pennsylvania State University.

Mazumder, S., and Modest, M. F., 1999, "A PDF Approach to Modeling Turbulence-Radiation Interactions in Nonluminous Flames," *International Journal of Heat and Mass Transfer,* Vol. 42, pp. 971–991.

Modest, M. F., 1993, *Radiative Heat Transfer,* McGraw-Hill, New York.

Pope, S. B., 1985, "PDF Methods for Turbulent Reactive Flows," *Progress in Energy and Combustion Science,* Vol. 11, pp. 119–192.

Song, T. H., and Viskanta, R., 1987, "Interaction of Radiation with Turbulence: Application to a Combustion System," *Journal of Thermophysics,* Vol. 1, No. 1, pp. 56–62.

Coupled Liquid and Vapor Flow in Miniature Passages With Micro Grooves

D. Khrustalev[1,2] and A. Faghri[1,3]

Friction factor coefficients for liquid flow in a rectangular microgroove coupled with the vapor flow in a vapor channel of a

[1] Department of Mechanical Engineering, University of Connecticut, Storrs, CT 06269.

[2] Present address: Thermacore, Inc., Lancaster, PA 17601. e-mail: khrustalev@thermacore.com.

[3] e-mail: faghri@eng2.uconn.edu. Mem. ASME.

Contributed by the Heat Transfer Division for publication in the JOURNAL OF HEAT TRANSFER and presented at '98 IMECE, Anaheim. Manuscript received by the Heat Transfer Division, Aug. 8, 1998; revision received, Feb. 22, 1999. Keywords: Flow, Heat Transfer, Heat Pipes, Two-Phase. Associate Technical Editor: A. Majumdar.

miniature two-phase device were calculated using finite element analysis. The results show that the effect of the vapor-liquid frictional interaction on the liquid flow decreases with curvature of the liquid-vapor interface. Shear stresses at the liquid-vapor interface are significantly nonuniform, decreasing towards the center of the liquid-vapor meniscus.

Nomenclature

A_i = cross-sectional area, m^2
C_i = constants
D_h = $4A/P$, hydraulic diameter, m
f = $2\bar{\tau}/(\rho\bar{w}^2)$ friction factor
L = length, m
n = unit vector normal to a boundary, m
p = pressure, Pa
P = wetted perimeter, m
Q_{max} = maximum heat transfer, W
Re = $\bar{w}D_h\rho/\mu$, axial Reynolds number
s = distance along the liquid-vapor interface (see Fig. 1), m
T = temperature, °C
t_{men} = height of the liquid domain (see Fig. 1), m
w = axial velocity, m/s
$\bar{w}$ = area-averaged axial velocity, m/s
z = axial coordinate, m

Greek Symbols

θ = contact angle
μ = dynamic viscosity, Pa-s
ρ = density, kg/m^3
τ = $\mu(\partial w/\partial n)$, shear stress, N/m^2

Subscripts

l = liquid
lv = liquid-vapor interface
men = meniscus
min = minimum
v = vapor
w = wall

Introduction

Miniature passages with axial micro grooves can be used as heat pipes or two-phase heat sinks for electronic cooling (Yang and Webb, 1996; Hopkins, 1996; Hopkins et al., 1997; Cao et al., 1996).

Theoretical prediction of performance characteristics of these two-phase devices is based on modeling of the working liquid flow in open capillary grooves affected by the vapor flow (Khrustalev and Faghri, 1995, 1996). However, fluid flow in axially grooved passages have often been modeled using numerous simplifying assumptions which can result in inaccurate predictions, if directly applied to miniature passages with high-velocity flows. For example, shear stress in liquid was assumed to be uniform along the liquid-vapor interface for a given cross section of the liquid flow by Longtin et al. (1992) and Khrustalev and Faghri (1994) in their modeling of micro heat pipes and also by Lin and Faghri (1997) and Ma et al. (1994). Schneider and DeVos (1980) and Hopkins et al. (1997) calculated friction factors for the liquid flow in axial grooves of heat pipes using analytical solutions obtained for the case of flat liquid-vapor interface affected by vapor flow. Also, liquid-vapor interaction can even be neglected in some situations, for example for low vapor velocities (Kamotani, 1976). However, simplifying assumptions mentioned above are not accurate enough for situations with high vapor velocities in constricted passages, especially when cross-sectional areas of vapor and liquid flows are comparable. Therefore a two-dimensional model of coupled liquid and vapor flow in miniature passages with axial grooves has been developed in this paper to more accurately calculate the friction factors. Based on these friction factors, longitudinal pressure gradients in liquid and vapor flows in a miniature heat pipe were calculated and the capillary limit was estimated and compared with existing experimental results of Hopkins et al. (1997). That comparison demonstrated that the coupled liquid-vapor solution is needed to predict performance characteristics of miniature axially grooved heat pipes with reasonable accuracy.

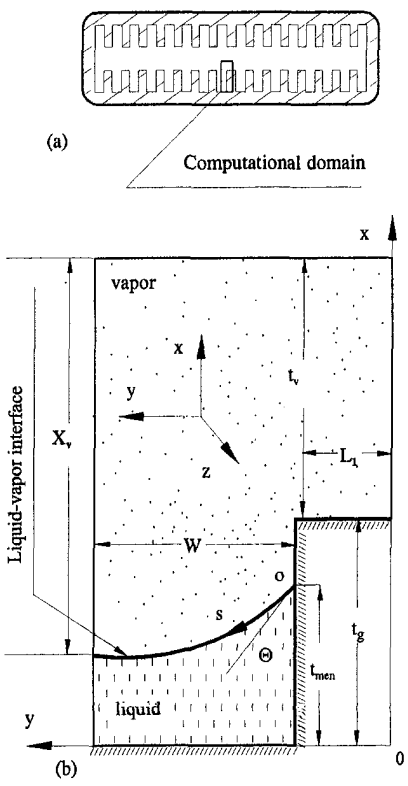

Fig. 1 Geometrical conventions and coordinate system: (*a*) computational domain, (*b*) cross section of a grooved passage

Mathematical Formulation

A fully developed flow in both vapor and liquid is typical for miniature passages with very large length to width ratios (Fisher and Martin, 1997). A cross section of a typical miniature passage with axial rectangular grooves is shown in Fig. 1(*a*). The liquid flows in the capillary microgrooves and the vapor flows in the central part of the passage free of liquid. The cartesian coordinate system used and the computational domain is shown in Fig. 1(*b*) where the vapor and liquid flow along the z-coordinate (cocurrent or countercurrent). A steady-state mathematical model is developed which includes coupled vapor and liquid flows with shear stresses at the liquid free surface due to the vapor-liquid frictional interaction. The model is based on the following simplifying assumptions:

1 Laminar fluid flow with fully developed velocity profiles.
2 Curvature of the liquid vapor interface is constant.
3 Symmetry conditions are applicable at the three exterior boundaries of the vapor domain (see Fig. 1(*b*)). This means that the number of grooves is large and the vapor channel height to width ratio is very small for a miniature passage with grooves.

For an incompressible fluid with constant vapor and liquid viscosities the momentum equation in Stokes approximation for both the vapor and liquid is

$$\frac{dp}{dz} = \mu \left(\frac{\partial^2 w}{\partial x^2} + \frac{\partial^2 w}{\partial y^2} \right). \quad (1)$$

Dimensionless velocity and coordinates are introduced as follows:

$$w^* = \frac{w\mu}{(W + L_1)(t_g + t_v)dp/dz}$$

$$x^* = x/[(W + L_1)(t_g + t_v)]^{0.5}$$

$$y^* = y/[(W + L_1)(t_g + t_v)]^{0.5}.$$

Therefore Eq. (1) takes the form

$$\left(\frac{\partial^2 w^*}{\partial x^{*2}} + \frac{\partial^2 w^*}{\partial y^{*2}} \right) - 1 = 0. \quad (2)$$

The boundary conditions defined as

$$\frac{\partial w^*}{\partial y^*} = 0 \quad \text{at} \quad y^* = 0 \quad \text{and} \quad y^* = \left[\frac{W + L_1}{t_g + t_v} \right]^{0.5} \quad (3)$$

$$\frac{\partial w^*}{\partial x^*} = 0 \quad \text{at} \quad x^* = [(t_g + t_v)/(W + L_1)]^{0.5} \quad (4)$$

$$w^* = 0 \quad \text{at} \quad x^* = 0 \quad \text{and} \quad \text{fin solid surfaces:} \quad (5)$$

$$(a) \quad x^* = t_g/[(t_g + t_v)(W + L_1)]^{0.5}$$

$$\text{for} \quad y^* \le L_1/[(W + L_1)(t_g + t_v)]^{0.5}$$

$$(b) \quad y^* = L_1/[(W + L_1)(t_g + t_v)]^{0.5}$$

$$\text{for} \quad x^* \le t_g/[(t_g + t_v)(W + L_1)]^{0.5}.$$

Equations (3) and (4) are symmetry conditions at three boundaries of the computational domain shown in Fig. 1(*b*): $y = 0$, $y = W + L_1$, and $x = t_g + t_v$. Equation (5) is no-slip condition on the solid surface. At the liquid-vapor interface, shear stresses and velocities in liquid and vapor should be equal. However, for miniature two-phase devices, mass flow rates of liquid and vapor are of the same order of magnitude as are the liquid and vapor cross-sectional areas (see Fig. 1). On the other hand, vapor density is usually less than 0.1 percent of liquid density. Therefore, average liquid velocity is negligibly small compared to the average vapor velocity. In this situation, when solving the vapor flow problem, vapor velocity at the liquid-vapor interface can be assumed zero.

$$\tau_l = \pm\tau_v \quad \text{or} \quad \frac{\partial w_l}{\partial n} = \pm \frac{\mu_l}{\mu_v} \frac{\partial w_v}{\partial n} \quad (6)$$

at every point of the liquid-vapor interface

$$w_v^* = 0 \quad \text{at the liquid-vapor interface.} \quad (7)$$

Note that Eq. (6) is used only for the liquid flow problem and Eq. (7) is only employed in the vapor flow problem. This approach is consistent with model of Longtin et al. (1992) where it is mentioned that the liquid film velocity at the liquid-vapor interface can be considered zero from the vapor flow perspective. Boundary condition Eq. (7) is sufficiently accurate and allows algebraic correlations for the friction factor-Reynolds number product to be obtained separately for liquid and vapor as will be shown in the following sections. The vapor and liquid flows are still precisely coupled via shear stress at the interface and approximately via interfacial velocities in this approach. The friction factor-Reynolds number products for both the vapor and liquid can be found from the numerically obtained velocity distributions using the definition of the friction factor.

$$(f\,\mathrm{Re}) = 2\bar{\tau}^*_{w=0} D^*_h / w^* \quad (8)$$

where $\bar{\tau}^*_{w=0}$ is dimensionless average shear stress on the boundaries with zero velocity and D^*_h is the dimensionless hydraulic diameter.

Numerical Procedure

The mathematical problem, Eqs. (2)–(7), for both liquid and vapor was solved using a finite-element method (Reddy, 1994) with triangular three-node elements and meshes generated for various values of parameters θ, W/L_1 and $t_v/(W + L_1)$ of the computational domain in Fig. 1(*b*). Accuracy of the numerical solution was checked by comparison of the results obtained for various numbers of elements and also comparison with analytical solutions available for limiting cases. The numerical solution was found to be essentially independent of the number of elements used. For example, the value of $(f\,\mathrm{Re})$ obtained with 256 elements was within three percent of the corresponding value obtained with 800 elements. The results presented below were obtained with the 800 element mesh. For the limiting case of flat liquid-vapor interface, $(f\,\mathrm{Re})_l$ was compared to corresponding values obtained from the analytical solution presented by Schneider and DeVos (1980). The agreement was very good with a maximum error of two percent for both shallow and deep grooves as well as for both negative and positive dimensionless shear stress at the interface, $\bar{\tau}^*$, defined by the following formula:

$$\bar{\tau}^* = \bar{\tau}^*_{lv} t^*_{\mathrm{men}} / \bar{w}^* \quad (9)$$

where $\bar{\tau}^*_{lv}$ is the average dimensionless shear stress at the interface and t^*_{men} is nondimensionalized similarly to x^*. Also the numerical solution for the vapor flow agreed favorably with an analytical solution for the case of $\theta = 90$ deg and $t_{\mathrm{men}} = t_g$ (Shah and Bhatti, 1987) with the maximum error of 0.2 percent.

The values of $(f\,\mathrm{Re})_v$ and $(f\,\mathrm{Re})_l$ were obtained for every set of parameters $t_v/(W + L_1)$, t_{men}/W and θ following a two-step procedure.

1 Solve Eq. (2) in the vapor region with boundary conditions (3)–(5) and (7) and find the dimensionless distribution of the shear stress at the liquid-vapor interface, $(f\,\mathrm{Re})_v$ and the ratio $\Phi_1 \equiv \bar{\tau}^*_{lv}/\bar{\tau}^*_{w=0}$.

2 Using the dimensionless distribution of the shear stress at the liquid-vapor interface obtained from the previous step, solve Eq. (2) in the liquid region with boundary conditions (3) and (5) for various values of $\bar{\tau}^*$ in liquid at the interface.

Coupling of the liquid and vapor flow can than be done by choosing the solutions from steps 1 and 2 where boundary condition Eq. (6) is satisfied. This can be easily achieved for a known ratio $(\mu_v \bar{w}_v)/(\mu_l \bar{w}_l)$ since

$$\bar{\tau}^* = -(f\,\mathrm{Re})_v \frac{\mu_v |\bar{w}_v|}{\mu_l |\bar{w}_l|} \frac{t_{\mathrm{men}}}{2D_{h,v}} \Phi_1. \quad (10)$$

Note that Eq. (10) is a dimensionless equivalent of Eq. (6) rewritten with respect to Eqs. (8) and (9).

Modeling of a two-phase miniature device could be essentially simplified if the numerical results for the coupled liquid and vapor flow for a fixed geometry of the miniature passage are approximated by some algebraic functions for the friction factor-Reynolds number products and Φ_1. For example, for the particular geometry considered in this paper and described in the following section these functions are presented as follows:

$$(f\,\mathrm{Re})_l = C_1[1 + C_2(\bar{\tau}^* - C_3)] + C_4(\theta - 90)(\bar{\tau}^* - C_5) \quad (11)$$

$$(f\,\mathrm{Re})_v = C_6 + C_7\theta + C_8\theta^2 + C_9\theta^3 \quad (12)$$

$$\Phi_1 = C_{10} + C_{11}\theta + C_{12}\theta^2 \quad (13)$$

where θ is in degrees.

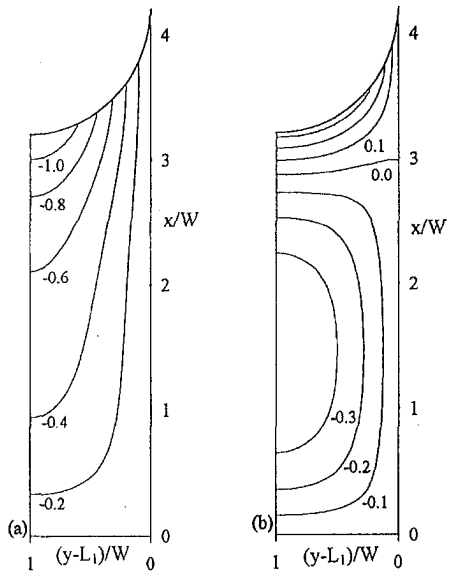

Fig. 2 Velocity contours in liquid: (*a*) cocurrent flow, $\bar{\tau}^* = -4.7$; (*b*) countercurrent flow, $\bar{\tau}^* = 11.0$

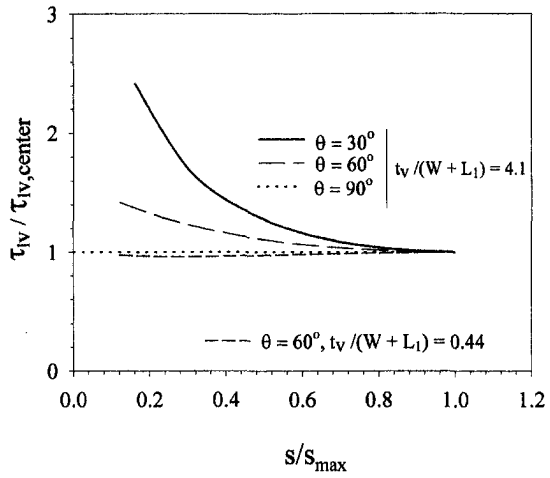

Fig. 4 Distribution of the dimensionless shear stress along the liquid-vapor interface

Results and Discussion

Previous analyses of grooved miniature heat pipes and heat sinks have shown that the grooves for the liquid flow should have a depth to width ratio of about 2 (Khrustalev and Faghri, 1995). Therefore, the results presented below are for the following geometrical parameters of the computational domain: $W/L_1 = 2$, $t_g/W = 4.2$ and $t_v/(W + L_1) = 4.1$ and $t_g = t_{men}$. These parameters are typical and represent a miniature heat pipe experimentally investigated by Hopkins et al. (1997).

Examples of velocity contours in liquid are shown in Fig. 2 for $\theta = 0$. For countercurrent vapor and liquid flow, reverse flow appears near the liquid-vapor interface, as seen in Fig. 2(*b*), due to the vapor-liquid frictional interaction. This interaction depends on the friction factor-Reynolds number product for the vapor flow that varies with the vapor channel size for small values of θ as shown in Fig. 3. However, $(f\,\mathrm{Re})_v$ does not depend on t_v for θ approaching 90 deg.

Distribution of the viscous shear stress at the liquid-vapor interface is not uniform as illustrated by Fig. 4. This nonuniformity increases with the interface curvature. The shear stress decreases towards the interface center. Friction factor-Reynolds number product for the liquid flow is given in Fig. 5 as a function of the dimensionless interfacial shear stress for several values of θ. Shear stress, τ^*, is defined by Eq. (9) and depends on the average liquid velocity. The resulting pressure gradient in liquid also depends on the hydraulic diameter. Overall, effect of the vapor flow on liquid reduces with curvature of the interface compared to the case when this interface is assumed to be flat in the calculations.

To illustrate the last statement, prediction of the capillary limit of a flat miniature copper-water heat pipe tested by Hopkins et al. (1997) was done. The values of constants C_i in the formulas Eqs. (11), (12), and (13) for $(f\,\mathrm{Re})$ and Φ_1 for $W/L_1 = 2$, $t_g/W = 4.2$ and $t_v/(W + L_1) = 4.1$ are: $C_1 = 20.8$, $C_2 = 0.01694$, $C_3 = C_5 = 7$, $C_4 = 0.007526$, $C_6 = 12.16$, $C_7 = 0.3496$, $C_8 = -0.004267$, $C_9 = 2.049 \times 10^{-5}$, $C_{10} = 0.7155$, $C_{11} = 4.85 \times 10^{-3}$, $C_{12} = -1.944. \times 10^{-5}$. With these C_i values, Eqs. (11), (12), and (13) describe the numerical results for functions $(f\,\mathrm{Re})_l$, $(f\,\mathrm{Re})_v$ and Φ_1 with an error less than ± 2 percent. The maximum heat transport of flat miniature axially grooved heat pipe, Q_{max}, was calculated using the fluid circulation model developed by Khrustalev and Faghri (1995). That model accounts for the capillary pressure, inertia effects in vapor, and meniscus curvature distribution along heat pipe axis. Since the model is fully presented in detail in Khrustalev and Faghri (1995), it is not repeated in the present paper. The only difference between the present heat pipe capillary limitation analysis and that in the cited paper is the values of the friction factor-Reynolds number product used in the calculations. Using values of the friction factors,

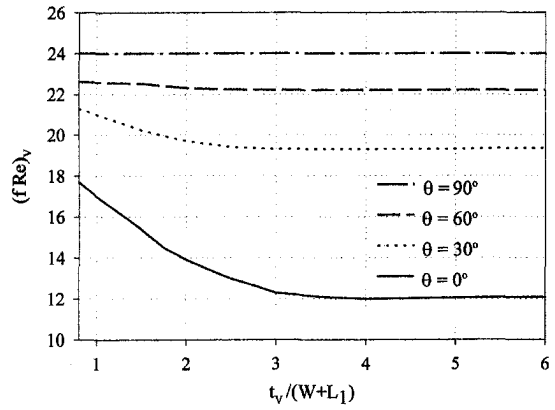

Fig. 3 Effect of the vapor channel size on the vapor friction factor-Reynolds number product

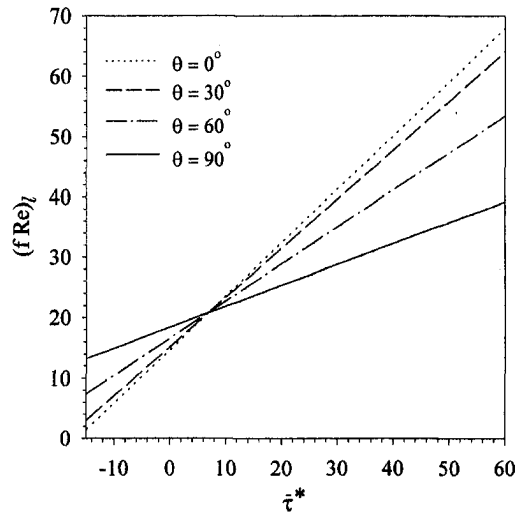

Fig. 5 Friction factor-Reynolds number product for liquid flow in a groove with curved liquid-vapor interface for $t_{men}/W = 4.2$

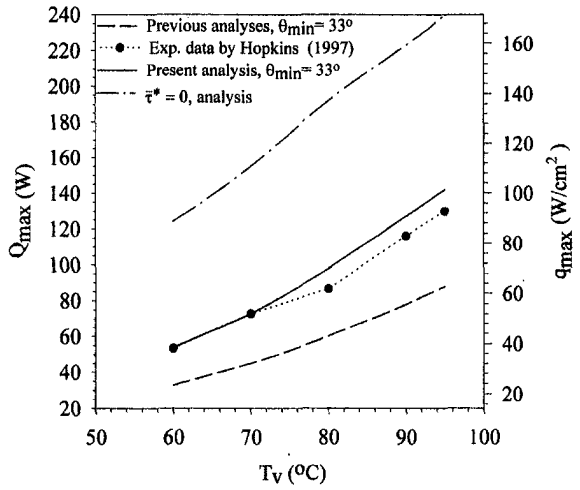

Fig. 6 Maximum heat transfer of a flat miniature heat pipe versus operating temperature in horizontal orientation

yielded by the present analysis, significantly improved agreement between theoretical prediction and experimental data obtained by Hopkins et al. (1997) as shown in Fig. 6. Previous analyses under predicted the experimental data by about 35 percent. Prediction obtained using results of the present coupled liquid and vapor flow analyses favorably agrees with the experimental data. Importance of accounting for the liquid-vapor interaction is seen from the upper curve in Fig. 6 obtained for zero shear stress at the interface that over predicts experimental data by 100 percent. This underlines that coupled solutions for liquid and vapor flow should be used in modeling of miniature grooved two-phase devices.

Conclusions

The numerical results describing the fluid flow in two-phase miniature passages with microgrooves are summarized as follows:

1 Shear stresses at the liquid-vapor curved interface are significantly nonuniform, decreasing towards the center of the liquid-vapor meniscus. This nonuniformity increases with curvature of the liquid-vapor interface.

2 The effect of the vapor flow on the liquid flow in the grooves decreases with curvature of the liquid-vapor interface.

3 Frictional vapor-liquid interaction significantly affects performance of two-phase miniature devices with axial grooves. Shapes of the liquid and vapor cross-sectional areas should be precisely accounted for when calculating the friction factor-Reynolds number products. Idealizing the liquid-vapor interface as flat can result in a significant error in prediction of fluid pressure drops in miniature two-phase devices.

Acknowledgments

Funding for this work was provided by NASA Grant NAG3-1870 and NSF Grant CTS-941458.

References

Cao, Y., Beam, J., and Donovan, B., 1996, "Air-Cooling System for Metal Oxide Semi-conductor Controlled Thyristors Employing Miniature Heat Pipes," *J. Thermophysics and Heat Transfer,* Vol. 10, No. 3. pp. 484–489.

Faghri, A., 1995, *Heat Pipe Science and Technology,* Taylor & Francis, London.

Fisher, L., and Martin, H., 1997, "Friction Factors for Fully Developed Laminar Flow in Ducts Confined by Corrugated Parallel Walls," *Int. J. Heat and Mass Transfer,* Vol. 40, pp. 635–639.

Hopkins, R., 1996, "Flat Miniature Heat Sinks and Heat Pipes with Micro Capillary Grooves: Manufacturing, Modeling and Experimental Study," Masters thesis, The University of Connecticut, Storrs, CT.

Hopkins, R., Faghri, A., and Khrustalev, D., 1997, "Flat Miniature Heat Pipes with Micro Capillary Grooves," *Proc. of the 1997 National Heat Transfer Conference,* HTD-Vol. 349, Vol. 11, pp. 71–80.

Jang, J. H., and Faghri, A., 1991, "Analysis of the One-Dimensional Transient Compressible Vapor Flow in Heat Pipes," *Int. J. Heat and Mass Transfer,* Vol. 34, pp. 2029–2037.

Kamotani, Y., 1976, "Thermal Analysis of Axially Grooved Heat Pipes," *Proc. 2nd Int. Heat Pipe Conf.,* Bologna, Italy, pp. 83–91.

Khrustalev, D., and Faghri, A., 1994, "Thermal Analysis of a Micro Heat Pipe," ASME JOURNAL OF HEAT TRANSFER, Vol. 116, pp. 189–198.

Khrustalev, D., and Faghri, A., 1995, "Thermal Characteristics of Conventional and Flat Miniature Axially-Grooved Heat Pipes," ASME JOURNAL OF HEAT TRANSFER, Vol. 117, pp. 1048–1054.

Khrustalev, D., and Faghri, A., 1996, "High Flux Evaporative Mini-Channel Heat Sink With Axial Capillary Grooves," *Journal of Enhanced Heat Transfer,* Vol. 3, No. 3, pp. 221–232.

Lin, L., and Faghri, A., 1997, "Steady-State Performance of a Rotating Miniature Heat Pipe," *Journal of Thermophysics and Heat Transfer,* Vol. 11, No. 4, pp. 513–519.

Longtin, J. P., Badran, B., and Gerner, F. M., 1992, "A One-Dimensional Model of a Micro Heat Pipe During Steady-State Operation," *Proc. 8th Int. Heat Pipe Conf.,* Beijing, China, Preprints, pp. C-5-1–C-5-7.

Ma, H. B., Peterson, G. P., and Lu, X. J., 1994, "The Influence of Vapor-Liquid Interactions on the Liquid Pressure Drop in Triangular Microgrooves," *Int. J. Heat and Mass Transfer,* Vol. 37, pp. 2211–2219.

Reddy, J. N., 1994, *The Finite Element Method in Heat Transfer and Fluid Dynamics,* CRC Press, Ann Arbor, MI.

Schneider, G. E., and DeVos, R., 1980, "Nondimensional Analysis for the Heat Transport Capability of Axially-Grooved Heat Pipes Including Liquid/Vapor Interaction," AIAA Paper No. 80–0214.

Shah, R. K., and Bhatti, M. S., 1987, "Laminar Convective Heat Transfer in Ducts," *Handbook of Single Phase Convective Heat Transfer,* Kakac et al., eds., John Wiley and Sons, New York.

Yang, C. Y., and Webb, R. L., 1996, "Friction Pressure Drop of R-12 in Small Hydraulic Diameter Extruded Aluminum Tubes With and Without Micro-Fins," *Int. J. Heat Mass Transfer,* Vol. 39, No. 4, pp. 801–809.

A Closure Model for Transient Heat Conduction in Porous Media

C. T. Hsu[1]

Equations governing the transient heat conduction in porous materials consisting of solids and fluids of different thermal properties were derived with a volumetric average scheme under the assumption of nonthermal equilibrium. The derivation leads to a macroscopic two-equation system which requires the closure modeling of new unknown terms due to interfacial transport, namely, the tortuosity term and the interfacial heat transfer term. Closure relations were obtained from the microscopic equations for temperature fluctuation under quasi-steady assumption. The closure coefficients appeared in the closure relations then depend on the media geometry as well as thermal properties. To demonstrate these dependencies, the closure coefficient for the thermal tortuosity is evaluated based on the effective stagnant thermal conductivity model proposed by Hsu et al. (1995) for periodically packed cubes, and the coefficient for interfacial heat transfer based on a quasi-steady heat conduction of dispersed spheres immersed in fluids. The salient features as well as the applicability and limitation of the newly proposed transient heat conduction model were discussed.

Nomenclature

a_{fs} = specific area of fluid-solid interface per unit volume
d = diameter

[1] Department of Mechanical Engineering, Hong Kong University of Science and Technology, Clear Water Bay, Kowloon, Hong Kong. e-mail: mechthsu@usthk.ust.hk. Mem. ASME.

Contributed by the Heat Transfer Division for publication in the JOURNAL OF HEAT TRANSFER. Manuscript received by the Heat Transfer Division, Mar. 31, 1997; revision received, Mar. 25, 1999. Keywords: Conduction, Porous Media, Transient and Unsteady Heat Transfer. Associate Technical Editor: M. Kaviany.

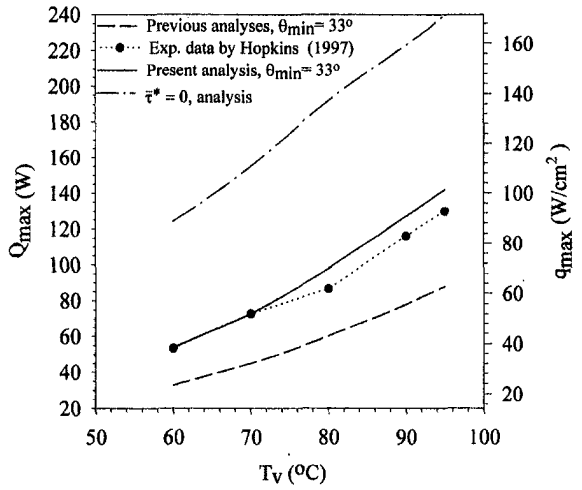

Fig. 6 Maximum heat transfer of a flat miniature heat pipe versus operating temperature in horizontal orientation

yielded by the present analysis, significantly improved agreement between theoretical prediction and experimental data obtained by Hopkins et al. (1997) as shown in Fig. 6. Previous analyses under predicted the experimental data by about 35 percent. Prediction obtained using results of the present coupled liquid and vapor flow analyses favorably agrees with the experimental data. Importance of accounting for the liquid-vapor interaction is seen from the upper curve in Fig. 6 obtained for zero shear stress at the interface that over predicts experimental data by 100 percent. This underlines that coupled solutions for liquid and vapor flow should be used in modeling of miniature grooved two-phase devices.

Conclusions

The numerical results describing the fluid flow in two-phase miniature passages with microgrooves are summarized as follows:

1 Shear stresses at the liquid-vapor curved interface are significantly nonuniform, decreasing towards the center of the liquid-vapor meniscus. This nonuniformity increases with curvature of the liquid-vapor interface.

2 The effect of the vapor flow on the liquid flow in the grooves decreases with curvature of the liquid-vapor interface.

3 Frictional vapor-liquid interaction significantly affects performance of two-phase miniature devices with axial grooves. Shapes of the liquid and vapor cross-sectional areas should be precisely accounted for when calculating the friction factor-Reynolds number products. Idealizing the liquid-vapor interface as flat can result in a significant error in prediction of fluid pressure drops in miniature two-phase devices.

Acknowledgments

Funding for this work was provided by NASA Grant NAG3-1870 and NSF Grant CTS-941458.

References

Cao, Y., Beam, J., and Donovan, B., 1996, "Air-Cooling System for Metal Oxide Semi-conductor Controlled Thyristors Employing Miniature Heat Pipes," *J. Thermophysics and Heat Transfer,* Vol. 10, No. 3. pp. 484–489.

Faghri, A., 1995, *Heat Pipe Science and Technology,* Taylor & Francis, London.

Fisher, L., and Martin, H., 1997, "Friction Factors for Fully Developed Laminar Flow in Ducts Confined by Corrugated Parallel Walls," *Int. J. Heat and Mass Transfer,* Vol. 40, pp. 635–639.

Hopkins, R., 1996, "Flat Miniature Heat Sinks and Heat Pipes with Micro Capillary Grooves: Manufacturing, Modeling and Experimental Study," Masters thesis, The University of Connecticut, Storrs, CT.

Hopkins, R., Faghri, A., and Khrustalev, D., 1997, "Flat Miniature Heat Pipes with Micro Capillary Grooves," *Proc. of the 1997 National Heat Transfer Conference,* HTD-Vol. 349, Vol. 11, pp. 71–80.

Jang, J. H., and Faghri, A., 1991, "Analysis of the One-Dimensional Transient Compressible Vapor Flow in Heat Pipes," *Int. J. Heat and Mass Transfer,* Vol. 34, pp. 2029–2037.

Kamotani, Y., 1976, "Thermal Analysis of Axially Grooved Heat Pipes," *Proc. 2nd Int. Heat Pipe Conf.,* Bologna, Italy, pp. 83–91.

Khrustalev, D., and Faghri, A., 1994, "Thermal Analysis of a Micro Heat Pipe," ASME JOURNAL OF HEAT TRANSFER, Vol. 116, pp. 189–198.

Khrustalev, D., and Faghri, A., 1995, "Thermal Characteristics of Conventional and Flat Miniature Axially-Grooved Heat Pipes," ASME JOURNAL OF HEAT TRANSFER, Vol. 117, pp. 1048–1054.

Khrustalev, D., and Faghri, A., 1996, "High Flux Evaporative Mini-Channel Heat Sink With Axial Capillary Grooves," *Journal of Enhanced Heat Transfer,* Vol. 3, No. 3, pp. 221–232.

Lin, L., and Faghri, A., 1997, "Steady-State Performance of a Rotating Miniature Heat Pipe," *Journal of Thermophysics and Heat Transfer,* Vol. 11, No. 4, pp. 513–519.

Longtin, J. P., Badran, B., and Gerner, F. M., 1992, "A One-Dimensional Model of a Micro Heat Pipe During Steady-State Operation," *Proc. 8th Int. Heat Pipe Conf.,* Beijing, China, Preprints, pp. C-5-1–C-5-7.

Ma, H. B., Peterson, G. P., and Lu, X. J., 1994, "The Influence of Vapor-Liquid Interactions on the Liquid Pressure Drop in Triangular Microgrooves," *Int. J. Heat and Mass Transfer,* Vol. 37, pp. 2211–2219.

Reddy, J. N., 1994, *The Finite Element Method in Heat Transfer and Fluid Dynamics,* CRC Press, Ann Arbor, MI.

Schneider, G. E., and DeVos, R., 1980, "Nondimensional Analysis for the Heat Transport Capability of Axially-Grooved Heat Pipes Including Liquid/Vapor Interaction," AIAA Paper No. 80–0214.

Shah, R. K., and Bhatti, M. S., 1987, "Laminar Convective Heat Transfer in Ducts," *Handbook of Single Phase Convective Heat Transfer,* Kakac et al., eds., John Wiley and Sons, New York.

Yang, C. Y., and Webb, R. L., 1996, "Friction Pressure Drop of R-12 in Small Hydraulic Diameter Extruded Aluminum Tubes With and Without Micro-Fins," *Int. J. Heat Mass Transfer,* Vol. 39, No. 4, pp. 801–809.

A Closure Model for Transient Heat Conduction in Porous Media

C. T. Hsu[1]

Equations governing the transient heat conduction in porous materials consisting of solids and fluids of different thermal properties were derived with a volumetric average scheme under the assumption of nonthermal equilibrium. The derivation leads to a macroscopic two-equation system which requires the closure modeling of new unknown terms due to interfacial transport, namely, the tortuosity term and the interfacial heat transfer term. Closure relations were obtained from the microscopic equations for temperature fluctuation under quasi-steady assumption. The closure coefficients appeared in the closure relations then depend on the media geometry as well as thermal properties. To demonstrate these dependencies, the closure coefficient for the thermal tortuosity is evaluated based on the effective stagnant thermal conductivity model proposed by Hsu et al. (1995) for periodically packed cubes, and the coefficient for interfacial heat transfer based on a quasi-steady heat conduction of dispersed spheres immersed in fluids. The salient features as well as the applicability and limitation of the newly proposed transient heat conduction model were discussed.

Nomenclature

a_{fs} = specific area of fluid-solid interface per unit volume
d = diameter

[1] Department of Mechanical Engineering, Hong Kong University of Science and Technology, Clear Water Bay, Kowloon, Hong Kong. e-mail: mechthsu@usthk.ust.hk. Mem. ASME.

Contributed by the Heat Transfer Division for publication in the JOURNAL OF HEAT TRANSFER. Manuscript received by the Heat Transfer Division, Mar. 31, 1997; revision received, Mar. 25, 1999. Keywords: Conduction, Porous Media, Transient and Unsteady Heat Transfer. Associate Technical Editor: M. Kaviany.

A = conduction layer thickness outside a sphere, normalized by the radius of sphere
A_{fs} = interfacial area between fluid and solid
B = conduction layer thickness inside a sphere, normalized by the radius of sphere
Cp = heat capacity
G = thermal tortuosity parameter
h_{fs} = interfacial heat transfer coefficient
$\mathbf{I}$ = unit matrix
k = thermal conductivity
k_e = effective stagnant thermal conductivity
M = interfacial transfer parameter
n = number of particles per unit volume
$\mathbf{n}$ = unit vector normal to the interface between fluid and solid
Nu = Nusselt number for interfacial heat transfer
Pr = Prandtl number
q = heat flux across the interface of a dispersed particle
Q_{fs} = interfacial heat transfer per unit volume
r = radius
Re = Reynolds number
$\mathbf{s}$ = area vector normal to the interface
t = time
T = temperature
V = volume

Greek

α = thermal diffusivity
β = thermal diffusivity ratio of solid to fluid
ϕ = porosity
γ_a = length ratio of particle to unit cell
γ_c = particle touching parameter
Λ_{fs} = interfacial thermal tortuosity
ρ = density
σ = thermal conductivity ratio of solid to fluid
τ = thermal diffusion time scale

Subscript

f = fluid
p = particle
s = solid

1 Introduction

Heat conduction in porous media consisting of fluid and solid phases has been encountered frequently in many engineering applications, such as manufacturing of composites, oil production, geothermal engineering, nuclear waste disposal, to name a few. For steady heat conduction, local thermal equilibrium between solids and fluids is usually assumed so that the macroscopic heat transfer processes of the two phases can be lumped into a single heat conduction equation for the mixture. The problem then becomes the construction of an appropriate composite model for the effective stagnant thermal conductivity in the lumped heat conduction equation. This type of approach can be traced back to the works of Maxwell (1873) and Rayleigh (1892). Continuing efforts in the past 40 years include those of Deissler and Boegli (1958), Kuni and Smith (1960), Zehner and Schlunder (1970), Nozad et al. (1985), Sahraoui and Kaviany (1993), and others. Most recently, Hsu et al. (1994, 1995, 1996) gave a more systematic account on the modeling of the effective stagnant thermal conductivity. Kaviany (1991) and Cheng and Hsu (1998) provided detailed reviews of the existing models for the effective stagnant thermal conductivity.

It has been generally realized for transient heat conduction that the local heat conduction process between the two phases is not in thermal equilibrium, especially when the difference in thermal conductivity of fluid and solid is large. This requires the separation of the macroscopic heat conduction equations for fluid and solid, respectively. One then encounters the so-called closure problem where the number of unknowns is more than the number of equations. As a result, closure modeling, a scheme to construct closure relations for the unknowns, is required. Furthermore, the final equations are usually coupled with each other, and their solutions can not obtained easily without employing complicated numerical procedure. For these reasons, there exist little works on the transient heat conduction in porous media. Amiri and Vafai (1994) performed a study of transient convective heat transfer in porous media based on a two-equation model. Quintard and Whitaker (1993) recently gave a comprehensive review of the closure modeling for the transient heat conduction based on a volumetric averaging scheme. They evaluated the closure coefficients by numerically solving the microscopic temperature fluctuation equations for periodic array of particles. More recently, Quintard and Whitaker (1995) investigated the constraints in using a local thermal equilibrium assumption for transient heat conduction. In this study, we shall follow Quintard and Whitaker (1993) by employing the volumetric averaging procedure to illustrate the closure problem and then construct the closure relations. However, unlike Quintard and Whitaker (1993), the evaluation of the closure coefficient for tortuosity effect is done analytically based on the lumped model of Hsu et al. (1995), and that for the interfacial heat transfer based on a quasi-steady assumption of microscopic heat conduction. The dependencies of these coefficients on the porosity and the thermal properties of fluids and solids are illuminated. The applicability and the limitation of the present model for transient heat conduction in porous media are discussed.

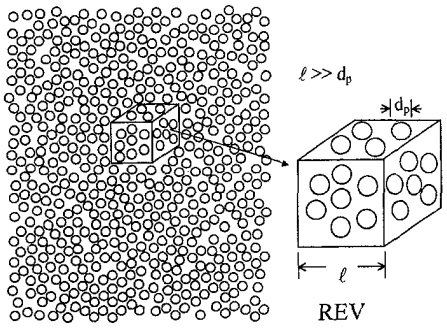

Fig. 1 The schematic of the porous media and the representative elementary volume (REV)

2 Macroscopic Transient Heat Conduction Equations

Let's assume that the porous material consists of packed solid particles surrounded by fluids as depicted in Fig. 1. For simplicity, we should consider the spherical particles of uniform size. The diameter, d_p, of the spheres characterizes the microscopic scale of the media. We also assume that d_p is much larger than the typical size of molecules such that fluid and solid microscopically are regarded as continuum. Hence, the microscopic transient heat conduction equations for the fluid and solid are given by

$$\rho_f Cp_f \frac{\partial T_f}{\partial t} = \nabla \cdot (k_f \nabla T_f) \tag{1}$$

and

$$\rho_s Cp_s \frac{\partial T_s}{\partial t} = \nabla \cdot (k_s \nabla T_s) \tag{2}$$

where the subscripts, f and s, refer to fluid and solid, respectively. The proper boundary conditions on the fluid-solid interface A_{fs} are

$$T_f = T_s \quad \text{on} \quad A_{fs} \tag{3}$$

and

$$\mathbf{n}_{fs} \cdot k_f \nabla T_f = \mathbf{n}_{fs} \cdot k_s \nabla T_s \quad \text{on} \quad A_{fs} \tag{4}$$

where $\mathbf{n}_{fs}$ is the unit vector out normal from fluid to solid.

It is impractical to solve the equation system (1)–(4) with details, especially when the number of solid particles is large. Alternatively, we are more interested in the global characteristics of heat conduction in the porous materials. To this end, we introduce a representative elementary volume (REV) of size V as depicted in Fig. 1. The length scale l of the REV is presumed to be much larger than d_p, but much smaller than the global scale of the domain under consideration. Hence, a quantity averaged over REV is regarded as continuum in the global domain.

If Eqs. (1) and (2) are averaged over REV for the respective fluid and solid phases, the volumetric phase-averaged equations after invoking the divergence theorem become

$$\rho_f C p_f \frac{\partial(\phi \bar{T}_f)}{\partial t} = \bar{\nabla} \cdot [k_f \bar{\nabla}(\phi \bar{T}_f)] + \bar{\nabla} \cdot (k_f \mathbf{\Lambda}_{fs}) + Q_{fs} \tag{5}$$

$$\rho_s C p_s \frac{\partial[(1-\phi)\bar{T}_s]}{\partial t} = \bar{\nabla} \cdot [k_s \bar{\nabla}((1-\phi)\bar{T}_s)] - \bar{\nabla} \cdot (k_s \mathbf{\Lambda}_{fs}) - Q_{fs} \tag{6}$$

where ϕ denotes the porosity and $\bar{\nabla}$ the macroscopic gradient operator. In Eqs. (5) and (6),

$$\mathbf{\Lambda}_{fs} = \frac{1}{V} \int\int_{A_{fs}} T_f d\mathbf{s} = \frac{1}{V} \int\int_{A_{fs}} T_s d\mathbf{s} \tag{7}$$

represents the thermal tortuosity effect and

$$Q_{fs} = \frac{1}{V} \int\int_{A_{fs}} k_f \nabla T_f d\mathbf{s} = \frac{1}{V} \int\int_{A_{fs}} k_s \nabla T_s d\mathbf{s} \tag{8}$$

represents the interfacial heat transfer. The last equalities in Eqs. (7) and (8) are evident from the interfacial boundary conditions (3) and (4). The negative sign in the last two terms of Eq. (6) reflects the fact that the source terms in Eq. (5) have to become the sink terms in Eq. (6), or vise versa. These last two integral terms represent the additional unknowns to the equation system (5) and (6). Closure modeling for these integral terms then becomes inevitable.

3 Closure Modeling

To close the equation system (5) and (6), we need to construct the constitutive equations which relate the integral terms to the macroscopically phase-averaged temperatures, $\bar{T}_f$ and $\bar{T}_s$. To this end, we first decompose T_f and T_s into

$$T_f = \bar{T}_f + T_f' \tag{9}$$

and

$$T_s = \bar{T}_s + T_s' \tag{10}$$

where T_f' and T_s' represent the microscopic temperature variations from the phase-averaged values. With the REV length scale being l, the time scale of the macroscopic conduction in fluid phase is l^2/α_f which is much larger than the time scale of the microscopic conduction given by d_p^2/α_f since $l \gg d_p$; similar argument applies to solid phase. With respect to the macroscopic process of long time scale, it is plausible to assume that the local microscopic heat conduction process is quasi-steady. Under this quasi-steady assumption, the substitution of (9) and (10) into (1) and (2) leads to

$$\nabla \cdot (k_f \nabla T_f') = 0 \tag{11}$$

and

$$\nabla \cdot (k_s \nabla T_s') = 0. \tag{12}$$

The interfacial boundary conditions (3) and (4) now become

$$T_f' = T_s' + (\bar{T}_s - \bar{T}_f) \quad \text{on} \quad A_{fs} \tag{13}$$

and

$$\mathbf{n}_{fs} \cdot \nabla T_f' = \mathbf{n}_{fs} \cdot \sigma \nabla T_s' + \mathbf{n}_{fs} \cdot (\sigma \bar{\nabla} \bar{T}_s - \bar{\nabla} \bar{T}_f) \quad \text{on} \quad A_{fs} \tag{14}$$

where $\sigma = k_s/k_f$ is the ratio of conductivity of solid to fluid.

Since Eqs. (11) and (12) are linear, the interfacial boundary conditions (13) and (14) suggest that the solutions to T_f' and T_s' will take the forms of

$$T_f' = f_0'(\bar{T}_s - \bar{T}_f) + \mathbf{f}_1' \cdot d_p(\bar{\nabla} \bar{T}_f - \sigma \bar{\nabla} \bar{T}_s) \tag{15}$$

and

$$T_s' = g_0'(\bar{T}_s - \bar{T}_f) + \mathbf{g}_1' \cdot d_p(\bar{\nabla} \bar{T}_f - \sigma \bar{\nabla} \bar{T}_s). \tag{16}$$

The substitution of Eqs. (15) and (16) into Eqs. (11)–(14) leads to equation systems and boundary conditions for f_0', $\mathbf{f}_1'$, g_0', and $\mathbf{g}_1'$. The details of their solutions depend on the structural geometry of the solid particles and require elaborated works. However, for the present aim of constructing the closure relations, the solution forms appearing in Eqs. (15) and (16) will suffice. The substitution of (15) or (16) into (9) and (10) and then into (7) and (8) results in

$$\mathbf{\Lambda}_{fs} = \mathbf{G}_0(\bar{T}_s - \bar{T}_f) + \boldsymbol{G}_1 \cdot (\bar{\nabla} \bar{T}_f - \sigma \bar{\nabla} \bar{T}_s) \tag{17}$$

where

$$\mathbf{G}_0 = \frac{1}{V} \int\int_{A_{fs}} f_0' d\mathbf{s} \quad \text{and} \quad \boldsymbol{G}_1 = \frac{d_p}{V} \int\int_{A_{fs}} \mathbf{f}_1' d\mathbf{s} \tag{18a, b}$$

and

$$Q_{fs} = M_0(\bar{T}_s - \bar{T}_f) + \mathbf{M}_1 \cdot (\bar{\nabla} \bar{T}_f - \sigma \bar{\nabla} \bar{T}_s) \tag{19}$$

where

$$M_0 = \frac{1}{V} \int\int_{A_{fs}} k_f \nabla f_0' \cdot d\mathbf{s} \quad \text{and} \quad \mathbf{M}_1 = \frac{d_p}{V} \int\int_{A_{fs}} k_f \nabla \mathbf{f}_1' \cdot d\mathbf{s}. \tag{20a, b}$$

The above derivations are basically in-line with those of Quintard and Whitaker (1993); however, here we provide a more concise treatment in obtaining the relations (17) and (19) which in form are slightly different from those of Quintard and Whitaker (1993). It is important to note that the closure coefficients, $\mathbf{G}_0$, $\boldsymbol{G}_1$, M_0, and $\mathbf{M}_1$, depend only on the detailed local geometry of particles, but not on the macroscopic quantities. For randomly distributed spherical particles, the volumetric averaged tensor $\boldsymbol{G}_1$ has to be axially symmetric to exhibit an isotropic property, i.e., $\boldsymbol{G}_1 = G\boldsymbol{I}$ where $\boldsymbol{I}$ is the unit matrix and G is a scalar quantity. According to Newton's law, the locally interfacial heat transfer is proportional to the total fluid-solid interfacial area A_{fs} in REV. Therefore, we have $M_0 = h_{fs} a_{fs}$ where a_{fs} $(= A_{fs}/V)$ is the specific interfacial area and h_{fs} is the interfacial heat transfer coefficient. From the physical point of view, a nonzero value in $\mathbf{G}_0$ or $\mathbf{M}_1$ will lead to a convective behavior associated with the macroscopic temperature gradient, where the vectors $\mathbf{G}_0$ and $\mathbf{M}_1$ resemble the convection velocities. Quintard and Whitaker (1993) had argued that this convective behavior does not have a physical ground since all these transfer processes are essentially from conduction. They also demonstrated mathematically that $\mathbf{G}_0 = \mathbf{M}_1 = 0$. Equations (17) and (19) then reduce to

$$\mathbf{\Lambda}_{fs} = G(\bar{\nabla} \bar{T}_f - \sigma \bar{\nabla} \bar{T}_s) \tag{21}$$

and

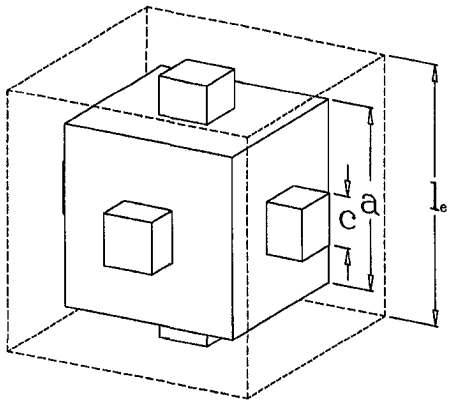

Fig. 2 The unit-cell geometry of the periodic array of in-line touching cubes

$$Q_{fs} = h_{fs}a_{fs}(\bar{T}_s - \bar{T}_f). \tag{22}$$

Equations (5) and (6) with the tortuosity and interfacial transfer terms given by Eqs. (21) and (22), respectively, are the governing equations for the transient heat conduction in porous media. The evaluation of the closure coefficients G and h_{fs} then becomes a critical task. We want to reemphasize that the values of G and h_{fs} depend only on the microscopic interfacial geometry and the thermal properties of solid and fluid.

4 Lumped Mixture Model Under Local Thermal Equilibrium Condition

Before evaluating the coefficients G and h_{fs}, we now examine the heat conduction in porous media under the local thermal equilibrium condition. This condition implies that

$$\bar{T} = \bar{T}_s = \bar{T}_f. \tag{23}$$

The constraints for invoking the local thermal equilibrium assumption were discussed in detail by Quintard and Whitkaer (1995). Equations (5) and (6), after invoking Eqs. (21), (22), and (23), are added together to lump into the following transient heat conduction equation for the solid-fluid mixture:

$$(\rho Cp)_m \frac{\partial \bar{T}}{\partial t} = \bar{\nabla} \cdot [k_e \bar{\nabla} \bar{T}] \tag{24}$$

where

$$(\rho Cp)_m = \phi \rho_f Cp_f + (1 - \phi)\rho_s Cp_s \tag{25}$$

is the heat capacitance and

$$k_e = \phi k_f + (1 - \phi)k_s + k_f(1 - \sigma)^2 G \tag{26}$$

the effective stagnant thermal conductivity of the mixture. Again, the value of k_e depends only on the microscopic interfacial geometry and the solid-fluid properties. Equation (24) resembles to the transient heat conduction of a pure substance whose solutions subjected to different initial and boundary conditions have been obtained extensively in open literature. Therefore, the main task becomes the determination of the effective stagnant thermal conductivity.

There exist several models for the effective stagnant thermal conductivity as mentioned in Section 1. For details of them, the readers are referred to the review article of Kaviany (1991) and Cheng and Hsu (1998). Here, we adopt the lumped composite layer model of Hsu et al. (1995) for in-line periodic array of three-dimensional cubes with the unit cell shown in Fig. 2. Using a composite layer scheme, they obtained the following expression for k_e/k_f:

$$k_e/k_f = 1 - \gamma_a^2 - 2\gamma_c\gamma_a + 2\gamma_c\gamma_a^2 + \sigma\gamma_c^2\gamma_a^2 + \frac{\sigma\gamma_a^2(1 - \gamma_c^2)}{\sigma + \gamma_a(1 - \sigma)} + \frac{2\sigma\gamma_c\gamma_a(1 - \gamma_a)}{\sigma + \gamma_c\gamma_a(1 - \sigma)} \tag{27}$$

with

$$1 - \phi = (1 - 3\gamma_c^2)\gamma_a^3 + 3\gamma_c^2\gamma_a^2 \tag{28}$$

where γ_c $(= c/a)$ is the touching parameter and γ_a $(= a/l_e)$ is length scale ratio of the cube particle to the unit cell. For given γ_c and ϕ, the value of γ_a is obtained from Eq. (28) and the results of k_e/k_f as a function of σ are then computed from Eq. (27). Figure 3 shows the results of k_e/k_f when $\phi = 0.36$ and $\gamma_c = 0.13$. The model predictions are in excellent agreement with the experimental data of Nozad et al. (1985). For nontouching cubes, $\gamma_c = 0$ and Eqs. (27) and (28) reduce to

$$\frac{k_e}{k_f} = [1 - (1 - \phi)^{2/3}] + \frac{\sigma(1 - \phi)^{2/3}}{\sigma + (1 - \sigma)(1 - \phi)^{1/3}}. \tag{29}$$

The predictions of k_e/k_f based on Eq. (29) for $\phi = 0.36$ are shown in Fig. 3. For comparison, the predictions based on Hsu et al.'s (1995) model for in-line two-dimensional array of cylinders are also included in Fig. 3.

5 Evaluation of Closure Coefficients

We now return to the transient heat conduction problem of local thermal nonequilibrium. To render Eqs. (21) and (22) applicable, analytical expressions for evaluating G and h_{fs} are required. They are described below.

Tortuosity Parameter G. Since the value of G depends only on the local interfacial geometry and on the solid and fluid thermal properties, it is plausible to assume that the expression for G obtained under the local thermal equilibrium condition can be extended to the thermal nonequilibrium regime. This bears the resemblance to the closure modeling of turbulent flows where a simple flow is usually used to evaluate the closure coefficient in a closure relation. Therefore, G is now obtained by solving Eq. (26):

$$G = \left[\frac{k_e}{k_f} - \phi - \sigma(1 - \phi)\right]/(1 - \sigma)^2 \tag{30}$$

where k_e/k_f is then determined by Eqs. (27) and (28).

To demonstrate the characteristics of G, the values of G were calculated from Eq. (30) over a wide range of ϕ, γ_c, and σ. Figure 4 shows the results of G for different γ_c with ϕ fixed at 0.36. The distinct feature is that G is always negative. This has to be the situation since $\phi + \sigma(1 - \phi)$, which represents the result of a lumped parallel two-layer model, is the upper limit of k_e/k_f. This implies that

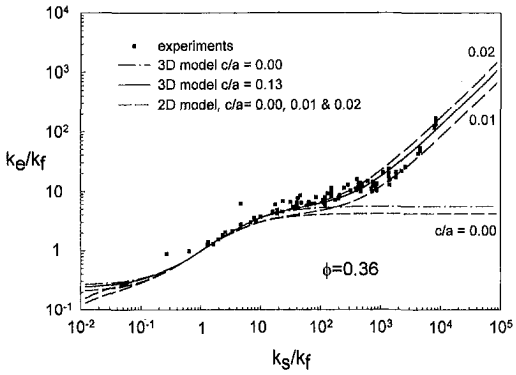

Fig. 3 The predictions of the effective stagnant thermal conductivity for media of in-line periodic array of three-dimensional cubes and two-dimensional cylinders, and their comparison to experimental data of Nozad et al. (1985)

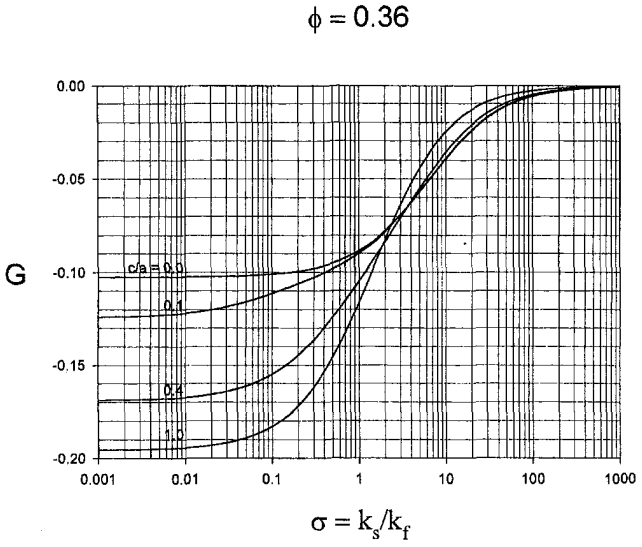

Fig. 4 The effect of particle-touching parameter on the tortuosity coefficient when the porosity is 0.36

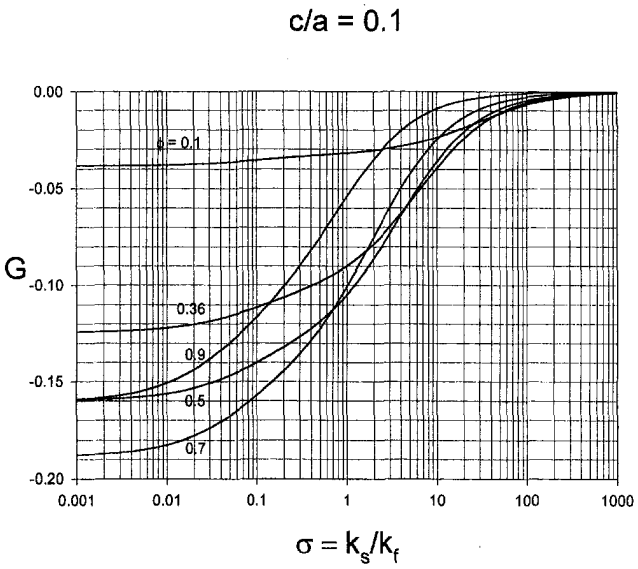

Fig. 5 The effect of porosity on the tortuosity coefficient when the particle-touching parameter is 0.1

the tortuosity effect is to reduce the effective thermal conduction by increasing the thermal path, i.e., the parallel layer model has the shortest thermal path. As shown in Fig. 4, the lower the thermal conductivity of solid than that of fluid, the more the thermal path undulates. The thermal path undulation is also enhanced by lateral particle touching. The lateral touching leads to a layer-in-series configuration to deter the thermal path. When $\sigma \ll 1$, a higher touching parameter means more lateral touching to produce more deterring of thermal path. The situation is reversed when $\sigma \gg 1$. The heat conduction is now dominated by the touching along the thermal path in reducing the tortuosity effect. At very high σ, the thermal lines are basically straight (i.e., $G \to 0$) since the solid particles have little thermal resistance as compared to fluids. These thermal lines are insensitive to the percentage of touching area. The case of $\sigma \to 1$ represents another interesting case where the solid and fluid have almost the same conductivity. Since $G \to -(1 - \gamma_a)[\gamma_a^3(1 - \gamma_c^2 - 2\gamma_c^3) + 2\gamma_a^2\gamma_c^2]$ when $\sigma \to 1$, the nonzero in G does not implies the tortuosity effect is nonzero under this limit as the change in the effective thermal conductivity due to tortuosity is given by $k_f(1 - \sigma)^2 G$. For normally packed spheres, the touching parameter γ_c is small and G can be approximated by $-[(1 - \phi) - (1 - \phi)^{4/3}]$, which equals to -0.088 if $\phi = 0.36$ as shown in Fig. 4.

Figure 5 shows the results of G when the touching parameter is fixed at $\gamma_c = 0.1$ while varying the porosity. Although the value of G is always negative, the variation of G with the porosity is not monotonic for different ranges of σ. In the range of $\sigma < 0.1$, minimal G occurs at ϕ near 0.7 and when $\sigma > 10$, near $\phi = 0.4$. Note that G becomes zero for both cases of $\phi = 0$ and 1, i.e., when the porous medium reduces to pure substance.

Interfacial Transfer Coefficient h_{fs}. To determine the interfacial transfer coefficient h_{fs}, we should base our analysis on dispersed particles undergoing quasi-steady heat conduction. Suppose a spherical particle at temperature $\bar{T}_s$ is suddenly introduced into a fluid of temperature $\bar{T}_f$ and, after a short time interval, the microscopic thermal diffusion at the interface has reached a quasi-steady state. This quasi-steady assumption for microscopic interfacial heat transfer is consistent with the quasi-steady closure-modeling scheme given in Section 3. By the same token, the validity of the quasi-steady model requires that the time scale of microscopic heat conduction is much smaller than that of macroscopic heat conduction. The stagnant interfacial heat transfer process then can be simplified to a model consisting of two heat conduction layers on the two sides of the interface as depicted in Fig. 6. By solving the steady-state heat conduction equation in a spherical coordinate system satisfying the boundary conditions $T_f = \bar{T}_f$ at $r = r_o$ and $T_s = \bar{T}_s$ at $r = r_i$, we obtain

$$T_f = \frac{q}{k_f 4\pi}\left(\frac{1}{r} - \frac{1}{r_o}\right) + \bar{T}_f \tag{31}$$

and

$$T_s = \frac{q}{k_s 4\pi}\left(\frac{1}{r} - \frac{1}{r_i}\right) + \bar{T}_s \tag{32}$$

where q is the heat flux through the interface. Positive q implies that the flux is from solid into fluid. By invoking the interface boundary condition, i.e., $T_f = T_s$ at $r = r_p$, into (31) and (32), we have

$$q = \frac{4\pi r_p k_f}{\dfrac{A}{1 + A} + \dfrac{B}{\sigma(1 - B)}}(\bar{T}_s - \bar{T}_f) \tag{33}$$

where $A = (r_o - r_p)/r_p$ and $B = (r_p - r_i)/r_p$ are the nondimensional thickness of the conduction layers. If there are n particles in REV, we have

$$Q_{fs} = nq/V \quad \text{and} \quad a_{fs} = n4\pi r_p^2/V = 6(1 - \phi)/d_p. \tag{34a, b}$$

Substituting (33) into (34a), invoking (34b), and then comparing the resultant equation to (22), we obtain

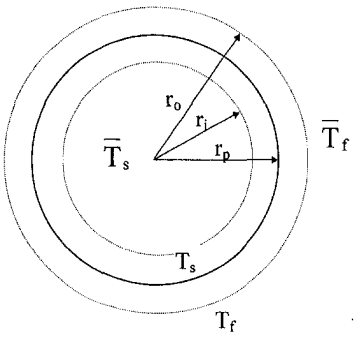

Fig. 6 The schematic of quasi-steady heat conduction of dispersed particles

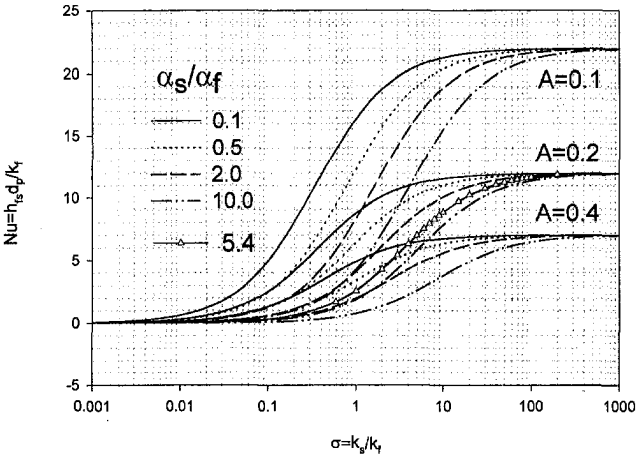

Fig. 7 The dependence of the Nusselt number of interfacial heat transfer on the local response time scale A and on the thermal properties of two phases, σ and β. The results of Quintard and Whitaker (1995) for ϕ = 0.36 are shown to be a special case of A = 0.2 and β = 5.4.

$$\mathrm{Nu} = \frac{h_{fs}d_p}{k_f} = \frac{2}{\dfrac{A}{1+A} + \dfrac{B}{\sigma(1-B)}} = \frac{2\sigma}{\alpha_A\sigma + \alpha_B} \tag{35}$$

where Nu is the Nusselt number for the interfacial heat transfer coefficient, $\alpha_A = A/(1 + A)$ and $\alpha_B = B/(1 - B)$. From the conservation of thermal energy, A and B are related by

$$\beta A^2 \frac{3 + A}{1 + A} = B^2 \frac{3 - B}{1 - B} \tag{36}$$

where $\beta = \alpha_s/\alpha_f$ is the thermal diffusivity ratio of solid to fluid.

The values of Nu are evaluated from Eqs. (35) and (36) for different values of A, σ, and β. The results are plotted in Fig. 7 as a function of σ for A = 0.1, 0.2, and 0.4, with β varying. Figure 7 indicates that Nu approaches zero when σ approaches zero. We also find that Nu approaches a constant when σ approaches infinite. When σ approaches zero, the solid particles behave as being nonconductive and little heat can transfer across the interface. On the other hand, when σ approaches infinite the particles become highly transmittable to thermal conduction and the heat flux across the interface depends solely on the thermal conductivity of fluids. In fact, the interfacial transfer coefficient h_{fs} becomes linearly proportional to the thermal conductivity of fluids and the proportional constant depends solely on A. The dependence of the interfacial transfer coefficient on the thermal diffusivity ratio β in the middle range of σ is interesting. From the quasi-steady model as depicted in Fig. 6, the effective thermal conductivity of the conduction layers near the solid-fluid interface resembles that of two layers in-series. This is implied from Eq. (35) where α_A/k_f and α_B/k_s are the effective thermal resistances for fluid and solid conduction layers, respectively. With the normalization of h_{fs} with respect to k_f, β is a measure of the relative thickness of the thermal layer inside the sphere. Higher β implies thicker thermal layer inside the sphere, and therefore lower value of Nu as implied by the layer-in-series model.

Quintard and Whitaker (1995) obtained an analytical expression for h_{fs} based on the unit cell of Chang (1983). Their expression for Nu can be rewritten into the same form as Eq. (35), but the coefficients α_A and α_B depend solely on the porosity. For comparison, the values of Nu are computed from their expression with ϕ = 0.36 and are also plotted in Fig. 7. We found that the results predicted from our present model become identical to those from Quintard and Whitaker's (1995) model if A = 0.2 and β = 5.4. However, it should be noted that the present model given by (35) and (36) is more general than Quintard and Whitaker's since their model depends only on ϕ and σ, but not on β. This β dependence is important as a consequence of enforcing the conservation of energy within the two phases.

Two limit cases for Nu are of interests and are discussed in the following. One is the case when the thermal diffusivities of solid and fluid are small that the thermal boundary layers are thin, i.e., A and B are small. Under the limit of small A and B, Eq. (36) reduces to $B = \sqrt{\beta}A$ which reconfirms the statement that the diffusion layer thickness is proportional to the root square of thermal diffusivity, and Eq. (35) becomes

$$\mathrm{Nu} = \frac{2}{A(1 + \sqrt{\beta/\sigma})}. \tag{37}$$

The other limit case occurs when β is very small, i.e., when the solid is thermally much less diffusive than fluid. Then B approaches zero and Nu $\rightarrow 2(1 + 1/A)$. This case behaves quite similarly to the case of $\sigma \rightarrow \infty$; it also resembles to the mass diffusion process in fluid phase, which depends solely on the mass diffusivity of fluid.

6 Concluding Remarks

In this study, a two-equation model is proposed for the transient heat conduction in porous media under the nonthermal equilibrium condition. Macroscopic equations for fluid and solid phases were obtained from the microscopic transient heat conduction equations through a phase averaging procedure. The averaging procedure leads to the closure problem where the number of unknowns become more than the number of equations. Closure relations for the two additional unknowns, namely, the tortuosity and interfacial heat transfer terms, are derived from the microscopic equations. The tortuosity constant G which appears in the closure relation is evaluated based on the lumped parameter model for the effective thermal conductivity proposed early by Hsu et al. (1995), while the interfacial heat transfer coefficient h_{fs} is based on a microscopic quasi-steady assumption.

The present result of G shows that G is always negative, i.e., the tortuosity effect is to reduce the effective thermal conductivities of fluid and solid. There is a minimum value of G at certain porosity because G approaches zero when the porosity approaches zero or one, i.e., when the media become pure substances. If the porosity is fixed, the absolute values of G appear to be largest as σ approaches zero, reduce monotonically as σ increases, and become zero as σ approaches infinite. This characteristics suggests that the results of G shown in Figs. 4 and 5 should apply only to media with packed solid particles as originally implied from the model of Hsu et al. (1995). For materials of different microscopic geometry such as sponges with phase symmetric property, other appropriate model for k_e/k_f such as the one proposed by Hsu et al. (1994) should be used. It is expected that the present two-equation model for transient heat conduction is applicable to a variety of media once the appropriate lumped parameter model for k_e/k_f is chosen.

The model for the interfacial heat transfer as proposed in this study indicates that Nu depends on the microscopic geometric parameter (or local response time scale parameter) A and the material thermal parameters σ and β. While the values of σ and β are determinative once the materials are chosen, the value of A depends on how the particles are packed, i.e., on the porosity. For dispersed particles immersed in fluid of large extent, the assessment of A is more subtle. However, for densely packed media it is expected that the thermal conduction in the fluid phase will be largely confined by the neighboring solid particles. The inverse dependence of Nu on A as shown in Eqs. (35) and (37) suggests that the interfacial transfer coefficient h_{fs} is sensitive to the time scale chosen for quasi-steady analysis. The equivalent radius r_e for the unit cell of Chang (1983) is given by $r_e/r_p = (1 - \phi)^{-1/3}$. If the microscopic interfacial heat transfer is assumed to reach a quasi-steady state when the diffusion length of thermal boundary layer in fluid becomes r_e, we have $1 + A = (1 - \phi)^{-1/3}$. For a medium with a typical value of ϕ = 0.36, we find that A = 0.16.

For medium with loosely packed particles, the value of A is expected to be larger than 0.16. We note that the proposed model for the interfacial Nusselt number Nu is based on spherical particles of uniform size. For media of nonuniform and/or nonspherical particles, the interfacial heat transfer coefficient h_{fs} is modified. Therefore, the dependence of Nu on A, σ and β may have to be resolved greatly by experiments, even though Nu may still behave similarly to that shown in Fig. 7.

It should be emphasized that the present model applies only for transient heat conduction, namely, only for stagnant heat conduction if the medium is filled with fluids. For fluids at motion, the interfacial heat transfer is enhanced strongly by heat convection. After compiled with earlier data Wakao, et al. (1979) suggested that the Nusselt number Nu* for interfacial heat transfer with convection could be correlated as

$$\mathrm{Nu}^* = h_{fs}^* d_p / k_f = 2 + 1.1\ \mathrm{Pr}^{1/3}\ \mathrm{Re}^{0.6} \tag{38}$$

where Pr is the Prandtl number and Re the Reynolds number based on the particle diameter. The correlation (38) indicates that $\mathrm{Nu}^* \rightarrow \mathrm{Nu} = 2$ (a constant) when $\mathrm{Re} \rightarrow 0$ (stagnant case). On the other hand, our present results shown in Fig. 7 indicates that the value of Nu for stagnant heat conduction depends strongly on the local geometry and the thermal properties of the two phases. In fact, the results compiled later by Wakao and Kaguei (1982) showed that there exists large scattering in the experimental data when Re is small. The scattering may have been due to this dependence of Nu on the local geometry and thermal property. The behavior of the interfacial heat transfer coefficient h_{fs}^* for transient heat convection in porous media remains unclear and will be investigated in a subsequent paper.

Acknowledgment

This work was supported by the Hong Kong Government through RGC Grant Nos. HKUST575/94E and HKUST815/96E. The author wishes to thank Mr. M. W. Wu and Mr. J. H. Sun for their assistance in carrying out the numerical work.

References

Amiri, A., and Vafai, K., 1994, "Analysis of dispersion effects and non-thermal equilibrium, non-Darcian, variable porosity incompressible flow through porous media," *Int. J. Heat Mass Transfer,* Vol. 37, pp. 939–954.

Chang, H. C., 1983, "Effective diffusion and conduction in two-phase media: A unified approach," *A.I.Ch.E. Journal,* Vol. 29, pp. 846–953.

Cheng, P., and Hsu, C. T., 1998, "Heat Conduction," *Transport Phenomena in Porous Media,* D. B. Ingham and I. Pop, eds., Pergamon Elsevier Science, London, pp. 57–76.

Deissler, R. G., and Boegli, J. S., 1958, "An Investigation of Effective Thermal Conductivities of Powders in Various Gases," *ASME Transactions,* Vol. 80, pp. 1417–1425.

Hsu, C. T., Cheng, P., and Wong, K. W., 1994, "Modified Zehner-Schlunder models for stagnant thermal conductivity of porous media," *Int. J. Heat Mass Transfer,* Vol. 37, pp. 2751–2759.

Hsu, C. T., Cheng, P., and Wong, K. W., 1995, "A Lumped Parameter Model for Stagnant Thermal Conductivity of Spatially Periodic Porous Media," ASME JOURNAL OF HEAT TRANSFER, Vol. 117, pp. 264–269.

Hsu, C. T., Wong, K. W., and Cheng, P., 1996, "Effective thermal conductivity of wire screens," *AIAA J. Thermophysics and Heat Transfer,* Vol. 10, pp. 542–545.

Kaviany, M., 1991, *Principles of Heat Transfer in Porous Media,* Springer-Verlag, New York.

Kuni, D., and Smith, J. M., 1960, "Heat transfer characteristics of porous rocks," *AIChE J.,* Vol. 6, pp. 71–78.

Maxwell, J. C., 1873, *A Treatise on Electricity and Magetism,* Clarenden Press, Oxford, p. 365.

Nozad, S., Carbonell, R. G., and Whitaker, S., 1985, "Heat conduction in multiphase systems, I: Theory and experiments for two-phase systems," *Chem. Engg. Sci.,* Vol. 40, pp. 843–855.

Quintard, M., and Whitaker, S., 1993, "One- and two-equation models for transient diffusion processes in two-phase systems," *Advances in Heat Transfer,* Vol. 23, pp. 369–367.

Quintard, M., and Whitaker, S., 1995, "Local thermal equilibrium for transient heat conduction: Theory and comparison with numerical experiments," *Int. J. Heat Mass Transfer,* Vol. 38, pp. 2779–2796.

Rayleigh, Lord, 1892, "On the influence of obstacles arranged in rectangular order upon the properties of a medium," *Philosophical Magazine,* Vol. LV1, pp. 481–502.

Sahraoui, M., and Kaviany, M., 1993, "Slip and non-slip temperature boundary conditions at interface of porous, plain media: Conduction," *Int. J. Heat Mass Transfer,* Vol. 36, pp. 1019–1033.

Wakao, N., Kaguei, S., and Funazkri, T., 1979, "Effect of fluid dispersion coefficients on particle-to-fluid heat transfer coefficients in packed beds," *Chem. Engg. Sci.,* Vol. 34, pp. 325–336.

Wakao, N., and Kaguei, S., 1982, *Heat and Mass Transfer in Packed Beds,* Gordon and Breach, New York, p. 294.

Zehner, P., and Schlunder, E. U., 1970, "Thermal conductivity of granular materials at moderate temperatures," [in German] *Chemie. Ingr.-Tech.,* Vol. 42, pp. 933–941 (in German).

Transient Temperature Computation for a System of Multiply Contacting Spheres in a 180-Degree Orientation

W. W. M. Siu[1,2] and S. H.-K. Lee[1,3]

Nomenclature

C = thermal constriction capacitance, W-s/K
Fo = Fourier number, $\alpha\tau/r^2$
q = heat flux, W/m^2
Q = total heat transfer, W
R = thermal constriction resistance, K/W
T = temperature, K

Greek

α = thermal diffusivity, m^2/s
γ = ratio of contact radius to sphere radius, r_c/r_s
τ = time, s

Subscripts

b = bulk temperature
c = contact
i = initial value
s = sphere, or length scale with r_s
ss = steady-state value

1 Introduction

Systems of contacting spheres are common in engineering applications such as cryogenic insulation, catalytic beds, and energy storage systems. For such systems, the heat transfer analysis can be quite complicated due to the complex geometrical contact arrangement and the transient behavior. Due to these complexities, most of the previous work in this area has adopted the porous media approach, where the effective thermal conductivity of a representative cell is either measured or computed analytically using some lumped-parameter model (cf. Hsu et al., 1994). However, this approach requires the length scale of the representative cell to be roughly three orders of magnitude larger than the size of the spheres (Kaviany, 1995). Consequently, the temperature solution obtained from the porous media approach may not be suitable for applications such as powder sintering where the spatial resolution requirement is significant.

Using a different approach Argento and Bouvard (1996) re-

[1] Department of Mechanical Engineering, The Hong Kong University of Science & Technology, Clear Water Bay, Kowloon, Hong Kong.

[2] Graduate Student. e-mail: meswm@ust.hk.

[3] Assistant Professor. e-mail: shklee@ust.hk. Mem. ASME.

Contributed by the Heat Transfer Division for publication in the JOURNAL OF HEAT TRANSFER and presented at '97 NHTC, Baltimore. Manuscript received by the Heat Transfer Division, July 1, 1998; revision received, Jan. 6, 1999. Keywords: Conduction, Contact Resistance, Heat Transfer, Packed beds, Porous Media. Associate Technical Editor: M. Kaviany.

For medium with loosely packed particles, the value of A is expected to be larger than 0.16. We note that the proposed model for the interfacial Nusselt number Nu is based on spherical particles of uniform size. For media of nonuniform and/or nonspherical particles, the interfacial heat transfer coefficient h_{fs} is modified. Therefore, the dependence of Nu on A, σ and β may have to be resolved greatly by experiments, even though Nu may still behave similarly to that shown in Fig. 7.

It should be emphasized that the present model applies only for transient heat conduction, namely, only for stagnant heat conduction if the medium is filled with fluids. For fluids at motion, the interfacial heat transfer is enhanced strongly by heat convection. After compiled with earlier data Wakao, et al. (1979) suggested that the Nusselt number Nu* for interfacial heat transfer with convection could be correlated as

$$\mathrm{Nu}^* = h_{fs}^* d_p / k_f = 2 + 1.1\ \mathrm{Pr}^{1/3}\ \mathrm{Re}^{0.6} \tag{38}$$

where Pr is the Prandtl number and Re the Reynolds number based on the particle diameter. The correlation (38) indicates that $\mathrm{Nu}^* \rightarrow \mathrm{Nu} = 2$ (a constant) when $\mathrm{Re} \rightarrow 0$ (stagnant case). On the other hand, our present results shown in Fig. 7 indicates that the value of Nu for stagnant heat conduction depends strongly on the local geometry and the thermal properties of the two phases. In fact, the results compiled later by Wakao and Kaguei (1982) showed that there exists large scattering in the experimental data when Re is small. The scattering may have been due to this dependence of Nu on the local geometry and thermal property. The behavior of the interfacial heat transfer coefficient h_{fs}^* for transient heat convection in porous media remains unclear and will be investigated in a subsequent paper.

Acknowledgment

This work was supported by the Hong Kong Government through RGC Grant Nos. HKUST575/94E and HKUST815/96E. The author wishes to thank Mr. M. W. Wu and Mr. J. H. Sun for their assistance in carrying out the numerical work.

References

Amiri, A., and Vafai, K., 1994, "Analysis of dispersion effects and non-thermal equilibrium, non-Darcian, variable porosity incompressible flow through porous media," *Int. J. Heat Mass Transfer,* Vol. 37, pp. 939–954.

Chang, H. C., 1983, "Effective diffusion and conduction in two-phase media: A unified approach," *A.I.Ch.E. Journal,* Vol. 29, pp. 846–953.

Cheng, P., and Hsu, C. T., 1998, "Heat Conduction," *Transport Phenomena in Porous Media,* D. B. Ingham and I. Pop, eds., Pergamon Elsevier Science, London, pp. 57–76.

Deissler, R. G., and Boegli, J. S., 1958, "An Investigation of Effective Thermal Conductivities of Powders in Various Gases," *ASME Transactions,* Vol. 80, pp. 1417–1425.

Hsu, C. T., Cheng, P., and Wong, K. W., 1994, "Modified Zehner-Schlunder models for stagnant thermal conductivity of porous media," *Int. J. Heat Mass Transfer,* Vol. 37, pp. 2751–2759.

Hsu, C. T., Cheng, P., and Wong, K. W., 1995, "A Lumped Parameter Model for Stagnant Thermal Conductivity of Spatially Periodic Porous Media," ASME JOURNAL OF HEAT TRANSFER, Vol. 117, pp. 264–269.

Hsu, C. T., Wong, K. W., and Cheng, P., 1996, "Effective thermal conductivity of wire screens," *AIAA J. Thermophysics and Heat Transfer,* Vol. 10, pp. 542–545.

Kaviany, M., 1991, *Principles of Heat Transfer in Porous Media,* Springer-Verlag, New York.

Kuni, D., and Smith, J. M., 1960, "Heat transfer characteristics of porous rocks," *AIChE J.,* Vol. 6, pp. 71–78.

Maxwell, J. C., 1873, *A Treatise on Electricity and Magetism,* Clarenden Press, Oxford, p. 365.

Nozad, S., Carbonell, R. G., and Whitaker, S., 1985, "Heat conduction in multiphase systems, I: Theory and experiments for two-phase systems," *Chem. Engg. Sci.,* Vol. 40, pp. 843–855.

Quintard, M., and Whitaker, S., 1993, "One- and two-equation models for transient diffusion processes in two-phase systems," *Advances in Heat Transfer,* Vol. 23, pp. 369–367.

Quintard, M., and Whitaker, S., 1995, "Local thermal equilibrium for transient heat conduction: Theory and comparison with numerical experiments," *Int. J. Heat Mass Transfer,* Vol. 38, pp. 2779–2796.

Rayleigh, Lord, 1892, "On the influence of obstacles arranged in rectangular order upon the properties of a medium," *Philosophical Magazine,* Vol. LV1, pp. 481–502.

Sahraoui, M., and Kaviany, M., 1993, "Slip and non-slip temperature boundary conditions at interface of porous, plain media: Conduction," *Int. J. Heat Mass Transfer,* Vol. 36, pp. 1019–1033.

Wakao, N., Kaguei, S., and Funazkri, T., 1979, "Effect of fluid dispersion coefficients on particle-to-fluid heat transfer coefficients in packed beds," *Chem. Engg. Sci.,* Vol. 34, pp. 325–336.

Wakao, N., and Kaguei, S., 1982, *Heat and Mass Transfer in Packed Beds,* Gordon and Breach, New York, p. 294.

Zehner, P., and Schlunder, E. U., 1970, "Thermal conductivity of granular materials at moderate temperatures," [in German] *Chemie. Ingr.-Tech.,* Vol. 42, pp. 933–941 (in German).

Transient Temperature Computation for a System of Multiply Contacting Spheres in a 180-Degree Orientation

W. W. M. Siu[1,2] and S. H.-K. Lee[1,3]

Nomenclature

C = thermal constriction capacitance, W-s/K
Fo = Fourier number, $\alpha\tau/r^2$
q = heat flux, W/m^2
Q = total heat transfer, W
R = thermal constriction resistance, K/W
T = temperature, K

Greek

α = thermal diffusivity, m^2/s
γ = ratio of contact radius to sphere radius, r_c/r_s
τ = time, s

Subscripts

b = bulk temperature
c = contact
i = initial value
s = sphere, or length scale with r_s
ss = steady-state value

1 Introduction

Systems of contacting spheres are common in engineering applications such as cryogenic insulation, catalytic beds, and energy storage systems. For such systems, the heat transfer analysis can be quite complicated due to the complex geometrical contact arrangement and the transient behavior. Due to these complexities, most of the previous work in this area has adopted the porous media approach, where the effective thermal conductivity of a representative cell is either measured or computed analytically using some lumped-parameter model (cf. Hsu et al., 1994). However, this approach requires the length scale of the representative cell to be roughly three orders of magnitude larger than the size of the spheres (Kaviany, 1995). Consequently, the temperature solution obtained from the porous media approach may not be suitable for applications such as powder sintering where the spatial resolution requirement is significant.

Using a different approach Argento and Bouvard (1996) re-

[1] Department of Mechanical Engineering, The Hong Kong University of Science & Technology, Clear Water Bay, Kowloon, Hong Kong.

[2] Graduate Student. e-mail: meswm@ust.hk.

[3] Assistant Professor. e-mail: shklee@ust.hk. Mem. ASME.

Contributed by the Heat Transfer Division for publication in the JOURNAL OF HEAT TRANSFER and presented at '97 NHTC, Baltimore. Manuscript received by the Heat Transfer Division, July 1, 1998; revision received, Jan. 6, 1999. Keywords: Conduction, Contact Resistance, Heat Transfer, Packed beds, Porous Media. Associate Technical Editor: M. Kaviany.

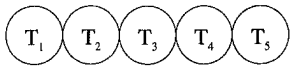

Fig. 1 Schematic of a multisphere system in a 180-deg orientation

cently completed a study in which the effective thermal conductivity of spheres in random packing was numerically determined by back-calculating from the steady-state temperature distribution within the packing. This distribution was obtained by using the constriction resistance to locally enforce conservation of energy. As defined in Eq. (1), the constriction resistance represents the resistance to the energy transfer between two objects with a temperature difference of ΔT, and is in addition to the contact resistance which is also neglected in the present study.

$$Q = \frac{\Delta T}{R} \Rightarrow R \equiv \frac{\Delta T}{Q} = \frac{\Delta T}{-kA \left.\dfrac{\partial T}{\partial r}\right|_{\text{contact}}} \tag{1}$$

Equation (1) seems straightforward and, as in the study by Argento and Bouvard (1996), it is typically used as a constitutive relation in the formulation of a steady-state energy equation. Although few have used it in a transient formulation, it would seem to be a natural extension. However, this extension is in fact not trivial. For one thing, the value of the constriction resistance (hereafter referred to as the resistance or R) is not a constant, and so different values are required for steady-state and transient formulations (Siu and Lee, 1997). In addition, the meaning of the driving potential, ΔT, requires further consideration for transient formulations. This is the motivation for the present study. The objective is to develop a transient formulation that could compute the temperature development of a packed-sphere system, but retains the spatial resolution to that of a sphere. To achieve this, the constriction resistance concept in Eq. (1) was utilized, and multiply contacting spheres in a 180-deg orientation was chosen as the vehicle as it introduced minimum geometrical effects. The present results demonstrate the necessity of a correction factor, which is herein referred to as the constriction capacitance.

2 Analysis

Shown in Fig. 1 is a schematic of a multisphere system in a 180-deg orientation. To compute the transient temperature of this system, the change in the internal energy of each sphere can be related to the net incoming energy from the immediately neighboring spheres. In turn, such energy can be computed with the driving potential, ΔT, which is the difference of the contacting spheres' bulk temperatures, and the corresponding resistance, R, between these two spheres. Applying these definitions, the energy conservation, for the jth sphere in a system containing M spheres, is given below by Eq. (2). In this equation, $j-1$ and $j+1$ are the spheres in contact with the jth sphere, T_b is the bulk temperature of the sphere as defined in Eq. (3), and R_{jk} is the resistance between the jth and kth spheres. In general, this resistance depends on the geometry and the boundary conditions, and, since very few of the existing relations are applicable for the present configuration, the relations derived earlier by Siu and Lee (1997) were used in this study.

$$\rho C_p V \frac{dT_{b,j}}{d\tau} = \sum_{k=j-1}^{j+1} \frac{(T_{b,k} - T_{b,j})}{R_{jk}}, \quad j = 1, M \tag{2}$$

$$T_b = \frac{1}{V} \int T(r, \theta, \phi) dV \tag{3}$$

Although Eq. (2) is conceptually correct, an error is incurred due to the usage of the bulk temperature, which causes an instantaneous redistribution of energy. Consider, for example, a three-sphere system where sphere-1 contacts sphere-2 which in turns contacts sphere-3. During the initial transient period, the interaction between sphere-1 and sphere-2 is limited to the immediate vicinity of the contacting area, as is the interaction between sphere-2 and sphere-3. Since these two contacting areas are physically apart from each other, a certain amount of time must pass before they affect each other. However, in using the bulk temperature as the driving potential, these two interactions become directly and immediately coupled with each other. Consequently, this leads to an error in the transient computation. Furthermore, as will be demonstrated later, this error is cumulative and can become substantial for a system containing a large number of spheres.

2.1 Constriction Capacitance. Thus, while Eq. (2) is correct in concept, the usage of the bulk temperature induces an error for transient computations. To adjust for this transient error, a correction factor is sought which could retain the usage of the bulk temperature and the form in Eq. (2). Since the error is directly related to the change of the temperature with respected to time, it is reasonable to assume the correction factor to take the form of a first-order derivative with respect to time. Thus, this correction factor has the form of a capacitance, and hence it is referred to as the constriction capacitance. This is not a real capacitance effect, but is used in the same spirit as the term constriction resistance. That is, neither the constriction resistance nor capacitance is real, but both are necessitated by the choice of the driving potential. Through numerical experiments, a proper correction factor was found, which when combined with the bulk temperature expression, yields the form given below in Eq. (4). Thus, the transient temperature of a multisphere system can be computed by applying Eq. (2), with the term inside the summation substituted by the right-hand side of Eq. (4). This modified equation is given below in Eq. (5). By applying Eq. (5) to each sphere of the system, a set of coupled, linear ordinary differential equations can be obtained and the solution to which is the bulk temperature development of each sphere in the system.

$$Q_{ij} = \frac{\Delta T_{ij}}{R} \pm C \left| \frac{dT_c}{d\tau} \right| \tag{4}$$

$$\rho C_p V \frac{dT_{b,j}}{d\tau} = \sum_{k=j-1}^{j+1} \left[\frac{(T_{b,k} - T_{b,j})}{R_{jk}} \pm C_{jk} \left| \frac{dT_c}{d\tau} \right| \right], \quad j = 1, M \tag{5}$$

$$T_c = \frac{T_{b,j} + T_{b,k}}{2} \tag{6}$$

In Eq. (5), C is the constriction capacitance and T_c is the temperature of the contact surface, which is simply the arithmetic mean of the contacting spheres' bulk temperatures as given in Eq. (6). The correction term is either added to or subtracted from the original expression in Eq. (2). There is a set of rules that determines whether to add or subtract the correction factor. For any spheres with two contacting areas, correction factors must be applied to both contact areas, which are referred to as site-A and site-B. At site-A, the correction factor is subtracted if heat is flowing in from site-B, and vice versa, the correction factor at site-A is added if heat is flowing out from site-B. This rule only applies for interior spheres with more than one contact areas. Spheres at the two ends having only one contact area will have the correction factor taking the opposite action as the immediately adjacent correction factor.

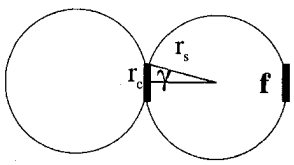

Fig. 2 Schematic of the contact area radius r_c, the sphere radius r_s, and their ratio γ

2.2 Configuration and Formulation. The solution to Eq. (5) hinges on the availability of the constriction capacitance, which is presently computed by utilizing a two-sphere system and applying Eq. (4) to area "f." As shown in Fig. 2, area f is the same size as the contact area, which is subtended by an angle, 2γ, with γ being less than 0.1 to minimize the error from physical deformation (Dellis et al., 1994). Since area f is fictitious, it has no particular relevance except the radial heat flow there is equal to zero. Thus, by applying Eq. (4) to this area, the capacitance can be computed from the expression given below in Eq. (7), where R is the resistance between the two contacting spheres, while T_f and T_b are both taken from the same sphere.

$$C = \left| \frac{\dfrac{T_f - T_b}{R/2}}{\dfrac{dT_f}{d\tau}} \right| \tag{7}$$

The solution to Eq. (7) requires the resistance, as well as the transient development of T_b and T_f. While the resistance can be taken from the previous study (Siu and Lee, 1997), the transient development of T_b and T_f would require knowledge of the temperature distribution within the spheres. These distributions are, in turn, obtained by directly solving Eq. (8) for a two-sphere system, in which the radii were taken to be 0.001 m, while the thermal conductivity, density, and specific heat were, respectively, taken to be 13.4 W/m-K, 8238 kg/m^3, and 468 J/kg-K. The two spheres were each initially at a different uniform temperature, and were suddenly brought into contact inside a vacuum environment. Continuity of temperature and energy were imposed at the contacting area while the remaining area was insulated. As given below in Eq. (9), these boundary conditions were implemented by iterating the contact temperature at the same time-step until convergence, which was typically less than 10^{-7}. Once Eq. (7) is solved, the capacitance values between two contacting spheres can be obtained and correlated for future usage.

$$\frac{\partial T}{\partial \tau} = \alpha \left[\frac{1}{r^2} \frac{\partial}{\partial r} \left(r^2 \frac{\partial T}{\partial r} \right) + \frac{1}{r^2 \sin\theta} \frac{\partial}{\partial \theta} \left(\sin\theta \frac{\partial T}{\partial \theta} \right) \right] \tag{8}$$

$$0 < \theta < \gamma \quad Q_1 = -Q_2$$

$$\Rightarrow -kA \left. \frac{\partial T}{\partial r} \right|_{r=r_s(\text{sphere 1})} = kA \left. \frac{\partial T}{\partial r} \right|_{r=r_s(\text{sphere 2})}$$

$$T\,(r = r_s,\ \text{sphere 1}) = T\,(r = r_s,\ \text{sphere 2})$$

$$\gamma < \theta < \pi \quad Q_1 = Q_2 = 0 \tag{9}$$

2.3 Method of Solution. The terms in Eq. (8) were approximated by a second-order finite volume scheme. The higher order of accuracy was necessary to properly capture the conditions at the contact. The finite volume scheme was utilized to simplify and increase the accuracy of the bulk temperature computation given in Eq. (3), which for a finite difference scheme would have required interpolation at the large gradient region near the contact.

After applying the finite volume approximation, the resulting algebraic expressions were solved on a nonuniform grid in order to further ensure the proper capturing of the large spatial gradients near the surface of the sphere and during the initial transient period. Thus, a constant-ratio grid was implemented in the radial and angular directions (Patankar, 1980). The resulting algebraic equations were solved using the TDMA in conjunction with a Crank-Nicolson scheme (Jaluria and Torrance, 1986). A time-step corresponding to the smallest grid size was chosen for the entire region.

Once the constriction capacitance has been determined, Eq. (5) was utilized to compute the temperature development in a system of multiply contacting spheres in a 180-deg orientation. Thus, for M spheres, each having two neighbors, the result was M equations, each having two heat-flux terms. This produced a system of coupled, first-order differential equations, which was also solved using the TDMA and Crank-Nicolson schemes.

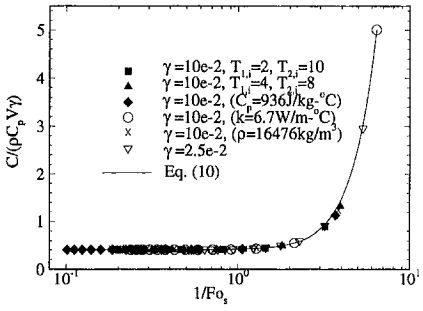

Fig. 3 Correlation of the dimensionless capacitance of the two-sphere system

3 Results and Discussion

For the present study, validation is required for the computations of the capacitance, which essentially translates to validating the solution to Eq. (8). As this has been validated in a previous study (Siu and Lee, 1997), it will not be repeated here. Validation is also required to verify the solution from Eq. (5), but this is, in fact, part of the results of this study, and will be discussed in Section 3.3.

3.1 Correlation of the Constriction Capacitance. The capacitance was back calculated from the two-sphere case as described in the previous section. In order for this to be useful, a correlation must be obtained. Since the capacitance should depend on the contact radius as well as parameters that affect the internal energy, it was scaled by the contact radius ratio, the density, the specific heat, as well as the volume of the spheres. The dimensionless capacitance was computed for several cases and over a wide range of Fourier number (based on sphere radius). As shown in Fig. 3, a correlation was obtained that collapsed these results onto a single curve. This correlation is given below in Eq. (10). Note in Fig. 3 the usage of a semi-log scale for clarification purpose and the critical Fourier number of unity, beyond which the capacitance reaches a steady-state value. For systems with a Fourier number smaller than 1, there will be difficulties in implementing Eq. (5), as the algorithm must then track the time scale for each sphere in the system. In the current study, and for most sintering systems, the Fourier number was around 10^4.

$$\frac{C}{\rho C_p V \gamma} = 0.40434 - 3.7789 \times 10^{-3} \frac{1}{\text{Fo}_s} - 6.545 \times 10^{-3} \frac{1}{\text{Fo}_s^2} + 1.87363 \times 10^{-2} \frac{1}{\text{Fo}_s^3} \tag{10}$$

where $\text{Fo}_s = \alpha\tau / r_s^2$.

3.2 Transient Computations for Multiply Contacting Spheres. To verify its applicability, Eq. (5) was used to compute the bulk temperatures in systems of three and five contacting spheres. For the three-sphere system, the radius, thermal conductivity, density, and specific heat of the sphere were taken to be 0.001 m, 13.4 W/m-K, 8238 kg/m^3, and 468 J/kg-K, respectively. For the five-sphere system, the properties of the spheres were changed in order to quickly obtain the steady-state solution. As such, the thermal conductivity, density, and specific heat of the sphere were change to 250 W/m-K, 5000 kg/m^3, and 500 J/kg-K, respectively. The resulting solution was then compared against the finite volume results obtained by solving Eq. (8) for each sphere in the system. For the three-sphere system the comparison is shown in Fig. 4, and for the five-sphere system the comparison is shown in Fig. 5. In both these figures, the agreement was excellent. Obviously, it would be preferable to make the above comparison for larger number of spheres, but the accompanying solution to Eq. (8) would require a tremendous amount of computational

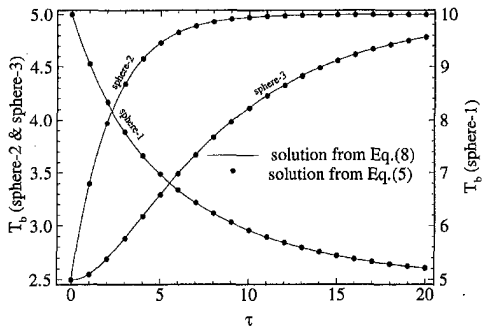

Fig. 4 Computation of the transient temperature development in a three-sphere system

resource. As is, solving Eq. (8) for five contacting spheres required over 100 CPU hours on the Sparc 20.

To verify the necessity of the correction factor, computations were made for systems of 5, 10, and 20 contacting spheres. The properties of these spheres were the same as those for the five-sphere system. For each system, the temperature was computed using both Eqs. (2) and (5). Thus, a comparison of the results indicates the importance of the correction factor. In all three cases, the temperature of sphere-1 was initially at 500°C, while the remaining spheres were initially at 5°C. Figure 6 shows the error incurred at the last sphere in the chain, if the computation were performed without the correction factor. This error decreases with time but increases with the number of spheres in the system. For the current parameters, there is a time period of two seconds prior to which the temperature distribution of a 20-sphere system would have a considerable error.

4 Conclusion

Due to its practical relevance, it is often of interest to compute the transient temperature of a system of spheres. In using the constriction resistance to compute the transient temperature of a multisphere system, it was discovered that a correction factor is required. This correction factor took the form of a capacitance, and it has been correlated against the Fourier number based on the sphere radius. Using this correction factor, the transient temperature of three and five contacting spheres in a 180-deg orientation was successfully computed. Finally, computations were also performed for systems of 5, 10, and 20 contacting spheres. The results showed that computations, which neglected this correction factor, produce results with a considerable error. This error decreased with increasing time periods and increased with the number of spheres in the system.

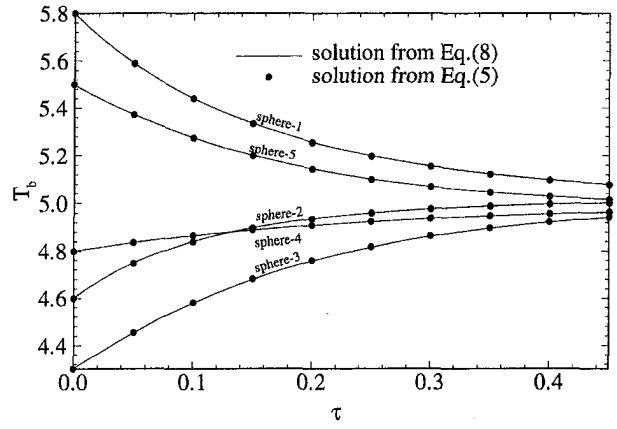

Fig. 5 Computation of the transient temperature development in a five-sphere system

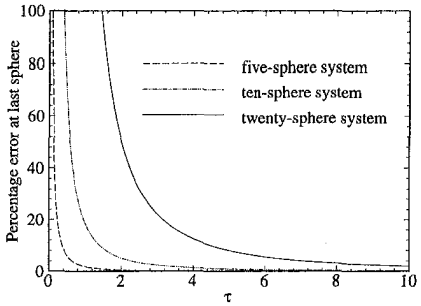

Fig. 6 Plot showing effect of neglecting the correction factor in computing the transient temperature of 5, 10, and 20 spheres

Acknowledgment

The authors acknowledge the financial support from the Department of Mechanical Engineering, the University Grant Council (Grant #DAG93/94.EG26) and the Research Grant Council of the Hong Kong SAR Government (Grant #HKUST807/96E).

References

Argento, C., and Bouvard, D., 1996, "Modeling the Effective Thermal Conductivity of Random Packing of Spheres through Densification," *International Journal of Heat and Mass Transfer,* Vol. 39, No. 7, pp. 1343–1350.

Dellis, C., Bouvard, D., and Stutz, P., 1994, "Numerical Modeling of Particle Deformation," *Hot Isostatic Pressing '93,* Elsevier Science, Amsterdam.

Hsu, C. T., Cheng, P., and Wong, K. W., 1994, "Modified Zehner-Schlunder Models for Stagnant Thermal Conductivity of Porous Media," *International Journal of Heat & Mass Transfer,* Vol. 29, pp. 2751–2759.

Jaluria, Y., and Torrance, K. E., 1986, *Computational Heat Transfer,* Hemisphere, New York.

Kaviany, M., 1995, *Principle of Heat Transfer in Porous Media,* Springer-Verlag, New York.

Patankar, S. V., 1980, *Numerical Heat Transfer and Fluid Flow,* Hemisphere, New York.

Siu, W. W. M., and Lee, S. H.-K., 1997, "Transient Temperature Computation for a System of Multiple Contacting Spheres in 180 degree Orientation," ASME HTD-Vol. 339, ASME, New York, pp. 151–160.

Analysis of Spray Cooling Heat Flux

G. W. Liu,[1] Y. S. Morsi,[2] and J. P. Van Der Walt[3]

Introduction

Spray cooling provides high heat flux through the continuous formation and evaporation of a thin liquid film on a hot surface. It is important for industry to predict the spray cooling heat transfer coefficient and critical heat flux for given spray and surface conditions. The spray cooling heat flux is a function of many parameters such as the spray hydrodynamic parameters, the properties of the coolant, as well as the properties and surface conditions of the hot metal. As a metallic block is

[1] Modeling and Process Analysis Group, School of Engineering and Science, Swinburne University of Technology, John Street, Hawthorn P. O. Box 218, Victoria 3122, Australia. e-mail: gwliu@swin.edu.au.

[2] Professor, Modeling and Process Analysis Group, School of Engineering and Science, Swinburne University of Technology, John Street, Hawthorn P. O. Box 218, Victoria 3122, Australia. e-mail: ymorsi@swin.edu.au.

[3] Doctor, Modeling and Process Analysis Group, School of Engineering and Science, Swinburne University of Technology, John Street, Hawthorn P. O. Box 218, Victoria 3122, Australia. e-mail: jvanderwalt@swin.edu.au.

Contributed by the Heat Transfer Division for publication in the JOURNAL OF HEAT TRANSFER. Manuscript received by the Heat Transfer Division, Aug. 15, 1998; revision received, Apr. 10, 1999. Keywords: Cooling, Evaporation, Heat Transfer, Impingement, Sprays. Associate Technical Editor: J. Han.

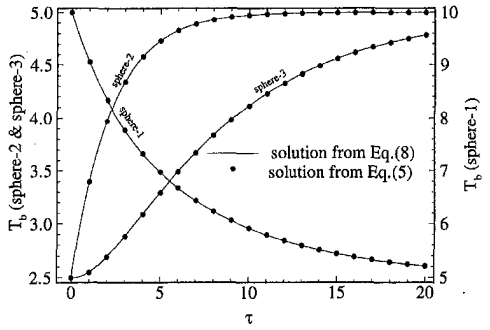

Fig. 4 Computation of the transient temperature development in a three-sphere system

resource. As is, solving Eq. (8) for five contacting spheres required over 100 CPU hours on the Sparc 20.

To verify the necessity of the correction factor, computations were made for systems of 5, 10, and 20 contacting spheres. The properties of these spheres were the same as those for the five-sphere system. For each system, the temperature was computed using both Eqs. (2) and (5). Thus, a comparison of the results indicates the importance of the correction factor. In all three cases, the temperature of sphere-1 was initially at 500°C, while the remaining spheres were initially at 5°C. Figure 6 shows the error incurred at the last sphere in the chain, if the computation were performed without the correction factor. This error decreases with time but increases with the number of spheres in the system. For the current parameters, there is a time period of two seconds prior to which the temperature distribution of a 20-sphere system would have a considerable error.

4 Conclusion

Due to its practical relevance, it is often of interest to compute the transient temperature of a system of spheres. In using the constriction resistance to compute the transient temperature of a multisphere system, it was discovered that a correction factor is required. This correction factor took the form of a capacitance, and it has been correlated against the Fourier number based on the sphere radius. Using this correction factor, the transient temperature of three and five contacting spheres in a 180-deg orientation was successfully computed. Finally, computations were also performed for systems of 5, 10, and 20 contacting spheres. The results showed that computations, which neglected this correction factor, produce results with a considerable error. This error decreased with increasing time periods and increased with the number of spheres in the system.

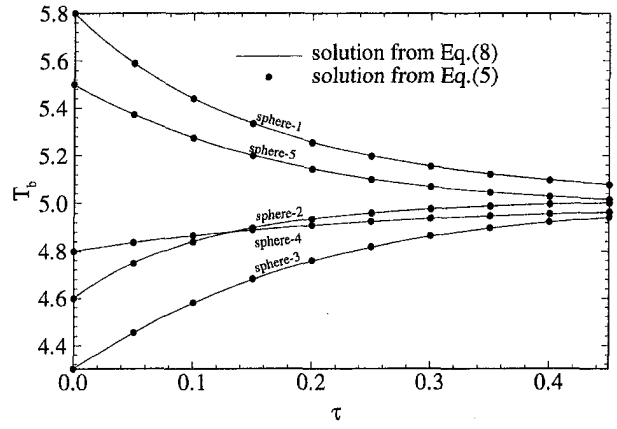

Fig. 5 Computation of the transient temperature development in a five-sphere system

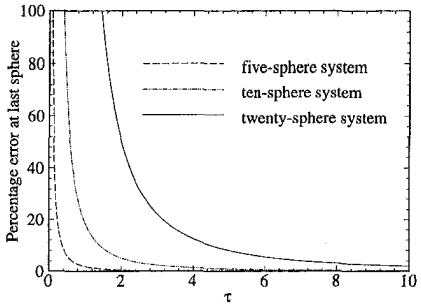

Fig. 6 Plot showing effect of neglecting the correction factor in computing the transient temperature of 5, 10, and 20 spheres

Acknowledgment

The authors acknowledge the financial support from the Department of Mechanical Engineering, the University Grant Council (Grant #DAG93/94.EG26) and the Research Grant Council of the Hong Kong SAR Government (Grant #HKUST807/96E).

References

Argento, C., and Bouvard, D., 1996, "Modeling the Effective Thermal Conductivity of Random Packing of Spheres through Densification," *International Journal of Heat and Mass Transfer,* Vol. 39, No. 7, pp. 1343–1350.

Dellis, C., Bouvard, D., and Stutz, P., 1994, "Numerical Modeling of Particle Deformation," *Hot Isostatic Pressing '93,* Elsevier Science, Amsterdam.

Hsu, C. T., Cheng, P., and Wong, K. W., 1994, "Modified Zehner-Schlunder Models for Stagnant Thermal Conductivity of Porous Media," *International Journal of Heat & Mass Transfer,* Vol. 29, pp. 2751–2759.

Jaluria, Y., and Torrance, K. E., 1986, *Computational Heat Transfer,* Hemisphere, New York.

Kaviany, M., 1995, *Principle of Heat Transfer in Porous Media,* Springer-Verlag, New York.

Patankar, S. V., 1980, *Numerical Heat Transfer and Fluid Flow,* Hemisphere, New York.

Siu, W. W. M., and Lee, S. H.-K., 1997, "Transient Temperature Computation for a System of Multiple Contacting Spheres in 180 degree Orientation," ASME HTD-Vol. 339, ASME, New York, pp. 151–160.

Analysis of Spray Cooling Heat Flux

G. W. Liu,[1] Y. S. Morsi,[2] and J. P. Van Der Walt[3]

Introduction

Spray cooling provides high heat flux through the continuous formation and evaporation of a thin liquid film on a hot surface. It is important for industry to predict the spray cooling heat transfer coefficient and critical heat flux for given spray and surface conditions. The spray cooling heat flux is a function of many parameters such as the spray hydrodynamic parameters, the properties of the coolant, as well as the properties and surface conditions of the hot metal. As a metallic block is

[1] Modeling and Process Analysis Group, School of Engineering and Science, Swinburne University of Technology, John Street, Hawthorn P. O. Box 218, Victoria 3122, Australia. e-mail: gwliu@swin.edu.au.

[2] Professor, Modeling and Process Analysis Group, School of Engineering and Science, Swinburne University of Technology, John Street, Hawthorn P. O. Box 218, Victoria 3122, Australia. e-mail: ymorsi@swin.edu.au.

[3] Doctor, Modeling and Process Analysis Group, School of Engineering and Science, Swinburne University of Technology, John Street, Hawthorn P. O. Box 218, Victoria 3122, Australia. e-mail: jvanderwalt@swin.edu.au.

Contributed by the Heat Transfer Division for publication in the JOURNAL OF HEAT TRANSFER. Manuscript received by the Heat Transfer Division, Aug. 15, 1998; revision received, Apr. 10, 1999. Keywords: Cooling, Evaporation, Heat Transfer, Impingement, Sprays. Associate Technical Editor: J. Han.

cooled by spray, its surface can experience four different heat transfer regimes: the film boiling regime, the transition boiling regime, the nucleate boiling regime, and the single-phase liquid cooling regime. The mechanism of spray cooling was investigated by many researchers in the field (Mesler, 1976, 1982; Bonacina et al., 1979; Choi and Yao, 1987; Deiters and Mudawar, 1989; Mudawar and Valentine, 1989; Yang, 1993; Yang et al., 1993, 1996a, b). However, due to the complexity of involved mechanisms, there has been no comprehensive model established for the heat transfer of the spray cooling process.

This paper proposes a simple model to predict the spray cooling heat flux which takes evaporation as the most important factor in the process. The model is capable of predicting the spray cooling heat flux during different heat transfer regimes. Furthermore, a correlation is given for predicting the evaporation ratio of the spray cooling involved in the high-pressure die-casting process. The predicted results were compared with the published data together with our experimental results and a good agreement was achieved.

Proposed Model Description

As shown in Fig. 1, the physics involved with the control volume is quite complicated. It incorporates the impingement of the droplets, liquid droplet interaction, liquid droplet and vapor interaction—the various heat transfer regimes depending on the spray and surface conditions. When spray droplets impinge on the hot surface, two basic phenomena will happen from a thermal viewpoint: (1) a droplet raises its temperature to the saturation temperature and (2) a droplet changes its phase from liquid to vapor and is evaporated. When these two phenomena occur, a large amount of heat is extracted, with some of the droplet running off as liquid at a temperature dependent on the spray conditions.

The amount of heat extracted from the hot surface, q can be calculated using the energy equation

$$q = \dot{m}_L C_p (T_{\text{Sat}} - T_L) + \dot{m}_{\text{vapor}} h_{fg} \tag{1}$$

where q is the spray cooling heat flux, $\dot{m}_L$ is the liquid mass flow rate, C_p is the specific heat, T_{Sat} is the liquid saturation temperature, T_L is the coolant temperature, $\dot{m}_{\text{vapor}}$ is the vapor mass flow rate, and h_{fg} is the latent heat. The evaporation ratio is defined as $r_e = \dot{m}_{\text{vapor}}/\dot{m}_L$, which is the ratio of the evaporated liquid and the liquid impinging on the hot surface. Hence, the heat flux is represented as

$$q = \dot{m}_L C_p (T_{\text{Sat}} - T_L) + \dot{m}_L r_e h_{fg}. \tag{2}$$

This is the proposed model to predict the spray heat flux. The evaporation ratio r_e, which combines all the parameters involved in the spray cooling process, has to be determined experimentally. The evaporation ratio falls into three regions: (1) $r_e = 0$, (2) $r_e = 1$, (3) $0 < r_e < 1$. In the first region, no evaporation is occurring. The heat transfer is in the single-phase cooling regime and forced convection is the only mechanism of the heat transfer. All liquid impinging on the surface runs off at a temperature lower than the liquid saturation temperature. Heat transfer in this regime will be very small. For the second region, the liquid evaporation rate $\dot{m}_{\text{vapor}}$ is equal to the liquid mass flow rate $\dot{m}_L$ ($\dot{m}_L = \rho Q$) impinging on the hot surface. All liquid impinging on the hot surface is evaporated. It is apparent that the liquid flow rate is the most important parameter influencing the spray cooling heat transfer which confines the maximum heat flux. In the third region, r_e is expressed by empirical relationships and this case is the most likely phenomenon to occur during a real spray cooling process.

Determination of r_e

A systematic experimental study was conducted by the authors (Liu et al., 1999) to examine the heat transfer characteristics from the hot die surface to the water spray involved in high-pressure die-casting processes. Temperature and heat flux measurements were made locally in the spray field using a heater made from die material H-13 steel and with a surface diameter of 10 mm. The spray cooling curve was determined in the nucleate boiling and critical heat flux, as well as the transition boiling regimes. The hydrodynamic parameters of the spray such as droplet diameters, droplet velocities, and volumetric spray flux were also measured at the position in the spray field identical to that of the test piece. Droplets size and velocity distributions were measured using a Dantec Particle Dynamics Analyzer system. An empirical correlation was developed to relate the spray cooling heat flux to the

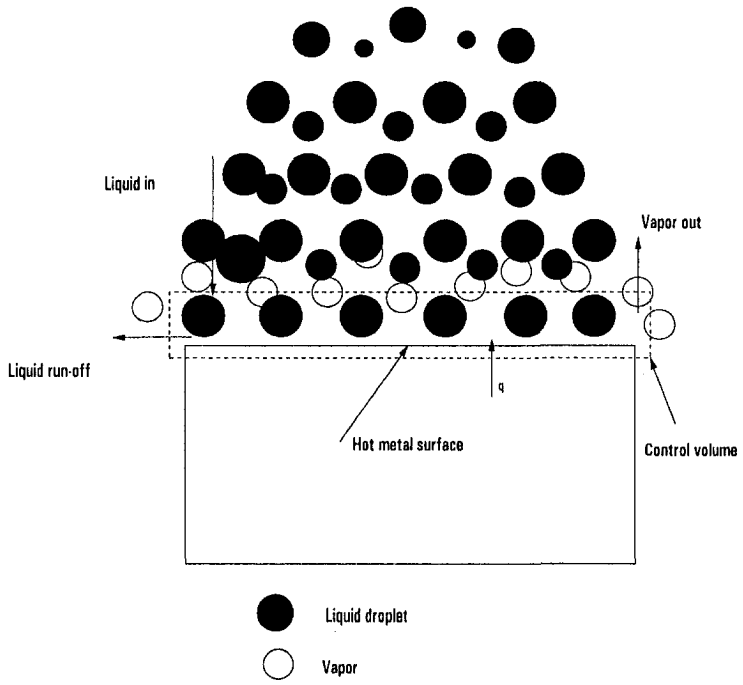

Fig. 1 The spray cooling process

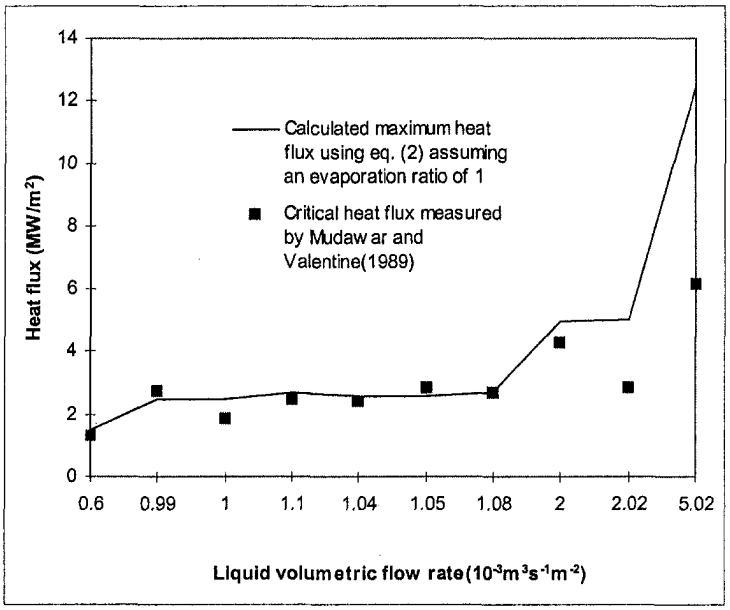

Fig. 2 Comparison between the calculated maximum heat flux and the critical heat flux measured by Mudawar and Valentine (1989)

spray hydrodynamic parameters, such as liquid volumetric flux, droplet size, and droplet velocity as follows:

$$q^* = AT^{*3} + BT^{*2} + CT^* + D \tag{3}$$

$$A = 10^{-4.05434}\,\mathrm{Re}^{1.45101}\,\mathrm{We}^{1.27899}\,\mathrm{RA}^{0.864281} \tag{4}$$

$$B = -10^{-3.6164}\,\mathrm{Re}^{1.31859}\,\mathrm{We}^{1.17256}\,\mathrm{RA}^{0.915949} \tag{5}$$

$$C = 10^{-3.64182}\,\mathrm{Re}^{1.21498}\,\mathrm{We}^{1.09276}\,\mathrm{RA}^{0.949317} \tag{6}$$

$$D = -10^{-4.15201}\,\mathrm{Re}^{1.13977}\,\mathrm{We}^{1.03674}\,\mathrm{RA}^{0.963274} \tag{7}$$

where

$q^* = \dfrac{q}{\rho Q h_{fg}}$ is the dimensionless heat flux;

$T^* = \dfrac{T_{\mathrm{sur}} C_p}{h_{fg}}$ is the dimensionless surface temperature;

$\mathrm{Re} = \dfrac{\rho \bar{u} d}{\mu}$ is the Reynolds number;

$\mathrm{We} = \dfrac{\sigma}{\rho \bar{u}^2 d}$ is the Weber number;

$\mathrm{RA} = \dfrac{\bar{u}}{Q}$ is the ratio of the droplet velocity and the volumetric liquid flux;

and ρ is the liquid density; Q is the liquid volumetric flow rate; T_{sur} is the surface temperature of the heater; $\bar{u}$ is the droplet mean

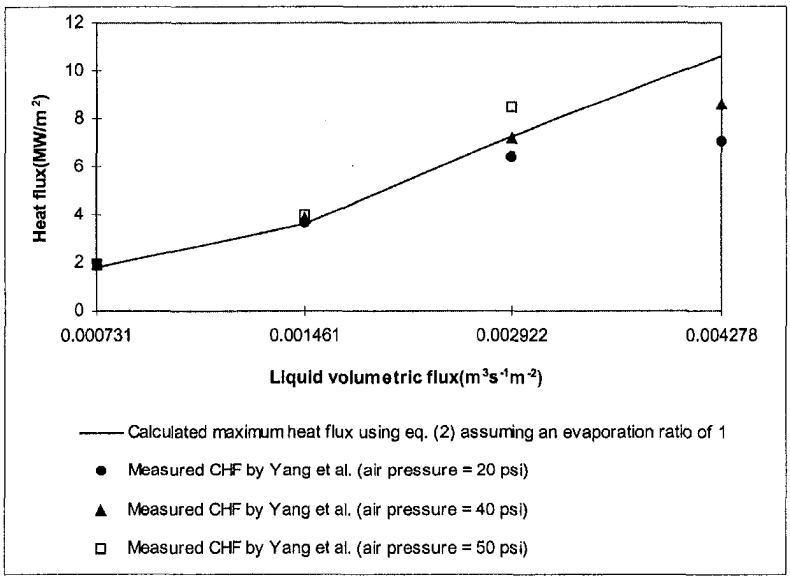

Fig. 3 Comparison between the calculated maximum heat flux and the critical heat flux measured by Yang et al. (1993)

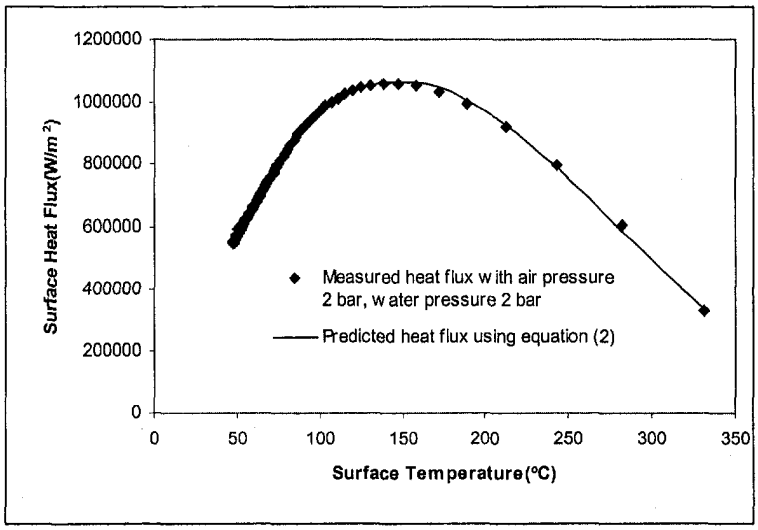

Fig. 4 Comparison between the predicted results and the measured surface heat flux of spray cooling involved in high-pressure die casting process

velocity; $\bar{d}$ is the droplet mean diameter; μ is the viscosity; and σ is the surface tension. From Eqs. (2) and (3), the correlation for evaporation ratio r_e can be easily derived:

$$r_e = AT^{*3} + BT^{*2} + CT^{*} + D - \frac{C_p(T_{sat} - T_L)}{h_{fg}}. \quad (8)$$

This correlation is only suitable for predicting the evaporation ratio of the spray cooling involved in a high-pressure die-casting process.

Results and Discussion

Figure 2 shows the comparison between the predicted maximum heat flux at different liquid volumetric flow rates assuming an evaporation ratio of 1 and the corresponding critical heat flux reported by Mudawar and Valentine (1989). They used a plain orifice spray with the test heater made from copper and with a cross-sectional area of 0.5 cm^2. As shown in the figure, at low liquid volumetric flow rates, the measured critical heat flux is in good agreement with the predicted one, which implies that at these conditions, all liquid impinging on the hot surface is totally evaporated. At liquid volumetric flow rates equal to 0.00202 and 0.00502 $m^3.s^{-1}.m^{-2}$, the measured critical heat flux is lower than predicted. This implies that at these spray conditions, only a portion of the liquid impinging on the hot surface is evaporated, the other runs off as liquid. Hence, the assumption of $r_e = 1$ is not suitable for these two cases.

Figure 3 shows the comparison between the calculated maximum heat flux for an evaporation ratio of 1 and the corresponding critical heat flux at various air pressure reported by Yang et al. (1993). Yang et al. used an air atomized spray nozzle, where the test heater was made from copper with square geometry (11 mm). Again as shown in the figure, for liquid volumetric flow rates of 0.000731 and 0.001461 $m^3.s^{-1}.m^{-2}$, the measured critical heat flux is in good agreement with the calculated one. Furthermore, at these liquid volumetric flow rates, increasing the air pressure from 20 psi to 50 psi did not change the critical heat flux. This can be explained that since the heat transfer has already reached its maximum at 20 psi, any further air pressure increases will not necessarily change the heat flux. On the other hand, at a liquid volumetric flow rate of 0.002922 $m^3.s^{-1}.m^{-2}$, the measured critical heat flux increases with increasing air pressure. Raising air pressure from 20 psi to 40 psi, the maximum heat flux is reached, so the measured critical heat flux is accurately predicted by the proposed model. However, at an air pressure of 50 psi, the measured critical heat flux is higher than the calculated maximum heat flux. This may be attributed to the strong air flow fields at a high air pressure, which causes forced convection heat transfer to take place. Finally, at a liquid volumetric flow rate of 0.004278 $m^3.s^{-1}.m^{-2}$, Fig. 3 shows that if the air pressure increases further, the critical heat flux will approach its maximum value.

Figure 4 shows the comparison between our measured surface heat flux and the calculated results using Eqs. (8) and (2), respectively. Agreement between the experimental data and the predicted results is excellent.

Conclusion

The results of this study indicate that the proposed model is capable of predicting the spray cooling heat flux. The model takes evaporation ratio as the most important factor in the spray cooling process. Provided the evaporation ratio is known, the model is capable of predicting the spray cooling heat flux during various heat transfer regimes. However, the evaporation ratio must be determined experimentally. The predicted results were compared with the published data together with our experimental results and good agreement was achieved.

References

Bonacina, C., Del Giudice, S., and Comini, G., 1979, "Dropwise Evaporation," ASME JOURNAL OF HEAT TRANSFER, Vol. 101, pp. 441–446.

Choi, K. J., and Yao, S. C., 1987, "Mechanisms of film boiling heat transfer of normally impacting spray," *Int. J. Heat Mass Transfer,* Vol. 30, pp. 311–318.

Deiters, T. A., and Mudawar, I., 1989, "Optimization of spray quenching for aluminum extrusion, forging, or continuous casting," *J. Heat Treating,* Vol. 7, pp. 9–18.

Deiters, T. A., and Mudawar, I., 1990, "Prediction of the temperature-time cooling curves for three-dimensional aluminium products during spray quenching," *J. Heat. Treating,* Vol. 8, pp. 81–91.

Liu, G. W., Morsi, Y. S., Van Der Walt, J. P., and Clayton, B. R., 1999, "Experimental Investigation of the Spray Cooling Heat Transfer Involved in a High Pressure Die Casting Process," *Journal of Experimental Heat Transfer,* submitted for publication.

Mesler, R., 1976, "A mechanism supported by extensive experimental evidence to explain high heat fluxes observed during nucleate boiling," *AIChE Journal,* Vol. 22, pp. 246–252.

Mesler, R., 1982, "Research on nucleate boiling," *Chemical Engineering Education,* Vol. 16, p. 152.

Mudawar, I., and Valentine, W. S., 1989, "Determination of the local quenching curve for spray-cooled metallic surface," *J. Heat Treating,* Vol. 7, pp. 107–121.

Yang, J., 1993, "Spray cooling with an air atomizing nozzle," Ph.D. dissertation, University of Kentucky.

Yang, J., Pais, M. R., and Chow, L. C., 1993, "Critical heat flux limits in secondary gas atomized liquid spray cooling," *Experimental Heat Transfer,* Vol. 6, pp. 55–67.

Yang, J., Chow, L. C., and Pais, M. R., 1996a, "An Analytical Method to Determine the Liquid Film Thickness Produced by Gas Atomized Sprays," ASME JOURNAL OF HEAT TRANSFER, Vol. 118, pp. 255–258.

Yang, J., Chow, L. C., and Pais, M. R., 1996b, "Nucleate Boiling Heat Transfer in Spray Cooling," ASME JOURNAL OF HEAT TRANSFER, Vol. 118, pp. 668–671.

Response of Counterflow Heat Exchangers to Step Changes of Flow Rates

F. E. Romie[1]

Introduction

The response of heat exchangers to changes of mass flow rates is of interest for control of systems containing heat exchangers. The purpose of this note is to find the responses of the outlet temperatures of counterflow exchangers to step changes of either or both flow rates. The problem is an initial value problem. Initially the exchanger operates in the steady-state condition for which the initial wall and fluid temperature distributions are computed using simple relations. At time zero either or both flow rates are abruptly changed without a change of fluid inlet temperatures. The ensuing transient occurs as the fluid and wall temperature distributions change from initial to final values.

The governing differential equations are linear and homogeneous with constant coefficients after the flow rate changes. If the inlet temperatures vary after or at the time of flow rate steps then responses to inlet temperature variations are additive to responses caused by the flow rate steps. Responses to inlet temperature variations have been given, for example, by Romie (1984) and Roetzel and Xuan (1992a).

Ontko and Harris (1990) use finite difference methods and Xuan and Roetzel (1993) use the Graver-Stehfest algorithm for numerical inversion of Laplace transforms to find combined responses to step changes of flow rates and inlet temperature variations. Although the response to step changes of flow rates is implicit in both references, the effect of flow rate excitation taken alone has not been made evident. Hence this note.

Analysis

The counterflow exchanger analyzed is defined by the following idealizations:

(1) Convective conductances are dependent on flow rate only and, in particular, are not dependent on time or position.

(2) The fluid capacitance rates before, $(wc)_{ai}$ and $(wc)_{bi}$, and after flow rate steps, $(wc)_a$ and $(wc)_b$, are uniform and constant. (Subscript i denotes values before the flow rate steps.)

(3) Thermal conductances $(hA)_{ai}$, $(hA)_{bi}$, $(hA)_a$ and $(hA)_b$ are uniform and constant as is the thermal capacitance, WC, of the exchanger core.

(4) The fluids are thermally insulated from the exchanger shell which thus has no influence on the transient.

(5) No heat is conducted axially.

Subscript a is assigned to the fluid that initially has the lesser capacitance rate and thus $C_i = (wc)_{ai}/(wc)_{bi}$ cannot exceed unity. The value of C following the steps may be greater than unity depending on the flow rate steps.

The overall thermal conductance is UA.

$$1/UA = 1/(hA)_a + 1/(hA)_b$$

Define $N_t = UA/(wc)_a$ and $R = (hA)_b/(hA)_a$. Using these definitions, $N_a \equiv (hA)_a/(wc)_a = N_t(1 + R)/R$ and $N_b \equiv (hA)_b/(wc)_b = N_aRC$. The subscript i can be appended to the preceding parameters to compute values before the flow rate steps. N_{ti} is the NTU (number of transfer units) of the exchanger before the steps and N_t is the NTU after the steps when C is not greater than unity.

Two additional parameters are the ratios of the thermal capacitances of the contained fluids to the thermal capacitance of the exchanger core and are independent of flow rates: $V_a = (wc)_a t_a/WC$ and $V_b = (wc)_b t_b/WC$. The dwell or transit times, t_a and t_b, are the times required for the fluids to fill the two fluid volumes of the exchanger. Define $t_c = WC/(wc)_a$ then $V_a = t_a/t_c$, $CV_b = t_b/t_c$ and, defining V, $V = V_a + CV_b = (t_a + t_b)/t_c$. The time variable used is $\theta = t/(t_a + t_b + t_c) = (t/t_c)/(1 + V)$ which has the advantage that the transient is effectively completed by the time $\theta = 2$ for all parameter values. (True also for steps of inlet temperatures.)

Without loss of generality a temperature scale is used that makes the inlet ($x = 0$) temperature of fluid a zero and the inlet ($x = 1$) temperature of fluid b unity. To compute the temperature distributions before the steps let $a = N_{ti}(1 - C_i)$ and $b = 1 - C_i \exp(-a)$.

$$T_{bi}(x) = (1 - C_i \exp(-ax))/b$$

$$T_{ai}(x) = (1 - \exp(-ax))/b$$

$$T_{wi}(x) = (T_{ai}(x) + R_i T_{bi}(x))/(1 + R_i)$$

When $C_i = 1$ these equations are indeterminate but $C_i = .9999$ can be used to avoid treatment of a special case.

The fluid a exit temperature before the step is $T_{ai}(1) = (1 - \exp(-a))/b$ and for fluid b is $T_{bi}(0) = 1 - C_i T_{ai}(1)$. To compute the final exit temperature of fluid a let $e_3 = \exp(-N_t(1 - C))$ to give $T_a(\infty, 1) = (1 - e_3)/(1 - Ce_3)$ and $T_b(\infty, 0) = 1 - CT_a(\infty, 1)$. The final response for fluid a is $T_a(\infty, 1) - T_{ai}(1)$ and for fluid b is $T_b(\infty, 0) - T_{bi}(0)$.

Energy balances give three equations governing the transient.

$$\partial T_w/\partial\theta = g(T_a - T_w) + Rg(T_b - T_w)$$

$$N_a(T_w - T_a) = u_1 \partial T_a/\partial\theta + \partial T_a/\partial x$$

$$N_b(T_w - T_b) = u_2 \partial T_b/\partial\theta - \partial T_b/\partial x$$

For notational simplification, $g = N_a(1 + V)$, $u_1 = V_a/(1 + V)$ and $u_2 = CV_b/(1 + V)$. The boundary conditions are $T_a(\theta, 0) = 0$ and $T_b(\theta, 1) = 1$. The initial conditions are $T_a(0, x) = T_{ai}(x)$, $T_b(0, x) = T_{bi}(x)$ and $T_w(0, x) = T_{wi}(x)$.

Note that $T_a(\theta, x)$, $T_b(\theta, x)$ and $T_w(\theta, x)$ are dependent on eight parameters: N_{ti}, C_i, R_i required to establish initial conditions, N_t, C, R required to establish conditions after the flow rate steps, and V_a and V_b. The three parameters N_t, C, and R are related to N_{ti}, C_i, and R_i by the flow rate steps as will be described in a following section.

The solution of the differential equations is found by first finding the double Laplace transforms ($\theta \to s$, $x \to p$) of T_a, T_b, and T_w. The double transforms can be partially inverted ($p \to x$) to give the transforms $T_a(s, x)$, $T_b(s, x)$, and $T_w(s, x)$. Expression of these transforms uses the following relations.

$$Q = s + g(1 + R), \quad d = N_a gR/Q, \; e = dC$$

$$f = N_a + u_1 s - d/R, \quad h = N_b + u_2 s - eR$$

$$u = N_b/(Q(1 + R_i)), \quad v = uN_a/N_b$$

$$a_1 = (v(1 + R_i C_i)(h + a + eR) + u_1(h + a) + u_2 dC_i)/b$$

$$a_2 = -(v(1 + R_i)(h + eR) + u_1 h + u_2 d)/b$$

$$a_3 = vR_i(1 - C_i)/b$$

$$b_1 = (u(1 + R_i C_i)(f - a + d/R) + u_1 e + u_2 C_i(f - a))/b$$

$$b_2 = -(u(1 + R_i)(f + d/R) + u_1 e + u_2 f)/b$$

[1] Palos Verdes Estates, CA 90274. Life Assoc. Mem. ASME.

Contributed by the Heat Transfer Division for publication in the JOURNAL OF HEAT TRANSFER. Manuscript received by the Heat Transfer Division, Oct. 5, 1998; revision received, Feb. 18, 1999. Keywords: Heat Transfer, Heat Exchangers, Transient. Associate Technical Editor: B. T. F. Chung.

$$b_3 = -(1 - C_i)(u_2 + uR_i)/b$$

$$w = de - fh,$$

$$r_1 = (f - h + ((f - h)^2 - 4w)^{1/2})/2, \quad r_2 = w/r_1$$

$$e_1(x) = \exp(-r_1x)/(r_2 - r_1)$$

$$e_2(x) = \exp(-r_2x)/(r_1 - r_2)$$

$$e_a(x) = \exp(-ax)/((a - r_1)(a - r_2))$$

$$g_1(x) = e_1(x)/(a - r_1) + e_2(x)/(a - r_2) + e_a(x)$$

$$g_2(x) = 1/w - e_1(x)/r_1 - e_2(x)/r_2$$

$$g_3(x) = e_1(x) + e_2(x)$$

$$g_4(x) = (f - r_1)e_1(x) + (f - r_2)e_2(x)$$

Using these relations,

$$T_b(s, 0) = (1/s - b_1g_1(1) - b_2g_2(1) - b_3g_3(1))/g_4(1)$$

$$T_b(s, x) = b_1g_1(x) + b_2g_2(x) + b_3g_3(x) + g_4(x)T_b(s, 0)$$

$$T_a(s, x) = a_1g_1(x) + a_2g_2(x) + a_3g_3(x) + dg_3(x)T_b(s, 0)$$

$$T_w(s, x) = ((T_a(s, x) + RT_b(s, x))g + T_{wi}(x))/Q.$$

Inversion ($s \rightarrow \theta$) of these transforms by analytic means is considered impossible and recourse is made to the Graver-Stehfest (Stehfest, 1970) algorithm for numerical inversion of Laplace transforms. The method has been discussed and applied to exchanger transients in several papers by Roetzel and Xuan, for example, Roetzel and Xuan (1992a, b) and Xuan and Roetzel (1993).

If $F(s)$ is the Laplace transform of $f(\theta)$ then the algorithm is

$$f(\theta) = \frac{\log(2)}{\theta} \sum_{m=1}^{M} K_m F\left(m \frac{\log(2)}{\theta}\right)$$

with

$$K_m = (-1)^{m+M/2} \sum_{k=(m+1)/2}^{\min(m, M/2)} \frac{k^{M/2}(2k)!}{(M/2 - k)!k!(k - 1)!(m - k)!(2k - m)!}$$

in which M is an even number and the lower limit on the sum is the integer part of $(m + 1)/2$. Good results for this note were obtained with $M = 6$ for which $K_1 = 1$, $K_2 = -49$, $K_3 = 366$, $K_4 = -858$, $K_5 = 810$, and $K_6 = -270$. Double precision is used because the algorithm involves the sum of differences of large numbers to produce a small number ($\Sigma K_m = 0$).

If a fluid is a gas then immediately after a step of its flow rate, before the wall temperature can change, the gas temperature will change abruptly. If fluid a is a gas then t_a will be much less than t_c and the ratio $t_a/t_c = V_a$ can be treated as zero ($u_1 = 0$). In this case just after its flow rate step, when N_{ai} becomes N_a, the gas a temperature distribution is given by the solution to

$$dT_a/dx = N_a(T_{wi}(x) - T_a)$$

with $T_a(0) = 0$. The solution for the outlet temperature is

$$T_a(0, 1) = \left(1 - e^{-N_a}\left(1 + \frac{N_a(1 + R_iC_i)}{(1 + R_i)(N_a - a)}(e^{N_a - a} - 1)\right)\right)/b$$

and the jump in gas a exit temperature response at $\theta = 0$ is $T_a(0, 1) - T_{ai}(1)$. Similarly, if fluid b is a gas then $V_b = 0$ and the gas temperature at $\theta = 0$ is the solution to

$$dT_b/dx = -N_b(T_{wi}(x) - T_b)$$

with $T_b(1) = 1$. The solution for gas b exit temperature at $\theta = 0$ is

$$T_b(0, 0) = e^{-N_b} + \left(1 - e^{-N_b} + \frac{N_b(1 + R_iC_i)}{(1 + R_i)(N_b + a)}(e^{-(N_b + a)} - 1)\right)/b$$

and the jump in gas b exit temperature response at $\theta = 0$ is $T_b(0, 0) - T_{bi}(0)$.

Calculation Results

If d_a and d_b are the fractional steps (+ or −) of the flow rates then $C = C_i(1 + d_a)/(1 + d_b)$. In general the thermal conductances include not only convective conductances but also recognition of fouling resistances, resistance to heat flow through the walls separating the fluids, and the effect of any extended surfaces. However, in the following conductances will be treated as purely convective for simplicity. The Nusselt number is proportional to Reynolds number to the power n: $hA \propto (wc)^n$. Thus $N_a = N_{ai}(1 + d_a)^{na-1}$, $N_b = N_{bi}(1 + d_b)^{nb-1}$, $R = R_i(1 + d_b)^{nb}/(1 + d_a)^{na}$ and $N_t = N_aR/(1 + R)$.

The fluid exit temperature responses are presented as the ratios, $B_a(\theta)$ and $B_b(\theta)$, of the fluid exit temperature response to the final exit temperature response: $B_a(\theta) = (T_a(\theta, 1) - T_{ai}(1))/(T_a(\infty, 1) - T_{ai}(1))$ and $B_b(\theta) = (T_b(\theta, 0) - T_{bi}(0))/(T_b(\infty, 0) - T_{bi}(0))$. The ratios thus vary from 0 before the steps to a final value of 1.

Figure 1 shows responses for a gas-to-gas exchanger with $d_a = d_b = 0.2$ and $na = nb = 0.6$ as is indicated at the top of the graph. The exchanger operates under symmetric conditions ($C = R = 1$ both before and after flow rate steps) which makes $B_a(\theta)$ and $B_b(\theta)$ identical. The 90 percent response occurs when $\theta = 0.22$ or, equivalently, when $t = 0.22t_c$.

Figure 2 shows responses with $d_a = 0.2$ and $d_b = 0$ for a liquid-to-liquid exchanger ($V_a = 1$ and $V_b = 2$). The 90 percent response occurs when $\theta = 1.22$ for fluid a and $\theta = 1.4$ for fluid b. The time t when $\theta = 1.22$ is $1.22(1 + V_a + CV_b)t_c = 5.08t_c$. The final response for fluid a is $(T_a(\infty, 1) - T_{ai}(1))(T_{bin} - T_{ain})$ in which T_{bin} and T_{ain} are the actual (unchanged) inlet temperatures. If $T_{bin} = 100$ deg. and

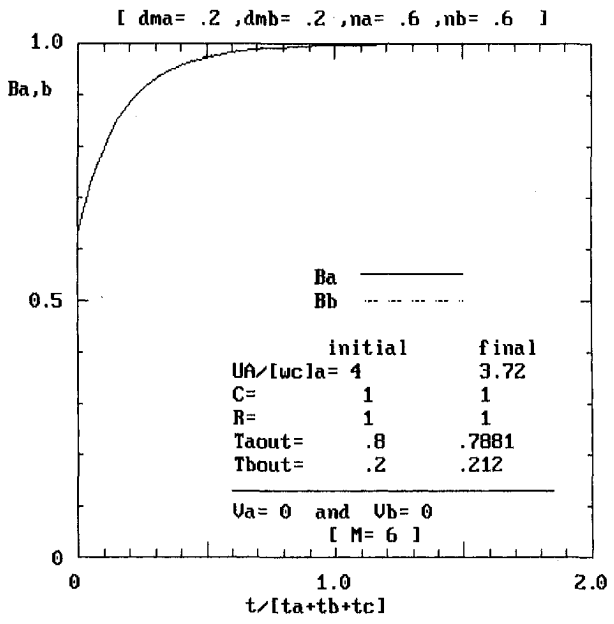

Fig. 1 Responses for a gas-to-gas exchanger operating under symmetric conditions ($C = R = 1$). B_a and B_b are identical.

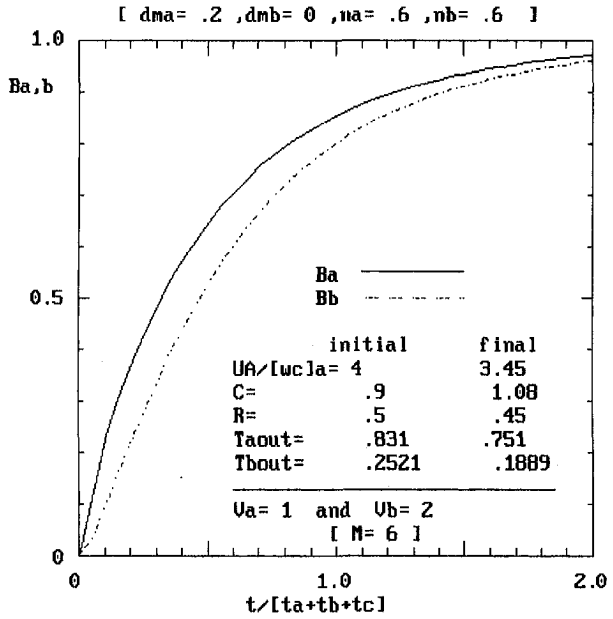

Fig. 2 Responses for a liquid-to-liquid exchanger with one capacitance rate unchanged

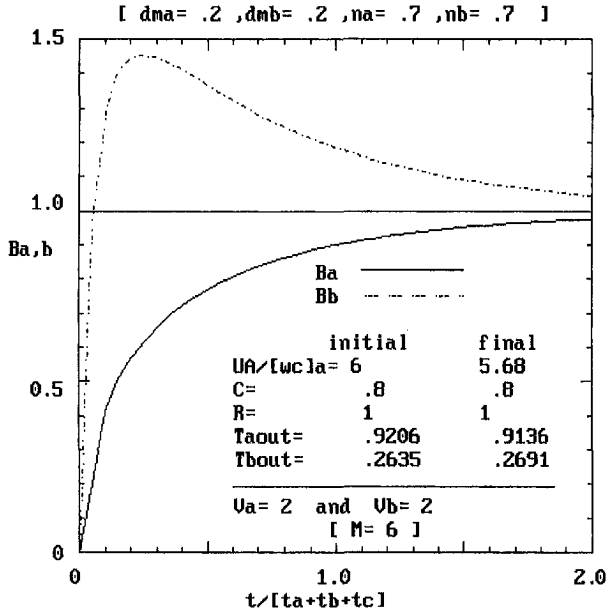

Fig. 3 Responses for a liquid-to-liquid exchanger with equal capacitance rate changes

T_{ain} = 200 deg. then, using the data on Fig. 2, the final response for fluid a is +8 deg. and for fluid b is +6.3 deg.

Figure 3 gives an example for which the fluid b response is greater than its final response during most of the transient. In general the responses B_a and B_b are found to be insensitive to the values of V_a and V_b which is attributed to the definition of θ.

The results of this note have been checked using a finite difference method. The advantage of the Graver-Stehfest algorithm is a much shorter solution time.

References

Ontko, J. S., and Harris, F. A., 1990, "Transients in the Counterflow Heat Exchanger," *Compact Heat Exchangers: A Festshrift for A. L. London,* Hemisphere, New York, pp. 531–548.

Roetzel, W., and Xuan, Y., 1992a, "Transient Response of Parallel and Counterflow Heat Exchangers," ASME JOURNAL OF HEAT TRANSFER, Vol. 114, pp. 510–512.

Roetzel, W., and Xuan, Y., 1992b, "Transient Behaviour of Multipass Shell-and-Tube Heat Exchangers," *Int. Journal of Heat and Mass Transfer,* Vol. 35, pp. 703–710.

Romie, F. E., 1984, "Transient Response of the Counterflow Heat Exchanger," ASME JOURNAL OF HEAT TRANSFER, Vol. 106, pp. 620–626.

Stehfest, H., 1970, "Numerical Inversion of Laplace Transforms," *Communications of the ACM,* Vol. 13, pp. 47–49.

Xuan, Y., and Roetzel, W., 1993, "Dynamics of Shell and Tube Heat Exchangers to Arbitrary Temperature and Step Flow Variations," *AIChE Journal,* Vol. 39, pp. 413–421.

Heat Transfer in Fin Assemblies: Significance of Two-Dimensional Effects—A Reexamination of the Issue

L. C. Thomas[1]

The purpose of this paper is to reexamine the significance and nature of two-dimensional effects in fin assemblies. In particular, consideration is given to concerns expressed in the literature that the standard approach commonly leads to large errors due to two-dimensional effects. In addition, for the purpose of establishing a practical means of evaluating the level of significance of two-dimensional effects, an approximate first-order two-dimensional thermal circuit approach to analyzing heat transfer in fin assemblies is developed.

Nomenclature

A = cross-sectional area of fin, m^2
A_F = surface area of fin, m^2
A_p = surface area of prime, m^2
A_t = $A + A_p$, m^2
A_o = fin/prime surface area, m^2
Aug = Augmentation, q_{2D}/q_{un}
Bi = Biot number, $h_2\delta/k_F$
Bi_1 = h_1P/k_w
Bi_2 = h_2P/k_w
E_{1D} = $q_{1D}/q_{2D} - 1$
$E_{(1)}$ = $1 - q_{(1)}/q_{2D}$
F_i = Rt/R_i
k = thermal conductivity, W/(m °C)
L = fin length, m
L_c = corrected fin length, $L + A/p$, m
P = half pitch, m
R = thermal resistance, °C/W
Rt = transverse thermal resistance, °C/W
q_F = fin heat transfer rate, W
q_p = prime heat transfer rate, W
q_o = fin/prime heat transfer rate, W
q_{2D} = fin/prime heat transfer rate—two-dimensional numerical solution, W
w = wall thickness, m

Greek Symbols

α = $A_o\eta_o/A_t$
δ = half-fin thickness, m

[1] Mechanical Engineering Department, King Fahd University of Petroleum & Minerals, Dhahran 31261, Saudia Arabia. Current address: 1424 Farrington Drive, Knoxville, TN 37923. Mem. ASME.

Contributed by the Heat Transfer Division for publication in the JOURNAL OF HEAT TRANSFER. Manuscript received by the Heat Transfer Division, Nov. 12, 1996; revision received, Jan. 22, 1999. Keywords: Augmentation and Enhancement, Finned Surfaces. Associate Technical Editor: R Boyd.

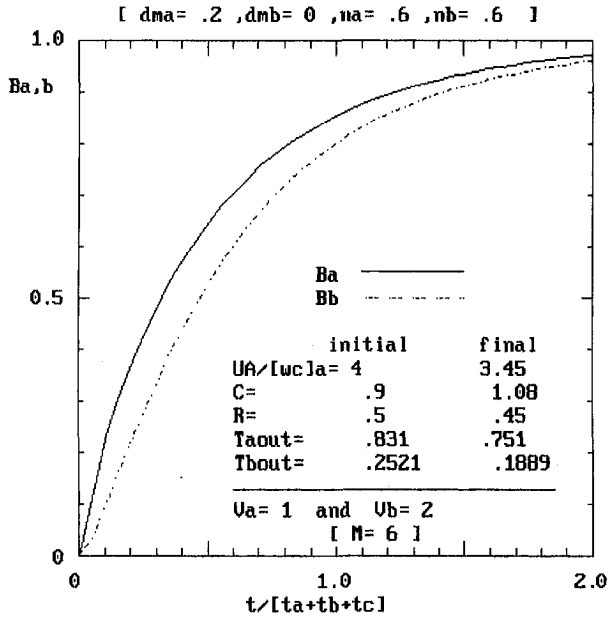

Fig. 2 Responses for a liquid-to-liquid exchanger with one capacitance rate unchanged

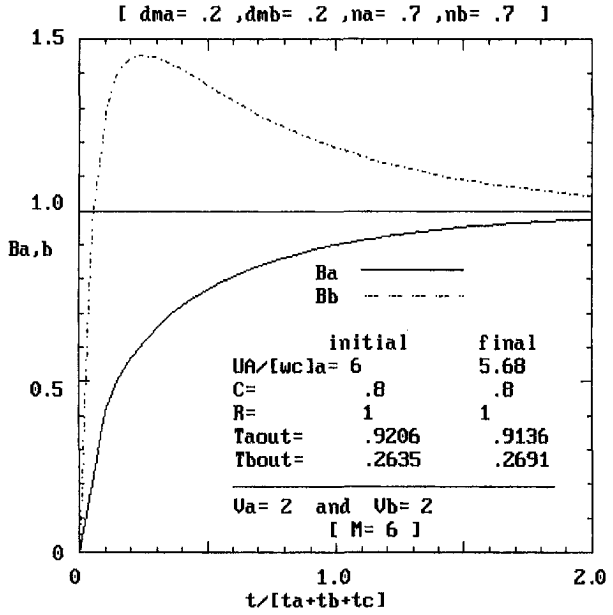

Fig. 3 Responses for a liquid-to-liquid exchanger with equal capacitance rate changes

T_{ain} = 200 deg. then, using the data on Fig. 2, the final response for fluid a is +8 deg. and for fluid b is +6.3 deg.

Figure 3 gives an example for which the fluid b response is greater than its final response during most of the transient. In general the responses B_a and B_b are found to be insensitive to the values of V_a and V_b which is attributed to the definition of θ.

The results of this note have been checked using a finite difference method. The advantage of the Graver-Stehfest algorithm is a much shorter solution time.

References

Ontko, J. S., and Harris, F. A., 1990, "Transients in the Counterflow Heat Exchanger," *Compact Heat Exchangers: A Festshrift for A. L. London,* Hemisphere, New York, pp. 531–548.

Roetzel, W., and Xuan, Y., 1992a, "Transient Response of Parallel and Counterflow Heat Exchangers," ASME JOURNAL OF HEAT TRANSFER, Vol. 114, pp. 510–512.

Roetzel, W., and Xuan, Y., 1992b, "Transient Behaviour of Multipass Shell-and-Tube Heat Exchangers," *Int. Journal of Heat and Mass Transfer,* Vol. 35, pp. 703–710.

Romie, F. E., 1984, "Transient Response of the Counterflow Heat Exchanger," ASME JOURNAL OF HEAT TRANSFER, Vol. 106, pp. 620–626.

Stehfest, H., 1970, "Numerical Inversion of Laplace Transforms," *Communications of the ACM,* Vol. 13, pp. 47–49.

Xuan, Y., and Roetzel, W., 1993, "Dynamics of Shell and Tube Heat Exchangers to Arbitrary Temperature and Step Flow Variations," *AIChE Journal,* Vol. 39, pp. 413–421.

Heat Transfer in Fin Assemblies: Significance of Two-Dimensional Effects—A Reexamination of the Issue

L. C. Thomas[1]

The purpose of this paper is to reexamine the significance and nature of two-dimensional effects in fin assemblies. In particular, consideration is given to concerns expressed in the literature that the standard approach commonly leads to large errors due to two-dimensional effects. In addition, for the purpose of establishing a practical means of evaluating the level of significance of two-dimensional effects, an approximate first-order two-dimensional thermal circuit approach to analyzing heat transfer in fin assemblies is developed.

Nomenclature

A = cross-sectional area of fin, m^2
A_F = surface area of fin, m^2
A_p = surface area of prime, m^2
A_i = $A + A_p$, m^2
A_o = fin/prime surface area, m^2
Aug = Augmentation, q_{2D}/q_{un}
Bi = Biot number, $h_2\delta/k_F$
Bi_1 = h_1P/k_w
Bi_2 = h_2P/k_w
E_{1D} = $q_{1D}/q_{2D} - 1$
$E_{(1)}$ = $1 - q_{(1)}/q_{2D}$
F_i = Rt/R_i
k = thermal conductivity, W/(m °C)
L = fin length, m
L_c = corrected fin length, $L + A/p$, m
P = half pitch, m
R = thermal resistance, °C/W
Rt = transverse thermal resistance, °C/W
q_F = fin heat transfer rate, W
q_p = prime heat transfer rate, W
q_o = fin/prime heat transfer rate, W
q_{2D} = fin/prime heat transfer rate—two-dimensional numerical solution, W
w = wall thickness, m

Greek Symbols

α = $A_o\eta_o/A_i$
δ = half-fin thickness, m

[1] Mechanical Engineering Department, King Fahd University of Petroleum & Minerals, Dhahran 31261, Saudia Arabia. Current address: 1424 Farrington Drive, Knoxville, TN 37923. Mem. ASME.

Contributed by the Heat Transfer Division for publication in the JOURNAL OF HEAT TRANSFER. Manuscript received by the Heat Transfer Division, Nov. 12, 1996; revision received, Jan. 22, 1999. Keywords: Augmentation and Enhancement, Finned Surfaces. Associate Technical Editor: R Boyd.

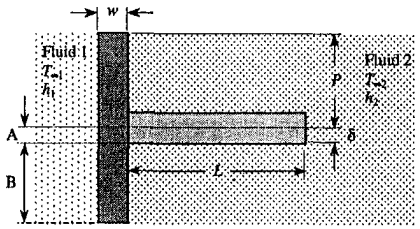

Depth $Z >> \delta$
$A = 2\delta Z$
$A_F = 2LZ$
$A_p = 2PZ$

$A_i = A_p + A$
$A_o = A_p + A_F$

$R_i = 1/(h_1 A_i)$
$R_w = w/(k_w A_i)$
$R_o = 1/(h_2 \eta_o A_o)$
$R_F = 1/(h_2 \eta_F A_F)$
$R_p = 1/(h_2 A_p)$

Fig. 1 Full fin/prime section of plane wall fin assembly

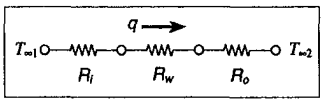

Fig. 2 Standard one-dimensional thermal circuit for full fin/prime section

$\Delta_{1D} = q_{1D}/q_{(1)} - 1$
η_F = fin efficiency
η_o = net surface efficiency
$\phi = \eta_F L_c/\delta$
$\psi = h_2/h_1 + h_2 w/k_w$

Subscripts

1D = standard one-dimensional method
2D = accurate two-dimensional method
(1) = first-order two-dimensional method
F = fin
i = surface 1 corresponding to fin/prime section
n_i = nodal temperatures; $i = 1, 2, 3, 4$
o = fin/prime section
p = prime surface
un = unfinned surface
w = wall

Introduction

The standard approach to characterizing heat transfer in a fin assembly involves the assumption of approximate one-dimensional transport within the supporting structure and fins, such that the temperature distribution within any transverse plane through the assembly is assumed to be uniform. Referring to Fig. 1, this underlying premise permits the representation of heat transfer through a cross section of the assembly that consists of an individual fin and its prime (unfinned) surface in terms of a one-dimensional thermal circuit. The standard one-dimensional thermal circuit is ordinarily sketched in the manner shown in Fig. 2. The thermal resistances associated with this circuit are given by $R_i = 1/(h_1 A_i)$, $R_w = w/(k_w A_i)$, and $R_o = 1/(h_2 A_o \eta_o)$, where the net surface efficiency η_o is expressed in terms of the fin efficiency η_F by $\eta_o = [1 - (A_F/A_o)(1 - \eta_F)]$. Figure 3 shows two equivalent forms of the corresponding one-dimensional thermal circuit associated with a fin/prime half-section, which is the smallest region that includes all of the essential features of the actual two-dimensional transport process. The longitudinal thermal resistances for the series/parallel circuit shown in Fig. 3(*b*) are given by $R_1 = 2/(h_1 A_p)$, $R_2 = 2/(h_1 A)$, $R_3 = 2w/(k_w A_p)$, $R_4 = 2w/(k_w A)$, $R_5 = 2w/(h_2 A_p)$, and $R_6 = 2/(h_2 A_F \eta_F)$. The one-dimensional thermal circuit approach provides the basis for developing a convenient approximate analytical relation for the rate of heat transfer across the fin assembly.

Concern pertaining to the significance of two-dimensional effects on heat transfer through convective fin assemblies was first expressed in the decade of the 1970s by Hennecke and Sparrow (1970), Klette and McCulloch (1972), Shih and Westwater (1974); Sparrow and Lee (1975), and Suryanarayana (1977). As demonstrated by these and other investigators, the actual temperature distribution within a fin is characterized by a temperature depression in the vicinity of the fin root which is a consequence of the relatively large rate of heat transfer through the fin as compared to the prime surface.

These early studies were followed up by a series of research papers by Stones (1980), Heggs et al. (1980a, b, 1982), Manzoor et al. (1981, 1982, 1983, 1984), and Houghton et al. (1991, 1993), which argued that the effective design of finned heat exchangers requires a two-dimensional analysis of the full fin assembly, with persistent warnings (primarily in reference to the study by Suryanarayana (1977))) that errors resulting from two-dimensional effects of up to 80 percent can occur in heat transfer prediction.

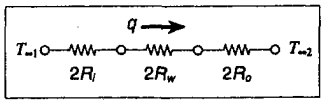

(a) Standard series circuit.

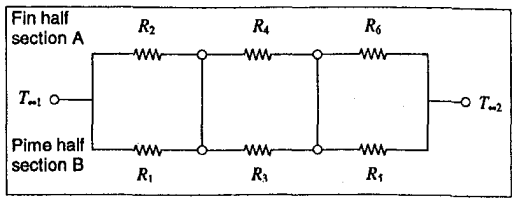

(b) Equivalent series/parallel circuit.

Fig. 3 Corresponding one-dimensional thermal circuits for fin/prime half-section

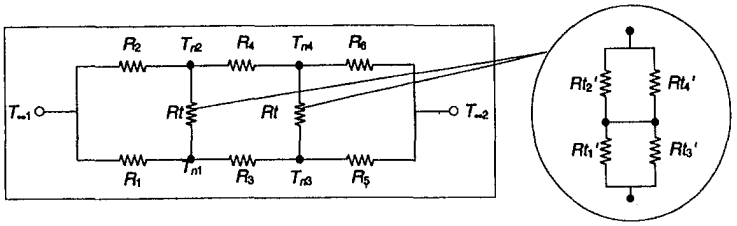

Fig. 4 First-order two-dimensional thermal circuit for fin/prime half-section

Table 1 Analytical solution relations: approximate first-order two-dimensional method

Dimensionless solution relations

$$\Theta_{n1} = \frac{T_{n1} - T_{\infty 2}}{T_{\infty 1} - T_{\infty 2}} = \frac{F_{24}(F_1 + F_3\Theta_{n3}) + F_2 + F_4\Theta_{n4}}{F_{13}F_{24} - 1}$$

$$\Theta_{n2} = \frac{T_{n2} - T_{\infty 2}}{T_{\infty 1} - T_{\infty 2}} = \frac{F_{13}(F_2 + F_4\Theta_{n4}) + F_1 + F_3\Theta_{n3}}{F_{13}F_{24} - 1}$$

$$\Theta_{n3} = \frac{T_{n3} - T_{\infty 2}}{T_{\infty 1} - T_{\infty 2}} = \frac{A_3 + B_3A_4}{1 - B_3B_4}$$

$$\Theta_{n4} = \frac{T_{n4} - T_{\infty 2}}{T_{\infty 1} - T_{\infty 2}} = \frac{A_4 + B_4A_3}{1 - B_3B_4}$$

Dimensionless parameters

$$A_3 = \frac{F_1Y_3 + F_2Y_3/F_{24}}{F_{35} - F_3Y_3} \qquad B_3 = \frac{1 + F_4Y_3/F_{24}}{F_{35} - F_3Y_3} \qquad Y_3 = \frac{F_3}{F_{13} - 1/F_{24}}$$

$$A_4 = \frac{F_2Y_4 + F_1Y_4/F_{13}}{F_{46} - F_4Y_4} \qquad B_4 = \frac{1 + F_3Y_4/F_{13}}{F_{46} - F_4Y_4} \qquad Y_4 = \frac{F_4}{F_{24} - 1/F_{13}}$$

$$F_1 = \mathrm{Bi}\frac{k_F}{k_w}\frac{h_1}{h_2}\frac{(P/\delta)(P/\delta - 1)}{w/\delta} \qquad F_3 = \frac{(P/\delta)(P/\delta - 1)}{(w/\delta)^2} \qquad F_5 = \mathrm{Bi}\frac{k_F}{k_w}\frac{(P/\delta)(P/\delta - 1)}{w/\delta}$$

$$F_2 = \mathrm{Bi}\frac{k_F}{k_w}\frac{h_1}{h_2}\frac{(P/\delta)}{w/\delta} \qquad F_4 = \frac{P/\delta}{(w/\delta)^2} \qquad F_6 = 2\mathrm{Bi}\frac{k_F}{k_w}\frac{P/\delta}{w/\delta}\phi$$

Considering the fact that the one-dimensional approach continues to be relied upon in the analysis and design of fin assemblies used in finned tube heat exchangers and other industrial equipment, the implication of the conclusion pertaining to the extent of two-dimensional effects put forth by Heggs, Manzoor, and associates is quite serious. It is the purpose of this paper to reexamine the significance and nature of two-dimensional effects in fin assemblies, with specific attention given to the proposition of Heggs, Manzoor, et al.

Approximate First-Order Two-Dimensional Method

To provide a basis for estimating the significance of two-dimensional effects within the supporting structure of fin assemblies, the heat transfer within a half-fin/prime section is approximated by the first-order two-dimensional thermal circuit shown in Figure 4.[2] This thermal circuit represents a generalization of the one-dimensional circuit shown in Fig. 3(*b*) that includes transverse thermal resistances *Rt* as well as longitudinal thermal resistances. Using finite difference formulation concepts, the transverse thermal resistances for this circuit are represented by $Rt = P/[k_w(w/2)Z]$.

Equations are obtained for the four unknown temperatures T_{n1}, T_{n2}, T_{n3}, and T_{n4} by performing an energy balance at each node. The resulting nodal equations are given by

$$\frac{T_{n1} - T_{\infty 1}}{R_1} + \frac{T_{n1} - T_{n3}}{R_3} + \frac{T_{n1} - T_{n2}}{Rt} = 0$$

$$\frac{T_{n2} - T_{\infty 1}}{R_2} + \frac{T_{n2} - T_{n4}}{R_4} + \frac{T_{n2} - T_{n1}}{Rt} = 0$$

$$\frac{T_{n3} - T_{\infty 2}}{R_5} + \frac{T_{n3} - T_{n1}}{R_3} + \frac{T_{n3} - T_{n4}}{Rt} = 0$$

$$\frac{T_{n4} - T_{\infty 2}}{R_6} + \frac{T_{n4} - T_{n2}}{R_4} + \frac{T_{n4} - T_{n3}}{Rt} = 0. \qquad (1)$$

An analytical solution for these nodal temperatures is given in Table 1. Using this solution result, the first-order two-dimensional approximation for the fin/prime half-section heat transfer rate $q_{(1)}$ becomes

$$q_{(1)} = \frac{T_{n3} - T_{\infty 2}}{R_5} + \frac{T_{n4} - T_{\infty 2}}{R_6}$$

$$= \frac{1}{R_5}\left(\frac{\Theta_{n3}}{R_6/R_5} + \Theta_{n4}\right)(T_{\infty 1} - T_{\infty 2}) \qquad (2)$$

where $\Theta_{n3} = (T_{n3} - T_{\infty 2})/(T_{\infty 1} - T_{\infty 2})$, $\Theta_{n4} = (T_{n4} - T_{\infty 2})/(T_{\infty 1} - T_{\infty 2})$, and $F_6/F_5 = \eta_F A_F/A_p$.

The significance of two-dimensional effects indicated by this first-order model can be determined by comparing Eq. (2) with solution results obtained by the one-dimensional model. Therefore, consideration is now given to solution results obtained on the basis of the standard one-dimensional method as well as the alternative one-dimensional method used by Suryanaryana (1977).

Standard One-Dimensional Method. The rate of heat transfer q_{1D} for the fin/prime half-section associated with the one-dimensional thermal circuits shown in Fig. 3 is given by

$$q_{1D} = \frac{T_{\infty 1} - T_{\infty 2}}{2(R_i + R_w + R_o)}$$

$$= \frac{T_{\infty 1} - T_{\infty 2}}{2[1/(h_1A_i) + w/(k_wA_i) + 1/(h_2A_o\eta_o)]}. \qquad (3)$$

Rearranging Eq. (3), the relation for q_{1D} takes the form

$$q_{1D} = \frac{h_2A_i(T_{\infty 1} - T_{\infty 2})}{2[h_2/h_1 + h_2w/k_w + A_i/(A_o\eta_o)]} = \frac{h_2A_i(T_{\infty 1} - T_{\infty 2})}{2(\psi + 1/\alpha)} \qquad (4)$$

where

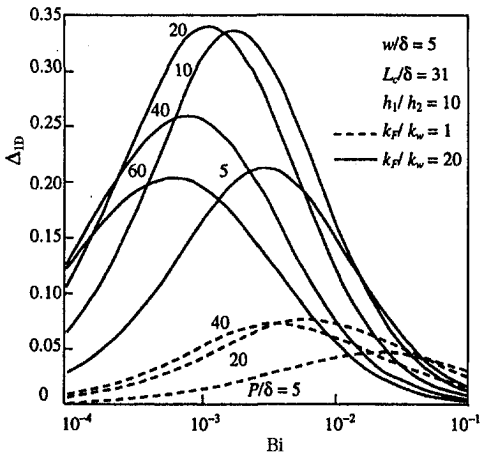

Fig. 5 Calculations for fin assembly difference function Δ_{1D} in terms of Bi and P/δ

[2] Higher-order thermal circuits can be formulated by subdividing the supporting structure into smaller subvolumes.

$$\psi = \frac{h_2}{h_1} + \frac{h_2 w}{k_w} = \frac{h_2}{h_1} + \frac{w}{\delta}\frac{k_F}{k_w}\,\mathrm{Bi}$$

$$\alpha = \frac{A_o \eta_o}{A_i} = 1 + \frac{\delta}{P}\left(\eta_F \frac{L_c}{\delta} - 1\right). \qquad (5,6)$$

The relative difference between the standard one-dimensional and first-order two-dimensional solutions is represented by the *fin assembly difference function* $\Delta_{1D} = q_{1D}/q_{(1)} - 1$. With $q_{(1)}$ and q_{1D} represented by Eqs. (2) and (4), the relation for Δ_{1D} takes the form

$$\Delta_{1D} = \frac{h_2 A_i R_F}{\psi + 1/\alpha}\frac{1}{(R_F/R_p)\Theta_{n3} + \Theta_{n4}} - 1$$

$$= \frac{P/\delta}{\phi(\psi + 1/\alpha)}\frac{1}{(F_5/F_6)\Theta_{n3} + \Theta_{n4}} - 1. \qquad (7)$$

A review of the solution details indicates that Δ_{1D} is a function of the six dimensionless parameters Bi, k_F/k_w, P/δ, L_c/δ, w/δ, and h_1/h_2. The usual ranges of these parameters in actual applications are as follows: Bi is considerably less than 0.1; k_F/k_w is equal to unity, except for bimetal construction, in which case k_F/k_w can be fairly large (>20); P/δ is between 5 and 20; L_c/δ is between 20 and 60; w/δ is between 2 and 10; and h_1/h_2 is considerably greater than 2. Representative calculations for Δ_{1D} are shown as a function of Bi and P/δ in Fig. 5. The calculations obtained in this study indicate that the greatest tendency for significant two-dimensional effects occurs in bimetal fin assembly construction with large values of k_F/k_w, moderately small values of Bi in the range 0.0002 to 0.01, moderate values of P/δ in the range 5 to 60, moderate to long lengths with L_c/δ greater than 20, and values of w/δ less than about 10 and any practical value of h_1/h_2. The calculations indicate that under a certain combination of operating conditions the value of Δ_{1D} can exceed 40 percent for $k_F/k_w = 20$, which is representative of some fin/wall alloy metal combinations. On the other hand, the tendency for significant two-dimensional effects to occur in fin assemblies of single metal construction ($k_F/k_w = 1$) is restricted to less common situations involving a very thin wall for which w/δ is less than 2, with the greatest effect found to occur for relatively small values of both w/δ and h_1/h_2.

The relations for q_{1D} and Δ_{1D} given by Eqs. (3) and (7) can readily be used to determine whether or not two-dimensional effects are significant and to estimate the fin/prime heat transfer rate q_o. The general viability of the method developed in this section for evaluating the significance of two-dimensional effects in fin assemblies is considered in the context of published two-dimensional solution results in a following section.

Alternative One-Dimensional Model. An alternative one-dimensional approach to approximating heat transfer in fin assemblies that was used in the study by Suryanarayana (1977) is based on the assumption that the fin root/prime surface temperature can be set equal to the surface temperature $T_{0,S}$ that would exist if the surface were unfinned.[3] Using this approach, Suryanarayana obtained approximations for the heat transfer rates from the fin and prime surfaces, which can be represented by $q_{P,S} = h_2 A_P (T_{0,S} - T_{\infty,S})$ and $q_{F,S} = h_2 A_F \eta_F (T_{0,S} - T_{\infty,S})$. Based on comparisons of calculations for $q_{P,S}$ and $q_{F,S}$ with numerical solution results for q_P and q_F associated with a fin assembly with Bi = 0.1, Suryanarayana reported large errors in the alternative one-dimensional model. Based on these results, Suryanarayana concluded that the assumption of equality of fin base temperature and the corresponding unfinned surface temperature leads to an overestimate of the heat-transfer rates, stating that "the magnitude of the error can be considerable—as high as 80%." Although Suryanarayana did not indicate the cause for the errors, when taken in the context of the entire paper which is entitled "Two-dimensional effects on heat-transfer rates from an array of straight fins," a possible inference of the conclusion is that the large errors are a consequence of two-dimensional effects.[4] However, in actuality, the errors reported by Suryanarayana are caused by the poor approximation represented by the magnitude of $T_{0,S}$, rather than by the assumption that the temperature distribution is one-dimensional.[5]

Two-Dimensional Solution Results: Published Literature

The solution results published by Heggs, Manzoor, and associates provide numerical calculations for fin/prime half-section heat transfer rate q_{2D} in the context of the augmentation factor Aug = q_{2D}/q_{un} for six cases. The numerical solution results reported for Aug are listed for specific values of the six dimensionless parameters $\mathrm{Bi}_1 = h_1 P/k_w$, $\mathrm{Bi}_2 = h_2 P/k_w$, k_F/k_w, δ/P, L/P, and w/P in Table 2(*a*) and for corresponding dimensionless parameters Bi, k_F/k_w, P/δ, L_c/δ, w/δ, and h_1/h_2 in Table 2(*b*). It should be noted that these cases involve values of Bi ranging from 0.00002 (case B2) to 0.375 (case A2), with Bi being less than 0.1 for all but one case. Thus, except for case A2, the values of Bi considered in these references span the range of conditions encountered in practice.

To determine the significance of two-dimensional effects associated with the five cases for which Bi < 0.1, the *fin assembly error function* is defined by $E_{1D} = q_{1D}/q_{2D} - 1$. This function is expressed in terms of Aug by

$$E_{1D} = \frac{q_{1D}}{q_{un}}\frac{q_{un}}{q_{2D}} - 1 = \frac{\mathrm{Aug}_{1D}}{\mathrm{Aug}} - 1 \qquad (8)$$

where Aug_{1D} is given by

$$\mathrm{Aug}_{1D} = \frac{q_{1D}}{q_{un}} = \frac{h_2/h_1 + h_2 w/k_w + 1}{h_2/h_1 + h_2 w/k_w + A_i/(A_o\eta_o)} = \frac{\psi + 1}{\psi + 1/\alpha}. \qquad (9)$$

Using Eqs. (8) and (9), the solution results for Aug listed in Table 2(*a*) are readily expressed in terms of E_{1D}. The corresponding calculations for E_{1D} are listed in Table 2(*b*). Calculations for E_{1D} are also listed in Table 2(*b*) for cases A1, A3, B1, B2, and B3.

The solution results for E_{1D} listed in Table 2(*b*) indicate that two-dimensional effects are small (less than one percent) for case B2 (E_{1D} = 0.087 percent) and case A1 (E_{1D} = 0.965), mild (one to five percent) for case A3 (E_{1D} = 1.38 percent) and case B1 (E_{1D} = 1.71 percent), and moderate (5 percent to 20 percent) for case B3 (E_{1D} = 10.7 percent). However, none of these cases involve strong (20 percent or greater) two-dimensional effects.

The error in the first-order two-dimensional method is represented by the *first-order fin assembly error function* $E_{(1)} = 1 - q_{(1)}/q_{2D}$. The function $E_{(1)}$ is expressed in terms of Δ_{1D} and E_{1D} by

$$E_{(1)} = (E_{1D} + 1)\left(\frac{1}{E_{1D} + 1} - \frac{1}{\Delta_{1D} + 1}\right) = \frac{\Delta_{1D} - E_{1D}}{\Delta_{1D} + 1}. \qquad (10)$$

Calculations for $E_{(1)}$ are listed in Table 2(*b*). The absolute errors in the calculations for $q_{(1)}$ are seen to range from less than one percent for cases A1, A3, B1, and B2 to 1.6 percent for case B3.

Conclusion

The approximate first-order two-dimensional formulation presented in this paper provides a means of estimating the significance

[3] The standard and alternative one-dimensional models are not equivalent. Thus, $T_{0,S}$ does not correspond to T_{n4}.

[4] Quoting from Heggs et al. (1982) and Manzoor et al. (1983, 1984), "Suryanarayana has reported that the difference between fin assembly heat-transfer rates predicted by one-dimensional analyses can be as much as 80 percent. It is therefore essential for the effective design of finned heat exchangers to consider the complete fin assembly and to employ a multidimensional analysis." More recently Houghton et al. (1993) have cautioned that the large dimensional variations claimed by Sparrow and Lee (1975) and Suryanarayana (1977) are for unrealistic values of the system parameters. However, the previous conclusions and warnings by Heggs, Manzoor, et al. were left unaddressed.

[5] This point is readily demonstrated by calculating the difference function Δ_{1D} associated with the most severe case studied by Suryanarayana. This calculation indicates Δ_{1D} = 0.012.

Table 2(*a*) Solution results: Heggs et al. (1982) and Manzoor et al. (1981, 1982, 1983, 1984)

Case	Bi_1	Bi_2	k_F/k_w	δ/P	L/P	w/P	Aug
A1	1.0	0.01	1	0.5	10	5.0	5.113
A2	2.25	0.75	1	0.5	10	5.0	1.043
A3	2.25	0.75	10	0.5	10	5.0	1.1375
B1	1.0	0.01	1	0.25	5	1.0	4.274
B2	0.2	0.001	10	0.2	2	0.5	2.963
B3	5.0	0.2	20	0.2	4	2.0	1.900

Table 2(*b*) Corresponding system parameters Bi, h_2/h_1, k_F/k_w, L_c/δ, P/δ, and w/δ

Case	Bi	h_1/h_2	k_F/k_w	P/δ	L_c/δ	w/δ	ψ	α	Δ_{1D} %	E_{1D} %	$E_{(1)}$ %
A1	0.005	100	1	2	21	10	0.06	6.90	0.435	0.9656	0.528
A2	0.375	—	—	—	—	—	—	—	—	—	—
A3	0.0375	3	10	2	21	10	4.08	3.08	0.679	1.38	0.696
B1	0.0025	100	1	4	21	4	0.02	4.66	2.262	1.708	0.542
B2	0.00002	200	10	5	11	2.5	0.0055	3.0	0.209	0.08739	0.121
B3	0.002	25	20	5	21	10	0.44	4.13	8.948	10.686	1.60

of two-dimensional effects on heat transfer in fin assemblies. The first-order two-dimensional formulation reduces to the standard one-dimensional formulation for $Rt = 0$. The general formulation results in an analytical relation that expresses the fin assembly difference function Δ_{1D} in terms of the key system parameters Bi, k_F/k_w, P/δ, L_c/δ, w/δ, and h_1/h_2. A comparison of calculations for Δ_{1D} with numerical calculations for E_{1D} published by Heggs, Manzoor, and associates indicates that the first-order two-dimensional method provides a very good approximation of the actual heat transfer rate for the range of conditions considered in their study.

Calculations based on the first-order two-dimensional method indicate that two-dimensional effects for a fin assembly constructed of a single material ($k_F/k_w = 1$) are normally small to mild (i.e., within one to five percent), such that the standard one-dimensional method is normally sufficiently accurate. However, this study also indicates moderately significant two-dimensional effects for less common operating conditions associated with relatively small values of w/δ and h_1/h_2. Of more practical concern, this study clearly indicates an increase in the significance of two-dimensional effects for bimetal construction, with values of the difference function Δ_{1D} exceeding 40 percent for operating conditions that can be expected to occur in practice. It follows that the potential for significant two-dimensional effects should be taken into account in the design and operation of bimetal fin assemblies. The first-order two-dimensional method presented in this paper provides a practical means of making this determination.

An examination of the solution results for heat transfer in fin assemblies reported by Suryanarayana (1977) indicates that the large differences reported in this early study are not due to two-dimensional effects, but are a consequence of the fact that the fin root/prime surface temperature is not well approximated by the unfinned surface temperature. Thus, the conclusion put forth in by Heggs, Manzoor, and associates based on their interpretation of the Suryanarayana study that the design of finned heat exchangers requires the use of multidimensional methods is generally not justified.

Acknowledgment

The author is pleased to acknowledge support for this work provided by Kind Fahd University of Petroleum & Minerals.

References

Heggs, P. J., and Stones, P. R., 1980, "The Effects of Dimensions on the Heat Flow Rate through Extended Surfaces," ASME JOURNAL OF HEAT TRANSFER, Vol. 102, pp. 180–182.

Heggs, P. J., and Stones, P. R., 1980, "Improved Design Methods for Finned Tube Heat Exchangers," *Trans. Inst. of Chemical Engineers,* Vol. 58, pp. 147–154.

Heggs, P. J., Ingham, D. B., and Manzoor, M., "The Analysis of Fin Assembly Heat Transfer by a Series Truncation Method," ASME JOURNAL OF HEAT TRANSFER, Vol. 104, pp. 210–212.

Hennecke, D. K., and Sparrow, E. M., 1970, "Temperature Depression at the Base of a Fin," ASME JOURNAL OF HEAT TRANSFER, Series C, Vol. 92, pp. 204–206.

Houghton, J. M., Ingham, D. B., and Heggs, P. J., 1991, "The Boundary Element Method Applied to Oscillatory Heat Transfer in a Fin," *Numerical Meth. Thermal Properties,* Vol. 7, pp. 52–62.

Houghton, J. M., Mobbs, S. D., Ingham, D. B., and Heggs, P. J., 1993, "An Application of the Boundary Element Technique to Periodic Heat Transfer in a Fin Assembly," *Numerical Heat Transfer,* Part A, Vol. 23, pp. 379–398.

Klette, D. E., and McCulloch, J. W., 1972, "The Effect of Thermal Conductivity and Base-Temperature Depression on Fin Effectiveness," ASME JOURNAL OF HEAT TRANSFER, Vol. 94, pp. 333–334.

Manzoor, M., Ingham, D. B., and Heggs, P. J., 1981, "Integral Element Analysis of Fin Assembly Heat Transfer," *Numerical Heat Transfer,* Vol. 4, pp. 285–301.

Manzoor, M., Ingham, D. B., and Heggs, P. J., 1982, "The Two-Dimensional Analysis of Fin Assembly Heat Transfer: A Comparison of Solution Techniques," *Proceedings, 2nd National Conference on Numerical Methods in Heat Transfer,* Hemisphere, Washington, DC.

Manzoor, M., Ingham, D. B., and Heggs, P. J., 1983, "Improved Formulations for the Analysis of Convecting and Radiating Finned Surfaces," *AIAA Journal,* Vol. 21, pp. 120–126.

Manzoor, M., 1984, *Heat Flow Through Extended Surface Heat Exchangers* (Lecture Notes in Engineering 5), Springer-Verlag, New York.

Shih, C. C., and Westwater, J. W., 1974, "Effect of Geometry and Wall Thickness on Heat Transfer From Longitudinal Fins to Boiling Liquids," Paper B1.4, *Fifth International Heat Transfer Conference,* Tokyo.

Sparrow, E. M., and Lee, L., 1975, "Effects of Fin Base-Temperature Depression in a Multifin Array," ASME JOURNAL OF HEAT TRANSFER, Vol. 97, pp. 463–465.

Stones, P. R., 1980, Ph.D. thesis, Leeds University, England.

Suryanarayana, N. V., 1977, "Two-Dimensional Effects on Heat Transfer from an Array of Straight Fins," ASME JOURNAL OF HEAT TRANSFER, Vol. 99, pp. 129–132.

Evaporative Heat Transfer and Enhancement Performance of Serpentine Tubes With Strip-Type Inserts Using Refrigerant-134a

S.-S. Hsieh,[1,3] K.-J. Jang,[2,3] and M.-T. Huang[2,3]

Nomenclature

A = nominal flow area

[1] Sun Yat-Sen Professor of Mechanical Engineering, Dean of Engineering. Fellow ASME.

[2] Graduate Student.

[3] Department of Mechanical Engineering, National Sun Yat-Sen University, Kaohsiung, Taiwan 80424, R.O.C.

Contributed by the Heat Transfer Division for publication in the JOURNAL OF HEAT TRANSFER. Manuscript received by the Heat Transfer Division, July 7, 1998; revision received, Jan. 25, 1999. Keywords: Boiling, Enhancement, Heat Transfer, Refrigeration. Associate Technical Editor: B. T. F. Chung.

Table 2(*a*) Solution results: Heggs et al. (1982) and Manzoor et al. (1981, 1982, 1983, 1984)

Case	Bi_1	Bi_2	k_F/k_w	δ/P	L/P	w/P	Aug
A1	1.0	0.01	1	0.5	10	5.0	5.113
A2	2.25	0.75	1	0.5	10	5.0	1.043
A3	2.25	0.75	10	0.5	10	5.0	1.1375
B1	1.0	0.01	1	0.25	5	1.0	4.274
B2	0.2	0.001	10	0.2	2	0.5	2.963
B3	5.0	0.2	20	0.2	4	2.0	1.900

Table 2(*b*) Corresponding system parameters Bi, h_2/h_1, k_F/k_w, L_c/δ, P/δ, and w/δ

Case	Bi	h_1/h_2	k_F/k_w	P/δ	L_c/δ	w/δ	ψ	α	Δ_{1D} %	E_{1D} %	$E_{(1)}$ %
A1	0.005	100	1	2	21	10	0.06	6.90	0.435	0.9656	0.528
A2	0.375	—	—	—	—	—	—	—	—	—	—
A3	0.0375	3	10	2	21	10	4.08	3.08	0.679	1.38	0.696
B1	0.0025	100	1	4	21	4	0.02	4.66	2.262	1.708	0.542
B2	0.00002	200	10	5	11	2.5	0.0055	3.0	0.209	0.08739	0.121
B3	0.002	25	20	5	21	10	0.44	4.13	8.948	10.686	1.60

of two-dimensional effects on heat transfer in fin assemblies. The first-order two-dimensional formulation reduces to the standard one-dimensional formulation for $Rt = 0$. The general formulation results in an analytical relation that expresses the fin assembly difference function Δ_{1D} in terms of the key system parameters Bi, k_F/k_w, P/δ, L_c/δ, w/δ, and h_1/h_2. A comparison of calculations for Δ_{1D} with numerical calculations for E_{1D} published by Heggs, Manzoor, and associates indicates that the first-order two-dimensional method provides a very good approximation of the actual heat transfer rate for the range of conditions considered in their study.

Calculations based on the first-order two-dimensional method indicate that two-dimensional effects for a fin assembly constructed of a single material ($k_F/k_w = 1$) are normally small to mild (i.e., within one to five percent), such that the standard one-dimensional method is normally sufficiently accurate. However, this study also indicates moderately significant two-dimensional effects for less common operating conditions associated with relatively small values of w/δ and h_1/h_2. Of more practical concern, this study clearly indicates an increase in the significance of two-dimensional effects for bimetal construction, with values of the difference function Δ_{1D} exceeding 40 percent for operating conditions that can be expected to occur in practice. It follows that the potential for significant two-dimensional effects should be taken into account in the design and operation of bimetal fin assemblies. The first-order two-dimensional method presented in this paper provides a practical means of making this determination.

An examination of the solution results for heat transfer in fin assemblies reported by Suryanarayana (1977) indicates that the large differences reported in this early study are not due to two-dimensional effects, but are a consequence of the fact that the fin root/prime surface temperature is not well approximated by the unfinned surface temperature. Thus, the conclusion put forth in by Heggs, Manzoor, and associates based on their interpretation of the Suryanarayana study that the design of finned heat exchangers requires the use of multidimensional methods is generally not justified.

Acknowledgment

The author is pleased to acknowledge support for this work provided by Kind Fahd University of Petroleum & Minerals.

References

Heggs, P. J., and Stones, P. R., 1980, "The Effects of Dimensions on the Heat Flow Rate through Extended Surfaces," ASME JOURNAL OF HEAT TRANSFER, Vol. 102, pp. 180–182.

Heggs, P. J., and Stones, P. R., 1980, "Improved Design Methods for Finned Tube Heat Exchangers," *Trans. Inst. of Chemical Engineers,* Vol. 58, pp. 147–154.

Heggs, P. J., Ingham, D. B., and Manzoor, M., "The Analysis of Fin Assembly Heat Transfer by a Series Truncation Method," ASME JOURNAL OF HEAT TRANSFER, Vol. 104, pp. 210–212.

Hennecke, D. K., and Sparrow, E. M., 1970, "Temperature Depression at the Base of a Fin," ASME JOURNAL OF HEAT TRANSFER, Series C, Vol. 92, pp. 204–206.

Houghton, J. M., Ingham, D. B., and Heggs, P. J., 1991, "The Boundary Element Method Applied to Oscillatory Heat Transfer in a Fin," *Numerical Meth. Thermal Properties,* Vol. 7, pp. 52–62.

Houghton, J. M., Mobbs, S. D., Ingham, D. B., and Heggs, P. J., 1993, "An Application of the Boundary Element Technique to Periodic Heat Transfer in a Fin Assembly," *Numerical Heat Transfer,* Part A, Vol. 23, pp. 379–398.

Klette, D. E., and McCulloch, J. W., 1972, "The Effect of Thermal Conductivity and Base-Temperature Depression on Fin Effectiveness," ASME JOURNAL OF HEAT TRANSFER, Vol. 94, pp. 333–334.

Manzoor, M., Ingham, D. B., and Heggs, P. J., 1981, "Integral Element Analysis of Fin Assembly Heat Transfer," *Numerical Heat Transfer,* Vol. 4, pp. 285–301.

Manzoor, M., Ingham, D. B., and Heggs, P. J., 1982, "The Two-Dimensional Analysis of Fin Assembly Heat Transfer: A Comparison of Solution Techniques," *Proceedings, 2nd National Conference on Numerical Methods in Heat Transfer,* Hemisphere, Washington, DC.

Manzoor, M., Ingham, D. B., and Heggs, P. J., 1983, "Improved Formulations for the Analysis of Convecting and Radiating Finned Surfaces," *AIAA Journal,* Vol. 21, pp. 120–126.

Manzoor, M., 1984, *Heat Flow Through Extended Surface Heat Exchangers* (Lecture Notes in Engineering 5), Springer-Verlag, New York.

Shih, C. C., and Westwater, J. W., 1974, "Effect of Geometry and Wall Thickness on Heat Transfer From Longitudinal Fins to Boiling Liquids," Paper B1.4, *Fifth International Heat Transfer Conference,* Tokyo.

Sparrow, E. M., and Lee, L., 1975, "Effects of Fin Base-Temperature Depression in a Multifin Array," ASME JOURNAL OF HEAT TRANSFER, Vol. 97, pp. 463–465.

Stones, P. R., 1980, Ph.D. thesis, Leeds University, England.

Suryanarayana, N. V., 1977, "Two-Dimensional Effects on Heat Transfer from an Array of Straight Fins," ASME JOURNAL OF HEAT TRANSFER, Vol. 99, pp. 129–132.

Evaporative Heat Transfer and Enhancement Performance of Serpentine Tubes With Strip-Type Inserts Using Refrigerant-134a

S.-S. Hsieh,[1,3] K.-J. Jang,[2,3] and M.-T. Huang[2,3]

Nomenclature

A = nominal flow area

[1] Sun Yat-Sen Professor of Mechanical Engineering, Dean of Engineering. Fellow ASME.

[2] Graduate Student.

[3] Department of Mechanical Engineering, National Sun Yat-Sen University, Kaohsiung, Taiwan 80424, R.O.C.

Contributed by the Heat Transfer Division for publication in the JOURNAL OF HEAT TRANSFER. Manuscript received by the Heat Transfer Division, July 7, 1998; revision received, Jan. 25, 1999. Keywords: Boiling, Enhancement, Heat Transfer, Refrigeration. Associate Technical Editor: B. T. F. Chung.

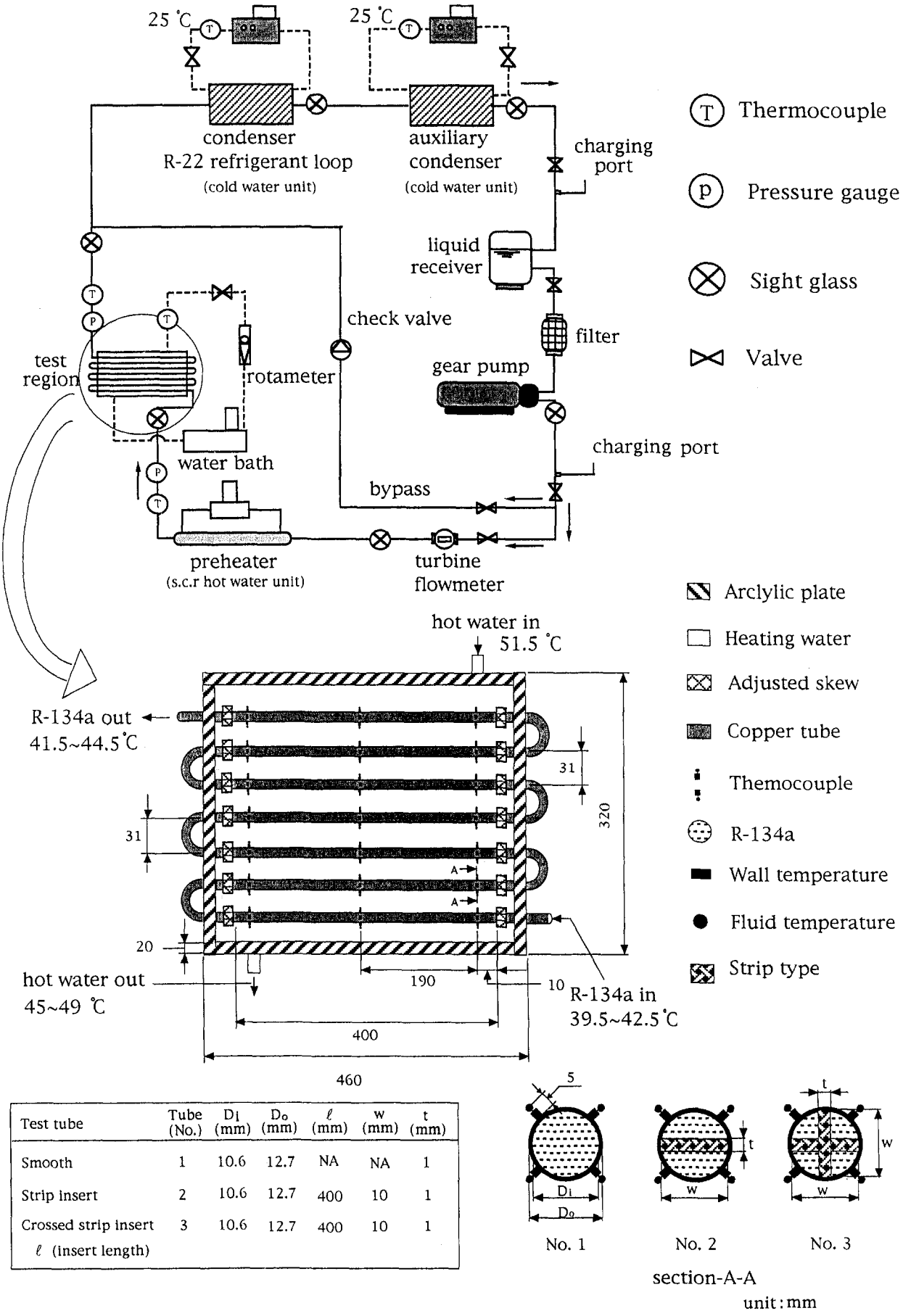

Test tube	Tube (No.)	Di (mm)	Do (mm)	ℓ (mm)	w (mm)	t (mm)
Smooth	1	10.6	12.7	NA	NA	1
Strip insert	2	10.6	12.7	400	10	1
Crossed strip insert	3	10.6	12.7	400	10	1

ℓ (insert length)

Fig. 1 Schematic of test apparatus and experimental setup (only for R-134a loop; R-22 refrigerant loop not included)

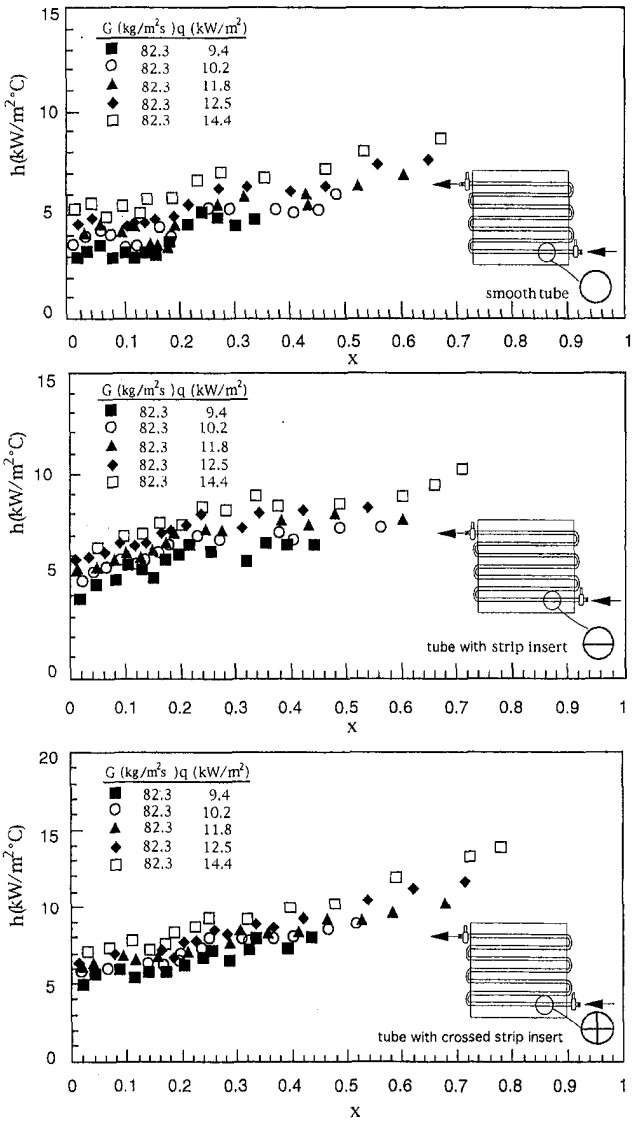

Fig. 2 *h* versus *x* for different tubes and heat flux levels at the same *G*

c_p = refrigerant constant pressure specific heat
D = tube diameter
G = mass velocity (flux) based on nominal flow area
h = local heat transfer coefficient (tube side)
i_{fg} = latent heat of evaporation
L = tube length
k = thermal conductivity of the refrigerant
Nu = Nusselt number, $\bar{h}D_h/k$
P = saturated pressure
Q_{net} = net heat input
T_{in} = refrigerant inlet temperature
T'_{sat} = saturation temperature at start of bulk boiling
T_{wz} = local wall temperature
T_z = local bulk fluid temperature
ΔT = temperature difference
x = local mass quality at downstream distance z
z = distance along the test tube
Δ = gradient/or difference
θ = enhancement performance ratio, $(\overline{h_a}/\overline{h_s})/(\Delta P_a/\Delta P_s)$
ρ = density
σ = surface tension

Subscripts

a = enhanced tube
H = heated
h = hydraulic
i = inside
l = liquid
o = outside
s = smooth tube
sub = subcooled
v = vapor
$\bar{}$ = averaged

1 Introduction

Recent technological implications have given rise to increased interest in enhancement of the in-tube evaporation used in many air conditioning and refrigeration systems. Various techniques have been used to improve heat transfer characteristics of in-tube flow. Several experimental studies have investigated evaporation of standard refrigerants inside internally finned tubes (see, for example, Bergles et al., 1983). Tubes with spiral fins had slightly better performance. Kubanek and Miletti (1979) conducted three finned tube tests with R-22 heated with water at high pressure. Ito and Kimura (1979) studied the heat transfer and pressure drop of R-22 in an internally finned horizontal tube. The fins were triangular. A later study by Kimura and Ito (1979) used the same apparatus to study heat transfer in 4.75-mm i.d. tubes at low flow rates. The best heat transfer performance in annular flow was obtained with tubes having 15-deg spiral fins.

Other surfaces, for instance rib-type surfaces which provide for more nucleation sites, are potentially more attractive as far as the boiling heat transfer is concerned. While the mouth of the cavity between two consecutive ribs determines the superheat required to nucleate, the internal shape and volume, together with the wetting characteristics of the cavity walls, determine the stability of the nucleating cavity. The concept of this type of roughened surface is known in France as the "Vapotron" (Franc et al., 1964) and is used to cool electronic power tubes dissipating heavy heat loads. Recently, Wen and Hsieh (1994) experimentally studied the evaporation heat transfer and enhancement effect of rib-roughened annuli with R-114. Heat transfer and pressure drop measurements were performed on three rib-type roughened tube annuli with two-phase flow of refrigerant R-114 under the evaporating condition.

Although many past studies have examined in-tube evaporative heat transfer enhancement and the associated pressure drop with internally finned tubes, in-tube evaporations with strip-type inserts, using R-134a as a refrigerant, have not been conducted. In addition, the fundamental phenomenon of nucleate boiling from a

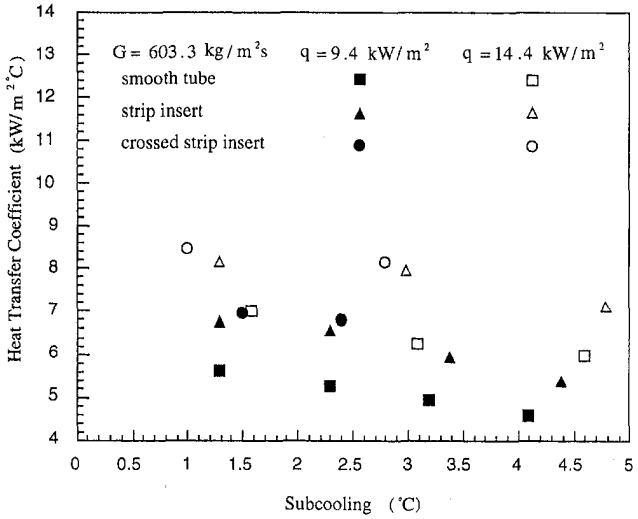

Fig. 3 Effect of subcooling on boiling on the present tubes under study

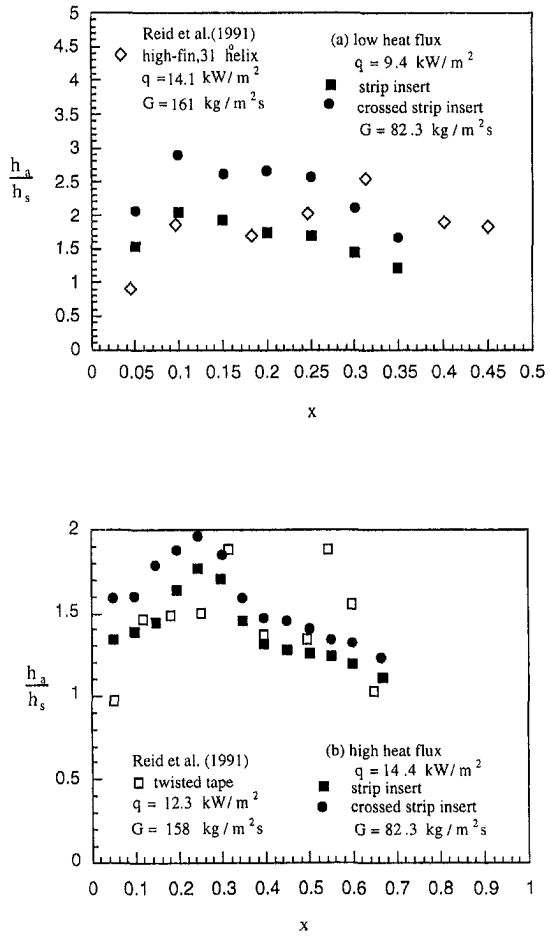

Fig. 4 Local heat transfer enhancement factor for tubes with inserts at q = 9.4 kW/m² and q = 14.4 kW/m²

heated wall subject to a strip-type insert is as yet not well understood, especially for the flow in serpentine tubes. In this study, flow boiling tests were conducted in serpentine coil with inserts. To accomplish these tasks, experiments were performed in a seven-pass serpentine test tube with longitudinal strip and cross-strip types inserts, 10.6-mm inside diameter with R-134a as the boiling fluid immersed in a hot water bath.

2 Experimental Apparatus and Instrumentation

The heat transfer test apparatus is shown schematically in Fig. 1. The apparatus consists of a closed-loop system that includes a gear pump with a variable speed drive, a rotameter, a set of condensers, a preheater, a turbine flowmeter, receiver, water bath and a sight-glass. The liquid receiver allows for stable control of system pressure. The size of the turbine flowmeter was chosen to a certain range of flow rates, from below 82.3 to over 603.3 kg/m² s and carefully calibrated by a stopwatch-and-bucket method to ensure that the experimental uncertainty was within ±0.5 percent of the reading.

The test section is also shown schematically in Fig. 1 and consists of a seven-pass serpentine flow channel. The flow channel consists of a copper tube (386 W/mK) with a total heated length of 2800 mm, and outside and inside diameters of 12.7 mm and 10.6 mm, respectively. Heating of the tubes is accomplished by pumping hot demineralized water into a water bath at a temperature of 51.5°C. The preheater heated R-134a to a subcooled condition (ΔT_{sub} = 1.0–4.8°C). As R-134a flowed through the test section, it was approximately uniformly circumferentially heated by the hot water bath and this was justified by using the Wilson plot technique. Moreover, thermal equilibrium of the vapor and liquid phases was assumed along the entire length of the tube.

The bulk temperatures of the liquid at the inlet and exit to the test section was measured with two in-stream, copper-constantan sheathed thermocouple probes positioned at midstream along the axis of the tubes. Intermediate inside-wall temperatures were obtained by measuring outside-wall temperatures at a certain distance (190 mm each from the inlet) along downstream locations (see Fig. 1 for details) with 28-gage Cu-Cn thermocouples through a correction (explained later in this section). The outside-wall temperature were measured by four thermocouples circumferentially spaced (90 deg apart) at these axial downstream locations and an average value was used to calculate the local heat transfer coefficient. The soldering point of the thermocouples to the tube wall was less than 1 mm in diameter. It is estimated that the temperature measurements were accurate to within ±0.2°C.

With knowledge of the input heat flux, inside-wall temperatures, and corresponding bulk temperature, local heat transfer coefficients were calculated based on

$$h = \frac{q}{(T_{wz} - T_z)}. \tag{1}$$

For a given mass velocity, outside-wall temperatures were obtained at 21 axial positions along the length of test tube as illustrated in Fig. 1. Because the temperature difference across the wall of the copper was large, the measured outside-wall temperatures were corrected to give the inside-wall temperature T_{wz} following Hsieh and Hsu (1994). To simplify the present analysis, q was found from the following equation:

$$q = \frac{Q_{net}}{\pi D_o L_H} \tag{2}$$

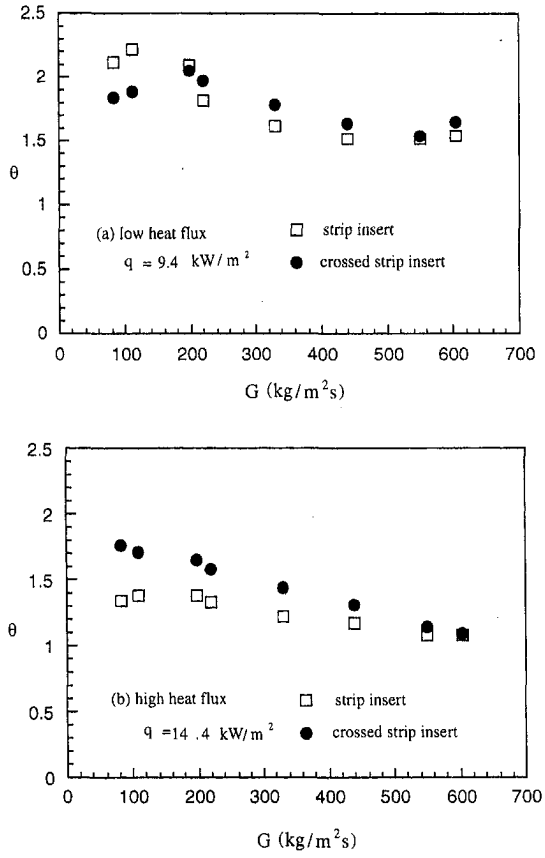

Fig. 5 Enhancement performance ratios versus mass velocity at q = 9.4 kW/m² and q = 14.4 kW/m²

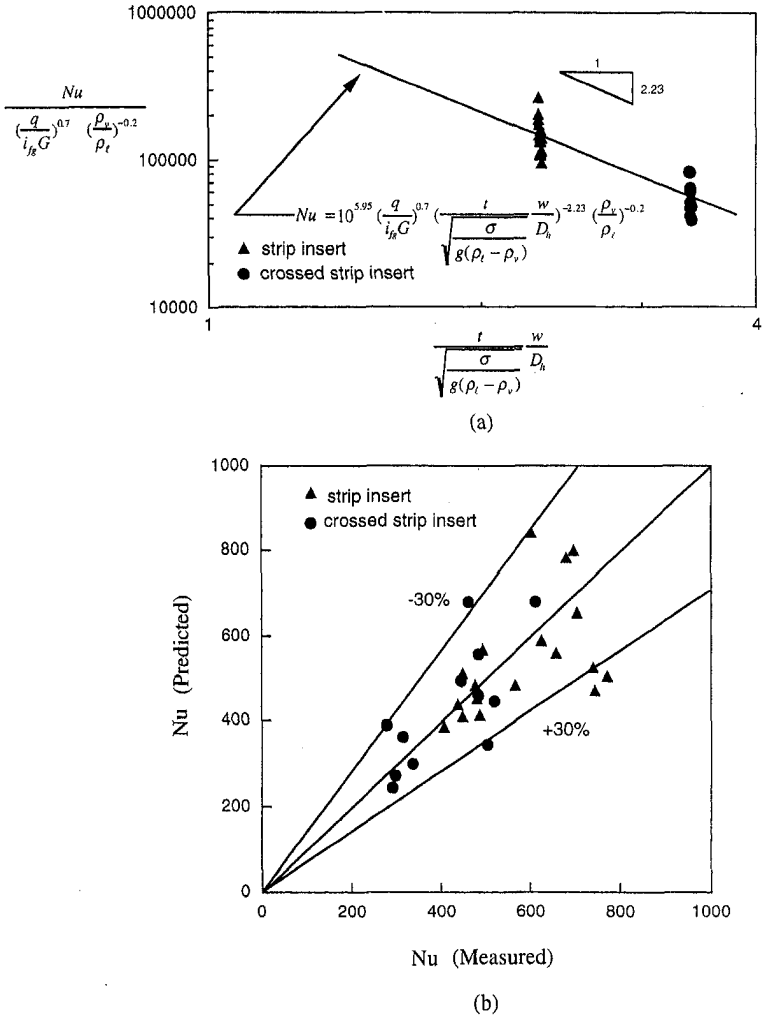

Fig. 6 (*a*) A correlation of flow boiling heat transfer performance for inserted tubes; (*b*) comparison between the predicted Nusselt numbers using the present correlation and the experimental values

where Q_{net} was obtained from the hot water. The local mass qualities x at measurement locations z were calculated from energy balance based on q as follows:

$$x = \frac{\pi D_i (z - L_{sc}) q}{AGi_{fg}} \tag{3}$$

where L_{sc} was determined by iteration from the following equation:

$$L_{sc} = \frac{GAc_p(T'_{sat} - T_{in})}{\pi D i_{fg}} \tag{4}$$

and a single-phase liquid pressure drop calculation for P at T'_{sat}. The saturation pressure at the exit was calculated from the bulk fluid temperature measured there. Linear interpolation was used to determine the fluid saturation pressure and, consequently, the corresponding bulk fluid temperature was thus obtained.

An uncertainty analysis was made to consider the error caused by the interpolation procedure of the measuring instruments. The estimated uncertainties in G, Q, x, $\bar{P}$, T_w, h, and θ are ± 1.26, ± 1.1, ± 6.4, ± 3.5, ± 0.2, ± 16.5, and ± 14.7 percent, respectively.

3 Results and Discussion

The heat transfer coefficient did increase with increasing mass flux at a fixed local mass quality but to a lesser degree than was observed for the smooth tube as evidenced from Fig. 2. On the other hand, in spite of the independence of heat flux on h in the forced convection vaporization region, the local h depends strongly on the mass flux and the quality as shown in Fig. 2. Heat transfer coefficients are more dependent on heat flux in regions of lower quality ($x < 0.5$), which represents a nucleate boiling region, as compared to a higher quality, which represents a forced convection vaporization region. However, this situation becomes less noted for the tubes with inserts. This indicates that an earlier onset of forced convection vaporization can occur with the inserted tubes. For each heat flux except $q = 14.4$ kW/m^2, the heat transfer coefficients dip (however, not found in the inserted tubes) at a certain quality ($0.1 \leq x \leq 0.2$) and then increase approximately linear with quality with a slow increase rate especially for the smooth tubes. This is because a part of the formed vapor bubbles in the core condense again and the liquid is thereby set into oscillatory motion, which leads to an increase in the heat transfer with the quality. This finding is similar to that of Reid et al. (1991). Among three tubes, the tube with the crossed strip insert has the highest heat transfer coefficients at $0 \leq x \leq 0.78$.

According to the present data, the performance of enhanced boiling arrangements (tube with inserts) would also decrease with subcooling. However, the performance of the tubes with inserts will diminish less because these tubes are thought to improve the resistance of trapped vapor nuclei to subcooling and have been

proven to have lower nucleation superheats once saturation conditions have been restored. This can be seen in Fig. 3. Furthermore, the evaporation process inside the enhancement will be isolated from the subcooled bulk liquid because increasing liquid will be preheated as it passes through the narrow passage ways due to the present inserts. On the other hand, for smooth surfaces, the boiling heat transfer coefficient would drop off rapidly with increasing subcooling. For instance, the heat transfer coefficient (h) from 5.6 drops to 4.2 kW/m^2°C as does the degree of subcooling from 1.3°C to 4.1°C for a smooth tube.

Of particular interest for studies of heat transfer enhancement is the question of how much the heat transfer coefficient is increased relative to an equivalent smooth tube at similar conditions. Local enhancement factors (h_a/h_s) were thus calculated by forming ratios of experimentally measured heat transfer coefficients for the inserted tube and a smooth tube of the same operating and geometry conditions. As shown in Fig. 4, with comparisons made for the relevant enhanced geometries included, the trend of enhancement factors for the two inserted tubes is similar. However, the factor seems to have a higher value at lower heat flux than that at high heat flux. In addition, the enhancement factors are more dependent on heat flux by comparing Figs. 4(a) and 4(b) in regions of lower quality. For instance, at a higher heat flux (Fig. 4(b)) enhancement factors in the low-quality region are approximately 1.6 for a crossed strip insert and 1.3 for a strip insert. As quality increases above 0.3, a level that corresponds to a forced-convection vaporization region, enhancement factors for both tubes decrease to a value of 1.2 or so. On the other hand, at a lower heat flux (Fig. 4(a)), enhancement factors in the low-quality region are about 2 for a crossed strip insert and 1.5 for a strip insert. As quality increases above 0.1, enhancement factors for both tubes decreased but did not reach a definite value, indicating an absence of a forced convection vaporization. This plot also demonstrates the effect of heat flux on enhancement factors and shows that the enhancement factors decreased as heat flux increased for both tubes.

Pressure gradient ratios, though not shown here, for both inserted tubes that correspond to the average heat transfer coefficients along the tube, were used to combine the heat transfer coefficient into one parameter termed the average enhancement performance ratio (θ), which is shown in Fig. 5. In Fig. 5(a), tubes with strip inserts have a higher θ (1.8–2) in $100 \leq G \leq 200$ kg/m^2 s. The value initially exhibited a slight rise to a peak and, then, it will be merged to a constant value ($\cong$1.5) as G increased to 600 kg/m^2 s for both inserted tubes. However, at high heat flux, this situation was changed as shown in Fig. 5(b) in which tubes with crossed strip inserts have a higher θ. The results shown in Figs. 5(a) and (b) suggest that the pressure drop in strip and crossed-strip type inserts is strongly dependent on heat flux in subcooled flow boiling. The distribution for both inserted tubes was followed by a monotonically decreasing curve and, finally, it again reached to a constant value ($\approx$1). At low heat flux (Fig. 5(a)), θ is dependent on G while at high flux (Fig. 5(b)), θ is most likely independent of G. This again suggests that at low heat flux the present study is in a nucleate boiling region for both inserted tubes while at high heat flux it is in a forced convection vaporization region.

Figure 6(a) indicates a correlation of the heat transfer coefficient versus a geometric parameter for all the inserted tubes under study. The correlation was derived by using standard procedures, and the dimensionless group ($q/i_{fg}G$), known as the boiling number, and ρ_v/ρ_l, will be familiar from other published boiling correlations. Although the range of ρ_v/ρ_l of the present study was limited, its effect is well known and is, therefore, included for completeness. The third dimensionless group $(t/\sqrt{\sigma/g(\rho_l - \rho_v)})(W/D_h)$ represents all the dimensions necessary to illustrate the present insert geometry configuration. In addition, it includes a term that is proportional to the bubble departure diameter and incorporates surface tension and buoyant forces, which are dominant in a hydrodynamic situation. Figure 6(b) showed the performance plot for the correlation of Fig. 6(a). The correlation predicts 85 percent of points within ±20 percent. Although there was considerable scatter in the data, the prediction still seems good and useful.

References

Bergles, A. E., Nirmalan, V., Junkhan, F. H., and Webb, R. I., 1983, "Bibliography on Augmentation of Convective and Mass Transfer-H," Heat Transfer Laboratory Report HFL-31, ISU-ERI-Ames-84221, Iowa State University, Ames, IA.

Franc, L., Brochner, J. B., Domenjond, H. P., and Morin, R., 1964, "Improvements Made to the Thermal Transfer of Fuel Elements by Using Vapotron Process," Paper A CONF 28/p/96 Presented at the 3rd International Conference on Peaceful Uses of Atomic Energy.

Hsieh, S. S., and Hsu, P. T., 1994, "Nucleate Boiling Characteristics of R-114, Distilled Water (H_2O) and R-134a on Plain and Rib-Roughened Tube Geometries," *Int'J. Heat Mass Transfer,* Vol. 37, pp. 1423–1432.

Ito, M., and Kimura, H., 1979, "Boiling Heat Transfer and Pressure Drop in Internal Spiral-Grooved Tubes," *Bull. Jap. Soc. Mech. Engrs.,* Vol. 22, No. 171, pp. 1251–1257.

Kimura, H., and Ito, M., 1979, "Evaporating Heat Transfer in Horizontal Internal Spiral-Grooved Tubes in the Region of Low Flow Rates," *Bull. Jap. Soc. Mech. Engs,* Vol. 24, No. 195, pp. 1602–1607.

Kubanek, G. R., and Miletti, D. L., 1979, "Evaporative Heat Transfer and Pressure Drop Performance of Internally Finned Tubes with Refrigerant 22," ASME JOURNAL OF HEAT TRANSFER, Vol. 101, pp. 447–452.

Reid, R. S., Pate, M. B., and Bergles, A. E., 1991, "A Comparison of Augmentation Techniques During in-Tube Evaporation of R-114," ASME JOURNAL OF HEAT TRANSFER, Vol. 113, pp. 451–458.

Wambsganss, M. W., France, D. M., Jendrzejczyk, J. A., and Tran, T. N., 1993, "Boiling Heat Transfer in a Horizontal Small-Diameter Tube," ASME JOURNAL OF HEAT TRANSFER, Vol. 115, p. 963.

Wen, M.-Y., and Hsieh, S. S., 1994, "Evaporative Heat Transfer and Enhancement Performance of Rib-Roughned Tube Annuil with Refrigerant 114," *Int' J. Heat Mass Transfer,* Vol. 37, pp. 425–436.

Effect of Buoyancy, Susceptor Motion, and Conjugate Transport in Chemical Vapor Deposition Systems

W. K. S. Chiu[1] and Y. Jaluria[2]

The fluid flow and heat transfer in the chemical vapor deposition (CVD) manufacturing process are studied numerically. Several crucial aspects such as thermal buoyancy, continuous processing, and conjugate transport are considered. For each aspect, the predicted heat transfer rate and the susceptor temperature are computed and qualitatively linked with the rate and uniformity of film deposition. It is shown that buoyancy effects in helium carrier gas commonly used in diffusion-limited CVD has a negligible effect on deposition rates. Susceptor motion is shown as a feasible alternative to improving the productivity. Conjugate heat transfer effects that arise demonstrate that reactor wall thickness and material may be judiciously chosen to improve temperature uniformity and enhance heat transfer rates, thereby improving deposition rate, film uniformity, and quality.

Nomenclature

Gr = Grashof number ($=g\beta\Delta TH^3/\nu_f^2$)

[1] Department of Mechanical and Aerospace Engineering, Rutgers University, New Brunswick, NJ 08903.

[2] To whom correspondence should be addressed. Department of Mechanical and Aerospace Engineering, Rutgers University, 98 Brett Road, Piscataway, NJ 08854-8058. e-mail: jaluria@jove.rutgers.edu. Mem. ASME.

Contributed by the Heat Transfer Division for publication in the JOURNAL OF HEAT TRANSFER and presented at the '97 NHTC, Baltimore. Manuscript received by the Heat Transfer Division, Apr. 6, 1998; revision received, Feb. 12, 1999. Keywords: Conjugate, Heat Transfer, Manufacturing, Materials, Mixed Convection, Thin Films. Associate Technical Editor: R. Mahajan.

proven to have lower nucleation superheats once saturation conditions have been restored. This can be seen in Fig. 3. Furthermore, the evaporation process inside the enhancement will be isolated from the subcooled bulk liquid because increasing liquid will be preheated as it passes through the narrow passage ways due to the present inserts. On the other hand, for smooth surfaces, the boiling heat transfer coefficient would drop off rapidly with increasing subcooling. For instance, the heat transfer coefficient (h) from 5.6 drops to 4.2 kW/m^2°C as does the degree of subcooling from 1.3°C to 4.1°C for a smooth tube.

Of particular interest for studies of heat transfer enhancement is the question of how much the heat transfer coefficient is increased relative to an equivalent smooth tube at similar conditions. Local enhancement factors (h_a/h_s) were thus calculated by forming ratios of experimentally measured heat transfer coefficients for the inserted tube and a smooth tube of the same operating and geometry conditions. As shown in Fig. 4, with comparisons made for the relevant enhanced geometries included, the trend of enhancement factors for the two inserted tubes is similar. However, the factor seems to have a higher value at lower heat flux than that at high heat flux. In addition, the enhancement factors are more dependent on heat flux by comparing Figs. 4(a) and 4(b) in regions of lower quality. For instance, at a higher heat flux (Fig. 4(b)) enhancement factors in the low-quality region are approximately 1.6 for a crossed strip insert and 1.3 for a strip insert. As quality increases above 0.3, a level that corresponds to a forced-convection vaporization region, enhancement factors for both tubes decrease to a value of 1.2 or so. On the other hand, at a lower heat flux (Fig. 4(a)), enhancement factors in the low-quality region are about 2 for a crossed strip insert and 1.5 for a strip insert. As quality increases above 0.1, enhancement factors for both tubes decreased but did not reach a definite value, indicating an absence of a forced convection vaporization. This plot also demonstrates the effect of heat flux on enhancement factors and shows that the enhancement factors decreased as heat flux increased for both tubes.

Pressure gradient ratios, though not shown here, for both inserted tubes that correspond to the average heat transfer coefficients along the tube, were used to combine the heat transfer coefficient into one parameter termed the average enhancement performance ratio (θ), which is shown in Fig. 5. In Fig. 5(a), tubes with strip inserts have a higher θ (1.8–2) in $100 \leq G \leq 200$ kg/m^2 s. The value initially exhibited a slight rise to a peak and, then, it will be merged to a constant value ($\cong$1.5) as G increased to 600 kg/m^2 s for both inserted tubes. However, at high heat flux, this situation was changed as shown in Fig. 5(b) in which tubes with crossed strip inserts have a higher θ. The results shown in Figs. 5(a) and (b) suggest that the pressure drop in strip and crossed-strip type inserts is strongly dependent on heat flux in subcooled flow boiling. The distribution for both inserted tubes was followed by a monotonically decreasing curve and, finally, it again reached to a constant value ($\approx$1). At low heat flux (Fig. 5(a)), θ is dependent on G while at high flux (Fig. 5(b)), θ is most likely independent of G. This again suggests that at low heat flux the present study is in a nucleate boiling region for both inserted tubes while at high heat flux it is in a forced convection vaporization region.

Figure 6(a) indicates a correlation of the heat transfer coefficient versus a geometric parameter for all the inserted tubes under study. The correlation was derived by using standard procedures, and the dimensionless group ($q/i_{fg}G$), known as the boiling number, and ρ_v/ρ_l, will be familiar from other published boiling correlations. Although the range of ρ_v/ρ_l of the present study was limited, its effect is well known and is, therefore, included for completeness. The third dimensionless group $(t/\sqrt{\sigma/g(\rho_l - \rho_v)})(W/D_h)$ represents all the dimensions necessary to illustrate the present insert geometry configuration. In addition, it includes a term that is proportional to the bubble departure diameter and incorporates surface tension and buoyant forces, which are dominant in a hydrodynamic situation. Figure 6(b) showed the performance plot for the correlation of Fig. 6(a). The correlation predicts 85 percent of points within ±20 percent. Although there was considerable scatter in the data, the prediction still seems good and useful.

References

Bergles, A. E., Nirmalan, V., Junkhan, F. H., and Webb, R. I., 1983, "Bibliography on Augmentation of Convective and Mass Transfer-H," Heat Transfer Laboratory Report HFL-31, ISU-ERI-Ames-84221, Iowa State University, Ames, IA.

Franc, L., Brochner, J. B., Domenjond, H. P., and Morin, R., 1964, "Improvements Made to the Thermal Transfer of Fuel Elements by Using Vapotron Process," Paper A CONF 28/p/96 Presented at the 3rd International Conference on Peaceful Uses of Atomic Energy.

Hsieh, S. S., and Hsu, P. T., 1994, "Nucleate Boiling Characteristics of R-114, Distilled Water (H_2O) and R-134a on Plain and Rib-Roughened Tube Geometries," *Int'J. Heat Mass Transfer,* Vol. 37, pp. 1423–1432.

Ito, M., and Kimura, H., 1979, "Boiling Heat Transfer and Pressure Drop in Internal Spiral-Grooved Tubes," *Bull. Jap. Soc. Mech. Engrs.,* Vol. 22, No. 171, pp. 1251–1257.

Kimura, H., and Ito, M., 1979, "Evaporating Heat Transfer in Horizontal Internal Spiral-Grooved Tubes in the Region of Low Flow Rates," *Bull. Jap. Soc. Mech. Engs,* Vol. 24, No. 195, pp. 1602–1607.

Kubanek, G. R., and Miletti, D. L., 1979, "Evaporative Heat Transfer and Pressure Drop Performance of Internally Finned Tubes with Refrigerant 22," ASME JOURNAL OF HEAT TRANSFER, Vol. 101, pp. 447–452.

Reid, R. S., Pate, M. B., and Bergles, A. E., 1991, "A Comparison of Augmentation Techniques During in-Tube Evaporation of R-114," ASME JOURNAL OF HEAT TRANSFER, Vol. 113, pp. 451–458.

Wambsganss, M. W., France, D. M., Jendrzejczyk, J. A., and Tran, T. N., 1993, "Boiling Heat Transfer in a Horizontal Small-Diameter Tube," ASME JOURNAL OF HEAT TRANSFER, Vol. 115, p. 963.

Wen, M.-Y., and Hsieh, S. S., 1994, "Evaporative Heat Transfer and Enhancement Performance of Rib-Roughned Tube Annuil with Refrigerant 114," *Int' J. Heat Mass Transfer,* Vol. 37, pp. 425–436.

Effect of Buoyancy, Susceptor Motion, and Conjugate Transport in Chemical Vapor Deposition Systems

W. K. S. Chiu[1] and Y. Jaluria[2]

The fluid flow and heat transfer in the chemical vapor deposition (CVD) manufacturing process are studied numerically. Several crucial aspects such as thermal buoyancy, continuous processing, and conjugate transport are considered. For each aspect, the predicted heat transfer rate and the susceptor temperature are computed and qualitatively linked with the rate and uniformity of film deposition. It is shown that buoyancy effects in helium carrier gas commonly used in diffusion-limited CVD has a negligible effect on deposition rates. Susceptor motion is shown as a feasible alternative to improving the productivity. Conjugate heat transfer effects that arise demonstrate that reactor wall thickness and material may be judiciously chosen to improve temperature uniformity and enhance heat transfer rates, thereby improving deposition rate, film uniformity, and quality.

Nomenclature

Gr = Grashof number ($=g\beta\Delta TH^3/\nu_f^2$)

[1] Department of Mechanical and Aerospace Engineering, Rutgers University, New Brunswick, NJ 08903.

[2] To whom correspondence should be addressed. Department of Mechanical and Aerospace Engineering, Rutgers University, 98 Brett Road, Piscataway, NJ 08854-8058. e-mail: jaluria@jove.rutgers.edu. Mem. ASME.

Contributed by the Heat Transfer Division for publication in the JOURNAL OF HEAT TRANSFER and presented at the '97 NHTC, Baltimore. Manuscript received by the Heat Transfer Division, Apr. 6, 1998; revision received, Feb. 12, 1999. Keywords: Conjugate, Heat Transfer, Manufacturing, Materials, Mixed Convection, Thin Films. Associate Technical Editor: R. Mahajan.

Gr/Re^2 = mixed convection parameter ($=g\beta\Delta TH/(U_\infty^*)^2$)
H = channel height
K = thermal conductivity ratio ($=k_s/k_f$)
k = thermal conductivity
Nu_x = local Nusselt number ($=hH/k_f$)
Pr = Prandtl number ($=\nu_f/\alpha_f$)
q_{ref} = reference heat flux used for dimensional scaling
Re = Reynolds number ($=U_\infty^* H/\nu_f$)
T_{ref} = reference temperature ($=q_{ref}H/k_f$)
ΔT = temperature difference ($=T_{sus} - T_\infty$)
α = thermal diffusivity ($=k/\rho c_p$)
β = coefficient of thermal expansion ($=-(1/\rho)(\partial\rho/\partial T)|_p$)
γ = susceptor tilt angle, with positive direction measured counterclockwise from horizontal
ν = kinematic viscosity
θ = dimensionless temperature ($=(T-T_\infty)/T_{ref}$)

Subscripts

f = fluid
insul = insulation
s = solid
sus = susceptor

Introduction

The use of chemical vapor deposition (CVD) to produce thin films represents an important and widely used manufacturing process in high technology applications. Thin films are deposited from a gas phase onto a solid substrate by means of chemical reactions at the deposition surface. The film thickness may range from a few nanometers to several millimeters. The quality of film deposition is judged by its purity, composition, thickness, adhesion, crystalline structure, and surface morphology. The level of desired quality depends largely on its application, with electronic and optical materials processing presenting the most stringent demands. Future trends in the semiconductor industry indicate the migration from 200-mm wafer CVD reactors to large diameter wafer (300 to 675 mm) systems (Semiconductor Industry Association, 1997). Market requirements for large wafer production with stringent deposition uniformity and high throughput requirements impose a formidable challenge for researchers. To improve deposition quality, one must understand the mechanisms governing access of film precursors to the substrate. Review papers by Jensen et al. (1991) and Mahajan (1996) provide a detailed overview of research on the CVD process to date.

It is seen from a review of the existing literature that, despite the growing importance of this materials processing technique, many basic and applied aspects remain to be investigated in detail. Among the most important considerations that need a detailed study include the effects of thermal buoyancy, susceptor motion for continuous processing, and conjugate heat transfer on the film quality and deposition rate. Buoyancy-induced flow in different reactor geometries and orientations have been shown to affect film quality, rate, and uniformity. A moving susceptor extends current CVD technology into a continuous processing technique, thereby enhancing productivity. Conjugate heat transfer raises significant issues in CVD reactor modeling and design. All three aspects have received little attention in CVD literature. The present work addresses these issues by initially tackling the fluid mechanics and heat transfer problem. This study is applicable to diffusion-limited CVD processes, where deposition rates may be approximated by the heat and mass transfer analogy. Details of this work are reported elsewhere (Chiu and Jaluria, 1997).

Numerical Model

Consider flow through a two-dimensional channel representing a horizontal CVD reactor. The full elliptic governing equations are solved using a finite volume method. The governing equations with constant properties under steady-state conditions are formulated for continuity, momentum, and energy conservation. Thermal buoyancy effects are modeled using the Boussinesq approximations (Gebhart et al., 1988). A conjugate heat transfer model couples conduction heat transfer in the solid region to convection heat transfer in the fluid region. Details of the formulation are given by Chiu and Jaluria (1997).

The boundary conditions for u, v, p, and θ arise from physical considerations of the problem. The flow entering the reactor is prescribed as the analytical parabolic profile $U = 6(y - y^2)$ from Panton (1984), while no-slip and impermeable assumptions are applied at the upper and lower boundaries. Flow exiting the reactor is assumed to become fully developed, thus the first gradient in the down-channel direction is set equal to zero. The top wall is prescribed at the ambient temperature (T_∞) because upper walls are often water cooled to preserve unreacted precursors for deposition on the substrate. The bottom boundary consists of three regions of finite thickness H_{sus}. The entrance and exit regions, defined as the insulation (K_{insul}), are stationary and insulated. In between the two regions, the susceptor K_{sus} moves at a uniform velocity U_{sus}^* and is heated electrically or by radiation, as approximated by an uniform heat source ($\partial\theta/\partial y = -1$). Since the reactor medium is composed mostly of an inert carrier gas, radiative heat transfer only occurs at the reactor walls. The current study calculates convective and conductive heat fluxes only; radiative heat fluxes may be calculated using a net radiative enclosure model.

Iterative convergence is ensured by comparing intermediate fluid and thermal fields, and by verifying mass and energy conservation to better than one percent and when two consecutive comparisons differ by less than 10^{-6}. Similarly, other parameters like grid size, initial guess, relaxation factor, outflow boundary conditions, and channel length are varied until their influence on the solution becomes negligible. Code validation with analytical solutions for developed fluid and thermal fields in a channel have a discrepancy of less than one percent. Experimental results from a developing thermal field with buoyancy (Kamotani and Ostrach, 1976) compared well with numerical solutions (Fig. 1), with less than ten percent deviation.

Results and Discussion

Results will be presented for a horizontal CVD reactor consisting of a 7 cm high channel, helium carrier gas entering under atmospheric pressure at an ambient temperature of $T_\infty = 300$ K, and deposition occurring at 400 K $\le T_{sus} \le$ 1300 K. Material properties are calculated at 0.5 ($T_{sus} + T_\infty$). Using a convective heat flux of 0.8 kW/m^2 $\le q_{ref} \le$ 8.7 kW/m^2 to reach the desired operating temperature and $\Delta T = (T_{sus} - T_\infty)$, parameters for the system are calculated as $Gr/Re^2 = 10$ and 50 and Re = 10 and 50. The influence of buoyancy effects on deposition rate and uniformity are studied, followed by a discussion on the feasibility of a moving susceptor in a converging horizontal reactor. Results will conclude with an analysis of conjugate parameters (K_{sus}, K_{insul}, H_{sus}) on temperature and heat transfer rate (Nu_x) at the susceptor surface. The susceptor temperature variation is related to film uniformity, while Nu_x provides qualitative deposition rates for a diffusion-controlled process.

Buoyancy Effects. The effect of buoyancy for a horizontal reactor is shown in Figs. 2(*a*) and (*b*) in terms of in the mixed convection parameter (Gr/Re^2). Figure 2(*a*) shows that the inclusion of buoyancy causes fluid entrainment near the susceptor leading edge, while fluid at the trailing edge attempts to settle back into a fully developed flow. As Gr/Re^2 increases from 0 to 50, flow disturbances become increasingly pronounced. If Gr/Re^2 is increased further, the onset of turbulence and secondary flow characteristics are expected to appear. Such phenomena are three dimensional in nature (Ouazzani et al., 1988), and are not considered in this study. Minimal susceptor temperature deviation is observed (Fig. 2(*b*)), indicating a weak buoyancy effect on temperature uniformity and consequently film uniformity. It was observed that a tilt angle of $\gamma = -6$ deg dampens out buoyancy

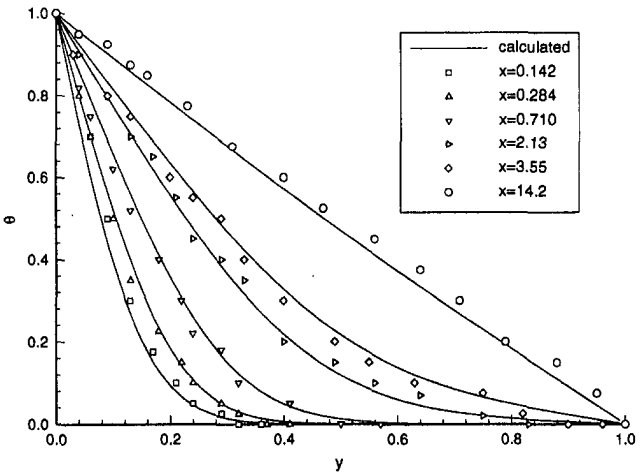

Fig. 1 Developing temperature profiles at Re = 50, Pr = 0.71, and Gr = 1000 in a horizontal parallel plate channel. Notation used: (—) calculated, (symbols) from Kamotani and Ostrach (1976).

forces by constricting flow across the converging region, resulting in larger local Re and hence a decrease in local Gr/Re^2.

Deposition rates for diffusion-limited CVD processes can often be qualitatively predicted by the heat transfer rate at the susceptor surface, namely, Nu_{avg}. From the cases studied, it was observed that fluid velocity (U_∞^*) and buoyancy have the strongest influence on Nu_{avg}. This dependence is illustrated by correlating Nu_{avg} in terms of Re and Gr/Re^2. The following correlation with susceptor heating by constant heat flux is obtained as

$$Nu_{avg} = 1.74\ Re^{0.25} \left(\frac{Gr}{Re^2}\right)^{0.01}. \quad (1)$$

The correlation coefficient r^2 is obtained as 0.943, indicating a good fit for Eq. (1). This correlation shows heat transfer having a relatively weak dependence on buoyancy, and the flow rate is dominating heat and mass transfer in this system. Therefore, buoyancy effects are small for parameters considered in this study.

Moving Susceptor. A moving susceptor is of considerable importance since it allows for continuous deposition, resulting in high production rates and low costs. This practice is currently used in different applications such as heat treatment and material extrusion, but the technique has received little attention for CVD reactors. There is obviously a significant gain in using a continuous CVD process, but one must first understand the resulting process, its effect on film quality, and proceed to evaluate the feasibility of such a continuous CVD process. This section will study the effects of a moving susceptor on fluid flow, heat transfer, and film deposition. The susceptor motion considered here is defined as either aiding (positive U_{sus}), where the susceptor moves with the flow, or opposing (negative U_{sus}), where the susceptor moves against the flow. Since carrier gases typically flow with small velocities (U_∞ small), deposition feasibility demands that U_{sus} be relatively small.

The flow field is solved for various values of the susceptor velocity (U_{sus}). The governing parameters are chosen as Re = 10, Pr = 0.71, and $\gamma = -6$ deg to represent a CVD reactor with dilute reactants, low flow rate, and helium as the carrier gas with previously shown negligible buoyancy effects ($Gr/Re^2 = 0$), depositing silicon. Aiding ($U_{sus} = 0.2$), stationary ($U_{sus} = 0.0$), and opposing ($U_{sus} = -0.2$) susceptor motion cases of a tilted susceptor are specified to simulate a continuous deposition horizontal reactor system. Results in the form of streamlines are plotted in Figs. 3(*a*) and (*b*). For opposing susceptor motion, streamlines show a recirculating region just above the susceptor surface. Such a phenomenon is expected to modify deposition homogeneity and deposition rate by isolating precursor availability near the reacting susceptor surface. Recirculation cells can also significantly alter deposition characteristics by modifying reactive gas flow within a reactor. The flow characteristics for aiding susceptor movement reveal fluid entrainment into a region near the susceptor leading edge. This can enhance deposition by drawing extra precursors into the reactive region. However, excessive fluid motion can also alter deposition, causing nonuniform layers of deposited material.

Figures 3(*c*) and (*d*) show the influence of aiding and opposing susceptor motion on temperature and heat transfer rate across a moving susceptor. Because aiding susceptor motion enhances convective heat transfer by reducing the thermal boundary layer thickness, positive U_{sus} will result in a cooler susceptor surface. An opposing susceptor has a countereffect due to an increasing thermal boundary layer. Although temperature differences for finite U_{sus} are apparent, moving susceptors with small U_{sus} do not significantly alter the temperature field. The local Nusselt number (Nu_x) for different susceptor velocities (Fig. 3(*d*)) show that peaks appear at the leading and trailing edges due to the presence of cooler fluid near the edges, allowing for greater heat removal at these locations. Aiding susceptor motion (positive U_{sus}) provides greater heat transfer due to cooler fluid entraining in the flow over the susceptor surface. Opposing susceptor motion (negative U_{sus}) recirculates warmer fluid upstream, causing a decrease in heat transfer. Results indicate that susceptor motion can be applied to the

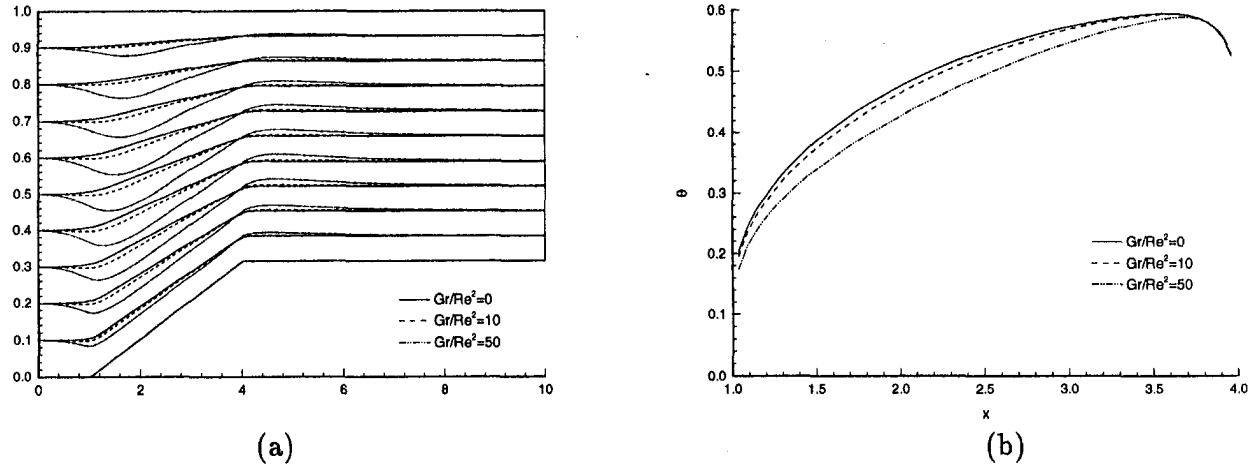

Fig. 2 (*a*) Buoyancy-induced streamlines and (*b*) susceptor surface temperature distributions for a horizontal reactor. The tilted susceptor is stationary and heated by uniform heat flux, at Re = 10, Pr = 0.71, and $\gamma = -6$ deg.

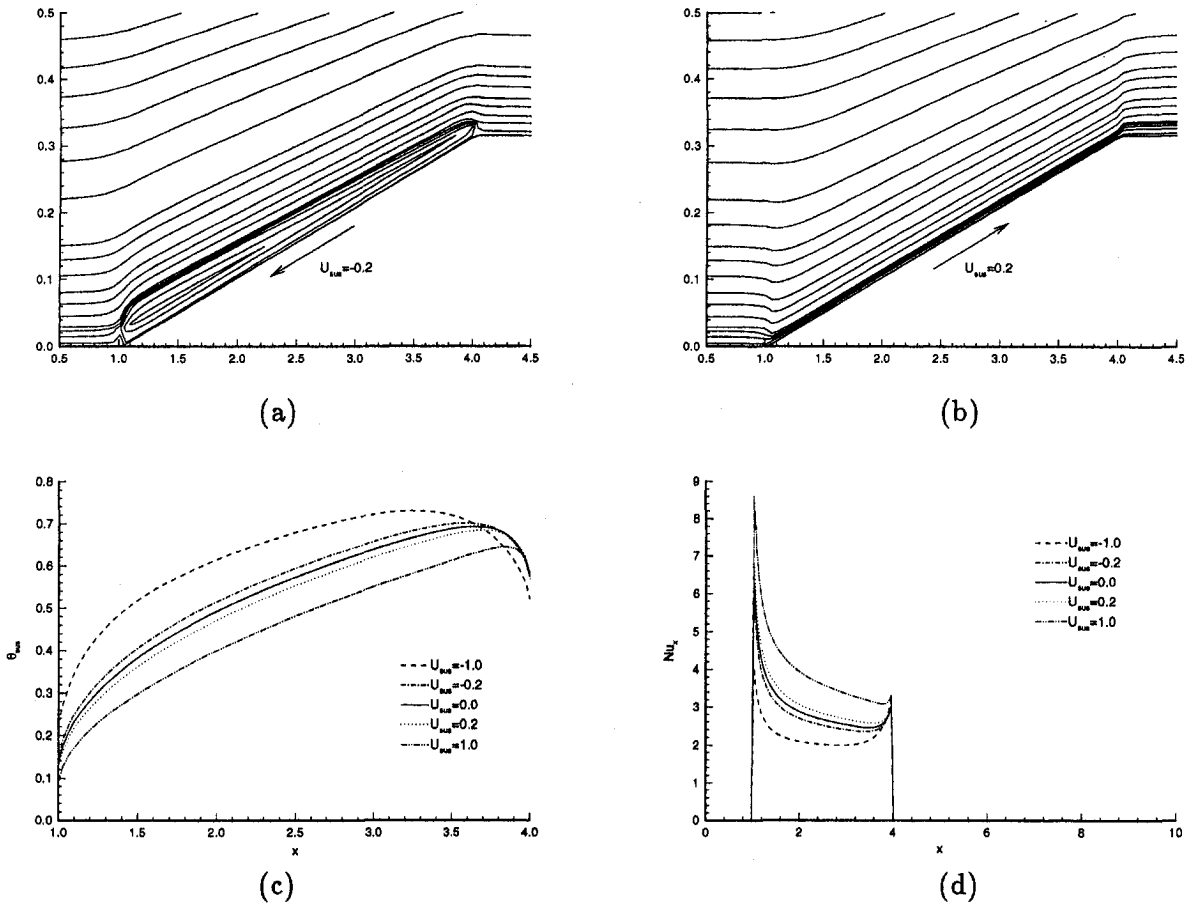

Fig. 3 Streamlines for (*a*) opposing ($U_{sus} = -0.2$) and (*b*) aiding ($U_{sus} = 0.2$) susceptor motion, (*c*) susceptor surface temperature, and (*d*) Nusselt number distributions for $\gamma = -6$ deg

current reactor geometry with slight changes in heat transfer and temperature distributions. Similar trends are also observed for other susceptor tilt angles and isothermal susceptor heating. Silicon deposition rate predictions on a moving susceptor for similar configurations are discussed by Chiu and Jaluria (1998).

Conjugate Heat Transfer. In the pursuit of high film uniformity, reactor designs require a uniform temperature distribution across the susceptor surface. Typical susceptor heating designs allow for thermal energy conduction loss into the surrounding reactor walls, resulting in a nonuniform temperature distribution at the susceptor surface. Since the deposition rate is strongly dependent on temperature, small temperature deviations will result in nonuniform deposition across the susceptor, especially near the edges. This phenomenon is known as an "edge effect." Although conjugate heat transfer has a significant impact on film quality, this aspect has not been considered in adequate detail in the literature.

Specific K_{sus} and K_{insul} values are chosen to simulate reactor wall materials consisting of He gas gap ($K = 1$), Borosilicate (Pyrex) Glass ($K = 4$), Titanium Dioxide ($K = 15$), and Silicon Dioxide ($K = 44$), as discussed by Pierson (1992). A parametric study of these combi-

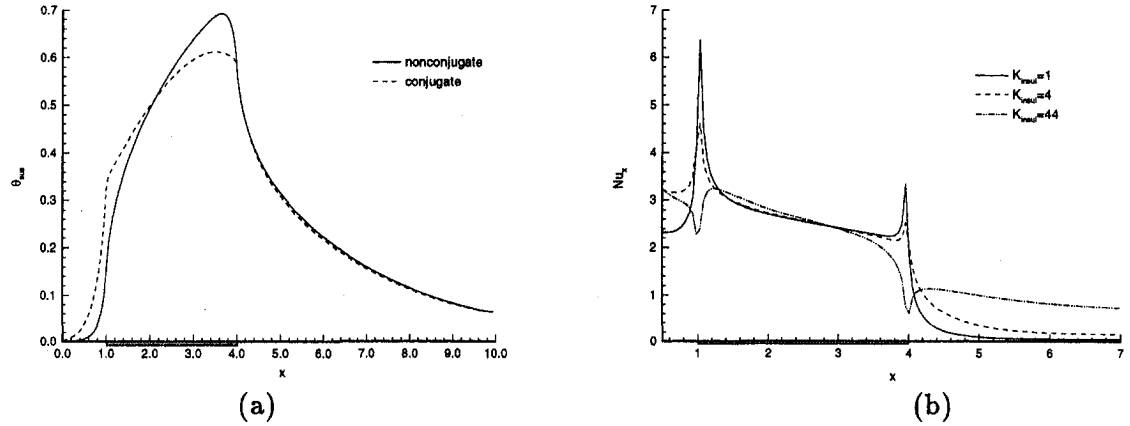

Fig. 4 (*a*) Comparison of susceptor temperature results obtained from conjugate and nonconjugate cases and (*b*) Nusselt number distribution for different insultation materials in a uniform heat flux heated reactor at Re = 10 and $\gamma = 0$ deg

Table 1 Susceptor temperature dependence on conjugate heat transfer effects for flow in a horizontal reactor with Re = 10, Pr = 0.71, Gr = 0, and γ = 0 deg

K_{sus}	K_{insul}	H_{sus}	θ_{sus} Range	Average	Standard deviation	Percent of variation
15	1	0.1	0.32–0.61	0.53	0.08	16%
44	1	0.1	0.42–0.64	0.57	0.06	10%
15	4	0.1	0.29–0.58	0.50	0.09	17%
15	44	0.1	0.19–0.50	0.41	0.09	21%
15	1	0.4	0.40–0.57	0.53	0.05	9%

nations are shown in Fig. 4 using Re = 10, Pr = 0.71, Gr = 0, γ = 0 deg, and U_{sus} = 0.0. Conjugate parameters are K_{sus} = 15, K_{insul} = 1 and H_{sus} = 0.1, unless specified otherwise. Figure 4(*a*) shows a comparison of susceptor surface temperatures for the conjugate and nonconjugate cases. In the nonconjugate case, a prescribed zero thickness wall (H_{sus} = 0) directs thermal energy input directly into the gas phase. When conjugate effects are considered, a redistribution of energy into finite region solid regions results in a warmer surface at the susceptor leading edge, while the susceptor trailing edge drops in temperature. The heat transfer rate at the susceptor surface decreases, with the largest drop occurring at the edges where energy is transferred to the fluid as well as to the insulating regions. These observations emphasize the importance of conjugate heat transfer effects in CVD reactor modeling.

The effect of K_{insul} variation on susceptor interface temperature and rate of heat transfer is shown in Fig. 4(*b*). A large K_{insul} results in a greater amount of energy drawn towards material surrounding the susceptor. Consequently, heat transfer rate over the susceptor surface decreases, with the largest drop occurring at the edges. Interestingly, the case of $K_{insul} > K_{sus}$ reveals two local Nu_x dips near the susceptor edges. Since the K parameter is obtained by scaling with the fluid thermal conductivity (k_f), solid regions with $K > 1$ have larger thermal conductivity than the fluid. If this condition is combined with $K_{insul} > K_{sus}$, most of the energy will travel from the susceptor into the insulating region rather than into the fluid and energy loss at the susceptor edges into the insulation becomes significant. In consequence, susceptor temperature uniformity may be controlled by proper wall material selection. These features may be incorporated in CVD reactors to avoid irregular deposition and reduce edge effects.

Since deposition uniformity is related to susceptor temperature uniformity, Table 1 tabulates θ_{sus} uniformity for different solid material properties and thicknesses. Minimal θ_{sus} variations occur by increasing K_{sus} or decreasing K_{insul}, allowing the system to direct thermal energy towards the susceptor surface. Furthermore, the solid region may be considered as an energy diffuser, acting to redistribute energy more evenly before heat is transfered into the fluid region. This observation is confirmed by the fact that a thicker solid region (H_{sus} = 0.4) has only a nine percent variation, which is significantly lower than other cases.

Conclusions

Heat transfer and fluid flow processes in horizontal CVD reactors have been simulated and used to predict diffusion-limited chemical vapor deposition through the heat and mass transfer analogy. Using this analogy, deposition rate and uniformity can be qualitatively predicted by the susceptor surface temperature and Nusselt number. Correlations indicate buoyancy as a weak effect under the operating conditions considered. A slow-moving susceptor with aiding and opposing motion was found to significantly alter the flow field, but to exhibit weak influence on heat transfer rate and susceptor temperature uniformity, emphasizing the feasibility of continuous processing. A comparison with the nonconjugate problem showed that conjugate effects represent an important factor in reactor design and operation. Further investigation into the use of materials with different size and properties revealed cases where certain material arrangements will lead to large temperature and heat transfer nonuniformities, and material combinations may be selected to enhance deposition quality, rate, and film uniformity.

Acknowledgments

The authors would like to thank the Pittsburgh Supercomputing Center for providing computing facilities under Grant No. CTS960015P.

References

Chiu, W. K. S., and Jaluria, Y., 1997, "Heat Transfer in Horizontal and Vertical CVD Reactors," *Proc. Nat. Heat Transfer Conf.*, ASME HTD-Vol. 347-9, pp. 293–311.

Chiu, W. K. S., and Jaluria, Y., 1998, "Heat and Mass Transfer in Continuous CVD Reactors," *Proc. 11th Int. Heat Transfer Conf.*, Vol. 5, pp. 187–191.

Gebhart, B., Jaluria, Y., Mahajan, R. L., and Sammakia, B., 1988, *Buoyancy-Induced Flows and Transport*, Hemisphere, New York.

Jensen, K. F., Einset, E. O., and Fotiadis, D. I., 1991, "Flow Phenomena in Chemical Vapor Deposition of Thin Films," *Ann. Rev. Fluid Mech.*, Vol. 23, pp. 197–232.

Kamotani, Y., and Ostrach, S., 1976, "Effect of Thermal Instability on Thermally Developing Laminar Channel Flow," ASME JOURNAL OF HEAT TRANSFER, Vol. 98, pp. 62–66.

Mahajan, R. L., 1996, "Transport Phenomena in Chemical Vapor-Deposition Systems," *Advances in Heat Transfer*, Vol. 28, Academic Press, San Diego, CA, pp. 339–425.

Ouazzani, J., Chiu, K. C., and Rosenberger, F., 1988, "On the 2D Modelling of Horizontal CVD Reactors and its Limitations," *J. Crystal Growth*, Vol. 91, pp. 497–508.

Panton, R. L., 1984, *Incompressible Flow*, John Wiley and Sons, Inc., New York.

Pierson, H. O., 1992, *Handbook of Chemical Vapor Deposition (CVD): Principles, Technology, and Applications*, Noyes Publications, Park Ridge, NJ.

The National Technology Roadmap for Semiconductors, 1997, Semiconductor Industry Association, San Jose, CA.